AMERICAN INSTITUTE OF PHYSICS

CONFERENCE PROCEEDINGS NO. 191

OPTICAL SCIENCE AND ENGINEERING SERIES 10

ADVANCES IN LASER SCIENCE-IV

ATLANTA, GA 1988

EDITORS: JAMES L. GOLE, DONALD F. HELLER, MARSHALL LAPP, & WILLIAM C. STWALLEY

CONFERENCE PROCEEDINGS 191

OPTICAL SCIENCE AND ENGINEERING SERIES 10

RITA G. LERNER
SERIES EDITOR

ADVANCES IN LASER SCIENCE–IV

PROCEEDINGS OF THE FOURTH INTERNATIONAL LASER SCIENCE CONFERENCE

ATLANTA, GA 1988

EDITORS:

JAMES L. GOLE, PROGRAM CHAIR
GEORGIA INSTITUTE OF TECHNOLOGY

DONALD F. HELLER, PROGRAM VICE-CHAIR
LIGHT AGE, INC., MT. BETHEL, NEW JERSEY

MARSHALL LAPP, CONFERENCE CHAIR
SANDIA NATIONAL LABORATORIES AND
LAWRENCE LIVERMORE NATIONAL LABORATORIES

WILLIAM C. STWALLEY, ADMINISTRATIVE VICE-CHAIR
UNIVERSITY OF IOWA

AIP
American Institute of Physics New York

Price: $85.00
American Institute of Physics
Per TELECON 1/16/90 CG

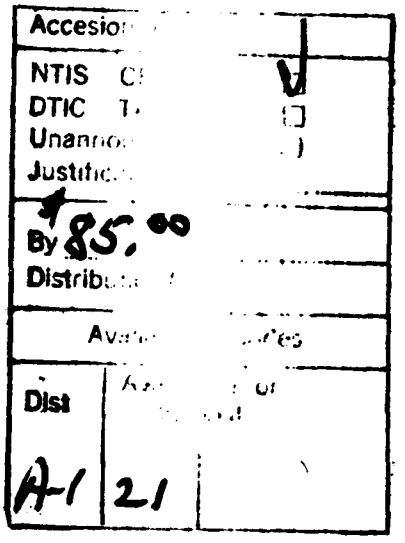

L.C. Catalog Card No. 89-085595
ISBN 0-88318-391-9
DOE CONF 8810399

Printed in the United States of America.

Symposia Contents

Preface xxvii

PANEL—Tunable Solid State Lasers (organized by D. F. Heller, Light Age, Inc., Mt. Bethel, NJ). Participants: R. L. Byer (Stanford University), L. Chase (Lawrence Livermore National Laboratory), R. C. Powell (Oklahoma State University), and J. C. Walling (Light Age, Inc., Mt. Bethel, NJ) 1

I. LASERS AND COHERENT SOURCES

I. A. New Developments in Solid State Sources (organized by C. R. Pollock, Cornell University)

Laser and Spectroscopic Properties of Chromium-Activated Fosterite (*invited*) 33
V. Petčević, S. K. Gayen, and R. R. Alfano

Laser Diode Pumped 1μ Nd:YAG and Nd:BEL Lasers 39
R. Scheps, P. Poirier, J. F. Myers, and D. F. Heller

Laser Performance and Tuning Characteristics of a Diode Pumped Nd:$YAlO_3$ Laser at 1083 nm 42
L. D. Schearer and P. Tin

Tunable CW Laser Action of Er^{3+} in Double Sensitized Fluoroaluminate Glass at Room Temperature 45
E. Heumann, M. Ledig, D. Ehrt, W. Seeber, E. W. Duczynski, H. J. v. d. Heide, and G. Huber

A Comparative Study of Nd:YLF and Nd:YAG Crystals for Solar-Pumped Laser Application 50
K. H. Kim and J. H. Lee

Parametric Conversion and Index of Refraction Measurements in Hydrothermally Grown in $KTiOPO_4$ 54
H. Vanherzeele, J. D. Bierlein, and F. C. Zumsteg

I. B. Novel Laser Systems—Modifications to Visible, Ultraviolet, and X-Ray Lasers (organized by R. A. Sauerbrey, Rice University)

Two-Laser Approach to X-Ray Lasers (*invited*) 57
W. Tighe, L. Meixler, C. H. Nam, and S. Suckewer

Superfluorescent Chemically Driven Visible Laser Transitions Using Fast Near Resonant Energy Transfer 63
J. R. Woodward, S. H. Cobb, and J. L. Gole

Continuous Chemical Laser Amplifiers in the Visible Region 68
S. H. Cobb, J. R. Woodward, and J. L. Gole

Ionic Alkali Halide Excimers Excited by a Laser-Produced Plasma 74
S. Kubodera, P. J. Wisoff, and R. Sauerbrey

An LNA Laser for Helium Experiments 77
T. Chuang and H. Metcalf
The Uniform Magnetic Field Free-Electron Laser with Higher Harmonic Emission 80
J. Soln
A One-Hertz Hypocycloidal Pinch Plasma Pump Source for Ultraviolet Dye Lasers 82
D. D. Venable, S. M. Lee, J. H. Lee, and K. S. Han
One Megawatt Blue–Green Laser by High Temperature Plasma Arrays 85
K. S. Han, K. Nam, and J. H. Lee
Increase of Dye Laser Energy by an Energy Converter Dye 88
C. H. Oh and U. C. Suh
Pulsed Laser Oscillation in Na_2 $B\,^1\Pi_u \rightarrow X\,^2\Sigma_g^+$ Pumped by the Dye Laser 91
Q. Wang, Z. W. Lu, T. Wu, Y. K. Cheng, and Z. G. Ma
Narrow Band, High Power Light from Diode Lasers 94
S.-Q. Shang and H. Metcalf

I. C. Spectroscopy of Materials for Solid State Laser Systems
(organized by R. C. Powell, Oklahoma State University)

Nd-Doped Tunable IR Lasers for Helium Optical Pumping (*invited*) 97
L. D. Schearer
Reduction of Tetravalent Chromium Induced Optical Loss in Nd:Cr:GSGG 103
A. J. Pertica, J. E. Marion, and S. E. Stokowski
Radiation Damage in KBr:Eu^{2+} and KCl:Eu^{2+} due to 350 nm Laser Irradiation 106
L. D. Merkle and P. K. Bandyopadhyay
Cr^{3+} to Nd^{3+} Energy Transfer in Substituted GGG in Relation to the Crystal Field Distribution 109
A. Monteil, C. Garapon, and G. Boulon

I. D. Modeling of Lasers and Laser Dynamics
(organized by A. M. Buoncristiani, NASA Langley Research Center)

Amplified Spontaneous Emission and Pulse Train Amplification in a KrF Amplifier (*invited*) 112
J. R. Ackerhalt, D. E. Hanson, R. G. Adams, T. D. Raymond, C. Reiser, J. K. Rice, and R. B. Michie
Modeling the Energy Deposition in the Aurora KrF Laser Amplifier Chain 119
J. C. Comly, S. J. Czuchlewski, D. P. Greene, D. E. Hanson, B. J. Krohn, and A. W. McCown
A Mathematical Model of the Dynamics of Titanium Doped Sapphire Lasers 125
L. F. Roberts, J. J. Swetits, and A. M. Buoncristiani
Non-Markovian Jump Processes in Lasers 128
A. M. Levine, A. G. Kofman, R. Zaibel, and Y. Prior

Quantum Initiation Effects on the Asymptotic Coherent On-Resonance Propagation of Two Different-Wavelength Probe and Pump Beams in a Three-Level System 131
F. P. Mattar, Y. Claude, and M. Burgess

Diffraction and Phase Effects on the Evolution of Raman Solitons 137
F. P. Mattar, Y. Claude, M. Burgess, and J. Teichmann

Diffraction, Phase and Quantum Fluctuation Effects in the Evolution of Raman Solitons 164
F. P. Mattar, Y. Claude, M. Burgess, and J. Teichmann

Cross-Phase Modulation and Cross-Focusing Effects in Optical Fibers 198
R. Du and F. P. Mattar

II. NONLINEAR OPTICAL PHENOMENA AND APPLICATIONS

II. A. Squeezed States and Quantum Optics
(organized by H. Pilloff, Office of Naval Research)

Prospects for Practical Use of Squeezed Light and Back Action Evasion (*invited*) 207
M. D. Levenson and R. M. Shelby

Quantum Nondemolition Detection of Optical Quadrature Amplitudes (*invited*) 210
R. M. Shelby

Photon Statistics of Multimode Squeezed Light 216
J. M. Huang and P. Kumar

Forward Hyper-Transient Stimulated Raman Scattering Including Laser Pump Depletion 219
F. P. Mattar, C. M. Burgess, Y. Claude, and J. Teichmann

Transverse Effects in Transient Stimulated Raman Scattering in Pump Laser Depletion 241
J. Teichmann, Y. Claude, M. Burgess, and F. P. Mattar

Quantum and Nonlinear Theory of Stimulated Raman Scattering (SRS) 249
F. P. Mattar, Y. Claude, M. Burgess, and J. Teichmann

Nonlinear Gaussian Expansions of Stochastic Processess: Non-Gaussian Effects in Coherent Anti-Stokes Raman Spectroscopy 262
A. M. F. Lau and R. L. Farrow

Second Stokes Generation in Deuterium 265
M. D. Duncan, R. Mahon, L. L. Tankersley, and J. Reintjes

II. B. Nonlinear Optical Phenomena in Atomic Vapors
(organized by C. R. Stroud, Jr., University of Rochester)

Influence of A. C. Stark Effect on Stimulated Hyper-Raman Profiles in Sodium Vapor 268
M. A. Moore, W. R. Garrett, and M. G. Payne

Attosecond Beats in Sodium Vapor 271
D. DeBeer, E. Usadi, and S. R. Hartmann

Suppression of Two-Photon Resonantly Enhanced Nonlinear Processes in Extended Media 273
W. R. Garrett, M. A. Moore, M. G. Payne, and R. K. Wunderlich

Experimental Studies of Self-Suppression of Vacuum Ultraviolet Generation in Xe 276
J. P. Judish, S. L. Allman, W. R. Garrett, and M. G. Payne

New Coherent Cancellation Effect Involving Four-Photon Excitation and the Related Ionization 279
M. G. Payne, W. R. Garrett, J. P. Judish, and M. P. McCann

Effect of the Coherent Cancellation of the Two-Photon Resonance on the Generation of Vacuum Ultraviolet Light by Two-Photon Resonantly Enhanced Four-Wave Mixing 282
M. G. Payne, W. R. Garrett, J. P. Judish, and R. Wunderlich

K $4\,^2S_{1/2} \rightarrow 8\,^2S_{1/2}$ Two-Photon Absorption by Near-Resonant Pumping of $6\,^2P_{1/2,3/2}$ State 285
Y. Z. Sun, X. H. Li, Q. Wang, and Y. K. Cheng

Diode Laser-Initiated, Two-Color Resonance Ionization Mass Spectrometry of Lanthanum 288
R. W. Shaw, J. P. Young, and D. H. Smith

Vacuum Enhanced Atomic Excitation 291
Y. Zhu, A. Lezama, and T. W. Mossberg

Two-Photon Resonant, Stimulated Processes in Krypton and Xenon 294
J. C. Miller

Dynamic Frequency Shift Effects on Coherent Propagation in Two-Level Systems 297
J. Manassah and F. P. Mattar

Self- and Cross-Phase Modulation, Pulse Compression Induced Chirping, Spectral Broadening and Focusing Effects in Co-Propagation Coherent Pulses in Three-Level Atoms 303
F. P. Mattar, J. Delettrez, and J. P. Babuel-Peyrissac

II. C. Nonlinear Optics in Semiconductors
(organized by A. L. Smirl, North Texas State University and R. B. James, Sandia National Laboratories, Livermore)

Saturation of Inter-Subband Transition in *p*-Type Semiconductor Quantum Wells 318
Y.-C. Chang and R. B. James

Optically Saturable Absorbing Centers Versus Deep-Level Traps in Semiconductor Lasers 324
X. Y. Liu and E. Bourkoff

Pulsed Laser Induced Photoconductivity in ZnS: Part II 327
R. D. Singh, A. Gaur, and A. K. Sharma

II. D. Short Pulse Lasers and Applications
(organized by D. F. Heller, Light Age, Inc., Mt. Bethel, NJ)

Intermolecular Vibration Observed in Liquid CS_2 at High Pressure 330
B. Kohler and K. A. Nelson
Femtosecond Time Resolved Absorption Spectroscopy of $Cr(CO)_6$ and $Mn_2(CO)_{10}$: Observation of Elementary Bond Breakage and Formation 333
A. G. Joly and K. A. Nelson
Picosecond Pulse Amplification in a Single Mode Neodymium Doped Fibre 336
A. S. Gouveia-Neto, A. S. B. Sombra, P. G. J. Wigley, and J. R. Taylor
Measurement of UV Femtosecond Light Pulses using Two-Photon Luminescence in CsI Crystals Doped with Na 339
F. Noack, W. Rudolph, R. Deijch, and W. E. Postovalos

III. CONDENSED MATTER, SURFACE, AND PARTICLE SPECTROSCOPY WITH EMPHASIS ON LASER–SURFACE INTERACTIONS
(organized by A. C. Tam, IBM Almaden Research Center)

III. A. Laser-Condensed Matter Interactions → next
(organized by E. E. Marinero, IBM Almaden Research Center)

Surface-Plasmons Enhanced Nonequilibrium Electronic and Lattice Heating in Thin Silver Films 345
T. Tsang and D. D. Smith
Transient Grating Probe of Recombination Dynamics in Cadmium Sulfide Colloids 348
L. V. Natarajan and J. R. Morgan
Time Resolved Measurements of Inelastic Scattering Processes from Micron Sized Droplets 351
A. Biswas, H. Latifi, R. L. Armstrong, and R. G. Pinnick
Two-Photon Induced Chemical Reactions in Liquids 354
C. H. Chen and M. P. McCann
Laser-Induced Reaction and Polymerization of Formaldehyde in Low Temperature Amorphous Solids 357
C. A. Wright, T. W. Tang, and E. S. Mansueto
Nonlinear Absorption in Liquids Studied by Laser-Induced Anharmonic Thermal Gratings 360
X. R. Zhu and J. M. Harris
Adsorption of Oxygen on a Polycrystalline Ag Surface: A Second-Harmonic Generation Study 363
L. Li, Y. H. Liu, G. D. Yu, W. C. Wang, and Z. M. Zhang
Visualization of Photogenerated Carrier Profiles at a Silicon Surface 366
K. Wan, R. Normandin, and P. Van der Meer
Optical Computing with Thin Films 369
R. Cuykendall and K. H. Strobl

III. B. Applications of Laser/Surface Interactions

Laser Induced Refractive Index Change in Polymers 375
D. S. Dunn and A. J. Ouderkirk
Photochemistry of $Ga(CH_3)_3$ at a Low Temperature Surface 379
E. Villa, J. A. Dagata, and M. C. Lin

III. C. Laser Modification of Surfaces

Excimer Laser-Controlled Photochemical Deposition of Thin Films and Artificially Structured Materials (*invited*) 382
D. H. Lowndes, D. Eres, D. B. Geohegan, J. Z. Tischler, D. N. Mashburn, and S. J. Pennycook
Laser Processed Zirconium: Study of Corrosion and Microstructure 391
W. Reitz and J. Rawers
Investigation of Surface Damage Thresholds by Photoacoustic Deflection 394
S. Petzoldt, A. P. Elg, J. Reif, and E. Matthias
Rotational Energy Accommodation of OH Produced in the Catalytic Reaction of NO_2+H_2 over Pt(111) 397
L. V. Novakoski, D. S. Y. Hsu, and M. C. Lin
ArF Excimer Laser Processing of PECVD and LECVD Silicon Oxynitride Thin Films: Local Changes in DUV Transparency and Composition 400
J. N. Cox, L. Friedrich, L. L. Heath, B. L. Sun, and R. Kolenkow
Laser Ablation/Fourier Transform Mass Spectrometry of Polymers 403
W. R. Creasy and J. T. Brenna

III. D. Surface Nonlinear Optics

Time-Resolved Laser Probes of Surfaces (*invited*) 406
H. W. K. Tom
Optical Second Harmonic Generation in Metal Monolayers and Metal Surfaces .. 412
T. E. Furtak and J. Miragliotta
Reflection at a Nonlinear Interface 415
K. H. Strobl, R. R. Cuykendall, B. Bockhop, and D. Megli

III. E. Laser Ionization, Ablation and Deposition

Studies of the Pulsed Laser Deposition Process for the Preparation of High Temperature Superconducting Films (*invited*) 420
T. Venkatesan, X. D. Wu, A. Inam, B. Dutta, M. S. Hedge, and C. C. Chang
Utilization of 1+1 REMPI as a Probe of Rotational Dynamics in Gas–Surface Scattering 426
D. C. Jacobs, K. W. Kolasinski, and R. N. Zare
Spectral Analysis of Fluorescence of Excited Species from 193 nm Photoablation of Polycarbonate and the High T_c Superconductors $Bi_2CaSr_2Cu_2O_9$ and $YBa_2Cu_3O_{7-d}$ 430
S. Deshmukh, E. W. Rothe, and G. P. Reck

Ion Acceleration in Threshold Level Photoablation of Metals 433
R. Welle and H. Helvajian
Laser Damage Studies of ZnS via Neutral Particle Emission 436
H. F. Arlinghaus, W. F. Calaway, C. E. Young, M. J. Pellin, D. M. Gruen, and L. L. Chase
Platinum Spots on Silicon Deposited by Photon Induced Chemical Vapor Deposition 439
C. Garrido, B. Leon, M. Perez-Amor, D. Braichotte, and H. van den Bergh
Laser Enhanced Selective Epitaxy of III–V Compounds 442
N. H. Karam, H. Liu, I. Yoshida, and S. M. Bedair
Rotational Temperature of SiF_2 Radicals Produced in the Thermal Etching of Silicon by Fluorine Containing Compounds 445
J. S. Horwitz, J. A. Dagata, D. W. Shinn, and M. C. Lin

IV. ATOMIC, MOLECULAR, AND IONIC SPECTROSCOPY

IV. A. Energy Resolved Ionization and Fragmentation Processes in Atoms and Small Molecules

(organized by J. E. Wessel, Aerospace Corporation)

Two-Color Studies of Autoionizing States in Small Molecules (*invited*) 451
S. T. Pratt, M. A. O'Halloran, F. S. Tomkins, J. L. Dehmer, and P. M. Dehmer
Multiphoton Ionization (MPI) of Vibrationally Excited NO ($v''=0$–9) in a Pulsed Molecular Beam 457
C. S. Feigerle and J. C. Miller
Molecular Two-Photon Spectroscopy 460
M. P. McCann, C. H. Chen, and M. G. Payne
Theory of Molecular Transition Moment Determination by Autler–Townes Spectroscopy: $D\,^1\Pi_u$–$E,F\,^1\Sigma_g^+$ Bands of H_2 463
A. M. F. Lau and W. M. Huo
Multiphoton Ionization Photoelectron Spectroscopy of Xenon: Experiment and Theory 466
S. J. Bajic, R. N. Compton, X. Tang, A. L'Huiller, and P. Lambropoulos
Observations of Excited State Photoionization of Xenon 469
J. Lahiri and S. T. Manson
A Spectroscopic Study of the $\tilde{X}\,^4\Sigma_g^-$ ($v=4$–7) Levels of C_2^+ Using the Stimulated Emission Pumping Technique 472
F. G. Celii and J. P. Maier
Two Photon Resonance Enhanced Multiphoton Ionization Detection and Spectroscopy of Gas Phase Germyl (GeH_3) Radicals 475
J. W. Hudgens, R. D. Johnson III, and B. P. Tsai
Raman-Induced Kerr Effect Spectroscopy of Rare Gas Dimers and Molecular Ions 478
R. H. Taylor, J. Borysow, and J. W. Keto
Single-Photon VUV Laser-Induced Fluorescence Spectrum of HCl 481
S. Arepalli, Y.-L. Huang, R. Callaghan, and R. J. Gordon

IV. B. Ionization Processes and Ion Spectroscopy of Polyatomic Species
(organized by J. E. Wessel, Aerospace Corporation)

Resonant Two-Photon Ionization Electronic Spectroscopy of the Silver Trimer 485
P. Y. Cheng and M. A. Duncan

Resonant Enhanced Multiphoton Dissociation Spectroscopy of Molecular Ions: Technique and Applications of CH_3I^+/CD_3I^+ 488
U. Boesl, R. Weinkauf, and K. Walter

Characterization of the Gas Phase Bromocyanogen Cation with Laser-Excited Fluorescence Spectroscopy 494
M. A. Hanratty, M. Roesslein, F. G. Celii, T. Wyttenbach, and J. P. Maier

Spectrum (310 to 360 nm) and Ionization Potential of the Silyl Radical 497
R. D. Johnson III, B. P. Tsai, and J. W. Hudgens

Aromatic Molecular Clusters and Their Predissociation Dynamics Studied by Picosecond Time-Resolved Fluorescence Spectroscopy 500
A. J. Kaziska, S. A. Wittmeyer, M. I. Shchuka, A. L. Motyka, and M. R. Topp

IV. C. Interaction of Strong Optical Fields with Matter
(organized by T. J. McIlrath, University of Maryland)

High-Order Harmonic Generation by Hydrogenic Ions (*invited*) 503
C. W. Clark, L. Pan, and K. T. Taylor

Dynamics of Coupled Single Particle Electron and Collective Nuclear Motion in a Laser Field 509
F. X. Hartmann, D. W. Noid, and Y. Y. Sharon

Self-Focusing of Very Intense CW Laser Beams in Saturable Absorbers 515
J. Teichmann, Y. Claude, M. Burgess, F. P. Mattar, J. P. Babuel-Peyrissac, J. P. Marinier, and C. Bardin

The Moment Theory for Cross-Coupling of Two Intense Fields through a Kerr Medium 529
J. Teichmann and F. P. Mattar

IV. D. Experiments with Laser Cooled and Trapped Atoms
(organized by J. E. Bjorkholm, AT&T Bell Laboratories, Holmdel)

Laser Cooling of Mg and Ca Atomic Beams 533
N. Beverini, E. Maccioni, D. Pereira, F. Strumia, and G. Vissani

IV. E. High Resolution Spectroscopy—From Atoms to Polyatomic Molecules
(organized by W. D. Phillips, NIST and M. C. Heaven, Emory University)

Bound-Continuum Transitions in Diatomic Molecules (*plenary*) 536
W. C. Stwalley

Precise Laser Wavelength Measurements: What Can we Learn from Classical Spectroscopy? (*invited*) 548
C. J. Sansonetti

Measurement of the Rydberg Constant by Doppler-Free Spectroscopy of Atomic Hydrogen 554
M. Allegrini, F. Biraben, B. Cagnac, J. C. Garreau, and L. Julien

State Mixing in Rydberg Atom–Noble Gas Collisions 557
K.-D. Heber, P. J. West, and E. Matthias

Line Shape Variations of Spin-Forbidden Two-Photon Transitions 560
H. R. Xia, J. W. Xu, and I. S. Cheng

High Resolution Resonance-Enhanced Dissociation Spectroscopy of Chlorobenzene Cation Prepared by MPI 563
X. Ripoche, F. Morlet-Savary, I. Dimicoli, F. Piuzzi, J. Le Calve, and R. Botter

The Absolute Vibrational Numbering and Molecular Constants of the Na_2 $2\,^3\Pi_g$ and $1\,^3\Delta_g$ States 569
X. Xie, R. W. Field, L. Li, A. M. Lyyra, J. T. Bahns, and W. C. Stwalley

OODR Fluorescence and Polarization Spectroscopy of K_2: Rydberg States and the $A\,^2\Sigma_u^+$ State (*invited*) 572
A. M. Lyyra, H. Wang, L.Li, W. T. Luh, V. Zafiropulos, and W. C. Stwalley

Na_2 $1\,^3\Sigma_g^+ \rightarrow 1\,^3\Sigma_d^+$ Lasing with Peak around 892.0 nm 578
Q. Wang, Z. W. Lu, W. Liu, T. Wu, D. Xing, and Z. G. Ma

Study of the New 600.0 nm Diffuse Band 581
Y. Z. Sun, X. H. Li, Q. Wang, and Y. K. Cheng

V. STATE-SPECIFIC PHOTOPHYSICS AND PHOTOCHEMISTRY

(organized by D. R. Crosley, SRI International and J. McDonald, Naval Research Laboratory)

Semiquantitative Laser-Induced Fluorescence Flame Measurements (*plenary*) 587
D. R. Crosley

State-Selective Photodissociation Dynamics of NOCl: Scalar and Vector Properties (*invited*) 593
A. Ogai, C. X. W. Qian, L. Iwata, and H. Reiser

Laser Induced Shifts in Chemical Equilibria 599
R. A. Bernheim, C. He, and G. Alzetta

Polarization Studies as a Probe of Photodissociation Dynamics 602
V. Zafiropulos, P. D. Kleiber, K. M. Sando, X. Zeng, A. M. Lyyra, and W. C. Stwalley

Self-Induced Polarization Effects in Gases 607
S. A. Bakhramov, A. T. Berdikulov, A. M. Kokharov, P. K. Khabibullaev, and V. V. Tikhonenko

Vibrational Predissociation Dynamics of Overtone-Excited HN_3 612
B. R. Foy, M. P. Casassa, J. C. Stephenson, and D. S. King

Vibrational and Rotational Energy Transfer in $X\,^2\Pi_i$ OH (*invited*) 615
D. R. Crosley, K. J. Rensberger, and J. B. Jeffries

Energy Transfer Collisions in Laser Excited Mixtures of Alkali Vapors (*invited*) 621
M. Allegrini, S. Gozzini, G. Squadrito, C. Gabbanini, and L. Moi

Photochemical Production of XeCl(B) Initiated by Two-Photon Excitation of Xe and Xe_2 627
M. R. Berman

Alignment Effects in Ca–He ($5\ ^1P_1$–$5\ ^3P_J$) Energy Transfer Half-Collisions 630
K. C. Lin, S. Ananthamurthy, P. D. Kleiber, J. X. Wang, W. C. Stwalley, and S. R. Leone

Spectroscopic Mapping of the OH–Ar Stretching Potential 634
M. T. Berry, M. R. Brustein, and M. I. Lester

Photodissociation Studies of Borane Carbonyl (*invited*) 637
H. H. Nelson

Photodissociation Dynamics of Ferrocene at 193 nm 642
U. Ray, M. Vernon, H.-Q. Ho, and Z. J. Zhang

Laser-Induced Fluorescence in the $B\ ^2\Sigma^+$–$X\ ^2\Pi_i$ System of OH 645
A. D. Sappey, D. R. Crosley, and R. A. Copeland

Photochemistry of Formyl Fluoride 648
B. R. Weiner and R. N. Rosenfeld

Energetics and Spin Selectivity in the Infrared Multiphoton Dissociation $HN_3(\tilde{X}\ ^1A') \rightarrow N_2(X\ ^1\Sigma_g^+) + NH(X\ ^3\Sigma^-, a\ ^1\Delta)$ (*invited*) 651
M. H. Alexander and P. J. Dagdigian

Study of Hydrogen Abstraction Reactions by Negative Ion Photoelectron Spectroscopy (*invited*) 657
S. E. Bradforth, A. Weaver, R. B. Metz, and D. M. Neumark

Double Resonance Studies of Rotational Energy Transfer in the $N_2\ B\ ^2\Pi_g$ State (*invited*) 664
P. J. Dagdigian and A. Ali

Collisional Quenching and Energy Transfer in NS $B\ ^2\Pi$ 670
I. J. Wysong, J. B. Jeffries, and D. R. Crosley

Statistical Spectroscopy: Insight or Nonsense? (*invited*) 673
J.-P. Pique, Y. Q. Chen, D. M. Jonas, J. K. Lundberg, C. E. Hamilton, G. W. Adamson, R. J. Silbey, and R. W. Field

Gas Phase Transition Metal Species: Electronic Structure and Reactivity (*invited*) 683
G. Eiden, S. Hanton, J. Harrington, D. Ritter, L. Sanders, and J. C. Weisshaar

Stability and Oxidation of Metal Based CO and CO_2 Complexes 687
M. J. McQuaid and J. L. Gole

Mode-Selective Intramolecular Vibrational Redistribution (IVR) to the van der Waals' Modes in *trans*-Stilbene van der Waals Complexes 692
T. S. Zwier

Dynamics of NCS Formation from Photolysis of RNCS 695
F. J. Northrup and T. J. Sears

The Resolution and Characterization of Distinct *ortho*- and *para*-D_2 Complexes with *trans*-Stilbene in a Supersonic Jet 698
D. O. DeHaan and T. S. Zwier

Application of Excitation Transfer to Studies of Collisional Deactivation of Vibrationally Excited Isotopically Labelled Nitrous Oxide by Sulfur Hexafluoride 701
M. C. Longuemare, R. Morrison, and R. D. Bates, Jr.

VI. DIAGNOSTIC AND ANALYTICAL APPLICATIONS OF LASERS

(organized by A. W. Miziolek, U. S. Army Ballistic Research Laboratory and D. M. Lubman, University of Michigan)

VI. A. Advances in Raman Spectroscopy

(organized by T. Vo-Dinh, Oak Ridge National Laboratory)

Surface Enhanced Raman Spectroscopy of Neurotransmitters (*invited*) **707**
M. L. McGlashen, K. L. Davis, and M. D. Morris

Observation of the SRS Spectrum of Secondary Vibrational Fundamental Frequency ν_2 in CH_4 ..... **713**
Y. Z. Wang, Q. Wang, D. Y. Lin, Y. K. Cheng, and Z. G. Ma

VI. B. Lasers and Chromatography

(organized by T. G. Nolan, Oak Ridge National Laboratory)

Novel Approaches in Detector Instrumentation for Process Liquid Chromatography (*invited*) **716**
R. E. Synovec

ArF Laser-Generated Microplasmas for Chemical Analysis **722**
J. B. Morris, A. W. Miziolek, R. C. Sausa, and B. E. Forch

VI. C. Advances in Photothermal Spectroscopy

(organized by M. D. Morris, University of Michigan)

Hadamard Transform Techniques in Photothermal Spectroscopy (*invited*) **725**
P. J. Treado and M. D. Morris

Intensity of the Spectral Lines in the Optogalvanic Effect **731**
B. R. Reddy, P. Venkateswarlu, and M. C. George

The OLD Technique Applied to Diagnostics of the Atmospheric Simulation Chamber **734**
R. Anderson

VI. D. Lasers in Trace Analysis

(organized by T. J. Whittaker, Battelle Northwest)

Quantum-Limited FM Spectroscopy with a Lead-Salt Diode Laser **737**
C. B. Carlisle and D. E. Cooper

Real-Time High Resolution Monitor for Ambient Methane Based on a Zeeman-Split HeNe Laser **741**
P. L. Kebabian and J. B. McManus

Imaging of Supersonic Flow Using Planar Laser-Induced Fluorescence **744**
P. H. Paul, J. Seitzman, M. P. Lee, B. McMillin, and R. K. Hanson

VI. E. Lasers in Combustion Analysis
(organized by B. E. Forch, Ballistic Research Laboratory)

***In-Situ* Detection of Gas Phase Species in the Filament-Assisted Diamond Growth Environment** 747
F. G. Celii, P. E. Pehrsson, H.-T. Wang, H. H. Nelson, and J. E. Butler

Simultaneous Determination of Temperature and Species Concentrations of High Temperature Gases using Tunable Laser Absorption Spectroscopy 750
X. Ouyang, P. L. Varghese, and D. S. Cline

Simultaneous Concentration Measurement of CO_2 and H_2 with Multiplex CARS in Combustion Environments 754
J. P. Singh and F. Y. Yueh

Laser-Induced Fluorescence and Dissociation of Acetylene in Flames 758
G. A. Raiche, D. R. Crosley, and R. A. Copeland

VI. F. Advances in Plasma Diagnostics

Laser-Induced Fluorescence Measurement of Plasma Ion Distribution Functions: Errors Due to Spatially Inhomogeneous Laser Intensities 761
M. J. Goeckner, J. A. Goree, and T. E. Sheridan

Measurement of H and H_2 Populations in a Low Temperature Plasma by Vacuum Ultraviolet Laser Absorption Spectroscopy 767
A. T. Young, G. C. Stutzin, A. S. Schlachter, J. W. Stearns, K. N. Leung, W. B. Kunkel, G. T. Worth, and R. R. Stevens

Photodetachment of He^-: Angular Distributions of Photoelectrons 770
J. S. Thompson, D. J. Pegg, R. N. Compton, and G. D. Alton

Author Index 773

PREFACE

Advances in Laser Science-IV is the Proceedings of papers presented at the Fourth International Laser Science (ILS) Conference. This meeting was established as a Topical Conference of the American Physical Society (APS) in order to provide a forum for the discussion of core research areas related to laser science. Its focus is on fundamental areas relating to laser physics, mechanisms, and properties; laser induced processes as they relate to materials characterization and modification; the underlying spectroscopy that forms the basis for the understanding of these laser-related processes; and the variety of recently developing laser applications associated with diverse new technologies.

Earlier ILS Conferences were held in Dallas in 1985 (ILS-I), in Seattle in 1986 (ILS-II), and in Atlantic City in 1987 (ILS-III). ILS-IV, from which the current volume is collected, was held in Atlanta, Georgia, October 2–7, 1988 with over 360 participants from the United States and other countries. An exciting aspect of the ILS Conferences has been their interdisciplinary nature, emphasized this past year by meeting concurrently with the American Vacuum Society (AVS). A major highlight of this meeting was a joint symposium with the AVS focused on laser–surface interactions, including such topics as surface etching to create new semiconductor and superconductor devices, laser processing to create surface modifications, and laser probes of the detailed mechanisms of gas–surface interactions.

Other meeting highlights covered a wide range of topics that included: a Sunday evening panel discussion on "Tunable Solid State Lasers," a keynote address by Professor Y. R. Shen of the University of California at Berkeley on "Nonlinear Optics and Surface Science"; plenary lectures presented by P. Andresen, A. Aspect, D. Crosley, W. Happer, E. Ippen, R. Osgood, and W. Stwalley; and a banquet talk presented by Professor Ali Javan of the Massachusetts Institute of Technology on the "Dawn of the Laser Era," reconstructing his discovery of the first gas phase (HeNe) laser with anecdotes of both a technical and personal nature.

The Conference Chair for ILS-IV was Marshall Lapp (Sandia National Laboratory and Lawrence Livermore National Laboratory), Andrew C. Tam (IBM Almaden Research Center) was Conference Vice-Chair, James L. Gole (Georgia Institute of Technology) was Program Chair, and Donald F. Heller (Light Age, Inc., Mt. Bethel, New Jersey) was Program Vice-Chair. Rolf W. F. Gross (Aerospace Corporation) was International Vice-Chair, a position of key importance in facilitating the attendance of overseas colleagues.

The Conference program was originated and assembled by the Program Chair and Vice-Chair, with Andrew Tam playing an additional vital role in organizing the joint ILS/AVS Laser–Surface Interactions Symposium. Substantial contributions were made by a number of session organizers and ILS program advisors. Many organizers worked on formulating the areas of laser science to be covered and the sessions within each area, with special efforts to arrange key invited speakers from the United States and abroad. These session organizers are acknowledged in the ILS-IV Conference Program printed in the *Bulletin of The American Physical Society*, Volume 33, No. 8 (1988) and in the Table of Contents of this volume.

This Proceedings Volume, as with earlier volumes, is not intended to replace the publication of new and complete research results in those technical journals that cover the field. Rather, the brief accounts of research summarized here are intended to provide summarized descriptions of the research topic chosen, with sufficient description (aided by a listing of the key references) to enable the reader to understand the basis of what has been accomplished and where to find more detailed information. In some instances, historical perspectives and thoughts on future directions are also presented.

The content of this volume is organized in a fashion designed for subsequent use rather than the chronological format of a technical digest provided at many conferences; the organization follows that of the general areas covered in the Conference rather than the order of presentation at the

Meeting. Also, to ensure quality and readability, each paper in this volume has been reviewed by at least one referee.

As for previous meetings, special thanks are extended to Lynn Borders, the ILS Conference Administrative Assistant, and to the secretarial staff at the University of Iowa for their tireless devotion to the countless administrative tasks for which they took responsibility. The extensive work involved in communicating with the authors of the papers in this volume and with the reviewers, as well as in providing manuscript correction capabilities and assembly of the volume was provided by Lynn. We thank James Spellos of the APS Meetings Department both for the extensive organization skills he has brought to ILS-IV and for his continued help with the organization of ILS-V, for which we have followed a similar format albeit with a slightly different name that connotes the interactive nature of the various disciplines encompassed by this Conference. The Fifth Interdisciplinary Laser Science Conference (ILS-V) will be held at Stanford University, August 28–31, 1989.

We gratefully acknowledge the organizations that provided generous support to ILS-IV—the National Science Foundation, the Office of Naval Research, the Petroleum Research Fund, the University of Iowa (Center for Laser Science and Engineering), the IBM Almaden Research Center, and Allied Signal Inc.—and trust that they will find this record of scientific results presented at the Conference to be of value.

The Editors:

James L. Gole, Program Chair
Georgia Institute of Technology

Donald F. Heller, Program Vice-Chair
Light Age, Inc., Mt. Bethel, New Jersey

Marshall Lapp, Conference Chair
Sandia National Laboratories and Lawrence Livermore National Laboratories

William C. Stwalley, Administrative Vice-Chair
University of Iowa

Sunday Evening Panel - Tunable Solid State Lasers

Organizer and Moderator: Donald F. Heller (Allied-Signal Inc.); Panelists: Robert L. Byer (Stanford University); Lloyd Chase (Lawrence Livermore National Laboratory); Richard C. Powell (Oklahoma State University); John C. Walling (Light Age, Inc., Warren, New Jersey)

D. F. Heller: Welcome to ILS-IV. In previous years we have traditionally opened ILS with a panel discussion on some area of science or technology that has been of interest and possibly some debate. Last year those of you who attended ILS-III in Atlantic City may recall that there was a panel discussion in prelude to the meeting that discussed dye lasers and the state of the technology: where the field is going, what we might expect to see evolve in our laboratories in our other applications as a result of progress being made by the scientists and engineers who are moving the field. This year, we'd like to do something similar with tunable solid state lasers. In fact, one of the questions that came to the fore during the discussion of dye lasers last year was what technologies, particularly in light of the new tunable laser technology, might come to be that may eventually either augment or displace dye lasers. So this panel, in a sense, is convened to address more broadly that question and the development of the last few years in tunable solid state lasers. The questions for the evening boil down, I think, principally to three major bodies, that is: 1) what is the status of the field of solid state lasers; 2) where are they going and what developments are likely to made that we should look forward to; and 3) why should any of us care. To help address those, we have chosen a panel of experts in the area of solid state lasers, people who have invented and developed these lasers, who have explored their physics, and who have helped to develop new and promising applications. These include Professor Robert Byer of Stanford, Dr. Lloyd Chase from Lawrence Livermore National Laboratory, Professor Richard Powell of Oklahoma State and Dr. John Walling of Light Age, Inc. So without further introduction, I'd like to turn the questions of the evening over to them with the hope that they will be able to set into some perspective these questions and issues that those of you in he audience may raise later. The last hour of this meeting is largely yours and the hope is that you will feel very free after either the initial discussions by each panel member or in the more general discussions that follow them, to ask any questions that may come to mind. You may target them toward a specific panel member or address them for general response. So I look forward to a very lively evening and to our first speaker of the evening who is Professor Richard Powell.

R. C. Powell: Thank you, Don. I think it's important to start the discussion by setting the parameters of the field and let me review for you the different mechanisms we have for creating tunability in solid state lasers. The first thing I'd list is simply the shift-

ing of lasing lines that we can achieve in the solid state by applying some kind of external perturbations such as changing the temperature or applying a magnetic field or external stress. This achieves only a limited tuning range but it can be important in materials such as semiconductor lasers, where the band gap is sensitive to these parameters and we want to tune into resonance with some specific transition for diode laser pumping or other applications. The next thing I listed was line selection. Many of the rare earth ion lasers lase in many different laser channels and we can switch back and forth from one lasing channel to another and get frequency agility in this way. What most of us think of when we think of tunable lasers are of course vibronic transitions that are broad band emitters with homogeneously broadened lines and we can tune across the spectral lines. We can have also broadband transitions due to inhomogeneously broadened lines, for example, ions in disordered materials such as glasses. This achieves tunability but of course all of the ions in the materials don't take part in this type of tuning so I've listed this as line narrowing, and then lastly we can tune the output of the laser through a nonlinear optic material. Now this may sound like it should be the topic of a separate discussion, but I think it is appropriate for this panel for several reasons. First of all, there have been a lot of advances recently in nonlinear optical materials: the borates that the Chinese have come up with. KTP and other materials are important. There are certain spectral ranges that are better hit by nonlinear optical tuning than by intrinsic tunable materials and there have been demonstrations by various groups such as R. Byer and others that we can use nonlinear optical materials as actual hosts for ions and have a monolithic device that's a tunable laser crystal through nonlinear optic tuning. So, with these as the areas for discussion, then, I'd like to give you a biased overview, my view of the field, from the point of view of someone whose main interest is basic, fundamental solid state spectroscopy of ions and solids.

It appears, at this point, from this perspective, that our field is driven by the user demand for lasers. NASA will have a requirement for lasers for remote sensing. Lawrence Livermore has a requirement for fusion lasers. The medical industry has requirements for lasers with very specific parameters. The rest of us, then, are trying to come up with lasers that have these exact parameters for optimum performance characteristics. Although we have many solid state lasers, at this point it would be fortuitous if one of them happened to have exactly what we needed for a certain application. Now the way the field is moving, there seems to be random attempts at simply trying to grow crystals and see what their laser characteristics are. This obviously isn't a very efficient way for the field to operate, but the reason it operates in this way is that we do not have a significant reliable data base of spectroscopic information and we do not have good models and theoretical work to interpret this spectral data so that we can develop a predictability that allows us to say: let's design a laser mater-

ial and go grow it and see what it's properties are and have predicted ahead of time what they should be. So I think the research areas that are of interest are obviously still looking for new hosts and new ions which is important, and new pumping schemes which is going on also, but we have to couple this with developing a data base of spectroscopic information and developing modeling techniques to understand what this spectroscopy is telling us in terms of what the laser characteristics will be. None of this is worth anything unless we can work closely with the crystal growers and materials people so we can grow the materials that we model and predict will be good lasers. The crystal growth of course requires defect work and trying to eliminate problems with these crystals.

The next thing I wanted to do, then, is to summarize some thoughts of what's going on in two different areas, firstly the broadband vibronic laser materials and then the line switching and the sharp line laser materials. Now broadband vibronic tunable lasers are generally made up of one of two classes of active centers: either color centers, that I'll leave for someone else to discuss; or 3d atoms and I've listed the various electronic configurations and normal valence states of the 3d ions. So far, chromium, of course, has been the real work horse. It lases in many different materials and has been the most successful of the tunable vibronic laser ions. There have been also some lasers based on trivalent titanium and some based on cobalt and a few of these other ions, but still there are many different 3d ions that have not yet been thoroughly studied and tried as lasers and of course many different hosts to look at. Some of us have played around a little with 4d and 5d transition metal ions. So far those haven't been very successful, but I would still hold out some hope for them in the future.

Well let's think about chromium for a minute since it's been so successful as a tunable laser ion. I've just, for the purposes of discussion, thrown up some emission spectra of chromium and different hosts. Ruby, of course, for those of you in the back, this scale is broken and these R lines in ruby actually, if the scale was the same as the rest of them, would go out the ceiling. It's a sharp line emitter, not broadband. But then as you go to lower crystal fields, you get the broad band emission. There's lots of chromium materials and we'll hear about some at this meeting like Fosterite that R. Alfano's group has developed and others. Are we interested in looking at more chromium built materials? Well, I think there's still a lot to learn. We know about how the crystal field changes the bandwidth and position of the emission but there are a lot of fundamental properties such as excited state absorption. L. Chase's group at Livermore has been looking at this but it's a very important property that's not completely characterized. Ion-ion interactions also can be important, especially if we use chromium as a sensitizer for other materials. Nonradiative decay processes are among a number of fundamental physical processes that have not yet been characterized in these chromium built materials,

and to fully understand the materials and predict better materials we need to spend some time understanding these processes. At a meeting I attended in Poland a couple of months ago, Alexander Kaminski from the Soviet Union, gave a nice talk reviewing all the work he's done recently on different lasing materials; these are all various chromium-doped materials with different lanthanum-gallium silicate and lanthanum-gallium niobate hosts and different tuning curves. The interest to me here is not so much the tuning curves but that in the niobate, which is a nonlinear optic material, you could see some second harmonic generation. In the chromium doped niobate and again, as I mentioned earlier, you have, through nonlinear optic tuning, a tuning range from the red back into the blue or green spectral region. About ten years ago when we had our first tunable laser workshop at Keystone, I suggested that one thing that would be interesting was to go back through all the phosphor literature and look at some of the really good broadband phosphor like the molecular ions of tungstates, vanadates and these sorts of materials. We've been trying to do this ever since and still haven't been successful; the major reason is crystal growth problems. This shows for example the emission spectra of the vanadate molecular ion and you can see that's a very nice strong broadband emission in a tuning range that matches a cesium filter. That ought to be a pretty interesting tunable solid state laser. But we're working right how with G. Loiacono at Philips trying to get some good single crystals of this but again it's a serious crystal growth problem and unless we work closely with crystal growers, we're not going to be able to make many advances in this field. Another problem here, if we really get into tunable lasers in the blue spectral region, we've got to have pump sources at higher energies and this is not easy for flashlamps, so this is something that I know several groups are working on, surface discharge pumping sources, but that will be another important issue. Another thing about some of these chromium doped materials or other 3d materials are optically induced color centers, especially the materials like the gallium garnets GSGG and GGG have these problems. The Livermore group has a talk at this meeting about the work they've done in trying to minimize optically induced color centers in GSGG. This shows some results. We were working with GSGG and GGG doing some laser induced grating spectroscopy but when we turn our laser beams off, there's a long lived refractive index change that we've induced into the material that is due to these optically induced color centers. And of course this is a loss mechanism and unless we get rid of these things they don't work well as lasers. So that kind of defect study is very important to the advancement of the field.

Let me shift gears, then, to the other topic and that is the sharp line materials and switching between laser channels. All of the lanthanide series rare-earth ions act as good laser ions and most of them have multiple lasing channels among all of these different energy levels. So the key, recently, has been various groups that have developed ways to switch between one lasing chan-

nel and another and get frequency agility in this way. One important thing that's going on with these rare-earth-doped laser materials is diode pumping which means that instead of flashlamp pumping in all of these visible levels, we selectively pump with diodes in a few of these low lying states. We've been simulating diode pumping in these regions by using an excellent alexandrite laser built by John Walling and this just shows some slope efficiency curves we've gotten with alexandrite-pumped neodymium YAG, BEL, and YLF. There's nothing special, really, about these curves but the thing that we've found when we laser pump selectively into these low lying excited state transitions, if we tune the alexandrite laser over the different Stark components, we can hit resonances with excited state absorption of the pump photons. And when we hit a resonance that turns off the infrared emission of neodymium at 106 microns and instead causes very bright blue emission. So we can, by tuning our pump laser over these Stark components, switch the frequency from an infrared output to a blue output and achieve tunability in that way. Tomorrow we have an invited talk by L. Schearer on work he's done trying to get tunable lasers at a very specific wavelength, 108.3 microns. The application is for pumping helium isotopes from magnetometers that are of interest to both NASA and the Navy. Here neodymium, of course, likes to lase at 1.06 microns but if you want to try to lase at this helium isotope transition, you have to do some fancy things, and I don't want to take Laird's talk which he will give tomorrow, but he's developed ways of narrow tuning ranges across some of the other Stark components of the neodymium emission to hit the exact wavelength of interest and this can be done in LNA. YAlO isn't quite as good. Neodymium in lithium niobate looks good. D. F. Heller (at Allied) and I have been talking about doing this with neodymium-doped BEL and you can see the spectrum of neodymium-doped BEL should have a nice broad tuning range in this region is another possible material for this application. But these kinds of applications, then, are what's driving us to find tunable ranges even if it's a very small range in a specific area. Milt Birnbaum's group at USC, among others, have been working on double-doped materials such as erbium and neodymium in YAG where you can get simultaneous lasing. This is the flashpump source and you can see the neodymium 1.06 m transition has a lower threshold and starts lasing and then the 2.90 μm transition of erbium comes in. Later they can do this also with with holmium and neodymium and then using frequency selective elements, they can tune back and forth between these wavelengths. There's a lot of work going on of this type of frequency selectively with up-conversion as a process for switching back and forth between lines, especially the IBM group of Will Lenth, among others. We did a very thorough study. One of my students, also working jointly with Leon Esterowitz at NRL, looked at barium terbium fluoride holmium. Holmium has several different laser transitions. By pumping differently we could turn on or off these transitions depending on how strong the various up-conversion processes were, and we did a fairly thorough spectroscopic study and computer model of this and really developed a good modeling scheme for pre-

dicting what we need for the optimum pumping for these different transitions. Again, this computer modeling is important.

Final ideas: tunable fiber lasers, rare-earth doped fiber lasers, and here of course the host is a glass, in this case a silicate glass, that means you've got an inhomogeneously broadened transition that you're tuning across. There is some Japanese work where they tuned by changing the length of the fiber. Payne's group in Great Britain used a similar tuning scheme for erbium doped fibers of the same length by putting a grating as a tuning element inside the cavity. So these are various ways to achieve tunability. Let me leave you now with the thought, again, in summarizing, that, along with the search for new ions and new hosts that's going on, the invention of novel pumping schemes is important but we need very definitely to develop some good spectroscopic data for a data base. Tie this with really good computer modeling to understand what the spectroscopy means in terms of laser capabilities and then work closely with our crystal growth friends in order to actually grow materials that work. Thank you, Don. I'll turn it back to you.

Question from R. Morris (Allied-Signal, Inc.): I'd just like to point out the way things have worked up till now, as far as I can tell the way things are still working, you're getting most of your new lasers from the crystal growth community. The process is not as you've described it. In my view it's the crystal growers who have been inventing the new lasers materials that are dirving the field, not the other way around. R. C. Powell: There's a point by Bob Morris at Allied who said that from his perspective as a crystal grower the way this is developing is the crystal growth people are coming up with materials that are good enough for those of us who are trying to make lasers to use and work in that way. You have to have a good enough crystal to make a laser or you're not going to make progress. I agree, I don't disagree with that at all.

Question from R. L. Byer: One quick question. Would you go into, a little bit, what you mean by computer modeling? What kind of modeling are you thinking of? R. C. Powell: Okay, I think that can take on a couple of different aspects, depending on the type of material. We've got a whole session here that Marty Buoncristiani put together on computer modeling that deals mostly with modeling of lasers and the cavity dynamics themselves which is one important area. In my case, what I'm talking about more is modeling the pumping dynamics. When you have multiple energy levels and have things like energy transfer, up-conversion and four or five different processes going on before you actually get a stimulated emitted photon, you have to go through a much more significant analysis. That can generally only be done on a computer, instead of saying we have a two-level atomic system that we can treat in a text book fashion. So there are really two aspects of the computer modeling I would push in that area.

D. F. Heller: I think that we'll defer further questions until after the session. Our next panel member is Dr. Lloyd Chase of Lawrence Livermore National Laboratories.

L. Chase: The main emphasis of what I want to say is to try to give you my impressions as a prospective end user of tunable lasers and also a person who has spent a few years intensively doing research and development on them, to give you some idea how research, development and applications have been coupled together, and where they haven't. Before I begin, I would like to spend some time explaining to you what a tunable vibronic laser is. The idea is fairly simple. There are energy levels of an ion like chromium or titanium as a function of some generalized vibrational coordinate describing the motions around the impurity ion. The important point to realize is that for different energy levels in an ion, the equilibrium configurations may not be the same. When you make a transition from the vibrational ground state to the excited states due to the pumping process and you end up in a metastable initial lasing level, there may be a configuration offset. What that does, essentially, is to give you emission which is primarily to the higher lying vibrational states of the ground electronic state. You pump "vertically" with no change in the nuclear configuration. You then go to a relaxed excited state. You emit vertically also and terminate on a highly excited state of the ground state. That Stokes shift, as it's called, is what gives you four-level laser operation from what can even be a two-level system. Titanium sapphire works exactly like this. The tuning range is then related to the width of that emission.

I'd like to try to make a distinction that may not be so obvious. There are two basic types of tunable laser applications. In one case you want tunability over a large wavelength range. For example, I'm a solid state spectroscopist. I use lasers to tune through spectra and I want something that will tune over a broad frequency range and the broader the better, because next month I may want to use it for something else. But there's another aspect to a tunable application, mainly something which is setable to a particular wavelength. There's no fixed frequency laser that works exactly there, so you're stuck with a tunable laser. The point I want to make is that, in fact, there may not be one laser medium that will be good in both types of applications.

The reason for that is that wavelength setable lasers should, in fact, have as <u>narrow</u> a tuning range as possible. Take, for example, CW operation where the gain of the medium at threshold, G_{TH}, is equal to the emission cross section times the population inversion at threshold times the length of the medium. That has to be equal to the sum of the round trip losses in the output from the laser. But on the other hand, that inversion population at threshold is proportional to the pump power you have available at threshold times the lifetime of the initial lasing level, and I'm assuming here, for simplicity, that it's the radiative lifetime. The

point is that the pump threshold power is something you have to supply in an application just to get in the ball game. You don't want that to be too big. In fact that's inversely proportional to the product of the emission cross section and the radiative lifetime. Now, there's a formula called the Fuchbauer-Ladenberg formula which is basically a restatement of the relationship between the Einstein A and B coefficients that tells you that the sigma tau product here is inversely proportional to the linewidth of the optical transition. So by going to broad linewidths to get very great tunability, you require high threshold powers. And if you want a laser that you set to a frequency and operate with a minimum of overhead, you don't want that. A similar thing happens if you go to short pulse operation. The stored energy, the product of the pumping power, times the lifetime of the initial level turns out to be inversely proportional to the product of cross section and lifetime, which is proportional to the bandwidth since the radiative lifetime is proportional to 1 over the emission cross section times bandwidth nu. Broad bandwidth is a disadvantage. So the argument here is that, either for CW or for pulsed application, if you want a setable laser, you want the narrowest tuning range that will do the job.

I'd like to go on to point out some possible applications for tunable lasers and see where tunability and setability are important. Spectroscopic research I already mentioned. You need something that can be broadly tunable or setable, but, really, in a laboratory, you don't care if a laser takes up a whole table. Whatever it takes to pump it you pump it with, and so a broadly tunable laser is preferred there even if you're going to use it for setable purposes. Frequency agility for a transmitter, for example, if the military wants something that will jump around in frequency so that no one can interdict it too easily, requires something that's broadly tunable, a cascade laser, or something of that sort. But the rest of these applications I've indicated all call for setability rather than tunability. In materials processing, a good example is laser isotope separation. You want to set the laser and forget it. A pump source for another laser. Resonant detection of absorbing or scattering species, like some NASA applications, environmental science applications, and most laser communications require setability. You can see that setability, at least in my opinion, wins out. And so it's going to be very rare to find the ultimate tunable laser in any given wavelength range.

Don Heller asked me to talk about applications. Now I'm not an expert about applications in the government, but I can point out some of the things that Bill Krupke and I discussed when I found out I was going to have to do his work for him tonight: mainly government applications of tunable solid state lasers. I'm going to talk about DOE and DOD as examples. In the Department of Energy, a big laser program is inertial confinement fusion. Here. for example, you might consider a laser pumped gain medium for a fusion laser. The other application is laser isotope separation.

Unfortunately everybody I talk to about the laser isotope separation process at Lawrence Livermore Laboratory says that there is no way in the near future that any kind of a tunable solid state laser is going to replace the copper vapor laser/dye laser type technology they have right now. The reason for that is that there's no reason to change. You have a dye that's very long lived to do the process. You have a copper vapor pump laser that gives you efficiencies of pumping that are the order of 50% for some of these dyes, and there's really nothing wrong with the dye. The main problem is the pump and that's not severe enough for someone to want to use an untried technology. So I think here's a case where dye lasers are going to be very hard to knock off the pedestal, except for what one could call niche applications: isotope separation of particular elements for which there is no good stable dye. And there is some work in that direction using lasers like alexandrite.

DOD applications give a couple of interesting examples of how maybe, and maybe not, tunable solid state lasers will be useful. The classic application, which has been around now for a number of years, is the much sought after blue-green laser for submarine laser communication. Blue-green because that's where sea water transmits the best. The idea is to put one of these in orbit to communicate with submarines. Many people have been looking for a solution to that problem, and many people have found a solution for the problem. But the question is: what's the right solution? You have to keep in mind that if you want something you are going to put up in orbit, that means you want it to not take too much pump power and it must be extremely reliable. You certainly wouldn't want to have to change flashlamps every two years, for example. And although the frequencies involved, 455 nm and 459 nm, can be generated by second harmonic conversion of a red laser operating at around 900 nm, right in the "wheel house" of a chromium tunable laser, it's going to be very difficult to make a tunable chromium laser with enough reliability to really do the job at a low enough pump threshold.

Another application that's been in the wind for a while is antisensor, namely the idea of blinding whatever the opponent is going to use to detect you if he wants to attack you with a missile or helicopter or something like that. What's needed here is a very broad wavelength tunability, and it's not clear what the solution for that problem is. What you really want is white light to blind everything in sight, otherwise a simple filter would be able to get rid of the threat.

Now let me very briefly mention the problem that we've been involved with that I think illustrates what it takes to find a solution to problem where you need a tunable solid state laser. It's a speculative idea, and it involves a way of generating a very high power fusion laser beam by pumping an energy storage medium with a tunable pump laser. In this case tunable very clearly means seta-

ble because once you've decided on this medium you know what that pump frequency will be. The thing that drives this whole concept is the efficiency of the pump laser. It's very hard to get a flashlamp-pumped pump laser that's 10% or more efficient. And so we set out looking for such a combination of a pump laser and a storage medium about a year and a half ago. We very quickly eliminated almost everything except for vibronic chromium lasers, and so we immediately set about finding out what was out there in vibronic chromium lasers. I think it's instructive to see that when you start trying to find out what's out there you immediately run into questions as to what the data means.

There are about thirty tunable chromium laser materials. But I think the thing that's very striking is that, if you're interested in efficiency as we are, then you see that there really were, at that time, two lasers, alexandrite and emerald, that looked good and then there was a large number of also-rans with low efficiency. What does that mean? What do the numbers mean? Did they mean that someone didn't do a very good job of building a cavity or the material was lousy? So when you look at a set of numbers in literature you really don't know enough to make an educated decision. What I want to point out here is that people who do research on tunable solid state lasers should probably do a better job of characterizing their measurements. Let me try to indicate to you how we approach this problem to try to eliminate some variables that are not necessarily intrinsic to the materials. If you use a very common expression for the slope efficiency, you can split that into two pieces. One is what I call an intrinsic or extrapolated efficiency and the other involves the hardware and the passive losses in the medium.

By plotting the reciprocal of the measured slope efficiency as a function of the reciprocal of the output coupling, the intrinsic efficiency and passive losses can be obtained from the slope and intercept of the plot. After you have done this for prospective laser hosts you have an ordering of laser candidates for your application, where now you know pretty well what the final numbers for the efficiency means. I think that if people are going to do research and development on tunable solid state lasers, they should go this extra step further and try to present a prospective user with a number that he can understand. Thank you.

Question from D. F. Heller: Were all of these measurements done at room temperature? As you know some of the intrinsics are thermally dependent. L. Chase: They're all room temperature measurements, particularly alexandrite which is the one that would vary quite a bit.

D. F. Heller: Our next panel member is Professor Robert Byer from Stanford University.

R. L. Byer: There's only one thing worse than talking to an audi-

ence after a two-martini lunch and that's talking to an audience after a wine and cheese reception on a Sunday evening. So instead of talking about credible lasers, I thought tonight we'd talk about incredible lasers. How do you make efficient lasers, and if you're going to make them efficient, how do you tune them? I'm the skunk at the picnic tonight because I don't build tunable lasers, I take lasers and tune them after we build them and I'm going to talk about trying to make efficient lasers and then turning these efficient lasers into tunable devices, and then after you learn how to tune them, I'll try to teach you how to make them into kilowatt average power lasers. I thought we'd take little bit of a tour through a widely tunable source that does not suffer from the gain bandwidth product that lasers suffer from and that's an optical parametric oscillator device and then a little bit about sub-kilohertz linewidth YAG lasers, some efficient harmonic generation and some CW and quasi-CW OPOs. I doubt in 15 minutes that I'll be able to teach you how to build a kilowatt average power laser by 1992 but believe me in the business of incredible lasers we can do it.

What's happened in the last few years? What's happened is 25 years of work in diode lasers suddenly got together with 25 years of work in solid state laser technology and somehow got coupled with 25 years of work in nonlinear optics. And what comes out of it is a lot of very incredible interesting things. I don't have time to give you the details so let me refer you to the special issue of the Journal of Quantum Electronics, June 1988. One of the editors there is Bill Krupke and in this special issue there's a series of papers on first diode laser pump sources, on diode pump and solid state lasers, and on efficient nonlinear conversion of these sources. And if you go back and read that, it will put you in the proper mood for understanding scientifically the kind of advance that's been made in the last couple of years.

Diode pumped solid state lasers have come a long way since first experiments in this renewed field. The field is very old. The first diode pumped solid state laser was built in 1963. This is not a young field, it is a very old field but with the advance in diode laser sources and the advanced understanding of the new doped materials, ion doped in crystals and with the new nonlinear crystals, we can make extensions on the early work. The extensions include low threshold, very high operating efficiency, q-switched operation of the lasers, mode-locked operation of the lasers, and frequency extension to a whole host of new wavelengths under diode laser pumping.

As an example, you can diode laser pump neodymium glass and when you diode pump glass, you can either q-switch or mode-lock it, if you wish. To mode-lock it, the record right now is output pulses of a cw diode pumped glass laser of 6 picosecond duration. That's not the limit, by the way, that's just where the state of the art is as of now. We'll see narrower pulses in the future. You can diode pump 3-level lasers like 946 nm in YAG, or in work

that took place with Huber's group in Germany, you can diode pump 2 micron transitions in thulium/holmium YAG and generate a laser that puts output into the micron spectra range. That laser has a particularly interesting feature. If you look at the energy scheme, you find that thulium/holmium YAG has a possibility of having a pump quantum efficiency of 2. For every pump photon of diode laser radiation that's absorbed you get a cross relaxation process that gives you two inversions. Two inversions transfer efficiently to holmium and you get a 2 micron laser. This laser has been operated under diode laser pumping at room temperature. Just last week in Germany, Huber reviewed results of their work of the flashlamp pumping and krypton ion laser pumping of this system. If you pump this laser with a krypton ion laser, you achieve a slope efficiency of greater than 30% and an average output power of 300 milliwatts at room temperature. If you pump this laser with flashlamp radiation, which has been done both in Scherbakov's laboratory and Huber's laboratory, the record to date for one kilojoule input is 17 joules of output energy at 2 microns with a slope efficiency of 3.3%.

Now diode lasers allow you to do something else unusual. That is you can control the linewidth of the diode pumped solid state laser and it turns out linewidth control is very important for efficient nonlinear interactions. One of the ways to make narrow linewidth lasers is to make a ring laser. If you make a ring laser you overcome spatial hole burning. If you overcome spatial hole burning, the laser runs in a single frequency. This laser, called a nonplanar ring oscillator, can be diode laser pumped. When it is, you can beat two of them together in a standard beat frequency experiment. If you lock two lasers onto a cavity to keep their relative frequency stable, and then beat them and look on the spectrum analyzer work that was done in the last few weeks showed that the linewidth of these lasers is now less than 150 hertz. Is that a record? No, it's just a step forward. The theoretical linewidth of this laser under these conditions is about 1 hertz. The goal is to achieve, some time in the next graduate student lifetime, which is 5 years, a laser with a linewidth of about a millihertz.

Now what would you do with such a laser? Well, I can tune it. How do I tune it? Suppose I take that single frequency laser and I injection seed a standard Q-switched neodymium YAG laser. That neodymium YAG laser becomes single axial mode. Under single axial mode operation maybe I can double and triple it and pump a parametric oscillator and make a tunable source. What is a parametric oscillator? It is a tunable coherent source first demonstrated in 1965 by Giordmain and Miller. It's a photon cutter. All it does is take a big pump photon and cut it arbitrarily into two pieces that have to add up to conserve energy by a conservation of energy equation. And, of course, physics says you have conserve momentum. There's conservation of momentum. If you do that and put a nonlinear crystal between two mirrors you build what's called a parametric oscillator. A parametric oscillator can have wide tuning de-

termined only by the dispersion of the material and at the same time can have a high gain cross section and it can have a low threshold. It doesn't have any restrictions on a gain bandwidth product that a laser does. In a joint experiment with Professor Wallenstein's group in Hanover, we built a beta barium borate parametric oscillator. This particular device is pumped by a standard q-switched off-the-shelf YAG laser with an injection seeder to get single mode. It's frequency tripled in the standard way and it pumps this crystal between two mirrors.

This device tunes from .4 microns, 4100 angstroms, that's blue, all the way to 2.5 microns in the infrared, that's near infrared, single crystal, angle tuning over a few degrees, that's the entire tuning range. The average output power is 140 milliwatts over this range. The conversion efficiency is 35%.

In the remaining two minutes I'm going to talk about nonlinear optics not in the high peak power regime but in the milliwatt regime and we'll talk about how do I generate very efficient frequency doubling when I only have a few milliwatts of CW narrow linewidth power. One way you do that is external resonance second harmonic generation and if you have such a nice green source then you can turn it around and make an optical parametric oscillator and have some fun making tunable radiation. Well, resonant harmonic generation has also been known since 1965 but what's different now is what we're talking about. You take your laser, you pump a cavity that contains a nonlinear material, you build up the field of this weak laser in this resonant cavity in order to make the nonlinear process efficient. What's changed since 1965 is we now have a single frequency very stable pump laser. We now have low-loss, well-known nonlinear materials and that combination allows us to do some rather fantastic things. Here's the experiment. You take this diode pumped single axial mode non-planar ring oscillator that puts out 50 milliwatts of 1.06 μm at 150 hertz linewidth. You don't need the linewidth that narrow, but it's sort of fun to know it exists. If you put it into a crystal that's a resonator at 1.06 μm, it's a ring resonator, the radiation builds up to 3 watts of circulating power, you convert some of that 3 watts to green and out comes green. How efficient is this frequency doubler? Up to 50 milliwatts was available at 1.06 μm this experiment. Up to 30 milliwatts of cw green was generated. The conversion efficiency of this cw doubler is 56%. Does it agree with theory and experiment? Yes. For those of you who want to read about it, go to the special June issue of the IEEE. It's published.

Now, if I have green, then I can build a parametric oscillator and maybe I can build it as a low threshold device. In fact, using exactly the same crystal as for harmonic generation, that is, a ring that resonates the signal in either way, you put in 30 milliwatts of green and you can begin to generate some tunable output in the infrared. The experiment is the single mode YAG, the frequency doubler, the OPO. In the experiments that we did, we pulsed the

YAG laser by causing relaxation oscillations. We frequency doubled and what we get out is the following: here's the pump pulse, 230 milliwatts of peak power, the depleted pump pulse is the amount of conversion to the tunable infrared. In this experiment we saw 80% pump depletion. That means we're going to convert 80% of the incident green into tunable infrared. This particular device is called a doubly resonant parametric oscillator. It was tuning over this range by tuning the crystal temperature. Lithium niobate is the nonlinear crystal. It tuned over the range shown in the boxes by changing the electric field across the crystal. By putting 0 to 400 volts on the lithium niobate crystal, we were able to tune continuously over more than 100 angstroms and the parametric oscillator ran in a single axial mode over that tuning range. It runs again at this very high efficiency. Well you may say, that's not a very wide tuning range. Indeed, it's not, it's limited by the coating on the crystal. We can get you a little wider tuning range if you give us a little bit more power and we can get a little bit more power by amplifying in a YAG amplifier so we take a 50 milliwatt source, amplified to a kilowatt in a slab YAG amplifier, frequency double and pump a parametric oscillator that has a widely tunable range, called a singly resonant oscillator which only resonates one of the ways, and this first device tuned from near 8000 angstroms out to 1.5 microns continuously tunable, except for a range where the coatings did not resonate. What is the extended range of this lithium niobate parametric oscillator? We know from previous work that we've tuned from about 6000 angstroms to 4 microns continuous tuning range. Was it an efficient device? Well the ring version of it ran at about 65% conversion efficiency and the standing wave version at about 45% conversion efficiency. That's low threshold cw and quasi-cw OPOs.

My final slide, if our chairman will give me a minute before the bell rings, how do we go from milliwatt to kilowatt average power levels? We do it in steps. You have to learn to crawl and then walk and then run. We have demonstrated a half watt average power diode pumped YAG slab oscillator. We are now designing and building a 20 watt CW YAG slab oscillator to be diode laser pumped, and that will be a step before we try to build a 20% wall plug efficient 1 kilowatt average power slab laser. Every time I show this slide of incredible lasers, the audience gets a big laugh. Here's our approach. We're going to buy 60 1-watt diode lasers coupled to fibers. These 60 1-watt diode laser sit off on the side and they pump a 3 cm long slab of neodymium YAG or neodymium glass. They're equally efficient and this device we think will generate 20 watts of TEM_{00} mode CW output power at about 10% wall plug efficiency. 10% efficiency, by the way, has already been achieved. What makes this possible? If I try to buy these diode lasers today, they cost $7000 a piece and 60 of them breaks even the bank of the Livermore National Labs so that's not going to work. What makes it possible is something our friends in the semiconductor industry taught us many years ago, and that's the cost savings associated with mass production. If you go to Siemans in Europe, you

go to Spectra Diode in the United States, or you go to Sony in Japan and you ask them please give me a cost per watt of diode laser power versus the volume, the number of lasers you produce per year, this is the curve you get. What does it show? If you only make a 1000 diode lasers a year, it's going to cost $1000 per watt. That's pretty expensive but with volume the price declines dramatically. That was last year's number, it's more than doubled that this year. They will quite readily make their million diode lasers a year and I think by 1992 we will indeed see $5 or $10 per watt per diode laser power. That's the story on incredible lasers this evening. Thank you.

D. F. Heller: Maybe we'll all live to see the day when solid state lasers become an economic driver in the semiconductor laser industry. Are there any questions at this point?

Question: What was the pump source for the OPOs you discussed?
R. L. Byer: That was pumped with the third harmonic neodymium YAG, a standard q-switched YAG laser frequency tripled. The key though is to injection seed to get single axial mode radiation for efficient OPO operation.

D. F. Heller: You must have given some thought to making OPOs for those high power lasers. To be sure, there are problems in just generating 1 kilowatt style lasers. Have you looked at the scaling for those things?

R. L. Byer: The problem is exactly the same as the problem of building high power lasers and that's how do you get the heat out and we've spent 10 years learning how to get the heat out of solid state lasers. We think we've learned how to do that relatively well. Now we're looking at how to remove the heat from the harmonic generation crystals and there are similar studies at Livermore on the same problem. You can reach 50 watts of average power without any heroic measures, standard crystals, working in the lab under normal circumstances. Above about 50 watts of average power, it's going to take some extra steps.

D. F. Heller: As we all appreciate, getting the heat out is the important concern there, but that is, to be sure, material dependent and not all of these nonlinear materials are conducive to that by at least the techniques I know.

Bob Byer: The problem in the nonlinear materials is exactly the problem in the laser material and that's reduce the losses of the material and in the nonlinear materials, the greatest advance has been reducing the losses, not increasing the nonlinear coefficient.

D. F. Heller: A lot of money has been put into that. Perhaps this will stimulate a similar kind of effort in nonlinear materials.

Our final panel member is Dr. John Walling of Light Age, who,

among us, is the only representative who has actually put his personal fortunes toward making all of this physics turn into something useful. So, perhaps, John, you can tell us about how this is progressing into a commercial role, and when we can see them in our laboratories, those of us who don't work at either Allied or Light Age.

J. C. Walling: I certainly hope that there's still some time to make some money in solid state lasers before all this happens, Bob. It certainly is an exciting area. For the time being, my attention has been pretty much directed at making the technology that we've been developing over the past several years a reality in the commercial market, and of course the emphasis in our company has been on the alexandrite laser. I would like to say just a few words regarding the markup for lasers in general and point out where things are today. The market for lasers at approximately $100 million is growing at about 10-25% per year on the average. What is particularly significant and interesting, is the fact that the solid state area, materials processing and R&D and medical therapy markets have rates of growth that are quite in excess of the average for the laser market in general. Also interesting is the excimer laser market which shows, again, significant growth increases and the dye laser market which we have been addressing as being one of the interesting targets for tunable solid state lasers, is growing approximately 40% per year in the medical area. This information is from Lasers and Optronics magazine. There is a growing interest in this area of tunable lasers and also solid state lasers throughout the industry. Applications that seem to be most talked about, and of most immediate apparent interest fall in the areas of R&D where there is spectroscopy and diode laser simulation. Remote illumination in the commercial area could be search and rescue and many other similar types of applications. Isotope separation schemes are highly varied and a great deal of interest is there for tunable solid state lasers. Also, in medicine there has been a great interest developing for solid state lasers to deal with some of the problems that they do experience with the dye lasers. Finally, whether atmospheric pollution analysis is an attractive area for such applications as the differential absorption lidar techniques.

Commercial alexandrite lasers are now on the market with the tunability in the 720-800 nm region in its fundamental. Ti: sapphire and cobalt doped magnesium fluoride presumably will be reaching the market pretty soon. Where to draw the line as to whether a new laser is truly on the market today is as difficult as drawing the line between R&D and other commercial applications. I'd like to say a few words regarding the commercial laser that we manufacture. I won't dwell upon this too greatly but I would like to point out that it is a commercially available laser that you can buy at this time and that it produces nominally one joule at 20 hertz and has about an angstrom linewidth. The output is better than three times the diffraction limited in normal mode operation. Multimode and untuned the ion produces 2 to 3 joules at 20 hertz,

around 50 to 60 watts. It can be q-switched to generate 200 to 500 millijoules depending on what other performance parameters you're trying to optimize. We offer many performance options to tailor performance to a specific application. It's basically a modularized system and is designed for applications of varying types. The performance of that laser as a tunable source is typical of alexandrite lasers. Here we show the tuning curves for both the pulsed and cw. The ordinate is in joules. I think the important thing to note is that they're very similar in average output power and the CW one is this one here which is around 3 watts of output power.

We are also involved in developing nonlinear shifting techniques which are somewhat more prosaic than the ones just described to us, but still none the less effective in covering much of the visible spectrum. These derived from the first order Stokes shift in these specific molecular species and then by doubling these and the fundamental you can cover frequencies in the visible and into the ultraviolet. With the new crystals, e.g., beta barium borate, it's becoming possible to get wavelengths as short as 200 nm with the alexandrite source. This represents simply one scheme. There are many combinations of materials that can be used to achieve broadband coverage. We also are looking into developing the CW laser. We've developed some custom systems but we haven't one as yet to provide commercially. It will be coming out before too much longer, I hope. It will produce very reasonable amounts of power on the order of 15 to 30 watts and has tunability as I just described.

I'd like to talk a little bit now about some of the applications, and particularly the medical applications for lasers to give you a rough idea of where some of there interests lie for different wavelengths. Nothing is absolute here but there are certain critical areas and other important areas that have developed for different wavelengths, and for different applications, in the medical area. The shorter wavelengths and wavelengths in the region of 2 or 3 microns and also for wavelengths as long as 10 microns, particularly when operating from a T-mode laser produce interesting effects on tissue and the absorption depth is very short and the tissue is removed, usually ablatively, from material. All of these have very similar effects but they are in constant question as to which of these three different areas of wavelength space are going to be important for this ablative type of procedure, such as would be used in corneal surgery. The angioplasty operation, which is, of course, the removal of the arterial plaque, seems to be focusing in the region of 300 to 400 nm and also somewhat shorter than that in the area of 400 to 450 nm. Again here there is an interest in obtaining wavelengths that will ablate the plaque preferentially and there is some interest in this wavelength region because of the particular natural pigmentation that occurs. For the longer wavelength region in the area between about 600 nm and 1 micron the body is fairly translucent, not absorbing very strongly at all, and it's in this region that applications in photodynamic therapy are

emerging. I'll say a word or two about that in just a moment.

Photodynamic therapy is a particularly interesting and important new procedure for treatment of cancer therapy. Basically it involves injection of a photosynthesizer which selectively localizes in the tumor tissue. There is a wait for a few hours while that localization occurs. Then the tumor is irradiated by light at the right wavelength and after a couple of days the tissue is cleaned out, and with luck the tumor will not reoccur. The only problem is that you have to protect the patient from sun for several weeks because of the sensitivity of the photosensitized skin, but the dramatic result is that the tumor is in many cases essentially eliminated and the morphology of the tissue returns to near to normal rather quickly, certainly by comparison with surgical techniques. One great advantage of photodynamic therapy is that recurrences can be retreated, in contrast to radiation therapy. Up to this point 3000 to 4000 patients have been treated world-wide since about 1982. Apart from the skin sensitivity, this technique is showing a great deal of promise for treating a wide range of different tumors. The laser requirements are on the order of 10 watts or less CW at wavelength between about 630 to 800 nm. The longer wavelength is somewhat prefered because of their increased tissue penetration. However, to use longer wavelength sources requires the development of new dyes to exploit them. This is a very important area for a tunable laser because it's necessary to assign a laser wavelength that will meet the most efficacious photosensitizers that are being produced.

Incidentally, Light Age has a program funded by NIH to explore the different dyes in the wavelength region of alexandrite in pulsed and CW laser operation. Another interesting area of application in the medical area for which alexandrite seems to be showing significant promise is that of laser lithotripsy. Basically the treatment here is for a kidney (or gall) stone trapped in the uretha or bladder or other organ. To be removed and by present technique requires fragmenting these stones with what they call a shock wave lithotripter. The patient lies on his back and a shock wave is produced and focused. Usually an ultrasonic shock wave is focused on the stone causing the stone to fracture and subsequently be passed. This particular laser technique utilizes a fiber optic which addresses the stone directly. The application is considered, presently, supplemental to the other technique but it does have certain advantages in that it does treat more types of clinical situations and indeed it is significantly less expensive with about $200,000 per unit versus the present $2,000,000 system. So there is a significant interest here in tunable lasers, indeed tunable dye lasers are currently being introduced in this application. But I believe alexandrite and other solid state lasers would prove preferable in most clinical environments.

I wanted to also discuss briefly with you some of the results of developments we've made, this time under funding by the United

States Air Force. We have produced an alexandrite laser in the output energy on the order of 100 joules. This laser's development was sponsored by the Air Force Space Technology Center through the Eastern Space and Missile Center and the objective was to generate a relatively long pulse, around 6 millisecond pulse, that would have certain other specifications and characteristics that would have divergence, for example, on the order of 30 times diffraction limited which doesn't particularly challenge us and for alexandrite which is able to do that and essentially halve the divergence requirement. The important thing to point out is that through a oscillator amplifier system that we were able to meet these specifications and provide a laser on the order of 100 joules. Also I would like to show you the temporal characteristics of the laser. The objective was that the laser would have a 6 millisecond pulse and that was the ultimate pulse duration that we were able to achieve. The objective was for the temporal pulse profile to be flat and we did have a few problems in getting and keeping it flat, but during the course of this work we have subsequently learned what the difficulties were and now, presently in the course of a phase 2 program, to develop a laser that is four times the size of the earlier one. I also want to show you the nature of the cross-section profile from that laser, which was essentially a top-hat profile characteristic for the multimode alexandrite laser. It's of particular interest for applications where you wish to illuminate at a distance and you'd like to have a more uniform pattern over the target. So the multimode alexandrite laser can be designed to provide a very uniform pattern. These are some of the things that we've been involved in and found very interesting and look forward to some degree of success. I would like to close at this point so that we can have an opportunity to carry on discussions. Thank you very much.

D. F. Heller: Are there any questions for the speaker?

Question from L. Chase: I just wonder, John, do you see any critical demand for alexandrite for medical purposes? Is there an alexandrite medical laser that is on the horizon or do you really need a quite different laser for different things?

J. C. Walling: Yes you do. I believe it is correct to say that within the medical area there is a need for a number of different types of lasers. They would like to have it all in one and perhaps Bob can tell us how to do that, but it is true that the lasers that are sought are sought over a very broad range and with a great number of different characteristics that include not just wavelength variation but also pulse duration variation and pulse duration is extremely important in the interaction process. So there is a great deal of opportunity there.

D. F. Heller: In order to open up the meeting more broadly, I'd like to take a couple of minutes to summarize quickly where we sit. We asked initially three questions: what is the status, where are

tunable solid state lasers going, and why should we care? As I understand from our speakers, at present, there are two sorts of commercially available lasers, presently color center lasers, of which precious little here has been spoken, and which I won't begin, and alexandrite, at this point, available from John Walling's company, and a few other places, I'm not aware of the development status of those, but I know there are some other companies attempting to develop commercial tunable solid state lasers. In the wings, we have titanium sapphire, which a fair amount of development has been put into in recent years, and that appears to be looking promising, for some other applications and I direct people who are interested in that also to various recent issues of JQE. Down the road, we discussed that there will be a variety of new vibronic lasers available. Just which ones will make it into the commercial world, I think it's safe to say that it's hard to speculate. It takes many years of development both of materials and spectroscopy and all of the other physical understandings that have to go into making new tunable solid state lasers. They'll probably be moved into the commercial arena, those that are successful; perhaps emerald, perhaps a few others. As they become available, they'll be moved more quickly than the first ones were, but I think it is safe to say that right now it's going to be some years before any new entries emerge. In the farther distance, perhaps, but looking promising, are diode pumped and solid state laser pumped OPOs which R. L. Byer talked about. They look very promising at least for low power applications and maybe even farther down the road, for higher power applications. Where are they going? There was tremendous agreement by everyone on the panel about what the most critical problem areas are that none affect the development of tunable solid state lasers: Dick Powell showed us how it is the spectroscopy, and perhaps admitting too to the fact that crystal growth is a major driver, and both are. I think it's safe to say that it's really pretty hard for either of those alone to drive everything. Enlightened crystal growth is of critical importance because you can't grow everything. It's the rate limiting step, in effect, in tunable solid state technology development, no question. Bruce Chai, who's one of my colleagues at Allied will talk some more about that and some new developments here tomorrow. The spectroscopy, though, does answer certain questions that simply can't be prejudged by the crystal grower, what excited state absorption is, for example, what are the effects of several different sites and materials on the laser performance. Lloyd Chase felt that, of course, one of the major drivers was the laser characterization and spoke to that. It is true that the only way you can assess how good a tunable solid state laser or any other laser is, is to make one and see. To do that you have to be reasonably enlightened in what figures of merit you use to compare all of the various characteristics of these rather different lasers, and it is a challenge to do that carefully. I'm glad that he did put that in some perspective for us. R. L. Byer talked about the importance of diode pumping and inferentially. The efficiency that can be realized by doing that. To be sure, frequency conversion of these lasers is

important because not everyone is interested only in spectral regions where a tunable solid state laser's fundamental frequency might be. All of these tunable sources are limited. It may be that the world comes to developing and commercializing five or ten different tunables. It may be the world gravitates toward using OPOs. It may be that there are other nonlinear processes that can be used to make one tunable solid state laser device or system the chosen path, and only time will tell. I have a word or two to say about that in a second. John Walling brought out that a lot of the emphasis in what gets developed is driven by the applications that emerge and by the markets. He's in the fortunate circumstance of having a relatively well developed laser material, from the point of view of physics and spectroscopy and crystal development, but he has to build and develop lasers for the commercial market and what form and substance they will take is largely driven by the whims of the community, of which you are all a part. It was good to see, by the way, that given four panel members, we had "unanimous agreement", that each of four different components was the most important in advancing the development. That is the nature, I think, of the beast.

In determining which applications develop one of the key issues is simply what laser wavelengths are available. That's what is driving tunables right now. That's why it's tunables. That's what developed dye lasers. The applications in each case, as L. Chase brought out, are driven largely by requirements for a particular spectral frequency. For research, or for medicine, as John Walling showed, perhaps a range of frequencies. One laser can't do it all. Although, it may turn out that with nonlinear methods one laser, such as alexandrite, can be used to make tunable light in virtually any region of the spectrum. Methods for doing this could be developed with titanium sapphire or, in principle, for other tunable lasers. But it is important to realize that, apart from OPOs that certainly seem very interesting for a present low power applications, that there are ways to get high power laser output at virtually any wavelength by using nonlinear methods in conjunction with presently known tunable solid state laser materials approaching 100% photon efficiency into the Stokes lines has been demonstrated using intracavity tunable solid state lasers. This shows that frequency conversion over much of the visible and IR can be achieved efficiently from a single tunable source: alexandrite's fundamental, it's first anti-Stokes, it's second anti-Stokes, were produced all of these tunable as the fundamental tunes.

The other thing driving the technology is, of course, not tunability, but the fact that these lasers can reach high peak and average powers. After all, there are perfectly good relatively inefficient, relatively low power, commercially available tunable laser sources, and many of you have them in your laboratories and have used them for many years. Why is something better needed? Well, for many of your applications, maybe nothing is, but for a large number of applications that were talked about today, clearly

something else is needed. This slide shows alexandrite laser it's a tunable solid state laser and it's melting this cinder block with about 100 watts of average power. This, from a single oscillator that is, as you can see, a very simple device. This one consisting of two mirrors and a pump chamber for a laser rod is operating at about 1 joule output and 100 hertz. The beauty of tunable solid state lasers, is their inherent simplicity and that's what permits us to contemplate their wide scale and wide-spread use not only as laboratory devices but as efficient devices for industry and medicine. And in fact, as the final summary, that is why we should care. Frequency agility implies, together with other properties like efficiency and high average power, that there will be new applications. Those we know now and those we don't, both in industry and in medicine and certainly in research as well. So, like all of the other laser technologies that have led before, tunable solid state lasers will follow this rather involuted road where the research drives the laser advancement and this advancement in turn drives new research and new applications. So with that I'd like to close this section of the panel discussion and open the meeting to further discussions from both the panel members and from any members of the audience. I hope you'll take part in it and I hope you won't be shy of asking questions of any of our panel members.

L. Chase: I think you mistook our diversity for disagreement. Dick and I were just trying to be orthogonal.

D. F. Heller: That may be but I think there is disagreement in the field and I think that's good. There are a lot of perspectives on what the most important questions are.

L. Chase?: I don't think either of us thinks that crystal growth and spectroscopy is more important than characterization.

D. F. Heller: I'm sure that's true, nor, in fact than laser development. The beauty of it is that it's now an advanced enough field so that this has become clear to any of us who may have earlier had other expectations: it just is not easy to make a good commercial quality laser or a good laser for any application.

Question from J. C. Walling: I have a question for Dr. Byer, if I may. I wonder, going back to the point I was raising regarding the dye lasers in the medical area. The major reason why they are so prevalent is that in the middle of the visible region there is a need for basically a tunable CW source. That gives you the maximum flexibility with respect to pulsed duration. Generally only a few watts are needed and of course there are applications where high peak power is required but there are many of the applications, particularly for eye surgery and for port wine stain and for some of these other applications and ophthalmological applications that require powers that are very modest. Could you comment on the practicality of achieving that in the next 2 or 3 or 4 years?

R. L. Byer: It's a good question and one that has interested not only the medical community but the community that likes to entertain the world. If you look back at coherent radiation from radios to microwaves to lasers and ask what is the biggest business opportunity in coherent radiation it is always historically been the entertainment business and my students have been interested in generating CW radiation at 455 nm not for submarine communication, which has no market whatsoever, but as the blue light source to be part of the blue, green and red projection system for high definition television. And what you need if you want to fill a movie theatre screen with high definition television images, which will be the way you will see movies in 4 or 5 years, is you need 3 watts of each primary color, CW and then modulated at 20 megahertz so that you can write and paint the images on that screen. So we purposely chose a diode pumped YAG laser at 20 watts of CW power such that we could follow that laser with the nonlinear harmonic conversion steps that I've mentioned and generate 3 watts of blue, 3 watts of green and 3 watts of red to allow us to project high definition television images. If I can generate those colors, I can also use the techniques of parametric devices to generate tunable CW radiation across the visible spectrum and I think that will follow shortly.

Question from floor: We are presently using the YAG laser to pump the dye laser for tuning. What is the advantage of the OPO over this?

R. L. Byer: The good news about the tripled YAG pumped dye laser or the doubled YAG pumped dye laser has been they've opened up a tremendous investigation of research and development over the last decade, but without exception they have not made the jump into commercial applications. You ask the question, why. The answer is that dye lasers by their nature aren't reproducable and don't tend to like to run for extended periods of time without some attention from a chemist or a physicist. On a production line on which you need to monitor something for a 1000 hours at a time at 99% operational reliability, it's not very easy to engineer a dye laser to do so. It is possible, and Livermore has engineered a dye laser that does exactly that for their application, but that's an application that doesn't meet a lot of needs where cost is a major driving factor. I think you'll find that the solid state laser approach will begin to interest a much wider application community because the devices are inherently reproducable, they're inherently long lasting, they're solid state, and that means they're beginning to meet a lot of the other requirements that make a product possible or an application possible. I gave you some room on that, Lloyd.

L. Chase: I object to these snide comments about Lawrence Livermore and money. Only Allied Signal can work on emerald lasers, right?

D. F. Heller: I think there may be some question to that. Our budget is finite also and I think that's one of the points with any of these technologies and their evolution are strongly money driven to get them to a point where they makes sense in an application requiring a high degree of refinement. An awful lot of money has gone into the engineering of dye lasers over the last 20 years or so and in the last 10 years, a fair amount of money, not nearly as much, has gone into the development of one, perhaps two, tunable solid state lasers. I think that you see some of that discrepancy at this time by the relative numbers of tunable solid state lasers that are out there in the user community compared to dyes. Would anyone like to speak, in fact, to the time scale that they think tunable solid state lasers are going to be broadly available to the users? Are they now? John, if someone here wanted to order 100 of them, would you be able to supply them with them next month?

J. C. Walling: Well, if they give us money up front, they'll have them. They are available at this point. It's a question of 3 or 4 months delivery time presently.

Question from Andy Tam: What about titanium sapphire. When will that be available?

J. C. Walling: Well, I would hesitate to speak for anyone else, I don't know what the plans truly are. From us it would be a little difficult to state at present but I would put it in terms of approximately a year, 6 months or a year, whatever.

Question from Andy Tam: Do you know how much that will cost per watt?

L. Chase: The trouble with titanium sapphire for scientific use is it's too easy to build them. I mean, we're building one in our lab right now. It's hard to get a market going when they're that easily put together.

D. F. Heller: I'm not sure. I think most of the community is driven by people who don't want to build their lasers. I mean, all of us up here do that and we all play with them and don't think too much about it. But having, myself, come from photochemistry background, you don't generally think, when you want to set up an experiment and do other hard things that may involve molecular beams or other rather tricky pieces of apparatus that you want to sit there and deal with the technology that you are not expert with nor equipped to handle the subtleties and diversities of, so I think it is important, exactly, that someone in the community seizes on that question with Ti:sapphire. The same statement, of course, could be made about alexandrite. It's terribly easy to buy and set up, yourself, an alexandrite laser and it will, but run in some highly nonoptimum fashion.

R. L. Byer: I think you're comparing a flashlamp pumped laser with

a laser pumped laser and it's much different technology.

D. F. Heller: That's true, but, nonetheless, I think somebody has to make a box, somebody has to make something that's relatively user friendly, just like with computers.

Question from Andy Tam: Is someone developing Ti:sapphire lasers in such a box?

D. F. Heller: I'm sure someone's working on it. I can virtually guarantee that.

Dick Powell: I think there are a couple of small companies like Larry DeShazer's company that will make you one if you want one. It depends on whether you want to have the krypton laser to pump it or you have one of your own. Because it is a laser pumped laser, it is a different ball game, in terms of buying one. It would be easy to buy the sapphire laser if you don't want the pump laser.

D. F. Heller: After all, it look a little bit more like dye laser technology with the box you put in front of something else for CW dye lasers.

Question from Bill Stwalley: You can ask the same question about a system that includes a tunable solid state and the OPO. When will that be available commercially?

R. L. Byer: Well, the first step in that, to ask the question is, are diode pumped solid state lasers commercially available now? The answer is that two years ago at the CLEO Conference there were at least seven start-up companies in diode pumped solid state lasers and today all seven exist and there are commercial diode pumped solid state lasers being delivered in reasonable numbers, meaning greater than 10s per month, out of each of these companies. Green radiation is now available, that is you can frequency double these sources, so the answer is, the first steps along that path have now been taken. Will there be a big enough market to drive the tunable source? That we have to wait and see but it's not much more difficult technology to make the tunable source once you have the harmonic generation products available. I might mention that I visited a number of laboratories in Japan in August and in virtually every lab I visited, was a diode pumped YAG laser frequency doubled to the green, so the technology is being investigated there at quite some length and quite rapidly for applications to read memory and compact discs.

D. F. Heller: I think it is an interesting observation that the larger laser companies in this country, commercial laser companies, have not been driving the new laser technologies, that they have been largely driven by small new venture start-up kinds of companies. Does anyone see a clear reason for that?

R. L. Byer: The reason is actually a very interesting economic reason. It's not hard to discern. If you're a large company, you're interested in markets that at least impact your bottom line to the degree that it shows up at the end of the year. Otherwise it doesn't make much sense to pursue that market and the risks are very high in pursuing new markets. Small companies don't need to have such large markets to justify either their existence or the development of new niche products, that might have the opportunity to grow large. The way our country is structured, if you start a small company, and it's successful, chances are very good you'll be purchased by a larger corporation when the market is established and the economics are known.

D. F. Heller: That's a philosophy that's done our steel industry a lot of good in the past, hasn't it?

R. L. Byer: It's been the philosophy in the laser industry, it's been the philosophy in the semiconductor industry. In the way our system is structured, that's the way it's tended to work.

D. F. Heller: I think you're right and it's pervasive for better and for worse.

R. L. Byer: It works pretty well because you give an opportunity for small companies to explore the market place in a myriad of different ways and those that are successful can either grow on their own or be purchased by larger companies when and if they need the economic resources to grow to a larger market scale.

D. F. Heller: Well, we have some fraction of the market place here, maybe we could take a market survey and find out... That would be interesting. How many people here have any interest at all in seeing one of these kinds of beasts of any of the sorts heard about in their laboratory in the near term. So not everyone is happy with present technologies.

Question from Jerzy Krasinski, Allied-Signal: I just wanted to point out that alexandrite, even before Ti:sapphire was pumped, and efficiently, by dye lasers and that diodes now exist that appear to be suitable for pumping alexandrite lasers.

L. Chase: I was going to ask Bob... You mentioned 400,000 diode lasers a month. I don't know what the power of those is. How does this figure into this 10^6 1 watt diodes a year. When do you think that will happen?

R. L. Byer: Let me give you the numbers as I understand them. Sony last year produced 400,000 diode lasers a month of the 10 milliwatt variety. These are index guided diode lasers particularly for compact discs. The production cost of those lasers is about $2. $1 goes for the case that holds the diode laser chip and the rest is the cost of the chip and the mounting. The MOCVD technol-

ogy, the reactor technology that is in place to build the 10 milliwatt laser is identical to the technology required to make a one watt laser. In fact, it is technically easier to construct a wide-striped one-watt laser than it is to construct a gain-guided 10 milliwatt laser. So it's not that the facilities are not in place, they are in place, it's that the market has to grow to a size such that the volume is up and the price can begin to fall. Will that happen? I think the answer is yes and it will happen in a time frame that has been understood in the semiconductor industry for more than two decades. And that time frame is traditionally that in semiconductors, whether you're buying memory, or you're buying power transistors, the performance improves a factor of two every year, and the price falls a factor of two every year and so you gain a price per performance of four each year. Now, I took that same number and tested it on the producers of diode lasers and asked them, has that been their experience, and it turns out, it has been. If you look at the price per performance of the gallium arsenide diode lasers that are in production now, a factor of four per performance number has held in the gallium arsenide diode laser business, and so the laser market is no different than the market in electronics that historically has been used as a guideline.

L. Chase: Except that the packaging here is a bit more crucial. If you want to get rid of one watt of electrical power in a diode laser, than that becomes a limiting problem rather than the MOCVD technology.

R. L. Byer: The packaging to remove the heat has indeed been a learning curve problem and that's what's held up the production of the one watt lasers until recently. One watt diode lasers are now being produced and the heat removal problem is solved to a degree not to the degree that a number of us would like, but you can buy one watt diode lasers that will last a few thousand hours if you operate them at room temperature and last 20,000 hours if you operate them at 10 degrees C. One watt is not a limit and the heat removal problem is being addressed both by all of the diode laser manufacturers and there are techniques including growing diamond heat sinks? and using the high thermal conductivity of diamond that are being approached as ways to remove the heat from each of these chips. The approach that we took is to couple diode lasers to fibers so that we separate the heat removal problem of heat from the diode laser by having the diode lasers distributed in their own power supply package. That becomes a separate engineering problem from the problem of removing heat from the YAG laser or glass laser or whatever other laser medium is being pumped by the diode laser radiation.

D. F. Heller: Well, that is a good point, isn't it, but you don't expect, certainly, the time scale factors for heat removal to go at the same rate as semiconductor development.

R. L. Byer: Semiconductor development has also been paced by heat

removal problems in exactly the same way and it has, in fact, been the heat removal technology in the semiconductor industry that is being applied to the heat removal in diode lasers. I expect them to go at the same rate.

D. F. Heller: No, I was speaking also to the fact that when you couple all of these into some solid state crystal and later into some OPO, then you have a problem that may be dealable with similar kinds of techniques but appears unlikely to scale that way. You'll hit some limits that may be hard to get around.

R. L. Byer: No, you need to think about it differently. The answer is the scaling and the heat removal will go along the same path. We can today build lamp pumped solid state lasers that operate at CW output powers of 1 1/2 to 2 kilowatts, neodymium YAG lamp pumped devices. The heat removal problem of those is about a factor of 5 worse than if they were diode laser pumped. So for free, I get a factor of 5 in performance improvement by diode pumping over lamp pumping. Is that the limit? The answer is no. There's a series of techniques that evolved over the last decade in slab laser technology which are heat removal techniques that allow you to scale these devices to much higher average powers. If you remember, it was three CLEOs ago that John Emmett was finally able to talk about average power solid state lasers approaching 50, 75 or 100 kilowatts. I didn't talk about, because of a lack of time, a 1 kilowatt module that we're working on that eventually will be diode laser pumped and not lamp pumped. But the lamp pumped devices are already in the laboratories being investigated. The diode pumping will occur later when the diode prices become appropriate. I don't believe there will be thermal limits that will set an absolute limit on the average power scalability of the laser source.

D. F. Heller: So, then, you believe that we'll have multikilowatt laser systems of that sort within the next 10 years.

R. L. Byer: Yes, there will be multikilowatt sources and there will be coherent sources and there will be the possibility of coherently adding the sources whether you coherently add the radiation in the diode array itself, which is a problem being pursued in a number of labs in the United States, or you coherently add the radiation in a solid state laser which has also been demonstrated, that is, independent CW YAG lasers of the type that I've shown have now been coherently added. The E fields have been added with greater than 95% efficiency. So you have the ability to scale in another way and that is to build modular lasers at the kilowatt power level or 100 watt power level or whatever and coherently add the radiation to gain a higher overall power while maintaining diffraction limited radiation. I told you I was going to talk about incredible lasers tonight, I need some way to wake up this audience.

D. F. Heller: I think everyone here hopes you are right. Maybe

everyone is just awe-struck.

Question from R. C. Morris, Allied-Signal: You talked about a factor of 4 in price to performance every year in semoconductor lasers. There's a lot of money in the communication business, but is there sufficient drive to carry the diodes needed for laser pumping at that same rate? Is there enough money in this business?

R. L. Byer: I think the answer is yes. It's a chicken and egg problem. Is there enough market to be able to drive the volume to get the prices down to open up new markets and that's been the problem that's been discussed the last four years in diode pumped solid state lasers. I didn't know the answer to that question until recently and I think recently, in the discussions I've had with companies in Europe and Japan, the answer is yes. The market potential is there to drive the diode pumped solid state laser and the harmonic processes as well as to continue to drive the diode laser industry directly.

Question from R. C. Morris, Allied-Signal: What is that market?

R. L. Byer: I gave one example. I think the entertainment business is the main driver, the up front driver and the one that in fact receives the most investment, in Japan, for example. Following that, it's the business of, I'll say broadly speaking, communication meaning computers and digital storage and communication links will be another market that will follow that one. There's a materials processing market that's equally as big and that's a whole other market that will drive and grow. I think J. C. Walling's figures show that as the case. A better way to say it, maybe it was the way it was said two years ago in the Laser Focus article that Gary Klaumenser published, is he plotted the growth of the laser industry versus the growth of the computer industry, only he shifted the axis of the laser industry 15 years and those industries grow at the same rate. Now most people would say that's unbelievable. There will never be as many applications for lasers as there are for computers in society but the answer is, historically, they're growing at the same rate and you can identify markets in the laser industry that are at least as big as the computer industry market.

Question from R. C. Morris: Well with the 15 year offset they never will be as big.

D. F. Heller: Well, something may saturate somewhere, but I think it is a good point that a lot of the development now as things go down the path from research toward initiation into commercialization the development becomes a very much more expensive process and must by necessity become driven by the demand of the market place. I think it's also fair to say that at this time, the market for tunable solid state lasers in particular, is effectively zero, so that's one of the things that clearly has to change and as the

quiet user, maybe Dick Powell might want to make a comment. You've been staying aloof and quiet recently, maybe out of wisdom.

Dick Powell: No comment, but let me pursue asking Bob questions, since that seems to be the way this is going. Bob, what happens if you pump one of your OPOs with a tunable laser source like alexandrite, does that help expand the tuning range?

R. L. Byer: It makes the tuning easy, assuming that the tunable laser behaves itself. In 1974, Richard Wallace used a dye laser to pump a lithium niobate OPO and he tuned the Rhodamine 6G dye laser wavelength but left the lithium niobate parametric oscillator parameters fixed and as a consequence you get tunable signal on either output without doing anything to the nonlinear crystals so it's a very convenient frequency converter much like Raman process that just is a fixed nonlinear element so that's a way to also extend the tuning range.

D. F. Heller: Well, unless there is some very pressing new question, perhaps we could just thank our panel members for a very lively and enlightening discussion and adjourn to tomorrow's session, which, I should mention, will continue with some considerable discussion of new developments in solid state lasers as well as several other sessions on applications of all lasers. Thank you all for your attendance.

I. LASERS AND COHERENT SOURCES

I.A. New Developments in Solid-State Sources

I.B. Novel Laser Systems--Modifications to Visible, Ultraviolet, and X-Ray Lasers

I.C. Spectroscopy of Materials for Solid-State Laser Systems

I.D. Modeling of Lasers and Laser Dynamics

LASER AND SPECTROSCOPIC PROPERTIES OF CHROMIUM-ACTIVATED FORSTERITE

V. Petričević, S. K. Gayen* and R. R. Alfano
Institute for Ultrafast Spectroscopy and Lasers
Departments of Physics and Electrical Engineering
City College of New York
New York, NY 10031

Abstract

Room-temperature pulsed laser action has been obtained in chromium-activated forsterite ($Cr:Mg_2SiO_4$) for both 532-nm and 1064-nm pumping. Free running laser emission in both cases is centered at 1235 nm and has bandwidth of ~ 30 nm. Slope efficiency as high as 22% has been measured. Using different sets of output mirrors and a single birefringent plate as the intracavity wavelength-selecting element tunability over the 1167-1268 nm spectral range has been demonstrated. Continuous-wave laser operation at room temperature has been obtained for 1064-nm pumping from a cw Nd:YAG laser. The output power slope efficiency is 6.8%. The gain cross section is estimated to be 1.1×10^{-19} cm^2. Spectroscopic studies suggest that the laser action is due to a 'center' other than the trivalent chromium (Cr^{3+}), presumably the tetravalent chromium (Cr^{4+}) in a tetrahedrally coordinated site.

I. INTRODUCTION

Recently, we have reported room-temperature pulsed laser action in chromium-doped forsterite ($Cr:Mg_2SiO_4$) for both 532-nm and 1064-nm excitation.[1-4] Laser emission is continuously tunable over the 1167-1268 nm spectral range,[5] with a potential for extending the tuning range beyond 1300 nm. This wavelength range is of great importance in optical communication and eye-safe ranging. The large bandwidth of the laser emission promises generation of ultrashort pulses through mode-locked operation. Large crystals of chromium-doped forsterite can be grown by Czochralski method, which means that this crystal has a potential to be used as an amplifier medium in the near infrared. Furthermore, the successful cw laser operation[6] of Cr forsterite has the practical implication that various types of laser and amplifier designs are possible.

On the other hand, spectroscopy of chromium-doped forsterite is very unusual and intriguing. It is the first chromium-activated laser crystal, to our knowledge, where the tetravalent chromium ion (Cr^{4+}) in a tetrahedral site is presumably responsible for laser action in the near infrared.[7]

In this paper we review the lasing and spectroscopic properties of this new and important tunable solid-state laser crystal.

II. CRYSTAL PROPERTIES AND SPECTROSCOPY

Forsterite is a member of the olivine family of crystals. A unit cell of forsterite has four formula units in an orthorhombic structure of the space group Pbnm. The unit cell's dimensions are: a=4.76Å, b=10.22Å, and c=5.99Å. The Cr^{3+} ion substitutes for the Mg^{2+} ion in two distinct octahedrally coordinated sites: one (M1) with inversion symmetry (C_i) and the other (M2) with mirror symmetry (C_s). The occupation ratio of the two sites by the Cr^{3+} ion is M1:M2=3:2.

Both the single crystals of $Cr:Mg_2SiO_4$ used for spectroscopic and laser experiments were grown by the Czochralski method at the Electronic Materials Research Laboratory of the Mitsui Mining and Smelting Co., Ltd., Japan. The first crystal, referred to as sample 1 hereafter, is a 9mmx9mmx4.5mm rectangular parallelepiped with the three mutually orthogonal axes oriented along the b, c, and a crystallographic axes of the crystal. It contains 0.04 at . % of Cr ions which is equivalent to a chromium ion concentration of 6.9×10^{18} ions/cm^3. The second crystal (sample 2) is a 6mmx6mmx30mm rectangular parallelepiped with the three mutually orthogonal axes oriented along the a, b, c, crystallographic axes of the crystal. It contains 2.8×10^{18} chromium ions per cm^3. The 6mmx6mm faces of the crystal were broad-band anti-reflection coated, such that the reflectivity over the 1050-1250 nm spectral range is less than 0.5%.

The room-temperature fluorescence and absorption spectra of $Cr:Mg_2SiO_4$ taken with sample 1 for E||b axis are shown in Fig. 1.

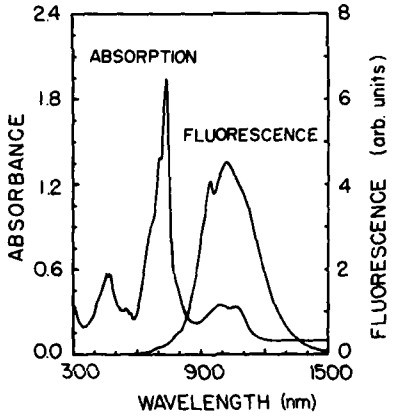

Fig. 1. Absorption and fluorescence spectra of $Cr:Mg_2SiO_4$ at room temperature. Both the spectra were taken for E||b axis and excitation along a axis. The thickness of the sample along a axis is 4.5 mm.

The room-temperature fluorescence is a broad band covering the wavelength range from 680-1400 nm. The absorption spectrum is characterized by two broad bands centered at 740 nm and 460 nm, attributed to the $^4A_2 \rightarrow {}^4T_2$ and $^4A_2 \rightarrow {}^4T_1$ transitions, respectively, of the Cr^{3+} ion. The broad, weak absorption band spanning the 850-1200 nm range is similar to the one observed in chromium-doped GSGG[6] and is attributed to transitions between states in another 'center', presumably the tetravalent Cr^{4+} ion in a tetrahedral site. This

absorption band overlaps a significant portion of $Cr:Mg_2SiO_4$ emission, and inhibits laser action in that region.

The absorption and fluorescence spectra of the 'center' in the near infrared spectral region are shown in Fig. 2. The room-temperature absorption spectrum is a double-humped band covering the 850-1200 nm wavelength range. The room-temperature fluorescence spectrum, excited by 1064-nm radiation from a cw Nd:YAG laser extends from 1000-1400 nm and peaks at 1140 nm. At liquid nitrogen temperature both the spectra show a sharp zero-phonon line at 1093 nm followed by elaborately structured sidebands. The fluorescence lifetime is 15 μs at room-temperature and 20 μs at liquid nitrogen temperature.

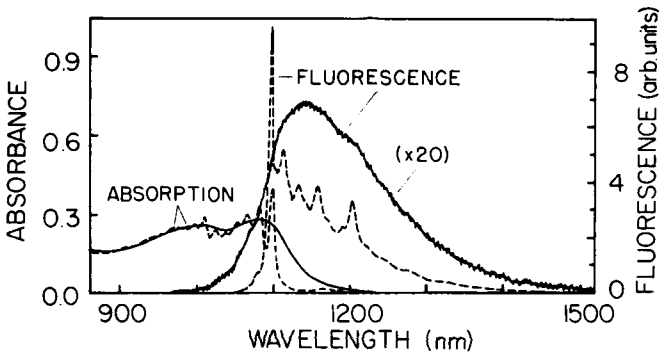

Fig. 2. Near infrared absorption and fluorescence spectra of $Cr:Mg_2SiO_4$ for 1064-nm excitation at room temperature (solid line) and liquid-nitrogen temperature (broken line) for E||b axis.

III. PULSED LASER ACTION

The first laser experiments were conducted with sample 1 in a stable cavity. Details of the cavity arrangement have been described elsewhere.[1] The fundamental and the second harmonic emissions from a Q-switched Nd:YAG laser operating at a 10-Hz repetition rate were used for excitation of the near-infrared and the visible bands, respectively. Pulsed laser action was observed for both the 1064-nm and the 532-nm pumping[4,7] at or above the respective thresholds of 1.25 mJ and 1.37 mJ of absorbed energy. The amplitude and duration of the $Cr:Mg_2SiO_4$ laser pulse, as well as its delay with respect to the pump pulse, varied with the pulse-to-pulse energy fluctuation of the pump pulses. However, for similar level of excitation and within the time resolution of the experiment, there was no appreciable difference in the delay between the pump pulse and the output laser pulse for the two pump wavelengths. The spectra of the free-running Cr:forsterite laser for both 1064-nm and 532-nm pumping peaked at 1235 nm and had FWHM of 30 nm and 27 nm, respectively. These facts clearly indicate that the same 'center' is active in laser action for both the 532-nm and 1064-nm excitations. For 532-nm pumping there is a fast transfer of excitation from the levels directly pumped to the lasing level. In case of 1064-nm pumping, the lasing level is directly populated. The output power slope efficiencies were 1.8%

for 1064-nm pumping and 1.4% for 532-nm pumping, indicating high losses in the cavity.

To improve the laser performance by reducing the losses anti-reflection-coated sample 2 was used, and care was taken to overlap the pump beam and cavity mode accurately. The sample was longitudinally pumped by the fundamental 1064-nm, 10-ns pulses from a Q-switched Nd:YAG laser in a cavity similar to that used earlier. An output power slope efficiency of 22% was obtained using an output coupler having 87% reflectivity over the lasing region.

IV. TUNABLE OPERATION OF FORSTERITE LASER

Tunable operation of Cr:forsterite laser has been obtained over the 1167-1268 nm spectral range.[5] A single birefringent crystalline quartz plate was inserted in the cavity at Brewster's angle with respect to the cavity axis as the intracavity wavelength-selective element. Smooth tuning over the 1167-1268 nm spectral range was obtained by rotating the tilted plate about an axis perpendicular to its surface and the result is displayed in Fig. 3.

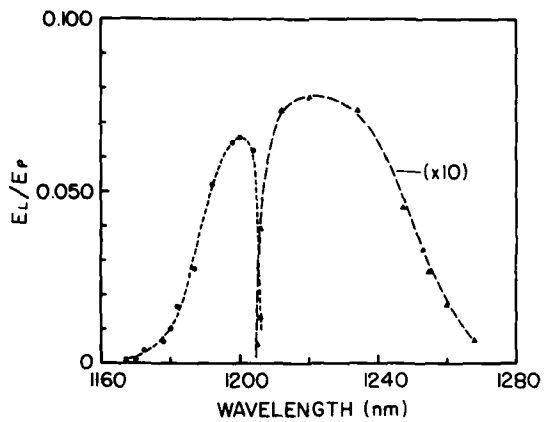

Fig. 3. The ratio of Cr:forsterite laser output (E_L) to the absorbed pump energy (E_p) as a function of wavelength. The curve to the right was taken with an output coupler having 98% reflectivity for 1200-1300 nm range, and one to the left with an output coupler with reflectivity that varied from 99% at 1150 nm to 87% at 1200 nm.

At the peak of the tuning curve at 1220 nm, the output laser energy is ~ 7 μJ/pulse for an absorbed pump energy of 0.9 mJ/pulse. Similar tunable operation has been obtained for 532-nm pumping as well.

IV. CW LASER OPERATION

To obtain cw laser action in Cr:forsterite, sample 2 was placed at the center of a nearly concentric cavity formed by two 5-cm radius mirrors. The output mirror had ~ 1% transmission for the 1175-1250 nm range. The 1064-nm radiation from a cw Nd:YAG laser was focused

by a 75-mm focal length lens to longitudinally pump the sample along the 30-mm path length. The pump beam propagated along the c axis and was linearly polarized along the b axis of the crystal. The pump beam was chopped at a duty factor of 9:1 to reduce heating effects. When the pump beam was not chopped, the Cr:forsterite laser operated at 40% reduced power, indicating the effect due to local heating.

Quasi-cw laser operation was readily obtained for pumping above the lasing threshold of 1.25 W of absorbed power. The spectrum of the free-running cw Cr:forsterite laser peaks at 1244 nm and has a bandwidth of 12 nm.

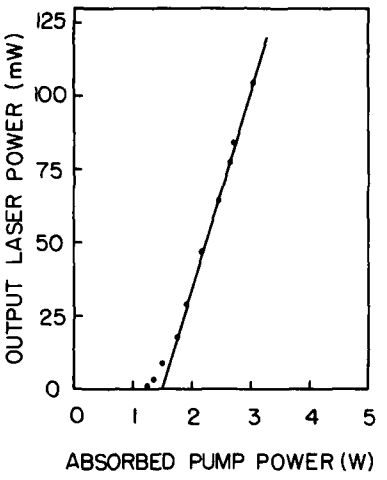

Fig. 4. Output power of the cw Cr:forsterite laser as a function of absorbed pump power.

The cw output power of the Cr:forsterite laser as a function of the absorbed pump power is displayed in Fig. 4. The measured slope efficiency is 6.8%. The experimentally obtained values of the absorbed pump power at the threshold and the slope efficiency together with known mirror reflectivities have been used to estimate a number of key laser parameters. The round-trip cavity loss is estimated to be 12.7%. The effective emission cross section is $\sim 1.1\times10^{-19}cm^2$, and threshold inversion density is $2\times10^{17}cm^{-3}$. Important laser and spectroscopic properties of Cr:forsterite are summarized in Table 1.

TABLE 1 Spectroscopic and laser properties of Cr:forsterite

Property	Value
Major pump bands	850-1200 nm, 600-850 nm, and 350-550 nm
Fluorescence band	680-1400 nm
Room temperature fluorescence lifetime	15 μs
Cr-ion concentration	~ $7x10^{18}$ions/cm^3
Lasing wavelength (center)	1235 nm (pulsed) 1244 nm (cw)
Spectral bandwidth	~ 30 nm (pulsed) ~ 12 nm (cw)
Slope efficiency	22% (pulsed) 6.8% (cw)
Tuning range	1167-1268 nm
Effective emission cross section	$1.1x10^{-19}cm^2$

V. ACKNOWLEDGEMENTS

We would like to acknowledge K. Yamagishi, H. Anzai and Y. Yamaguchi of Mitsui Mining and Smelting Co., Japan for providing us the crystals used in these measurements. The research is supported by Army Research Office, National Aeronautics and Space Administration, and City College of New York Organized Research.

*Present Address: Department of Physics and Engineering Physics, Stevens Institute of Technology, Hoboken, New Jersey 07030.

REFERENCES

1. V. Petričević, S. K. Gayen, R. R. Alfano, K. Yamagishi, H. Anzai, and Y. Yamaguchi, Appl. Phys. Lett. 52, 1040 (1988).
2. V. Petričević, S. K. Gayen, and R. R. Alfano, Phot ıics Spectra 22(3), 95 (1988).
3. V. Petričević, S. K. Gayen, R. R. Alfano, K. Yamagishi and K. Moriya, in Proceedings of the International Conference on Lasers '87, F. J. Duarte, Ed., STS, McLean, VA(1988), p. 423.
4. V. Petričević, S. K. Gayen, and R. R. Alfano, Appl. Opt. 27, 4126 (1988).
5. V. Petričević, S. K. Gayen, R. R. Alfano, Appl. Opt. (submitted).
6. V. Petričević, S. K. Gayen, R. R. Alfano, Optics Lett. (submitted).
7. V. Petričević, S. K. Gayen, R. R. Alfano, Appl. Phys. Lett. (to be published).
8. J. A. Caird, M. D. Shinn, T. A. Kirchoff, L. K. Smith, and R. E. Wilder, Appl. Opt. 25, 4294 (1986).

LASER DIODE PUMPED 1μ Nd:YAG AND Nd:BEL LASERS

R. Scheps, P. Poirier, and J.F. Myers
Naval Ocean Systems Center, Code 843, San Diego, California 92152

D.F. Heller
Allied-Signal Inc., Corporate Technology Center, PO Box 1021R,
Morristown, New Jersey 07960

ABSTRACT

Performance data for laser diode-pumped cw Nd:YAG and Nd:BEL lasers are presented. Two single stripe laser diodes are used as the pump source, each emitting 1 W in the pump band. The heat sink for the lasers is temperature controlled to allow for wavelength tunability. The resonator is based on a hemispherical design. Output and pump threshold measurements were made and gain and loss for Nd in both hosts were measured. The output power from the Nd:YAG rod was in excess of 870 mW with a slope efficiency of 58% and an overall electrical efficiency of 13%. In Nd:BEL, the output power was in excess of 635 mW with a slope efficiency of 49% and an electrical efficiency of 9.5%.

INTRODUCTION

Of the various hosts for diode pumped Nd based lasers, BEL offers several unique advantages. These include a relatively broad spectral absorption bandwidth, a lower sensitivity to laser diode wavelength than Nd:YAG, and the capability of being made athermal. In addition, the crystal growth and polishing technology of this material is relatively mature. Unlike some other hosts, the absorption bandwidth is centered near the Nd:YAG absorption band, so that in many cases the same diode pumps can be used for both BEL and YAG. In this work we present a comparative study of laser diode pumped cw Nd:BEL and Nd:YAG. We show that both hosts perform well, and specify under what conditions BEL might be the better host.

EXPERIMENT

The outputs of two 1 Watt laser diodes were collimated and combined using a polarizing beamsplitter cube. The laser diodes are mounted on active heat sinks for wavelength control. The output spectrum of the laser diodes was measured with an OMA and typically show eight longitudinal modes operating simultaneously with a total bandwidth of about 2.5 nm. With both arrays operating at 1 Watt, approximately 1.6 Watts could be focussed onto the face of a 1 cm long Nd:host rod. This face was coated HR at 1.06μ and measured to be 96% transmitting at 808 nm. The focussed spot size consists of two unequal intensity lobes separated by 50μ; 99% of the pump energy was contained in a rectangular area 75μ wide by 10μ high. The

resonator geometry was hemispherical.

RESULTS

The output power in the IR as a function of laser diode pump power is shown for both hosts in Figure 1. The comparison was performed using the optimum output coupling for each host. This was found to be 97% for YAG and 98% for BEL. It can be seen that the slope efficiency for Nd:YAG is 58%, while for Nd:BEL it is 49%. The threshold power measured at the optimum output coupling is 35 mW for Nd:YAG and 97 mW for Nd:BEL.

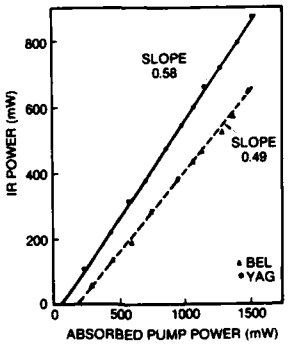

Figure 1. Output power dependence on pump power.

The dependence of the output power on the mirror reflectivity was measured for reflectivities between 95% and 99.9%. The results indicate that BEL is somewhat more sensitive to output reflectivity than YAG. From the dependence of the threshold power on output coupling one can derive the single pass loss for BEL and YAG (.002 and .0009, respectively) and the small signal gain dependence on pump power. For BEL this number was 2.6×10^{-4}/mW, while for YAG it is 8.1×10^{-4}/mW. The ratio of the two slopes is approximately the same as the ratio of stimulated emission cross sections for Nd in the two hosts.

We have calculated the overall efficiency from a consideration of the various factors which influence it, but the details of that calculation are too lengthy to include here; they will be published separately[1]. However, from an empirical point of view one can factor the overall efficiency into the product of three measurable quantities, as shown in Table I for BEL and YAG. The first factor is the electrical to optical pump light conversion efficiency for the laser diode. Although this efficiency is lower than the best reported devices, it is typical of currently available 1 Watt laser diodes. The power consumption of the coolers is not included in the overall efficiency. The collection efficiency of the optics is a function of the numerical aperture of the lenses and the reflectivity of the anti-reflective (AR) coating. The third factor is the pump-to-IR optical conversion efficiency of the laser rod, and is given for the optimum output coupling for each host. The lower number for BEL is due to the higher pump threshold.

Table I. Measured efficiency factors for Nd:host lasers

Host	Electrical to 808/810 nm	Collection optics	808 nm to 1.06μ or 810 nm to 1.07μ @R	Overall efficiency (%)
YAG	.30	.78	.56 @ 97%	13.0
BEL	.30	.78	.41 @ 98%	9.5

Future improvements in the diode and collection efficiencies are expected. One might anticipate diodes whose efficiencies exceed 40%, and improved optics and coatings that provide collection efficiencies exceeding 90%. Improvements in the optical conversion efficiencies (the fourth column in Table I) are less likely. This column is determined by the slope efficiency and the pump threshold, and is essentially the product of the quantum defect, the extraction efficiency and the laser quantum efficiency. A lower pump threshold would improve the BEL performance more than that of YAG, and can be achieved by reducing the loss, and pumping with a smaller spot size. The measured loss is most likely due to the AR coating on the interior face of the rod, and the focussed spot size is limited by the partial incoherence of the laser diode. Additional improvements would result from an increased laser quantum efficiency, which is possible to the extent that non-radiating "dark sites" contribute, and only if they could be removed from the rod.

CONCLUSIONS

Under the conditions used in the present work, both BEL and YAG perform comparably well. The broader absorption band in BEL did not appear to enhance it's operation because of the long absorption path length and the relatively narrow spectral bandwidth of the laser diode arrays. However, for side pumping or for pumping with broader spectral bandwidth arrays, the broader absorption in BEL will become a factor. In addition, it is important to recognize that a minimum of 24% of the pump light is converted to heat (the quantum defect) so that at high pump fluence athermal BEL might prove a superior host.

ACKNOWLEDGEMENTS

The authors wish to acknowledge the financial support of the NOSC IED program administered by Dr. John Silva and Mr. Kenneth Campbell, and the technical support of J. Krasinski, and R.C. Morris from Allied Corporation.

REFERENCES

1. R. Scheps, to be published.

LASER PERFORMANCE AND TUNING CHARACTERISTICS OF A DIODE PUMPED Nd:$YAlO_3$ LASER at 1083 nm

L.D. Schearer and P. Tin
Physics Department
University of Missouri-Rolla, Rolla, MO 65401

ABSTRACT

We have obtained more than 100mW of laser emission at 1079.5 nm when a small "a" axis crystal of Nd-doped $YAlO_3$ was end-pumped by a 500 mW laser diode emitting at 805 nm. Laser emission was also obtained at 1064.5 nm, 1072.9 nm, 1090.9 nm, 1084.5 nm and 1098.9 nm when a Lyot filter is added to the cavity for frequency selection. Each of these bands was tuned through several nm with the addition of an uncoated, 0.25 mm thick etalon to the cavity.

INTRODUCTION

Laser generation in Nd:$YAlO_3$ (YAP) was first reported by Massey and Yarborough[1] in 1971. In 1986 cw laser emission on seven YAP laser lines at 1064.5, 1072.9, 1079.5, 1084.5, 1090.9, 1092.1 and 1098.9 nm within the $^4F_{3/2}$-$^4I_{11/2}$ transition was reported by Schearer and Leduc[2] using a modified cw, Nd:YAG laser cavity. They also tuned through the laser lines at 1079.5 and 1084.5 nm. Scarl et al.,[3] recently obtained laser emission at 1341.1 nm ($^4F_{3/2}$ $-^4I_{13/2}$ transition) in Nd:$YAlO_3$ when it was pumped by an 0.5 W, 40 stripe laser diode. In this article we report the lasing performance and tuning characteristics of Nd:YAP laser lines originating from the $^4F_{3/2}$ - $^4I_{11/2}$ transitions when pumped with a 500mW high power laser diode.

EXPERIMENTAL SETUP

The YAP crystal we used in this experiment was obtained from Airtron[4]. It had 1 wt% Nd content and was cut along the crystal "a" axis. One end of the YAP rod had a high reflectivity coating at 1080 nm and high transmission at 800 nm. The other end was AR coated at 1080 nm. Thus, one end of the crystal also formed one end of the cavity providing a straight way of coupling in the pump power and also minimizing the threshold power.

The laser diode output was collimated by an 8 mm focal length lens. A 3x anamorphic prism was used to correct the astigmatism

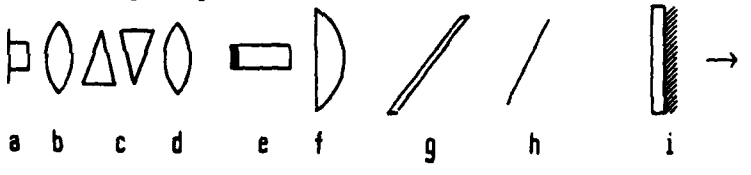

Fig. 1 Laser diode pumped YAP laser cavity.

of the laser diode light before focussing onto the YAP crystal by a 25mm focal length lens. The cavity as shown in figure 1 was about 40 cm in length providing space for a Lyot filter and one or more solid etalons for tuning purposes.

LASER PERFORMANCE AND TUNING CHARACTERISTICS.

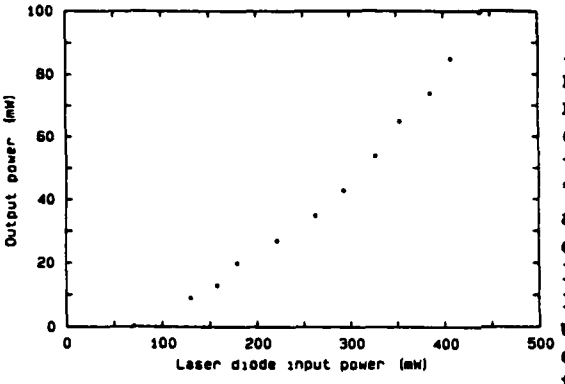

Fig. 2 YAP laser gain curve @ 1079.5 nm (95% output coupler R @ 1080 nm).

Figure 2 is the YAP laser gain curve at 1079.5 nm obtained with a 95% reflectivity output coupler. The YAP laser threshold occurred with 75mW of diode power. It absorbed more than 90% of the incident diode light at 805 nm. Over 100 mW of output power was achieved with 450 mW of laser diode light on the crystal. The laser thresholds and gain coefficients of the various transitions for Nd^{3+} in $YAlO_3$ are dependent on the crystallo graphic orientation of the rod axis. Without polarization selective optics in the cavity, the oscillation is always polarized along the c axis either at 1079.5 nm or 1341.1 nm[2].

Oscillation on the main peak at 1079.5 nm was suppressed by inserting a Lyot filter with thicknesses of 0.76 mm and 6 mm, between the intra-cavity lens and the output mirror. When the c crystallographic axis was parallel to the laser polarization, laser emission at 1072.9, 1079.5 and 1084.5 nm was obtained by tuning with the Lyot filter. When the b axis of the crystal was made parallel to the laser polarization, three other lines at 1064.5, 1090.9, and 1098.9 nm were obtained.

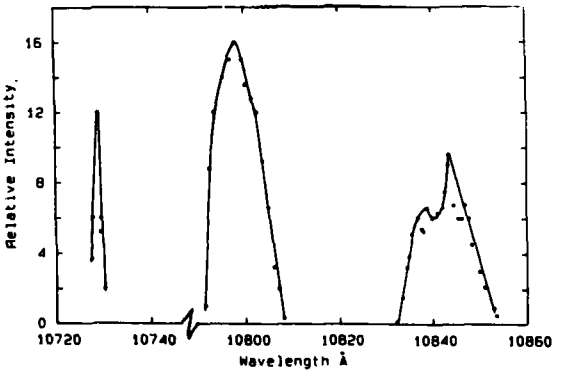

Fig. 3 YAP laser tuning curves @ 10729 Å 10795 Å and 10845 Å.

Tuning within a band was performed by inserting an 0.25mm uncoated etalon inside the cavity. Fig 3 is the tuning range of the laser lines at 1072.9 nm, 1079.5 nm and 1084.5 nm with a 98% ouput coupler.

We also tune this YAP laser at the other three laser lines: 1064.5 nm, 1090.9 nm and 1098.9 nm when the crystalline b axis was parallel to the polarization of the laser output. A single plate Lyot filter of thickness 1.5 mm and a 0.25 mm uncoated etalon was used for tuning of these three lines as shown in Fig. 4. All these tuning curves were obtained by using the 98% output coupler.

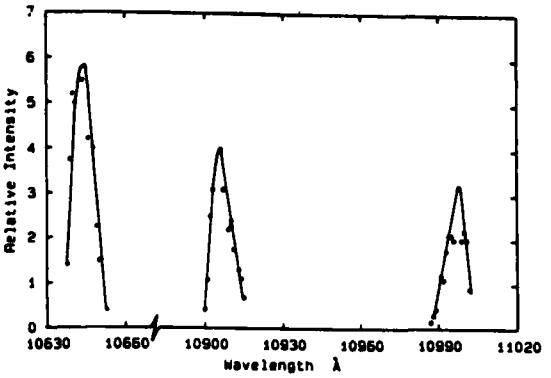

Fig. 4 YAP laser tuning curves @ 10645 Å, 10909 Å and 10989 Å.

Conclusions

We have obtained all the energy levels pertinent to the Nd^{3+}:YAP laser lines of the $^4F_{3/2}$ - $^4I_{11/2}$ transition manifold[5] by pumping the Nd^{3+}:YAP crystal with the laser diode. The tuning curves of Fig. 3 show that we can obtain laser emission, although weak, near 1083.1 nm which is the resonance transition in Helium-3 (7mw in an 0.012 nm bandwidth). Using an arc-lamp pumped Nd:YAP laser to optically pump helium atoms, spin-polarized Helium-3 nuclei and polarized metastable Helium-4 atoms have been obtained[6]. Nuclear targets of polarized He^3 nuclei have been developed using the arc-lamp YAP system. The work reported here suggests that diode-pumped systems may be useful in this application as more powerful diodes become available.

The absence of high voltages, high temperature load, and UV radiation encountered with arc lamps leads to a more benign operating environment for all solid state laser systems employing laser diode pumps. Thus, the diode-pumped, Nd:YAP system may be a useful alternative to Nd:YAG where tunability, efficiency, and portability are required.

References

1. G.A. Massey and J.M. Yarborough, Phys. Lett. 18, 576-579 (1971).
2. L.D. Schearer and Michele Leduc, IEEE J. Quantum Electron. QE-22, 756-758, (1986).
3. D. Scarl, B. Fieldman, and R. Burnham, Topical Meeting on Tunable Soild State Lasers, Technical Digest, p 23-25, MC 3-1, 1987.
4. AIRTRON, Inc. Morristown, NJ
5. M. Bass and M. J. Weber, App. Phys. Lett., 17, 395 (1970).
6. C. L. Bohler, L.D. Schearer, M. Leduc, P.J. Nacher, L. Zachorowski, R. Milner, R.D. Mckeown, and C.E. Woodward, J. Appl. Phys., 63, 15 (1988).

TUNABLE CW LASER ACTION OF ER^{3+} IN DOUBLE SENSITIZED FLUOROALUMINATE GLASS AT ROOM TEMPERATURE

E. Heumann, M. Ledig, D. Ehrt, W. Seeber
University of Jena, DDR-6900 Jena, German Democratic Republic

E. W. Duczynski, H.J. v.d. Heide, G. Huber
University of Hamburg, BRD-2000 Hamburg 36, Federal Republic of Germany

INTRODUCTION

Lasers emitting in the 1.5 to 1.6 µm band have interesting applications in navigation, meteorology, optical communication and medicine. One possibility to generate such wavelength is the utilization of the transition $^4I_{13/2} - {}^4I_{15/2}$ of Er^{3+} ions in different crystal and glass hosts[1].

Due to the three-level nature of this transition lasing can be obtained only for rather low erbium concentration, less than 1 %. Therefore, the weakly absorbing transitions of erbium cannot ensure efficient absorption of the pump light. Codoping with suitable sensitizer ions increases the efficiency of the erbium laser[2]. In this paper we report on an efficient energy transfer from chromium via ytterbium to erbium and our first lasing results in fluoroaluminate glass.

EXPERIMENTAL

The main components of the fluoroaluminate glass used are aluminiumfluoride and alkaline earth metaphosphates. In such glass samples the temperature dependence of the refractive index is weak negative at room temperature. After heating e. g. by irradiation nearly full temperature compensation will be reached.

Absorption and fluorescence measurements were carried out using glass samples of several compound and dopant combination.

Figure 1 shows the transmission of Yb,Er-glass compared to the Cr,Yb,Er-glass in the spectral range between 300 and 900 nm. The addition of Cr yields strong broad band absorption with maxima near 450 and 650 nm.

Fluorescence spectra of Cr and Yb by excitation of Cr with a Kr-ionlaser (647.1 nm) are shown in figure 2.

The glass sample containing Cr^{3+} only shows broad band fluorescence with a maximum around 820 nm. This fluorescence signal completely vanishes by codoping with Yb^{3+} at concentrations above $5 \cdot 10^{20} cm^{-3}$ and a strong fluorescence of Yb appears. Additional doping with Er^{3+} leads to strong decrease of the Yb-fluorescence intensity. These results indicate an efficient energy transfer from Cr via Yb to Er in the glass host used (Fig. 3).

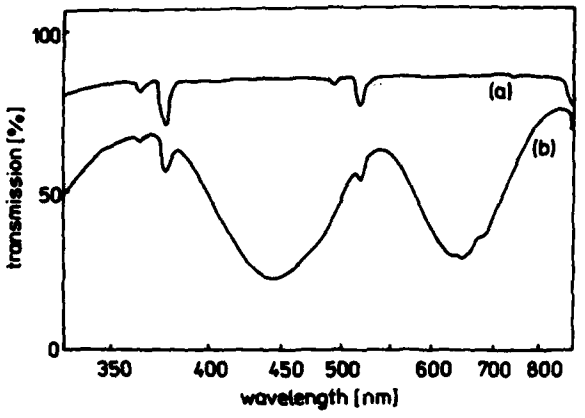

Figure 1.
Transmission of Yb,Er-glass (a) and Cr,Yb,Er-glass (b)

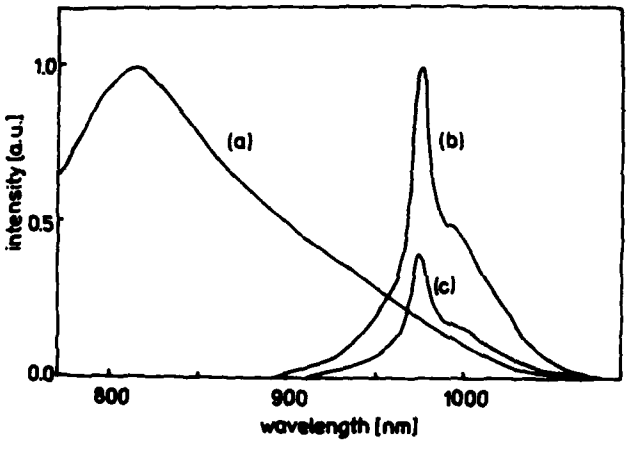

Figure 2.
Fluorescence of Cr^{3+} and Yb^{3+},(a)Cr-glass, (b) Cr,Yb-glass, (c)Cr,Yb,Er-glass

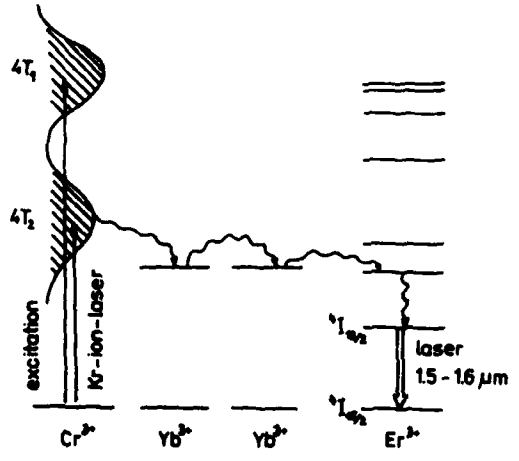

Figure 3.
Scheme of energy transfer processes in Cr,Yb,Er-fluoro-aluminate glass

In Figure 4 the monitored Er^{3+} fluorescence around 1.5 µm is shown.

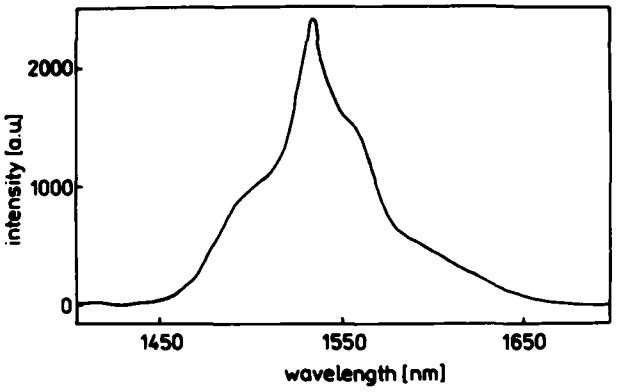

Figure 4. $^4I_{13/2}$-$^4I_{15/2}$ fluorescence of Er^{3+} in Cr,Yb,Er-fluoroaluminate glass

From time resolved fluorescence measurements of Cr, Yb and Er at several glass hosts and dopant concentration important parameters of the energy transfer processes were estimated. The best results for the time being have been obtained using the glass compound AlF_3 (80 %), $Sr(PO_3)_2$ (20 %) and the dopant concentration Cr^{3+}= 2 . 10^{19} cm^{-3}, Yb^{3+} = 1 . 10^{21} cm^{-3}, Er^{3+} = 3 . 10^{19} cm^{-3}. The energy transfer is characterized by the microparameter c(Cr-Yb) = 5.5 . 10^{-38} cm^6s^{-1} and the efficiencies η(Cr-Yb) ~ 1.0, η(Yb-Er) ~ 0.8. The fluorescence of Er^{3+} decays exponentially with a time constant of 7 ms. This value proves the high storage capacity of the material.

For lasing experiments a glass sample of 4 mm in length was placed into a nearly concentric cavity formed by two 7.5 cm radius mirrors with high reflectivity at 1.55 µm. The glass was pumped longitudinally via the $Cr^{3+}(^4T_2)$absorption band by a krypton laser. As a result we have obtained cw lasing of the glass at room temperature for the first time [3].

According to the spectral bandwidth of about 100 nm of the Er-fluorescence we have tried to tune the laser wavelength. Using mirrors of different spectral reflection characteristic the wavelength can be shifted between 1.5 and 1.6 µm. Figure 5 shows input/output curves of the Cr, Yb, Er-cw glass laser at three discrete wavelength.

The results of continuus tuning are shown in figure 6. The experimental setup used is similar to a dye laser resonator with a prism as a tuning element. The tuning range proved is about 60 nm.

Due to the broad band absorption of Cr and the strong absorption of Yb this glass is also an attractive material for flashlamp pumped lasers. First results are shown in fig. 7.

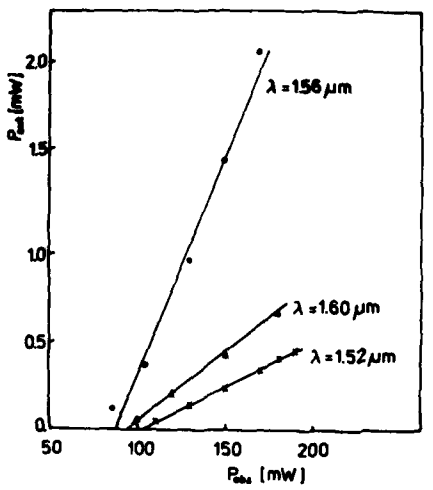

Figure 5.
cw lasing of Cr,Yb,Er-glass of three discrete wavelength

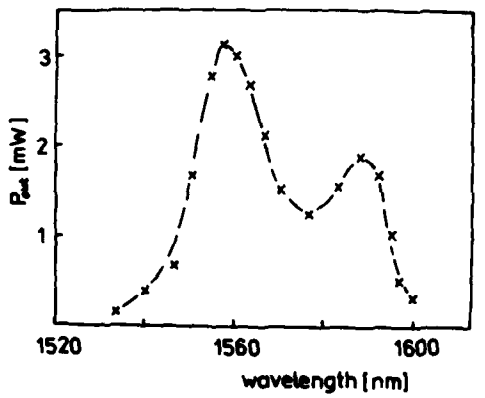

Figure 6.
Tuning curve of the cw Cr,Yb,Er-glass laser

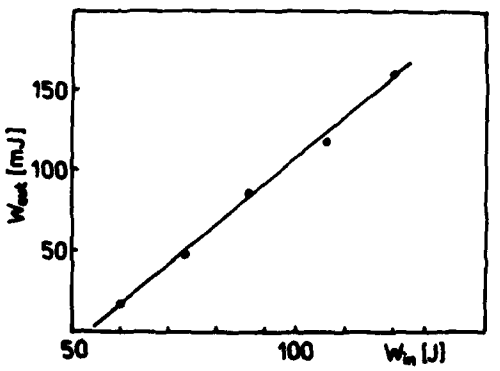

Figure 7.
Input/output characteristic of the flashlamp pumped laser (rod length 50 mm, diameter 5 mm)

Using glass samples of excellent optical quality in optimized cavities substantially better results can be expected.

Efficient lasing of this Cr, Yb, Er-fluoroaluminate glass should be possible too by excitation via Yb nearly 940 nm using high power diode lasers or LED-arrays.

REFERENCES

1. E. Snitzer, R. Woodcock, Appl. Phys. Lett. 6, 45 (1965)
2. C. G. Lunter et al., Opt.Spectrosc.(USSR) 55, 345 (1983)
3. E. Heumann et al., Appl.Phys.Lett. 52(4), 255 (1988)

A Comparative Study of Nd:YLF and Nd:YAG Crystals for Solar-Pumped Laser Application

Kyong H. Kim
Physics Dept., Hampton University, Hampton, Virginia 23668

Ja H. Lee
NASA Langley Research Center, Hampton, Virginia 23665

ABSTRACT

The cw laser performances of Nd:YLF and Nd:YAG crystals were compared under solar-simulator pumping. The measured threshold pump powers were 129 W for a 1.5 atomic % Nd:YLF rod and 143 W for a 1.1 atomic % Nd:YAG rod. The size of both crystals was 3.2 mm in diameter and 76 mm in length. The corresponding pump beam intensities on the rod surfaces were 211 s.c. (solar constants) and 236 s.c., respectively. The slope efficiency of the Nd:YLF was measured to be about 1-1.4 times better than that of the Nd:YAG in the pump beam intensity range from 200 s.c. (=27 W/cm^2) to 650 s.c. (=88 W/cm^2). Negative thermal lensing effect of the Nd:YLF rod was calculated and compared with experimental results.

INTRODUCTION

The Nd:YLF crystal has been known as a material having long upper state lifetime (≈480 μs) and low thermal lensing effect[1-3] and requiring a low threshold pump power compared to the Nd:YAG in cw laser operation.[4,5] This material has been tested in this research as a alternate laser material for a solar-pumped laser in space. Nd:YAG has already been used for solar pumping to produce a cw power of 100 W by Weksler and Shwartz[6].

EXPERIMENT AND RESULTS

Experimental setup used in this research is shown in Fig.1. The solar simulator which consists of a Xe-arc lamp and an elliptical reflector provided a spectral beam similar to the air-mass-zero solar spectrum and the beam was converged by a conical aluminum collector along the axis of 3.2 mm dia. x 76 mm long laser rods. The one end of the rods had a highly reflective mirror coated with a curvature of 5 m, and the other end had flat anti-reflection coating. The crystal was cooled by circulating water and the water jacket glass tube was surrounded by two or three diffused glass tubes to have a uniform pumping and to achieve low pump powers. The laser resonator length was 165 mm.

Fig.2 shows the results of the laser output measurement

of the Nd:YAG and Nd:YLF crystals with various output mirrors. The lowest threshold was achieved with a highly reflective output mirror and was 129 W (or 211 s.c.) for the Nd:YLF and 143 W (143 s.c.) for the Nd:YAG. The solar beam absorption efficiencies of the crystals was 3.8 percent for the π-polarization of 1.5 at. % Nd:YLF (2.8 percent for the σ-polarization) and 5.7 percent for the 1.1 at. % Nd:YAG. The corresponding absorbed pump power densities were 8.1 W/cm^3 and 13.5 W/cm^3, respectively, whose ratio agrees with the expected $p(\text{Nd:YLF})/p(\text{Nd:YAG}) = \sigma\tau(\text{Nd:YAG})/\sigma\tau(\text{Nd:YLF}) \approx 0.6$ value by Pollak, et al.[4] Here σ is the emission cross section and τ is the upper state lifetime. The slope efficiency of Nd:YLF was observed to be better up to 1.4 times than or at least equal to that of Nd:YAG within our system error in the optical pump power range from 100 W to 370 W. When a 1/4 inch diameter Nd:YLF rod was compared to the 1/8 inch rod, the slope efficiency of the former rod was increased around twice but its threshold increase was less than 2. When a flat output mirror was used for the Nd:YLF rod, no cw laser was possible because of its negative thermal lensing effect even though it was possible with the Nd:YAG crystal.

NEGATIVE THERMAL LENSING EFFECT

The radial variation of refractive index of the laser rod caused by radial temperature variation within the rod under a uniform pumping scheme is written as[7]:

$$n(r) = n_o[1 + P_a\{(dn/dt)/2n_o - n_o^2\,\alpha Q\}/2\pi KL - P_a r^2\{(dn/dt)/2n_o + n_o^2\,\alpha C_{r,\phi}\}/2\pi r_o^2 KL] \quad (1)$$

where n_o is the refractive index at rod surface, P_a is absorbed pump power by rod, dn/dt is temperature variation rate of the rod's refractive index, α is linear thermal expansion coefficient, Q is an elasto-optic constant of the crystal, K is thermal conductivity, L is rod length, $C_{r,\phi}$ is elasto-optic constants for light with radial and tangential polarization, respectively, and r_o is rod radius. Using this n(r) in ray equation to trace paraxial rays in a lens like medium[8], we obtain

$$n_o\, d^2x/dz^2 = \pm\, 4n_o x/b^2 \quad (2)$$

where $b^2 = 1/[P_a(\pm\, dn/dt)/8\pi r_o^2 KLn_o]$, x direction is taken as the radial direction and z direction is taken along the rod axis. The + sign is applied to positive dn/dt materials such as Nd:YAG, and the - sign is applied to negative dn/dt materials such as Nd:YLF.[9] The solution of the differential equation for the + sign is given in Ref.8 and that for the - sign is given as

$$\begin{vmatrix} x \\ x' \end{vmatrix} = \begin{vmatrix} \cosh(2z/b) & (b/2)\sinh(2z/b) \\ (2/b)\sinh(2z/b) & \cosh(2z/b) \end{vmatrix} \begin{vmatrix} x_o \\ x_o' \end{vmatrix} \quad (3)$$

where x,x' are output ray position and direction with respect to the rod axis, respectively, after traveling a certain distance of z and x_0, x_o' are input ray position and direction, respectively. Applying this relation in our laser resonator geometry, we obtain the following relation:

$$\begin{vmatrix} x_3 \\ x_3' \end{vmatrix} = \begin{vmatrix} 1 & d \\ 0 & 1 \end{vmatrix} \begin{vmatrix} 1 & 0 \\ 0 & n_o \end{vmatrix} \begin{vmatrix} \cosh(2L/b) & (b/2)\sinh(2L/b) \\ (2/b)\sinh(2L/b) & \cosh(2L/b) \end{vmatrix} \begin{vmatrix} x_o \\ x_o' \end{vmatrix} \quad (4)$$

$$= \begin{vmatrix} \cosh(2L/b)+(2n_od/b)\sinh(2L/b) & (b/2)\sinh(2L/b)+n_od\cosh(2L/b) \\ (2n_o/b)\sinh(2L/b) & n_o\cosh(2L/b) \end{vmatrix} \begin{vmatrix} x_o \\ x_o' \end{vmatrix}$$

where x_3, x_3' are the ray position and direction at the output mirror surface, respectively, and x_o, x_o' are the ray position and direction at the highly reflective mirror coated end of the laser rod. Here the rod end distortion was ignored because the both ends were located under shaded area from the pump beam to protect the HR or AR coatings. Then, the thermal focus is written as

$$f=-1/[(2n_o/b)\ \sinh(2L/b)]^{-1} \quad (5)$$

and cavity parameters are

$$G_1 = (a_1/a_2)\ [\cosh(2L/b) + (2n_od/b)\sinh(2L/b) - \{(b/2)\ \sinh(2L/b) + n_od\ \cosh\ (2L/b)\}/R_1] \quad (6)$$

$$G_2 = (a_2/a_1)\ [n_o\ \cosh(2L/b) - \{(b/2)\sinh(2L/b) + n_od\ \cosh(2L/b)\}/R_2] \quad (7).$$

where a_1 and a_2 are the radii of HR mirror and output mirror, respectively. Thus, the laser resonator is stable when the condition $-1 \le G_1G_2 \le 1$ is satisfied. Our calculation shows that thermal focusing of Nd:YLF is less than that of Nd:YAG as expected[2,3], and the laser resonator with a Nd:YLF rod turns out to be always unstable when the flat output mirror is used even at near threshold pump powers, while that with a Nd:YAG in the same resonator configuration is stable for pump powers from 940 W to 5030 W. This agrees with what we observed from experiment except stable cw laser operations were possible with the Nd:YAG even at pump powers lower than 940 W.

CONCLUSION

Our results show that neither Nd:YLF or Nd:YAG laser material is suitable for pumping with cylindrical parabolic solar collectors which can provide only up to 200 s.c. (=27 W/cm^2). Therefore, these laser systems must adopt parabolic dish collectors to obtain the pump power above their thresholds. Although the Nd:YLF has negative thermal lensing effect, its lower threshold, higher efficiency and less thermal lensing effect indicate that it is a superior or at least equivalent alternative to the Nd:YAG for solar

pumping. The thermal lensing may be overcome by inserting compensating optical lens(es) in the laser resonator.

REFERENCES

1. A. L. Harmer, A. Linz and D. R.Gabbe, J. Phys. Chem. Solids, 30, 1483 (1969).
2. J. E. Murray, IEEE J. Quantum Electron., QE-19 (4), 488 (1983).
3. H. Vanherzeele, Opt. Lett. 13 (5), 369 (1988).
4. T. M. Pollak, W. F. Wing, R. J. Grasso, E. P. Chicklis, and H. P. Jessen, IEEE J. Quantum Electron. QE-18 (2), 159 (1982).
5. N. P. Barnes, D. J. Gettemy, L. Estrowitz, and R. E. Allen, IEEE J. Quantum Electron. QE-23 (9), 1434 (1987).
6. M. Weksler and J. Shwartz, SPIE, New Slab and Solid-State Laser Technology and Applications (SPIE, Bellingham, WA, 1987), Vol. 736, p.84.
7. J. D. Foster and L. M. Osternik, J. Appl. Phys., 41 (9),3656 (1970).
8. H. Kogelnik, BSTJ, 44, 455 (1965).
9. N. P. Barnes and D. J. Gettemy, J. Opt. Soc. Am. 70 (10), 1244 (1980).

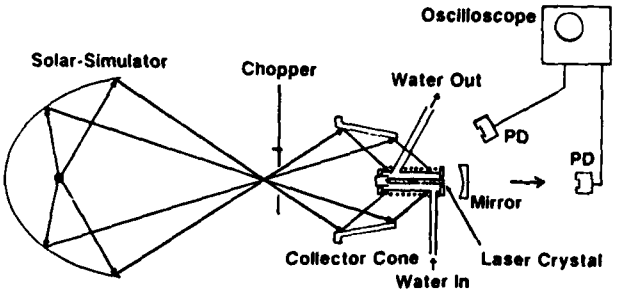

Figure 1. Schematic diagram of experimental setup.

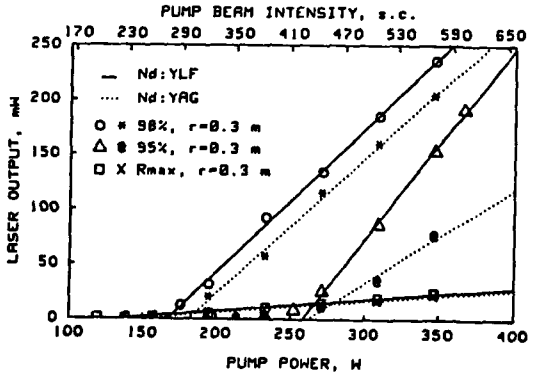

Figure 2. Laser output of Nd:YLF and Nd:YAG crystals as a function of input pump power at various output mirror reflectivities.

PARAMETRIC CONVERSION AND INDEX OF REFRACTION MEASUREMENTS IN HYDROTHERMALLY-GROWN $KTiOPO_4$

Herman Vanherzeele, J. D. Bierlein and F. C. Zumsteg
E. I. DuPont de Nemours & Company, Experimental Station, Wilmington, Delaware 19880

ABSTRACT

We report accurate index of refraction measurements and the first observation of optical parametric generation and amplification in hydrothermally-grown $KTiOPO_4$. By pumping with the second harmonic of a Nd:YLF laser system (526 nm), we have obtained picosecond pulses tunable from 600 nm to 4.3 μm.

INTRODUCTION

$KTiOPO_4$ (KTP) is a widely used material for frequency doubling Nd:YAG lasers and other Nd-doped laser systems emitting around 1.06 μm.[1] Recently, second harmonic generation at other wavelengths and sum-frequency mixing of the outputs of a Nd:YAG and a near infrared dye laser has been reported in KTP.[2,3] Here, we report the first observation of single-pass optical parametric generation and amplification in hydrothermally-grown KTP.[4] By pumping with the second harmonic of a picosecond Nd:YLF laser system (526 nm), we have obtained high peak power radiation tunable from 600 nm to 4.3 μm. The calculated tuning curves, derived from Sellmeier equation fits to measured refractive index data, agree well with experimental data.

SELLMEIER EQUATIONS AND TUNING CURVES

The refractive indices of hydrothermally-grown KTP were measured at forty seven wavelengths ranging from 350 nm to 2.4 μm using the minimum deviation method. From these data we have constructed one-pole Sellmeier equations with an IR correction of the form :

$$n^2 = A + \frac{B}{1 - (C/\lambda)^2} - D\lambda^2$$

where λ is the vacuum wavelength in μm and A, B, C, D are given in Table I. In KTP only type II phase matching is efficient, with optimum phase matching directions in the three principal planes. From the Sellmeier equations, we have calculated phase matching curves for second harmonic generation, sum and difference frequency mixing, and parametric generation.[5] Here, we will restrict ourselves to parametric generation and amplification. For this application, KTP can be most suitably pumped by the fundamental or the second harmonic of a Nd laser, or by any other laser source with intermediate wavelength (such as a visible or near infrared dye laser oscillator-amplifier). Only in the y-z and the x-z planes is the birefringence large enough to allow a broad tuning range for a visible or near infrared pump. In these planes, the effective nonlinear coefficient (in pm/V) is respectively [6.1 $\sin(\vartheta)$] and [7.6 $\sin(\vartheta)$], where ϑ is the phase matching angle with respect to the z-axis. As an example, Fig.1 represents the calculated tuning curves (solid lines) for a 526 nm pump (second harmonic of Nd:YLF) propagating as an ordinary beam in the y-z (left) and the x-z plane (right), thereby generating an extraordinary signal and an ordinary idler. Although phase matching in the x-z plane is somewhat more efficient than in the y-z plane, the tuning curve in the x-z plane has a gap from 1.007 μm to 1.103 μm when pumping with the second harmonic of Nd:YLF. Regardless, it is clear that a broad (>14,000 cm^{-1}) tuning range can be achieved with one crystal. This feature

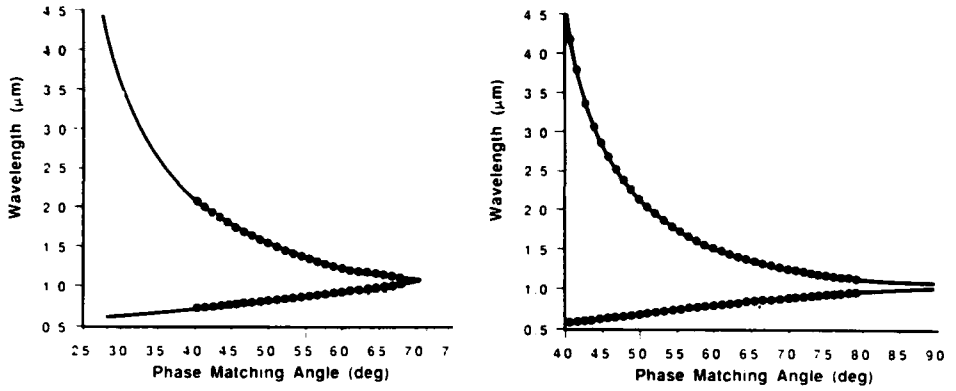

Figure 1 : Angle tuning curve in the y-z plane (left) and x-z plane (right) for a KTP parametric generator pumped by the second harmonic of Nd:YLF. Angles refer to internal propagation in the crystal.The dots represent the experimental data.

makes KTP particularly attractive for optical parametric generation, especially since such a device does not require any external dielectric mirrors whose bandwidths inevitably would limit the tunability.

PARAMETRIC GENERATION AND AMPLIFICATION : EXPERIMENTAL RESULTS

The laser system used to pump the parametric generator has been described elsewhere.[6] The front-end of the system consists of a cw pumped, harmonically mode-locked Nd:YLF laser, which generates a 100 MHz train of 35 ps pulses, with an average power of 10 Watts at 1.053 μm. About 10% of the output of the YLF laser is used to seed a Nd:YLF regenerative amplifier. The remaining beam is frequency doubled to pump a synchronously mode-locked dye laser which generates nearly bandwidth and diffraction limited 1 ps pulses with typically 1 nJ energy. The dye laser operates from 0.56 μm to 1.03 μm. The output of the regenerative amplifier is further amplified twice, and spatially filtered in vacuum, to generate a collimated Gaussiam beam with about 100 mJ of energy per pulse. After frequency doubling and filtering out the remaining IR beam, about 50 mJ per pulse at 526 nm is available with an excellent pulse-to-pulse stability for various pumping schemes.

The KTP crystals were cut parallel to the natural (201) or (011) faces for propagation in the x-z or y-z plane, respectively. The experimentally observed angle tuning data are shown in Fig.1 by the dots. Clearly, a good agreement between calculated and experimental data is obtained over the entire tuning range (0.6 μm - 4.3 μm), thus validating the accuracy of our Sellmeier equations.

Single-pass amplification measurements were carried out in a 20 mm long crystal with a (201) cut. Fig.2 represents the power gain as a function of pump energy at 526 nm, for a signal at 630 nm derived from the dye laser. The solid line corresponds to the calculated gain, while the dots represent the experimental data. From the results, it is obvious that exponential amplification takes place with a saturation setting in at a pump energy of about 5 mJ. At this pump level an amplification of $2x10^5$ is obtained, which compares favorably to a dye laser amplifier with several stages of amplification. This illustrates the great potential of KTP as an easily tunable and efficient parametric amplifier or seeded parametric generator for producing high peak-power ps pulses.

In the absence of a seed, the parametric process starts from noise, and parametric emission generally occurs over a relatively large divergence with a resulting wide frequency

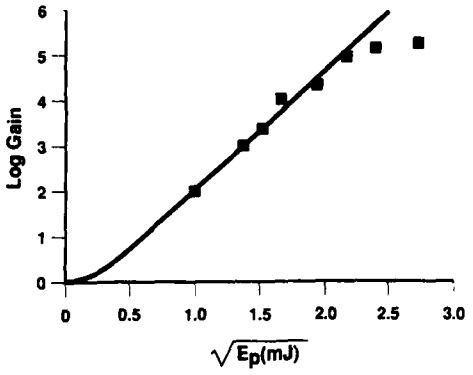

Figure 2 : Single-pass amplification at 630 nm in a 20 mm long KTP crystal, pumped by 526 nm as a function of pump energy. The solid line corresponds to the calculated gain, while the dots represent the experimental data.

band. Therefore, a parametric generator is usually followed by an amplifier in which amplification starts from those frequency components which are contained in the narrow pump beam. Using two 20 mm long KTP crystals in this configuration, we typical obtain 10% energy conversion for a 5 mJ pump at 526 nm. Optical damage in KTP does not present a problem for this application. We measured a damage threshold of 30 GW/cm^2 for 30 psec green pulses.

CONCLUSIONS

In summary, we have presented Sellmeier equations derived from accurate index of refraction measurements over a large wavelength range in hydrothermally-grown KTP. With these data we have calculated tuning curves for parametric three photon interaction in this material. Single-pass optical parametric generation, pumped by the second harmonic of a Nd:YLF laser, has been demonstrated from 600 nm to 4.3 μm. The observed angle tuning curves are in excellent agreement with the calculated ones. The large tuning range and the high conversion efficiencies that can be achieved in short crystals make KTP a material of choice for this application.

REFERENCES

1. F. C. Zumsteg, J. D. Bierlein and T. E. Gier, J. Appl. Phys. 47, 4980 (1976).
2. J.-C. Baumert, F. M. Schellenberg, W. Lenth, W. P. Risk and G. C. Bjorklund, Appl. Phys. Lett. 51, 2192 (1987).
3. K. Kato, IEEE J. Quantum Electron. QE-24, 3 (1988).
4. H. Vanherzeele, J. D. Bierlein and F. C. Zumsteg, Appl. Opt. 27, 3314 (1988).
5. J. D. Bierlein and H. Vanherzeele, J. Opt. Soc. Am. B 6 (to be published, May 1989).
6. H. Vanherzeele, Appl. Opt. 27, 3608 (1988).

Table I
Sellmeier equation coefficients for hydrothermally-grown KTP

	A	B	C	D
n_x	2.1146	0.89188	0.20861	0.01320
n_y	2.1518	0.87862	0.21801	0.01327
n_z	2.3136	1.00012	0.23831	0.01679

TWO-LASER APPROACH TO X-RAY LASERS

W. Tighe, L. Meixler, C.H. Nam, S. Suckewer*,
Princeton University Plasma Physics Laboratory,
Princeton, New Jersey 08543

ABSTRACT

Progress in X-ray laser studies at Princeton University's Plasma Physics Laboratory (PPPL) is proceeding along many fronts. Along with finding applications for the recombination soft X-ray laser operating at 18.2 nm, there are intense efforts to generate shorter wavelength output and higher energy output. There are multi-laser approaches involved in attaining both of these goals but here we will primarily discuss the effort to develop shorter wavelength X-ray lasing by using two pump lasers. The motivation for this approach will be presented along with a description of the status of the experiment and initial spectra obtained from preliminary solid-target interaction experiments.

INTRODUCTION

The X-ray laser system, operating at 18.2 nm, has been successfully applied to contact microscopy and shows promise for use in X-ray lithography.[1] However, at shorter wavelengths (around 4 nm) there exists the water window for X-ray absorption providing higher contrast in the examination of hydrated biological cells. Shorter wavelength would also have the potential to provide higher resolution and better penetration which would be important in general applications.

It is our goal to demonstrate X-ray lasing significantly below 10 nm, perhaps as short as 1 nm. However, with present X-ray schemes based on recombining or collisionally pumped transitions, these goals may be difficult to reach and a new approach may be required. For example, the ideas of Duguay and Rentzepis[2] with the modifications by McGuire[3] have already been verified in experiments in which VUV lasing near 100 nm was demonstrated.[4,5] There have also been recent results in cesium by the Stanford Group.[6] There are also very promising approaches using autoionizing metastable levels for storage of pumping energy[7] and ion core excitation using an extremely high power density laser.[8] All these approaches may provide a route to much shorter wavelengths.

As one moves toward shorter wavelengths in a recombination X-ray scheme the input pump intensity scales as severely as λ^{-4}. That is, to reduce the wavelength by a factor of ten requires an increase in input laser power of four orders of magnitude. However, the pumping time required, τ, actually decreases as λ^{2}. So, the practical approach toward shorter

*Princeton University Mechanical and Aerospace Engineering Dept.

wavelength emission should make use of short pulse length, high power lasers. This is what has motivated our construction of the powerful, picosecond laser (PP-laser).

In general, however, in order to obtain shorter wavelength emission, one must access transitions which arise from excited levels of highly ionized species. The laser characteristics which one needs to excite the short wavelength transition and produce a population inversion are very different from those needed to produce plasma consisting of highly ionized species. While a single laser might be able to perform these tasks, a two-laser approach, which separates these processes, promises to be a more effeicient one. This is the primary approach which is being followed at Princeton.

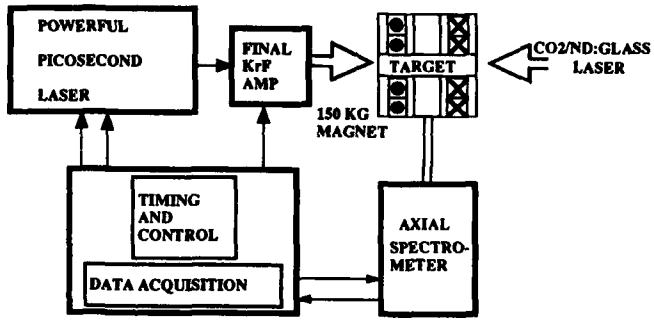

Fig. 1 Block diagram of the two-laser approach shorter wavelength X-ray lasers.

The two-laser scheme to produce a shorter wavelength X-ray laser (Fig. 1) consists of several elements. A high energy CO_2 or Glass laser is line-focused onto a target producing a plasma column. A large magnetic field (up to 150 kG) is used to confine the plasma and provide the desired plasma conditions. The short pulse, high power laser is used at the appropriate time (the occurrence of the correct ionization stage), to create an inversion. The interaction is examined using various diagnostics, primarily axial and transverse XUV spectrometers. All the essential elements for this experiment are now in place. Temporal synchronization between the lasers, the magnetic field, and the diagnostics has been verified.

THE POWERFUL PICOSECOND LASER (PP Laser)

In designing a high power laser for this application, several elements were considered. Excimer systems offer a large bandwidth which will support extremely short pulses and may be scaled to large aperture for energy extraction. The short wavelength of the ultraviolet system also allows for smaller focal spots and, so, very high power intensity. A high order multi-photon absorption mechanism is also made more attractive when higher energy photons from these ultraviolet systems are used.

The KrF* excimer amplifier, which (at 248 nm) still allows (in most cases) the preferred use of fused silica optics, was selected. To generate short (< 1 psec) pulses at 248 nm a relatively sophisticated scheme is employed[9-11] (Fig. 2).

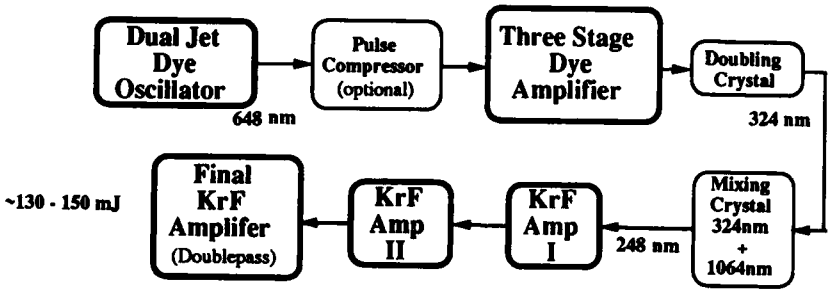

Fig. 2 Picosecond Laser System; simplified block diagram.

The oscillator is a 1 psec, synchronously modelocked, dye system operating at 648 nm. An optional fiber/grating compressor is then used to provide pulses of $\sim$ 200 fsec duration.[12] A single pulse from the oscillator is selected and then amplified through a three-stage dye amplifier. Using KDP crystals, the dye amplifier output is first doubled to 324 nm and this is then mixed with 1.06 μm radiation to produce a 248 nm seed pulse. This seed pulse is then injected through a chain of KrF* amplifiers. These amplifiers are well separated to prevent self-oscillation and spatial filters are employed between stages to restrict the growth of amplified spontaneous emission (ASE). The pulse width is monitored at the dye oscillator and has been measured after the dye amplifier and before injection into the final KrF amplifier. This was done for cases with and without pulse compression. For the most part the pulse width at the oscillator is maintained throughout.

The output for the first stage of the system, that is without the final KrF* amplifier and without pulse compression, was in the vicinity of 20-30 GW and was focussed to power densities of $\sim 10^{16}$ W/cm^2. Results from target experiments using this output will be presented in the next section. The final KrF* amplifier was constructed at PPPL.[13]

The cross sectional area of the final amplifier is 5 cm by 10 cm, and the length of the discharge is $\sim$ 80 cm. The amplifier is UV preionized by a row of 40 pins which span the length of the active laser region. The amplifier is double passed with the seed pulse derived from the output of the first stage. The pulse is expanded to fill the aperture as it traverses the amplifier on the initial pass. The beam is reflected by a spherical mirror and slowly converges on its return trip, before being focussed onto the target. In this configuration output energies of 1 J have been observed using a 20 ns seed pulse from the first two KrF amplifiers, and pulse energies in the range of 200 mJ (with $\sim$ 20% ASE) have been obtained using a 300 fsec seed pulse. If the pulse width is maintained through

the final amplifier, this provides us with output power levels of 1/3-1/2 TW. These results are still preliminary and there remains room for improvement.

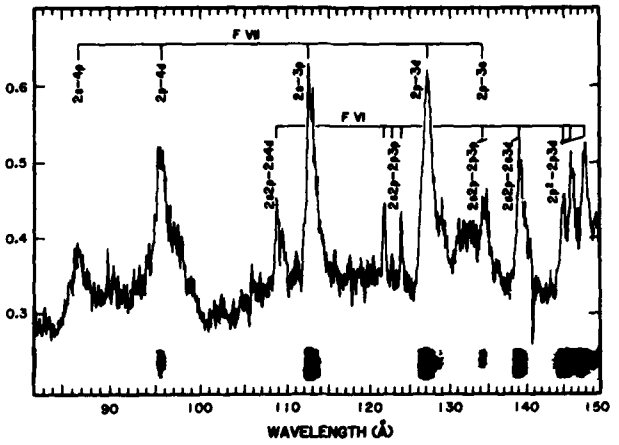

Fig. 3 Fluorine spectra resulting from psec interaction with teflon target [ref. 14].

INITIAL SPECTRA FROM SOLID TARGET INTERACTION

The output of the 1st stage (20-30 GW) was initially used in solid target experiments[14] using a 3-m high resolution XUV spectrometer. The highlights of the resulting spectra were the observation of highly ionized species (for eg. from an ion target Fe XVI) and very significant line broadening for certain transitions. This may be a result of either Stark broadening in high density ($> 10^{22}$ cm^{-3}) plasma or the extremely high electric field associated with the laser pulse (10V/Å). Modelling, based on Stark broadening, indicated that in some cases a mixing of wavefunctions and subsequent emission from otherwise forbidden transitions occurred, leading to asymmetry in certain lines (F 2p-3d, Fig. 3). Recently, Koshelev[15] noted that the asymmetry may be the result of the contribution of satellite lines to the transition.

The laser-target experiments were continued using a different spectrometer (SOXMOS) which utilized a more sensitive detection element. This allowed the effect of a prepulse on the interaction to be examined.[16] The prepulse is contained in the amplified spontaneous emission (ASE) of the two KrF* amplifiers. Even though the ASE signal is 10^4 times longer in duration and more than 10^5 times weaker in intensity than the main picosecond pulse, it significantly changes the condition of interaction of the main pulse with the target. The amount of prepulse energy was changed by varying the injection timing of the psec seed pulse. Injection timing of T = 0 ns corresponds to injection at the peak of the ASE pulse.

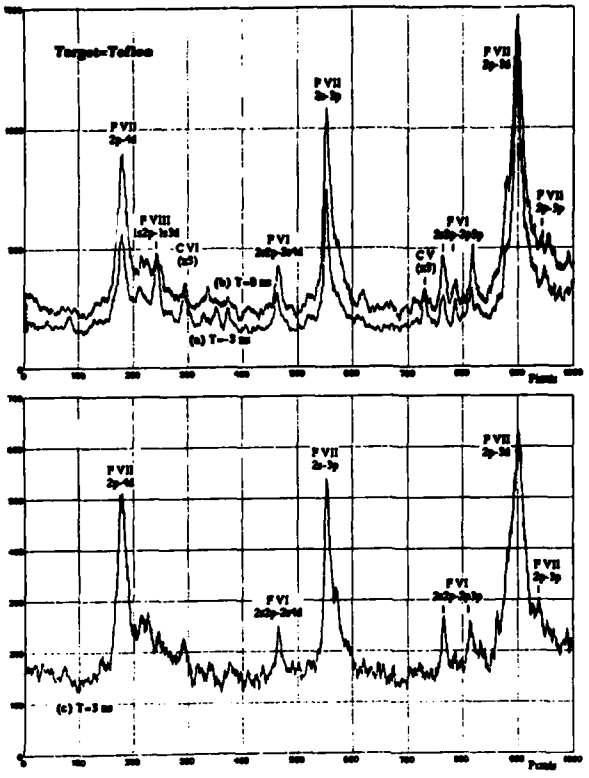

Fig. 4 Fluorine spectra with varying amount of prepulse energy
a) T = -3 nsec (min. prepulse) b) 0 nsec
c) 3 nsec (max. prepulse)

The spectra shown in Figs. 4(a),(b), and (c) were obtained with a teflon target at injection times of T = -3, 0, and 3 ns, respectively. The estimated amount of prepulse energy in each case is 0.3, 7, and 15%, respectively, of the picosecond pulse energy. As the injection time is delayed (more prepulse) F VII lines become broader, and more asymmetric. If the effects of the electric field of the laser pulse are ignored this would imply that as the amount of prepulse increases, the F VII ions are created at higher electron density. Assuming a freely expanding plasma, calculations,[16] based on the observed spectral intensities and the linewidths of Li-like F VII, indicate that with decreasing prepulse the electron temperature increases. This is supported by the presence of much stronger resonance lines of CV and C VI (in third order) for the case of weak prepulse than those observed for a stronger prepulse.

It is expected that the prepulse creates a low temperature plasma which expands prior to the arrival of the picosecond pulse.As the amount and duration of prepulse increases,the number of ions interacting with the picosecond pulse will get larger, with the result that the peak temperature will decrease.

Finally, we have recently obtained spectra using the higher output characteristics of the laser system. Though not yet carefully analyzed, the resultant spectra do show very different

features from those obtained from a lower power condition. There was some indication of increased line broadening and the onset of significant satellite lines. The spectral line intensities in the 30-100 Å wavelength region which were obtained with only 5 shots in the higher power case were comparable to those obtained with 200 shots from the output of the 1st stage of the PP-Laser.

CONCLUSION

All elements of the two laser approach to the development of shorter wavelength X-ray lasers are now in place and we are now proceeding toward our first experiments. The first step will be to perform experiments which will clearly identify the effects due to the extremely large electric field associated with the laser pulse.

ACKNOWLEDGEMENTS

We gratefully acknowledge the support of the other members of the X-ray Laser Division at PPPL, the helpful discussion and suggestions of R. Miles and M. Littman of Princeton Univ., J. Fujimoto of MIT, and T.J. McIlrath and J. Goldhar of Univ. of Maryland, and the support of H. Furth and T. Stix of PPPL.

This work received financial support from DOE contract KC-05-01 and the AFOSR.

REFERENCES

1. C.H. Skinner et al., IEEE, Trans. Plasma Sci., 16, 512 (1988).
2. M.A. Duguay and P.M. Rentzepis, Appl. Phys. lett., 10, 350 (1967).
3. E.J. McGuire, Phys. Rev. Lett., 35, 844 (1975).
4. H.C. Kapteyn, R.W. Lee and R.W. Falcone, Phys. Rev. Lett. 57, 2939 (1986).
5. M.H. Sher, J.J. Macklin, J.F. Young, and S.E. Harris, Opt. Lett. 12, 891 (1987).
6. K.D. Pedrotti et al., Opt. Lett., 11, 425 (1986).
7. S.E. Harris, et al., Laser Technology V, McKeller, Oka, and Stoicheff ed., (Springer-Verlag, NY, 1981) p. 437.
8. A.P. Schwarzenbach, et al., Opt. Lett., 2, 499 (1986).
9. W. Tighe, et al., Rev. Sci. Inst., 59, No. 10, 2235, (1988).
10. S. Szatmari et al., Opt. Comm., 63, 305 (1987).
11. S. Watanabe, et al., SPIE, Vol. 664, p. 194 (1986).
12. Work performed with J. Fujimoto, MIT.
13. Work performed with J. Goldhar, Univ. of Maryland.
14. C.H. Nam, et al., Phys. Rev. Lett., 59, 2427 (1987).
15. K.N. Koshelev, J. Phys. B, 21, L 593 (1988).
16. C.H. Nam, Doctoral Thesis, Princeton Univ., April 1988.

"Superfluorescent Chemically Driven Visible Laser Transitions Using Fast Near Resonant Energy Transfer"

J. R. Woodward, S. H. Cobb, and J. L. Gole

High Temperature Laboratory
Center for Atomic and Molecular Science
School of Physics
Georgia Institute of Technology
Atlanta, Georgia 30332

Abstract

Highly exothermic metal oxidations have been employed to develop the first chemically driven pulsed laser amplifiers operative in the visible spectral region. These amplifiers rely on ultrafast near resonant energy transfer from chemically created metastable storage states of SiO and GeO to subsequently lasing thallium (535nm) and gallium (417nm) atoms from which superfluorescent pulses are monitored.

Pulsed thallium and gallium laser amplifiers have resulted from the pursuit of studies in our laboratory whose focus has been to characterize the constraints of spin conservation, internal excited electronic state relaxation, and fast energy transfer associated with the formation of copious quantities of the metastable SiO and GeO $a^3\Sigma^+$ and $b^3\pi$ states as the products of the primarily spin conserving Si-N_2O,[1] Si-NO_2,[2] Ge-N_2O, and Ge-O_3 reactions. We have used these long-lived triplet states as an energy reservoir for fast intermolecular energy transfer to excite potentially lasing atomic transitions. Using this approach we have obtained amplification from thallium at 535nm[3] (gain coeff. $\alpha \geq 2.5$/cm) and gallium at 417nm[3] ($\alpha \sim 2$).

One might envision the SiO and GeO "$a^3\Sigma^+$" and "$b^3\pi$" states as forming a combined metastable triplet state reservoir which is, at best, weakly coupled to the ground electronic $X^1\Sigma^+$ state (minimal nonradiative transfer). Thus, these states are maintained and can be made to transfer their energy to pump the atom of interest. We carry out an efficient intermolecular energy transfer process

$$SiO,\ GeO(a^3\Sigma^+, b^3\pi) + X \rightarrow SiO, GeO(X^2\Sigma^+) + X^* \qquad (1)$$

where X^* represents the electronically excited atomic species from which we wish to obtain lasing action and the energy transfer process involves the formation of SiO or GeO ground state molecules.

The success of the above scheme depends on the rate constants for the reactions of interest,[4] the branching ratio for formation of SiO or GeO $a^3\Sigma^+$ and $b^3\pi$, and the rate of the MO^* (M=Si,Ge) - X intermolecular energy transfer strongly influenced by near resonances between the MO^* and X^* energy levels. All of these parameters must at present be inferred from a plethora of independent information, however, using a Nd:YAG pumped pulsed dye laser system, it will be possible to quantitatively assess the time dependence of these interlocking processes. We can say that the energy transfer step is extremely efficient proceeding at rates much in excess of gas kinetic.

The Group IIIA metals, gallium, indium, and thallium were chosen as promising candidates for the transfer scheme considered because these atoms have regular ground electronic ^2P states with substantial spin-orbit splittings,[5] 826.24 cm^{-1} (Ga), 2212.56 cm^{-1} (In), and 7792.7 cm^{-1} (Tl) and excited $^2S_{1/2}$ upper states which for thallium and gallium are in very near resonance with the SiO and GeO triplet states. Photodissociation lasers involving this upper $^2S_{1/2}$ atomic state were already known to exist operating on the strongly allowed

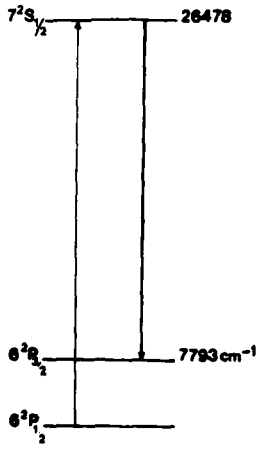

Figure 1: Energy levels associated with the Tℓ atom which allow for the creation of a population inversion for the $7^2S_{1/2}$ level relative to the $6^2P_{3/2}$ level after energy transfer pumping of the $7^2S_{1/2}$ - $6^2P_{1/2}$ transition.

$^2S_{1/2}$ - $X^2P_{3/2}$ transition and producing laser action[6] at 417 (Ga), 451 (In) and 535 nm (Tl).

We have thus made use of the scheme (Figure 1)

$$\text{Pump:} \quad MO^* + X^2P_{1/2} \rightarrow X^* (^2S_{1/2}) + MO^t \tag{2}$$

$$\text{Lasing:} \quad X^* (^2S_{1/2}) \rightarrow X (^2P_{3/2}) + h\upsilon \tag{3}$$

Here, the metal oxide excitation is transferred to the Group IIIA atom, pumping from the $X^2P_{1/2}$ to the energetically accessible electronically excited $^2S_{1/2}$ level, this level subsequently undergoing the (potential laser) transition $^2S_{1/2}$ - $X^2P_{3/2}$ to what corresponds to an initially unpopulated $^2P_{3/2}$ spin orbit component ($N_{3/2} \leq e^{-10} (N_{1/2})$ at $T \leq 1100K$) in the Tl system.

The efficiency of the outlined process for X = $T\ell$ ($^2P_{1/2}$), which does not react to form the metal monoxide, is such that a "superfluorescent" laser spike (Fig. 2) some 25 times the normal $^2S_{1/2}$-$^2P_{3/2}$ fluorescent intensity (after correction for instrumental response) is generated on less than a 5ns time scale. A similar albeit less pronounced effect is observed in the more complex gallium system (Fig. 3) where both the initial thermal population of the Ga $^2P_{3/2}$ level and the possible reaction of both the $^2P_{3/2}$ and $^2P_{1/2}$ spin orbit components complicates a detailed analysis of the system. As the population of the $P_{3/2}$ metastable level builds in these systems, the $^2S_{1/2}$ - $^2P_{3/2}$ population inversion is lost and lasing ceases. The light level in the remainder of the temporal scan corresponds to $^2S_{1/2}$ - $^2P_{3/2}$ fluorescence. A more detailed discussion of the experimental configurations can be found elsewhere.[3]

We have obtained strong evidence for the development of laser amplifiers from fast near resonant energy transfer. We also wish to develop the corresponding laser oscillators optimizing the efficiency

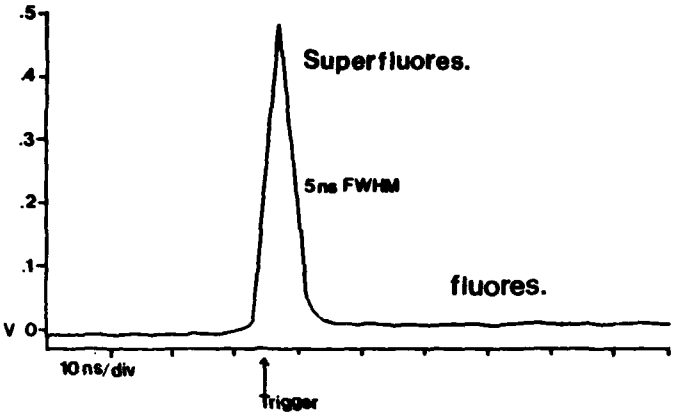

Figure 2: Temporal behavior of the $^2S_{1/2}$ - $^2P_{3/2}$ emission from Tℓ atoms excited via fast energy transfer from metastable GeO. The sharp spike corresponds to superfluorescence triggered by relative signal intensity and not mixing. The signal level required for triggering superfluorescence substantially exceeds the level of fluorescence which is apparent for times following the superfluorescent pulse.

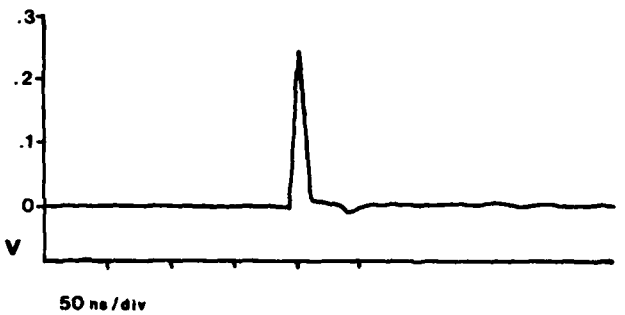

Figure 3: Temporal behavior of the $^2S_{1/2}$ - $^2P_{3/2}$ emission from Ga atoms excited via fast near resonant energy transfer from metastable GeO. The sharp spike corresponds to superfluorescence triggered by relative signal intensity and not mixing. The signal level required for triggering superfluorescence substantially exceeds the level of fluorescence which is apparent for times following the superfluorescent pulse.

of the Ga and Tℓ amplifiers in a cavity configuration. While our initial efforts have focused on a pump of thallium and gallium excited states, we envision extension of the near resonant energy transfer concept as an efficient pump for somewhat longer lived emitters (allowing a further increase in energy storage in a laser cavity). If we replace the $^2P_{3/2}$ spin orbit component (Fig. 1) with a low-lying

electronic state in a variety of atomic receptors,[5] we generalize the near resonant intermolecular energy transfer pump-amplification concept to a broader range of possibilities. Further, it may be feasible to replace the metastable states of SiO and GeO with selectively formed and long-lived states of the Group IIIB halides.

As applied to Tℓ, Ga and In atoms, our studies have thusfar indicated (1) the importance of the near matchup of SiO and GeO energy level increments with the energy level spacing of the receptor atoms of interest and (2) the potential for operation over a rather wide range of intermediate ($P_{3/2}$) and ground state ($P_{1/2}$) level separations. With the extension to low-lying electronic states, the three level excitation scheme offers a considerable range of radiative configurations (lifetimes) cor nensurate with a variety of potential lasing transitions.[7]

References

1. G. J. Green and J. L. Gole, Chemical Physics 100, 133 (1985).

2. R. W. Woodward, J. S. Hayden, and J. L. Gole, Chemical Physics 100, 133 (1985).

3. See Science News 132, 261 (1987). "A Chemically Driven Visible Laser Transition Using Fast Near Resonant Energy Transfer", R. Woodward, S. H. Cobb and J. L. Gole, submitted.

4. P. M. Swearengen, S. J. Davis, and T. M. Niemczyk, Chem. Phys. Lett. 55, 274 (1978).

5. C. E. Moore, "Atomic Energy Levels", N. B. S. Circular 467.

6. S. Chilukuri, Appl. Phys. Lett. 34, 284 (1979). H. Hemmati and G. J. Collins, Appl. Phys. Lett. 34, 844 (1979). R. Burnham. Appl. Phys. Lett. 30, 132 (1977).

7. See for example, R. W. F. Gross and J. F. Bott, Handbook of Chemical Lasers, Wiley and Sons, New York, 1976.

Continuous Chemical Laser Amplifiers in the Visible Region

S. H. Cobb, J. R. Woodward and J. L. Gole

High Temperature Laboratory
Center for Atomic and Molecular Science
and School of Physics
Georgia Institute of Technology
Atlanta, Georgia 30332

Abstract

The high cross section (pumping efficiency), highly selective sodium trimer-halogen atom reactions (Na_3 - X (X = Br,I)) are used to create a continuous electronic population inversion based on the chemical pumping of Na_2. Optical gain through stimulated emission is demonstrated in regions close to 527 (3.8% for individual rovibronic level ($\alpha = 8 \times 10^{-3}$/cm)) 492, and 460.5nm. Extensions into the ultraviolet and conversions to laser oscillators will be considered.

We have been concerned with the high cross section, highly exothermic Na_3 - X (Cl,Br,I) reactions which form Na_2^* in several of its excited electronic states.[1] The optical signatures for the processes

$$Na_3 + Cl,Br,I \rightarrow Na_2^* + NaX \ (X = Cl,Br,I)$$

encompass emission from a limited number of Na_2 band systems. Surprisingly, the observed emission is characterized by sharp well defined emission regions[2] (Figures 1,2) superimposed on a much weaker but perceptible background. As Fig. 2 demonstrates, these sharp emission features are not readily explained by invoking a purely fluorescent process.[2]

The sharp nature of several of the B-X, C-X, and C'-X Na_2 fluorescence features (Fig. 1) and their correlation in certain regions to the emission characteristic of optically pumped Na_2 laser systems[3] (ex: @528.2nm (v',v") = (6,14)B-X) suggested the possibility that stimulated emission analogous to that obtained in alkali dimer optical pumping experiments might be associated with certain of the

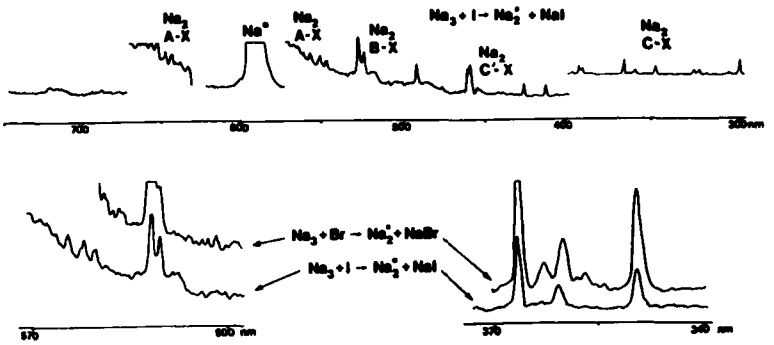

Figure 1: Chemiluminescent emission from the Na_3 + Br and Na_3 + I reactions forming excited states of Na_2, whose optical signature dominates the observed emission, and the sodium halide. Sharp emission features superimposed on a broad background are apparent including those at ~ 527, ~ 492, ~460.5 nm. Spectral resolution is 0.6+ nm. See text for discussion.

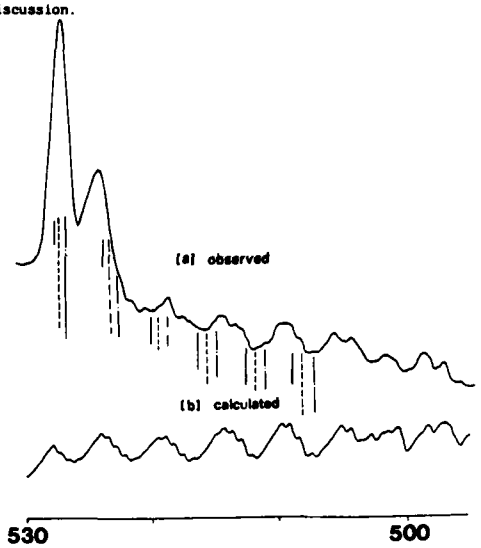

Figure 2: Comparison of (a) observed and (b) calculated emission spectra for the Na_2 B-X emission system. The experimental spectrum corresponds to the chemiluminescence from the Na_3-Br reaction. The calculated spectrum, which was obtained for a rotational temperature, T_{Rot} ~ 1000K, represents an estimate of effective rotational temperatures for Na_2 product formation under near single collision conditions and therefore not at equilibrium. Relative vibrational populations input for Na_2 B-X, v' = 0-6 were in the ratio 1.00:1.17:1.33:1.50:1.58:1.67:1.54. The location of contributions from vibrational levels v' = 6 (——), 5 (---), and 4 (-·-) of the Na_2 B state in transition to vibrational levels v" = 14-9, v" = 13-8, and v" = 12-7 of the Na_2 ground state are indicated. See text for discussion.

Na_2 emission products. We have carried out laser gain measurements to assess this possibility.

Using argon ion pumped dye lasers to study the Na_3 + Br reaction we have scanned the entire wavelength region from 420 to 600nm (Figure 1) at 0.5 cm^{-1} resolution (FWHM)[2,4] and the region around 527nm (Fig. 2) at 0.007 cm^{-1} resolution using a ring dye laser.[2,4] We find that laser gain and hence amplification is characteristic of certain select regions and that several of the sharper and more pronounced emission features apparent in the spectra depicted in Figure 1 correspond to a stimulated process and to the establishment of a population inversion. Our ring dye laser studies demonstrate that the strong feature at ~ 527nm (Fig. 2) corresponds to stimulated emission from between four and seven unresolved rotational levels.

Optical gain through stimulated emission has been measured at 0.5 cm^{-1} resolution in the regions 527nm (1% gain), 492nm (0.3% gain) and 460.5nm (0.8% gain), correlating precisely with the reactive process and the relative intensities of those features observed while monitoring the light emitted from the Na_3-Br and Na_3-I reactions (Figs. 1,2). High resolution ring dye laser scans in the 527nm region indicate that the gain for the system is close to 3% for an individual rovibronic transition with approximately four to seven transitions showing gain. These results demonstrate the amplifying medium for a visible chemical laser in at least three wavelength regions.[2,4] At no other scanned wavelengths have we observed gain of any kind. In the region of the sodium D-line, a substantial absorption and hence loss is monitored as a function of the trimer-halogen atom reaction.

Because of the low Na_3 ionization potential and the high halogen electron affinities,[5] the Na_3-halogen atom reactions are expected to proceed via an electron jump mechanism with extremely high cross sections,[6] producing substantial Na_2 excited state populations. The created population inversions monitored thusfar are thought to be sustained by the large number of free halogen atoms reacting with the Na_2 molecules in those ground state levels on which the transitions emanating from the Na_2 excited states terminate. The cross section

for reaction of vibrationally excited ground state Na_2 is expected to be quite substantial relative to that corresponding to collision induced vibrational deactivation of the Na_2 manifold. Extremely efficient reactions rapidly deplete the lower state levels in this system allowing one to sustain a continuous population inversion.

Our major efforts thusfar have focused on the Na_2 B-X spectral region and the potential development of a laser oscillator at wavelengths in the vicinity of 527nm. However, because the Na_2 B-X radiative lifetime is only 12 nanoseconds, we are also concerned with the extension of these studies further into the ultraviolet region primarily as they access states of considerably longer radiative lifetime.

The Na_2 ~ 395, ~ 365, and ~ 350nm emission features depicted in Fig. 3 represent a portion of the optical signatures for the Na_3-Br

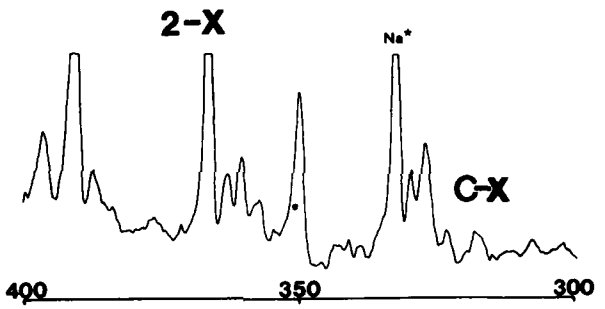

Figure 3: Chemiluminescence from the reaction $Na_3 + Br \rightarrow Na_2^* + NaBr$. The spectrum is dominated by the Na_2 $C^1\Pi_u$-$X^1\Sigma_g^+$ and $2^1\Sigma_u$-$X^1\Sigma_g^+$ emission features.

reaction. They are of interest for they correspond again to sharp emission features, on a broad and weak background, whose appearance cannot be readily explained in terms of a purely fluorescent process. They are tentatively associated, at least in part with a very recently ascribed double minimum excited electronic state[7] ($2^1\Sigma_u^+$-$X^1\Sigma_g^+$). The 395nm region corresponds to emission from the outer turning point of the outer potential minimum, the 365nm features to emission from the central potential barrier region, and the 350nm feature to the inner

turning point of the inner potential well.

The radiative lifetimes associated with this double minimum state are complex. The outer potential well is best associated with an ion pair configuration whose radiative lifetime is short and comparable to that of the Na_2 B and A states (~10ns). However the radiative lifetime associated with the inner well levels is of order 40ns, and the transition moments for the inner well decrease in traversing the level structure up to and including the inner barrier region. Transitions emanating from the inner barrier region are in fact favorable but have smaller transition probabilities and thus the 365nm region is to be associated with even longer radiative lifetimes. These longer lifetimes of course enhance the potential energy storage in a laser cavity. This, in turn, suggests that the laser gain studies already performed should be extended to this spectral region in order to assess the feasibility of using these transitions as laser amplifiers extending far into the ultraviolet. Further, we will want to extend these studies to the other alkali metals, taking advantage of the possibility for forming laser amplifiers extending both to considerably shorter and longer wavelength. Of course, simultaneously we hope to convert these laser amplifiers to laser oscillators.

References

1. W. H. Crumley, J. L. Gole, and D. A. Dixon, J. Chem. Phys. 76, 6439 (1982).

2. S. H. Cobb, J. R. Woodward, and J. L. Gole, Chem. Phys. Lett. 143, 205 (1988).

3. B. Wellegehausen, in "Metal Bonding and Interactions in High Temperature Systems with Emphasis on Alkali Metals", A. C. S. Symposium Series 179, edited by J. L. Gole and W. C. Stwalley, (Am. Chem. Soc., Washington, D. C.), p. 462. B. Wellegehausen, J. of Quantum Electronics 15, 1108 (1979).

4. S. H. Cobb, J. R. Woodward, and J. L. Gole, "Continuous Chemical Amplification of Single and Multimode Lasers in the Visible Region", submitted (Chem. Phys. Lett.).

5. See for example, R. S. Berry and C. W. Reimann, J. Chem. Phys. 38, 1540 (1963), R. S. Berry, J. Chem. Phys. 27, 1288 (1957), W. S. Struve, J. R. Krenos, D. L. McFadden, and D. R. Herschbach, J. Chem. Phys. 62, 404 (1975). R. C. Oldenborg, J. L. Gole and R. N. Zare, J. Chem. Phys. 60, 4032 (1974).

6. Given Na_2 and Na_3 ionization potentials of 4.87 and 3.97 eV (A. Hermann, E. Schumacher, and L. Wöste, J. Chem. Phys. 68, 2327 (1978) and an electron affinity of 3.363 eV for atomic bromine, we determine a very substantial electron jump cross section $\sigma \tilde{=} \pi$ (14.38/3.97-3.36) = 1746 Å^2 (1.75 x 10^{-13} cm^2) for the Na_3 - Br reaction and $\sigma \tilde{=} \pi$ (14.38/(4.87-3.36)) = 285 Å^2 (2.85 x 10^{-14} cm^2) for the Na_2 - Br reaction.

7. W. C. Stwalley, private communication.

Ionic Alkali Halide Excimers Excited By A Laser-Produced Plasma*

S. Kubodera, P.J. Wisoff, and R. Sauerbrey

Department of Electrical and Computer Engineering
Rice University
Houston, Texas 77251-1892

Abstract

We have observed ultraviolet (UV) and vacuum ultraviolet (VUV) emission from ionic alkali halide molecules and ionic rare gas alkali metal molecules excited by the soft x-rays from a laser-produced plasma and relativistic electron beams. The excitation process of the ionic excimer has been investigated using a simple kinetic model. The emission behavior of those ionic excimers in the UV and VUV region has been experimentally studied.

The existence of ionic excimers was predicted based on isoelectronic scaling of the well-known neutral excimer molecules [1]. Molecules such as $Cs^{2+}F^-$, which is isoelectronic to XeF, emit further into the UV and VUV than their rare gas halide counterparts. We have already observed the VUV emission of the $Cs^{2+}F^-$ ionic alkali halide excimer at 185 nm using the soft x-rays from a laser-produced plasma to photoionize neutral CsF vapor [2]. Here we briefly summarize a simple kinetic model describing some fundamental kinetics of alkali halide ionic excimers excited by soft x-rays, as well as present experimental spectroscopic studies of CsF^+, RbF^+, and $CsCl^+$ [3].

The experimental setup is discussed in Ref. 2. An oscillator-amplifier injection-controlled KrF excimer laser beam was focused onto a rotating tantalum target inside a heat pipe cell where stable alkali halide vapors were created. The focused laser beam intensity was about $10^{11}\ W\,cm^{-2}$ with a 30 ns pulse width. The laser-produced plasma generates soft x-rays in the range of 10-100 eV, which can photoionize inner-shell electrons of alkali halide molecules in the heat pipe cell. UV and VUV emission from the excited vapor inside the cell was detected using a vacuum spectrometer and a photomultiplier with a scintillator.

Fig. 1 shows a time-integrated fluorescence spectrum of the $Cs^{2+}F^-$ emission. A main continuum extending between 170 nm and 190 nm with a peak at 185 nm corresponds to the $B(^2\Sigma_{1/2}, Cs^{2+}F^-) \rightarrow X(^2\Sigma_{1/2}, Cs^+F)$ transition, and a second peak at 154 nm has been identified as the $D(^2\Pi_{1/2}, Cs^{2+}F^-) \rightarrow X(^2\Sigma_{1/2}, Cs^+F)$ transition. The undulated structure is due to vibrationally-excited $Cs^{2+}F^-$. Fig. 2 shows a time-integrated fluorescence spectrum of $Rb^{2+}F^-$. A continuum between 125 nm and 135 nm with a peak at 130 nm has been identified as the $Rb^{2+}F^-(^2\Sigma_{1/2}, B) \rightarrow Rb^+F(^2\Sigma_{1/2}, X)$ transition which was predicted to occur between 100 nm and 126 nm [1]. The other continuum peak around 158 nm is due to

*This work was supported by the National Science Foundation, the Robert A. Welch Foundation, and the Air Force Office of Scientific Research.

F_2^* emission. Since asymptotic states of Rb^+F^* lie only 2 eV above the potential minimum of $Rb^{2+}F^-$, the crossing of the potential curves can occur at relatively small internuclear distances leading to predissociation into Rb^+ and F^*. F_2^* molecules can then be formed by collisions between ground state F atoms and excited state F^* atoms. Contrary to this case, no F_2^* emission was observed in the $Cs^{2+}F^-$ fluorescence spectrum. Since there is a larger energy difference between Cs^+F^* asymptotic states and the potential minimum of $Cs^{2+}F^-$ molecules, the potential curve crossing should occur at a larger internuclear distance. The predissociation probability should thus be smaller for $Cs^{2+}F^-$ compared to $Rb^{2+}F^-$. For the ionic excimer $Cs^{2+}Cl^-$, Cl_2^* emission at 258 nm due to the predissociation has been observed in addition to the ionic excimer emission at 208 nm (Fig. 3).

In order to analyze the kinetic behavior and estimate the feasibility of producing a CsF^+ ionic excimer laser, a simple kinetic model is proposed [3]. The soft x-rays from the laser plasma on a high Z target is assumed to have the character of a blackbody radiator and could thus be described by an effective plasma temperature. Photoionization of the neutral CsF vapor was assumed to be the only excitation mechanism of $Cs^{2+}F^-$ and the only source of electrons. A three body recombination process was included in the model in the vicinity of the target to regulate electron density, and electron de-excitation of the $Cs^{2+}F^-$ upper state was assumed to be only significant loss process, having a relatively large rate constant. All processes considered in this model were faster than our 30 ns laser pulse, so that equilibrium could be assumed.

The calculated number density of electrons and $Cs^{2+}F^-$ is shown in Fig. 4. For this calculation, two plasma temperatures, 10 and 20 eV, were chosen [4]. Based on these calculations for a 10 eV plasma, the peak number density of the $Cs^{2+}F^-$ was estimated to be $10^{14}\,cm^{-3}$, leading to 3×10^{14} radiative decays for a CsF pressure of 3 Torr in the observable volume. Reasonable agreement was found with the experimentally estimated number of $10^{13}-10^{14}$ emitted photons. This excited state number density of $Cs^{2+}F^-$ could produce a gain coefficient of several percent per centimeter, assuming a calulated stimulated cross section of $1.5\times10^{-16}\,cm^2$ [1] and assuming little absorption at the laser wavelength. The measured absorption cross section of $3\times10^{-18}\,cm^2$ [2] for CsF vapor at 185 nm implies that the production of a laser in CsF vapor should be attempted near the target where little ground state CsF remains, due to the high soft x-ray flux.

In addition to these ionic alkali halide excimers, we have recently observed VUV emission from new rare gas-alkali metal ionic molecules. Spectroscopic studies have already been performed for Xe^+Rb ionic molecules at 165 nm, excited by the soft x-rays fro[illegible] a laser-produced plasma [5]. A new VUV emission at 160 nm from Xe^+Cs i[illegible].c molecules has been studied using relativistic electron beam excitation.

In summary, we have observed fluorescence spectra from three ionic alkali halide excimers and two rare gas alkali metal ionic excimers in both the UV and VUV regions and proposed a kinetic model to describe some of the fundamental excitation and quenching processes of such molecules excited by the soft x-rays from a laser-produced plasma.

References

[1] R. Sauerbrey and H. Langhoff, IEEE J. Quan. Electron. QE-21, 179 (1985).

[2] S. Kubodera, L. Frey, P.J. Wisoff, and R. Sauerbrey, Opt. Lett. 13, 446 (1988).

[3] L. Frey, S. Kubodera, P.J. Wisoff, and R. Sauerbrey, J. Opt. Soc. Amer. B (submitted).

[4] P. Mora, Phys. Fluids 25, 1071 (1982).

[5] P. Millar, T. Petersen, G. Warwar, P.J. Wisoff, and R. Sauerbrey, Opt. Lett. (to appear).

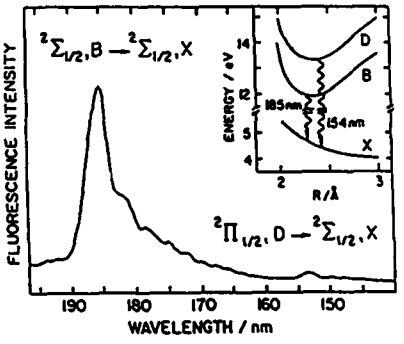

Figure 1. Time-integrated fluorescence spectrum of $Cs^{2+}F^-$ ionic excimers.

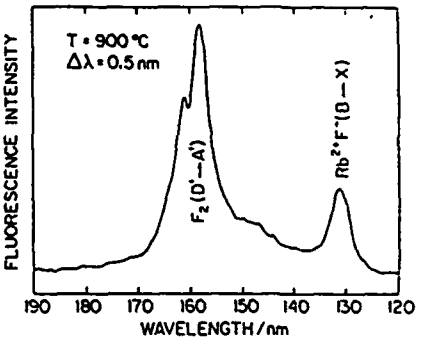

Figure 2. Time-integrated fluorescence spectrum of $Rb^{2+}F^-$ (B→X) transition.

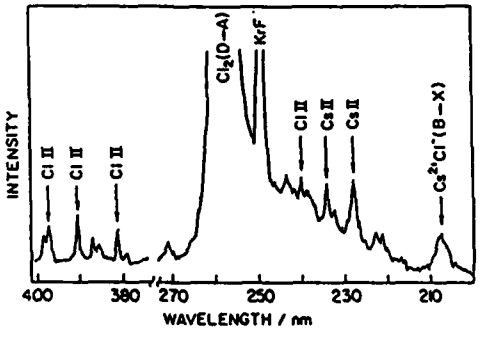

Figure 3. Time-integrated fluorescence spectrum of $Cs^{2+}Cl^-$ ionic excimers.

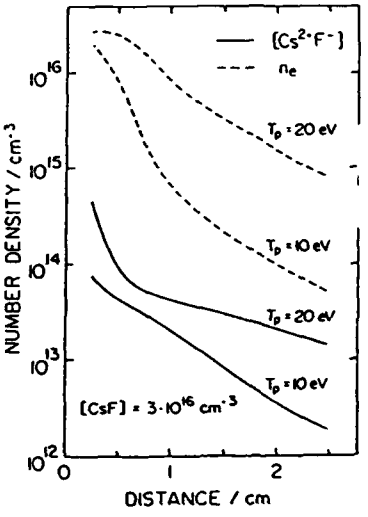

Figure 4. Calculated electron number density and $Cs^{2+}F^-$ population density in laser produced plasmas.

AN LNA LASER FOR HELIUM EXPERIMENTS*

Ti Chuang and Harold Metcalf
Physics Dept., SUNY Stony Brook, NY 11790

We have designed, built and operated an LNA laser, end pumped by a high power diode laser array, for the purpose of exciting the He resonance transition $2^3S \rightarrow 2^3P$ near $\lambda = 1.083$ μm. LNA is a host lattice for Nd^{+3} ($La_{1-x}Nd_xMgAl_{11}O_{19}$) chosen because it can be tuned to the transition of interest in helium because it splits and shifts the laser frequency relative to Nd:YAG at $\lambda = 1.064$ μm.

We have made the laser cavity as short as possible to separate its modes and thereby enhance single mode operation because we are interested in the application to atomic beams rather than Doppler broadened vapors of He. While previous workers[1] have used an intracavity Lyot filter to discriminate against the strong LNA peak at $\lambda = 1.054$ μm in favor of the weak one at $\lambda = 1.083$ μm (resonant with the He transition), we used a dichroic coating on the output mirror that reflects about 98% at 1.083 μm but only 60% at 1.054 μm. This results in one less element to adjust and a much more compact cavity that both eases alignment and separates the modes.

Our S = 37 mm (optical length) long laser cavity, bounded by this curved, dichroic output mirror and the crystal's end coating, which is also dichroic, has a mode separation of about 4 GHz (0.15 A). We use a solid quartz intracavity etalon 1/4 mm thick with reflection coefficient R = 60% on each surface, thus having FSR of 400 GHz (15 A), finesse of $\pi\sqrt{R}/(1-R) = 6$, and resolution ~ 67 GHz. This etalon therefore has about 17 cavity modes between its 50% points, so that it can select a single one of them sufficiently well.

The Nd^{+3} ions in the cylindrical LNA crystal are excited by 794 nm light from a Spectra Diode Labs 2420C diode laser array whose 200 mW output is collimated, circularized by a pair of anamorphic prisms, and focussed by a 6.5 mm working distance lens to a ~100 μm spot just inside the dichroic coated end of the crystal. This coating transmits more than 90% of the pump light. The lowest order mode of our semiconfocal cavity has a spot size $\sqrt{(\lambda S/\pi)} \sim 100\mu$m, so the pumped volume of atoms is well matched to it. Because the other end of the 10 mm long crystal is anti-reflection coated at 1.08 μm, the only other effective surface in the cavity is the curved output mirror at its end (also dichroic to suppress laser action at 1.05 μm).

We have also built a slightly different cavity using a plane mirror and a lens instead of a curved mirror, and by tilting the etalon in the parallel beam part of this cavity, we have tuned this laser to the He resonance frequency. We observed the tuning using optogalvanic spectroscopy on a dc discharge in a hollow cathode He lamp, and at the same time we used a wavemeter to observe that the spectrum of the laser remained single mode throughout the tuning range.

We have been studying the properties of LNA crystals and coatings on them for the purpose of designing the best laser. We obtained several crystals from different boules, first from Airtron Corp. and later from Union Carbide Corp. The Airtron crystals were properly coated for end-pumped diode laser excitation, and we will soon coat those from Union Carbide. In order to compare crystals, we measure the absorption length at the pump wavelength to establish efficiency (LNA absorbs a 15 nm wide band between 790 and 805 nm with a strong peak near 794 nm), and at the laser wavelength to establish the loss (we use one crystal as a laser to test others).

These measurements must be corrected for reflection losses, which we measure by recording the intensity of the reflected spots (we tilt the crystal just a few degrees to do this). For the coated crystals, the reflectance of the dichroic face of the crystal at 794 nm determines how much pump light will be admitted to the crystal, and at 1.083 μm determines how much loss there is from the laser cavity.

All these measured numbers are combined into a single "figure of merit" given by FM = $(1-r_d)(1-e^{-L/x})(R_d)(e^{-L/X})(1-R_a)$ for each crystal where r,R are reflection coefficients, x,X are absorption lengths, (lower case x and r refer to λ = 794 nm and upper case X and R refer to λ = 1.08 μm), L is the length of the crystal, d refers to the dichroic coated end of the crystal, and a refers to the anti-reflection coated end (at 1.08 μm). We expect that FM provides a measure of the crystal's performance as a laser. Because more than 95% of the diode laser light is absorbed, we are not concerned with the properties of the anti-reflection coating at 794 nm (r_a).

For the six coated crystals we tested[2] (five were ~10 mm long and one was 5 mm long, all were 3-5 mm diam.), the values of FM ranged from just below 0.7 to 0.9. We also measured the laser threshold and efficiency of four of these six in order to compare the results with FM. (Two of the crystals would not operate in our lab: the FM of one was the lowest of all six but that of the other was near the average. Both of these worked at the University of Missouri with higher pump power. We have recently obtained a 500 mW model 2430C diode array from Spectra Diode Labs that we will soon use for pumping the crystals.) Typical "good" operation has a threshold of ~90 mW of 794 nm pump light and slope efficiency ~15%, but the four crystals have very different values of these parameters. In Fig. 1 we show a typical laser efficiency curve and in Fig. 2 we plot efficiency (circles) and threshold (triangles) vs. FM for the four crystals we could get to work.

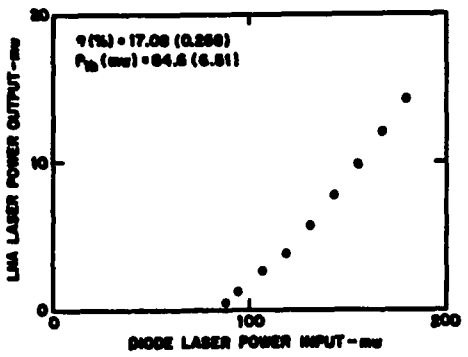

Figure 1

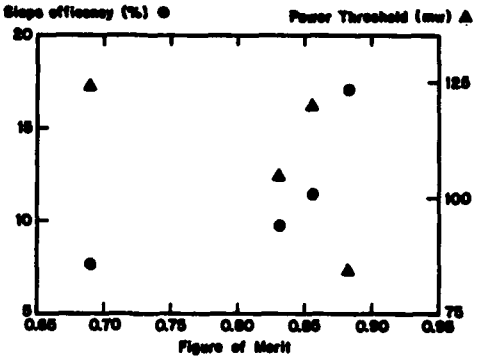

Figure 2

Because the value of FM for the one crystal whose performance was so poor was not exceptionally low, we set out to determine why it behaved so badly. We began by X-ray analysis[3] of the four Stony Brook crystals, and this showed that they were all cut within a few degrees of the crystal axis, but that the "bad" one was probably cut with the cylinder axis along the crystal a-axis instead of the more laser efficient c-axis. This was later confirmed by polarization analysis, thus explaining its poor performance.

The absorption length at λ = 794 nm of the three uncoated crystals from Union Carbide averaged 4.5 mm, compared with 3.5 mm for the Airtron crystals, and we therefore expect that their performance will be about the same. We plan to cut and coat both 5 and 10 mm long crystals from the same Union Carbide rod to measure their laser threshold and efficiency coefficients, and will report on the results of those measurements in a later paper.

We are evaluating different cavity configurations such as a ring and/or coupled cavities for wavelength selection as well as a number of design parameters for optimal choices.

We wish to acknowledge the capable assistance of Dan Downs in analyzing some of the data.

*Supported by NSF and ONR

REFERENCES

1. L.Schearer et al., IEEE J.Quant.Elect.QE22, 713(1986); J. Hamel et al., Opt. Commun. 63, 114 (1987).
2. We thank Laird Schearer of the University of Missouri for kindly loaning us two of these coated crystals.
3. We thank Yusheng Li of the Materials Science department at Stony Brook for allowing us to use the X-ray equipment.

THE UNIFORM MAGNETIC FIELD FREE-ELECTRON LASER WITH HIGHER HARMONIC EMISSION

Josip Šoln
Harry Diamond Laboratories, Adelphi, Maryland 20783

ABSTRACT

Within the multiphoton formalism, the study of the spontaneous and the stimulated emission with the fundamental and the higher harmonic frequencies in the uniform magnetic field free-electron laser is being pursued.

INTRODUCTION

The uniform magnetic field free-electron laser (FEL) is one of the more interesting wiggler-free FEL's.[1,2] As is the case with the usual FEL with a helical wiggler magnet, this FEL also has no on-axis higher harmonic emission (where the axis direction coincides with the direction of the uniform magnetic field). Nevertheless, the multiphoton formalism predicts[2] that the on-axis gain is easily 20 percent for plane-wave-like 100 GHz stimulated radiation with an interaction length (L) of 75 cm, a magnetic field (B) of 0.75 T, a total beam energy (E) of 1.2 MeV, and a beam density of 10^8 cm^{-3}. Now the requirement that in the uniform magnetif field FEL the radiation be Doppler-shifted[3] means that the perpendicular (with respect to the uniform magnetic field) component of the electron velocity be no more than 10-20 percent of the parallel component of the electron velocity. Consequently, the emission into higher harmonics (occurring only off-axis) could be observed with Doppler-shifted frequencies at very small angles with respect to the uniform magnetic field. The spontaneous emission covers a wide spectral region (since it is due to all the harmonics); as such it should be able to stimulate the radiation with the fundamental and higher harmonic frequencies from electrons further along the interaction region for sufficiently wide electron beams.

HIGHER HARMONIC EMISSION

The Fourier transform of the electron current density[2] can already tell us that the resonance radiation angular frequencies are of the form

$$\omega_\ell = \ell \bar{\omega}$$

where $\ell = 1$ corresponds to the fundamental frequency, while $\ell \geq 2$ corresponds to the higher harmonic frequencies. The fundamental radiation angular frequency $\bar{\omega}$ is the Doppler-shifted angular cyclotron frequency whose dependence on the angle at which the radiation occurs can be found in reference 2.

With the assumption that the interaction time is much larger than the period of the electron helical motion,[2] the multiphoton formalism can give, in principle, partial (for each ℓ separately) and total expressions for quantities such as the average number and the radiated energy per unit solid angle for spontaneously emitted photons. Preliminary investigations seem to indicate that in order to generate radiation in the microwave/far-infrared spectral region one would need $E \leq 10$ MeV, $B \leq 4T$, and $L \leq 100$ cm. With such an energetic beam, we can have spontaneous emission both on-axis (with the fundamental frequency) and just slightly off-axis (with the first few harmonic frequencies); i.e., from the practical point of view interesting radiation is occurring essentially in the forward direction.

REFERENCES

1. S.K. Ride and W. B. Colson, Appl. Phys. 20, 47 (1979).
2. J. Šoln, J. Appl. Phys. 58, 3374 (1985).
3. T. C. Marshall, Free-Electron Lasers, MacMillan, New York (1984).

A ONE-HERTZ HYPOCYCLOIDAL PINCH PLASMA PUMP SOURCE FOR ULTRAVIOLET DYE LASERS

D. D. Venable, S. M. Lee, J. H. Lee and K. S. Han
Hampton University, Hampton, VA 23668

ABSTRACT

We have utilized a repetitively operated hypocycloidal pinch plasma device (HCP) as a broadband optical pump source for ultraviolet (uv) lasers. This presentation discusses enhancements in the system previously reported[1] to allow 1 Hz operation. The dye selected for testing the system is BBQ which has an absorption peak at a wavelength of 305 nm and a fluorescence peak at a wavelength of 385 nm. We have measured a slope efficiency of 0.01% for pumping BBQ. Dependence of the laser performance on firing rates (up to 1 Hz) and on dye flow rates has been characterized. Our system compares favorably with coaxial flashlamp pumped uv dye lasers with similar input energies and repetition rates and can, however, be scaled to input energies higher than those achievable with flashlamps.

INTRODUCTION

Comparisons of various dye laser pump sources typically utilized in the ultraviolet (uv) portion of the spectrum indicate that the hypocycloidal pinch (HCP) device has distinct advantages over other sources.[2] The HCP device has been extensively utilized in our laboratories as a pump source for ultraviolet and blue-green dye lasers. Appropriate references on these works are given in the recent theses by S. M. Lee[3] and by K. S. Nam.[4] In this paper we discuss the operation of an HCP device in a repetitive mode of operation for pumping BBQ dye.

EXPERIMENTAL RESULTS

The new HCP prototype had a net resistance of 178 mΩ and a total inductance of 135 nH. These values were, respectively, 4.5 and 0.68 times higher than those given for the prototype of reference 1. The capacitive storage energy was 1 kJ and 68% of this energy was converted to stored energy within the HCP device. This resulted in a peak current of 64 kA for the system. A complete listing of the electrical characteristics of the prototype is given in Table I. It should be noted that because of the metal construction of the device, higher charging energies can be achieved by replacement of appropriate circuit elements.

The HCP continuum light emission approximated that of a 15,000 K blackbody when operated at the optimum filling gas pressure of 10 Torr of argon. The measurement system was calibrated at wavelengths above 250 nm by comparison to NBS traceable light emission standards. Because of the weak sensitivity of our measuring instruments, we were unable to make quantitative measurements below 250 nm. The time integrated emission within the BBQ absorption band (285-325 nm) was 45 kW/cm^2 which corresponded to a 13% spectral efficiency for the system. The total useful light energy incident on the

lasing medium was 1.2 J.

The pump intensity was monitored for long term operation (greater than 100 shots) and found to fluctuate by less than 8% for the 1 Hz operation mode. Even though the pump light was stable the uv dye laser output showed a strong dependence on the thermal gradients produced in the dye solvent at each firing of the system. To characterize this effect, the beam of a reference He-Ne laser was directed through the HCP laser tube and the defocusing of this probe beam was monitored as the HCP system discharged. The time required for the probe beam to refocus after each firing represented a useful upper limit on the laser repetition rate. Figure 1 shows the laser output energy as a function of the number of shots for various repetition rates. This data show that the laser output energy fluctuates by less than 15% for a given firing rate but decreases from 60 to 8 mJ for near single shot to 1 Hz operation. The data in Fig. 1 were obtained with a dye circulation rate sufficient to refresh the laser tube 15 times per second (a refresh rate of 15 Hz.) Figure 2 shows the laser output energy dependence at 0.5 Hz operation as a function of refresh rate. The smaller laser energies at low refresh rates and high repetition rates result from the heating of the boundary layer of the dye solution by the hot uv irradiance of the HCP pump. Characteristics of the dye laser are given in Table II. The overall system efficiency, defined as the ratio of laser output energy to electrical input energy, of 0.01% compares favorably with other broadband pump systems in this region of the spectrum.

Table I. Electrical circuit parameters.

Power Supply Capacity	40 kV, 200 mA, P_{max} = 8 kW
Operating Rate	1 Hz at V_0 = 30 kV
Stored Capacitor Energy	630 J (1.1 kJ for V_0 = 40 kV)
Damping Factor	7.8 x 10^6 Hz
System Inductance	135 nH
System Resistance	178 mΩ
Average HCP Inductance	80 nH
Average HCP Resistance	150 mΩ
Cycle Period	2.7 μs
Maximum Current	94 kA
Ringing Frequency	370 kHz
Percentage Reversal	12%
Electrode Materials	Molybdenum
Insulator Material	Ceramic

All parameters measured at 10 Torr (Ar).

Table II. Parameters of BBQ dye laser.

Absorption Wavelength (Peak)	307 nm
Untuned Laser Wavelength	386 nm
Laser Energy-Single Shot (for V_0 = 30 kV)	60 mJ
Optimum Filling Pressure	10 Torr
Optimum Output Coupler	50%
Extracted Energy Density	50 mJ/cm^3
Maximum Power	260 kW
Pulse Width (FWHM)	0.23 μs
Divergence Angle	2 mrad
Repetition Rate	1 Hz
Laser Energy (at 1 Hz)	8 mJ

SUMMARY

A 1 Hz HCP laser operating at 1 kJ input energy has been fabricated and tested. The time integrated continuum emission of the pump light approximated that of a 15,000 K blackbody at wavelengths above 250 nm. The pump emission was

found to be stable at 1 Hz operation. However thermal effects introduced by heating of the dye solution resulted in a reduction of the laser output as repetition rates increased. The overall efficiency of the system was found to be 0.01% for single shot operation and reduced by 85% for operation at 1 Hz.

This research was supported in part by AFOSR grant AFOSR-86-0345.

REFERENCES

1. W. J. Yi, D. D. Venable and Ja H. Lee, Proceedings of the International Conference on Lasers '86, edited by R. W. McMillan, (STS Press, McLean, VA, 1987), pp. 411-415.
2. W. J. Yi, Ultraviolet Dye Lasers Pumped by Hypocycloidal Pinch Plasmas, M. S. Thesis, Hampton University, Hampton, VA 23668, 1987.
3. S. M. Lee, One Hertz Ultraviolet Source for Laser Excitation, M. S. Thesis, Hampton University, Hampton, VA 23668, 1988.
4. K. S. Nam, Megawatt Blue-Green Dye Laser Excitation by A Hypocycloidal Pinch Plasma, M. S. Thesis, Hampton University, Hampton, VA 23668, 1988.

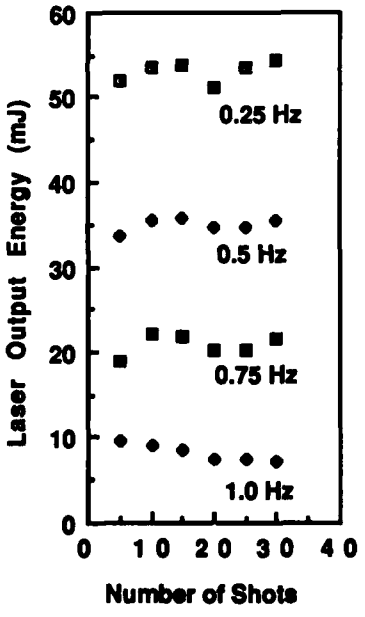

Figure 1. Stability of the laser output at different firing rates. In all cases the refresh rate was 15 Hz.

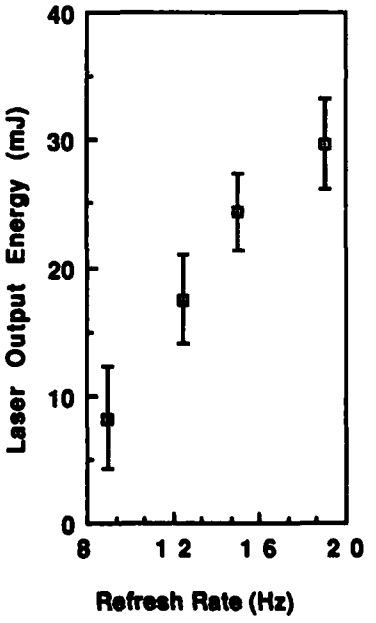

Figure 2. Output laser energy dependence on refresh rate. In all cases the firing rate was 0.5 Hz.

ONE MEGAWATT BLUE-GREEN LASER BY HIGH-TEMPERATURE PLASMA ARRAYS

KWANG S. HAN, KIESEO NAM AND JA H. LEE
Hampton University, Hampton, VA 23668

ABSTRACT

An output enhancement of blue-green laser with an array of multiple-stage hypocycloidal-pinch plasmas (HCP) has been achieved.[1] The maximum untuned laser power obtained with LD490 dye (λ_p=500nm) exceeded 1.97 MW with a pulse width of 0.69 μs (FWHM). The system was improved from earlier unit by adopting a large pump length, higher input energies, and an inverse-pinch switch. The thermal effect on laser medium was observed at high peak pump power. The characteristics of the pumping source and optical coupling configuration indicate that the system can be developed for repetitive and high average power operation (>2MW or 1 J).

INTRODUCTION

Description of the HCP plasma source for pumping blue-green dye laser is reported elsewhere.[1] In order to scale up the output power (> 1 MW) and energy (> 1 J) of blue-green dye laser, the previous HCP system[1] was improved by increasing number of HCP array from 6 to 12 units, and using an inverse-pinch switch[2] and transmission line for the reduction of the system inductance. The overall system efficiency improved to 0.04% which is higher by one order of magnitude compared with that of the previous system.

EXPERIMENT AND RESULTS

As shown in figure 1, The HCP array consists of 14 electrodes (brass) and 13 insulators (Macor). The electrodes are connected by three resistor chains as voltage dividers. The HCP array is encased by the cyclindrical electrode which is connected to a plate transmission line. The stored energy 4 kJ in the capacitor bank (three capacitors: 2.7 μF, 18nH, 32 kV each) is transferred to the HCP through transmission line when the breakdown occurs in the inverse-pinch switch. As shown in Fig. 2, the risetime (≈1μs) of the pumping light decreases as the input energy increases and the filling gas pressure decreases because the rise time depends on the rundown speed of the current sheet in the HCP chamber. As shown in Fig. 3, peak intensity of the pumping light increases with the input energy and also depends on argon fill gas pressure. The optimum pressure for this experiment was found to be 20 Torr for laser output energy, and 5 Torr for output power at the input voltage of 35 kV. Fig. 4 shows temporal shape of laser pulse and pumping light pulse. As argon fill gas pressure decreases to 5 Torr, the risetime of pumping light becomes shortest and the laser power reachs maximum. Fig. 5 indicates that both laser output energy and power reach the maximum values of 1.36J/1.97MW at the dye concentration of 4 x10^{-4} M and the input energy of 4 kJ, but both laser energy and power decreases with concentration (> 4x10^{-4} mol). The extracted energy density was 412J/liter. It has been observed that the laser output tends to saturate with the

input energy > 4 kJ (instead of linear increase) due to the thermal lensing effect on the dye.

Conclusion

Laser excitation of LD490 dye was achieved with an improved HCP device and laser output energy/ power of 1.36J/1.97MW were obtained with the pulse width of 0.69 μs. With further improvement by reducing thermal effect and using higher driving energy (> 10 kJ) etc., the system could be scaled up beyond the megawatt level suitable for the applications to the ocean optics. We acknowledge that this work was supported by ONR Contract No. N00014-80-C-957.

References

1. K. S. Han, S. H. Nam and J. H. Lee, J. App. Phys. 55, 4113 (1984).
2. S. H. Choi and J. H. Lee, 22nd Intersociety Energy Conversion Engineering Conf. (IECEC), Philadelphia, Aug. 10-14, 1987, Paper 979130.

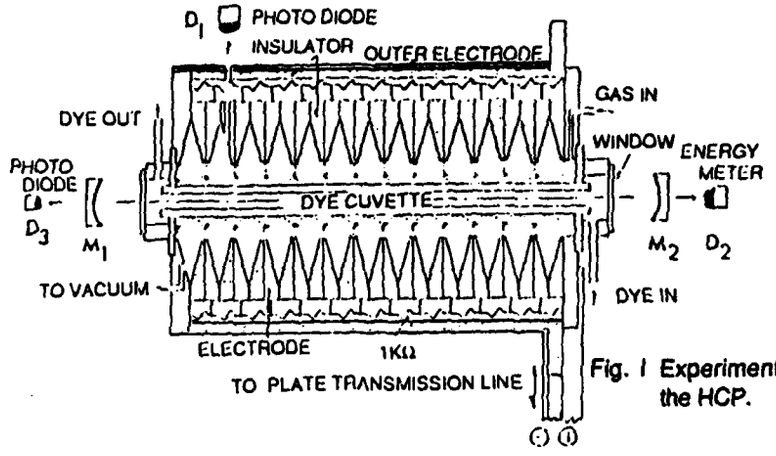

Fig. 1 Experimental Set up of the HCP.

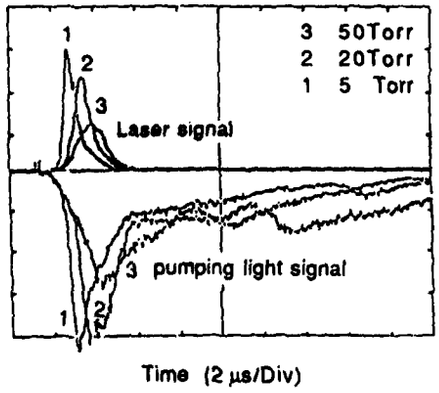

Fig. 2 Temporal shape of laser pulse and pumping light pulse for the input energy of 4 kJ.

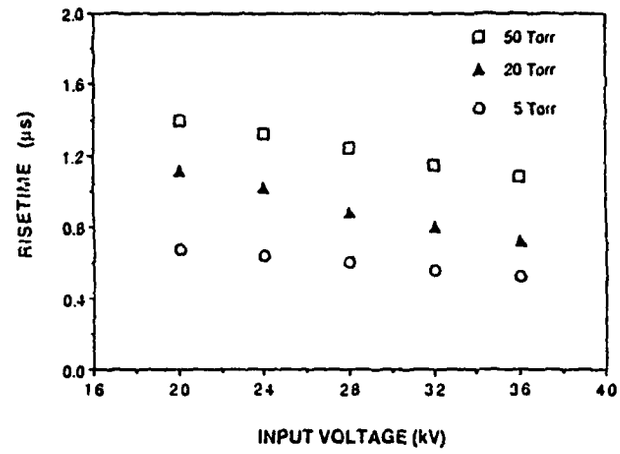

Fig. 3 Risetime of pumping light vs. the input voltage.

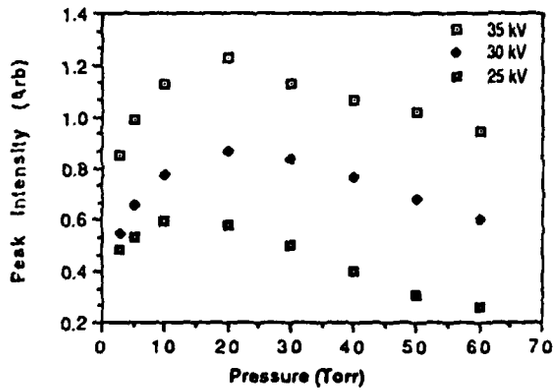

Fig. 4 Peak intensity of pumping light vs. argon fill pressure.

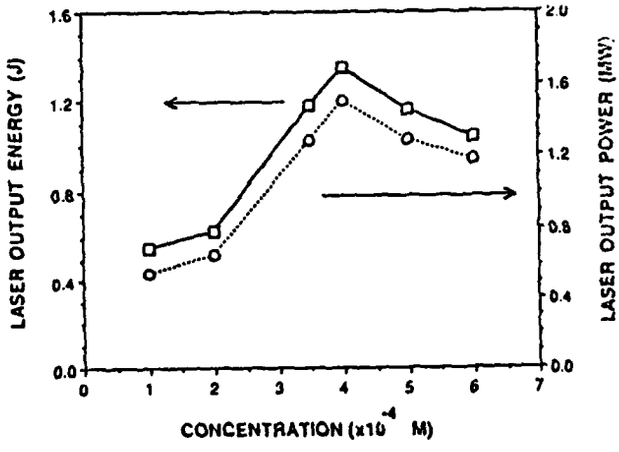

Fig. 5 Laser output energy /power vs. LD490 dye concentration for the input energy of 4 kJ.

INCREASE OF DYE LASER ENERGY BY AN ENERGY CONVERTER DYE

C. H. OH and U. C. Suh
Kyungpook National University, Taegu, 702-701, Korea

ABSTRACT

In order to increase the laser energy through spectrum conversion of the pumping light, the converter dye, BBQ was mixed in the laser dye solutions. The laser was pumped by an Ar flashlamp with a longer pulse width. Various concentrations of laser dye mixture LD490+BBQ in methanol were used. The experimental results show that the laser output energy increases by 180% with a dye mixture made of 4.5×10^{-6} mol/l over the maximum output obtainable with the laser dye alone, while the laser power increases by 92% with the same conditions. Comparison with the previous results was discussed.

INTRODUCTION

The mixed dye method for enhancement of dye laser efficiency has been developed in several years. K.S.Han et al at Hampton University employed this method for enhancement of a blue-green laser efficiency and they obtained better than 80% increase of laser energy for LD490+BBQ and coumarin 503+BBQ.(1) The pumping source was a hypocycloidal pinch (HCP) array which was modified slightly for laser pumping.(2)

Here, we employed the same mixed dye method as stated above except the pumping source which was an Ar flashlamp. However, more increase (180%) of dye laser energy was obtained and reported on this paper.

EXPERIMENTAL METHOD

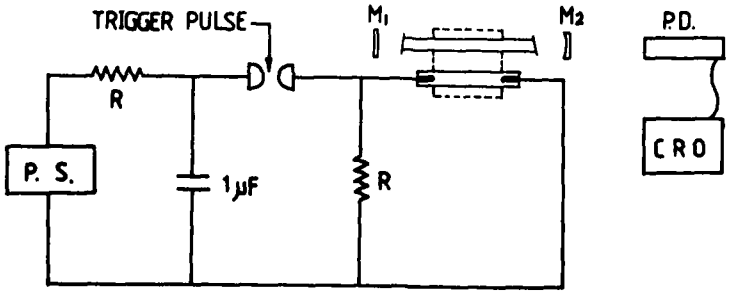

Fig.1. Experimental arrangement

Fig. 1 shows the experimental arrangement of electrical circuit, laser cavity and light detector system. The stored energy used to operate the Ar-flash-lamp was 80J when the capacitor was charged at 12.6kv. The risetime of the pumping light was 0.5μs and its pulse width (FWHM) 2.5μs. The laser oscillator consists of a quartz cuvette and two laser cavity mirrors. The cuvette has an inner diameter of 6mm and a length of 100mm. The laser mirror M_1 (in Fig.1) has a flat HR surface for a central wavelength of 500nm with a bandwidth of 70nm. The output coupling mirror M_2 with a 2m radius of curvature has its reflectivity of 98% for the same central wavelength and band width. The laser dye LD490 is dissolved in pure methanol and the converter dye BBQ is slow to dissolve in methanol. Therefore, the saturated solution of BBQ in methanol is added to LD490 solution in the same solvent to make different concentrations of BBQ.

RESULTS AND DISCUSSION

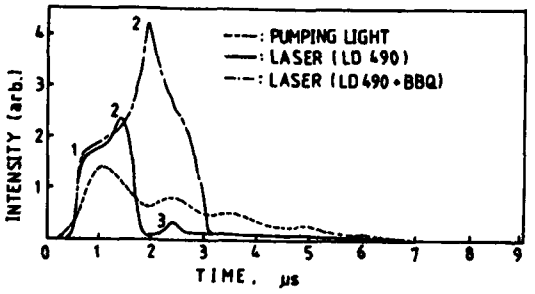

Fig.2. pulse shapes of pumping light and dye lasers

Fig.2 shows the typical pulse shapes of pumping light and dye laser. The rise time of pumping light was 0.5μs and its pulse width is about 2.5μs and it is ringing slightly due to the L - C component in the discharge circuit. The laser pulse of LD490 shows 3 peaks as noted in the figure. As the addition of BBQ to LD490, peak 1 does not change but peak 2 and 3 increase rapidly. It means that the conversion effect of BBQ on LD490 dye laser pulse is very small on first peak and large on later peaks. Thus it seems likely that the conversion effect takes some times about a few 100 ns. The analysis of peak 1, 2,3 of laser pulse, the laser output power and energy (laser pulse area) as function of BBQ concentration were plotted in Fig.3. The laser output power and energy increase as the BBQ concentration increases until it reaches 4.4×10^{-6} mol/l where the power enhancement is 92% and the energy enhancement is 180%. These increases are expected partially by the converter effect mentioned on the previous paper(1) However, the energy enhancement is much more than the expected value by the spectrum conversion

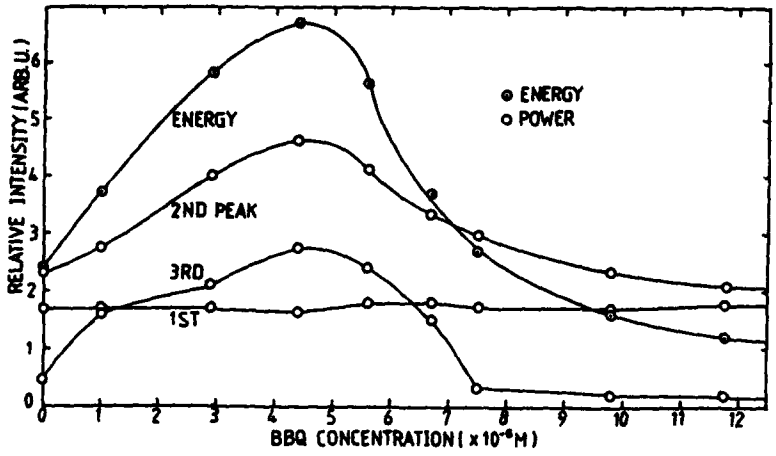

Fig.3 The laser energy and power vs BBQ concentration and analysis of peak 1.2.3.

theory. On the other hand, the laser energy calculation (energy=power×time) involves the time factor, i.e, the pulse width. Therefore, the energy increase is due to both the power increase and the pulse width increase. The later may caused by the increase of BBQ concentration and the longer pulse width of pumping light.

In practice, the pulse width of pumping light used in this experiment was longer than 2.2μs which was nearly twice as larger as that used in previous work [1] in that case the energy increase of 80% was obtained. Consequently, if the longer pulse of light source is applied for the pumping of mixed dyes, the laser energy enhancement is better than that of the laser power. If the BBQ concentration is more than 4.5×10^{-4}mol/l, then the laser output decreases as BBQ concentration increases. This may be due to the increased triplet-triplet absorption by BBQ of fluorscence of the laser dye. Thus the optimum concentration of BBQ for LD490 laser dye is 4.5×10^{-4}mol/l. This is nearly the same value as that of previous work.

In conclusion, it was observed that the use of dye mixture LD490+BBQ resulted in 92% increase of the laser power and 180% increase of the laser energy. This result indicates that if the longer pulse of light source is applied for the pumping of mixed dye, the better enhancement of laser energy than that of laser power is obtainable with the spectrum conversion theory.

ACKNOWLEDGMENT

This work is supported in part by Korea Science and Engineering Foundation(1987)

REFERENCES

1. K.S.Han, C.H.OH and J.H.Lee, J.Appl. Phys.60,3414(1986)
2. K.S.Han, S.H.Nam and J.H.Lee,J.Appl.Phys.55,4113(1984)

PULSED LASER OSCILLATION IN THE $B^1\Pi_u \rightarrow X^1\Sigma_g^+$ TRANSITION OF Na_2 PUMPED BY A DYE LASER*

Wang Qi, Lu Zhiwei, Wu Tao, Cheng Yongkang and Ma Zuguang
Institute of Opto-Electronics, Harbin Institute of Technology, China

ABSTRACT

The pulsed laser oscillations at 525.9 nm, 530.0 nm and 541.4 nm in the $B^1\Pi_u \rightarrow X^1\Sigma_g^+$ transition in Na_2 pumped by a dye laser at 488.00 nm are first obtained with a plane-plane resonator in the temperature range of 580°C-720°C. The pulsed laser oscillations are also observed by using other pumping wavelengths.

INTRODUCTION

In the Na_2 $B^1\Pi_u \rightarrow X^1\Sigma_g^+$ transitions, the laser oscillations which have been achieved are all pumped by a cw argon ion laser[2-6]. By pumping with the pulsed laser, only superfluorescent emission has been achieved[7]. In this paper, the pulsed laser oscillation in the $B^1\Pi_u \rightarrow X^1\Sigma_g^+$ transition in Na_2 pumped by the pulsed dye laser is first reported.

EXPERIMENTAL SYSTEM

The pumping light beam is from a dye laser (Coumarin 102) pumped by an excimer laser (XeCl) and is incident into a heat pipe, in which sodium vapor is produced with 10 torr argon buffer gas. At both ends of the heat pipe, two plane reflecting mirrors form an optical resonator, the transmissivity of which is not optimized for maximum output. The laser oscillation separated from the pumping laser with a grating and is measured by an optical multichannel analyzer (OMA-II).

DISCUSSION ON LASER OSCILLATION

Under the conditions of pumping energy density of 0.5 mJ/cm^2 at the wavelength of 488.00 nm in the heat pipe and the operating temperature range of 580°C-720°C, the three pulsed laser oscillation lines are obtained (see Table I). By dispersing the lines on a grating, the green laser spots

Table I. The pulsed laser transitions in $B^1\Pi_u \rightarrow X^1\Sigma_g^+$ system Na_2 of pumped by 488.00 nm

pump transition v' J' ← v" J"	laser oscillation lines (nm)	laser transitions v' J' → v" J"
2, 39 ← 0, 40	525.9	2, 39 → 10, 39
	530.0	2, 39 → 11, 39
	541.4	2, 39 → 14, 38

* Supported by the Science Fund of the Chinese Academy of Science.

are observed on the screen, shown in Figure 1, and the divergence angle of each of them is about 5 mrad. The laser spectrum recorded by the OMA-II is shown in Figure 2. In comparison with the fluorescence, the intensity of the laser oscillation increases over 10^4 times, which is identical with the calculated result. The linewidth of the laser oscillation lines decreases to about half of that of the fluorescence. With detuning of the resonator, the laser oscillation output decreases rapidly and disappears at detuning of the mirror about 15'. When the pumping laser is attenuated by optical filters, the threshold is obviously observed and is 50 $\mu J/cm^2$ at 640°C.

↑ pumping dye laser

↑ pulsed laser oscillations in Na_2 B-X

Figure 1. The pulsed laser oscillation spots in the Na_2 $B^1\Pi_u \rightarrow X^1\Sigma$ transition (The limit of the rectangle-heat pipe windo makes the laser spots rectangular. To photograph conveni ently, the grating is tilted, so that the laser spots ar parallelograms in this photograph).

The dependence of the pulsed laser oscillation intensity on tl temperature is shown in Figure 3. For each laser line there is .

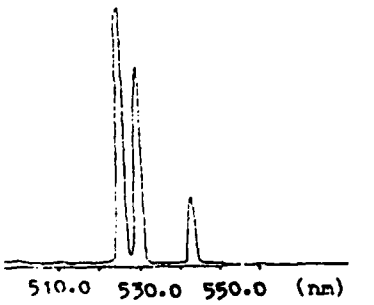

Figure 2. The laser spectrum in Na_2 B-X transitions pumped by a dye laser at 488.00 nm.

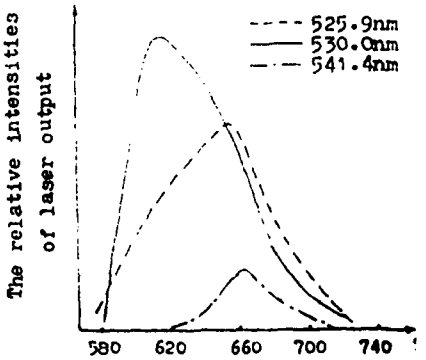

Figure 3. The dependence of r tive intensities among the l lines on the temperature.

optimum temperature. This is because as the temperature is going up, the density of Na_2 increases and the intensity of the laser oscillation also increases with them. However, if the temperature continuously goes up, the increase of the population in the lower laser level causes a rise of the self-absorption larger than that of the laser intensity, so the laser output decreases.

According to the spectroscopic constants given by Kusch and Hessel[8], the possible pump transitions are calculated when the pumping wavelength is 488.00 nm and the linewidth 0.016 nm. Meanwhile, taking account of the population distribution, we confirm that the most probable pump transition is:

$$Na_2\ B^1\Pi_u\ (v' = 2,\ J' = 39) \leftarrow Na_2\ X^1\Sigma_g^+\ (v'' = 0,\ J'' = 40)$$

Taking the $Na_2\ B^1\Pi_u$ ($v' = 2$, $J' = 39$) as the upper laser level, the frequencies of the $Na_2\ B^1\Pi_u \rightarrow X^1\Sigma_g^+$ transitions are calculated, which agree well with the fluorescence lines measured in the experiment. Thus the transitions of the pumping laser and the pulsed laser oscillation lines are confirmed and shown in Table I.

When changing the pumping wavelength, we obtain many other pulsed laser oscillations, typically with less than a 1 Å pumping wavelength spacing over a wide range of the pumping wavelengths. More intense laser output at some pumping wavelengths than at 488.00 nm are obtained. It is seen from this experiment that the $B^1\Pi_u \rightarrow X^1\Sigma_g^+$ system of Na_2 has a low threshold and wide tunable range.

CONCLUSION

The pulsed laser oscillation in the $B^1\Pi_u \rightarrow X^1\Sigma_g^+$ transition in Na_2 pumped by a dye laser is first obtained with a plane-plane resonator. By pumping at 488.00 nm, the three laser oscillation lines at 525.9 nm, 530.0 nm and 541.4 nm are achieved. The wavelengths of pulsed laser oscillation in the experiment are identical with those calculated from spectroscopic constants.

REFERENCES

1. B. Wellegehausen, IEEE J. Quant. Electron. QE-15, 1108 (1979).
2. B. Wellegehausen, S. Shahdin, D. Friede and H. Welling, Appl. Phys. 13, 97 (1977).
3. H. Welling and B. Wellegehausen, Laser Spectroscopy III (Springer-Verlag, New York, 1977), p. 365.
4. B. Wellegehausen and H. H. Heitmann, Appl. Phys. Lett. 34, 44 (1979).
5. C. N. Man-Pichot and A. Brillet, IEEE J. Quant. Electron. QE-16, 1103 (1982).
6. R. Schmiele, W. Luthy and H. P. Weber, J. Appl. Phys. 53, 1356 (1982).
7. M. A. Henesian, R. L. Herbst and R. L. Byer, J. Appl. Phys. 47, 1515 (1976).
8. P. Kusch and M. M. Hessel, J. Chem. Phys. 68, 2591 (1978).

NARROW BAND, HIGH-POWER LIGHT FROM DIODE LASERS*

Song-Quan Shang and Harold Metcalf
Physics Dept., S.U.N.Y., Stony Brook, NY 11790

Because of their ease of use and low cost, tunable diode lasers will have significant impact on experimental atomic physics, and especially on laser spectroscopy. For example, it is now quite reasonable to consider single experiments that use several different lasers for state preparation, optical pumping, opto-mechanical steering and cooling, saturation, probing, etc. Some of the limitations of diode lasers are imposed by their spectral width, frequency stability, spatial beam quality, and low power output. We have found that many of these limitations can be overcome by injecting light from another source into a diode laser array. Many authors have reported successful experiments of this kind[1,2].

We report here extensions and improvements of this prior work[1,2], as well as a simple physical model of the process. We inject only 2 mW from a spectrally narrowed master diode laser[3] into a 100 mW free-running array (Spectra-Diode Labs 2410-C), and we find that it dramatically narrows both its spectrum and beam divergence. We have modelled this injection process, and have found that the dominant feature is phase matching of the injected wave with the free running wave in a single stripe of the array. This model provides an accurate description of both the main output beam features as well as certain secondary behavior.

We use a 10 mW Sharp LT-021 diode as a master laser and focus it onto a single stripe of a Spectra-Diode Labs model 2410-C diode array with a cylindrical and spherical lens. One of these has a PZT to target an individual array stripe (10 μm apart) for light from the master laser. We find that often there is enough optical feedback from the cavity formed between the two lasers to stabilize and narrow the master laser without an auxilliary cavity[3]. The free running array emits in two lobes directed about $\pm 3^0$ from the axis, and the master laser beam is directed close to, but not coincident with, one of these lobes. Typically it is at about 4^0 from the laser axis, about 1^0 larger than the free-running lobes. The main output beam is directed close to the other lobe, and thus the properly injected array can appear almost like a mirror with gain.

Although the free running array has characteristically many spectrally broad, weak longitudinal modes spread over ~1000 GHz, injection of the master laser's light collapses the spectrum into a single mode at the master laser frequency. Fig. 1a shows the many weak modes of the free running array spread over hundreds of GHz, folded by the 2 GHz FSR of the analyzer (finesse ~50). Fig. 1b shows that when the master laser light is admitted, the spectrum condenses dramatically into a single narrow mode whose strength is 50-100 times

stronger (note change of scale). When this beam is mixed on a fast photodiode with light from a separate, independently locked and narrowed diode laser[3], the beat note is observed to be less than 300 kHz wide. (This width actually appears to be about ten times smaller, but overall frequency instabilities presently limit our measurement capability.) The spectral purity is therefore very high.

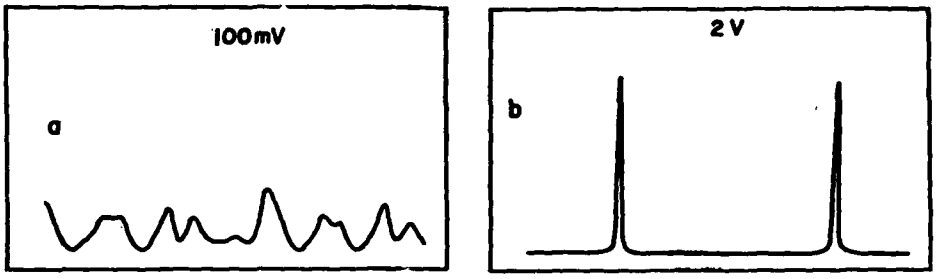

Fig. 1. Note the difference in scale of the two parts.

We have achieved injection locking at many different frequencies, including modes so weak that they don't even oscillate when the array is free running, but they are still within the gain region. The implications are that a laser diode array can generate light at frequencies many hundreds of GHz away from its free running output spectrum, and therefore may not require very careful wavelength selection from the manufacturer.

Injection of the master laser light also has a profound effect on the spatial distribution of the array output. The far-field pattern of the free-running array has two asymmetric lobes a few degrees wide and ~6° apart (Fig. 2a). When the master laser light is admitted, these are collapsed into a single, nearly diffraction limited beam directed at a 1° larger angle from the laser axis than either of the two original lobes (Fig. 2b). The 0.27° spread of the beam is the diffraction angle determined by the full width of the array, suggesting that all the stripes are coherently phase locked together. This beam contains most of the power of the array (typically 90% or 90 mW).

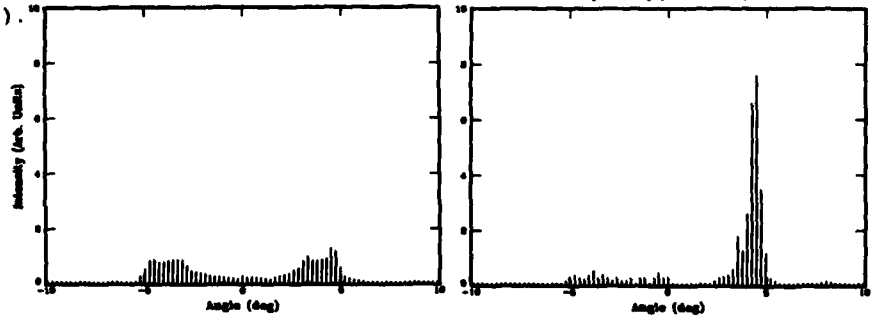

Discussion of the spectral properties of diode laser arrays begins with the free-running mode structure. The separation between these $\Delta\nu$ is not simply the spacing between resonant longitudinal modes of the dielectric Fabry-Perot cavity (index of refraction = n) constituting the laser, but must also account for the dispersion of the medium[4]. Differentiating the resonance condition $m\lambda = 2nL$ gives the spacing $\Delta\nu = c/2n'L$, where L is the channel length and $n' \cong n - \lambda(dn/d\lambda)$ has a surprisingly large correction for the dispersion. Our measured $\Delta\nu$ = (127±3) GHz, and the specified length of the SDL-2410-C laser array (250±10 μm), combine to give $n' = 4.72 \pm 0.30$.

Successful injection locking can be achieved when the external light from the master laser (k_e) is nearly resonant with and matched into one of the resonant modes of a single channel of the slave laser array (k_s). This requires $2k_eL\cos\theta_s = 2\pi j_e$ where j_e is an integer, and Snell's law relates the internal angle θ_s to the angle θ_e between the external beam and the channel axis. For the free-running array, the individual channel resonance condition is $2k_sL = 2\pi j_s$ where j_s is an integer near j_e. Subtracting this from the relation above we find $\cos\theta_s = 1 + \Delta k/k_e + \lambda j/2nL$ where $\Delta k = k_s - k_e$ is the detuning between the injected light and that of the free-running array, λ is the free space wavelength, and $j = j_e - j_s$ is a small (negative) integer.

When the master laser light was focussed by only spherical lenses, we observed one or more small secondary beams at discrete angles from the main beam correponding to different values of j. Careful measurements of the angular dependence of these peaks on frequency corroborates the model of injection locking above. We also found that use of the cylinder lens to compress the master laser light resulted in the appearance of just one of these peaks at a time, selectable by the injection angle.

Also, we have changed k_e (and therefore Δk) by varying the current of the master laser and have observed the resulting angular steering of the beam for various values of j. We use $dk/d\lambda = -2\pi n'/\lambda^2$ and the small angle approximation to find $d\theta_e/d\lambda \cong -nn'/\lambda\theta_e$ where θ_e depends on j. Using the measured value of $d\theta_e/d\lambda$ and $n' = 4.72$ from the mode spacing as determined above, we find the index of refraction n for each j. The average of these is $n = 3.02 \pm 0.20$. Then the definition of n' above gives $E(dn/dE) = -\lambda(dn/d\lambda) = 1.7$ which can be compared with other data[5]. We find that $dn/dE = 1.06$ at E = 1.6 eV (λ=780 nm, the Rb resonance line) fits the data of Ref. 5 very well.

* Work supported by the NSF and the ONR.

1. J. Hohimer et al., Appl. Phys. Lett. 48, 1504 (1986).
2. L. Goldberg and J. Weller, App. Phys.Lett. 51, 871 (1987).
3. B. Dahmani et al. Opt. Lett. 12, 876 (1988).
4. Frank Stern, Phys. Rev. 133, A1653 (1964).
5. M. Afromowitz, Solid State Commun. 15, 59 (1974).

Nd-doped, Tunable IR Lasers for Helium Optical Pumping

L.D. Schearer
Laboratory for Atomic and Molecular Research
University of Missouri-Rolla, Rolla, MO 65401

ABSTRACT

We have investigated the tuning characteristics of several Nd-doped, IR lasers for use as a cw source to optical pump helium atoms at 1083 nm. We report the gain and tuning curves obtained for $LaMgAl_{11}O_{19}$, $YAlO_3$, and $LiNbO_3$. The materials are pumped with a variety of laser sources including Ar^+, and Kr^+ ion lasers, Kr arc lamps, and GaAlAs diodes. Single-mode laser power at the helium resonance wavelength is greater than 15 mw when LNA is pumped with a 450 mw diode. Tunable power up to 1 w is obtained with $Nd:YAlO_3$ in a cw, arc-lamp pumped cavity. Applications for laser-pumped, spin-polarized ensembles of ^3He and metastable ^4He range from space-based magnetometers to nuclear targets.

INTRODUCTION

Our motivation in this work is to obtain tunable cw laser radiation at 1083 nm which can be used in helium optical pumping experiments. The interaction of an appropriately prepared source of radiation with metastable 2^3S_1 helium atoms can produce spin polarized ensembles of metastable ^4He atoms and ground state ^3He nuclei[1]. The pumping process requires cw laser power ranging from several milliwatts single mode to 1 watt in bandwidths ranging from 10 MHz (the natural linewidth) to 1.8 GHz (the Doppler broadened linewidth), depending on the particular application.

In the sections below we describe the results we have obtained for 3 Nd hosts when pumped with several types of laser sources. The final section is devoted to a description of several interesting applications which are currently being explored.

$Nd:LaMgAl_{11}O_{19}$

This material has strong absorption peaks at 514.5, 752, and 800 nm. Consequently, it may be conveniently pumped with the Ar and Kr ion lasers and GaAlAs diodes. The cavity used with an ion laser as the pump source is shown in fig.1.

Fig. 1

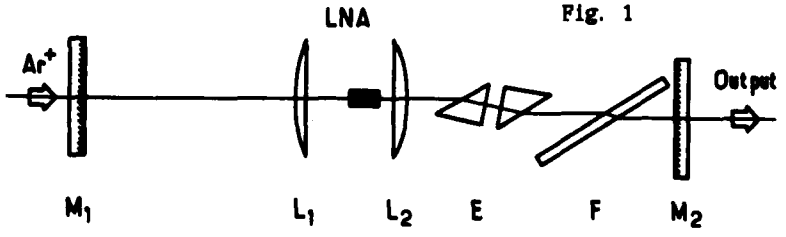

M_1 is the entrance mirror and is highly reflective at 1083 nm while transmitting the pump radiation. L_1 and L_2 are focussing and collimating lenses. The Brewster prism pair, E, is an air-spaced etalon with 50% reflective surfaces. One of the Brewster prisms is mounted on a piezo-electric transducer so that the etalon thickness can be varied electronically. A Lyot filter at F is used for course tuning.

Fig.2 is the fluorescence spectrum of LNA with the arrow indicating the helium resonance wavelength. When pumped with 6 watts at 514.5 nm from an Ar^+ laser more than 300 mw at 1083 nm are obtained in three longitudinal modes separated by 150 MHz. Similar results are obtained with a Kr^+ pump laser at 752 nm[2].

The LNA can also be pumped with a GaAlAs diode operated at 800 nm. With the cavity of fig.3, 300 mw of absorbed pump light yields 15 mw of single-mode laser emission at 1083 nm.

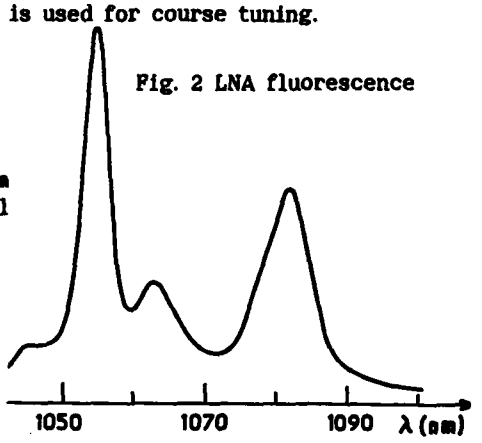

Fig. 2 LNA fluorescence

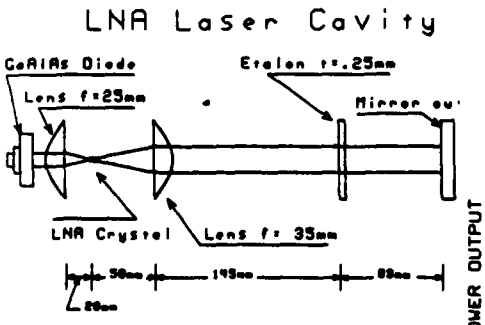

Fig. 3 LNA diode-pumped laser cavity. Output mirror is coated to be transmitting at the 105.4 nm band and 98% reflecting at the 1083 nm band.

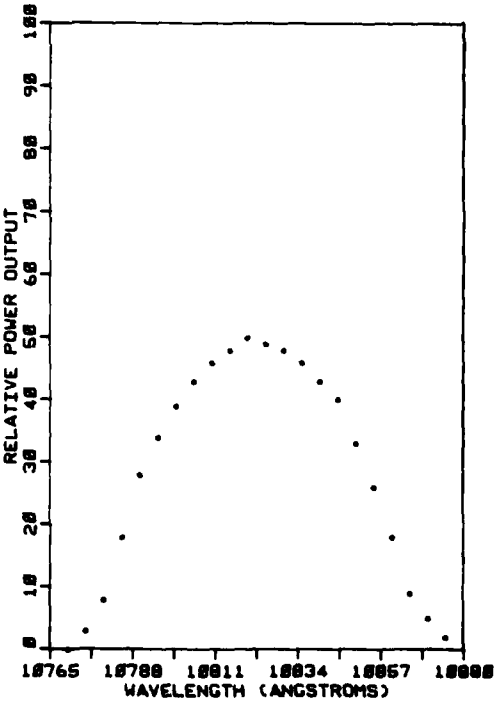

Fig. 4 LNA tuning curve obtained with above cavity as etalon is tilt-tuned. Peak power out is about 15 mw, single mode. Etalon has 50% reflective coatings.

Tuning curves obtained with this cavity are shown in fig.4. The linewidth of the tunable laser is less than 40 MHz, the instrumental width of our scanning Fabry-Perot interferometer.

$Nd:YAlO_3$

A commercial cw, arc-lamp pumped Nd:YAG cavity was modified by replacing the YAG rod with $Nd:YAlO_3$ of the same dimensions and adding a Lyot filter and a solid, uncoated etalon to the cavity[3]. The YAP has gain and thresholds comparable to YAG, the laser output is however, polarized along one of the crystalline axes. Depending on the orientation of the Lyot filter with respect to the crystal the laser lines shown in fig.5 can be tuned with the Lyot filter. The solid and dashed lines represent the transitions obtained for the two crystalline axes. The solid etalon permits one to tune within one of these bands. The tuning curve obtained for the band containing the helium transition is shown in fig.6. Despite being well off the peak of the gain curve, we have nonetheless obtained over 1 w at the helium transition in an emission bandwidth of about 3 GHz.

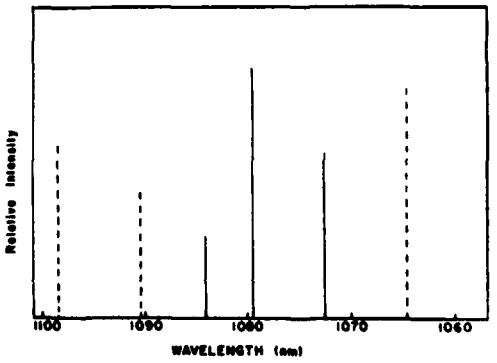

Fig. 5 YAP laser bands tuned with Lyot filter.

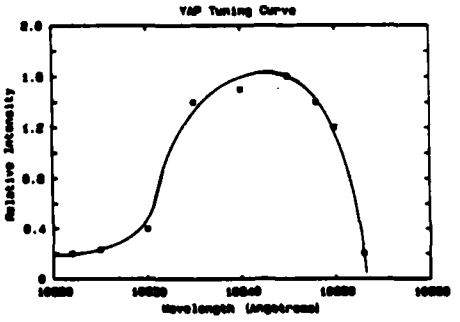

Fig. 6 YAP laser tuning curve on the 1064nm band obtained with solid etalon.

If a small YAP crystal is end-pumped with a 500 mw GaAlAs diode, more than 100 mw of laser emission at 1079.5 nm is obtained. The insertion of a Lyot filter permits us to tune the diode-pumped YAP rod to each of the bands shown in fig.5. A solid, uncoated etalon is used to tune to the helium transition yielding about 9 mw in an 0.0125 nm bandwidth.

$Nd:LiNbO_3$

A small crystal of Nd-doped $LiNbO_3$ has been end-pumped with a cw Kr^+ laser at 752 nm. With 1 watt of absorbed pump power, more than 260 mw of laser emission is obtained at 1084.5 nm. With the addition of a solid etalon the tuning curve of fig.7 is obtained. Apoproximately 60 mw of laser emission at the helium transition is obtained[4].

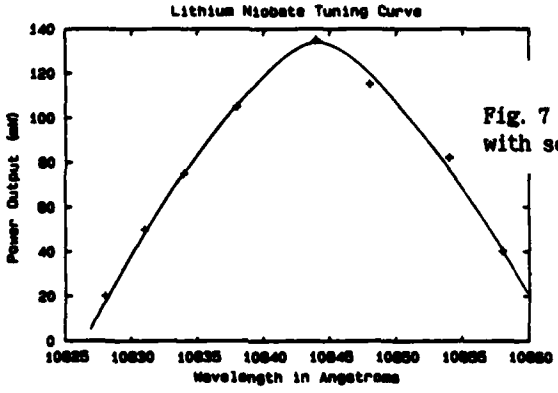

Fig. 7 $LiNbO_3$ tuning curve obtained with solid etalon.

Applications: Spectroscopy

If the tunable emission from an LNA laser is directed through a helium cell in which a weak electrical discharge is used to populate the metastastable state, one can observe fluorescence as the metastable atoms absorb the laser emisssion. A fluorescence spectrum from ^4He is shown in fig.8. The line labelled D_0, is the 2^3S_1-2^3P_0 transition at 1083.29 nm. The D_1 transition is approximately 0.1 nm longer wavelength. The helium metastable atoms may be efficiently optically pumped with either the D_0 or D_1 lines. The excitation of the metastable atoms may also be detected by observing the change in the conductivity of the discharge as the laser is scanned, the optogalvanic effect. Similar results are obtained with ^3He; the spectrum is slightly shifted toward longer wavelengths and is somewhat more complicated due to the presence of a nuclear spin, I=1/2.

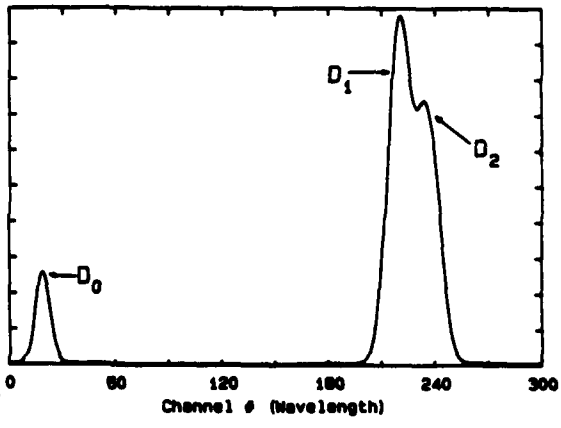

Fig. 8 Fluorescence spectrum of ^4He when the solid etalon in the cavity of fig. 3 is tilt-tuned.

Applications: Magnetometry

The optical pumping process may be used to measure the magnetic field in which the spin-polarized ensemble is located. Using a discharge lamp to pump the spins, for example, one is able to observe changes in the earth's magnetic field[5] at the level of 1 part in 10^7. Such a device is used by the

U.S. Navy to detect submarines. One may also measure changes in fields near zero with a similar sensitivity. Several space probes have carried helium magnetometers to measure planetary magnetic fields. The most recent probe measured the magnetic field of Uranus and is currently on its way to Neptune. We have recently demonstrated an improvement of 2 orders of magnitude in sensitivity of the magnetometer while reducing the power requirements by 1/3 by using a diode pumped, LNA laser for the optical pumping[6].

If the optical pumping process is applied to the mass three isotope of helium, the nuclear spins become polarized. A maser magnetometer at the nuclear frequency has been demonstrated[7]. We anticipate a similar increase in sensitivity and efficiency when our LNA laser is applied to this system.

Applications: Nuclear Targets

Several interesting applications for ensembles of spin-polarized ^{3}He samples have been investigated. For the most part the applications require large polarizations at densities greater than 10^{17} cm^{-3}. These include an investigation of the quantum properties of a spin-polarized Fermi system. The phase diagram of spin-polarized ^{3}He is substantially different from its unpolarized counterpart with the nuclear polarization reducing the domain of existence of the liquid phase. Experiments to investigate these quantum properties of this system are presently under investigation by a group at the Ecole Normale Superieure in Paris[8]. The laser pump sources described here are critical to the success of this program.

Experiments have been proposed to investigate the quark structure of the neutron using a polarized ^{3}He target. With an LNA laser or the Nd:YAP laser described above one can obtain nuclear polarizations exceeding 60%. The nuclear polarization obtained with an LNA laser as a function of laser pump power is shown in fig.9. The laser and target development are discussed in ref. 9.

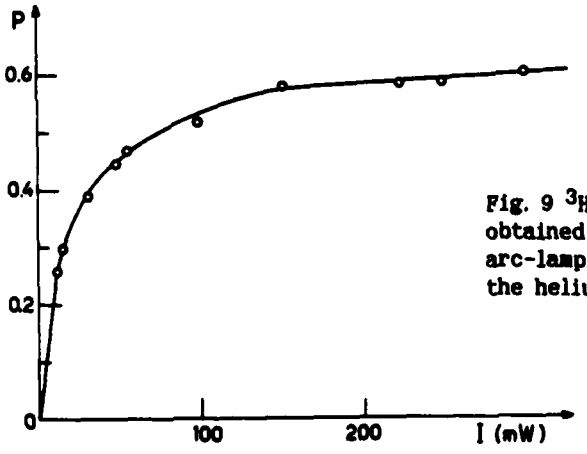

Fig. 9 ^{3}He nuclear polarization obtained with a modified, commercial, arc-lamp pumped YAP laser tuned to the helium resonance transition.

Summary

We have developed several solid state, tunable lasers which can be employed in the helium optical pumping process. Increases in ensemble polarization of 1-2 orders of magnitude are obtained when the laser source replaces the conventional discharge lamp and increases of more than 2 orders of magnitude in the sensitivty of magnetometers have been demonstrated. A variety of new and exciting applications have been suggested which depend critically upon the availability of the lasers described here.

References

1. L.D. Schearer, "Polarization of 2^3S_1 Metastable Helium Atoms by Optical Pumping", in Advances in Quantum Electronics, J.R. Singer, ed.,Columbia University Press, NY, 239-251, 1961. and F.D. Colegrove, L.D. Schearer, and G.K. Walters, Phys. Rev. 132, 2561 (1963).
2. L.D. Schearer, M. Leduc, D. Vivien, A.M. Lejus, and J. Thery, IEEE J. Quant. Electr.22, 713 (1986).
3. L.D. Schearer and M. Leduc, IEEE J. Quant. Electr. 22, 756 (1986).
4. L.D. Schearer, M. Leduc, and J. Zachorowski, IEEE J. Quant. Electr.23, 1996 (1987).
5. J. Rice, L.D. Schearer, anf A. Keyser, J. Geophys. Res.66, 4163 (1961).
6. R.E. Slocum, L.D. Scherare, P. Tin, and R. Marquedant, to be published, Dec 1988, J. Appl. Phys.
7. H.G. Robinson and Than Myint, Appl. Phys. Lett.5, 116 (1964).
8. D.S. Betts and M. Leduc, Ann. Phys. Fr.11, 267 (1986).
9. C.L. Bohler, L.D. Schearer, M. Leduc, P.J. Nacher, J. Zachorowski, R.G. Milner, , R.D. McKeown, and C.E. Woodward, J. Appl. Phys.63, 2497 (1988).

REDUCTION OF TETRAVALENT CHROMIUM INDUCED OPTICAL LOSS IN Nd:Cr:GSGG*

A. J. Pertica, J. E. Marion and S. E. Stokowski
Lawrence Livermore National Laboratory, Livermore, CA 94550

ABSTRACT

We report on methods for elimination of optical absorption in neodymium, chromium doped gadolinium scandium gallium garnet (Nd:Cr:GSGG) due to tetravalent chromium at the laser wavelength. These methods include doping of the crystal melt with specific additives as well as post growth heat treatments.

Nd:Cr:GSGG CRYSTAL DEVELOPMENT

Neodymium:chromium:gadolinium:scandium gallium garnet (Nd:Cr:GSGG) is among the best material available for high-average-power (HAP) laser operation because of its exceptional laser efficiency.[1] We are developing this material under a contract to Allied Signal Corporation.[2] Our goal is stable growth of >10-cm-diam by >20-cm long crystals and low absorption at the laser wavelength. Divalent calcium is added to the melt to promote stable growth, but gives high absorption because of the conversion of Cr^{3+} to absorbing Cr^{4+}. Addition of Ce^{3+} to the melt compensates the Ca^{2+}, keeping Cr in its trivalent state without destabilizing the growth. Unfortunately, a slight amount of Cr^{4+} remains in the large boules; absorption ranges from about 1% cm^{-1} at the top of the crystals to about 8% cm^{-1} at the bottom.[3] For efficient laser operation, the loss must further be reduced to <1% cm^{-1} over the entire length of crystal.

Current inventory of Nd:Cr:GSGG includes four boules, all grown with Ca and Ce additions, which are available for laser experiments. The largest boule is 96 mm in diameter by 194 mm long.

ONE MICRON ABSORPTION IN Nd:Cr:GSGG

We believe that the absorption in the present GSGG is attributable to Cr^{4+} that occupies fourfold coordination sites in the garnet lattice. During the three years of this contract, we scaled GSGG crystal growth from 1" diameter to 4 to 5" diameter boules. This scaling decreased the thermal gradients at the melt/crystal growth interface, leading to growth instabilities and spiral growth morphology. Although divalent Ca additions to the

*Work performed by the Lawrence Livermore National Laboratory under the auspices of the Defense Advanced Research Projects Agency, ARPA Project Order 5358, and US DOE/UC Contract No. W-7405-ENG-48.

melt controlled the spiraling, uncompensated Ca^{2+} ions and a slightly oxidizing growth atmosphere (necessary to prevent volatilization of gallium suboxide) induced the formation of undesirable Cr^{4+}.

To alleviate this problem, cerium oxide was added to the melts. Because of its electrochemistry, Ce changes its valence state from 3+ to 4+ (to compensate Ca^{2+}) more readily than Cr. Ce in either valence state does not contribute to an absorptive loss at the laser lines of GSGG and only negligibly in the pump bands. The addition of Ce resulted in material with losses <10% cm^{-1}, a tenfold improvement over previous boules. The spatial distribution of loss in GSGG depends on the segregation coefficients of the various dopants and on the annealing effects imposed by the growth atmosphere as the boules are grown.

Two Cr^{4+} spectral absorption features are seen in Ce:Cr:Nd:GSGG. We denote the primary center as CR4, which consists of a double peak in the near-IR region with accompanying bands in the red and blue-green spectral regions. CR4 absorptions can be intermixed with absorptions from a second center (denoted as CR4'), which is believed to arise from energy perturbations of Cr^{4+} from local defect sites. Figure 1 shows absorption spectra for each center. Although CR4' also absorbs at the laser band, its peak is shifted further towards the IR and thus results in lower loss than CR4. Exposure to blue photons at room temperature transforms CR4 into CR4', whereas the reverse transformation occurs upon heating above about 375°C. Both CR4 and CR4' occupy one of the tetrahedrally coordinated sites in GSGG. Since these sites lack a center of symmetry, the intensity of transitions is very high, such that even minute amounts of Cr^{4+} result in relatively strong absorptions and high loss.

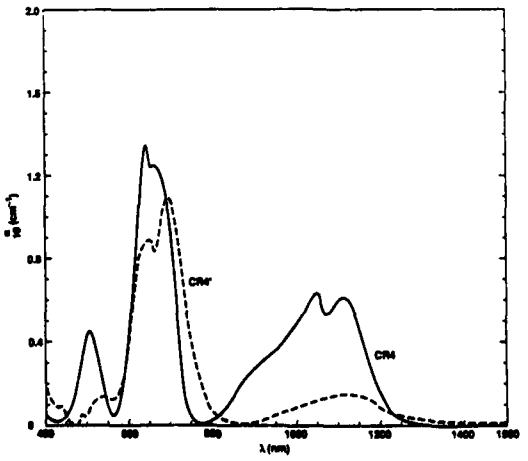

Figure 1. Absorption spectra of CR4 and CR4' in Nd:Cr:GSGG

To further improve the material, we subject the slabs to a high temperature treatment in a reducing atmosphere to reduce the residual Cr^{4+}. The most effective results have been obtained by annealing small samples for 24 hr at 1300°C in a platinum tube furnace with a reducing atmosphere of a 1:1 ratio volume of $CO:CO_2$. The absorption loss in samples treated in this manner were studied spectrophotometrically, calorimetrically, and using a cavity ring-down loss meter technique. In combination, the three methods indicate that the overall loss is less than 0.5% cm^{-1}.

Scaling the heat treatments to the larger slabs has been difficult. While the absorption losses can be decreased by this approach, treatments on large samples often results in high losses due to creation of fine scattering sites or by the migration and reduction of metal ions along dislocations. An early treatment (0.5% H_2 in Ar for 24 hr in a tungsten-lined furnace) resulted in a slab that has lased. While performance was primarily limited by amplified spontaneous emission, residual 1-μm loss was >1%cm^{-1} and there was significant scattering inhomogeneously distributed (~0.5% cm^{-1}).

REFERENCES

1. J. A. Caird, M. D. Shinn, T. A. Kirchoff, L. K. Smith and R. E. Wilder, "Measurements of losses and lasing efficiency in GSGG:Cr:Nd and YAG:Nd laser rods," Appl. Opt. 25, 4294-4304 (1986).
2. Synthetic Crystal Products Division, Allied-Signal Inc., Charlotte, NC 28241.
3. S. E. Stokowski, M. H. Randles, and R. C. Morris, "Growth and Characterization of Large Nd,Cr:GSGG Crystals for High Average Power Slab Lasers," IEEE J. Quantum Electron. 24, (6) 934-948, (1988).

RADIATION DAMAGE IN KBr:Eu^{2+} AND KCl:Eu^{2+} DUE TO 350 nm LASER IRRADIATION*

L. D. Merkle
Physics Department, University of Arkansas, Fayetteville, AR 72701

P. K. Bandyopadhyay
Physics Department, Hendrix College, Conway, AR 72032

ABSTRACT

In the course of a study of excited state absorption in alkali halides doped with Eu^{2+} we have observed changes in the absorption spectra similar to those induced by ionizing radiation. Comparison of these data and observed changes in the Eu^{2+} fluorescence spectra in KBr and KCl with studies of thermally induced aggregation of Eu^{2+}-alkali vacancy dipoles indicate that laser enhancement of such aggregation is primarily responsible for these spectral changes. In KBr:Eu irradiation also produces F-center absorption. The initial rate of F-center production varies as the cube of the laser intensity, suggesting that the irradiation effects are due to three photon generation of electron-hole pairs. This also indicates that near ultraviolet excited state absorption by Eu^{2+} observed in these hosts is not due to ionization of the europium.

INTRODUCTION

Its broad, allowed emission band and strong ultraviolet absorption bands make divalent europium interesting as a short wavelength tunable laser ion in solids. However, strong excited state absorption attributed to ionization prevents laser action in CaF_2:Eu.[1,2] We are studying excited state absorption by Eu^{2+} in hosts in which the ionization model predicts this transition to be removed well into the ultraviolet. In the course of such studies in alkali halides, long-lived laser-induced spectral changes have been observed. These effects and their implication for the mechanism of Eu^{2+} excited state absorption in these hosts are the subjects of this paper.

RADIATION DAMAGE

Single crystals of KBr:Eu^{2+} and KCl:Eu^{2+} were obtained from the crystal growth facility of Oklahoma State University and irradiated by the 350 nm output of a XeF excimer laser. The absorption spectra were probed before and after irradiation using a pulsed Xe lamp whose beam traversed the sample about 0.8 mm behind the irradiated face of each sample. The transmitted probe beam was detected by a Tracor Northern system based on an intensified

*Supported by an Arkansas Science and Technology Authority grant.

photodiode array.

The changes in absorbance of two samples due to irradiation with several thousand pulses at fluences between 0.1 and 0.2 J/cm^2 are shown in Figure 1. The results are similar to those reported in europium doped alkali halides due to x-ray irradiation.[3] In such radiation damage studies the spectral changes are attributed in part to a change in the charge state of some of the europium ions and in part to radiation enhanced aggregation of the Eu^{2+}-alkali vacancy pairs. In the present case no evidence has been found in absorption or emission for Eu^{3+} or Eu^{+}, but the ultraviolet absorbance changes are quite similar to those induced by thermal aggregation of Eu^{2+}.[4] Laser-induced broadening of the Eu^{2+} emission band is also observed, and is consistent with the thermal aggregation studies. It is thus concluded that radiation-enhanced aggregation of the europium occurs in these materials, with charge state changes apparently less important.

The strong F-center absorption band evident in Figure 1 for KBr:Eu is evidence that 350 nm laser irradiation produces free electrons in this material. Since no such F-band is evident in KCl:Eu, a simple thermoluminescence experiment has been performed in this host. Following laser irradiation at 80 K a glow peak does indeed appear at about 130 K, indicating that charges must have been freed by the radiation and subsequently trapped until the warming occurred. The initial rate of growth of the F-band in two KBr:Eu samples has been measured as a function of incident pulse energy, with the results given in Figure 2. The cubic dependence clearly indicates that the production of free charges occurs by three photon absorption. Since the energy of three 350 nm photons excedes the band gap in both hosts, this explains the similarity of the present results to x-irradiation data.

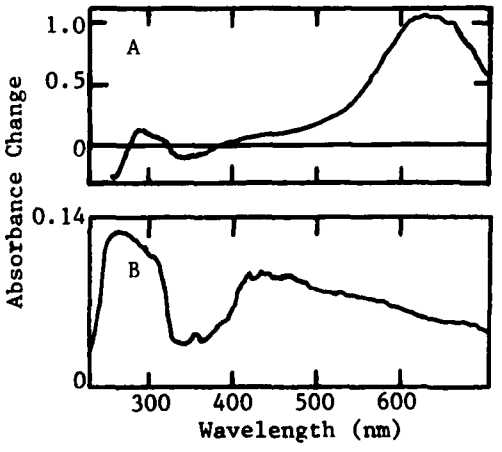

Figure 1. Laser-induced absorption changes in (A) KBr:Eu and (B) KCl:Eu.

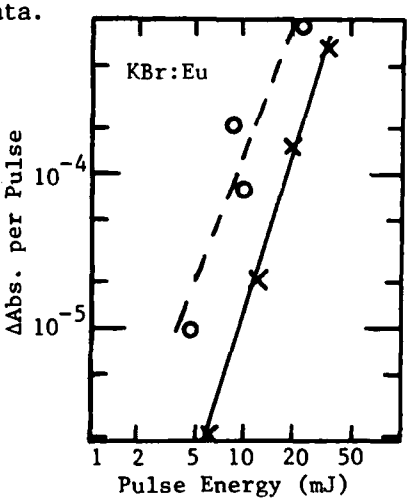

Figure 2. Intensity dependence of the initial rate of F-band growth in two KBr:Eu samples.

IMPLICATION FOR EXCITED STATE ABSORPTION

It has been oberved by the authors that Eu^{2+} in KBr and KCl exhibits an excited state absorption (ESA) band peaking near 4 eV, with the onset of absorption probably below 3.5 eV.[5] Application of the ionization model used in references 1 and 2 to these materials, however, predicts the onset of ESA at about 7 to 9 eV.[5] The question thus arises as to the nature of the near ultraviolet ESA. The three photon nature of the free charge generation noted above helps to address this question. The density of conduction band electrons, n_{cb}, produced by three photon electron-hole generation at a typical pulse fluence of 0.2 J/cm^2 may be estimated using the rate equation

$$dn_{cb}/dt = n_{vb}S_3F^3 \qquad (1)$$

where S_3 is the cross section for three photon ionization, n_{vb} is the density of valence band electrons, and F is the peak photon flux. For a pulse duration of 8 ns, and estimating the cross section as 10^{-80} cm^6-s^2,[6] n_{cb} is on the order of 10^{12} cm^{-3}. The same pulse fluence excites an estimated 9 % of the Eu^{2+} ions and the ESA cross section is large enough that the majority of these should undergo ESA during the pulse as well.[5] Thus for a typical Eu concentration of 1.75×10^{18} cm^{-3} roughly 10^{17} cm^{-3} conduction band electrons should be produced if the ESA is an ionizing transition. Since this process occurs by two single photon steps, the production of free electrons should have been dominated by a quadratic intensity dependence in this case. Therefore the observed cubic dependence strongly suggests that the ESA observed in these materials is not due to an ionizing transition.

As noted in reference 5, the observed ESA may be due to a charge transfer transition, but further study will be required to test this possibility. The presence of a strong excited state transition other than that due to ionization further complicates the optical properties of Eu^{2+}. However, depending on the host dependence of this transition it remains possible that Eu^{2+} doped materials may be found with properties favorable for laser action.

REFERENCES

1. J. F. Owen, P. B. Dorain, and T. Kobayasi, J. Appl. Phys. 52, 1216 (1981).
2. C. Pedrini, D. S. McClure, and C. H. Anderson, J. Chem. Phys. 70, 4959 (1979).
3. K. J. Kao and M. M. Perlman, Phys. Rev. B 19, 1196 (1979).
4. M. Aguilar G., J. Rubio O., F. J. Lopez, J. Garcia-Sole, and H. Murrieta S., Sol. St. Commun. 44, 141 (1982).
5. L. D. Merkle and P. K. Bandyopadhyay, unpublished.
6. G. Brost, P. Braunlich, and P. Kelly, Phys. Rev. B 30, 4675 (1984).

Cr^{3+} TO Nd^{3+} ENERGY TRANSFER IN SUBSTITUED GGG IN RELATION TO THE CRYSTAL FIELD DISTRIBUTION*

A. Monteil, C. Garapon, G. Boulon
UA CNRS n°442 - Université Lyon I - 69622 Villeurbanne (France)

ABSTRACT

In the garnet $(Gd, Ca)_3 (Ga, Mg, Zr)_2 Ga_3 O_{12}$, Cr^{3+} is located in sites of intermediate crystal field strength. This induces a fast energy transfer to Nd^{3+}. We have shown that it is possible to differentiate Cr^{3+} in sites of rather strong field against sites of rather weak crystal field. Different spectroscopic measurements allow us to conclude that Cr^{3+} ions in weaker crystal fields are mainly responsible for the energy transfer to Nd^{3+}.

RESULTS

We have studied a substitued Gadolinium Gallium Garnet (GGG) : $(Gd, Ca)_3 (Ga, Mg, Zr)_2 Ga_3 O_{12}$, which was grown by Crismatec (Grenoble France). In a previous paper [1], we have shown that in such a crystal Cr^{3+} ions are in multisites of varying intermediate crystal field strength. While at room temperature all the ions emit only the $^4T_2$-$^4A_2$ band, at low temperatures, weak crystal field ions emit the $^4T_2$-$^4A_2$ band and strong crystal field ions emit the ^2E-$^4A_2$ line with its phonon-sideband.

In codoped samples, (Cr^{3+} : 0.33%, Nd^{3+} : 2.8%) the emission spectrum (fig 1) consists of both ^2E and $^4T_2$ emission for chromium and several lines belonging to neodymium; also the dips that appear in the $^4T_2$ band correspond to absorption of neodymium. This indicates a Cr→Nd radiative energy transfer. Shortening of chromium emission decay times in the presence of neodymium, indicates a Cr→Nd non-radiative energy transfer (fig 2).

We have made selective excitation near the ^2E-$^4A_2$ transition of Cr^{3+}. Exciting at the maximum of the transition, i. e. exciting both ions in stronger and weaker field sites, we obtained the same emission spectrum as in the case of broadband excitation.

---

* Supported by DRET Grant 86-123

Exciting on the lower energy side of the line, i. e. exciting mostly ions in weaker field sites, we obtained only emission of the $^4T_2$-$^4A_2$ band and of Nd^{3+} lines (fig 3).

It follows from this result that it is the excitation of weak field ions which gives transfer to Nd^{3+}. Moreover, decay of Nd^{3+} emission does not show any long decay time for several orders of magnitude as would be seen if transfer came from ions in strong fields. Comparison of the excitation spectrum of Nd^{3+} near the ^2E-$^4A_2$ transition with the excitation spectrum of weak field ions and strong field ions gives the same conclusion.

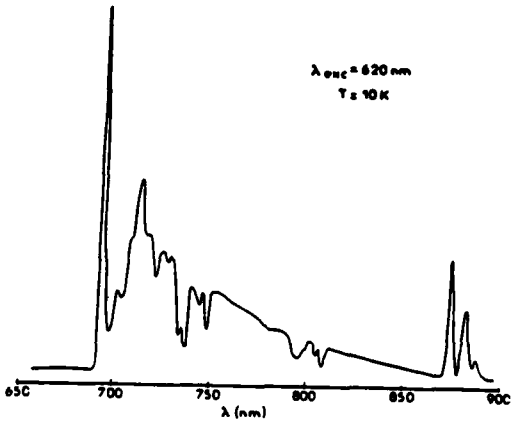

Figure 1. Emission spectrum of G(CMZ)GG Cr^{+3}, Nd^{3+} with excitation in the $^4T_2$ state of Cr^{3+}. The lines near 870 nm belong to Nd^{3+}.

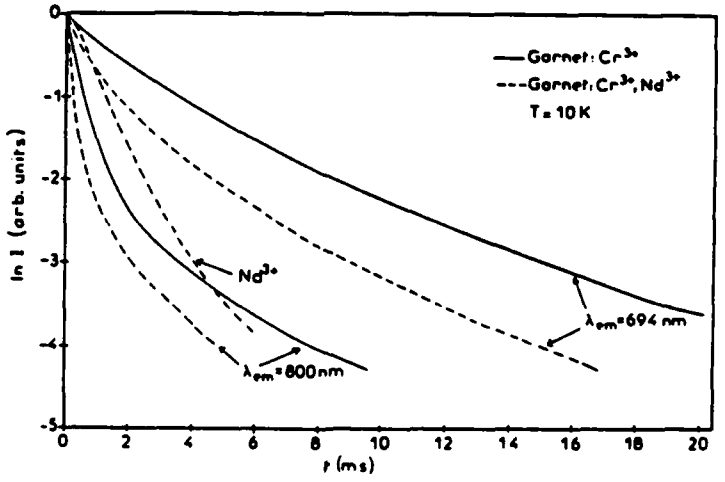

Figure 2. Luminescence decays of Cr^{3+} with and without Nd^{3+} for two different wavelength (694 nm for strong field ions, 800 nm for weak field ions). Nd^{3+} decay showing no long decay time unlike strong field Cr^{3+} ions.

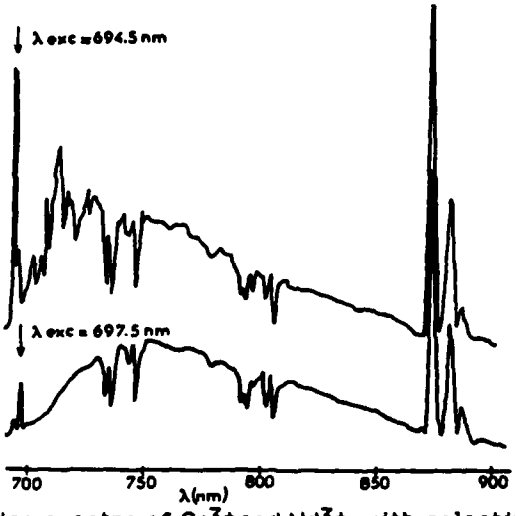

Figure 3. Emission spectra of Cr^{3+} and Nd^{3+} with selective excitation.

Table I. Mean transfer time τ_t and quenching of Chromium emission.

T	10K	90K
$\tau_t(^2E)$	1.3ms	1.2ms
$\tau_t(^4T_2)$	0.7ms	0.4ms
	without Nd	with Nd
$\frac{Emi\ ^4T_2}{Emi\ ^2E}$	5.7	2.7

From emission spectra and decay measurements we have computed transfer times by standard methods and quenching of chromium emission in comparison to the two kind of sites for chromium. Results are summarized in Table I.

CONCLUSION

All these experiments are in agreement with the main conclusion : In G(CMZ)GG : Cr, Nd, the fast and efficient Cr→Nd energy transfer proceeds mainly from the Cr^{3+} ions located in sites of weaker crystal strength.

REFERENCE

[1] A. Monteil, C. Garapon, G Boulon, J. of Lum. 39, 167 (1988).

AMPLIFIED SPONTANEOUS EMISSION AND PULSE TRAIN AMPLIFICATION IN A KrF AMPLIFIER

Jay R. Ackerhalt and David E. Hanson
Los Alamos National Laboratory,T-12,MS-J569,
Los Alamos,NM 87545

Richard G. Adams, T.D. Raymond, Christopher Reiser,
and James K. Rice
Sandia National Laboratory,Albuquerque,NM 87185

Robert B. Michie
Mission Research Corporation,Albuquerque,NM 87106

ABSTRACT

We present modeling studies of pulse-train amplification experiments conducted at Sandia National Laboratory in Albuquerque (SNLA) with an e-beam pumped KrF laser amplifier. The laser geometry is such that the dominant amplified spontaneous emission (ASE) growth is along the propagation axis. Our numerical studies include the propagation of on axis co- and counter-propagating fields for both the pulse train and ASE simultaneously. The time-dependent gain, absorption,formation and quenching rates are obtained from a state-of-the-art kinetics code developed at Los Alamos National Laboratory (LANL).

INTRODUCTION

This paper presents some preliminary results of a collaboration between the experimental groups at SNLA and the theoretical groups at LANL. The SNLA experiments being modeled were conducted using a λ-cell KrF amplifier described elsewhere.[1] The 5.7 cm diameter KrF gas cell was longitudinally pumped over 92 cm of its 1.3 m length by a 20 nsec e-beam. The e-beam profile contained 68% of its energy in the central 30% of the cell area. This results in an average pump rate of 4 MW/cm^3 at a gas pressure of 1 atmosphere. Because of the high aspect ratio we have modelled this system using a plane-wave on-axis co- and counter-propagating representation for the electromagnetic fields in Maxwell's equations, i.e., right and left propagating ASE pulses and a right propagating injected pulse train. Due to the very fast lower-level lifetime we need only model the fields' intensities as opposed to their amplitudes, and have treated the KrF^* excited states as the only species present in the cell which can create photons.[2]

The theoretical model used here is a simplification of our more sophisticated kinetics model[3] where we compute the e-beam energy deposition while simultaneously solving 70 kinetics reactions including photon propagation. Because of the long run times for this computer code we have studied the impact of the photon dynamics on the e-beam excitation physics, and have found that it is possible to characterize the KrF^* formation rate, both the saturable and non-saturable absorption coefficients, and the KrF^* quenching rate almost completely from the strength and temporal profile of the e-beam excitation assuming a uniform transverse profile. Therefore, we simply solve the dynamics of the photon intensities and the upper-state population in a one-dimensional, time-dependent formalism using the look-up tables provided by the kinetics code. The only other quantities that are necessary for describing the dynamics are the stimulated and spontaneous emission rates for the KrF^* species and the saturable-absorption saturation intensity. In addition, since we are trying to represent all the dominant ASE as on-axis ASE, we have used a position dependent aperture function to more accurately represent the source of the ASE photons, i.e., the farther a gain sheet is from the end of the cell the smaller the solid angle into which ASE photons are radiated in the near on-axis region.

ASE THEORY AND EXPERIMENT

From a modelling perspective, it is important to calibrate the theoretical model to ASE experiments before beginning calculations for pulse train extraction, as this represents a baseline check of the initial assumptions. Without a pulse-train seed, we measured 2.7 J of ASE from one end of the λ-cell. Agreement between theory and experiment was obtained when the theoretical aperture area was limited to 35% of the cell area. This suggests that the dominant ASE is nearly on-axis and that this model is appropriate for treating the pulse train experiments.

Although the time dependence of the output ASE was not measured in the experiments, the theoretical waveforms show damped oscillations in the ASE intensity. In order to better understand this result we made the e-beam temporal profile flat-topped. The results are shown in Figs. (1)-(3). The observed steady-state is consistent with well-known analytic solutions.[4-10] A scan of the literature revealed no previous studies of transient ASE. However, in discussing these results with colleagues we have found that other research groups have noticed these relaxation oscillations in their theoretical modelling, but as of today no one has observed them in their experiments.[11,12] The oscillation period depends primarily on the stimulated emission cross section and to a lesser degree on the

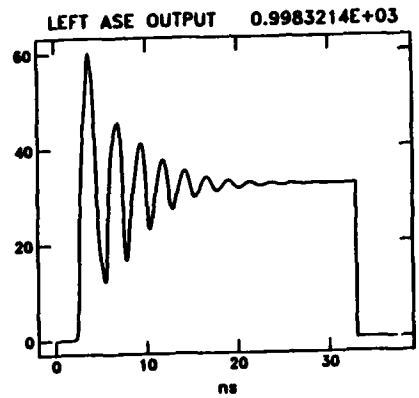

Figure 1. Left ASE intensity on output from the cell vs. time (ns).

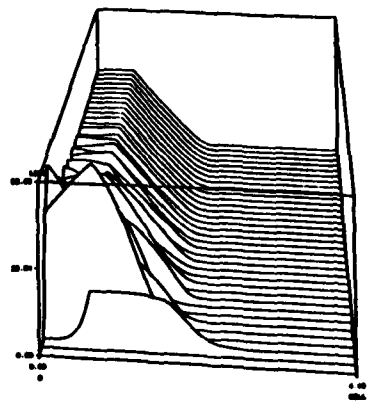

Figure 2. Left ASE intensity within the cell. Each successive trace refers to one nanosecond later in time. The left edge of the cell corresponds to Fig. 1.

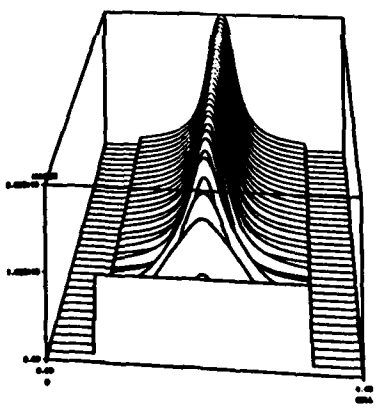

Figure 3. Excited-state species within the cell. Each successive trace refers to one nanosecond later in time.

cell length. Whereas, the oscillation's magnitude and fall-off depend most strongly on the pumping rate and damping of the excited-state population.

PULSE TRAIN DYNAMICS

In Figs. (4) and (5) we show measurements of the input and output waveforms, respectively, acquired with 0.5 ns resolution. The theoretical output waveform, calculated using the data from Fig. (4), is shown in Fig. (6). The model predicts strong amplification of the intensity between pulses and over estimates the output energy. Further investigation suggests that the actual baseline intensity is not accurately represented in the data. Data supporting this conjecture is shown in Figs. (7) and (8) where the temporal resolution is 0.2 nsec. In addition to revealing structural details within each pulse, these figures show little baseline intensity between pulses.

Because of these difficulties with the data we began a theoretical study assuming a zero baseline. In Figs. (9) and (10) we show a theoretical simulation of the same pulse train. The pulses are super Gaussian functions with a fourth-order exponent. Notice the high gain on the leading edges of the output pulses. When we repeated the calculation with standard second-order exponent Gaussian functions, the output pulses did not show this high gain on the leading edge. This sensitivity of the output pulse temporal profile with respect to the rise time of the leading edge of the input pulse temporal profile makes modelling of these experiments very difficult. Returning our attention to Fig. (10) notice that the ouput energy is reduced as compared with Fig. (5), but is still larger than found experimentally. In Figs. (11) and (12) we show the right travelling (co-propagating) ASE and left travelling ASE, respectively. The co-propagating ASE builds up between successive pulses in the train. The counter-propagating ASE has an initial peak with a subsequent tail. Both these results are qualitatively consistent with experimental observations from the λ cell, since the energy in the ASE pulses is not known.

FUTURE WORK

We plan to continue modelling pulse train data from the λ cell with the expectation that modifications in the experimental apparatus and theoretical model will improve the consistency between them. SNLA personnel are currently working to improve the temporal resolution of the input, output, and ASE waveforms. Other suggested experimental improvements include baffling of the electron beam to improve uniformity, and baffling the λ-cell to reduce the ASE reflections at the walls. Possible improvements to the model are the inclusion of ASE bandwidth, off-axis ASE propagation, and radial profiles of the e-beam and input seed energies. The present code does, however, contain the essential physics of the ASE and pulse-train dynamics.

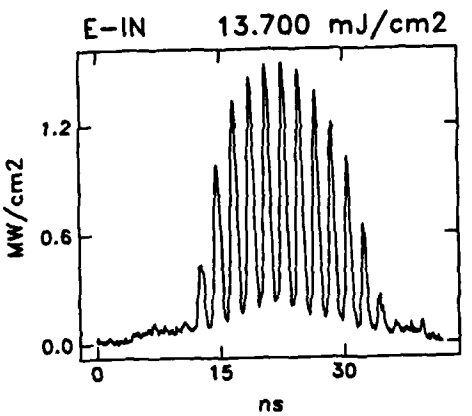

Figure 4. Input pulse train intensity vs. time digitized from a streak camera.

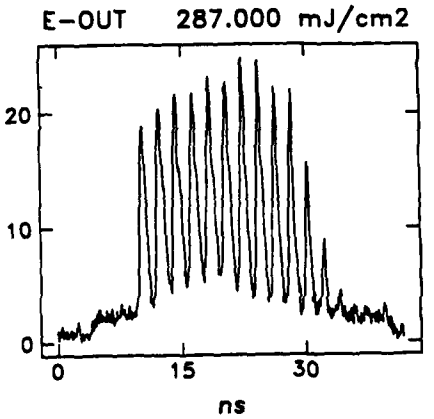

Figure 5. Output pulse train intensity vs. time digitized from a streak camera, corresponding to the input shown in Fig. 4.

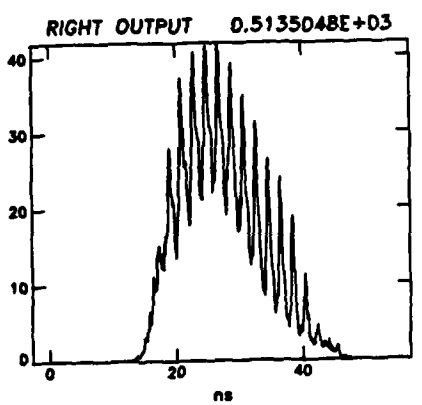

Figure 6. Theoretical output pulse train intensity vs. time for the input pulse shown in Fig. 4, Energy in mJ/cm^2.

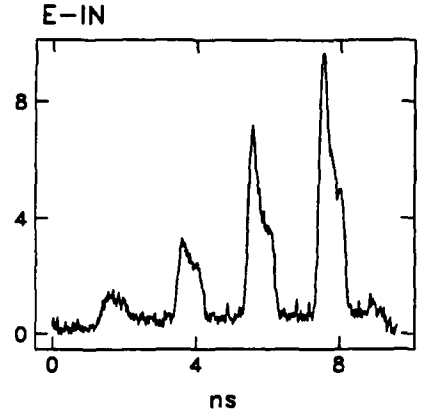

Figure 7. Input pulse train intensity vs. time for a small initial region of a total pulse train. Not the same run as shown in Fig. 4.

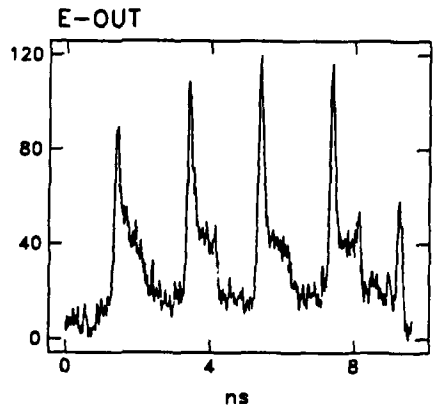

Figure 8. Corresponding output pulse train intensity vs. time from Fig. 7.

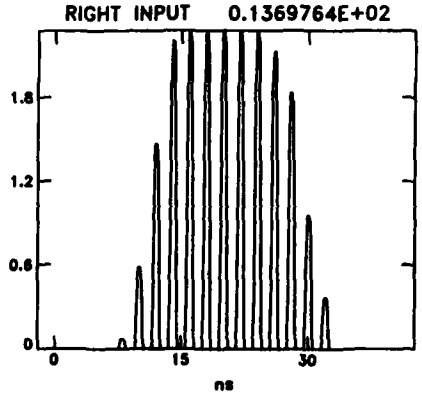

Figure 9. Simulated input pulse train from Fig. 4 with zero baseline. Energy measured in mJ/cm^2.

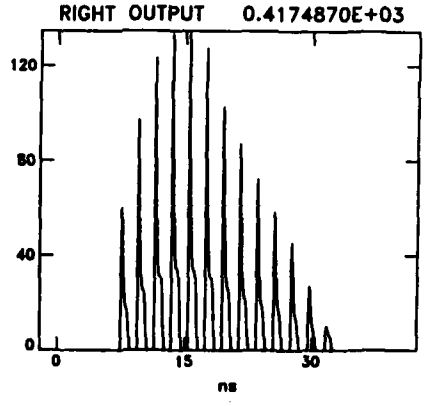

Figure 10. Output pulse train based on input from Fig. (9).

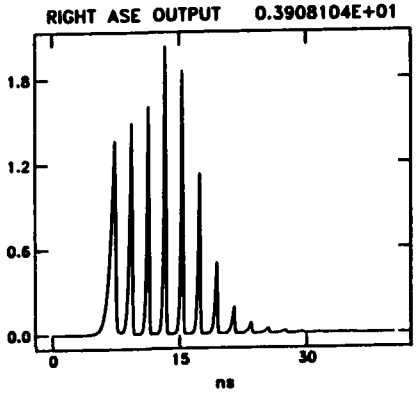

Figure 11. ASE output (co-propagating with the injected pulse train) at the right end of the cell vs. time.

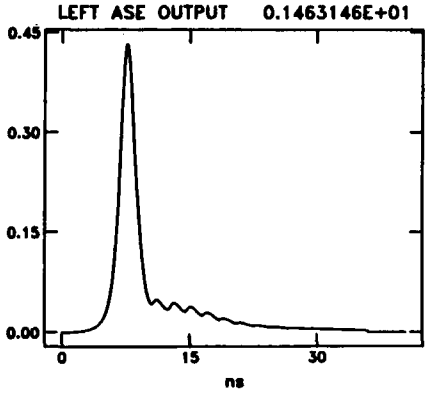

Figure 12. ASE output (counter-propagating with the injected pulse train) at the left end of the cell vs. time.

REFERENCES

1. E.L. Patterson, J.K. Rice, and G.C. Tisone, Appl. Phys. Lett. 36, 188 (1980).
2. P.W. Milonni, R.B. Gibson, and A.J. Taylor, JOSA B5,1368 (1988).
3. S.J. Czuchlewski, D.E. Hanson, B.J. Krohn, and A.R. Larson, Fusion Tech. 11, 560 (1987).
4. U. Ganiel, A. Hardy, G. Neumann and D. Treves, IEEE JQE QE-11, 881 (1975).
5. G. Haag, M. Munz and G. Marowsky, IEEE JQE QE-19, 114 (1983).
6. L. Allen and G. Peters, Phys. Rev. A8, 2031 (1973).
7. G. DuJardin and P. Flamant, Opt. Commun. 24, 243 (1978).
8. N. Abraham, J. Huang, D. Kranz and E. Rockower, Phys. Rev. A24,, 2556 (1981).
9. A. Hunter and R. Hunter, IEEE JQE QE-17, 1879 (1981).
10. D. Lowenthal and J. Eggleston, IEEE JQE QE-22, 1165 (1986).
11. D. Casperson, J. Comly and G. Schappert, private communication.
12. R. Chiao, M. Nathel, R. Minich and J. Garrison, private communication.

MODELING THE ENERGY DEPOSITION IN THE AURORA KrF LASER AMPLIFIER CHAIN

J.C. Comly, S.J. Czuchlewski, D.P. Greene, D.E. Hanson,
B.J. Krohn, and A.W. McCown,
U. of California, Los Alamos National Laboratory, Los Alamos, NM 87545

ABSTRACT

Monte Carlo calculations model the energy depositions by highly energetic electron beams into the cavities of the four KrF laser amplifiers in the Aurora chain. Deposited energy density distributions are presented and studied as functions of e–beam energy and gas pressure. Results are useful for analyzing small signal gain (SSG) measurements and optimizing deposition in future experiments.

INTRODUCTION

The KrF laser is a potential driver for inertial confinement fusion (ICF), and as part of the ICF program at Los Alamos, a large KrF laser system, called Aurora,[1] is under construction. Aurora consists of a front–end KrF laser resonator and a chain of four electron–beam pumped KrF laser amplifiers, whose names are abbreviated by SAM, PA, IA, and LAM. (See Fig. 1; more details of the design appear in Fig. 2 of Ref. 1.) Compression of the laser output pulse to 5 ns is achieved[1] by angular multiplexing (not illustrated in Fig. 1). The amplifiers have rectangular cavities 1–3 m in length (see Table I) with extraction volumes between 12 ℓ and 2100 ℓ.

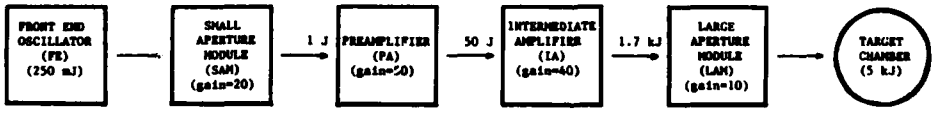

Figure 1. Simplified schematic of the Aurora laser chain.

TABLE I. Model Parameters for E-Beam Pumping

Property \ Laser	SAM	PA	IA	LAM	Avco[4]
Cavity dimensions					
Width, Δx	22.2	31.5	53.3	107.0	13.0
Height, Δy	19.05	30.0	56.0	106.0	10.0
Length, Δz	120.0	320.0	320.0	280.0	100.0
Pumped height, Δy_p	12.0	20.0	40.0	102.0	10.0
Pumped length, Δz_p	100.0	280.0	280.0	208.0	2.0
Materials					
Foil (thickness, mil)	Ti(2)	Ti(2)	Ti(2)	Ti(1)	Kapton(2)
Walls	Cu	Cu	Cu	Cu	Al
Ends	SiO_2	SiO_2	SiO_2	SiO_2	CaF_2
Gas: Pressure (Torr)	900	750	400-1400	700	380-1520
% comp., Kr/F_2/(balance Ar)	10/0.4	10/0.4	20/0.4	10/0.4	4/0.3
No. of pumped sides	1	1	1	2	1
E-beam energy (keV)	320	520	400-900	660	275
Appl. mag. field (kG)	0	1.2	1.2	1.6	4.0

MODELING METHODS

We have used a Monte Carlo code that originally modeled electron energy deposition in e–beam pumped CO_2 lasers[2]. The generic configuration for each of the four laser amplifiers (Fig. 2) includes a rectangular cavity containing a $Kr/F_2/Ar$ gas mixture, surrounded by six solid volumes. In present notation x measures distance (in the cavity) from the inner edge of the foil, y = 0 at half the height of the cavity, and z = 0 at the midpoint between end pieces.

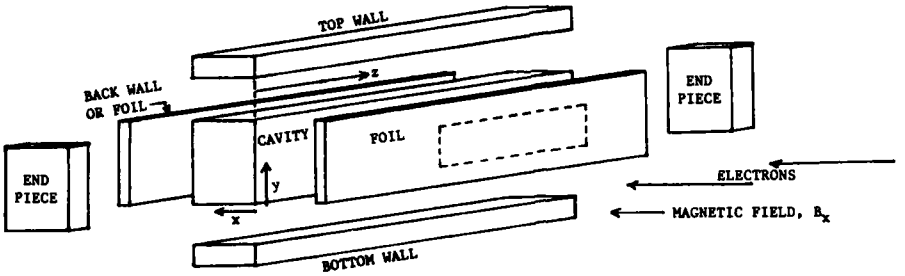

Figure 2. Geometrical configuration of modeled lasers.

Calculations are accomplished in two stages. The first stage employs the "microscopic" physics of collisions and generates, for each material within the seven volumes, a data file consisting of (i) probability distribution functions for electron scattering into various angles and (ii) distribution for electron energy loss per unit path length (stopping power). For electron scattering, Monte Carlo techniques are used, assuming a "shielded Coulomb" form of the cross section with a shielding angle specified by Molière's formula.[2,3] For the energy loss, the straggling distribution follows Landau's theory, with the mean loss rate normalized to Bethe's formula.[3]

The second stage models the "macroscopic" deposition using as input the physical dimensions of the laser, the applied fields, and the gas density. The Monte Carlo technique follows many electron trajectories, with each trajectory consisting of small substeps. Within each substep the relativistic equations of motion are time–integrated, including effects of Lorentz forces from the applied fields and the continuous stopping–power force. Scattering occurs at the end of each substep. Output from the second stage consists of fractional absorptions in the objects surrounding the cavity and a three–dimensional density function for the energy (per electron) deposited in the gas. The energy is accumulated at 51 positions (including the end points) in each dimension, and the complete density function is the collection of evaluations in the $(51)^3$ sub–volumes. Summation over one or two dimensions allows a graphical routine to illustrate the density by a curve in one dimension, or to represent the distribution in two dimensions by a contour plot.

The Monte Carlo energy per electron deposited in the gas, W_g, is an integral of the density function over three dimensions. W_g is related to the average energy density deposited in the gas, E_d, by the approximate formula,

$$E_d = W_g I_b \Delta t / v, \qquad (1)$$

where I_b is the electron beam current, Δt is the duration of the input pulse (here taken to be fwhm), and v is the volume of the cavity.

The present code has modeled a small signal gain (SSG) experiment at the Avco Everett Research Laboratory.[4] The cavity of their KrF laser resonator was much smaller than those of our amplifiers (see Table I), and their e–beam operated at lower energy than ours. Our calculated one–dimensional distributions are in good agreement with their (normalized) data presented in Fig. 7 of Ref. 4. (Our x–direction is equivalent to z in their notation.)

RESULTS

The energy distributions for the Aurora amplifiers are plotted within the cavity dimensions specified in Table I. Fig. 3 refers to gain probe experiments on the SAM laser, in which four probe beams were aligned parallel to the z–axis

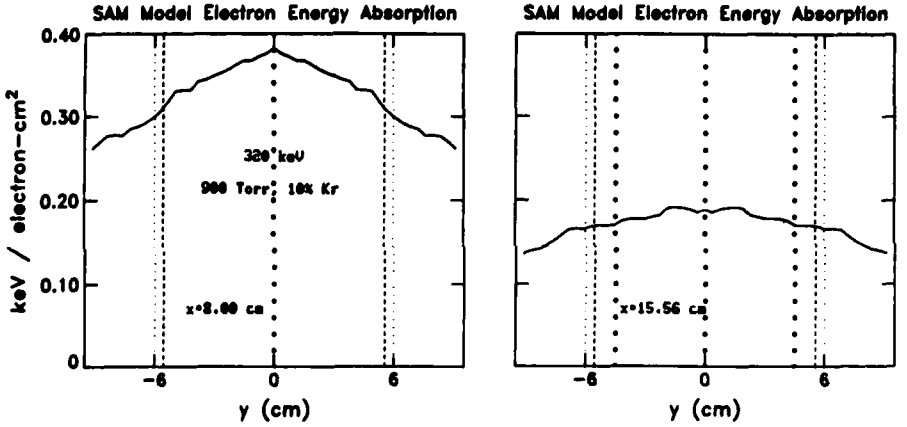

Figure 3. Deposition profiles in y at the two x–coordinates of gain probes. Dashed lines show top and bottom edges of the foil. Dotted lines mark aperture edges. Heavy dots indicate the gain probe lasers.

and were placed at the following (x,y) coordinates (in cm): (7.8, 0), (15.3, 0), (15.3, ±4.5). SSG coefficients of 3.6, 1.8, 1.6, and 1.6 %/cm were measured at the four respective positions. The two y–profiles were obtained by integrating the 3–dimensional distribution over z, with x fixed at the sub–interval center nearest the probe position. Reflection symmetry was imposed about y=0 to reduce statistical noise. Calculated relative energy absorptions at the positions of the gain probes are in excellent agreement with the observed ratios of gains.

Figure 4 shows one–dimensional (twice integrated) distributions across the cavity of the PA laser. The degradation of pumping in the y direction is gradual near ±10 cm (the edges of the foil), rather than abrupt, and only the central 10 cm interval is nearly uniformly pumped. Figure 5 gives the contour plot for the xy–distribution. Here the three–dimensional density function was smoothed, symmetrized about y=0, and summed over the z–direction.

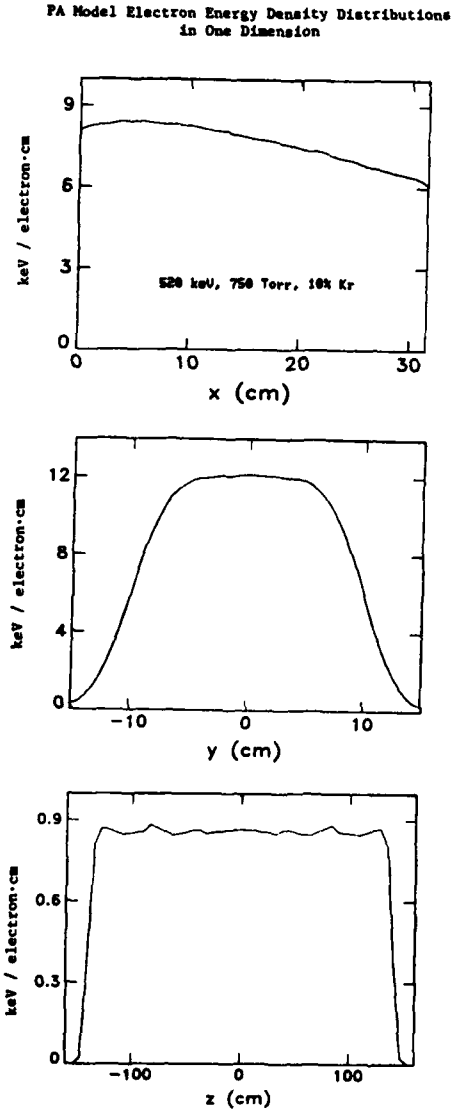

Figure 4

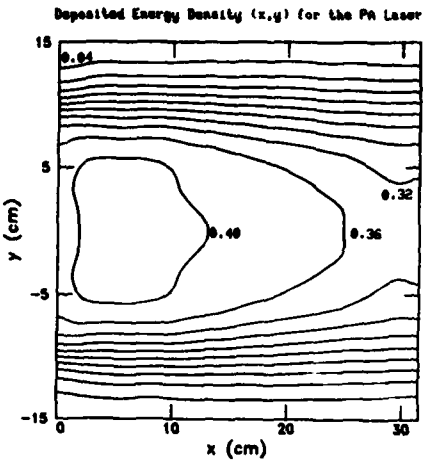

Figure 5. A smoothed (symmetrised) two–dimensional energy distribution function. The ten contours are evenly spaced in the deposited (once integrated) density: 0.04, 0.08, ..., 0.40 keV/electron–cm².

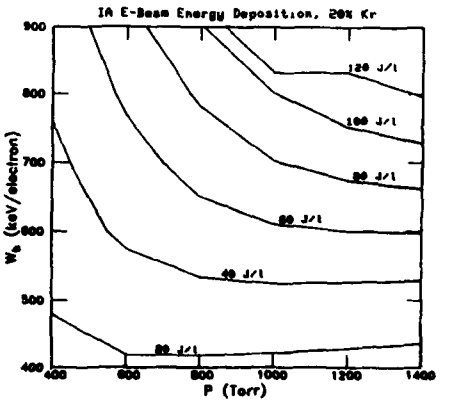

Figure 6

Electron energy deposition in the cavity of the IA laser is modeled as a function of the e–beam energy (W_b) and gas pressure (P) in Fig. 6. Contours were derived from the values of W_g calculated at 36 points in the (P,W_b)–plane corresponding to P = 400, 600, ..., 1400 Torr and to W_b = 400, 500, ..., 900 keV. At each point the average energy density, E_d, was obtained from Eq. (1), using the Child–Langmuir law[5,6],

$$I_b \propto W_b^{3/2}, \qquad (2)$$

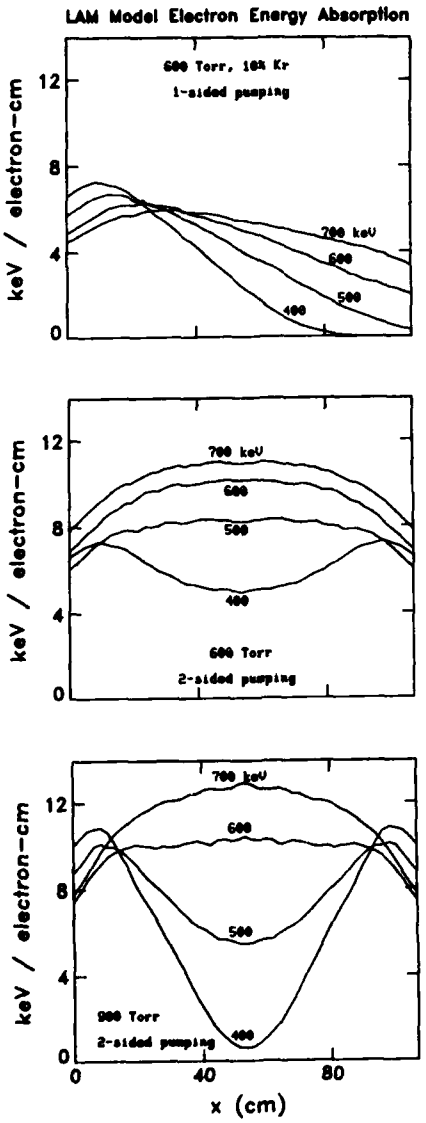

Figure 7. Families of one–dimensional deposited energy distributions for the LAM laser.

to scale the beam current, whose value of 97 kAmp was deduced at $W_b = 520$ keV from results of kinetics calculations[7] and a measurement of SSG.

The LAM laser is the largest in the Aurora chain, and is designed for symmetrical 2–sided pumping to enhance uniform deposition across the 1 m width of its cavity. Table II gives the relative energies absorbed in the cavity and surrounding volumes, for single–sided pumping. Because of the magnetic field, the end pieces (see Fig. 2) are too far from the foil to absorb electrons. Figure 7 shows one–dimensional (twice integrated) energy distributions within the cavity as a function of the e–beam energy and gas pressure. Each curve for two–sided pumping is the superposition of the one–sided pumping curve with its reflection about the central value of x.

DISCUSSION

Parametric studies, such as Table II, reveal trends in relative energy absorptions in the seven volumes of Fig. 2 and guide future experiments to optimize pumping conditions. Column 3 of Table II is the gas pumping efficiency. Presently the LAM has the most efficient deposition of the four amplifiers (primarily because of its cavity width), as approximately 80% of the electron energy is absorbed by the gas. In the three smaller lasers, the fractions are typically 30–40% for the SAM and 40–45% for the PA and IA. Contours of pumping performance for the IA, in Fig. 6, were derived from calculated fractional electron energies deposited in the gas. Other practical questions are addressed. For example, in Table II, calculated absorptions by the first and second foils indicate that, on the average, an electron deposits substantially less energy in the second foil than in the first. Therefore, the stress at a given foil is not greatly increased by the incidence of a second e–beam (from the opposite side of the cavity).

TABLE II. Monte Carlo[a] Electron Energy Deposition for the LAM Laser

P_b (Torr)	V_b (keV)	Fractional Absorptions of Energy per Electron					V_g [c] (keV)
		Gas	1st foil	2nd foil	Top/bott	Lost[d]	
600	400	0.815	0.112	0.000	0.008	0.066	326
	500	0.833	0.082	0.004	0.012	0.070	417
	600	0.823	0.058	0.023	0.015	0.080	494
	700	0.773	0.047	0.035	0.018	0.128	541
900	400	0.815	0.113	0.000	0.007	0.066	326
	500	0.841	0.080	0.000	0.010	0.068	421
	600	0.870	0.058	0.000	0.014	0.058	522
	700	0.870	0.046	0.006	0.018	0.060	609

[a]Each row represents calculation of 20300 independent electron trajectories.
[b]T=295°K is assumed for calculating densities.
[c]This is the product of entries in the second and third columns of this table.
[d]Electrons are lost to the vacuum either by backscatter from the first foil or by penetration of the second foil. By assumption, 50% of such electrons (selected randomly) are lost.

On the subject of detailed energy density in the gas, the close agreement between SSG measurements and calculated deposition for the SAM laser suggests that Monte Carlo distributions faithfully indicate regions of relatively high gain in the cavity. In particular, the contours in Fig. 5 should accurately characterize the SSG in the PA laser. Figure 7 shows that the energy distribution (and gain) in the cavity can be very sensitive to beam energy and gas pressure. Finally, deposited energy densities E_d, and temporal pulse shapes, provide the power input to time–dependent kinetics calculations of SSG and laser extraction.[7] A future application will be to model the spatial profiles of beam intensity at the exit aperture of each laser amplifier in the Aurora chain.

REFERENCES

1. L.A. Rosocha, J.A. Hanlon, J. McLeod, M. Kang, B.L. Kortegaard, M.D. Burrows, and P.S. Bowling, Fusion Technol. 11, 497 (1987).
2. J.C. Comly, W.T. Leland, C.J. Elliott, A.M. Hunter, and M.J. Kircher, IEEE J. Quantum Electron. QE17, 1786 (1981).
3. M.J. Berger, Meth. Comp. Phys. 1, 135 (1963).
4. A. Mandl, D. Klimek, and J.H. Parks, J. Appl. Phys. 55, 3940 (1984).
5. C.D. Child, Phys. Rev. Ser. I, 32, 492 (1911).
6. I. Langmuir, Phys. Rev. Ser. II, 2, 450 (1913).
7. S.J. Czuchlewski, D.E. Hanson, B.J. Krohn, A.R. Larson, and E.T. Salesky, Fusion Technol. 11, 560 (1987).

A MATHEMATICAL MODEL OF THE DYNAMICS OF TITANIUM DOPED SAPPHIRE LASERS

L. F. Roberts †
Randolph-Macon Woman's College, Lynchburg, Virginia 24503
J. J. Swetits ††
Old Dominion University, Norfolk, Virginia 23529
A. M. Buoncristiani ††
Christopher Newport College, Newport News, Virginia 23606

ABSTRACT

We have developed a model of an end-pumped Titanium doped Sapphire ring laser. The model was created as a means to study in detail the spatial and temporal evolution of the electron population in the laser rod as well as the development of the right and left traveling photon fluxes in the active medium and the cavity. It is based upon a four-level model of the vibronic transitions of the Titanium ion and consists of a system of first order semilinear partial differential equations that is symmetric hyperbolic. The task of solving the system of equations numerically is considered and results from several numerical schemes are compared.

INTRODUCTION

During the last several years, solid state lasers having the potential to meet the rigorous performance requirements for space-based remote sensing of the atmosphere have been developed. In order to design a stable, efficient laser capable of line-narrowed operation it is necessary to have an understanding of the temporal evolution of the dynamical processes in the laser cavity. We have developed a model of the spatial and temporal dynamics of a tunable solid state laser so that the time evolution of the dynamic quantities may be studied at each position in the laser cavity. The laser that is modeled is an end pumped Titanium doped Sapphire ring laser that allows for injection seeding through the output coupler. The model consists of a system of two sets of partial differential equations that describe the evolution of the dynamic variables in the active region and in the remainder of the cavity and which are coupled via boundary conditions that describe the optical environment of the active medium. In addition, we have developed a stable and efficient procedure for numerical solution of the system of equations.

MODEL

The photon flux distribution at time t at a position x in the active medium is given by the two functions $F_{\pm}(x,t;\lambda)$. The active medium is assumed to be homogeneous with index of refraction, n and concentration of optically active ions n_T. The continuity equations that govern the spatial and temporal development of the photon fluxes moving through the active medium with a speed $v = c/n$ are

$$\frac{1}{v}\frac{\partial F_{\pm}}{\partial t} \pm \frac{\partial F_{\pm}}{\partial x} = \left[\sigma(\lambda) - \alpha(\lambda)\right] F_{\pm} + S_{\pm}(x,t;\lambda) \qquad (1)$$

† Supported by NASA under Training Grant NGT-47-003-804 ; †† National Researach Council Resident Research Associates at NASA Langley Research Center.

Here, $\sigma(\lambda)$ and $\alpha(\lambda)$ represent the emission cross-section and absorption coefficient, respectively. The functions $S_{\pm}(x,t;\lambda)$ represent the contribution to the photon flux due to spontaneous emission. In the remainder of the cavity, the equations for the propagation of the photon flux are the same as (1) except that v is replaced by the speed of light in a vacuum, c, and the right hand sides of (1) replaced by zero.

The rate equations based on a four-level model of the transitions between the electronic levels of the titanium ion that describe the spatial and temporal evolution of the electron concentrations n (x,t), at the i energy level are given below.

$$\frac{\partial n_2}{\partial t} = W_P - \left[n_2 - \frac{g_2}{g_1} n_1 \right] \int d\lambda\, \sigma(\lambda)\, F(\lambda) - \frac{n_2}{\tau_2}$$

$$\frac{\partial n_1}{\partial t} = \frac{n_2}{\tau_{fl}} - \left[n_2 - \frac{g_2}{g_1} n_1 \right] \int d\lambda\, \sigma(\lambda)\, F(\lambda) - \frac{n_1}{\tau_1} \qquad (2)$$

$F(\lambda) = (F_+(x,t;\lambda) + F_-(x,t;\lambda))$ is the total photon flux at position x at time t, represents the transition rate from level i to level j, and τ_{fl} represents the fluorescence lifetime for the material. W (x,t) is the rate at which the upper lasing level is populated and the equation that describes the propagation of the pumping pulse through an active medium is given by

$$\frac{1}{v}\frac{\partial W_P}{\partial t} \pm \frac{\partial W_P}{\partial x} = -\sigma_{ab}\left[n_T - (1 + g_2/g_1)\, n_1 - n \right] W_P \qquad (3)$$

Equations (1)-(3) are subject to initial conditions and boundary conditions that describe the optical elements in the cavity.

NUMERICAL SOLUTIONS

By dividing the emission spectrum of Ti:Sapphire into m intervals of length $\Delta\lambda$, then the above system of partial differential equations is reduced to a system of 2m + 3 equations that is symmetric hyperbolic and semilinear. The system can then be reduced using standard methods [1] to a system of ordinary differential equations along the characteristics. The method of integration along the characteristics [2] can be employed to approximate the solutions numerically using ordinary differential equation methods. We used both the first order accurate Euler's Method and the second order accurate Modified Euler Method, as in [3], to compute approximate solutions to the system. Results are shown in Fig. 1 giving the computed population inversion using Euler's Method with 5 and 10 spatial grid points in the crystal and the Modified Euler Method with 5 grid points in the crystal. Increasing the accuracy of the procedure results in a numerical solution in which there is an earlier decrease in the population inversion that corresponds to the onset of stimulated emission. In order to achieve

accuracy from Euler's Method comparable to the Modified Euler Method with 5 grid points in the crystal it was necessary to increase the number of grid points to 20. This represents considerable expense in terms of computer time necessary to compute the solutions. In addition, there was no significant increase in the accuracy obtained from the Modified Euler Method by increasing the number in grid points to 10.

The results obtained by integration along the characteristics were compared to those obtained using a stable, first order accurate finite difference algorithm [1]. The finite difference procedure required 50 spatial grid points in the crystal to obtain comparable accuracy to the Modified Euler procedure and required approximately 40 times the computing time necessary to compute the solutions.

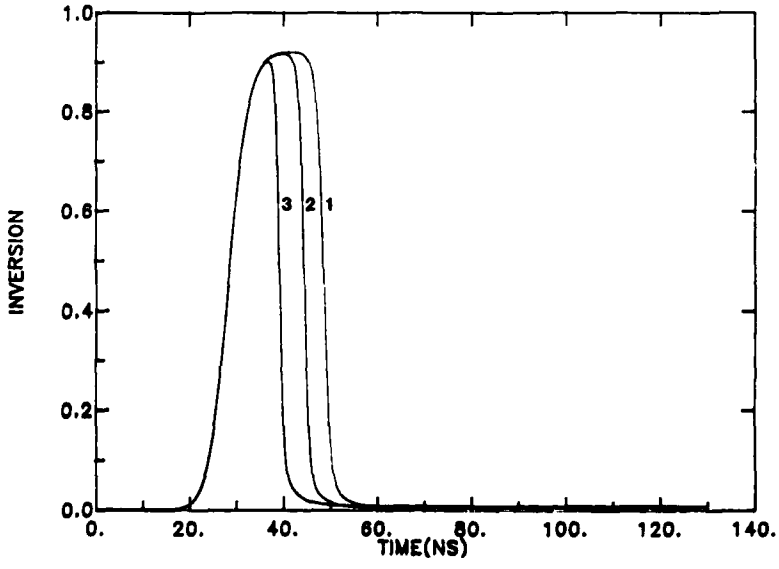

Figure 1. Evolution of the computed population inversion at corresponding spatial grid points using Euler's Method and the Modified Euler Method. (1) corresponds to Euler's method with 5 spatial points in the crystal; (2) corresponds to Euler's method with 10 spatial points in the crystal; (3) corresponds to Modified Euler's method with 5 spatial points in the crystal

REFERENCES

1. Garabedian, P. Partial Differential Equations, Chelsea, New York, 1964.

2. Courant, R. and P.D. Lax, Pure Appl. Math., Vol 2, 1949, pp. 253-273.

3. Burden, R.L. and D.T. Fares, Numerical Analysis, Prindle, Weber, and Schmidt, Boston, 1978.

4. Buoncristiani, A.M. et.al, American Institute of Physics Conference Proceedings , No.172, Optical Sciences and Engineering Series 9, 1988.

Non-Markovian Jump Processes in Lasers*

A.M. Levine
The College of Staten Island, CUNY, NY 10301
A.G. Kofman, R. Zaibel, Yehiam Prior
Weizmann Inst., Rehovot, Israel, 76100

Abstract

A new model for stochastic fluctuations in lasers is introduced where successive phase jumps are correlated to previous jumps. The model is applicable in the generalized phase diffusion limit, the generalized Kubo oscillator limit, and the generalized telegraph noise limit.

An ideal laser produces light at a single frequency. Real lasers produce light in which the electromagnetic fields fluctuate stochastically with a narrow spectrum centered around the nominal laser frequency. We have recently introduced a new non-Markovian jump model[1] that describes real lasers. In this model the phase $\phi(t)$ is assumed to undergo sudden "jumps" at random times. Unlike previous jump models, the "jumps" are allowed to be correlated. We have developed the formalism for calculating the consequences of these fluctuating fields in non-linear optics experiments. In this paper, we will present a generalization of that work that allows us to describe any laser using a small number of experimentally obtained parameters.

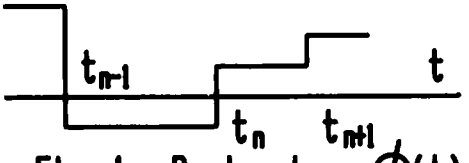

Fig. 1a. Random phase $\phi(t)$

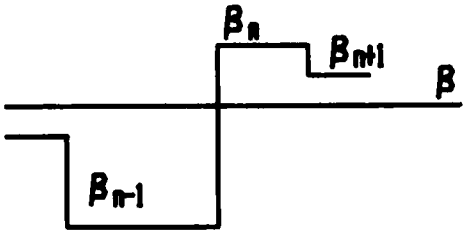

Fig. 1b. Random jumps $\beta(t)$

The non-Markovian jump model can best be understood by referring to Figure 1. The phase of the electromagnetic wave $\phi(t)$ is assumed to undergo random jumps of size β_n at random time t_n. This defines two jump processes $\phi(t)$ and $\beta(t)$.

*Work supported by the U.S.-Israel Binational Science Foundation.

The random time between jumps $\tau_{n+1} = t_{n+1} - t_n$ is given by a Poisson distribution

$$P\left[\tau_{n+1}\right] = \frac{1}{\tau_0(\beta_n)} \exp\left\{\frac{\tau_{n+1}}{\tau_0(\beta_n)}\right\} \qquad (1)$$

One extension of our earlier work is to allow $\tau_0(\beta_n)$ to be a function of the jump magnitude β_n. The magnitude of the random jump is described by an unconditional distribution $f(\beta)$ whose second moment $\langle \beta^2 \rangle = B^2$ characterizes the jump size.

The key feature of the new model is that it incorporates correlated jumps by defining a conditional distribution $h(\beta', \beta)$ that describes the present jump β in terms of the previous jump β'. Thus $\phi(t)$ is now a non-Markovian random variable. The vector $\{\phi(\epsilon), \beta(t)\}$, however, is a jump Markovian vector, and the method introduced by Burshtein[2] can be used to obtain an exact description of the process.

In our previous work, $f(\beta)$ and $h(\beta', \beta)$ were assumed to be Gaussian functions. In this paper, we use quite general forms for these functions, and define the following physically meaningful parameters. The weighted average of jump times is

$$\frac{1}{\tau_{av}} = \frac{1}{\beta^2} \int d\beta \, \frac{\beta^2 f(\beta)}{\tau_0(\beta)} \qquad (2)$$

The fluctuating frequency deviation is

$$\epsilon(t) = \frac{\beta(t)}{\tau_0(\beta(t))} \qquad (3)$$

The reciprocal jump process memory time is:

$$\frac{1}{\nu_\beta} = \frac{\tau_{av}^2}{\beta^2} \int_0^\infty \langle \epsilon(0)\, \epsilon(t) \rangle \, dt \qquad (4)$$

We may now define a generalized correlation parameter γ by the formula:

$$\gamma = 1 - \nu_\beta \, \tau_{av} \qquad (5)$$

When each jump is independent of the previous jump, $\gamma = 0$ and the jumps are uncorrelated. If succeeding jumps are likely to be of the same sign as the previous jumps, $0 < \gamma \leq 1$, and the jumps are positively correlated. When succeeding jumps are likely to be of the opposite sign as the previous jumps, $-1 \leq \gamma < 0$, and the jumps are negatively correlated.

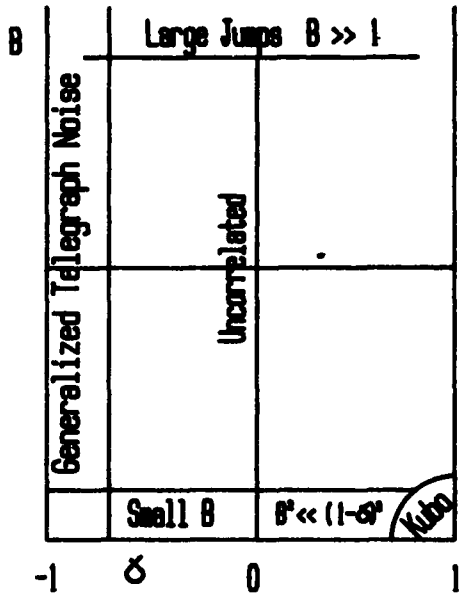

Fig. 2. B,σ plane showing regions defining the nature of the process.

The three parameters r_{av}, γ and B serve to characterize most lasers. One of them, r_{av}, serves to define the time scale of the process. The other two: γ (the correlation parameter) and B (the jump size) define the nature of the process. This is described graphically on Figure 2 which shows a B, γ plane. When $\gamma = 0$, the jumps are uncorrelated. When the jump size is small $B^2 << (1-\gamma)^2$, the Born approximation presented in our earlier paper is valid. For large jumps, $B >> 1$, the process appears uncorrelated. When $\gamma \approx +1$ and B is small, the new model recovers a generalized form of the Kubo oscillator. When $\gamma \approx -1$, the new model yields a generalization of the telegraph noise model.

In each of these regions, we have derived formula for both the field correlation function and the spectrum of the fluctuating laser field. The analytical expressions allow the experimental determination of the three parameters r_{av}, γ, and B. We have also analyzed the predicted spectrum for the output of a particular non-linear process, namely resonance fluorescence. In all cases, the output lineshape depend critically on the parameters B and γ. Detailed formulae will be given in a later publication.

References

1. A.G. Kofman, R. Zaibel, A.M. Levine, Y. Prior, Phys. Rev. Lett. **61**, 251 (1988).
2. A.I. Burshtein, Sov. Phys. JETP **22**, 939 (1966).

QUANTUM INITIATION EFFECTS ON THE ASYMPTOTIC COHERENT ON-RESONANCE PROPAGATION OF TWO DIFFERENT-WAVELENGTH PROBE AND PUMP BEAMS IN A THREE-LEVEL SYSTEM*

Farrès P. Mattar*,#, Yves Claude* and Michel Burgess*
Department of Physics, New York University, New York, NY 10003 and
Photonics Engineering Center, Department of Electrical Engineering,
City College of New York,New York, NY 10031

ABSTRACT

The coherent energy transfer from a strong pump beam at a given frequency to a weak probe beam initiated by quantum noise at another frequency is reported. Effects of self- and cross-phase modulation were also examined. An optimal energy exchange is maintained in the presence of fluctuations by matching the oscillators strengths to insure maximum pulse overlap throughout the motion. The central role of pump depletion, transverse effects, quantum initiation and time- and radial-dependent phase variations in an asymptotic co-propagation in a three-level medium is revealed. An ensemble of statistical calculations is carried out. For most trajectories a stabilization of the pulse area is inhibited. Probe pulse sharpening and pump laser pulse peak retardation along with amplitude dimension, have been observed.

I. INTRODUCTION

Previous analyses of coherent on-resonance propagation have included transverse effects in either two-field pump and superfluorescence SF three-level with quantum fluctuations accounted for as the initiation process[1] or asymptotic evolution of probe and pump solitary waves[2] from deterministic pulses instead but never both. This study reports simultaneous treatment of both effects, quantum fluctuations and propagation into the asymptotic regime. The calculation strives to achieve rigorous analysis of this nonlinear interaction with maximum accuracy and minimum computational effort by introducing adaptive stretching and rezoning transformations[3].

The primary objective of this paper is to extend the analysis of asymptotic swept-gain superradiance evolution[4] in a pre-excited two level system to one that accounts for a finite pumping mechanism as well as to account for quantum initiation in a three-level atomic vapor[5]. Spontaneous probe pulse formation and evolution is now accounted for. We investigate how the quantum initiation modifies the stabilized profile of the pump and probe beam areas and how the diffraction acts on the noise-modulated distorted spatial-temporal shape.

We have adopted for the description of the probe initiation process a formulism[5] developed in conjunction with optically-pumped three-level SF. The initiation process is achieved through the application of two Langevin forces: one in each of the one-photon allowed transition. We have derived, rather than assumed, the transverse field variation (TFV) as self-similar.

We have determined the TFV such as would develop for arbitrary input pulses into an initially grounded three-level system. The longitudinal profile of the pulses gets distorted by interaction with the medium, while the atomic transient dynamics is altered by the two different wavelength pulses. The modified medium then re-affects the field profile.

In this study we have examined how the fluctuations modify the profile structure and affect the diffraction coupling in conjunction with the propagation of two strongly-overlapped pump and probe pulses

* Supported by ARO, AFOSR, ONR and NSF at NYU.

3Z5ILS4 5/16,20,21; 6/29,30

of distinct areas in a three-level system with a λ configuration initially at ground state. A continuously-varying instantaneous frequency shift associated with the time derivative of the pump and probe phases arises due to the presence of diffraction, co-propagation, cross-coupling and fluctuations. New spectral effects are reported.

II. THE PHYSICAL MODEL

The semiclassical formalism (which amounts to representing the field classically & describing the atomic system quantum-mechanically) is adopted. The pulse length is considerably shorter than any depopulation or dephasing relaxation times. This type of interaction originated with the discovery of Self-Induced-Transparency (SIT)[6] and superradiance SF[7]. The Maxwell-Bloch formulism was shown[8] adequate to describe the SF emission. The equations of motion consist of two paraxial-Maxwell equations coupled through a three-level density matrix. The initiation is provided through a temporally- & spatially-varying bichromatic Langevin source right in the density matrix. The numerical algorithm that solved for this two-field three-level interaction is implemented as LR2CFS©.

In the presence of quantum initiation[9], the atomic dynamics for a given propagational distance, i.e., a specific Beer-length Fresnel number, can significantly vary from one trajectory to the other and throughout the medium as well, i.e., for different propagational distances, within the same trajectory.

III. THREE-LEVEL CALCULATIONS

The medium provides amplification[10] for the probe while the transverse communication across the beam imposes a diffractive loss. The beam reshapes longitudinally and transversely. A measure of the gain/loss condition would be F_g, a Fresnel number defined in terms of the Beer's length transition associated with a specific radial profile of N, the pre-excited atomic density.

In a rigorous two-field three-level atom on-resonance interaction, the strong pump depletes its energy (ENRGYa) both temporally and spatially so that the probe energy (ENRGYb) builds up. At the input plane, the on-axis pump area is 2π, while the on-axis input seed area which represents the probe is only zero. However, quantum noise acts as a seed that varies from one shot to the other. The probe emerges with appreciable statistically different output power peak and delay amplitude after a certain propagation distance. The pump depletion which accompanies the probe growth is shown. The output power (OPOWRa,b) of both pump and probe exhibits a strong temporal distortion[11] that varies from shot-to-shot and departs from the input Gaussian profile.

In the absence of quantum fluctuations[12,13] for sufficiently large $\alpha_b \ell$, the probe buildup slows down, tapers, or even changes sign. Its area may also stabilize. Depending on the relative phase shift between the probe and the pump, the pump may reduce then interrupt its depletion and may even renew its energy, that is, it may anomalously reverse its depletion and even stabilize. The area stabilization is the coherent counterpart of self-trapping that was discussed by Haus [14] and reviewed Shen[15a] and by Marburger[15b]. Moreover, the diminution, cessation and reversal of pump depletion is consistent with what has been reported by Carlsten's group in Raman, i.e., off-resonance interaction.

However, when the initiation is quantum instead of a deterministic seed, the role of self-phase, cross-phase modulation and diffraction is enhanced and self-focusing may occur for some specific trajectories. The probe does not always display the z-independent on-axis area stabilizations as its two-level swept-gain superradiance counter-

part[4]. For some trajectories, the stabilization is exhibited while for most others it is inhibited.

This statistically-dependent emergence of solitary wave is controlled by the relative phase variations between pump and probe. In the presence of quantum initiation, diffraction plays a more predominant role. It is important to note that beyond a certain optical thickness for a given trajectory, the feedback of the probe buildup can strongly affect the pump. In summary, partial spontaneous depletion reversal has been observed to occur randomly whilst complete reversals are seen to occur less frequently.

We have evaluated the standard deviation of the stabilized area to quantify the statistical behavior of the ensemble of trajectories. We are displaying in Fig. the on-axis area for different initial shots. We report the evolution of significant temporal distortion profile vis-a-vis a Gaussian variation of the output power. A multi-peak behavior, in which the first peak is not the highest peak, results. Such unusual trajectories occur occasionally perhaps once in every twenty to fifty trajectories and characterized as phase waves as discussed by Hopf[16a]. These phase waves were respectively reported in two-[16b] and three-level[16c] SF, and in Raman soliton computational studies[16d] as well. MacPherson et al.[16e] ascertained their validity in Stimulated Raman Scattering soliton observations.

$$\epsilon = \frac{\sigma(\Delta\tau_D)}{\langle\Delta\tau_D\rangle} = \left\{ \frac{\Sigma[\Delta\tau_d^i - \overline{\Delta\tau}_D]^2/N}{\Delta\tau_D} \right\}^{1/2} \left[1 \pm (N-1)^{-1/2}\right]$$

where $\overline{\Delta\tau}_D$ is the mean value of the delay or advance of the peak of the probe with respect to the peak of the pump, σ is the standard deviation and N is the number of elements in the statistical ensemble.

V. CONCLUSION

Rigorous calculations accounting for the interplay of diffraction coupling quantum fluctuations with the nonlinear medium inertial response in conjunction with pump depletion exhibit in the asymptotic regime the inevitable spatial and temporal redistribution of pump and probe energy as well as stabilization of the time-integrated area for some of the trajectories of the statistical ensemble. Variation of the energy conversion profiles between the input and output (after propagation) and from shot-to-shot has been invariably seen. Both the threshold of the area stabilization, and the probability of its occurrence (less than 1) vary from shot to shot.

REFERENCES

1. [a] F.A. Hopf et al., Phys. Rev. A12, 2534 (1975); F.A. Hopf, et al. Rev. A13, 777 (1976); [b] F.A. Hopf et al., Phys. Rev. A19, 1180 (1979); and [c] F.A. Hopf, Phys. Rev. A20, 2064 (1979).
2. F.P. Mattar, in Advances in Laser Sciences III, ed. A.C. Tam, J.L. Gole & W.C. Stwalley, (AIP, 1988) (a) probe soliton: pp. 524-529 and (b) pump soliton: pp. 530-536.
3. F.P. Mattar, Appl. Phys. 17, 53 (1978); and F.P. Mattar and M.C. Newstein, Comp. Phys. Commun. 20, 139 (1980).
4. C.M. Bowden & F.P. Mattar, SPIE 288, 364 (1981) and 369, 151 (1983); and in Coherent and Quantum Optics V, ed. L. Mandel and E. Wolf (Plenum Press, 1984) pp. 87-94.
5. [a] C.M. Bowden and C.C. Sung, Phys. Rev. Lett. 50, 156 (1983); [b] F.P. Mattar and C.M. Bowden, Phys. Rev. A27, 343 (1983); [c] F.P.Mattar et al., in Coherent and Quantum Optics V, ed. L.Mandel & E. Wolf, (Plenum Press, 1984) p. 507; & [d] F.P. Mattar et al., in Multiple-Photon Excitation and Dissociation of Polyatomic

Molecules, ed. C.D. Cantrell, (Springer-Verlag, 1986) pp.223-283.
6. S.L. McCall and E.L. Hahn, Phys. Rev. 183, 457 (1969). SIT is a solution to the Sine-Gordon equation.
7. R.H. Dicke, Phys. Rev. 93, 99 (1954).
8. [a] N.Skribanowitz et al., Phys. Rev. Lett. 30, 309 (1973); & [b] M.S. Feld & J.C. MacGillivray, in **Coherent Nonlinear Optics**, ed. M.S.Feld & V.S.Letokhov, (Springer-Verlag,1980) p.7; Q.H.F.Vrehen & H.M. Gibbs, in **Dissipative Systems in Quantum Optics**, ed. R. Bonifacio, (Springer-Verlag,1981) pp.111-147; M.Gross & S.Haroche Phys.Rep. 93, 301-396(1982); & F.P.Mattar, SPIE 380,508-542(1983)
9. [a] D. Polder et al., Phys. Rev. A19, 1192 (1979); [b] F. Haake et al., Phys. Rev. A20, 2047 (1979); [c] F.P. Mattar, SPIE 288, 364 (1981); [d] P.D. Drummond and J.H. Eberly, Phys. Rev. A25, 3446 (1982); & [e] E. Watson et al., Phys. Rev. A27, 1427 (1983).
10. F.P. Mattar et al., Phys. Rev. Lett. 46, 1121 (1981).
11. [a] See Ref. 1b,c for the introduction of phase waves; [b] See Ref. 9c,e for the evolution of phase in diffraction calculations of two-level SF; [c] See Ref. 5b,c for strong temporal distortion in three-level SF especially for shorter pulses. As τ_p the pump pulse length decreases the occurrence of phase waves in the SF transitions increases; [d] The prediction of phase wave in Raman Soliton: see C.M. Bowden & J.C. Englund, Opt. Commun. 67, 71 (1988); [e] The observation of phase waves: D.C. MacPherson et al., Phys. Rev. Lett. 61, 66 (1988).
12. F.P. Mattar, Program of the International Laser Science Conference ILS-III, Bull. Am. Phys. Soc. 32, 1644 (1987) paper #WO-6 and in **Advances in Laser Sciences III**, ed. A.C. Tam, J.L. Gole and W.C. Stwalley, (AIP, 1988) pp. 537-547 and to appear in **Progress in Quantum Electronics** (Pergamon Press, 1989).
13. F.P. Mattar, Transverse On-Resonance Reshaping in Coherent (a) Probe and (b) Pump Soliton Asymptotic Evolution in a Three-Level System, submitted to **Prog. Quantum Electronics**, Bull. Am. Phys. Soc. 32, 1644 (1987) paper #WO-5 & in **Advances in Laser Science-III (ILS-3)**, ed.A.C. Tam, J.L. Gole & W.C. Stwalley, (AIP, 1988) (a) probe soliton: pp. 524-529; (b) pump soliton: pp. 530-536.
14. [a] H.A. Haus, Appl. Phys. Lett. 8, 128 (1966); and [b] H.A. Haus, **Waves and Field in Opto Electronics** (Prentice Hall, 1984).
15. [a] Y.R.Shen, **Self-Focusing:Experimental**, Prog. Quantum Electron. 4, 1-34 (Pergamon Press,1975); & [b] J.H.Marburger, **Self-Focusing Theory**, Prog. Quantum Electron. 4, 35-110 (Pergamon Press, 1975).
16. [a] See Ref. 11a; [b] See Ref. 11b; [c] See Ref. 11c; [d] See Ref. 11d; and [e] See Ref. 11e.

LR2CFS SIMULATION NO. 1309

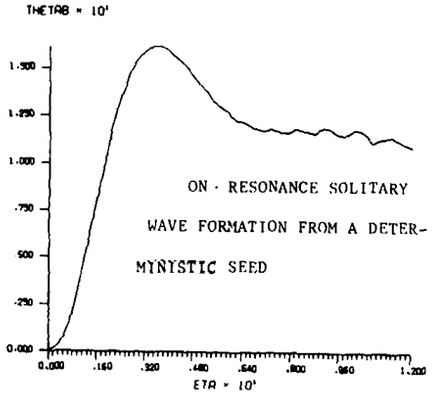

LR2CFS SIMULATION NO. 1310

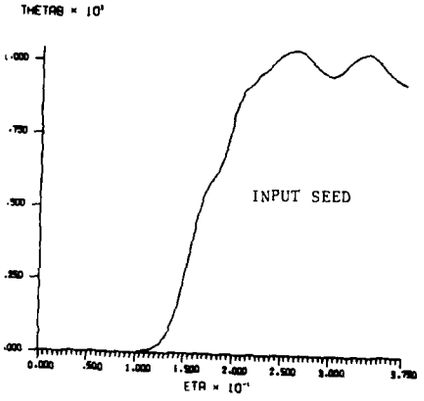

LR2CFS SIMULATION NO. 1315

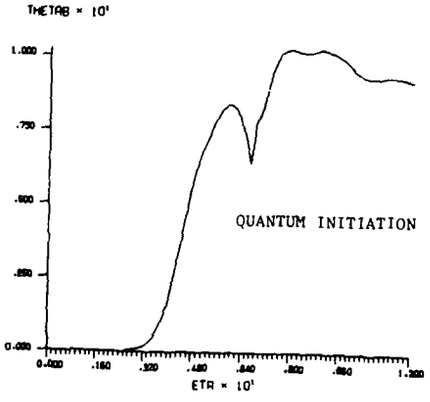

LR2CFS SIMULATION NO. 1316

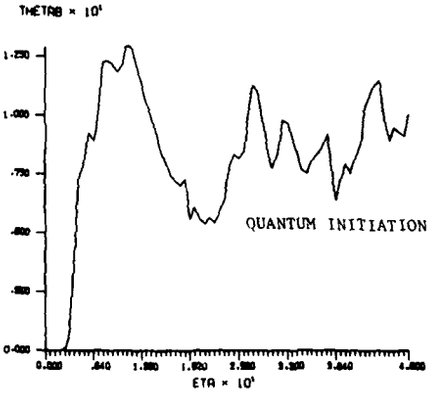

LR2CFS SIMULATION NO. 1321

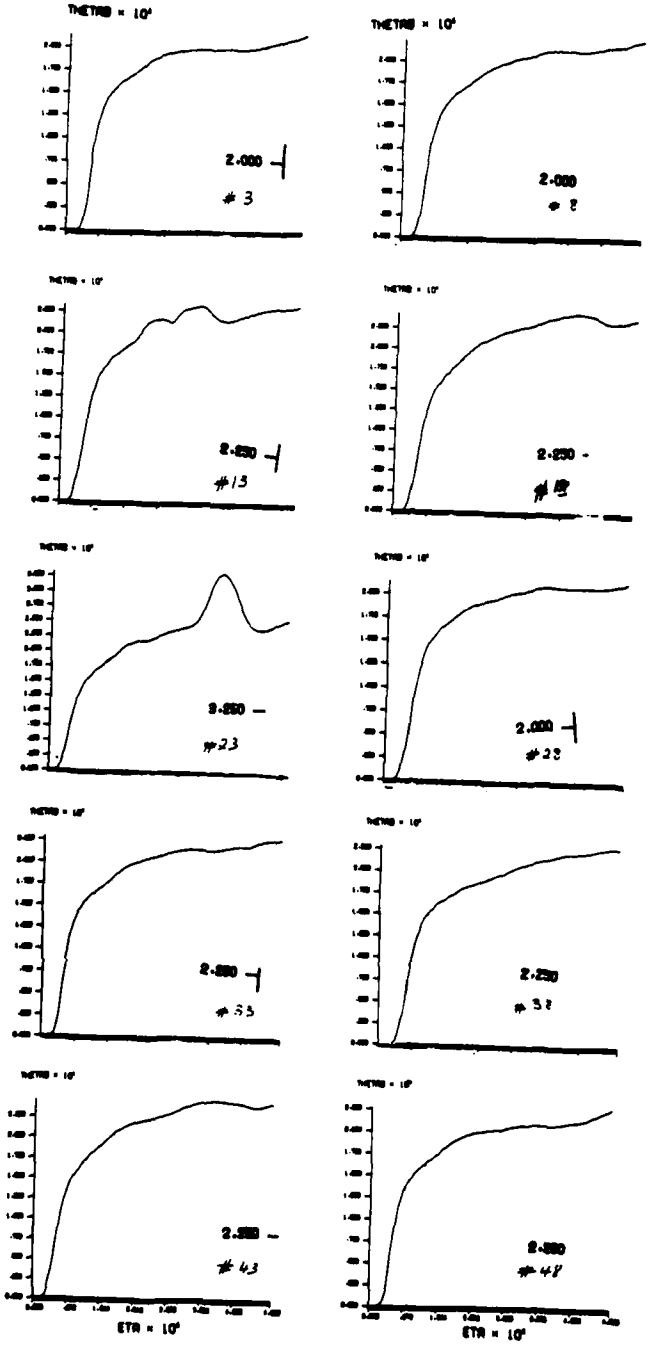

DIFFRACTION AND PHASE EFFECTS ON THE EVOLUTION OF RAMAN SOLITONS

F.P. Mattar#, Y. Claude*, M. Burgess* and J. Teichmann*
Department of Physics, New York University#, New York, NY 10003 and
Department of Electrical Engineering, City College of New York#,
New York, NY 10031; and
Departement de Physique, Université de Montreal*, Montreal, Canada

ABSTRACT

Transverse effects are shown to modify the evolution of off-resonant Stimulated Raman Scattering (SRS) solitons. The diminution of pump depletion, its cessation and reversal in a single-pass cell is demonstrated numerically. The verification of the conservation of energy confirms the validity of the computations.

I - INTRODUCTION

Solitons are waves that propagate without distortion. Their shape is preserved while subjected to the influence of competing mechanisms such as dispersion and Kerr nonlinearity in optical fibers[1] as predicted by Hasegawa and Tappert. Subsequently nearly distortionless propagation was demonstrated by Stolen and Lin[2]. Spatially solitary waves can result whenever diffraction and coherent nonlinear absorption that lead to self-trapping[3a]/self-focusing[3b] in Self-Induced-Transparency (SIT)[4]. (The SIT phenomenon occurs in a resonant two-level atomic system whose response is not instantaneous.) Associated with the inertia of the medium the pulse experiences delay and reshapes asymptotically into a distortionless hyperbolic secant pulse.

The solitons or solitary waves were discovered by Kruskal et al. [5] in 1967. In 1973 Scott et al.[6] reviewed the soliton as a distortionless carrier. Then, Chu and Scott[7] reported a two-photon soliton formation which was confirmed by Tan-no et al.[8] and Makhviladze[9].

Recent interest on soliton arose when Drühl et al.[10] reproduced numerically their observation of a Raman Soliton formed when a π phase-shift is electro-optically induced in the Stokes field. The Raman soliton appears with the repletion of the pump and a pulse compression. A bright pump soliton results. A companion dark soliton at the Stokes frequency was also found. The calculation was semi-classical uni-dimensional with the introduction of π phase shift for the Stokes pulse at the input plane. The Raman soliton formation was subsequently rederived by Ackerhalt et al.[11] and by Kaup[12]. More recently, Englund et al.[13] reported the spontaneous generation of Raman solitons from quantum noise while Teichmann and co-workers[14] analyzed the role of transverse effect which lead to self- and cross-phase modulation on Raman solitary waves.

A related on-resonance coherent co-propagation of a strong pump and a weak probe in three-level atoms with diffraction accounted for, has led to the discovery of two solitary waves: first a probe, followed by a pump[15]. The probe and pump solitons do not occur simultaneously. The renewal of the pump, i.e., the anomalous interruption of pump depletion as observed by Drühl et al. does take place.

In this communication, we analyze the interplay of diffraction-induced self-phase and cross-phase modulation. This situation was previously studied in conjunction with two- and three-level superfluorescence emission[16] and in Stimulated Raman Scattering[17].

#Supported by ARO, AFOSR, ONR & NSF at NYU & by NSERC at U.de Montreal

II - PHYSICAL MODEL

Stimulated Raman Scattering, which consists of of two beams co-propagating in nonlinear Raman medium with a time-delayed response, is described in a moving frame by the following system of coupled equations:

$$\frac{\partial}{\partial \tau} Q = - \Gamma Q + i\kappa_1 E_L E_S^* \tag{1}$$

$$\frac{\partial}{\partial \eta} E_S - i F_S^{-1} \nabla_T^2 E_S = i\kappa_2 E_L Q^* \tag{2}$$

$$\frac{\partial}{\partial \eta} E_L - i F_L^{-1} \nabla_T^2 E_L = i\kappa_3 E_S Q \tag{3}$$

where E_L and E_S represent respectively the Raman pump and the Stokes field amplitude, while Q the effective polarization. Γ, which is the reciprocal of the relaxation time, represents the decay of coherence associated with collisions. The second term in the LHS of Eq. (2) and Eq. (3) is the transverse Laplacian term which represent the diffraction coupling. The interplay of diffraction and nonlinearity is characterized by the Beer-length absorption Fresnel number F_L for the Raman pump and F_S the Stokes fields. Note that no prevision for the variation of the population inversion density has been made.

The initial conditions are

$$E_L(\rho,\tau,0) = \tau \exp(-\tau/\tau_p)\exp[-(r/r_p)^2] \qquad 0 \le \tau \le \infty \tag{4}$$

with ρ the radial variable $\rho = r/r_p$ (5). The input Stokes field is a small seed.

$$E_S(\rho,\tau,0) = 10^{-4} E_L(\rho,\tau,0) \exp[i\phi] \tag{6}$$

with $\phi_S(\rho,\tau,0) = \pi/2 \qquad 0 < \tau < \tau_{peak}$ (7a)

$$= - \pi/2 \qquad \tau_{peak} < \tau < \tau_{max} \tag{7b}$$

$$Q(\rho,0,\eta) = 0 \tag{8}$$

Whenever diffraction is not accounted for, Drühl et al.'s [10] equations of motion are obtained. A Raman simulation computer program has been developed as L22P©.

III - NUMERICAL RESULTS

At first we reproduced Drühl et al.'s uniform plane wave calculation. The physical parameters analyzed by Drühl et al. are as follows:

ℓ=0.2m, FWHM=140 ns; τ_{max}=160 ns, T_2=3.333 ns, γ=1/T_2=3 nsec^{-1}

for $0 < \tau < 71$ ns, $\phi_S = 0$; and 71 ns $< \tau <$ 160 ns, $\phi_S = \pi$,

$\omega_L = 970.55$ cm^{-1}, $\omega_S = 616.19$ cm^{-1}; $\delta_0 = \omega_L/\omega_S = 1.5751$

$I_L \simeq 5.5$MW, $I_S = 10^{-4} I_L$; g = 15 m/MW

$s_L = 9.26$ and $s_S = 0.0926$ with $s_{L,S} = \int_0^{\tau_{max}} |E_{L,S}| d\tau$

We present in Fig. 1 a comparison versus z the propagation distance the temporal reshaping of the pump energy in graph a and the Stokes energy in graph b. From graph a, one can follow the pump depletion from the incident profile for successive distances of propagation until one in which the pump ceases to deplete and begins to rebuild into two side lobes one at the front and the other at the trailing edges and an ultra-narrow pulse of constant amplitude, shape and temporal width. In graph b one sees the continuous growth of the Stokes until this specific z-plane at which a bright soliton evolves at the pump frequency while a dark soliton emerges at the Stokes frequency. The Stokes loss of energy is the source of the pump renewal. The conservation of the total energy has been verified throughout the propagation in the Raman media (Graph 1c).

In Figs. 2 and 3 we respectively provide for diffraction calculation two plot family of on-axis energies and radially-integrated energies, i.e., output power (OPOWRa,b). The input radial dependence of the beam is Gaussian. The temporal collapse of the pump width is quite striking - its persistence over z is significant. A sizeable pump pulse compression results in this regime. The depletion of the Stokes energy in favor of a repletion of the pump energy persists for different radii and can be observed even for a larger detector. The Raman soliton formation only occurs after the peak of the pulse at the incident plane. The peak amplitude of the Raman soliton is largest than the first peak. This temporal distortion was discussed by Hopf [16] in connection with fluctuation calculations in superfluorescence. Hopf referred to it as a phase wave. When diffraction effects are included the output power displays a stronger second peak (see L22P#41 at η=0.120), exhibited by the one-dimensional energy counterpart.

In Fig. 4 we compare the influence of the Fresnel number for incident Gaussian beam and that of the HWHM width r_p (TBRHO^{-1}) on the soliton formation by displaying a composite comparison of the on-axis energies (ENRGYa & ENRGYb) in graph a or the output powers in graph b for three different propagation lengths. Significant spatial and temporal energy reshaping is observed. As the diffraction coupling gets stronger, energy redistribution within the same beam can occur causing at some instances an on-axis enhancement, i.e., a self-focusing. For narrower beams (as in L22P#51) the inflow of radial flux becomes sufficiently important to first reduce the pump soliton amplitude and eventually to eliminate the dark Stokes soliton altogether.

The Fresnel number associated with a Raman gain length g^{-1} is the critical universal parameter $F_g = \pi r_p^2/\lambda g^{-1}$. The ratio of the Stokes to Raman pump gain is the second critical parameter. The ratios of $F_{gpump}/F_{gStokes}$, of g_{Stokes}/g_{pump} as well as of the input incident powers are sufficient to characterize the energy conversion and the Raman soliton formation for a given pulse shape. The emergence of **anomalous pump reversal** appears for an earlier propagation distance z and with a lesser on-axis time-delay from the first peak.

The influence of the pulse shape was also studied hence their rising time and the steepness of the trailing/leading edges on the emergence of the Raman soliton. The pulse shapes considered were the hyperbolic secant, sech τ, hyperbolic secant square sech$^2\tau$, the Gaussian exp($-\tau^2$), the super-Gaussian exp[$-\tau^4$] and time-weighted exponential τexp($-\tau$).

By enhancing the input relative Stokes phase one establishes a

chirp which in turn accelerates the emergence of the Raman solitary wave.

In summary, the presence of transverse variations plays an important role in accelerating or delaying the formation of the solitary wave since it controls the relative self- and cross-phase modulation of each beam. For example, the on-center portion of the Stokes beam can experience self-focusing in the same temporal region where an annular shell whose radius is smaller than the HWHM exhibits the conditions for Raman soliton formation. This duality of processes occurring within the same beam but at different radii is displayed in calculation L22P45 and L22P49 (see Fig. 5).

Should one vary the pulse shape while keeping its area constant (or equivalently, the fluence) one modifies the pulse sharpening thus the rate of buildup of the phase which ends up affecting the evolution of the Raman soliton.

Finally we present in Fig. 6 the transverse energy current versus τ and ρ for different η. The energy current is defined as the energy-weighted phase gradient; i.e., it is the product of the energy with the phase variation. When the phase curvature is focusing the flux is negative. This means that the energy current is flowing inwardly from the beam wings to the beam center. The on-axis energy will experience an enhancement while the beam widths will narrow. If the phase curvature is positive the energy flux is flowing outwardly illustrating the blooming of the beam. In our calculations we have found that the pump beam generally experiences narrowing while the Stokes beam expands. This demonstrates that the phase variations are crucial to the description of the physics.

IV - CONCLUSION

We have presented both phase and diffraction effects on the Raman soliton evolution for input Gaussian beams. We obtain a degree of realism in our analysis by assuming that the radial profile of the beam does not remain Gaussian. **Our computation demonstrates that transverse effect is an inherent fundamental process and cannot be taken as an unnecessary extension to one dimensional analytical studies. Transverse effects leads to the evolution of self-phase and cross-phase modulation.** This conclusion was reached in our earlier analysis of superfluorescence[17] and of SRS[18]. The significance of self-phase modulation has been recently recognized in a one-dimensional calculation on soliton regeneration[19].

Finally, if the Lorentz local field(s) correction[20-23] is also accounted for, a population-dependent frequency offset emerges in the density matrix. The effective detuning becomes a time (and radial) dependent function. An additional phase variation results. The resultant chirp, i.e., the frequency modulation modifies the characteristics of the Raman co-propagation. The rate of energy conversion from the pump to the Stokes and the depletion of the pump and the growth of the Stokes emission become more complicated. The analytical tractability vanishes. One must resort to numerical experiments to appreciate the physical nuances and domain.

REFERENCES

1. A.Hasegawa & F.Tappert, Appl. Phys. 23, 142(1973) & 23, 171(1973).
2. R.H. Stolen & C. Lin, Phys. Rev. A17, 1448 (1978).
3. [a] J. Marburger, **Progress in Quantum Electronics**, ed. (Pergamon Press, 1975) pp. 35-105; and [b] F.P. Mattar & M.C. Newstein, Opt. Commun.18, 70(1976) & IEEE J.Quantum Electronics QE-13, 507(1977).

4. S.L. McCall & E.L. Hahn, Phys. Rev. Lett. 28, 308 (1967); Phys. Rev. 183, 457 (1969) and Phys. Rev. A2, 861 (1970).
5. N.J. Zabusky & M.D. Kruskal, Phys. Rev. Lett. 15, 240 (1965).
6. A.C. Scott et al., IEEE Proc. 61, 1443-1483 (1973).
7. R.Y.F. Chu & A.C. Scott, Phys. Rev. A12, 2060 (1975).
8. N. Tan-no et al., Phys. Rev. A12, 159 (1975).
9. T.M. Makhviladze et al., Sov. Phys. JETP 42, 255 (1976).
10. [a] K.J. Drühl et al., Phys. Rev. Lett. 51, 1171 (1983); [b] J.L. Carlsten et al., in **Refereed Proceedings Los Alamos Conference on Optics**, ed. R.S. McDowell & S.C. Stotlar SPIE 380, 201 (1983); [c] R.G. Wenzel et al., J. Stat. Phys. 39, 621 (1985) and 615 (1985); [d] K.J. Drühl & G. Alsing, Physica 20D, 429 (1986); and [e] D.C. MacPherson et al., J. Opt. Soc. Am. B4, 1853 (1987).
11. J.R. Ackerhalt & P.W. Milonni, Phys. Rev. A33, 3185 (1986).
12. D. Kaup, Physica 19D, 125 (1986).
13. [a] J.C. Englund & C.M. Bowden, Phys. Rev. Lett. 57, 2661 (1986); and [b] C.M. Bowden & J.C. Englund, Opt. Commun. 67, 71 (1988).
14. J.Teichmann & F.P.Mattar, Bull.Am.Phys.Soc. 33, 1637 (1988) paper M17 & to appear in **Advances in Laser Sciences IV**, Am. Inst. Phys. Conf. Proc. for the Fourth International Laser Science Conference.
15. F.P. Mattar, in **Advances in Laser Science III**, ed. A.C. Tam, J.L. Gole & W.C. Stwalley, (AIP, 1988) (a) probe soliton pp. 524-529 & (b) pump soliton pp. 530-536; & J. De Physique 49, C2, 463 (1988).
16. F.A. Hopf, Phys. Rev. A20, 2064 (1979).
17. [a] F.P. Mattar et al., Phys. Rev. Lett. 46, 1121 (1981); and [b] F.P. Mattar & C.M. Bowden, Phys. Rev. A27, 343 (1983).
18. [a] R.L. Carman et al., Phys. Rev. A2, 60 (1970); [b] M. Maier et al., Phys. Rev. 177, 580(1969); [c] G.I. Kachen & W.H. Lowdermilk, Phys. Rev. A14, 1472 (1976); & [d] S.M. Georges & C.B. Harris, Phys.Rev. A28, 863 (1983).
19. R. Wolfson & K.J. Drühl, Opt. Lett. 15, 125 (1989).
20. J. Marburger, L. Huff, J.D. Reichert & W.G. Wagner, Phys. Rev. 184, 255 (1969).
21. [a] R. Friedberg, S.R. Hartmann & J.T. Manassah, Phys. Lett. 35A, 161 (1971), ibid 40A, 395 (1972) & Phys. Report 7C, 101-179 (1973); [b] J.T. Manassah, Phys. Report 101, 359-427 (1983); [c] R. Friedberg, S.R. Hartmann & J.T. Manassah, Phys. Rev. A39, 93 & 3444 (1989); and [d] J.T. Manassah, Phys. Rept. 101, 359-427.
22. [a] F.A. Hopf, C.M. Bowden & W.H. Louisell, Phys. Rev. A29, 2591 (1983); [b] in **Optical Bistability II**, ed. C.M. Bowden, H.M. Gibbs & S.L. McCall (Plenum Press, 1984) pp. 361-368; and [c] in **Optical Instabilities**, ed. R.W. Boyd, M.G. Raymer & L.M. Narducci (Cambridge University Press, 1986) pp. 308-311.
23. J.T. Manassah & F.P. Mattar, in Proc. Intl. Laser Sci. ILS-IV, **Advances in Laser Science IV** (Am. Inst. Phy., 1989).

FIGURE CAPTIONS

Fig. 1a A comparison of the on-axis energies is respectively shown versus τ for the pump and the Stokes at three different propagation distances. The conservation of the sum of the fluences validates the calculation.

Fig. 2a The on-axis pump and Stokes energies (L22P#49) are respectively shown as two- and three-dimensional plots.

Fig. 2c In Graph c the soliton formation is exhibited for different diffraction couplings.

Fig. 3 A comparison of the pump and Stokes output power is carried out at three η for large (L22P#40, at η=0.120) and narrow (L22P#44 & 45 at η=0.2) beams. The temporal region in which the Stokes energy profile ceases to exhibit a diminition and experiences an enhancement is enlarged.

Fig. 4 The effect of the diffraction coupling on the emergence of the Raman soliton. Graph a consists of two-dimensional composite plots for the on-axis energies of L22P#43, 44, 45 and 46 while Graph b consists of three-dimensional energy plots for L22P#47 & 48.

Fig. 5 The importance of diffraction coupling in modifying the on-axis dark Stokes soliton energy evolution is illustrated. In graph a the change of transverse flux is presented as a function of the Fresnel number. In graph b, the on-axis pump and Stokes energies are displayed for three successive propagational distances for a narrow and a large beam.

Fig. 6 Three-dimensional plots of the transverse energy current for each pump and Stokes pulses.

L22P SIMULATION NO. 49

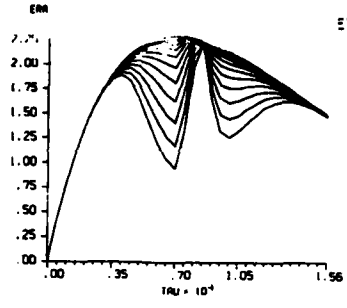

ERA

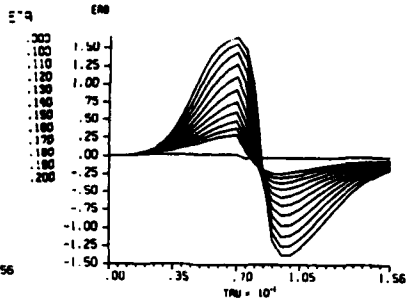

ERB

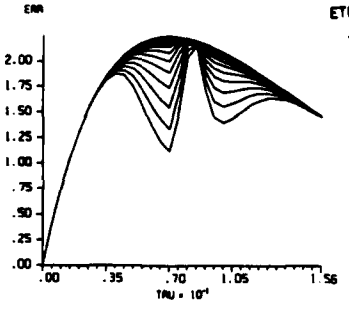

ERA

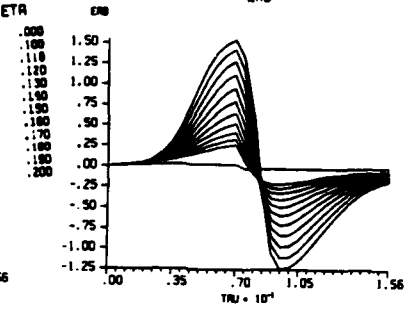

ERB

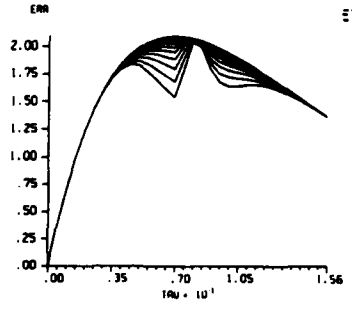

ERA

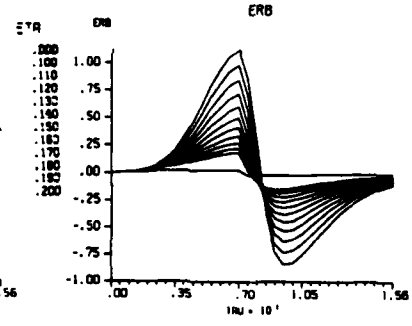

ERB

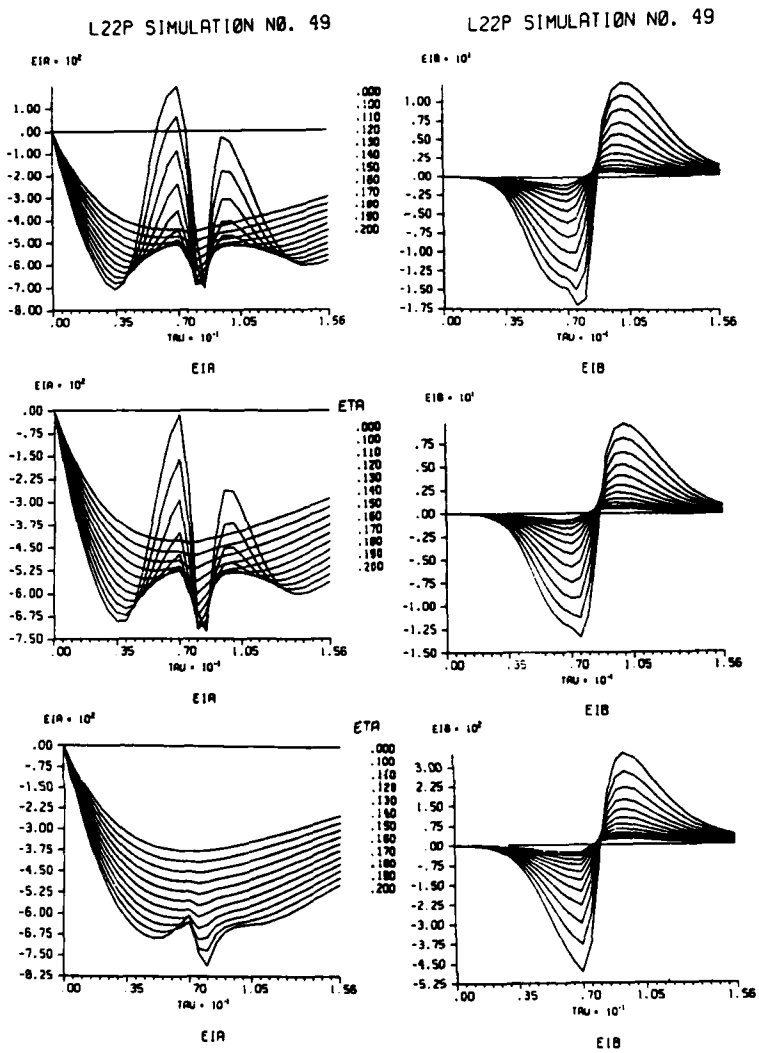
L22P SIMULATIØN NØ. 49
L22P SIMULATIØN NØ. 49
EIA
EIB
ETA
EIA
EIB
ETA
EIA
EIB

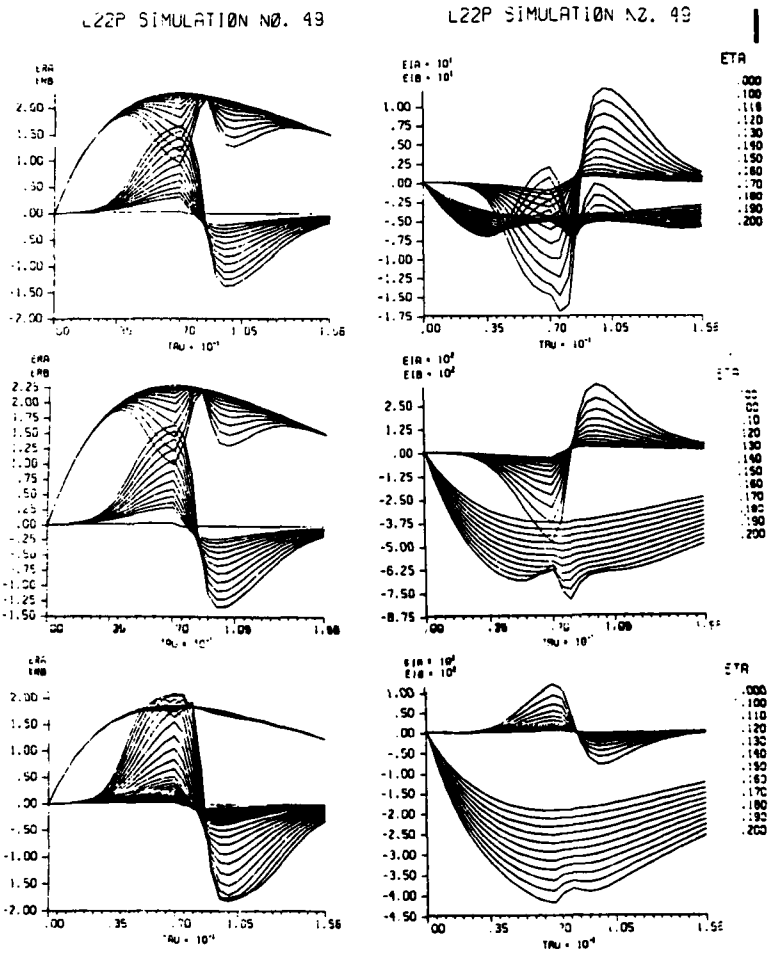
L22P SIMULATION NO. 49
L22P SIMULATION NO. 49
ETA

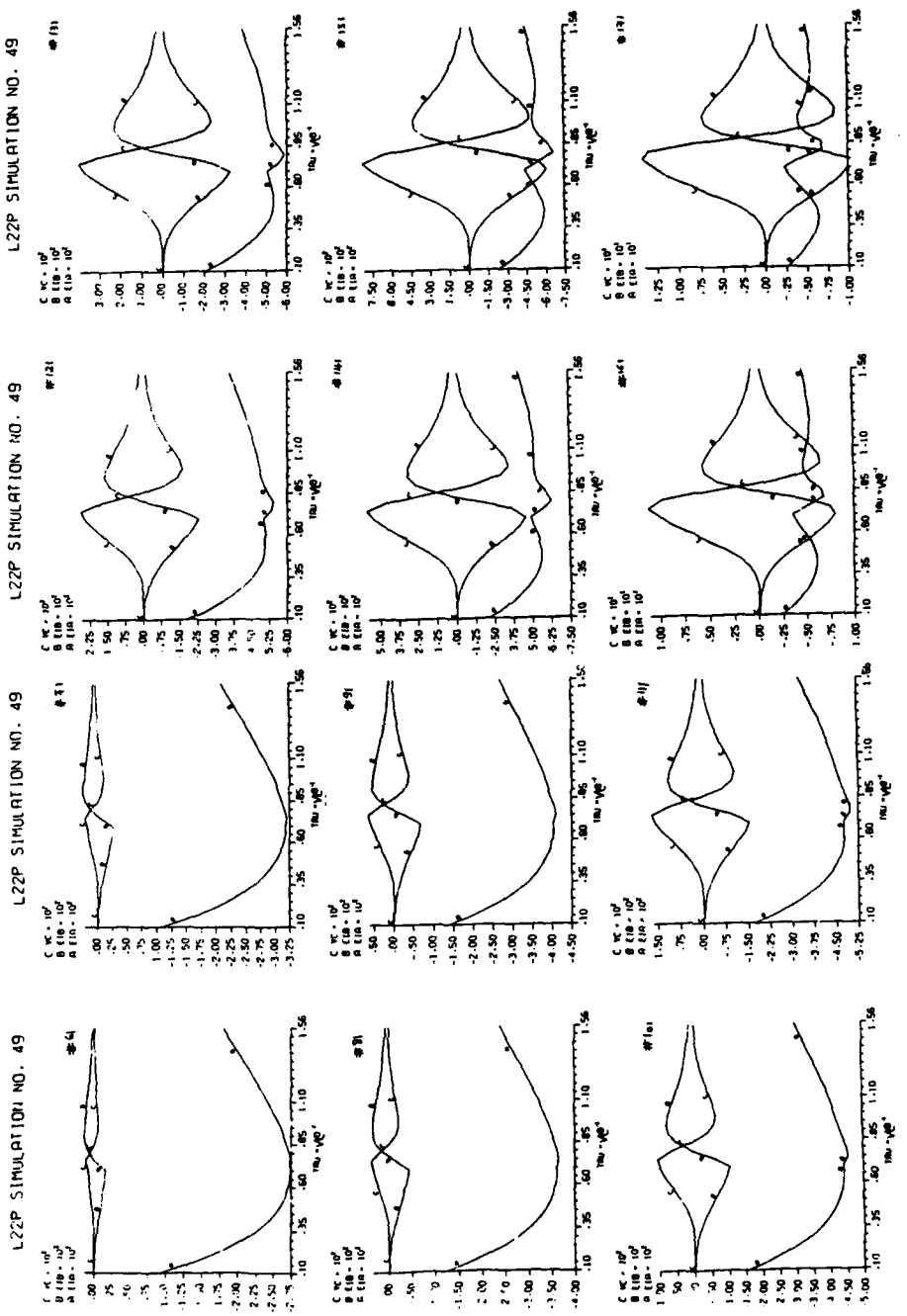
L22P SIMULATION NO. 49
L22P SIMULATION NO. 49
L22P SIMULATION NO. 49
L22P SIMULATION NO. 49

L22P SIMULATION NO. 25

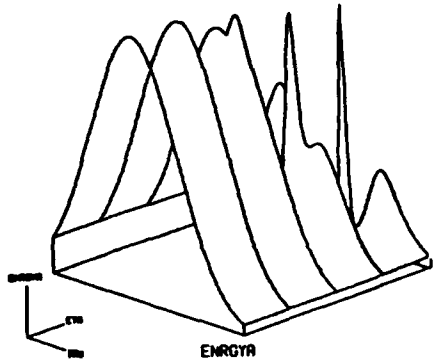

L22P SIMULATION NO. 26

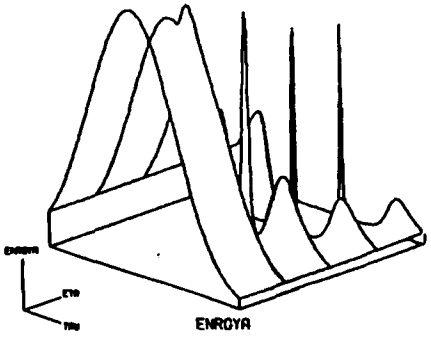

L22P SIMULATION NO. 27

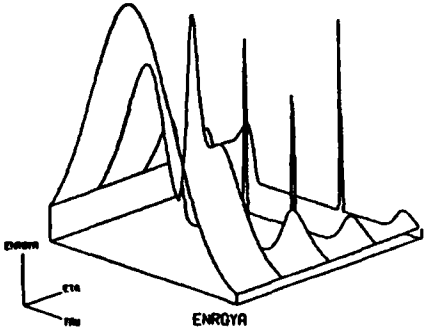

L22P SIMULATION NO. 40

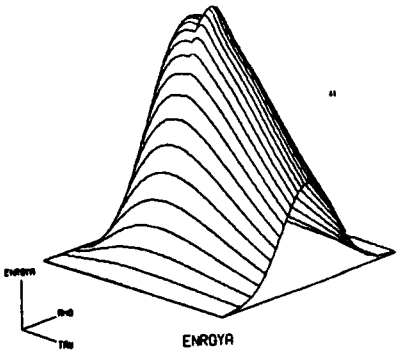

L22P SIMULATION NO. 40

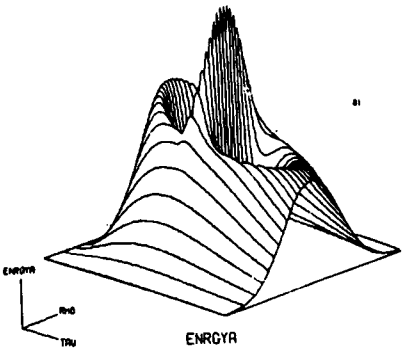

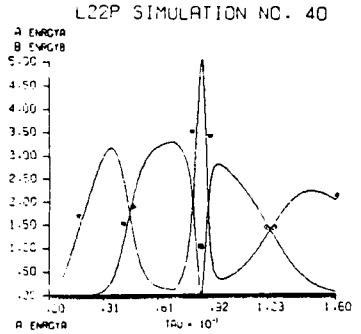
L22P SIMULATION NO. 40
A ENRGYA
B ENRGYB
TAU x 10⁻⁴

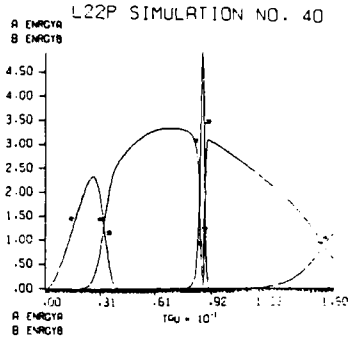
L22P SIMULATION NO. 40
A ENRGYA
B ENRGYB
TAU x 10⁻⁴

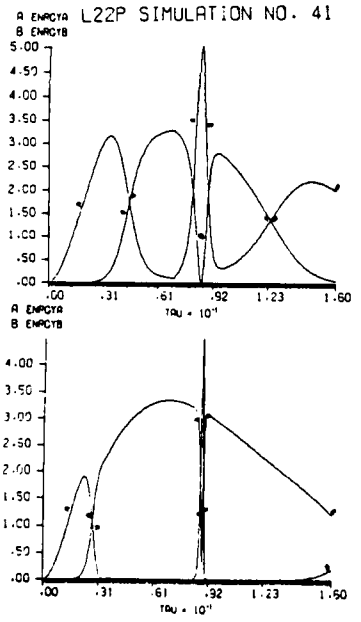
L22P SIMULATION NO. 41
A ENRGYA
B ENRGYB
TAU x 10⁻⁴

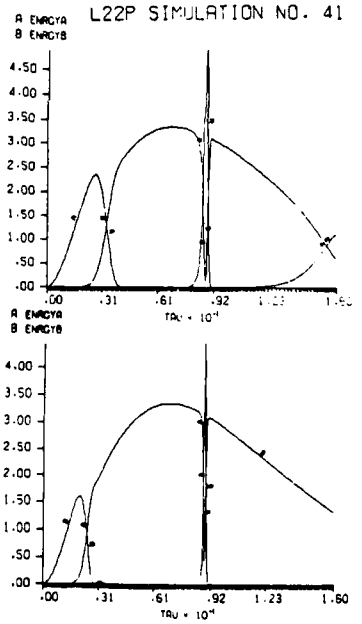
L22P SIMULATION NO. 41
A ENRGYA
B ENRGYB
TAU x 10⁻⁴

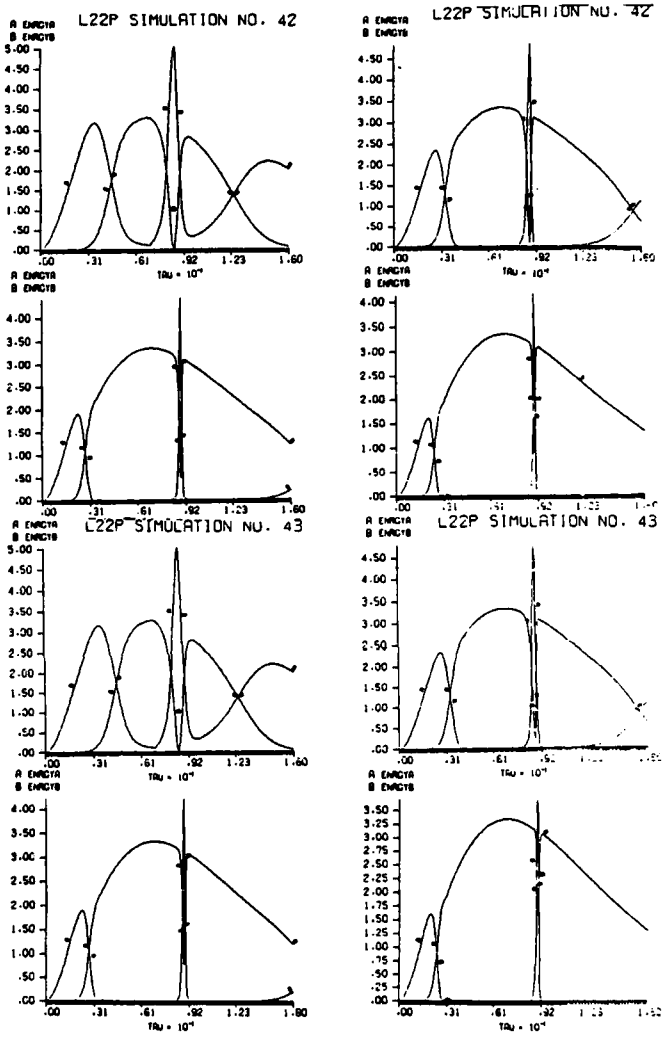
L22P SIMULATION NO. 42
L22P SIMULATION NO. 42
L22P SIMULATION NO. 43
L22P SIMULATION NO. 43

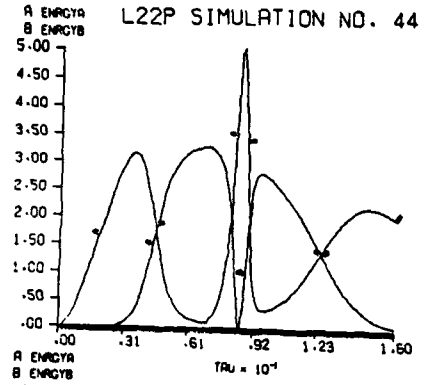
A ENRGYA
B ENRGYB
L22P SIMULATION NO. 44
5.00
4.50
4.00
3.50
3.00
2.50
2.00
1.50
1.00
.50
.00
.00
.31
.61
.92
1.23
1.60
TAU = 10⁻⁴

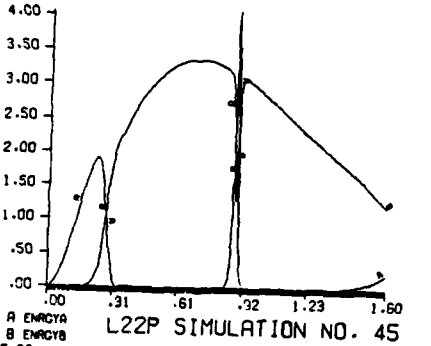
A ENRGYA
B ENRGYB
4.00
3.50
3.00
2.50
2.00
1.50
1.00
.50
.00
.00
.31
.61
.92
1.23
1.60

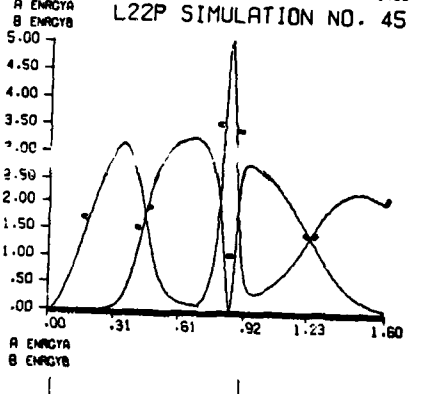
A ENRGYA
B ENRGYB
L22P SIMULATION NO. 45
5.00
4.50
4.00
3.50
3.00
2.50
2.00
1.50
1.00
.50
.00
.00
.31
.61
.92
1.23
1.60
TAU = 10⁻⁴

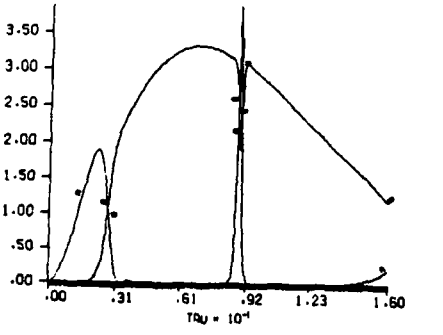
A ENRGYA
B ENRGYB
3.50
3.00
2.50
2.00
1.50
1.00
.50
.00
.00
.31
.61
.92
1.23
1.60

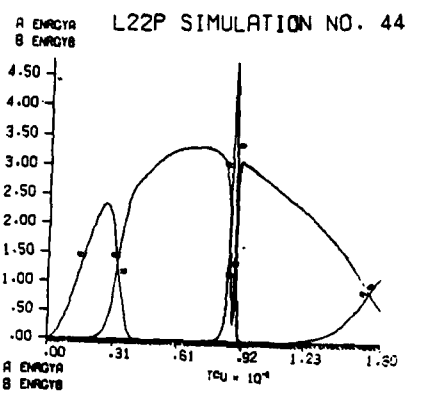
A ENRGYA
B ENRGYB
L22P SIMULATION NO. 44
4.50
4.00
3.50
3.00
2.50
2.00
1.50
1.00
.50
.00
.00
.31
.61
.92
1.23
1.60
TAU = 10⁻⁴

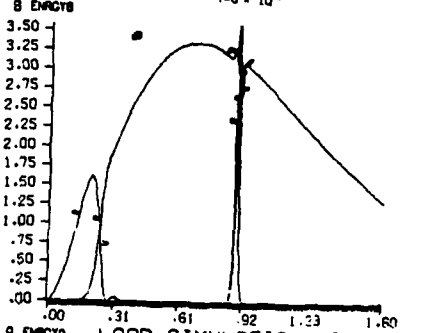
A ENRGYA
B ENRGYB
3.50
3.25
3.00
2.75
2.50
2.25
2.00
1.75
1.50
1.25
1.00
.75
.50
.25
.00
.00
.31
.61
.92
1.23
1.60

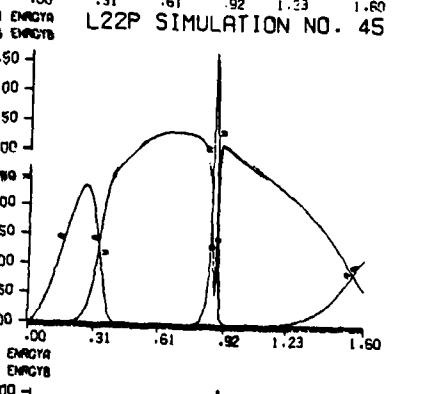
A ENRGYA
B ENRGYB
L22P SIMULATION NO. 45
4.50
4.00
3.50
2.00
1.50
1.00
.50
.00
.00
.31
.61
.92
1.23
1.60

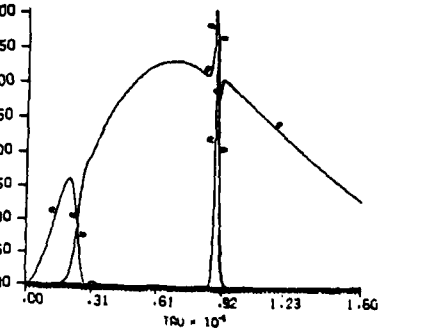
A ENRGYA
B ENRGYB
4.00
3.50
3.00
2.50
2.00
1.50
1.00
.50
.00
.00
.31
.61
.92
1.23
1.60
TAU = 10⁻⁴

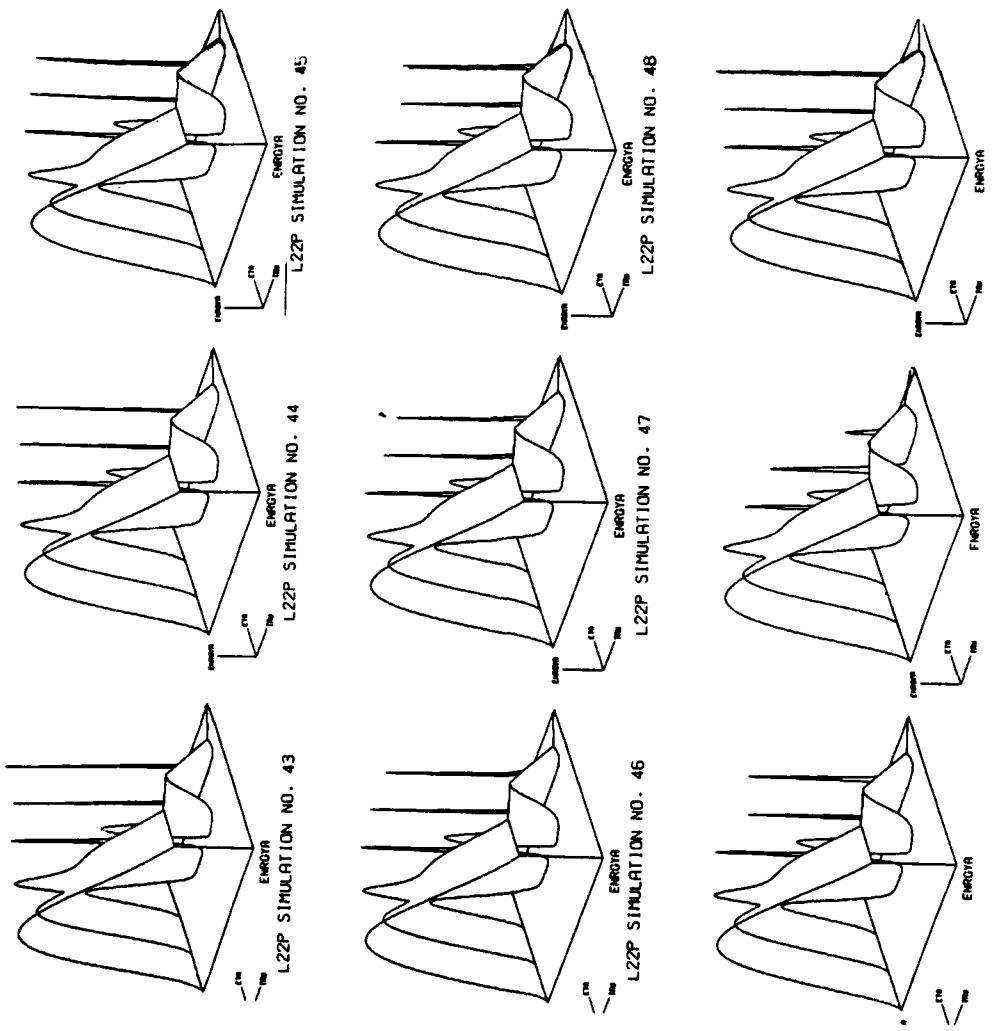
L22P SIMULATION NO. 45
L22P SIMULATION NO. 48
L22P SIMULATION NO. 44
L22P SIMULATION NO. 47
L22P SIMULATION NO. 43
L22P SIMULATION NO. 46
ENROYA

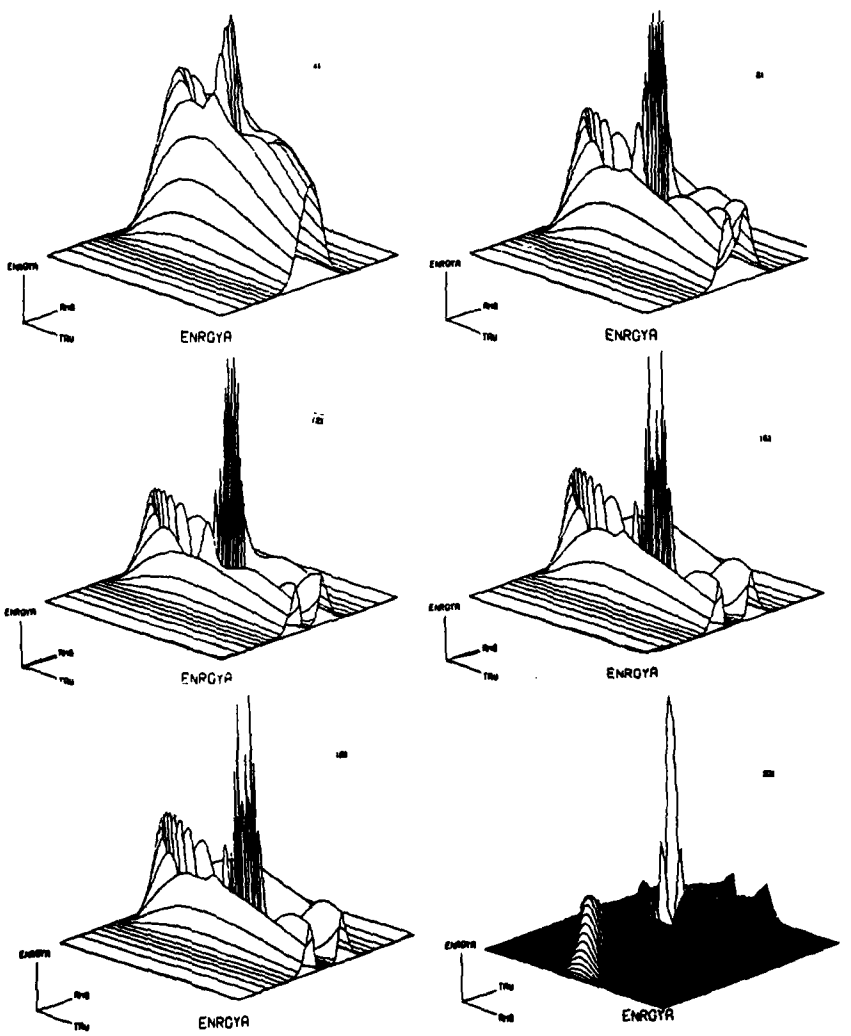
ENRGYA
ENRGYA
ENRGYA
ENRGYA
ENRGYA
ENRGYA

L22P SIMULATIØN NØ. 45

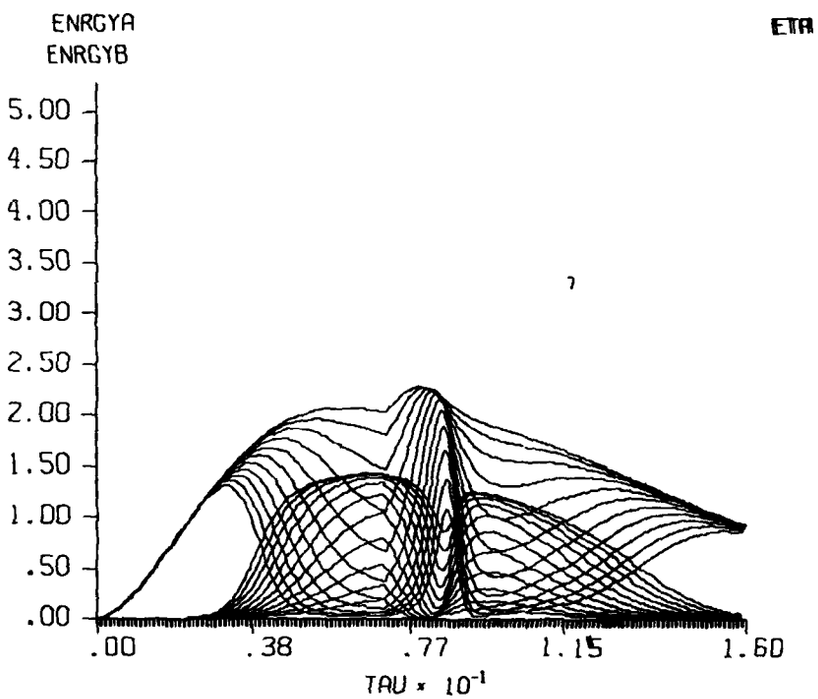

L22P SIMULATIØN NØ. 45

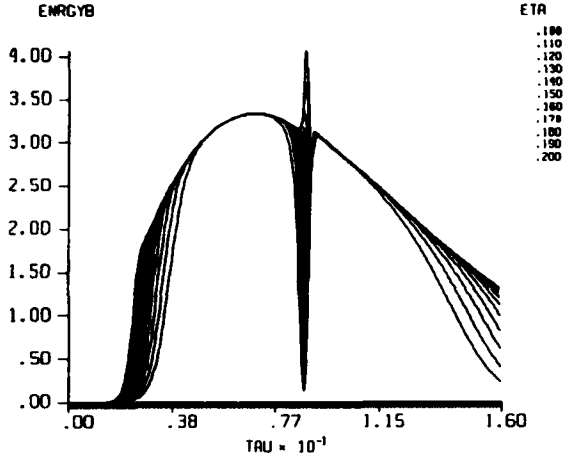

ENRGYB

SCALE	GLOBALE	AXIS	TOT.PT	SYM	RANGE	NB.SEL	RANGE OF VALUES
MIN =	0.	RHO	32	NB	1	1	0.0
MAX =	4.0888821	ETA	201	NB	(10).201)	11	(0.1.0.2)
		TAU	256	NB	(1.256)	256	(0.0.16.0)

on-axis

L22P SIMULATIØN NØ. 45

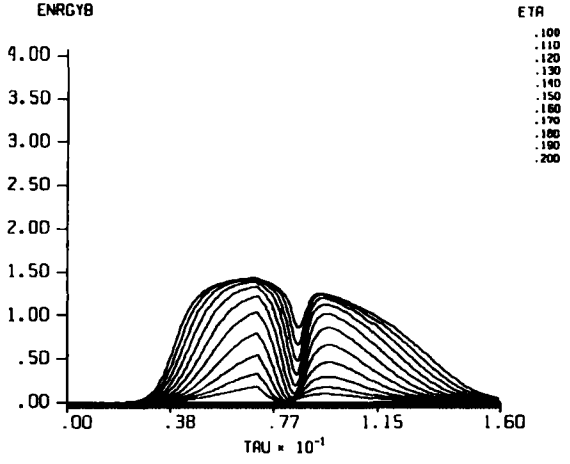

ENRGYB

SCALE	GLOBALE	AXIS	TOT.PT	SYM	RANGE	NB.SEL	RANGE OF VALUES
MIN =	0.	RHO	32	NB	7	1	0.001585
MAX =	4.0888821	ETA	201	NB	(10).201)	11	(0.1.0.2)
		TAU	256	NB	(1.256)	256	(0.0.16.0)

off-axis

L22P SIMULATION NO. 45

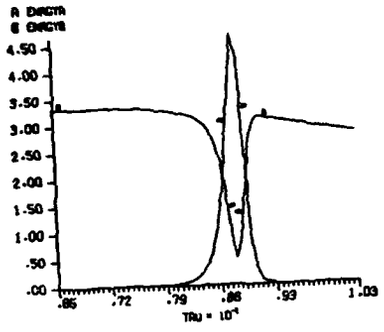

L22P SIMULATION NO. 45

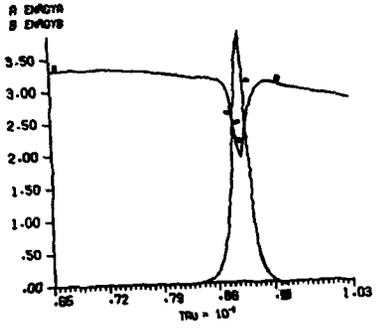

L22P SIMULATION NO. 45

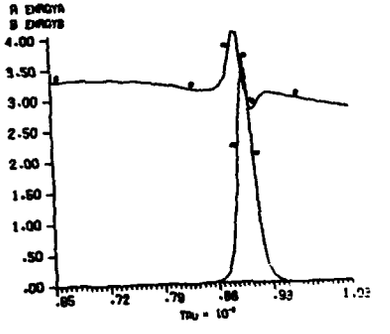

L22P SIMULATION NO. 46

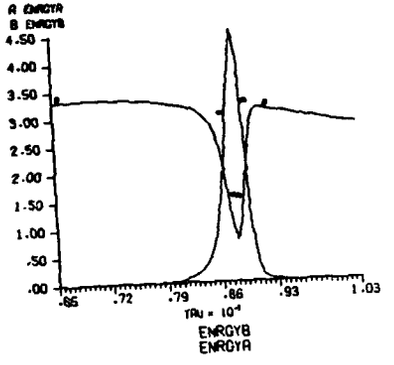

L22P SIMULATION NO. 46

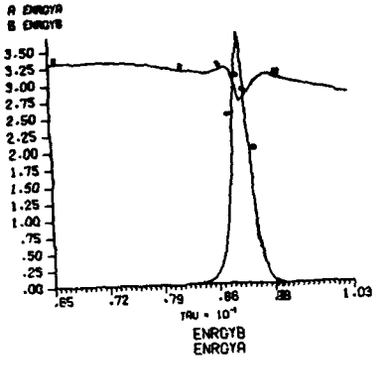

L22P SIMULATION NO. 46

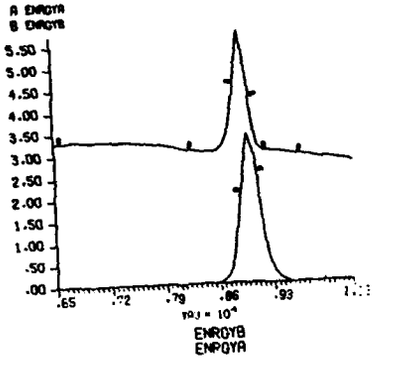

L22P SIMULATION NO. 49

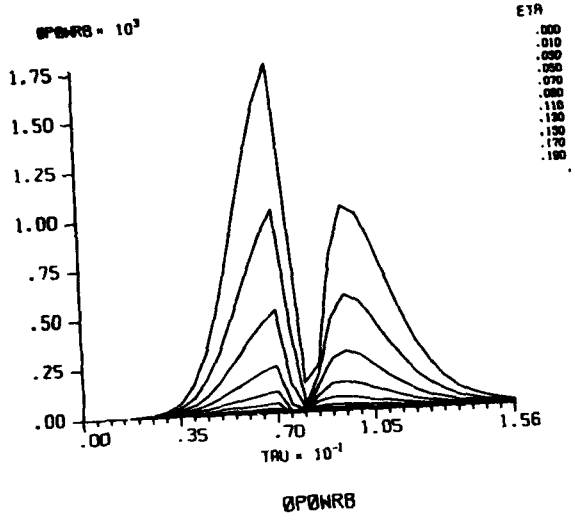

L22P SIMULATION NO. 45

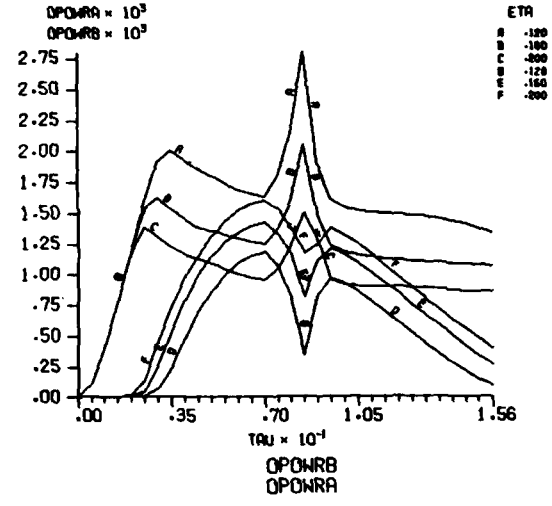

RADIALLY-INTEGRATED ENERGY ,i.e.,OUTPUT POWER AS FONCTION OF THE PROPAGA -GATIONAL DISTANCES. THE FORMATION OF BRIGHT RAMAN PUMP SOLITONS AND OF DARK STOKES SOLITONS IS CLEARLY DEMONSTRATED.

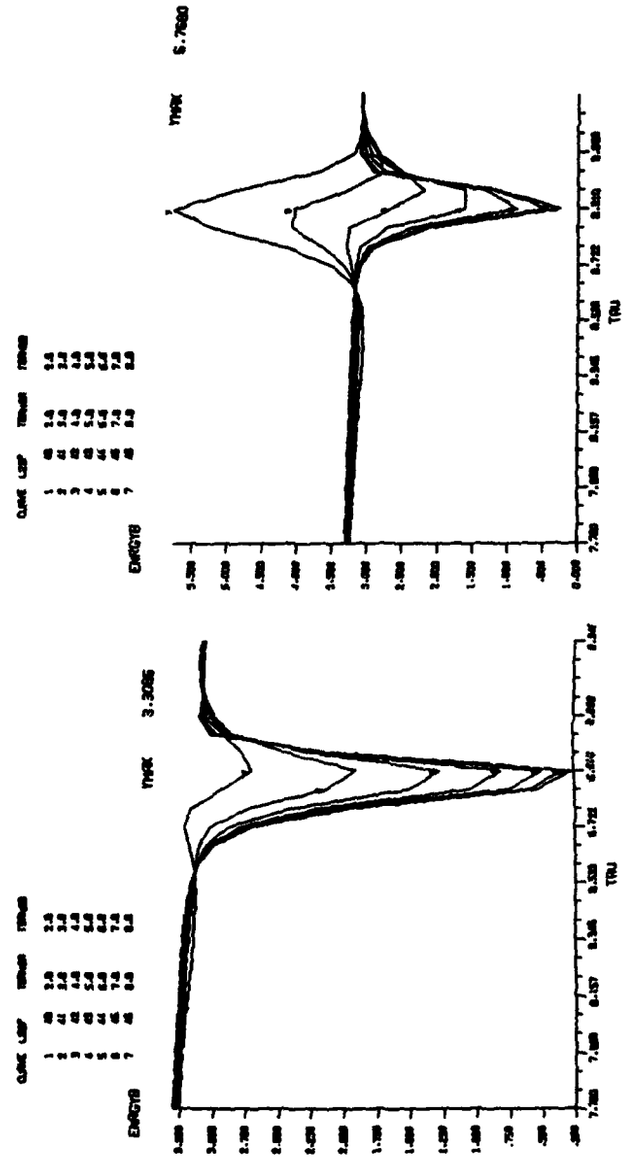

L22P SIMULATION NO. 47

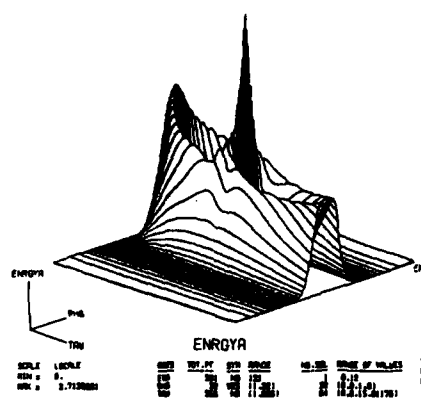

L22P SIMULATION NO. 47

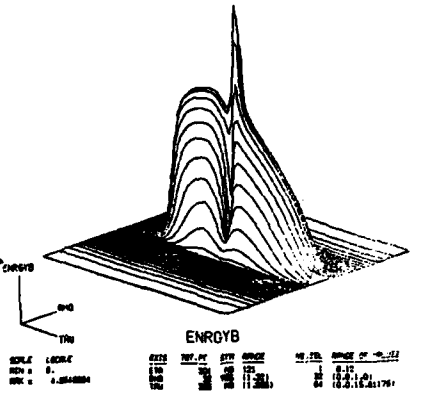

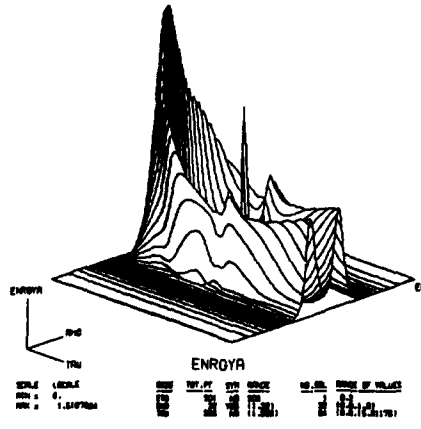

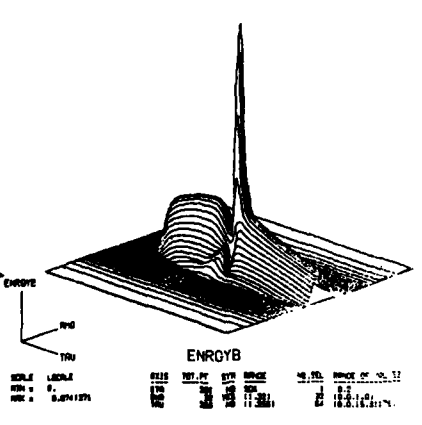

L22P SIMULATIØN NØ. 49

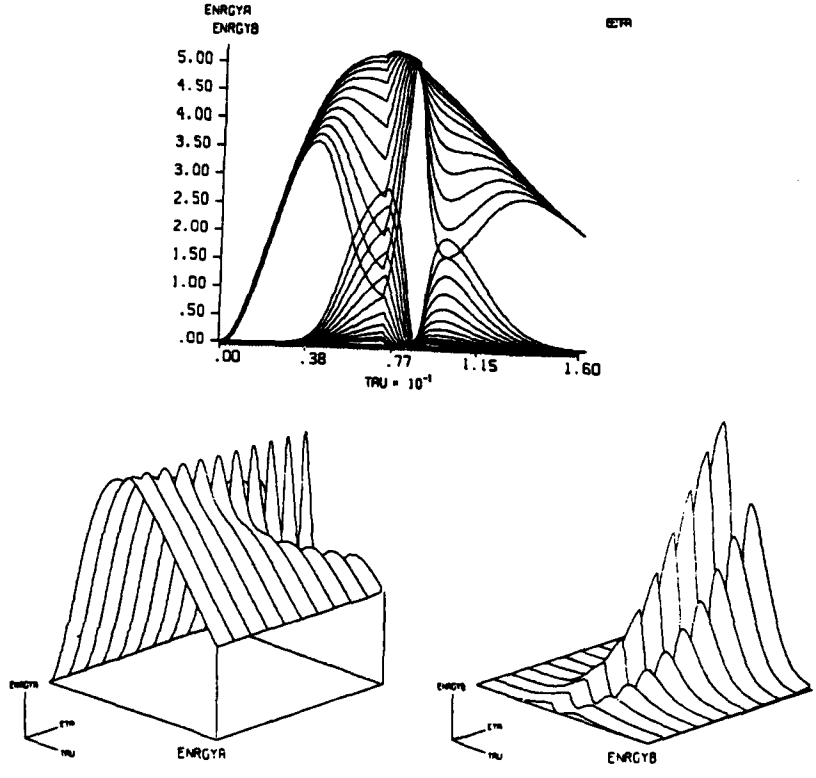

RAMAN SOLITON FORMATION OUT OF DIFFRACTION

DIFFRACTION REPRESENTS A SOURCE OF SELFPHASE AND OF

CROSS PHASE MODULATION IN THE PRESENCE OF DISSIPATION

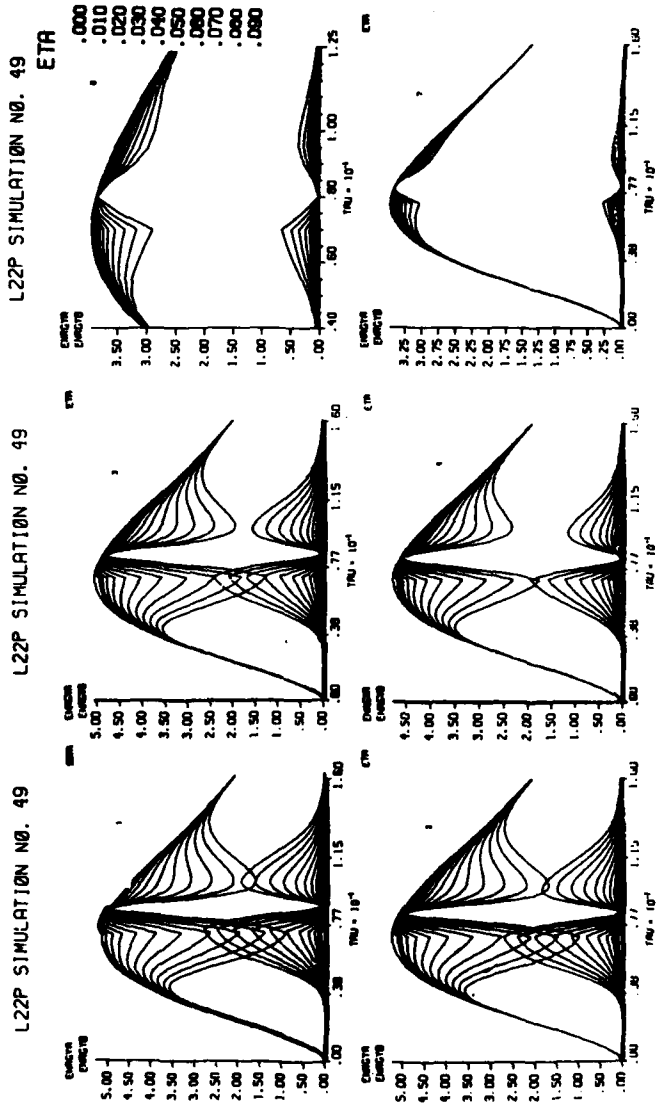
L22P SIMULATION NO. 49
ETA
.000
.010
.020
.030
.040
.050
.060
.070
.080
.090
L22P SIMULATION NO. 49
L22P SIMULATION NO. 49

L22P SIMULATIØN NØ. 49

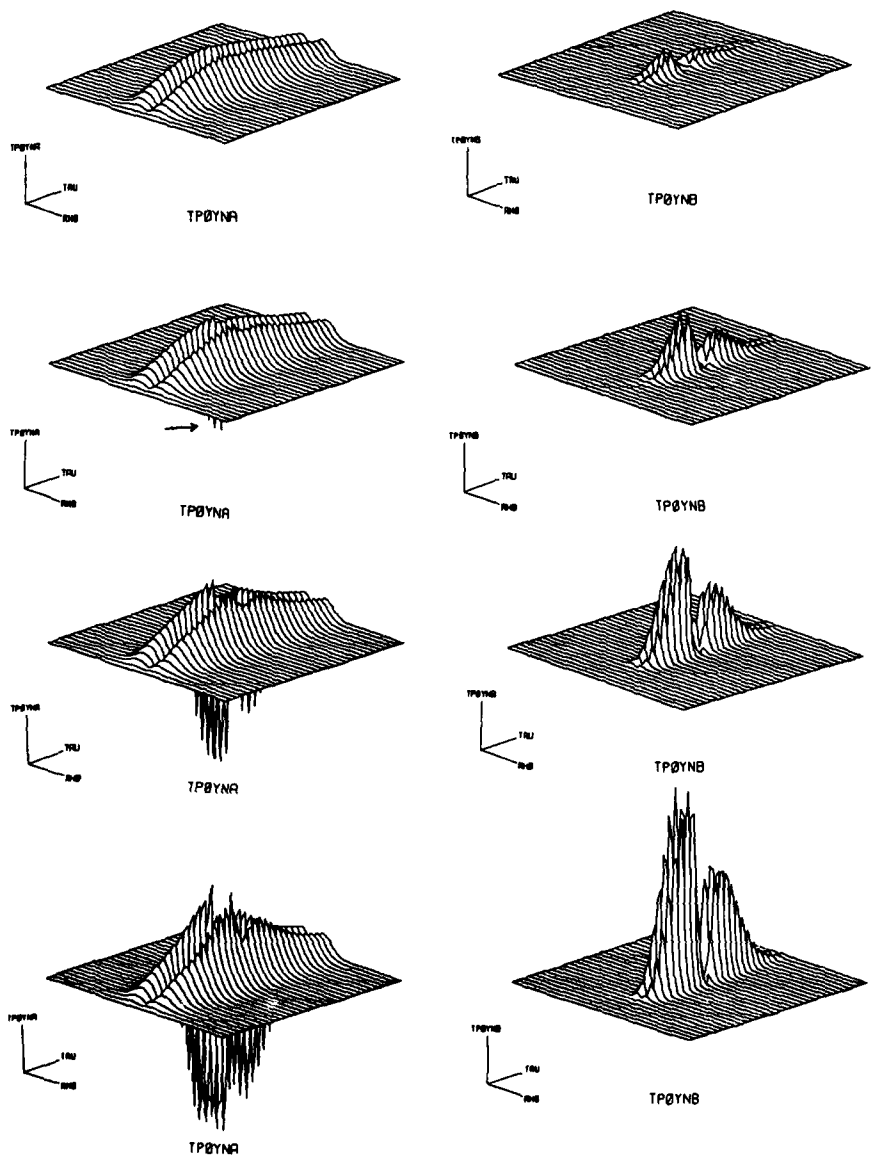

L22P SIMULATIØN NØ. 49

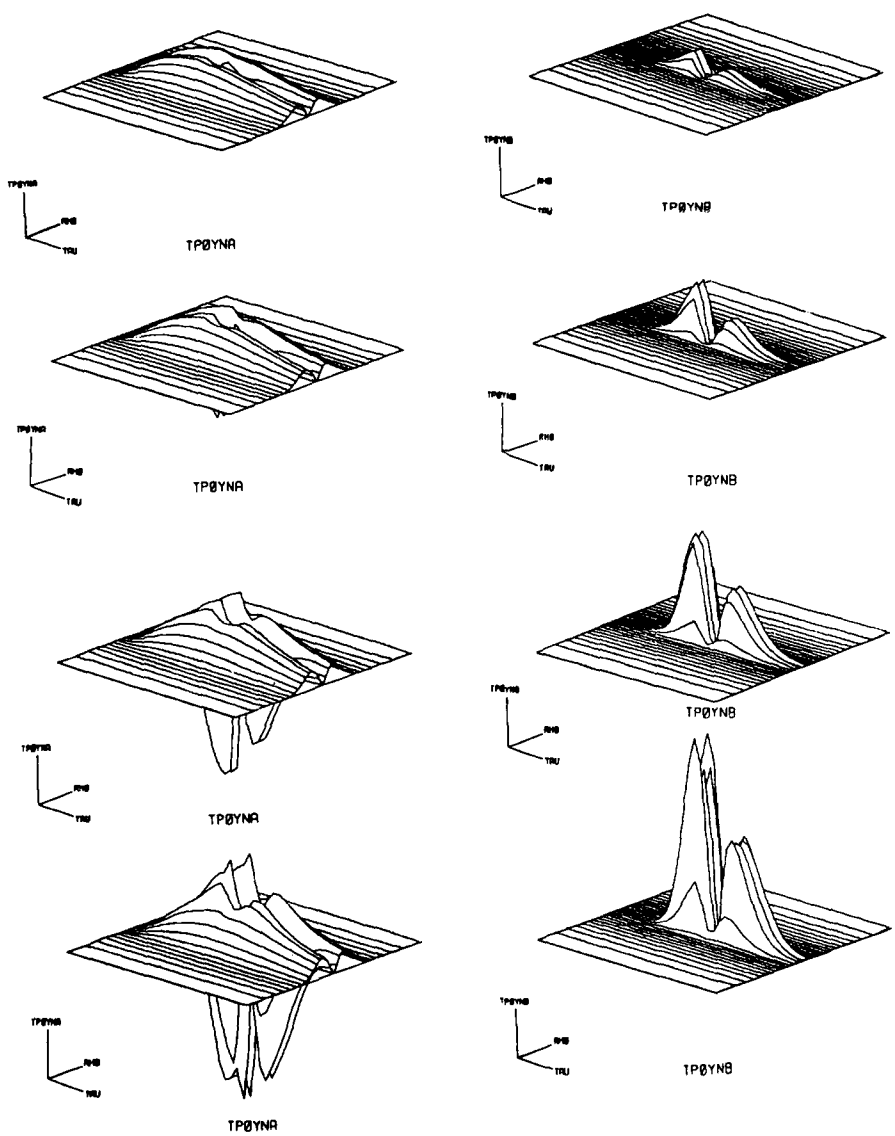

DIFFRACTION, PHASE AND QUANTUM FLUCTUATION EFFECTS IN THE EVOLUTION OF RAMAN SOLITONS

F.P. Mattar#, Y. Claude*, M. Burgess* and J. Teichmann*
Department of Physics, New York University#, New York, NY 10003 and
Department of Electrical Engineering, City College of New York#,
New York, NY 10031; and
Departement de Physique, Université de Montreal*, Montreal, Canada

ABSTRACT

Transverse and phase effects are shown to alter the spontaneous emergence of off-resonant Stimulated Raman Scattering (SRS) bright Raman pump and dark Stokes solitons from quantum fluctuations in a single-pass cell.

I - INTRODUCTION

Solitons are waves that propagate without losing their shape while subjected to the influence of competing mechanisms such as dispersion and Kerr nonlinearity in optical fibers[1].

Kruskal et al.[2] in 1967 were the first to coin the term but it was not until 1973 that Scott et al.[3] presented the soliton as a universal self-preserved information carrier. Then, Chu and Scott[4] reported a bi-chromatic soliton formation which was confirmed by Tan-no et al.[5] and Makhviladze[6].

Solitary waves, on the other hand, ha· been demonstrated as the resultant between diffraction and coherent nonlinear absorption that lead to self-trapping[7a]/self-focusing[7b] in Self-Induced-Transparency SIT[8]. The SIT phenomenon occurs in a resonant two-level atomic system whose response is not instantaneous. Associated with the inertia of the medium the pulse experiences delay in the absence of diffraction and reshapes asymptotically into a distortionless hyperbolic secant pulse in the presence of loss.

More recently, interest on soliton formation was catalyzed when Carlsten and co-workers[9], Drühl et al.[10] reproduced numerically their observation of a Raman Soliton formed only when a π phase-shift is electro-optically induced in the Stokes field with respect to the Raman pump. The Raman solitons are associated with the repletion of the propagating pump instead. The calculation was semiclassical uni-dimensional with the introduction of an external π phase shift to the Stokes field at the input plane. Without an induced phase change of π in the Stokes field, SRS solitons do not emerge.

The Raman soliton evolution was subsequently reproduced analytically by Ackerhalt et al.[11] and by Kaup[12]. More recently, Englund and Bowden EB[13a] reported the spontaneous generation of Raman solitons from quantum noise with random initial phase. Their results are in accordance to experimental observations by Wenzel, Drühl and Carlsten that exhibited soliton formation in the absence of apparent relative phase shift in the Stokes field. EB based their theory on the fact that amplified processes originating from stochastic phase noise may cause solitons to occur spontaneously. The origin of the stochastic generation which remain undefined were partly explained by EB. As discussed by Carlsten and co-workers additional experiments are needed to elucidate the exact source of the quantum fluctuation. Do the solitary wave fluctuations stem from the quantum initiation as predicted by Bowden and Englund or does the nonlinear amplification enhance the noise? More analysis is necessary. For example, the effect of finite beam extent should be investigated.

#Supported by ARO, AFOSR ONR & NSF at NYU & by NSERG at U.de Montreal

The role of transverse effects in deterministic Raman soliton formation was examined perturbatively by Teichmann and co-workers[14]. It revealed the emergence of self- and cross-phase modulation and their effect on Raman solitary waves.

On the other hand, asymptotic on-resonance coherent propagation of a strong pump and a weak probe in three-level atoms, with diffraction rigorously accounted for, had led to the discovery of a sequence of two solitary waves. That solitary wave is characterized by a time-integrated area that stabilizes over the propagation distance. A probe soliton emerged first and is followed by a pump soliton[15]. The probe and pump solitary waves do not occur simultaneously, they occur successively. The renewal of the pump, i.e., the anomalous interruption of pump depletion as observed by Carlsten et al., takes place. A semiclassical formulism was adopted. It consisted of two paraxial wave equations coupled by a three-level density matrix. This model was first analyzed in the context of three-level superfluorescence[16] and of simulton[17]. Only deterministic initiation was considered.

In this communication, we examine the interplay of fluctuation-induced phase and diffraction-induced self- SPM and cross-phase XPM with the computer program L22P®. We also note that the time-derivative of the phase, which is non-zero, represents an instantaneous frequency offset. The propagating Stokes beam is not on Raman resonance. The amount of pump depletion tends to vary with the instantaneous detuning. We herein address simultaneously the quantum initiation advocated by Bowden and Englund and the transverse coupling analyzed by Teichmann and Mattar. This situation was previously studied in conjunction with two- and three-level superfluorescence emission[18] and two- and three-level swept-gain super-radiance evolution[19].

II - NUMERICAL RESULTS

The quantum SRS soliton yield depends upon a number of experimental parameters namely, the Raman gain, the collisional dephasing time, the pump and Stokes wavelengths, the peak pump and probe amplitudes, the Raman gain, the medium length, the cell cross-section, the atomic density and its radial variation. It also depends on the temporal pulse length and pulse shape as well as on the radial beam width and beam profile.

The sharpness of the soliton necessitates a higher resolution than available by the nonuniform mesh. To characterize and localize the soliton one has to adopt a highly-dense uniform mesh.

From the ensemble trajectories carried out, one calculates peak-output power and delay-peak distributions of the bright Raman pump or dark Stokes solitons. One must also calculate a cross-correlation function that ties the Stokes initiation quantum source and the response Q of the Raman medium

$$C(\rho,\tau,\eta) = |\langle E_S^*(\rho,\tau,\eta)\, Q(\rho,\tau,\eta)\rangle_R| \left[\langle |E_S(\rho,\tau,\eta)|^2\rangle_R \langle |Q(\rho,\tau,\eta)|^2\rangle_R\right]^{-1/2} \quad (1)$$

In agreement with recent modeling and follow up experiments, the amplitudes and widths of the solitons vary from one propagation distance to the other within the same shot/trajectory. While the evolving pulse is generally referred to as soliton, this term is not really correct since the soliton characteristics are not invariant.

As in superfluorescence theories[16-19], the Langevin stochastic noise sources f_L, E_S or equivalently Q are defined as follows:

$$f_L = |f_L| \exp(i\theta_L) \quad (2a)$$

where the probability of the amplitude

$$P(|f_L|^2) = [1/\pi\sigma_L]\exp[-|f_L|^2/\sigma_L^2] \text{ bivariant Gaussian distribution} \quad (2b)$$

$$0 \le \theta_L \le 2\pi \qquad \text{phase is uniformly random distribution} \quad (2c)$$

and $\sigma_L = N\, r_R \ell/c$ (3a) with $r_R = 1/(\Gamma N)$ (3b)

III - NUMERICAL RESULTS

We have first reproduced Englund and Bowden's results then pursued calculations that account for transverse effects.

In Fig. 1, we present one-dimensional energy computation L22P71 of bright Raman soliton and dark Stokes soliton as a function of the optical thickness η within the same trajectory.

In Fig. 2, we display Amplitude Dynamics of the energy of the Raman soliton for two different trajectories at distinct propagational distances. The peak of the soliton occurs at a time in the front edge of the input pump. The peak value of the Raman soliton energy varies from shot to the other, i.e., from one trajectory to the other.

In Fig. 3, we report a one-dimensional calculation of the Raman pump and Stokes energies with σ, the width of the probability distribution function changing, L22P71 and L22P72, by a factor of a thousand for the same trajectories at the identical propagational distances.

In Fig. 4, a one-dimensional calculation of the pump and Stokes energies for a third value of σ L22P73 for two different trajectories is presented. In this large σ (a factor of a million) case, two solitary waves can appear simultaneously.

In Fig. 5, we display amplitude dynamics of the on-axis energy of the bright Raman pump soliton and the dark Stokes soliton for the same trajectory at different propagational lengths η with diffraction L22P76 accounted for. We show two plots, the first one graph (a) consists of two planes while graph (b) is a three-dimensional plot.

In Fig. 6, we show the results of a diffraction calculation L22P76 of Raman solitons output power at the same optical thickness but for different trajectories.

In Fig. 7, we present Raman pump soliton formation for two different trajectories from the ensemble computed to reflect the quantum statistics at distinct propagational distances. We also note that the time at which the soliton peak occurs varies from one graph to the other. For one trajectory the soliton occurs at the front edge of the Raman pump pulse while at another trajectory it occurs at the trailing edge.

As shown in Fig. 8, we also find in plots of θ_b versus ρ and η that surprisingly a number of distinct structures occur on-axis for four different trajectories of an ensemble of ten.

In Fig. 9, we find that that several trajectories do not exhibit spontaneous anomalous pump depletion reversal takes place at several propagational distances for which it does occur at other trajectories.

In Fig. 10, three-dimensional representation of the Raman pump energy for two different trajectories are presented. The quantum initiation modifies the field phase as well as the resulting amplitude and the location of the Raman pump soliton whenever it appears.

In Fig. 11 we show three-dimensional plots of the pump and Stokes energies versus τ and ρ for different η within the same trajectory.

IV - CONCLUSION

We have presented rigorous computation that accounts for both quantum and diffraction effects on the Raman soliton evolution. This nonlinear analysis, which examines self- SPM and cross-phase XPM modulation systematically[20], attains a degree of realism long sought for[21-23] by including quantum initiation in conjunction with diffraction coupling. The same phase waves that were reported for some trajectories in superfluorescence calculations by Hopf, and by Watson et al. and in spontaneous Raman soliton calculations by Englund et al. are observed occasionally in our numerical experiment. Only a few of the phase waves yield soliton while some others do not lead to Raman pump repletion whence Raman solitons. Furthermore, the amplitude of the evolving soliton decays while their widths varying as the propagation distance, i.e.,the effective length of the Raman cell, increases. This is consistent with MacPherson et al.'s recent observations[24].

Finally, if the Lorentz local field(s) correction[25-28] is also accounted for. A population-dependent frequency offset emerges in the density matrix. The effective detuning becomes a time (and radial) dependent function. The resultant chirp, i.e., the frequency modulation modifies the characteristics of the Raman co-propagation. The rate of energy conversion from the pump to the Stokes and the depopulation of the pump and the growth of the Stokes emission become more complicated. The analytical tractability vanishes. One must resort to numerical experiments to appreciate the physical nuances and domain.

REFERENCES

1. A.Hasegawa & F.Tappert, Appl.Phys. 23, 142(1973) & 23, 171(1973).
2. N.J. Zabusky & M.D. Kruskal, Phys. Rev. Lett. 15, 240 (1965).
3. A.C. Scott et al., IEEE Proc. 61, 1443-1483 (1973).
4. R.Y.F. Chu & A.C. Scott, Phys. Rev. A12, 2060 & 2065 (1975).
5. N. Tan-no et al., Phys. Rev. A12, 159 (1975).
6. T.M. Makhviladze et al., Sov. Phys. JETP 42, 255 (1976).
7. [a] J. Marburger, Progress in Quantum Electronics V, (Pergamon Press, 1975) pp. 35-105; [b] N. Wright & M.C. Newstein, Opt.Commun. 9, 8 (1973); & [c] F.P.Mattar & M.C.Newstein, Opt. Commun.18, 70(1976) & IEEE J.Quantum Electronics QE-13,507(1977).
8. S.L. McCall & E.L. Hahn, Phys. Rev. Lett. 28, 308 (1967); Phys. Rev. 183, 457 (1969) and Phys. Rev. A2, 861 (1970).
9. J.L. Carlsten et al., SPIE 380, 201 (1983).
10. [a] K.J. Drühl et al., Phys. Rev. Lett. 51, 1171 (1983); [b] R.G. Wenzel et al., J. Stat. Phys. 39, 621 (1985) & 615 (1985); & [c] D.C. MacPherson et al., J. Opt. Soc. Am. B4, 1853 (1987).
11. J.R. Ackerhalt & P.W. Milonni, Phys. Rev. A33, 3185 (1986).
12. D.J. Kaup, Physica 19D, 125 (1986).
13. [a] J.C.Englund & C.M.Bowden, Phys.Rev.Lett. 57, 2661 (1986) & SPIE 874, 218 (1988); & [b] C.M.Bowden & J.C.Englund, Opt.Commun. 67, 71 (1988).
14. J. Teichmann & F.P. Mattar, Bull. Am. Phys. Soc. 33, 1637 (1988) paper M17 & to appear in Advances in Laser Sciences IV, AIP, 89.
15. F.P. Mattar, in Advances in Laser Science III, ed. A.C. Tam, J.L. Gole & W.C. Stwalley, (AIP, 1988) (a) probe soliton pp. 524-529 & (b) pump soliton pp. 530-536; & J. De Physique 49, C2, 463(1988).
16. [a] F.P. Mattar & C.M. Bowden, Appl. Phys. B29, 149 (1982) & Phys. Rev. A27, 345 (1983); & [b] C.M. Bowden, in Laser Physics, ed. J.D. Harvey & D.F. Walls, (Springer-Verlag, 1983).

17. [a] F.P. Mattar et al., in **Advances in Laser Sciences-I**, ed. W.C. Stwalley (AIP, 1986) pp. 324-328; [b] F.P. Mattar et al., in **Optical Instabilities**, ed. R.W. Boyd, M.G. Raymer & L.M. Narducci (Cambridge University, 1986) pp. 343-345.
18. [a] R. Glauber & F. Haake, Phys. Lett. 68A, 29 (1978); [b] D. Polder et al., Phys. Rev. A19, 1192 (1979); [c] F. Haake et al., Phys. Rev. Lett. 45, 558 (1980); [d] F.A. Hopf, Phys. Rev. A20, 2064 (1979); [e] F.P. Mattar, SPIE 288, 353 (1981); and ibid 380, 508 (1983); [f] E.A. Watson et al., Phys. Rev. A27, 1427 (1983); [g] P.D. Drummond & J.H. Eberly, Phys. Rev. A25, 3446 (1982); [h] F.P.Mattar et al.,in **Coherent and Quantum Optics IV**, ed. L.Mandel & E.Wolf (Plenum Press,1984) pp. 507-514; & [i] F.P.Mattar et al. in **Multiple-Photon Excitation & Dissociation of Polyatomic Molecules**, ed. C.D. Cantrell, (Springer-Verlag, 1986) pp. 223-283.
19. [a] R. Bonifacio et al., Phys. Rev. A12, 2568 (1975); [b] F.A. Hopf & P. Meystre, Phys. Rev. A12, 2534 (1975); and F.A. Hopf et al., Phys. Rev. A13, 777 (1976); [c] F.A.Hopf et al., Phys. Rev. Lett. 35, 511 (1975); [d] F.A. Hopf & E.A. Overman II, Phys. Rev. A19, 1180 (1979); and [e] C.M. Bowden & F.P. Mattar, SPIE 288, 364 (1981) and SPIE 369, 151-163 (1983).
20. M. Lax, Phys. Rev. 145, 110 (1966).
21. [a] C.M. Bowden & C.C. Sung, Phys. Rev. Lett. 50, 156 (1983); and [b] B. Sobolewska, Opt. Commun. 46, 170 (1983).
22. [a] M.G. Raymer & J. Mostowski, Phys. Rev. A32, 332 (1985); and [b] M.G. Raymer et al., Phys. Rev. A32, 332 (1985).
23. F.P. Mattar, "Transverse Physical Mechanisms in Coherent On-Resonance Propagation of Two Beams Cross-Coupled in a Three-Level System", to appear in **Prog. of Quantum Electronics**, 1989.
24. [a] D.C. MacPherson et al., Phys. Rev. Lett. 61, 66 (1988); and [b] D.C. MacPherson & J.L. Carlsten, **Advances in Laser Sciences III**, ed. A.C.Tam, J.L.Gole & W.C.Stwalley, (AIP,1988) pp.204-206.
25. J. Marburger, L. Huff, J.D. Reichert & W.G. Wagner, Phys. Rev. 184, 255 (1969).
26. [a] R. Friedberg, S.R. Hartmann & J.T. Manassah, Phys. Lett. 35A, 161 (1971), ibid 40A, 395 (1972) & Phys. Report 7C, 101-179 (1973); [b] J.T. Manassah, Phys. Report 101, 359-427 (1983); [c] R. Friedberg, S.R. Hartmann & J.T. Manassah, Phys. Rev. A39, 93 & 3444 (1989); and [d] J.T. Manassah, Phys. Rept. 101, 359-427.
27. [a] F.A. Hopf, C.M. Bowden & W.H. Louisell, Phys. Rev. A29, 2591 (1983); [b] in **Optical Bistability II**, ed. C.M. Bowden, H.M. Gibbs & S.L. McCall (Plenum Press, 1984) pp. 361-368; and [c] in **Optical Instabilities**, ed. R.W. Boyd, M.G.Raymer & L.M. Narducci (Cambridge University Press, 1986) pp. 308-311.
28. J.T. Manassah & F.P. Mattar, in Proc. Intl. Laser Sci. ILS-IV, **Advances in Laser Science IV** (Am. Inst. Phy., 1989).

FIGURE CAPTIONS

Fig. 1 One-dimensional energy Raman soliton and dark Stokes soliton as a function of the optical thickness η within the same trajectory.

Fig. 2 Amplitude Dynamics of the Raman soliton energy for two different trajectories at distinct propagational distances.

Fig. 3 One-dimensional calculations of the Raman pump and Stokes energies with two unequal σ, the width of the probability distribution function.

Fig. 4 One-dimensional calculation of the pump and Stokes energies for a third value of σ L22P73 for two different trajectories.
Fig. 5 On-axis energy of the Raman solitons for the same trajectory at different propagational lengths η with diffraction L22P76 accounted for. Graph (a) consists of a two dimension plot while graph (b) is a three-dimensional plot.
Fig. 6 Raman solitons output power.
Fig. 7 Raman pump soliton formation for two different trajectories.
Fig. 8 Three-dimensional AREA for four trajectories.
Fig. 9 Trajectory without spontaneous anomalous pump depletion reversal occurring.
Fig. 10 Three-dimensional representation of the Raman pump energy for two different trajectories.
Fig. 11 We show three-dimensional plots of the pump and Stokes energies versus τ and ρ for different η within the same trajectory.

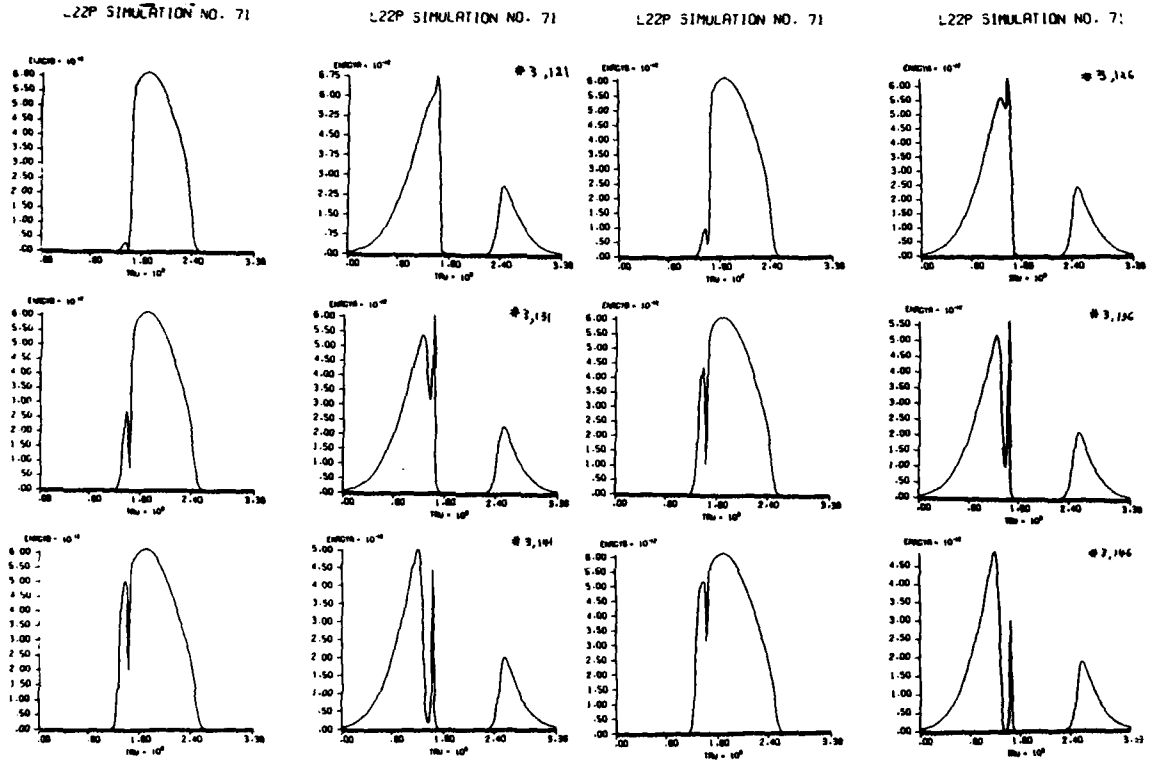

SPONTANEOUS RAMAN SOLITON FORMATION IS DYNAMICALLY SHOWN FOR THREE DIFFERENT PROPAGATION DISTNCES
THE SOLITARY WAVE OCCURS AT THE FRONT OF THE PULSE IN THIS TRAJECTORY

L22P SIMULATION NO. 72

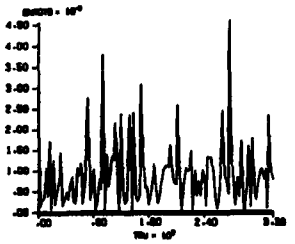

ENROYB

L22P SIMULATION NO. 72

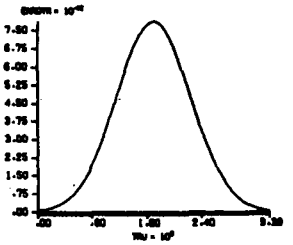

ENROYR

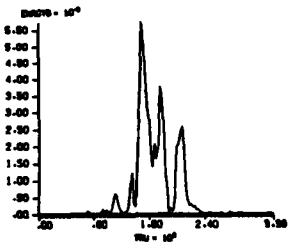

ENROYB

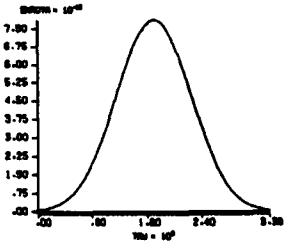

ENROYR

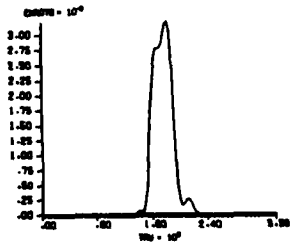

ENROYB

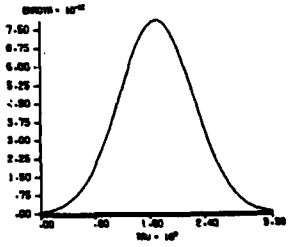

ENROYR

L22P SIMULATION NO. 72

L22P SIMULATION NO. 72

$\eta = 75$

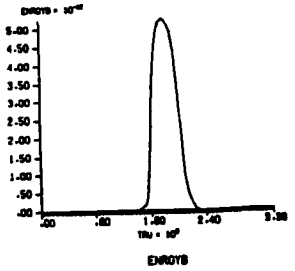

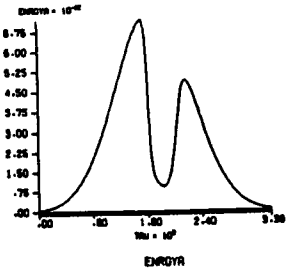

$\eta = 101$

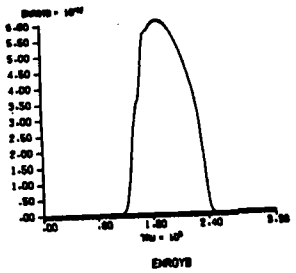

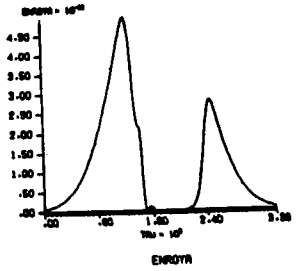

$\eta = 1$

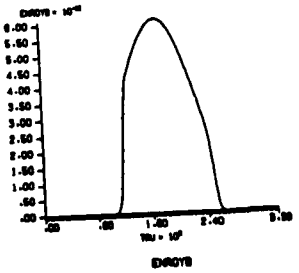

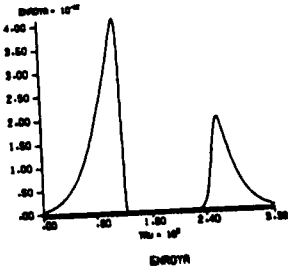

L22P SIMULATION NO. 72

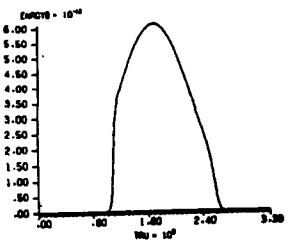

L22P SIMULATION NO. 72

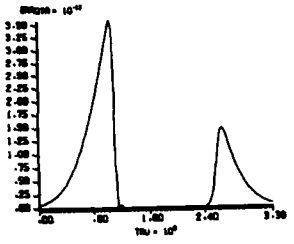

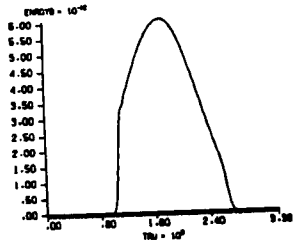

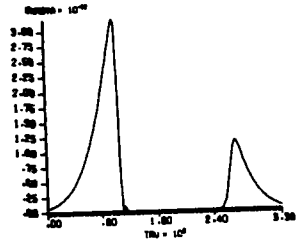

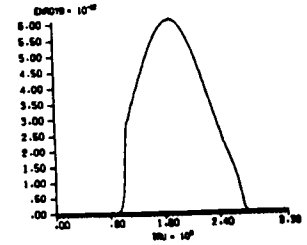

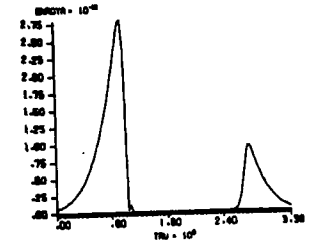

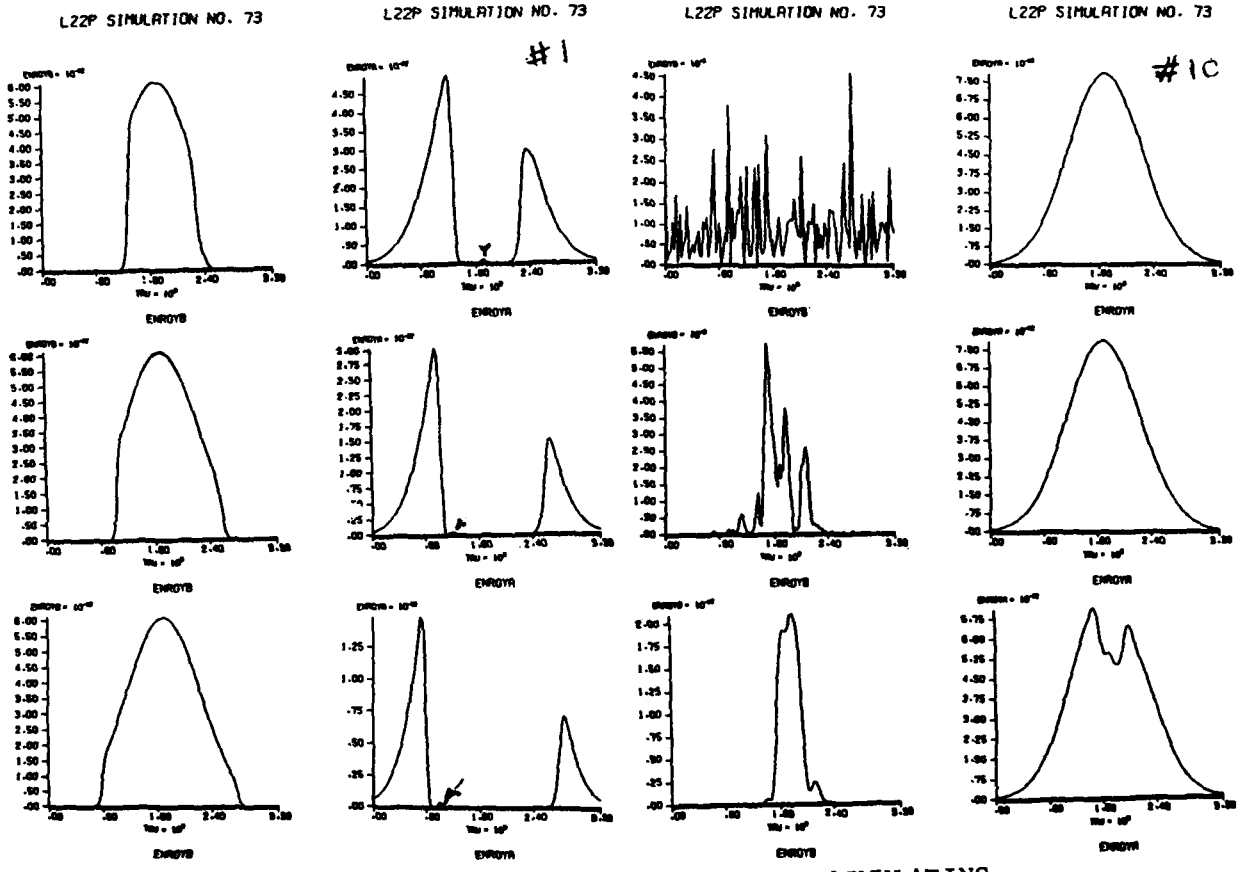

COMPARISON OF TWO TRAJECTORIES #1 AND #10 SIMULATING

THE SPONTANEOUS FORMATION OF RAMAN SOLITONS

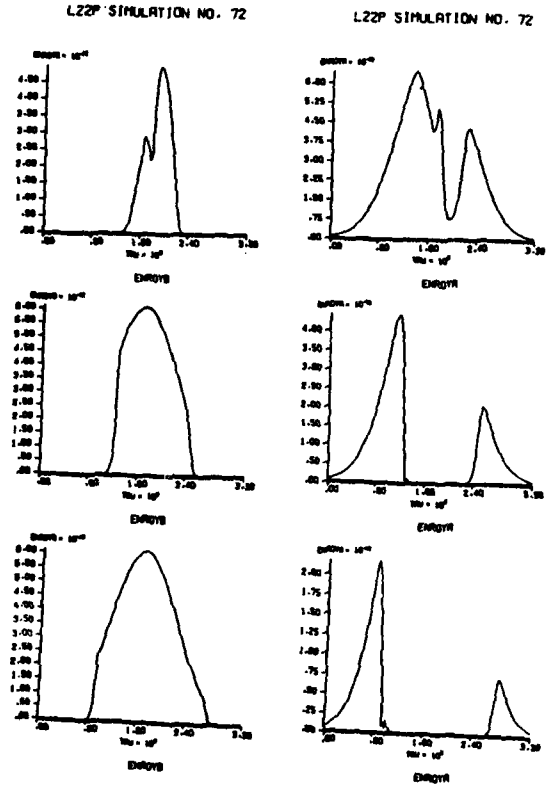
L22P SIMULATION NO. 72
L22P SIMULATION NO. 72
ENRGYS
ENRGYR
ENRGYS
ENRGYR
ENRGYS
ENRGYR

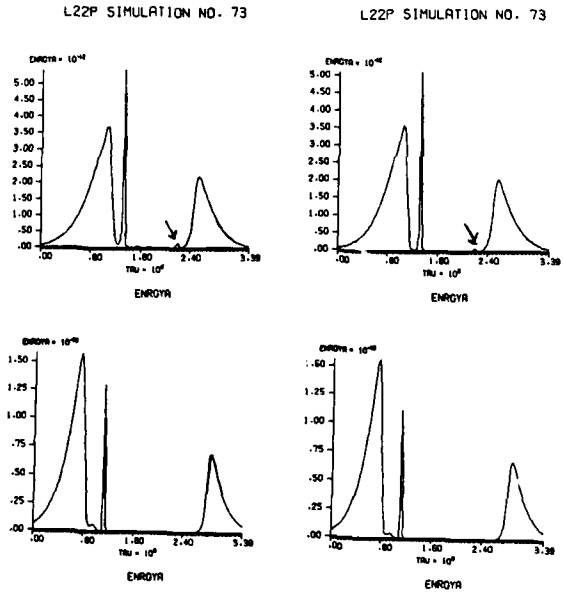

COMPARISON OF TWO TRAJECTORIES SIMULATING
THE SPONTANEOUS FORMATION OF RAMAN SOLITONS

THE SOLITARY WAVE CAN OCCUR EITHER AT THE FRONT EDGE OR AT THE TRAILING EDGES OF THE PULSE.

OCCASIONALLY THE SOLITARY WAVES MAY HAPPEN AT BOTH EDGES SIMULTANEOUSLY.

3C261IS4

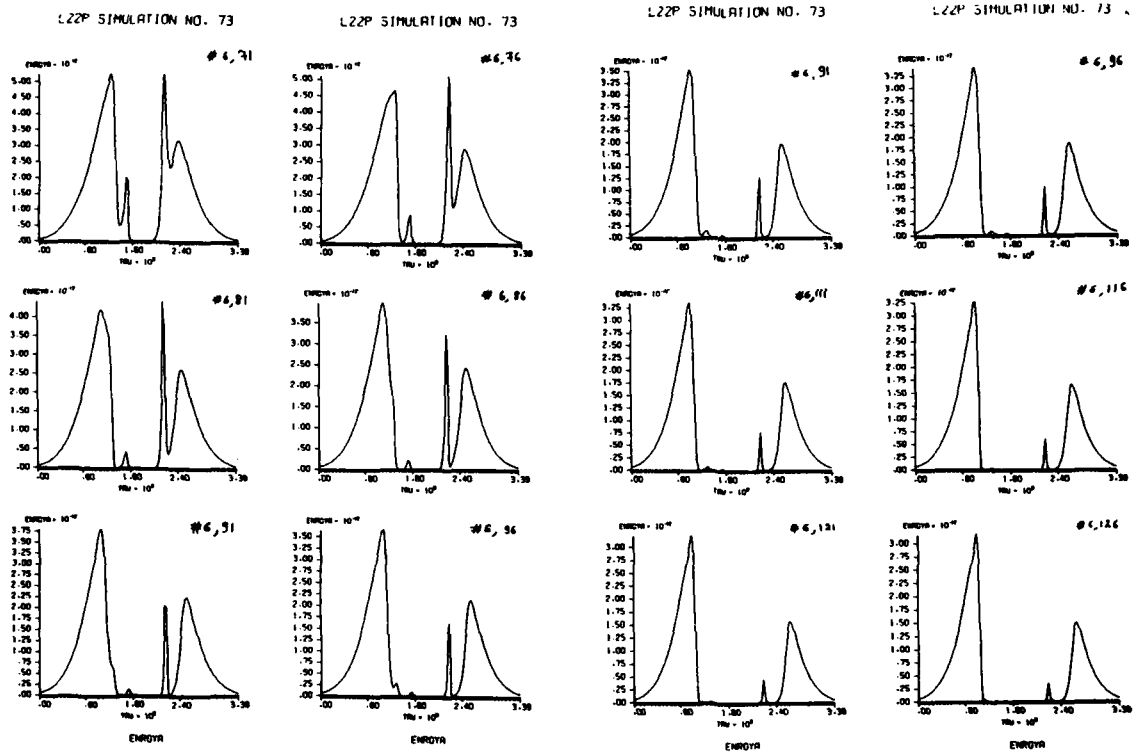

SPONTANEOUS RAMAN SOLITON FORMATION FOR TRAJECTORY #6 OF AN ENSEMBLE OF TRAJECTORIES.

THE SOLITARY WAVE CAN OCCUR EITHER AT THE FRONT EDGE OR AT THE TRAILING EDGES OF THE PULSE.

OCCASIONALLY THE SOLITARY WAVES MAY HAPPEN AT BOTH EDGES SIMULTANEOUSLY.

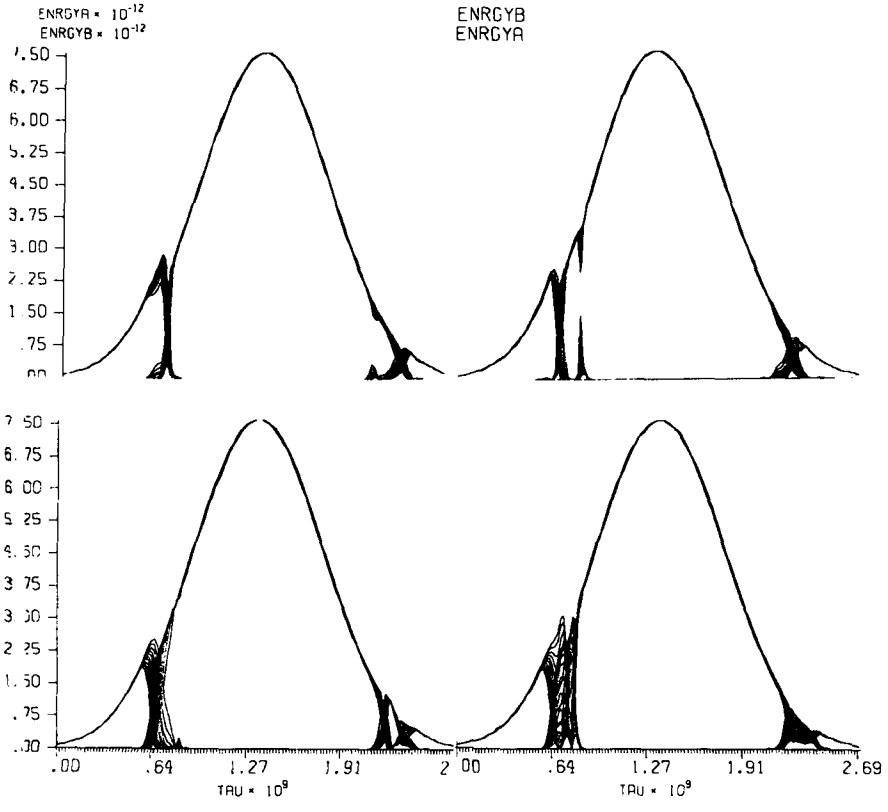
ENRGYA × 10⁻¹²
ENRGYB × 10⁻¹²
ENRGYB
ENRGYA
7.50
6.75
6.00
5.25
4.50
3.75
3.00
2.25
1.50
.75
.00
.64
1.27
1.91
2.00
2.69
TAU × 10⁹
TAU × 10⁹

L22P SIMULATIØN NØ. 75

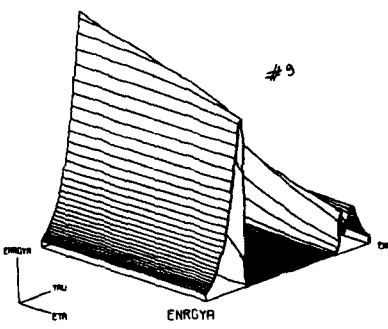

L22P SIMULATIØN NØ. 75

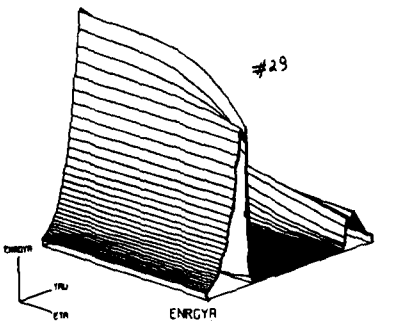

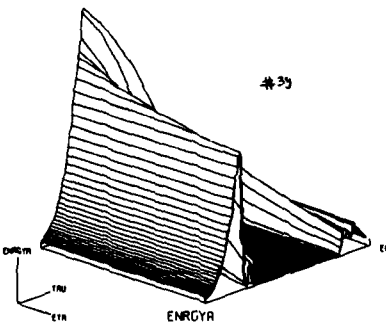

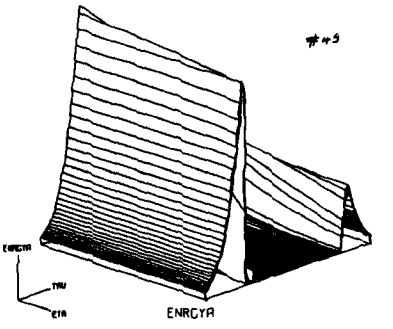

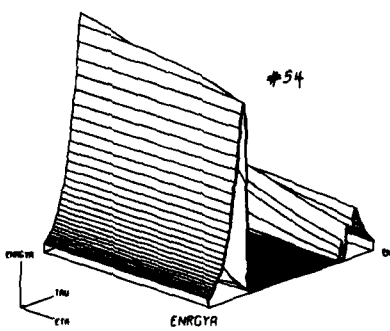

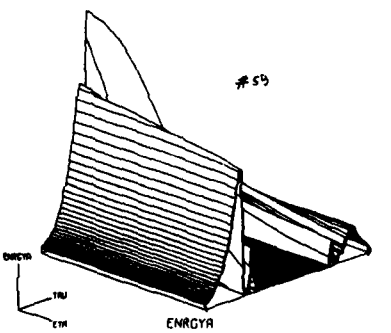

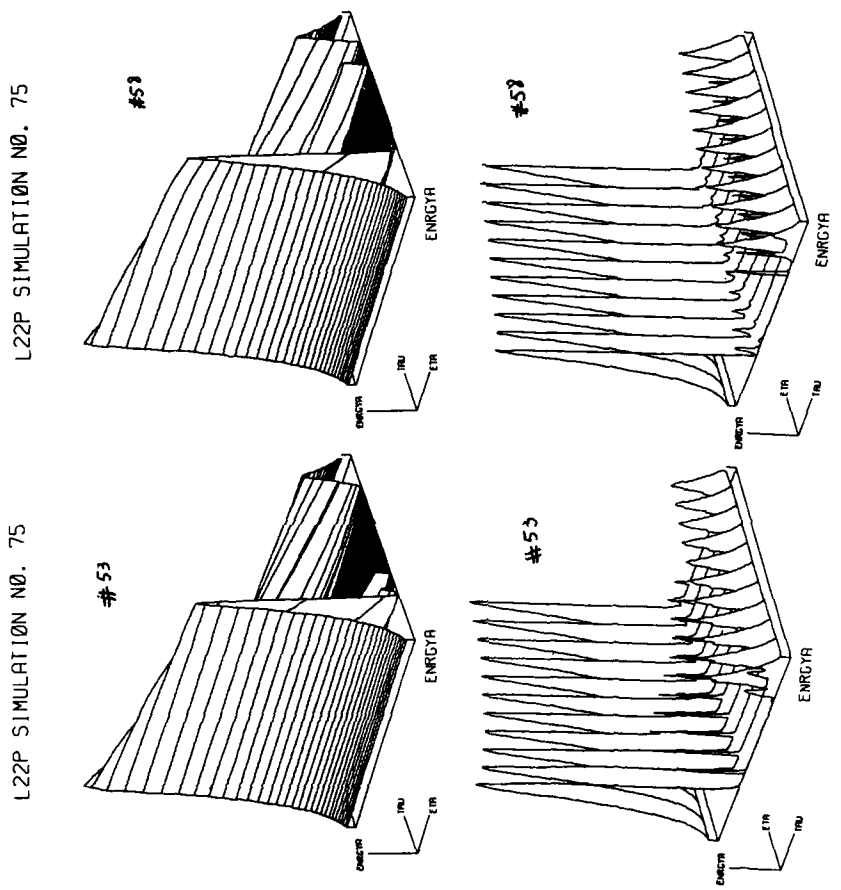
L22P SIMULATIØN NØ. 75
#53
ENRGYA
TRU
ETR
L22P SIMULATIØN NØ. 75
#53
ENRGYA
TRU
ETR
#53
ENRGYA
ETR
TRU
#53
ENRGYA
ETR
TRU

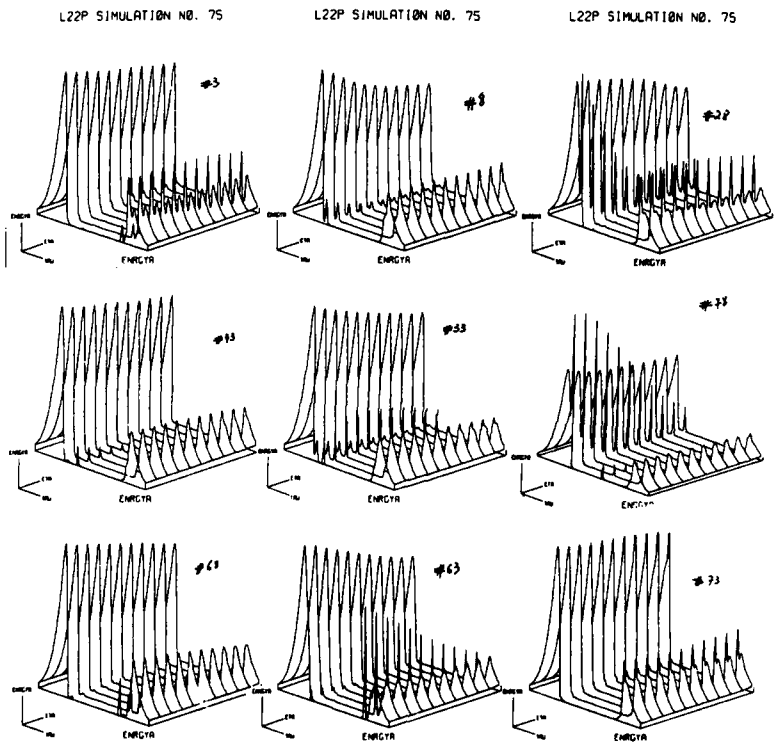
L22P SIMULATI0N N0. 75
L22P SIMULATI0N N0. 75
L22P SIMULATI0N N0. 75
ENRGYA
ENRGYA
ENRGYA
ENRGYA
ENRGYA
ENRGYA
ENRGYA
ENRGYA
ENRGYA

L22P SIMULATIØN NØ. 75

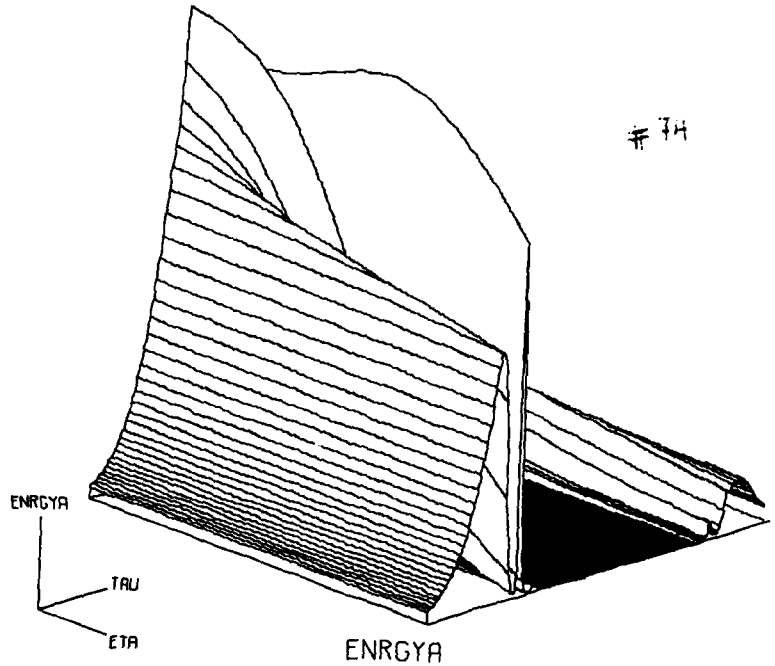

ENRGYA

SCALE	LØCALE
MIN =	53192.653
MAX =	.31882596E+13

AXIS	TØT.PT	SYM	RANGE	NB.SEL	RANGE ØF VALUES
STAT	100	NØ	74	1	74.0
ETA	201	NØ	(151,201)	11	(0.15,0.2)
TAU	256	NØ	(1,256)	128	(0.0,0.26894E-8

L22P SIMULATIØN NØ. 75

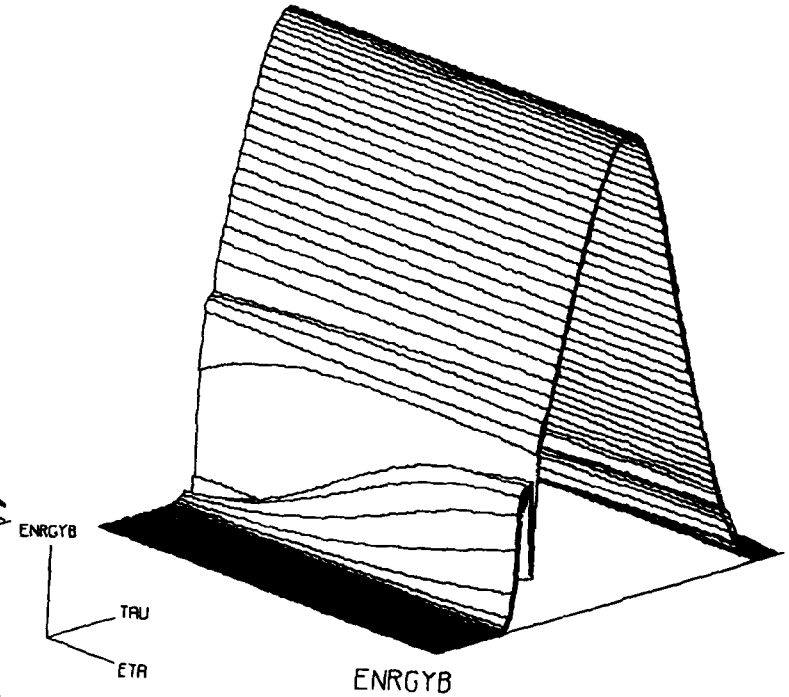

ENRGYB

SCALE	LØCALE
MIN =	37980.624
MAX =	.75992853E+13

AXIS	TØT.PT	SYM	RANGE	NB.SEL	RANGE ØF VALUES
STAT	100	NØ	74	1	74.0
ETA	201	NØ	(151,201)	11	(0.15,0.2)
TAU	256	NØ	(1,256)	128	(0.0,0.26994E-8)

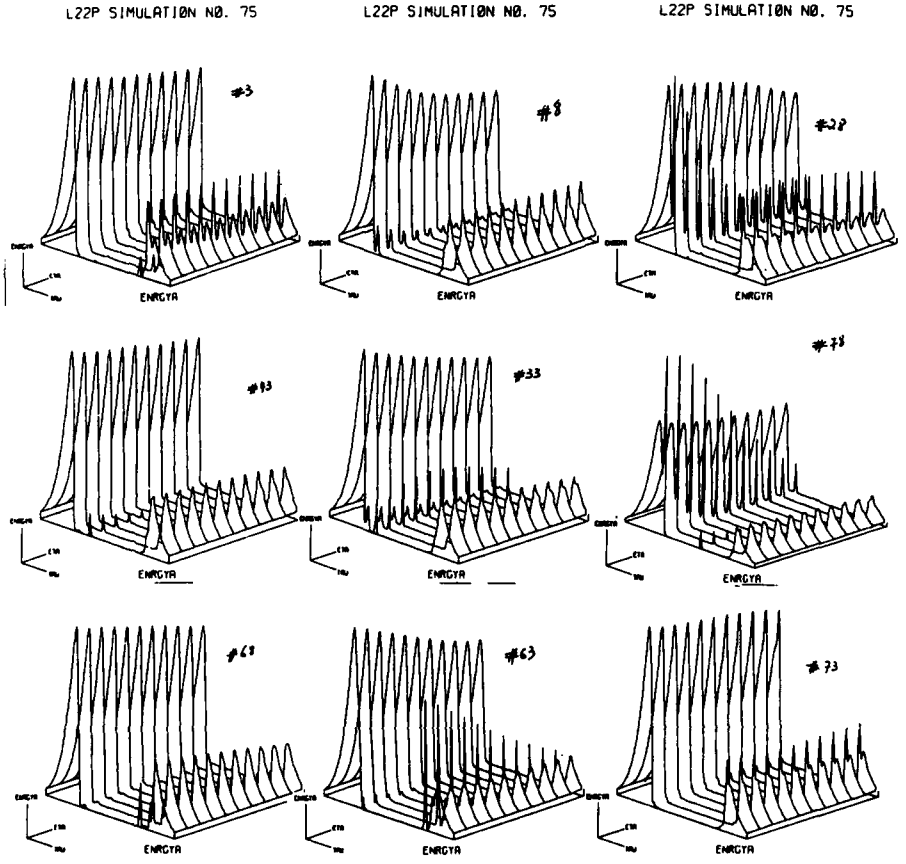
L22P SIMULATIØN NØ. 75
L22P SIMULATIØN NØ. 75
L22P SIMULATIØN NØ. 75
#3
#8
#28
#33
#38
#43
#63
#73
ENRGYA
ENRGYA
ENRGYA
ENRGYA
ENRGYA
ENRGYA
ENRGYA
ENRGYA

L22P SIMULATION NO. 76

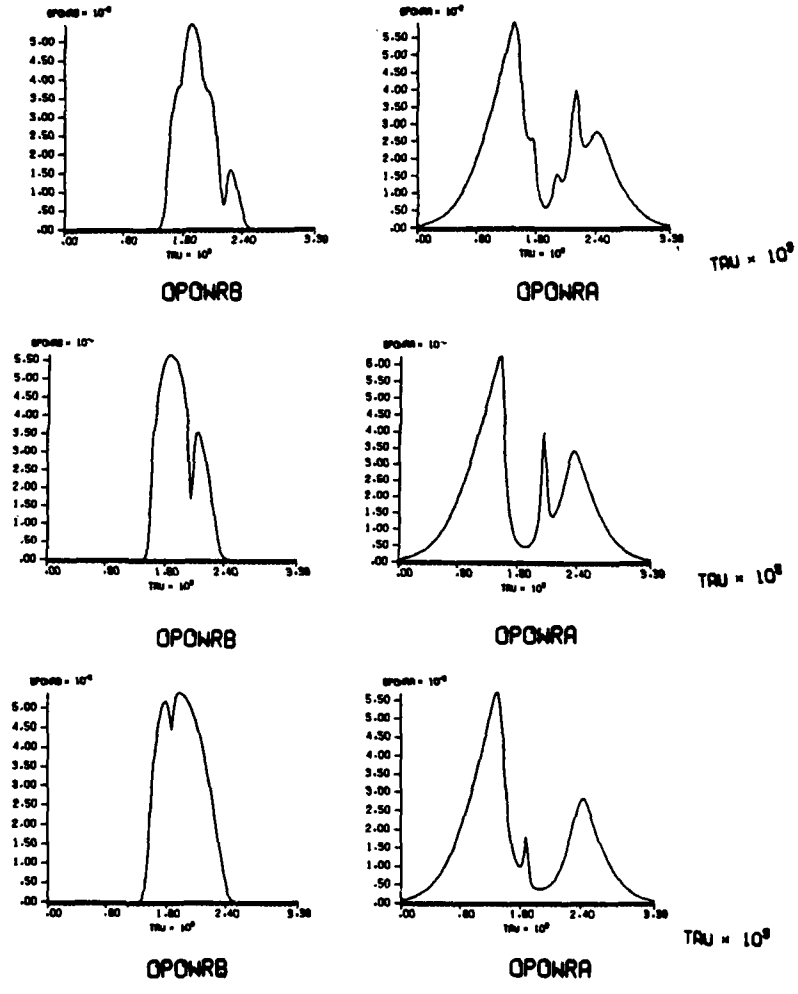

DISPLAY OF RAMAN SOLITON FORMATION IN A CONFIGURATION THAT ACCOUNT FOR DIFFRACTION IN A SINGLE PASS CELL

L22P SIMULATION NO. 76

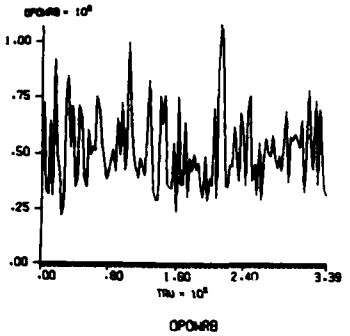

L22P SIMULATION NO. 76

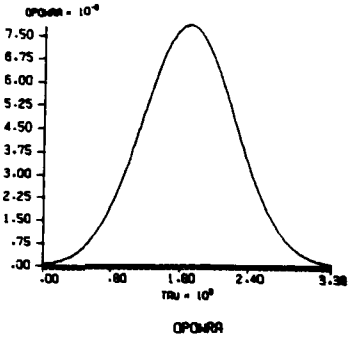

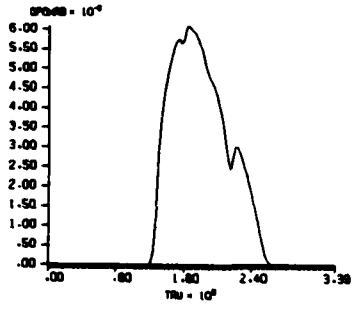

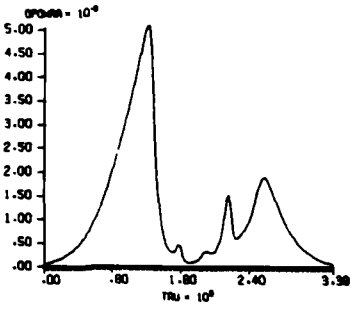

COHERENT MACROSCOPIC FORMATION OF A RAMAN SOLITON FROM MICROSCOPIC NOISE IN THE PRESENCE OF DIFFRACTION

L22P SIMULATION NO. 76

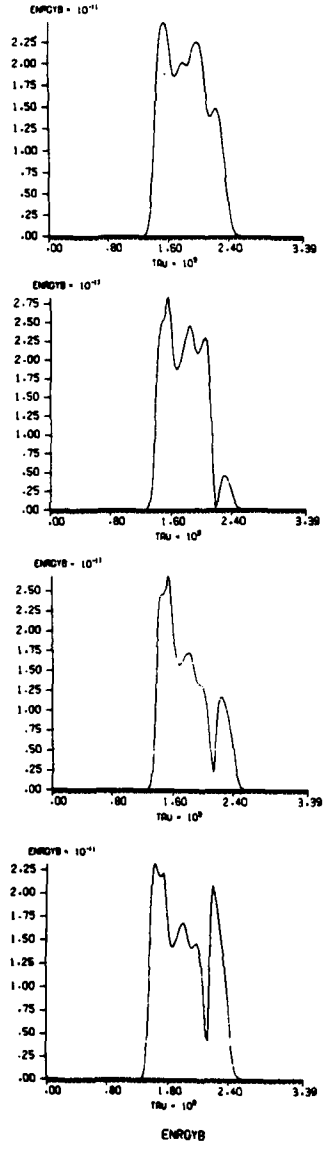

ENRGYB

L22P SIMULATION NO. 76

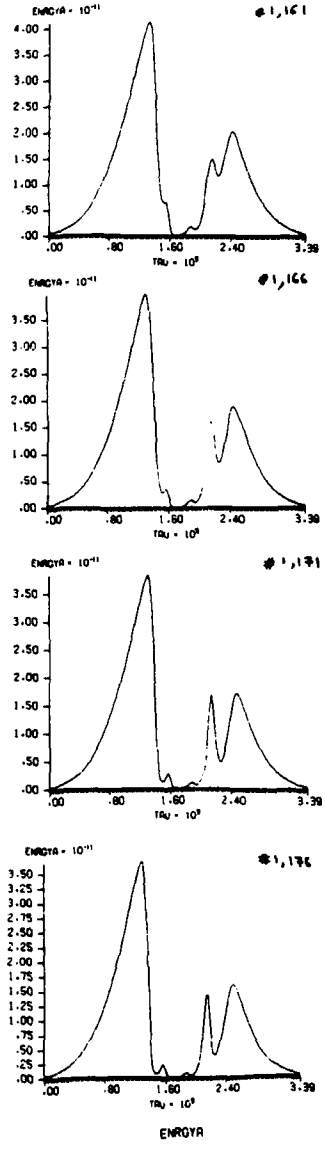

ENRGYA

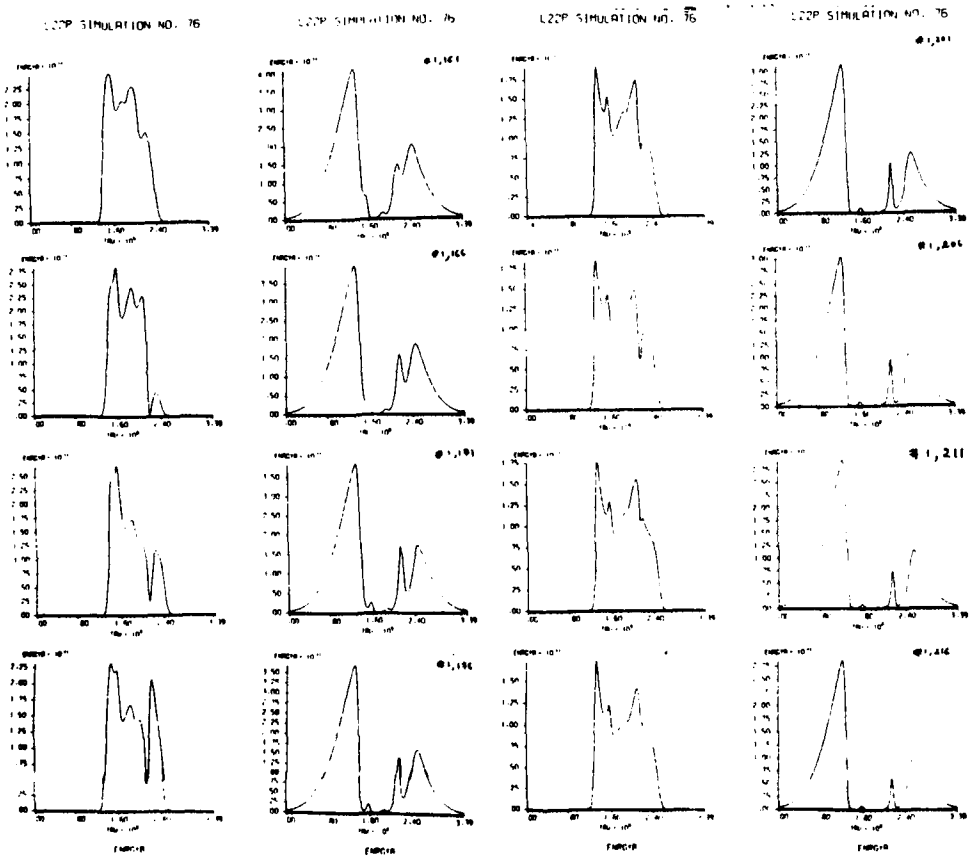

SPONTANEOUS RAMAN SOLITON FORMATION FROM QUANTUM FLUCTUATIONS. PUMP & STOKES ENERGIES ARE SHOWN FOR TRAJECTORY #1. THE SOLITARY WAVE OCCURS IN THE TRAILING EDGE

L22P SIMULATION NO. 76

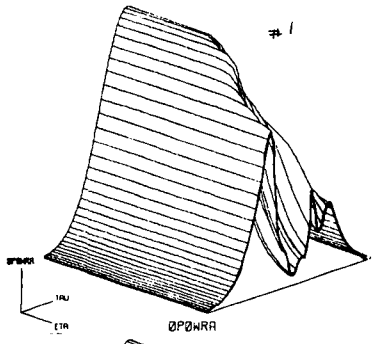

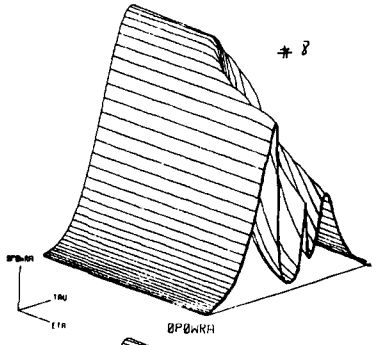

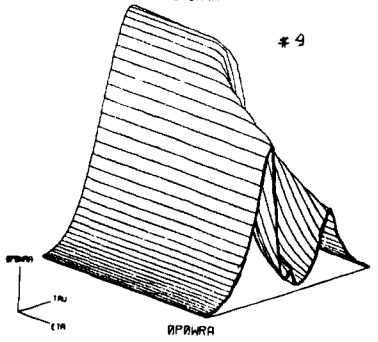

L22P SIMULATION NO. 76

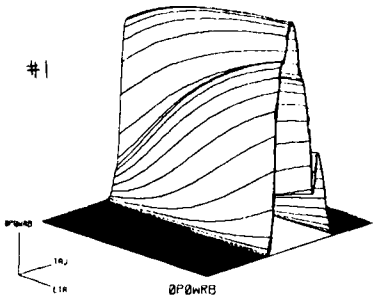

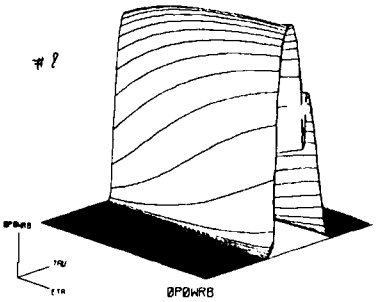

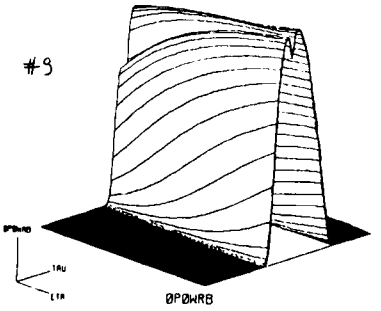

L22P SIMULATION NØ. 76

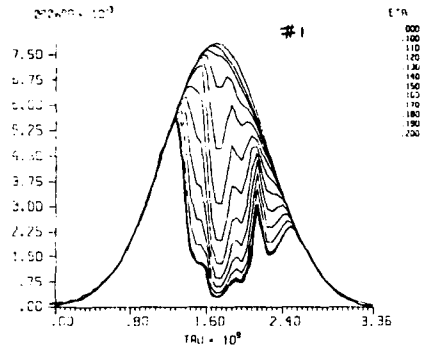

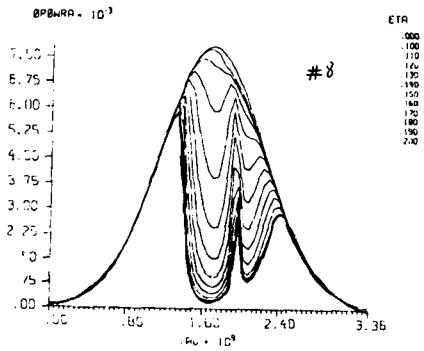

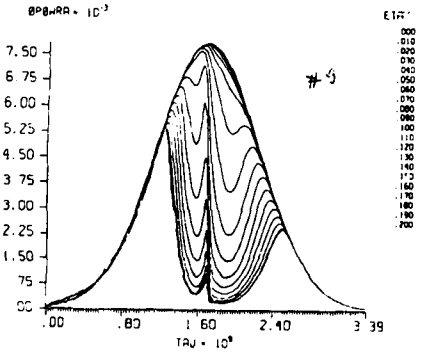

L22P SIMULATION NØ. 78

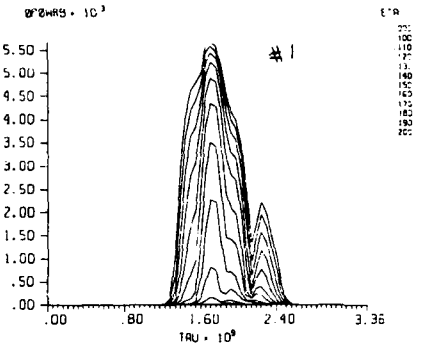

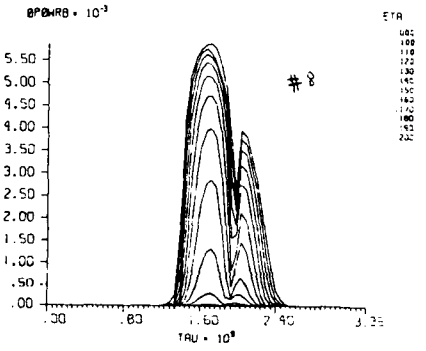

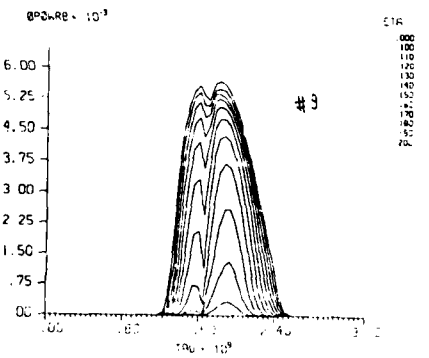

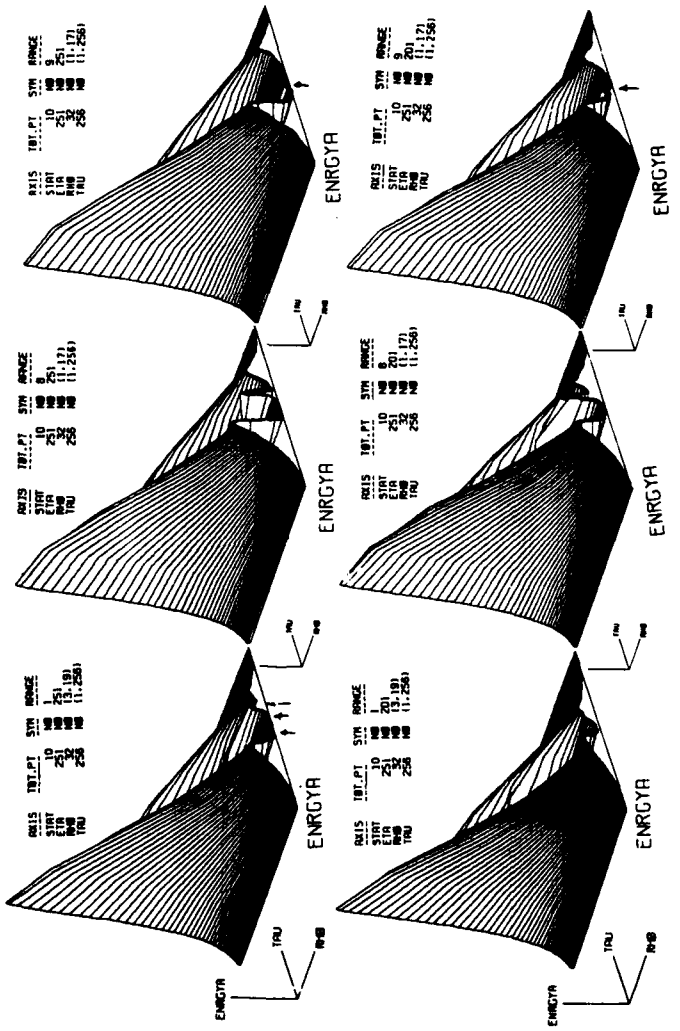
L22P SIMULATIØN NØ. 76
ENRGYA
TRU
RHØ

L22P SIMULATIØN NØ. 76

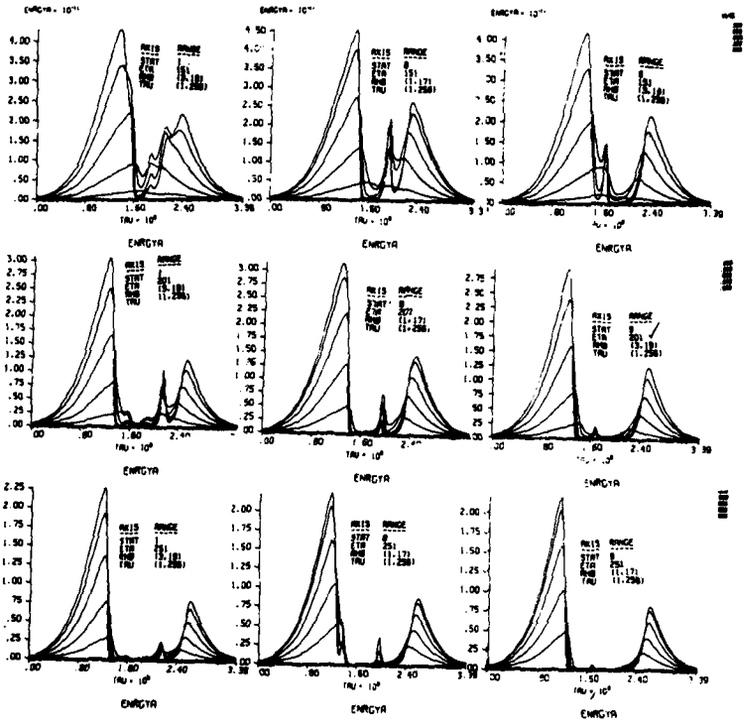

RAMAN SOLITONS ARE DISPLAYED AS A FUNCTION OF RADIUS FOR DIFFERENT PRO-PROPAGATIONAL DISTANCES. THE RAMAN SOLITONS ARE SHOWN TO SURVIVE DIFFRACTION EFFECTS.

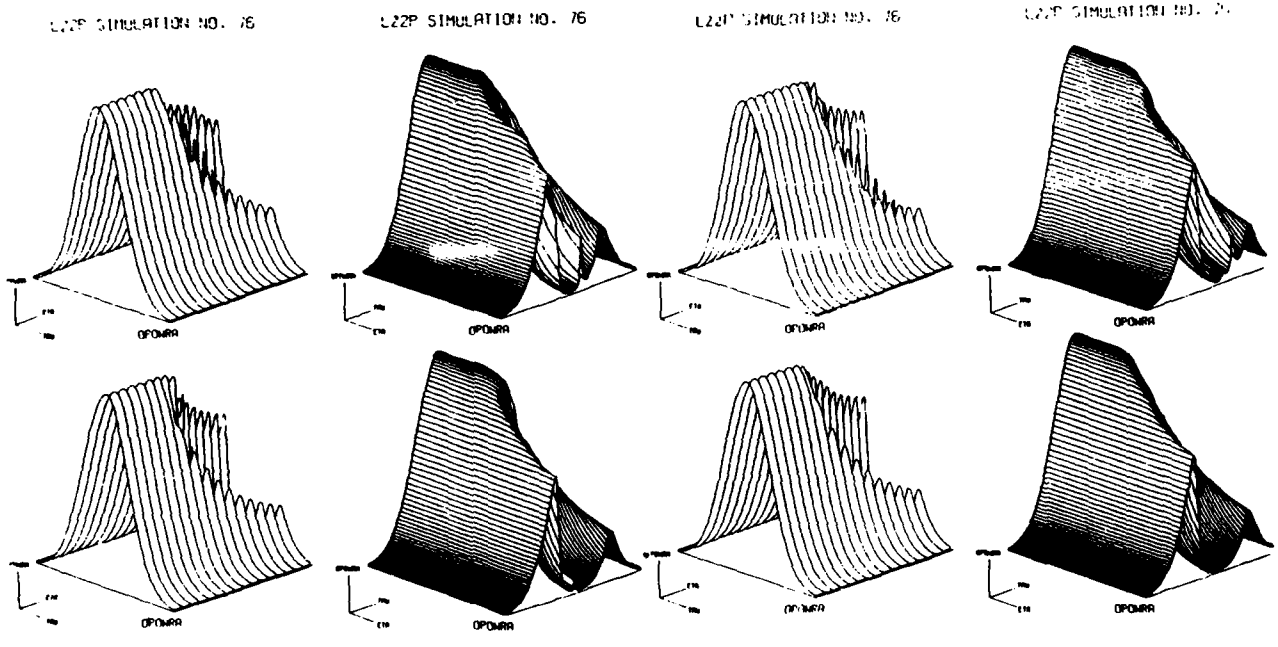

VARIOUS PUMP-DEPLETION REVERSAL SURVIVE THE AVERAGING ACROSS THE BEAM
THE RADIALLY-INTEGRATED ENERGY ,i.e.,THE OUTPUT POWER DISPLAYS RAMAN SOLITON.
DIFFRACTION EFFECTS OBSERVED WITH A LARGE DETECTOR DEMONSTRATE THAT RAMAN SOLITON
ARE NOT WASHED OUT AND THEY SURVIVE NON-PLANAR CONFIGURATIONS

L22P SIMULATIØN NØ. 76

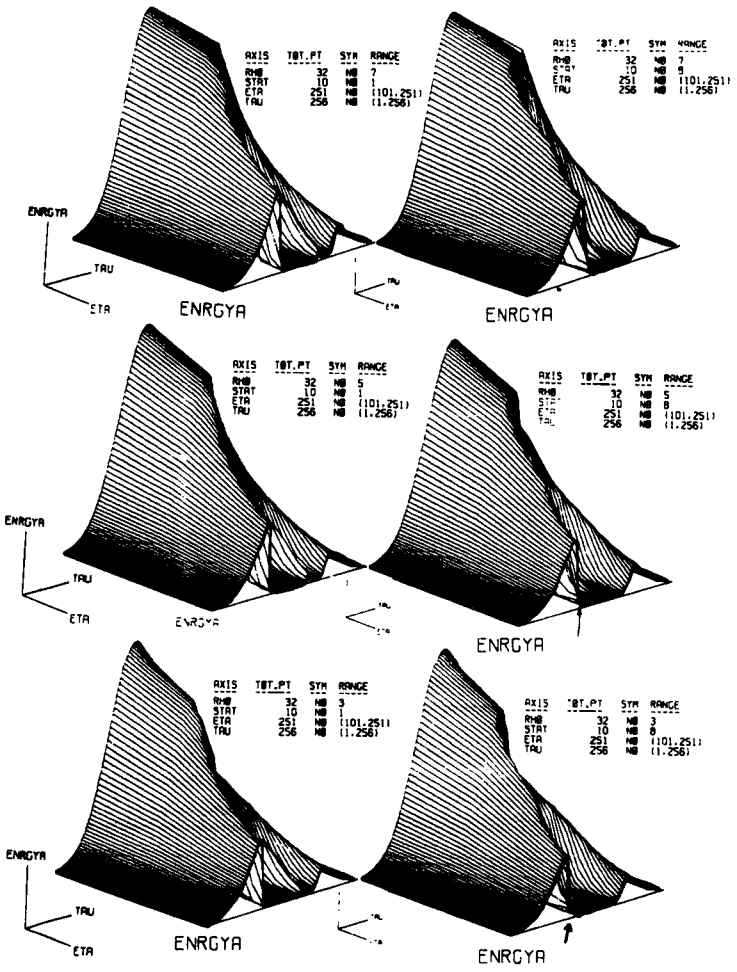

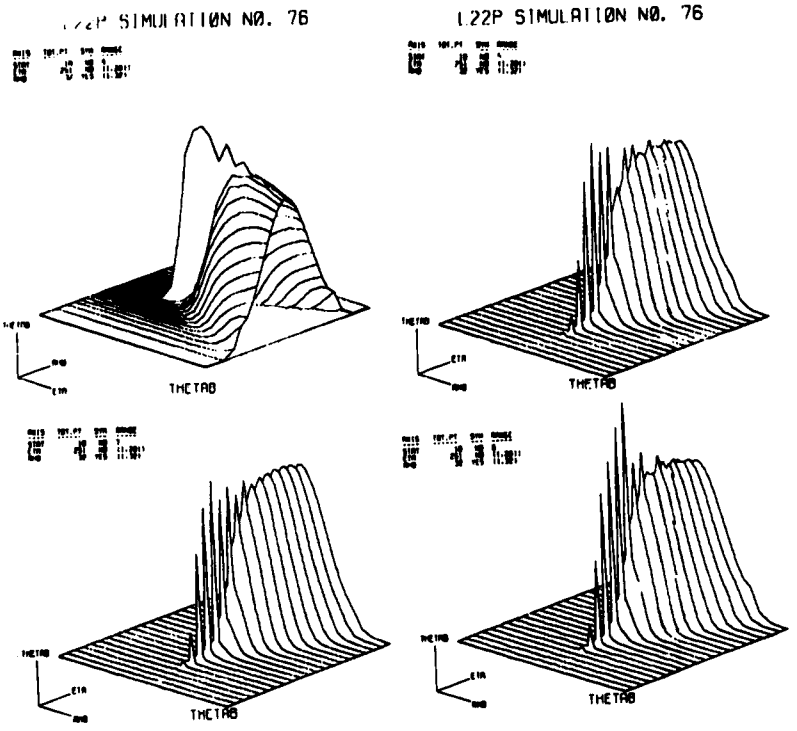
L22P SIMULATIØN NØ. 76
THETAB
L22P SIMULATIØN NØ. 76
THETAB
THETAB
THETAB

L22P SIMULATIØN NØ. 76

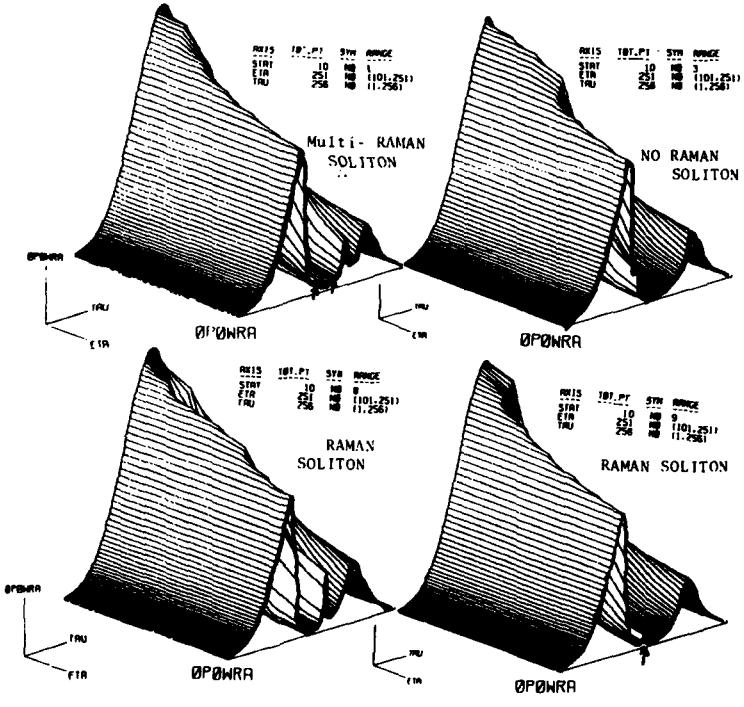

L22P SIMULATIØN NØ. 76

L22P SIMULATION NØ

L22P SIMULATION NØ. 76

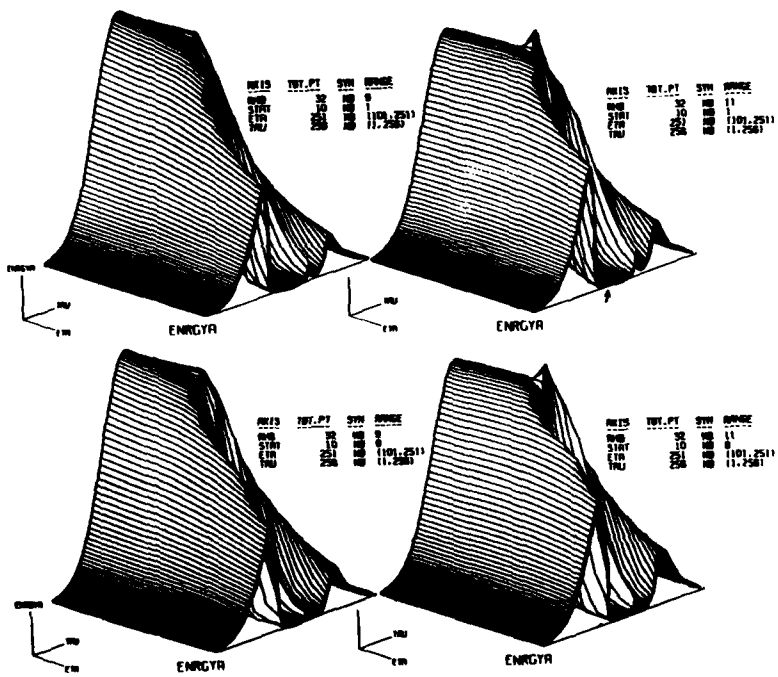

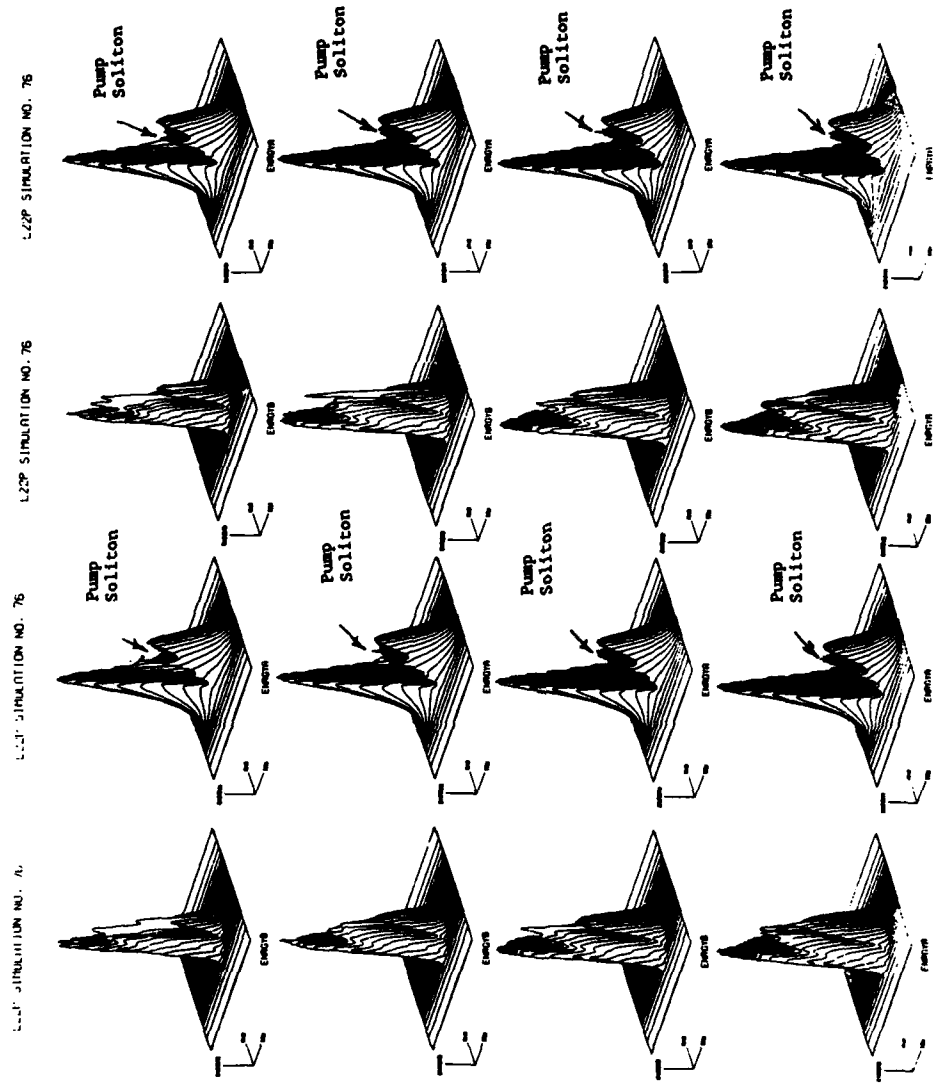
Pump Soliton
Pump Soliton
Pump Soliton
Pump Soliton
L22P SIMULATION NO. 76
L22P SIMULATION NO. 76
Pump Soliton
Pump Soliton
Pump Soliton
Pump Soliton

CROSS-PHASE MODULATION & CROSS-FOCUSING EFFECTS IN OPTICAL FIBERS

Rose Du*,#and Farres Mattar#
Stuyvesant High School*, New York, NY & Physics Dept., New York University & Electrical Engineering Dept., City College of New York #, New York, NY

The effects of diffraction, self-, and cross-phase modulation on the spatial profile of copropagating CW beams are analytically examined in parabolic graded-index fiber that sustains a Kerr nonlinearity. A self-similar solution, which does not restrict the strength of the probe beam as compared to the strength of the pump beam, is obtained.

We begin with the nonlinear wave equation:

$$\nabla^2 E - \frac{n^2}{c^2}\frac{\partial^2 E}{\partial t^2} - \frac{2nn_2}{c^2}\frac{\partial^2}{\partial t^2}\left(|E|^2 E\right) = 0$$

The following approximations are made: 1)effects of group velocity dispersion are neglected , 2)effects of self-steepening are neglected, and 3)the graded index is approximated by

$$n^2 = n_0^2\left(1 - k_2 r^2/(kn_0)\right)$$

The electric field is described by $E(r,z,t) = 1/2\left[E(r,z,t)\exp[i(\omega_0 t - kz)] + \text{c.c.}\right]$

where $E(r,z) = E_0 \exp\left(-r^2/r_0^2\right)$ is the initial condition.

In the slowly varying envelope approximation we have

$$\nabla_r^2 E_{\alpha,\beta} - 2ik\frac{\partial E_{\alpha,\beta}}{\partial z} - kk_2 r^2 E_{\alpha,\beta} + \left(n_2 k^2/n_0\right)\left(|E_{\alpha,\beta}|^2 + 2|E_{\beta,\alpha}|^2\right)E_{\alpha,\beta} = 0$$

in which the first term denotes the transverse component of the Laplacian. Note that the cross-term is twice the self-term.

An approximate solution to the above equation can be described by the Gaussian profile [1]:

$$E(r,z) = E_0^2/w(z)\exp\left\{-r^2/\left[r_\rho^2 w^2(z)\right] - i(k/2)\rho(z)r^2 + ik\psi(z)\right\}$$

where w is the normalized beam radius, ρ^{-1} is the radius of curvature, and $k\varphi$ is the longitudinal phase along the fiber axis.

Let $w'_\alpha = \partial w_\alpha/\partial z$ and $\rho' = \partial \rho_\alpha/\partial z$

The following relationships are derived by separating the equation into real and imaginary components. From the imaginary component an equation for the inverse of the radius of curvature is obtained.

$$\rho_{\alpha,\beta} = w'_{\alpha,\beta}/w_{\alpha,\beta}$$

Making the following aberrationless assumption:

$$\exp\left[-2r^2/\left(r_{\rho\alpha,\rho\beta}^2 w_{\alpha,\beta}^2\right)\right] \approx 1 - \left(-2r^2\right)/\left(r_{\rho\alpha,\rho\beta}^2 w_{\alpha,\beta}^2\right)$$

we can separate the real component into two parts. The radially dependent part simplifies into

$$-B_{\alpha,\beta}/w_{\alpha,\beta}^3 + w''_{\alpha,\beta} + A_{\alpha,\beta} w_{\alpha,\beta} + 2C_{\alpha,\beta}/w_{\alpha,\beta}^3 + 4C_{\beta,\alpha} w_{\alpha,\beta}/w_{\beta,\alpha}^4 = 0$$

where the constants describing the graded-index, free space, and Kerr nonlinearity are

$$A_{\alpha,\beta} = \frac{k_{\alpha,\alpha\beta}}{k_{\alpha,\beta}} = \frac{1}{l_{w\alpha,w\beta}^2}, B_{\alpha,\beta} = \frac{4}{r_{\rho\alpha,\rho\beta}^4 k_{\alpha,\beta}^2} = \frac{1}{l_{d\alpha,\alpha}^2}, \text{and } C_{\alpha,\beta} = \frac{n_2 E_{\alpha,\alpha\beta}^2}{n_0 r_{\rho\alpha,\rho\beta}^2} = \frac{1}{l_{nl\alpha,\alpha\beta}^2}$$

respectively. l_d is the Rayleigh diffraction length, l_w is the waveguiding length, and l_{nl} is the nonlinear interaction length [1]. The diffraction length corresponds to the distance of propagation at which the Fresnel number is one, the waveguiding length refers to the period at which the beam width spreads and focuses, and the nonlinear interaction length characterizes the distance at which the accumulated diffraction will be equal to the self-focusing. Letting

$D_{\alpha,\beta} = B_{\alpha,\beta} - 2C_{\alpha,\beta}$ describing the competition between diffraction and Kerr self – focusing

$H_{\alpha,\beta} = A_{\alpha,\beta} + 4C_{\beta,\alpha}/w_{\beta,\alpha}^4$ defining the competition between parabolic and Kerr nonlinearity

If we assume that $4C_{\beta,\alpha}/w_{\beta,\alpha}^4$ is slowly varying, then the equation can be solved analytically. Using the trial periodic solution

$$w_{\alpha,\beta} = \left[\eta_{\alpha,\beta}\cos(\gamma_{\alpha,\beta}) + \delta_{\alpha,\beta}\right]^{1/2}$$

we find that $\gamma_{\alpha,\beta} = 2(H_{\alpha,\beta})^{1/2}$, $\eta_{\alpha,\beta} = \dfrac{w_{\beta,\alpha}^3 H_{\alpha,\beta} - D_{\alpha,\beta}}{2H_{\alpha,\beta}}$, $\delta_{\alpha,\beta} = \dfrac{w_{\beta,\alpha}^3 H_{\alpha,\beta} + D_{\alpha,\beta}}{2H_{\alpha,\beta}}$

The radially independent part can be solved to give

$$\phi_{\alpha,\beta} = \frac{(B_{\alpha,\beta} - C_{\alpha,\beta}) r_{\rho\alpha,\rho\beta}^2}{2\left(\delta_{\alpha,\beta}^2 - \eta_{\alpha,\beta}^2\right)^{1/2}} \tan^{-1}\left[(\delta_{\alpha,\beta} - \eta_{\alpha,\beta})\tan(\gamma_{\alpha,\beta} z/2)\right]$$

By using the fact that

$$\delta_{\alpha,\beta} + \eta_{\alpha,\beta} = w_{\beta,\alpha}^3$$

and making the appropriate substitutions

$$\Psi_{\alpha,\beta} = \left[(B_{\alpha,\beta} - C_{\alpha,\beta}) r_{\rho\alpha,\rho\beta}^2/2\right](H/D)^{1/2}\tan^{-1}\left[(D/H)^{1/2}\tan(\gamma_{\alpha,\beta} z/2)\right]$$
$$- C_{\beta,\alpha} r_{\rho\beta,\rho\alpha}^2 (H/D)^{1/2}\tan^{-1}\left[(D/H)^{1/2}\tan(\gamma_{\alpha,\beta} z/2)\right]$$

Using the results for the normalized beam radius w, we can now derive an expression for the inverse of the radius of curvature

$$\rho_{\alpha,\beta} = -\eta_{\alpha,\beta}\gamma_{\alpha,\beta}\sin(\gamma_{\alpha,\beta} z)/\left\{2\left[\eta_{\alpha,\beta}\cos(\gamma_{\alpha,\beta} z) + \delta_{\alpha,\beta}\right]\right\}$$

From the solutions, it is readily seen that the normalized beam waist varies periodically with z

The periodicity depends on the waveguiding length, l_w, and the nonlinear effect due to the copropagating beam. Because of this periodicity, the beam will not collapse at all if it does not do so in the first cycle. In a homogeneous medium, where $k_2 = 0$ and the copropagating beam is weak, the periodicity does not exist. w eventually approaches zero and the beam collapses into one point [1].

We can also express the result in a simpler form sometimes used[2], [3]

$$E_{\alpha,\beta} = \frac{1}{w_{\alpha,\beta}(z)}\exp\left[-r^2/\left(r_{\rho\alpha,\rho\beta}^2 w_{\alpha,\beta}^2(z)\right) - \frac{1}{2}ik_{\alpha,\beta}\rho_{\alpha,\beta}(z)r^2 + ik_{\alpha,\beta}\Psi_{\alpha,\beta}(z)\right]$$

$$= \exp\left[-i\left(L_{\alpha,\beta}(z) + \frac{1}{2}Q_{\alpha,\beta}^{-1}(z)r^2\right)\right]$$

where $L_{\alpha,\beta}(z) = -i\ln w_{\alpha,\beta} - k_{\alpha,\beta}\Psi_{\alpha,\beta}$ is the longitudinal phase

and $Q_{\alpha,\beta}^{-1}(z) = -2i/\left(r_{\rho\alpha,\rho\beta}^2 w_{\alpha,\beta}^2\right) + k_{\alpha,\beta}\rho_{\alpha,\beta}$ is the complex radius of curvature.

Then use the following expression for the beam power from the conservation of energy and the theory of moments [4],[5].

$$P_{\alpha,\beta} = \frac{1}{2}\int_V \left|E_{\alpha,\beta}\right|^2 dV = \frac{1}{4}E_{0\alpha,0\beta}^2 r_{\rho\alpha,\rho\beta}^2 \pi$$

to obtain the power P and critical power P_C (minimum power at which the beam collapses) in terms of the fiber parameters [6]

$$P_{c\alpha,c\beta} = n_0 \pi / \left(2k_{\alpha,\beta}^{\ 2} n_2\right) \text{ and } P_{\alpha,\beta} = E_{0\alpha,0\beta}^{\ 2} \pi r_{p\alpha,p\beta}^{\ 2}/4$$

and an expression relating the power and critical power with the previous length constants.

$$P_{\alpha,\beta} / P_{c\alpha,c\beta} = 2C_{\alpha,\beta} / B_{\alpha,\beta} = N_{\alpha,\beta}$$

This is the normalized peak power [1]. Finally, letting

$$G_{\alpha,\beta} = \frac{4C_{\beta,\alpha}}{w_{\beta,\alpha}^{\ 4}}; w_{0\alpha,0\beta}^{\ 2} = \frac{B_{\alpha,\beta}}{A_{\alpha,\beta}}; F_{\alpha,\beta} = -\frac{G_{\alpha,\beta} B_{\alpha,\beta}}{A_{\alpha,\beta}\left(A_{\alpha,\beta} + G_{\alpha,\beta}\right)}; J_{\alpha,\beta} = w_{0\alpha,0\beta}^{\ 2} + F_{\alpha,\beta}; \text{ and } M_{\alpha,\beta} = J_{\alpha,\beta}\left[1 - N_{\alpha,\beta}\right]$$

we have after some calculations

$$\phi_{1\alpha,1\beta} = \frac{\left(1 - N_{\alpha,\beta}/2\right)}{\left(1 - N_{\alpha,\beta}\right)^{1/2}} \tan^{-1}\left\{\left[M_{\alpha,\beta}\right]^{1/2} \tan\left(2H_{\alpha,\beta}^{\ 1/2}\right)\right\}$$

$$w_{\alpha,\beta} = \frac{1}{\sqrt{2}}\left\{\left[1 - M_{\alpha,\beta}\right]\cos\left(2H_{\alpha,\beta}^{\ 1/2}\right) + \left[1 + M_{\alpha,\beta}\right]\right\}^{1/2}$$

$$\rho_{\alpha,\beta} = -\frac{\left[1 - M_{\alpha,\beta}\right] H_{\alpha,\beta}^{\ 1/2} \sin\left(2H_{\alpha,\beta}^{\ 1/2} z\right)}{\left\{\left[1 - M_{\alpha,\beta}\right]\cos\left(2H_{\alpha,\beta}^{\ 1/2}\right) + \left[1 + M_{\alpha,\beta}\right]\right\}}$$

The total phase is given by

$$\phi_{T\alpha,T\beta} = \omega_{\alpha,\beta} t - k_{\alpha,\beta} z + k_{\alpha,\beta} \varphi_{\alpha,\beta} - k_{\alpha,\beta} \rho_{\alpha,\beta} r_{\alpha,\beta}^{\ 2}/2$$

where the longitudinal phase is [1], [2]

$$\phi_{1\alpha,1\beta} = k_{\alpha,\beta} w_{\alpha,\beta}$$

and the radial phase is [2], [3]

$$\phi_{r\alpha,\beta} = -k_{\alpha,\beta} \rho_{\alpha,\beta} r_{\alpha,\beta}^{\ 2}/2$$

The solutions are valid for $M_{\alpha,\beta} >= 0$. Therefore the critical field can be described using the equation $M_{\alpha,\beta} = 0$. This can be examined by separating the expression into two cases. First of all,

$$E_{\alpha,\varphi}^{\ 2} = 4n_0 / \left(r_{p\alpha,p\beta}^{\ 2} k_{\alpha,\beta}^{\ 2} n_2\right)$$

which is the usual result for one beam [1]. This is true if the beam has a high intensity. In the second case,

$$E_{0\alpha,0\beta}^{\ 2} = -\left(4n_0 w_{\beta,\alpha}^{\ 4} + r_{p\alpha,p\beta}^{\ 4} k_{\alpha,\beta} k_{2\alpha,2\beta} n_0 w_{\beta,\alpha}^{\ 4}\right) / \left(4r_{p\alpha,p\beta}^{\ 2} k_{\alpha,\beta}^{\ 2} n_2\right)$$

From this expression, it can be seen that the critical field may be dependent upon the copropagating beam, that is, if both beams are of sufficient intensity, then each will not only self-focus but causes the copropagating beam to focus as well, and vice versa, enhancing the focusing effect. Furthermore, it may be concluded that it is possible for a beam to be below its threshold power and yet focus if the copropagating beam has a sufficiently high power (satisfy the above equation) and n_2 is negative.

From the solutions, it is readily seen that the normalized beam waist varies periodically with z. The periodicity depends on the waveguiding length, l_W, and the nonlinear effect due to the copropagating beam. Because of this periodicity, the beam will not collapse at all if it does not do so in the first cycle. In a homogeneous medium, where $k_2 = 0$ and the copropagating beam is weak, the periodicity does not exist. w eventually approaches zero and the beam collapses into one point [1].

The above general equations may be simplified under specific conditions. The effect of regions of varying intensity and the propagating medium of different characteristics on the longitudinal phase are examined. Similar conclusions can be drawn for the normalized beam radius and the inverse of the radius of curvature.

We shall now examine the region of high intensity where P is close to P_C. Under this condition, we obtain the following expression

$$\phi_{\alpha,\beta} = \left(l_{w\alpha,w\beta}^{\ 2} / l_{d\alpha,d\beta}^{\ 2} + F_{\alpha,\beta}\right)^{1/2} \tan\left(2H_{\alpha,\beta}^{\ 1/2}\right) - \left(l_{w\alpha,w\beta}^{\ 2} + F_{\alpha,\beta} l_{d\alpha,d\beta}^{\ 2}\right)^{1/2} l_d / l_{nl}^{\ 2} \tan\left(2H_{\alpha,\beta}^{\ 1/2} z\right)$$

Notice that the phase is now dependent upon both the beam itself and its companion beam.

For the propagation of two beams in a low intensity regime for one pulse, that is, $P_\alpha << P_{c\alpha}$, the longitudinal phase takes the following form

$$\phi_{\alpha,\beta} = \tan^{-1}\left[J_{\alpha,\beta}^{1/2}\tan\left(2H_{\alpha,\beta}^{1/2}z\right)\right]$$

If the two strong beams travel in a homogeneous medium, the phase becomes

$$\phi_{\alpha,\beta} = \frac{(1-N_{\alpha,\beta}/2)}{(1-N_{\alpha,\beta})^{1/2}}\tan^{-1}\left[(1-N_{\alpha,\beta})^{1/2}\left(\frac{B_{\alpha,\beta}}{G_{\alpha,\beta}}\right)^{1/2}\tan\left(2G_{\alpha,\beta}^{1/2}z\right)\right]$$

If one of those two beams is weak then the phase takes the following forms

$$\phi_{\alpha,\beta} = \tan^{-1}\left[\frac{1}{I_{c\alpha,\alpha\beta}}\left(G_{\alpha,\beta}^{1/2}\right)\tan\left(2G_{\alpha,\beta}^{1/2}z\right)\right]$$

and

$$\phi_{\alpha,\beta} = \frac{(1-N_{\alpha,\beta}/2)}{(1-N_{\alpha,\beta})^{1/2}}\tan^{-1}\left[(1-N_{\alpha,\beta})^{1/2}z/I_{c\alpha,\alpha\beta}\right]$$

The first equation describes the situation in which the weak pulse is the pulse we are describing, while the second equation describes the case in which the weak pulse is the copropagating pulse. Notice that the phase is no longer dependent upon the intensity of the weak pulse, but still retains its dependence upon the stronger copropagating pulse.

If the results of the two beam propagation are placed under the condition of low intensity for both beams, then the equation simplifies into the equation for one beam which is also in the low intensity regime. This equation may be derived using Yariv's method for one beam without the Kerr effect in a graded-index fiber[2].

$$\phi_l = \tan^{-1}\left[I_w/I_d\tan(z/I_w)\right]$$

For the low intensity regime in a homogeneous medium, we obtain a result whose description is similar to the one given above. This equation may also be arrived at by using Yariv's method, but in a homogeneous medium [2].

$$\phi_l = \tan^{-1}\left[z/I_d\right]$$

From the above solutions and from the graphical solutions we can make the following conclusions. The longitudinal phase of two weak beams propagating in free space increases and reach a limit. The longitudinal phase periodically increases and decreases if two weak beams propagate in a graded-index fiber. The same effect occurs for the propagation of two strong beams without the influence of the graded-index. With both effects combined, we again have the same resulting behavior as shown in Fig. 1. However, in this case, the period of oscillation depends mostly on the graded-index and not the Kerr effect.

A change in power will not affect the period of oscillation of the longitudinal phase. Also, the graded-index has a much greater effect on the period than the Kerr effect.

Using similar procedures, we can readily derive the equations for and analyze the beam radius under various conditions. The beam radius for two strong beams in a graded-index fiber is

$$w_{\alpha,\beta} = \frac{1}{\sqrt{2}}\left\{\left[1-\left(w_{0\alpha,\alpha\beta}^{4}+F_{\alpha,\beta}\right)(1-N_{\alpha,\beta})\right]\cos\left(2H_{\alpha,\beta}^{1/2}z\right)+\left[1+\left(w_{0\alpha,\alpha\beta}^{4}+F_{\alpha,\beta}\right)(1-N_{\alpha,\beta})\right]\right\}^{1/2}$$

If the power of the beam we are describing reaches critical power, the expression changes to

$$w_{\alpha,\beta} = \frac{1}{\sqrt{2}}\left[\cos\left(2H_{\alpha,\beta}^{1/2}z\right)+1\right]^{1/2}$$

In the low intensity regime in a graded-index fiber where one of the two propagating beams is weak, the beam width takes the forms

$$w_{\alpha,\beta} = \frac{1}{\sqrt{2}}\left\{\left[1-w_{0\alpha,\alpha\beta}^{4}(1-N_{\alpha,\beta})\right]\cos\left(2A_{\alpha,\beta}^{1/2}z\right)+\left[1+w_{0\alpha,\alpha\beta}^{4}(1-N_{\alpha,\beta})\right]\right\}^{1/2}$$

and

$$w_{\alpha,\beta} = \frac{1}{\sqrt{2}}\left\{\left[1-\left(w_{0\alpha,\alpha\beta}^{4}+F_{\alpha,\beta}\right)\right]\cos\left(2H_{\alpha,\beta}^{1/2}z\right)+\left[1+\left(w_{0\alpha,\alpha\beta}^{4}+F_{\alpha,\beta}\right)\right]\right\}^{1/2}$$

where the first expression describes the situation in which the weak pulse is the pulse we are describing, while the second one describes the case in which the weak pulse is the copropagating pulse.

When two strong beams are propagating in a homogeneous medium, the beam radius is

$$w_{\alpha,\beta} = \frac{1}{\sqrt{2}}\left\{\left[1-\left(\frac{B_{\alpha,\beta}}{G_{\alpha,\beta}}\right)(1-N_{\alpha,\beta})\right]\cos\left(2G_{\alpha,\beta}^{1/2}z\right)+\left[1+\left(\frac{B_{\alpha,\beta}}{G_{\alpha,\beta}}\right)(1-N_{\alpha,\beta})\right]\right\}^{1/2}$$

If one of the two beams is weak, that is, $P_\alpha << P_{co\alpha}$,then we have

$$w_{\alpha,\beta} = \frac{1}{\sqrt{2}}\left\{\left[1-\left(\frac{B_{\alpha,\beta}}{G_{\alpha,\beta}}\right)\right]\cos\left(2G_{\alpha,\beta}^{1/2}z\right)+\left[1+\left(\frac{B_{\alpha,\beta}}{G_{\alpha,\beta}}\right)\right]\right\}^{1/2}$$

Similar to the longitudinal phase, when both beams are weak, their beam radii are not affected by one another, we thus have the expressions for the propagation of one weak beam which can be derived using Yariv's methods [2]. In a graded-index fiber, we have

$$w = \frac{1}{\sqrt{2}}\left\{\left[1-w_o^2\right]\cos(2z/l_m)+\left[1+w_o^2\right]\right\}^{1/2}$$

In a homogeneous medium, we have

$$w = w_o\left(1+z^2/l_o^2\right)^{1/2}$$

From the above solutions and the graphical solutions we observe the following. For the propagation of one or two weak beams in free space, the beam radius spreads due to diffraction. If the medium of propagation is a graded-index fiber, the beam radius periodically spreads and focuses, with the period depending on the wavelength of the light beam as shown in Fig. 2. The beam also periodically spreads and focuses with the period depending on the power under the influence of the Kerr effect only as shown in Fig. 3. With the Kerr effect and the graded-index combined, as in Fig. 4, the period of oscillation depends on both the power and the wavelength of the copropagating beam.

From our results, we can also conclude that if the light beam focuses first, it will not spread beyond its original width and it spreads first, it similarly will not focus beyond its original width. An increase in power always enhance the focusing effect while an increase in wavelength will lead to a shorter period if the beam width is spreading and focusing periodically except when there is no graded-index. This suggests that the graded-index plays a key role in this phenomenon.

This problem may be further investigated by examining the propagation in a multimode optical fiber and also by considering the case with a fifth order nonlinearity.

The equations of motion correspond to those governing the on-resonance CW propagation of two light beams in a three level atom with a radially dependent atomic density. Since the beam intensities are weaker than the saturation intensity, the nonlinear response is approximated by a cubic term.[7]

ACKNOWLEDGEMENT

We would like to thank Mr. Q. Z. Wang of the Ultrafast Laser and Spectroscopy Institute at CCNY for the helpful discussions we had and the NYU Academic Computing Facility for access to the Microcomputer Laboratory.

REFERENCES.

[1] J. T. Manassah, P. L. Baldeck, and R. R. Alfano, Opt. Lett.,13,589(1988).
[2] A. Yariv,Quantum Electronics, (Wiley, 1989).
[3] H. A. Haus, Waves and Fields in Optoelectronics, (Prentice-Hall,1984).
[4] S. N. Vlasov, V. A. Petrishchev, and V. I. Talanov, Izvestiya Uyashikh Radiofizika, 14, 1353, (1971).
[5] S. A. Akhmanov, R. V. Khokhlov, A. P. Sukhorukov, in Laser Handbook, Volume 2, (North Holland, 1972).
[6] J. H. Marburger, Progress in Quantum Electronics, 4, 35, (1975).
[7] J. Teichmann, and F. P. Mattar, in Advances in Laser Science IV, (Am. Inst. Phys., 1989).

Figure 1. Two beams,phase, Kerr, graded-index, different powers, N=.25, .5, .75, .9,5

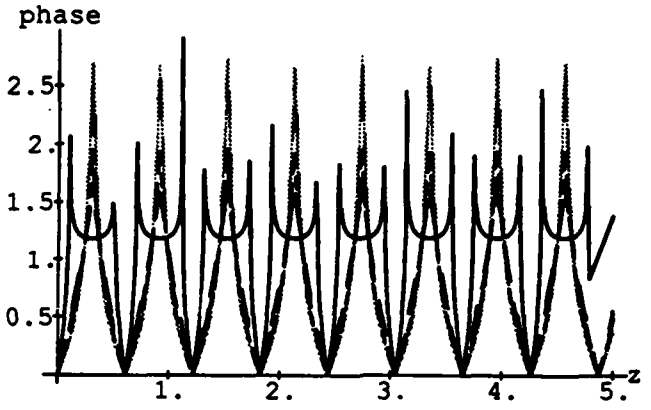

Figure 2. No Kerr, graded-index, one beam or two weak beams different wavelengths- .53, 1.06, and 1.5 μm.

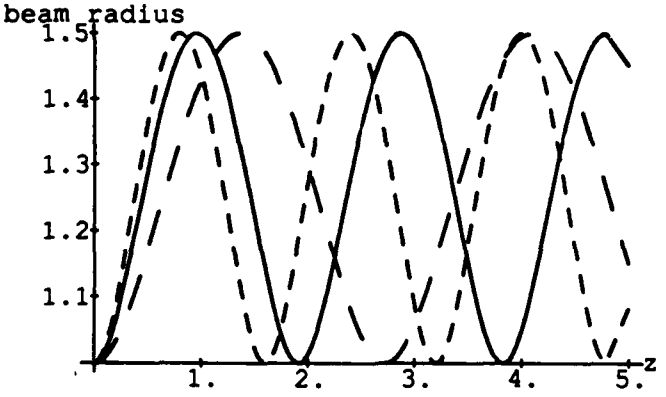

Figure 3. Kerr, no graded-index,different powers, N=.25, .5, .75, .9,5

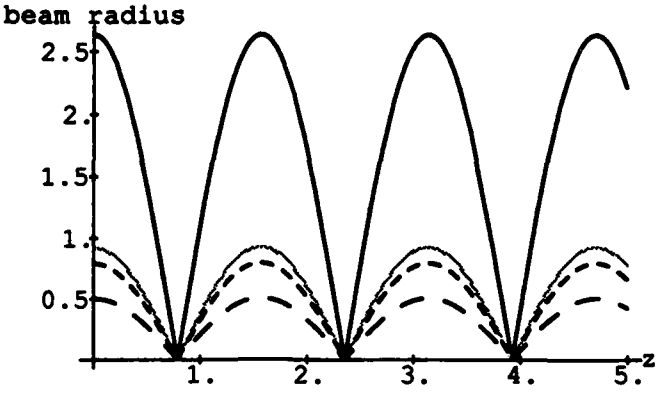

Figure 4. Two beams, beam radius, graded-index, Kerr,different powers, N=.25, .5, .75, .9,5

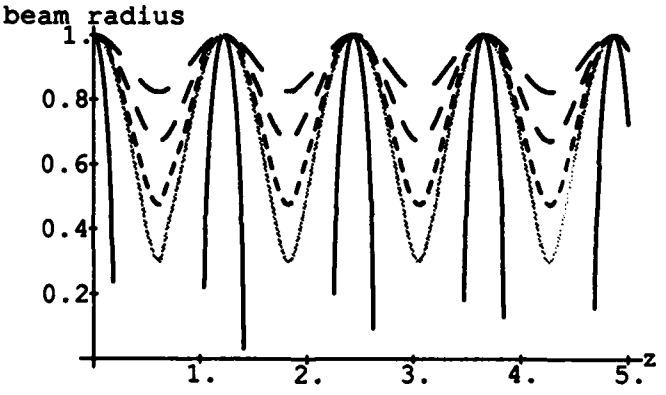

II. NONLINEAR OPTICAL PHENOMENA AND APPLICATIONS

II.A. Squeezed States and Quantum Optics

II.B. Nonlinear Optical Phenomena in Atomic Vapors

II.C. Nonlinear Optics in Semiconductors

II.D. Short-Pulse Lasers and Applications

PROSPECTS FOR PRACTICAL USE OF SQUEEZED LIGHT AND BACK ACTION EVASION

M.D. Levenson and R.M. Shelby
IBM Almaden Research Center, San Jose, CA 95120

ABSTRACT

The most powerful method to date of reducing quantum noise - Kimble's cavity parametric deamplifier - eliminates 95% of this noise but requires a full optical table of sophisticated equipment. The questions remains whether such methods can be made useful. In some very difficult and esoteric experiments, such as gravity wave detection, even quite laborious techniques may make the overall experiment only marginally more difficult. In other types of measurement, such as infra-red spectroscopy and optical data storage and retrieval, much simpler and more flexible devices with similar power will be required.

Squeezed states of light and back action evading optical measurements promise to reduce the noise level in a variety of experiments. The question remains when this promise will be made useful outside the quantum optics laboratory. Now, these phenomena have already been useful scientifically; they have forced a paradigm shift in which the vacuum fluctuations responsible for quantum noise have become more real and susceptible to manipulation.

The basic science of squeezed state generation is now well known, and the specifics of individual processes have been extensively reviewed (1). Back action evading or quantum nondemolition detection is less familiar (2-4). Basically these processes allow the measurement of one quantum variable (such as the amplitude of a light wave) without perturbing that variable. A conjugate variable, decoupled from the measured quantity, is perturbed instead (4). To prove the success of such a measurement, one must show that the process has no loss, adds no noise, and produces a signal that correlates with that from a conventional detector, even for quantum fluctuations.

To date, the most successful squeezing experiments have been the parametric oscillator projects of Kimble et. al.(5-7). Kimble has inferred a 95% reduction of quantum noise at the output of his device, but because of loss in his optics and

detectors, the actual noise is lowered by only 50%. The apparatus is quite complex and expensive; however, recent developments in GaAs pumped monolithic Nd:YAG lasers and lithium niobate resonant nonlinear devices promise major simplification (8). Such a device would be useful in gravity wave detection (9).

Giacobino et. al. have developed an intrinsically tuneable parametric oscillator that reduces the quantum noise in the difference in the intensity of signal and idler waves by 70% (10). This sort of apparatus will be useful in infra-red spectroscopy.

Machida et. al. have shown that semiconductor diode lasers with high total quantum efficiency and quiet pumping currents can produce noise below that expected for a coherent state (11). Such lasers are very sensitive to feedback, and it has proven very difficult to achieve even 30% noise reduction.

It appears that a 50% reduction in quantum noise can be plausibly achieved using known techniques. The question is: How much is such a reduction worth in an experiment? In gravity wave detection, such a noise reduction increases the volume of space from which a gravity wave source can be detected. Such an increase might be worth as much as $30,000,000, much more than the cost of the squeezed state generator. However, today's reliability must be improved, and the experiment optimized for squeezed light (9).

In spectroscopy, decreasing quantum noise by 50% might be worth $3,000. There have been a wide variety of proposals for using squeezed light or back action evasion in spectroscopy (12-15), but all appear to cost too much.

In optical data storage, a 3dB reduction in the quantum noise level could be quite important, but economics indicates that the necessary hardware must cost less than $30. While the technology for decreasing the noise level in magneto-optic detection has been successfully demonstrated, there is little chance for meaningful application (16).

Thus while the practical application of non-classical light does not seem imminent, the field has produced a lot of important science. The technical barriers can likely be overcome. One must work on cost and convenience.

* This Research was supported by the Office of Naval Research under contract N00014-82-C-0694.

1. H.J. Kimble, D.F. Walls (eds.) Special Issue On Squeezed States J.O.S.A. B 4 , 10 (1987); E.R. Pike and R. Loudon (eds.) J. of Mod. Optics Special Issue 34 , 6/7 (1987)
2. V.B. Braginsky, Y.I. Vorontsov and K.S. Thorne; Science 209 , 547 (1980)
3. N. Imoto, H.A. Haus and Y. Yamamoto; Physical Review A32 , 2287 (1985)
4. M.D. Levenson, R.M. Shelby, M. Reid, and D.F. Walls; Physics Review Letters 57 , 2473 (1986)
5. L.A. Wu, H.J. Kimble, J.L. Hall and H. Wu; Physical Review Letters 57 , 2520 (1986)
6. M. Xiao, L.A. Wu and H.J. Kimble; Physical Review Letters 59 , 278 (1987)
7. M. Xiao, L.A. Wu, and H.J. Kimble; Optics Letters 13 , 476 (1988)
8. C.D. Nabors, W.J. Kozlovsky, R.C. Eckardt and R.L. Byer; I.E.E.E. J. Quantum Elect (Submitted 1988)
9. J. Geà Banacloche, G. Leuchs J.O.S.A. B 4 , 1667 (1987)
10. A. Heidmann, R.J. Horowicz, S. Reynaud, E. Giacobino, C.Fabre and G. Camy; Physical Review Letters 59 , 2555 (1987)
11. S. Machida and Y. Yamamto; Physical Review Letters 60 , 792 (1988)
12. B. Yurke and E.A. Whittaker; Optics Letters 12 , 239 (1987)
13. M.D. Levenson in Lasers Spectroscopy and New Ideas, W.M. Yen and M.D. Levenson, (eds.) Springer Series in Optical Sciences 54 (Springer Verlag Heidelberg (1987)
14. N. Imoto (Private Communication)
15. A.S. Lane, M.D. Reid and D.F. Walls, Physical Review Letters 60 , 1940 (1988)
16. P. Grangier, R.E. Slusher, B. Yurke and A. La Porta; Physical Review Letters 59 , 2153 (1987)

Quantum Nondemolition Detection of Optical Quadrature Amplitudes

Robert M. Shelby

IBM Almaden Research Center, San Jose, CA 95120

ABSTRACT

The concept of quantum nondemolition (QND) measurement is outlined in the context of quantum optics. As a prototypal QND measurement scheme, the interaction of a light beam with a classical mechanical oscillator via radiation pressure is outlined. Results of QND experiments using cross-phase modulation of two co-propagating beams in single mode optical fibers are reviewed, and the prospects for improved schemes briefly discussed.

INTRODUCTION

The Heisenberg Uncertainty Principle is one of the basic tenets of quantum theory: the theory which we believe correctly describes the microscopic world. The uncertainty principle requires that when any physically observable quantity of some system is measured, the measuring apparatus interacts in an essential way with the system being measured. This interaction results in perturbation of the system being measured by the measurement process itself, i.e. so-called "back-action." The state of the system after a measurement is different from before. This is required to preserve the minimum uncertainty product for the variable being measured and the complementary or quantum-mechanically conjugate variable.[1]

A quantum nondemolition (QND) measurement is one that measures a physical observable of some system without altering its value. This is possible when the desired observable can be made a constant of the motion of the coupled system and measuring apparatus. Subsequent measurements of the same observable will yield an identical value, and this makes it possible to observe changes in this physical quantity with a precision that is in principle not limited by quantum fluctuations. The back action perturbation is confined to the variable that is conjugate to the QND observable. These concepts were first developed in the context of the detection of gravitational radiation via its interaction with a mechanical oscillator.[2] However, the first experimental demonstration of a QND measurement has been done with electromagnetic oscillations, i.e. laser beams. Conventional photodetectors perform a demolitional measurement of light intensity. They absorb light quanta and convert them into an electric current which can be measured by an external circuit. The more efficiently they absorb the light, the more accurately they determine its intensity, but in the process the light beam is destroyed and is unavailable for further measurements.

The photocurrent signal is accompanied by noise: fluctuations in the current which limit the sensitivity with which small changes in the light amplitude can be detected. Ultimately, the noise is determined by the quantum nature of the light being detected, which enforces a minimum noise floor known as the "shot noise limit." This noise is now understood to originate from the quantum mechanical uncertainty in the electric field amplitude which must be present in order that the Heisenberg Uncertainty Principle be obeyed, even in

the vacuum state. It is the interference of the vacuum fluctuation fields with the coherent mean field of the light wave that is the physical origin of the shot noise. This paper will introduce the basic ideas of quantum nondemolition measurement in the context of optics and illustrate with a conceptually simple example, the radiation pressure of a light beam reflected from a mirror. The optical Kerr effect in glass fibers provides an experimentally realizable scheme in which QND correlations have been observed in the laboratory, allowing measurement of optical amplitude with a noise level that is lower than that of the vacuum.

RADIATION PRESSURE

When a light beam is reflected from a mirror, momentum is transferred to the mirror. If the mirror (of mass m) is mechanically constrained by a spring (spring constant k), measurement of its displacement allows the amplitude of the light to be inferred, yet the entire beam is reflected and available for further measurements. If the mirror is perfectly reflecting, the amplitude of the light is unchanged; only its phase is perturbed by the induced motion of the mirror. If the light intensity fluctuates, e.g. due to vacuum noise, these fluctuations will also be transferred to the motion of the mirror, with a maximum response at the resonant frequency, $\delta_0 = \sqrt{k/m}$, and with no change in the amplitude fluctuations of the reflected beam. This interaction is a QND measurement of the light amplitude. The fluctuating mirror position induces additional phase fluctuations on the output beam.

Mathematically, the light is a sinusoidal oscillation of the field at frequency ω_0 with superimposed vacuum fluctuation fields:

$$\hat{E}(t) = (E_0 + \delta\hat{E}_A(t)) \sin \omega_0 t + (\delta\hat{E}_\phi(t)) \cos \omega_0 t. \qquad (1)$$

In eq. (1) E_0 is the average amplitude of the electric field part of the light wave, and the fluctuations are due to the two independent vacuum fields $\delta E_A(t)$ and $\delta E_\phi(t)$. Since δE_A is in phase with the field amplitude E_0, it produces noise on the amplitude of the light, while δE_ϕ causes uncertainty in the phase of the wave. These two vacuum field quadratures are non-commuting quantum operators. Therefore, the uncertainty principle sets a minimum value for the product of the mean square of these two fluctuating fields. The QND measurement of the amplitude allows δE_A to be known; thus this field is no longer "noise," and the uncertainty in the amplitude is reduced. In order that the uncertainty principle not be violated, the phase uncertainty must increase accordingly, and it can be shown that the fluctuating mirror position is sufficient to ensure that this is the case.

Consider the Fourier components of the amplitude and phase fluctuations, the quadrature amplitudes,

$$\hat{X}_A(\delta) = \int \delta\hat{E}_A(t) \exp(i\delta t)dt, \qquad (2)$$

the corresponding Fourier amplitudes for phase fluctuations, X_ϕ, and the mirror position $\zeta(\delta)$. The response of the oscillator to the radiation pressure fluctuations at frequency δ is given by

$$\zeta(\delta) = \frac{i\kappa |E_0| \hat{X}_A}{\Gamma + i(\delta - \delta_0)}, \qquad (3)$$

where Γ is the damping constant of the mechanical oscillator, $\kappa = (\hbar\omega_0)/(mc\tau\mathbf{E})$, with τ being the characteristic time constant which defines the measurement bandwidth and $\mathbf{E}^2 = (4\pi\hbar\omega_0/cA\tau)$ is the mean square electric field per photon for the optical beam. Thus, the mirror position provides a readout of the amplitude quadrature operator X_A. This readout faithfully reproduces the quantum amplitude fluctuations of the light, limited by the thermal background noise in the mechanical oscillator. An analysis of the magnitude of thermal noise yields the signal to noise ratio

$$\frac{S}{N} = \frac{(\hbar\omega_0)^2 P}{4c^2 R k_B T} \tag{4}$$

where P is the optical power in quanta per second, k_B is Boltzmann's constant and T the ambient temperature of the oscillator. $R = Q/\sqrt{km}$ is a figure of merit for the mechanical oscillator. To achieve a signal to noise ratio of unity, $R = 10^{11}$cm/dyne-sec is required which may prove very difficult.

OPTICAL FIBER QND

A different approach using cross-phase modulation in an optical Kerr medium has recently succeeded in demonstrating QND correlations. Two beams of light of different wavelength co-propagate in a single-mode optical fiber (see Figure 1). The refractive index depends on the intensity of the light as

$$n = n_0 + n_2 |E|^2, \tag{5}$$

where n_0 is the usual refractive index, n_2 is the nonlinear refractive index, and $|E|^2$ is the total intensity. Equation (5) shows that at the output of the fiber of length ℓ the refractive index and therefore the phase shift experienced by each of the waves will depend on the intensity of the other wave. Let the wavelengths of the two beams be λ_1 and λ_2 and their average amplitudes be E_1 and E_2. At the output of the fiber, the two beams can be separated by a prism and their amplitude and phase measured. The phase of the beam at wavelength λ_1 (the "readout" beam) will be modulated by fluctuations in the amplitude (X_2^A) of the beam at λ_2 (the "signal" beam):.

$$\hat{X}_1^{\phi}(\ell) = \hat{X}_1^{\phi}(0) + \hat{X}_{bgd}^{\phi} + \frac{8\pi\ell}{\lambda_1} n_2 |E_1| |E_2| \hat{X}_2^A. \tag{6}$$

The term in eq. (6) proportional to X_2^A provides a means of inferring the quantum amplitude fluctuations of the signal beam. In the process, the signal beam itself has not been absorbed. Furthermore, the nonlinear interaction between the signal and readout beams takes the form of an intensity-dependent index of refraction; changes of the index of refraction are incapable of modulating the amplitude of either beam. Therefore, the amplitude fluctuations of the signal beam could not have been modified in any way by the measurement process, and the back action has been evaded. The other terms in eq. (7) are noise backgrounds which limit the accuracy of the measurement, due to initial phase fluctuations of the readout beam ($X_2^{\phi}(0)$) or to phase noise from other sources, e.g. from thermal fluctuations of the refractive index of the fiber (X_{bgd}^{ϕ}). A subsequent measurement of the amplitude of the signal beam would then give an identical result, to within this uncertainty.

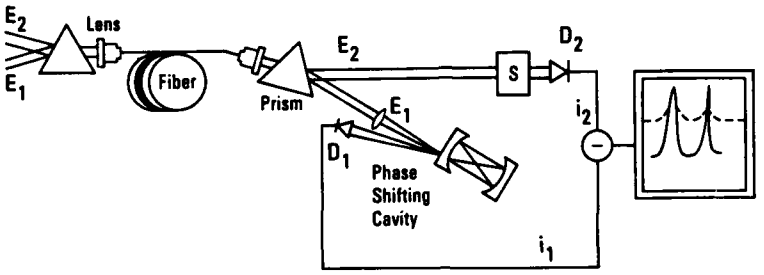

Figure 1. A quantum nondemolition scheme for quantum noise suppression. The signal and readout beams are coupled in an optical fiber by the intensity-dependent index of refraction. A phase-shifting interferometer is used to measure the phase fluctuations of the readout beam, from which the quantum amplitude fluctuations of the signal beam can be inferred. The amplitude noise of the signal beam due to quantum fluctuations can be subtracted from the signal beam photocurrent.

The phase of the signal beam is perturbed by the amplitude fluctuations of the readout beam, maintaining the required minimum uncertainty product.

A possible application of this QND scheme is shown schematically in Figure 1. The signal beam amplitude is first determined by a QND measurement in an optical fiber. The signal beam then interacts with some optical apparatus that can make very small changes in its amplitude which one then desires to detect. By comparing the QND and conventional measurements of the intensity, a noise level better than any conventional technique can result.

Figure 2 depicts experimental data[3] demonstrating a reduction of the noise level below the vacuum level for a configuration similar to that shown in Figure 1. The signal beam amplitude noise at the fiber output was at the vacuum level, consistent with back-action evasion for the amplitude. The probe beam fluctuations were detected as a mixture of amplitude and phase as parameterized by the phase angle Φ, amplified, and subtracted from the signal beam amplitude fluctuations. For an optimum range of phase shifts, Φ, the noise level was decreased by about 5%. This rather modest noise reduction was limited by thermal fluctuations of the refractive index of the fiber even at 2°K.

Improved performance of such a QND scheme can be obtained at the expense of reduced measurement bandwidth by enclosing the nonlinear medium (the optical fiber) in a resonant optical cavity. A single-mode fiber ring resonator has been constructed using an integrated variable directional coupler.[4] *Using a room temperature ring resonator constructed with a* 10 m long fiber, QND correlations have been observed with signal to noise ratio that is comparable to that of the 100 m cryogenic fiber experiment above, over a bandwidth of ~1 MHz.

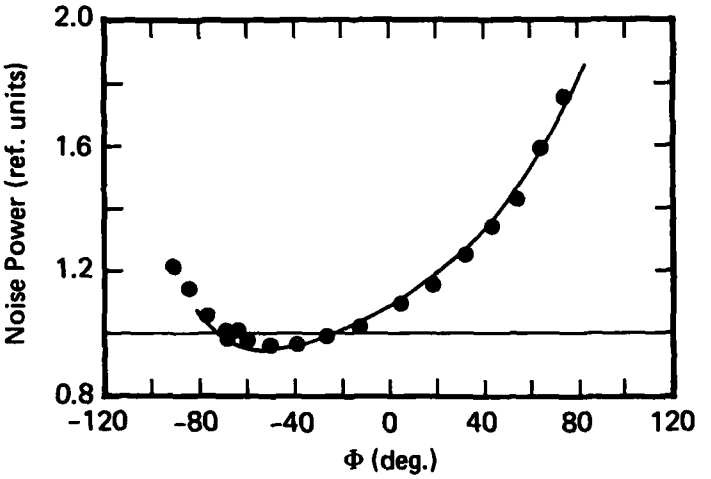

Figure 2. Experimental data for the QND scheme shown in Fig. 2. For optimum choice of the phase Φ at which the probe beam fluctuations are measured, a reduction of the noise level in the signal-probe difference photocurrent by 5% relative to the signal beam vacuum noise is possible, limited by thermal phase noise from the fiber.

DISCUSSION

These experiments clearly demonstrated the quantum correlations expected for QND measurement using the optical Kerr nonlinearity of fused silica fibers. Back-action evasion is expected from the theory to be very well obeyed, but is difficult to verify rigorously due to the limited signal to noise ratio. A more satisfying verification of back-action evasion could be obtained by demonstrating quantum correlations between the readouts of two independent QND measurements of the same signal wave, requiring significant reduction of the readout background noise level. A promising scheme for an improved QND measurement of optical amplitude utilizes optical parametric amplification in a Type II phase-matched crystal such as KTP.[5] The nonlinear Hamiltonian for parametric amplification has only part of the interactions necessary for back-action evasion, and additional "mode-conversion" interactions must be provided which mix the two subharmonic waves with a coupling in proportion to the parametric gain. In a Type II phase-matched device, the required mixing can by achieved by polarization rotation. Such a device offers the potential for high signal to noise ratio because the pump wave is at twice the frequency of the signal and readout, and pump light scattering cannot add background noise.

Quantum nondemolition measurement can be used to reduce quantum noise in schemes such as that discussed above and shown in Figure 1. In many ways it is complementary to other quantum noise reduction methods, such as the use of squeezed vacuum fluctuations or twin photon beams. In optical communication or measurement techniques where the essential information is carried by the quantum state of the light itself, the back-action evasion of QND will be required to provide a useful means for nondestructively detecting this quantum information.

ACKNOWLEDGMENT

The author wishes to thank M.D. Levenson, D.Z. Anderson and G.M. Mcclelland for contributions to the ideas discussed here.

REFERENCES

1. J.A. Wheeler and W. H. Zurek, eds., **Quantum Theory and Measurement,** Princeton University Press, (Princeton, N.J., 1983).

2. C.M. Caves, K.S. Thorne, R.W.P. Drever, V.D. Sandberg, and M. Zimmerman, Rev.Mod.Phys. **57,** 341 (1980).

3. M.D. Levenson, R.M. Shelby, M.D. Reid and D.F. Walls, Phys.Rev.Lett. **57,** 2473 (1986); M.D. Levenson and R.M. Shelby, J.Modern Optics **34,** 775 (1987).

4. H.A. Bachor, M.D. Levenson, D.F. Walls, S.H. Perlmutter and R.M. Shelby, Phys. Rev. A **38,** 180 (1988).

5. R.M. Shelby and M.D. Levenson, Opt. Commun. **64,** 553 (1987); S.F. Pereira, H.J. Kimble, P. Alsing, and D.F. Walls, J.Opt.Soc.Am. A **4,** P11 (1987).

PHOTON STATISTICS OF MULTIMODE SQUEEZED LIGHT*

Jianming Huang and Prem Kumar
Northwestern University, Evanston, Illinois 60208

ABSTRACT

In this paper, we present photon-counting distributions of multimode squeezed light of bandwidth B. By expanding the electric-field operator into relevant modes over the counting internal T and applying the Bogoliubov transformation that generates squeezing, we calculate the counting distributions under both $T \simeq 2\pi/B$ and $T \gg 2\pi/B$ conditions. Effect of nonunity quantum efficiency of the photodetector is also considered.

INTRODUCTION

Squeezed light has recently been generated in a variety of physical systems and its quadrature noise behavior verified using the balanced homodyne detection technique.[1] Squeezed states also exhibit interesting photon-counting distributions showing oscillatory behavior under appropriate conditions.[2] Although these distributions for single-mode squeezed light are well known,[3] not much attention has been paid to those of multimode squeezed light of the kind generated by an intracavity parametric down-converter[4] – the most successful light squeezer todate. In this paper, we present a characteristic function technique[3] to calculate the photon-counting distribution of squeezed light of bandwidth B and examine conditions under which the oscillatory behavior might be observable.

MODE EXPANSION AND CHARACTERISTIC FUNCTION

We start by expanding the positive frequency part of the electric-field operator $\hat{E}^{(+)}(t)$ in terms of the relevant field modes over the photon-counting interval $[t-T/2, t+T/2]$ as $\hat{E}^{(+)}(t) = AT^{-1/2}\sum_{\ell=-N}^{N}\hat{a}_\ell \exp\{-i(\ell 2\pi/T+\omega_0)t\}\cdot \mathrm{rect}(t/T)$, where ω_0 is the center frequency of the squeezed light, $\{\hat{a}_\ell\}$ are the modal annihilation operators, and A is a constant. Taking the Fourier transform, the corresponding spectrum of $\hat{E}^{(+)}(t)$ is given by $\hat{E}^{(+)}(\omega) = AT^{1/2}\sum_{\ell=-N}^{N}\hat{a}_\ell \,\mathrm{sinc}[(\omega - \omega_0)T/2\pi + \ell]$, where $N = \mathrm{int}(BT/2)$, and $2N+1$ is the total number of modes required to describe the field of bandwidth B over the time interval T.

To obtain the photon-counting distribution, we define a joint antinormally-ordered characteristic function associated with the density operator $\hat{\rho}$ as:

$$\chi_A(\eta_i, \eta_i^*) = \mathrm{Tr}\{\hat{\rho}\exp(\sum_{i=-N}^{N}\eta_i^*\hat{a}_i)\exp(\sum_{i=-N}^{N}-\eta_i\hat{a}_i^\dagger)\}. \tag{1}$$

Using normal-ordering techniques, the density operator $\hat{\rho}$ of the multimode field can be recovered from the above characteristic function, and is given by

$$\hat{\rho} = \int \chi_A \exp(\sum_{i=-N}^{N}-\eta_i\hat{a}_i^\dagger)\exp(\sum_{i=-N}^{N}\eta_i^*\hat{a}_i)\prod_{i=-N}^{N}\frac{d^2\eta_i}{\pi}. \tag{2}$$

The joint probability $P(n_{-N},\ldots,n_N) \equiv < n|\hat{\rho}|n >$ for counting $n_{-N},\ldots,n_N$ photons in modes $-N,\ldots,N$, respectively, is then

$$\begin{aligned} P(n_{-N},\ldots,n_N) &= \int \chi_A < n|\exp(\sum_{i=-N}^{N} -\eta_i \hat{a}_i^\dagger)\exp(\sum_{i=-N}^{N} \eta_i^* \hat{a}_i)|n > \prod_{i=-N}^{N} \frac{d^2\eta_i}{\pi} \\ &= \int \chi_A \prod_{i=-N}^{N} L_{n_i}(|\eta_i|^2)\frac{d^2\eta_i}{\pi}, \end{aligned} \tag{3}$$

where $|n >\equiv \prod_{i=-N}^{N} |n_i >_i$ is the n-mode number state, and $\{L_{n_i}\}$ are the Laguerre polynomials.

In the Heisenberg picture, χ_A is easily calculated by applying the squeezed-state generating Bogoliubov transformation[5]

$$\hat{a}_i = \mu_i \hat{b}_i + \nu_i \hat{b}_{-i}^\dagger, \tag{4}$$

where $\mu_{\pm i} \equiv \mu(\omega_0 \pm \omega_i), \nu_{\pm i} \equiv \nu(\omega_0 \pm \omega_i), \omega_i = 2\pi i/T$, and $\hat{b}_i$ for $i = -N$ to N are the annihilation operators of the input modes to the device generating squeezed light. Substituting (4) into (1), we obtain

$$\begin{aligned} \chi_A &= \mathrm{Tr}[\hat{\rho}_0 \exp\{\sum_{i=-N}^{N} \eta_i^*(\mu_i \hat{b}_i + \nu_i \hat{b}_{-i}^\dagger)\}\exp\{\sum_{i=-N}^{N} -\eta_i(\mu_i^* \hat{b}_i^\dagger + \nu_i^* \hat{b}_{-i})\}] \\ &= \prod_{i=-N}^{N} \exp\{\mathrm{Re}(\eta_i \eta_{-i} \mu_i^* \nu_{-i}^* - |\eta_i \mu_i|^2)\}, \end{aligned} \tag{5}$$

where $\hat{\rho}_0$ is the density operator for the input to the squeezer, and in the second equality we have assumed it to be $\prod_{i=-N}^{N} |0 >_i {}_i< 0|$. Such is the case in the Wu et al.[4] experiment.

PHOTON COUNTING DISTRIBUTIONS

Because both $\hat{a}_i$ and $\hat{b}_i$ must obey bosonic commutators, the following relations exist between μ_i and ν_i : $|\mu_i| = |\mu_{-i}|$, $|\nu_i| = |\nu_{-i}|$, $|\mu_i|^2 = 1 + |\nu_i|^2$, and $\mu_i \nu_{-i} = \mu_{-i}\nu_i$. Using these relations and substituing (5) in (3), the following joint counting probability for the multimode squeezed light is obtained:

$$\begin{aligned} P(n_{-N},\ldots,n_N) = \int \exp\{\mathrm{Re}(\eta_0^2 \alpha_0 - |\eta_0|^2 \beta_0)\} L_{n_0}(|\eta_0|^2)\frac{d^2\eta_0}{\pi} \prod_{i=1}^{N} \int \frac{d^2\eta_i}{\pi}\frac{d^2\eta_{-i}}{\pi} \\ \cdot \exp\{2\mathrm{Re}(\eta_i \eta_{-i}\alpha_i) - \beta_i(|\eta_i|^2 + |\eta_{-i}|^2)\} L_{n_i}(|\eta_i|^2) L_{n_{-i}}(|\eta_{-i}|^2), \end{aligned} \tag{6}$$

where $\mu_i^* \nu_{-i}^* \equiv \alpha_i$, and $|\mu_i|^2 \equiv \beta_i$. The manifestly factored nature of the above expression reflects the fact that photons are generated pair-wise independently

in modes $0, \pm 1, \ldots,$ to $\pm N$. A practical photodetector, however, will not distinguish between the photons in each pair. Therefore, we define a total count variable $z_i = n_{-i} + n_i$ ($z_0 = n_0$) for each pair and Eq. (6) becomes

$$P(z_0, z_1, \ldots, z_N) = \int \exp\{\mathrm{Re}(\eta_0^2 \alpha_0 - |\eta_0|^2 \beta_0)\} L_{z_0}(|\eta_0|^2) \frac{d^2\eta_0}{\pi} \prod_{i=1}^{N} \int \frac{d^2\eta_i}{\pi} \frac{d^2\eta_{-i}}{\pi}$$
$$\cdot \exp\{2\mathrm{Re}(\eta_i \eta_{-i} \alpha_i) - \beta_i(|\eta_i|^2 + |\eta_{-i}|^2)\} L^1_{z_i}(|\eta_i|^2 + |\eta_{-i}|^2). \quad (7)$$

For short counting times ($T \simeq 2\pi/B$), only the $i = 0$ mode is required to describe the field. The first factor in the above equation then gives the well known photon distribution for a single-mode degenerate squeezed-vacuum state:[3]

$$P_{n=2k+1} = 0, \; P_{n=2k} = (2k-1)!!\, \bar{n}^k / 2^k k! (\bar{n}+1)^{k+1/2}, \quad (8)$$

where $\bar{n}$ is the average number of counted photons during T.

For long counting times ($T \gg 2\pi/B$), a photodetector will count all the photons in the $2N+1$ modes. Defining a total count variable $n = \sum_{i=0}^{N} z_i$, Eq. (7) leads to the following distribution for multimode squeezed-vacuum light:

$$P_n = \int \exp\{\sum_{i=-N}^{N} \mathrm{Re}(\eta_i \eta_{-i} \alpha_i - \beta_i |\eta_i|^2)\} L_n^{2N}(\sum_{i=-N}^{N} |\eta_i|^2) \prod_{i=-N}^{N} \frac{d^2\eta_i}{\pi}. \quad (9)$$

Using a generating function technique, we still get $P_{n=2k+1} = 0$ and

$$P_{n=2k} = [2(N+k)-1]!!|\nu|^{2k} / 2^k k! (2N-1)!! (1+|\nu|^2)^{N+k+1/2} \xrightarrow{N\to\infty} e^{-\bar{n}/2} [\bar{n}/2]^k / k!, \quad (10)$$

where we have assumed $|\nu_i| = |\nu|$ for all i.

NONUNITY QUANTUM EFFICIENCY

Nonunity quantum efficiency q of the photodetector is easily taken into account by coupling each mode to a loss reservoir represented by $\hat{d}_i = q^{\frac{1}{2}} \hat{a}_i + (1-q)^{\frac{1}{2}} \hat{c}_i$, where $\{\hat{c}_i\}$ are in vacuum state and q is assumed frequency independent. Substituting in (5), the characteristic function becomes $\chi_A = \prod_{i=-N}^{N} \exp\{\mathrm{Re}(q\eta_i \eta_{-i}\alpha_i) - q|\eta_i \mu_i|^2 - (1-q)|\eta_i|^2\}$. The details will be presented elsewhere, however, we note that $q \neq 1$ modifies P_n in a drastic way because the pair-correlated photons are lost independently.

* Supported in part by the National Science Foundation Grant EET-8715275.

REFERENCES

1. J. Opt. Soc. Am. B 4, (1987); squeezed states feature issue.
2. R. S. Bondurant, B. S. Thesis, MIT, 1978, unpublished;
   W. Schleich and J. A. Wheeler, J. Opt. Soc. Am. B 4, 1715 (1987).
3. H. P. Yuen, Phys. Rev. A 13, 2226 (1976).
4. L.-A.Wu, H.J.Kimble, J.L.Hall, and H.Wu, Phys. Rev. Lett. 57, 2520 (1986).
5. C. W. Gardiner and C. M. Savage, Opt. Commun. 50, 173 (1985).

FORWARD HYPER-TRANSIENT STIMULATED RAMAN SCATTERING INCLUDING LASER PUMP DEPLETION

F.P. Mattar*, C.M. Burgess*, Y. Claude* and J. Teichmann#
Department of Physics*, New York University, New York, NY 10003 and
Department of Electrical Engineering, City College of New York,
New York, NY 10031; and
Departement de Physique#, Université de Montreal, Montreal, Canada

ABSTRACT

Diffraction calculations which lead to self- and cross-phase modulation are reported in the coherent buildup regime of Stokes emission. Spatio-temporal reshaping of the pump and Stokes beams have been calculated.

PHYSICAL MODEL

The coupled equations for forward hyper-Transient Stimulated Raman Scattering SRS from a homogeneously broadened vibrational linewidth are well known[1-4]. A number of simplifying assumptions were introduced: the laser and Stokes fields are assumed to be monochromatic. Their spectral bandwidths are accounted for by the Fourier transform of their time dependent envelopes. Coupling to anti-Stokes and higher-order Stokes fields is ignored. The population difference between the initial and final vibrational states is set equal to a constant. Dispersion between the laser and Stokes fields and associated phase mismatch are neglected. However, the laser beam's spatial profile is herein accounted for. Transverse beam reshaping is dealt with rigorously.

Using these assumptions, the normalized on-resonance equations in retarded time and z space can be written as discussed by Georges & Harris[5]:

$$\partial\zeta_L/\partial z = -\,1/2\; g(\omega_L/\omega_S)q\zeta_S \tag{1}$$

$$\partial\zeta_S/\partial z = 1/2\; g\; q^*\zeta_L \tag{2}$$

$$\partial q/\partial\tau + q/T_2 = \zeta_S^*\zeta_L/T_2 \tag{3}$$

where j is the SRS steady-state gain constant.

For energy consideration one can rearrange and combine the equations of motion as follows:

$$\frac{\partial}{\partial z}\,[|\zeta_L|^2 + (\omega_L/\omega_S)|\zeta_S|^2] = 0 \tag{4a}$$

$$\frac{\partial}{\partial\tau}\,|q|^2 = (q'^*_S\,\zeta_L^*\,\zeta \;+ q'\,\zeta_S\,\zeta_L^*)/T_2 \tag{4b}$$

TRANSVERSE EFFECTS

Motivated by the importance of dynamic transverse effects in Self-Induced-Transparency (both numerical prediction[6] and actual SIT experiments[7]) and in superfluorescence (both SF observations [8] and actual SF computations[9]), we have allowed one transverse degree of freedom in the SRS computations. The development of both self- and cross-phase modulation can now be analyzed. One must add to the right-hand side of Eq. (2) and Eq. (3) the Laplacian term

$$[1/4\; F_{L,S}\ell]\;\nabla_T^2\,\zeta_{L,S},\ \text{where}\ \nabla_T^2\zeta_{L,S} = \frac{1}{\rho}\frac{\partial}{\partial\rho}\left[\rho\,\frac{\partial\zeta_{L,S}}{\partial\rho}\right] \tag{5a}$$

* Supported by ARO*, AFOSR*, ONR* and NSF* at NYU and NSERC# at U. de Montreal

$$- i F_L^{-1} \nabla_T^2 \zeta_L + \partial\zeta_L/\partial z = - 1/2\ g(\omega_L/\omega_S)q'\zeta_S \tag{5b}$$

$$- i F_S^{-1} \nabla_T^2 \zeta_S + \partial\zeta_S^*/\partial z = 1/2\ g\ q'\ \zeta_L \tag{5c}$$

with diffraction accounted for, one obtains additional terms in the energy conservation expression, namely, the transverse energy flux

$$i((\tfrac{1}{4}F_L\ell)\nabla_T(\zeta_L^*\nabla_T\zeta_L - \zeta_L\nabla_T\zeta_L^*) + [\tfrac{\omega_L}{\omega_S}](\tfrac{1}{4}F_S\ell)\nabla_T(\zeta_S^*\nabla_T\zeta_S - \zeta_S\nabla_T\zeta_S^*)) + \frac{\partial}{\partial z}[|\zeta_L|^2 + (\frac{\omega_L}{\omega_S})|\zeta_S|^2] = 0 \tag{5d}$$

with $\rho = r/r_p$ is the radius of the initial inversion at half maximum, ℓ is the sample length and $F_{L,S} = \pi r_p^2/\lambda_{L,S}\ell$ is the Fresnel number. The fields $\zeta_{L,S}$ are complex so that phase variations introduced by diffraction can be included systematically[10]. Thus, neither the mean-field approximation that neglects propagation effects nor the substitution of a loss term for diffraction coupling or even a linearization of the interaction[11] is used. Instead, a self-consistent numerical algorithm[12] is adopted which takes into account full paraxial propagation and transverse (both spatial profile and Laplacian coupling) effects. Thus our model possesses a degree of realism long sought for.

Finally, if the Lorentz local field(s) correction[13-16] is also accounted for. A population-dependent frequency offset emerges in the density matrix. The effective detuning becomes a time (and radial) dependent function. The resultant chirp, i.e., the frequency modulation modifies the characteristics of the Raman co-propagation. The rate of energy conversion from the pump to the Stokes and the depopulation of the pump and the growth of the Stokes emission become more complicated. The analytical tractability vanishes. One must resort to numerical experiments to appreciate the physical nuances and domain.

NUMERICAL RESULTS

The equations for transient stimulated Raman scattering from homogeneously broadened vibrational linewidths have been carefully studied in the low and high laser depletion limit by Carman et al.[1] and by Georges & Harris[5] respectively. We then analyzed the influence of diffraction coupling on the Raman pump and Stokes dynamics using a rigorous computer program L22P©. Induced phase modulation and cross-self-action phenomena are invariably seen. Stokes pulse compression is obtained from the transverse reshaping. Laser pump beam narrowing, Stokes beam blooming, and self-lensing evolution are revealed.

The physical parameters studied are as follows:

τ_p = 7 psec, FWHM = $7 \times 10^{-12} s^{-1}$, τ_{window} = 35 ps

T_2 = 7 psec, $\gamma = 1/T_2 = 0.142857 \times 10^{-12}$ sec^{-1}

ω_L = 18,846 cm^{-1}, ω_S = 15,913 cm^{-1}, $\delta_0 = \omega_L/\omega_S = 1.1843$

$$g = 25\ \text{m/TW} = 2.5 \times 10^{-11}\ \text{m/W},\ \eta_{max} = 0.2,\ \ell = 0.2\ \text{m}$$

$$I_L = 40\ \text{TW/m}^2 = 40 \times 10^{12}\ \text{W/m}^2,\ I_S = \exp[-13]\ I_L$$

$$s_L = 12.5 \text{ and } s_S = 0.28254 \times 10^{-4} \text{ with } s_{a,b} = \int_0^{\tau_{window}} |\varsigma_{L,S}| d\tau$$

For the Georges & Harris's[5] case, we display as a function of propagational distance η a composite of two-dimensional plots in which we compare versus τ the real part of the pump field and Uc the real component of the induced polarization Q of the effective two-level system. When diffraction is neglected and on-resonance interaction is considered, the fields without initial phase variations do not acquire a phase throughout the propagation in the sample see L22P18. The pump depletion and the Stokes buildup is clearly visualized.

When diffraction is included we find that self- and cross-phase modulation SPM and XPM result even though no initial phase or incident frequency variation were included in the field. To illustrate the role of transverse effects we display calculations L22P21 and L22P24 projection plots versus τ for different propagational distances η. The on-axis real ERa,b and imaginary EIa,b of the two fields and of (Uc,Vc) Q. We also exhibit in a three-dimensional representation the on-axis energy ENRGYa,b and of the radially-integrated energy of the field referred to as output power OPOWRa,b as a function of τ and η. The on-axial distribution is quite different from the output power plots substantiating that transverse effects are not nonessential complications of the physics analyzed in one-dimensional models. The on-axis energy can display, for small Fresnel numbers, an enhancement, i.e., a self-focusing while off-center energies for radii that are smaller than the HWHM can display self-defocusing behavior.

We have also computed the phase diagrams of the on-axis two fields and of Q for a family of propagational distances. In these parametric representations in which the variable τ is eliminated, the horizontal x-axis represents the in-phase (real part) component while the out-of-phase (imaginary part) is displayed on the vertical y-axis.

In Fig. 1 we show as a function of η for a uniform-plane-wave calculation a parametric representation with the real component of the pump field ERA plotted along the vertical axis and the Stokes field ERB plotted along the horizontal axis. The gradual depletion of the pump and the simultaneous buildup of the Stokes field are clearly illustrated as calculated in L22P18.

In Fig. 2, we displayed another phase plot for the Raman calculation L22P18 over a family of η, the propagational distance, to illustrate the temporal dynamics of the real part of the Stokes field initiated ERB by a seed (as a vertical axis) and of UC the real component of the inertial medium response.

In Fig. 3 we present three-dimensional plots of the one-dimensional simulation versus η and τ namely the real component of the pump field ERA, the real component of the Stokes field ERB and the real component UC of the Raman medium response Q.

We present in Fig. 4 three-dimensional plots of the time-integrated energy PSI pump and Stokes fluences for simulation LR22P11 to display the simultaneous longitudinal and radial reshaping as well as the energy conversion from the pump to the Stokes seed.

We also show side-to-side in Fig. 5 three-dimensional plots for the time- integrated area THETA versus ρ and η and of the radially-integrated energy, i.e., the output power OPOWR versus τ and η to substantiate the multi-dimensional dependence of the light-matter interaction.

In Fig. 6, we show a comparison of two-dimensional composites of the on-axis pump and Stokes energies L22P24. The depletion of the pump and the buildup of the Stokes are clearly exhibited.

A three-dimensional representation versus τ of the pump and Stokes output power for different η is shown in Fig. 7 to substantiate that energy conversion does take place for finite beam, i.e., in the presence of diffraction.

In Fig. 8 and in Fig. 9 we respectively display results from a diffraction. In particular we show for a given radius a composite of two dimensional plots versus time as a function of the propagational distance. The interplay of diffraction and copropagation is studied. We show the imaginary components of the field and of the material response. The variation of EIA and VC oppose each other. The dependence of the real component of the field and the material response is also presented. The dependence of ERB follows that of UC in the same direction. Thus EIA and VC are out of synchronization while ERB and UC are in synchronization. Beyond a certain propagational distance ERA and EIB develop negative values. Furthermore the positive peaks of UC and ERB occurs about the same time slice at which the minimum of ERA the pump field occurs. Nearly the same temporal coincidence evolves between EIA and VC and the time delayed medium response and the Stokes field EIB as displayed in additional graphs of Figs. 8 and 9.

The evolution of the on-axis imaginary component of the pump EIA, the Stokes EIB fields and VC the imaginary component of the material response is also shown in a three-dimensional plot that varies in terms of the propagational distance and the time (see Fig. 10). The phase of the Stokes field is almost out of synchronization of the phase of the pump field. Without the diffraction self-coupling and the medium cross-coupling the fields that are initially collimated do not acquire any phase (see Fig. 11).

In Fig. 12 we display for the diffraction calculation the radially-integrated energy, i.e., the output power versus time and propagational distances. The pump exhibits absorption and non-negligible depletion while the Stokes exhibits first a linear buildup followed by a nonlinear buildup. This buildup occurs beyond a threshold time which is larger than the initial time-peak occurrence at the input plane.

We contrast the output power with on-axis energy plots (see Fig. 13) to substantiate the role of diffraction of any other transverse effect. We construct a family of on-axis energy to illustrate the frequency conversion as it was shown in Figure 12. As the Stokes builds up and its peak advances in a frame that moves with respect to the velocity of light, the pump energy gets severely depleted in its trailing edge. This on-axis energy behavior displays a temporal ringing which tends to average out for large detectors. The one-dimensional temporal ringing remains for every cylindrical shell of the beam. Only its average will be a single pulse. The diffraction does not eliminate the temporal ringing. Thus the output power and the on-axis energy have totally different signatures.

Finally we present in Fig. 14 the transverse energy current versus τ and ρ for different η. The energy current is defined as the energy- weighted phase gradient; i.e., it is the product of the energy with the phase variation. When the phase curvature is focusing the flux is negative. This means that the energy current is flowing inwardly from the beam wings to the beam center. The on-axis energy will experience an enhancement while the beam widths will narrow. If the phase curvature is positive the energy flux is flowing outwardly illustrating the blooming of the beam. In our calculations we have found that the pump beam generally experiences narrowing while the Stokes beam expands. This demonstrates that the phase variations are crucial to the description of the physics.

CONCLUSION

We have demonstrated that transverse effects causes strong departures from the uniform-plane-wave cases.

REFERENCES

1. R.L. Carman et al., Phys. Rev. 2A, 60 (1970).
2. S.A. Akhmanov et al., JETP 32, 266 (1971).
3. [a] M. Maier & W. Kaiser, in **Laser Handbook**, ed. F.T. Arecchi & S.O. Shultz-DuBois (North Holland, 1972) pp. 1077-1150; and [b] A. Laubereau & W. Kaiser, Rev. Mod. Phys. 50, 607 (1978).
4. G.I. Kachen & W.H. Lowdermilk, Phys. Rev. A14, 1472 (1976).
5. S.M. Georges & C.B. Harris, Phys. Rev. A28, 863 (1983).
6. [a]N.Wright & M.C.Newstein, Opt.Commun. 9, 8(1973); [b]F.P.Mattar & M.C.Newstein, Opt.Commun. 18, 70 (1976), IEEE J. Quantum Electron 13, 507 (1977); & [c] F.P.Mattar et al., in **Coherence & Quantum Optics IV**, ed. L.Mandel & E.Wolf (Plenum,1978) pp.143-164
7. [a] S.L. McCall & E.L. Hahn, Phys. Rev. 183, 487 (1969); [b] A. Zembrod & T. Gruhl, Phys. Rev. Lett. 27, 287 (1971); [c] C.K. Rhodes et al., Phys. Rev. 184, 25 (1969) & Phys. Rev. Lett. 21, 1151 (1968); [d] H.M. Gibbs et al., Phys. Rev. Lett. 37, 1743 (1976); [e] W.Krieger et al., Z. Phys. B25, 297 (1976), & F.P. Mattar et al., Kvantovaya Electronika 5, 1818 (1978); & [f] J.J. Bannister et al., Phys. Rev. Lett. 44, 1062 (1980).
8. [a] N. Skribanovitz et al., Phys. Rev. Lett. 30, 309 (1973); [b] H.M. Gibbs et al., Phys. Rev. Lett. 39, 547 (1977); & [c] D.J. Heinzen et al., Phys. Rev. Lett. 54, 677 (1985).
9. [a] F.P.Mattar et al., Phys. Rev. Lett. 46, 1123 (1981); [b] F.P. Mattar, SPIE 288, 353-361 (1981) and ibid 380, 508-542 (1983); [c] P.D.Drummond & J.H.Eberly, Phys. Rev. A25, 1427 (1982); [d] E.Watson et al., Phys. Rev. A27, 1427 (1983); & [e] J.Mostowski & B.Sobolewska, Phys. Rev. A28 2573 (1983); & ibid A30, 610 (1984).
10. J.H. Marburger, **The Theory of Self-Focusing**, in Progress in Quantum Electronics, Vol. 4, Ed. J.H. Sanders and S. Tenholm (Pergamon Press, 1975) pp. 35-110.
11. M.G. Raymer et al., Phys. Rev. A32, 332 (1986).
12. F.P. Mattar, App. Phys. 17, 53 (1978); F.P. Mattar & M.C. Newstein, Comp. Phys. Commun. 20, 139 (1980); & B.R. Suydam & F.P. Mattar, SPIE 380, 439(1983).
13. J. Marburger, L. Huff, J.D. Reichert & W.G. Wagner, Phys. Rev. 184, 255 (1969).
14. [a] R. Friedberg, S.R. Hartmann & J.T. Manassah, Phys. Lett. 35A, 161 (1971), ibid 40A, 395 (1972) & Phys. Report 7C, 101-179 (1973); [b] J.T. Manassah, Phys. Report 101, 359-427 (1983); [c] R. Friedberg, S.R. Hartmann & J.T. Manassah, Phys. Rev. A39, 93 & 3444 (1989); and [d] J.T. Manassah, Phys. Rept. 101, 359-427.

15. [a] F.A. Hopf, C.M. Bowden & W.H. Louisell, Phys. Rev. A29, 2591 (1983); [b] in **Optical Bistability II**, ed. C.M. Bowden, H.M. Gibbs & S.L. McCall (Plenum Press, 1984) pp. 361-368; and [c] in **Optical Instabilities**, ed. R.W. Boyd, M.G.Raymer & L.M. Narducci (Cambridge University Press, 1986) pp. 308-311.
16. J.T. Manassah & F.P. Mattar, in Proc. Intl. Laser Sci. ILS-IV, **Advances in Laser Science IV** (Am. Inst. Phy., 1989).

FIGURE CAPTION

Fig. 1 Parametric representation of ERa and ERb Raman Energy conversion L22P18.
Fig. 2 Parametric plot of ERb and Uc.
Fig. 3 Two-dimensional animation of the fields (ERa, ERb) and Uc with respect to η for simulation L22P18.
Fig. 4 Fluence ψ plots for the Pump and Stokes Field for calculation L22P11.
Fig. 5 Three-dimensional Pump and Stokes Area θ and output power O for simulation L22P11.
Fig. 6 Comparison composite for on-axis pump and Stokes energies: graph a L22P21 and graph b L22P24.
Fig. 7 Comparison of Pump OPOWRa and Stokes output power.
Fig. 8 Detailed evolution over η of the on-axis EIz, EIb and Vc in two-dimensional plots versus τ to quality the phase effects.
Fig. 9 Three-dimensional evolution of EIa, EIb and Uc.
Fig. 10 Detailed evolution over η of the on-axis ERa, ERb and Uc in two-dimensional plots versus τ.
Fig. 11 Three-dimensional plots of the field ERa, ERb and material Uc in which ERa=ERb=Vc=0 for all ρ,η and τ variables in the absence of phase and transverse effects.
Fig. 12 Three-dimensional plots of the pump and Stokes soliton of the output power.
Fig. 13 Contrast of the on-axis energy and the radially-integrated energy to substantiate the contribution of the diffraction.
Fig. 14 Three-dimensional plots of the transverse energy current for each pump and Stokes pulses.

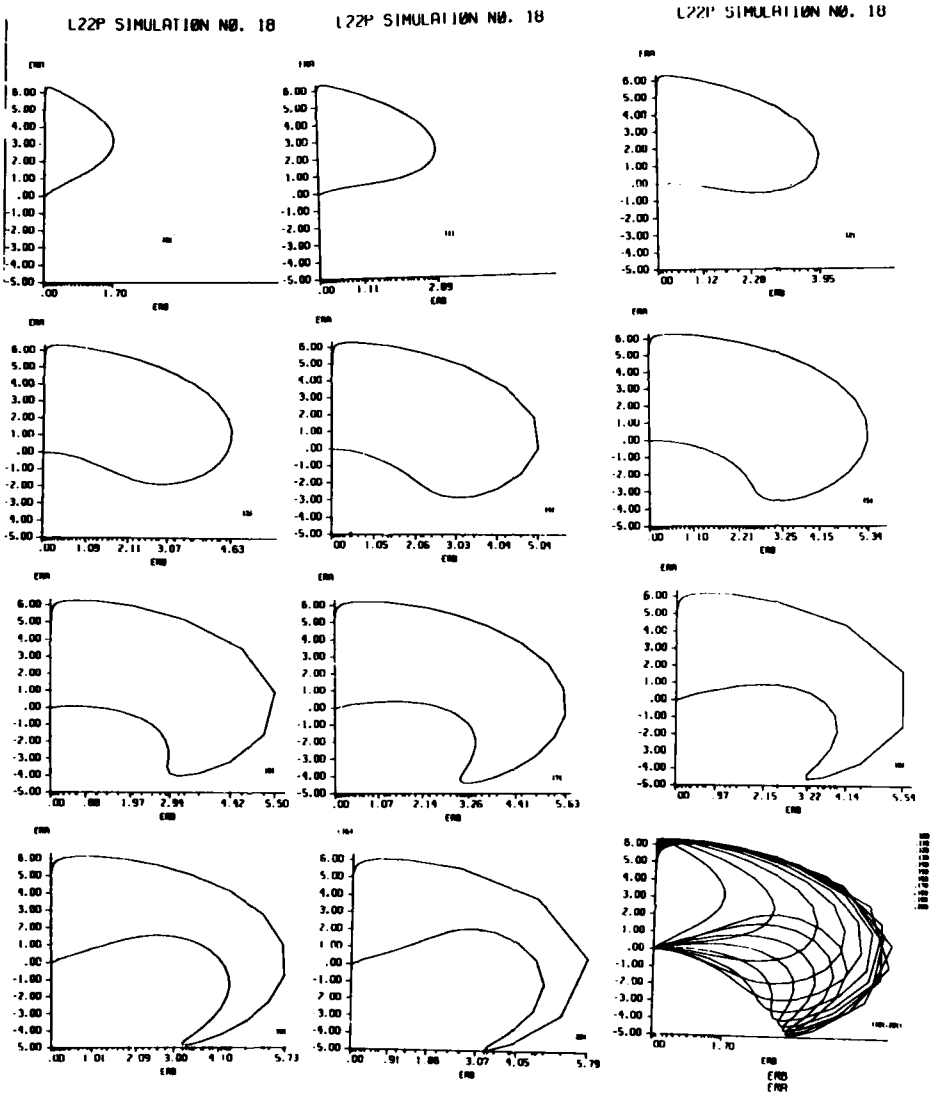

PHASE DIAGRAMS FOR THE UNI-DIMENSIONAL PLANAR NONLINEAR CALCULATION

L22P SIMULATION NO. 18

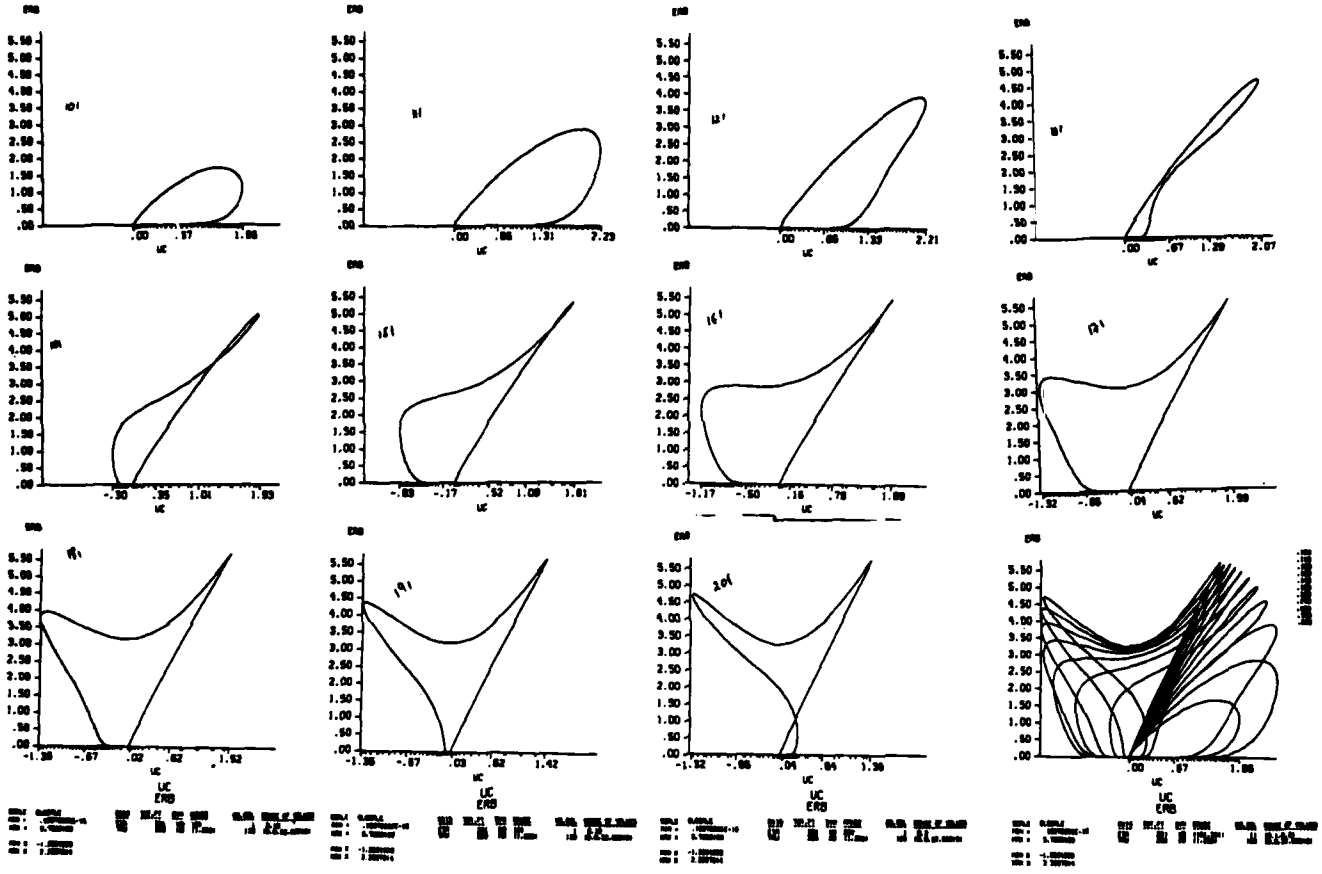

L22P SIMULATION NO. 18

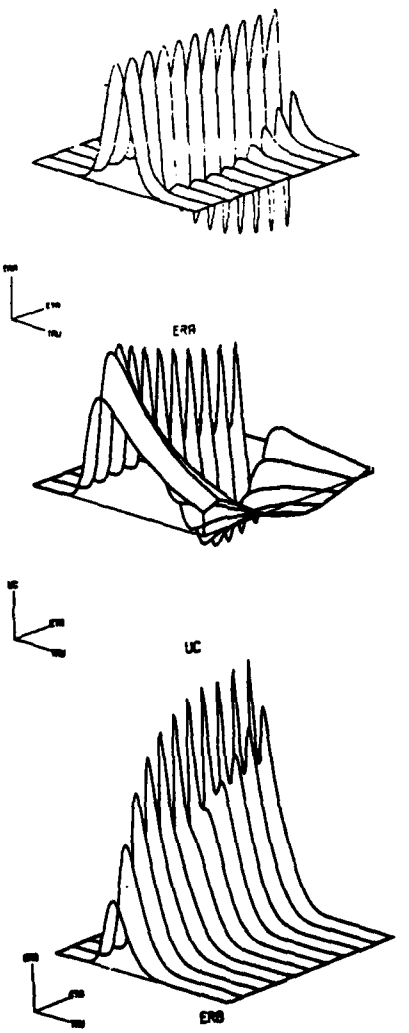

L22P SIMULATION NO. 11

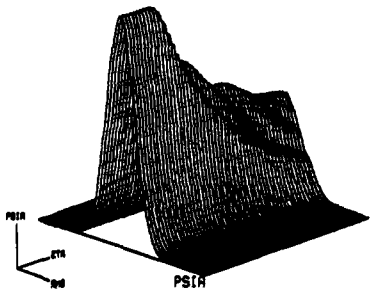

L22P SIMULATION NO. 11

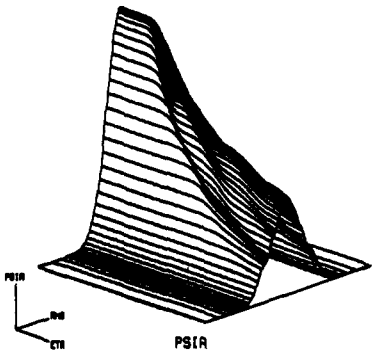

L22P SIMULATION NO. 11

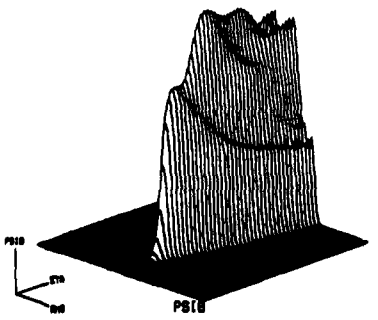

L22P SIMULATION NO. 11

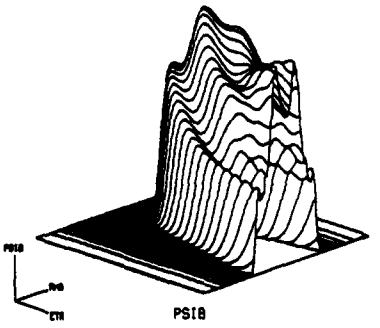

L22P SIMULATION NO. 11

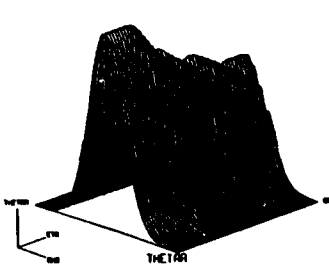

L22P SIMULATION NO. 11

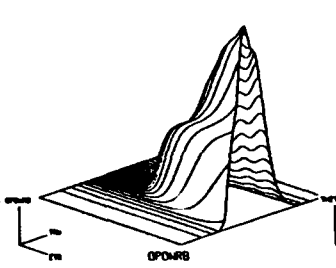

L22P SIMULATION NO. 11

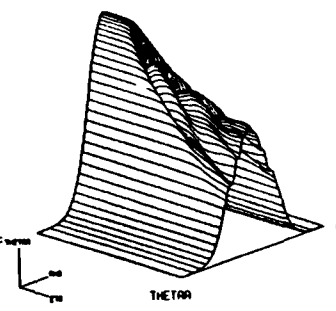

L22P SIMULATION NO. 11

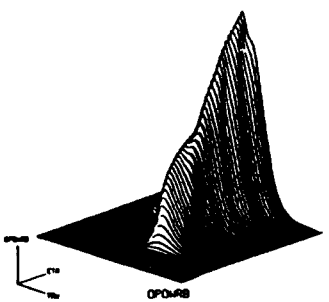

L22P SIMULATION NO. 11

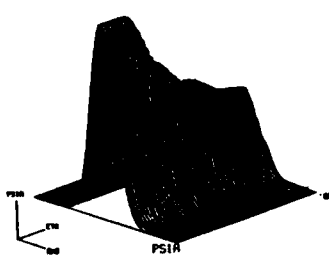

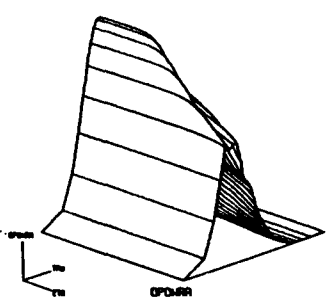

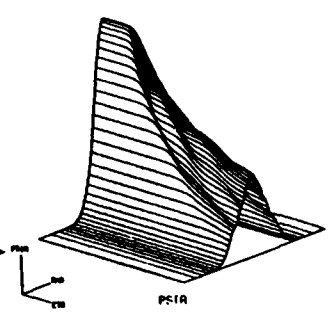

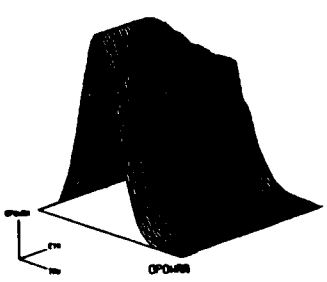

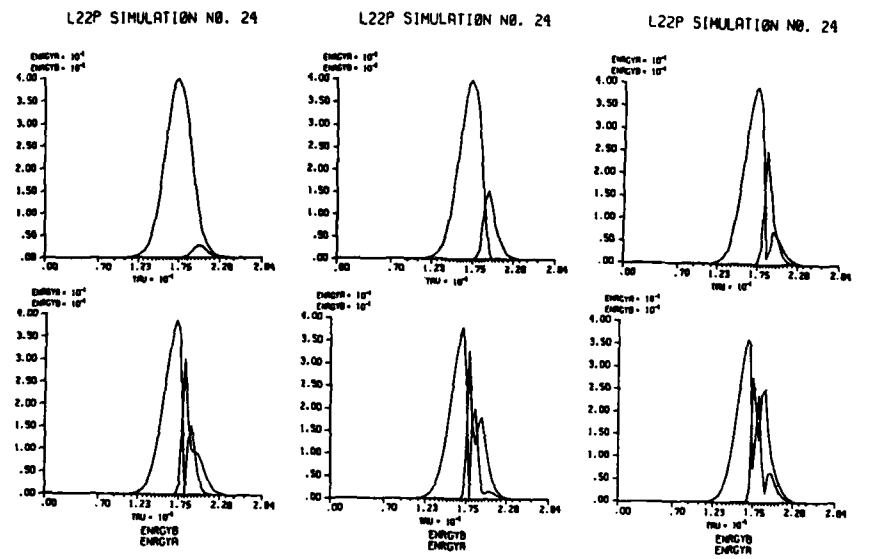
L22P SIMULATIØN NØ. 24
L22P SIMULATIØN NØ. 24
L22P SIMULATIØN NØ. 24
ENRGYB
ENRGYA
ENRGYB
ENRGYA
ENRGYB
ENRGYA

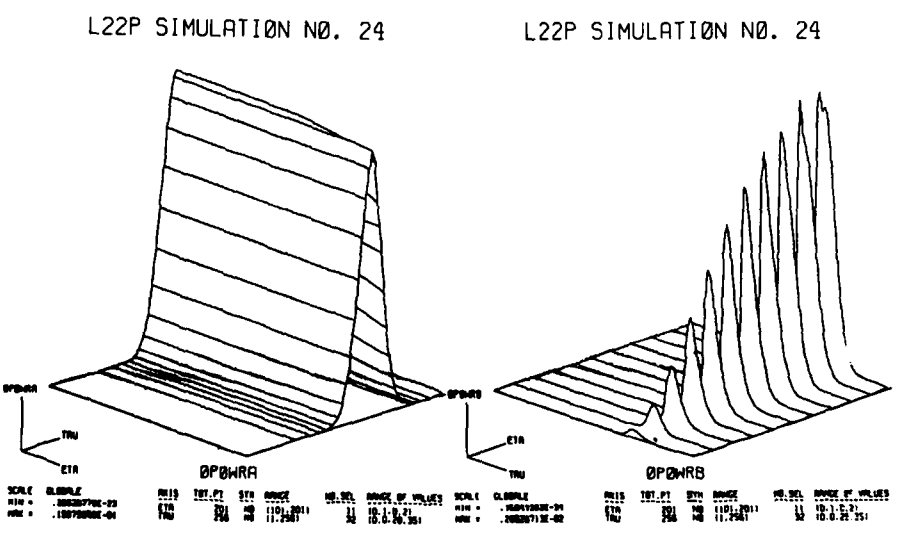
L22P SIMULATIØN NØ. 24
L22P SIMULATIØN NØ. 24
TAU
ETA
ØPØWRA
ETA
TAU
ØPØWRB

L22P SIMULATION NO. 24

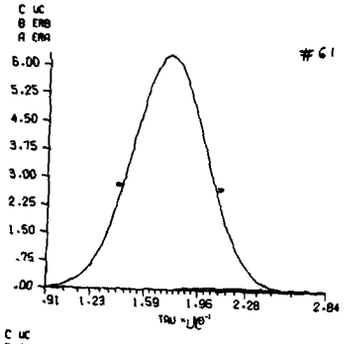

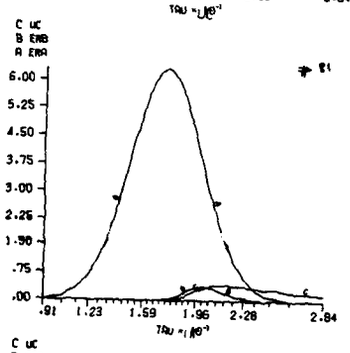

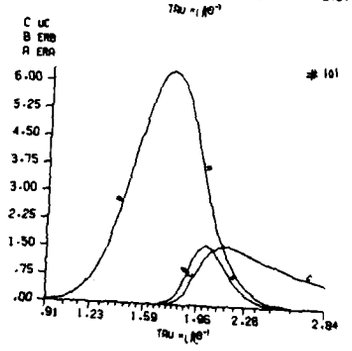

L22P SIMULATION NO. 24

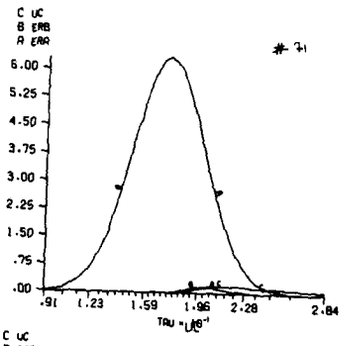

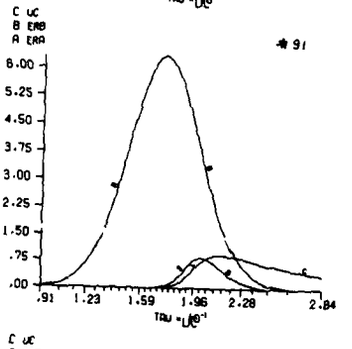

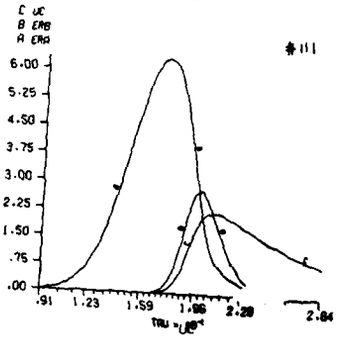

L22P SIMULATIØN NØ. 21

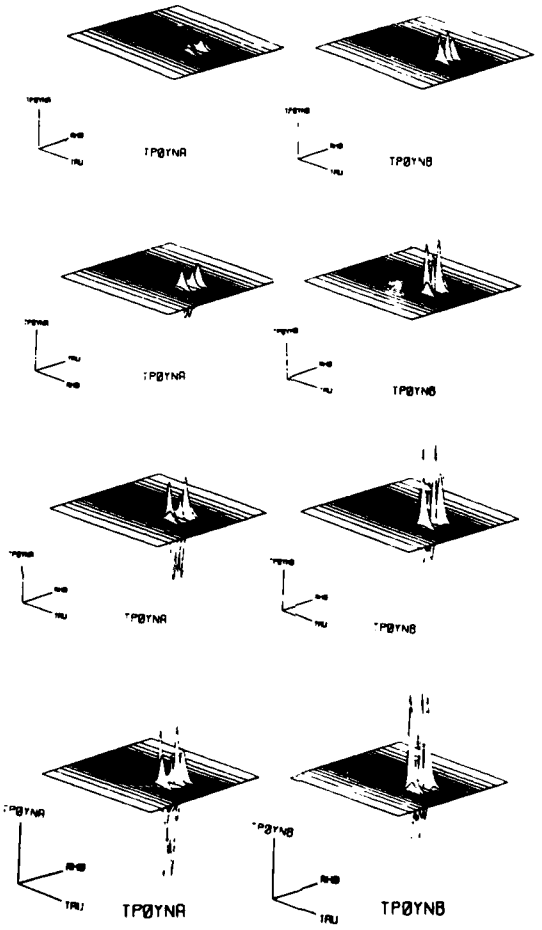

L22P SIMULATION NO. 24

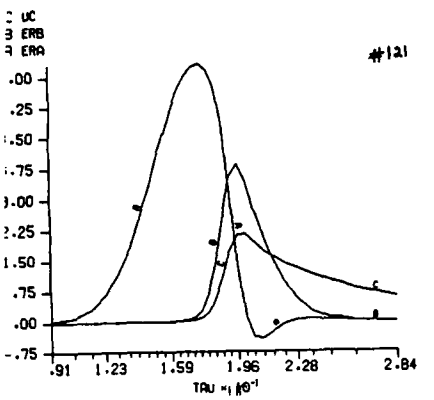

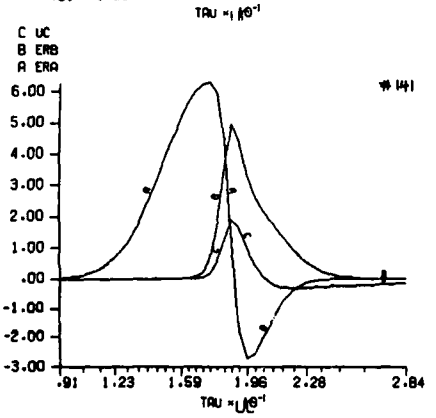

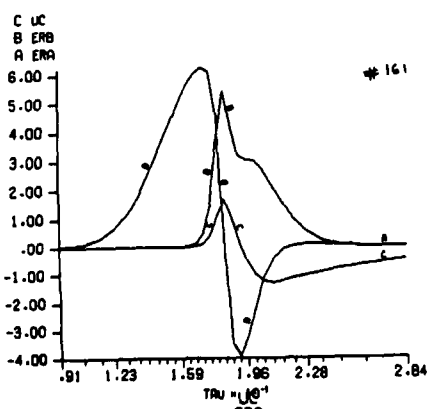

L22P SIMULATION NO. 24

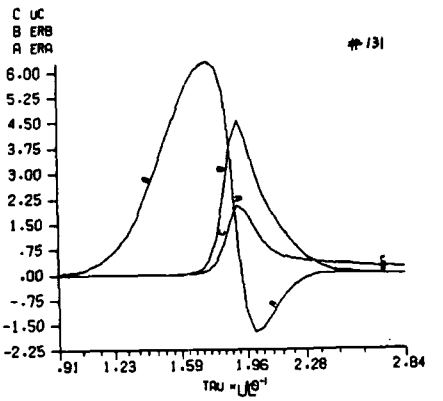

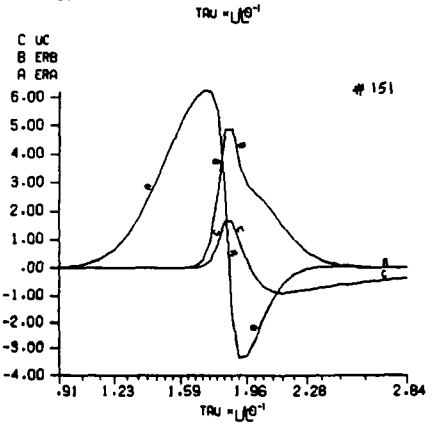

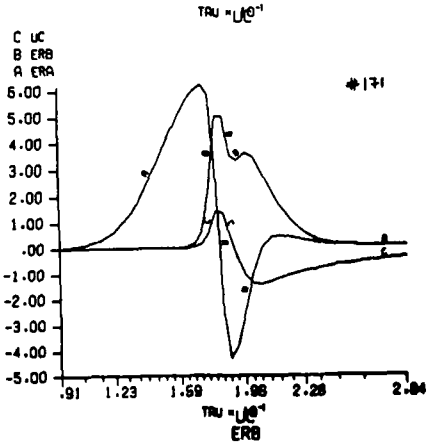

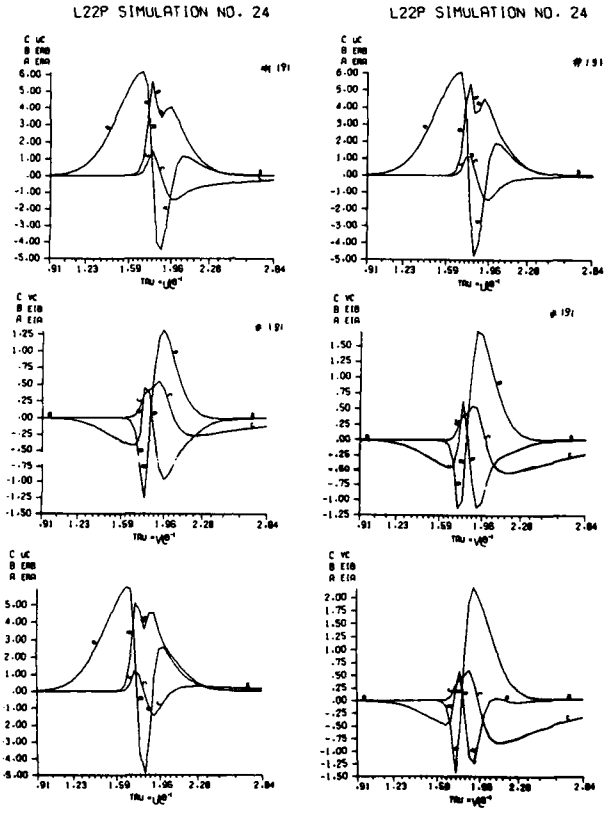
L22P SIMULATION NO. 24
L22P SIMULATION NO. 24

L22P SIMULATION NO. 24

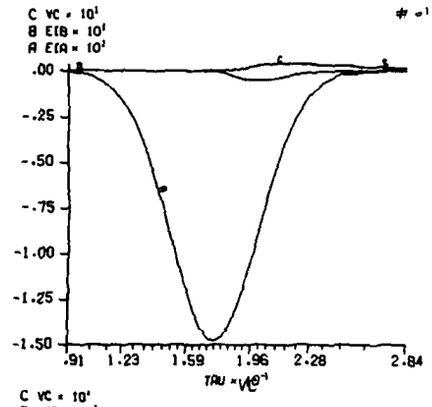

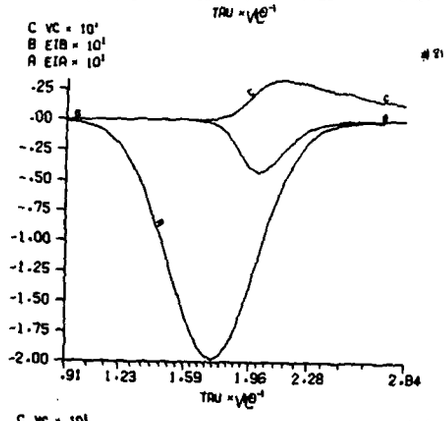

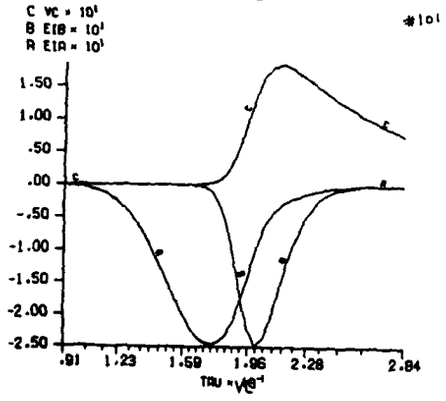

L22P SIMULATION NO. 24

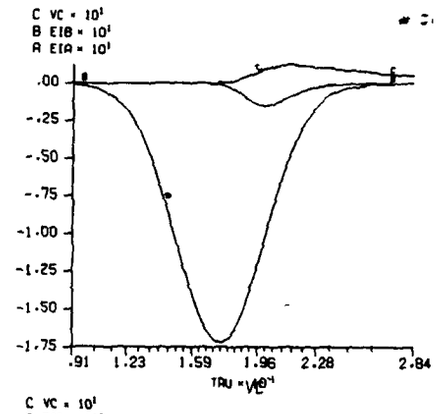

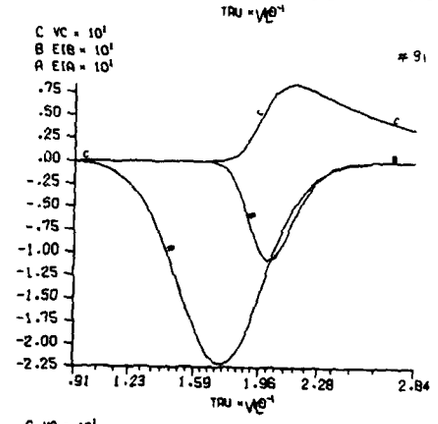

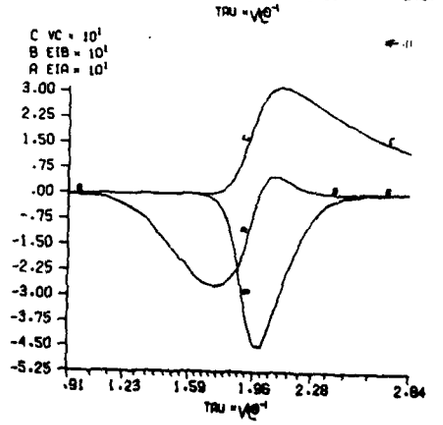

L22P SIMULATION NO. 24

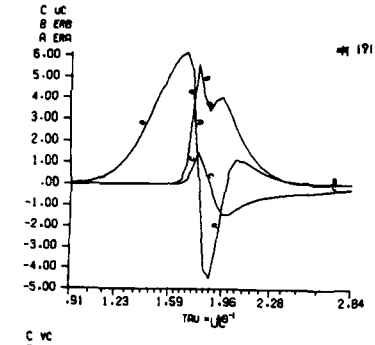

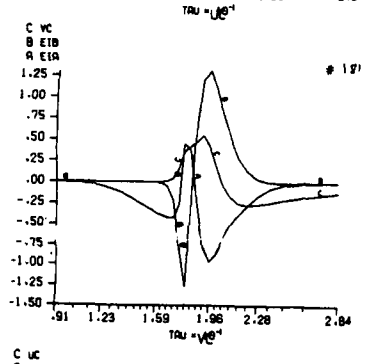

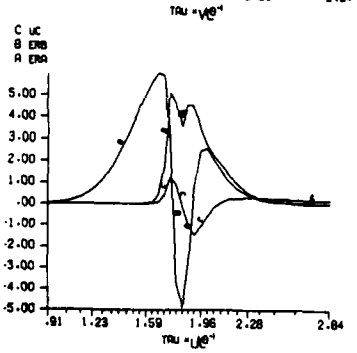

L22P SIMULATION NO. 24

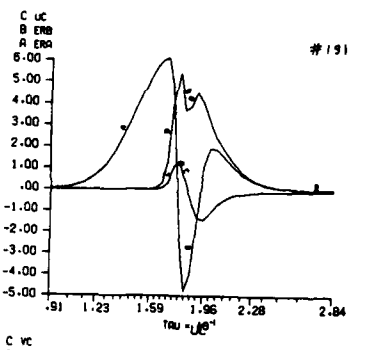

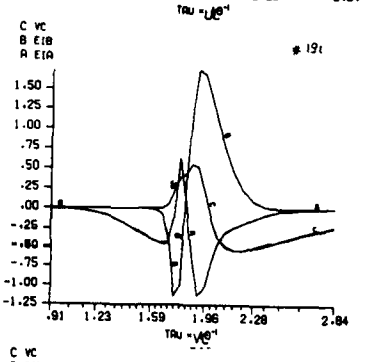

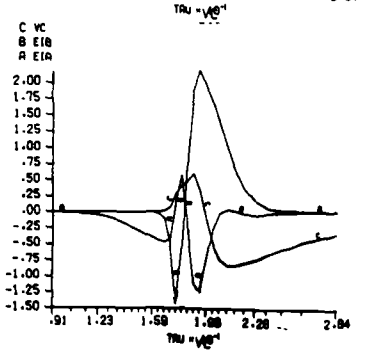

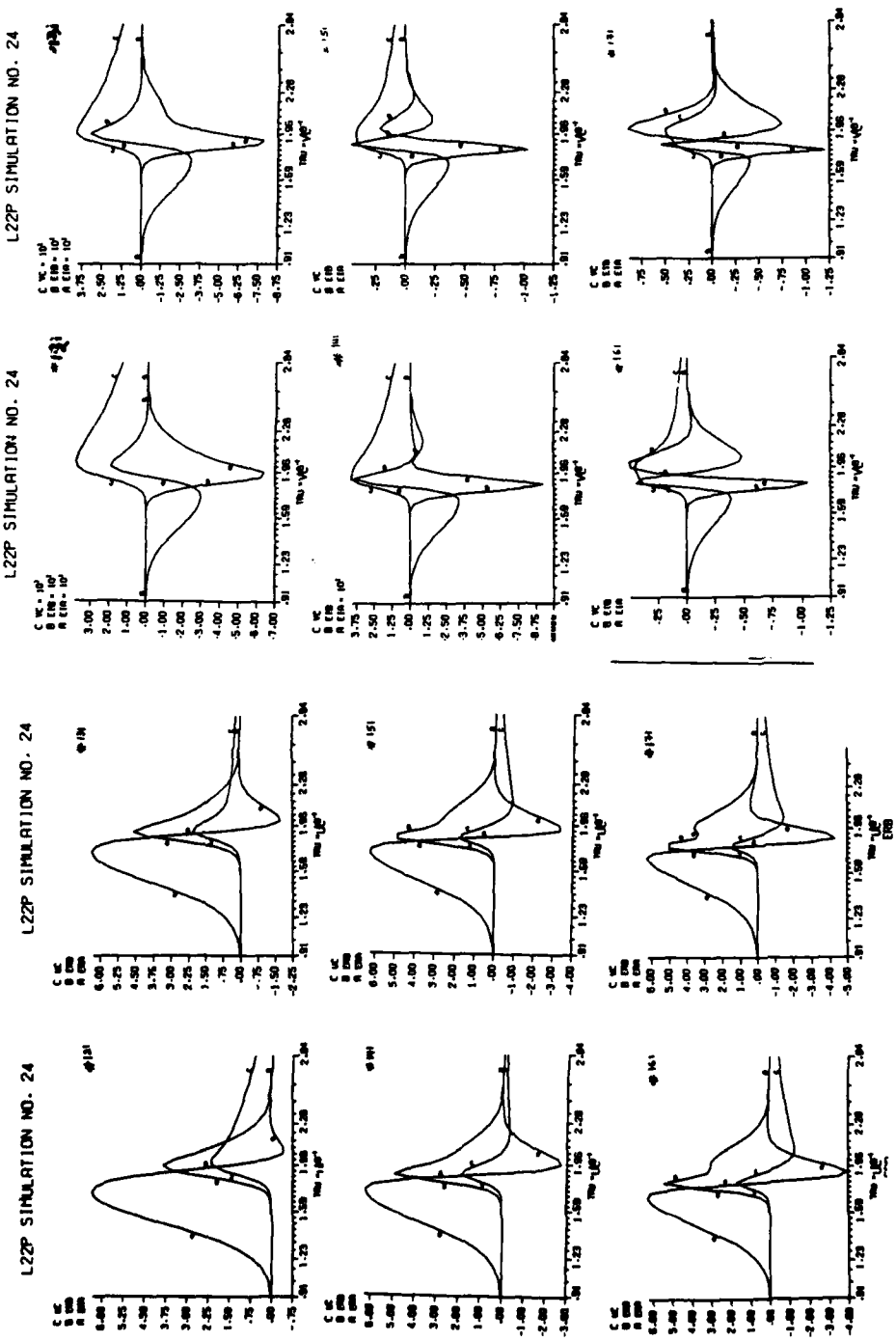
L22P SIMULATION NO. 24
L22P SIMULATION NO. 24
L22P SIMULATION NO. 24
L22P SIMULATION NO. 24

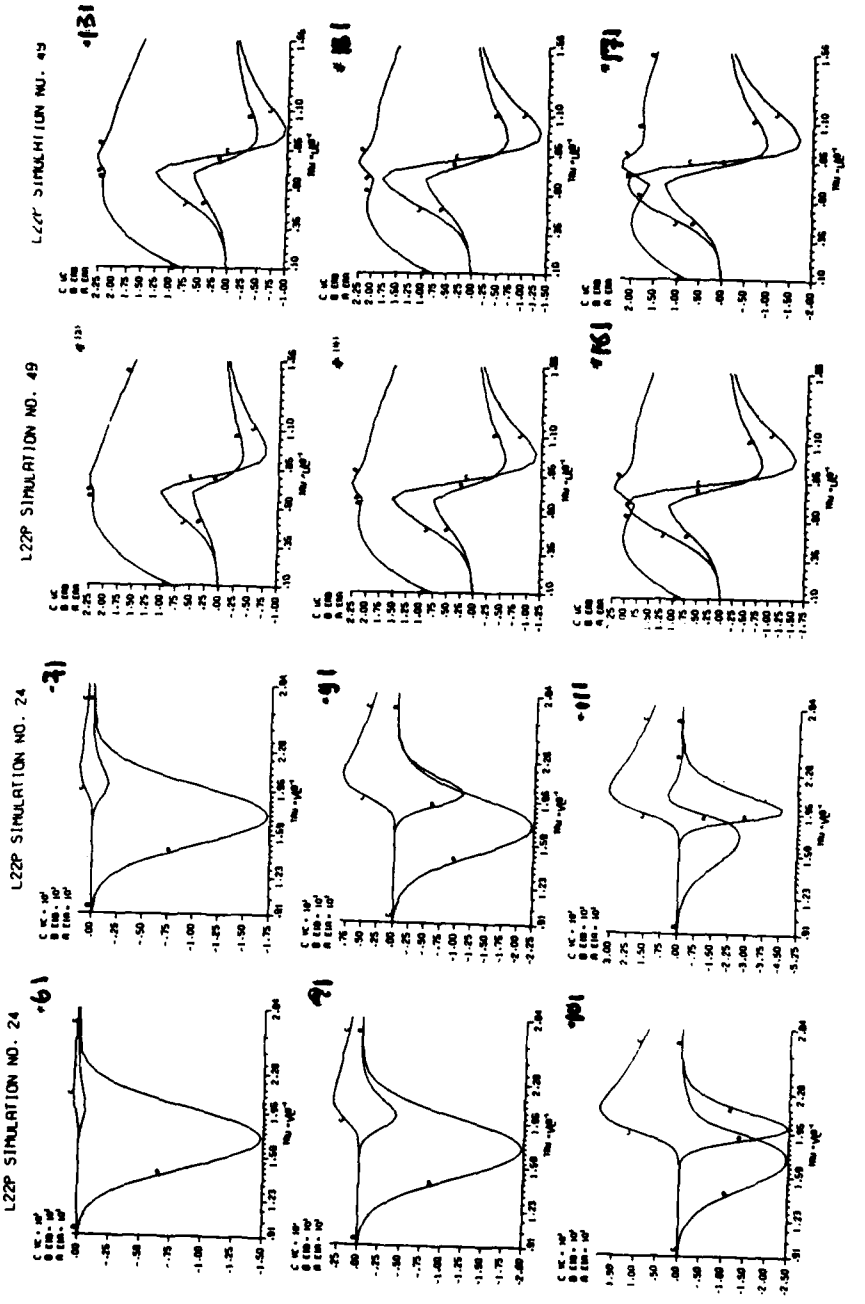
L22P SIMULATION NO. 49
L22P SIMULATION NO. 49
L22P SIMULATION NO. 24
L22P SIMULATION NO. 24

L22P SIMULATION NO. 21

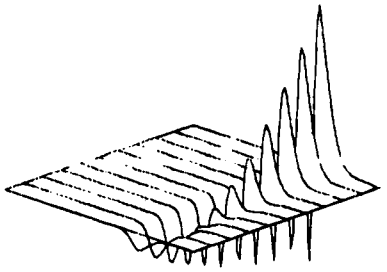

CIB

L22P SIMULATION NO. 21

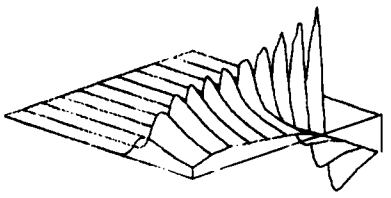

VC

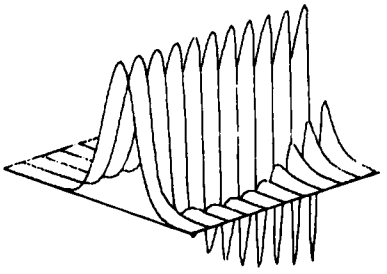

ERR

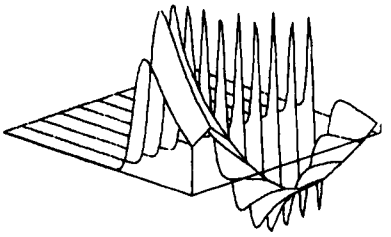

UC

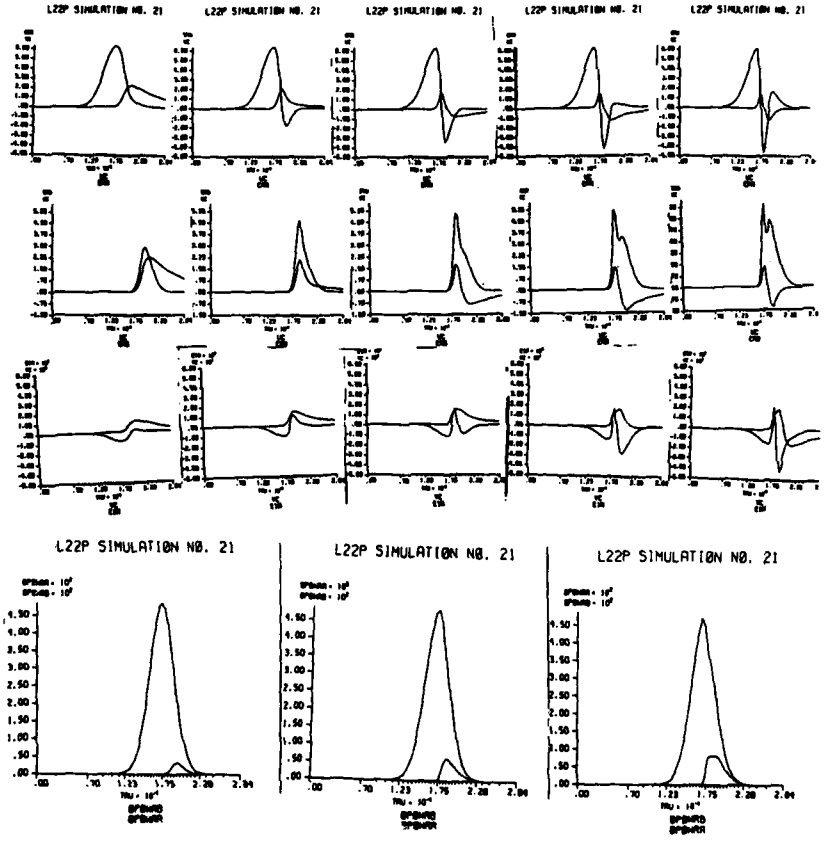
L22P SIMULATION NO. 21
L22P SIMULATION NO. 21
L22P SIMULATION NO. 21
L22P SIMULATION NO. 21
L22P SIMULATION NO. 21
L22P SIMULATION NO. 21
L22P SIMULATION NO. 21
L22P SIMULATION NO. 21

TRANSVERSE EFFECTS IN TRANSIENT STIMULATED RAMAN SCATTERING IN PUMP LASER DEPLETION

J. Teichmann*, Y. Claude*, M. Burgess** and F.P. Mattar**
Department de Physique, Université de Montreal*, Montreal, Canada and Physics Department, New York University**, New York and Electrical Engineering Department, City College of New York**, New York

ABSTRACT

Perturbative treatment of diffraction coupling onto the Raman soliton evolution is reported here. The evolution of self- and cross-phase modulation is established in a single-pass cell.

I. INTRODUCTION

The transient Stimulated Raman Scattering (SRS) has been extensively studied in the past[1-4]. However theoretical analysis of co-propagation of pulses in three-level system[5,6] and in Raman medium [6] has been limited essentially to a one-dimensional approximation. A semi-classical formulism introduced by McCall and Hahn[7] to describe the Self-Induced-Transparency phenomenon is adopted. A three-dimensional description of the Stimulated Raman Scattering was done recently in the linearized regime[8] in view of the influence of the large Fresnel numbers on the energy depletion of the Stokes pulses. Nevertheless this theory assumes that the pump field E_L is constant over the cross-section of the beam and constant in time.

In our earlier analyses of the Self-Induced-Transparency SIT, we have found[9] that transverse effects - diffraction and nonlinear pulse compression are rather important in formation of pulse shape. These effects depend critically on the transverse energy distribution of propagating optical pulses.

In the present study we developed a simple perturbation theory, based on an approach used in the study of cw propagation of intense laser in saturable two-level absorber[10] and of simulton propagation [11] where similar transverse effects take place.

II. PHYSICAL MODEL

Assuming a homogeneously broadened vibrational line shape under which the system of coupled differential equations are transient Stimulated Raman Scattering in the form[12] complement a transverse Laplacian:

$$\frac{\partial}{\partial \tau} Q = - \Gamma Q + i \kappa_1 E_L E_S^* \tag{1a}$$

$$\frac{\partial}{\partial \eta} E_S - i f_S \nabla_T^2 E_S = i \kappa_2 E_L Q^* \tag{1b}$$

$$\frac{\partial}{\partial \eta} E_L - i f_L \nabla_T^2 E_L = -i \kappa_3 E_S Q \tag{1c}$$

In these equations, the laser pump field(E_L) and the Stokes field(E_S) are assumed to be monochromatic. Coupling to anti-Stokes and to higher order states modes is ignored. The population difference between the initial & final vibrational Stokes is assumed to be equal & constant.

The equations (1) are written in the usual slowly varying envelope approximation (SVEA) in the local retarded time $\tau = t - (n/c)z$ (2a). The wave propagates in the z direction (η=z). The radial variation is described by the normalized coordinate $\rho = r/r_o$ (2b), with r_o being the transverse waist of the beam.

Supported by ARO, AFOSR, ONR and NSF at NYU

The quantities f_S and f_L are the reciprocal Fresnel numbers $f_{S,L}=\lambda_{S,L}\ell/\pi r_o^2$ (3). The term $\Gamma=1/T$ (4) represents the collisional damping with the relaxation time T, $\kappa_1 = \Lambda/2\omega_L$ (5a), $\kappa_2 = 2\pi\Lambda\omega_S/cm$ (5b), $\kappa_3 = 2\pi\Lambda\omega_L/cm$ (5c), with Λ being the coupling constant, $\Lambda = N\frac{\partial\alpha}{\partial Q}$ (6), where N is the molecular number density and $\frac{\partial\alpha}{\partial Q}$, is the rate of change of the molecular polarizability with the vibrational coordinate Q.

III. EQUATIONS OF MOTION

In the hypertransient limit $\Gamma = 0$. For large Fresnel numbers $f_S = f_L = f << 1$ we can develop the field amplitudes and the vibrational coordinate in series in f:

$$E_{L,S}(\eta,\rho,\tau) = E_{Lo,So}(\eta,\rho,\tau)+ifE_{L1,S1}(\eta,\rho,\tau)+f^2E_{L2,S2}(\eta,\rho,\tau) + \ldots \quad (7a)$$

$$Q(\eta,\rho,\tau) = iQ_o(\eta,\rho,\tau) + fQ_1(\eta,\rho,\tau) + if^2Q_2(\eta,\rho,\tau) + \ldots \quad (7b)$$

The zeroth-order system takes the form

$$\frac{\partial}{\partial\tau} Q_o = \kappa_1 E_{Lo}E_{So}^* \quad (8a)$$

$$\frac{\partial}{\partial\eta} E_{So} = \kappa_2 E_{Lo}Q_o^* \quad (8b)$$

$$\frac{\partial}{\partial\eta} E_{Lo} = -\kappa_3 E_{So}Q_o \quad (8c)$$

subjected to

$$\frac{\partial}{\partial\eta} |E_{So}|^2 + [\kappa_2/\kappa_3]\frac{\partial}{\partial\eta} |E_{Lo}|^2 = 0 \quad (8d)$$

Generalizing Drühl et al's.[13] radially-independent solitary solution to (8) we can write a single soliton solution to (7):

$$Q_o = A\,\mathrm{sech}\,K\xi \ (9a), \quad E_{Lo} = B\,\mathrm{sech}\,K\xi \ (9b), \quad E_{So} = C\tanh K\xi \ (9c)$$

where $\xi=\tau-\lambda\eta$(10a), $\Lambda=1/v_p-n/c$(10b), v_p being the propagation speed of the pulses in the laboratory frame of reference. Then $A=-\frac{\Lambda K}{\sqrt{\kappa_2\kappa_3}}$ (11a), $B=\frac{K\sqrt{\Lambda}}{\sqrt{\kappa_1/\kappa_2}}$ (11b), $C=\frac{K\sqrt{\Lambda}}{\sqrt{\kappa_1\kappa_3}}$ (11c). The parameter $K(\rho)$ is determined from the initial conditions. For $\kappa_2 = \kappa_3$ one has $B = C$ thus $|E_{Lo}|^2+|E_{So}|^2 = B^2[\mathrm{sech}^2K\xi+\tanh^2K\xi] = B^2$ = constant, the energy is conserved.

The first-order system

$$\frac{\partial}{\partial T} Q_1 = \kappa_1(E_{Lo}E_{S1}^* - E_{L1}E_{So}^*) \quad (12a)$$

$$\frac{\partial}{\partial\eta} E_{S1} = \nabla_T^2 E_{So} + \kappa_2(E_{Lo}Q_1^* + E_{L1}Q_o^*) \quad (12b)$$

$$\frac{\partial}{\partial\eta} E_{L1} = \nabla_T^2 E_{Lo} + \kappa_3(E_{So}Q_1 - E_{S1}Q_o) \quad (12c)$$

can be solved by iterations[14].

IV. PERTURBATIONAL ANALYSIS RESULTS

We assume that the laser pump has initially a Gaussian/super-Gaussian transverse profile in the field amplitude and a reciprocal Gaussian/superGaussian variation of the pulse length.

The first iterates for the pump $\hat{E}_{L1}$ and Stokes $\hat{E}_{S1}$ amplitudes represent the "free space" Fresnel diffraction and are obtained from the linearized system (5):

$$\hat{E}_{S1} = \int d\eta \ \nabla_T^2 E_{So} \quad (13a); \quad \hat{E}_{L1} = \int d\eta \ \nabla_T^2 E_{Lo} \quad (13b)$$

using these approximations, we may construct the next iterates to obtain

$$Q_1 = \kappa_1 \int d\tau \ \{ - E_{Lo} \int d\eta \ \nabla_T^2 E_{So} + E_{So} \int d\eta \ \nabla_T^2 E_{Lo}\} \quad (14a)$$

$$E_{S1} = \hat{E}_{S1} + \kappa_2 \int d\eta \ \{E_{Lo} \kappa_1 \int d\tau [- E_{Lo} \int d\eta \ \nabla_T^2 E_{So} + E_{So} \int d\eta \ \nabla_T^2 E_{Lo}] - Q_o \int d\eta \ \nabla_T^2 E_{Lo}\} \quad (14b)$$

$$E_{L1} = \hat{E}_{L1} + \kappa_3 \int d\eta \ \{E_{So} \kappa_1 \int d\tau [- E_{Lo} \int d\eta \ \nabla_T^2 E_{So} + E_{So} \int d\eta \ \nabla_T^2 E_{Lo}] - Q_o \int d\eta \ \nabla_T^2 E_{So}\} \quad (14c)$$

Higher order iterates and higher order terms E_{L2}, E_{S2} and Q_2 in the parameter f for the fields E_L and E_S and Q amplitudes can be obtained in the same way.

VI. ROLE OF INPUT TRANSVERSE PROFILE

We have plotted the lowest order perturbations of the pump field ($\hat{E}_{L1}$) and the Stokes field ($\hat{E}_{S1}$) in Figs. 1,2 for the Gaussian radial distribution. The evolution of the $\hat{E}_{L1}$ profile shows typical diffraction patterns for the soliton sech($K\xi$) pulse. For the Stokes and pump fields, rapid variations of phase take place in the wings (ρ~1) where radial energy flows occur. The total energy of the pump pulse shows concentration of the energy into the wing area and, more significantly, enhancement in the central region of the pulse. For the Stokes mode, the focusing of energy into the wing area is dominant.

For beams, having steeper radial dependence at the wing ~$\exp(-\rho^n)$, $n > 2$ than the Gaussian, no perturbation occurs at the axis (ρ=0). However the phase variations and radial energy flows in the wing area is much more enhanced. The critical dependence of radial variations of the perturbations on the initial radial pump profile was computed. The first order perturbations and total energy distribution for pump and Stokes pulses are calculated for initially super-Gaussian pulse profiles, (n=4). Figure 3 shows the increase of perturbation activity with increasing reciprocal Fresnel numbers.

Diffraction induced phase profiles are represented in Fig. 4 for the initially Gaussian pump.

VII. CONCLUSION

We have calculated diffraction effect on coherent Raman soliton evolution. Expressions for the onset of self-phase modulation have been obtained for Gaussian and superGaussian profiles. Even in a perturbational analysis, strong departure from the uniform-plane-wave soliton solutions are found. Rigorous diffraction computation need to be addressed as well as local field correction[14-18] for dense media.

REFERENCES

1. R.L. Carman et al., Phys. Rev. A2, 60 (1970).
2. M. Maier et al., Phys.Rev. 177, 580 (1969).
3. A. Akhmanov et al., IEEE J. Quantum Electron QE-4, 598 (1968).
4. M.G. Raymer & J. Mostowski, Phys. Rev. A28, 1980 (1981).
5. M.J. Konopnicki & J.H. Eberly, Phys. Rev. A24, 2567 (1981).
6. B.J. Herman et al., Phys. Rev. A30, 2462 (1984).
7. S.L. McCall & E.L. Hahn, Phys. Rev. 183, 457 (1969).
8. (a) J. Mostowski & B. Sobolewska, Phys. Rev. 30A, 610 (1984); and (b) M.G. Raymer et al., Phys. Rev. A32, 332 (1985).
9. (a) M.C. Newstein & N. Wright, IEEE J. Quantum Electron QE-10, 743 (1974); (b) F.P. Mattar & M.C. Newstein, Opt. Commun. 18, 70 (1976); IEEE J. Quantum Electron QE-13, 507 (1977), and in **Cooperative Effects in Matter and Radiation**, ed. C.M. Bowden, D.W. Howgate & H.R. Robl (Plenum, 1977) pp. 139-191; and (c) F.P. Mattar et al., in **Coherence and Quantum Optics IV**, ed. L. Mandel & E. Wolf (Plenum, 1978) pp. 143-164.
10. (a) M.LeBerre et al., Phys.Rev. A25, 1604 (1982); (b) M. LeBerre et al., SPIE 369, 269-274 (1983); (c) M.LeBerre et al., in **Coherence and Quantum Optics V**, ed. L. Mandel & E. Wolf (Plenum, 1984) pp. 347-353; (d) M. LeBerre et al., Phys. Rev. A29, 2669 (1984); & (e) J. Teichmann et al., Opt. Commun. 54, 33 (1985).
11. (a) F.P.Mattar, Final Report to ONR-Physics Contract N000-14-80-C-0174, Tech.Rept.M/AE 83- 84, Polytechnic Inst. of NY (b)J. Teichmann & F.P.Mattar ILS-III paper #WO7, Bull.Am.Phys.Soc. 32, 1644(1987); in **Advances in Laser Science-III**, ed. A.C.Tam, J.L. Gole & W.C.Stwalley, (AIP, 1988) pp. 548-553; & (c) J.Teichmann, CAP-APS Congress, paper #PK6 Bull.Amer.Phys.Soc. 33, 1240 (1988).
12. S.M. George & C.B. Harris, Phys. Rev. A 28, 863 (1983).
13. (a) J.L.Carlsten et al., SPIE 380, 201-207 (1983); (b) K.J.Drühl et al., Phys.Rev.Lett. 51, 1171 (1983); (c) J.L.Carlsten et al., **Proc.Intern.Conf.Lasers '84**, 144 (1984); (d) K.J.Drühl et al., J. Stat.Phys. 39, 615 (1986); & (e) R.G.Wenzel et al., J.Stat.Phys. 39, 621 (1986).
14. H.A. Lorentz, **Theory of Electrons**, reprinted (Dover, 1952)
15. J. Marburger, L. Huff, J.D. Reichert & W.G. Wagner, Phys. Rev. 184, 255 (1969).
16. [a] R. Friedberg, S.R. Hartmann & J.T. Manassah, Phys. Lett. 35A, 161 (1971), ibid 40A, 395 (1972) & Phys. Report 7C, 101-179 (1973); [b] J.T. Manassah, Phys. Report 101, 359-427 (1983); [c] R. Friedberg, S.R. Hartmann & J.T. Manassah, Phys. Rev. A39, 93 & 3444 (1989); and [d] J.T. Manassah, Phys. Rept. 101, 359-427.
17. [a] F.A. Hopf, C.M. Bowden & W.H. Louisell, Phys. Rev. A29, 2591 (1983); [b] in **Optical Bistability II**, ed. C.M. Bowden, H.M. Gibbs & S.L. McCall (Plenum Press, 1984) pp. 361-368; and [c] in **Optical Instabilities**, ed. R.W. Boyd, M.G.Raymer & L.M. Narducci (Cambridge University Press, 1986) pp. 308-311.
18. J.T. Manassah & F.P. Mattar, in Proc. Intl. Laser Sci. ILS-IV, **Advances in Laser Science IV** (Am. Inst. Phy., 1989).

FIGURE CAPTIONS

Fig. 1. First order pump field amplitude E_{L1} $(K\xi,\rho)$.

Fig. 2. First order Stokes field amplitude E_{S1} $(K\xi,\rho)$.

Fig. 3. Total intensity in the pump & Stokes pulses. p=0.002. $p=(\frac{16f}{r})^2$

Fig. 4. Diffraction induced phase variation ϕ_L^g for the pump field E_L^{pg} with a Gaussian profile for $K(\rho)$.

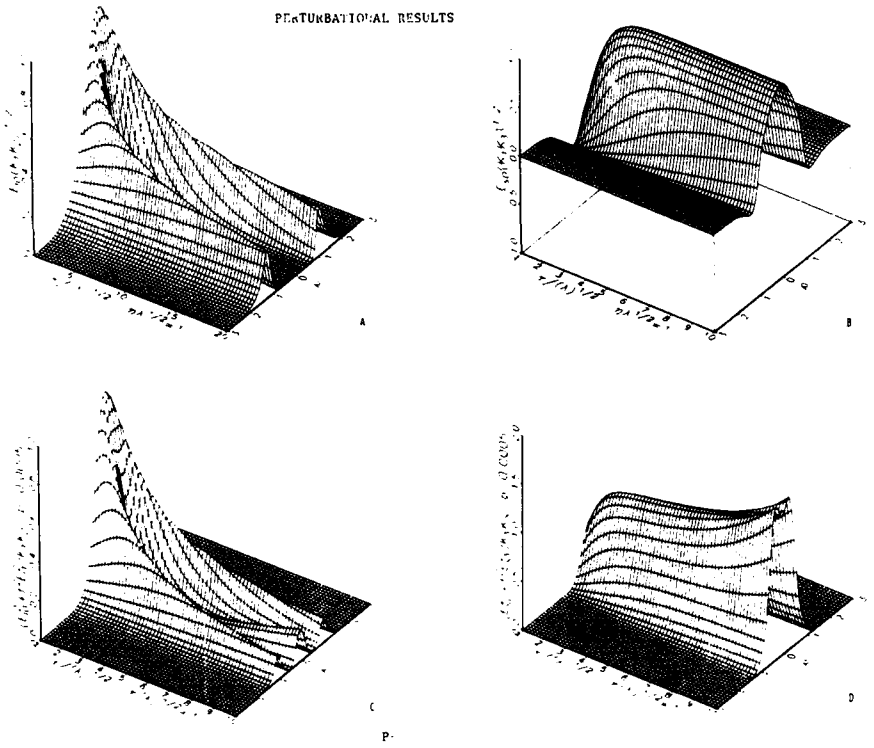
A
B
C
D

L22P SIMULATION NO. 2

RIGOROUS COMPUTATIONAL RESULTS

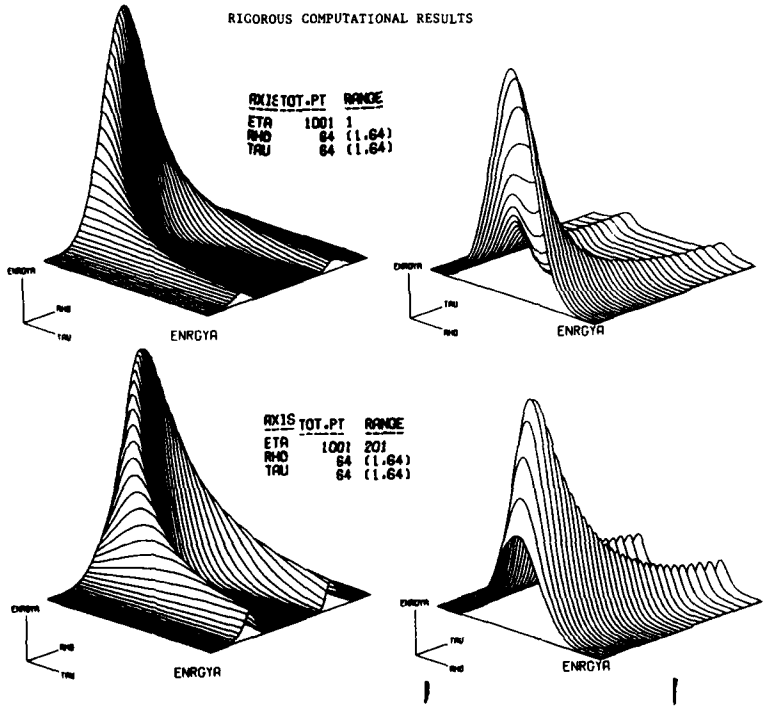

PERTURBATIONAL RESULTS

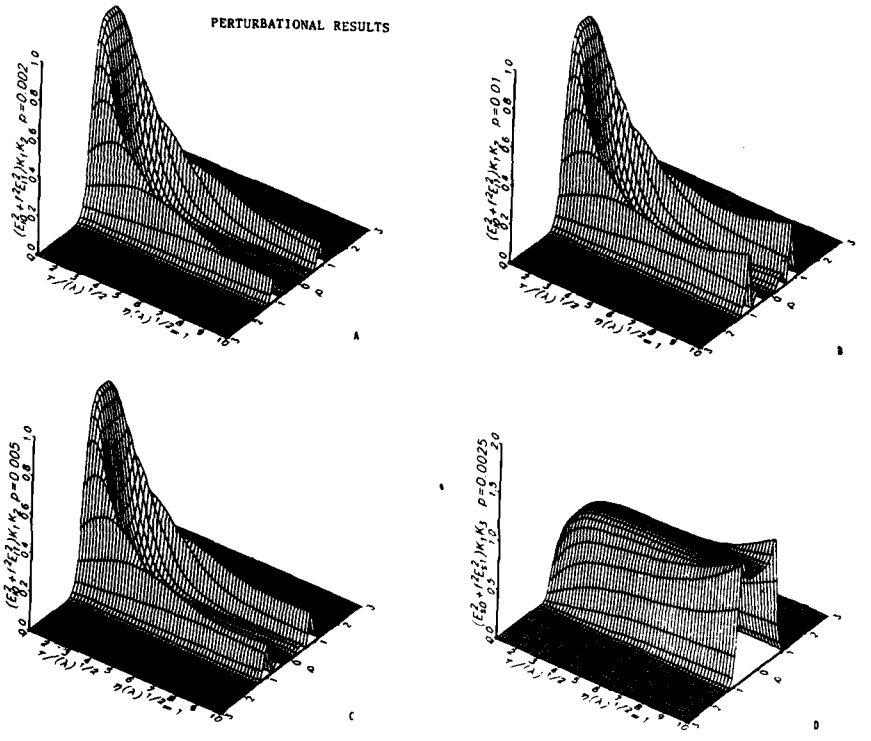

PERTURBATIONAL RESULTS

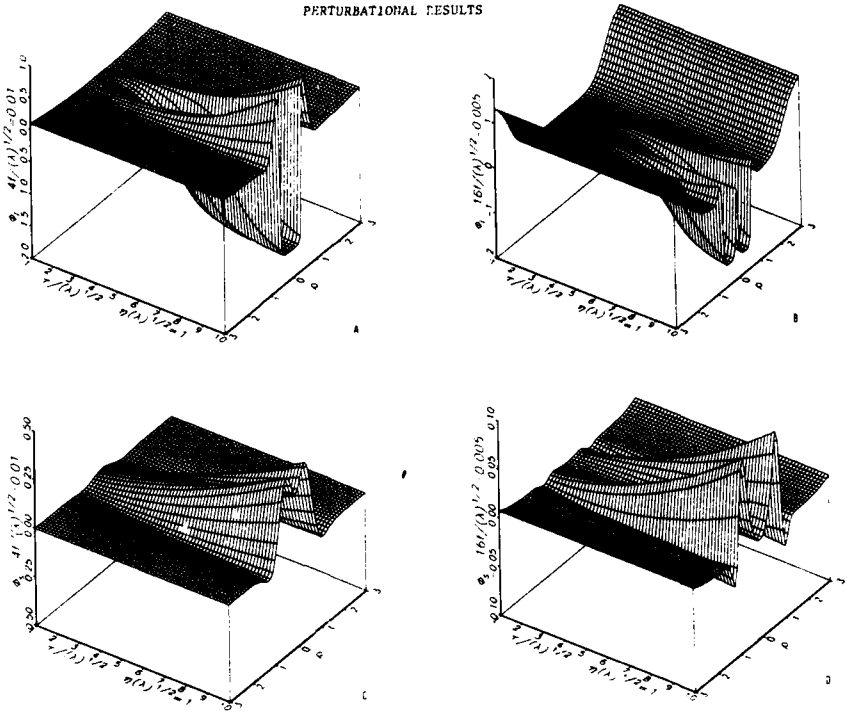

QUANTUM AND NONLINEAR THEORY OF STIMULATED RAMAN SCATTERING (SRS)

F.P. Mattar*, Y. Claude*, M. Burgess* and J. Teichmann#
Department of Physics*, New York University, New York, NY 10003 and
Department of Electrical Engineering, City College of New York,
New York, NY 10031; and
Departement de Physique#, Université de Montreal, Montreal, Canada

ABSTRACT

Experimental studies of spatial and temporal coherence of SRS in hydrogen[1] have pointed out the need of a quantum theory in the nonlinear regime. Previous studies have dealt either with diffraction in a linearized regime[2] or with a nonlinear light-matter description in the uniform-plane-wave regime[3]. Both diffraction and nonlinear effects are examined herein. The Stokes pulse builds up from quantum initiation as does the superfluorescence SF emission[4]. The interplay of diffraction coupling, transverse variations of the atomic density and quantum fluctuations on the Stokes buildup was simulated using a self-consistant numerical algorithm[5] previously developed for finite beam effects in Self-Induced-Transparency[6,7].

I - INTRODUCTION

Stokes emission profiles are calculated using a one-way paraxial Maxwell-Bloch Raman computer code L22P©. Backward scattering is not included in the analysis. Transverse effects are included in the cylindrical-symmetry case. Even through our SF formulism[8] includes Cartesian treatment of diffraction and quantum fluctuations, we restrict our analysis of the Stokes evolution to the cylindrical geometry with azimuthal symmetry. This configuration is valid for small Fresnel numbers. Full three-spatial-dimension calculations are required for describing short-scale phase and magnitude fluctuation at the initiation process. In the large Fresnel number regime, multi-directional output emission with hot spots results. The Stokes field evolution resembles that of an SF emission. This analogy was first recognized by Raymer & Mostowski[1]. Mostowsky & Sobolewska[2] developed an analytical treatment. To maintain its tractability they had to linearize the matter description.

Stokes initiation from quantum fluctuations approximated by a random polarization source (in the effective two-level atomic system) with a completely random phase and root mean-square tipping angle of $2/\sqrt{N_i}$ where N_i is the number of atoms in each annular area and corresponds to N the number of atoms in each. As observed in SF observations and computations[4], the quantum fluctuations reduces the tail of the output pulses obtained with transverse effects alone with a seed for Stokes initiation. We make use of the methodology developed by Haake et al.[9] and Vrehen et al.[10] and Hopf[11] for studying the quantum initiation including propagation in the uniform-plane-wave regime. Quantum effects occur during the very beginning of the pulse evolution when the problem is still linear. During the later nonlinear evolution when the number of photons is sufficiently important that the dynamic description is accurately describable semi-classically. The quantum initiation is described by a statistical ensemble of trajectories with different initial conditions[8-13]. The initial Q has a magnitude which is a bivariate Gaussian distribution with rms value $2/\sqrt{N_i}$ and a random phase ϕ.

Supported by ARO,AFOSR*,ONR* & NSF* at NYU & NSERC# at U.de Montreal

This article is the first calculation of a Stokes emission in which quantum initiation, self-phase modulation and transverse effects are included simultaneously in the nonlinear regime. The primary objective of this paper is to show the various subtleties of the physics such as spontaneous evolution of phase waves[14] using the computational apparatus of SF without any linearization.

II - THE MASTER EQUATIONS OF MOTION

Within the slowly varying envelope approximation SVEA, the physical model for SRS consists of two paraxial field equations (ζ_p pump and ζ_s Stokes) cross-coupled through an effective two-level atomic system. Q pseudo-polarization and W_c the effective inversion two-level density. These equations constitute a subset from those analyzed by Mattar and Bowden in optically-pumped three-level superfluorescence[15]. The second source term was suggested by Raymer.

$$-\frac{i}{4F_s}\nabla_T^2\zeta_S + \frac{\partial\zeta_S}{\partial\eta} = \kappa_2\zeta_L Q^* + \zeta_S[a_S(1+W_c) + b_S(1-W_c)] \tag{1a}$$

$$-\frac{i}{4F_p}\nabla_T^2\zeta_L + \frac{\partial\zeta_L}{\partial\eta} = \kappa_1\zeta_S Q + \zeta_L[a_L(1+W_c) + b_L(1-W_c)] \tag{1b}$$

$$\frac{\partial Q}{\partial\tau} = -\gamma Q - (\zeta_L\zeta_S + \zeta_L\zeta_S)W_c + 2\Gamma^* \tag{2a}$$

$$\frac{\partial W_c}{\partial\tau} = (\zeta_L^*\zeta_S Q + \zeta_L\zeta_S^* Q^*) \tag{2b}$$

In the uniform-plane-regime, with infinite relaxation times and without pump depletion the equations of motion can be rearranged to exhibit

$$\frac{\partial}{\partial\eta}|\zeta_S|^2 = (\kappa_2/\kappa_1)\ \frac{\partial}{\partial\tau}|Q|^2 \tag{3}$$

With pump depletion accounted for one readily sees that the sum of the two pump and probe energies is constant

$$\frac{\partial}{\partial\eta}[|\zeta_L|^2 + \kappa_1/\kappa_2|\zeta_S|^2] = 0 \tag{4}$$

with Q and W_c. For infinite relaxation time, a conservation of the Bloch vector length must be satisfied.

$$W_c^2 + |Q|^2 = 1 \tag{5}$$

with F_s and F_p the geometric Fresnel number the scaling

$$\tau = (t-z/v)/\tau_{SF}\ (6)\quad \eta = z/c\tau_{SF}\ (7),\quad \rho = r/r_p\ (8)$$

$$\zeta_{s,p} = (2\frac{\mu_{eff}}{\hbar}\zeta_{s,p})\tau_{SF} \qquad \text{where E is a complex slow varying envelope} \tag{9}$$

and with

$$\beta=(1/2)\kappa_2\kappa_3\ell\ (10)\quad \gamma=\Gamma\tau_{SF}\ (11)\quad \tau_{SF}^{-1} = (1/2)\Gamma g\ell = (3/8\pi)\lambda_s^2 NL/\tau_0\ (12)$$

$$\mu_{eff} = \kappa_1\zeta_p\ (13)\quad \tau_0^{-1} = |\wp\,\mu_{eff}|^2\omega_s^3/c^3\ (14)\quad \tau_{SF}^{-1} = \kappa_1\kappa_2|\zeta|^2 L\ (15)$$

The input pump field is Gaussian in time $\zeta_0 \exp[-(\tau/\tau_p)^2]$ and in radius $\exp[-(r/r_p)^2]\rho$. The on-axis time-integrated optical area is 2π. An initial phase can be introduced to allow the compensation self-action processes.

The input Stokes field is zero as in superfluorescence SF emission. The input effective pseudo-dipole moment Q at $\tau = 0$ is initiated as an input Gaussian noise $\delta(\vec{r}-\vec{r}')$ by $\hat{f}$ a Langevin force

$$\langle \hat{f}(\vec{r},\tau)\hat{f}(\vec{r}',\tau')\rangle = \tau_{SF}^2\ 2\ \Gamma\ N^{-1}\delta(\vec{r}-\vec{r}')\ \delta(\tau-\tau') \qquad (16)$$

This Langevin force introduced by Raymer[1,3] is different from the one defined by Bowden et al.[16] with the probability distribution of $Q\ \delta(\vec{r}-\vec{r}')$

$$P(Q_i) = (1/2\ \pi\sigma_i^2)\ \exp[-|Q_i|^2/2\sigma_i^2] \qquad (17)$$

with $2\sigma_i = (\Delta v_i N)^{-1}$ (18) where N is the number atomic density. The magnitude $|Q| = (2/\sqrt{N})[\ell n(1/R)]^{1/2}$ (19) with R a random number between 0 and 1. While the phase is a uniform random number of value between 0 and 2π.

The above equations account for pump depletion. It generalizes Raymer et al.'s[2a] and [3] model which does assume infinite pump strength. Only one field equation is retained. We have carried out two sets of computations, one without the pump depletion but with the medium not linearized and one with the pump depletion rigorously accounted for. Both plane wave and non-plane wave regime were investigated.

III - DISCUSSION OF THE PHYSICAL MODEL

In this analysis we address four different transverse effects. The first one is the diffraction coupling. The cross-coupling of the two finite beams is the second one. The radial dependence of the Raman gain through the atomic density N is the third effect while the randomly-generated initiation of the Stokes (amplitude and phase) is the fourth. These four processes vary from one shell to the other, that is, nonuniformly across the beam.

Both self-phase SPM and cross-phase XPM results in the Raman analysis. Moreover, the diffraction-induced phase competes with that generated by quantum-initiation. Their interference can be either constructive or destructive.

Should one allow for dispersion through detuning, one obtains an additional contribution to the phase. The dispersion-associated phase can enhance or reduce the combined SPM and XPM.

Finally, if the Lorentz local field(s) correction[17-20] is also accounted for, a population-dependent frequency offset emerges in the density matrix. The effective detuning becomes a time and a radially dependent function. The resultant chirp, i.e., the self- and cross frequency modulation modifies the characteristics of the Raman co-propagation. The rate of the energy conversion from the pump to the Stokes and the depletion of the pump and the growth of the Stokes emission become more complicated. The analytical tractability vanishes. One must resort to numerical experiments to appreciate the physical nuances and domain.

IV - NUMERICAL CALCULATION

The growth of the Stokes emission from quantum noise has been studied for an ensemble of trajectories. The evolution of a coherent pulse from initial fluctuations is clearly demonstrated in terms of the on-axis energy and of the radially-integrated energy, i.e., the output power as the function of the retarded time τ and distance of propagation η. The peak value of the Stokes energy and its location vary from one shot to the other within the same simulation. This calculation was achieved in the uniform-plane-wave calculation where diffraction coupling is neglected and in the transverse regime for small Fresnel numbers where diffraction coupling is inportant. The detailed fluctuation statistics have been compiled for presentation elsewhere.

We first reproduce Raymer et al.'s calculation with quantum initiation.

In Fig. 1, we display the on-axis Stokes energy at a given propagational distance η=1001 for three different trajectories out of an ensemble of fifty (stat=1,25,50). The amplitude, the pulse width and the delay of the energy peak, with respect to an observer travelling with the velocity of light, vary from one shot-to-the other. For example the peak values are respectively 0.162×10^{-3}, 0.493×10^{-3} and 0.241x10-4. The third pulse exhibits a precursor which is weaker.

In Fig. 2 we display for two other trajectories stat=16 and 21 in the same set of 50 quantum initiated calculation, the Stokes energy for different propagational distances. In one instance a precursor develops and the peak energy is reduced while in the other trajectory the Stokes pulse does not develop a secondary lobe but retains a peak strength four times as large.

In Fig. 3, we displayed for a given trajectory, stat=1, the evolution of the on-axis Stokes energy in the Raman cell (η=101,201, 301,401,501,601,701,801,901 and 1001). The longitudinal reshaping of the Stokes pulse is quite clear from quantum fluctuation, i.e., noisy source into a (smooth) coherent symmetric pulse. Again the peak and temporal width vary with the propagational distance.

The standard deviation and the mean of the time-integrated Stokes pulse area $\langle\theta_b\rangle$ $\sigma(\theta_b)$ and the time-integrated Stokes energy $\langle\psi_b\rangle$ $\sigma(\psi_b)$ have been respectively evaluated as follows: the area

$$\langle\theta_b\rangle = 0.545 \times 10^{-10}$$

$$\sigma(\theta_b) = 0.258 \times 10^{-10}$$

$$\varepsilon(\theta_b) = \sigma(\theta)/\langle\theta\rangle = 0.437 \times 10^{2}$$

with a fiability percentage of 1/7 the fluence

$$\langle\psi_b\rangle = 0.544 \times 10^{-12};$$

$$\sigma(\psi_b) = 0.592 \times 10^{-12};\ \text{and}$$

$$\varepsilon(\psi_b = \sigma(\psi_b)/\langle\psi_b\rangle = 0.919 \times 10^{2}$$

$\langle \psi_b \rangle = 0.544 \times 10^{-12}$;

$\sigma(\psi_b) = 0.592 \times 10^{-12}$; and

$\varepsilon(\psi_b = \sigma(\psi_b)/\langle \psi_b \rangle = 0.919 \times 10^{2}$

The Stokes energy $I=\zeta_S \zeta_S^*$ statistics have been evaluated at six time slices τ_{101}, τ_{111}, τ_{121}, τ_{131}, τ_{141} and τ_{151} to reflect the incurred delay/advance.

τ	101	111	121	131	141	151
I_b	0.827×10^{-8}	0.202×10^{-6}	0.327×10^{-5}	0.265×10^{-4}	0.113×10^{-3}	0.187×10^{-3}
$\sigma(I_b)$	0.780×10^{-8}	0.208×10^{-6}	0.315×10^{-5}	0.220×10^{-4}	0.105×10^{-3}	0.185×10^{-3}
$\varepsilon(I_b)$	0.94×10^{2}	0.103×10^{3}	0.963×10^{2}	0.829×10^{2}	0.93×10^{2}	0.987×10^{2}

Moreover, the statistics fluctuation of the peak Stokes values and the associated time-location have been calculated as follows

$\sigma(\tau_{peak})/\langle \tau_{peak} \rangle =$

$\sigma(I_{peak}) =$

with I_{peak} the peak energy

$\sigma(I_{peak})/\langle I_{peak} \rangle =$

Beginning with a delta-correlated Stokes emission we obtain numerically a qualitative agreement with Raymer, Walmsley, Sobolewska and Mostowski's results in the linear regime with pump depletion accounted for. In simulation L22P78 we have followed up the buildup of the Stokes emission. As shown in Fig. 4 the Stokes energy builds up as the distance of propagation increases. The value of the peak energy for the first one thousand steps in periods of one hundred space increments beginning at η=101 with 0.154×10^{-6}, η=201 with 0.13×10^{-6} it gradually increases until it reaches at η=801, 0.574×10^{-5}, afterwards the energy goes through a sudden nonlinear Stokes buildup η=901, the peak energy equal to 0.84×10^{-4} and η=1001 to the value of 0.12×10^{-2} W/m^2. Correspondingly the pump experiences absorption and depletion. The pump energy decreases to the benefit of the Stokes. Energy conversion from one frequency to the other one is demonstrated to occur in the nonlinear regime. The buildup of the Stokes is thus similar to the one of superfluorescence.

In Fig. 5 we display three isometric plots of the Stokes energy ENRGYb versus τ and η at nine specific trajectories stat=1-9. The obtained on-axis peak Stokes energy varies from shot-to-shot in simulation L22P80. Their amplitude in $Watt/m^2$ takes the following values (1) 2.31×10^{8}; (2)6.02×10^{7}; (3) 2.23×10^{7}; (4) 1.84×10^{7}; (5) 1.34×10^{5}; (6) 3.3×10^{16}; (7) 2.95×10^{7}; (8) 3.84×10^{7} and 9.08×10^{7}. The

composite plot substantiates the evolution of linear buildup as in superfluorescence followed by a sudden nonlinear buildup. A threshold in time and η along the propagation distance does occur for the macroscopy formation of the Stokes.

The results correspond to those of the optically-driven three-level SF in which the gain in the SF transition should be larger than that of the pure two-level SF and herein corresponding Stokes emission with an infinite strong non-depleting pump.

For Fig. 6 we present the Stokes energy results of simulation L22P in a set of two-dimensional plots versus τ for a given set of propagational distances η. The peak on-axis energies for a distinct (stat=1,6,11,16,21,26,31,36 and 41) number of trajectories out of an ensemble of 50. The microscopic fluctuations at the initiation process display macroscopic variations that can be observed in the Stokes energy. The on-axis Stokes energy peak values in the presence of a finite pump pulse are as follows: (1) Stat #1, 2.25×10^{-7}; (2) stat #6, 3.25×10^{-6}, (3) stat #11, 2.25×10^{-7}; (4) stat #16, 1.50×10^{-7}; (5) stat #21, 2.0×10^{-7}; (6) stat #26, 1.25×10^{-7}; (7) stat #31, 2.5×10^{-7}; (8) stat #36, 5.5×10^{-6}; and (9) stat #41, 1.0×10^{-7}.

V - CONCLUSION

We have presented a rigorous formulism that covers pump depletion, diffraction and quantum initiation for a nonlinear medium. We are planning precise comparisons with Raymer's and co-workers experimental effort.

VI - FUTURE EFFORT

The rigorous account of the anti-Stokes emission for Raman beam calculations are in the process of being realized.

REFERENCES

1. [a] M.G. Raymer et al., Phys. Rev. A32, 332 (1985); and [b] I.A. Walmsley & M.G. Raymer, Phys. Rev. A33, 382 (1986).
2. J. Mostowski & B. Sobolewska, Phys. Rev. A30, 610 (1984); and ibid A32, 332 (1985).
3. [a] M.G. Raymer & J. Mostowski, Phys. Rev. A24, 1980 (1981); [b] J. Mostowski & M.G. Raymer, Opt. Commun. 36, 237 (1981); [c] M.G. Raymer, K. Rzazewski & J. Mostowski, Opt. Lett. 7, 71 (1982); & [d] K. Rzazewski et al., Opt. Commun. 43, 451 (1982).
4. [a] R.H. Dicke, Phys. Rev. 93, 99 (1954); [b] M.S. Feld & J.C. Mac Gillivray, in Coherent Nonlinear Optics, ed. M.S. Feld & V.S. Letokhov (Springer-Verlag, 1980) pp. 7- ; [c] Q.H.F. Vrehen & H.M. Gibbs, in Dissipative Systems in Quantum Optics, ed. by R. Bonifacio, (Springer-Verlag, 1981) pp. 111-147; [d] M.F.H. Schuurmans et al., in Advances in Atomic and Molecular Physics, Vol. 17, ed. D.R. Bates and B. Bederson (Academic, 1981) pp. 168-228; [e] M. Gross & S. Haroche, Phys. Rep. 93, 301-396 (1982); [f] F.P. Mattar, SPIE 380, 508-542 (1983); and [g] F.P. Mattar et al., in Multiple-Photon Excitation and Dissociation of Polyatomic Molecules, ed. C.D. Cantrell, (Springer-Verlag, 1986) pp. 223-283.
5. [a] F.P.Mattar, Appl.Physics 17, 53(1978); & [b] F.P.Mattar & M.C. Newstein, Comp.Phys.Commun. 20, 139 (1980) & ibid 32, 225 (1984).
6. S.L. McCall & E.L. Hahn, Bull. Am. Phys. Soc. 10, 1189 (1965); Phys. Rev. Lett. 28, 308 (1967); Phys. Rev. 183, 457 (1969) and Phys. Rev. A2, 861 (1970).

8. [a] F.P. Mattar, SPIE Vol. 288, 353-361 (1981); and [b] E.A. Watson et al., Phys. Rev. A27, 1427 (1983) (see Sect. IIIc).
9. [a] R. Glauber & F. Haake, Phys. Lett. 68A, 29 (1978); [b] F.Haake et al., Phys. Rev. Lett. 42, 1740 (1979); & [c] F. Haake et al., Phys. Rev. Lett. 45, 558(1980).
10. D. Polder et al., Phys. Rev. A19, 1192 (1979).
11. [a] F.A. Hopf, Phys. Rev. A20,2064 (1979); and [b] F.A. Hopf & E.A. Overman II, Phys. Rev. A19, 1180 (1979).
12. M. Lewenstein, Z. Physics B56, 69 (1984).
13. P.D. Drummond & J.H. Eberly, Phys. Rev. A25, 3446 (1982).
14. [a] Ref. 11; and [b] Ref. 8b Fig. 7.
15. F.P. Mattar & C.M. Bowden, Phys. Rev. A27, 345 (1983).
16. [a] J.C. Englund & C.M. Bowden, Phys. Rev. Lett. 57, 2661 (1986) & SPIE 874, 218 (1988); [b] C.M.Bowden & J.C.Englund, Opt. Commun. 67, 71 (1988); and [c] For the on-resonance three-level quantum initiation see C.M. Bowden & C.C. Sung, Phys. Rev. Lett. Vol. 50, 156 (1983).
17. J. Marburger, L. Huff, J.D. Reichert & W.G. Wagner, Phys. Rev. 184, 255 (1969).
18. [a] R. Friedberg, S.R. Hartmann & J.T. Manassah, Phys. Lett. 35A, 161 (1971), ibid 40A, 395 (1972) & Phys. Report 7C, 101-179 (1973); [b] J.T. Manassah, Phys. Report 101, 359-427 (1983); [c] R. Friedberg, S.R. Hartmann & J.T. Manassah, Phys. Rev. A39, 93 & 3444 (1989); and [d] J.T. Manassah, Phys. Rept. 101, 359-427.
19. [a] F.A. Hopf, C.M. Bowden & W.H. Louisell, Phys. Rev. A29, 2591 (1983); [b] in **Optical Bistability II**, ed. C.M. Bowden, H.M. Gibbs & S.L. McCall (Plenum Press, 1984) pp. 361-368; and [c] in **Optical Instabilities**, ed. R.W. Boyd, M.G.Raymer & L.M. Narducci (Cambridge University Press, 1986) pp. 308-311.
20. J.T. Manassah & F.P. Mattar, in Proc. Intl. Laser Sci. ILS-IV, **Advances in Laser Science IV** (Am. Inst. Phy., 1989).

FIGURE CAPTIONS

Fig. 1 A sample of the Stokes energy at a given distance of propagation, η=1001, evolution from a bouquet of trajectories.

Fig. 2 A composite representation of Stokes energies for a family of propagational distances for two trajectories.

Fig. 3 Propagational effects on the Stokes energy. Pump depletion was not rigorously accounted for in the analysis.

Fig. 4 Stokes buildup with pump depletion accounted for.

Fig. 5 A set of Stokes energy three-dimensional plots versus τ and η for different trajectories in an ensemble of 10 shot-to-shot simulations.

Fig. 6 A set of two-d plots Stokes energy versus τ and ρ for a larger ensemble of 50 trajectories to verify the occurrence of either a precursor or a secondary plot, i.e., temporal ringing.

L22P SIMULATION NO. 77

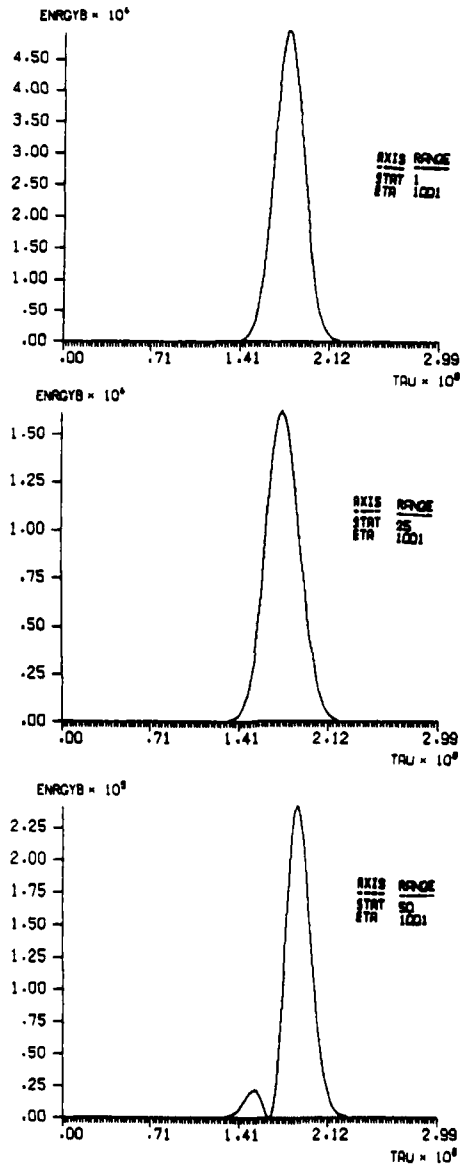

ENRGYB

L22P SIMULATIØN NØ. 77

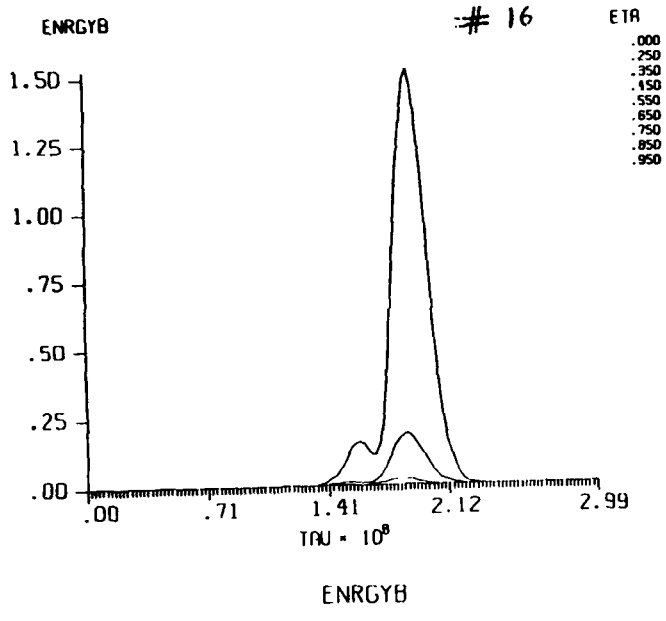

L22P SIMULATIØN NØ. 77

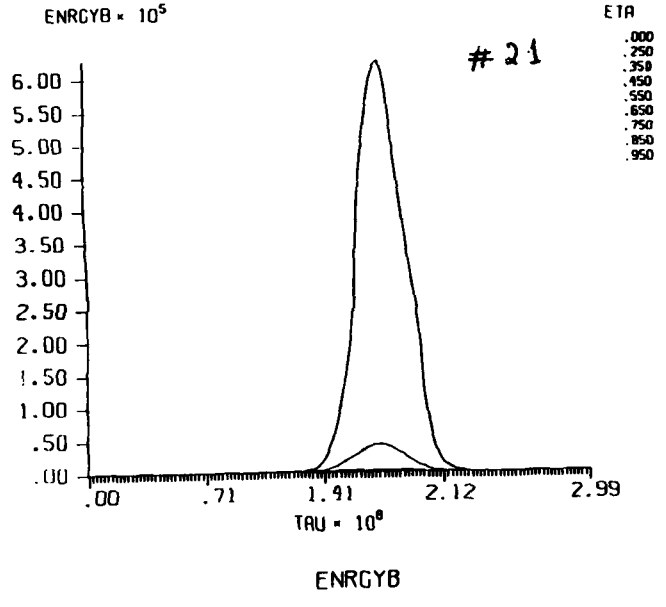

L22P SIMULATIØN NØ. 77

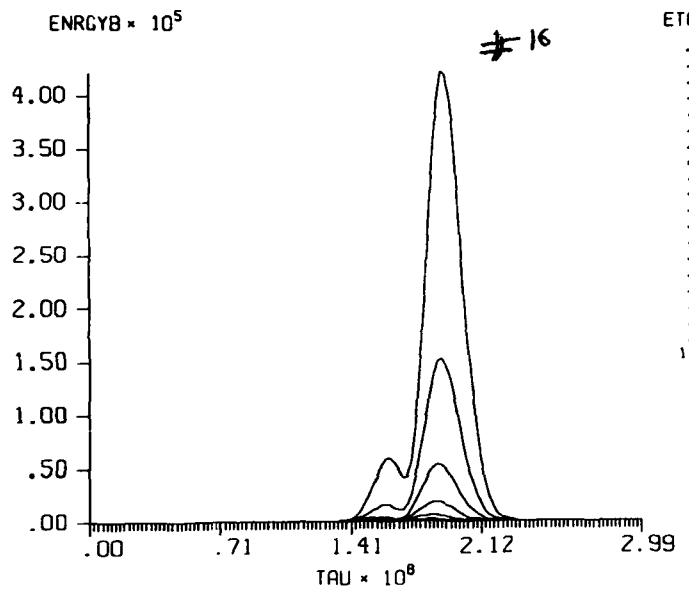

ENRGYB

L22P SIMULATIØN NØ. 77

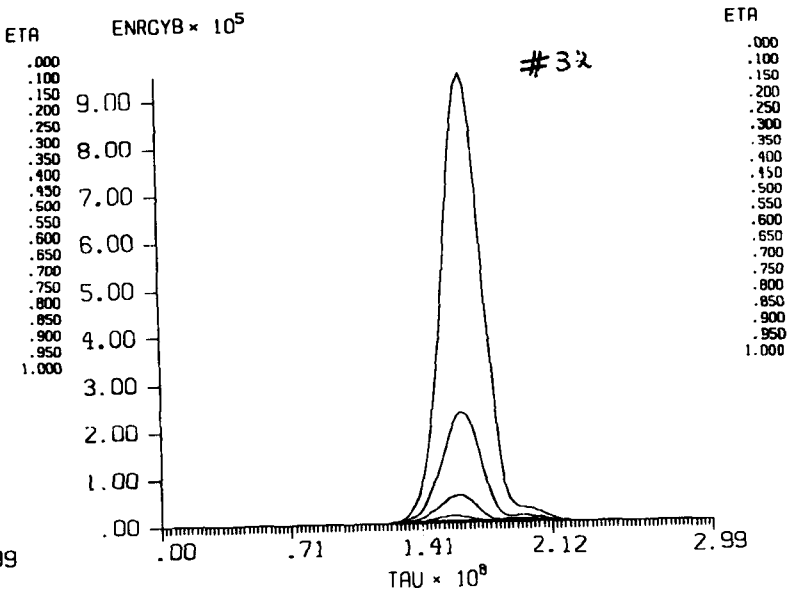

ENRGYB

L22P SIMULATIØN NØ. 24

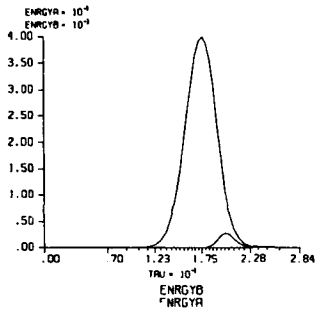

L22P SIMULATIØN NØ. 24

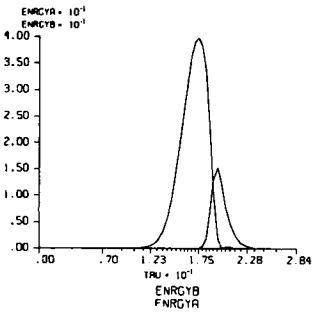

L22P SIMULATIØN NØ. 24

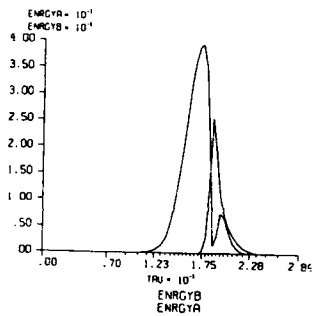

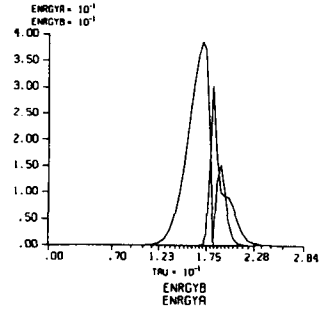

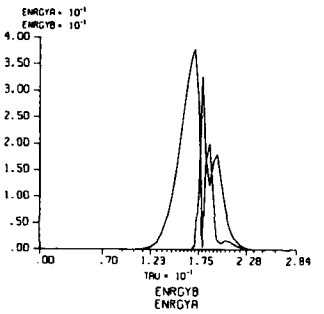

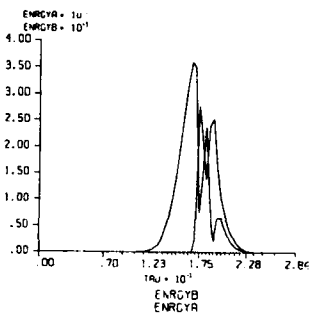

L22P SIMULATION NO. 77

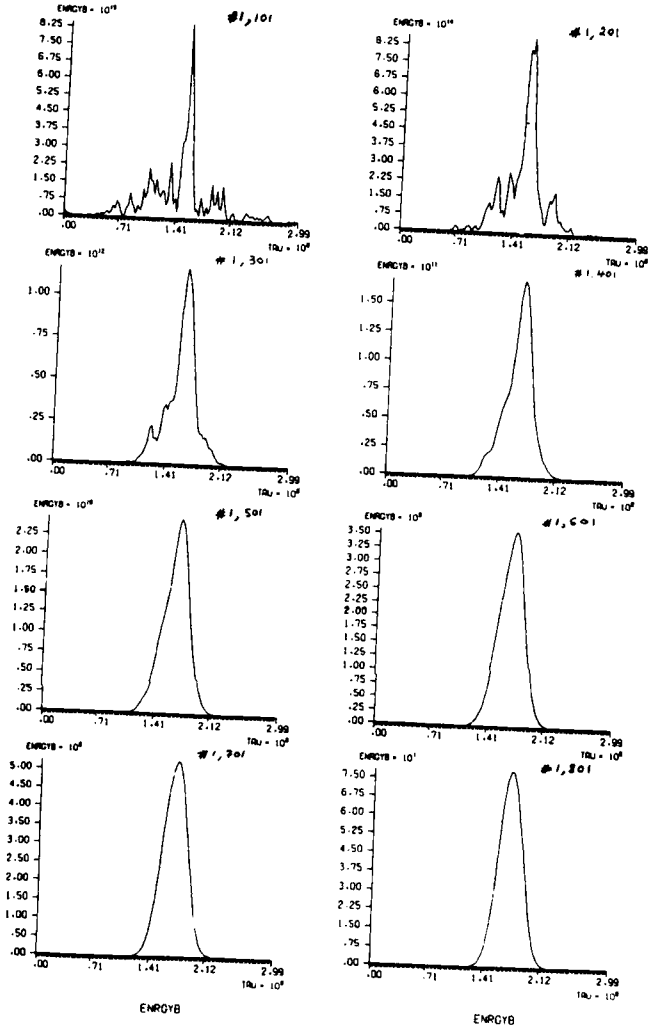

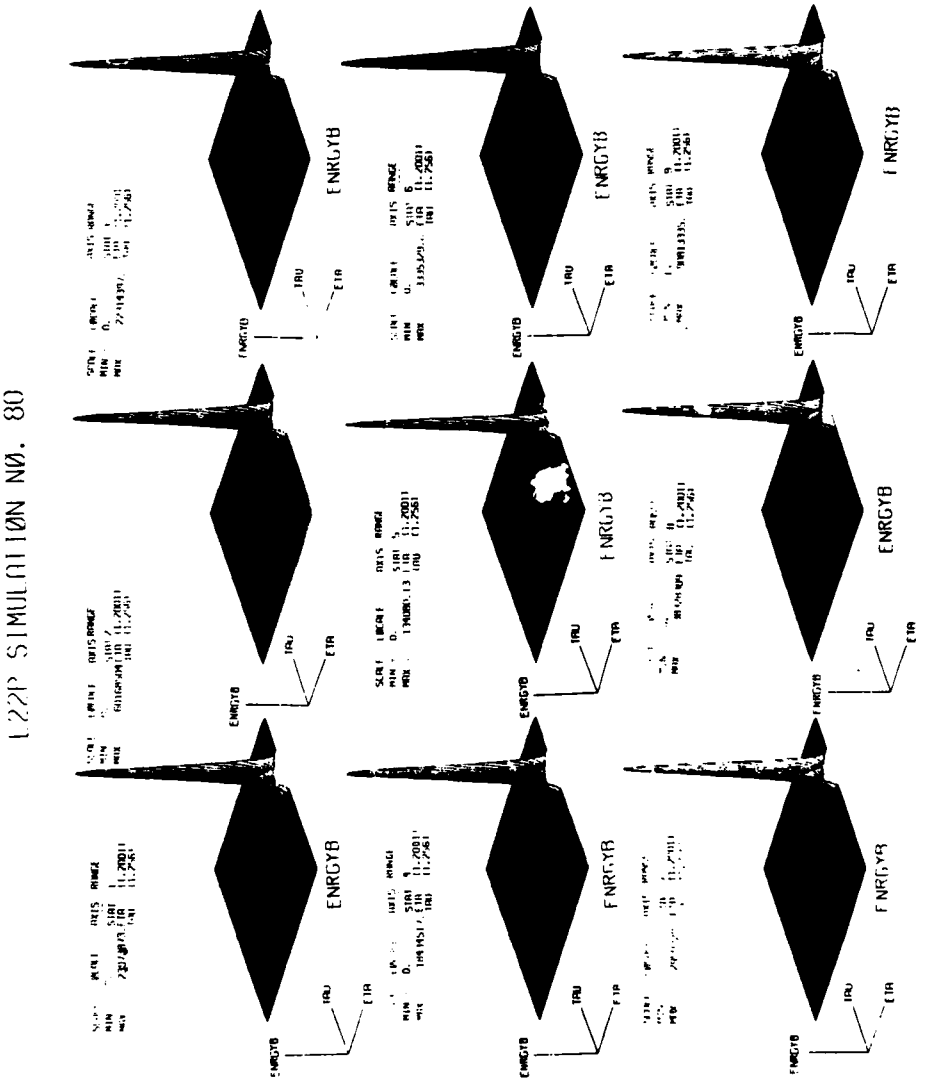

F22P SIMULATION NO. 80

Nonlinear Gaussian Expansions of Stochastic Processes: Non-Gaussian Effects in Coherent Anti-Stokes Raman Spectroscopy

Albert M. F. Lau and Roger L. Farrow
Combustion Research Facility, Sandia National Laboratories,
Livermore, CA 94550

Abstract

We propose a new approach to the analysis of stochastic processes (such as fluctuating laser fields) with non-Gaussian statistics: the expansion of stochastic processes in terms of first and higher powers of Gaussian components, which are used like a basis set. This approach is applied to treat the non-Gaussian correlation effects observed in coherent anti-Stokes Raman scattering experiments using frequency-doubled pump-laser fields. Our results give much better agreement with experimental data than previous theories.

Many nonlinear laser spectroscopic measurements are known to be sensitive to the fluctuations in the laser fields. In order to obtain the frequencies needed in many experiments, the laser fields are produced from a multimode fundamental field by n-harmonic generation. At present, there is no reliable method of *a priori* predicting the fluctuation statistics of the resulting n-harmonic generated fields. The question addressed in this paper is thus quite general: What are the field statistics of the resulting laser field after n-harmonic generation from a multimode fundamental field?

We propose here a novel approach to the analysis of stochastic processes E(t) containing non-Gaussian statistics (such as the n-harmonic fields generated from multimode fields) based on a flexible and systematic expansion in terms of first and higher powers of basis components $G_m(t)$,

$$E(t) = \sum_{m=1}^{n} [G_m(t)]^m , \qquad (1)$$

where each $G_m(t)$ is statistically independent and obeys Gaussian *statistics*. Previous approaches[1,2] neglect all other intermediate powers of G_m as well as either $G_1(t)$ or $G_n^n(t)$. A mathematical advantage of the above expansion is that because all the stochastic components are Gaussian, higher-order correlation functions of each component G_m can be decorrelated rigorously.[3]

We demonstrate this approach by applying it to analyze the non-Gaussian effects observed in the CARS measurements on the O(18) transition of nitrogen.[1] In these measurements, two pump beams split from a dye laser pumped by a frequency-doubled, multimode Nd:YAG laser (1.0 cm^{-1} FWHM linewidth at 532 nm) and an independent Stokes beam were focused into a gas cell containing pure nitrogen to generate the coherent anti-Stokes beam using a crossed-beam CARS geometry. The anti-Stokes intensity was monitored as a function of the variable relative delay (small compared with the temporal pulse width) between the two pump beams. Therefore its magnitude depends on the statistics of the field fluctuations in the pump beams and their correlation. For example, in a set of measurements performed on the O(18) transition at 500 Torr and 296 K, the resonant and the nonresonant anti-Stokes intensity components versus delay were measured separately by splitting the anti-Stokes beam and

using dual polarizers and detectors. Their ratio was found to vary by almost a factor of 2 when the delay changed from 0 cm to 2 cm (see data plotted in Fig.1).

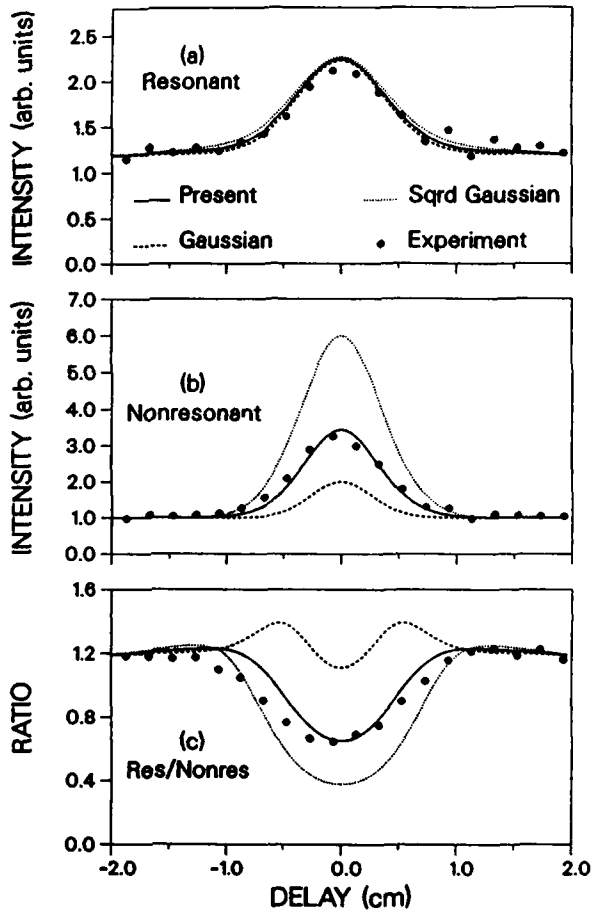

Figure 1. Comparison of experimental (solid dots) resonant and nonresonant CARS intensities and their ratios (measured on the O(18) transition of nitrogen at 500 Torr and 296 K) with theoretical results using the present theory (solid lines), Gaussian (dashed lines) and squared-Gaussian (dotted lines) statistics to model the fluctuations in the pump laser fields.

Using only the first and second terms in Eq.(1), we fit our calculated results to the *nonresonant* CARS data of nitrogen at 500 Torr as shown in Fig.1, thus determining the only adjustable parameter, namely the relative intensity between the two terms. With no further adjustment of this parameter, our results give much better agreement with the data at 500 and 4500 Torr, than the Gaussian[1] and the the squared-Gaussian model,[2] as shown in Figs. 1 and 2. The results at 4500 Torr serve as an independent test of the theory and the small discrepancies are due to uncertainties in the experimental measurements.[4]

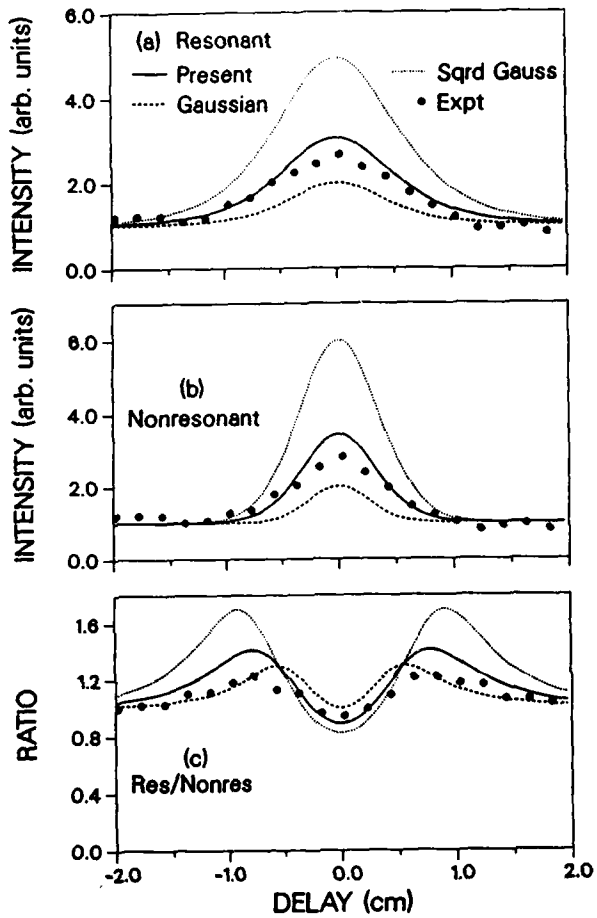

Figure 2. Comparison of experimental (solid dots) resonant and nonresonant CARS intensities and their ratios (measured on the O(18) transition of nitrogen at 4500 Torr and 296 K) with theoretical results using the present theory (solid lines) with the same field statistics determined from the 500 Torr data. Results of the Gaussian (dashed lines) and squared-Gaussian (dotted lines) models are also presented for comparison.

This work was supported by the U.S. Department of Energy, Office of Basic Energy Sciences, Chemical Science Division.

REFERENCES:

1. L. A. Rahn, R. L. Farrow, and R. P. Lucht, Opt. Lett. 9, 223 (1984).
2. G. S. Agarwal and R. L. Farrow, J. Opt. Soc. Am. B 3, 1596 (1986).
3. L. Mandel and E. Wolf, Rev. Mod. Phys. 37, 231 (1965).
4. A. M. F. Lau and R. L. Farrow, to be published.

SECOND STOKES GENERATION IN DEUTERIUM

M. D. Duncan, R. Mahon, L. L. Tankersley, and J. Reintjes
Laser Physics Branch, Code 6540, Optical Sciences Division
Naval Research Laboratory, Washington, D.C. 20375

ABSTRACT

We have investigated the growth, the spatial mode profiles and the pulse energy statistics of the first and second Stokes generated in a transient stimulated Raman self-generator experiment. In particular, we have observed two distinct regions of second Stokes growth. The first region is characterized by a low signal level due to 4-wave mixing. The second region appears to be one of stimulated growth seeded by spontaneous scattering at the second Stokes wavelength, an assumption supported by the rapid growth of the second Stokes signal and the observation of pulse energy statistics indicative of growth from noise. The absolute level of the Stokes signal in the 4-wave mixing region varied as a function of deuterium gas pressure, increasing for lower pressures as a result of stronger 4-wave mixing. We have also measured the second Stokes threshold as a function of deuterium pressure and have observed results consistent with first Stokes threshold measurements made at high pressures. At lower gas pressures, the threshold for second Stokes generation is lowered, indicating some seeding of the stimulated process due to 4-wave mixing.

EXPERIMENTAL APPARATUS

The general experimental apparatus used in these studies has been described elsewhere.[1] In brief, a frequency-doubled Nd:YAG mode-locked laser with spatially filtered pulses of 40 ps duration and 5 mJ of energy at 532 nm was used to pump a Fresnel number one, single-pass Raman self-generator. The Raman cell was filled with deuterium at a pressure in the range of 45 to 145 atm. A separate seed-Stokes generator was operated well into saturation with a depletion level of about 15% to provide stable Stokes outputs at 633 nm and 780 nm for the purpose of calibrating photodiodes at these two wavelengths. The 532 nm pump beam had a confocal parameter well in excess of the 100 cm length amplifier cell used for these experiments. A two cell arrangement was used at certain times to clarify the role of first Stokes beam quality in the generation of the second Stokes. In those cases the first Stokes was generated in a separate cell and then spectrally isolated before being used to generate the second Stokes.

The input pump and the generated first and second Stokes pulse energies were measured with calibrated photodiodes. Gain and pulse energy statistics data were acquired automatically with a microcomputer-based data-acquisition system. Statistical data on the Stokes energy distributions were collected with 5% and 1% windows on the incident pump energy. Typical samples contained data from 2000 laser shots in the energy window with the data being collected into 100 energy bins of equal width. For gain measurements the natural scatter of pump pulse energies was utilized in generating complete curves showing the dependences of the 1st and 2nd Stokes energies on pump energy. Spatial profiles of the pump, the 1st Stokes, and the 2nd Stokes were measured using a digital camera placed 35 cm after the exit window of the self-generator cell.

RESULTS AND DISCUSSION

The growth of the first and second Stokes in a single cell as a function of the 532 nm pump energy for two different deuterium pressures is shown in Fig. 1. The

first Stokes follows the expected form of exponential growth followed by saturation.[1,2] The second Stokes, however, has two separate growth regions, most clearly seen at high pressure in Fig. 1(a). The first is a 4-wave mixing region which is followed by a region of exponential growth. As seen in Fig. 1, the 4-wave mixing contribution is greater at lower pressures. At higher pressures, the phase-matching angle is greater and falls farther outside the angular spread of the pump and Stokes beams, reducing the strength of the 4-wave mixing process.[3] At the lower pressure the 4-wave mixing region is not as distinct a region and seems to blend somewhat with the eventual exponential growth that the second Stokes undergoes. Figure 2 shows pulse energy statistics of the second Stokes measured at various points on the second Stokes growth curve of Fig. 1(a). Figure 2(a) shows pulse energy statistics characteristic of pulses produced by a well-stabilized source.[4] This is

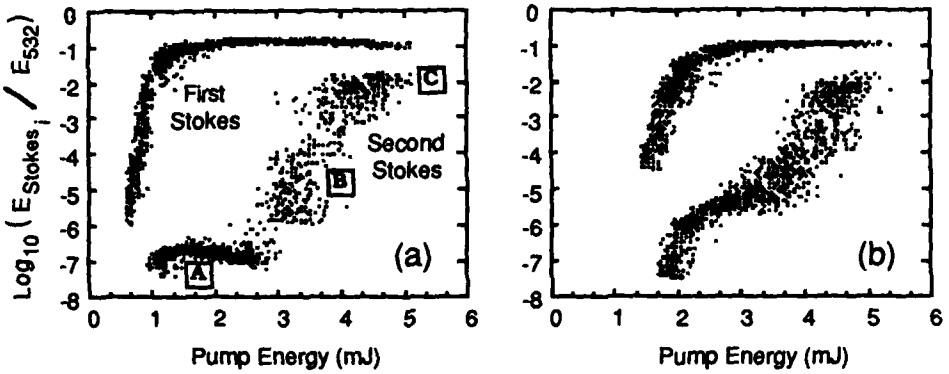

FIG 1. First and second Stokes generation from deuterium gas at two different pressures as a function of 532 nm pump energy. (a) Deuterium pressure of 1950 psi; (b) deuterium pressure of 700 psi. The boxed letters in figure (a) indicate regions where pulse energy statistics were measured (see Figure 2).

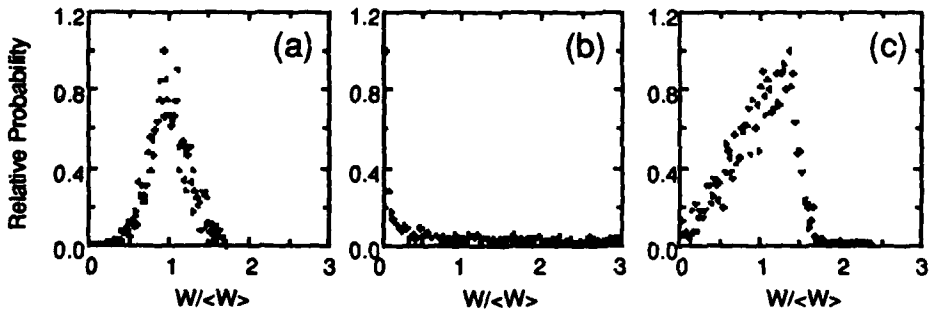

FIG. 2. Pulse energy statistics for the second Stokes signal from three different regions of Fig. 1(a): (a) from the 4-wave mixing region identified as A; (b) from the exponential growth region identified as B; (c) from the saturated region identified as C. W is the pulse energy and <W> is the average pulse energy.

consistent with production of the second Stokes signal by 4-wave mixing from a relatively constant energy pump and a saturated first Stokes. Figure 2(b) shows a pulse energy distribution measured in the exponential growth region for the second Stokes in Fig. 1(a). Here the distribution is highly peaked at a very low energy value, an indication that the pulses are generated from an extremely noisy source, such as quantum noise. However, the distribution is different than would be expected if the source was simply quantum noise.[4] A further experiment performed with separate Raman cells for first Stokes and second Stokes generation showed that the excessively noisy nature of the distribution in Fig. 2(b) was caused by spatial beam degradation in the first Stokes light. When the degradation of the first Stokes beam quality was removed by spatial filtering, the distribution returned to a more normal negative exponential distribution typical of that produced by quantum noise. Figure 2(c) shows a pulse energy distribution taken from the region in Fig 1a where the second Stokes is beginning to saturate. The form of the distribution is consistent with a saturated process.

We have made threshold measurements for both first and second Stokes generation. We define threshold to be when the Stokes order of interest has reached an energy level that is 0.1% of that Stokes' pump energy. At high pressures we found that the threshold for second Stokes generation matched the first Stokes generation threshold very well. The values were obtained in a single cell and were corrected for effects such as reduced cell length for second Stokes generation and slightly reduced beam quality of the generated first Stokes. Other experiments have reported anomalously high thresholds for second Stokes generation.[5,6] Explanations proposed have concentrated on the gain narrowing of the first Stokes beam and the subsequent reduction of second Stokes generation due to the diverging beam.[7] Our experiments were performed using a collimated 532 nm pump beam to minimize any divergence problems. Detailed measurements indicate that the first Stokes does pick up some excess divergence even though we saw no large effects of this divergence on the second Stokes threshold. At lower deuterium pressures the threshold for second Stokes is well below the first Stokes threshold. This is consistent with our observation of an increase in 4-wave mixing at lower pressures.

Unanswered questions remain concerning the generation of second Stokes light. At high pressures, why doesn't the second Stokes light generated from 4-wave mixing seed the stimulated gain and dominate the apparent growth from spontaneous scattering? A possible explanation is that the spectral content of the first Stokes light is shifted sufficiently by self-phase modulation of the pump pulse that it is ineffective in seeding the second Stokes. Further work using rotational Raman scattering in hydrogen, where the 4-wave mixing contribution can be turned on and off by using either circularly polarized or linearly polarized light, is underway.

REFERENCES

1. M. D. Duncan, R. Mahon, L.L. Tankersley, and J. Reintjes, J. Opt. Soc. Am. B, **5**, 37, (1988).
2. M. D. Duncan, R. Mahon, L.L. Tankersley, and J. Reintjes, SPIE, **874** ,200 (1988).
3. M. D. Duncan, R. Mahon, L.L. Tankersley, and J. Reintjes, Optics Lett. **11**, 803 (1986).
4. M. G. Raymer, I. A. Walmesley, J. Mostowski and B. Sobolewska, Phys. Rev. A **32**, 332 (1985).
5. J. L. Carlsten, J. M. Telle and R. G. Wenzel, Optics Lett. **9**, 353 (1984).
6. R. G. Wenzel and J. M. Telle, J. Opt. Soc. Am. B, **3**, 1483 (1986).
7. B. Bobbs and C. Warner, Optics Lett. **11**, 88 (1986).

INFLUENCE OF A.C. STARK EFFECT ON STIMULATED HYPER-RAMAN PROFILES IN SODIUM VAPOR

Mary Anne Moore,* W. R. Garrett, and M. G. Payne
Chemical Physics Section, Oak Ridge National Laboratory
Oak Ridge, Tennessee 37831-6378

ABSTRACT

When pumping near the two-photon 3d resonance in pure sodium vapor and observing the backward hyper-Raman emission to the 3p substates, an asymmetry in ratios of $3p_{1/2}, 3p_{3/2}$ associated emissions was observed dependent upon the direction of the initial laser detuning from the resonance. It has been determined that this asymmetry can be attributed to the a. c. Stark effect induced by the hyper-Raman emission itself.

Stimulated hyper-Raman (SHR) emission characteristics in pure sodium vapor have been well documented.[1] It has been shown that the three-photon SHR process is suppressed in the direction of the laser photons due to interference with a four-wave mixing (FWM) pumping of the atomic transition that is exactly 180 degrees out of phase with the SHR excitation process.[2,3] However, the backward propagating SHR emission is unaffected by this suppression effect because of the absence of FWM in that direction due to phase-matching considerations.

The SHR process studied in this paper is produced by two laser photons tuned near, but not on the two-photon resonance with the Na 3d states. The fine structure levels (j= 5/2, 3/2) are not resolved by the Lumonics excimer-pumped dye laser used in the experiments. The subsequent SHR emission to the $3p_{1/2}$ and $3p_{3/2}$ states ($\lambda \sim 818.5$ nm and 819.7 nm, respectively) was monitered by a Jarrell-Ashe spectrometer with a resolution of 0.03 nm (see Fig. 1 for an energy level diagram of the process involved).

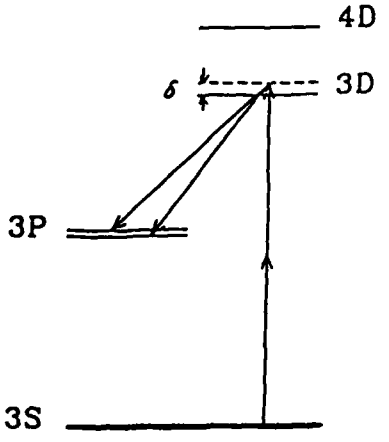

Figure 1. Energy level schematic of hyper-Raman process in sodium vapor.

The gain for the SHR process is inversely proportional to the square of the initial laser detuning, δ, and not sensitive to the direction of that detuning (i.e., whether the laser photons are tuned to the high or low energy side of the 3d resonance). When tuned to the low energy side of the 3d states it was noted that the intensity of the backward directed $3p_{1/2}$ SHR emission was always more suppressed than the $3p_{3/2}$ SHR intensity (Fig. 2b). The opposite would occur when detuned to the high energy side of the two-photon 3d resonance; the $3d - 3p_{3/2}$ signal was reduced in intensity more than the peak at 818.5 nm (Fig. 2c).

The asymmetry of SHR peak suppression due to the direction of incident laser detuning was consistently reproducible, and became understandable in light of other work involving the a.c. Stark effect.[3] The a.c. Stark effect causes either the apparent splitting or shifting of atomic sublevels coupled by an electromagetic field. For near resonant processes it is quadratic with respect to the field and proportional to the product of electromagnetic field amplitude and the dipole matrix element connecting two states, and inversely proportional to the energy mismatch of the photon field that couples the states.

Now note that the sign of the energy mismatch (detuning) of the coupling field determines the direction of the shift. If the photon energy, $\hbar\omega$, couples to states at exact resonance, the levels appear to be split into sublevels with equal amplitudes. If the photon has less energy than the transition between levels (i.e., is tuned to the red side) the splitting evolves into a shifting of levels with the atomic states pushed apart. The opposite happens when the photon is more energetic or is tuned to the blue side of the resonance.

The a.c. Stark shift can now be used to explain the backward SHR asymmetry discussed earlier. If one tunes the incident laser to the red side (low energy) side of the two-photon 3d resonance (see Fig. 3), SHR is emitted between the virtual state and both the $3p_{1/2}$ and $3p_{3/2}$ states, labeled ω_1 and ω_2. If one redraws these transitions so that they start from the d state (dotted lines) it is easily seen that while ω_1 is on the red side of both of the $3d-3p$ transitions, ω_2 is to the blue side of $3d-3p_{3/2}$ transition, but to the red side of $3d-3p_{1/2}$ transition. The ω_1 photon pushes the 3d states away from both of the 3p levels, while ω_2 pushes the $3d-3p_{1/2}$ levels even further apart, while pushing together the $3d-3p_{3/2}$ levels. The net effect is to have a total Stark shift which is greater for the $3d-3p_{1/2}$ transition than it is for the $3d-3p_{3/2}$ one. Since the total Stark shift is larger for the $3d-3p_{1/2}$ transition, it has a lower transition rate and will, therefore, be suppressed in intensity compared to the case where the laser is tuned exactly to the two-photon resonance. The exact opposite occurs when tuned to the blue (high energy) side of the resonance. Both ω_1 and ω_2 tend to push the $3d-3p_{3/2}$ states together, while ω_1 pushes $3d-3p_{1/2}$ states apart and pulls the $3d-3p_{3/2}$ together. The net effect is to have the Stark shift greater for the $3d-3p_{3/2}$ transition, and to suppress its transition probability with respect to the $3d-3p_{1/2}$ emission. Put in other terms, when the laser is detuned to the red side of the two-photon 3d resonance, the 818.5 nm emission should be more suppressed than the 819.7 nm emission when compared to intensities at zero detuning. When detuned to the blue side the opposite should occur.

This is exactly what the wavelength scans in Fig. 2 show. One expects the intensity of both peaks to be decreased when detuned from resonance, but if one does not include the a.c. Stark effect it is expected that both peaks are affected by the same amount. It is only when one takes the a.c. Stark effect into account that this asymmetry phenomenon becomes understandable. It is also direct experimental proof that the a.c. Stark effect can suppress the gains for resonant processes such as SHR and amplified spontaneous emission.[3] It should be noted that differences in the shifts at these laser intensities and detunings are small (~10%), and in a region where the gain is still in exponential growth (i.e., not yet limited by saturation effects). Thus, even these small differences can significantly affect peak intensities.

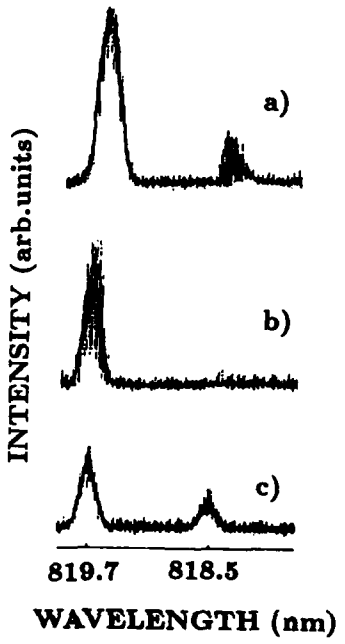

Figure 2. Backward SHR emission from near the Na 3d states to $3p_{3/2}$ and $3p_{1/2}$ states, respectively, at different laser detunings. (a) On resonance, (b) 0.03 nm to the low energy side, $3p_{1/2}$ transition suppressed, (c) 0.05 nm to the high energy side, $3p_{3/2}$ transition suppressed.

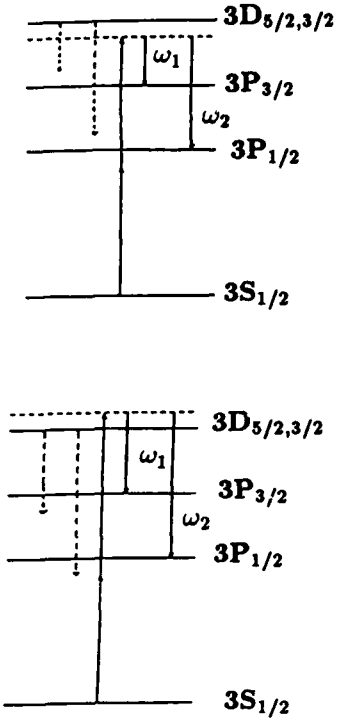

Figure 3. Schematic of backward SHR emission out of 3d states illustrating the radiation responsible for the asymmetric suppression of the 3p states as a function of the direction of pump laser detuning due to the a.c. Stark effect.

Research sponsored by the Office of Health and Environmental Research, U.S. Department of Energy under contract DE-AC05-84OR21400 with Martin Marietta Energy Systems, Inc. M. A. Moore is a postdoctoral fellow, University of Tennessee, Knoxville, Tennessee.

REFERENCES

1. M. A. Moore, W. R. Garrett, and M. G. Payne, Optics Comm. (in press),1988.
2. W.R. Garrett and M. G. Payne, Phys. Rev. A 26, 356 (1982).
3. W. R. Garrett, M. A. Moore, M. G. Payne, and R. K. Wunderlich, "Suppression Effects in Two-Photon Resonantly Enhanced Nonlinear Processes" (to be published).

ATTOSECOND BEATS IN SODIUM VAPOR

D. DeBeer, E. Usadi and S. R. Hartmann
Columbia Radiation Laboratory and Department of Physics
Columbia University, New York, NY 10027

ABSTRACT

Transient time-delayed four-wave mixing (TDFWM) experiments have been performed on the Na D doublet and modulations of 980 attoseconds have been observed. This period corresponds to the sum frequency of the two Na D lines. The experiments were performed using 7 ns pulses of light with frequency components at each of the D-line transitions. The effects of superposition-state modulations are observed in the integrated TDFWM signal as a function of the time delay. As the time delay is varied, the lowest diffraction order mixing signal is modulated. Higher diffraction order mixing signals contain modulation components at integral multiples of the beat frequency.

INTRODUCTION

Intensity modulations of a four-wave mixing signal as a function of time delay between the excitation pulses have been observed using both incoherent[1] and coherent[2] light. The modulation arises from the interference of two transitions in the sample. In both cases the modulation was at the difference frequency of the two transitions. We report here the observation of beats at the sum frequency of the two transitions.[3]

EXPERIMENTAL

The experiments were done on the D-lines in sodium. A schematic diagram of the apparatus is shown in Fig. 1. The dye-laser pulses were 7 ns in duration and were tuned to 589.6 and 589.0 nm, the wavelengths of the sodium $3S_{1/2}$-$3P_{1/2}$ and $3S_{1/2}$-$3P_{3/2}$ transitions, respectively. The dye-laser outputs were split and recombined to provide two double-frequency pulses in such a way that the 589.0 nm component was delayed by τ in one beam and the other frequency component was delayed by the same amount in the other beam. The two double-frequency beams were angled at $\theta \approx 0.3$ mrad. These pulses overlapped spatially throughout a 100 mm long sodium cell which was held at a constant temperature. A pinhole in the focal plane of a 300 mm lens passed the TDFWM signal in the phase-matched $\mathbf{k}_2 + n(\mathbf{k}_2 - \mathbf{k}_1)$ direction while blocking the excitation pulses. Here $\mathbf{k}_1$ and $\mathbf{k}_2$ refer to the wavevectors of the

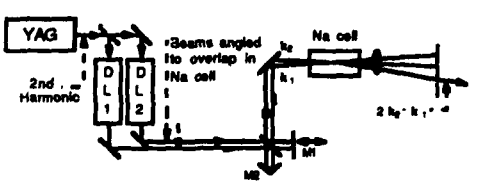

Fig 1.Schematic diagram of the apparatus

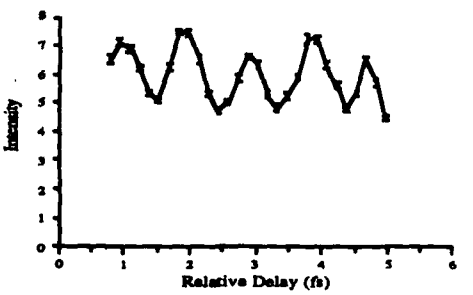

Fig. 2 Data showing 980 as beats

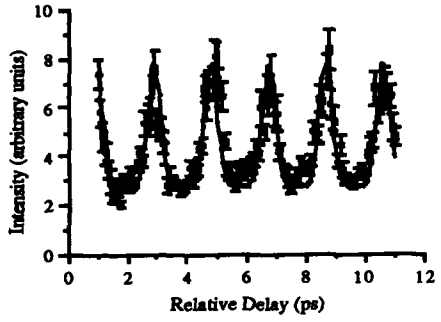

Fig. 3 Fourth order diffraction signal data

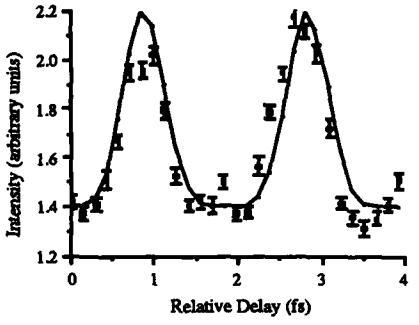

Fig. 4 Data obtained on a single transition

excitation pulses and n is the diffraction order. The signal was detected with a photodiode and integrated over its full 7 ns duration. In a typical run, the TDFWM signal was monitored as the relative delay was varied by moving mirror M1. The result of such a run is shown in Fig. 2.

DISCUSSION

The origin of the beats can be simply understood in terms of an induced-grating picture. The two angled excitation pulses at 589.0 nm set up a stationary intensity grating in the sample which induces a population grating. As one of the pulses is delayed with respect to the other the grating sweeps across the sample. The light at 589.6 nm similarly sets up a population grating. The geometry makes the gratings sweep in opposite directions as a function of the time delay. As the two gratings go in and out of phase the four-wave mixing signal is modulated at just the sum frequency of the two transitions. Difference-frequency beats are also easily explained in this model. In this case the geometry is such that the gratings sweep in the same direction; however, they sweep at slightly different rates and go in and out of phase very slowly at just the difference of the two transition frequencies.

When the analysis is done more rigorously[3] interesting effects are predicted. 1) The modulation of higher order diffraction signals (those into the directions $\mathbf{k}_2 + n(\mathbf{k}_2 - \mathbf{k}_1)$) is expected to narrow according to $I_n \propto [1 + \cos((\Omega + \Omega')\tau)]^n$. We have not seen this effect in the sum-frequency beats. We believe this is due to inadequate vibrational stability in the apparatus. The effect, however, has been observed in difference-frequency beats as shown in Fig. 3. 2) The modulation is also expected to narrow for large pulse areas. We have looked at beats in this pulse area regime but have not observed the expected narrowing. 3) In the limit where $\Omega' \rightarrow \Omega$ the modulation is at Ω, not at 2Ω, but the modulation pattern narrows according to $I_n \propto [1 + \cos(\Omega\tau)]^{2n+1}$. Fig. 4 shows the expected narrowing of the beats observed in the first diffraction order when working on a single transition.

This work was supported by the U. S. Office of Naval Research and by the Joint Services Electronics Program (U. S. Army, U. S. Navy, U. S. Air Force) under Contract No. DAAG29-85-K-0049.

[1]R. Beach, D. DeBeer, and S. R. Hartmann, Phys. Rev. A 32, 3467 (1985)
[2]D. DeBeer, L. G. Van Wagenen, R. Beach, and S. R. Hartmann, Phys. Rev. Lett. 56, 1128 (1986)
[3]D. DeBeer, E. Usadi, and S. R. Hartmann, Phys. Rev. Lett. 60, 1262 (1988)

SUPPRESSION OF TWO-PHOTON RESONANTLY ENHANCED NONLINEAR PROCESSES IN EXTENDED MEDIA

W. R. Garrett, Mary Anne Moore,*
M. G. Payne, and Rainer K. Wunderlich**
Chemical Physics Section, Oak Ridge National Laboratory
Oak Ridge, Tennessee 37831-6378

ABSTRACT

On the basis of combined experimental and theoretical studies of nonlinear processes associated with two-photon excitations near 3d and 4d states in Na, we show how resonantly enhanced stimulated hyper-Raman emission, parametric four-wave mixing processes and total resonant two-photon absorption can become severely suppressed through the actions of internally generated fields on the total atomic response in extended media.

INTRODUCTION

A number of nonlinear optical studies have established that certain strongly resonant multiphoton phenomena which are readily observed under very low density conditions may become almost undetectable at higher number densities, though from simple considerations they would be expected to scale with pressure.[1-3] In a series of studies in Na vapor, we have demonstrated some new suppression mechanisms which become operative in near resonant nonlinear processes and we have illustrated new features of previously known suppression effects.

Some facts associated with two-photon excitations of $s \rightarrow d$ transitions in "extended" alkali vapors are the following: 1) at two-photon resonance, laser absorption is much smaller than that predicted on the basis of atomic beam photoionization experiments; 2) stimulated hyper-Raman (SHR) emission is suppressed in the forward direction and backward SHR, parametric four-wave mixing (PFWM), and amplified spontaneous emission (ASE) show saturation behavior at high laser power and/or high number density; 3) the saturation effect mention in 2) has a very sharp onset with pressure at constant laser power, or with laser power at constant pressure; 4) the backward propagating SHR profiles show a power and pressure dependent dip in lineshape at the two-photon resonance, and 5) although in these experiments SHR emission should have higher gain than PFWM, nevertheless PFWM processes are comparable in intensity to SHR emissions. All of these effects can be operative in regimes where laser beam attenuation and population transfer are not significant.

We have delineated the respective roles of a.c. Stark effects and PFWM interferences in suppressing expected results for two-photon resonantly enhanced phenomena, and explained quantitatively the features listed in the above paragraph.

Experimental elements included a stainless steel heat pipe oven and an excimer pumped dye laser system of 3 mm beam diameter, maximum unfocused power densities of $5 \times 10^6 \mathrm{W/cm^2}$, and $\approx 0.08 \mathrm{cm^{-1}}$ FWHM bandwidth.

RESULTS

In an earlier study of nonlinear wave mixing phenomena in Na vapor, we have shown that the three-photon resonant interference effect, in which an internally generated four-wave mixing field interferes with direct three-photon

excitation,[3,4] manifests itself in SHR emission.[5] Indeed we have shown that forward directed SHR emissions are suppressed for hyper-Raman processes involving excitation of a dipole allowed transition.[5] It is easy to show that the same behavior should result for the five-photon hyper-Raman process shown in Fig. 1. The predicted behavior has been established in two-photon pumping near 4d states in Na. In the lower trace in Fig. 1, backward directed five-photon hyper-Raman emissions near 8000 Å, associated with $3p_{3/2}$ and $3p_{1/2}$ excitations, as shown (corresponding to ω' and ω'' in the diagram). In the upper trace the forward axial emissions are recorded under identical circumstances. The SHR lines are absent, due to interference by the internally generated six-wave mixing fields at the $3p_{1/2} - 3s_{1/2}$ and $3p_{3/2} - 3s_{1/2}$ frequencies. (The single line is due to axially phase matched parametric six-wave mixing.)

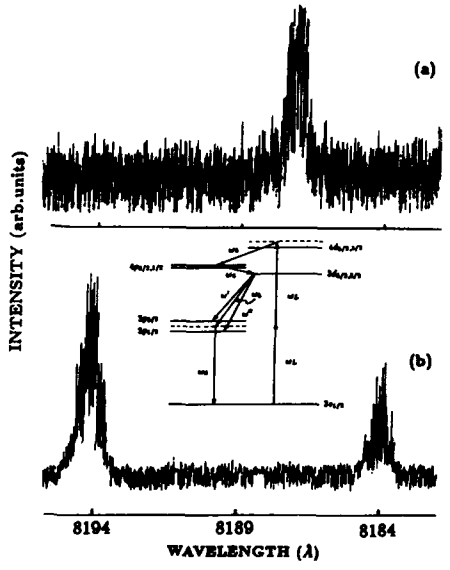

Figure 1. Insert: Five-photon SHR emissions, ω', ω'', in Na. Lower trace, backward SHR profiles. Top trace, forward emission. No SHR in forward direction.

The backward directed SHR (one of which is ω_3 in Fig. 1) causes large a.c. Stark shifting of the $4d$ and $4p$ states. This effect limits the gain of backward SHR, causing it to go from a quadratic laser intensity, I_L^2, over to linear dependence for SHR output. This effect is demonstrated in Fig. 2 for ≈819 nm emissions associated with $3p_{3/2}$ and $3p_{1/2}$ SHR excitations when tuning near two-photon resonance with the $3d$ states. The Stark shifting also causes the SHR excitation profiles to show a dip at two-photon resonance.

Additionally, when tuned to two-photon resonance, the generation of PFWM fields can cause a different class of interference to occur between direct two photon pumping by the laser field and two photon pumping by the PFWM fields.[6,7] The generated fields grow until the interference cancels the two-photon pumping mechanism and thereafter no additional PFWM generation occurs unless the driving field changes. Thus at fixed laser power the intensity of a PFWM signal should increase with pressure until the interference occurs, then saturate. This type of behavior is shown in Fig. 3 where the PFWM wave at 2.33μ generated when tuning near the $4d$ state, is shown as a function of Na number density (fixed laser intensity of 34 MW/cm^2).

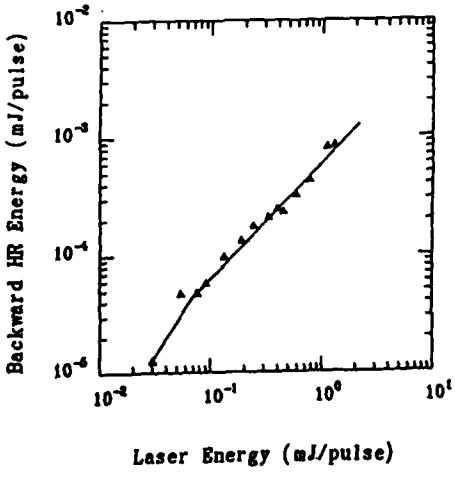

Figure 2. Intensity of backward SHR emissions near 8100 Å when tuning near Na 3d state, showing quantative and linear power dependent regions. $P_{Na} = 0.07$ Torr.

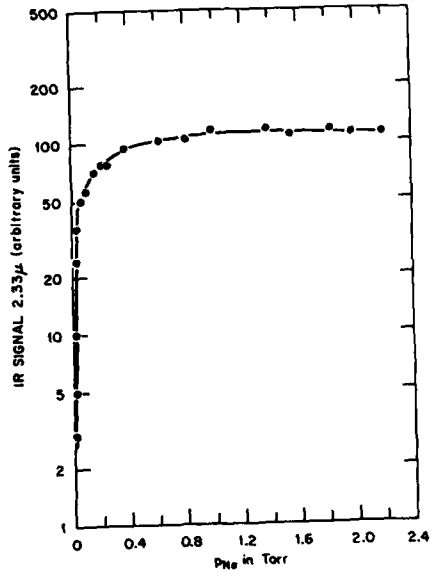

Figure 3. PFWM output at 2.33 μm as a function of P_{Na}. Laser intensity 34 MW/cm^2, detuned 0.3 Å from 4d resonance.

Finally, we show that with increasing laser intensity the two-photon interference will set in at a given intensity (for fixed number density and column length). When this occurs we predict that the power dependence of I_{PFWM} will go over from quadratic in I_L to linear in I_L. This feature has been shown to occur again for the 2.33μ component of PFWM generated at two-photon resonance with $4d$.

We get quantitative agreement between experimental findings and theoretical predictions on these and other features of the nonlinear behavior associated with near resonant pumping of two-photon resonances in Na.

Research sponsored by the Office of Health and Environmental Research, U.S. Department of Energy under contract DE-AC05-84OR21400 with Martin Marietta Energy Systems, Inc. Mary Anne Moore present address: Harvard-Smithsonian Center for Astrophysics, Cambridge, MA. Rainer K. Wunderlich permanent address: Max-Planck-Institut fur Kernphysik, West Germany.

REFERENCES

1. J. C. Miller, R. N. Compton, M. G. Payne, and W. R. Garrett, Phys. Rev. Lett. 75, 114 (1980).
2. M. G. Payne, W. R. Garrett, and H. C. Baker, Chem. Phys. Lett. 75, 468 (1980).
3. W. R. Garrett, W. R. Ferrell, M. G. Payne, and J. C. Miller, Phys. Rev. A 34, 1165 (1986).
4. W. R. Garrett, S. D. Henderson, and M. G. Payne, Phys. Rev. A 34, 3463 (1986).
5. M. A. Moore, W. R. Garrett, and M. G. Payne, Optics Commun. 68, 310 (1988).
6. E. A. Manykin and A. M. Afanas'ev, Sov. Phys. JETP 21, 619 (1965); 25, 828 (1967).
7. M. S. Malcuit, D. J. Gauthier, and R. W. Boyd, Phys. Rev. Lett. 55, 1086 (1985).

EXPERIMENTAL STUDIES OF SELF-SUPPRESSION OF VACUUM ULTRAVIOLET GENERATION IN Xe

J. P. Judish, S. L. Allman, W. R. Garrett, and M. G. Payne
Chemical Physics Section, Oak Ridge National Laboratory
Oak Ridge, Tennessee, USA, 37831-6378

ABSTRACT

Vacuum ultraviolet light in the range 116 nm to 117 nm was produced by using a two-photon resonant four-wave mixing scheme in Xe. The buildup of coherent cancellation of the two-photon resonant transition employed in the generation of the vacuum ultraviolet, with resulting limitations imposed on the achievable vacuum ultraviolet intensity was investigated. Under certain predicted conditions, increases in the intensity of one of the pumping beams, ≈1500 nm infrared, or tuning this beam towards resonance with the $5p^5 7s(3/2)_1$ level of Xe led, not to increases, but decreases in the vacuum ultraviolet generated.

INTRODUCTION

Generation of vacuum ultraviolet (VUV) by four-wave mixing (FWM) in Xe has both practical and theoretical interest. For instance, this method has been used successfully[1] to produce tunable VUV for the selective excitation and subsequent ionization of Kr as part of a way to quantitatively detect small amounts of Kr isotopes in a gas sample. On the other hand, a careful theoretical analysis[2,3] of this process predicts some subtle effects whose importance we have only recently recognized. Under certain conditions, as the generated VUV propagates through the generation cell along with the 252.5 nm ultraviolet (UV) and the 1507 nm infrared (IR) pumping beams, a two-photon effect can become operative and cause cancellation of the two-photon resonant enhancement in the generation process. This comes about when the Xe level pumped by the two-photon UV transition is also two-photon pumped by the VUV and the second laser field, but out of phase. The theory predicts that, for certain predicted conditions, the generated VUV intensity will decrease rather than increase when the intensity of the IR is increased or when the IR is tuned closer towards resonance with the $5p7s(3/2)_1$ level of Xe. We undertook experiments to make checks on the theory's predictions. In the present study we present results that appear to verify some of these predictions.

RESULTS

Figure 1 shows the energy level diagram involved. The doubled frequency of a YAG laser pulsed at 10 Hz is split to pump two dye lasers. The output of one dye laser is mixed with a residual 1064 nm beam from the YAG to produce the 252.5 nm UV. It is kept tuned for an exact two-photon resonance with the $5p^5 6p[3/2]_2$ state of Xe. The output of the second dye laser is injected into a hydrogen filled Raman-shifter. By tuning this dye laser, the second stokes output (≈1507 nm) of the Raman shifter can be set at a desired energy $\hbar\delta$ above the $5p^5 7s[3/2]_1$ level of Xe. The theory predicts how the VUV intensity will depend on the laser bandwidths, laser intensities, amount of detuning, δ,

Xe pressure, and distance into the VUV generation cell. The prediction, for one simplified example, is that at one point in the cell under certain conditions the relationship between the beam intensities and detuning δ is given by $I_{VUV} \propto \frac{I_{UV}^2 \delta^2}{I_{IR}}$.

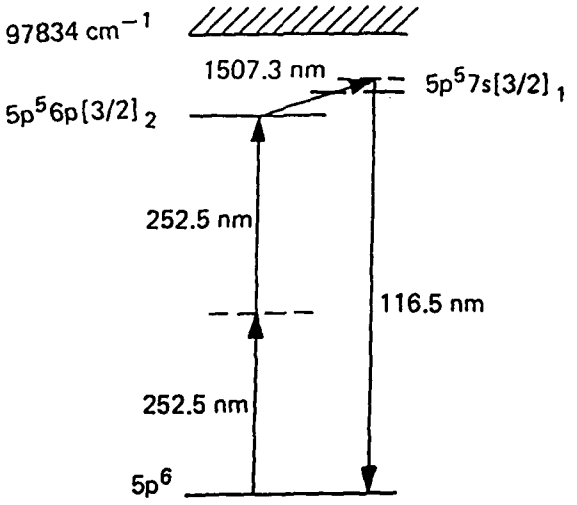

Figure 1. Two-photon resonant four-wave mixing scheme in xenon

Our experimental results shown in Figs. 2 and 3 are for a fixed δ of 0.048 nm on the high energy (negatively dispersive) side of the $7s[3/2]_1$ state with 8 torr of Xe in the VUV cell. Figure 2 shows the relative VUV intensity as a function of UV intensity. Figure 3 shows the relative VUV intensity as a function of IR pump intensity.

These results, in particular the location of the knee of the curve in Fig. 3, closely follow predictions of the theory which takes into account all the parameters previously mentioned. Our study of this cancellation process for different values of the parameters is continuing.

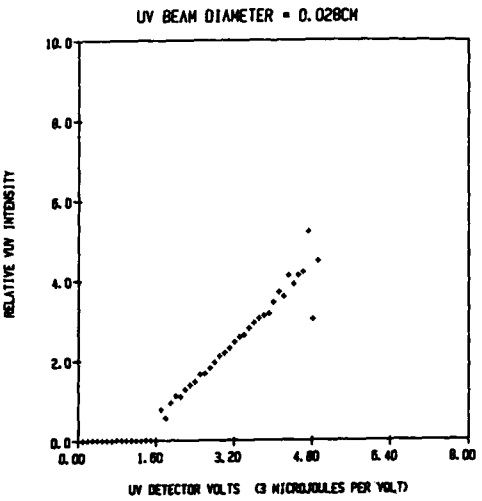

Figure 2. Relative VUV intensity as a function of UV intensity

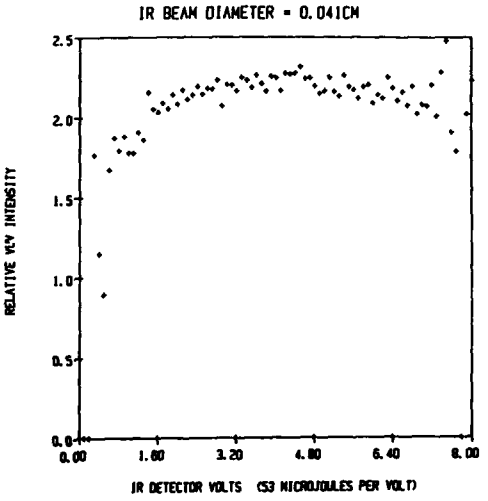

Figure 3. Relative VUV intensity as a function of IR intensity

Research sponsored by the Office of Health and Environmental Research, U.S. Department of Energy under contract DE-AC05-84OR21400 with Martin Marietta Energy Systems, Inc.

REFERENCES

1. S. D. Kramer, C. H. Chen, M. G. Payne, G. S. Hurst, and B. E. Lehmann, Appl. Optics 22 (20), 3271-3275 (1983).
2. E. A. Manykin and A. M. Afanas'ev, Soviet Physics JETP 21, 619-623 (1965).
3. M. G. Payne, W. R. Garrett, J. P. Judish, and Rainer Wunderlich, Proceeding of the Fourth International Laser Science Conference (ILS-IV) in ADVANCES IN LASER SCIENCES - IV (to be published by the American Institute of Physics).

NEW COHERENT CANCELLATION EFFECT INVOLVING FOUR-PHOTON EXCITATION AND THE RELATED IONIZATION

M.G. PAYNE, W.R. GARRETT,
J.P. JUDISH, AND M.P. MCCANN
CHEMICAL PHYSICS SECTION, OAK RIDGE NATIONAL LABORATORY,
OAK RIDGE, TENNESSEE 37831-6378

ABSTRACT

We describe here an effect which occurs when a first laser is tuned near a dipole allowed three-photon resonance and a second laser is used to complete a dipole allowed four-photon resonance between the ground state $|0>$ and an excited state $|2>$. In this process three photons are absorbed from the first laser and one photon from the second; so that if the $|0>$ to $|2>$ transition is two-photon allowed the transition is also pumped resonantly by the third harmonic field due to the first laser and the second laser field. When the second laser is strong enough to cause strong absorption of the third harmonic light, and the phase mismatch, Δk is large and dominated by the nearby resonance, a destructive interference occurs between the pumping of the $|0>$ to $|2>$ transition by two- and four-photon processes.

I. INTRODUCTION

Blazewicz and Miller[1] studied five-photon ionization in the region near several three-photon resonances in Xe and Kr. These three-photon resonances were $J = 0$ to $J = 1$ transitions, which are also dipole allowed in one photon. Two colors of light were used, with the first laser being tuned through the phase matching region for third harmonic generation while the second was fixed at a frequency such that four-photon resonance was achieved for some preselected frequency for the first laser. Even without the second laser considerable ionization was seen in this situation, with the ionization lineshape being similar to the phase matching curve for the third harmonic generation. For several different transitions, and for a wide range of pressures, they observed that when the four-photon resonance occurred on the side of the peak of the phase matching curve closest to three-photon resonance a dip in ionization coincided with four-photon resonance. On the other hand, when resonance occurred on the side of the peak with $-\Delta kb < 4$ a peak was observed in the ionization. The observed dips were found to occur only when the power density of the second laser was sufficiently high so that observations of the third harmonic photons showed a deep dip at the resonance. We suggest here that the dips are due to an interference between four- and two-photon pumping of the $|0> \leftrightarrow |2>$ transition which with a broad bandwidth laser is pumped at a rate $R \simeq |\Omega_{0,1}^{eff}\Omega_{1,2}|^2/(\delta_1^2\sqrt{3\Gamma_{L1}^2 + \Gamma_{L2}^2})$. Here,

$\Omega_{0,1}^{eff}$ is half the Rabi frequency for $|0>$ to $|1>$ (including both channels) and $\Omega_{1,2}$ is half of the Rabi frequency between $|1>$ and $|2>$ due to the second laser. δ_1 is the detuning of the second laser from the three-photon resonance, Γ_1 and Γ_2 are the laser bandwidths. When the cancellation occurs $\Omega_{0,1}^{eff} \simeq 0$, thereby leading to no population in $|2>$. The four-photon resonant cancellation to be described here is closely related to the odd-photon resonance cancellation effect first observed by Miller et al[2] and treated theoretically by Payne and Garrett[3-5] and others.[6,7]

II. SUMMARY OF RESULTS

We treat this problem as a three state problem, with states $|0>$ and $|1>$ being coupled coherently by both a three-photon Rabi frequency, $2\Omega_{0,1}^{(3)}$, due to the laser and by a one-photon Rabi frequency, $2\Omega_{0,1}^{(1)}$, due to third harmonic light generated in the medium. The states $|1>$ and $|2>$ are coupled by a one-photon Rabi frequency $2\Omega_{1,2}^{(1)}$ due to the second laser. In dealing with the generation of third harmonic light we assume that the nonlinear susceptibility is dominated by the near resonant terms due to the nearby three-photon resonance. The latter can be related to the three-photon Rabi frequency and δ_1. Since $|0>$ and $|1>$ are coupled by both three-photon and one-photon Rabi frequencies we write an effective coupling parameter as

$$\Omega_{0,1}^{eff} = e^{-3ik(\omega_{L1})z}\Omega_{0,1}^{(3)} + e^{-ik(3\omega_{L1})z}\Omega_{0,1}^{(1)}, \tag{1}$$

where ω_{L1} is the frequency of the first laser and $k(\omega)$ is the length of the propagation vector for an electromagnetic wave with frequency ω. It is this coupling parameter which enters the equations of motion for the density matrix when both coupling channels are included.

We find for the polarization at $3\omega_{L1}$:

$$\mathcal{P}_{3\omega_{L1}} = -ND_{0,1}\frac{\Omega_{1,0}^{eff}}{\delta_1}e^{-3i\omega_{L1}t}\left(1 + i\frac{<<|\Omega_{1,2}|^2>>}{\delta_1\sqrt{3\Gamma_{L1}^2 + \Gamma_{L2}^2}}\right) + cc., \tag{2}$$

where the quantity $D_{0,1}$ is the dipole matrix element between states $|0>$ and $|1>$ and N is the concentration of the active gas.

This polarization can now be combined with Maxwell's equations in order to determine the third harmonic field. As a consequence of our few state approximation Eq. (2) contains only one term linear in the third harmonic field. To properly deal with the dispersive properties of the medium we add on linear polarization terms at $3\omega_{L1}$ due to all other dipole allowed transitions in both the active atoms and any buffer gas atoms that may be present.

We let $\kappa_{0,1} = 2\pi(3\omega_{L1})N|D_{0,1}|^2/(\hbar c)$, $\Delta_s = << |\Omega_{1,2}^{(1)}|^2 >> /\delta_1$, and

$$\alpha = \frac{\kappa_{0,1}}{\delta_1} \frac{\Delta_s}{\sqrt{3\Gamma_{L1}^2 + \Gamma_{L2}^2}},$$
$$\Delta k \equiv \frac{3\omega_{L1}}{c}(n(3\omega_{L1}) - n(\omega_{L1})) = -\frac{\kappa_{0,1}}{\delta_1} + \Delta k_0. \tag{3}$$

2α is the absorption coefficient for the third harmonic light due to two-photon absorption, Δ_s is the a.c. Stark shift in level $|2>$ due to the second laser, and Δk_0 is what needs to be added to the near resonant $|0> \rightarrow |1>$ contribution to the phase mismatch in order to get Δk. Using the slowly varying amplitude and phase approximation with Maxwell's equations and the nonlinear part of the polarization from Eq. (2) ($\Omega_{1,0}^{(1)} = D_{1,0}E_{3\omega_{L1}}^{(0)}/(2\hbar)$)

$$\Omega_{1,0}^{(1)} = -\Omega_{1,0}^{(3)}\left[1 - \frac{\Delta k_0}{\Delta k + i\alpha}\right]\left(e^{-i\Delta kz} - e^{-\alpha z}\right). \tag{4}$$

If $\alpha z >> 1$ and $\sqrt{\Delta k^2 + \alpha^2} >> |\Delta k_0|$ Eq.(4) yields $\Omega_{1,0}^{(1)} \simeq -\Omega_{1,0}^{(3)}e^{-i\Delta kz}$. In this limit Eq. (1) becomes $\Omega_{0,1}^{eff} \equiv 0$. Thus, no population transfer to state $|2>$ occurs for z such that $\alpha z >> 1$.

Research sponsored by the Office of Health and Environmental Research, U.S. Department of Energy under contract DE-AC05-84OR21400 with Martin Marietta Energy Systems, Inc. M. P. McCann, postdoctoral fellow, University of Tennessee, Knoxville, Tennessee.

REFERENCES

1. P.R. Blazewicz and J.C. Miller, Phys. Rev. A38, 2863 (1988). See also:P.R. Blazewicz, M.G. Payne, W.R. Garrett, and J.C. Miller, Phys. Rev. A34, 5171 (1986).
2. J.C. Miller, R.N. Compton, M.G. Payne, and W.R. Garrett, Phys. Rev. Lett. 45, 114 (1980).
3. M.G. Payne, W.R. Garrett, and H.C. Baker, Chem. Phys. Lett. 75, 468 (1980).
4. M.G. Payne and W.R. Garrett, Phys. Rev. A26, 356 (1982).
5. M.G. Payne and W.R. Garrett, Phys. Rev. A28, 3409 (1983). See also: M.G. Payne, W.R. Ferrell, and W.R. Garrett, Phys. Rev. A27, 3053 (1982).
6. D.J. Jackson and J.J. Wynne, Phys. Rev. Lett. 49, 543 (1982).
7. D.J. Jackson, J.J. Wynne, and P.H. Kess, Phys. Rev. A28, 781 (1983).

EFFECT OF THE COHERENT CANCELLATION OF THE TWO-PHOTON RESONANCE ON THE GENERATION OF VACUUM ULTRAVIOLET LIGHT BY TWO-PHTON RESONANTLY ENHANCED FOUR-WAVE MIXING

M.G. Payne, W.R. Garrett, J.P. Judish, and Rainer Wunderlich*
Chemical Physics Section, Oak Ridge National Laboratory,
Oak Ridge, Tennessee 37831-6378

ABSTRACT

Many of the most impressive demonstrations of the efficient generation of vacuum ultraviolet (VUV) light have made use of two-photon resonantly enhanced four-wave mixing to generate light at $\omega_{VUV} = 2\omega_{L1} \pm \omega_{L2}$. The two-photon resonance state is coupled to the ground state both by two photons from the first laser, or by a photon from the second laser and one from the generated VUV beam. We show here that these two coherent pathways destructively interfere once the second laser is made sufficiently intense, thereby leading to an important limiting effect on the achievable conversion efficiency.

INTRODUCTION

Various aspects of the two-photon cancellation effect were first discussed in a series of papers by Manykin and Afanas'ev[1] published more than 20 years ago. However, detailed experimental confirmation of the predicted effects have only recently been presented.[2-4] We discuss here the ramifications of this effect on the use of two-photon resonances to enhance nonlinear susceptibilities used in the generation of VUV light. Not only do these effects distort the radial intensity profile of the generated light, but they also limit the conversion efficiency to a few percent.

RESULTS

We describe as a three state system the atomic response when a first laser at frequency ω_{L1} is tuned on or near resonance between the ground state $|0>$ and an excited state $|2>$, and a second laser at ω_{L2} causes a near three-photon resonance between $|0>$ and $|3>$ at $2\omega_{L1} + \omega_{L2}$. Neglecting population transfer from the ground state, but including the possible absorption of the generated VUV due to resonant absorption in which a VUV photon is absorbed and an emission is stimulated at the frequency of the second laser, we find for the nonlinear polarization at angular frequency $2\omega_{L1} + \omega_{L2}$

$$\mathcal{P}_{VUV}^{NL} = e^{i\Phi} \frac{N D_{3,0} \Omega_{23}^{(1)}}{\delta_3(\delta_2 + i\Gamma)} \left[\Omega_{02}^{(2)} e^{-i\Delta k z} - \frac{\Omega_{32}^{(1)} \Omega_{03}^{(1)}}{\delta_3} \right] + c.c. \qquad (1)$$

In Eq. (1) $2\Omega_{02}^{(2)}$ is the two-photon Rabi frequency for the transition $|0> \leftrightarrow |2>$ due to the first laser, $2\Omega_{23}^{(1)}$ is the one-photon Rabi frequency for the transition $|2> \leftrightarrow |3>$ due to the second laser, and $2\Omega_{03}^{(1)}$ is the one photon Rabi frequency for the $|0> \leftrightarrow |3>$ transition due to the generated field at $2\omega_{L1} + \omega_{L2}$. N is the concentration of the active gas, $\Phi \equiv k_{VUV}z - \omega_{VUV}t$, δ_2 is the detuning from exact resonance between the first laser and the $|0>$ to $|2>$ resonance, δ_3 is the detuning of $2\omega_{L1} + \omega_{L2}$ from resonance between $|0>$ and $|3>$, Γ is the collisional width of the two-photon resonance, $\Delta k \equiv k_{VUV} - 2k_{L1} - k_{L2}$ is the phase mismatch, and $D_{0,3}$ is the matrix element of the electronic dipole operator between states $|0>$ and $|3>$. The term $\Omega_{03}^{(1)}\Omega_{32}^{(1)}/(\delta_3)$ is a two-photon Rabi frequency for driving transitions between $|0>$ and $|2>$ by the absorption of a VUV photon and a stimulated emission of a photon at ω_{L2}. The term in $\mathcal{P}_{VUV}^{NL}$ involving the latter combination includes in the polarization both the absorption of the VUV wave by this process and the power dependent phase mismatch due to the strong coupling between $|2>$ and $|3>$ when $\delta_2 \neq 0$. If we use Eq. (1) in Maxwell's equations and implement the slowly varying phase and amplitude approximation we find for $\Delta k = 0$

$$\Omega_{03}^{(1)} = \frac{\Omega_{02}^{(2)}\delta_3}{\Omega_{32}^{(1)}}(1 - e^{-\beta z}), \tag{2}$$

where $\kappa_{03} = 2\pi\omega_{VUV}N|D_{0,3}|^2/(\hbar c)$, and $\beta = i\kappa_{03}(|\Omega_{23}^{(1)}|^2)/[\delta_3^2(\delta_2 + i\Gamma)]$. If $|\beta L|$ is much larger than unity the exponential term is small and we see that by the time the exit end of the cell (z = L) is reached $\Omega_{03}^{(1)}\Omega_{32}^{(1)}/\delta_3 = \Omega_{02}^{(2)}$. This is just the condition for the total destructive interference of the two pathways for pumping the transition between state $|0>$ and state $|2>$. The approach to this limit involves a true cancellation of the two-photon resonance if $\delta_2 = 0$. However, when $|\delta_2| >> \Gamma$ the solution oscillates about this limit as a function of z due to a large power dependent phase mismatch induced by the near two-photon resonance. We see that the VUV signal becomes limited by the cancellation of the pumping of the two-photon resonance. On the other hand, if $|\beta L| << 1$ the result becomes exactly equivalent to the conventional result.

One thing which is easily seen from the cancellation condition is that making the power density at ω_{L2} too large can actually decrease the generation of light at ω_{VUV}. The optimum intensity at frequency ω_{L2} is such that the absoption of the VUV due to two-photon excitation satisfies $N\sigma_a L/2 \simeq 1.5$. Either less or more power density at this wavelength decreases the generated intensity of the VUV light. When the intensity is made far too large we must consider the power densities as a function of radial distance away from beam center carefully if we are to be able to interpret the manifestations of the effect in an actual experiment. We assume that the radial power densities are such that $\Omega_{23}^{(1)} = \Omega_{23}^{(1)}(0)e^{-\rho^2/R_2^2}$, and $\Omega_{02}^{(2)} = \Omega_{02}^{(2)}(0)e^{-2\rho^2/R_1^2}$.

We will now integrate over the radial power densities for the lasers and derive an expression for the number of VUV photons passing through a cross

section of the beam at z during the pulse for the case $\delta_2 = 0$ and $\Delta k = 0$. Let $x = \beta(0)z$ and $y = (R_2/R_1)^2$, then after some substitutions

$$N_\gamma = \frac{1}{2} N_e W(\beta(0)z, (R_2/R_1)^2), \tag{3}$$

with $N_e = [2|\Omega_{02}^{(2)}(0)|^2\tau/\Gamma](N\pi R_1^2 z)$ = number of excited atoms produced in state 2 from cell entrance to z, and τ is the pulse length of the lasers. Above, $\beta(0)$ is the value of beta at beam center, R_1 and R_2 are the radii of the laser beams and the function W is given by

$$W(x,y) = yx^{-2y}\int_0^x \frac{ds}{s^{2(1-y)}}\left(1-e^{-s}\right)^2 = 2xy\sum_{n=0}^{\infty}(-1)^n\frac{[2^{n+1}-1]}{(n+2)!}\frac{x^n}{n+2y+1}.$$

W is usually less than 0.2, where this value is reached for $\beta(0)L$ values between 1 and 5 if the beam radii are not widely different. This suggests that an overall efficiency in generating VUV photons is limited to about 10% of N_e. It is probable that an N_e large enough to attenuate the laser significantly would spoil the phase matching by changing the index of the medium. Another effect which becomes probable when the power density of the first laser is large enough to produce strong attenuation of the first laser beam is the initiation of parametric four-wave mixing which can grow from noise to the point where it leads to greatly reduced absorption of the laser beam. Exactly this effect is known to greatly reduce the absorption of laser beams tuned near the 3s to 4d two-photon resonance in sodium.[4]

Research sponsored by the Office of Health and Environmental Research, U.S. Department of Energy under contract DE-AC05-84OR21400 with Martin Marietta Energy Systems, Inc. Rainer Wunderlich permanent address: Max-Planck-Institut fur Kernphysik, Heidelberg, West Germany.

REFERENCES

1. E.A. Manykin and A.M. Afanas'ev, Soviet Physics JETP 21, 619 (1965). See also: A.M. Afanas'ev and E.A. Manykin, Soviet Physics JETP 21, 323 (1965).
2. M.S. Malcuit, D.J. Gauthier, and R.W. Boyd, Phys. Rev. Lett. 55, 1086 (1985).
3. M.A. Moore, W.R. Garrett, and M.G. Payne, Optics Commun. 68, 310 (1988).
4. W. R. Garrett, Mary Anne Moore, M. G. Payne, and Rainer K. Wunderlich (Proceeding of the Fourth International Laser Sience Conference (ILS-IV), Atlanta, Ga, October 1988 (to be published by American Institute of Physics).

K $4^2S_{1/2} \rightarrow 8^2S_{1/2}$ TWO-PHOTON ABSORPTION BY NEAR-RESONANT PUMPING OF $6^2P_{1/2,3/2}$ STATE

Yuezhen Sun, Xinghua Li, Qi Wang and Yongkang Cheng
Institute of Opto-electronics, Harbin Institute of Technology,
Harbin, China

ABSTRACT

Using a pulsed dye laser near-resonantly pump the 6^2P_J state of potassium atom, we have observed the $4^2S_{1/2} \rightarrow 8^2S_{1/2}$ two-photon absorption.

INTRODUCTION

There are some papers reporting the equal frequency two-photon absorption of potassium atoms to the $8s^2S_{1/2}$, $7s^2S_{1/2}$, $5d^2D_J$ states and the related nonlinear phenomenon. Here, we use a UV pulsed dye laser near-resonant pumping K $6p^2P_J$ state, having observed the emission of $8s^2S_{1/2} \rightarrow 4p^2P_J$ and a series of cascade stimulated emission resulting from the stimulated Raman scattering. Analysis of the theoretical and experimental results shows that the $8s^2S_{1/2} \rightarrow 4p^2P_J$ emission originates from the two-photon absorption in which the two photons are different.

EXPERIMENTAL SET-UP

An excimer laser(XeCl) is used to pump the PTP dye laser. The linewidth of the dye laser is 0.016nm. The dye laser energy is about 1mJ per pulse when the laser wavelength is 344.6nm. The dye laser beam is reflected into the stainless steel heat pipe containing potassium vapor. Passing through the dichroic plate, the fluorescence is focused into the monochromator by a focal lens. After spectral analysis, the signal is received by the photomultiplier tube or PbS detector. Then it is sent to the boxcar averager and recorded by the recorder.

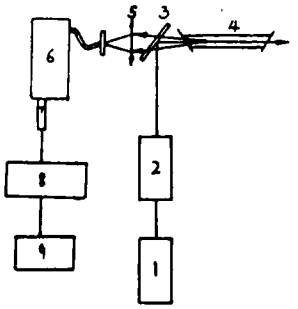

1. Excimer laser; 2. Dye laser;
3. Dichroic plate; 4. Heat pipe;
5. Focal lens; 6. Monochromator
7. Detector; 8. Boxcar averager;
9. Chart recorder.

Fig.1 Experimental set-up

RESULTS AND ANALYSIS

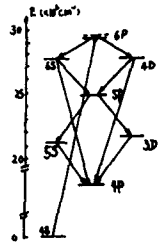

Fig.2 Partial energy level of potassium atom

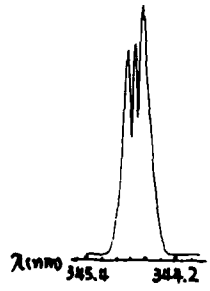

Fig.3 The intensity of $6^2S_{1/2} \rightarrow 4^2P_{1/2}$ vs λ_L

Fig.2 is the partial atomic energy diagram of potassium. When UV laser near-resonantly pump the $6p^2P_J$ state, the atom in the $4s^2S_{1/2}$ is scattered to the $6s^2S_{1/2}$ or $4d^2D_J$ states, producing a Stokes photon. The population inversion of the $6^2S_{1/2}$, 4^2D_J to the 5^2P_J and 4^2P_J is formed, resulting in the production of a seris of near infrared and visible cascade emission. Fig.3 is the variation of the intensity of $6^2S_{1/2} \rightarrow 4^2P_{1/2}$ transition (691.1nm) versus the laser wavelength. From Fig.3, we see that the tuning range of the Raman scattering is about 1.0nm. In the experiment we have measured the cascade emission in the near infrared range. The final state of the cascade stimulated emission is $4^2S_{1/2}$. The $4^2P_J \rightarrow 4^2S_{1/2}$ emission doesn't appear in low temperature(below 600℃) due to the strong self-absorption. The whole process can be expressed,

$$K(4s)+\hbar\omega_L \rightarrow K^*(6s \text{ or } 4d)+\hbar\omega_s$$
$$K^*(6s) \rightarrow K^*(5p)+\hbar\omega(6s-5p)$$
$$K^*(6s) \rightarrow K^*(4p)+\hbar\omega(6s-4p)$$
$$K^*(4d) \rightarrow K^*(5p)+\hbar\omega(4d-5p)$$
$$K^*(4d) \rightarrow K^*(4p)+\hbar\omega(4d-4p)$$
$$K^*(5p) \rightarrow K^*(5s)+\hbar\omega(5p-5s)$$
$$K^*(5p) \rightarrow K^*(3d)+\hbar\omega(5p-3d)$$
$$K^*(5s) \rightarrow K^*(4p)+\hbar\omega(5s-4p)$$
$$K^*(3d) \rightarrow K^*(4p)+\hbar\omega(3d-4p)$$
$$K^*(4p) \rightarrow K(4s)+\hbar\omega(4p-4s)$$

As the laser wavelength is tuned to 344.39nm or 344.61nm, the strong $8s^2S_{1/2} \rightarrow 4p^2P_J$ (532.33nm, 533.97nm) emission also appear in the cascade emission. Fig.4 is the excitation function of the $\lambda = 533.97$nm fluorescence.

From Fig.4 we see that the population of the $8s^2S_{1/2}$ state doesn't originate from the collisional relaxation, but originates from a higher order nonlinear process. Based on the energy calculation, it is obtained,

$$\lambda_L = 344.39\text{nm}, \quad \omega_L + \omega(6^2S_{1/2} \rightarrow 5^2P_{3/2}) = \omega_{8s-4p}$$
$$\lambda_L = 344.61\text{nm}, \quad \omega_L + \omega(6^2S_{1/2} \rightarrow 5^2P_{1/2}) = \omega_{8s-4p}$$

and the seperation of the two peaks in the excitation function of $8^2S_{1/2} \rightarrow 4^2P_{3/2}$ equals to the fine splitting of the 5^2P state.

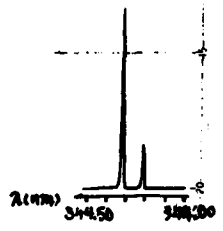

Fig.4 Excitation function of 5339.7nm

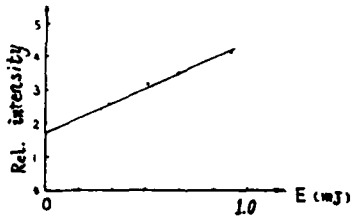

Fig.5 Logrithmic curve of the 533.97 nm intens. vs pumping energy

Because there is a resonance $\omega_L+\omega_{4s-ns}=\omega_{4s-ns}$, the third-order susceptibility is greatly enhanced. At present, the population of the $8^2S_{1/2}$ state is linear with the result of the laser intensity multiplying the intensity of the $6^2S_{1/2}\rightarrow 5^2P_j$ transition. The logrithmic curve of the fluorescence intensity of the $8^2S_{1/2}\rightarrow 4^2P_{3/2}$ transition versus the pumping energy is done as Fig.5. Using the least square fit method we obtain the slope of the experimental line is 2.02. In the experiment we exclude the possibility of three-photon or more than three-photon process and the recombination of the two-photon ionization, proving that the population of the $8^2S_{1/2}$ originates from the two-photon absorption, one is a laser photon, the other is a $6^2S_{1/2}\rightarrow 5^2P_j$ photon produced by the cascade transition.

The generation of 532.3nm and 539.7nm can be interpreted as being due to the four-wave mixing process among the laser photon, a $6^2S_{1/2}\rightarrow 5^2P_j$ transition photon (if λ_L=344.39nm, j=3/2; if λ_L=344.61nm, j=1/2) and a $4^2P_j\rightarrow 4^2S_{1/2}$ transition photon. In the collinear phase-matching condition we have approximately calculated the detuning of this four-wave mixing process, $\Delta k=k_L+k_{4s-ns}-k_{4s-4p}-k_{4p-4s}$, $k=2\pi\times n/\lambda$. The refractive index n can be calculated from the Sellmeier formula,

$$n(\nu)=1+N\times r_e/(2\pi)\times\sum_{n,j} f_{np,j}/(\nu^2_{np,j}-\nu^2)$$

in which $r_e=2.818\times10^{-13}$cm, $\nu_{np,j}$ is the energy of the (nP,j) level, expressed in wavenumber. The calculation shows that the $\Delta k\approx 0$, that is, the detuning of the above-mentioned process is very small. That is why the 8s→4p transition is easily obtained.

REFERENCE

1. P. L. Zhang et al, J. Opt. Soc. Am., B1, 9 (1984)
2. P. L. Zhang, Acta Physica Sinica, Vol.34, (1985)
3. Z. G. Wang et al, Optica Sinica, Vol.6, (1987)
4. A. N. Nesmeyanov, Vapor Pressure of the Chemical Elements (Academic Press, New York, 1963)
5. S. Bashkin, J. O. Stoner, Jr., Atomic Energy-level and Grotrian Diagrams, Vol. II, (North Holland, Amsterdam, 1978)

DIODE LASER-INITIATED, TWO-COLOR RESONANCE IONIZATION MASS SPECTROMETRY OF LANTHANUM*

R. W. Shaw, J. P. Young, and D. H. Smith
Oak Ridge National Laboratory
Oak Ridge TN 37831

ABSTRACT

A GaAlAs semiconductor diode laser tuned to 753.93 nm was utilized to excite the first step of three-photon resonance ionization processes of lanthanum. A practical resonance ionization mass spectrometric (RIMS) instrument based solely on diode laser optical excitation is envisioned.

INTRODUCTION

Tunable semiconductor diode lasers[1] will have a great impact on high resolution optical spectroscopy. They will be particularly important for analytical chemical applications where simplicity of operation is required for routine methods. These devices are inexpensive and compact, but exhibit narrow bandwidth and coherence similar to single frequency dye lasers that cost in the neighborhood of $100,000. The price of the diode laser system used for the experiments reported here was approximately $5000. We utilized a 750 nm GaAlAs diode laser to initiate a resonance ionization scheme for resonance ionization mass spectrometry (RIMS) of lanthanum. The diode laser provided only the first photon of the three-photon (overall) ionization scheme, but, as we will propose, photo-ionizations driven by multiple diode lasers are eminently feasible.

The optical ionization scheme selected was as follows. One photon from the CW diode laser excited ground state ($^2D_{3/2}$) atoms to the $^4F^o_{3/2}$ level at 13260 cm^{-1}. A photon from a pulsed, tunable dye laser further excited the atom to the $^4D_{5/2}$ level at 30354 cm^{-1}. Finally, an additional photon from the same dye laser was of sufficient energy to promote the lanthanum atom to above its ionization potential at 44981 cm^{-1}.

EXPERIMENTAL

The diode laser (model ML-4405, Mitsubishi Electronics America) used exhibited single longitudinal mode operation at 748 nm at room temperature. The bandwidth was 150 MHz, as measured with a scanning Fabry-Perot optical spectrum analyzer, and was probably limited by the current noise of the power supply. The output was collected and focused using a 0.5 N. A. lens. The diode laser was temperature- and current-tuned to produce 753.93 nm light; the operating temperature and current were 45 C and 75 mA. This relatively high current was required to position the operating point for the desired

*Research sponsored by the Office of Energy Research, U. S. Department of Energy, under contract DE-AC05-84OR21400 with Martin-Marietta Energy Systems, Inc.

wavelength at a point remote from a mode hop. The output power was 8 mW, substantially above the nominal rating of 3 mW. The dye laser used was a 6 KHz copper vapor laser-pumped dye laser (model 351HR, Plasma Kinetics Corporation and model DL13P, Molectron Corporation, respectively) with a nominal linewidth of 0.3 cm^{-1}. Rhodamine 6G laser dye in methanol was used, and the overall tuning range was 560 to 600 nm. A single-stage magnetic sector mass spectrometer tuned to mass 139 was used to detect ionization. The diode and dye laser beams crossed at right angles between a 1400 K rhenium filament and the ion lens of the mass spectrometer. The filament had been loaded with approximately 1 mg of lanthanum metal and overcoated with aquadag. An electron multiplier, discriminator, and rate meter were used to count the ions produced.

RESULTS AND DISCUSSION

Over the 40 nm tuning range of the dye laser, more than 80 single color resonance ionization lines of lanthanum were seen.[2] These lines are thought to arise from three-photon processes: two bound-bound atomic transitions, followed by a non-resonant excitation to the continuum. The first two steps require wavelengths that fall within the linewidth of the dye laser, and thus must be nearly iso-energetic. Concerted two-photon processes can not be ruled out in some cases. The strongest single-color lanthanum resonance ionization line in this range is at 579.0 nm.

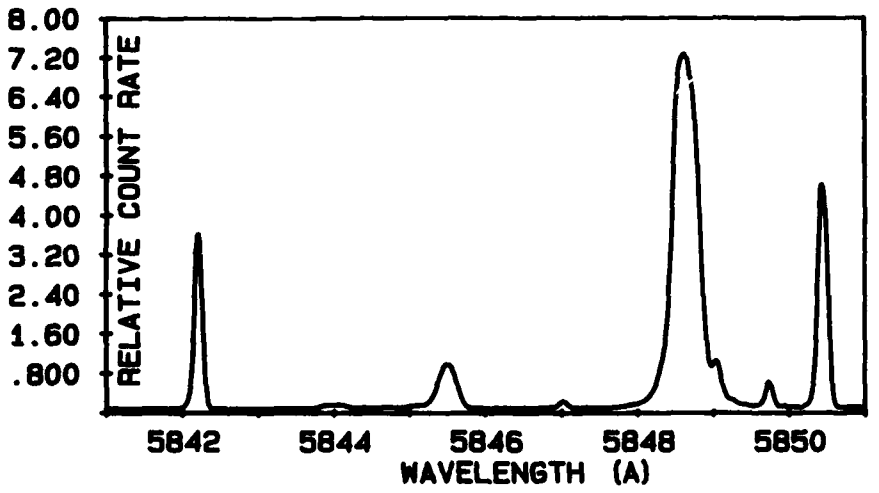

Fig. 1. Lanthanum resonance ionization spectrum

A spectrum resulting from excitation with both lasers (diode laser fixed at 753.93 nm and dye laser scanned) is shown in Figure 1. With the exception of the strong line at 584.86 nm, this spectrum is identical to that using the dye laser alone for this narrow 1 nm range. The 584.86 nm line is completely absent when the 753.93 diode laser is blocked from the experiment; likewise it is

missing if the diode laser is detuned by as little as 0.025 nm. It represents the diode plus dye laser double resonance ionization outlined above. The maximum of the line represents 13,000 counts/second for diode and dye laser powers of 8 mW and 2.1 kW, respectively. The small shoulder to the long wavelength side also is present in the spectrum due to the dye laser only. The width of the 584.86 nm double resonance line indicates saturation. Indeed, it was necessary to reduce the diode laser power to below 2 mW to attain a linear count rate response.

In addition to the two-color line shown in Figure 1, two others were identified. Both were initiated with the diode laser-pumped 0-13260 cm^{-1} transition as above. The second line was found at 566.46 nm and involves excitation to the $^4D_{5/2}$ level at 30909 cm^{-1}. This is a known level[3], but this particular transition is not seen in emission.[4] The final line occurs at a dye laser wavelength of 586.54 nm and corresponds to a $^2F_{5/2}$ intermediate state at 30305.6 cm^{-1}.

CONCLUSIONS

We have demonstrated the utility of an inexpensive semiconductor diode laser for RIMS. Although this study utilized a diode laser for only the first excitation step of a three photon process, the obvious extension would be to employ diode lasers for all of the optical steps. The resulting technique would be much like the cwDRIMS method pioneered by Cannon et al,[5] except that lasers that are both inexpensive and simple to operate are used. The final step, excitation to the continuum, has a much lower cross section and a method such as electric field or carbon dioxide laser ionization probably will be required. Counterpropagating beam methods for Doppler-free linewidths will permit isotopic selectivity in many cases and a practical instrument for isotope ratio determinations can be envisioned.

REFERENCES

1. A. Yariv, Optical Electronics (3rd Edition), Chapter 15, Semiconductor Lasers - Theory and Applications (Holt, Rinehart, and Winston, New York, 1985), p. 467-498.

2. R. W. Shaw, J. P. Young, and D. H. Smith, Analytical Chemistry, submitted for publication.

3. W. C. Martin, R. Zalubas, and L. Hagan, Atomic Energy Levels-The Rare Earth Elements (National Standard Reference Data System, NBS-60, 1978), p. 27.

4. W. F. Meggers, C. H. Corliss, and B. F. Scribner, Tables of Spectral-Line Intensities (NBS Monograph 145, Part 1, National Bureau of Standards, 1975), p. 128.

5. B. D. Cannon, B. A. Bushaw, and T. J. Whitaker, J. Opt. Soc. Am. B 2, 1542 (1985).

VACUUM ENHANCED ATOMIC EXCITATION

Yifu Zhu, A. Lezama, and T. W. Mossberg
Department of Physics
University of Oregon
Eugene, Oregon 97403

ABSTRACT

We report an experimental study of the steady-state behavior of strongly driven,two-level atoms relaxing into a frequency dependent vacuum reservoir. Enhancement or suppression of the atomic excitation has been observed by tuning the resonance frequency of the cavity from one sideband of the strong-field fluorescence triplet spectrum to the other. This effect results from the modification of the population distribution among the atom-field dressed states in the presence of a cavity-modified vacuum reservoir. It may be useful in achieving significant steady-state inversions of two-level atomic samples.

Properties of spontaneous radiative decay of atoms under the influence of an environment other than free space have attracted considerable attention in recent years. In the case of atoms coupled to a cavity-modified vacuum reservoir, several radiative properties, such as spontaneous emission rates,natural decay lineshapes, and radiative level shifts, have been studied recently.[1-3] A new aspect of this problem concerns the properties of strongly driven atoms in a frequency dependent reservoir. New phenomena such as vacuum-field dressed-state pumping, and dynamical suppression of spontaneous emission, have been predicted to occur if the vacuum reservoir changes on a frequency scale comparable or finer than the atomic resonance width.[4] Atomic relaxation dynamics are perturbed because of the finite correlation time in the cavity-modified vacuum reservoir.

Consider the atom-field system in terms of the dressed-state picture[5] which consists of a ladder of doublets separated in frequency by the laser frequency and split by the generalized Rabi frequency. The spontaneous emission process corresponds to the transitions between adjacent dressed-state doublets with emission of fluorescent photons. The transition rates can be controlled by changing the mode density of vacuum field at the various dressed-state transition frequencies as demonstrated in the experiments showing enhanced and inhibited spontaneous emission rates for undriven atoms. By changing the relative mode density at various dressed-state transitions, one modifies the relative

transition rates and consequently changes the distribution of population within each dressed-state doublet. At nonzero laser-atom detuning, owing to the different weights of the dressed-state in terms of bare atomic states, this change leads to modifications in the population of the atomic states.[6] With sufficiently large imbalance of dressed-state population, significant population inversion can be achieved, then the spontaneous emission process will preferentially leave the atom in its excited state.

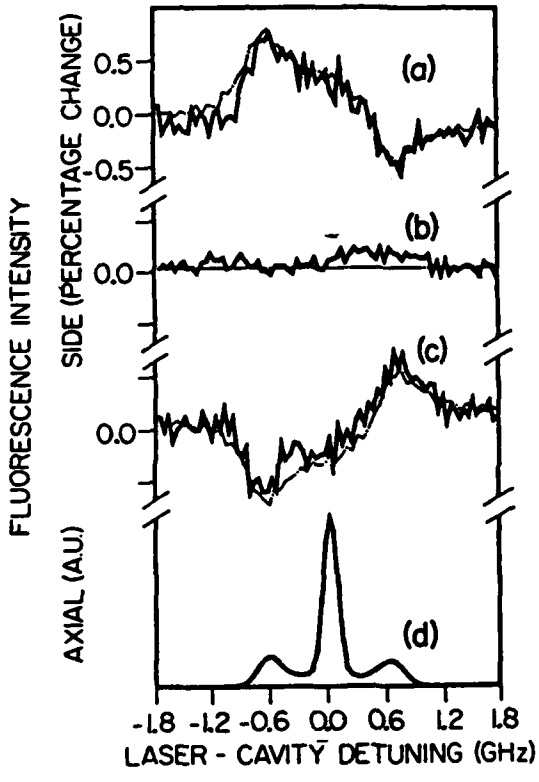

Fig.1. Atomic fluorescence intensity vs Laser-cavity detuning. a-c: Percent change in fluorescent intensity from the open sides of the cavity with laser-atom detuning of 320, 0, and -320 MHZ, respectively. In a-c, each vertical division represents 0.5 percent change. d: Fluorescence out the end of the cavity recorded simultaneously with (a) above. In d, the Mollow triplet is evident. In a-c, the thick solid line is experimental data and the thin dash-dotted line is theoretical fit based on the measured cavity-induced mode density change of 5%. Increases in side fluorescence intensity indicate cavity-induced increases in excited state population.

To demonstrate the basic mechanism described above, an experiment was performed in which Ba atoms were made to pass through the center of a mode degenerate, symmetric, 1-cm-long confocal cavity with mirror reflectivity 99.3%. The mode density is increased by about 5% relative to the free-space value in the vicinity of the cavity resonance frequency as measured by the change of the spontaneous emission rate in a weak excitation field for the cavity on and off the atomic resonance frequency. A CW dye laser drove the 553.5 nm Ba $6s^2$ $^1S_0$ - 6s6p $^1P_1$ transition resonantly or detuned by ±320 MHZ. The cavity resonance frequency was swept across the dressed-state transition frequencies with a voltage ramp applied to a piezoelectric transducer attached to one of the cavity mirrors. The fluorescence intensity was collected from the open side of the cavity through spatial filtering and imaging optics, and thus provided a direct measure of the excited-state population of the atoms. The results are shown in Fig.1. The presence of suppression and enhancement in the side fluorescence intensity is evident, and presents the cavity-induced increases in the excited state population as well as decreases. By comparing the positions of the fluorescence triplet observed through the end of one of the cavity mirrors with the locations of the enhancement and suppression of the side fluorescence intensity, it is clear that the changes of the excited-state population occur when the cavity is tuned to be resonant with the sidebands of the Mollow triplet (and hence enhances the mode density at the blue or red dressed-state transition frequency).

In conclusion, a cavity-induced modification of steady-state population for driven two-level-like atoms has been observed. With a suitably designed cavity, a steady-state population inversion of two-level atomic samples should be achievable.

We gratefully acknowledge financial support from NSF and AFOSR.

REFERENCES

1. R. G. Hulet, E. S. Hilfer, and D. Kleppner, Phys. Rev. Lett.55,2137(1985).
2. W. Jhe, A. Anderson, E. A. Hinds, D. Meschede, L. Moi, and S. Haroche, Phys. Rev. Lett. 58, 666(1987)
3. D. J. Heinzen, J. J. Childs, J. E. Thomas, and M. S. Feld, Phys. Rev. Lett. 58,1320(1987), and references therein.
4. M. Lewenstein and T. W. Mossberg, Phys. Rev. A, 37,2048(1988).
5. C. Cohen-Tannoudji and S. Reynaud, J. Phys. B 10,345(1977).
6. Y. Zhu, A. Lezama, and T. W. Mossberg, Phys. Rev. Lett. 61,1946(1988).

TWO-PHOTON RESONANT, STIMULATED PROCESSES IN KRYPTON AND XENON

John C. Miller
Chemical Physics Section, Oak Ridge National Laboratory
P.O. Box 2008, Oak Ridge, Tennessee, 37831-6125

ABSTRACT

Both on-axis and conical emissions have been observed following two-photon pumping of the 5p states of krypton and the 6p′, 7p, 8p, and 4f states of xenon. In the former case, coherent emissions from the 5p states to the 5s are observed and in the latter case, many p→s, d→p, and f→d cascade emissions are observed. By analogy to the well-studied alkali and alkaline earth examples, the emissions are discussed in terms of amplified spontaneous emission (ASE), stimulated hyper-Raman scattering, and parametric four-wave mixing. The physical processes responsible for the conical emission and for intensity anomolies in the xenon p→s emissions are not understood at present. Interference effects due to coherent cancellation between competing excitation pathways may be occurring.

INTRODUCTION

Ever since the first report in 1967 of the production of coherent vacuum ultraviolet radiation via third-harmonic generation (THG) in rare gases, techniques for increasing its efficiency have been explored.[1] The use of two-photon resonance enhancement of the non-linear susceptibility was recognized very early for metal vapor systems.[1] Along with the increased efficiency of THG, however, came the observation that a panoply of competing non-linear processes also became important when exciting at or near two-photon resonance. These may include multi-photon ionization (MPI), stimulated electronic Raman scattering (SERS), stimulated hyper-Raman scattering (SHRS), and amplified spontaneous emission (ASE). These new emissions present in the laser focus can also interact with the pump radiation to generate new waves by a parametric four-wave mixing (PFWM) scheme.

In contrast to the accessibility of the two-photon levels in metal systems, the corresponding studies in rare gases require intense, tunable, ultraviolet light (210-225 nm) which has only recently become available. The present paper presents the first results from a comprehensive study of these very interesting processes in krypton and xenon.

EXPERIMENTAL

The frequency-doubled beam of an excimer-pumped dye laser (Lambda Physik) is loosely focussed (50 cm lens) into an MPI cell with suprasil windows. The emerging light is refocussed into either an optical multichannel analyzer (VIS-IR), an infrared spectrometer and diode detector, or a vacuum ultraviolet spectrometer equipped with a solar-blind phototube. Rearrangement of the optics and addition of a dichroic mirror allowed detection of backward-directed light. More details may be found elsewhere.[2]

RESULTS AND DISCUSSION

A. Krypton

Two-photon excitation at 214.7 or 216.6 nm excites the $5p[\frac{3}{2}]_2$ and $5p[\frac{5}{2}]_2$ levels, respectively of Krypton (Figure 1). Once populated, these levels are inverted relative to the lower-lying 5s′ and 5s states. Amplified spontaneous emission to the former lies in the mid-infrared and was not observed. The latter emissions to both 5s levels were observed in the forward and backward direction as shown in Figure 2 for the forward ASE. The relative intensity of the two lines are in accord with their calculated line strengths.[3] The time profile of the emission (~8 ns) is similar to that of the excitation laser pulse and shorter than the radiative lifetime of 20-50 ns. The emission was polarized with its polarization parallel to the input laser for $\Delta J = 1$ transitions and perpendicular for $\Delta J = 0$ transitions. The excitation spectrum of the ASE was very narrow (laser linewidth limited) and peaked at the $5p[\frac{3}{2}]_2$ or $5p[\frac{5}{2}]_2$ transition energies as monitored by (2+1) MPI. No other emissions were observed for excitation on or near these levels. All of the above observations are consistent with the assignment of the emissions as ASE.

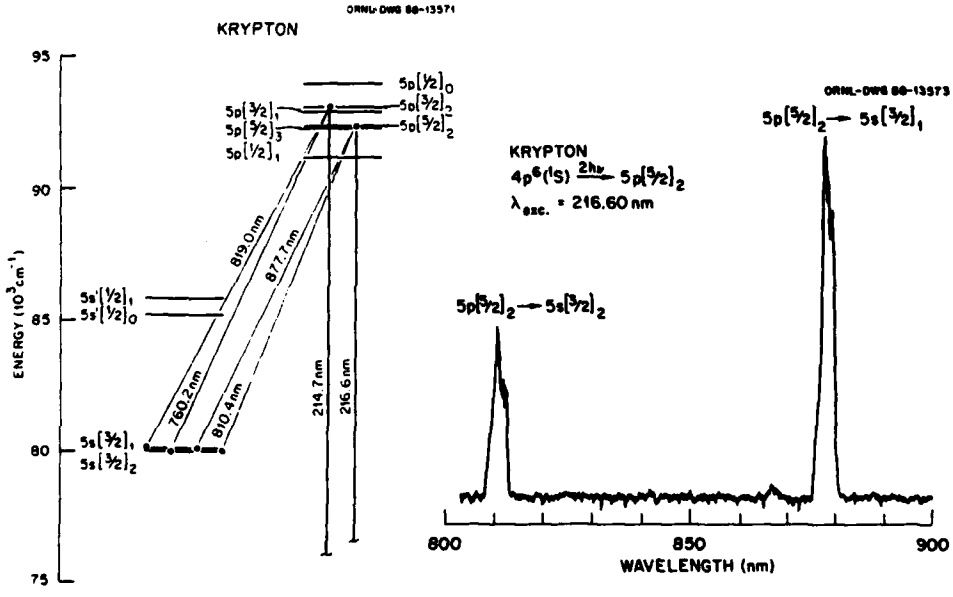

Figure 1. Energy levels of krypton. Figure 2. ASE from krypton.

B. Xenon

In xenon the accessible tuning region overlaps the two-photon wavelengths for excitation of the 6p, 7p, 6p′, and 4f manifolds. Figure 3 shows the relative energies of these levels as well as a summary of the observed emissions. The straight arrows indicate emissions observed connecting the various manifolds. The wavy arrows indicate nonobserved emissions whose existence can be inferred from the observed "cascade" ASE. For most of the emissions the observed linestrengths, polarizations, and forward-backward intensity ratios were similar to those expected on the basis of the krypton results.

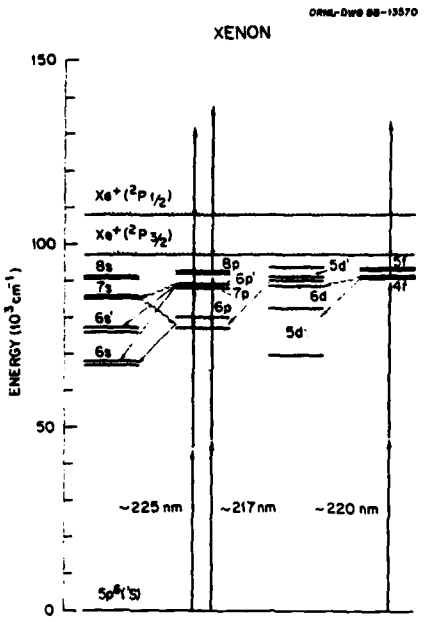

Figure 3. Energy levels of xenon.

Two anomolies were observed, however, which are presently not understood. First, for excitation of the $6p'[\frac{3}{2}]_2$ and $7p[\frac{3}{2}]_2$ levels, only emission to the $6s[\frac{3}{2}]_2$ state is observed. Emission to the corresponding J=1 level is less than 5% although branching ratios from theory[3] and spontaneous[4] fluorescence are more nearly equal. Furthermore, in the latter case emission to the $6s'[\frac{1}{2}]_1$ state should be observable based on the published branching ratios. The second anomoly concerns the visual observation of conical emission at higher pressures (100 torr) for the same two excitations. Although conical emission is usually associated with the phase-matching requirements of PFWM, this process is not possible in this case as the terminal level, the $6s[\frac{3}{2}]_2$ state cannot optically connect to the ground state by dipole selection rules. Six-wave mixing processes can be envisioned,however.

Although not understood at the present time, the unusual ASE branching ratios and the presence of wave-mixing processes may implicate interference effects between various coherent pathways between states. Additional experiments are currently being performed in order to further characterize these two-photon resonant stimulated processes in rare gases.

Research sponsored by the Office of Health and Environmental Research, U.S. Department of Energy under contract DE-AC05-84OR21400 with Martin Marietta Energy Systems, Inc.

REFERENCES

1. C. R. Vidal in Tunable Lasers, L. F. Mollenauer and J. C. White, eds., (Springer-Verlag, Berlin, 1987), pp. 56-113.
2. P. R. Blazewicz and J. C. Miller, Phys. Rev. A 38, 2863 (1988); J. C. Miller, to be published.
3. M. Aymar and M. Coulombe, Atomic Data and Nuclear Data Tables 21, 537 (1978).
4. H. Horiguchi, R.S.F. Chang, and D. W. Setser, J. Chem. Phys. 75, 1207 (1981).

DYNAMIC FREQUENCY SHIFT EFFECTS ON COHERENT PROPAGATION IN TWO-LEVEL SYSTEMS

Jamal Manassah and Farrès P. Mattar
Photonic Engineering Center, Department of Electrical Engineering,
City College of New York, New York, NY 10036

Abstract

We report the local field correction in the evolution of coherent propagation using the slowly-varying envelope approximation. To demonstrate this phenomenon we have dealt with mathematical atomic densities that are larger than the physical ones. The Lorentz correction leads to a self-frequency shift that causes dynamic self-phase modulation. The interplay of Lorentz induced-phase and fraction induced-phase is rigorously analyzed herein.

I. Introduction

In Lorentz's classical treaty[1] he proved that the local field correction leads to a frequency shift in the atomic susceptibility. Except for Marburger et al.[2], in most of the propagational studies the local field correction was not discussed. This description was reported by Marburger et al. when they accounted for high density media from a liquid instead of the dilute gas. The traditional Kerr cubic nonlinearity disappears. The modified susceptibility is now saturable. The theory of self-action phenomena could be exceptionally sensitive to the Lorentz correction.

We have examined the role of the local field in the density matrix that describes the resonant atomic two-level system and like Friedberg et al.[3a,c] and subsequently, Hopf et al.[4] found that an additional frequency offset term must be included with analysis. Those two studies were carried out for an optimally thin sample. This additional inversion-weighted detuning varies with τ and introduces novel atomic dynamics. The induced phase ϕ can compensate the phase evolving due to diffraction in optically thick medium [5,6]. One sees that the Lorentz local field correction causes a dynamic inversion-dependent frequency shift $\partial\phi/\partial\tau$ in the off-diagonal elements. Upon substitution the local field correction drops out of the equation for the inversion. The numerical factor that relates the Beer length α to B the coefficient of the local-correction time-dependent detuning (BW/T_2) are appreciable. Since B is the shift in the central frequency relative to linewidth, it follows that for any appreciable shift, the absorption coefficient is of the order of or much greater than λ^{-1}. The associated wavefront curvature $\partial\phi/\partial\rho$ and energy flux $A^2\partial\phi/\partial\rho$ can be altered significantly. The propagation effects definitely play a major role. It appears [3] that the slowly-varying-envelope approximation may not apply in the domain of physical parameters. Additional dispersion effects associated with the second and higher temporal derivatives of the field and material response must be accounted for. This signifies that the full Helmhotz equation must be solved.

II. Equations of Motion

The field that drives the two-level atoms appears in the density matrix as follows:

$$\mathcal{E}_{loc} = \mathcal{E} + i\delta P \tag{1}$$

where $\delta = 4\pi/3+\sigma$ with σ a constant which is due to correlations with

respect to atomic positions that occur in crystal

$$\frac{\partial P}{\partial \tau} = -(i(\Delta\omega)+1/T_2)P + \zeta_{loc} W \tag{2a}$$

$$\frac{dW}{d\tau} = -1/2\,(\zeta^*_{Loc}P + \zeta_{loc}P^*) - (W-W^e)/\tau_1 \tag{2b}$$

Upon substitution of Eq. (J.1) in Eq. (J.2), one obtains

$$\frac{dW}{d\tau} = -1/2\,(\zeta^*P+\zeta P^*) - (W-W^e)/\tau_1 \tag{3}$$

Thus the local field drops from the equations for the population difference. The local field equation can then be rearranged to read as follows:

$$\frac{dP}{d\tau} = -i\,((\Delta\omega) - [BW/\tau_2] + 1/\tau_2)\,P + \zeta W \tag{4}$$

$$\text{with } B = \delta\,\frac{\mu^2 N}{2h}\,T_2 \tag{5}$$

with N the atomic density which sustains transverse variations

One therefore sees that the local field correction introduces an inversion-dependent frequency shift that can vary radially. Hopf et al. showed that this shift leads to Clausius-Mosatti relationship when taken off-resonance.

$$\text{If } \sigma = 0 \qquad \beta = \frac{\lambda\delta}{8\pi^2}\,\alpha \tag{6}$$

where α the on-resonance absorption coefficient

$$\alpha = \frac{4\pi\omega\mu^2 N}{ch}\,T_2 \text{ with } \omega/c = 2\pi/\lambda \tag{7}$$

Should one allow for quantum initiation in the superfluorescence (SF) problem or Langevin driving force to emulate collisional effects (CE) one obtains three distinct sources of phase evolution. The first one is due to diffraction. The second one is associated with the effective detuning; it reflects the static input frequency-offset (between the carrier laser frequency and the two-level atoms frequency transition) and the dynamic frequency offset (due to the local field correction). The third term varies according to the quantum initiation of superfluorescence and the Langevin driving forces that describe the evolution of amplified spontaneous emission (ASE). The interplay of the diffraction-, dispersion-, and Lorentz-induced phases can lead to constructive or destructive interference. The resultant propagation of the beam in the two-level system will be strongly modified.

III. Numerical Results

To illustrate how much the evolution of the fields are modified by the local field correction we have considered two cases: the first is self-induced-transparency while the second is superfluorescence. As shown in Figs. 1 and 2 the energy is exhibited as a three-dimensional function versus ρ and τ for a given η. We contrast the traditional physical situation with that where the corrections are accounted for.

The departure can be quite profound. Now that we have demonstrated that longitudinal and transverse reshaping are associated with the propagation of the light in an optically-thick medium we need to generalize the physical model without any simplifying assumption. We expect that the phenomenon of self-frequency shift will be observable in physical parameters.

IV. Addendum

Recently Stroud, Bowden and Allen[7] have reported an analytical theory in the uniform-plane-wave regime of a self-induced-transparency evolution subjected to chirp. This chirp is a consequence of local field correction. Their result substantiates the validity of our computations. Propagational effects in a highly dense medium require a local field correction.

References

1. H.A. Lorentz, Theory of Electrons, reprinted (Dover, 1952)
2. J. Marburger, L. Huff, J.D. Reichert & W.G. Wagner, Phys. Rev. 184, 255 (1969).
3. [a] R. Friedberg, S.R. Hartmann & J.T. Manassah, Phys. Lett. 35A, 161 (1971), ibid 40A, 395 (1972) & Phys. Report 7C, 101-179 (1973); [b] J.T. Manassah, Phys. Report 101, 359-427 (1983); [c] R. Friedberg, S.R. Hartmann & J.T. Manassah, Phys. Rev. A39, 93 & 3444 (1989); and [d] J.T. Manassah, Phys. Rept. 101, 359-427.
4. [a] F.A. Hopf, C.M. Bowden & W.H. Louisell, Phys. Rev. A29, 2591 (1983); [b] in Optical Bistability II, ed. C.M. Bowden, H.M. Gibbs & S.L. McCall (Plenum Press, 1984) pp. 361-368; and [c] in Optical Instabilities, ed. R.W. Boyd, M.G.Raymer & L.M. Narducci (Cambridge University Press, 1986) pp. 308-311.
5. F.P. Mattar & J.T. Manassah, unpublished.
6. F.P. Mattar & M.C. Newstein, IEEE J. Quant. Elect., 13, 507 (1977), and Comp. Phys. Commun. 20, 139 (1980).
7. C.R. Stroud, Jr., C.M. Bowden & L. Allen, Opt. Commun. 67, 387 (1988).

LRICFS SIMULATIØN NØ. 109

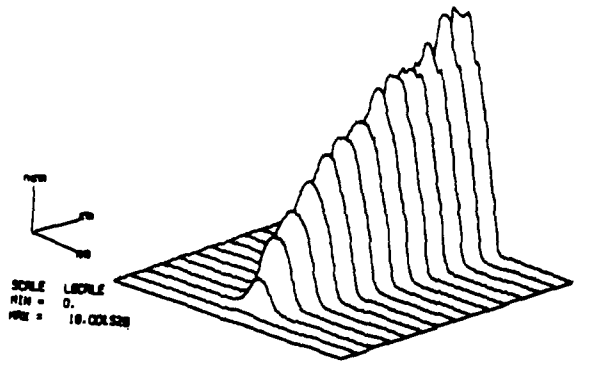

LRICFS SIMULATIØN NØ. 116

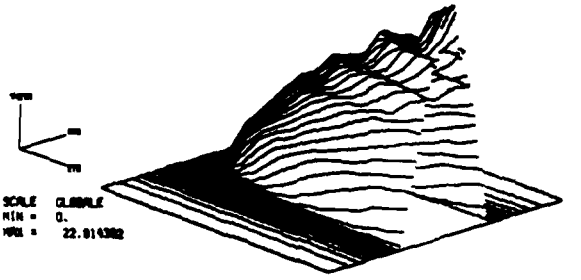

LRICFS SIMULATIØN NØ. 117

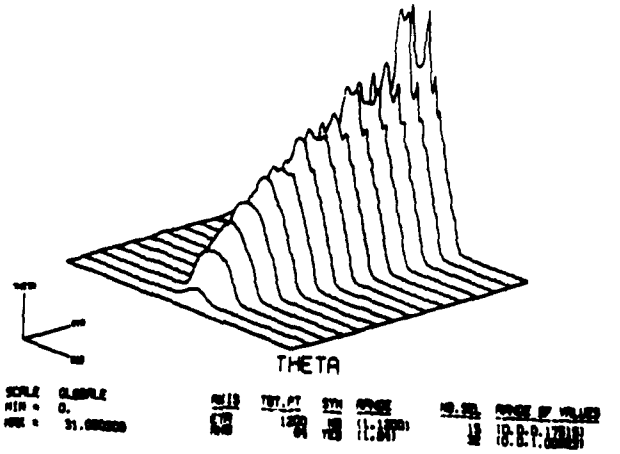

Fig. 1

LRICFS SIMULATIØN NØ. 158 LRICFS SIMULATIØN NØ. 160

ENERGY

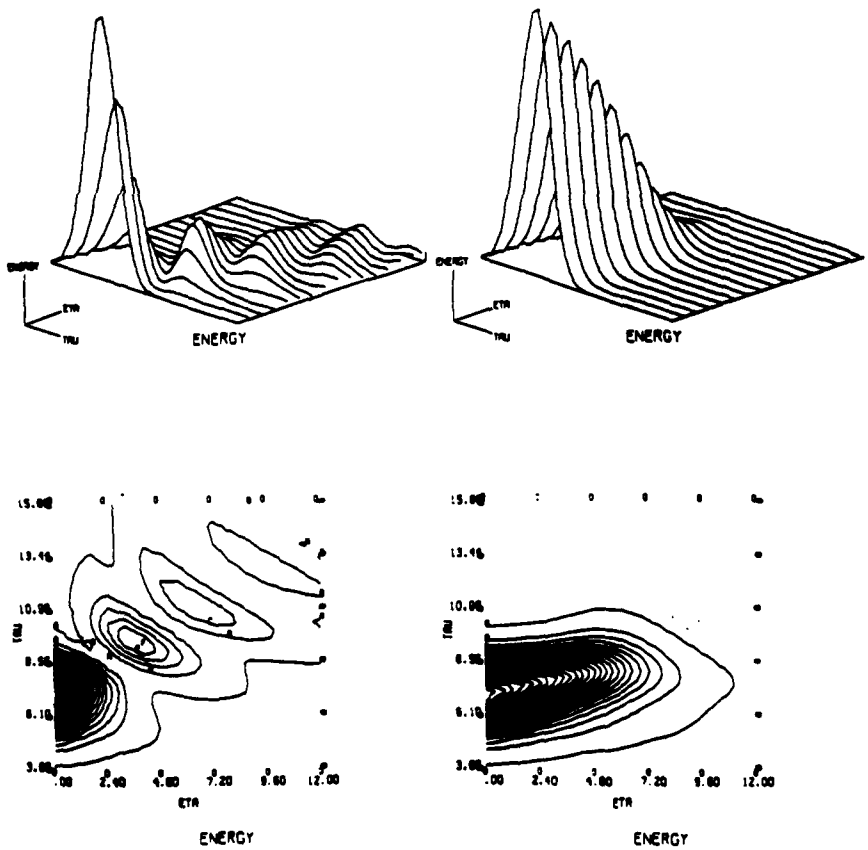

Fig. 2a

LRICFS SIMULATIØN NØ. 163

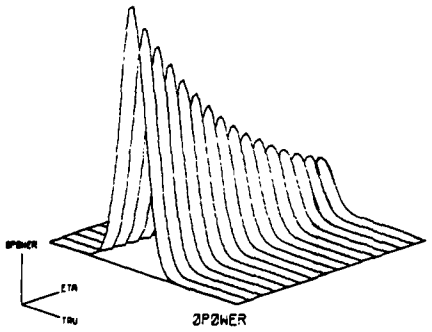

LRICFS SIMULATIØN NØ. 164

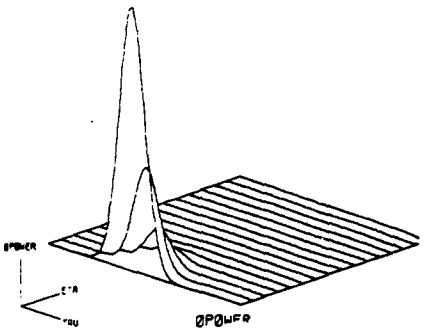

LRICFS SIMULATIØN NØ. 158

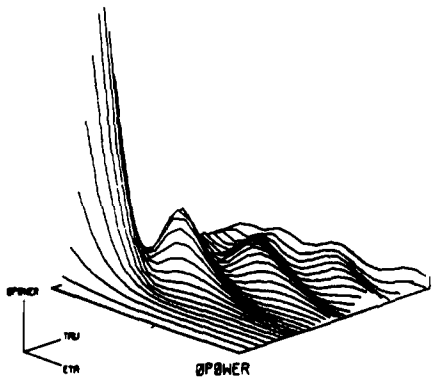

LRICFS SIMULATIØN NØ. 160

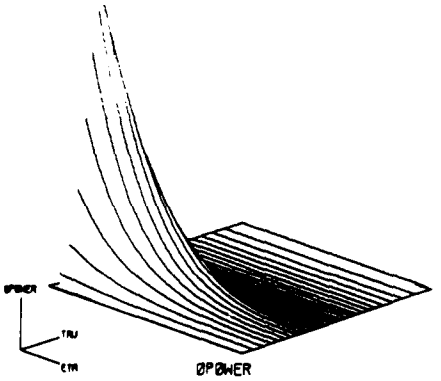

Fig 2b

SELF- AND CROSS-PHASE MODULATION, PULSE COMPRESSION INDUCED CHIRPING, SPECTRAL BROADENING AND FOCUSING EFFECTS IN CO-PROPAGATION COHERENT PULSES IN THREE-LEVEL ATOMS

F.P. Mattar*,#, J. DeLettrez*,** and J.P. Babuel-Peyrissac#
Physics Department, New York University*, New York, NY &
Electrical Engineering Dept., City College of New York*, New York, NY;
Laboratory for Laser Energetics, University of Rochester**,
Rochester, NY 14627; and
Departement de Physico-Chimie#, Centre d'Etudes Nucleaires, Saclay
Gif/Yvette, France

ABSTRACT

We have examined the influence of the formation of self-phase and cross-phase modulation on the simultaneous propagation of two different-wavelength beams in a three-level system. The temporal and spectral variations of the field are shown as a function of the optical thickness.

I - INTRODUCTION

Phase and transverse effects were previously considered as unimportant extensions of the one-dimensional results. In this communication, we substantiate that phase and diffraction are fundamental inherent processes that are closely intertwined and that can not be neglected. Self- and cross-action phenomena are discussed.

Our physical model is formulated in the semi-classical regime. The fields are described by the paraxial Maxwell equations. The atomic medium necessitates a three-level density matrix description[1-6].

At the input plane the beams are collimated. They acquire their phase due to self-and cross-diffraction.

The emergence of phase variations is critical since its temporal derivatives act as an instantaneous frequency offset. The resultant absorptive and dispersive characteristics of each transition are locally altered and in their turn modify the propagating fields.

II - DISCUSSION OF THE PHYSICAL MODEL

In this analysis we address four different transverse effects. The first one is the diffraction coupling. The cross-coupling of the two finite beams is the second one. The radial dependence of the Raman gain through the atomic density N is the third effect while the randomly-generated initiation of the Stokes (amplitude and phase) is the fourth. These four processes vary from one shell to the other, that is, nonuniformly across the beam.

Both self-phase modulation (SPM) and cross-phase modulation (XPM) results in the Raman or pump/probe analysis. Moreover, the diffraction-induced phase competes with that generated by quantum-initiation. Their interference can be either constructive or destructive.

Should one allow for dispersion through detuning, one obtains an additional contribution to the phase. The dispersion-associated phase can enhance or reduce the combined SPM and XPM.

Finally, if the Lorentz local field(s) correction[17-20] is also accounted for. A population-dependent frequency offset emerges in the density matrix. The effective detuning becomes a time (and radial)

* Supported by the U.S. ARO, AFOSR, ONR, NSF and the French CEA at NYU

dependent function. The resultant chirp, i.e., the frequency modulation modifies the characteristics of the Raman co-propagation. The rate of energy conversion from the pump to the Stokes and the depopulation of the pump and the growth of the Stokes emission become more complicated. The analytical tractability vanishes. One must resort to numerical experiments to appreciate the physical nuances and domain.

III - NUMERICAL RESULTS

To substantiate the longitudinal and transverse effects we have kept track in time- and frequency domain for each field the on-axis field Energy, its associated spectrum (known as the power spectrum), the field output power and the spectrum of the output power, the phase spectrum and its derivative spectrum as a function of η the distance of propagation.

The rigorous computations substantiate that assumptions of self-similar, i.e., shape-preserving are not valid. Spatio-temporal radial and spectral distortions result for each of the diagnostic physical functions. Even the shape of the pulses modifies the evolution in the nonlinear medium. The time-integrated-pulse area theorem that governs SIT or simultons do not apply here especially when diffraction and phase effects are analyzed.

The group velocity dispersion changes the phase of each spectral component of the pulse by an amount that depends on the frequency and the propagated distance. Even though such phase changes do not affect the pulse spectrum, they can modify the pulse shape.

Although the incident pulse is unchirped (with no phase modulation), the transmitted pulse becomes chirped. The time dependence of the phase implies that the instantaneous frequency changes across the pulse from the central frequency. This behavior changes if the input pulse has an initial frequency chirp. The pulse spectral width is enhanced and can drastically change the presence of linear chirp. The spectrum does not only rely on the pulse shape but also on the initial chirp imposed on the pulse.

The dispersion-induced broadening is sensitive to steepners of pulse. A pulse with steeper leading and trailing edges broadens more rapidly with propagation simply because such a pulse has a wider spectrum to start with. For example a superGaussian pulse becomes square shaped with sharper leading and trailing edges; its rise time is shorter than the one corresponding for the Gaussian pulse.

- While the Gaussian pulse can maintain its shape during propagation in a weakly nonlinear medium, the super-Gaussian pulse not only broadens at a faster rate but also distorts in shape. The differences between the two can be attributed to the steeper leading and trailing edges associated with the super-Gaussian pulse. Similarly the Gaussian pulse has a shorter rise time than a hyperbolic secant pulse.

- The most notable feature of the spectral evolution is that diffraction-induced phase and spectral broadening is accompanied by an oscillatory structure covering the entire frequency range. The origin of the oscillatory structure can be understood by referring to a plot displaying the time-dependence of the phase and of the phase-induced chirp. The same chirp occurs at two values of t showing that the pulse has the same instantaneous frequency but different phases at two distinct points. Depending on the relative phase difference between the two waves, represented by the two points, the phases can interfere constructively or destructively. Shimuzu showed that the multipeak structure is a result of such interference.

We first calculate the propagation of two Gaussian pulses of equal Rabi frequencies. A nonuniform frequency structure develops. We show in Fig. 1 the evolution of (a) the power spectrum, (b) the spectrum of the output power, (c) the phase spectrum and (d) the spectrum of the phase derivative for four propagational distances. This was done for a Gaussian pulse. The distances of interest are z=0.6, 1.0, 1.4 and 1.6. In Graph a, the on-axis characteristics are exhibited while those in Graph b represent the off-axis ones. In the off-center shell, namely at r=0.065, the spectrum of the phase and its derivative develop a significantly more important structure than the corresponding on-axis.

In Graph a of Fig. 2 we present for the beam center the same diagnostic function for an input hyperbolic secant pulse. The frequency pattern is more uniform than it is for the Gaussian pulse. However, longer propagational distances are required so that a macroscopic spectral variation evolves. The distances of interest are now z=0.0, 20.2, 40.4 and 60.6. In Graph b of Fig. 2 we show for the same z the on-axis energy and output power which are functions of τ.

In Fig. 3 we compute the propagation of a strong pump and a weak probe both Gaussian in pulse and beam shape. We keep the same diagnostic function. We demonstrate at five different propagational distances z=2.1, 4.0, 6.1, 8.1 and 10 for on-axis and off-axis shells that a frequency structure develop especially for the spectrum of the phase and of its derivative. We also display, in Graph c, the spectrum of the output power. It is noteworthy that a radially integrated energy does not develop a structure with respect to frequency as z increases.

In Fig. 4 we present the radial profile of the field phase at six different propagational distances z=1.1, 2.1, 4.0, 6.1, 8.1 and 10 for three temporal slices. The selected time slices are respectively chosen to represent those at which the rising half-maximum, the peak and the falling half-maximum occur. The gradual formation of the frequency pattern is readily observable.

IV - CONCLUSION

We have presented a detailed analysis of self- and cross-phase modulation associated with the co-propagation of two beams of finite extent in a metallic vapor characterized by a time delay nonlinearity. The motivation of this effort is a re-evaluation of the impact of propagational effect on laser isotope separation. The above calculation qualitatively agree with a recent observation[11] of a spatial temporal behavior in conical emission.

V - ADDENDUM

The formation of new frequencies[12] and of transverse structures has been confirmed by an extensive calculation performed by Crenshaw & Cantrell[13].

REFERENCES

1. S.L. McCall & E.L. Hahn, Phys. Rev. 183, 457 (1969).
2. F.A. Hopf & M.O. Scully, Phys. Rev. 179, 399 (1969).
3. A. Icsevgi & W.E. Lamb, Jr., Phys. Rev. 185, 517 (1969).
4. G. Lamb, Jr., Rev. Mod. Phys. 43, 94 (1971); J.C. Diels & E.L. Hahn, Phys. Rev. A10, 2501 (1974); E. Courtens, in **Laser Handbook**, ed., F.T.Arecchi & E.O. Shultz-DuBois, (North-Holland, 1972) pp. 493-556; R.E. Slusher, **Progress in Optics XII**, ed. E. Wolf (North-Holland, 1974) pp. 53-100.

5. F.Y.F. Chu et al., Phys. Rev. A12, 2060 (1975).
6. M.J. Konopnicki and J.H. Eberly, Phys. Rev. A24, 2567 (1981).
7. F.P. Mattar, in **Advances in Laser Science II**, ed. M. Lapp, W.C. Stwalley & G.A. Kenney-Wallis, Am. Inst. Phys. 1987 pp. 422-429.
8. F.P. Mattar, J. Delettrez, J.P. Babuel-Peyrissac, J.P. Marinier & C. Bardin, in **Modeling & Simulation XVII**, ed. W.G. Vogt & M.H. Mickle, (Instr. Soc. Am., 1987) pp. 1387-1558 and in **Advances in Laser Science II**, ed. M. Lapp, W.C. Stwalley & G.A. Kenney-Wallis (Am. Inst. Phys., 1987) pp. 247-253.
9. F.P. Mattar, in **Advances in Laser Science III**, ed. A.C. Tam, J.L. Gole & W.C. Stwalley (Am. Inst. Phys., 1988) pp. 537-547.
10. F.P. Mattar, J. Delettrez, J. Teichmann & J.P. Babuel-Peyrissac, in **Advances in Laser Science III**, ed. A.C. Tam, J.L. Gole & W.C. Stwalley (Am. Inst. Phys., 1988) pp. 517-523.
11. P.H. Kupecek, M. Chomte, J.P. Marinier, J.P. Babeul-Peyrissac and C. Bardin, Opt. Commun. 65, 306 (1988).
12. F.P. Mattar & P.R. Berman, in **Advances in Laser Science III**, ed. A.C. Tam, J.L. Gole & W.C. Stwalley (Am. Inst. Phys., 1988) pp. 504-516.
13. M.E. Crenshaw & C.D. Cantrell, Opt. Lett. 13, 386 (1988) and Phys. Rev. A39, 126 (1989).

FIGURE CAPTIONS

Fig. 1 Graph a on-axis spectral behavior of the four characteristic functions for equal simulton with a Gaussian shape. Graph b off-axis spectral behavior of the four characteristic functions for equal simulton with a Gaussian shape.

Fig. 2 Graph a on-axis spectral behavior of the four characteristic functions for equal simulton with a hyperbolic secant pulse shape. Graph b temporal behavior of the on-axis energy and the output power for equal simulton with a hyperbolic secant pulse.

Fig. 3 Graph a on-axis spectral behavior of the four characteristic functions for unequal pump and probe with a Gaussian shape. Graph b off-axis spectral behavior of the four characteristic functions for unequal pump and probe with a Gaussian shape. Graph c on- and off-axis spectral variation of the characteristic functions at the exit plane of the cell.

Fig. 4 Propagation evolution of the phase front for two unequal pump and probe with a Gaussian shape.

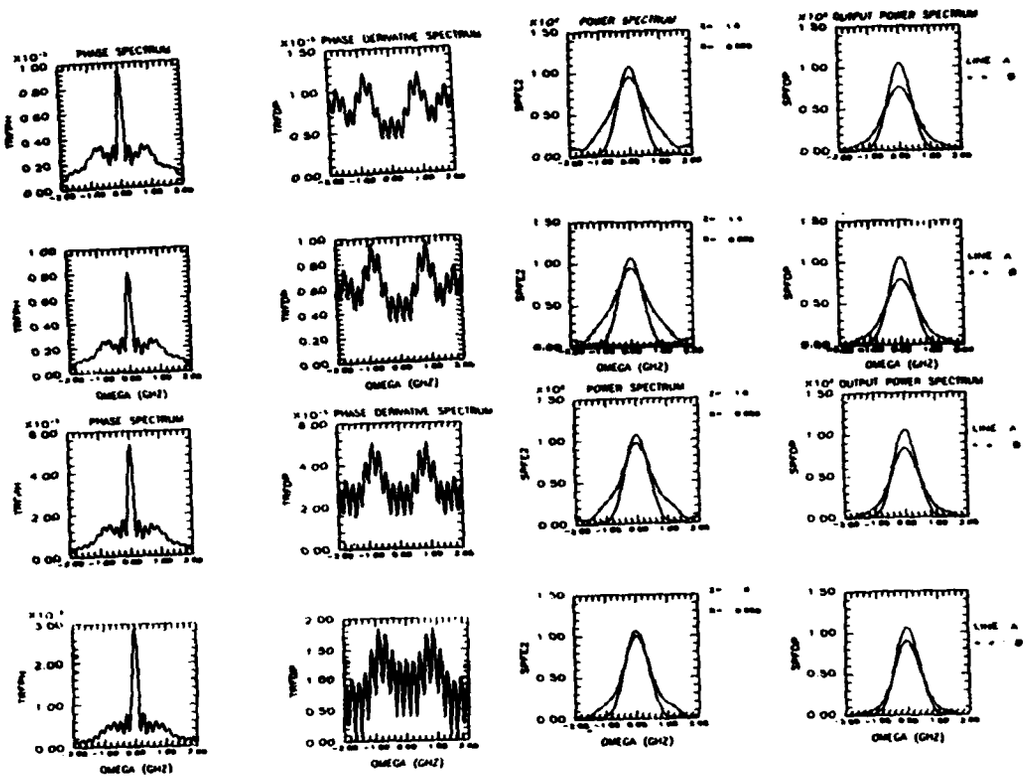
PHASE SPECTRUM
PHASE DERIVATIVE SPECTRUM
POWER SPECTRUM
OUTPUT POWER SPECTRUM
OMEGA (GHZ)
LINE A
LINE B

fig 1 Graph a

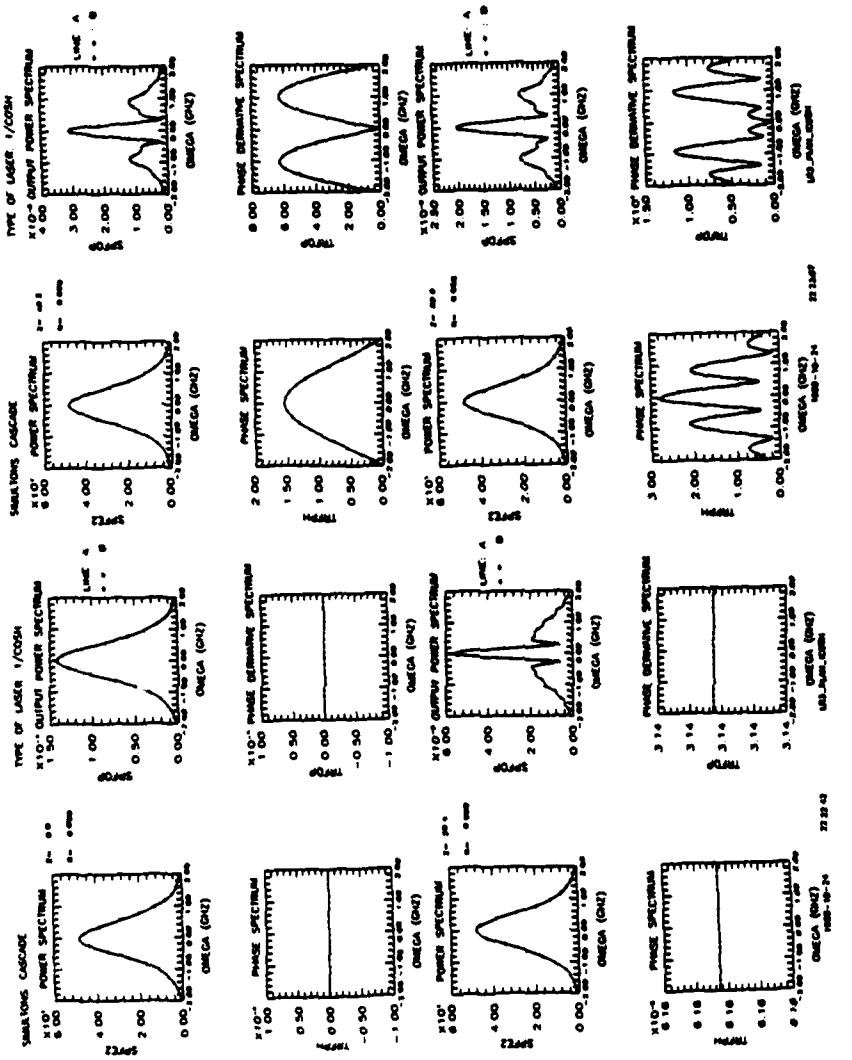

Fig. 1 Graph b)

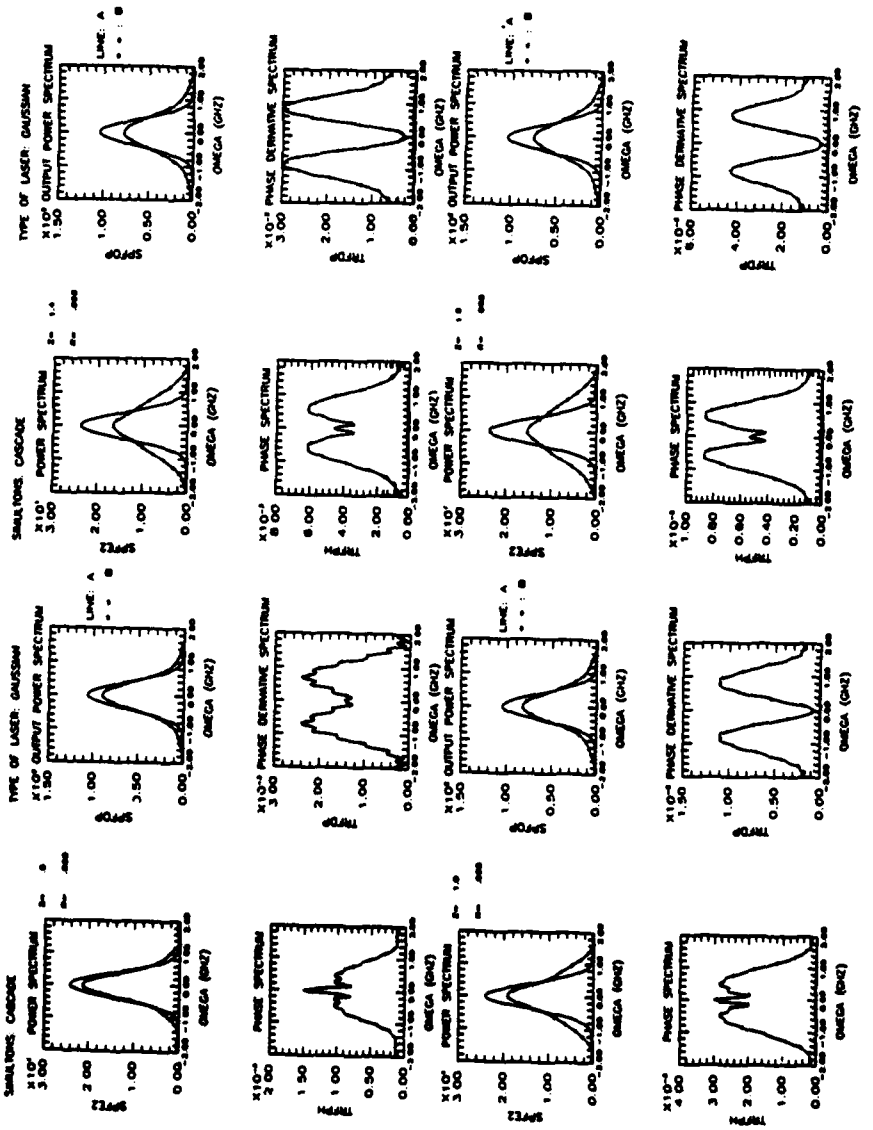

Fig. 1 graph b

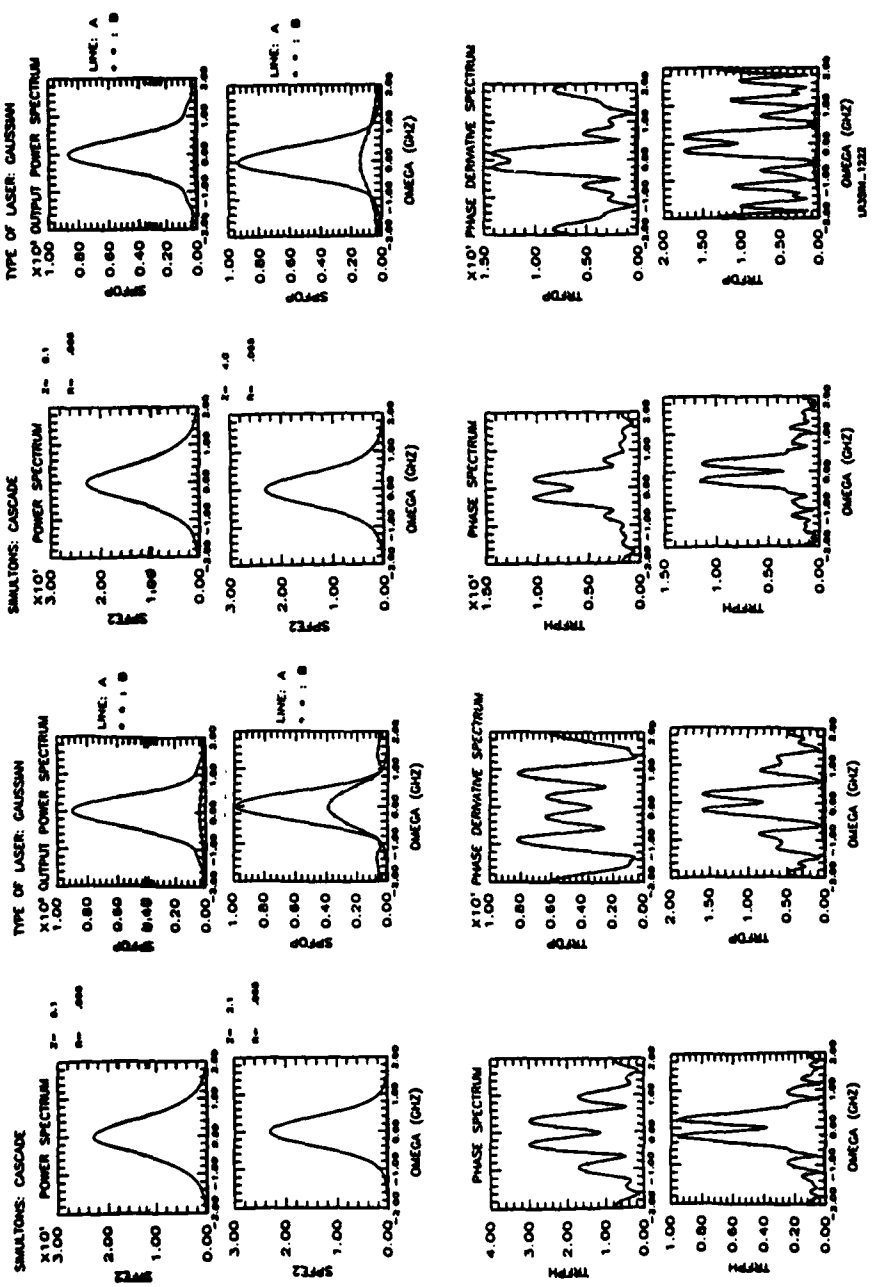
SIMULTONS: CASCADE
TYPE OF LASER: GAUSSIAN
X10' POWER SPECTRUM
X10' OUTPUT POWER SPECTRUM
X10' PHASE SPECTRUM
X10' PHASE DERIVATIVE SPECTRUM
SPEC2
SPECP
PHSPH
TMSPH
OMEGA (GHZ)
LINE: A
LINE: B

Fig. 2 Graph a

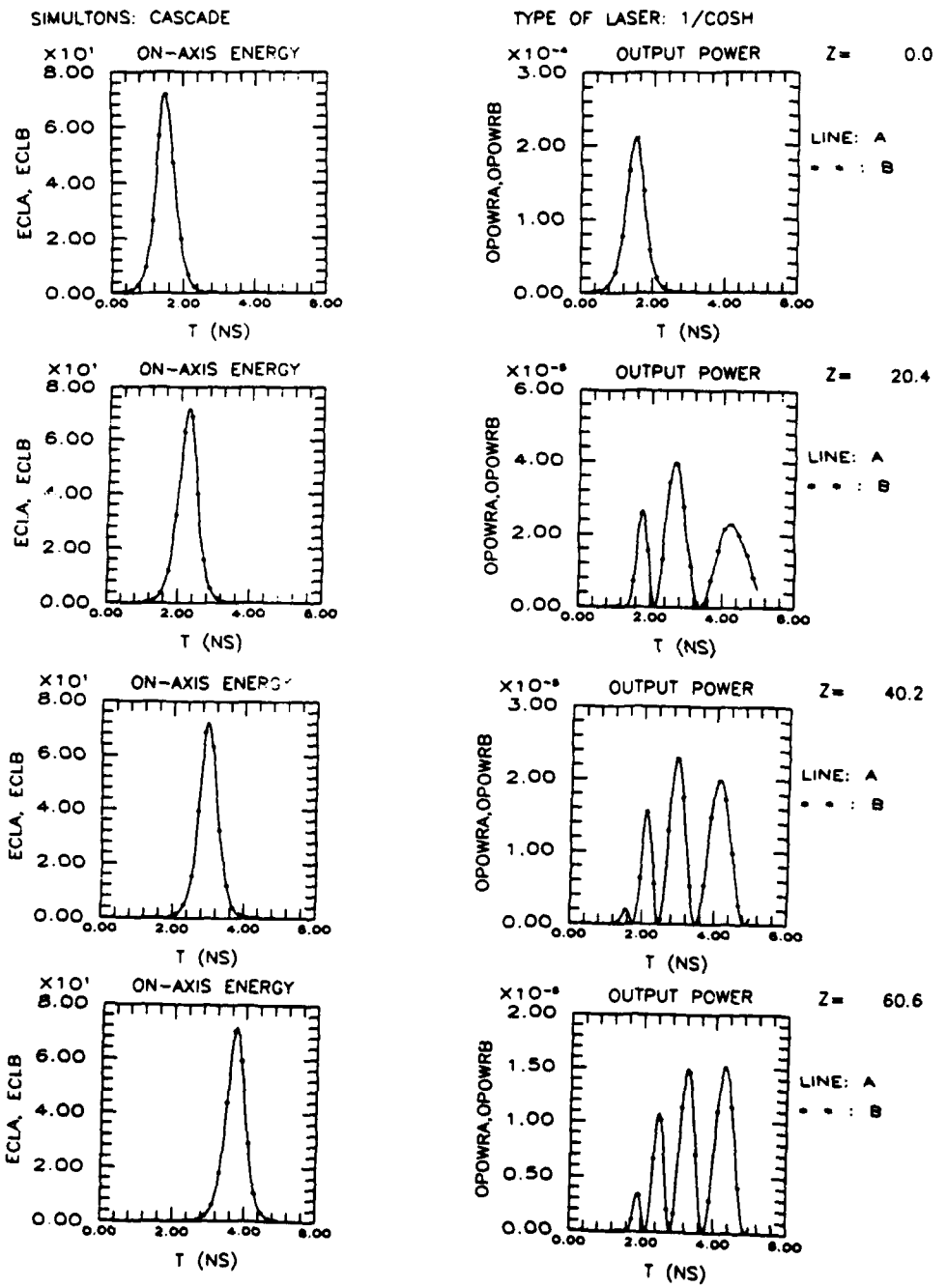
SIMULTONS: CASCADE
TYPE OF LASER: 1/COSH
X10' ON-AXIS ENERGY
ECLA, ECLB
T (NS)
X10⁻⁴ OUTPUT POWER Z= 0.0
OPOWRA,OPOWRB
LINE: A
* * : B
X10' ON-AXIS ENERGY
X10⁻⁵ OUTPUT POWER Z= 20.4
X10' ON-AXIS ENERGY
X10⁻⁵ OUTPUT POWER Z= 40.2
X10' ON-AXIS ENERGY
X10⁻⁵ OUTPUT POWER Z= 60.6

Fig. 2 Graph b

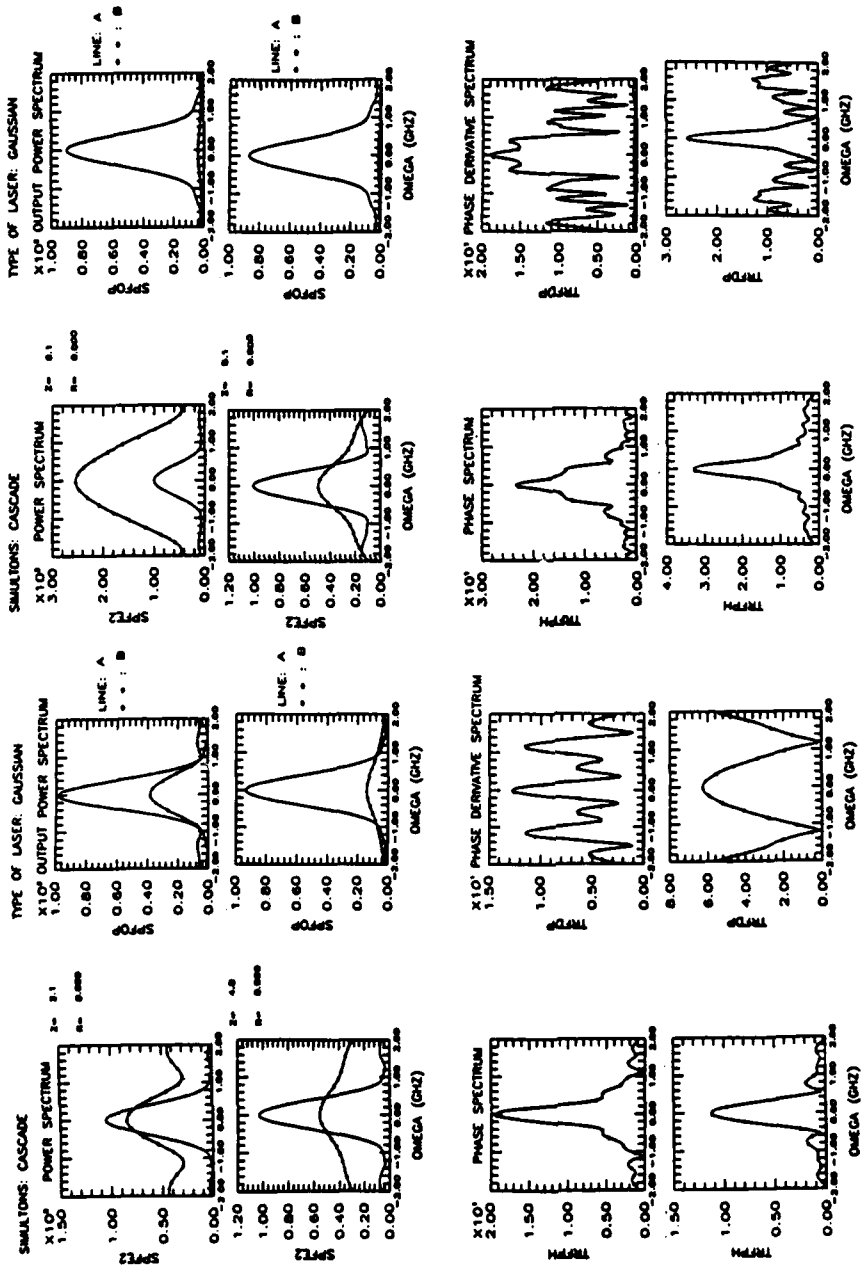

Fig. 3 Graph a 1

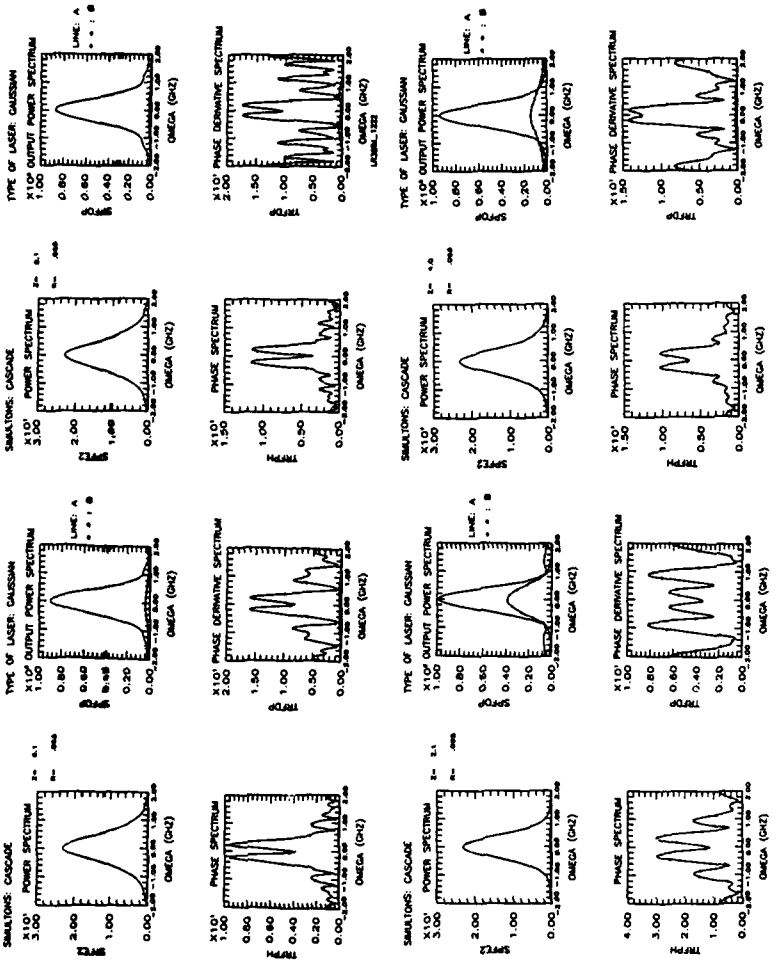

Fig. 3 Graph b1

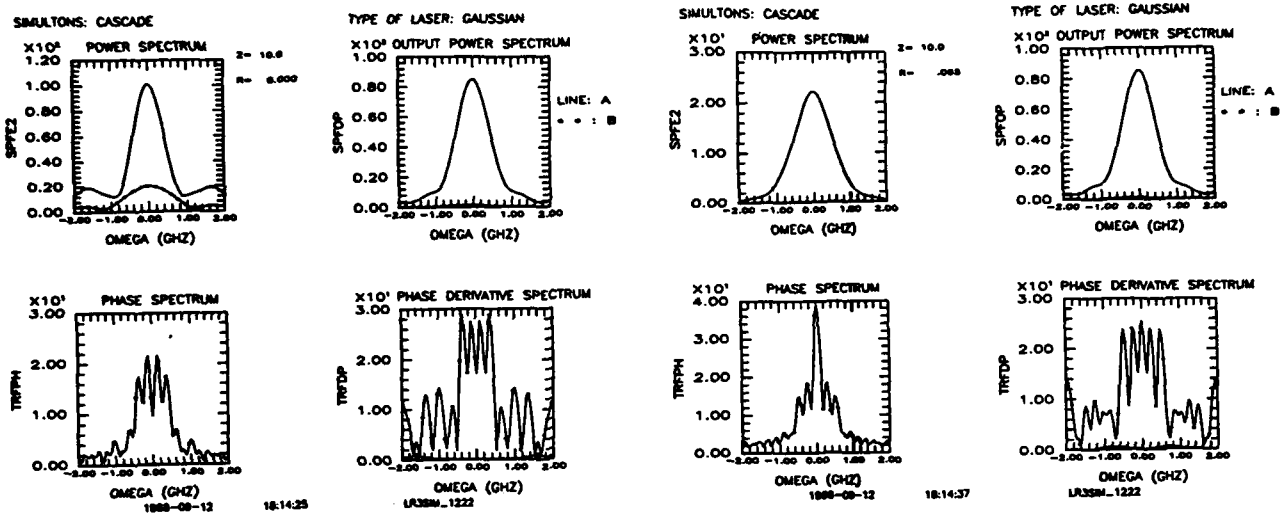

Fig. 3 Graph a 2

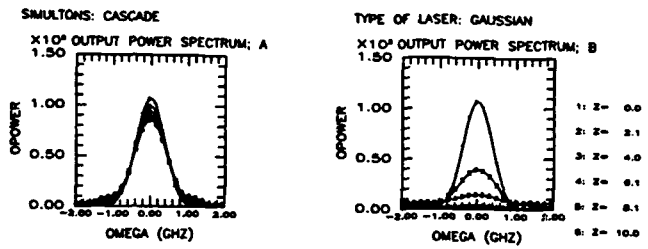

Fig. 3 Graph c 1

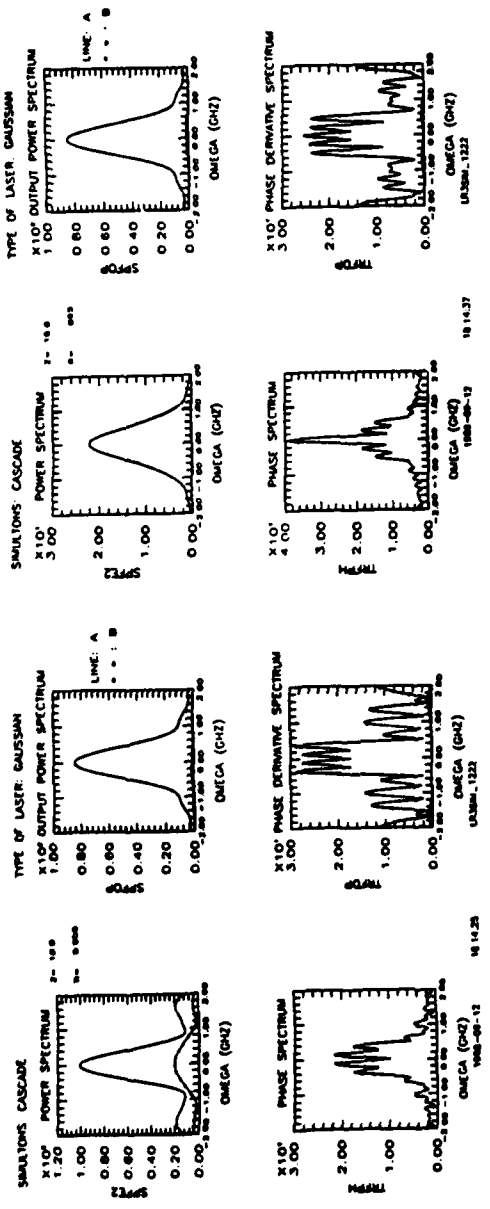

Fig. 3 Graph b 2

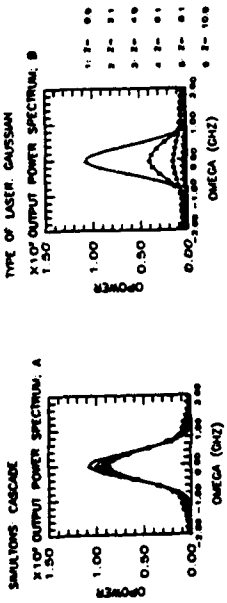

Fig. 3 Graph c 2

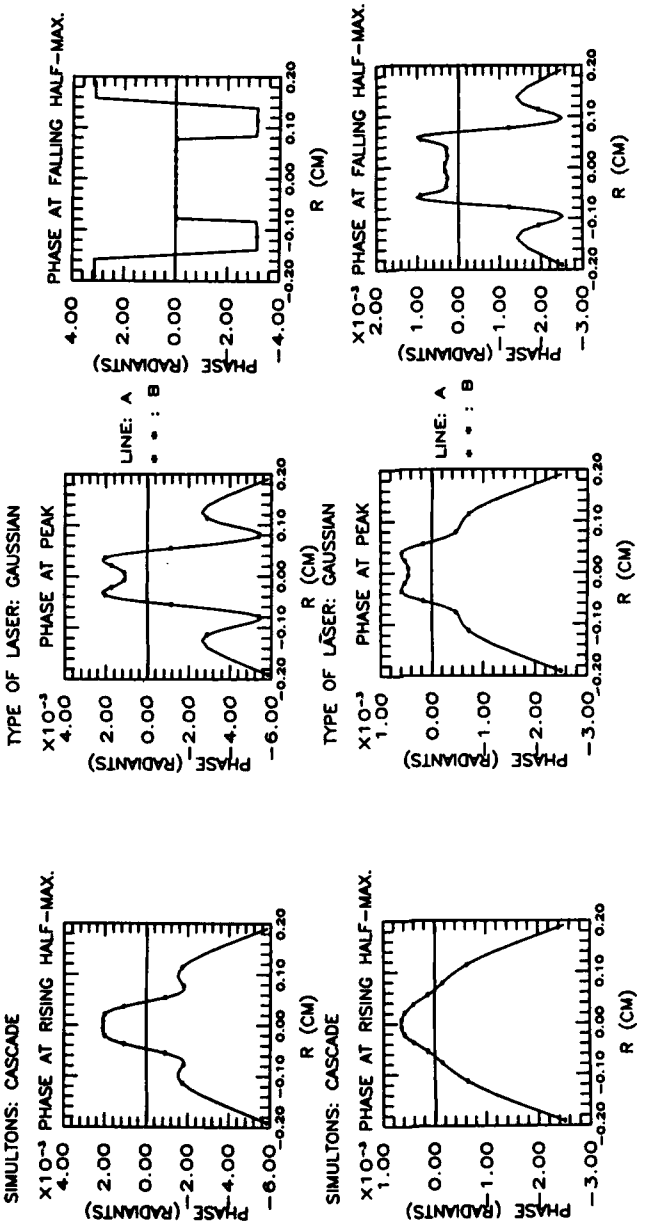
SIMULTONS: CASCADE
PHASE AT RISING HALF-MAX.
PHASE AT PEAK
PHASE AT FALLING HALF-MAX.
TYPE OF LASER: GAUSSIAN
LINE: A
* * : B
PHASE (RADIANTS)
R (CM)

Fig. 4 Graph a

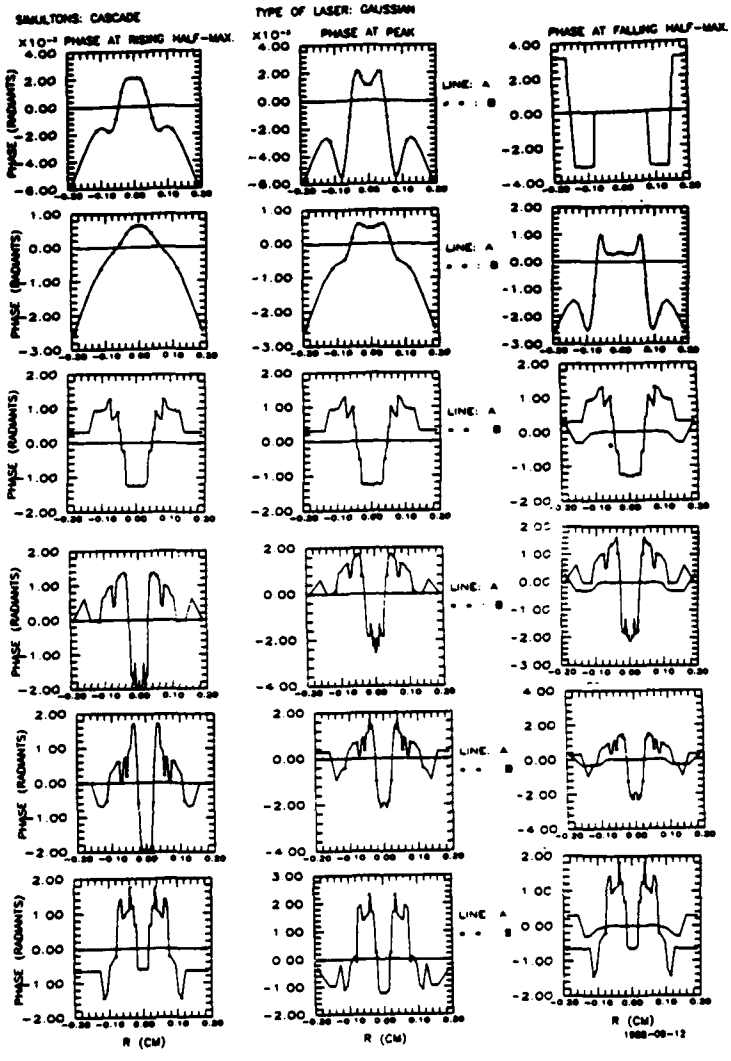
SIMULTONS: CASCADE
TYPE OF LASER: GAUSSIAN
PHASE AT RISING HALF-MAX.
PHASE AT PEAK
PHASE AT FALLING HALF-MAX.
PHASE (RADIANTS)
LINE: A
B
R (CM)
1988-08-12

Fig. 4 Graph b

SATURATION OF INTER-SUBBAND TRANSITIONS IN p-TYPE SEMICONDUCTOR QUANTUM WELLS

Yia-Chung Chang
University of Illinois at Urbana-Champaign, Urbana, IL 61801

R. B. James
Sandia National Laboratories, P. O. Box 969, Livermore, CA 94550

ABSTRACT

Saturation behavior of inter-subband optical transitions in p-type semiconductor quantum wells is examined theoretically. Carrier-phonon scatterings are taken into account within the deformation-potential approximation. Deviation of the hole distribution from thermal equilibrium due to optical pumping is calculated by solving coupled rate equations. Pump-and-probe absorption spectra are also studied and possible applications for light-by-light modulation are discussed.

THEORY

To calculate the absorption due to inter-subband transitions in p-type GaAs-$Al_xGa_{1-x}As$ quantum wells, we need a suitable description of the valence band structures. For p-type modulation doped GaAs-$Al_xGa_{1-x}As$ quantum wells, the valence subband structures can be well described by a multi-band effective-mass theory[1] in which the hole kinetic energy term is modeled by a 4×4 Luttinger-Kohn Hamiltonian matrix $H^{(0)}(\vec{k})$.[2]

The variational method reported in Ref. 1 was used to calculate the valence band structures. The absorption coefficient for intervalence-band transitions between subband n and subband n' is given by[3]

$$\alpha_{nn'}(\omega) = \frac{4\pi^2 e^2}{\sqrt{\epsilon_1} m_0^2 \omega c} \sum_{\vec{k}_{||}} [f_n(\vec{k}_{||}) - f_{n'}(\vec{k}_{||})] |\hat{\epsilon} \cdot \vec{P}_{nn'}(\vec{k}_{||})|^2 \frac{\hbar\Gamma_{nn'}(\vec{k}_{||})/\pi}{(\Delta_{nn'}(\vec{k}_{||}) - \hbar\omega)^2 + (\hbar\Gamma_{nn'}(\vec{k}_{||}))^2}, \quad (1)$$

where $\vec{k}_{||}$ designates the in-plane wave vector, $\Delta_{nn'}(\vec{k}_{||}) \equiv |E_{n'}(\vec{k}_{||}) - E_n(\vec{k}_{||})|$, $E_n(\vec{k}_{||})$ is the energy of subband n, $\vec{P}_{nn'}(\vec{k}_{||})$ is the momentum matrix element, $f_n(\vec{k}_{||})$ is the carrier distribution function associated with subband n, and $\Gamma_{nn'}(\vec{k}_{||})$ is the average scattering rate for the electronic states $(n\vec{k}_{||})$ and $(n'\vec{k}_{||})$ due to the electron-phonon interaction. The momentum matrix element $\vec{P}_{nn'}(\vec{k}_{||})$ for

the intervalence-band transitions can be derived from the $\vec{k} \cdot \vec{p}$ theory[4]. The derivations can be found in Ref. 5.

The average scattering rate is given by

$$\Gamma_{nn'}(\vec{k}_{||}) = \frac{1}{2}\sum_{m\vec{k}'_{||}}(R_{n\vec{k}_{||}\to m\vec{k}'_{||}} + R_{n'\vec{k}_{||}\to m\vec{k}'_{||}}) \equiv \frac{1}{2}[\Gamma_n(\vec{k}_{||}) + \Gamma_{n'}(\vec{k}_{||})], \qquad (2)$$

where $R_{n\vec{k}_{||}\to m\vec{k}'_{||}}$ is the rate in which a hole in subband state $(n, \vec{k}_{||})$ is scattered into subband state $(m, \vec{k}'_{||})$. In this paper we only include scatterings from longitudinal acoustical and optical phonons. The scattering rate is calculated within the deformation-potential approximation.

At low input light intensities, the carrier distribution is approximately given by the equilibrium distribution $f^e_n(\vec{k}_{||})$, and Eq. (1) gives the linear absorption coefficient. At high input light intensities, the optical transitions deplete the population of initially filled states so fast that the electron-phonon scattering cannot maintain the equilibrium distribution of carriers. The nonequilibrium distribution $f_n(\vec{k}_{||})$ is calculated by solving the rate equations[5]

$$\frac{\partial f_n(\vec{k}_{||})}{\partial t} = \qquad (3)$$
$$-\sum_m \beta_{nm}(\vec{k}_{||})[f_n(\vec{k}_{||}) - f_m(\vec{k}_{||})] - \Gamma_n(\vec{k}_{||})f_n(\vec{k}_{||}) + \sum_{m\vec{k}'_{||}} R_{m\vec{k}'_{||}\to n\vec{k}_{||}} f_m(\vec{k}'_{||}),$$

where

$$\beta_{nm}(\vec{k}_{||}) \equiv \frac{2\pi^2 e^2 I}{\sqrt{\epsilon_1} m_0^2 \hbar\omega^2 c}|\hat{\epsilon}\cdot\vec{P}_{nm}(\vec{k}_{||})|^2 \frac{\hbar\Gamma_{nm}(\vec{k}_{||})/\pi}{(\Delta_{nm}(\vec{k}_{||}) - \hbar\omega)^2 + (\hbar\Gamma_{nm}(\vec{k}_{||}))^2}. \qquad (4)$$

Here I is the input light intensity. The first term on the right-hand side represents the optical depumping rate with carriers being photoexcited from subband n to all other subbands m, the second term represents the scattering rate of subband n, and the third term represents the feeding rate with carriers being scattering into the subband n from all other subbands m. Note that at zero input light intensity the equilibrium distribution $f^e_n(\vec{k}_{||})$ satisfies the rate equation

$$\Gamma_n(\vec{k}_{||})f^e_n(\vec{k}_{||}) - \sum_{m\vec{k}'_{||}} R_{m\vec{k}'_{||}\to n\vec{k}_{||}} f^e_m(\vec{k}'_{||}) = 0. \qquad (5)$$

To solve for the non-equilibrium distribution $f_n(\vec{k}_{||})$, we assume that the light intensity is turned on suddenly at $t = 0$. We use an iterative method to calculate $f_n(\vec{k}_{||})$ as a function of t subject to the initial condition $f_n(\vec{k}_{||}) = f^e_n(\vec{k}_{||})$.

RESULTS

Figure 1 shows the valence subband structures of a $50\mathring{A}$ GaAs-AlAs quantum well whose optical properties will be discussed extensively below. The vertical arrow in the figure indicates the possible optical transitions for an incident photon energy of $0.117eV$.

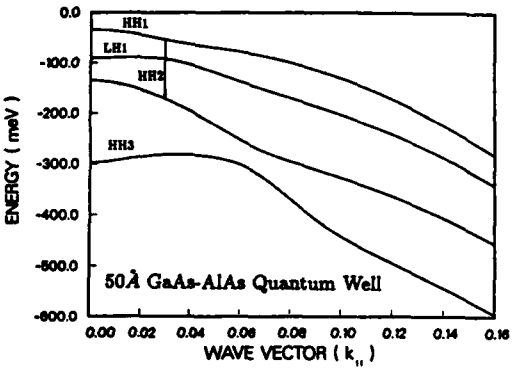

Figure 1. Valence subband structures of a $50\mathring{A}$ GaAs-AlAs quantum well.

Figure 2 shows the squared momentum matrix elements, $2|\hat{\epsilon} \cdot \vec{P}_{nn'}|^2/m_0$ for a $50\mathring{A}$ GaAs-AlAs quantum well as functions of the wave vector. In this paper we only consider the normal experimental set-up in which the incident light is propagating along the growth direction (the z direction) of the quantum well. Thus the polarization vector ($\hat{\epsilon}$) is in the $x-y$ plane. Examining the subband structure of Figure 1, we see that the energy separation between the first and third subbands at $k_{||} = 0.03\mathring{A}^{-1}$ is around $120meV$, which coincides with the CO_2 laser energy of interest. Thus we expect the $1-3$ transition at $k_{||} \approx 0.03\mathring{A}^{-1}$ to play an important role in the intersubband absorption.

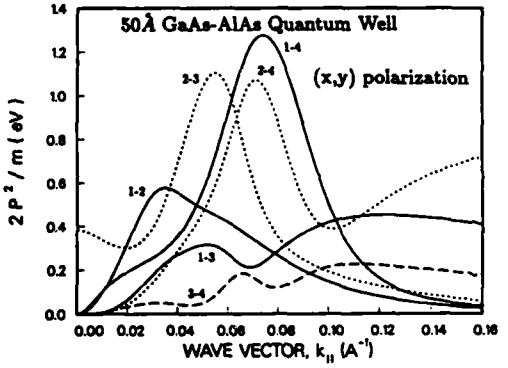

Figure 2. Squared momentum matrix elements for a $50\mathring{A}$ GaAs-AlAs quantum well as functions of the wave vector.

Figure 3 shows the distribution functions (solid and dashed curves) for various valence subbands of a $50\mathring{A}$ GaAs-AlAs quantum well at $300K$ and $77K$ for a pump beam with $\hbar\omega = 0.117eV$ and $I = 50\,MW/cm^2$. Also included for comparison are the corresponding equilibrium distribution functions (dotted curves). In the semilog graph, the equilibrium distribution as a function of $\vec{k}_{||}$ resemble the subband structure, because in the nondegenerate regime, the carrier distribution is proportional to the Boltzman factor. For the first subband, carriers are partially depleted (due to optical depumping) at wave vectors

near $0.03\mathring{A}^{-1}$ and back filled (due to carrier-phonon scattering) at larger wave vectors. As a result of optical pumping the carrier distribution in the third subband at $k_{||} \approx 0.03\mathring{A}^{-1}$ is substantially increased, giving rise to a peaked structure. The other structures, which appear at subband energies separated by integer multiples of the optical phonon energy, are due to carrier-optical phonon scatterings.

Figure 4 shows the intensity dependence of the nonlinear absorption coefficient $[\alpha(I)]$, normalized to the linear absorption coefficient (α_0), of a $50\mathring{A}$ quantum well for incident photon frequencies of $0.11, 0.117$, and $0.14eV$. We find that the saturation curve can be approximated by an inhomogeneously broadened two-level model, i.e. $\alpha(I)/\alpha_0 \approx (1 + I/I_s)^{-1/2}$, where I_s is the saturation intensity. The saturation intensity can be determined by finding the value of I at which $\alpha(I)/\alpha_0 = 0.707$. From this figure, we find that the saturation intensity ranges from 7 to $8\,MW/cm^2$ at $77K$ and 10 to $15\,MW/cm^2$ at $300K$. These values are comparable to those of bulk GaAs.[3]

I_s can be significantly reduced by increasing the well width to approximately $80\mathring{A}$. For the $80\mathring{A}$ quantum well, the energy separation between the first and fourth

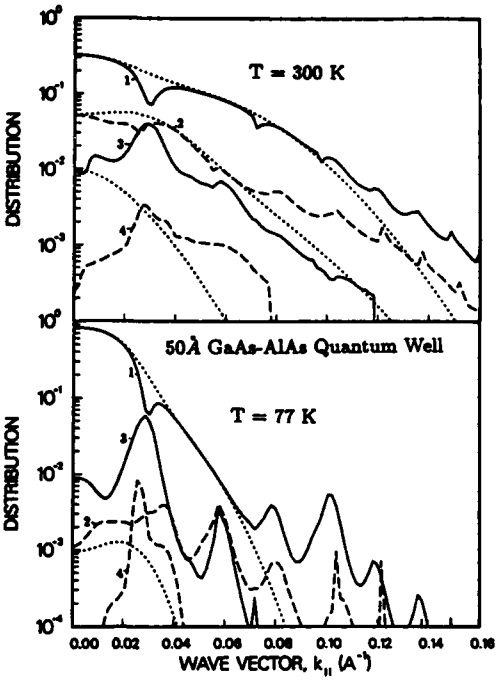

Figure 3. Distribution functions for various valence subbands of a $50\mathring{A}$ GaAs-AlAs quantum well under optical pumping.

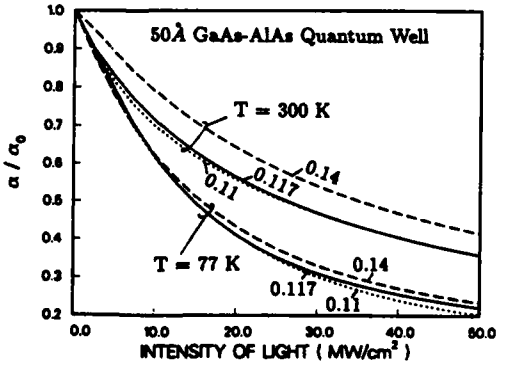

Figure 4. $\alpha(I)/\alpha_0$ versus I for a $50\mathring{A}$ GaAs-AlAs quantum well for $\hbar\omega = 0.11, 0.117$, and $0.14eV$.

subbands matches the CO_2 laser energies at $k_{||} \approx 0.05\mathring{A}^{-1}$ and the $1-4$ optical matrix element also peaks around there. For photon energies from 0.11 to 0.14 eV, the saturation intensity is found to range from 1 to 3 MW/cm^2 at $77K$ and 5 to 10 MW/cm^2 at $300K$.

A possible application of the inter-subband absorption saturation in p-type semiconductor quantum wells is as light-by-light modulator. Because of the rich structures in the valence subbands in quantum wells, there are many ways of modifying the absorption spectrum of a weak probe beam by an intense pump beam. To the first-order approximation, the absorption coefficient for the probe beam is described by (1) with the carrier distribution determined by solving (3) for the pump beam.

Figure 5 shows the absorption spectra of the $50\mathring{A}$ GaAs-AlAs quantum well with and without a $50MW/cm^2$ pump beam at $\hbar\omega = 0.117meV$. The absorption coefficient is substantially reduced for $\hbar\omega$ near the pump frequency as a result of carrier depletion. The change of absorption at other photon energies reflects the intensity-dependent nonequilibrium carrier distribution set up by the pump beam. The absorption coefficient is reduced to various degrees at almost all photon energies shown in this figure. We found negative absorption coefficient for $\hbar\omega \approx 0.07-0.09eV$ indicating a gain. In the semilog plot, we show the absolute value of α with the understanding that the sign of α is negative for $\hbar\omega \approx 0.07 - 0.09eV$.

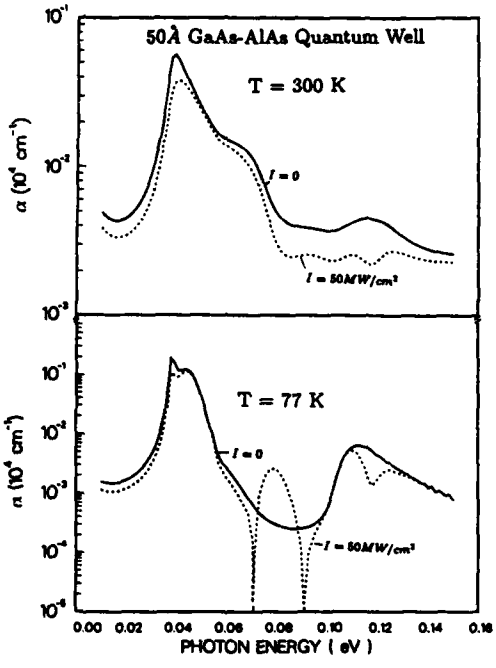

Figure 5. Absorption spectra of a $50\mathring{A}$ GaAs- AlAs quantum well with and without optical pumping for doping density of $10^{12}cm^{-1}$.

The appearence of the gain is due to the inverted population of the third subband relative to the second subband at $k_{||}$ near $0.03\mathring{A}^{-1}$ (see Figure 3) and the sizable 2-3 transition at that wave vector (see Figure 2). The peak position of the gain is around $0.08eV$ which agrees well with the energy separation of subbands 2 and 3 at $k_{||} \approx 0.03\mathring{A}^{-1}$ (see Figure 1). Thus in a pump-and-probe experiment, one can map out the energy difference of various subbands as a function of $\vec{k}_{||}$ by sweeping the frequency of the pump beam and measuring the probe absorption spectrum.

ACKNOWLEDGMENTS

We would like to thank D. L. Smith and M. Baskes for fruitful discussions. One of us (Y.C.C.) would like to thank Sandia National Laboratories, Livermore for the support via a summer faculty program. This work was supported in part by the U. S. Office of Naval Research (ONR) under Contract N00014-81-K-0430. One of us (R.B.J.) would like to acknowledge support from the U. S. Department of Energy.

REFERENCES

1. G. D. Sanders and Y. C. Chang, Phys. Rev, **B31**, 6892 (1985); Phys. Rev. **B36** (1987).
2. J. M. Luttinger and W. Kohn, Phys. Rev. **97**, 869 (1955).
3. R. B. James and D. L. Smith, Phys. Rev. Lett. **42**, 1495 (1979); Phys. Rev. **B21**, 3502 (1980).
4. E. O. Kane, J. Phys. Chem. Solids **1**, 82 (1956).
5. Y. C. Chang and R. B. James, Quantum Well and Superlattice Physics (SPIE Proceedings Vol. 792, Washington, 1987), edited by G. H. Döhler and J. N. Schulman, p. 214.

OPTICALLY-SATURABLE ABSORBING CENTERS VERSUS DEEP-LEVEL TRAPS IN SEMICONDUCTOR LASERS

X. Y. Liu and E. Bourkoff
The Johns Hopkins University, Dept. of Electrical & Computer Engineering
Baltimore, MD 21218

ABSTRACT

We compare the model of deep-level traps with that of the optically-saturable absorbing centers in semiconductor lasers. Their dynamic behavior is simulated by numerically solving the rate equations. The dependence on various laser parameters of the oscillation frequencies, the onset of the self-sustained pulsations (SSP), and the damping rate of the relaxation oscillations (RO) is also investigated. The results predicted by the two models are then compared with each other.

INTRODUCTION

The mechanism for self-sustained pulsations of semiconductor lasers has been an interesting topic for many years. There has been much interest in self-sustained pulsation phenomena, which has significant effects on the dynamic characteristics of semiconductor lasers and is an important factor in high-speed modulation. There has been, however, much controversy over the mechanism of this phenomena. Some authors claim that deep-level traps are responsible for SSP, while others conclude that the optically-saturable absorbers are responsible. Each viewpoint is supported by certain experimental results. Looking at the physics behind these two theories, we can see that the difference lies in how the traps/absorbers interact with photons and carriers. In the trap model, an empty trap that has captured an electron can then release the electron by absorbing a photon. In the absorber model, however, an absorber will interact with a photon only by absorbing it. Due to the difference in the physics between these two models, it is naturally expected that the dynamic characteristics predicted by the two models will be different.

RATE EQUATIONS

The rate equations we use for the trap model can be found in our previous paper[1]. For the purpose of comparison, we list them here again:

$$\frac{dS}{dt} = g(N-N_e)S - \frac{S}{\tau_p} + \gamma\frac{N}{\tau_c} - \sigma_o c S(T_o - T) \tag{1}$$

$$\frac{dN}{dt} = \frac{J}{ew} - g(N-N_e)S - \frac{N}{\tau_c} + \frac{dT}{dt} \tag{2}$$

$$\frac{dT}{dt} = \sigma_o c S(T_o - T) - \sigma_e v_t N T \tag{3}$$

where

$$g(S) = g_o/(1+\frac{S}{S^*}) \tag{4}$$

S, N, and T are the photon, carrier, and trap densities, respectively; J is the injection current density; g is the gain parameter, for which we adopt the gain saturation relation in a two-level system; S^* is

the gain saturation parameter, γ the probability of spontaneous emission into the lasing mode, N_e the minimal carrier density to achieve transparency; τ_c and τ_p are the carrier and photon lifetimes; T_o is the total trap density; σ_o and σ_e are the optical and electron capture cross-sections; c is the light speed in the active layer; v_t the carrier thermal velocity; and w the thickness of the active layer. For the absorber model, we adopted the rate equations given by the paper in Chik, Dyment, and Richardson[2] with the incorporation of gain saturation and spontaneous emission. The rate equations follow:

$$\frac{dS}{dt} = g(N-N_e)S - \frac{S}{\tau_p} + \gamma\frac{N}{\tau_c} - c\sigma_o nS \tag{5}$$

$$\frac{dN}{dt} = \frac{J}{ew} - g(N-N_e)S - \frac{N}{\tau_c} \tag{6}$$

$$\frac{dn}{dt} = \frac{(n_o-n)}{\tau} - c\sigma_o nS \tag{7}$$

n_o is the total density of saturable absorbers, n the density of empty absorbers, and τ the average lifetime of absorbers in excited state. All the other parameters are identical to those in the trap model. We derived the expressions for the threshold current density for the two models as follows:

$$J_{th}^{trap} = (\frac{ew}{g_o\tau_c\tau_p})(1+g_o\tau_p N_e+\sigma_o c\tau_p T_o) \tag{8}$$

$$J_{th}^{abso} = (\frac{ew}{g_o\tau_c\tau_p})(1+g_o\tau_p N_e+\sigma_o c\tau_p n_o) \tag{9}$$

Both expressions are consistent with the numerically-calculated DC responses. As expected, the presence of traps or absorbers will increase the threshold current density slightly, since the traps or absorbers will cause additional loss.

RESULTS

The frequency of SSP or RO is one of the most important characteristics of the dynamics of a laser. By numerically solving the rate equations we obtained the dependence of oscillation frequency on various laser parameters.

The oscillation frequency vs. photon lifetime as predicted by the trap model is given in our previous paper[1]. The absorber model also predicts similar behavior. The dependence of the oscillation frequency on the carrier lifetime is similar to that on the photon lifetime in both models. When the trap or absorber density is varied, or the injection current density is varied, both models predict similar behavior for the oscillation frequency. Fig. 1 gives the required trap density for the onset of the self-sustained pulsations and the corresponding frequency as a function of the gain saturation parameter. The larger s^* is, the less its effect. As s^* decreases, the damping rate for RO increases, resulting in a higher trap density required for the onset of SSP. At the same time, the oscillation frequency will decrease due to increasing trap density. The absorber model also gives similar results when the gain saturation parameter is varied. For both models, the spontaneous emission has very similar effects as the gain saturation. However, the two models give different phase relationships among the carrier, photon, and trap/absorber densities. In the trap case, the carrier and trap densities are 180^o out of phase. In the absorber case, they are neither in phase nor 180^o out of phase. The phase relationship between the carrier and the photon densities is the same in both models. The absorber model also gives a broader pulse width (compared to the pulsation period) than for trap model. When a semiconductor laser is self-pulsing, the pulse width predicted by the trap model is usually one-tenth of the pulsation period, or even narrower, while the absorber model usually gives a

pulse width about one-third to one-half of the pulsation period.

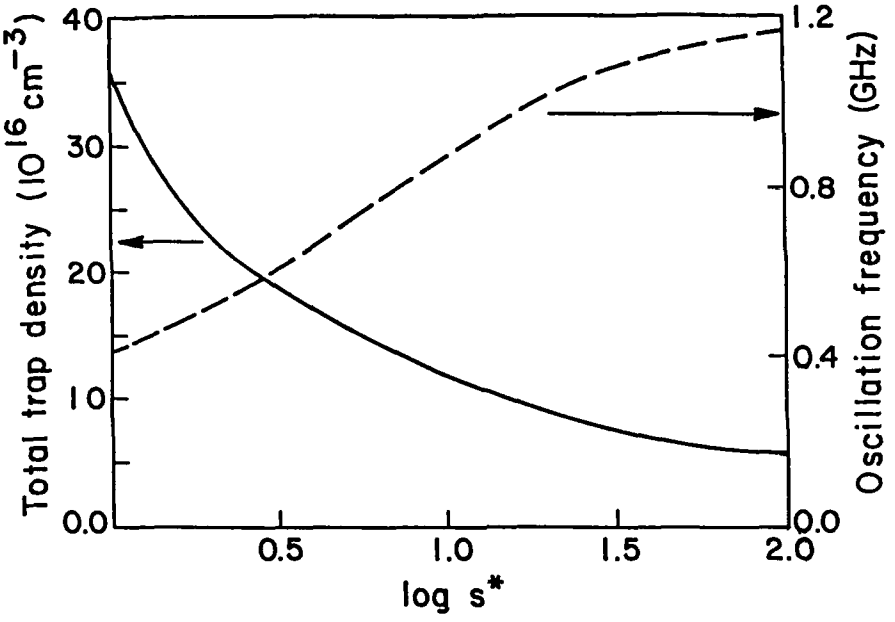

Fig. 1. The effect of gain saturation. Here, $s^* = S^* \frac{g_o \tau_c}{1+g_o \tau_p N_e}$

SUMMARY

Even though the trap model and the absorber model are different in terms of the interaction among the traps/absorbers, carriers, and photons, we found little difference between the dynamic characteristics predicted by the two models when the laser is directly modulated. We discussed the dependence on various laser parameters of the oscillation frequency, the onset of SSP, and the damping rate of RO, and obtained similar results from both models. However, the pulse width compared to the pulsation period given by the absorber model is much broader than that given by the trap model. The two models also give slightly different phase relationships between the carrier and trap/absorber densities. A promising way to distinguish traps from absorbers is to investigate the dynamic characteristics of the semiconductor lasers in external cavities, which is now in progress.

REFERENCES

1. E. Bourkoff, X. Y. Liu, and T. L. Worchesky, in *Advances in Laser Science-III*, Ed. by A. C. Tamm, J. L. Gold, W. C. Stwalley, American Institute of Physics Conference Proceedings, No. 172, Subseries: Optical Science and Engineering, No. 9, pg. 41, New York, NY (1988).
2. K. D. Chik, J. C. Dyment, and B. A. Richardson, J. Appl. Phys. 51, 4029 (1980).

PULSED LASER INDUCED PHOTOCONDUCTIVITY IN ZnS: PART II

R.D.Singh, Arun Gaur & A.K.Sharma
Department of Physics, M.D.University Rohtak-124001
(India)

ABSTRACT

The photoconductivity properties of ZnS crystal have been studied using XeCl excimer laser, N_2-laser, N_2-laser pumped dye laser, fundamental and frequency doubled Nd:YAG lasers. The controversy between the superlinearity and multiphoton photoconductivity of V-C'-C type has been resolved. At low photon density, charge vs photon density (Q vs Ip) characteristics show space charge generated currents. Extremely low values of the electron mobility indicate laser induced absorption.

INTRODUCTION

Multiphoton processes in crystalline solids have become a subject of wide interest for physicists as well as technologists because of their varied applications in high power laser technology and fundamental solid state physics. The small value of the absorption coefficients, however, make the experiments more difficult to perform and the complexity of the equation describing the processes make the theoretical calculations cumbersome. Therefore, an attempt to find a system which has relatively large multiphoton absorption coefficient is of significant importance. Mylnikov and Kozyrev[1] have suggested that the nonlinear photoconductivity observed in the case of ZnS at a small photon density of the order of 10^{23}photons/cm^2/sec should be attributed to the two photon process of V-C'-C type transition (where C' refers to the intermediate band) involving the lower valence band reported by Koren and Yakoby.[2] Ashkinadze et al[3] have studied non-linear luminescence in single crystal GaP excited by Nd:YAG laser at 77K. The minimum of the direct band gap in this case lies at 2.9 ev while the indirect band gap is 2.33 ev. The observed luminescence in this case was thus either due to the absorption of three photon with no phonon participation or due to a two-photon phonon-assisted transition. Since there exists wide differences between the values of the absorption coefficients calculated by the different workers and between the theoretical and experimental values, we have studied the lux-ampere and current voltage characteristics in the case of ZnS crystal using XeCl excimer laser, N_2-laser, N_2-laser pumped dye laser, fundamental and frequency doubled Nd:YAG laser.

EXPERIMENTAL DETAILS

The experimental set up used for the detection of the photoconductivity signal was the same as described elsewhere.[4]

RESULTS AND DISCUSSION

The band gap of the crystal using N_2-laser pumped dye laser

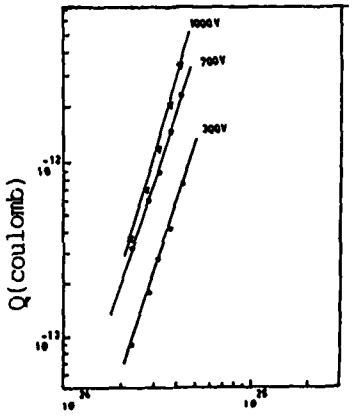

Ip(Photons/cm²/sec)

Fig.1. Q vs Ip characteristics using N_2-laser.

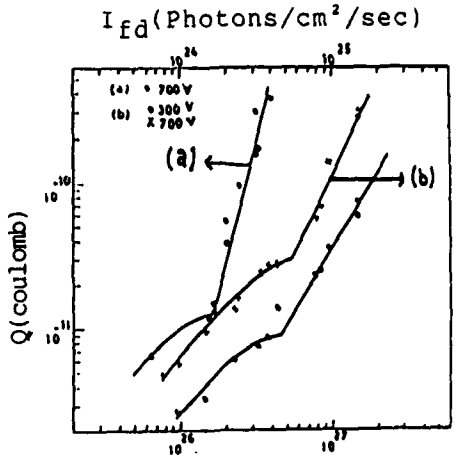

I_f (Photons/cm²/sec)

Fig.2. Q vs Ip characteristics using (a) fundamental Nd:YAG laser and (b) frequency doubled Nd:YAG laser.

was found to be 3.58 ev. The charge vs photon density characteristics using N_2-laser and Nd:YAG laser (fundamental and frequency doubled) are shown in Figs.1 and 2, where I_f and I_{fd} represent the photon densities in case of fundamental and frequency doubled Nd:YAG laser. The former obeys the relations $Q \propto I_p^n$, with n=3. On the basis of the theoretical calculations made by the earlier workers this can easily be understood to be due to the three photon absorption process. Since the band gap of the crystal is less than the energy of the exciting photon (3.78 ev), the observed photoconductivity signal can be due either to a phonon assisted two photon absorption starting from the lower valence band as reported by Koren and Yacoby[2] or to the space charge generated currents. The former possibility though quite stimulating is ruled out on the basis of Q vs I_p characteristics using Nd:YAG laser and XeCl excimer laser. In the former case using fundamental as well as frequency doubled Nd:YAG laser, the curves start with a large slope, indicating saturation and then nonlinear behaviour with a slope of two in case of the second harmonic and four in case of the fundamental. The large slope can be understood to be due to the space charge generated currents as reported by Smith and Rose[5] and the plateau shows the saturation of the one photon process. The characteristics observed in case of N_2-laser excitation may correspond to the first process of space charge generated current. Also the photon density observed in the two cases are similar. Interestingly the Q vs I_p characteristics using XeCl laser show only the slope one, indicating band to band transitions.

The electron mobilities (μ) obtained in the present case are quite interesting in view of their extremely low values, in conformity

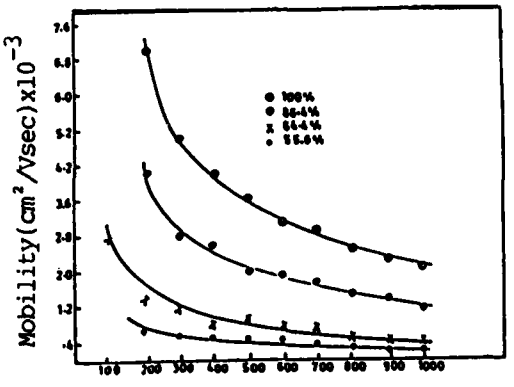

Fig.3. Mobility vs electric field (E) characteristics using N_2-laser.

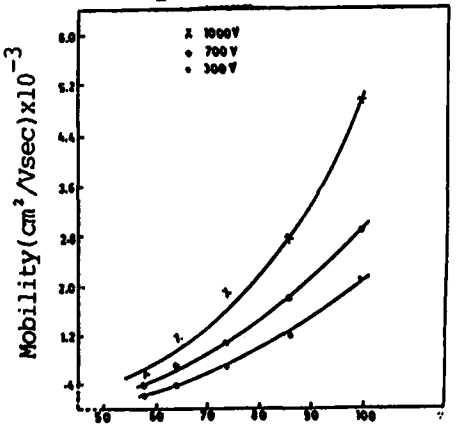

Fig.4. Mobility vs intensity(I) characteristics using N_2-laser.

with the studies reported by Mylnikov and Kozyrev[1]. This is attributed to the laser induced absorption.Thus we find that the photocurrent using high power pulsed laser increases manyfold, but the mobility of the charge carriers drops. However, unlike the case of ZnSe crystal where we observed an increase in the electron mobility with applied voltage at extremely low photon densities, in the present case the electron mobility drops with voltage at all the photon densities used.

ACKNOWLEDGEMENTS

Authors thank to Mr.N.K. Abbi for technical assistance.

The work has been sponsored by the Dept. of Atomic Energy Bombay (India).

REFERENCES

1. V.S.Mylnikov and V.K. Kozyrev, Sov.Phys.Semicond. 11, 127(1977).
2. G.Koren and Y. Yacoby, Phy.Rev. Lett. 30, 920 (1973).
3. B.M. Ashkinadze, I.P. Kretsu, S.L.Pyshkin and I.D. Yaroshets kii, Sov. Phys. Semicond. 2, 1261 (1969).
4. R.D.Singh, A.K.Sharma, Arun Gaur and Devendra Mohan, Solid State Commun. 68, 39 (1988).
5. R.W. Smith and A. Rose, Phys. Rev. 97, 1531 (1955).

INTERMOLECULAR VIBRATION OBSERVED IN LIQUID CS_2 AT HIGH PRESSURE

Bern Kohler and Keith A. Nelson
Department of Chemistry, Massachusetts Institute of Techonology, Cambridge, MA 02139

ABSTRACT

Impulsive stimulated scattering (ISS) experiments were performed on liquid CS_2 at high pressure. As pressure is increased the observed response becomes weakly oscillatory, revealing underdamped intermolecular vibrations. These are interpreted as librational oscillations similar to those observed in ISS experiments on CS_2 at low temperatures.[1]

INTRODUCTION

By varying the pressure of a molecular liquid and thereby forcing molecules to sample different regions of their intermolecular potentials, it is possible to learn a great deal about intermolecular interactions in the liquid state. Spontaneous light scattering has been used as a probe of liquid-state molecular dynamics in several pressure-dependent studies. In CS_2, a soft shoulder in the depolarized Rayleigh spectrum was observed to increase in intensity at elevated pressures.[2] This shoulder has been attributed to vibrational motions between neighboring molecules.

Impulsive stimulated scattering (ISS) experiments carried out with femtosecond time resolution permit real-time observation of intermolecular motions in liquids, in some cases revealing dynamics that are difficult to extract from spontaneous light-scattering spectra. In a temperature-dependent ISS study of liquid CS_2, oscillatory temporal responses were observed at low temperatures and interpreted in terms of rotational vibrations, or librations, between neighboring molecules.[1] Here we present initial results of an ISS study on CS_2 in which pressure was varied with a diamond anvil cell. At high pressure the response is again weakly oscillatory due to underdamped librational motion.

EXPERIMENTAL

The ISS experiment has been described extensively elsewhere.[3] Amplified 90 femtosecond pulses at 620 nm were used for both the excitation pulses and the variable delayed probe pulse in a transient grating geometry. The polarizations of the three incoming pulses and of the diffracted light were set to minimize the electronic contribution to signal at t=0, as has been described elsewhere.[4] Pressure was generated in a standard Merrill-Bassett type diamond anvil cell. An 0.78 mm thick, 304 stainless steel gasket was used to contain the CS_2 within a hole of 0.7 mm diameter. We have estimated the pressure values by comparing single-exponential fits to our data at times greater than 1.2 ps (after the librational response is over) to reorientational correlation times determined from high-pressure Raman spectra.[5] We estimate ±1 kbar accuracy in our reported pressures.

DISCUSSION

In figure 1, ISS data from CS_2 liquid is shown at 3 different pressures together with fits to be discussed below. The signal around t=0 is due to the purely electronic (instantaneous) response which lasts only as long as the excitation pulses are in the sample. This response cannot be eliminated completely because of depolarization due to the diamond anvil cell. The dip in signal just after t=0 occurs because the signal contributions due to electronic and nuclear responses cancel each other.[3] The reponse shortly after the dip is due entirely to CS_2 molecular dynamics and is of primary interest to us.

The topmost scan was recorded upon first loading the cell and just squeezing out trapped air. All the features of the data, including the 1.5-ps decay time at $t > 1.2$ ps, are identical with those observed earlier at 1 atmosphere. At the two higher pressures the signal decays more rapidly initially. A weak second oscillation is barely visible at 2.5 kbar and clearly apparent at the highest pressure of 5 kbar.

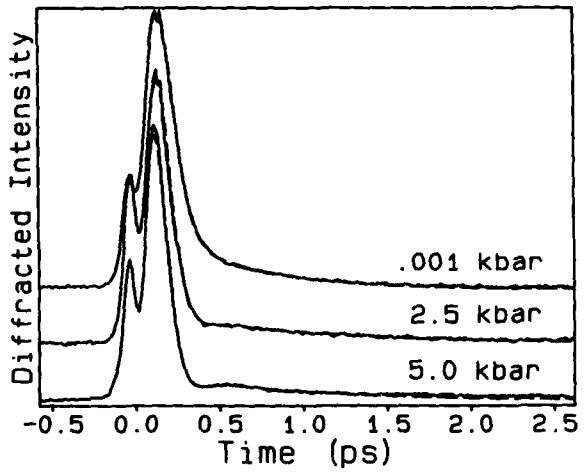

Figure 1. ISS data from room temperature CS_2 liquid at different pressures.

In the ISS experiment, the ultrashort excitation pulses exert impulsive torques on molecules through single-molecule polarizability anisotropies (essentially, stimulated rotational Raman scattering or optical Kerr effect). The resulting orientational motions lead to a net alignment of molecules which is detected by the probe pulse (also through single-molecule polarizability anisotropies). As in earlier analyses of ISS data, we neglect higher-order contributions to signal and interpret the response in terms of orientational motion only. The librational response at short times is fit assuming an inhomogeneous distribution of librational frequencies.The "modified Gaussian" distribution[3] is characterized by an average frequency, ω_A, whose value measures the configuration-averaged intermolecular torques in the liquid, and by a width, Δ, whose value measures the extent of inhomogeneity in the liquid. At long times the signal is assumed to decay exponentially with collective orientational relaxation rate Γ. The functional form used to fit the data is

$$I(t) = \left(Ae^{-\Delta^2 t^2/2}\sin\omega_A t + Be^{-\Gamma t}\right)^2.$$

The parameters determined from the fits appear in Table 1.

We observe that the average intermolecular librational frequency ω_A increases as the pressure increases. As a molecule's neighbors become closer on average with increasing pressure, the greater importance of repulsive interactions is expected to cause higher frequencies. The values of the average frequency at 5 kbar (295K) and 1 bar (165K) are similar, as are the CS_2 densities. The extent of inhomogeneity, as measured by Δ, is larger than at low temperature, probably indicative of a greater number of local structures accessible at room temperature even under pressure.

CONCLUSIONS

In this initial study we have observed oscillatory time responses in liquid CS_2 at high pressures similar to those reported previously at low temperatures. Further study is planned over a wider range of pressures and temperatures to allow for more detailed interpretation of the results in terms of simple models and molecular dynamics simulations.

To our knowledge these are the first time-resolved spectroscopy experiments with under 100-fs time resolution carried out in a diamond anvil cell. Our results demonstrate that dispersion and intensity-dependent optical responses in the diamonds do not cause significant loss of time resolution or present any other serious obstacles to this type of work, even with amplified femtosecond pulses in the microjoule energy range.

This work was supported in part by NSF Grant No. DMR-8704352.

TABLE I. Best-fit parameters for pressure-dependent ISS data from CS_2 liquid at room temperature.

Pressure (kbar)	ω_A (ps^{-1})	Δ (ps^{-1})	Γ (ps^{-1})	A	B	ρ (gm/cm^3)
.001	1.2	6.9	1.0	50	5.5	1.29
2.5	8.2	5.9	.55	10	3.6	1.43
5	9.9	6.1	.64	9	3.3	1.53
Temperature (K) (from reference 1)						
165 (1 bar)	7.5	4.4	.65	9	3.7	1.42

REFERENCES

1. S. Ruhman, B. Kohler, A. G. Joly, and K. A. Nelson, Chem. Phys. Lett. 141, 16 (1987).
2. B. Hegemann and J. Jonas, J. Chem. Phys. 82, 2845 (1985).
3. S. Ruhman, A. G. Joly, B. Kohler, L. R. Williams and K. A. Nelson, Revue Phys. Appl. 22, 1717 (1987).
4. J. Etchepare et al., Opt. Comm. 63, 329 (1987).
5. S. Ikawa and E. Whalley, J. Chem. Phys. 86, 1836 (1987).

FEMTOSECOND TIME RESOLVED ABSORPTION SPECTROSCOPY OF $Cr(CO)_6$ AND $Mn_2(CO)_{10}$: OBSERVATION OF ELEMENTARY BOND BREAKAGE AND FORMATION

Alan G. Joly and Keith A. Nelson
Massachusetts Institute of Technology, Cambridge, Massachusetts 02139

ABSTRACT

Femtosecond transient absorption measurements have been used to study CO dissociation in three simple transition metal carbonyls, $Cr(CO)_6$ and $M_2(CO)_{10}$ [M = Mn, Re] in solution. In all compounds, CO dissociation is seen to occur within one picosecond. $Cr(CO)_6$ shows subsequent solvent coordination within 2.5 ps which is consistent with previous results. All compounds show slow spectral evolution on a 10 to 50 ps timescale which is interpreted as relaxation of the resulting photoproducts.

INTRODUCTION

$Cr(CO)_6$ and $Mn_2(CO)_{10}$ have long been considered prototypes for transition metal carbonyl photochemistry. In the gas phase, irradiation of $Cr(CO)_6$ with ultraviolet light produces $Cr(CO)_n$ fragments with n varying between 0 and 5. In contrast, in solution or matrix environments, a single CO dissociates. In methanol, subsequent solvent coordination of the "naked" $Cr(CO)_5$ fragment is known to occur within 2.5 ps[1]. However in $M_2(CO)_{10}$ [M = Mn, Re], photolysis results in either metal-metal [M-M] bond cleavage or CO dissociation within 25 ps[2]. After CO dissociation, in $Mn_2(CO)_{10}$, subsequent intramolecular rearrangement to form a semi-bridging compound is known to occur[3]. In $Re_2(CO)_{10}$, a CO bridge does not form[4] but solvation or solvent coordination to the empty site may occur. Perhaps the most interesting point is that laser pulses centered at 308 nm excite predominantly a metal-metal (M-M) $\sigma \rightarrow \sigma^*$ transition[5]. This reduces the formal bond order to zero and should lead to homolytic cleavage of the M-M bond. However, CO dissociation is preferred over M-M bond cleavage indicating that there exists a nearby electronic state from which CO dissociation occurs. Using 100 fs laser pulses, we hope to observe the evolution of the initial excited states and subsequent CO dissociation in these compounds and relate this to their photochemistry.

EXPERIMENTAL

The femtosecond laser system used has been described previously[6]. Briefly, a synchronously pumped and amplified femtosecond laser system is employed whose output consists of 60 fs pulses of 6 μjoule energy at 615 nm. A portion of this output is frequency doubled to provide the 308 nm pump pulse. The remaining red light is focussed into a 2 mm cell of D_2O to produce white light continuum probe pulses, which are overlapped with the pump pulse in a 2 mm flow cell containing the sample. Cross-correlation of the pump and probe pulses indicates an instrument response time of 95 fs which is consistent with the fastest rise times observed in the experiment.

RESULTS AND DISCUSSION

Ultraviolet pulses at 308 nm excite predominantly the $^1A_{1g} \rightarrow {}^1T_{1g}$ ligand field transition[7] in $Cr(CO)_6$. This transition reduces π backbonding and places electron density in a Cr-CO σ^* orbital which labilizes the Cr-CO bonds. Figure 1 shows transient absorption measurements taken with 480-nm probe pulses. This wavelength corresponds to the absorption maximum of $Cr(CO)_5(MeOH)$. The data show three distinct regions: a pulse duration-limited rise, a rapid (< 500 fs) nonexponential decay, and a slower 2.5 ps exponential rise. The 2.5 ps risetime is in agreement with the solvent coordination time obtained by Simon and Xie[1] and so can be assigned as the time required for formation of $Cr(CO)_5(MeOH)$. The pulse duration limited rise is due to electronic absorption into the $^1T_{1g}$ state which ab initio calculations suggest should have symmetry allowed absorptions in the blue[7]. This state then undergoes dissociation of a single CO within 500 fs, resulting in formation of the bare $Cr(CO)_5$ complex. The dissociation process gives rise to a rapid blue shift of the excited state absorption spectrum which produces a nonexponential decay of absorption at 480 nm. Data taken at nearby wavelengths support this conclusion. Therefore we believe that the initially excited state ($^1T_{1g}$) is purely dissociative and excitation to this state leads to CO dissociation within 500 fs.

Longtime data, which is not shown, show slow spectral evolution which suggests that the spectrum is blue shifting on a 50 ps timescale. This is consistent with vibrational and/or electronic relaxation of the solvated complex. Ab initio calculations and matrix isolation studies suggest that the bare $Cr(CO)_5$ species is formed in an electronic excited state[8]. It is not certain whether electronic relaxation occurs on the time scale of solvent complexation or slower. The slow spectral evolution could therefore reflect electronic as well as vibrational relaxation of the initially formed $Cr(CO)_5(MeOH)$.

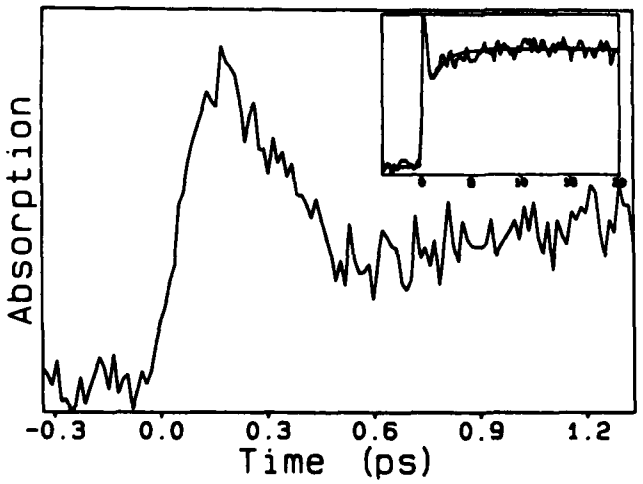

Figure 1. Transient absorption data of $Cr(CO)_6$ using 480 nm probe pulses. The inset shows solvent coordination that occurs after dissociation is complete.

In contrast to $Cr(CO)_6$, $M_2(CO)_{10}$ forms two photoproducts, $M_2(CO)_9$ and $M(CO)_5$. Figure 2 shows transient absorption measurements for the two different compounds using hexane as the solvent. The probe wavelength is set to the maximum of the $M_2(CO)_9$ absorption. Here different dynamics should be observed

since $Mn_2(CO)_{10}$ forms a bridged species while $Re_2(CO)_{10}$ does not. However the data in figure 2 are remarkably similar in their short time behavior. Both scans show two distinct temporal regions: a pulse-duration limited rise, and an 800 fs exponential decay. It is improbable that this decay reflects the CO bridging time as it is identical in both species; however it may reflect the CO dissociation time. Since the initial pulse at 308 nm excites the M-M $\sigma \rightarrow \sigma^*$ transition[5], CO dissociation must result from electronic curve crossing and thus requires more time to occur. Bridging or solvent complexation may follow rapidly, so that in both $M_2(CO)_{10}$ species the rate-limiting photochemical processes may be electronic curve crossing and CO dissociation.

The long time $M_2(CO)_{10}$ data (not shown) do show significant differences, due presumably to the formation of quite different products with different electronic and/or vibrational relaxation times. The results of more detailed studies using different probe wavelengths and solvents to better understand both CO dissociation and M-M bond cleavage are forthcoming.

This work was supported in part by NSF and private contributions to a Presidential Young Investigator Award.

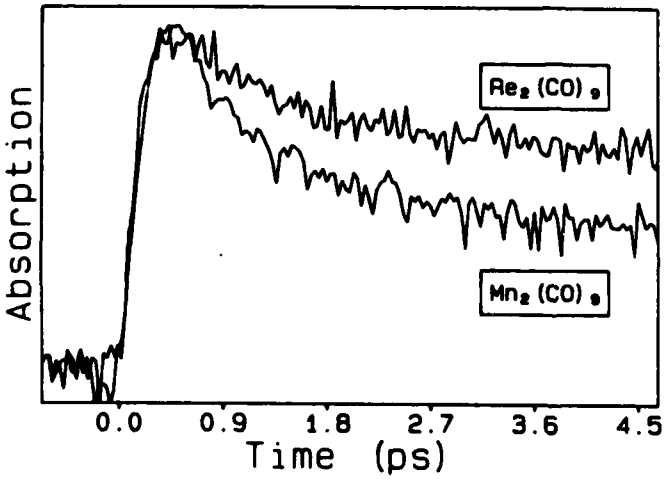

Figure 2. Transient absorption data for $M_2(CO)_{10}$ using probe pulses centered at the peak of the $M_2(CO)_9$ absorption.

REFERENCES

1. J. D. Simon and X. Xie, J. Phys. Chem. 90, 6751 (1986).
2. L. J. Rothberg, N. J. Cooper, K. S. Peters, and V. Vaida, J. Am. Chem. Soc. 104, 3536 (1982).
3. (a) A. F. Hepp and M. S. Wrighton, J. Am. Chem. Soc. 105, 5934 (1983). (b) S. P. Church, H. Hermann, F. W. Grevels, and K. Schaffner, J. Am. Chem. Soc. 785 (1984).
4. S. Firth, W. E. Klotzbucher, M. Poliakoff, and J. J. Turner, Inorg. Chem. 26, 3370 (1987).
5. R. A. Levenson and H. B. Gray, J. Am. Chem. Soc. 97, 6042 (1975).
6. S. Ruhman, B. Kohler, A. G. Joly, and K. A. Nelson, IEEE J. Quantum Elec. QE-24, 470 (1988).
7. H. B. Gray and N. A. Beach, J. Am. Chem. Soc. 90, 5713 (1968).
8. (a) P. J. Hay, J. Am. Chem. Soc. 100, 2411 (1978). (b) J. K. Burdett, J. M. Grzybowski, R. N. Perutz, M. Poliakoff, J. J. Turner, and R. F. Turner, Inorg. Chem. 17, 147 (1978).

PICOSECOND PULSE AMPLIFICATION IN A SINGLE MODE NEODYMIUM DOPED FIBRE

A.S. Gouveia-Neto, A.S.B. Sombra, P.G.J. Wigley & J.R. Taylor
Femtosecond Optics Group, Physics Department, Imperial College,
Prince Consort Road, London SW7 2BZ

ABSTRACT

The pulses from a fibre-grating compressed mode locked c.w. pumped Nd:YAG laser have been amplified in a Nd doped single mode fibre using a counter propagating pumping geometry. Gains of up to times ten were measured for signal energies of up to 0.2pJ per pulse.

INTRODUCTION

In the past three years there has been a renewed interest in rare earth doped fibres [1,2] primarily as laser sources [3] which have been Q-switched [4] and mode locked [5]. Additionally, rare earth doped fibres have been used as sensors [6] and nonlinear elements [7]. However, it is as amplifiers [8,9] particularly at telecommunications wavelengths that these devices should play an important role. We report here, the first measurements on picosecond pulse amplification at 1.06μm in neodymium doped fibre.

EXPERIMENTAL AND RESULTS

A schematic of the experimental arrangement is shown in Figure 1.

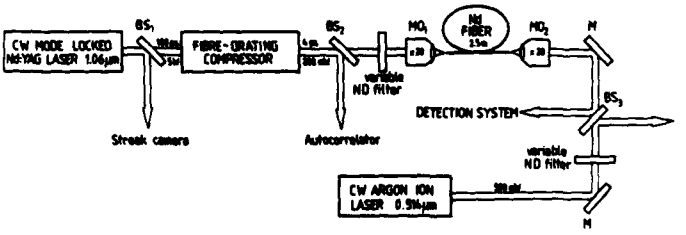

Figure 1. Schematic of the experimental arrangement.

The source of pulses was derived from a conventional mode locked, c.w. pumped Nd:YAG laser which delivered an average power of around 8W in 100ps pulses at a 100MHz repetition rate. A standard optical fibre-grating pair was used to compress the output pulses from this laser, providing a source of signal pulses of 4ps in duration with a bandwidth of ~0.8nm and with average powers of up to 300mW. These pulses were coupled into and out of the amplifying medium, a Neodymium doped fibre, using conventional times twenty microscope objectives.

The Neodymium doped fibre was a conventional GeO_2-SiO_2 based design with a 8μm core diameter and a Nd doping of 300ppm and medium phosphorus content. At 1.06μm the fibre exhibited a loss of about 2dB/Km and at 514nm the measured absorption coefficient was $1.46 \times 10^{-2} cm^{-1}$. A 2.5m fibre length was used.

The pump power to the fibre was provided by a c.w. argon ion laser and at maximum an average power of 40mW was launched counter-propagating to the input picosecond signal. In addition to a conventional photodiode oscilloscope combination, a scanning autocorrelator and a synchroscan streak camera were used to directly measure the gain provided by the excited fibre and to monitor any temporal changes in the amplified and transmitted pulse profile.

Taking typical values for Nd in glass for a gain cross section of $3 \times 10^{-20} cm^2$, the saturation energy density for incident picosecond pulses is around $6 Jcm^{-2}$. This would correspond to a saturation energy of about 420nJ into the fibre. Typically, the maximum signal pulse energies were around 25pJ.

For an average pump power of 36mW saturation of the amplification was observed at average signal levels of ~0.5mW. This corresponded to approximately an energy of 5pJ in the 100MHz repetition rate picosecond signal pulses. Figure 2 shows the variation of the directly measured gain with average signal power for an average pump power of 35mW at 514nm. It can be seen that for signal pulse energies of ~0.2pJ gains approaching times ten were achieved.

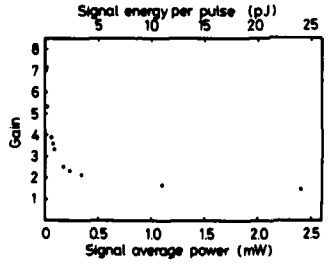

Figure 2. Variation of the gain with signal power at a fixed pump power of 35mW.

The Neodymium doped fibre was not single mode at 514nm and problems were encountered ensuring that the mode of the pump laser provided sufficient overlap with the signal mode to obtain the optimum amplification. It was necessary to vary the launch conditions of the pump laser in order to achieve this condition.

Although providing adequate amplification, the wavelength of operation is of little consequence for pulsed communication. The

more important system is that based on Erbium doped systems operating in the 1.55μm window. Sub-picosecond pulse amplification studies are presently being undertaken in our laboratory in this material.

The provision of the optical fibres by British Telecom Research Laboratories is very gratefully acknowledged.

REFERENCES

1. S.B. Poole, D.N. Payne, R.J. Mears, M.E. Fermann & R.I. Laming
IEEE J. Lightwave Tech. LT4, 870 (1986).
2. B.J. Ainslie, S.P. Craig & S.T. Davey
IEEE J. Lightwave Tech. LT6, 287 (1988).
3. L. Reekie, R.J. Mears, S.B. Poole & D.N. Payne
IEEE J. Lightwave Tech. LT4, 956 (1986).
4. I.P. Alcock, A.C. Tropper, A.I. Ferguson & D.C. Hanna
Electronics Lett. 22, 84 (1986).
5. I.N. Duling, L. Goldberg & J.F. Weller
Electronics Lett. 24, 1334 (1988).
6. M.C. Farries, M.E. Fermann, R.I. Laming, S.B. Poole & D.N. Payne
Electronics Lett. 22, 419 (1986).
7. M.W. Phillips, H. Gong, A.I. Ferguson & D.C. Hanna
Optics Commun. 61, 215 (1987).
8. R.J. Mears, L. Reekie, I.M. Jauncey & D.N. Payne
Electronics Lett. 23, 1026 (1987).
9. E. Desurvire, J.R. Simpson & P.C. Becker
Optics Lett. 12, 888 (1987).

MEASUREMENT OF UV FEMTOSECOND LIGHT PULSES USING TWO-PHOTON LUMINESCENCE IN CsI CRYSTALS DOPED WITH Na

F. Noack, W. Rudolph
Physics Department, Friedrich-Schiller-University Jena, GDR

R. Deijch
Academy of Science Salaspils-1, USSR

W.E. Postovalos
Institute of General Physics IOFAN Moscow , USSR

ABSTRACT

UV femtosecond light pulses can easily be used to excite alkali-halides by two-photon absorption and to measure two-photon absorption coefficients. In CsI doped with Na the two photon absorption is followed by luminescence centered around 420nm. This nonlinear-optical process of second-order can be utilized to measure correlation functions for determining durations of UV femtosecond light pulses with high sensitivity and without critical requirements for the alignment.

INTRODUCTION

At present, high power subpicosecond light pulses in the UV can easily be obtained by amplification of frequency-doubled femtosecond light pulses in excimer gain modules [1,2] and have gained great deal of interest in various fields of application. The handling of such pulses requires an exact knowledge of their parameters, in particular of the pulse duration. Common techniques as the measurement of pulse autocorrelations through second harmonic generation (SHG) in nonlinear crystals fail due to the high one photon absorption below 200nm. We propose to use luminescence excited by two-photon absorption (TPL) in doped alkali-halides as nonlinear process. This technique distinguishes itself by its simplicity and sensitivity as compared with surface SHG [3] and two-photon ionization [4]. Moreover, it provides the principal possibility of single-shot measurements similar to the two-photon fluorescence in organic dyes which has been applied for the measurement of ps pulses in the VIS and NIR for a long time.

CsI doped with Na is a promising candidate for this purpose because of its relatively high two-photon absorption (TPA) coefficient and the fact that the TPA is not followed by the formation of color centers. Firstly, we will describe measurements of the TPA-coefficient in CsI with UV fs light pulses. Secondly, we describe the measurement of femtosecond pulse autocorrelations using TPL.

MEASUREMENT OF THE TPA-COEFFICIENT IN CsI

TPA coefficients can be determined from the measured dependence of the reciprocal optical transmission on the incident light energy[4]. The measurements were performed with amplified pulses of a CPM laser[5] which after frequency doubling were reamplified in a XeCl module at 308nm. The pulse intensity was varied by means of color glass filters calibrated for 308nm, where care was taken to avoid contributions of nonlinear absorption. From Fig. 1 the TPA coefficient can be estimated and yields $\beta \approx (4.5 \pm 2) 10^{-9}$ cm/W The error in this absolute value results mainly from uncertainties in the determination of the pulse and beam profile. Obviously for input energies exceeding a critical value A, or more strictly speaking if the product of TPA coefficient β, sample length L and input intensity I_o is larger than an certain value, the ideal linear behavior is violated.

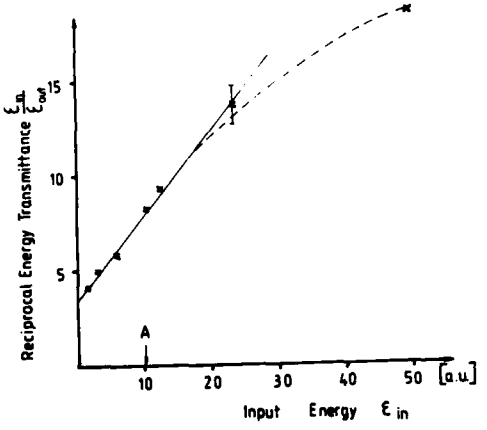

Figure 1. Reciprocal energy transmission as a function of the input energy for TPA in CsI $A \approx (6 mJ/cm^2)$

MEASUREMENT OF UV FEMTOSECOND PULSES BY MEANS OF TPL

To prove that the luminescence arises from a nonlinear process of second-order we measured the luminescence energy as a function of the input energy, see Fig. 2. Obviously for input energies smaller than a critical value A the ascent of two of the curve in a double-logarithmic plot shows the expected behavior.

In autocorrelation measurements an ideal contrast ratio of 3 (defined as the ratio of the signals at zero pulse delay and infinite pulse delay) requires $(\beta L I_o) < 1$. To estimate the error caused by violation of this condition for the determination of the full width at half maximum of the autocorrelation we calculated the correlation parameters for different values of $(\beta L I_o)$, see Fig. 3.

For measuring the pulse autocorrelation the pulses were sent through a usual Michelson-interferometer. The two partial pulses were then focussed into the crystal and the luminescence energy was measured by a photodiode. Figure 4 shows a typical recording. The contrast ratio was about 2.1 resulting in a corrected correlation width of about 490fs. For Gaussian pulses this corresponds to a pulse duration of about 350fs. The satellites are typical for femtosecond pulse amplification in XeCl in the weak saturation regime. This as well as their constant separation of about 1.3ps is due to the action of several inhomogenously broadened amplifying transitions[6].

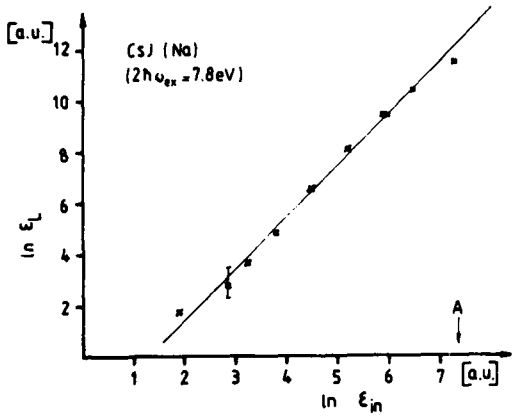

Figure 2. Double logarithmic plot of the luminescence energy after TPA in CsI(Na) as a function of the input energy A≈ 6mJ/cm²

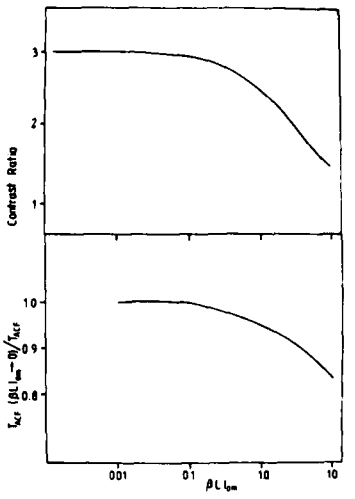

Figure 3. Contrast ratio and factor by which the measured autocorrelation width T_{ACF} has to be multiplied to get the true value $T_{ACF}(\beta L I_0\ 0)$. (The curves are calculated for Gaussian pulses with a constant intensity across the beam profile. Curves obtained for other typical pulse shapes do not differ significantly.)

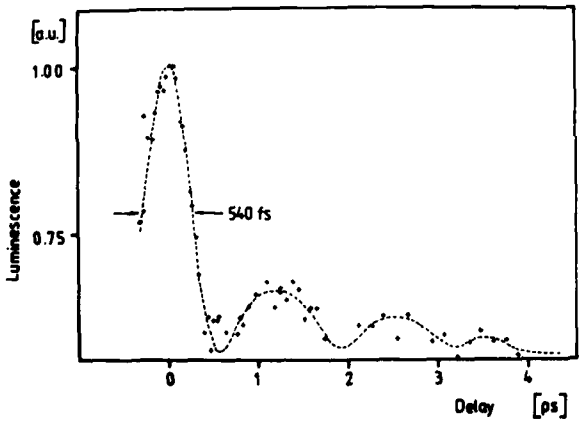

Figure 4. Autocorrelation function of UV femtosecond pulses recorded by means of TPL in CsI(Na).

LITERATURE

1 J.H.Glownia, G.Arjavalingham, P.P.Sorokin, J.E.Rothenberg: Opt.Lett. 11 (1986) 79

2 S.Szatmari, B.Racz, F.P.Schäfer: Opt.Commun. 62 (1987) 271

3 E.S.Kintzel, C.Rempel: Appl.Phys. B42 (1987) 91

4 N.Bloembergen: IEEE J.Quant.Electr. QE10 (1974) 375

5 W.Dietel, E.Döpel, V.Petrov, C.Rempel, W.Rudolph, B.Wilhelmi, G.Marowsky, F.P.Schäfer: Appl.Phys B46 (1988) 1

6 B.Dick, S.Szatmari, B.Racz, F.P.Schäfer: Opt.Commun. 62(1987) 277
V.Petrov, W.Rudolph: to be published

III. CONDENSED MATTER, SURFACE, AND PARTICLE SPECTROSCOPY WITH EMPHASIS ON LASER/SURFACE INTERACTIONS

III.A. Laser--Condensed Matter Interactions

III.B. Applications of Laser/Surface Interactions

III.C. Laser Modification of Surfaces

III.D. Surface Nonlinear Optics

III.E. Laser Ionization, Ablation, and Deposition

SURFACE-PLASMONS ENHANCED NONEQUILIBRIUM ELECTRONIC AND LATTICE HEATING IN THIN SILVER FILMS

T. Tsang[+] and D. D. Smith[*]
Purdue University, W. Lafayette, Indiana 47907

ABSTRACT

We report the first observation of nonequilibrium heating of electronic and lattice in a thin silver film enhanced due to the excitation of single metal-boundary surface plasmons at the metal-air interface. The surface-plasmon-enhanced heating is probed on a picosecond time scale by thermally-induced changes in the ultra-violet reflectivity of the thin film. The heating enhancement due to plasmon decay is more than 2 orders of magnitude as compared to heating by a directly incident laser beam.

In this proceedings, we report a new surface-enhanced effect, namely, surface-plasmon-enhanced electronic and lattice heating in thin silver films. Surface Plasmon-Polaritons (SPP) are collective oscillations of electron charge density that are confined to the surface(s) of thin films. They are electromagnetic waves propagating along a metal-dielectric interface. The oscillation of these surface charges can be coherently and resonantly excited by an optical field via evanescent field using a prism coupler. Because the phase velocity of SPP is slower than that of a photon of the same energy, direct coupling of a photon field to a SPP is forbidden in a smooth free-standing metal film. However, employing the Attenuated-Total-Internal Reflection (ATR) technique (the Kretchmann configuration), the parallel component of the incident photon momentum wave vector $k_{\parallel}$ can be extended with the aid of a coupling prism. The phase matching is achieved by adjusting the incident angle of an incoming laser until $k_{\parallel}$ of the photon and plasmon match at the point dictated by the SPP dispersion curve,[1]

$$k_{\parallel} = \frac{\omega}{c}\sqrt{\frac{\varepsilon_1\varepsilon_2}{\varepsilon_1+\varepsilon_2}}, \qquad (1)$$

where ω is the excitation frequency, ε_1 and ε_2 are the complex dielectric constant of dielectric (air) and metal, respectively.

The active medium employed in this study is a 490 Å thick Ag film which was thermally evaporated under vacuum onto the hypotenuse side of a high-index of refraction glass prism (Schott Lak8). The laser beam entered from the glass side of the prism and resonantly excited the Single Metal-Air boundary Surface Plasmon-polaritons (hereafter SMSP) at the metal-air interface. The excitation source was a cavity-dumped dye laser pumped by the frequency doubled output of an actively mode-locked Nd:YAG laser. The dye laser optical pulse train has a 4 MHz repetition rate with a pulse duration of 4.5 ps at 624 nm. Figure 1 shown the experimental detail. Part of the dye laser beam was diverted to a stepper-motor controlled optical delay line and was then frequency doubled by a $LiIO_3$ nonlinear crystal to be used as the probe. The probe beam was focused to a spot size of $\sim 3\times10^{-4}$ cm^2 at the near-normal incidence onto the Ag film from the air side of the glass prism.

Meanwhile, the *p*-polarized and amplitude modulated pump beam was focused to the same spot size as the probe and was spatially overlapped with the probe spot on the Ag film. However, the pump beam irradiated the metal film through the glass prism instead and therefore excited the SMSP. A transient optical heating-induced thermoreflectance of the metal film was performed at room temperature. The measurement interrogates the change of the intensity of the reflected UV probe beam as a function of the time delay between the pump and the probe pulse.

The excitation of the SMSP is confirmed by taking a *p*-polarized ATR spectrum where a reflectance of <0.6 was obtained. When conduction electrons are heated on a time scale shorter than the electron-phonon energy relaxation time, a nonequilibrium temperature difference between the electrons and the lattice results.[2] This nonequilibrium heating due to direct optical heating has been investigated.[3,4] The electron temperature in the metal film is dramatically increased by the enhanced field density due to the excitation of SMSPs. The heating produced by decay of the collective electronic excitation mode results in a change in the Fermi distribution of the occupied electron states at a probe frequency ω_{probe},[3,5]

$$\rho = \frac{1}{1 - e^{[\hbar\omega_{probe} - (E_F - E_d)]/kT}} \tag{2}$$

and

$$\frac{\partial\rho}{\partial T} \propto \hbar\omega_{probe} - (E_F - E_d)\,, \tag{3}$$

where E_d and E_F are the energy of the *d* band electron and the Fermi energy. Therefore, when $\hbar\omega_{probe}<E_F-E_d$ a decrease in the reflected probe beam intensity due to the temperature modulation of the Fermi distribution is expected. Our picosecond time-resolved measurements probe the heat-induced change of the reflectance by interrogating the *d* band to Fermi level absorption of Ag. The temporal reflectance change is a direct indication of the electron and lattice temperatures. These temporal decays are depicted in Figure 2, where the dashed line is the normalized intensity of the laser pulse autocorrelation. When the polarization of the pump beam is switched from *p* to *s*, the temporal signal disappeared. Therefore, it is clear that the thermoreflectance signal is a consequence of the SMSP and has two decay components. The fast component that occurs in less than 5 ps and is not completely resolved is due to the ultrafast heating and energy relaxation of the electrons to the lattice. The slow component has a 1/e relaxation lifetime of ~50 ps is due to the relaxation of the lattice.

To compare and demonstrate the SMSP-enhanced heating, the *p*-polarized pump beam is redirected and incident on the metal film from the air side (see Figure 1), thus no SMSP is involved. The thermoreflectance signal is significantly reduced (light solid line near the baseline of Figure 2). By signal averaging, it was determined that a factor of ~100 in signal reduction is obtained for direct heating vs. SMSP-heating. Because the electron mean free path and the optical skin depth in the UV regime are both ~40 nm, the heating enhancement can be calculated using the ratio of the total field density within the metal film. For the case of SMSP-enhanced heating to that of the direct heating, this ratio, $\int | E_{sp\text{-}enhanced} |^2 dz / \int | E_{direct} |^2 dz$, is ~110,[6] and is comparable with the

experimental value. Because the modulation of the Fermi distribution is related to the energy density deposited in the metal film, the peak signal strength of the electron energy temporal relaxation profile, which is determined by the Fermi smearing,[3] is thus a direct measurement of the in-situ total energy density.

One of the authors+ would like to thank Brookhaven National Laboratory for the travel arrangments to the ILS Conference.

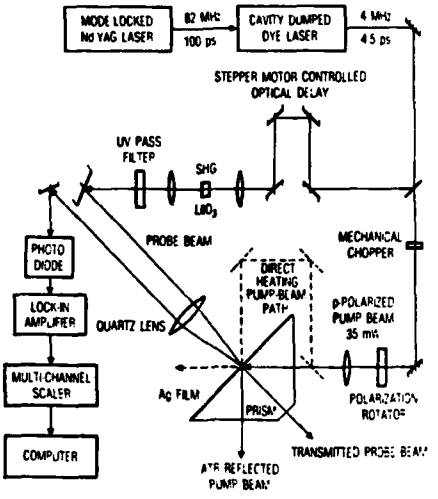

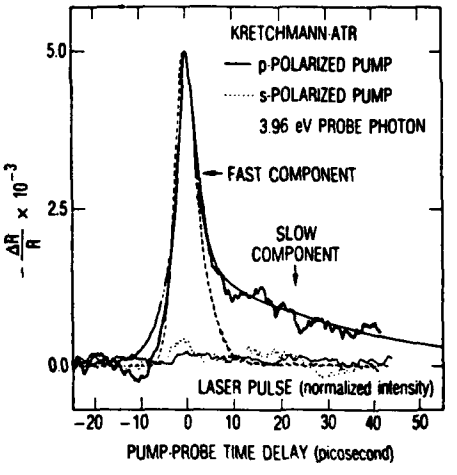

Fig. 1 The experimental arrangement. **Fig. 2** Transient thermoreflectance of a 49 nm Ag film.

+ Present address: Brookhaven National Lab., Upton, NY 11973.
* Present address: The Aerospace Corp., Los Angeles, CA 90009-2957.

REFERENCES

1. E. Kretchmann, Z. Phys. 241 (1971) 313.
2. R. Yen, J. M. Liu, and N. Bloembergen, Opt. Comm. 35 (1980) 277.
3. G. L. Eesley, Phys. Rev. B3 (1986) 2144.
4. R. W. Schoelein, W. Z. Lin, J. G. Fujimoto, and G. L. Eesley, Phys. Rev. Lett. 58 (1987) 1680.
5. R. Rosei and D. W. Lynch, Phys. Rev. B5 (1972) 3883.
6. T. Tsang and D. D. Smith, submitted to Opt. Comm.

TRANSIENT GRATING PROBE OF RECOMBINATION DYNAMICS IN CADMIUM SULFIDE COLLOIDS

L. V. Natarajan and J. R. Morgan
Department of Chemistry
University of Nevada-Reno, Reno, Nevada 89557

ABSTRACT

The recombination dynamics of charge carriers in room temperature aqueous cadmium sulfide (CdS) colloids containing 5 nm size CdS particles is examined by transient grating methods with subnanosecond pulses. The technique is found to be sensitive to excitation levels corresponding to less than one absorbed photon per CdS particle on the average. Multiexponential decays were observed. The technique is also found to be sensitive to photo-induced electron transfer to surface adsorbed species.

INTRODUCTION

The recombination of photo-induced charge carriers near semiconductor surfaces and interfacial charge transfer are important processes in surface mediated chemical reactions. These processes have been examined in small particles (< 10 nm diameter) of semiconductors in solution. These systems are interesting as photo-initiators for chemical transformations.[1] The colloid systems provide a large surface to volume ratio with negligible scattered Rayleigh light for sufficiently small particles and are also convenient systems to examine the effects of confinement of the charge carriers to a limited volume. In order to understand the photophysical and photochemical processes involved in semiconductor colloids, several studies have made use of luminescence[2] and transient absorption.[3] In this work, our effort has been to apply the transient grating technique to semiconductor colloids on picosecond timescales to elucidate the charge carrier[4] and interfacial electron transfer[5] dynamics. The technique has been found to be an extremely sensitive probe of dynamics in colloid systems where luminescence quantum yields are low.

The transient grating technique[6] involves excitation of the colloid with two crossed excitation beams of an identical wavelength corresponding to energies above the bandgap. The holographic charge carrier production leads to a modulation of the index of refraction (phase grating). Diffraction of a probe beam at energies below that of the bandgap can be used to monitor the time dependence of charge carrier density.

EXPERIMENTAL

The third harmonic (355 nm) of a single pulse (100 ps pulse width) extracted from a Spectra-Physics mode-locked, Q-switched YAG laser was split with a 50% beamsplitter and recombined at the sample for the excitation pulses. The 1064 nm fundamental

traversed a variable delay line and was focused at the Bragg angle on the spot formed by the pump beams.

Aqueous CdS colloids were prepared by methods previously reported in the literature.[2] The method used yielded 5 nm size particles with equal concentrations of Cd^{2+} and S^{2-} ions. The quantum yield for luminescence is $1x10^{-3}$. All measurements were performed at room temperature.

RESULTS AND DISCUSSION

The charge carrier relaxation is found to be nonexponential. Lifetime components ranging from <100 psec to 12 nsec are observed for the low intensity data in Fig. 1.

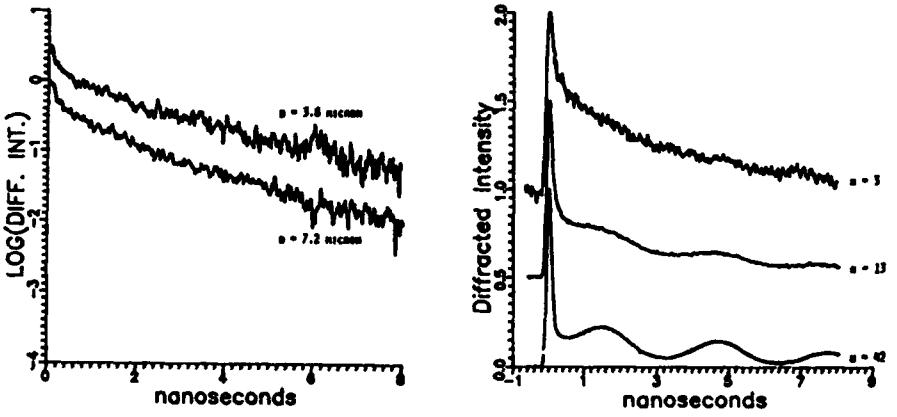

Fig. 1: left: The transient grating decay for different grating fringe spacings with N = 0.5 absorbed photons/particle. right: Intensity dependence of grating decay.

Fig. 1 shows that when the grating fringe spacing is varied by changing the angle between the pump beams that the decay is unchanged. This shows that diffusive processes such as interparticle excitation transfer do not occur on these distance scales. These results also show that diffraction by a thermal grating is unimportant since thermal diffusion would also lead to faster decays at smaller fringe spacings.

The intensity dependence of the transient grating decay is also shown in Fig. 1. As excitation intensities increase above a few absorbed photons per CdS particle, a larger portion of the decay occurs within 100 psec. Second order recombination has been observed in bulk CdS crystals at high intensities.[7] In the case of 5 nm diameter CdS particles the charge carriers are confined to a diameter not much larger than the exciton diameter. Second order recombination occurs rapidly and efficiently in this limited volume. The data in Fig. 1 also show a periodic modulation in diffracted intensity at high excitation levels. This results from the launching of counterpropagating acoustic waves due to the rapid deposition of heat at high intensities indicating that the short

time, second order recombination is largely nonradiative.

Methylviologen (MV^{2+}) is an acceptor of conduction band electrons in CdS via

$$e^-_{cb} + MV^{2+} \rightarrow MV^+$$

where MV^{2+} is adsorbed to the particle surface. This process is known to occur within 100 psec. The transient grating signal for several concentrations of MV^{2+} is shown in Fig. 2. It is observed that the intensity of the peak decreases with increasing MV^{2+} concentration and the long time components corresponding to electrons trapped on defects also increase in decay rate. The increase in decay rate indicates that the electron transfer to MV^{2+} either competes more effectively with trapping by long lived traps than short lived traps or that MV^{2+} is preferentially bound to surface sites with long recombination times.

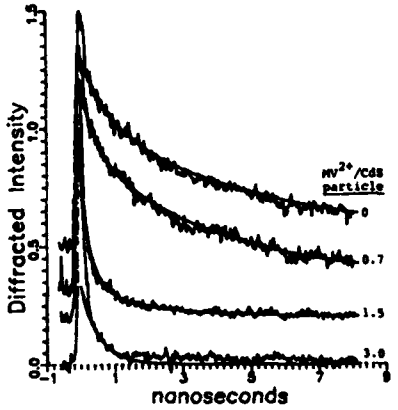

Fig. 2: Transient grating decay for aqueous CdS colloid with various MV^{2+} concentrations.

Acknowledgements Acknowledgement is made to the donors of The Petroleum Research Fund, administered by the American Chemical Society, for the support of this research.

REFERENCES

1. M. A. Fox, Acc. Chem. Res. 16, 314 (1983).
2. J. J. Ramsden and M. J. Gratzel, Chem. Soc., Faraday Trans. 1 80, 919 (1984).
3. Y. Nosaka, H. Miyama, M. Terauchi, and T. Kobayashi, J. Phys. Chem. 92, 255 (1988).
4. J. R. Morgan and L. V. Natarajan, J. Phys. Chem., in press.
5. L. V. Natarajan and J. R. Morgan, manuscript in preparation.
6. M. D. Fayer, Ann. Rev. Phys. Chem. 33, 63 (1982).
7. H. Saito and E. O. Gobel, Phys. Rev. B 31, 2360 (1985).

TIME RESOLVED MEASUREMENTS OF INELASTIC SCATTERING PROCESSES FROM MICRON SIZED DROPLETS

A. Biswas, H. Latifi, R. L. Armstrong
Physics Department, New Mexico State University, Las Cruces, NM 88003

R. G. Pinnick
Atmospheric Sciences Laboratory, White Sands Missile Range, NM 8802

ABSTRACT

Micron-sized droplets of Rhodamine 6G solution in water and ethanol (3 x 10^-4 M) are irradiated with a ~10 ns pulse from a frequency doubled Nd:YAG laser. Coupling of the inelastic fluorescence emission with the natural resonant modes of the spherical droplets result in stimulated emission, with each droplet behaving like a laser cavity. The droplet lasing exhibits faster rise times and is shorter lived than corresponding bulk liquid fluorescence. Lasing in droplets generally initiates almost simultaneously with the elastic scattered light, unlike stimulated Raman scattering (SRS) which is significantly delayed.

INTRODUCTION

Lasing[1,2] and SRS[3,4] observed in pulsed laser irradiated micron-sized spherical droplets have been attributed to the coupling of Lorenz-Mie structure resonances with the inelastic scattering (fluorescence and spontaneous Raman) inside the droplet. Recently it has been shown[5,6,7] that the SRS emission from transparent droplets show significant delays with respect to the elastic scattered light. This motivated us to study the temporal behavior of lasing in droplets.

EXPERIMENT AND RESULTS

The experimental arrangement used has been described elsewhere[7]. The technique consists of temporal measurement of lasing from dye-doped water and ethanol droplets ejected from a Bergland-Liu generator, and irradiated with a pulsed Nd:YAG laser (0.1 - 1 GW/cm^2). A spectrometer with appropriate blocking filters provides wavelength discrimination. The temporal signal is recorded by a photomultiplier tube (rise time 0.8 ns, bandwidth 0.8 nm) routed to a transient digitizer (0.742 ns per bin).

The lasing spectra consists of quasi-periodic peaks which turn on in the vicinity where the difference

between fluorescence emission and absorption reaches a peak[1,2,8]. Temporal profiles of the lasing were measured on and off resonance. Fig. 1a shows the temporal profile for the bulk liquid fluorescence (the dashed line indicates the time history of the elastically scattered laser light). Signals from the off-resonance portion of the lasing spectra appear similar to the bulk signal (Fig. 1b) with slightly faster rise times. This similarity with bulk behavior is expected since, in the absence of resonances, the spontaneous emission originates from a volume averaged region of the droplet. The on-resonance signals which are stronger and associated with lasing (Fig. 1c) have faster rise times and narrower widths. These signals are dominated by stimulated emission from near the droplet surface.

Multiple time peaks are observed sporadically, Fig.1d and these occur with highest frequency at the spectral region where the lasing peaks are strongest. The second peak is delayed by relatively long times (8-11 ns). These peaks could be evidence of relaxation oscillations.[1,9]

For dye-doped ethanol drops simultaneous SRS and lasing is observed at 630 nm. Fig. 1e shows the temporal profiles for simultaneous lasing and SRS. The second peak is due to SRS emission; in its absence (achieved by lowering the incident pump laser energy below SRS but above lasing threshold) the first peak remains unaltered. A slightly longer delay occurs for the SRS compared to that observed in pure transparent ethanol drops. This may suggest competition between the stimulated emissions inside the droplet.

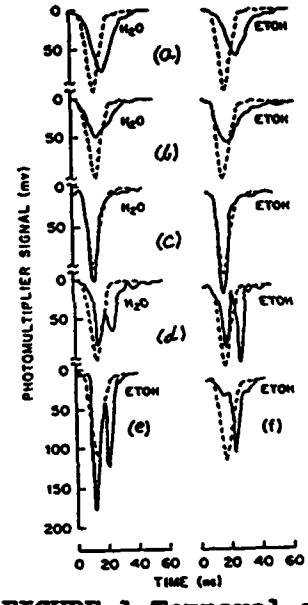

FIGURE 1 Temporal signals from different wavelength regions.

For the ethanol drops an additional region of sporadic and irreproducible lasing is identified to occur towards the higher absorption region. These lasing peaks when observed display significant initiation delays, Fig. 1f.

For dye-doped ethanol droplets the initiation and rise time (T_I and T_{RT}) for lasing exhibits wavelength dependence. Fig. 2 shows these times plotted as a function of wavelength. This behavior is suggestive of Q-switched[9] laser operation in that the delayed initiation caused by higher absorbtion is associated with

faster rise times. Moreover the temporal variation is much like that of the bulk emission intensity profile; consistent with the picture of the lower emission edges (570- 580 nm and 630 nm) requiring longer times to attain requisite gain.

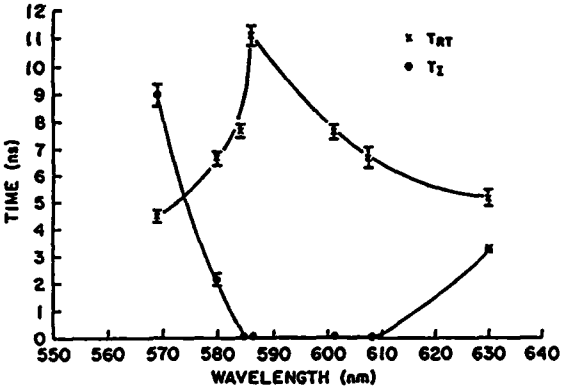

FIGURE 2 Rise time T_{RT} and initiation time T_I for droplet lasing as function of wavelength.

CONCLUSION

Long delays previously found in SRS are not generally observed in lasing. This may be attributed to the lowering of the cavity Q caused[10] by increased absorption due to the presence of dye in the droplets. However, the delays observed for the sporadic peaks (Fig. 1f) are not consistent with this explanation.

REFERENCES

1. H. M. Tzeng, K. F. Wall, M. B. Long, and R. K. Chang, Opt. Lett., 9, 499, (1984)
2. H. -B. Lin, A. L. Huston, B. L. Justus, and A. J. Campillo, Opt. Lett., 11, 614, (1986)
3. J. B. Snow, S. X. Qian, R. K. Chang, Opt. Lett., 10, 37, (1985)
4. S. X. Qian, R. K. Chang, Phys. Rev. Lett., 56, 926, (1986)
5. J. Zhang, D. H. Leach, R. K. chang, Opt. Lett., 13, 270, (1988)
6. W. F. Hsieh, J. Zheng, R. K. Chang, Opt. Lett., 497, (1988)
7. R. G. Pinnick, A. Biswas, P. Chylek, R. L. Armstrong, H. Latifi, E. Creegan, V. Srivastava, M. Jarzembski, G. Fernandez, Opt. Lett., 13, 494, (1988)
8. A. Biswas, H. Latifi, R. L. Armstrong, R. G. Pinnick, Opt. Lett. (In Press)
9. A. Yariv, "Optical Electronics", 3rd Ed., 188,177, Holt, Rinehart and Winston (1986).
10. S. C. Hill and R. E. Benner, J. Opt. Soc. Am. B, 3, 1509, (1986).

TWO-PHOTON INDUCED CHEMICAL REACTIONS IN LIQUIDS

C. H. Chen and M. P. McCann*
Chemical Physics Section, Oak Ridge National Laboratory
Oak Ridge, Tennessee 37831-6378

ABSTRACT

A two-photon absorption process has been used for the first time to produce significant quantities of reaction products between halogen containing organic compounds and silver containing inorganic compounds in the condensed phase. The mechanisms for these chemical reactions were also studied and confirmed by two-photon absorption spectra and optoaccoustic methods.

Chemists have hoped for some time to be able to use the laser for reactions which could not be done by conventional means. Most laser induced chemical reactions have been done in the gas phase in order to take advantage of the high brightness per unit wavelength. There has been very limited progress on excitation of selected vibrational modes which might lead to selected chemical reactions. Excitation of a particular vibrational mode quickly relaxes by transfering the vibrational energy to other vibrational modes, thus precluding the dissociation of a particular bond.[1] If the laser induced chemical reaction involves a multiphoton excitation then the quantum yield is, in general, too low to produce significant quantities of product.

Two-photon induced chemical reactions in liquids offer some advantages. These reactions can not be done by a conventional ultraviolet light source since these reactions involve nonlinear processes. With laser sources, the quantum yield can be high due to the high density of the liquid. With a typical two-photon absorption cross section of 1×10^{-50} cm^4 sec molecule^{-1} and moderate focusing in a liquid, the quantum yield is close to 0.5 for a 5-cm cell.

Below are some of the laser induced chemical reactions which have been studied.[2]

$$AgNO_3 + CCl_4 \xrightarrow{2h\nu} AgCl\downarrow$$

$$AgNO_3 + CH_2Cl_2 \xrightarrow{2h\nu} AgCl\downarrow$$

$$AgNO_3 + C_6H_5Br \xrightarrow{2h\nu} AgBr\downarrow$$

$$AgNO_3 + C_6H_5I \xrightarrow{2h\nu} AgI\downarrow$$

The reactions took place in the cell shown in Figure 1. A pulsed Nd:YAG - dye laser system was used to actuate the reaction. The solutions were transparent and the precipitate formation was proportional to the square of the laser intensity, which indicates that the reactions were occurring due to two-photon absorptions.

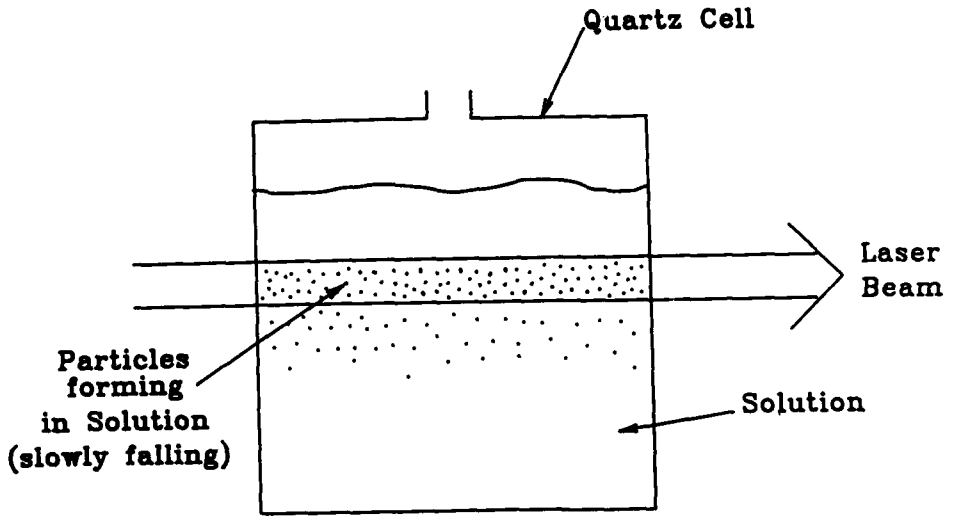

Figure 1. Two-Photon Induced Reaction Cell

There are two mechanisms for these reactions. The first mechanism is a photodissociation process.

$$RX \xrightarrow{2h\nu} R + X$$
$$X + H_2O \rightarrow X^- + H^+ + OH$$
$$X^- + Ag^+ \rightarrow AgX \downarrow$$

The second mechanism is an electron detachment process.

$$NO_3^- \xrightarrow{2h\nu} NO_3 + e^-$$
$$e^- + RX \rightarrow R + X^-$$
$$X^- + Ag^+ \rightarrow AgX \downarrow$$

Using pH or ion selective electrodes as shown in Figure 2, laser induced changes in ion concentrations were also studied. Two-photon induced dissociation cross sections were measured.

$$CCl_4(aq) \xrightarrow{2h\nu} CCl_3 + Cl \qquad \sigma = 6 \times 10^{-51} cm^4 sec\ mol^{-1}$$

$$C_6H_5Br(aq) \xrightarrow{2h\nu} C_6H_5 + Br \qquad \sigma = 2 \times 10^{-50} cm^4 sec\ mol^{-1}$$

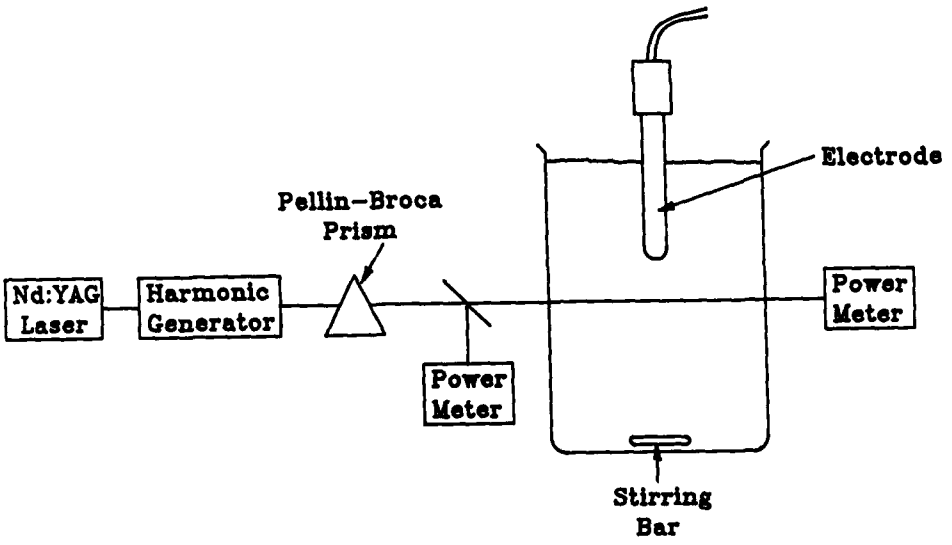

Figure 2. Ion Selective Apparatus

Using the laser to generate radical species at a very well defined time and a very well defined volume in a solution, some new chemical reactions can be studied and their reaction rates measured. The radical species can be generated so that diffusion rates can also be measured.

Research sponsored by the Office of Health and Environmental Research, U.S. Department of Energy under contract De-AC05-84OR21400 with Martin Marietta Energy Systems, Inc. M. P. McCann is a postdoctoral fellow, University of Tennessee, Knoxville, Tennessee.

REFERENCES

1. Ralph H. Page, Y. R. Shen, and Y. T. Lee, J. Chem. Phys. 88(9), 5362-5376 (1 May 1988).
2. C. H. Chen and M. P. McCann, Chem. Phys. Lett. (to be published).

LASER-INDUCED REACTION AND POLYMERIZATION OF FORMALDEHYDE IN LOW-TEMPERATURE AMORPHOUS SOLIDS[a)]

Charles A. Wight,[b)] Thomas W. Tang and Edward S. Mansueto
Chemistry Department, University of Utah, Salt Lake City, UT 84112

ABSTRACT

Photochemical reactions of formaldehyde with chlorine have been investigated in thin films from 10-77 K. The amorphous films are formed by deposition of gaseous formaldehyde doped with small amounts of Cl_2 onto an optical window mounted at the cold tip of a closed-cycle refrigerator. Excimer laser irradiation at 308 nm dissociates some of the chlorine molecules to atoms, initiating chemical reactions within the solid. Polymerization of the solid is initiated in the presence of a strong acid (e.g., HCl). Photopolymerization has also been achieved by photoexcitation of small amounts of 2-nitrophenol doped into solid formaldehyde.

INTRODUCTION

Photochemical reactions in solids are of current interest from the standpoint of inducing changes in optical and chemical properties with a high degree of spatial selectivity (e.g., using focussed lasers). This is important, for example, in fabricating holographic gratings and high-density optical memories. In our laboratory, we have been investigating fundamental aspects of photochemical chain reactions in amorphous thin films at low temperature (10-100 K). Chain reactions are attractive systems from the standpoint that many reactant molecules can be converted to products for each photon absorbed by the sample. Thus, we can utilize the chemical energy in the solid to do most of the work, rather than relying on the "brute force" of high power laser pulses.

In this article we summarize some of our most recent experimental results in the chain polymerization of solid formaldehyde. The reaction is initiated in the presence of a strong acid. We have thus far accomplished this three ways:

- by codepositing a sample of formaldehyde with HCl.
- by laser photolysis of Cl_2 molecules doped in solid CH_2O.
- by photoexcitation of 2-nitrophenol (an excited-state acid) doped into solid CH_2O.

Photochemical quantum yields for consumption of CH_2O and formation of reaction products are analyzed by obtaining transmission IR spectra of the thin films before and after laser photolysis.

a) Research supported by the Air Force Astronautics Laboratory (F-04611-87-0023) and the Utah Laser Institute (Office of Naval Research N-0014-86-K-0710).

b) Author to whom correspondence should be addressed.

EXPERIMENTAL SECTION

Samples are prepared by vapor deposition of formaldehyde and reaction initiator onto the surface of an optical window (typically CsI for infrared studies). Sample size is typically 30-60 μmoles, and the sample thickness is 5-10 μm. The window is mounted in a copper retainer at the cold tip of a liquid nitrogen dewar vessel (77 K nominal temperature). In some experiments, a closed-cycle helium refrigerator has been used to cool the sample to 10 K. No significant temperature dependence has been observed in the photopolymerization of formaldehyde over this temperature range.

The sample is photolyzed with the 308 nm output of a XeCl excimer laser (1-4 mJ/cm^2/pulse) through a quartz window mounted on the vacuum shroud.

Photochemical reactions in the sample are characterized by obtaining transmission FTIR spectra of each sample before and after laser photolysis. Integrated IR band intensities are used to determine photochemical quantum yields for consumption of reagents and formation of the various products.

RESULTS AND DISCUSSION

Figure 1 shows several IR spectra of solid formaldehyde under various conditions. Trace a) is an unphotolyzed sample of CH_2O and Cl_2. Trace b) is the same sample after 308 nm laser photolysis. Absorption bands of CH_2O have diminished intensities, while new product bands are observed at 1763 cm^{-1} (CHClO) and 850-1150 cm^{-1} (polyoxymethylene, POM). The photochemical reaction mechanism is:

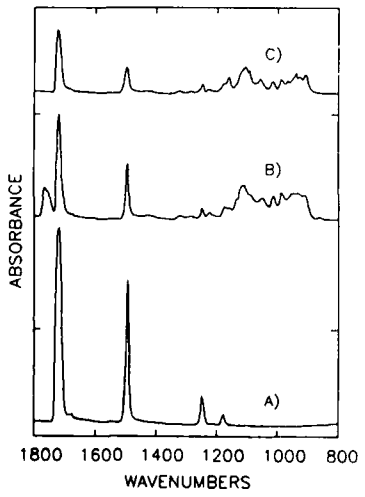

$$Cl_2 \xrightarrow{h\nu} 2\ Cl\bullet \quad (1)$$

$$Cl\bullet + CH_2O \longrightarrow HCl + CHO\bullet \quad (2)$$

$$Cl\bullet + CHO\bullet \longrightarrow CHClO \quad (3)$$

$$HCl + n\ CH_2O \longrightarrow H(OCH_2)_n^+ + Cl^- \quad (4)$$

The fact that HCl is responsible for initiating the polymerization reaction is confirmed by experiments in which HCl is co-deposited with CH_2O directly onto the surface of the optical window, as shown in trace c). No CHClO is formed in this case, but the POM has nearly the same spectral characteristics as in the photochemical reaction, trace b).

Figure 1. A) 11:1 mixture of CH2O:Cl2 at 77 K.
B) Same sample after 15,000 laser pulses @308 nm.
C) 10:1 mixture of CH2O:HCl at 10 K.

Photochemical quantum yield measurements in the CH_2O/Cl_2 system show photodissociation of Cl_2 and formation of CHClO occur with approximately unit probability following absorption of a UV photon. The average chain length (n) of the POM is 6.4 ± 1.5.

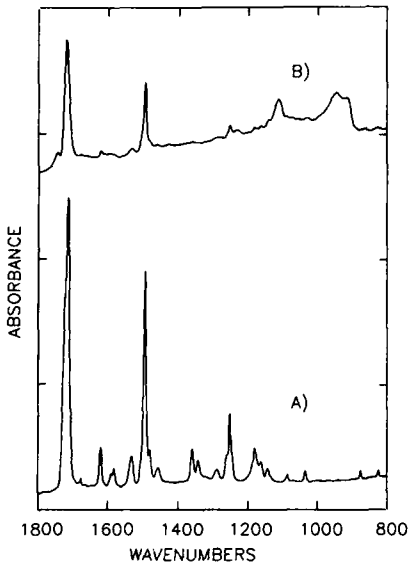

Figure 2. A) 20:1 mixture of CH2O:2-nitrophenol. B) Same sample after 50,000 pulses @ 308 nm.

Polymerization of formaldehyde has also been accomplished by co-depositing CH_2O with small amounts of 2-nitrophenol. This molecule is a weak acid in its ground S_0 electronic state, but becomes a strong acid in its S_1 state when excited at 308 nm. Proton transfer from the excited molecule to a nearby CH_2O molecule begins a sequence of polymerization steps forming POM. Figure 2 shows IR spectra of 2-nitrophenol in CH_2O before and after photolysis. Note that the POM formed in this reaction has a somewhat different spectral signature compared with that shown in Figure 1. Collapse of the C-O-C stretch/bend vibrational frequencies into distinct bands at 900, 1100, and 1250 cm^{-1} is characteristic of high molecular weight POM rather than short chain oligomers. This indirect evidence indicates that the average POM chain length is probably greater than 10 monomer units. The quantum yield for formation of POM is in the range 0.01-0.05 monomer units consumed per UV photon absorbed by 2-nitrophenol. From these two results, we infer that the probability of initiating the reaction is small (less than 0.5% per photon). One possible explanation is that depolymerization of short chain length oligomers may occur after the nitrophenoxide anion returns to its ground state and becomes a strong base. If the polymerization reaction propagates a long distance from the initiation site, the reaction is rendered effectively irreversible.

Additional experiments are now underway to further characterize excited-state proton transfer polymerization in the solid state, and to explore additional chemical reactions which can be initiated by this technique.

NONLINEAR ABSORPTION IN LIQUIDS STUDIED BY LASER-INDUCED ANHARMONIC THERMAL GRATINGS

X. R. Zhu and J. M. Harris
University of Utah, Salt Lake City, Utah 84112

ABSTRACT

Laser-induced anharmonic thermal gratings have been used to study nonlinear absorption of 3,3'-diethyloxatricarbocyanine iodide (DOTCI) in ethanol. Observed anomalous dependence of diffraction efficiency on the excitation intensity is explained by using a recently developed, general numerical method for diffraction from anharmonic Gaussian volume gratings in terms of an excited-state absorption and trap-state formation model.

INTRODUCTION

The cyanine dye 3,3'-diethyloxatricarbocyanine iodide (DOTCI) is an important material for near infrared dye lasers.[1] In a recent paper, Speiser and Shakkour[2] have indicated that DOTCI has a large excited-state absorption cross-section at 532 nm. Although it is well known that excitation of most cyanine dye molecules produces thermodynamically unstable photoisomers, there is little direct evidence about the photoisomerization of DOTCI. In this paper, we present a laser-induced anharmonic thermal grating study of the excited-state absorption and photoisomerization of DOTCI in ethanol.

In a medium having temperature dependent index of refraction, nonlinear absorption at the crossed-beam interference pattern creates, through thermalization of the absorbed energy, a Bragg thermal grating containing harmonics of the spatial frequency present in the interference pattern. Detection of the diffraction with a probe beam incident at Bragg angles of the higher order harmonic gratings provides a sensitive measurement of the deviation from linear absorption.

EXPERIMENTAL RESULTS AND DISCUSSIONS

The anharmonic thermal grating experimental setup was previously described in Ref.3-6. The excitation beams, having pulse duration 67 ns FWHM, are from a Q-switched Nd:YAG laser operating at the second harmonic, λ_e = 532 nm. A 488 nm laser-beam from an air-cooled argon ion laser is used as the probe beam. DOTCI was obtained from Eastman Kodak and used without purification.

The thermal diffraction signal transients of DOTCI in ethanol measured at the first- and second-Bragg angles have single exponential time dependence, with time constants satisfying $\tau_1 = 4\tau_2$, consistent with Bragg diffraction from independent thermal gratings decaying by thermal diffusion across fringe spacings which differ by a factor 2.[3] This observed 1:1/4 ratio insures that we are observing second-order diffraction from a second-order spatial

frequency caused by nonlinear absorption.[3-6] To assess accurately the nonlinear absorption of DOTCI by this experiment, the dependence of diffraction efficiency on the excitation intensity is measured, and the results are plotted in Fig.1. One notes that diffraction intensity shows anomalous dependence on the excitation intensity, that is, the second-order diffraction intensity has a minimum at a modest excitation intensity, while the first order diffraction intensity continuously increases as the excitation intensity increases. Based on the large excited-state absorption cross-section of DOTCI at 532 nm and importance of photoisomerization as a nonradiative decay path of the first excited-state of cyanine molecules, we propose a five-level excited-state absorption and trap-state formation model, as shown in Fig.2, to discuss our results.

The time evolution of the population of the molecule in each level can be described by a set of first-order kinetic equations.[7] The rate of heat deposited due to the nonradiative decay of excited-states is given by[7],

$$\frac{dQ}{dt} = N\sigma_1 I S_0(t)\left[\frac{hc}{\lambda_e} - \frac{hc}{\lambda_f}\right] + NS_1(t)k_1'\left[\frac{hc}{\lambda_e}\phi_{nr} - \phi_t E_t + \frac{hc\,\sigma_2 I}{\lambda_f\, k_1'}\right] \quad (1)$$

where N is the number density of solute molecules, σ_1 and σ_2 are the ground-state and excited-state absorption cross sections, S_0 and S_1 are fractions of molecules in the ground-state and the first excited-state, hc/λ_e is the excitation photon energy, λ_f is the wavelength for the 0-0 transition from S_1 to S_0, ϕ_{nr} is the nonradiative yield of S_1, $k_1' = k_1 + k_3$, k_1 is the sum of radiative and nonradiative decay rates from S_1 to S_0, k_3 is the trap-state formation rate, ϕ_t is the trap-state yield, and E_t is the ground-state energy of the trap-state. The total heat being generated during an excitation pulse can be calculated by integrating the Eq.(1) over the entire pulse. Eq.(1) and the recently developed numerical method for diffraction from anharmonic volume gratings[7] are then used to reproduce the measured data.

We have taken the literature values of kinetic parameters $\sigma_1(532\ nm) = 1.5\times10^{-18}\ cm^2$, $\sigma_2(532\ nm) = 6.19\times10^{-17}\ cm^2$ and $1/k_1' = 1.2\ ns$[2], $\phi_f = 0.25$[2,8] and $\lambda_f = 716\ nm$.[8] With these values, we have fit the measured data to the model, as shown by the solid line in Fig.1. From the fit, we have the photoisomerization yield $\phi_t = 0.27 \pm 0.03$; the fit is insensitive to parameter k_2 for values exceeding $1.5\times10^{10}\ sec^{-1}$. We have neglected the absorption of photoisomer, which, in general, should be included to provide a complete picture of nonlinear absorption processes. While additional parameters in the model may improve the fit of the data, the simplest model which provides a fit within the experimental error has been used to identify the major photophysical pathways.

In conclusion, we have used diffraction from anharmonic thermal grating to study excited-state absorption and photoisomerization of DOTCI in liquid. The photoisomerization yield of DOTCI in ethanol is 0.27 ± 0.03.

Work is supported in part by the National Science Foundation under Grant No. CHE-8506667, and by a fellowship grant (to JMH) from Alfred P. Sloan Foundation.

REFERENCE

1. Y. Miyazoe and M. Maeda, Appl. Phys. Lett. 12, 206 (1968).
2. S. Speiser and N. Shakkour, Appl. Phys. B38, 191 (1985).
3. D. J. McGraw and J. M. Harris, Phys. Rev. A10, 4829 (1986).
4. D. J. McGraw and J. M. Harris, J. Chem. Phys. 86, 2536 (1987).
5. X. R. Zhu and J. M. Harris, Chem. Phys. 124, 321 (1988).
6. X. R. Zhu and J. M. Harris, J. Phys. Chem. (in press).
7. X. R. Zhu, Ph.D. Dissertation, University of Utah (1989).

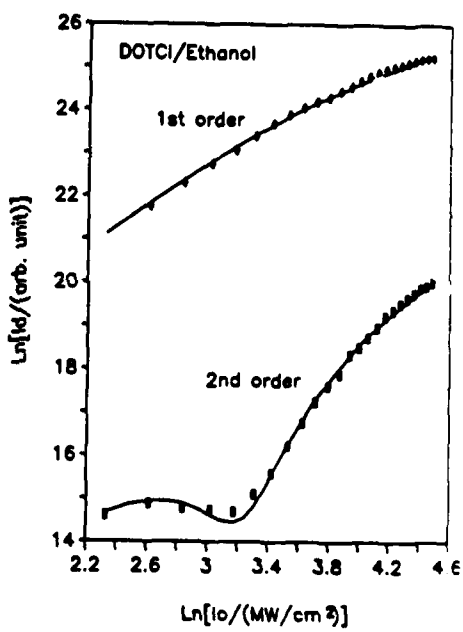

Fig.1 Diffraction intensity vs excitation intensity for grating induced by non-linear absorption of DOTCI in ethanol. Points are experimental data and solid lines are fit to the model in Fig.2.

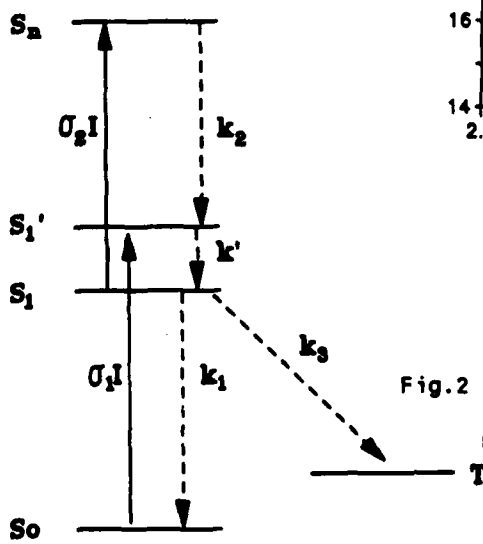

Fig.2 Excited-state absorption and trap-state formation model.

ADSORPTION OF OXYGEN ON A POLYCRYSTALLINE Ag SURFACE: A SECOND-HARMONIC-GENERATION STUDY

Li Le, Liu Yanghua, Yu Gongda, Wang Wencheng
and Zhang Zhiming

Lab of Laser Physic & Optics
Fudan University, Shanghai, P.R.China

The interaction of oxygen with Ag surface is of considerable fundamental and practical interest in silver catalysts due to the wide spread industrial use of Ag partial oxidation catalysts. In this paper, we'll report on the study of oxygen adsorption on a polycrystalline Ag surface with optical Second-Harmonic-Generation(SHG) in an Ultra-High Vacuum(UHV) system. Experimental results on the adsorption dynamics, the temperature dissociation of adsorbed oxygen and the influence of the pre-state of Ag surface will be presented and discussed. Also, the charge transfer between Ag and oxygen, both in atomic and molecular state, will be inferred.

The details of the UHV chamber as well as SHG measurement apparatus have been described elsewhere(1). The polycrystalline silver with purity of 4N was mechanically polished and cleaned by re-peated argon ion sputtering plus an annealing process. High purity oxygen sample was introduced into the UHV chamber through a leakage valve. Fundamental beam at 1.06um from a Q-switched YAG laser was impinged onto the sample and the reflected SH signal was detected. First, the dynamics of oxygen adsorption on Ag at low temperature of 120K was measured. The result is depitched in Fig.1, in which the solid line represents the theoretical fitting by the formula(1) derived based upon the Langmuir model. It's seen that the SHG intensity increases with oxygen exposure,which is believed due to the charge transfer between Ag and oxygen. Backx et al(2) have observed a molecularly adsorbed oxygen on Ag(110) at low temperature(<150K) and they suggested that a dual channel mechanism of the charge transfer might exist between Ag and the oxygen. Since SHG intensity is an increasing function of conducting electron density in a metal, our measured result in Fig.1 corresponds to the increase of the conducting electrons in silver upon molecular oxygen adsorption. According to the dual channel mechanism by Backx et al(2), it might be inferred that the electrons donated to Ag from oxygen π filled orbital be more than that transfered from Ag to oxygen π^* anti-bonding orbital,which didn't be proved experimentally by Backx et al(2). Recently, there was a report(3) that accompanying with the appearence of the desorption peak of molecular oxygen, the work function of an oxygen-covered Ag surface was found to

be increased, which could be regarded as a support for our conclusion.

We also studied the temperature dependence of oxygen dissociation on Ag.After the Ag surface has been covered by a saturated layer of molecular oxygen ,it's then heated to a high temperature 400K at a rate of 0.04K/s, meanwhile the SH sigal was recorded as a function of temperature. The result is shown in Fig.2, where the dotted-dash line represents the SHG intensity from a clean Ag. The constant curve labelled with the reverse arrow corresponds to the same SHG measurement but during a cooling process. This result clearly shows that the temperature variation of the SHG intensity within an annealing circle is irreversible, which simbolizes a dissociation of the adsorbed oxygen. At the temperature region below 175K, the constant SHG intensity against the temperature as shown in Fig. 2 implies a stable adsorption of molecular oxygen. Heating upto 175K leads to a decrease of SHG intensity due to the dissociation of the oxygen molecules, which could be explained by the fact that the electron density in Ag metal is decreased by the charge transfer from Ag to the oxygen atoms resulted from the dissociation. It's clear from Fig.2 that this dissociation process could take place in a rather wide temperature ranged from 175K to 330K since the SHG intensity variates remarkablly. Above 330K, the plateau in Fig.2 becomes again insensitive to the temperature, demonstrating the completion of such a dissociation. However, the dissociated oxygen atoms in each adsorption site will

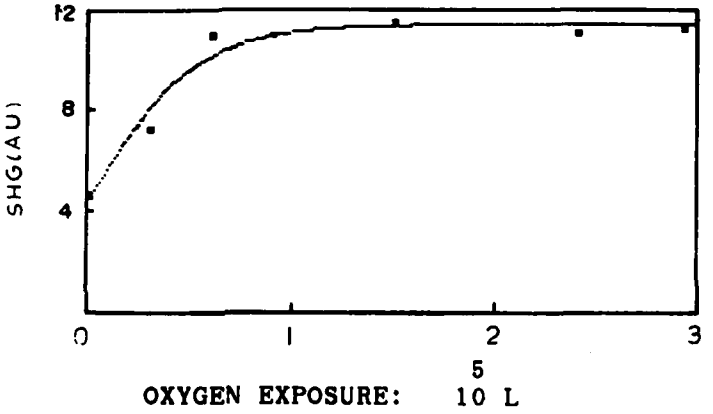

Fig.1 SHG measurement of oxygen adsorption dynamics onto a polycrystalline Ag, where "---" is the theoretical fit by the formula $I \propto |1+B/A*(1-\exp(-kpt/\Theta_s))|^2$ which gives out $k/\Theta_s=0.98*\exp(-171^*)$ and $B/A=0.35*10^{-4}$ /layer, respectively, $T_s=124K$.

not form molecular oxygen again because the SH signal keeps constant during the recooling process. This is why an irreversible temperature variation of the SH signal was ob-served for the molecular oxygen covered Ag surface within an annealing circle.

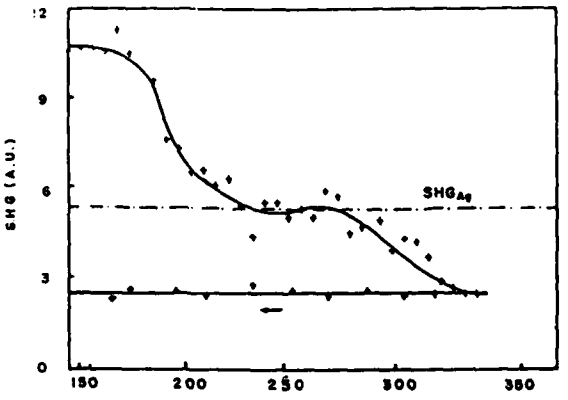

Fig.2 SHG measurement of annealing an oxygen-adsorbed Ag surface, where "-·-·-" represents the SH signal from the clean Ag and the constant curve labelled with the reverse arrow represents the reverse measurement.

Finally, the adsorption of molecular oxygen on the Ag surface which is pre-adsorbed with a saturated layer of atomic oxygen was studied. It's found that the Ag surface even at low temperature of 124K didn't show any activity in adsorbing the molecules. The reason is simply that the adsorption active sites have been pre-occupied by the oxygen atoms, so that molecular oxygen could be hardly adsorbed.

In conclusion, we've shown that optical SHG is a potential tool for surface studies. It could yield much useful information on surfaces or interfaces.

---

* From Dept. of Phys., Suzhou University, Suzhou, China

References

1. Li Le, Ph.D Dissertation, Fudan University, Shanghai China, 1988.

2. C.Backx, C.P.M.DeGroot and P.Biloen, Surf.Scie.104, 300(1981).

3. Bao Xinhe, Ph.D Dissertation, Fudan university, Shanghai, China.

Visualization of Photogenerated Carrier Profiles at a Silicon Surface

K. Wan, R. Normandin and P. Van der Meer
National Research Council, Ottawa, Canada K1A 0R6

ABSTRACT

We demonstrate the use of far field diffraction (DP) to estimate the transport properties of photoexcited carriers near a semi-insulating silicon surface. The DP is produced by placing the cleaved edge of a 0.5 mm thick Si slab at the focal plane of a low power, 1.06 μm laser probe beam, such that half of its 12 μm diameter is in the Si slab. This DP depends partly on the local index of refraction of the sample, which is modified by the carrier density profile in the probing volume. This profile results from the diffusion of the photoexcited carriers generated at the cleaved surface by a 0.53 μm laser beam derived from the probe. We showed that the phase shifts of the DP caused by the 0.53 μm pump beam can be related semi-quantitatively to the carrier transport properties.

INTRODUCTION

There is renewed interest in the dynamics of photoexcited carriers in semiconductors because of its importance in the understanding of high speed optoelectronic devices. Many different optical techniques, such as Raman scattering [1], photoexcited carrier transient diffraction gratings, photoreflectivity, photoluminescence and photothermal deflection, have been introduced to study nonequilibrium carriers for different time scales. However, many of these techniques do not probe directly the spatial profile of the photoexcited plasmas. Here we demonstrate the use of diffraction from the plasma to extract the carrier density profile at an interface. The diffracted probe beam passes through the sample perpendicular to the excitation surface, as outlined in Fig. 1, and probes directly the depth profile of the photoexcited carriers. Although a silicon sample was used for this demonstration, this technique should be applicable to many other semicor ctor geometries.

EXPERIMENTAL LAYOUT

The probe beam was the residual 1.06 μm light from a Q-switched, frequency doubled Nd:YAG laser with a 1 KHz repetition rate and 100 ns pulses. This beam was then focussed to a 12 μm spot size. Harmonic generation by a KDP crystal was used to derive the needed 0.53 μm for the pump beam with an average power of less than 2 mW, also at 1 kHz. These beams were then positionned at the cleaved edge of a 0.5 mm thick Si slab, as outlined in Fig. 1. Half the probe beam passed through

the photoexcited plasma at the Si interface. The delay between the probe and pump beam is negligible compared with the pulse duration. A computer controlled rotating mirror was used to scan the diffraction pattern across a photodiode. The detected signal was then amplified and filtered by a lock-in amplifier and stored in a computer.

RESULTS AND DISCUSSION

Because of the probe beam width, the diffraction pattern is a mixture of circular and straight fringes, as observed by a CCD camera. The photodiode records only a cross-section of this pattern perpendicular to the edge. A comparison of the patterns obtained without (solid) and with (dashed) the 1.5 mW pump beam is shown in Fig. 2 . The azimuth goes from the air side to the sample side of the pattern. With the pump beam on, each of the three recorded fringes shifted away from the sample side by a different amount. A linear dependence of these shifts on the pump power up to about 10 MW/cm^2 was observed, as shown in Fig. 3 for one of the peaks.

The change in diffraction pattern is due to a decrease in optical path of the probe beam passing through the electron-hole plasma. A 1-dimensional diffusion model, using the appropriate parameters for the pump beam and for the sample suggests that the free carriers within the interaction region diffused about 40 μm down into the sample at the end of the probe pulse, with a maximum concentration of about 10^{17} cm^{-3} at the surface. Therefore, the size of the photoexcited plasma in our experiment is much larger than the probe beam. Furthermore the fluence of the pump pulse is so small, the change in refractive index due to heating contributions [2] is much smaller than the one induced by free carriers.

COMPUTER SIMULATION

We also performed a computer simulation to demonstrate that the carrier spatial profile can be, in principle, extracted from the modifications in the diffraction pattern. The diffraction intensity was calculated using the Kirchhoff diffraction theory with a source field assumed to be a Gaussian beam with the appropriate complex refractive indices. The calculated 2-dimensional diffraction intensity gave similar fringes as observed in the experiments. The solid line in Fig. 4 is the cross section without pump beam. To reduce computation time, the effects of the photoexcited carriers were modelled by a negative refractive index with a Gaussian depth profile with minimum at the excitation surface. This minimum and its half width was assumed to be -0.001 and 40 μm respectively. The dashed line in Fig. 4 was calculated using a lensing of 30% with the probe beam shifted down by 5% relative to the probe beam center radius.

CONCLUSION

To conclude, the effects of a photoexcited plasma on the diffraction pattern of a semiconductor interface were investigated. The carrier profile reduced the local refractive index and therefore the local optical path of the probe beam passing through it. This resulted in a measurable shift in the diffraction pattern. A simulation was performed and demonstrated that when a proper model is incorporated, the photoexcited carrier spatial profile can theoretically be extracted from the diffraction pattern.

REFERENCES

[1] K. Wan, J. F. Young and A.J. SpringThorpe, Can. J. of Phys. 65, 831 (1987).

[2] L.A. Lompré, J.M. Liu, H. Kurz and N. Bloembergen, Appl. Phys. Lett. 43, 168 (1983).

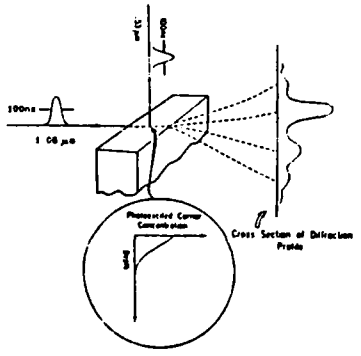

Fig. 1. A close-up view of the sample region.

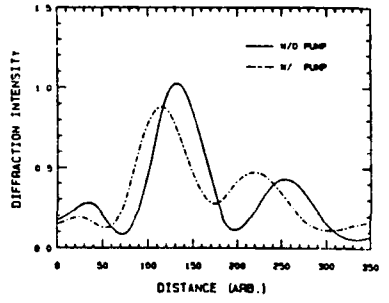

Fig. 2. Observed diffraction pattern.

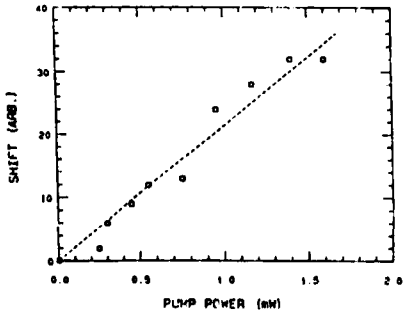

Fig. 3. Pump power dependence.

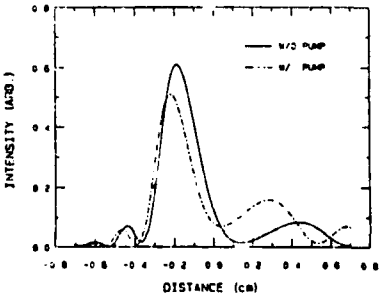

Fig. 4. Calculated diffraction profile.

OPTICAL COMPUTING WITH THIN FILMS

Robert Cuykendall+ and Karlheinz Strobl
Center for Laser Science and Engineering, University of Iowa, Iowa City, IA 52242

ABSTRACT

An optical integration technique using thin film technology can be based on the topology of an interface with a diffusive Kerr-like nonlinearity. Solid state multiplexing is implemented with thin film multilayer stacks resulting in polarizers and phase retarders matched to the interface. This effort is justified by the results of 2-d simulations of the nonlinear interface carried out on the CRAY X-MP/48 showing nearly whole-beam switching with high contrast.

INTRODUCTION

High-contrast switching at an interface between diffusive nonlinear media having opposite Kerr coefficients has been reported[1] based on 2-d simulations of the optical field redistribution effects. The calculation results indicate that nearly whole-beam switching at a nonlinear interface should be possible with real (gaussian) input beams. We have recently found similar behavior[2] at the interface between linear and diffusive nonlinear media. With polarization-coded inputs these interfaces implement a symmetric self-controlled logic structure more powerful than a NAND gate, which is both noise tolerant and optically reversible[3]. Such a switching device has the additional advantage of computing the input signals at a surface, not while traveling through a bulk material. This is ideal for integration purposes since absorption losses can be minimized.

THIN FILM INTEGRATION

Switching based on a nonlinear interface having one linear material leads to an intriguing integration architecture. Idealized switching behavior is assumed in order to assess the ultimate worth of such an expedient approach to optical computers if

+ also with Department of Electrical & Computer Engineering

appropriate materials could be identified. Both computing and multiplexing elements can in principle be constructed with thin films having the low-index linear material (L) in common. Since the computing of the input signals occurs at a surface the nonlinear medium (NL) can be reduced to a very thin film. A schematic diagram of a thin film realization of a nonlinear interface is shown in Fig 1. The logic table defines the allowable cases, based on the assumption that a beam with intensity 1 is reflected while a beam with intensity 2 is transmitted through the diffusive nonlinear film. The thin film gate can be used, with some restriction (e.g. I_1=2 implies I_2=0), both from the top (I_1) and from the bottom (I_2) side, allowing some limited polarization-independent multiplexing with the computing element itself. Note that I_1 is the computing input while the I_2 input only reflects (multiplexes). The minimum thickness (5 λ) of the nonlinear thin film follows from the requirement to guarantee total internal reflection for the case when I_1=I_2=1.

Earlier numerical work[2] indicates that the behavior of a diffusive nonlinear interface follows this logic table. Based on this we were inspired to investigate the possibility of circuit integration using the thin film gate as the single computing element. This led to designs for a high incident-angle (85°) 'single frequency' thin film polarizer (v-mirror) and lambda-half reflector matched to the thin film gate, providing multiplexing functions. The simplest thin film polarizer is a symmetrical three-layer stack (HLH) formed by alternating thin linear films with high and low refractive indices, itself enclosed by the same material L which forms the middle layer. A $\lambda/2$ - mirror can be made using the fact that during total internal reflection both polarizations suffer (in general) a different phase delay. With presently available materials it is not possible to make a phase delay of $\lambda/2$ with a single total reflection. But by adding an additional layer H between the incident medium L and the total reflection layer T, the desired phase delay can be obtained.

The simplicity of the integration architecture is demonstrated by designing a half-adder. Three different thin film realizations of a half-adder are shown in Fig. 2. The pictures are drawn to scale (except for the thickness of the nonlinear medium) for an incident angle $\theta_0 = 85^\circ$. The thickness of the individual films follows from the standard model parameter n_L=1.5 and corresponding materials with n_H=2.35 and n_T=1.38. The H and T materials have been chosen from the viewpoint of commercial availability, with n_H as high as possible and n_T lower than n_L. The y-dimension has been blown up by a factor of eleven for improved visualization. The solid lines show

the computing beams while the dashed lines show additional unavoidable signal channels (duplication and inversion of the input signals) characteristic of the thin film logic. The half-adder version in Fig. 2a requires the smallest amount of space. The version in Fig. 2b is roughly 5% longer than that in Fig. 2a, but uses the least number of circuit elements. It is also the most flexible design: (1) it is transparent to an h-beam traveling from V_1 to V_3 (or vice versa) and can therefore be used to communicate with circuits in planes above or below the actual half-adder, and (2) substitution of the polarizer V_1 or V_3 with a conventional mirror M allows redirectioning of some of the inputs and outputs. The third half-adder, shown in Fig. 2c, is twice as high as the others and needs an additional pump beam, but it has the definite advantage of a continuous rather than interrupted nonlinear thin film, and is therefore easiest to manufacture. The design (c) is 'independent' of the nonlinear film thickness, while designs (a) and (b) have a small such dependence. Fig. 3 shows the half-adder in Fig. 2c emphasizing the layered structure, comprising 15 layers. Note that the minimum-layer design (Fig. 2b) requires only 12 layers.

One important feature of this thin film architecture is that the layers have no restriction in the third dimension, so that with the same amount of manufacturing steps hundreds of self-similar circuits can be produced. The number is limited only by the film extension in the third dimension, and the minimum distance between two adjacent circuits necessary to avoid channel interference due to diffraction. The minimum separation is therefore about twice the beam waist of the input signals. This indicates the high potential that this kind of integration has for parallel calculation. The problem of depositing strips of different materials on the same horizontal plane has to be solved only in one direction, and requires an accuracy of only tens of microns, which is within present state-of-the-art. Ion or laser enhanced chemical vapor deposition, or similar techniques, could possibly be used to produce the desired structure.

Only four materials are necessary to build the thin film half-adders: a nonlinear material NL, the corresponding linear material L, another linear material H with an index of refraction as high as possible, and a material for the mirrors. The mirrors M could be a simple thin film aluminum or gold coating, depending upon the wavelength of light used. The combination of NL and L forms the nonlinear thin film gate which computes and allows some polarization-independent multiplexing,while the combination of L and H forms the v-mirror for polarization-sensitive multiplexing. The T material is only used in designs requiring a polarity exchange, such as full-

adders. Having the L material in common avoids additional interfaces, and therefore beam splitting between different linear materials, which at high incident angles would cause non-negligible reflections, greatly complicating the circuits. Another feature is the multiple use of component layers, leading to simple compact circuits in two dimensions. Some circuit elements can also be used from the back side for another computing circuit, minimizing the necessary total number of computing and multiplexing elements.

CONCLUSION

In this paper we have demonstrated that thin film optical computing circuits, at least in principle, can be constructed based on idealized behavior of the nonlinear interface. Further work is necessary[4] in determining the actual switching characteristics of the nonlinear thin film gate in order to assess beam regeneration and re-focusing, etc. requirements in real circuits.

References

1. R. Cuykendall, Appl. Opt. 27, 1772 (1988).
2. R. Cuykendall and K.H. Strobl, submitted to JOSA-B.
3. R. Cuykendall and D.R. Andersen, Opt. Lett. 12, 542 (1987).
4. We are presently conducting an experiment to study the effects of diffusion on the behavior of the nonlinear interface. Results [Proc. ILS-IV (1988)] show much higher switching contrast than obtained in a previous experiment reported by P.W. Smith and W.J. Tomlinson, IEEE J. Quant. Elect. 20, 30 (1984).

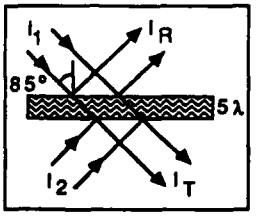

I_1	I_2	I_R	I_T
0	0	0	0
0	1	0	1
1	0	1	0
1	1	1	1
2	0	0	2

Fig. 1: Nonlinear Thin Film Gate / Multiplexer.

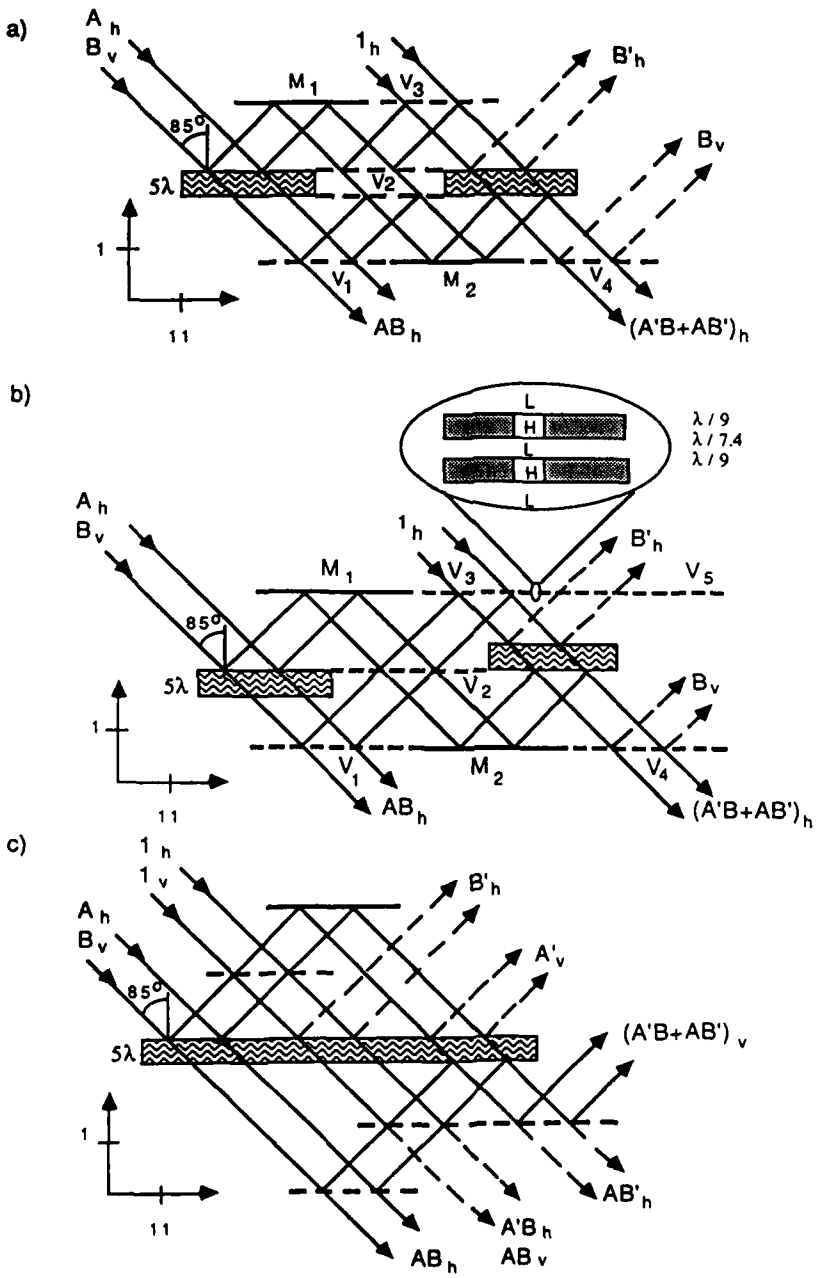

Fig. 2: Thin film half-adder: a) smallest volume, b) most flexible and c) simplest to manufacture.

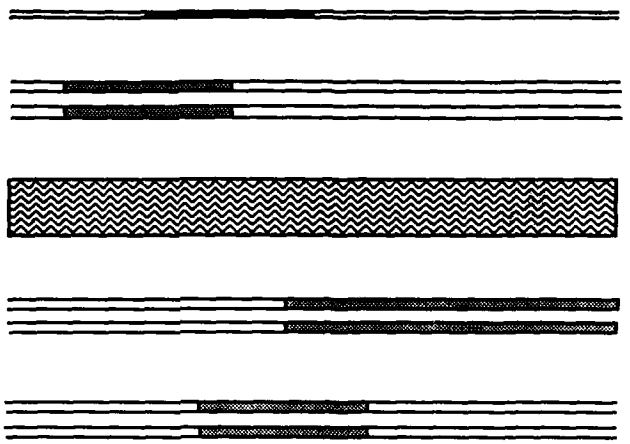

Fig. 3: Schematic layout for thin film half-adder corresponding to figure 2c.

LASER-INDUCED REFRACTIVE INDEX CHANGE IN POLYMERS

D. S. Dunn and A. J. Ouderkirk
3M Corporate Research Process Technologies Laboratory
208-1-01 3M Center, St. Paul, Minnesota 55144

ABSTRACT

Pulsed uv laser irradiation of semicrystalline polymers at low fluences has been shown to produce a thin amorphous layer on the polymer surface. For poly(ethylene terephthalate) (PET) this amorphous layer results in a reduced refractive index of the polymer surface and the production of an antireflective coating. The melting occurring in this surface amorphization is very rapid, approximately 10^6 times faster than predicted by current polymer melting theories.

INTRODUCTION

Etching of polymer surfaces by pulsed excimer laser irradiation has been extensively studied because of its ability to remove material with little residual thermal degradation of the polymer surface.[1] This ablation generally requires the deposition of 3000-4000 J/cm^3 in the polymer near-surface region.[2] In this paper we report the discovery of a new process for laser surface modification of polymers that requires approximately 10% of the energy density necessary for ablation. The effects of this new process are described for the particular example of laser irradiation of PET at the wavelengths of 193 and 248 nm. The laser surface modification is most easily observed by the change in optical properties of the PET.

EXPERIMENTAL

The PET used in this work had a number average molecular weight of 27,000. The semicrystalline PET was a 4 mil. thick, biaxially oriented film. This film had a crystallinity of approximately 50%. The amorphous PET was a 12 mil. thick film prepared by quenching from the melt. This material was amorphous as determined by x-ray diffraction. In some experiments thinner semicrystalline PET films were prepared by dissolving the amorphous PET in o-chlorophenol and spin casting films on polished silicon wafers. The films were dried in vacuum at 70-90 C to remove residual solvent and thermally crystallized in vacuum at 200 C.

Either a Lambda Physik 201 MSC or a Questek 2460 excimer laser, both with a nominal pulse width of 15 nsec., was used to irradiate the PET samples. Laser fluence was varied by changing the distance between the sample and a diverging cylindrical lens placed in the laser beam. Laser fluences were measured with a Gentec joulemeter. All laser exposures were done in air.

RESULTS AND DISCUSSION

The change in the optical properties of semicrystalline PET on excimer laser irradiation is shown in Fig. 1. This figure shows the transmission spectrum in the visible and near IR at near normal incidence for biaxially oriented, semicrystalline PET before and after laser treatment on both sides at 248 nm and a fluence of 17 mJ/cm^2. On laser treatment the transmission of the PET increased over a large wavelength region by 3-4%. Measurement of the total reflection spectrum of this polyester sample showed that the increase in transmission was due to a decrease in reflectivity of the polymer surface.

The dependence of the laser induced antireflectivity, measured at 550 nm, on laser fluence at a laser wavelength of 193 nm is shown in Fig. 2. All samples were given the same total laser exposure, 20 mJ/cm^2, so the values plotted along the x-axis are laser

fluences per pulse. The data clearly show that this process exhibits a fluence threshold. Below the threshold fluence there is no antireflectivity, above the threshold the antireflectivity increases with laser fluence. From the figure, the threshold fluence at 193 nm is approximately 3 mJ/cm^2. For laser treatment at 248 nm the threshold is 4 mJ/cm^2. This dependence on laser wavelength is in good agreement with the absorption spectrum of PET in the ultraviolet, as measured in our laboratory.

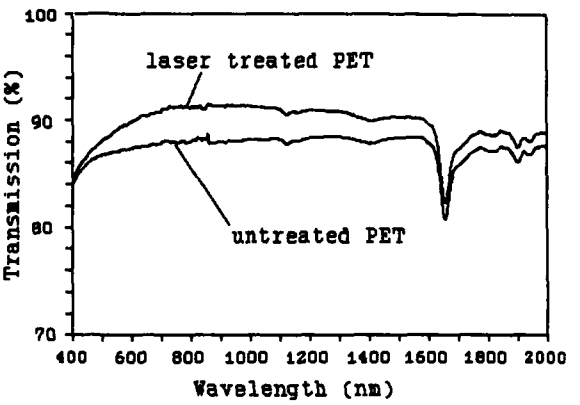

Figure 1. Transmission spectra in the visible and near IR of the laser treated biaxially oriented PET.

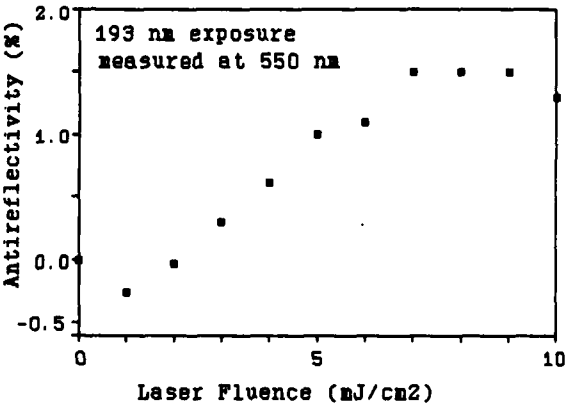

Figure 2. Dependence of laser induced antireflectivity at 550 nm for biaxially oriented PET on laser fluence.

The laser induced antireflectivity is due to the formation of a layer on the PET surface with a lower refractive index than that of the bulk polymer. Fig. 3 shows plots of the refractive index and thickness as a function of laser fluence for a spin cast semicrystalline PET thin film, as determined by ellipsometry at 632.8 nm. For fluences below 4 mJ/cm^2 the refractive index of the PET thin film was constant; above this fluence the refractive index decreased as fluence was increased. The film thickness remained constant below threshold, increased by a few percent (reflecting the lower density of the low index material which was formed) at intermediate fluences, and then finally decreased as material was ablated from the film surface at high fluences (above 16-17 mJ/cm^2). It is important to note that the formation of the low index layer occurs at fluences well below the ablation threshold of PET at 193 nm.[3] The formation of this low index layer is not a manifestation of ablation.

There are several possible processes which could be responsible for the formation of this lower index material on uv laser irradiation. The most likely mechanisms are: microtexturing of the PET to produce a graded density surface layer, photodecomposition to produce monomeric or oligomeric material on the surface, or rapid melting and quenching to produce an amorphous layer on the surface. High resolution SEM examination of laser antireflected PET (at either 193 or 248 nm) showed no laser texturing on the scale of 20 nm or larger. This is well below the texture size required for antireflection in the visible.[4,5] Surface texture is not the source of the laser induced antireflectivity.

XPS analysis of PET laser treated at 248 nm showed no detectable chemical change. PET laser treated at 193 nm did show evidence of some decarboxylation in the XPS spectrum. The amount of decarboxylation was, however, very small, less than a

monolayer in equivalent thickness. There was also no change in the water contact angle of PET laser antireflected at 193 nm and no detectable decrease in molecular weight, as determined by gel permeation chromatography. These results, taken in concert, eliminate photodecomposition as the source of the lower index material.

In order to determine whether surface amorphization was the source of the observed antireflectivity, amorphous PET was laser treated. A plot of the change in transmission of amorphous PET as a function of laser fluence at 193 nm is shown in Fig. 4. The optical transmission of amorphous PET did not change on laser irradiation, even though it was exposed to laser fluences well above the antireflectivity threshold for semicrystalline material. The surface region of this material is already amorphous so we would expect no change in optical transmission on laser exposure. It is not possible to further decrease the refractive index of amorphous PET without decomposition.

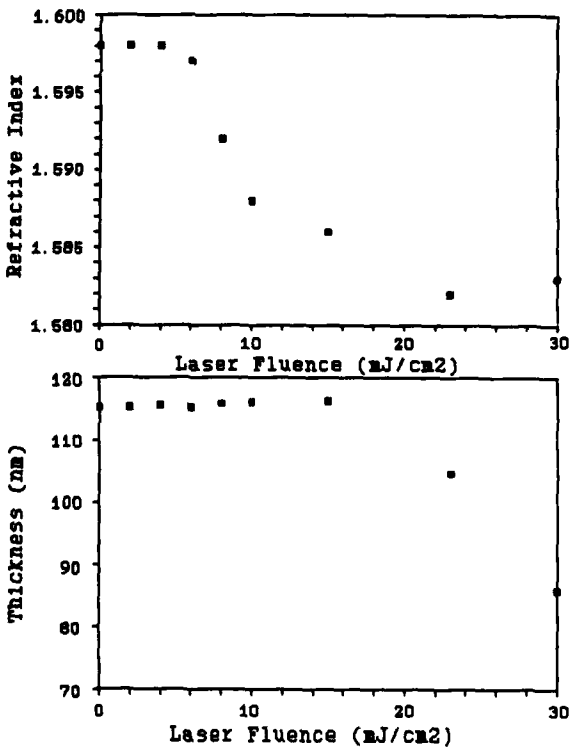

Figure 3. Dependence of refractive index and thickness of PET on laser fluence.

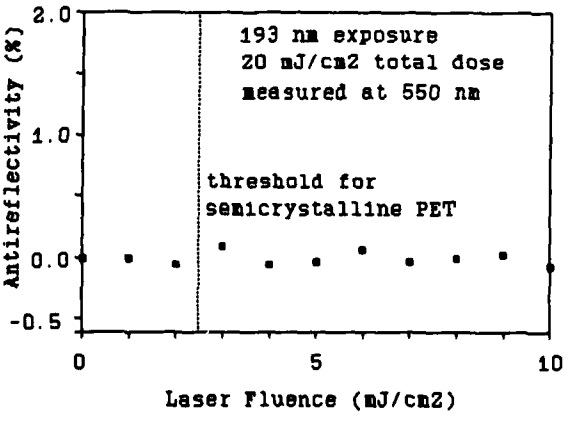

Figure 4. Dependence of laser induced antireflectivity at 550 nm for amorphous PET on laser fluence.

CONCLUSION

We report here the discovery of a new excimer laser process which amorphizes the surface region of semicrystalline polymers. Since this surface amorphization involves a phase change, it quite naturally exhibits a threshold laser fluence below which it will not occur. Amorphization thresholds for PET are in the range of 3-5 mJ/cm^2 for laser exposure in the uv. This fluence region is well below the ablation threshold for PET. We believe that the melting involved in this process takes place during the 15 nsec laser pulse. This means that it occurs at a rate approximately 10^6 times faster than current theories

of polymer melting predict.[6] For the particular case of PET, the surface amorphization results in a relatively large change in refractive index. This produces a durable antireflective coating on the PET surface.

REFERENCES

1. R. Srinivasan, Nature 234, 559 (1986).
2. P. E. Dyer and J. Sidhu, J. Appl. Phys. 57, 1420 (1985).
3. S. Lazare and V. Granier, J. Appl. Phys. 63, 2110 (1988).
4. K. N. Maffitt and R. F. Willson, U. S. Patent No. 4,340,276 (1982).
5. D. J. McClure, in Proceedings of the 29th Annual Technical Conference of the Society of Vacuum Coaters (Society of Vacuum Coaters, Washington, 1986).
6. B. Wunderlich, Macromolecular Physics, Vol. 3 Crystal Melting (Academic Press, New York, 1980), p. 215.

Photochemistry of $Ga(CH_3)_3$ at a Low Temperature Surface

E. Villa and J. A. Dagata
Chemistry Division, N. R. L., Washington, D.C. 20375-5000

M. C. Lin
Department of Chemistry, Emory University, Atlanta, GA 30322

ABSTRACT

The photochemistry of adsorbed $Ga(CH_3)_3$ on LiF(100) maintained at 150 K has been studied with a KrCl (222 nm) laser using resonance-enhanced multiphoton ionization/mass spectrometry (REMPI/MS) and electron impact/mass spectrometry (EI/MS) techniques to detect desorbed photodissociation products. The time-of-flight mass spectra of various fragments such as Ga, CH_3 and $Ga(CH_3)_x$ have been measured. The combination of these two different ionization techniques allows us to differentiate the origins of these neutral photofragments.

INTRODUCTION

The laser has been increasingly employed for the processing of materials, particularly for the patterning of microelectronic devices on solid surfaces, because of its high power, spectral brightness and directionality (coherency). One such application is laser chemical vapor deposition (LCVD) for direct writing of submicron metal lines[1-2]. The physico-chemical processes involved in these surface photochemical reactions are very complex and their reaction mechanisms are yet to be fully elucidated.

In an attempt to elucidate the deposition mechanism of the GaAs semiconductor by LCVD, we have recently studied the photochemistry of adsorbed $Ga(CH_3)_3$ (TMG), which is one of the most common sources of gallium in LCVD or OMCVD (organometallic chemical vapor deposition). This study concludes that adsorbed TMG could be readily photodissociated at low temperatures with 222 nm laser irradiation to produce CH_3, Ga and other photofragments, $Ga(CH_3)_x$, $x \leq 2$. The time-of-flight mass spectra measured for these fragments using both electron impact (EI) and resonance-enhanced multiphoton ionization (REMPI) mass spectrometry detection, allow us to differentiate the origins of some of the detected fragments. The mechanism of the photodissociation reaction and the translational energy distributions of these photofragments are reported herein.

EXPERIMENTAL

The experimental arrangement is similar to the one employed recently in our laboratory to study the chemistry of silicon etching reaction[3]. The only modification made in this system is the replacement of a rigid sample mount for Si single crystals with an XYZ-manipulator which can be cooled down to 150 K with LN_2. The reaction and mass spectrometer chambers, which were separated with a 3-mm skimmer, could be readily pumped down to a base pressure of 2x10-8 torr using two separate diffusion pumps with LN_2 cold traps. The chambers were also cryo-pumped with two separate LN2-cooled copper shields.

The LiF substrate was positioned 26 cm away from the ionization region of the quadrupole mass spectrometer (Extranuclear). The TMG sample was introduced into the system by a capillary tubing held 1.5 cm away from the substrate. A steady-state dosing rate was maintained by monitoring the TMG-EI signal in such a manner that the deposited TMG on LiF was totally removed by each laser shot. The laser pulse energy was about 10 mJ. The photodissociation laser light (222 nm KrF) was directed onto the substrate surface, covering .1 cm^2 of the surface area. The angle between the laser beam and the surface normal was measured to be 80°.

The time-of-flight detection of the desorbed photofragments was made alternately

with EI/MS or REMPI/MS. EITOF measurements were carried out at 30 ev. REMPI detection was carried out by an excimer-pumped dye laser (Lambda Physik EMG 101/FL 2002). Ionization was carried out by focusing the dye laser beam into the ionizer of the QMS using a 12" focal length lens. Methyl radicals and gallium atoms could be readily detected by REMPI/MS at 333.46 and 287.40 nm respectively as we had demonstrated before in conjunction with our GaAs-OMCVD studies. The mass selected EI and REMPI signals were amplified with a current amplifier, digitized by a transient recorder and sent to an IBM PC for further processing.

RESULTS AND DISCUSSION

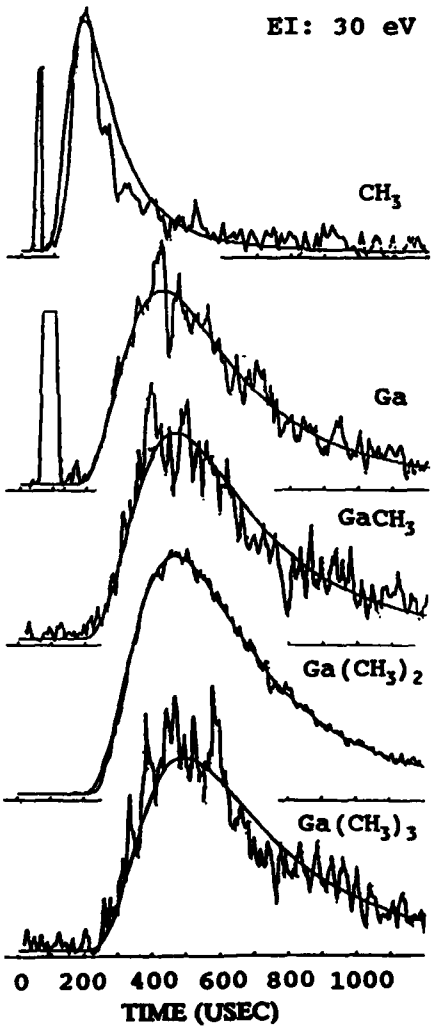

Figure 1. Time of flight spectra of desorbed $Ga(CH_3)_x$ species from the surface. The solid curve represents the fitted M-B distributions to the experimental data.

The time of flight spectra of various desorbed species obtained by EI using 30 ev ionization energy are shown in Figure 1. A sharp intense peak observed at 110 usec was determined to be from desorbed Ga^+. Similarly, a weaker CH_3^+ peak was also noted in the TOF spectrum at 25 usec. The TOF profiles, except for CH_3, could be qualitatively accounted for by Maxwell-Boltzmann (M-B) distributions with an approximate translational temperature of 950 K as indicated by the calculated curves presented in the figure.

The CH_3 is characterized by a narrow TOF distribution peaking at ~225 usec. This narrower distribution, as opposed to the broader one for Ga and $Ga(CH_3)_x$ species, strongly suggests that the observed CH_3 EI signal is derived primarily from desorbed CH_3 radicals rather than fragmentation of the $Ga(CH_3)_x$ in the mass spectrometer ionizer. This point is confirmed by the similarity of the methyl radical TOF distributions as detected by REMPI and EI techniques[4].

REMPI detection of Ga atoms, however, revealed a distinctively different TOF distribution[4] from that obtained by EI, as shown in Figure 2. The broad TOF distribution obtained by EI can be fitted by a 950 K translational M-B. In contrast, the REMPI/TOF profile can be characterized by a M-B distribution with a translational temperature of ~1500 K. The small population of the neutral Ga atom desorbed by the laser has a distinctly different origin and clearly did not derive from the cracking of $Ga(CH_3)_x$ ions.

The most likely source of Ga atom as well as the fast Ga^+ ion is believed to be the Ga metal film generated by repetitive photodissociation of adsorbed

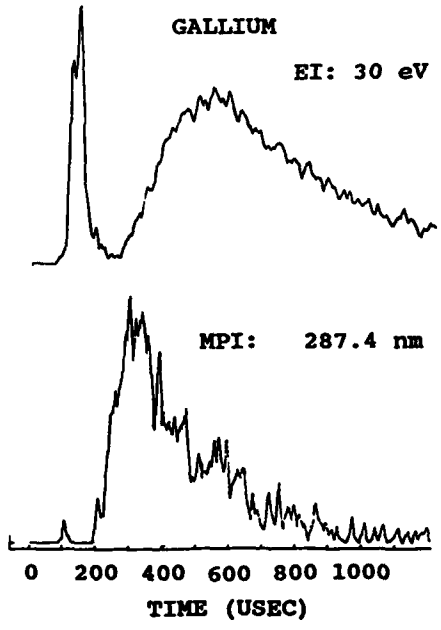

Figure 2. Gallium EI and MPI time of flight spectra. The TOF/EI spectrum corresponds to fragmentation of $Ga(CH_3)_x$ species. The TOF/MPI spectrum corresponds to gallium desorbed from the surface.

TMG. Since the Ga film can be readily ionized by visible or UV photons, the appearance of the Ga^+ ion is not surprising at all. The photoexcitation of the deposited film also desorbed some of neutral atoms with considerably higher translational energy than $Ga(CH_3)_x$ species.

A more detailed analysis of the observed $Ga(CH_3)_x$ TOF distributions, using the cracking pattern of the TMG molecule, suggests that the majority of $GaCH_3^+$ and $Ga(CH_3)_2^+$ signals derived from the $Ga(CH_3)_2$ radical, rather than TMG[5]. This conclusion, aided by the fact that CH_3 radicals were actually detected, indicates that the photodissociation of adsorbed TMG at 222 nm produces CH_3 and $Ga(CH_3)_2$ as the major photodissociation products.

ACKNOWLEDGEMENTS

E. Villa and J. A. Dagata thank the National Research Council (NRC) and the Office of Naval Research (ONR) respectively for their support.

REFERENCES

1. D. Bauerle ed., Laser Processing and Diagnostics, Springer-Verlag, NY 1984.
2. R. M. Osgood, Ann. Rev. Phys. Chem. 34 77 (1983).
3. J. A. Dagata, D. W. Squire, C. S. Dulcey, D. S. Y. Hsu and M. C. Lin, J. Vac. Sci. Technol. B 5 1495 (1987).
4. J. A. Dagata, E. Villa and M. C. Lin, CPL submitted.
5. E. Villa, J. A. Dagata and M. C. Lin, in preparation.

EXCIMER LASER-CONTROLLED PHOTOCHEMICAL DEPOSITION OF THIN FILMS AND ARTIFICIALLY STRUCTURED MATERIALS

D. H. Lowndes, D. Eres, D. B. Geohegan, J. Z. Tischler, D. N. Mashburn, and S. J. Pennycook
Solid State Division, Oak Ridge National Laboratory, PO Box 2008, Oak Ridge, Tennessee 37831-6056

ABSTRACT

Excimer laser photolysis is attractive for low-temperature film deposition because high resolution in film thickness can be combined with useful deposition rates, at temperatures that are too low for pyrolysis. Examples of ArF (193 nm) laser photolysis of hydride molecules to deposit amorphous superlattices are presented. Transmission electron microscopy demonstrates that thin (5–25 nm) layers with reproducible thickness and sharp boundaries can be deposited under photonic control. Results of low-temperature growth of crystalline and amorphous Ge films by pyrolysis and photolysis of digermane also are described. Experimental limitations encountered using these, and other, parent molecules are discussed, and general principles are outlined for efficient low-temperature photoepitaxial film growth using excimer lasers.

INTRODUCTION

In conventional thermal chemical vapor deposition (CVD), a gas stream containing parent molecules flows over a hot substrate and bond-breaking occurs following excitation to high vibrational levels. The substrate must be sufficiently hot to produce substantial numbers of the atoms or radicals that are the actual precursors to film growth, via these pyrolytic reactions. This typically requires >900°C for crystalline (c) Si, 600–800°C for c-GaAs, and 300–600°C for II–VI compound thin films to grow at useful rates. Unfortunately, the use of thermal energy to drive film-growth reactions also can degrade thin films and multilayered structures in two ways. Thermal generation of native defects such as vacancies and vacancy-dopant atom complexes can prevent control of crystalline thin-film electrical properties. Thermal diffusion from the substrate to the film or between adjacent layers in multilayered structures also can occur, resulting in graded interfaces or contaminated layers. Vacancy-enhanced diffusion can produce structural imperfections such as precipitates and associated grain boundaries in crystalline films.[1,2] For several technologically important classes of materials (e.g., the II–VI compounds), problems such as these have prevented the formation of well-defined interfaces, or abrupt compositional changes, and made it difficult to dope epitaxial thin films grown at conventional pyrolysis temperatures.[1,2]

Laser photochemical vapor deposition (LPVD) is a process in which ultraviolet (UV) photons are used to electronically excite and photodissociate parent molecules in the gas stream just above the growing surface, for example using a pulsed excimer laser beam directed parallel to the substrate.[3-8] Using this parallel-beam geometry, film nucleation

and growth are controlled by the nonthermal photon-induced chemical environment, instead of by the substrate temperature (T_S). The potential advantage is that the film growth rate can be controlled by the photon flux and becomes only a weak function of T_S, as T_S is reduced. Under optimum conditions, it may be possible to combine high resolution in the photon-controlled film thickness and growth rate with low-substrate temperatures, resulting in multilayered structures with well-defined layer thickness and sharp boundaries, at substrate temperatures too low for pyrolysis.[3,8] However, the properties and quality of the resulting thin films then depend sensitively on the precise nature of the precursors that are produced by the gas-phase photodissociation reactions, since the subsequent surface reactions and atomic diffusion that are necessary to grow high-quality films will be slowed or eliminated as T_S is reduced.[4]

In this paper, we review results of experiments in which disilane, germane and digermane parent molecules were used for ArF (193 nm) laser photolytic growth and for pyrolytic growth of Si and Ge thin films. Practical and fundamental limitations to achieving photon-controlled growth then are summarized. Finally, based both on our work and on experiments elsewhere using other parent molecules, we outline some general principles for excimer laser photon-controlled growth of crystalline (epitaxial) thin films.

AMORPHOUS SUPERLATTICES BY ArF LASER PHOTOLYSIS

Multilayered amorphous structures were deposited in a turbo-pumped chamber (base pressure ~10^{-6} Torr) based on a six-way stainless steel cross and equipped with 5 cm diameter Suprasil windows.[3,4,8] The ArF laser beam (~15 ns full-width half-maximum pulse duration) was unfocused but passed through a rectangular slit before entering the chamber, to precisely define its cross section (6 x 20 mm^2). The excimer beam traveled parallel to the substrate with its lower edge set 1 mm above the substrate surface. Depositions were made onto 2.5 cm square (100) c-Si substrates, whose temperature was monitored with an infrared radiation thermometer (IRCON Type W). A high stability HeNe (632.8 nm) laser beam was reflected at near-normal incidence from the gas–film and film–substrate interfaces and the interference oscillations in the reflected intensity, as the film was deposited, were used for in situ film thickness monitoring.[3,8] Helium was used to flush the inside of the two windows through which the excimer laser beam entered and exited the chamber; a He flow in the range of 150–250 sccm per window nearly eliminated deposition of Si or Si_3N_4 window films.

Previous work has established that single layers of either amorphous semiconductor (a-Si:H, a-Ge:H) or dielectric (SiO_2, Si_3N_4) films can be deposited photolytically, and that deposition conditions can be found to produce films having properties similar to those obtained using conventional thermal CVD-based methods. (See Refs. 3, 4, and 9 and references therein for discussions of the photochemical reaction paths leading to film growth.) In our experiments, hydrogenated amorphous Si (a-Si:H) was deposited by photolysis of disilane (Si_2H_6); Si_3N_4 was deposited by photolysis of mixtures of disilane and ammonia (NH_3); and hydrogenated a-Ge (a-Ge:H) was deposited by photolysis of germane (GeH_4). Photolytic deposition of a-Ge:H from germane is limited by a very

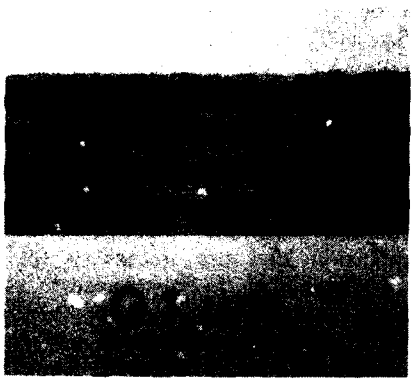

Figure 1. TEM cross section view of a nine-layer a–Si(light)/ a–Ge(dark) structure deposited on (100) c–Si by ArF laser photolysis at 250°C.

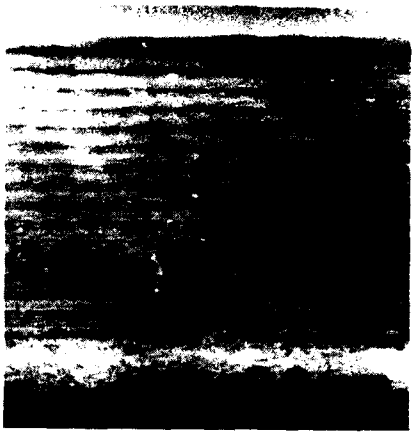

Figure 2. TEM cross section view of a 32-layer Si_3N_4/a–Si amorphous superlattice deposited at 350°C by ArF laser photolysis.

small (~3 x 10^{-20} cm^2) absorption cross section at 193 nm. The use of high ArF laser pulse energies to speed deposition results in the gradual decay of laser power within the chamber, due to Ge film buildup on the chamber windows, even with a He window flush.[3] This window film buildup can be forestalled by operating the excimer laser at a low fluence. Consequently, structures containing thin (<10 nm) a–Ge:H layers can be grown entirely by ArF laser photolysis, but thicker layers were grown from germane by pyrolysis (at an increased substrate temperature), in order to obtain reasonable deposition times and to avoid eventual loss of laser power due to window film deposition. The film growth experiments using digermane that are reported below were motivated by this experience with germane.

Completely photolytic a–Ge:H/a–Si:H structures were deposited at 250°C. The a–Ge:H layers used 140 sccm of a 10% germane/90% He mix at p = 50 Torr, 60 Hz laser repetition rate and 420 mW transmitted power. The a–Si:H layers used 40 sccm of a 10% disilane/90% He mix at p = 5 Torr, 40 Hz laser repetition rate and 200 mW of transmitted power. A 450 sccm (total) He window purge was used continuously. It was found[9] that for T < 400°C ArF laser photolysis of disilane results in entirely photon-controlled film deposition (ratio of laser deposition rate to background pyrolysis rate > 1000).

Figure 1 shows a photolytically grown nine-layer a–Si:H/a–Ge:H structure, for which layer thickness was controlled by keeping the product of laser power and deposition time a constant for corresponding layers. The average thickness of the a–Si:H layers is 10.7 ± 0.4 nm, while for the first, third and fourth a–Ge:H layers the average thickness is 5.4 ± 0.2 nm. The second a–Ge:H layer was deposited with the power–time

product increased by approximately 24%, resulting in a layer 30% thicker (7.0 ± 0.3 nm) than the average of the other layers.

Figure 2 shows a 626 nm thick 32-layer (16-period) Si_3N_4/a-Si:H superlattice that was deposited using ArF laser photolysis at 350°C and p = 5 Torr. For the a-Si:H layers a 10% disilane/90% He mix was used at 20 sccm; for the Si_3N_4 layers, 60 sccm of NH_3 and 20 sccm of the disilane mix (30:1 NH_3:Si_2H_6 ratio) were used. After the first layer, the a-Si:H layer thicknesses are 13.3 ± 0.4 nm, while the Si_3N_4 layer thicknesses are 26.6 ± 2 nm, as determined by TEM cross section views.

CONDITIONS FOR PHOTOEPITAXIAL FILM GROWTH

Several groups have explored laser photochemically controlled epitaxy, using either normally incident or parallel radiation, and both pulsed and continuous lasers. Here we briefly review problems encountered in recent excimer laser epitaxial film growth experiments and the experimental conditions needed to deal with them.

As described above, a flow of gas across the inside surface of the windows through which the excimer beam enters and leaves the chamber is needed to avoid window film deposition. Both inert gases and halogen-based etchant gases[10] have been used successfully.

Efficient matching of the parent molecule's photodissociation cross section, σ, to at least one of the available excimer laser wavelengths is needed, for several interrelated reasons. For $\sigma \geq 3 \times 10^{-18}$ cm^2, the parent molecule's partial pressure can be kept sufficiently low (in the mTorr range) that gas phase (homogeneous) nucleation does not occur, and "dust" deposits on the growing film are avoided.[1,2] This value of σ, combined with the high repetition rate of excimer lasers, also ensures that reasonable deposition rates can be obtained at these low pressures, while still maintaining high resolution "photonic" control of film thickness (typically, <0.1 monolayer deposited per laser pulse[3,7]).

A second constraint on the choice of the parent molecule and laser wavelength is that carbon contamination of semiconductor thin films must be avoided. For simple parent molecules such as hydrides no problem results from using high-energy UV photons (e.g., 6.4 eV from the ArF laser). However, in using metalorganic alkyls to grow III-V or II-VI compound semiconductors, it is important to avoid secondary photolysis reactions of carbon-bearing ligands, after the primary photolytic bond-breaking reaction has released the atomic species of interest.[7] For example, Donnelly, McCrary and co-workers[5,6,11] found carbon contamination ~2% during ArF laser growth of GaAs from trimethylgallium and trimethylarsenic. Normally incident ArF laser fluences of >0.1 J/cm^2 were sufficient to reduce carbon contamination to <0.1%, but interference between the normally incident laser beam and scattered surface waves then caused periodic twin growth within the epitaxial film, with a spatial period equal to the laser wavelength.[11] In practice, avoiding secondary photolysis reactions requires using UV wavelengths >220 nm. It appears from recent experiments on II-VI film growth that by keeping the C-bearing ligands intact, C is carried off in the gas phase.[7]

These results strongly suggest that the excimer beam should be kept parallel to the film surface, passing through the gas just above the

growing surface but not directly irradiating it. High intensity excimer laser pulses are needed to obtain useful deposition rates, but normally incident radiation can damage or even melt the growing film surface, with formation of growth defects.

However, for many parent molecules it is found that if the substrate temperature is reduced to allow gas-phase photolytic reactions to dominate over pyrolysis, then only amorphous or polycrystalline films are obtained, under parallel-beam, gas–phase–photolysis initiated growth conditions.[3-6,11] This conflict between epitaxy and gas-phase photon-controlled deposition occurs whenever photolysis does not directly produce the atomic species needed for crystalline growth, but only produces intermediate radicals that must undergo further surface reactions to free the atomic species. Consequently, when T_s is lowered to allow photolysis to dominate for such a parent molecule, then some alternative energy input to the growing film surface (other than thermal) will be needed to stimulate low-temperature epitaxy.

Thus, there appear to be two different routes[12] to epitaxy under parallel-beam, gas-phase-photolysis initiated conditions, depending on the nature of the gas-phase photoproducts. If the atomic species needed is produced directly in the gas phase, and is not involved in secondary recombination reactions, then it is only necessary that these atoms be able to diffuse to lattice sites, after adsorption on the growing surface. This is the simplest case, and appears to be what happens in low-temperature KrF laser photolytic growth of II–VI compounds such as CdTe and HgTe from MO alkyls. In such cases, the desired reduction of T_s, to minimize thermal defect generation and interdiffusion in crystalline thin-film layers, can be achieved via parallel-beam gas-phase photolysis. On the other hand, if gas-phase photolysis produces only intermediate radicals that must undergo both further surface reactions and diffusion after adsorption, then either the substrate temperature or another energy input must drive these surface reactions, and entirely gas-phase photon-controlled epitaxy may not be possible with such a parent molecule.

The combination of requirements just listed is sufficiently restrictive that alternatives to gas-phase photolysis also are being explored for photon-controlled epitaxy. In particular, direct surface illumination and surface photochemical reactions of adsorbed molecular layers are being studied for spatially selective growth (growth limited to the laser–illuminated region). Two examples of this approach are the photochemical prenucleation of an aluminum film in a UV laser-exposed region[13] followed by conventional thermal MOCVD growth, and the laser-selective decomposition of an adsorbed trimethylgallium layer resulting in GaAs atomic layer epitaxy[14] in the laser–illuminated region.

Ge FILM GROWTH FROM DIGERMANE

Because the very small absorption cross section of germane at 193 nm results in a low ArF laser photolytic deposition rate, we have

instead grown Ge films from digermane (Ge_2H_6).[15] A mixture of 4.9% digermane in helium was used; the only significant impurity was about 300 ppm of germane. In the studies reported here, both the a– and c–Ge films were grown on (100) GaAs substrates, which are nearly lattice-matched to Ge (a[GaAs] = 5.6535 Å, a[Ge] = 5.6577 Å).[16,17] Both pyrolytic and ArF laser photolytic film growth were studied, for substrate temperatures 200°C < T_S < 560°C. Because both types of reaction proceed easily, it was possible to obtain useful deposition rates at quite low partial pressures: 0.05 mTorr < p(Ge_2H_6) < 20 mTorr for pyrolytic growth, and at total pressures of up to 5 Torr when a He window purge was used during laser photolytic growth.

Figure 3 illustrates the transition from crystalline to amorphous film growth that was observed with decreasing T_S. For T_S = 380°C

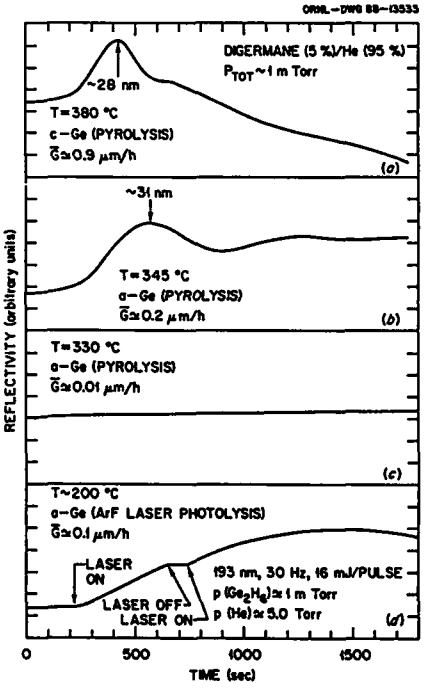

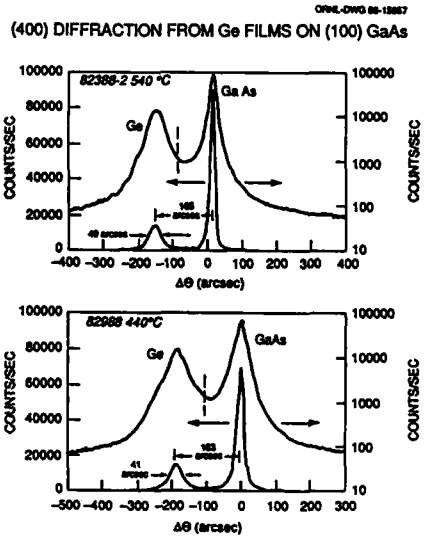

Figure 4. (400) Bragg diffraction from c–Ge film (left hand peak), and from the GaAs substrate (right hand peak), for films deposited at T_S = 540°C (top) and T_S = 440°C (bottom). The vertical dashed line marks the expected position of the (400) peak from an incommensurate (relaxed) Ge film.

Figure 3. Comparison of film growth rates and HeNe laser reflectivity signals during growth of Ge films from 4.9% Ge_2H_6/95% He. (a) c–Ge (epitaxial growth) by pyrolysis at T_S = 380°C (G ~ 0.92 μm/hr); (b) a–Ge:H by pyrolysis at T_S = 345°C (G ~0.21 μm/hr); (c) a–Ge:H by pyrolysis T_s = 330°C (G~0.013 μm/hr); (d) a–Ge:H by ArF laser photolysis at T_S = 200°C. For (a)–(c) p(total) ~1 mTorr, while in (d) p(Ge_2H_6) ~1 mTorr and p(He) 5 Torr.

pyrolytic growth of epitaxial Ge occurs at a rate of ~0.9 μm/hr, even at a digermane partial pressure of only 0.05 mTorr. Under these conditions the HeNe reflectivity signal does not exhibit the attenuated oscillations expected for a c–Ge layer with uniformly increasing thickness. Instead, the reflectivity displays an initial peak (at a film thickness ~300 Å), followed by either a shoulder (Fig. 3a) or second oscillation, and then a long slow decay. Model calculations and both SEM and optical microscope studies show that this reflectivity behavior results from roughening or (under some conditions) (111) faceting of the growing c–Ge surface, and is associated with an island growth mechanism. The surface roughness increases with film thickness and produces a non-specular reflectivity component at visible wavelengths. Figure 3b shows the oscillating reflectivity signal observed as an a–Ge:H film is deposited by pyrolysis in smooth, specularly reflecting layers at T_s = 345°C. At T_s = 330°C (Fig. 3c) the pyrolytic deposition rate is reduced to ~0.01 μm/hr, under these low pressure conditions. The rapid decrease of pyrolytic deposition with decreasing T_s corresponds to an apparent activation energy E_a = 1.4 (± 0.2) eV.

Rapid ArF laser photolytic deposition of a–Ge:H is possible at still lower substrate temperatures, as shown in Fig. 3d. It should be noted, though, that Eres et al.[4] recently showed that the optical properties of a–Si:H films deposited by ArF laser photolysis of disilane in the parallel-beam geometry do depend sensitively on the combination of T_s and deposition rate, because short polysilane, $(SiH_2)_n$, chains must be eliminated from the deposit through formation of Si–Si and monohydride bonds, accompanied by H_2 desorption from the surface. A covalently bonded a–Si:H network cannot be formed if there is not sufficient time for these surface reactions to occur before the next layer is deposited. Thus, longer times and lower deposition rates are required to produce films with the same optical properties, as T_s is reduced.[4] We anticipate that similar considerations will apply to a–Ge:H films, i.e., their optical and electrical properties are expected to depend sensitively on both T_s and deposition rate.

An important result of this work was that high quality, coherently strained epitaxial Ge films were grown on (100) GaAs by digermane pyrolysis, for temperatures in the range 380 < T_s < 560°C. Because the bulk lattice constant for Ge is larger than that for GaAs[16,17], a completely commensurate epitaxial Ge film is under compression in the plane parallel to the GaAs surface, and so is in tension perpendicular to the (100) GaAs substrate. The perpendicular lattice constant is measured by the (400) x-ray diffraction peak. For a completely commensurate, coherently strained Ge film, the Ge (400) peak is expected to occur at −173 arc sec from the GaAs (400) peak, while if the Ge film has its bulk (relaxed) lattice constant the Ge (400) peak should be found at −100 arc sec. As Fig. 4 shows, all of our thin (<500 nm) Ge films had the (400) peak at −173 (±10) arc sec, indicating that they were completely commensurate with the GaAs substrate. A much thicker (~1.5 μm) Ge film was found to be partially relaxed ($\Delta\theta$ = −129 arc sec); cross section TEM revealed what may be an array of edge dislocations, spaced at intervals of ~0.8 μm, in the plane of the interface. However, even in this case there were no dislocations or extended defects of any kind extending into either the Ge film or the GaAs substrate.

The full-width at half-maximum (FWHM) intensity of the Ge (400) x-ray peaks also was measured, and was compared with the minimum width possible for diffraction from the finite number of lattice planes, for each c–Ge film. The Ge (400) peaks were found to have the minimum possible FWHM for $T_s \geq 500°C$, and to increase to only about 75% more than the minimum for films grown near 400°C. Thus, even the films grown at relatively low temperatures are of high crystalline quality. The slight increase in FWHM may be due to voids or vacancies that are not annealed out during low-temperature growth.

SUMMARY

ArF laser photolysis of disilane and digermane results in completely photon-controlled deposition of a–Si:H and a–Ge:H films, at substrate temperatures <400°C and <300°C, respectively. At such temperatures the photon fluence provides excellent control of deposition, in that the laser deposition rate is much greater than the background pyrolysis rate. Under these conditions, the high pulse repetition rate and average power of excimer lasers make it possible to combine "digital" control of film deposition with useful overall deposition rates. Consequently, amorphous superlattice structures can be deposited using entirely photon-controlled reactions. Structures that we have grown have reproducible layer thicknesses and sharp interlayer boundaries, and are believed to be the first superlattices grown entirely under laser photolytic control. However, amorphous film properties do depend sensitively on the combination of substrate temperature and deposition rate, because the rate-limiting steps in forming high quality amorphous films by photolysis of hydrides are not the gas-phase photolysis reactions, but instead are thermally activated surface reactions involving bond rearrangement and hydrogen desorption.[4]

Detailed consideration of the problems and conditions necessary for photoepitaxial growth after gas-phase laser photolysis leads to the conclusion that there are two different routes to epitaxy, depending primarily on the species produced by photolysis. If the atomic species needed in the crystalline film is produced directly in the gas phase and is not involved in secondary recombination reactions, then only surface diffusion to lattice sites is necessary after their adsorption, and photoepitaxial growth may be possible at relatively low temperatures. This appears to be the case for II–VI compound growth by excimer laser photolysis of appropriate MO alkyls. On the other hand, if only intermediate radicals result from gas-phase photolysis, then surface reactions must occur to produce the atomic species; higher substrate temperatures, or some other surface energy input, are required for epitaxial growth. However, if higher substrate temperatures are used then they may cause pyrolysis to dominate photolysis. Nevertheless, rapid, easily controlled pyrolytic epitaxial growth may be still possible at low reactant partial pressures. This appears to be the situation for Ge films grown from digermane, under the conditions we have explored. In particular, we find that fully commensurate, coherently strained epitaxial Ge films can be grown on GaAs by pyrolysis of digermane, at substrate temperatures $380 < T_s < 560°C$.

Our analysis of the conditions for excimer laser-controlled photoepitaxy, together with the recent demonstrations of amorphous superlattice growth[3] and of epitaxial II–VI thin film growth[7] under excimer laser control, strongly imply that excimer laser-controlled growth of crystalline superlattice structures is now possible, at least for selected crystalline materials.

ACKNOWLEDGMENTS

We would like to thank P. H. Fleming, J. T. Luck, and C. W. Boggs for skilled technical assistance This work was sponsored by the Division of Materials Science, U. S. Department of Energy under contract DE-AC05-840R21400 with Martin Marietta Energy Systems, Inc.

REFERENCES

1. S.J.C. Irvine and J. B. Mullin, *J. Vac. Sci. and Technol.* A 5, 2100 1987).
2. S.J.C. Irvine and J. B. Mullin, *Chemtronics* **2**, 54 (1987).
3. D. H. Lowndes, D. B. Geohegan, D. Eres, S. J. Pennycook, D. N. Mashburn, and G. E. Jellison, Jr., *Appl. Phys Lett.* **52**, 1868 (1988); D. H. Lowndes, D. B. Geohegan, D. Eres, D. N. Mashburn, and S. J. Pennycook. *Mat. Res. Soc. Symp. Proc.* **103**, 23 (1988).
4. D. Eres, D. B. Geohegan, D. H. Lowndes, and D. N. Mashburn, accepted for publication in *Applied Surface Science.*
5. V. M. Donnelly, V. R. McCrary, A. Appelbaum, D. Brasen, and W. P. Lowe, *J. Appl. Phys. 61*, 1410 (1987).
6. V. M. Donnelly, D. Brasen, A. Appelbaum, and M. Geva, *J. Appl. Phys.* **58**, 2022 (1985).
7. J. J. Zinck, P. D. Brewer, J. E. Jensen, G. L. Olson, and L. W. Tutt, *Appl. Phys. Lett.* **52**, 1434 (1988).
8. D. H. Lowndes, D. B. Geohegan, D. Eres, S. J. Pennycook, D. N. Mashburn, and G. E. Jellison, Jr., accepted for publication in *Applied Surface Science.*
9. D. Eres, D. H. Lowndes, D. B. Geohegan, and D. N. Mashburn, *Mater. Res. Soc. Symp. Proc.* **101**, 355 (1988).
10. A. A. Langford, B. L. Stafford, and Y. S. Tsuo, *Proc. of 19th IEEE Photovoltaic Specialists Conf.* (Inst. Electrical and Electronics Engineers, New York 1987). p. 573–6.
11. V. R. McCrary, V. M. Donnelly, D. Brasen, A. Appelbaum, and R. C. Farrow, *Mat. Res. Soc. Symp. Proc.* **75**, 223 (1987).
12. P. M. Dryburgh, *J. Crystal Growth* **87**, 397 (1988).
13. G. S. Higashi and C. G. Fleming, *Appl. Phys. Lett.* **48**, 1051 (1986); G. S. Higashi, G. E. Blonder, and C. G. Fleming, *Mater. Res. Soc. Symp. Proc.* **75**, 117 (1987).
14. Y. Aoyagi, A. Doi, S. Iwai, and S. Namba, *J. Vac. Sci. Technol.* B **5**, 1460 (1987).
15. Digermane was purchased from Voltaix, Inc. (North Branch, NJ).
16. J.F.C. Baker and M. Hart, *Acta Cryst.* A**31**, 364 (1975).
17. J.F.C. Baker, M. Hart, M.A.G. Halliwell and R. Heckinbottom, *Sol. St. Electronics* **19**, 331 (1976).

LASER PROCESSED ZIRCONIUM: STUDY OF CORROSION AND MICROSTRUCTURE

W. REITZ[a] AND J. RAWERS[b]

[a] Resident Engineer, Babcock and Wilcox Co., Lynchburg, VA.
[b] Metallurgist, U.S. Department of the Interior, Bureau of Mines, Albany, OR.

Abstract

Zirconium alloys have been laser processed with a 10 kw continuous wave CO_2 laser. Corrosion tests were conducted in room temperature 10% $FeCl_3$ (immersion weight loss) and steam autoclave. The corrosion rates showed a 10 to 100-fold improvement for the laser processed material. There appeared to be a direct relationship between corrosion rate and type of microstructure transformation induced by the laser processing.

INTRODUCTION AND EXPERIMENT

Laser surface melting (LSM) is a technique whereby a small surface volume is melted and subsequently rapidly quenched by the substrate material. Quench rates on the order of 10^5 to 10^8 °C/sec have been reported (1).

Several studies have shown that corrosion performance can be affected by existing microstructure. The alloys systems studied included: aluminum (2), nickel (3), iron (4), and zirconium (5,6). Many of these works also address the importance that pitting plays in the corrosion behavior of the metal systems (2,4,5).

In this study surfaces of Zr-4 were LSM and the resulting microstructure and corrosion characteristics were investigated. The experimental procedure and materials used have been described previously (7).

ANALYSIS AND DISCUSSION

MICROSTRUCTURE

Optical microscopy revealed the structural changes (Figure 1) in the transverse microstructure. The energy densities of 4 (3kw-200ipm-1mm dia), 7 (7-100-3), 10 (5-50-3) kJ/cm² are shown in the 'a, b, c' portions. The lowest energy density produced the shallowest melt pool of about 0.53 mm, whereas the 7 and 10 kJ/cm² energy densities produced melt pool depths of about 1.19 mm each.

A close examination of Figure 1 revealed that the resulting microstructure is strongly dependent upon the laser energy deposited in the material. Low energy densities generate a martensitic type structure that is characterized by lenticular formation and extremely fine alpha - beta distribution. The martensitic structure typically results from extremely fast quenching from the melt temperature through the beta-phase.

The other two energy densities of 7 and 10 kJ/cm² produce similar melt pool depths. The highest energy density generates the coarsest microstructure. When examining the topmost surface layer, it is possible to discern the wider spacing of the parallel platelets within each colony and the large colony sizes, which is indicative of a slower quench rate.

CORROSION TESTING

Autoclave - Autoclave testing was performed at 1500 psig for 400 hours at 400°C. LSM resulted in corrosion rates of 0.6 mg/dm² and 1.0 mg/dm²

for energy densities of 7 and 4 kJ/cm². The control samples (non-LSM) yielded the best corrosion resistance with corrosion rates of 0.3 mg/dm².

LSM of Zr-4 also produced a change in visual appearance. The non-LSM samples were shiny and black with a minimal amount of white corrosion product, which is a standard response for this material in a steam autoclave environment. LSM produced a surface with numerous areas of tightly adhering nodular corrosion.

Immersion - The sand-blasted surface condition resulted in high corrosion rates of 300 mpy, which is typical for fabricated surfaces. The as-received surface condition yielded a corrosion rate of 20 mpy. This surface has a fabrication history which generated a deep surface oxide that provides beneficial protection in a $FeCl_3$ environment. The polished sample surface (1 micron alumina) produced a corrosion rate of 5 mpy. All LSM samples yielded corrosion rates between 0.6 and 8 mpy. The best corrosion resistance was generated by laser processing with the lowest energy density of 4 kJ/cm².

Immersion coupons were then examined for their propensity towards pitting. The tendency towards pitting is directly related to the energy density and resulting microstructure as demonstrated by Figure 2 . The lowest energy density, which had the martensitic type structure, produced the fewest and smallest pits. This indicates that general corrosion predominates over localized, pitting corrosion. The middle energy density, which was a Widmanstatten type structure, generated slightly larger pits and a corresponding higher number of pits. Whereas, the highest energy density produced not only a coarser microstructure, but also a tremendous increase in pit size and frequency. This is indicative of the localized corrosion phenomena dominating the general corrosion. The weight losses of these three groups showed that the martensitic type structure was overall slightly more corrosion resistant than the basketweave and coarse structure. However, the pitting histogram demonstrates that the pitting propensity is extremely high for the basketweave and coarse microstructure, which indicates a serious compromise in corrosion performance.

CONCLUSIONS

1. Laser processing controls microstructure. The higher the energy density the coarser the microstructure.
2. Microstructure controls corrosion rate and type of corrosion.
3. Laser processing produces lower corrosion rates than sand-blasted or as-received surfaces.
4. Martensitic type structure has the least tendency to pit and lowest overall corrosion rates.

REFERENCES

1. R. B. Schwarz, MRS Bulletin, v. XI, No. 3, 1986, pp 55-58.
2. O. Lunder and K. Nisancioglu, NACE, 44, 7, July 1988, pp 414-422.
3. Y. C. Lu, T. L. Lin, L. Y. Chen and B. R. Su, Mat'ls Letters, 6, 7, April 1988, pp 229-232.
4. J. D. Peggs and D. P. Skrastins, Corrosion, Microstructure and Metallography, D.O. Northwood, W.E. White, and G.F. VanderVoot, (eds.), 12, ASM, Metals Park, OH, 1985, pp 25-35.
5. C. W. Draper and C. A. Ewing, J. of Mat'l Sci, 19, 1984, pp 3815-25.
6. G. C. Palit and H. S. Gadiyar, NACE, 43, 3, March 1987, pp 140-148.
7. J. Rawers and W. Reitz, 1988 TMS Symposium, Laser Processed Materials, to be published.

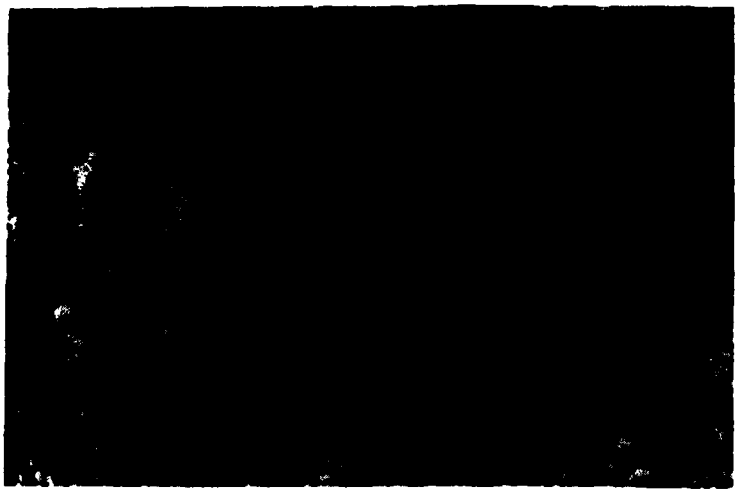

Figure 1. Transverse Microstructure of Zr-4, ingot 214267, cold rolled, a. 10 kJ/cm², b. 7 kJ/cm², c. 4 kJ/cm² .

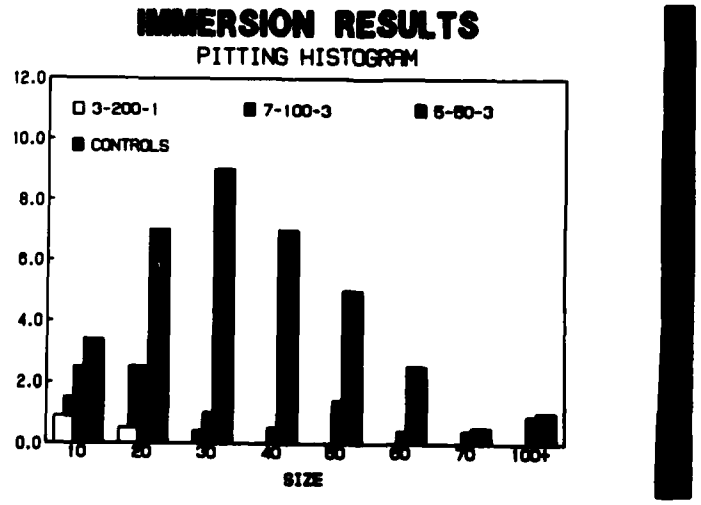

Figure 2. Immersion Test Pitting Histogram. The abcissa indicates relative size and the ordinate indicates the average number of pits for a given size per coupon.

INVESTIGATION OF SURFACE DAMAGE THRESHOLDS BY PHOTOACOUSTIC DEFLECTION *

S. Petzoldt, A.P. Elg, J. Reif, and E. Matthias
Freie Universität Berlin, Fachbereich Physik, D-1000 Berlin 33, FRG

ABSTRACT

Intensity dependent laser surface damage of optical materials in air was studied by photoacoustic probe beam deflection. The technique permits a reliable determination of damage thresholds and yields information about the basic energy coupling mechanisms between radiation and surface. For highly inert surfaces, like polished fused silica, MgF_2, and CaF_2, thresholds of about 1 GW/cm^2 due to dielectric breakdown are found. Defect rich surfaces exhibit thresholds an order of magnitude lower, which appear to result from multiphoton surface ionization.

INTRODUCTION

The increasing application of high power lasers is often confronted with the problem of irreversible damage in optical materials, caused by extremely high laser intensities[1]. It is highly desirable to learn more about the underlying physical mechanisms. Also, for optimizing optical components for beam handling, their damage thresholds need to be known. In this contribution, we report on a technique which can yield reliable information on both questions, and we present first results obtained for halide crystals and fused silica.

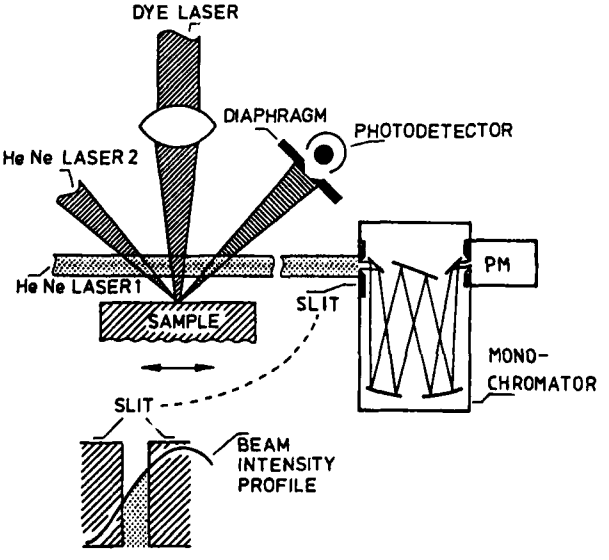

Figure 1. Schematic experimental set-up. HeNe laser 1 probes the acoustic pulse generated in the damaging explosion, HeNe laser 2 cross-checks the reflectance.

EXPERIMENT

The technique (cf. Fig. 1) makes use of the fact that laser surface damage is always accompanied by a shock wave, expanding away from the surface. This acoustic pulse causes a transient change in refractive index of the air close to the surface and leads to a time dependent deflection of a probe laser. In a recent publication[2], we have de-

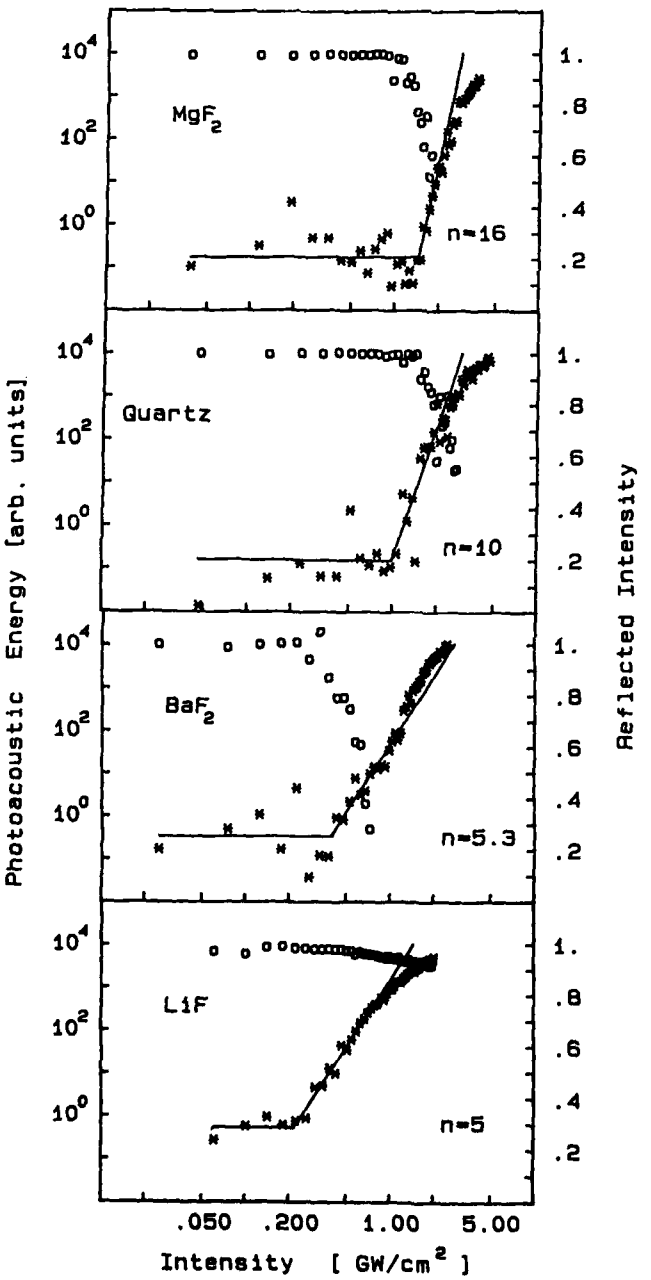

Figure 2. Photoacoustic energy (*) and reflected intensity (o) as a function of damaging laser intensity for MgF_2, quartz, BaF_2, and LiF. (λ=530 nm, pulse width 4 ns).

monstrated that the photoacoustic energy derived from this deflection is a measure of the produced damage. the results were cross-checked by simultaneously probing the reflection from the interaction spot.

RESULTS

We have applied this technique to investigate several frequently used optical materials like LiF, BaF_2,CaF_2,MgF_2, and fused silica. Typical single shot (1-on-1) results are presented in Fig. 2. A strikingly different behavior is observed between the upper two materials (polished MgF_2 and quartz) and BaF_2 and LiF in the lower two plots. The latter two crystals exhibit thresholds between 200 and 500 MW/cm^2, and the photoacoustic energy increases with the fifth power of the damaging intensity. In contrast, for MgF_2 and quartz the damage threshold lies above 1 GW/cm^2 and the intensity dependence is much steeper. In all cases, the damage thresholds determined by the deflection technique agree well with those obtained by the reflectance method.

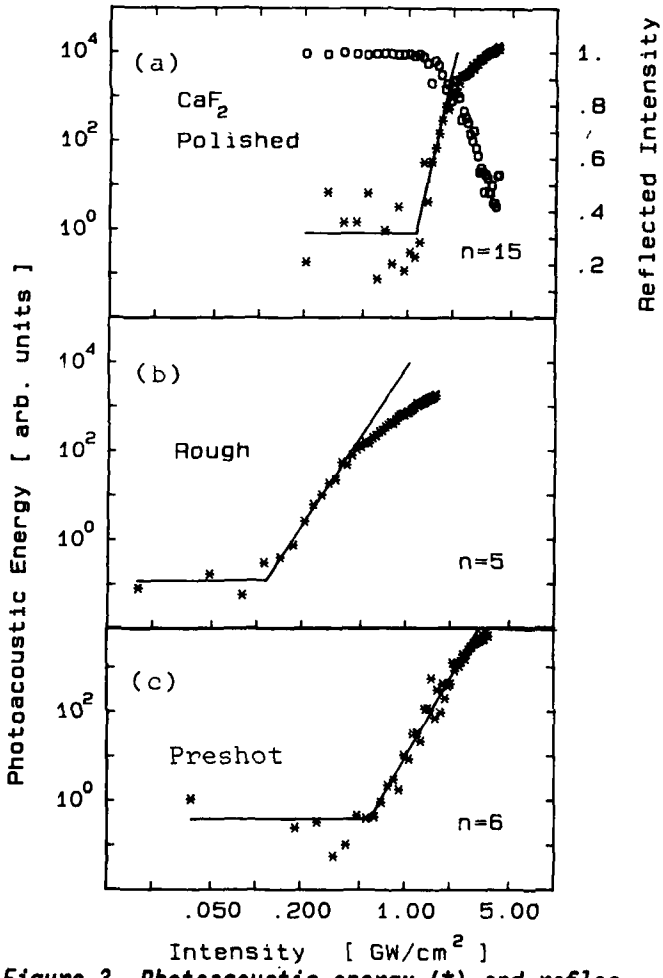

Figure 3. Photoacoustic energy (*) and reflected intensity (o) as a function of damaging laser intensity for CaF_2. (λ=530 nm).

In Fig. 3 we show the result for CaF_2. Part (a) was recorded under the same conditions as all previous results in Fig. 2, i.e. virgin surface spots were irradiated by single laser pulses. Threshold and slope of CaF_2 are similar to those MgF_2 and quartz. Figs. 3 (b) and (c) represent results obtained under different conditions: from a rough surface instead of a polished one (b), and with each damaging pulse being preceded by a preshot well below threshold intensity (c). The results in Figs. 3 (b) and (c) are more similar to those observed for LiF and BaF_2. These surfaces apparently have a high density of states in the band gap, caused by either adsorbates or structural defects. The slopes indicate that the intensity dependence is consistent with the idea of multiphoton surface ionization[3] being the basic absorption mechanism. The very steep slopes observed for the highly inert materials MgF_2, CaF_2, and quartz, on the other hand, point more toward dielectric breakdown[1,4] as the principal energy coupling.

REFERENCES

* Work supported by the Deutsche Forschungsgemeinschaft, Sfb 337

1. R.M.Wood; *Laser Damage in Optical Materials* (Adam Hilger, 1986)
2. S.Petzoldt, A.P.Elg, M.Reichling, J.Reif, and E.Matthias; Appl. Phys.Lett.53, 2005 (1988)
3. E.Matthias,H.B.Nielsen, J.Reif, A.Rosén, and E.Westin; J.Vac.Sci. Technol. B5, 1415 (1987)
4. M.vonAllmen; *Laser-Beam Interactions with Materials*(Springer,1988)

ROTATIONAL ENERGY ACCOMMODATION OF OH PRODUCED IN THE CATALYTIC REACTION OF $NO_2 + H_2$ OVER Pt(111)

Leo V. Novakoski, D. S. Y. Hsu, M.C. Lin
Naval Research Laboratory, Washington, D.C. 20375-5000

ABSTRACT

Laser induced fluoresence has been used to study the desorption dynamics of OH radicals produced by the reaction of NO_2 and H_2 over Pt(111), under UHV conditions. We measure an apparent Arrhenius activation energy for desorption that increases from 25 to 38 kcal/mole as the NO_2 to H_2 ratio in the dosing mixture, X, decreases from 2 to .05. Boltzmann-like rotational energy distributions with relatively high rotational to surface temperature ratios (α = Tr/Ts = .69 - .87) are reported for crystal temperatures between 1078 and 1433 K. α exhibits a small but definite dependence on both Ts and X. These results are compared with earlier data from the $O_2 + H_2$ system and interpreted in terms of O-coverage.

INTRODUCTION

The apparent Arrhenius activation energy, Ea, and the rotational accommodation coefficient, α, of OH desorbing from Pt(111) exhibit behavior that can be attributed in part to variations in the surface oxygen coverage, [O(ads)]. For the Ea data, the NO_2 and O_2 systems exhibit dosing ratio dependences readily explained by the much greater sticking probability and consequent higher [O(ads)] of the former[1]. Due to the smaller signals and larger uncertainties of the $O_2 + H_2$ system, a comparison of the results is made only for the 1:1 mixtures. However, the influence of [O(ads)] is still apparent.

The data presented here was obtained using a UHV system that has been fully described elswhere[2]. The Pt surface was dosed with reaction mixtures composed of various NO_2 to H_2 ratios, X. The incident flux was maintained at a constant rate of about 10^{15} cm^{-2} s^{-1}, independently of X. This corresponds to a chamber pressure of 2 x 10^{-5} torr. All results are based on excitation of the $(^2\Sigma^+, v'=1 \leftarrow {}^2\Pi, v''=0)$ transition near 281 nm.

ROTATIONAL ACCOMMODATION

In fig. 1 we have plotted α vs Ts for X = .1, .25, 1, and 2. Each data point represents an average of 10 to 15 spectral scans. The dashed line corresponds to α = .87, obtained for the H_2 rich, X = .1, dosing mixture. For the NO_2 rich mixtures, X = 2 and 1, there is a dip in α at 1183 K (α = .69 for X = 1). This minimum suggests at least two different processes are competing to produce the measured rotational accommodations. Note that for high Ts, α approaches .87 for all X. In this same temperature range (Ts > 1280 K), Arrhenius plots for the $NO_2 + H_2$ system (ln(signal) vs 1/T), exhibit a marked fall off in signal attributed to a decrease in the sticking coefficient of the reactants and consequent decrease in the surface coverage[3]. This suggests .87 is the low coverage limit of α. The absence of variations in α with Ts in the H_2 rich, X = .1 and .25 mixtures indicates it is the O-coverage in particular that is affecting the rotational accommodation.

Below 1183 K, this surface temperature dependence reverses and α increases with decreasing Ts for X = 1 and 2. Without further information we can only speculate as to what the mechanism for this might be. For instance, it's possible the coverage and Ts dependence of α is associated with specific sites on the surface. Higher [O(ads)] occuring at lower Ts could then block these sites, leading to the observed behavior.

For the $O_2 + H_2$ system, sufficient data for a meaningful comparison was collected only for the 1:1 reaction mixture. In this case, α = .89, .81, and .85 for Ts = 1183,

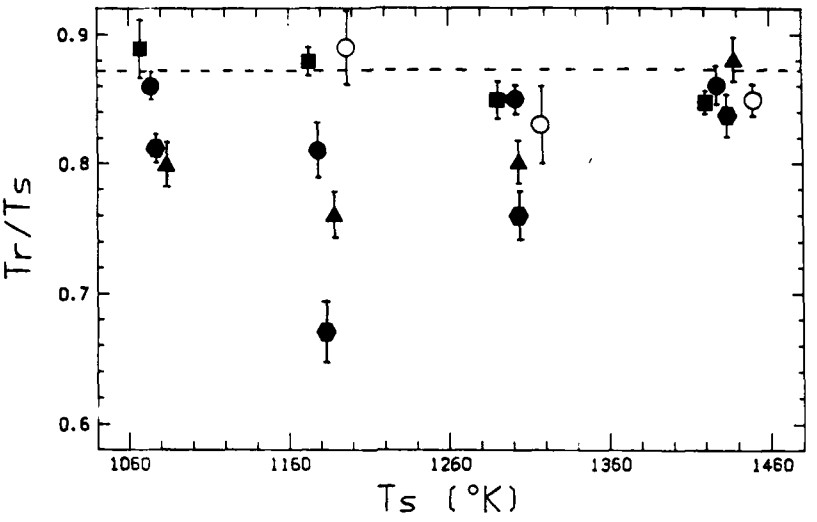

Fig. 1 Rotational accommodation versus Ts for different dosing mixture ratios. X = .1, ■; X = .25, ●; X = 1, ⬢; X = 2, ▲, for the NO_2 system and X = 1, ○, for the O_2 system.

1303, and 1433 K. OH signal levels at 1080 K were too low to be detected. The results are indicated in fig. 1 by open circles and are in good agreement with the low O-coverage results of the $NO_2 + H_2$ system as well as with those in reference 2. This is consistent with the fact that for Ts < 450 K, O_2 dosing leads to an O (2 X 2) overlayer on Pt(111) with a saturation coverage of $\theta = .25$[1]. Consequently, kinetic effects limit the $O_2 + H_2$ system to low O-coverage. For sufficiently high NO_2 dosing fluxes, on the other hand, adsorbed O occupies additional surface sites within the 2 x 2 overlayer, leading to saturation coverages of $\theta = .75$. This coverage difference is consistent with a site specific mechanism for the surface temperature dependence of α.

APPARENT ACTIVATION ENERGY FOR OH DESORPTION

Only the apparent activation energy for OH desorption is measured in these experiments since no attempt is made to account for the variation in OH coverage resulting from shifts in the surface chemical equilibia and changes in the reactant sticking probabilities with Ts. Ea is determined by monitoring the rate of OH desorption vs Ts via the $R_1(5)$ rotational transition. This approximation is justified by the agreement between the value of Ea obtained in this manner and the value obtained by summing intensities from all R_1 transitions[2]. In fig. 2 we present results for the $NO_2 + H_2$ and $O_2 + H_2$ systems, the latter taken from ref. 2. Both sets of data exhibit a rise in Ea as the dosing mixture becomes increasingly H_2 rich. For the $NO_2 + H_2$ case, Ea varies from 25 to 38 kcal/mole as X decreases from 2 to .05. The dependence of Ea on the dosing ratio for the $O_2 + H_2$ case is similar except the increase in the apparent activation energy occurs for lower oxidant to H_2 ratios. Since the rise in Ea correlates with decreasing [O(ads)], the difference between the two systems is consistent with the greater sticking probability and consequent higher O coverages of NO_2. The dependence of Ea on [O(ads)] has been reproduced in a kinetic model and

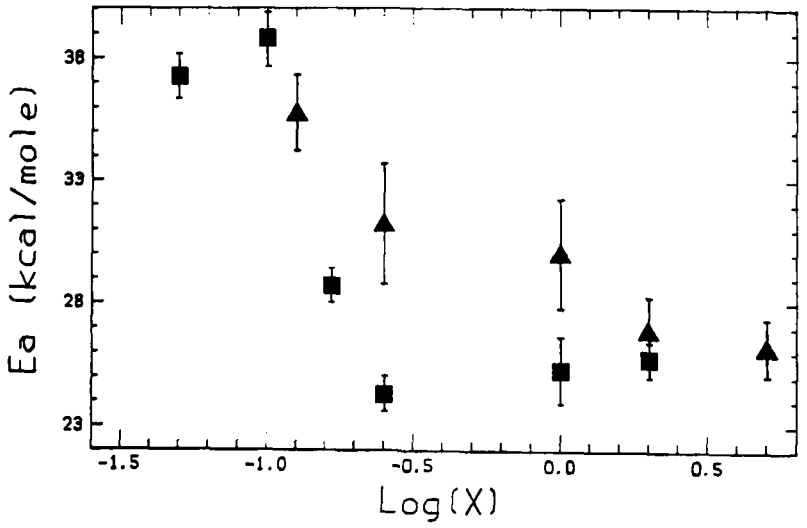

Fig. 2 Apparent activation energy for desorption, Ea, versus Log(X) for the NO_2 (■) and O_2 (▲) systems.

attributed to complex changes in the equilibria of the surface reactions[2]. Repulsive lateral interactions between adsorbed O-containing species might also contribute to the Ea dependence, as has been shown to occur in the desorption of NO following dissociative adsorption of NO_2 on Pt(111)[3].

CONCLUSIONS

We have presented evidence for the influence of surface coverage on the desorption dynamics of OH radicals on a Pt(111) surface. While the Ea dependence on coverage has been previously discussed for the $O_2 + H_2$ system[2], the Ts and X dependence of α is new. There is good evidence that α decreases with increasing [O(ads)] for Ts > 1183 K. However, the mechanism responsible for α's behavior at temperatures < 1183 K is open to further speculation until more evidence becomes available. In either case, there are no obvious mechanisms by which the O coverage influences the rotational energy of the desorbing OH radicals. Further understanding in this area must await the development of better gas-solid potential energy surfaces.

REFERENCES

1) D. Dahlgren, J. Heminger, Surface Science, 123, (1982), L739
2) D.S.Y. Hsu, M.A. Hoffbauer, M.C. Lin, Surface Science, 184 (1987), 25
3) J. Segner, W. Vielhaber, G. Ertl, Israel J. of Chem., 22 (1982), 375

ArF EXCIMER LASER PROCESSING OF PECVD AND LECVD SILICON OXYNITRIDE THIN FILMS: LOCAL CHANGES IN DUV TRANSPARENCY AND COMPOSITION

J. Neal Cox, L. Friedrich, L. L. Heath, and B. L. Sun
Intel Corp, Components Research, Santa Clara, CA 95051

Robert Kolenkow
General Signal Thinfilm Co., Fremont, CA 94539

ABSTRACT

The deep ultra-violet (DUV) transparency and composition of silicon oxynitride (SiNO) and silicon nitride (SiN) thin films formed by plasma enhanced chemical vapor deposition (PECVD) and excimer laser enhanced CVD (LECVD) were measured. Deposited onto silicon (SI), sapphire (SA), and quartz (QZ) wafers, the films were characterized by Fourier transform infrared (FTIR), wavelength dispersive x-ray (WDX), and ultraviolet/visible (UV/VIS) spectroscopies. In addition to varying these properties by altering the reactor deposition parameters, changes also were studied as a function of single pulse and high repetition rate exposures of the films to the output of an ArF excimer laser at different pulse energies. Single pulse experiments caused no changes, while high repetition rate exposures modified the films. The effects were greater for the QZ and SA samples, which are the more thermally insulating substrates, than the SI samples, suggesting that the changes occur via local heating of the film. The major effect on composition caused by laser exposure was the loss of hydrogen bound to silicon (SiH) and to nitrogen (NH). Overall, a decrease in the SiH had the strongest correlation with an increase in UV transparency. Adjusted to the basis of a one micrometer film, exposure of a PECVD QZ sample increased its transmittance at 200 nm from 1% before irradiation to 10%, a contrast of 10, while an SA sample increased from 10% to 25%, a contrast of 2.5. Laser exposure of LECVD SiN films--produced with silicon-rich, nearly stoichiometric, and silicon-deficient Si:N ratios--showed maximum contrasts of 1 (no effect), 7, and 50, respectively, but the films were strongly absorbing at the wavelengths of maximum contrast. The nature of the photo-modifiable, UV-absorbing defect is discussed.

INTRODUCTION

SiN (Si_xN_y:SiH_a,NH_b) and SiNO ($Si_xN_yO_z$:SiH_a,NH_b,OH_c) thin films are widely used in VLSI manufacturing. Applied in the device itself as an interlayer dielectric and as the top passivation, they are also used as sacrificial layers in etch and implant steps. Effort has been devoted to their development as thin gate dielectrics, as well as in X-ray and DUV mask technologies. Deposited by a variety of processes, SiN films are not typically stoichiometric Si_3N_4, but contain from 10 to 30 atomic percent hydrogen as SiH and NH. When oxygen is added to form SiNO, the hydroxyl group (OH) is also present as a contaminant.

These films exhibit a UV absorption band edge that, depending upon composition and processing, can be found at wavelengths as long as 450 nm. Early work on SiN films demonstrated a positive correlation between a blue shift in the edge and a decrease in hydrogen content as the films were furnace annealed above 600 °C, too high a temperature for many applications in VLSI manufacture.[1] Thermal sensitivity and optical absorption in the UV provide mechanisms for thin film processing subsequent to deposition. The availability of ArF excimer lasers opens the possibility for film-selective thermal annealing in which only the SiNO layer reaches the maximum temperature. Direct electronic excitation may also lower the required minimum temperature. The ability to focus the laser beam to a submicron spot size would be desirable in certain applications, such as DUV mask generation or performance as a passive programming element for an EPROM device in which UV-transparent windows are selectively opened. This feasibility study defines the critical factors for ArF laser processing, explores the compositional space available to SiNO films, examines the nature and structure of the modifiable UV-absorbing defect, and gives estimates of the optical contrast obtained by laser exposure.

RESULTS

When PECVD SiNO films on SI, SA, and QZ were subjected to single pulse and to high energy/high repetition rate (40-110 mJ avg pulse energy/cm^2, 100 Hz for 30 sec) laser exposures, the former exposure mode caused no changes in the film, while the latter caused a marked increase in UV transparency (measured by UV/VIS transmission and reflection) and a decrease in both SiH and NH (measured by FTIR). The effects were greatest for the QZ, and least for the SI, samples. With QZ being the most thermally insulating, and SI the least, the data is consistent with a thermally controlled, rather than a direct electronic mechanism.

Film composition and UV transparency can also be modified by varying the deposition conditions used in the PECVD reactor. For the composition matrix examined in this study, experiments showed that an increase in UV transparency was accompanied by a decrease in SiH and an increase in NH. A very slight decrease in Si content, measured by WDX, was also observed. Thus, for both the laser exposure and composition matrix studies, the increase in UV transparency is consistent only with a decrease in SiH. The photo-modifiable defect, then, is associated with hydrogen bound to silicon, while the changes in NH are coincidental.[2]

SiH is not the entire story. LECVD was used to produce three different compositions of silicon nitride films on QZ substrates.[3] WDX showed the compositions were as follows (Atomic Percent Si:N): 52:48 (Si-rich), 45:55 (nearly 'stoichiometric' 3:4, or 45:60), 39:61 (Si-deficient). The atomic percent of hydrogen was not factored into this data. Upon laser irradiation, the Si-rich sample showed no change, the 'stoichiometric' sample showed a slight increase, while the Si-deficient sample showed a marked increase in UV transparency. Thus the photo-modifiable site may involve a nitrogen defect structure. Fig 1. shows the spectra for the 39:61 sample before and after exposure. "Contrast" is defined as the ratio,

$$C(t,\lambda) = T_i/T_u \qquad (1)$$

of irradiated (i) to unirradiated (u) transmittances at a given wavelength, λ, for a film of thickness, t. For the 1 μm film in Fig 1., a maximum contrast of 50 was achieved near 200 nm, which unfortunately is also a region of strong absorption. However, a contrast of 10 occurs near 225 nm, where the film is reasonably transmissive.

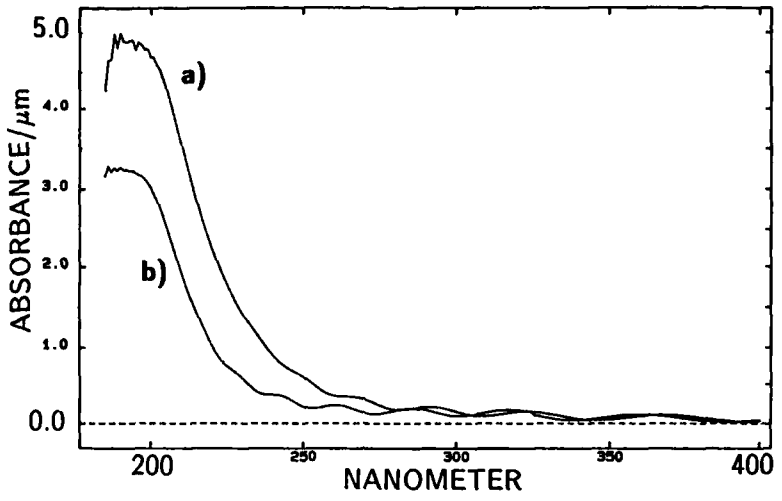

Figure 1. Transmission spectra in absorbance units of an LECVD silicon-deficient SiN thin film on a QZ substrate, a) before and b) after exposure to the output of an ArF laser.

CONCLUSIONS

ArF lasers can be used to modify the UV transparency of SiNO and SiN thin films. The mechanism is thermally controlled, but a possible electronic enhancement of the effect in comparison with furnace anneals has not been ruled out. The photo-modifiable site involves SiH, possibly associated with a nitrogen-related defect structure. Contrasts of 10 have been observed at wavelengths where the films are reasonably transparent. Still, the results show that the class of SiNO and SiN materials present a very large compositional space that must be explored in order to optimize the laser process.

REFERENCES

1. H. J. Stein, V. A. Wells, R. E. Hampy, J. Electrochem. Soc., **126**, 1750 (1979).
2. J. N. Cox, L. B. Friedrich, L. L. Heath, and B. L. Sun, J. Vac. Sci. Techol. B, to be published (1989).
3. G. A. Roche and R. S. Zorich, Technical Proceedings, SEMICON WEST, 264 (1988).

LASER ABLATION/FOURIER TRANSFORM MASS SPECTROMETRY OF POLYMERS

William R. Creasy and J. T. Brenna
IBM Corporation, 1701 North St. (T43)
Endicott, NY 13760

ABSTRACT

Laser ablation/ionization followed by Fourier transform mass spectrometry is used to identify and characterize polymers. The mass spectra of several polymers are discussed, including polyimide, polyamic acid, Dupont Tefzel, and polyphenylene sulfide.

INTRODUCTION

A difficult problem in surface science and analytical chemistry is the identification of organic contaminants on surfaces, especially nonconducting surfaces. This problem is particularly important in electronics packaging, due to the large variety of polymers and organic compounds used in manufacturing processes.

In order to address this problem, a laser microprobe system has been developed for use on a Fourier transform ion cyclotron resonance mass spectrometer (FTMS). This system is being characterized by analyzing known reagent-grade polymers to determine their mass spectra. In addition, it is helpful to understand the physical processes in laser ablation/ionization that relate to ion formation. This understanding makes it simpler to relate the observed mass spectrum to the polymer composition, and it may also be important in materials processing applications.

EXPERIMENTAL

The laser microprobe system is described in detail in a publication.[1] The system is used with a Nicolet FTMS/2000 Fourier transform mass spectrometer to provide high mass resolution and a large mass range for detection and identification of ablated ions. In addition, FTMS has the capability of multiple stages of ion separation and fragmentation, called MS/MS, for identification of ion fragmentation patterns for structural determination. FTMS is a pulsed mass spectrometry technique which allows measurement of a complete mass spectrum with a single laser pulse, or signal averaging using many pulses, to optimize either spatial resolution or signal. The laser system which is used is a Quantel Nd:YAG laser at a wavelength of 266 nm. The spatial resolution of the optical system used to focus the laser beam has been characterized to be 5-10 um.

RESULTS AND DISCUSSION

Polyimide (Dupont Kapton®) is used extensively in packaging applications, and a study of its laser ablation/ionization properties using this technique has already been published.[2] The ions consist of carbon cluster ions and hydrogenated carbon cluster ions, which are not related to the polyimide structure. These ions probably arise from gas phase or plasma reactions following laser ablation of the polymer. The negative ion mass spectrum has large peaks for the ions CN^-, OCN^-, and C_3N^-, which are formed from fragmentation of the ablated material into small species. The mass spectra are unique to polyimide, and they can be obtained from nanogram quantities of material.

Polyamic acid, which is the precursor to polyimide before curing, has also been studied. The positive and negative ion mass spectra are distinct from polyimide. The ions which are observed can be related to fragments of the polymer chain. The large differences in the mass spectra between polyamic acid and polyimide suggest that studies of the curing process may be possible with this technique.

A polymer with interesting laser ablation properties is Dupont Tefzel®, which is a copolymer of ethylene and tetrafluoroethylene.[3] Laser ablation for 50 to 70 laser pulses on one spot produces a distribution of high mass carbon cluster ions, including a large C_{60}^+ peak. However, after 70 pulses, the mass spectrum changes dramatically, and lower mass fragment ions are observed, including a large peak at mass 77. The change in the mass spectrum is accompanied by visible blackening of the surface of the polymer. This result provides a dramatic example of the modification of a polymer surface by laser radiation.

Polyphenylene sulfide has an unusual positive ion mass spectrum,[4] as shown in Figure 1. The polymer consists of a chain of phenyl groups attached by sulfur atoms. The ions in the mass spectrum can be assigned to combinations of different numbers of phenyl groups (designated by "P" in Figure 1) with zero to five sulfur atoms (shown by vertical lines). There is also a considerable amount of dehydrogenation, shown by the groups of peaks at each combination.

The mass spectra for these polymers show that several different ionization mechanisms can occur for different polymers. The mechanisms range from direct fragmentation of the polymer chains to gas phase fragmentation, recombination, and condensation reactions in the laser-generated plasma.

In addition to the polymers which have been discussed, approximately twelve other reagent-grade polymers have been studied. All of them give distinct mass spectra, showing that unequivocable identification of small quantities of unknown polymers is possible. However, the observed ions are not

necessarily structurally related to the polymers. Therefore, determination of the identity of an unknown requires that its mass spectra be compared to those of known polymers. Further work is in progress to determine the effects of additives in the polymers, and to measure depth profiles.

REFERENCES

1. J. T. Brenna, W. R. Creasy, W. McBain, and C. Soria, Rev. Sci. Instrum. 59, 873 (1988).
2. W. R. Creasy and J. T. Brenna, Chem. Phys., in press.
3. W. R. Creasy and J. T. Brenna, J. Phys. Chem., submitted for publication.
4. W. R. Creasy and J. T. Brenna, manuscript in preparation (Anal. Chem.).

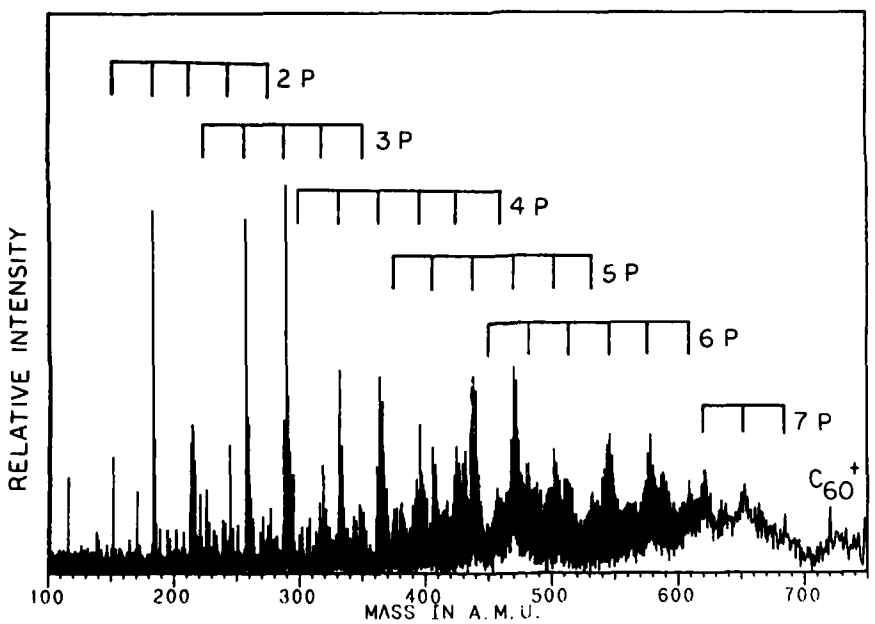

Figure 1: Positive ion mass spectrum of polyphenylene sulfide. Numbers with "P" designate numbers of phenyl groups in the ions, and vertical lines show different numbers of sulfur atoms, 0 to 5 S except for 7 P, which is 3-5 S.

Time-Resolved Laser Probes of Surfaces

H. W. K. Tom
AT&T Bell Laboratories, Holmdel, NJ 07733

ABSTRACT

Laser-based probes can be used to study the dynamics of surface reactions and phase transitions on timescales as short as a few femtoseconds. Here we report the results of an experiment in which visible frequency second harmonic generation is used to follow the change in structural symmetry of crystalline silicon as it evolves, after the silicon has been electronically excited with a 100 femtosecond optical pulse. We also report development of a picosecond high-repetition rate infrared source which may be used for time-resolved vibrational studies of molecular adsorbates on surfaces.

INTRODUCTION

One of the most compelling reasons for using laser-based probes of surfaces is that processes can be time-resolved down to a few femtoseconds. A typical use of time-resolved probes is to measure excited state lifetimes. A measurement of electronic and vibrational lifetimes as well as transfer times between excited states should give great insight into the microscopic dynamics of surface electronic structure, adsorbate-substrate and adsorbate-adsorbate interactions. Another use of time-resolved probes is to use the time-delayed probe to follow changes in state due to the photo-initiating pump pulse. In this way chemical or structural intermediates in a reactions may be identified. A more subtle use of time-resolved probes is to discriminate the role of a particular degree of freedom by probing the effect of exciting one degree of freedom before energy equilibrates to other degrees of freedom. In particular, because the electron-phonon relaxation time in semiconductors is around 100 fsec, it is possible to photo-excite a semiconductor with 100 fsec optical pulses and create an electronically excited but vibrationally cold system. Reactions that occur before substantial energy can be transferred to the vibrational degrees of freedom may be considered to be induced by the electronic excitation.

In the first section of this talk, I will briefly summarize an experiment[1] of the latter kind, in which we explore the question posed several years ago by Van Vechten, *et al*[2], whether or not crystalline Si can be driven to disorder by electronic excitation without the lattice modes equilibrating at a temperature above the melting temperature. We use visible frequency second-harmonic generation to follow the time evolution of the crystal symmetry after electronic excitation with 90 fsec pulses. While second harmonic generation is sensitive to surface structure and to some extent surface composition, it lacks chemical specificity. In the second section, I will describe a new high-repetition rate, picosecond mid-infrared source more suitable for studies of molecular adsorbates.

SECOND HARMONIC GENERATION PROBE OF SURFACE SYMMETRY

Second harmonic (SH) radiation at frequency 2ω is generated in reflection from an interface illuminated with laser radiation at fundamental frequency ω. Surface sensitivity is obtained at interfaces between centrosymmetric media because SH is dipole-allowed at interfaces where centrosymmetry is broken but dipole-forbidden in centrosymmetric bulk media. In the present case of Si excited with 2 eV fundamental, the escape depth of the 4 eV SH limits the contribution of the bulk to the top 75 - 130 Å of the sample. In contrast, the interface contribution to SH comes from the Si-SiO_2 interface which is 5-10 Å thick.

The dipole-allowed source polarization for the SH from the surface can be written $P(2\omega) = \chi:E(\omega)E(\omega)$ where χ is the nonlinear susceptibility tensor. The sensitivity of SH to structure[4] comes from the symmetry of χ. This symmetry is easiest to observe by noting the anisotropy of the SH intensity as a crystalline sample is rotated about its surface normal. Three elements of χ are nonzero for all symmetries: these isotropic elements contribute to the SH regardless of the sample orientation. For the (111) surface which is 3m symmetric, there is an additional element $\chi_{\xi\xi\xi}$, where the ξ-axis is the $[2\bar{1}\bar{1}]$-axis in the surface plane. The element $\chi_{\xi\xi\xi}$ produces 3-fold rotational anisotropy in the SH. The dipole-forbidden source polarization for the cubic bulk media is $P_i(2\omega) = \gamma\nabla_i E^2(\omega) + \zeta E_i(\omega)\nabla_i E_i(\omega)$ where the axes i are the principal axes of the cubic crystal. The isotropic susceptibility γ contributes to the SH equally for any crystal orientation, while the anisotropic susceptibility ζ produces rotational anisotropy.

It can be shown using the equations in Ref. 4 that it is possible to choose the polarization of fundamental and detected SH and to choose the sample orientation to isolate the anisotropic susceptibility tensor elements. If one orients the Si(111) so the $[2\bar{1}\bar{1}]$ axis is perpendicular to the plane of incidence and uses *p*-polarized fundamental radiation, the *p*-polarized SH will be from isotropic elements of χ and γ while the *s*-polarized SH will be from $\chi_{\xi\xi\xi}$ and ζ. If cubic symmetry is lost the latter (*s*-polarized SH) should become zero, while the former (*p*-polarized SH) should only change if the net order-independent susceptibility in the sample changes, for example if the material becomes less covalent or more metallic.

STUDY OF LASER-INDUCED DISORDER OF Si

The possibility of laser-inducing disorder before achieving melting temperatures has obvious practical importance in laser-assisted semiconductor processing and surface photochemistry in general. It is of fundamental interest because the dynamics of electron-phonon equilibration may directly effect the evolution of the phase transition. Moreover, the physical picture of how Si might be disordered by non-equilibrium electronic excitation is appealing. Silicon is well described by a tight-binding model in which the valence band acts as bonding charge while the conduction band electronically screens coulomb interaction. Electronic excitation should weaken the interatomic bonding and thus lower the vibrational energy required to disorder.

The experiments are very similar to those reported in Refs. 5 and 6. Laser pulses of 75 fsec duration (110 fsec FWHM autocorrelation) were obtained by dispersion-compensating the amplified output of a colliding pulse mode-locked laser operating at 610 nm. To make the excitation relatively uniform over the probe spot we used a smooth spatially filtered beam profile (central Airy spot) and focussed the excitation and probe beam to diameters of 75 and 25 μm respectively. Our sample was a Si wafer (B-doped, 1800 Ω-cm) with a native oxide and the experiments were conducted in air. The excitation and probe beams were incident at -20° and 30° to the surface normal, respectively, to avoid scattered SH from the excitation pulse from dominating the much weaker probe SH signals. A different position on the sample was used for each shot of the laser.

In Fig. 1, the top two panels show the *s*- and *p*-polarized SH signals from a Si(111) sample as a function of probe time delay with respect to the excitation pulse. The crystalline axes and polarizations were oriented as discussed above so that the *s*-SH is proportional to $\chi_{\xi\xi\xi}$ and ζ and the *p*-SH is the isotropic signal. The two SH polarizations were separated by a beam-splitting polarizer, and simultaneously detected with a pair of photomultiplier tubes and gated electronics. The third panel, Fig. 1c, shows the sum-frequency signal obtained from mixing the excitation pulse and probe pulse on the surface. This signal emerged near normal to the surface and was detected with a third PMT. It measures the arrival of the pump pulse with respect to the probe and the effect of the non-collinear excitation geometry in increasing the intensity cross-correlation FWHM to 180 fsec. The dashed line is a fit with the autocorrelation of intensity $I(t) = \mathrm{sech}^2(t/t_p)$ where t_p = 67 fsec. Fig. 1d shows the *p*-polarized linear reflection of the probe as a function of probe time delay. All four traces were obtained with laser excitation at twice threshold (0.2 J/cm^2 peak intensity) where the after-the-fact melt spot was measured with an optical microscope to be 75 μm.

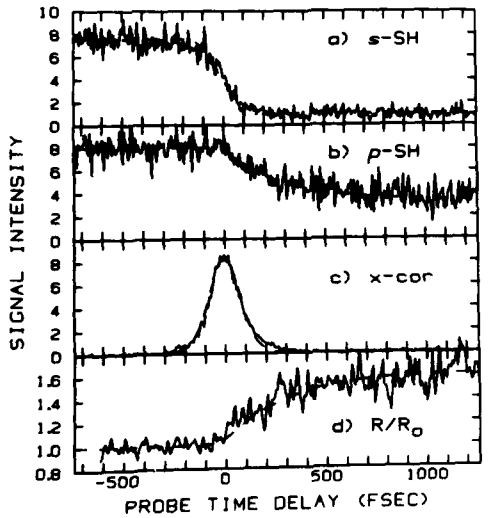

Fig. 1. Signal intensity from Si(111) surface vs. probe time delay after a 2 X threshold pump pulse. Panels from top: a) *s*-polarized SH, b) *p*-polarized SH, c) pump-probe cross-correlation, d) *p*-polarized linear reflection. Solid line: data. Dashed line: fits explained in text.

This fluence was sufficient to photoexcite 1.25% of the valence band (4 electrons per Si atom) assuming linear absorption[7] since the excitation energy, 2 eV, was far above the bandgap we may estimate that the maximum excitation density including such nonlinear absorption effects[8] as free-carrier absorption, bandgap renormalization, and two-photon absorption was 2.5% of the valence band. The probe intensity was kept below 0.02 J/cm^2 to insure that only the pump pulse induced the phase transition.

One sees in Figs. 1a and b that the order-dependent SH signal $|E_{s,111}|^2$ disappears in less than 150 fsec while the order-independent signal $|E_{p,111}|^2$ decreases in 500 fsec to a lower value. The data in Fig. 1a can be fit with the dashed curve $E_{s,111}(t)=A_f+(A_0-A_f)\exp((t_0-t)/t_A)$ where t_0 = 53.3 fsec and t_A = 100 fsec for $t>t_0$. $E_{s,111}(t)$ has been convolved with the sech^2 time profile of the probe pulse. An abrupt change in $E_{s,111}(t)$ does not fit the data as well. The action seems to begin well before the excitation pulse is over. We have given $E_{s,111}(t)$ a constant background A_f which we attribute to material at the edges of the probe beam that was excited below threshold. We can fit the data of Fig. 1b with $E_{p,111}(t)=B_f+(B_0-B_f)\exp(-t/t_B)$, where t_B = 333 fsec. The ratio between final and initial values of B_f/B_0 = 0.633. For lower pump intensity the SH signals change on the same timescales but to different saturation values consistent with the size of the after-the-fact damage spot decreasing. No change is seen in either SH signal for pump intensity at half the melting threshold when the damage spot is only a few microns in diameter.

The most striking result is the sudden loss of cubic structural symmetry shown by the rapid decrease in the anisotropic *s*-polarized SH. To resolve whether this loss of order was due to a change in symmetry at the surface (through $\chi_{\xi\xi\xi}$) or in the bulk (through ζ), we performed analogous experiments on the (100) surface of Si. For the (100) surface which is 4m symmetric, rotational anisotropy in SH comes only from ζ [Ref. 4]. We found[1] the *s*- and *p*-polarized SH from Si(100) could be fit by the same time functions as used for the Si(111) data. This showed that the fast changes are due to changes of the electronic properties of the topmost 75 to 130 Å of bulk silicon rather than from the Si-SiO$_2$ interface. The uncertainty in the 75 to 130 Å depth is due to uncertainty of the Si linear dielectric constant which lies between liquid[9] and solid values, respectively.

The fast decrease of ζ implies that the top 75 to 130 Å is disordered in < 150 fsec. Atomic disorder in less than 2 electron-phonon relaxation times requires that the atoms move out of lattice positions directly because the electronic states have been changed. In a local picture, the fast atomic disorder is perhaps not surprising. Such rapid configurational relaxation probably occurs in

excited molecules as the Franck-Condon effect and in defects in solids as Jahn-Teller (symmetry-breaking) distortion. In a delocalized picture, however, it is somewhat more surprising. Photoexcitation reduces the forces holding the lattice together by both depleting bonding charge and by increasing the electronic screening between charges. Van Vechten, *et al*[2] originally proposed that if around 10% of the valence band were promoted to the conduction band (40% of the Si atoms were singly excited) then the bonding would be sufficiently weakened to make the lattice unstable to shear stress. Biswas and Ambegaokar[10] calculated the phonon spectrum of Si as a function of excited electron-hole density and showed that TA phonons go soft at the [111] zone boundary when 4.5% of the valence band is excited. Because the lattice modes are equilibrium properties and do not take into account the dynamics of random atomic motion during the sudden change in bonding charge, the 4.5% density is the value at which the bonding is so much weakened that there is no restoring force to bond shearing ($\perp$ to the [111] direction). In the experimental case, not only are bonds weakened upon the initial photoexcitation, but also coherent phonons can be created (through phonon-assisted absorption) and there is time during the first 100 fsec for each carrier to excite a phonon. Under these conditions restoring forces may become sufficiently weak for local atomic motion to disorder the lattice. It may then be reasonable that disorder could occur at the experimental excited carrier densities which are 2 to 4 times less than the 4.5% calculated figure. While the excitation of some phonon modes may be essential to the disordering process, it is clear that the lattice disorders while still vibrationally cold compared to the equilibrium melt.

The slow decrease in the order-independent (*p*-SH) signal shows that once threshold for disorder is exceeded, the highly excited system does not attain equilibrium for at least several hundred fsec. This conclusion applies equally well if we model the process as occurring homogeneously in the top 130 Å layer with a 333 fsec time constant or as occurring in a thin expanding layer (as in Ref. 5) but with the nonlinear susceptibility approaching liquid value equal to 0.633 times the solid value in approximately 300 fsec. In the latter case, we use a fit (shown in dashed line) to the *p*-polarized linear reflection in Fig. 1d to set the layer expansion rate at $v=2X10^6$ cm/sec. The fact that neither the SH nor the linear reflection change dramatically during the first 50 fsec of excitation strongly suggests that the disordered Si remains a semiconductor rather than changes to a metal. The semiconductor-metal transition must change the valence from 4 to >6 and in equilibrium is accompanied with a 10% volume reduction.[11] The 300 fsec time delay may be due both to the time delay required for vibrational excitation to exceed melting threshold (in analogy to the Lindemann criterion[12]) or for lattice contraction.

We must mention one caveat to the analysis. That is that optical probes in the visible and UV measure electronic susceptibilities rather than atomic structure directly. We can not rule out the possibility that the laser excitation bleaches the valence-conduction band transition or that the high carrier density screens the cubic ionic potential. However, severe bleaching is probably unlikely because there are no abrupt changes in linear reflection or *p*-polarized SH. We can argue that screening[13] is also unlikely to cause a complete loss of the cubic electronic symmetry, since for Si even the carriers in the conduction band see a fairly strong cubic potential as evidenced by the non-spherical band structure.[14] While these arguments are not a proof, there is convincing reason to believe that the rapid reduction in the *s*-SH is due to atomic disorder in < 150 fsec.

We have shown that second harmonic generation has great potential as a time-resolved probe of laser-induced reactions on surfaces. Similar experiments on laser-induced melting of other materials such as metals, laser-induced diffusion across interfaces, and laser-induced reactions such as molecular desorption are in progress. However, one major problem with second harmonic generation is that it is not chemically specific and will be less useful for investigating chemical reactions. We have therefore begun to develop a laser source for time-resolved infrared vibrational spectroscopy.

TIME-RESOLVED VIBRATIONAL STUDIES OF MOLECULES ON SURFACES

Several laser-based techniques for time-resolved vibrational studies of adsorbates on surfaces have been developed. The main technical difficulty is that the vibrational spectrum of an adsorbate is <1% in reflection and transient changes in that spectrum require detection of 10^{-3} or better. Raman spectroscopy[15], and IR-visible sum-frequency mixing on the surface[16,17] can both exploit low noise visible photon detectors. While IR detectors are considerably more noisy than photomultiplier tubes, the IR photon flux from an IR laser can be sufficiently high that measurements are not limited by detector noise. Direct IR reflection has been used with 10 ns IR pulses to obtain the spectra of CO on Pt(111)[18] and picosecond time-resolved measurements of adsorbates vibrational lifetimes have been measured in dispersed media.[19]

To specifically address the problem of small signal detection we built a high repetition rate IR source compatible with lock-in techniques.[3] The heart of our system (see Fig. 2) is a cw mode-locked Nd:YAG laser which produces 90 psec 1.06 μm pulses at 76 MHz. The frequency-doubled output at 0.532 μm is used to synchronously-pump a dye laser running with Exciton LDS 867. Using three different output couplers we can tune the dye laser over the three ranges 833-907 nm, 857-932 nm, and 883-953 nm. The remaining radiation at 1.06 μm is fiber-grating compressed to ~4 psec. Approximately 800 mW of 1.06 μm radiation is then mixed with 4 to 40 mW of dye laser output in Type I phase-matched $AgGaS_2$ to generate IR.[20,21] The input beams are focussed to ~50 μm diameter and the $AgGaS_2$ crystal is 1.2 mm long. For the three different dye laser output couplers, we can then tune the difference frequency over the ranges: 1626-2606 cm^{-1}, 1457-2254 cm^{-1}, and 1094-1926 cm^{-1}.

In Fig. 3 we show the IR output power vs. frequency for the second dye output coupler. An average power of 54 μW at 2200 cm^{-1} was obtained by mixing 800 mW of 1.064 μm with 45 mW of 862 nm. The output power and the phase- matching angles agree well with calculation using crystal data[21]. The fall off in power at longer wavelengths is mostly due to the decrease in dye laser output. For 3-, 2-, and 1-plate birefringent filters, the dye laser pulse duration was 2, 1.2, and 0.7 psec. Using the 3-plate filter in the dye laser, the difference frequency IR pulse duration was measured to be about 2 psec by comparing the cross-correlations of the 2200 cm^{-1} and the 2 psec 862 nm pulses with the 4 ps 1.064 μm pulse. It is reasonable to believe that the IR pulse width follows closely the dye laser pulse width considering the group velocity dispersion is negligible for the 1.2 mm crystal and the phase-matching efficiency falls to half maximum when the frequency detuning is swept from -20 to +20 cm^{-1}. The pulses were close to transform-limited. The frequency full-width half-max was measured to be 25 cm^{-1} and 7 cm^{-1} for the 0.7 and 2 ps pulse cases. Currently, both IR pulse width and wavelength are limited by the dye laser.

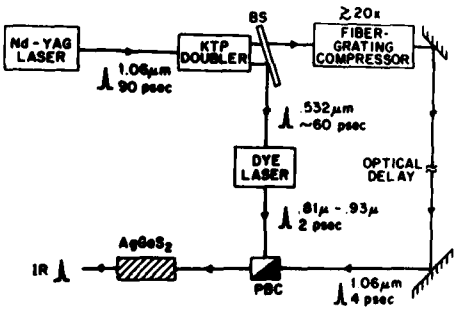

Fig. 2: Schematic of the laser system used to generate IR. BS represents a dichroic beam splitter, PBC represents a polarizing beam combiner.

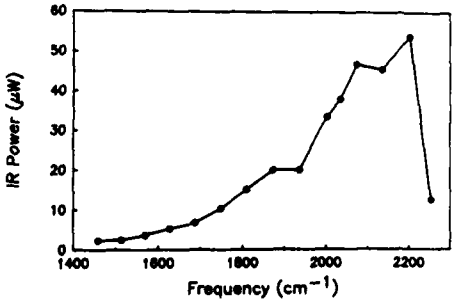

Fig. 3: IR output power as a function of IR wavelength. The circles are data. The line is a guide to the eye.

Because of the high laser fluence, we expect intrinsic IR detector noise to limit our sensitivity to differential reflectivities only at the 10^{-6} level for 60 sec averaging times. This corresponds to a 10^{-4} change in the IR spectra of CO on a metal substrate. An experiment to measure changes in the CO stretching frequency as the metal-adsorbate system is electronically excited and heated by a visible laser pulse is in progress.

SUMMARY

Time-resolved visible frequency second-harmonic generation experiments on Si suggest strongly that electronic excitation can induce reactions in bulk media. They further suggest that one should be able to observe photo-induced substrate-mediated surface reactions on 100 fsec time-scales. While studies of such reactions should give us a more fundamental understanding of this first step in photochemistry at surfaces, the community should push forward on techniques such as vibrational spectroscopy that can reveal how adsorbates or reactants change during photochemical reactions.

I would like to acknowledge useful discussions about the Si work with C. H. Brito-Cruz, C. V. Shank, R. L. Fork, D. Chemla, Y. R. Shen and I. Boyd and the technical assistance of G. D. Aumiller and F. Beiser. The IR laser source was developed jointly with A.G. Yodh, with assistance at earlier times by S. Chu and M. Feller.

REFERENCES

1. H. W. K. Tom, G. D. Aumiller, and C. H. Brito-Cruz, *Phys. Rev. Lett. 60*, 1438 (1988).
2. J. A. Van Vechten, R. Tsu, and F. W. Saris, *Physics Letters 74A*, 422 (1979).
3. A.G. Yodh, H.W.K. Tom and G.D. Aumiller: "Generation of Tunable Mid-IR Picosecond Pulses at 76 MHz," Proceedings of Conference on Lasers and Electro-Optics, 25-29 April, 1988, Anaheim, CA, paper THX5.
4. H. W. K. Tom, T. F. Heinz, and Y. R. Shen, *Phys. Rev. Lett. 51*, 1983 (1983).
5. C. V. Shank, R. Yen, and C. Hirlimann, *Phys. Rev. Lett. 50*, 454 (1983).
6. C. V. Shank, R. Yen, and C. Hirlimann, *Phys. Rev. Lett. 51*, 900 (1983).
7. M. C. Downer and C. V. Shank, *Phys. Rev. Lett. 56*, 761 (1986).
8. T. F. Bogess, Jr., A. L. Smirl, S. C. Moss, I. W. Boyd, E. W. Van Stryland, *IEEE J. Quantum Electron. 21*, 488 (1985).
9. G. E. Jellison, Jr. and D. H. Lowndes, *Appl. Phys. Lett. 47*, 718 (1985); K. M. Shvarev, B. A. Baum, and P. V. Gel'd, *Sov. Phys. Sol. St. 16*, 2111 (1974).
10. R. Biswas and V. Ambegaokar, *Phys. Rev. B 26*, 1980 (1982).
11. V. M. Glazov, S. N. Chizhevskaya, and N. N. Glagoleva, *Liquid Semiconductors*, (Plenum, New York, 1969), p. 61.
12. J. M. Ziman, *Principles of the Theory of Solids* (Cambridge Univ. Press, Cambridge, England, 1972), p. 65.
13. H. M. van Driel, *Appl. Phys. Lett. 44*, 617 (1984).
14. M. L. Cohen and V. Heine, in *Solid State Physics*, eds. H. Ehrenreich, F. Seitz, and D. Turnbull (Academic, New York, 1970) Vol. 24, p. 38.
15. X. Jiang and A. Campion, *Chem. Phys. Lett. 140*, 95 (1987).
16. P. Guyot-Sionnest, J. H. Hunt, and Y. R. Shen, *Phys. Rev. Lett. 59*, 1597 (1987).
17. A. L. Harris, C. E. D. Chidsey, N. J. Levinos, D. N. Loiacono, *Chem. Phys. Lett. 141*, 350 (1987).
18. D. S. Bethune, M. D. Williams, and C. A. Luntz, *J. Chem. Phys. 88*, 3322 (1988).
19. E. J. Heilweil, J. C. Stephenson, and R. R. Cavanagh, *J. Phys. Chem. 92*, 6099 (1988).
20. T. Elsaesser, H. Lobentanzer and A. Seilmeier, *Opt. Comm. 52*, 355 (1985).
21. G. D. Boyd, H. Kasper and J. H. McFee, *IEEE J. Quantum Electronics QE-7*, 563 (1971).

OPTICAL SECOND HARMONIC GENERATION IN METAL MONOLAYERS AND METAL SURFACES

T. E. Furtak
Physics Department
Colorado School of Mines
Golden, Colorado 80401

J. Miragliotta
Exxon Research and Engineering Co.
Annandale, New Jersey 08801

ABSTRACT

Information about the structure of foreign metal monolayers can be obtained through measurements of the polarization dependence of optical second harmonic generation. We have used this phenomenon to monitor electrochemically controlled deposition of hexagonal metals on the (111) face of Ag. In the process, we have learned more about resonant second harmonic effects involving intrinsic excitations of the monolayer as well as surface influences within the Ag substrate.

Optical second harmonic generation (SHG) has been recently applied to a variety of interface characterization problems [1-4]. Its utility comes from the lower symmetry at the interface between centrosymmetric media. Under these conditions, normally forbidden electric dipole contributions to the second-order susceptibility lead to a surface-specific nonlinear polarization. The resulting SHG is related to the electronic structure of the interface and, through control of the orientation of the incident and detected electric field vector, can be used to reveal the symmetry of the interfacial region. This is particularly valuable in electrochemical experiments [1,2,5] where most alternative microscopic probes carry symmetry information only indirectly.

In experiments of this type it is important to carefully separate the field orientation dependence coming from the surface crystallinity from that due to p- and s-polarization effects, and also from the non-forbidden higher multipole contributions coming from the bulk [6]. We have avoided the first complication by performing our experiments at normal incidence. The second problem can only be overcome through surface modification.

We have studied Cd, Tl, and Zn electrochemically deposited on Ag(111) using a thin-layer sample chamber. The background electrolyte was an inert salt at a concentration of 0.3M, adjusted for suitable pH. Monolayer (ML) deposition could be separated from bulk plating through control of the applied potential. In all three cases a well-defined binding energy difference existed between the ML and multilayer conditions. We used an inexpensive 1 W CW Nd-YAG laser for excitation (focussed to a diffraction-limited spot on the sample), filters and a monochromator for spectral separation of the SHG, and a cooled photomultiplier with a lock-in amplifier for the electronic detection. The Ag crystal was mechanically and chemically polished to produce a strain-free, clean surface with an orientation uncertainty of one degree. Data were recoreded in two modes: (a) without polarizers in the light path the SHG was measured as a function of the coverage of the metal, and (b) at constant coverage and with a polarizer in front of the detector the SHG was measured as a function of the orientation of the optical field of the incident light.

In mode (a) all three metals led to dramatic increases in SHG just as the first ML was complete. We attribute this to resonant SHG within the ML caused by pseudo-interband transitions that are related to the parallel-band absorption in this class of hexagonal metals [7,8]. For Cd, the SHG intensity dropped to 50% of the maximum at the end of the second ML, while for the other metals the intensity leveled off to a nearly constant value for subsequent layers.

The optical field orientation experiments for the three metals were different. In the case of Cd the symmetry of the SHG fell into two types of behavior correlated with the two observed signal levels in mode (a). The ML structure showed a four-lobed pattern consistent with a 3m point-group having a mirror-plane perpendicular to [211] [9]. This is to be contrasted with expected contributions from the substrate, whose mirror-plane is perpendicular to [011]. We feel this behavior was caused by a buckled $\sqrt{3}x\sqrt{3}$ R30° overlayer which could be maintained only for one ML. The 3% compression was apparently relaxed at the completion of the second ML where the SHG intensity dropped and the altered symmetry pattern was observed. The latter consisted of a two-fold dependence on the incident field orientation. The resulting structure was most likely an incommensurate close-packed Cd lattice with arbitrary alignment over the Ag substrate.

The mode (b) experiments on Zn also showed a transition to an incommensurate phase after 2 ML. However

the first ML result had the same symmetry as the substrate, a reflection of an 8.6% expanded epitaxial relationship at low coverage. Similar symmetry information was obtained with Tl at low coverage. This metal would have to be compressed by 16.4% to achieve epitaxy--an unlikely possibility. We feel that Tl grows with a (6x6)-25Tl coincidence structure which would align with the Ag(111) surface within 0.2%. The Tl symmetry was maintained for higher coverages (up to 4 layers), a result of the unstrained primary layer structure.

We expect that optical SHG will grow in importance as a structural and electronic measurement tool for interfacial studies. We have demonstrated here how straightforward experiments can lead to an understanding of the symmetry of an electrochemically controlled system.

ACKNOWLEDGEMENT

This work was supported by the U. S. Department of Energy through the office of Basic Energy Sciences, grant number DE-FG02-86ER45253.

REFERENCES

1. G. L. Richmond, J. M. Robinson and V. L. Shannon, Prog. Surf. Sci. 28, 1 (1988).
2. J. Miragliotta and T. E. Furtak, Phys. Rev. B37, 1028 (1988).
3. J. F. McGilp and Y. Yeh, Solid State Commun. 59, 91 (1986).
4. H. W. K. Tom, T. F. Heinz and Y. R. Shen, Phys. Rev. Letters 51, 1983 (1983).
5. J. Miragliotta and T. E. Furtak, Surf. Int. Anal. 14, in press (1989).
6. J. E. Sipe, V. Mizrahi and G. Stegeman, Phys. Rev. B35, 9091 (1987).
7. P. Sinha and S. Chatterjee, J. Phys. F. 7, 105 (1977).
8. M. A. E. A. Ament and A. R. deVroomen, J. Phys. F. 7, 97 (1977).
9. J. E. Sipe, D. J. Moss and H. M. van Driel, Phys. Rev. B35, 1129 (1987).

REFLECTION AT A NONLINEAR INTERFACE

K. H. Strobl, R. R. Cuykendall, B. Bockhop and D. Megli
Center for Laser Science and Engineering
University of Iowa, Iowa City, IA 52242-1294

ABSTRACT

Numerical calculations[1] have led to interesting new aspects of the behavior of a light beam crossing an interface between linear and nonlinear media when a Gaussian beam instead of a plane wave is used. We report initial experimental results investigating that predicted behavior. Significantly increased switching was found compared with similar experiments[2] and the existence of hysteresis could not be confirmed. Our results disagree both quantitatively and qualitatively with the 2-d Gaussian model predictions.

INTRODUCTION

The Nonlinear Interface (NI) is commonly known in the literature as a plane interface between an ordinary dielectric and a nonlinear dielectric material with an intensity dependent index of refraction. If the nonlinear medium has a diffusion mechanism which delocalizes the induced index change (not strictly proportional to the local intensity value) we term it a Diffusive Nonlinear Interface (DNI) in order to distinguish it from the diffusionless case. Kaplan[3] studied the intensity dependence of the reflection of an NI in the plane wave case. He found that under certain conditions the reflectivity would exhibit a threshold behavior as a function of the incident electromagnetic field: for intensities below the threshold value the interface would be totally reflecting, and for intensities above the threshold, the interface would have significant transmission. He further predicted a bistable behavior (hysteresis) of the reflectivity of the NI for a range of input intensities just below the threshold value.

The predicted threshold behavior suggested a possible application of the NI for ultrafast optical switches, scanners, logic elements, etc. As a result, several theoretical and experimental investigations were started in order to study the behavior of the NI under more realistic situations. For example, Tomlinson et al.[1] studied the reflection of a focused Gaussian beam at an NI with a 2-d computer simulation and found a multiple threshold behavior associated with the creation of additional self-focused channels in the transmitted beam. An experiment performed by Smith and Tomlinson[2] showed qualitative agreement (strong indication for the existence of multiple thresholds). The quantitative disagreement was explained by the difference between the 2-d theoretical model and the 3-d experiment. They found a maximum reflectivity change (100% to 70%) for low and high incident intensities, which is significantly less than the 2-d theoretical model predicted (100% to 50%). The possible existence of hysteresis in connection with the NI is suggested

tensity case) in general decayed with time. Furthermore, we observed a slope decrease with time (due to laser-induced particle aggregation). For these reasons, we repolished the LiF crystal every time we exposed it to the nonlinear liquid, to achieve, as closely as possible, identical starting points.

DISCUSSION AND CONCLUSION

We found that the presence of surfactant strongly influenced the intensity dependence of the reflectivity. This can be seen clearly in Fig. 2 which shows the measured intensity dependence of the reflectivity for an incident glancing angle of $\Psi = 7.3°$ taken without (Fig. 2a) and with (Fig. 2b) surfactant. Each curve is normalized against the low intensity value for easier comparison. Without surfactant we got a reflectivity increase (Fig. 2a) with increasing intensity while we found a reflectivity decrease (Fig. 2b) for the case where we added some surfactant. The switching contrast thus depended on the amount of surfactant (Triton X-100) added.

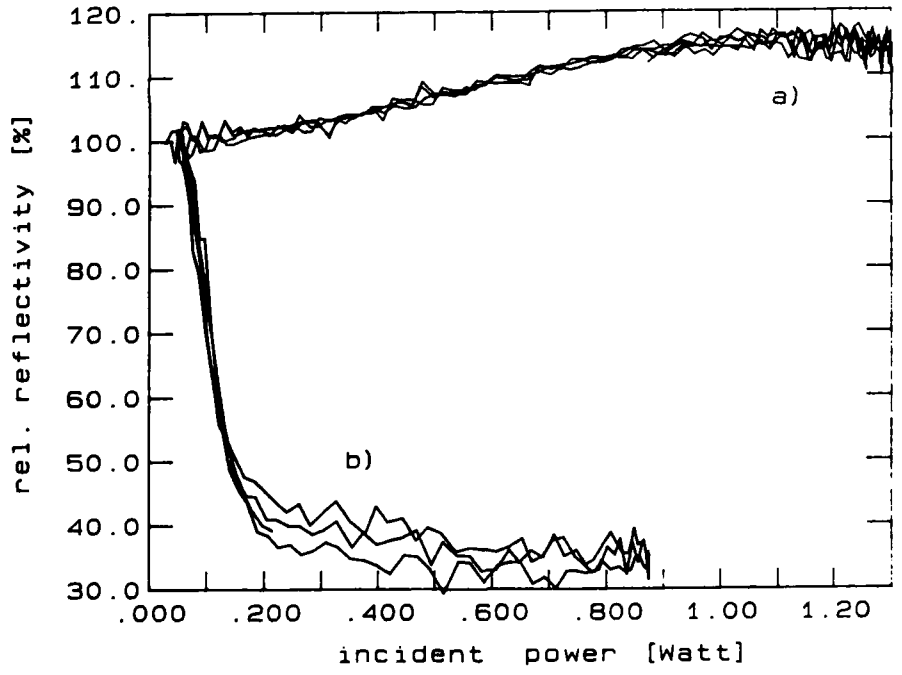

Fig. 2: Intensity dependence of the relative reflectivity for a) no surfactant; and b) roughly .5% surfactant.

(polarization in the incident plane). By rotating the $\lambda/2$-plate (45°/111 sec.), the transmission of these variable attenuators could be changed with a minimum of beam deviation and wavefront distortion. Roughly 5% of the incident beam was reflected by a wedged beamsplitter to a Newport 835 SL-03 power meter (I). An identical power meter (R) was used to measure the intensity of the laser beam after the reflection from the interface. Additional beamsplitters were used as attenuators in order to avoid saturation effects in the R-power meter. Both power meters (I and R) were connected to an IBM-AT computer for data acquisition. Both power meters where triggered simultaneously each second, and the actual values transmitted to the computer.

The linear medium was an optically polished single crystal (6 cm × 1 cm × 1 cm) of LiF which has an index of refraction of $n_{LiF} = 1.391$ at $\lambda = 514.5$ nm. The crystal was mounted in a Precision 360° Rotator with encoder drive (Oriel Corp.), which allowed a relative (absolute) angle determination of 0.75 arc sec (<.3°). The nonlinear medium was an aqueous suspension of .277 μm polystyrene spheres with a volume concentration of 7.7% (Interfacial Dynamics Corp.).

An explanation of the nonlinear behavior of these suspensions of dielectric particles in a electromagnetic field gradient has appeared[2,7]. In short, the particles experience a force which attracts the particles in the high intensity region, changing therefore the particle density locally, resulting in a refractive index change. These light forces are opposed by thermal diffusion (Brownian motion) of the particles. In the limit of quasi-stationarity the Brownian diffusion counterbalances the optical pressure resulting in a density distribution which follows the intensity variation for moderate intensities. In this particular system the effect of diffusion is to simulate a diffusionless case where the local induced index change varies with the local intensity (kerr-like nonlinearity). Therefore we are investigating here a diffusionless NI. Unfortunately, when these particles come too close together they tend to agglomerate, irreversibly changing the nonlinear medium (see discussion below). Using eq. (3) and (4) from Ref. 7, we obtain an effective nonlinear Kerr coefficient $n_2 \approx .44$ cm^2/MW, a scattering loss $\alpha_0 \approx 4.2\times10^3$ cm^{-1} and calculate (see Ref. 7) a low intensity index of refraction for this nonlinear medium of $n \approx 1.353$. The calculated critical angle for this interface is then $\Psi_{crit.} = 13.4°$ and the (low intensity) refractive index difference (Δ) between the two media forming the NI is $\Delta = 3.8\times10^{-2}$.

In addition to polystyrene and water, the nonlinear liquid contained some surfactant (<1%), and was saturated with LiF. The saturation with LiF avoided the surface etching with water, so that the reflected intensity no longer decreased with time due to increasing surface roughness. Exposure of the LiF crystal to the nonlinear liquid for 5 hours did not cause any visible damage to the crystal surfaces. On the other hand, we observed that the switching contrast (maximum change in reflectivity between the low and high in-

by the pulsed experiment[4] and in part also by the CW experiment[2], but in neither case is bistability conclusive. Recently, theoretical 2-d modeling[5] of a diffusive nonlinear interface has found a much more plane wave like behavior with significantly reduced beam break-up, and no clear indication of multiple threshold behavior for the reflectivity at the DNI. Based on that indicated behavior, an optical integration architecture was developed[5,6] with an ideal NI (or DNI) as the single computing element in order to assess the potential worth of such a device for optical computing.

In order to study the NI also from nature's point of view, we set up an experiment which is similar to the CW experiment by Smith and Tomlinson at Bell Labs[2]. We report in this paper the first results showing that significantly enhanced switching is obtainable by adjusting the parameter region. No hysteresis was found in the parameter region explored and our results disagree with the 2-d prediction of a diffusionless NI.

EXPERIMENTAL STUDIES

Our experiments were performed with the apparatus shown in Fig. 1. The input 514.5 nm beam of an argon ion laser was focused with a 4.7 cm lens to a theoretical 1/e amplitude radius of the order $w_o \approx 4\ \mu m$ and a far-field diffraction angle $\Psi_D \approx 1.3°$ at the interface. The laser beam was attenuated by a $\lambda/2$-plate polarizer combination

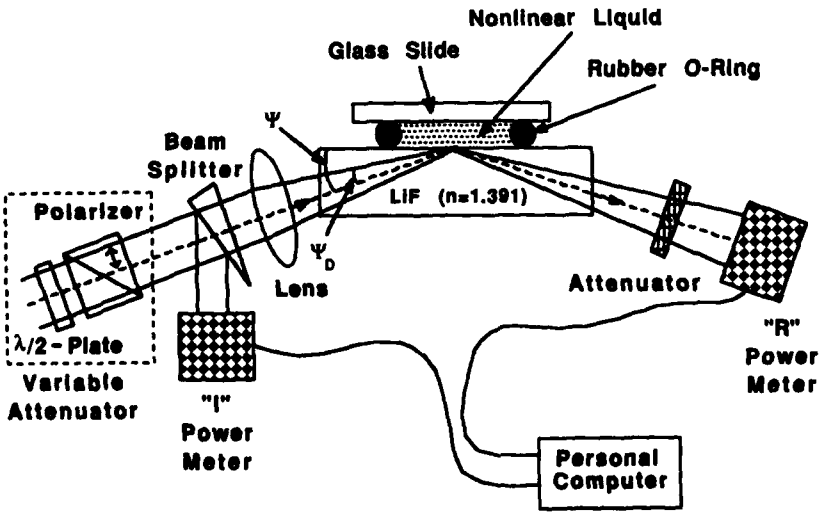

Fig. 1: Experimental Setup

The effect of the added surfactant needs further investigation since it is not yet totally clear if it influences only the laser induced particle aggregation, or changes the interface and diffusion parameters too.

The intensity dependence of the reflectivity found has no second bump. It therefore looks much more like the plane wave case studied by Kaplan[3] than the 2-d treatment of a Gaussian beam incident at a diffusionless nonlinear interface[1], suggesting that the 2-d model is not adequate to describe the experimental behavior of an NI.[8]

In the early days of the experiments we observed some hysteresis. But after isolating and fixing some 'flaws' in the experimental set-up and nonlinear interface preparation, no hysteresis could be found in the explored parameter region. See, for example, the curves in Fig. 2 which contain several intensity cycles (low-high) for each case. For that reason, we think that laser-induced particle growth could be a possible explanation for the hysteresis reported earlier[2].

These preliminary experiments have shown that under certain conditions a nonlinear interface can have a much better switching contrast (100% to 35% and possibly lower) than previous experiments (100% to 70%) and theoretical analysis[1] (100% to 50%) have indicated. Further work is necessary to assess the optimum parameter set and the limitation of the nonlinear interface for the use of the NI as an all optical computing element.

ACKNOWLEDGMENT

The authors wish to thank J. Feinstein and G. Jwo for their contribution to the setup of the experiment. We would also like to express our appreciation for the support and assistance received from the Iowa Laser Facility.

REFERENCES

[1] W. J. Tomlinson, J. P. Gordon, P. W. Smith and A. E. Kaplan, Appl. Opt. 21, 2041 (1982).
[2] P. W. Smith and W. J. Tomlinson, IEEE QE-20, 30 (1984).
[3] A. E. Kaplan, JETP Lett. 24, 114 (1976).
A. E. Kaplan, Sov. Phys. JETP 45, 896 (1977).
[4] P. W. Smith, W. J. Tomlinson, P. Maloney and J.-P. Hermann, IEEE QE-17, 340 (1981).
[5] R. R. Cuykendall and K. H. Strobl, JOSA-B, (1989) to be published.
[6] K. H. Strobl and R. R. Cuykendall, submitted to Appl. Opt.
[7] P. W. Smith, P. J. Maloney and A. Ashkin, Opt. Lett. 7, 347 (1982).
[8] K. H. Strobl and R. Cuykendall, submitted to Opt. Lett. (1989)

Studies of the Pulsed Laser Deposition Process for the Preparation of High-Temperature Superconducting Films

T. Venkatesan, X. D. Wu[a], A. Inam[a]
B. Dutta[b], M. S. Hegde[c,d], and C. C. Chang,
Bellcore, Red Bank, NJ 07701
[a]Physics Dept., Rutgers Univ., Piscataway, NJ 08854
[b]Physics Dept., Middlebury College, Middlebury, VT 05753
[c]Solid St. Struct. Chemistry Unit, Indian Inst. of Sci., Bangalore, 560012
[d]Ceramics Research, Rutgers Univ., Piscataway, NJ 08854

ABSTRACT

The pulsed laser deposition technique can produce films with compositions similar to those of the target pellets on a variety of substrates. This deposition process has been explored by laser ionization mass spectrometry including post ablation ionization, Rutherford backscattering analysis, and optical spectroscopy. We find that binary and ternary suboxides are emitted from the target with kinetic energy equivalent of several eV's corresponding to effective temperatures of 10^4K thus facilitating crystallization at low substrate temperatures. The laser plume has a forward directed component with the correct stoichiometry, which increases with laser energy density, and a non-stoichiometric broad component due to evaporation. Optical emission from oxide species increased with oxygen pressure, and films with the highest T_c's and J_c's were obtained when deposited under conditions of intense emission from the oxides.

INTRODUCTION

The pulsed laser deposition technique (PLD)[1] [2] is emerging as a leading method for depositing high temperature superconducting films of complex composition. We will describe only our work with the Y-Ba-Cu-O superconducting material, for which there is now quite a respectable materials technology. Our PLD films have shown some of the highest reported superconducting temperatures and supercurrents for this material, with demonstrated capabilities for producing smooth films and multi-layered structures that can be deposited at the lowest reported growth temperatures. Most of these capabilities are related to the laser ablation process. The study of these unique laser processes that lead to the correct superconducting phase with the desired chemical, physical, and electrical properties is the subject of this paper.

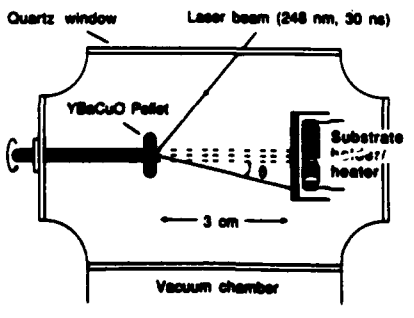

Fig. 1. Schematic of deposition system.

EXPERIMENTAL

The laser deposition apparatus is shown in Fig. 1. A beam of a few mm diameter was focused onto a superconducting target pellet prepared in the usual way[3], using a KrF excimer laser, as described previously.[1][2] The 30 ns, 248 nm laser was pulsed at 1 Hz at a power density of about 10^8W/cm^2. Film composition and thickness were measured using a General Ionex Rutherford backscattering (RBS) instrument operated

at 4 MeV using a He^+ beam of about 1 mm diameter. The nature of the ablated material was investigated by laser ionization mass spectrometry (LIMS)[4], [5] in which a quadrupled Nd:YAG laser (266 nm, 5ns pulse) with a smaller beam (2μ m) but higher power density (over $10^9 W/cm^2$) than for our PLD system was used.[2] Emitted neutrals were studied with a post ablation ionization (PAI) technique in which a second Nd:YAG beam was focused 0.6mm above the target surface.[6] The beam of ablated material was also examined by optical spectroscopy. An RCA 8850 photomultiplier tube with different filters was used and the data recorded with a digitizer or on an oscilloscope.[7]

DEPOSITION THRESHOLD ENERGY DENSITY AND ANGULAR DEPENDENCE

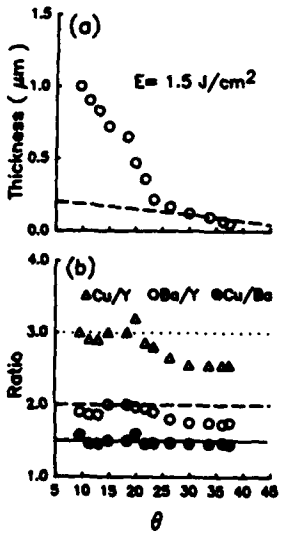

Fig. 2. At 1.5 J/cm^2 laser energy density, the angular distribution of the deposited film (a) thickness (the dashed line is the cosθ fit) and (b) composition.

The ablated plume is somewhat cone shaped with its axis nearly normal to the target surface and the apex at the target. There are two components to this plume[6], a broad, evaporative, cosθ component, and a directed (narrow) central core, as shown in the RBS data of Fig. 2a. The forward-directed beam is stoichiometric, but the broad one is deficient in Cu and Ba, as shown in Fig. 2b. As the laser power density was decreased, the directed component decreased faster than the evaporative part -- in fact, the evaporative component is fairly constant with energy. The threshold energy density for creating the directed beam was $0.4 J/cm^2$,[6] compared to $0.1 J/cm^2$ for pulsed laser etching.[8] We conclude that the lower energy threshold is for evaporation.

LIMS INVESTIGATIONS

The greatest advantage of the PLD process is the stoichiometric deposition. One possible mechanism is that clusters of the correct stoichiometry are vaporized by the laser. The mass-to-charge ratios (m/z) ratios of such clusters will exceed 650 and they maintain short range order similar to that of the bulk superconductor. In order to identify the species in the plume, LIMS studies were performed in both the + ve and -ve ion modes. PAI was also performed, but only in the + ve mode. Typical rise time of our time-of-flight detection system was <20 ns and mass resolution was better than 250; neutral velocity distributions were obtained by varying the time delay of the post-ionization laser pulse with respect to the ablating pulse.

Figs. 3a and 3b are positive LIMS spectra taken at power densities of 5.5×10^9 and 1.2×10^{10} W/cm^2, respectively. The LIMS laser was different from our PLD laser, and the threshold for detectable emission was about 7×10^8 W/cm^2, almost three times that for PLD. At the lower power (Fig. 3a) the intense peaks are from diatomic and suboxide species; intensities of higher mass clusters fall off rapidly. Even at the higher power density, no significant higher mass peaks are detected. This is also true for the neutrals, as shown in the PAI spectrum of Fig. 3c. The ablation irradiance was 7 x

10^9W/cm^2 and the ionizing irradiance was $5x10^{10}$W/cm^2 with a 2.6μs delay. Mostly elemental, diatomic, and triatomic species are detected, again indicating that significant amounts of high mass neutral clusters are not emitted.

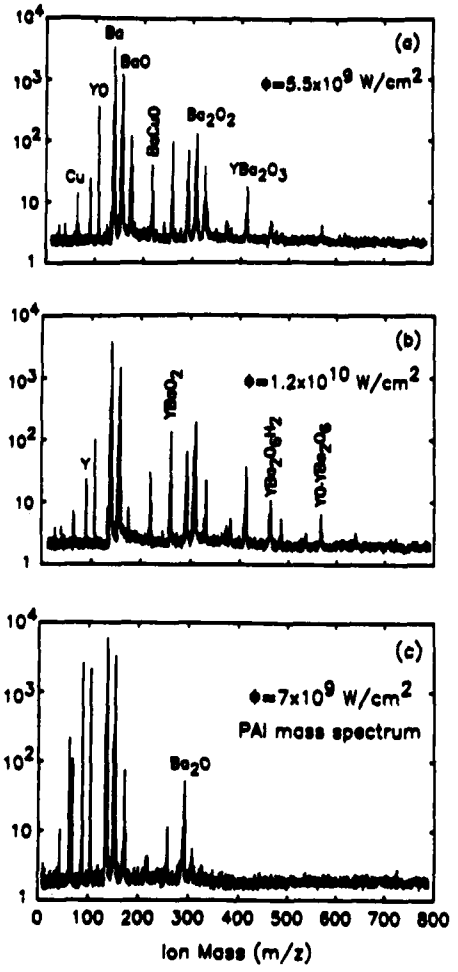

Fig. 3. LIMS spectra at: (a) 5.5 x 10^9 W/cm^2, (b) 1.2 x 10^{10} W/cm^2, and (c) PAI spectra at: ablation laser irradiance of 7 x 10^9 W/cm^2. The vertical axis is the ion count in arbitrary units.

At the wavelength of 248 nm, the superconducting material efficiently absorbs the laser energy within the first 50 nm from the surface.[8] The surface temperature can significantly exceed 1300°C[9] in a few ns, whereby the material can rapidly evaporate from the surface. We know that atomic or molecular species (see below), crystalline particles, and molten droplets are dislodged.[10] Although the precise mechanisms are not known, shock waves,[11] subsurface explosion,[12] and surface superheating with recoil pressure,[13] have been discussed in the literature. A few general phenomena have been established. Initially, there is preferential evaporation of material which changes the surface composition until at steady state, the evaporated material has nearly the right composition.[14] At low power, this condition may not be reached.[15] The explosive ablation process results in non-thermal energy distribution normal to the target surface, and large velocities have been measured and calculated.[16] [17] We also reported on the first measurements of the velocity distribution of the neutrals using PAI,[6] giving rise to effective plume temperatures of 10^4K.

We conclude that PLD proceeds by deposition of atomic and molecular species, and not by cluster deposition. The explanation for correct stoichiometric deposition is mostly the near-total vaporization of everything in the surface region. The remaining slight non-stoichiometric vaporization is compensated by the change in target surface composition at steady state.

OPTICAL SPECTROSCOPIC STUDIES

We had previously shown[18] that as-deposited films, made at substrate holder temperature of 650°C in 5-10 mTorr of oxygen, were superconducting at 30K.

Subsequent annealing at 450 °C in oxygen improved the zero resistance temperature (T_{c0}) of the films (on $SrTiO_3$) to 86 K, indicating that as-deposited films were oxygen deficient. By introducing a jet of oxygen directly into the plume, and keeping the system pressure and substrate holder temperature the same, we were able to obtain as-deposited films with T_{c0} of 89 K,[19] demonstrating the importance of the interaction of oxygen directly with the plume. Optical spectroscopy has been used to study plasmas used in semiconductor technology,[20] [21] as well as laser induced plasmas from Y-Ba-Cu-O targets.[22] [23] [24] Those studies were restricted to the identification of emission lines, and we show below that the parameters of laser power density and oxygen pressures they investigated are not the optimum.

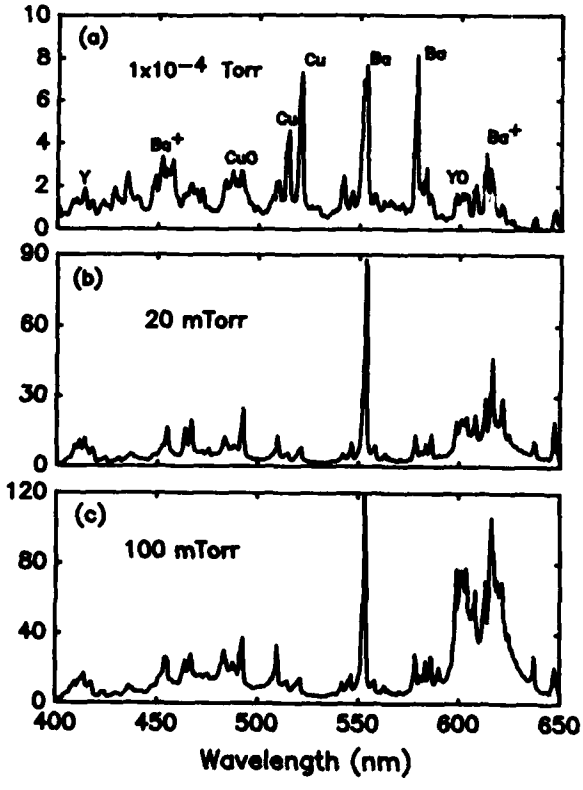

Fig. 4. Optical spectra of the laser produced plume at an oxygen pressure of (a) $<10^{-4}$, (b) 20, and (c) 100 mTorr, taken at laser energy density of 1.5 J/cm^2. The vertical axis is the photon count in arbitrary units.

Optical spectra from the plume in our instrument for different oxygen pressures are shown in Fig. 4. Based on data from earlier work[25] [26] [27] [28] and previous experiments,[21][23] the following major lines were identified (in nm): YO (614.84, 613.21, 605.93, 601.99, 600.36, 597.20); CuO (584.77) or Ba (584.857), Ba^+ (582.225); BaO (580.5); Ba (553.54) or Y (552.7); Ba (551.9); Cu (521.766, 515.404); CuO (463.5); and Y (423.594, 416.7, 412.831, 410.238, 408.3). Also, emission bands[26] from YO ($A^2\Pi \rightarrow X^2\Sigma$), BaO ($A^1\Sigma \rightarrow X^1\Sigma$ and CuO ($A^2\Sigma \rightarrow X^2\Pi$) were observed at 570-616.5, 460-710, and 584-640 nm, respectively. As the oxygen pressure is increased, the intensity of almost all emission lines and bands increase, as seen from Figs. 4b and 4c. The dominance of the elemental and monoxide species is in agreement with the LIMS results.

Data from dynamical optical measurements are shown in Fig. 5 a-d. Figure 5a shows the emission at 410 nm from Y atoms and 5b at 632.8 nm from YO, both taken in vacuum below 10^{-4} Torr. There is a 'prompt' emission and a 'slow' emission a few μs later; the former was insensitive to oxygen pressure, but the latter was quite sensitive, especially for the oxide species, as seen in Fig. 5d.

Details of the prompt emission are shown in Fig. 6. Optical emission begins after a 7 ns delay which represents the time required to pump enough energy into the surface to start vaporization. The onset of Y emission is delayed by 10 ns whereas that for YO is 20 ns.

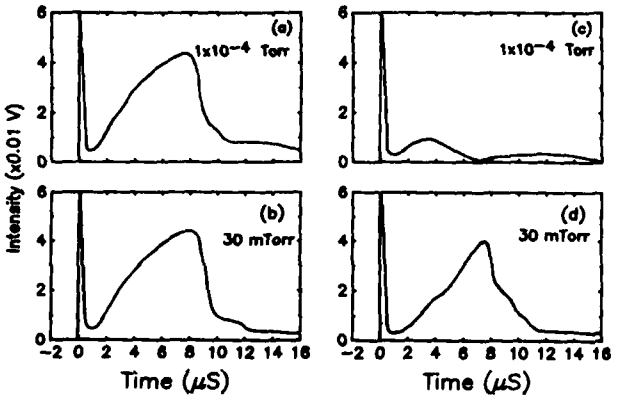

Fig. 5. Time-resolved measurements of the secondary emission with a narrow band filter centered at 410 nm at (a) $<10^{-4}$ and (b) 30 mTorr, and at 632.8 nm at (c) $<10^{-4}$ and (d) 30 mTorr.

We think that material is ejected in atomic form and subsequently form molecular species due to near surface collisions. We have used these data to optimize the oxygen pressure for maximum emission from the oxides; for example, for deposition at a given oxygen pressure, deposition at 10 mTorr resulted in a film with T_{c0} of only 30K whereas deposition near the maximum emission pressure of 100 mTorr gave a film with T_{c0} of 93K.

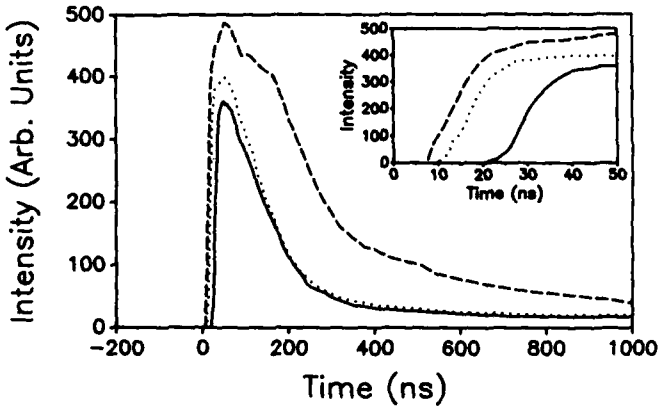

Fig. 6. Time-resolved measurements of the prompt plasma emission with narrow band filters (<10 nm) centered at 410 nm (solid line), 632.8 nm (dotted line) and wide band emission (dashed line).

DISCUSSION

It is clear that the process of laser ablation is not well understood. The processes by which atomic, then molecular species, and the fractured particles and molten droplets are created at these high power densities have not been sufficiently studied. On the other hand, the monitoring techniques we used have enabled us to optimize our deposition process to provide some of the best films to be described in the literature. The unique properties of lasers are central to these successes which demonstrate that further work along these lines will provide exciting new results, not only for

superconductivity, but also for understanding the way in which laser light interacts with matter.

REFERENCES

1. D. Dijkkamp, T. Venkatesan, X. D. Wu, S. A. Shaheen, N. Jisrawi, Y. H. Min-Lee, W. S. McLean and M. Croft, Appl. Phys. Lett. 51, 619 (1987).
2. T. Venkatesan, X. D. Wu, A. Inam, M. S. Hegde, E. W. Chase, C. C. Chang, P. England, D. M. Hwang, R. Krchnavek, J. B. Wachtman, W. L. McLean, R. Levi-Setti, J. Chabala, and Y. L. Wang, in *Chemistry of High Temperature Superconductors II, ACS Symposium Series 377,* Ed. D. L. Nelson and T. F. George, American Chemical Society, Washington, DC, (1988), P. 234.
3. J. M. Tarascon, W. R. McKinnon, L. H. Greene, G. W. Hull, and E. M. Vogel, Phys. Rev. B36, 226 (1987).
4. R. W. Odom, C. J. Hitzman and B. Schueler, Mat. Res. Soc. Symp. Proc. 69, 265 (1986).
5. T. Venkatesan, X. D. Wu, A. Inam, Y. Jeon, M. Croft, E. W. Chase, C. C. Chang, J. B. Wachtman, R. W. Odom, F. Radicati di Brozolo, and C. A. Magee, Appl. Phys. Lett. 53 (15), 1431 (1988).
6. B. Schueler and R. W. Odom, J. Appl. Phys. 63, 4642 (1987).
7. X. D. Wu, B. Dutta, M. S. Hegde, A. Inam, T. Venkatesan, E. W. Chase, C. C. Chang, and R. Howard, unpublished.
8. A. Inam, X. D. Wu, T. Venkatesan, S. B. Ogale, C. C. Chang, and D. Dijkkamp, Appl. Phys. Lett. 51, 1112 (1987).
9. S. Leng, N. Narita, K. Higashida, and H. Mazaki, Japan. J. Appl. Phys. 26, L1394 (1987).
10. T. Venkatesan, C. C. Chang, D. Dijkkamp, S. B. Ogale, E. W. Chase, L. A. Farrow, D. M. Hwang, P. J. Miceli, S. A. Schwarz, and J. M. Tarascon, J. Appl. Phys. 63(9), 4591 (1988).
11. A. M. Bonch-Bruevich and Y. A. Imas, Sov. Phys. Tech. 12, 1407 (1968).
12. F. P. Gagliano and U. C. Paek, Appl. Opt. 13, 274 (1974).
13. J. F. Ready, *J. Appl. Phys.* 36, 462 (1965).
14. U. Kaiser and J. C. Huneke, MRS Bulletin 12(6), 48 (1987).
15. T. Venkatesan, X. D. Wu, A. Inam and J. B. Wachtman, Appl. Phys. Lett. 52, 1193 (1988).
16. D. Lubben, S. A. Barnett, K. Suzuki, S. Gorbatkin and J. E. Greene, J. Vac. Sci. Technol. B3(4), 963 (1985).
17. R. Kelly and R. W. Dreyfus, to appear in Surface Sci., (1988).
18. X. D. Wu, A. Inam, T. Venkatesan, C. C. Chang, E. W. Chase, P. Barboux, J. M. Tarascon and B. Wilkens, Appl. Phys. Lett. 52, 1554 (1988)
19. X. D. Wu, T. Venkatesan, A. Inam, E. W. Chase, C. C. Chang, Y. Jeon, M. Croft, C. Magee, R. W. Odom and F. Radicati de Brozolo, in *Proceedings of SPIE: High Tc Superconductivity - Thin Films and Devices,* Newport Beach, Ca, 16 March, 1988.
20. V. M. Donnelly, V. R. McCrary and D. Brasen, in *Photon, Beam and Plasma Stimulated Chemical Processes at Surfaces,* Eds. V. C. Donnelly, I. P. Herman and M. Hirose, Materials Research Soc., Pittsburgh, 1987, Vol. 75, P.567.
21. P. J. Hargis, Jr. and M. J. Krushner, Appl Phys. Lett. 40, 779 (1982).
22. W. A. Weimer, Appl. Phys. Lett. 52, 2171 (1988).
23. O. Auciello, S. Athavale, O. E. Hankins, M. Sito, A. F. Schreiner and N. Biunno, Appl. Phys. Lett. 53, 72 (1988).
24. H. S. Kwok, P. Mattocks, L. Shi, X. W. Wang, S. Witanachchi, Q. Y. Ying, J. P. Zhang and D. T. Shaw, Appl. Phys. Lett. 52, 1825 (1988).
25. M. L. Parsons, B. W. Smith and G. E. Bentley, *Handbook of Flame Spectroscopy,* Plenum, NY, 1975.
26. R. W. B. Pearse and A. G. Gaydon, *The Identification of Molecular Spectra,* Chapman and Hall, NY, 1976.
27. *Handbook of Chemistry and Physics,* 68th ed., CRC, NY 1988.
28. F. M. Phelps, *MIT Wavelength Table,* MIT, Cambridge, 1982, Vol. II.

UTILIZATION OF 1+1 REMPI AS A PROBE OF ROTATIONAL DYNAMICS IN GAS-SURFACE SCATTERING

D. C. Jacobs*, K. W. Kolasinski and R. N. Zare
Department of Chemistry, Stanford University, Stanford, CA 94305

ABSTRACT

The spectroscopic technique of 1+1 resonance enhanced multiphoton ionization (REMPI) spectroscopy gives a quantitative measure of the rotational population and alignment distributions of molecules that have interacted with a surface. The two distinct dynamical regimes of trapping/desorption and inelastic scattering are studied for the NO/Pt(111) system. In the case of molecular desorption, molecules which desorb with a large amount of angular momentum (J>12.5) prefer to rotate in the plane of the surface. Those molecules which inelastically scatter from the surface show the opposite preference for rotational alignment, i.e., they preferentially rotate in a plane perpendicular to the surface. The rotational population distribution reveals that surface vibrational energy is efficiently transferred into rotational energy in the scattering process.

INTRODUCTION

Resonance enhanced multiphoton ionization (REMPI) is an ideal method for studying the rotational dynamics of gas-surface scattering. This is because it is generally regarded as the most sensitive technique for measuring low densities of small gas-phase molecules in a state-specific manner. The NO/Pt(111) system is chosen for a few salient reasons. Nitric oxide can be detected at pressures as low as 10^{-10} Torr using 1+1 REMPI through the $A^2\Sigma^+(v=0)$ state. Moreover, the treatment for reducing 1+1 REMPI spectra to population and alignment distributions has been developed and tested for the NO system.[1,2] The Pt(111) surface is the only metal substrate on which NO has a large binding energy (25-35.5 kcal/mole) and yet does not readily dissociate.

Nitric oxide is believed to bind to Pt(111) through the nitrogen atom with the internuclear axis lying normal to the surface.[3-6] The initial sticking probability lies between 0.85 and 0.90, independent of surface temperature.[7,8] The internal state distributions associated with NO/Pt(111) have been described by rotational temperatures that fall on or below the surface temperature.[9-14] Prior to this study, rotational alignment in the scattered and desorbed NO has not been observed for Pt(111).[11,14]

This paper discusses the rotational dynamics of NO from Pt(111) for two distinct regimes -- trapping/desorption and inelastic scattering. Inelastic scattering refers to a collision of short duration (one or a few bounces) between the molecule and surface. Trapping/desorption involves a relatively long surface residence time in which the molecule loses "memory" of its initial conditions. Our probe of the system is the measure of both the relative rotational population and the quadrupole moment of the alignment distribution $|A_0^{(2)}(J)|$ for each quantum state J. Population refers to the relative number of molecules in a particular rotational state while alignment concerns the spatial distribution of the rotational angular momentum vector. The cartoons in Fig. 1 show two limiting cases for rotational alignment: "helicopter" motion where the plane of rotation lies parallel to the surface and "cartwheel" motion where the plane of rotation is perpendicular to the surface. The values of the quadrupole moment which correspond to these two limits are +2 and -1, respectively.[2]

* Present Address: Department of Chemistry, University of Notre Dame, Notre Dame, IN 46556.

EXPERIMENTAL

The experimental apparatus is described in detail elsewhere.[15] Briefly, a differentially-pumped pulsed molecular beam is directed at normal incidence to a clean Pt(111) sample. The neat supersonic expansion of NO (characterized by an 85 meV translational energy, a 40 K rotational temperature, and a 100 μs temporal width) provides the Pt surface with 0.006 Langmuir pulses of NO at 10 Hz. A sizable fraction of the incident pulse of NO scatters from the surface. The remainder traps on the surface and desorbs later. Both LEED and Auger surface diagnostics are used to ensure the order and cleanliness of the Pt crystal.

A pulsed Nd:YAG pumped dye laser system is employed to provide state-selective detection of the nascent molecules via 1+1 REMPI spectroscopy. The tunable 225 nm radiation is generated by Raman shifting in H_2 the doubled output of a Moya cavity dye laser. The resulting 6 ns laser pulse (200 mJ/shot) passes 2 mm above the Pt crystal face and excites a portion of those molecules that have interacted with the surface. The ions created by REMPI are accelerated, mass-selected according to their time-of-flight, and collected by a charged particle multiplier (CEMA multichannel plates). The linear polarization direction of the laser is controlled on a shot-to-shot basis by a photoelastic modulator. This allows for the characterization of both rotational population and alignment distributions.[1,2,15] The dose/detect cycle is repeated at 10 Hz while the laser wavelength is scanned. Magnetic fields in the laser interaction region are minimized through the use of external Helmholtz coils and by interruptin the heater filament current during the laser pulse.

RESULTS

The regime of trapping/desorption is isolated by firing the laser 200 μs after the end of the nozzle pulse. Here the laser detects only those molecules that have remained on the 553 K surface for 200-300 μs. The laser is tuned to a particular rotational transition and ions are collected for 1,000 - 10,000 laser shots at alternating laser polarization directions. The polarization dependence of a given rotational transition is directly related to the quadrupole moment of the rotational alignment distribution.

Figure 1 shows the measured rotational alignment as a function of rotational quantum number J for desorption at 553 K. For J < 12.5, there appears to be little to no rotational alignment. However, molecules with J > 12.5 show increasing values of the quadrupole moment. The maximum measured quadrupole moment (+0.15) implies that 1.2 - 1.5 times as many molecules desorb with their plane of rotation resembling that of a helicopter as those resembling a cartwheel motion (See cartoons in Fig. 1).

The regime of inelastic scattering is explored when firing the laser synchronously with the rising edge of the

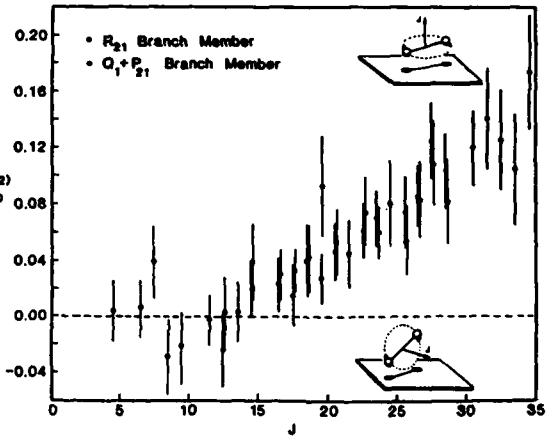

Figure 1. The quadrupole moment of the alignment distribution , $A_0^{(2)}(J)$, for NO desorption from a 553 K Pt(111) surface. Positive values indicate a preference for "helicopter" motion over "cartwheel" motion.

nozzle pulse. For the 450 K surface temperature reported here, this discriminates in favor of those molecules that have bounced once or a few times on the surface. The laser is scanned at a rate which permits for each rotational line profile approximately 50 shots of signal averaging for each of the two orthogonal laser polarizations. The REMPI line intensities are then reduced to both rotational population and alignment distributions.

Figure 2 shows a Boltzmann plot of the rotational populations for NO inelastically scattered from a Pt(111) surface at 450 K. The data do not fall on a single line. In fact there appear to be three somewhat linear portions to the Boltzmann plot. These are marked with temperatures only to show the relative amount of rotational excitation in each of these three regions. The temperatures are not meant to imply that the rotational distribution is "thermal" or even "trimodal". The vertical dashed line at 690 cm^{-1} represents the total energy of the incident supersonic beam. In the rigid surface limit, rotational excitation beyond this energy would be strictly forbidden. However, the experiment reveals that a significant fraction of the molecules escape the surface with more energy in rotation than they initially possessed as total energy in the incident beam.

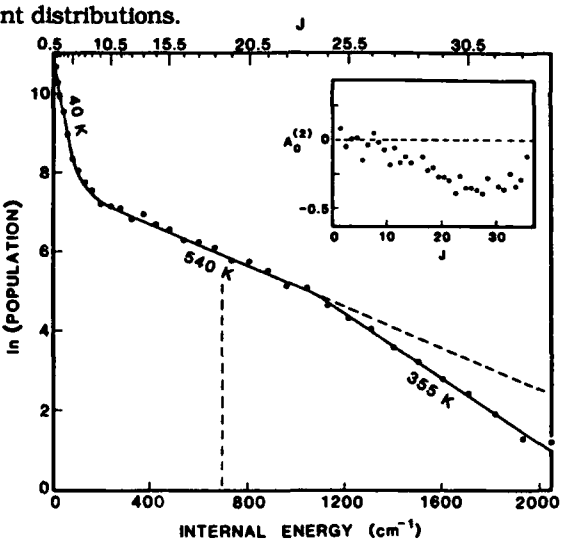

Figure 2. Boltzmann distribution for inelastic scattering of NO from a 450 K Pt(111) surface. The inset shows the corresponding rotational

The corresponding quadrupole moment, $A_0^{(2)}(J)$, is plotted in the inset of Fig. 2. For $J < 10.5$ there is no appreciable alignment. However, beyond $J = 10.5$ there is a steady increase in the magnitude of the quadrupole moment until it reaches a maximum around $J = 25.5$. This implies that scattered molecules prefer to rotate in a plane normal to the surface, i.e., to undergo cartwheel motion (See cartoon in Fig. 1). This preference has also been seen for the scattering of NO[16-18] and N_2[19-21] from Ag(111).

DISCUSSION

These experiments mark the first observation of rotational alignment in desorption. They also represent the first study of inelastic scattering in which rotational states up to three times more energetic than the incident beam energy are examined for rotational alignment. The opposite preference in rotational alignment for desorption and inelastic scattering suggests that these two processes have very different dynamical pathways on the same potential energy surface.

Molecules that desorb from the surface with a large amount of rotational angular momenta prefer to rotate in the plane of the surface. This result suggests that molecules are free to rotate on the surface immediately prior to desorption. Rotation of an adsorbed molecule in the plane of the surface is less hindered than rotation in a plane normal to the surface. This dynamical bias for the adsorbed species leads to the observed preference in rotational alignment.

The Boltzmann plot of Fig. 2 reveals the presence of a surface vibration to rotational energy transfer mechanism in inelastic scattering. In general, if the surface atom closest to the molecule is translating out of the bulk during the surface collision, then the molecule will gain translational and/or rotational energy. The degree of rotational excitation in the scattered distribution increases with increasing surface temperature. Although significant surface to rotational energy transfer is responsible for populating states with rotational energy exceeding the beam energy, rotational alignment is created in these states and is preserved in the final distribution. In scattering, the molecule experiences predominantly an out-of-plane force from the surface. Hence the associated torque exerted on the molecule leads to a preference for scattering with a "cartwheel" motion.

Resonance enhanced multiphoton ionization is an invaluable technique for examining gas-surface interactions. Rotational population and alignment distributions provide a sensitive probe of gas-surface dynamics. In particular, such studies reveal information about energy transfer processes at surfaces and anisotropies in the molecule-surface potential near the transition state.

ACKNOWLEDGEMENTS

This work was supported by the Office of Naval Research (N0014-87-K-00265). We gratefully acknowledge the assistance of Stacey F. Shane.

REFERENCES

1. D. C. Jacobs and R. N. Zare, J. Chem. Phys. **85**, 5457 (1986).
2. D. C. Jacobs, R. J. Madix and R. N. Zare, J. Chem. Phys. **85**, 5469 (1986).
3. H. Ibach and S. Lehwald, Surf. Sci. **76**, 1 (1978).
4. J. L. Gland and B. A. Sexton, Surf. Sci. **94**, 355 (1980).
5. B. E. Hayden, Surf. Sci. **131**, 419 (1983).
6. M. Kiskinova, G. Pirug and H. P. Bonzel, Surf. Sci. **136**, 285 (1984).
7. J. A. Serri, M. J. Cardillo and G. E. Becker, J. Chem. Phys. **77**, 2175 (1982).
8. C. Campbell, G. Ertl and J. Segner, Surf. Sci. **115**, 309 (1982).
9. F. Frenkel, J. Häger, W. Krieger, H. Walther, C. Campbell, G. Ertl, H. Kuipers and J. Segner, Phys. Rev. Lett. **46**, 152 (1981).
10. M. Asscher, W. Guthrie, T. Lin and G. Somorjai, Phys. Rev. Lett. **49**, 76 (1982).
11. J. Segner, H. Robota, W. Vielhaber, G. Ertl, F. Frenkel, J. Häger, W. Krieger and H. Walther, Surf. Sci. **131**, 273 (1983).
12. M. Asscher, W. Guthrie, T. Lin and G. Somorjai, J. Chem. Phys. **78**, 6992 (1983).
13. D. S. King, D. A. Mantell and R. R. Cavanagh, J. Chem. Phys. **82**, 1046 (1985).
14. D. A. Mantell, R. R. Cavanagh and D. S. King, J. Chem. Phys. **84**, 5131 (1986).
15. D. C. Jacobs, K. W. Kolasinski, S. F. Shane and R. N. Zare, J. Chem. Phys., *submitted*.
16. A. Luntz, A. Kleyn and D. Auerbach, Phys. Rev. B **25**, 4273 (1982).
17. A. Kleyn, A. Luntz, and D. Auerbach, Surf. Sci. **117**, 33 (1983).
18. A. Kleyn, A. Luntz, and D. Auerbach, Surf. Sci. **152**, 99 (1985).
19. G. O. Sitz, A. C. Kummel and R. N. Zare, J. Vac. Sci. Technol. A **5**, 513 (1987).
20. G. O. Sitz, A. C. Kummel and R. N. Zare, J. Chem. Phys. **87**, 3247 (1987).
21. G. O. Sitz, A. C. Kummel, R. N. Zare and J. C. Tully, J. Chem. Phys. **89**, 2572 (1988).

SPECTRAL ANALYSIS OF FLUORESCENCE OF EXCITED SPECIES FROM 193 nm PHOTOABLATION OF POLYCARBONATE AND THE HIGH T_c SUPERCONDUCTORS $Bi_2CaSr_2Cu_2O_9$ AND $YBa_2Cu_3O_{7-d}$

Subhash Deshmukh, Erhard W. Rothe, and Gene P. Reck
Wayne State University, Detroit, MI 48202

ABSTRACT

Samples are photoablated in a vacuum and the resulting emission spectra are obtained. The relative and absolute line intensities depend upon the number of laser shots. Our observations show that the emission can be used to characterize the bulk materials as well as the films.

INTRODUCTION

An understanding of laser ablation of materials is relevant to macroscopic applications and to microscopic interpretations. The 193 nm photoablation yields a plume of material above the sample surface that emits at continuous and discrete wavelengths. We present here a shot-to-shot study of photoablation of polycarbonate (PC), $Bi_2CaSr_2Cu_2O_9$ (BCSCO), and $YBa_2Cu_3O_{7-d}$ (123).

EXPERIMENTAL

The photoablation was done in a vacuum by 193 nm excimer laser pulses that were approximately 20 ns long, were repeated at 1 Hz and had an average energy of 50 mJ. The shot-to-shot energy variations were about 10%. The laser beam was transmitted onto a 3 mm by 1mm surface area: i.e., an average fluence of 1.6 J/cm^2. For targets we used commercial PC, a hot pressed pellet of 123, annealed and unannealed 123 films on a sapphire substrate that we prepared with 193 nm deposition from the pellets of 123, and a cold pressed pellet of BCSCO.

The entire ablated plume was observed through a wavelength calibrated monochromator connected to an intensified 1024 diode array. The resolution was about one nm. The spectra were obtained on a shot-to-shot basis. The time required to acquire each spectrum was 10 ms. Different diode-array gains can be used. Relative gains are noted in the figure captions. Zero of the intensity scales is arbitrary. Peak amplitudes can be compared among all the figures by dividing the height shown by the stated gain.

The laser beam was applied to different surface areas. The data reported for PC, for example, for 10 shots, is an average of the 10th shot from 5 different areas. For BCSCO and 123 samples the data is for the average of 10 pulses from 2 areas.

RESULTS AND DISCUSSION

Figure 1 shows averaged spectra from PC from 1, 10, and 30 shots. That from the first shot is much richer because it probably does not represent the bulk material but rather the surface history. Subsequent spectra are more representative of the bulk. The atomic C line is at 495.6 nm in second order.

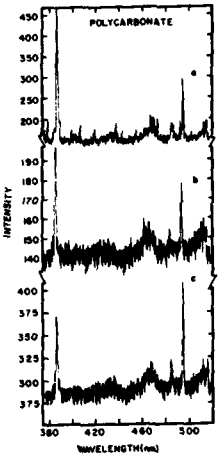

Figure 1. Emission spectra of plume from PC at a) shot one b) shot ten and c) shot thirty. Note that the gain for c is twice that of a and b so that the main peak at 388 nm in a is 290 units larger than that in b and 303 units larger than that in c.

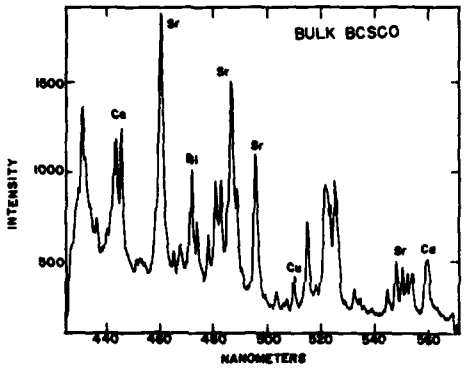

Figure 2. Emission from bulk BCSCO. The ordinate is in arbitrary units.

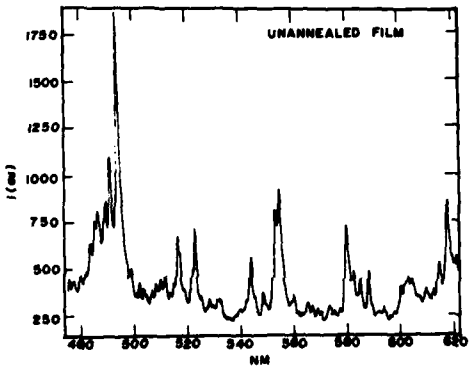

Figure 3. Emission from an unannealed 123 film. The ordinate is in arbitrary units but is the same for Figures 3 and 4.

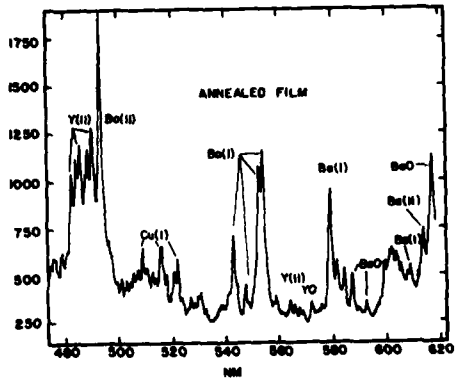

Figure 4. Emission from an annealed 123 film.

Molecular features are the C_2 Swan ($A^3\Pi_g$-$X^3\Pi_u$) system at 466-472 nm and 512-516 nm, a CO band at 485 nm due to the fourth positive system ($A^1\Pi$-$X^1\Sigma$) in second order, and a well developed CH band at 431-432 nm from ($A^2\Delta$-$X^2\Pi$). The band at 387-388 nm was previously identified as the CN ($B^2\Sigma$-$X^2\Sigma$) system.[1] The bands are best seen after 100 shots. Further details on our polycarbonate work are available.[3]

Figure 2 has the spectrum from BCSCO. Atomic lines from Bi, Ca, Cu, and Sr are present. In order to identify the emission lines, we also used pure Bi_2O_3, CaO, CuO, and $Sr(OH)_2 \cdot 8H_2O$ and compared with standard compilations. Further details on our BCSCO work are available.[2]

Figures 3 and 4 are emission spectra from ArF laser deposited films of 123 on sapphire substrate before and after annealing, respectively. These two spectra are virtually the same except between 480-500 nm, where there is a difference. The spectra from the 123 pellets and the annealed films are identical. As with BCSCO, we also used pure BaO, CuO, and Y_2O_3. Lines from Ba, Cu, Y, Ba^+, Y^+, BaO, and YO are identified in Figs. 3 and 4. Further details on our 123 work are available.[4]

CONCLUSIONS

The initial pulses from polycarbonate produce irregular spectra from surface absorbates. Subsequent pulses produce similar spectra that indicate that the mechanism of ablation remains the same after fresh surface is exposed. The major emitters in the BCSCO plume are atomic Bi, Ca, Cu, and Sr. The laser induced plume from non-superconducting and superconducting films of 123 prepared by laser ablation deposition shows that the emitting species are Ba, Cu, Y, Ba^+, Y^+, BaO and YO. Emission studies from superconducting materials should be useful in monitoring the composition of certain key species in the plume during the deposition process and hence in characterizing the films. Care should be taken in future studies to distinguish between photoablation products and those made in the plasma.

ACKNOWLEDGEMENTS

We would like to thank NSF, AFOSR, and the Institute for Manufacturing Research of Wayne state University for support of this work.

REFERENCES

1. G.M. Davis, M.C. Gower, C. Fotakis, T. Efthiniopoulos, and P. Argyrokis, Appl. Phys. 36, 27 (1985).
2. Subhash Deshmukh, Erhard W. Rothe, Gene P. Reck, T. Kushida, and Zai Gui Xu, Appl. Phys. Lett., 53 (26), 2698 (1988).
3. Subhash Deshmukh, Erhard W. Rothe, and Gene P. Reck, J. Appl. Phys., submitted for publication.
4. Subhash Deshmukh, Erhard W. Rothe, Gene P. Reck, T. Kushida, and Zai Gui Xu, Superconductor Science and Technology, scheduled for Mar. 1989.

ION ACCELERATION IN THRESHOLD LEVEL PHOTOABLATION OF METALS

R. Welle and H. Helvajian
Laser Chemistry and Spectroscopy Department
The Aerospace Corporation, Los Angeles, CA 90009

INTRODUCTION

Intense laser sources can create plasmas at metallic surfaces when the radiation fluxes are above 10^6 W/cm^2. These plasmas, in an air environment, grow rapidly and develop into either a laser supported detonation or laser supported combustion wave which absorbs the laser radiation through the inverse Bremsstrahlung process and strongly influences the laser coupling to the surface. If the surface is in a vacuum, at sufficient intensities a plasma is formed in the material removed from the surface. The net effect of the opaque fully absorbing plasma is to reduce the coupling of the laser to the surface. Furthermore, at these very high laser fluence levels, the initial ablation mechanism (thermal evaporation or photochemical) is usually masked by the avalanching ionization process. To have any hope of understanding the mechanisms of laser ablation, it becomes necessary to conduct experiments where the laser fluences are near threshold levels. We have prepared an experiment which measures, for a single laser shot, the nascent velocity distributions of ablated ionic species at laser fluences near threshold for ion production. Since we acquire data for each laser firing, we are able to monitor changes as we remove successive layers of the material.

EXPERIMENTAL

The experiment is described in more detail elsewhere,[1] but briefly, the target is mounted in a UHV chamber (10^{-10} torr), normal to the axis of a time-of-flight mass spectrometer (TOF). A laser beam is brought into the chamber and strikes the target at 45° to the surface normal. The target mounting plate acts as the first plate of the TOF, with a positive potential, thereby accelerating positive ions produced at the surface into the TOF extractor plate, and from there to the microchannel plate detector. For each laser firing, the signal from the detector is amplified and then digitized by a fast transient recorder and stored by computer along with the TOF voltages, and the incident laser energy. The targets used were several single crystals of silver of unknown orientation. The methods described will detect only the ions produced in the ablation process. Information about the behavior of the neutrals would also be of interest, and we are currently working on applying multi-photon ionization methods to this question.

RESULTS AND DISCUSSION

Figure 1 shows high resolution (10 nsec) TOF mass spectra of the three principal ions generated in threshold level (~30 mJ/cm^2) laser ablation of the silver target at 248 nm. As expected, we see the silver monomer and dimer ions. In addition, iron ions are present as an impurity due to sputtering from the accelerator plates of the TOF. Each spectrum is the sum of 300 laser shots each individually measured, with the laser fluence maintained at the threshold for Ag^+ ion production. For an ion with a given mass to charge ratio (m/q), the flight time from target to detector depends only on the initial kinetic energy of the ion and the TOF dimensions and voltages. There is a

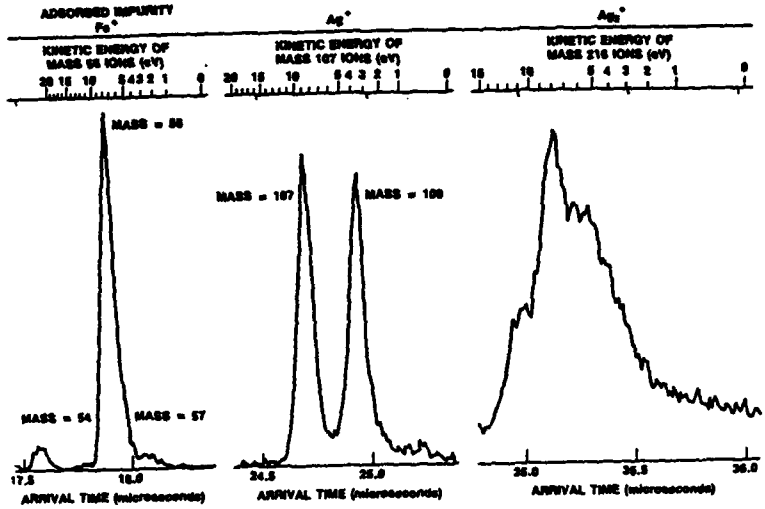

fixed relation between the ion arrival time and its initial kinetic energy which is used to generate the upper axes of Figure 1. From this we see that, at the laser fluence threshold for Ag^+ production, each of the ions generated are ejected with a mean kinetic energy (KE) of ~9 eV and a narrow distribution (~3 eV FWHM). Ablation experiments also were conducted at 351 nm, with similar results.

The observation of hypervelocity ions in high fluence laser ablation of solid targets is not uncommon. Even in moderate laser fluence experiments, high kinetic energy species have been observed. In those experiments, the average kinetic energy tends to be a function of the laser intensity, with the energy distribution being very broad and fitting a hot Maxwellian distribution. The excitation mechanism at these higher laser fluences involves inverse Bremsstrahlung absorption above the surface, where there are significant densities of electrons and ions. The observed ion acceleration at these fluences can result from ambipolar diffusion processes and plasma dynamical effects. To our knowledge, our results are the first to show that threshold laser ablation of silver, where plasma effects are negligible, results in hypervelocity ions with very narrow KE distributions. In addition, our data show no change in the KE distribution with laser fluence variation up to 20% above threshold. However, with further increase in laser fluence, well above the threshold for ion production, we observe the production of ions with very high kinetic energies (30 - 50 eV).

An explanation consistent with our results is that the ions are generated on or very near the surface and are accelerated either by a transient laser induced electric field or via a collective charge excitation in the sample. Several possible mechanisms suggest themselves, although none is fully consistent with the data.

In silver, electronic states (image potential states) outside the solid (5 to 20 Angstroms) have been observed. The energies of the image potential states follow a hydro-

genic series converging to the vacuum energy (4.49 eV), thereby allowing a large electron population to exist in the high density of states outside the solid. Assuming the incident laser light could excite electrons into these states, this would provide a possible mechanism for generating a transient electric field necessary for the ion acceleration. Our results cannot, however, be easily explained using the image potential state argument. For a single photon excitation, the 248 nm laser photon energy is above the work function for silver, while at 351 nm, the photon energy is insufficient to excite even the lowest (n=1) image potential state Therefore any excitation of electrons to these states cannot be through a simple excitation process. At the very least, one would expect that between 351 nm and 248 nm laser ablation there would be a measurable difference in the KE, since at the higher photon energy an excited electron is no longer bound.

Our results of laser induced fast ion desorption have some similarity to those derived from electron stimulated desorption (ESD) studies. In those experiments it has been shown that a beam of electrons (10 - 300 eV) bombarding a substrate can remove adsorbate ions while imparting to them a high kinetic energy. The models used to explain the ESD process agree that the initial excitation mechanism is an electronic excitation (either valence or core electronic states) in the adsorbate/substrate system. The specific mechanism for converting the electronic energy to nuclear motion of the ejected ion is described either through a Franck-Condon type excitation to a repulsive surface from which the ion is ejected, or in the case of a core excitation/ionization process, through an interatomic Auger decay which leaves the desorbate ion near a bound ionized neighbor, and the kinetic energy is gained by the desorbate via coulombic repulsion. The difficulty in this analogy is the mechanism by which multiple UV photons must be absorbed to lead to a core excitation or ionization. Since the core excitation mechanism predicts ion desorption thresholds at core ionization thresholds, the appropriate experiment would be tunable x-ray photon stimulated desorption on silver.

In silver, the value of the kinetic energy of the ions has a fortuitous coincidence to the bulk longitudinal plasmon energy (8 eV). It is known from x-ray photoelectron spectroscopy that a specific excitation (core hole creation) in a medium can result in a relaxation in the form of a plasmon excitation. If silver were a free electron metal with one 5s electron per atom, the plasmon energy would be 9.025 eV. Because of the strong d band electron interactions, this plasmon is split into two hybrid plasmons with energies at 4 and 8 eV. Our results show ablated ions only with 9 eV kinetic energy, and if the ion energies are produced by a plasmon interaction, it is not clear why the lower energy plasmon should be excluded from the interaction. For silver it is known that the two plasmon energies correspond to oscillations where the s-electron (valence) and d-electrons (bound) are out of phase for the low energy (4 eV) plasmon and in phase for the 8 eV higher energy plasmon. Intuitively, the collective electron oscillations which are in phase should be more efficient in ejecting ions from the surface. Clearly more experiments using different metal substrates (different plasmon energies) or perhaps insulators are necessary to obtain a more positive correlation between the laser ablated ion KE enhancement and the substrate plasmon energy.

1. R.P. Welle and H. Helvajian, "Threshold Level Photoablation of Metals: Ejected Ion Energy Distributions," AIAA-88-2776, 1988.

Laser Damage Studies of ZnS via Neutral Zn Particle Emission

H.F. Arlinghaus,* W.F. Calaway, C.E. Young, M.J. Pellin, and D.M.Gruen
Argonne National Laboratory, Argonne, Illinois 60439

L.L. Chase
Lawrence Livermore National Laboratory, Livermore, California 94550

ABSTRACT

Emission of neutral atoms from ZnS surfaces due to laser irradiation has been observed at power densities two orders of magnitude below the single pulse damage threshold of the material. We have measured the velocity distribution and absolute yield of neutral Zn atoms generated by exposure of ZnS single crystals to XeCl excimer laser irradiation (308 nm) using time-of-flight and high-resolution two-photon laser-induced fluorescence spectroscopy. The distributions are in agreement with Maxwell-Boltzmann distributions. The characteristic temperature increases from 2000 to 9000 K as the fluences are raised from 17 to 80 mJ/cm^2, respectively. The absolute Zn yield also increases from 10^8 to 10^{12} atoms per laser pulse as the laser fluence is increased. The results suggest formation of a plasma that interacts with the surface and leads to catastrophic failure. For consecutive laser shots at constant laser fluences, a nearly exponential increase in the Zn particle density is observed, yet visible damage did not occur until 150,000 laser shots. Our results show that neutral particle emission is of considerable importance in the identification of fundamental damage mechanisms and that microscopic damage occurs far below the single-pulse damage threshold.

INTRODUCTION

The application of high-power laser systems is limited in part by the inability to produce optical components capable of transmitting intense laser beams without incurring surface damage. To improve surface treatments and coating processes for optical components designed for high-power laser applications, an understanding of the fundamental physical and chemical origins of optical surface damage is required. In this work, time-of-flight (TOF) measurements employing high-resolution two-photon laser-induced fluorescence spectroscopy (LFS) have been used to determine the absolute yield and velocity distributions of Zn atoms ejected from ZnS single crystals under laser irradiation. The velocity distribution was measured by detecting the ejected particles at a known distance from the target at various times after the ablating laser strikes the target. By comparing LFS measurements of Zn atoms sputtered from pure metal targets by Ar^+ ions with the yield of laser-ablated Zn atoms, the absolute Zn yield was determined. The dependence of the damage threshold on the number of laser shots striking the surface was examined by determining the velocity distribution and the neutral yield from ablated surfaces as a function of the number of laser shots.

EXPERIMENTAL

The experimental arrangement, recently described in detail,[1,2] consists of an ablating laser, an ion gun, a LFS detection system, an ultrahigh vacuum (UHV) chamber (base pressure 3×10^{-8} Pa), and computer-controlled electronics. The interaction of the ablation laser [XeCl excimer laser (308 nm)] with the sample causes atoms to be ejected from the surface. At predetermined delay times after the ablating laser, a narrow-band probe laser (85 MHz bandwidth, 1.3 mJ/pulse, 15 ns pulse) is triggered. This laser is tuned across a 10-GHz frequency range near 320 nm , one-half the frequency of the Zn transition, $4s^2\ ^1S_0$ - $4d\ ^1D_2$ (160 nm). The induced fluorescence is detected at 636 nm

* Present address: Atom Sciences, Inc., Oak Ridge, TN 37830

($4d\ ^1D_2 - 4p\ ^1P^0_1$) by light collection optics which image the fluorescence from a well-defined volume, a known distance from the sample through a narrow bandpass interference filter onto a photomultiplier.

RESULTS AND DISCUSSION

The absolute yield of Zn atoms produced by laser irradiation was ascertained by comparison of its fluorescence signal with that of Zn atoms ejected from an ion-bombarded metallic Zn target since the absolute ion sputtering yield is well known (for details see Ref. 1). The absolute Zn yield from ZnS, due to 0.9 mJ irradiation at 308 nm on a 3 mm^2 (30 mJ/cm^2) area, was determined to be 10^9 atoms/pulse, corresponding to ~10^{-6} atoms/photon. Assuming stoichiometric ablation it was estimated that $4x10^{-4}$ of a monolayer is removed per laser pulse.

The velocity distribution was obtained by measuring the fluorescence signal at the appropriate frequency for each delay time and plotting those values against the velocity determined from that delay time. The velocity distributions were found to fit a Maxwell-Boltzmann distributions quite well. Figure 1 shows the calculated kinetic temperatures obtained from the Maxwell-Boltzmann fits for a series of experiments as a function of ablation laser fluence. The temperature increases slowly with increasing fluence until ~55 mJ/cm^2 where a significant temperature rise occurs. After the sharp rise, the temperature slowly increases further with increasing fluence. It should be noted that for each temperature measurement a new ablating area was used on the target. Visible damage was only observed for the three measurements made at an ablation fluence of ~80 mJ/cm^2. The solid line is a modelled surface temperature using the solution of the heat-flow equation from Bechtel[3] where the absorption coefficient $\alpha \rightarrow \infty$. As can be seen, the measured temperatures are much higher than the calculated maximum expected surface temperature. The poor fit led us to consider a model where a very thin layer of ZnS is isolated from the bulk, thus preventing thermal conductivity. The dotted line in Fig. 1 is a plot of temperature versus fluence for an isolated slice of ZnS with a thickness of 100 nm. The high kinetic temperatures at low fluences, obtained in our multiple-pulse experiments, may be caused by cumulative surface modification, such as thermally-induced cracking, leading to a reduction of the thermal conductivity compared to the bulk value. Single-pulse experiments showed only an increase of ~500 K at low ablation fluences.[4] This suggests that different ejection mechanisms are at work for single-pulse versus multiple-pulse laser ablation. Also shown in Fig. 1 is the sudden temperature rise observed near 60 mJ/cm^2. This step may indicate that a critical combination of particle density and laser intensity has been reached which causes formation of a plasma. The laser pulse could be absorbed directly by the plasma, thus causing additional heating of the ablated particles. In additon, the plasma would in turn bombard the surface and lead to the damage observed during the measurements of the velocity distributions at 80 mJ/cm^2. This idea is supported by the small sizes of the damage spots (μm) in comparison to the irradiated area (mm) and may indicate that local breakdown is the mechanism for component failure.

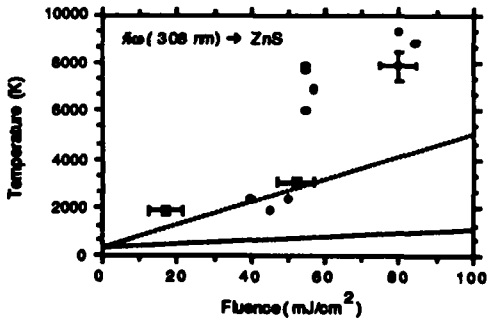

Fig. 1. Increase of the kinetic temperatures as a function of ablation fluence. The lines represent calculated surface temperatures.

In Fig. 2 the increase of the absolute neutral Zn yield is plotted as a function of inverse temperature. The Zn yield follows an Arrhenius relation for fluences between 20 and 60 mJ/cm^2 with an activation energy of 2.5 eV. This is approximately the heat of vaporization of ZnS and may indicate that a thermal process, such as sublimation, can account for the emission. At higher fluences, the measured temperatures deviate significantly from the straight line. This also occurs as an abrupt step, similar to Fig. 1, indicating that a second process has started. The absolute yield as a function of the inverse fluence[1] also suggests that Zn particles produced by an additonal mechanism such as interaction of the plasma with the surface and fragmentation of molecules and clusters in the plasma region leads to a rise of the measured yield.

Examination of the Zn yield and velocity distribution as a function of laser shots[1] reveals that the particle density increases nearly exponentially with consecutive laser shots for constant laser ablation fluences (45 mJ/cm^2) even though the kinetic temperature (~1900 K) of the ejected particles did not change. Most likely a change in both the surface morphology and the surface stoichiometry with repeated laser shots causes the increase of the Zn yield. After 150,000 shots (corresponding approximately to a removal of 60 monolayers) the first visible damage occurred. Clearly, the results suggest that microscopic damage increases with the number of laser shots and eventually leads to catastrophic failure at lower laser fluence than the single-pulse damage threshold.

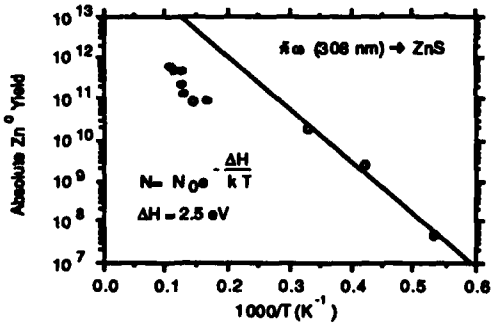

Fig. 9.Arrhenius plot of the absolute neutral Zn yield as a function of the inverse temperature. The solid line is a least-squares fit to the three data points obtained at low ablation fluences.

CONCLUSIONS

The LFS TOF technique has been shown to be a very sensitive and effective method for obtaining information on yields and velocity distributions of ejected particles from laser-irradiated surfaces. The ability to detect laser-induced particle emission at fluences two orders of magnitude below the single-pulse macroscopic damage threshold appears to be a powerful method for the study of optical surface damage and unambiguously shows that microscopic damage occurs much earlier, suggesting that first particles emission from clean surfaces should be defined as the damage threshold.

ACKNOWLEDGEMENTS

Work performed under the auspices of the U.S. Department of Energy, BES-Materials Sciences, under Contract W-31-109-ENG-38 (ANL) and Contract W-7405-ENG-48 (LLNL).

REFERENCES

1. H. F. Arlinghaus, W. F. Calaway, C. E. Young, M. J. Pellin, D. M. Gruen, and L. L. Chase, J. Appl. Phys., Dec. 1988.
2. H. F. Arlinghaus, W. F. Calaway, C. E. Young, M. J. Pellin, D. M. Gruen, and. L. L. Chase, to be published in J. Vac. Sci. Technol.
3. J. H. Bechtel, J. Appl. Phys. 46, 1585 (1975).
4. L. L. Chase and L. K. Smith, in Proceedings of the Symposium on Laser Induced Damage in Optical Materials, Boulder, CO (1987), in press.

PLATINUM SPOTS ON SILICON DEPOSITED BY PHOTON INDUCED CHEMICAL VAPOR DEPOSITION.

C. Garrido, B. Leon and M. Perez-Amor
Appl.Phys.Dept., Univ. Santiago, Apdo. 62, 36280-VIGO (SPAIN)

D. Braichotte and H. van den Bergh
Ecole Polytechnique Federale, CH-1015-LAUSANNE (SWITZERLAND)

ABSTRACT

Laser induced photolytic and pyrolytic deposition spots on silicon are studied for different laser powers,partial pressure and deposition time. In the photolytic case at low powers, the reaction takes place in the adsorbed phase on the surface, whereas at higher powers it is a predominantly gas phase process. Schottky diodes have been tested to demonstrate the good quality of platinum deposits.

INTRODUCTION

The term Laser Chemical Vapor Deposition (LCVD) describes a wide variety of processes in which material is deposited by means of laser irradiation starting from the gas phase [1] . Several LCVD experiments have been performed to deposit metals, such as copper[2], gold[3], nickel[4], platinum[5], etc., materials which are suitable to be used in microelectronics. We have studied the deposition of platinum on silicon substrates starting from organometallic platinum bis-hexafluoroacetyl-acetonate, $Pt(HFAcAc)_2$, whose absorption and vapor pressure are known[6].

EXPERIMENTAL

The experimental set up has been described previosly[7] . Briefly, the UV radiation (351-363 nm) of an argon ion laser is focalized through a microscope objetive inside a vacuum cell, in which independent control of the reactant partial presure, the substrate temperature and the laser spot diameter is possible.

Samples were characterized by profilometry and SEM to determine their geometry, morphology and structure.

RESULTS AND DISCUSSION

The thickness of the deposited material as a function of the exposition time obtained from the experimental results is shown in fig.1 for different laser powers (vapor pressure=0.15 mbar; laser spot diameter=50 μm) and it follows, apparently an anomalous behaviour. This fact led us to investigate in detail the deposition rate in function of power which is represented in figure 2. From powers up to 10 mW the deposition rate increases linearly with power (slope unity) and it decreases as the substrate temperature increases. Between 15 and 250 mW the rate decreases and with powers above 250

mW the rate increases again.

Looking across the microscope at the deposits obtained with laser powers between 2 and 250 mW they show the same morphology, their diameters are aproximately the same as the laser spot diameter and their profils are of square shape. The process in this range is photolytic and it takes place in the adsorbed phase[8]. From powers higher than 15 mW the deposition rate decreases, because the temperature increases due to the radiation absorption. For powers above 250 mW the morphology of the deposits changes, their grain size becomes bigger and their diameters increase quickly as power and exposition time increase, whereas the profil becomes gaussian or, in some cases, of volcanic form. For very short times the process is still photolytic and it takes place in the vapour phase. Once the pyrolytic temperature is reached , the process changes (fig.2 represents only the deposition rate due to photolysis).

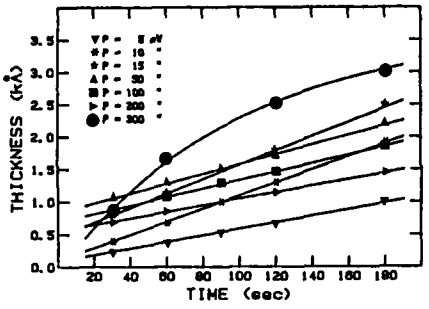

Fig.1. Thickness of the deposits for different powers

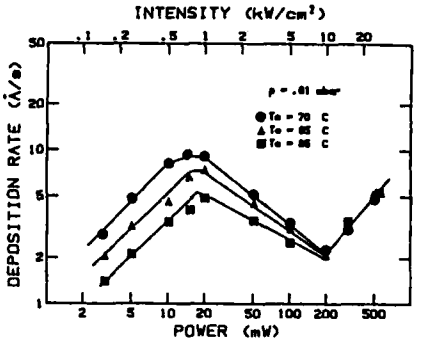

Fig.2. Photolytic deposition rate as a function of powers for different temperatures of the substrate

Figures 3 and 4 show the diameter and thickness obtained from the pyrolytic stage for a vapor pressure of 0.1 mbar and an initial substrate temperature of 90 °C (the laser spot diameter is 5 μm). The obtained growth in this stage is appreciably higher than that of the photolytic one. The gaussian form and the bigger diameters of the deposits in this case is due to the silicon high thermal conductivity, which leads up to a quick heat diffusion at areas rather far from the center of the spot.
The activation energy of the process[8] calculated by means of the Arrhenius plot gave the value of 6 Kcal/mol.

The deposits were analysed by Auger microscópy and their platinum content was 96% for the photolytic deposits containing also oxygen and carbon, while pyrolytic deposits contained 99% Pt. No contaminants were detected , at least in the detection range of the apparatus (1%).

For the purpose of testing our samples, Schottky diodes were built on epitaxial silicon (0.124 Ω .cm) on Si wafers with aluminium ohmic contacts on the back face. The value of the Pt-Si interface barrier was 0.82 V, slightly lower than the theorical value (0.9 V) and the value of the ideality factor n was 1.5, much greater than

the unity. These desviations arise probably from the oxide and contaminants present at the interface owing to the low vacuum used (5.10^{-3} torr).

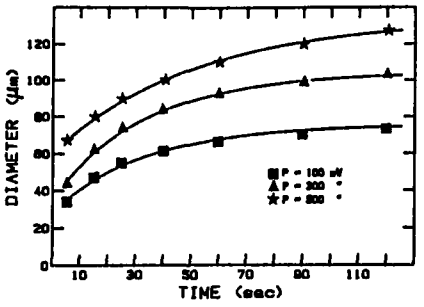

Fig.3. Diameter of the deposits for different powers

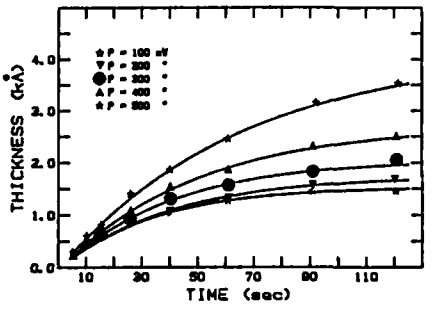

Fig.4. Thicknees of the deposits for different powers.

CONCLUSIONS

We have studied with some detail in our experiments the photolytic and pyrolytic platinum deposition process by LCVD. In spite of pyrolysis gives deposition rates higher than those which corresponds to the photolytic process, pyrolysis is more difficult to control, specially to obtain films with the apropiate shape, because their profiles take in general the form of a bell with a very extended base (very big diameters). On the other hand, the photolytic deposition provides films with square profiles and the same diameter as the laser spot diameter. The characteristics of the laser processed Schottky diodes are a demostration of the feasibility of the method, taking into account the experimental limitations. In the same way the results obtained by the photo- and pyrolytic diodes were practically the same, which points out that the slight difference in the composition of the films has no influence on the properties of the diodes, which arise only from the presence of states at the interface metal-silicon.

REFERENCES

1.- D. Bauerle, "Chemical Processing with Laser"; Springer-Verlag, Berlin, Heildelberg (1986)
2.- C.R. Moyan, T.H. Baum and C.R. Jones; Appl.Phys.A 40, 1 (1986)
3.- T.H. Baum and C.R. Jones, J.Vac.Sci.Technol.B 4, 1187 (1986)
4.- S.D. Allen; J. Appl. Phys. 52, 6501 (1981)
5.- C. Garrido-Suarez, D. Braichotte and H. van den Bergh; Appl. Phys.A 46,285 (1988)
6.- D. Braichotte and H. van den Bergh; Proceedings of the International conference on Lasers'85.
7.- D. Braichotte and H. van den Bergh; Appl. Phys.A 45, 337 (1988)
8.- C.Garrido, D.Braichotte, H.van den Bergh, B.Leon and M.Perez-Amor, to be publied.

TR-88-107

LASER ENHANCED SELECTIVE EPITAXY OF III-V COMPOUNDS

N.H. Karam* H. Liu, I. Yoshida, and S.M. Bedair
Electrical and Computer Eng. Dept. North Caroline State University,
Raleigh, N.C. 27695

ABSTRACT

Laser assisted epitaxy is a potential technique for low temperature deposition, selective growth and maskless direct writing of device structures. The selective deposition nature of this laser CVD process makes it especially attractive for monolithic integration of devices, lateral compositional grading and direct writing of microscale structures (waveguides). Successful selective epitaxial growth of device quality GaAs and monolayer control of its growth rate has been achieved at low temperatures (250° C) using Ar+ ion laser. Selective p and n-type doping has also been realized using Dimethylzinc and Hydrogen Selinide respectively. We will report on some of the potential applications of this new technique and the characterization tools employed.

INTRODUCTION

Recently, there has been considerable interest in Laser Assisted Chemical Vapor Deposition (LCVD) as a low temperature means for high quality selective epitaxy of III-V compounds [1-5]. In this paper, we will consider LCVD work on GaAs using Ar ion laser (514.5 nm) which seems to be most promising for producing device quality material [1-8]. Generally, two basic techniques exist for laser induced CVD namely, laser assisted atomic layer epitaxy (LALE) [3,7] and conventional LCVD. Detailed treatment of LALE is published elsewhere by the authors [1,3] and others [7].

In the case of conventional LCVD, the substrate is simultaniously exposed to the reactants during laser irradiation [1,2]. Low temperature (250° C) selective epitaxy of device quality GaAs has recently been reported by the authors [4,6] using LCVD multiple scanning technique [1]. The laser beam is tightly focused to a spot on a thermally biased substrate where locally controlled deposition takes place at a rate determined by the laser power density, scanning speed, thermal bias and mole fraction of reactants. Multiple scanning gives precise control over the deposited layer thickness. In this paper, we will report on the progress in low temperature selective epitaxy and doping of GaAs as well as the first maskless direct writing of a p-n junction by LCVD.

EXPERIMENTAL

Details of the MOCVD reactor and basic LCVD experimental procedure were previously reported [2]. Trimethylgallium (TMG, -13° C), AsH_3, Trimethylzinc (TMZn), Diethylzinc (DFZn), and H_2Se were the sources for Ga, As, P and n-type dopants respectively. Laser power P, spot sizes, thermal bias and scanning speed were in the range 0.5-3W, 500-620 μm, 250-400° C and 200 μm/sec respectively. Laser beam associated temperature rise and damage have been reported elsewhere [1,4].

*Currently with Spire Corporation, Patriots Park, Bedford, MA 01730

RESULTS AND DISCUSSION

Laser direct writing of single crystal III-V compound films on GaAs was first reported by the authors where epitaxy was verified by Transmission Electron Microscopy [1]. The substrates were mounted on a graphite susceptor that could be biased to a constant temperature T_b. An Ar ion laser was focused on the sample to induce localized decomposition of the reactants for deposition to take place. The selective LCVD growth traced the path of the laser beam and the growth rate was found to increase with the laser power density, T_b, and the TMG flow rate, and to decrease with increasing scanning speed.

Figure 1 shows a photo-luminescence (PL) spectrum at liquid He of LCVD GaAs deposited at T_b = 250°C and P = 2.5 W. This is the lowest temperature reported for GaAs epitaxy using organo-metallic and AsH_3 sources. Growth of GaAs by other techniques such as MBE at such low temperatures gave heavily compensated material with no PL reponse. The LCVD deposited line has two main PL peaks, the higher energy peak is at 1.514 eV which may correspond to excitonic related transition for GaAs. The lower energy peak (1.489 eV) is broad and probably due to impurities incorporated during LCVD, possibly from the TMG source. Such a problem may be reduced by the use of triethylgallium as a column III precursor, where the carbon elimination by formation of C_2H_6 is more stable than CH_4.

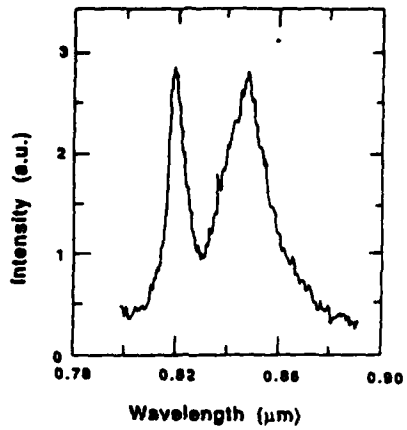

Figure 1. Low Temperature (4.2 K) Photoluminescence Spectrum for LCVD at T_b = 250° C.

ELECTRICAL PROPERTIES AND DOPING BEHAVIOR OF LCVD GaAs FILMS

Incorporation of dopants such as Si from SiH_4, Se from SeH_2 and Zn from DEZn or DMZn in conventional MOCVD is critically dependent on the growth temperature. Thus, doping behavior in the temperature range of LCVD (250 - 400°C) is expected to be different from that estimated in conventional MOCVD. The presence of laser irradiation can also enhance or retard the dopants incorporation. Table 1 shows the estimated carrier concentration and resistivity for LCVD samples deposited at different temperatures and laser power. Estimates of carrier concentrations were based on resistivity measurements and mobility 100 cm^2/ V-sec. Selective p-type doping with DEZn

Substrate Temp. °C	Laser Power	Dopant	Resistivity (Ω.cm)	Estimated Carriers Concentraton
400	1.3-4W	undoped	high resistivity	less than $10^{14}/cm^3$
250	3.5W	undoped	high resistivity	
400	2W	DMZn	0.02	$P = 10^{18}/cm^3$ range (or higher) Zn everywhere on GaAs substrate
300	3W	DMZn	0.06	$P = 10^{18}/cm^3$ range. Zn deposited in the vicinity of the LCVD lines
300	3W	H_2Se	0.6	$n = 10^{17}/cm^3$

Table 1. Electrical Properties of GaAs Grown by LCVD.

was not successful due to its efficient cracking using Ar^+ laser which results in uniform Zn incorporation over the entire wafer. Successful selective doping of GaAs was achieved using DMZn at T_b 300°C yielding carrier concentration in the $10^{18}/cm^3$ range. LCVD n-type doping was achieved at 300°C yielding carrier concentration in the $10^{17}/cm^3$ range.

A p-n rectifying junction was achieved by LCVD of p^+ GaAs lines on Si doped GaAs substrate (n = $10^{18}/cm^3$) at 300°C. The junction (100 x 200 m^2) was fabricated using standard photolithographic techniques; its I-V characteristics is shown in Figure 2. The diode showed a soft breakdown probably due to the high doping on both sides of the junction.

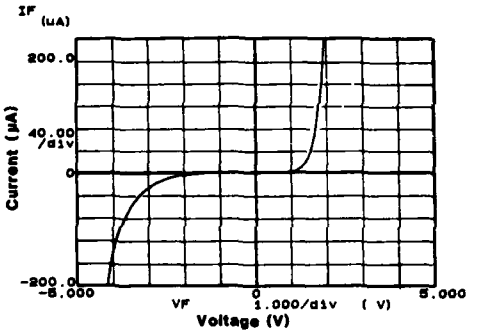

Figure 2. I-V Characteristics of p-n Junction Selectively Deposited by LCVD on GaAs at 300° C.

In conclusion, LCVD has been successfully demonstrated as a new approach for low temperature selective epitaxy of III-V compounds. GaAs has been deposited using this LCVD technique at a substrate temperature as low as 250° C. DMZn and H_2Se have been successfully used as p- and n-type dopants, respectively, and a GaAs p-n junction was selectively grown using this LCVD approach.

REFERENCES

1. N.H. Karam, N.A. El-Masry, and S.M. Bedair, Appl. Phys. Lett. 49, 880 (1986); N.H. Karam, S.M. Bedair, N.A. El-Masry, and D. Griffis, Mat. Res. Soc. Symp. B, 75, 241. (1987).

2. S.M. Bedair, J.K. Whisnant, N.H. Karam, D. Griffis, N.A. El-Masry, and H.H. Stadelmayer, J. Cryst. Growth 77, 229 (1986).

3. Y. Aoyogi, S. Masuda, S. Namba, and A. Doi, Appl. Phys. Lett. 47, 95 (1985).

4. N.H. Karam, H. Liu, I. Yoshida and S.M. Bedair, Appl. Phys. Lett. 53, 767 (1988).

5. N.H. Karam, H. Liu, I. Yoshida, and S.M. Bedair, Appl. Phys. Lett. 52, 1144 (1988).

6. N.H. Karam, H. Liu, I. Yoshida, B.L. Jiang, and S.M. Bedair, in Proc. of the 4th Int. Conf. on MOVPE, Hakone, Japan, 1988.

7. A. Doi, Y. Aoyagi, and S. Namba, Appl. Phys. Lett. 49, 785 (1986).

8. V. Donnely, Mat. Res. Soc. Symp B proc. (MRS) meeting, Boston, MA 101, 8, (1988).

This work is supported by the National Science Foundation (DMR 8303916-95).

ROTATIONAL TEMPERATURE OF SiF_2 RADICALS PRODUCED IN THE THERMAL ETCHING OF SILICON BY FLUORINE CONTAINING COMPOUNDS

J. S. Horwitz[a], J. A. Dagata[b], D. W. Shinn[c] and M. C. Lin[c]

Chemistry Division, Naval Research Laboratory, Washington, D.C. 20375

ABSTRACT

The rotational constants of the B^1B_2 state of SiF_2 have been determined by fitting the (2+1) resonance-enhanced multiphoton ionization (REMPI) spectrum at 321 nm using the asymmetric rigid rotor approximation. Ionization spectra, obtained in a thermally equilibrated flow cell at 200 and 350 K, establish a bond length of 1.5975 Å and a bond angle of 103.2° for the $\tilde{B}^1B_2$ state of SiF_2. Computer simulations of the SiF_2 REMPI bandshape for the F_2 etching of silicon single crystals under single collision conditions indicate that the radicals which desorb from the fluorosilyl surface layer do so with poor rotational energy accommodation: i.e., $T_{rotational}$ ~350-450 K for 600 K < $T_{surface}$ < 1000 K.

INTRODUCTION

Plasma etching of silicon remains an important process in semiconductor device fabrication. The complex nature of plasma-surface interactions has stimulated interest in the more fundamental gas-surface interactions seen in thermally activated processes. The reaction of silicon with F_2 is spontaneous at room temperature, with SiF_4 as the major gas phase product. SiF_x (x=1-3) species have been detected both on the surface[1-3] and in the gas phase[4-6], although not all are believed to be primary products of the gas-surface interaction. While the techniques that have been applied to the study of the etching mechanism are quite diverse, they share as a common goal the identification of products formed on the surface or in the gas phase and the relative distribution of these products. The dynamics of this process is inferred from these measurements.

Recently, we demonstrated that resonance enhanced multiphoton ionization/mass spectrometry (REMPI/MS) can be used to identify the gas phase products in spontaneous etching under single collision gas-surface conditions. Under these conditions, SiF_2 has been observed as a nascent product in the reaction of silicon single crystals with F_2, XeF_2 and NF_3[7-9]. The REMPI of SiF_2 was assigned to the (2+1), $\tilde{B}^1B_2 \leftarrow \tilde{X}^1A_1$ transition. Both the one-photon VUV absorption[10] and the (2+1) REMPI spectra are moderately structured and can provide not only information regarding product identification but can also be used to determine radical temperature. For radicals formed in a single collision gas-surface environment, the spectroscopy serves as a probe of the conditions in which the radical was formed.

In this study, an asymmetric rigid rotor approximation has been used in conjunction with Boltzmann populations for ground state vibrational and rotational levels to model the thermally equilibrated one-photon VUV absorption and the (2+1) REMPI for SiF_2. The model is found to be extremely sensitive to the excited state geometry. The experimentally determined geometry is then used to measure the temperature of SiF_2 radicals formed under single collision gas-surface conditions. The spectral modeling indicates that desorbed SiF_2 radicals are not equilibrated with the surface and are characterized by rotational temperatures close to room temperature for crystal surface temperatures ranging from 600 to 1000 K.

[a]NRC/NRL Postdoctoral Associate.
[b]ONT/NRL Postdoctoral Associate, present address: NIST, Gaithersburg, MD.
[c]present address: Chemistry Department, Emory University, Atlanta GA.

EXPERIMENTAL

The frequency doubled output (500-700 μj/pulse) of a Nd:YAG-pumped dye laser was focused with a 6" focal length lens into one of two reaction chambers used to study the REMPI spectra. In a pyrex flow cell, maintained at a total pressure of ~6 torr, SiF_4 (1.6% in He) reacted with polycrystaline Si heated to 970 K. The photoionization region was about 50 cm downstream from the crystals. The drift region and ionization region were in good thermal contact with a bath that was used to regulate the temperature of the gas inside the cell. Under these conditions, radicals were assumed to be in thermal equilibrium with the He buffer gas. Alternatively, REMPI spectra were measured for SiF_2 radicals generated in the reaction of F_2 (10% in He) with a Si(100) single crystal under single gas-surface collision conditions. This experiment has been described in detail in reference 9.

THEORETICAL METHODS

The calculation of the (2+1) REMPI bandshape of the $\tilde{B}\ ^1B_2 \leftarrow \tilde{X}\ ^1A_1$ transition of SiF_2 at 321 nm was performed as follows. Molecular and intertial axes were associated according to the type I^r convention[11] for ground and excited electronic states in the asymmetric rigid rotor approximation. All subsequent derivations of nonvanishing matrix elements, statistical weights, and selection rules were carried out using this convention. In the calculation, the lower and upper state rotational levels of all possible J ($\leq$ 100) were expressed in the Wang basis of symmetric-top functions and diagonalized.[12] Expressions for two-photon transition probabilities and amplitudes for rotating, asymmetric-top molecules have been given previously by Metz, et al.[13] For the case of absorption of two identical photons by a molecule with C_{2v} symmetry, the only nonvanishing (Cartesian) two-photon absorption tensor elements[14] for a ($B_2 \leftarrow A_1$) transition are (yz,zy). The resulting intensity for each line was convoluted with a Lorentzian linewidth and summed over a 250 cm^{-1} region about T_0, determined to be 62293±15 cm^{-1}. Contributions to the overall bandshape arising from v_2 sequence bands[10] were accounted for by multiplying the (0,0) envelope by a Boltzmann factor and using the displacements given in Ref. 10. Since the ground state rotational constants of SiF_2 are known,[15] the only free parameters to be determined from the calibrated spectra at 200 and 350 K are the bond length and bond angle of the upper state. A best-fit was obtained with r=1.5975 Å and θ=103.20°. Finally, a one-photon absorption bandshape was generated using these parameters and was found to be in good agreement with the spectrum published by Gole, et al.[10]

RESULTS AND CONCLUSIONS

Shown in Figure 1a are the REMPI spectra obtained for the $\tilde{B}^1B_2 \leftarrow \tilde{X}^1A_1$ transition of SiF_2 obtained in the thermally equilibrated flow cell at 200 and 350 K. The spectra have been normalized to the square of the laser power and have been scaled such that the integrated intensity is constant (i.e., the two-photon cross-section is independent of temperature). As the bath temperature is lowered, the spectrum narrows and increases in intensity. This is a result of a decrease in the number of rotational levels that can be thermally populated in the ground state. Shown in Figure 1b are the calculated spectra for similar temperatures. The temperature dependence of modeled spectra are in good agreement with the experimental spectra.

In Figure 2a the thermally equilibrated room temperature spectrum is compared to the spectrum obtained for the reaction of F_2 with a Si(100) crystal heated to 1000 K. At 10^{-5} torr, the mean free path for collisions is long compared to the distance between the surface and the photoionization region. As a consequence of the low pressure, the measured internal energy should be the same as when the radical was desorbed from the surface. The two spectra are quite similar in intensity and spectral width. For comparison, the modeled spectra for thermally equilibrated SiF_2 radicals at 300 K and 1000 K are shown in Figure 2b. At the high temperature, the modeled spectrum becomes

extremely broad and unstructured. As a consequence of this, the maximum intensity of the transition decreases.

Clearly, the SiF_2 generated in the reaction of F_2 with a silicon surface at 1000 K is not characterized by a rotational temperature (T_r) similar to the crystal surface temperature (T_s). For a wide range of crystal temperatures (600 to 1000 K), the SiF_2 REMPI is best described by a rotational temperature of ~350-450 K.

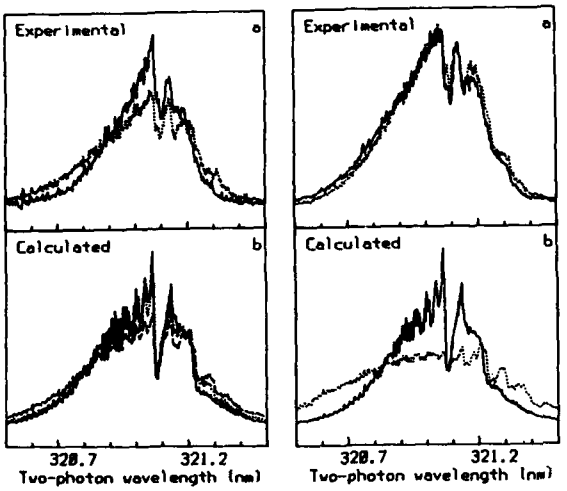

Figure 1 (left). Spectra for thermally equilibrated radicals for the (2+1) $\tilde{B}^1B_2 \leftarrow \tilde{X}^1A_1$ REMPI of SiF_2. a) Experimental specrta at 200 K (—) and 350 K (·····). b) Calculated spectra for T_r at 200 K (—), 350 K (····) and 500 K (– –).

Figure 2 (right). A comparison of a thermally equilibrated spectrum with a spectrum observed under single collision gas-surface conditions. a) Measured spectra for thermally equilibrated radicals at 300 K (—) and under single collision gas-surface conditions with T_s=1000 K (····). b) Calculated spectra for thermally equilibrated radicals for T_r at 300 K (—) and 1000 K (···).

REFERENCES

1. J. A. Mucha, V. M. Donnelly, D. L. Flamm and L. M. Webb, J. Phys. Chem., 85 3529 (1981).
2. M. J. Vasile and F. A. Stevie, J. Appl. Phys., 53 3799 (1982).
3. H. F. Winters and F. A. Houle, J. Appl. Phys., 54 1218 (1983).
4. F. R. McFeely, J. Morar, N. D. Shinn, G. Langren, F. J. Himpsel and Y. Jugnet, Mat. Res. Soc. Proc., 25 341 1984.
5. B. Roop, S. Joyce, J. C. Schultz, N. D. Shinn and J. Steinfeld, Appl. Phys. Lett., 46 1187 (1985).
6. F. R. McFeely, J. F. Morar and F. J. Himpsel, Surf. Sci., 165 277 (1986).
7. J. A. Dagata, D. W. Squire, C. S. Dulcey, D. S. Y. Hsu and M. C. Lin, Chem. Phys., Lett. 134 151 (1987).
8. J. A. Dagata, D. W. Squire, C. S. Dulcey, D. S. Y. Hsu and M. C. Lin, J. Vac. Sci. Tech. B, 5 1495 (1987).
9. D. W. Squire, J. A. Dagata, D. S. Y. Hsu, C. S. Dulcey and M. C. Lin, J. Phys. Chem., 92 2827 (1988).
10. J. L. Gole, R. H. Hauge, J. L. Margrave, and J. W. Hastie, J. Mol. Spec., 43 441 (1972).
11. G. W. King, R. M. Hainer and P. C. Cross, J. Chem. Phys., 11 27 (1943).
12. F. Creutzberg and J. T. Hougen, J. Mol. Spec., 38 257 (1971).
13. F. Metz, W. E. Howard, L. Wunsch, H. J. Neusser and E. W. Schlag, Proc. Roy. Soc. Lond., A363 381 (1978).
14. W. M. McClain, J. Chem. Phys., 55 2789 (1971).
15. V. M. Rao, R. F. Curl, P. L. Timms, and J. L. Margrave, J. Chem. Phys., 43 2557 (1965).

IV. ATOMIC, MOLECULAR, AND IONIC SPECTROSCOPY

IV.A. Energy-Resolved Ionization and Fragmentation Processes in Atoms and Small Molecules

IV.B. Ionization Processes and Ion Spectroscopy of Polyatomic Species

IV.C. Interaction of Strong Optical Fields with Matter

IV.D. Experiments with Laser-Cooled and Trapped Atoms

IV.E. High-Resolution Spectroscopy--From Atoms to Polyatomic Molecules

TWO-COLOR STUDIES OF AUTOIONIZING STATES IN SMALL MOLECULES*

S. T. Pratt, M. A. O'Halloran,† F. S. Tomkins, J. L. Dehmer, and P. M. Dehmer
Argonne National Laboratory, Argonne, Illinois 60439

ABSTRACT

Two-color resonantly enhanced multiphoton ionization (REMPI) is used to study rotational autoionization of molecular hydrogen and nitric oxide. In contrast to conventional, single-photon techniques, the REMPI technique can be used to study autoionizing levels of H_2 that can decay only through very weak interactions such as p-f mixing and singlet-triplet mixing. In addition, rotational autoionization that occurs with a change in rotational quantum number greater than 2 can also be examined (i.e., $\Delta N^+ > 2$). In homonuclear molecules, symmetry considerations require that ΔN^+ be even; in heteronuclear molecules, ΔN^+ may be even or odd. It is found, however, that NO is in some sense quasi-homonuclear, and that processes with ΔN^+ = even appear to be more efficient than processes with ΔN^+ = odd.

ROTATIONAL AUTOIONIZATION OF H_2

Two-color REMPI was used to study pure rotational autoionization of np Rydberg states of H_2 near the first ionization threshold. One laser was used to excite the two-photon transition to the E,F $^1\Sigma_g^+$, v'=E0, J'=0-4 intermediate levels, and a second laser was used to probe single-photon transitions to autoionizing Rydberg series converging to the X $^2\Sigma_g^+$, v^+=0, N^+=1-6 rotational levels of the ion. In this paper, we focus on the series excited from the J'=2 level, and Figure 1 shows a schematic diagram of the allowed transitions from this level to np Rydberg states in which the spins are assumed to remain coupled into a singlet state. Transitions to levels with $\ell \neq 1$ are not observed. Only transitions to Rydberg states with J=1,2,3 are allowed (ΔJ=0, ±1), and because of symmetry considerations, the series must converge to even rotational levels of H_2^+. Figure 1 shows that for excitation from E,F $^1\Sigma_g^+$, J'=2, one Rydberg series with J=1 converges to the N^+=0 level of the ion (corresponding to P(1)np0 transitions), three Rydberg series with J=1,2,3 converge to the N^+=2 level of the ion (corresponding to P(2)np2, Q(2)npπ, and R(2)np2 transitions), and one Rydberg series with J=3 converges to the N^+=4 level of the ion (corresponding to R(2)np4 transitions). The Rydberg series are traditionally denoted by Hund's case (b) notation for low values of principal quantum number (e.g., P(J')npσ $^1\Sigma_u^+$ and P(J')npπ $^1\Pi_u$) and by Hund's case (d) notation for high values of principal quantum

*Work supported by the U.S. Department of Energy, Office of Health and Environmental Research, under Contract W-31-109-Eng-38.
†Present address: Department of Physics and Astronomy, University of Oklahoma, Norman, Oklahoma 70319.

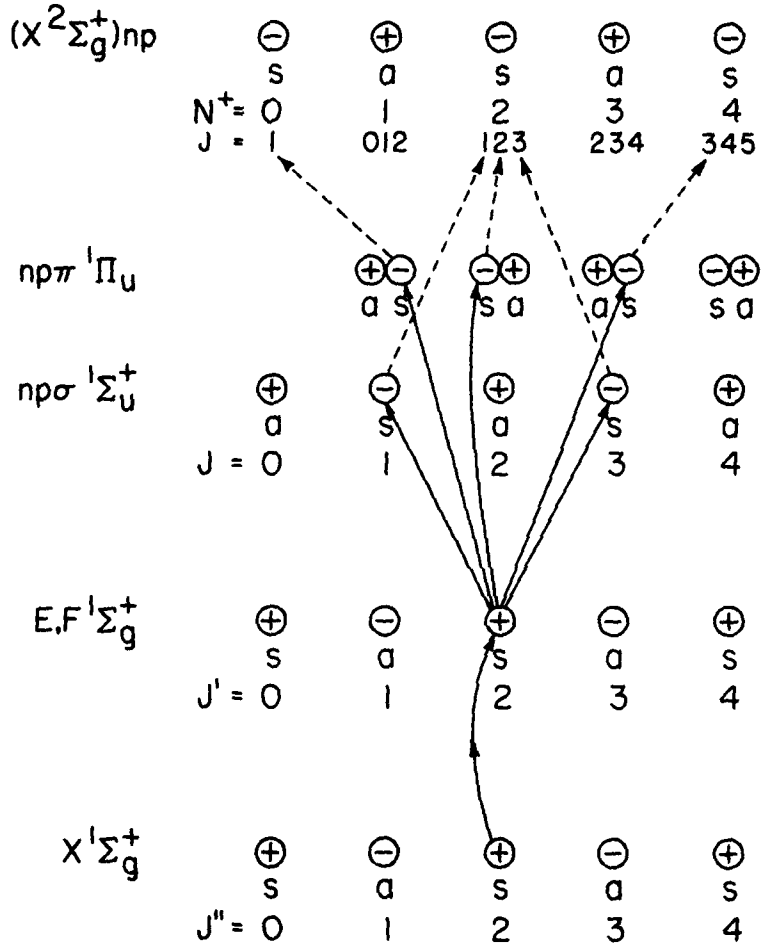

Figure 1. Schematic illustration of the allowed rotational transitions for two-color (2+1') ionization of H_2 via the $E,F\ ^1\Sigma_g^+$ state. The processes shown are (1) the two-photon Q(2) transition from the $X\ ^1\Sigma_g^+$, J"=2 ground state to the $E,F\ ^1\Sigma_g^+$, J'=2 state; (2) the single-photon transition from the $E,F\ ^1\Sigma_g^+$, J'=2 state to the $np\sigma\ ^1\Sigma_u^+$ and $np\pi\ ^1\Pi_u$ Rydberg states in Hund's case (b) coupling; and (3) the transition from Hund's case (b) to Hund's case (d) coupling (shown as dashed lines).

number (e.g., $R(J')npN^+$). Since the Q(J') series have pure π character for all values of n, they are denoted by $Q(J')np\pi$ rather than $Q(J')npN^+$ at high n.

Of the five series shown in Figure 1, the four series that converge to $N^+=2$ and 4 are energetically allowed to autoionize above the $N^+=0$ threshold; however, the selection rules for autoionization require that the autoionizing rotational level must have the same parity (+ or -), nuclear exchange symmetry (a or s), and total

angular momentum (J) as the ion core plus electron. Using the assumptions of outgoing p-wave and singlet coupling of the spins of the outgoing electron and the ion core, the P(2)np2 series may autoionize into the P(2)np0 continuum, and, above the $\bar{N}^+=2$ threshold, the R(2)np4 series may autoionize into the R(2)np2 continuum. These autoionization processes are illustrated in Figure 2. In this coupling scheme and in the absence of external perturbations, the Q(2)npπ and R(2)np2 series cannot autoionize as no continua with the correct total angular momenta exist. In

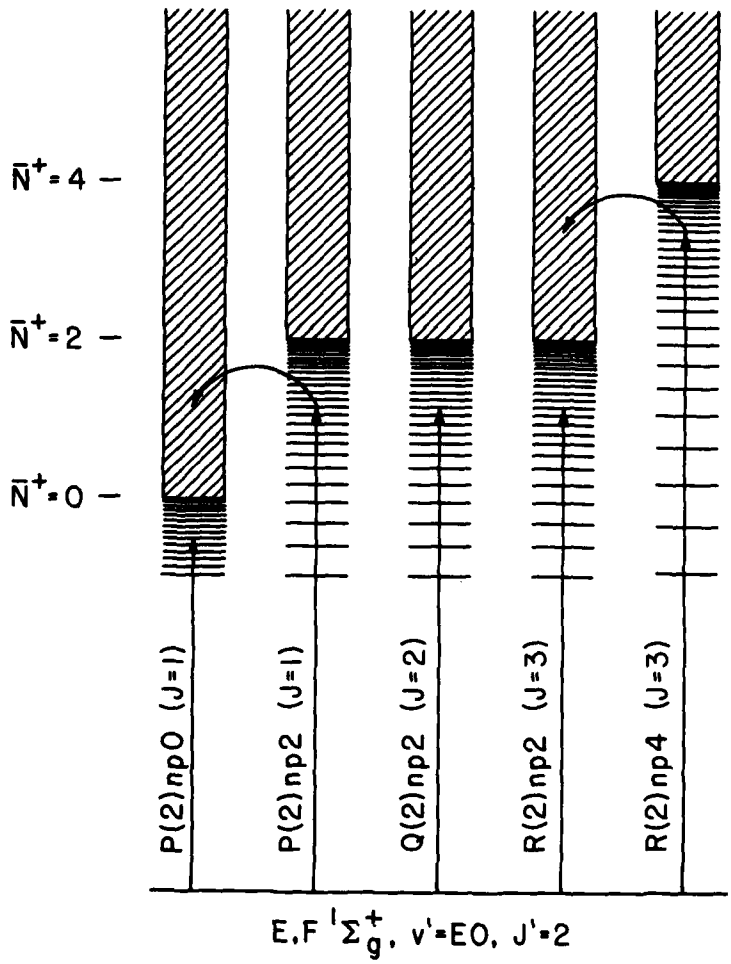

Figure 2. Schematic illustration of the allowed autoionization paths for the Rydberg series excited from the E,F $^1\Sigma_g^+$, J'=2 level, and decaying into the H_2^+ X $^2\Sigma_g^+$, v$^+$=0, $\bar{N}^+$+ep singlet continuum.

addition, below the $N^+=2$ ionization threshold, the R(2)np4 series can only autoionize via $\Delta N^+=4$, which is also forbidden according to the approximations of Figure 1.

The two-color excitation spectrum determined via the E,F $^1\Sigma_g^+$, v'=0, J'=2 level by monitoring the photoelectron signal is shown in Figure 3.[1] The $N^+=0$ continuum is very weak, as is expected, because

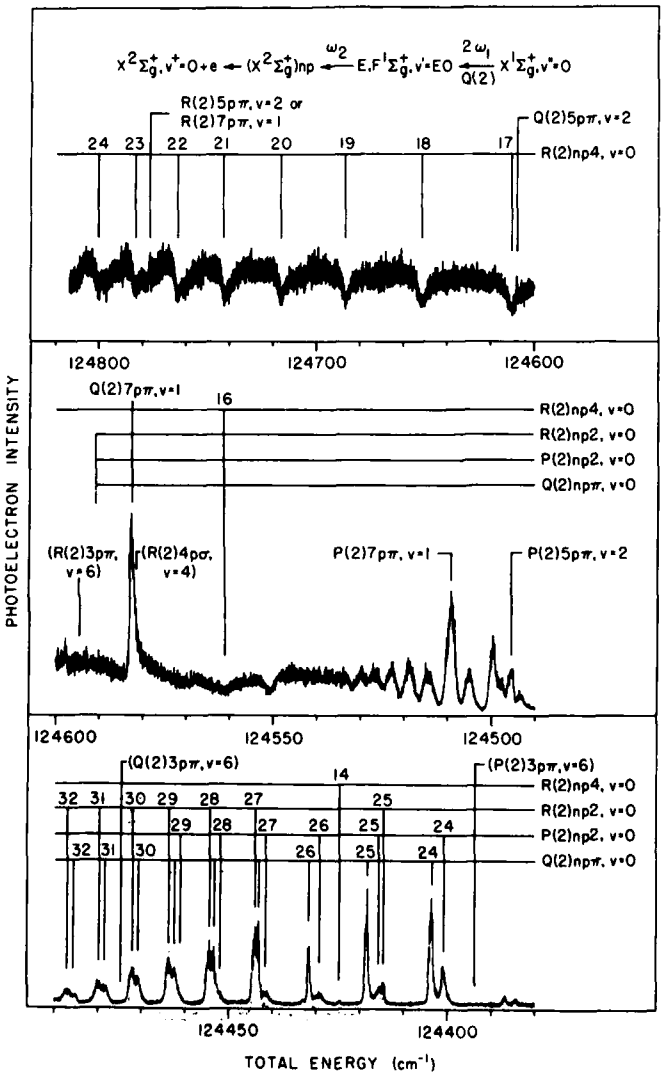

Figure 3. Two-color (2+1') excitation spectrum of autoionizing np Rydberg states of H_2 excited from E,F $^1\Sigma_g^+$, v'=E0, J'=2. The abscissa gives the total energy from the H_2 $^1\Sigma_g^+$, v=0, J''=0 ground state.

$\Delta N^+ \neq 0$, and it cannot be distinguished from the background low-energy electron signal. One broad series is observed between the $N^+=0$ (124417.42 cm^{-1})[2] and $N^+=2$ (124591.72 cm^{-1})[2,3] ionization thresholds; this series is identified as P(2)np2, which couples strongly with the X $^2\Sigma_g^+$, $v^+=0$, $N^+=0+\varepsilon p$ continuum, as is shown in Figure 2. Two previously unobserved sharp series with instrumentally limited linewidths are also observed in this energy region and are identified as the Q(2)npπ (J=2) and the R(2)np2 (J=3) series.

As was discussed above, the Q(2)npπ and R(2)np2 series cannot decay within the approximations of Figure 2, because no $N^+=0$, εp, $J^+=2$ or 3 continua exist. However, general considerations[1] show that the rates of the decay mechanisms that compete with autoionization (i.e., fluorescence and predissociation) are not particularly fast, so that autoionization via relatively weak interactions can occur. This is confirmed in Figure 3. Autoionization of the J=3 Rydberg series into the $N^+=0$ continuum can occur with an εf outgoing partial wave, while autoionization of the J=2 series into the $N^+=0$, εp continuum can occur if the spins recouple into a triplet state rather than a singlet state. Thus, the study of the autoionization of the J=2 and 3 series provides information on the weak singlet-triplet and p-f interactions in H_2, respectively. Higher resolution is necessary to measure the widths of these levels and to determine the interaction matrix elements more precisely.

Above the $N^+=2$ ionization limit in Figure 3, the R(2)np4 series is observed as a series of window resonances. Below the $N^+=2$ threshold, autoionization of the R(2)np4 series members must proceed by $\Delta N^+=4$, in contrast to the P(2)np2, Q(2)npπ, and R(2)np2 series, which decay by $\Delta N^+=2$. Evidence for at least two of the R(2)np4 transitions below the $N^+=2$ threshold is observed in the present spectra. In particular, a very weak peak at 124424.7 cm^{-1} is assigned as R(2)14p4. The half-width of the R(2)14np4 level is resolution limited (0.6 cm^{-1}), while the higher members of the same series above the $N^+=2$ threshold (which autoionize by $\Delta N^+=2$) are approximately a factor of 20 broader. Thus, the rate of the $\Delta N^+=4$ process is at least a factor of 20 slower than the rate of the $\Delta N^+=2$ process. This is reasonable because the $\Delta N^+=4$ process requires an f-wave component in the continuum, while the $\Delta N^+=2$ process can involve either p- and f-waves. Higher resolution is necessary for a precise determination of the relative rates.

ROTATIONAL AUTOIONIZATION OF NO

Two-color REMPI was also used to probe Rydberg states of NO converging to the first ten rotational levels of NO^+ X $^1\Sigma^+$, $v^+=0$ by using the A $^2\Sigma^+$, $v'=0$ intermediate state. Above the $N^+=0$ threshold, rotational autoionization of Rydberg series converging to higher thresholds is observed. In contrast to H_2, predissociation of the Rydberg states of NO is found to compete with rotational autoionization in much the same manner as predissociation competes with vibrational autoionization in the region of the first few

vibrational limits of NO^+.[4,5] Aside from a scaling factor of $1/n^3$, the predissociation rate is expected to vary slowly in the wavelength region of the present study; and, in particular, it is not expected to change significantly as the probe laser is scanned through an N^+ threshold. Thus, predissociation provides an approximately constant decay rate to which the rotational autoionization rates for different values of ΔN^+ can be compared. Because NO is a heteronuclear molecule, rotational autoionization can occur for both even and odd values of ΔN^+. However, rotational autoionization by $\Delta N^+=2$ is found to be faster than that by $\Delta N^+=1$ or 3.[6] This results from the symmetry requirement that ΔN^+ = even processes require interactions between levels that both have even or both have odd values of orbital angular momentum ℓ, while ΔN^+ = odd processes require interactions between levels of which one has even ℓ and the other has odd ℓ. The latter interactions are known to be weak in NO.[7]

CONCLUSION

In this paper, we have presented new results on the rotational autoionization of H_2 and NO. The fundamental conclusion is that two-color excitation of Rydberg states of small molecules allows the detailed study of selected levels that can only decay by interactions that are normally too weak to be observed.

REFERENCES

1. M. A. O'Halloran, P. M. Dehmer, S. T. Pratt, J. L. Dehmer, and F. S. Tomkins, J. Chem. Phys., in press.
2. E. E. Eyler, J. Gilligan, E. McCormack, A. Nussenzweig, and E. Pollack, Phys., Rev. A 36, 3486 (1987).
3. M. Kuriyan and H. O. Pritchard, Can. J. Chem. 55, 3240 (1977).
4. W. A. Chupka, in Ion-Molecule Reactions, edited by J. L. Franklin (Plenum, New York, 1972) Vol. I, p. 33.
5. A. Giusti-Suzor and Ch. Jungen, J. Chem. Phys. 80, 986 (1983).
6. S. T. Pratt, J. L. Dehmer, and P. M. Dehmer, to be published.
7. See, for example, S. Fredin, D. Gauyacq, M. Horani, Ch. Jungen, G. Lefevre, and F. Masnou-Seeuws, Mol. Phys. 60, 825 (1987), and references therein.

MULTIPHOTON IONIZATION(MPI) OF VIBRATIONALLY EXCITED NO (v"=0-9) IN A PULSED MOLECULAR BEAM

C. S. Feigerle
University of Tennessee, Knoxville, Tennessee 37996-1600

J. C. Miller
Chemical Physics Section, Oak Ridge National Laboratory,
Oak Ridge, Tennessee 37831-6125

ABSTRACT

Vibrationally excited (v" =0-9) yet rotationally cold (<100K) NO has been produced by electrically discharging N_2O in a pulsed molecular beam. The MPI spectrum of this sample has been recorded from 420 to 460nm and 212 to 225nm. Numerous new bands have been observed in this region and assigned as A ← X and C ← X transitions originating from vibrationally excited NO. In particular the 420 to 460nm region is dominated by C ← X hot band transitions which produce NO^+ in a (2+1) ionization scheme. Comparison of spectra of (1+1) ionization through the A state with compu r simulations show the one-photon resonance transition to be nearly saturated.

INTRODUCTION

The field of multiphoton ionization spectroscopy has grown rapidly, developing from an emerging spectroscopy to being increasingly utilized as a probe of photochemical and chemical reaction dynamics. In these applications, it is paramount that the underlying spectroscopy be understood if meaningful results are to be obtained. The present paper describes experimental and theoretical studies of MPI spectroscopy of NO. New MPI bands are described and the importance of the C-state intermediate is demonstrated for a region of the spectrum previously attached to ionization through the A-state. Simulations of a "saturated" spectrum are presented, saturation being an experimentally useful condition for population analysis[1,2].

EXPERIMENTAL

The apparatus used in these experiments has been previously described[3]. Briefly, gas from a 10 Hz pulsed nozzle is ignited into a glow discharge by applying a 1-2kV potential across wire electrodes placed in the gas expansion. The molecular beam is skimmed and then crossed at 90° with the focused output from an excimer pumped dye laser. Ions formed by multiphoton ionization are extracted and analyzed in a Wiley-McLaren type time-of-flight mass spectrometer. MPI spectra are obtained by time-gating the mass of interest and recording the boxcar averaged signal as a function of laser wavelength. Spectra were recorded from 420nm to 460nm using the direct output of the coumarin 440 dye laser beam, and 212nm to 230nm using a β-barium borate crystal(CSK Co) to double the beam.

NO SPECTRAL ASSIGNMENTS

The wavelength regions studied are those that span the A(v'=1) ← X(v"=0) and A(v'=0) ← X(v"=0) one- and two-photon excitations. In the absence of a discharge, these transitions provide the only significant (1+1) or (2+2) ionization signal in these regions. However, when the discharge is ignited many new bands appear. An example of the spectra obtained with the discharge on, using the direct and doubled dye laser output to scan the A(2,2) and C(0,4) bands, is shown in Figures 1(a) and (b) respectively. The notation A(v',v") is used to denote the A(v') ← X(v") transition to the intermediate A-state in route to ionization. The most striking feature of these spectra is the strength of the C(0,4) band compared to the absent A(2,2) band in Fig. 1(a). This is easily understood when one considers the energetics involved. For the C(0,4) band, only a single photon is necessary to ionize the C(v'=0) intermediate making this a (2+1) ionization process. With the A(2,2) band, two photons are required to ionize the A(v'=2) intermediate. Due to the reduced order in the ionization step, (2+1) ionization through the C-state dominates the 420 to 460nm discharge MPI spectrum; C(1,5), C(0,3), and C(1,4) bands also being observed in this region. For one photon excitation, ionization through the A- and C-states have to compete in the same order and (1+1) ionization signals involving these two intermediate states are of roughly comparable intensity. In addition to the C-state bands observed in both (1+1) and (2+1) MPI, nine hot bands involving the A-state intermediate have been observed in (1+1) MPI with the discharge: A(1,1), (2,2), (3,3), (4,4), (6,6), (5,6), (7,8), (8,9), and (2,1). Only four of these bands have been previously characterized. Analysis of the new discharge bands can be found elsewhere[3].

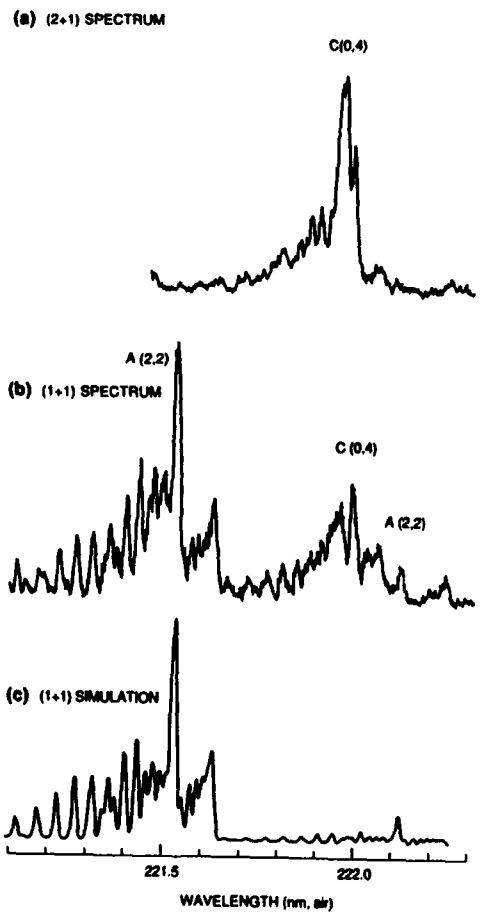

Figure 1. Experimental a) (2+1) and b) (1+1) MPI spectrum of NO. Part c) shows computer simulated A-state part of (1+1) spectrum.

SATURATION EFFECTS

The weak field intensity of a rovibronic transition will be

$$F_i(\lambda_i) \propto N_{v''J''} S(J',J'')/(2J''+1) \quad (1)$$

where $N_{v''J''}$ is the initial state Boltzmann population and $S(J',J'')$ is the one-photon Honl-London factor. The intensity at any λ

$$I_{abs}(\lambda) = \sum_i F_i(\lambda_i)\, f(\lambda - \lambda_i), \quad (2)$$

is the sum of all transitions weighted by the lineshape function $f(\lambda - \lambda_i)$. Attempts to simulate the (1+1) MPI spectrum of the A(2,2) band with these formula failed to adequately represent the data in Fig. 1(b). An excellent simulation of the experiment was obtained by assuming that the excitation step was saturated. The experimental result is shown compared with this saturated transition simulation in Figures 1(b) and (c). There is a subtlety that arises in simulating saturation for the A ← X transition in NO. For the $^2\Pi_{1/2}$ component of the X-state, the problem arises in the P_{21}+Q_{11} (and R_{11}+Q_{21}) branches. Here $P_{21}(J'')$ and $Q_{11}(J'')$ lines terminate on the same K' and are only separated by the small spin-rotation *splitting in* the A-state. These pairs are typically not resolved in a MPI spectrum. Consequently, if one simulates saturation by replacing the Honl-London factors by 1, and sums the intensities treating the P_{21} and Q_{11} branches independently, this in effect counts the rotational population twice. To simulate saturation correctly requires treating the P_{21} and Q_{11} branches as a pair, as the true intensity is limited by the initial rotational state population. The spectrum predicted for the A(0,0) band at 300K by a) the weak field limit, b) setting the Honl-London Factors to 1, and c) treating the required "degenerate" branches as pairs (the correct simulation of saturation), is shown in Fig. 2(a), (b), and (c) respectively.

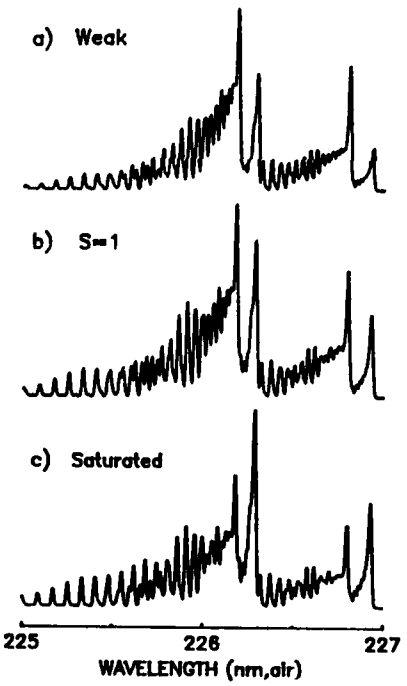

Figure 2. Calculated A(0,0).

REFERENCES

1. I. C. Winkler, R. Stachnik, J. I. Steinfeld, S. Miller, Spectrochim. Acta Part A 42, 339 (1986).
2. D. C. Jacobs and R. N. Zare, J. Chem. Phys. 85, 5457(1986).
3. C. S. Feigerle and J. C. Miller, J. Chem. Phys.(in press).

MOLECULAR TWO-PHOTON SPECTROSCOPY

M. P. McCann,* C. H. Chen, and M. G. Payne
Chemical Physics Section, Oak Ridge National Laboratory
Oak Ridge, Tennessee, USA, 37831-6378

ABSTRACT

Two-photon transitions are examined in molecular oxygen in the region of 8 to 9 eV Using a pulsed nozzle - quadrupole mass spectrometer apparatus, absolute two-photon constants can be determined.

There has been a great deal of interest in the two-photon spectrum of molecular oxygen, because it has a center of symmetry and thus many electronic levels are accessible only by two-photon transitions.[1,2,3]

In this experiment with only one tunable pulsed ultraviolet (UV) laser, the following expression can be used to calculate the two-photon constant.[4,5]

$$T_2 = \frac{\pi (\hbar\omega)^2 r_0 \theta_{1/2} \Delta \tau N_I}{N \epsilon^2 \left[\tan^{-1}\left(\frac{r_0 L}{2 f^2 \theta_{1/2}}\right)\right]} \tag{1}$$

where

T_2 = two-photon constant (cm^4)
$\hbar\omega$ = two-photon energy (J)
r_0 = half-width to e^{-1} drop in intensity (cm)
$\theta_{1/2}$ = half-angle beam divergence of the initial beam before focusing (rad)
Δ = spectral full width at half-maximum of the UV laser (rad/s)
τ = laser pulse duration (s)
N_I = number of O_2^+ cation
N = number density of oxygen molecules in the detection region (cm^{-3})
ϵ = energy of laser pulse (J)
L_0 = is the distance along the laser beam axis over which O_2^+ cations can be detected
f = lens focal length (cm).

The two-photon constant is useful in the case where the laser bandwidth is of comparable or greater size than the width of the state which is being probed. This is certainly the case where broadband pulsed lasers are being used to examine electronic levels in gases.

The apparatus is shown in Figure 1. The pulse nozzle and the Nd:YAG laser both run at 10 Hz. The Nd:YAG laser is frequency doubled to yield a visible beam at 532 nm. The second harmonic is used to pump a dye laser. The output of the dye laser is frequency doubled to yield tunable ultraviolet (UV) light. The UV beam enters the chamber where the pulsed nozzle has emitted a supersonic jet of 10% oxygen in argon. The rotationally cooled oxygen molecules absorb two ultraviolet photons. Once in the two-photon excited state, the oxygen molecule then absorbs an additional UV photon and is ionized. The oxygen cation is repelled into the quadrupole mass spectrometer by the anode plate. The oxygen cation is then detected by the channeltron at the end of the mass spectrometer. By scanning the wavelength of the UV beam and monitoring the signal a spectrum can be obtained as in Figure 2. The signal intensity is directly proportional to the two-photon constant.

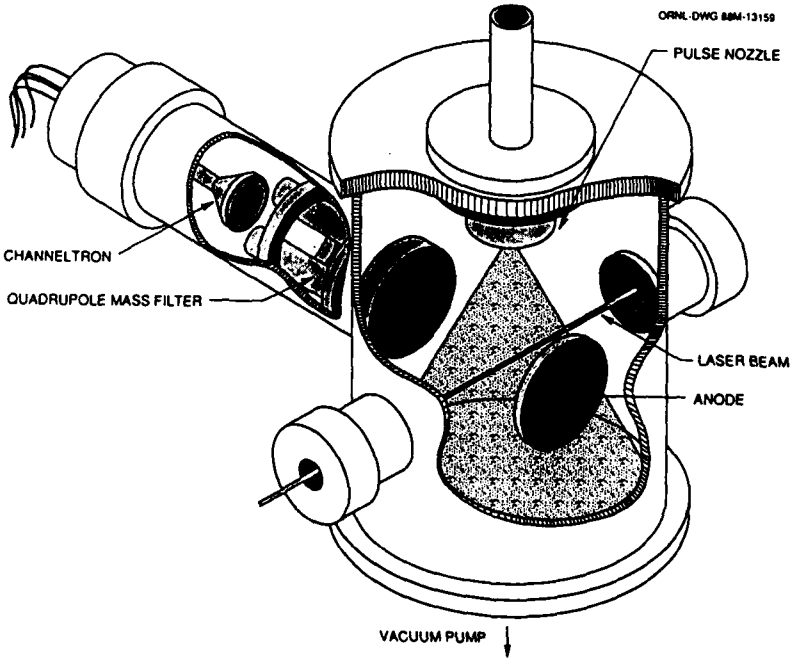

Figure 1. Experimental Apparatus

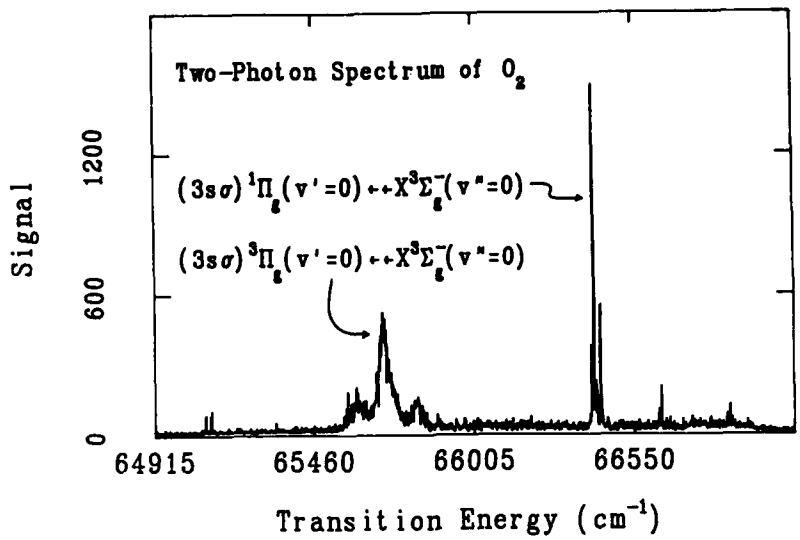

Figure 2. Two-Photon Spectrum of O_2

Research sponsored by the Office of Health and Environmental Research, U.S. Department of Energy under contract DE-AC05-84OR21400 with Martin Marietta Energy Systems, Inc. M. P. McCann, postdoctoral fellow, University of Tennessee, Knoxville, Tennessee.

References

1. Abha Sur, C. V. Ramana, William A. Chupka, and Steven D. Colson, J. Chem. Phys. 84(1), 69-72 (1986).
2. J. A. Stephens, M. Braunstein, and V. McKoy, J. Chem. Phys. 89(6), 3923-4061 (1988).
3. P. J. Miller, W. A. Chupka, J. Winniczek, and M. G. White, J. Chem. Phys. 89(7), 4058-4061 (1988).
4. M. P. McCann, C. H. Chen, and M. G. Payne, J. Chem. Phys. 89(9), 5429-5442 (1988).
5. M. P. McCann, C. H. Chen, and Irene Datskou (in preparation).

Theory of Molecular Transition Moment Determination by Autler-Townes Spectroscopy: D $^1\Pi_u$ - E,F $^1\Sigma^+_g$ Bands of H_2*

Albert M. F. Lau
Combustion Research Facility, Sandia National Laboratories, Livermore, CA 94550
and
Winifred M. Huo
NASA Ames Research Center, Moffett Field, CA 94035

ABSTRACT

We investigate the determination of vibronic transition moments between two electronic states of a molecule by the Autler-Townes effect (also known as ac, optical or dynamical Stark splitting). For some representative bands of H_2(D $^1\Pi_u$ - E,F $^1\Sigma^+_g$), we calculate their Autler-Townes spectra and examine their dependences on laser detuning, intensity, bandwidth, and the Doppler effect. As input to our calculation, the D - E,F electronic transition moment and the (v' = 0 - 14, v = 1, 4 and 6) vibronic transition moments have been computed. Our investigation shows that with moderate laser requirement, the Autler-Townes splitting of a large number of D - E,F vibronic transitions in H_2 should be observable so that their transition moments may be deduced.

Recently, Quesada *et al.*[1] have observed the Autler-Townes effect in the two-color four-photon ionization of H_2 via the double resonant levels E,F $^1\Sigma^+_g$ (v=6, J=1) and D $^1\Pi_u$ (v'=2, J' =2). By fitting the calculated spectra with the observed spectra, they deduced the vibronic transition moment between these two states. They noted that pairwise state-selectivity, insensitivity to other molecular parameters (such as relaxation rates) in the *strong saturation* regime of the effect, and the need to measure only external laser parameters (such as intensity and frequency detuning) but not absolute state population are some of the advantages of the Autler-Townes measurement of transition moments over other methods. Coupled with multiphoton excitation to high-lying levels and multiphoton ionization or fluorescence monitoring techniques, this method seems particularly well-suited for measuring *absolute* values of transition moments between *excited electronic* states.[1]

In order to deduce the *electronic* transition moment by various known methods (including the R-centroid approximation),[2] it is necessary to measure a number of vibronic transition moments between the same pair of electronic states. The vibronic transition moment measured in Ref.1 is probably the strongest among the D - E,F band system. In this paper, we investigate which other D - E,F vibronic transition moments should also be observable by this method and what would be the requirements on the laser parameters.

The *ab initio* results of vibronic transition moments between the (E,F) state, v=6 and the D state, v'= 1 - 14 are shown in Table I. The v'=2 - v=6 transition for which Autler-Townes splitting was observed in Ref.1 is clearly among the strongest transitions. By far the majority of the vibronic transition moments are not as strong. Therefore in addition to the v'=2 - v=6 transition, we choose a few representative bands of lesser strengths and investigate the dependencies of their Autler-Townes spectra on laser detuning, intensity, bandwidth, and the Doppler effect. The ionization spectra as functions of the two-photon resonance detuning Δ_2 of the uv probe laser are

calculated using density-matrix equations of motion for the molecule coupled to the laser field. We use the same experimental and theoretical parameters as those given in Ref. 1, except where it is stated otherwise.

v'	Franck-Condon factor	r-centroid (au)	transition moment (au)
0	0.1169 (-3)[a]	1.7270	-0.04156
1	0.1732 (-1)	4.3545	0.3600
2	0.7878	2.3520	1.9700
3	0.6823 (-3)	19.1136	0.007036
4	0.3569 (-1)	2.4922	0.1883
5	0.3049 (-2)	4.7549	0.01148
6	0.1250 (-2)	4.6346	-0.04034
7	0.1205 (-1)	3.5842	-0.02696
8	0.3857 (-3)	3.8802	0.006737
9	0.1003 (-1)	4.0355	0.01182
10	0.3303 (-3)	3.4731	-0.003019
11	0.7270 (-2)	3.5485	0.01396
12	0.2718 (-1)	5.7412	0.06901
13	0.7607 (-1)	5.5254	0.08645
14	0.6747 (-2)	4.2914	0.004418

[a](n) denotes the powers of ten.

Table I. Franck-Condon factors, r-centroids and transition matrix elements between H_2, (E,F) state, v=6 and D state, v'=1 - 14.

One set of our results shows that by reducing the probe laser bandwidth in the experiment in Ref.1, the resolution of the Autler-Townes doublet is dramatically improved, enabling the observation of weaker transitions with moderate laser power. The experimental uv (probe) laser bandwidth in Ref.1 was 0.7 cm^{-1}. For the two-photon (E,F)-X transition, this becomes effectively a 1.4 cm^{-1} bandwidth and is the dominant contribution in the transverse relaxation rates Γ_{21} and Γ_{31}. It is feasible experimentally to reduce the uv laser bandwidth by a factor of 5 and still maintain enough signal. In Fig.1, we present our results showing the major improvement of spectral resolution of the Autler-Townes doublets for the narrow-band case (solid lines) over the previous broad-band case (dotted lines). For the (v'=2,4 - v=6) transitions, even the *Doppler-averaged narrow-band* spectra (dashed lines) are better resolved than the *Doppler-free broad-band* spectra. On the other hand, comparison among the narrow-band spectra shows that the elimination of the Doppler effect dramatically improves the spectral resolution of the doublet. Fig.1(c) shows a previously unresolved doublet in the broad-band case can be resolved in the narrow-band case.

The above and other results[4] show that with moderate pump laser intensity (≤ 1 GW/cm^2) and narrow probe laser bandwidth (≤ 0.14 cm^{-1}), Doppler-free Autler-Townes spectra of H_2 (D - E,F) can be resolved for those bands with a vibronic transition moments greater than 0.05 au. The experimental conditions assumed in these calculation are not very stringent.[1] Clearly Autler-Townes spectroscopy of weaker transitions can be achieved with even narrower laser bandwidths and weaker probe (ionization) laser intensity.

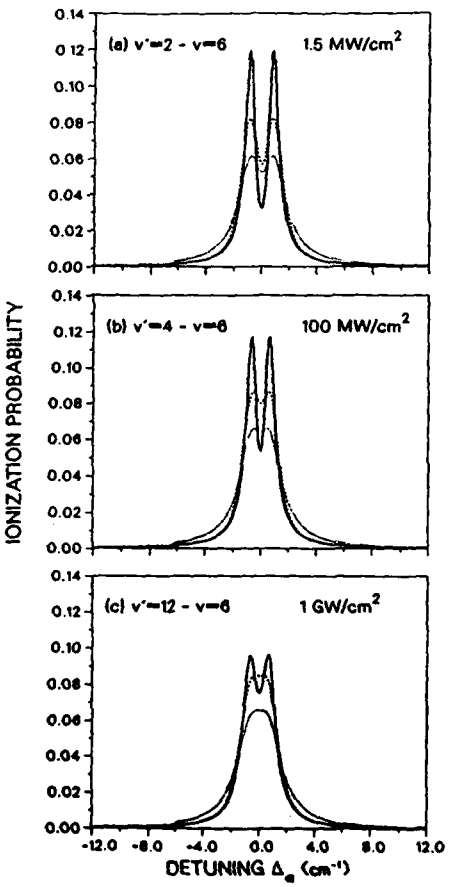

Figure 1

This work was supported in part by the U.S. Department of Energy, Office of Basic Energy Sciences, Division of Chemical Sciences.

REFERENCES

1. M. A. Quesada, A. M. F. Lau, D. H. Parker, and D. W. Chandler, Phys. Rev. A 36, 4107 (1987).
2. H. Klemsdal, Physica Norvegica 5,123 (1971) and references therein.
3. W. M. Huo and R. L. Jaffe, Chem. Phys. Lett. 101, 463 (1983) and W. M. Huo, unpublished data.
4. A. M. F. Lau and W. M. Huo, to be published.

MULTIPHOTON IONIZATION PHOTOELECTRON SPECTROSCOPY OF XENON: EXPERIMENT AND THEORY

S. J. Bajic and R. N. Compton
Oak Ridge National Laboratory, Oak Ridge, Tennessee 37831-6125
and Department of Chemistry, The University of Tennessee
Knoxville, Tennessee 37996

X. Tang, A. L'Huiller,* and P. Lambropoulos
Department of Physics, University of Southern California,
Los Angeles, California 90089

ABSTRACT

Photoelectron energy and angular distributions for resonantly enhanced multiphoton ionization (REMPI) of xenon via the three-photon-allowed $7s[\frac{3}{2}]_1^0$ and $5d[\frac{3}{2}]_1^0$ states have been studied both experimentally and theoretically. The electron kinetic energy spectra give the probability of leaving Xe^+ in either the $^2P_{1/2}$ or $^2P_{3/2}$ core. The measured branching ratio for leaving each ionic core is used to test the theoretical description of the REMPI process. Measurements of *both* the angular distributions and the [3+1] REMPI via the 5d state are adequately reproduced by multichannel quantum defect theory. However, measurements of angular distributions for the electrons resulting from [3+1] via the $7s[\frac{3}{2}]_1^0$ state into Xe^+ $^2P_{3/2}$ (core preserving) or Xe^+ $^2P_{1/2}$ (core changing) are in striking disagreement with theory.

INTRODUCTION

Coupling experimental and theoretical studies of REMPI and photoelectron spectroscopy (PES) can provide unique information about the photoionization dynamics of excited states. REMPI-PES studies of the rare gases have mostly been confined to xenon primarily because the lowest Rydberg states are easily accessible using available lasers. Recently, Blazewicz et al.[1] found resonable agreement between multichannel quantum defect theory (MQDT) and experiment in the description of the [3+2] and [3+1] REMPI processes via the Xe $6s[\frac{3}{2}]_1^0$ and $6s'[\frac{1}{2}]_1^0$ states, respectively. We have extended this work to the $7s[\frac{3}{2}]_1^0$ and $5d[\frac{3}{2}]_1^0$ states of xenon. The apparatus for this experiment has been described elsewhere[1] and will not be discussed here.

RESULTS

Figure 1 shows the energy distribution of the photoejected electrons for the [3+1] REMPI process via the $5d[\frac{3}{2}]_1^0$ level of Xe at 357.6 nm. Electrons with an energy of 1.7 eV dominate the spectrum. This corresponds to a non-core-changing ionization process. In addition, a small signal at 0.4 eV is seen which corresponds to photoelectrons leaving the Xe^+ $^2P_{1/2}$ ionic core. The approximate ratio of the two observed signals is comparable with that predicted

*Permanent Address: CEN SACLAY, Sevice de Physique des Atomes et des Surfaces, 91190 Gief-Sur-Yvette, France.

from MQDT calculations. Figure 1 also shows the polar plot of the measured angular distribution for the electrons resulting from REMPI via the $5d[\frac{3}{2}]^0_1$ level. The electron signal corresponding to leaving the $^2P_{1/2}$ core was too weak to obtain a reliable angular distribution measurement. Fitting the angular distribution data to a Legendre polynomial expansion required terms up to $P_8(\cos\theta)$:

$$Xe^+\ ^2P_{3/2} : I(\theta) = 1 + 1.23P_2 + 0.75P_4 + 0.20P_6 - 0.70P_8$$

The calculated angular distribution from MQDT for the $^2P_{3/2}$ electrons quantitatively reproduces the angular distribution observed in the experiment.

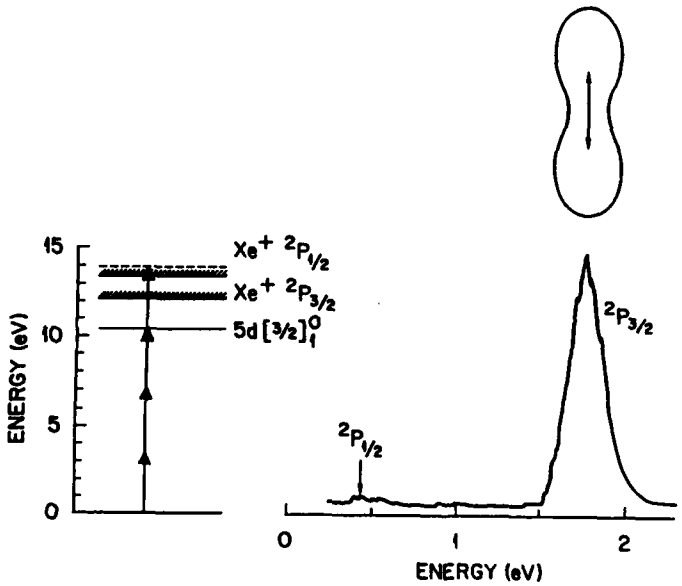

Figure 1. PES and angular distribution for REMPI via the 5d state.

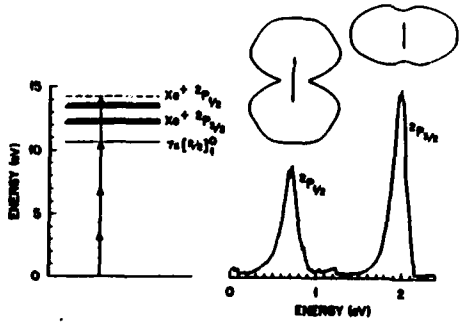

Figure 2. PES and angular distributions for REMPI via the 7s state.

Figure 2 shows the energy distribution of the photoelectrons for the [3+1] REMPI process through the $7s[\frac{3}{2}]^0_1$ state of Xe at 351.1 nm. Two groups of electrons are observed at 0.7 eV and 2.0 eV which correspond to leaving the $Xe^+\ ^2P_{1/2}$ and $^2P_{3/2}$ ionic cores respectively. The ratio of the two signals (approx. 2:1) compares favorably with that predicted from MQDT.

The polar plots of the experimental angular distributions for the two groups of electrons are shown above their respective energy distributions. As

can be seen, the two groups yield quite different angular distributions. The experimental angular distributions were also fitted to a Legendre polynomial expansion. It was found that terms up to $P_8(\cos\theta)$ were needed to fit both the $^2P_{1/2}$ and $^2P_{3/2}$ data.

$$Xe^+\ ^2P_{3/2}: \quad I(\theta) = 1 - 0.33P_2 + 0.02P_4 - 0.03P_6 - 0.04P_8$$

$$Xe^+\ ^2P_{1/2}: \quad I(\theta) = 1 + 0.78P_2 - 0.42P_4 + 0.30P_6 - 0.16P_8$$

MQDT calculations semiqualitatively agree with the general shape of the experimental angular distribution for the $^2P_{1/2}$ electrons except for a predicted small maximum at $\pi/2$ where a sharp minimum is observed in the experiment. MQDT calculations predict that the angular distribution for the $^2P_{3/2}$ core-preserving electrons should have a deep and somewhat broad minimum at $\pi/2$ and a maximum at 0 and π. However the experiment shows that the angular distribution is somewhat isotropic with an unexpected maximum at $\pi/2$ and minimum at 0 and π. This discrepancy is not understood at this time.

Research sponsored by the Office of Health and Environmental Research, U.S. Department of Energy under contract DE-AC05-84OR21400 with Martin Marietta Energy Systems, Inc.

REFERENCE

1. P. R. Blazewicz, X. Tang, R. N. Compton, and J.A.D. Stockdale, J. Opt. Soc. Am. B., 4(5), 770 (1987).

OBSERVATIONS OF EXCITED STATE PHOTOIONIZATION OF XENON*

Jayanti Lahiri
Department of Physics & Chemistry
Southern College of Technology, Marietta, GA 30060

Steven T. Manson
Department of Physics & Astronomy
Georgia State University, Atlanta, GA 30303

INTRODUCTION:

Excited state photoionization cross sections were calculated for Xe using the central field Hartree model.[1] The calculations included photoelectron energy 0 to 5 Rydbergs and all $n\ell$ excited states up to $n = 9$, $\ell = 3$. Emphasis was placed on the existence and positions of Cooper minima,[2] zeros in the dipole matrix elements, which affect the spectral shapes of the cross sections so drastically. Previous work on excited alkali atoms has shown that excited states, owing to their extent, exhibit many more Cooper minima than do ground states despite the fact that the potential is pure Coulomb over most of their extent. In addition a simple relationship between the Cooper minima and the quantum defects (threshold phase shifts for continuum states) induced by the inner non-Coulomb region of the potential has been found for the alkalis.[3] In particular in an $n\ell \rightarrow \epsilon\ell'$ transition, if the difference between the quantum defect $\mu_{n\ell}$ and the threshold phase shift (in units of π) $\delta_{\ell'}(0)$ is greater than about 0.5, a maximum of one zero is expected; if it is greater than about 1.5, a maximum of two zeros is possible, etc. In this work then we investigate this relationship as applied to Xe.

RESULTS AND DISCUSSION:

The phase shift differences for Xe are calculated to be 0.42, 1.29, and 2.17 for $s \rightarrow p$ (and $p \rightarrow s$), $p \rightarrow d$ (and $d \rightarrow p$) and $d \rightarrow f$ (and $f \rightarrow d$) transitions respectively. Thus we expect a minimum near threshold (above or below) for $s \rightarrow p$ transitions, a minimum well above threshold for $p \rightarrow d$ transitions, and two minima for $d \rightarrow f$ transitions, based on previous experience.

To exemplify our results, cross sections for $n = 6$ states are presented. The 6s photoionization cross section, shown in Fig. 1, is dominated by a Cooper minimum just above threshold, in keeping with our expectation based on phase shift difference. Our results also show that other ns states behave similarly.

The 6p cross section, given in Fig.2, shows a $6p \rightarrow \epsilon d$ Cooper minimum well above threshold, at about 4 Rydbergs. Since the phase shift difference here is much larger than for the $6s \rightarrow \epsilon p$ case, our expectation is that the minimum here appears at much larger energy, which

---

*Work supported by NSF and US ARO

indeed occurs. The 6p → εs transition however shows no Cooper minimum although the relative phase shift difference is the same as the s → p which does show a minimum. To explain this, note that the inner non-Coulomb region of the potential always mitigates against zeros. In terms of a phase amplitude formalism, the phase shift can be viewed as a function of distance starting with zero at the nucleus and reaching its asymptotic value δ_ℓ at large distances. The phase shifts and phase shift differences are smaller in the inner region so that even if two transitions have the same phase shift difference their zeros may be very different if one transition has a much larger contribution from the inner region.[3] Since the 6p → εs does in fact, have much more of a contribution from the inner region than the 6s → εp transition, we expect its zero to be at a lower energy, which in this case, is below threshold.

Note further that the total cross section does not show a minimum, despite the dominance of the p → d channel, because of the p → s contribution. Nevertheless, the zero shows up as a rather distinct change of slope in the total cross section.

With a d → f phase shift difference of 2.17, well above 1.5, two Cooper minima are possible in 6d → εf. The first zero is seen at about 0.7 Rydbergs (Fig. 3); a second zero (not shown) appears near 7.2 Rydbergs. The 6d → εp $\ell \rightarrow (\ell-1)$ transition, with phase shift difference of 1.29, far above 0.5, shows a zero in the continuum at about 0.6 Rydbergs, much below the energy of the 6p → εd minimum indicated above. This occurs for reasons discussed in connection with the 6p → εs transition. Since both the d → p and the d → f transitions have Cooper minima in the same energy range, a sharp minimum in the total photoionization cross section appears around 0.7 Rydbergs.

CONCLUSION:

In conclusion, the relationship between phase shift differences and Cooper minima predicted for alkali atoms[3] also holds for Xe, a noble gas. Further the $\ell \rightarrow (\ell+1)$ minima are found to occur at higher energies than $(\ell+1) \rightarrow \ell$ for reasons discussed. Finally we infer that similar phase shift differences imply similar excited state photoionization over the entire periodic system.

REFERENCES:

1. S.T. Manson and J.W. Cooper, Phys.Rev. 165, 126 (1968)
2. J.W. Cooper, Phys.Rev. 128, 681 (1962)
3. J. Lahiri and S.T. Manson, Phys.Rev. A33, 3151 (1986)

Figure 1

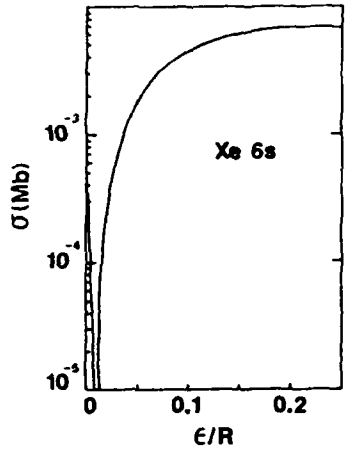

Figure 2

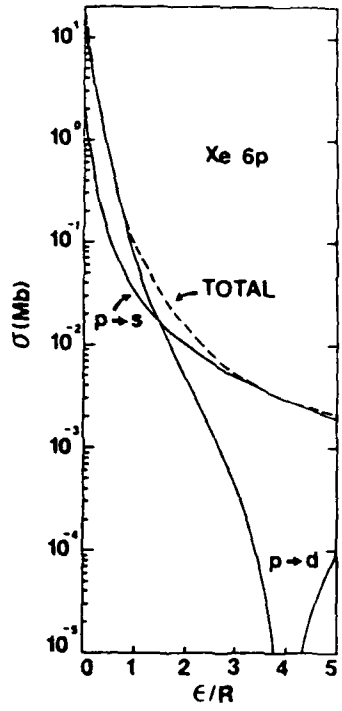

Figure 3

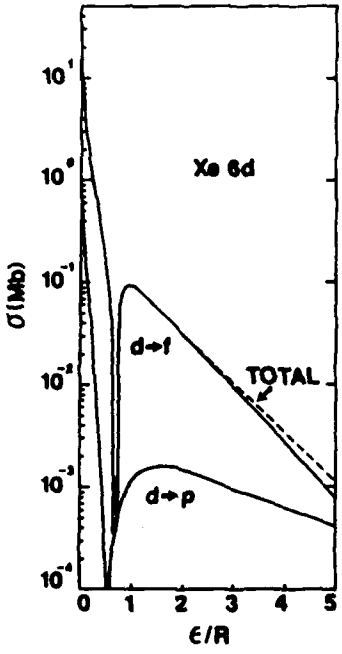

Total and partial photoionization cross sections for Xe 6s, 6p, and 6d vs photoelectron energy ε.

A SPECTROSCOPIC STUDY OF THE $\tilde{X}\,^4\Sigma_g^-(v = 4-7)$ LEVELS OF C_2^+ USING THE STIMULATED EMISSION PUMPING TECHNIQUE

F. G. Celii* and J. P. Maier
Institut für Physikalische Chemie, Universität Basel, Basel, Switzerland

ABSTRACT

Stimulated emission pumping (SEP) spectroscopy was utilized to characterize vibrationally excited levels (v=4–6) of the $\tilde{X}\,^4\Sigma_g^-$ ground electronic state of C_2^+. Transitions were detected by decreased total fluorescence from laser-excited $\tilde{B}\,^4\Sigma_u^-$ levels. To obtain the 2-photon spectra, a modulation scheme which discriminated against one-photon fluorescence signals was successfully employed.

INTRODUCTION

The C_2^+ ion, although important in interstellar chemistry[1] and tractable for theoretical studies,[2] has only recently been characterized spectroscopically.[3-5] Rösslein, *et al.*,[4] guided by the calculations of Rosmus, *et al.*,[2] discovered a band system whose lower state was identified as the ground $\tilde{X}\,^4\Sigma_g^-$ state of C_2^+. A recent ESR study[6] of matrix-isolated C_2^+ identified the ground electronic state of C_2^+ as having $^4\Sigma$ symmetry, in agreement with the theoretical predictions[2] and laser-excited fluorescence (LEF) observations.[4,5] With this well-characterized band system, the means now exist for monitoring this interesting and reactive species. In addition, 2-photon spectroscopies, such as stimulated emission pumping (SEP) and optical-optical double resonance (OODR), can now be used to probe other vibrational levels and electronic states. We report here the preliminary results of an SEP study of C_2^+ in which transitions were observed to the $\tilde{X}\,^4\Sigma_g^-(v'' = 4-7)$ levels.

EXPERIMENTAL

The experiments were conducted in an apparatus, described previously,[7] designed for the study of fluorescent molecular cations. Briefly, a liquid nitrogen-cooled Penning ionization source is employed which provides rotationally-cooled molecular ions of sufficient quantity for interrogation with LEF and SEP spectroscopies. For these studies, a flow of He across a DC discharge produced metastable He which in turn reacted with acetylene to form C_2^+ (as well as other fragments). Because of the reactivity of C_2^+, it was imperative to have the C_2H_2/He^* mixing area as close as possible to the laser interaction region.

The laser system (Fig. 1) consisted of two dye lasers (Lambda Physik, FL-2002), designated PUMP and DUMP, which were excited by a single excimer laser. As will be detailed below, the excimer was fired at twice the frequency of an optical chopper which blocked alternate pulses from the PUMP laser. The two beams were spatially overlapped using a dichroic mirror and focussed into the reaction chamber through a single port. Fluorescence from C_2^+ excited by the PUMP laser was collected using a photomultiplier tube with appropriate filters and optics. The various analog signals were averaged using boxcar integrators and stored in a microcomputer, which also scanned both dye lasers.

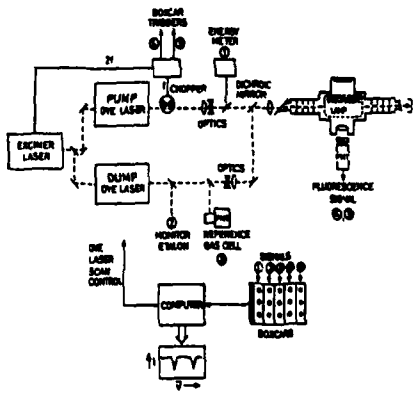

Figure 1: Schematic of the apparatus used for LEF and SEP studies. The signals collected include the molecular fluorescence (from C_2^+, C_2^+, etc.), etalon, reference cell (I_2 or Te_2) and PUMP laser power signals.

RESULTS AND DISCUSSION

Wavelength scans of the PUMP laser (with the DUMP laser blocked) generated LEF spectra which could be assigned to the known bands of C_2^+.[4,5] The $\widetilde{B}\,^4\Sigma_u^- \leftarrow \widetilde{X}\,^4\Sigma_g^-$ $(2-0)$ band was selected as the PUMP transition in the SEP double resonance scheme. The PUMP laser, with wavelength fixed to excite a single rotational state of the $\widetilde{B}\,^4\Sigma_u^-(v'=2)$ level, produced a constant level of fluorescence, I_P. The SEP experiment could, in principle, be performed by scanning the DUMP laser and detecting transitions to $\widetilde{X}\,^4\Sigma_g^-(v'')$ levels by observing loss of the I_P fluorescence signal, as was shown in an earlier SEP study of the $C_4H_2^+$ ion.[8] It was found, however, that the DUMP laser also excited fluorescence from other species present in the chamber, most notably from C_2. To discriminate against these signals, the PUMP laser beam was blocked on alternate excimer laser shots using an optical chopper. The two resultant fluorescence signals, I_{P+D} (PUMP and DUMP together) and I_D (DUMP alone), were electronically subtracted and normalized to the average value of I_P to yield a signal whose only wavelength dependence was the desired 2-photon (SEP) contribution:

$$\frac{I_{P+D}(\lambda) - I_D(\lambda)}{I_P} = 1 + \frac{I^{SEP}(\lambda)}{I_P}, \tag{1}$$

Application of the modulation technique is depicted in Figure 2, which shows the $\widetilde{B}\,^4\Sigma_u^- \leftrightarrow \widetilde{X}\,^4\Sigma_g^-(2-5)$ region of the C_2^+ spectrum. The two traces of I_D (upper) and the SEP signal (lower) were recorded simultaneously. The SEP transitions were extracted from regions which were severely overlapped by C_2 LEF transitions. Note also that the C_2^+ $\widetilde{X}\,^4\Sigma_g^-(v=5)$ level is populated under the discharge conditions, so that $I_D(\lambda)$ also contains contributions from $\widetilde{B}\,^4\Sigma_u^- \leftarrow \widetilde{X}\,^4\Sigma_g^-(2-5)$ LEF transitions. The modulation scheme similarly discriminates against these signals as well. The extent of the discrimination can be seen clearly from the scan in Figure 2 which demonstrates that for PUMP laser excitation of the $(2-0)$ R(5) transition, DUMP laser features due only to the expected R(5) and P(7) $(2-5)$ SEP transitions are observed.

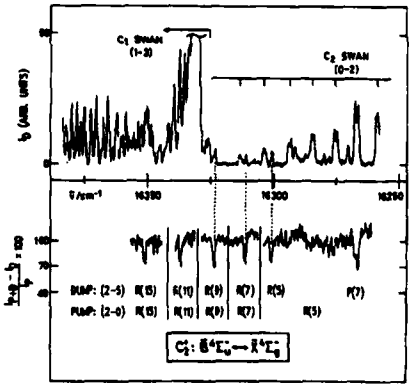

Figure 2: LEF (upper) and demodulated SEP spectra (lower trace) in the C_2^+ $\widetilde{B}\,^4\Sigma_u^- \leftrightarrow \widetilde{X}\,^4\Sigma_g^-(2-5)$ transition region.

To derive spectroscopic constants for the $\widetilde{X}\,^4\Sigma_g^-(v=4\text{–}7)$ levels, individual rovibronic transitions of the $\widetilde{B}\,^4\Sigma_u^- \rightarrow \widetilde{X}\,^4\Sigma_g^-(2-5), (2-6)$ and $(2-7)$ bands were recorded using SEP as outlined above. Line positions of the $(2-4)$ band were obtained using LEF. All line positions measured in this work were combined with those of the 10 previously determined[5] C_2^+ $\widetilde{B}\,^4\Sigma_u^- \leftarrow \widetilde{X}\,^4\Sigma_g^-$ bands and fit to the Hund's case (b) Hamiltonian whose rotational dependence is modelled by:

$$F(N) = B(v)\cdot N(N+1) - D(v)\cdot N^2(N+1)^2, \tag{2}$$

where $B(v)$ and $D(v)$ are the rotational and centrifugal distortion constants of each vibrational level. The preliminary results of fitting all but the $(2-7)$ band are collected in the table, where B_e and ω_e have their usual meaning:

$$B(v) = B_e - \alpha_e(v+1/2) \tag{3}$$

$$G(v) = \omega_e(v + 1/2) - \omega_e x_e(v + 1/2)^2 \quad (4)$$

The resulting spectroscopic constants agree quite well with extrapolations of those previously derived. Figure 3 compares the vibrational frequencies determined from this study with those of the LEF work.[5]

Table 1: Spectroscopic Constants Determined for $^{12}C_2^+$ §

	$\tilde{X}\,^4\Sigma_g^-$	$\tilde{B}\,^4\Sigma_u^-$
T_e	0.0	19652.2(4)
ω_e	1351.7(2)	1508.1(5)
$\omega_e x_e$	12.18(2)	12.69(11)
B_e	1.4258(3)	1.5465(5)
α_e	0.01762(8)	0.01704(25)
D_e†	$6.3(5)\times10^{-6}$	$6.5(5)\times10^{-6}$

§ All values in cm^{-1}.
† Value held constant.

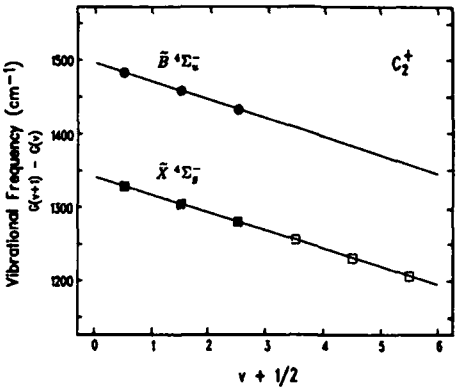

Figure 3: Vibrational frequencies of C_2^+ *vs.* the vibrational quantum number. Filled symbols from Ref. [5], open squares from this work.

We have demonstrated a general method for obtaining SEP spectra in the presence of competing background LEF signals, and have used this technique to refine the molecular constants for C_2^+ to include the $\tilde{X}\,^4\Sigma_g^-(v{=}4\text{–}6)$ levels. A full report to include the $\tilde{X}\,^4\Sigma_g^-(v{=}7)$ level will be published elsewhere. Extensions of this work include the use of double resonance techniques to locate the $\tilde{A}\,^4\Pi_g$ electronic state, predicted[2] to lie close in energy to the $\tilde{X}\,^4\Sigma_g^-(v{=}8)$ level, as well as to assist analysis of the spin-spin splittings which are partially resolved in the $\tilde{B}\,^4\Sigma_u^- \leftarrow \tilde{X}\,^4\Sigma_g^-$ system.

ACKNOWLEDGEMENTS

This work is part of "Schweizerischer Nationalfonds zur Föderung der wissenschaftlichen Forschung." Ciba-Geigy SA, Sandoz SA, and F. Hoffmann-la Roche & Cie SA, Basel are also thanked for financial support. FGC also gratefully acknowledges receipt of a fellowship from the Erziehungsdepartement des Kantons Basel-Stadt.

REFERENCES

* Present address: Code 6174, Naval Research Lab, Washington, D.C., 20375-5000.
1. G. Winnewisser, *Topics Current Chem.*, **99**, 39 (1981).
2. P. Rosmus, H.-J. Werner, E.-A. Reinsch and M. Larsson, *J. Electron. Spectrosc.* **41**, 289 (1986), and references therein.
3. D. Forney, H. Althaus and J. P. Maier, *J. Phys. Chem.* **91**, 6458 (1987).
4. M. Rösslein, M. Wyttenbach and J. P. Maier, *J. Chem. Phys.* **87**, 6770 (1988).
5. J. P. Maier and M. Rösslein, *J. Chem. Phys.* **88**, 4614 (1988).
6. L. B. Knight, Jr., S. T. Cobranchi and E. Earl, *J. Chem. Phys.* **88**, 7348 (1988).
7. D. Klapstein, J. P. Maier and L. Misev, in "Molecular Ions Spectroscopy, Structure and Chemistry," edited by T. A. Miller and V. E. Bondybey (North Holland, Amsterdam, 1983), p. 175.
8. F. G. Celii, J. P. Maier and M. Ochsner, *J. Chem. Phys.* **85**, 6230 (1986).

TWO PHOTON RESONANCE ENHANCED MULTIPHOTON IONIZATION DETECTION AND SPECTROSCOPY OF GAS PHASE GERMYL (GeH_3) RADICALS

Jeffrey W. Hudgens, Russell D. Johnson III and Bilin P. Tsai
Chemical Kinetics Division, Center for Chemical Technology,
National Institute of Standards and Technology (Formerly, the
National Bureau of Standards), Gaithersburg, MD 20899

ABSTRACT

GeH_3 radicals were observed by resonance enhanced multiphoton ionization (REMPI) spectroscopy in the region of 370 - 430 nm. The spectrum arises from two-photon resonances with the 5p $^2A_2''$ (D_{3h}) Rydberg state which has its origin at 419.1 nm (ν_{0-0} = 47,705 cm^{-1}). Absorption of a third photon ionized the radicals. A vibrational progression of ~756 cm^{-1} was assigned to the "umbrella" mode, ν_2'. The observed $\tilde{X}$ $^2A_1$ (C_{3v}) v_2''=2 to v_2''=0 vibrational interval is 663 cm^{-1}.

INTRODUCTION

Resonance enhanced multiphoton ionization (REMPI) spectroscopy has become an effective tool for discovering electronic states of free radicals.[1] Using this technique we have observed the only known optical (or infrared) spectrum of the germyl radical, GeH_3. ESR spectroscopy[2] and molecular orbital calculations have shown that GeH_3 has an ammonia-like, pyramidal structure of the C_{3v} point group.[3,4] The potential energy along the out-of-plane bending (ν_2'' "umbrella" mode) coordinate is described by a double-minimum potential function. For GeH_3 these potential minima are predicted to lie at $\theta_m = \pm 18.4°$ where θ is the angle formed between the hydrogen atom plane and a Ge-H bond (when planar, $\theta_m = 0°$).

EXPERIMENTAL

The apparatus used in this study consisted of a flow reactor which produced GeH_3 radicals, an excimer pumped dye laser which ionized the radicals, a time of flight mass spectrometer, and a computer/data acquisition system. In a flow reactor fluorine or chlorine atoms were produced by a microwave discharge. Downstream from the microwave discharge the halogen atoms mixed and reacted with germane, GeH_4, to produce GeH_3 radicals. A fraction of these GeH_3 radicals effused into the ion source of the mass spectrometer where they were ionized by a focussed laser beam (Energy = 5-20 mJ/pulse; Bandwidth = 0.2 cm^{-1} FWHM; fl = 250 mm). The laser generated ions were mass selected and detected by the mass spectrometer. The ion signal was recorded as a function of wavelength to produce the REMPI spectra. Pressure within the ion source was about 5×10^{-5} torr. Under typical operating conditions and assuming 100% conversion of GeH_4 into GeH_3, the radical concentration in the ion optics was estimated to be ~10^9 cm^{-3}.

RESULTS AND ANALYSIS

Figure 1 displays the composite REMPI spectrum of $^{74}GeH_3$ (m/z 77) radicals between 370-430 nm. Similar REMPI spectra were also carried by m/z 73, 75, 76, and 79 ions. The signal from these masses is consistent with the assignment of the spectral carrier to GeH_3 because elemental germanium has significant (>7% abundance) isotopes at masses 70, 72, 73, 74, and 76. The strength of these REMPI signals depended upon the relative concentrations of GeH_3 and halogen and required the presence of the microwave discharge. Thus, all chemical and mass spectral data support the assignment of the m/z 77 REMPI spectrum to GeH_3 radical. Further confidence in this assignment is derived from the similarity of the spectrum in Fig. 1 to the REMPI spectrum of the isovalent radical, SiH_3.[5]

To ionize, GeH_3 radicals must absorb three laser photons to exceed its calculated 8.0 eV[4] ionization potential. The REMPI spectrum can arise from two classes of candidate states: 1) Rydberg states or 2) excited valence states. The Rydberg formula predicts that GeH_3 Rydberg states reside at the energy of two laser photons. Excited valence state candidates may reside at the energy of one or two laser photons. Analysis of the ν_2' "umbrella" mode of the excited state will resolve the excited state assignment.

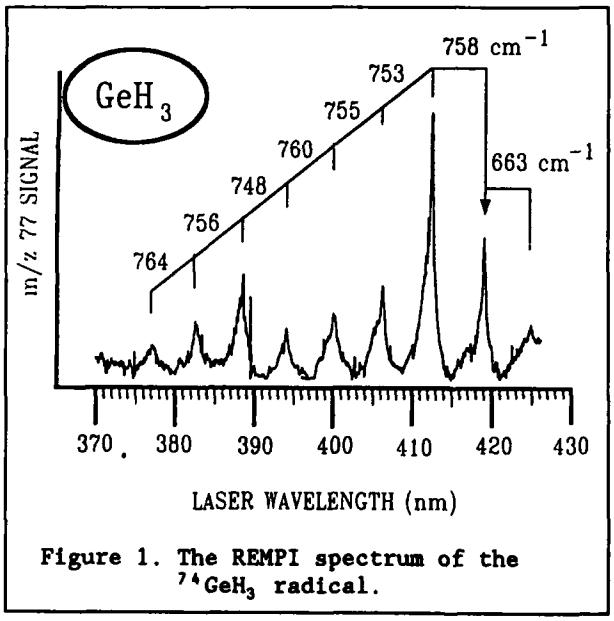

Figure 1. The REMPI spectrum of the $^{74}GeH_3$ radical.

The vibrational bands in the REMPI spectrum arise from activity in the ν_2 "umbrella" mode. This activity reflects the large changes in the pyramidal angle, θ_m, upon excitation from the ground state into a higher electronic state. Excited valence states have doubly occupied p_z-orbitals which impel the radical to form a more acute pyramid (larger θ_m). In contrast, Rydberg states feature empty p_z-orbitals which favor the planar GeH_3 radical geometry ($\theta_m = 0°$). In all cases the large change in equilibrium pyramidal angle causes electronic transitions to have large nondiagonal ν_2 Franck-Condon factors that favor $\Delta\nu_2 > 0$ transitions.

In Figure 1 festoons show the two photon energy intervals between adjacent REMPI bands. One regularly spaced progression with band separations of 756 ± 5 cm^{-1} is formed from the eight bands that lie between 370-419.1 nm. These bands are assigned to ν_2' vibrational levels of the upper electronic state. The red-most member of this progression at 419.1 nm ($2h\nu$ = 47,705 cm^{-1}) is assigned to the electronic origin. The weak ninth band at 425.0 nm, 663 cm^{-1} from the origin is assigned as a ground state vibrational "hot" band.

All spectroscopic evidence supports an assignment of the REMPI spectrum to two-photon excitation of a Rydberg state. The regular ν_2' vibrational intervals shows that the "umbrella" mode potential energy coordinate is harmonic. This can occur only for a planar Rydberg state. The electronic origin assignment of 47,705 cm^{-1} leads to a reasonable solution of the Rydberg equation, δ=2.45 for n=5, which indicates that the resonant state is a 5p Rydberg state. This 5p Rydberg state ionizes after a third photon is absorbed. All candidate excited valence state assignments are discarded because valence states should exhibit irregularly spaced ν_2' progressions. This irregularity would be in the form of unresolved v_2'=2n,2n+1 doublets that exhibit a negative anharmonicity of about 100-150 cm^{-1} between doublet bands. Irregular spacing occurs because valence states of GeH_3 have pyramidal geometries and significant inversion barriers.

The 5p Rydberg complex is comprised of $^2A_2''$ and E' states (in the D_{3h} point group). In the closely related radical, SiH_3, the E' Rydberg state manifold is predicted to be mixed with the lowest E' valence state.[6] Because the properties of SiH_3 and GeH_3 are very similar, we believe that the E' Rydberg manifold of GeH_3 suffers a similar plight. If so, the E' Rydberg states of GeH_3 will display irregular vibrational intervals. Since the spectrum presented here appears unperturbed, we favor assignment of the REMPI spectrum to 5p $^2A_2''$ (D_{3h}) ← $\tilde{X}$ $^2A_1$ (C_{3v}) transitions.

ACKNOWLEDGEMENT

Prof. Tsai thanks the University of Minnesota for support through the Bush Foundation.

REFERENCES

1) J. W. Hudgens, Advances in Multi-photon Processes and Spectroscopy, Vol. 4, S. H. Lin, ed. (World Scientific Publishing Co., Singapore, 1988), pp. 171-296.
2) G. S. Jackel, J. J. Christiansen, W. Gordy, J. Chem. Phys. 45, 4274 (1967).
3) K. Ohta, H. Nakatsuji, I. Maeda and T. Yonezawa, Chem. Phys. 67, 49 (1982).
4) J. Moc, Z. Latajka, H. Ratajczak, J. Mol. Struct. (Theochem) 150, 189 (1987).
5) R. D. Johnson III and J. W. Hudgens, Chem. Phys. Lett. 141, 163 (1987).
6) G. Olbrich, Chem. Phys. 101, 381 (1986).

RAMAN-INDUCED KERR EFFECT SPECTROSCOPY OF RARE GAS DIMERS AND MOLECULAR IONS*

Roger H. Taylor, Jacek Borysow,† and J. W. Keto
The University of Texas at Austin, Physics Department, Austin, TX 78712-1081

ABSTRACT

A high-sensitivity Raman-Induced Kerr Effect (RIKE) spectrometer designed for the spectroscopy of rare gas dimers and molecular ions is presented. One highly linearly polarized, pulsed dye laser beam (probe) is crossed with a tunable, circularly polarized, pulsed dye laser beam (pump) in a sample. The nonlinear interaction between these beams and the sample induces a birefringence that creates a polarization component of the probe laser orthogonal to its original polarization whose magnitude peaks at Raman resonances. Adjusting the polarization of the pump laser can decrease nonresonant contributions to the birefringence and thereby increase the signal-to-noise ratio. Subtraction of a fraction of the magnitude of a reference beam from the signal further enhances the sensitivity by reducing pulse-to-pulse fluctuations. Spectra from solutions with fractional particle densities of 1000 ppm and from gases at low pressure have been recorded. Based on these data, the feasibility for using this technique for studies of the structure of ions in discharges and of rare gases at high pressure is discussed.

INTRODUCTION

Study of the formation and dynamics of molecular ions in discharges has been slowed by the low particle densities and high background luminosities inherent in these environments. Coherent Raman techniques promise to be ideal probes for these environments as they generate coherent signals, but their sensitivity must be improved to enable them to detect low density species. Coherent Raman probes sensitive enough to detect species in discharges will also be useful for rare gas dimers.

Coherent Raman spectrometers have traditionally used cw probe lasers to carry the signal from the sample to the detector so that laser power fluctuations are minimized and shot noise limits the sensitivity. Since the signal scales linearly with the probe laser power while shot noise scales as the square root of the power, increasing the laser power will increase the signal-to-noise ratio. Pulsed lasers produce greater peak powers than cw lasers and so afford the opportunity to increase the sensitivity of coherent Raman spectrometers if their larger power fluctuations can be reduced.[1]

The RIKES birefringence induced by overlapping laser beams in a medium peaks when the frequency difference between two applied laser fields equals a Raman resonance. If the intensity of the probe laser is measured through crossed polarizers as a function of this frequency difference, a signal is seen against a background having smaller fluctuations.[2] These fluctuations can be reduced by subtracting from the signal a reference laser's intensity having similar fluctuations. RIKES also allows the background due to nonresonant Raman interactions to be minimized.[3]

*Supported by the Robert A. Welch Foundation, by the Texas Advanced Research Program and the U. S. DOE, Office of Basic Energy Sciences, Division of Chemical Sciences..

†Present address: Joint Institute for Laboratory Astrophysics, University of Colorado, Boulder, CO 80309-0440

Coherent Raman processes can be described by the third-order electric susceptibility tensor $\chi^{(3)}$. In RIKES, the interaction of two laser fields with $\chi^{(3)}$ of a medium produces a polarization wave which can be written as

$$P_1(\omega_1) = K \left| \chi_{1221} e^{i\phi} - \chi_{1212} e^{-i\phi} \right|^2 E_2(\omega_1)\, I^2(\omega_2), \qquad (1)$$

where χ_{ijkl} is a component of the third-order electric susceptibility, $E_2(\omega_1)$ is the probe laser field, $I(\omega_2)$ is the pump laser irradiance , ϕ is an adjustable phase between polarization components of the pump laser, and K is a proportionality constant. Nonresonant susceptibility tensor elements are nearly equal; so, tuning ϕ with retardation optics in the pump beam can minimize the background and optimize the signal.

Stray birefringence in the optical path of the probe laser should also be minimized, though some birefringence will remain to produce a nonzero background. Accounting for this leakage light, the detected irradiance is

$$I_{sig}(\omega_1) = I_{back}(\omega_1) + 2\sqrt{\alpha_R \gamma}\, I(\omega_1) I(\omega_2) + \alpha_R I(\omega_1) I^2(\omega_2), \qquad (2)$$

where γ is the fraction of the leakage light coherent with the signal, and α_R is proportional to $\chi^{(3)}$. For small signals--$2\sqrt{\alpha_R \gamma} >> \alpha_R I(\omega_2)$--the cross-term dominates. Controlling the fraction of the probe light $\sqrt{\gamma} I(\omega_1)$ that leaks through the polarizers to heterodyne with the signal can enhance this term. With sufficient probe laser power, the major noise source is probe laser intensity fluctuations which can be minimized if a reference sample of the probe laser having similar fluctuations is monitored and subtracted from the signal beam intensity.

APPARATUS

The Raman-induced Kerr effect spectrometer used to test these techniques consists of two Nd:YAG pumped dye lasers with the detectors and signal processing electronics. The probe laser is polarized and analyzed with Glan-Thompson polarizers having an extinction ratio of 10^{-7}. The pump laser's polarization is controlled by wave-plates and compensators. The reduction of laser power fluctuations by the pulse-to-pulse subtraction of a reference laser's intensity from the signal is performed on voltage signals from photodiodes. Each beam is detected by EG&G FND-100 photodiodes mounted on a printed-circuit board where the diodes' outputs are subtracted immediately. This circuit can subtract two laser pulses to within a factor of 0.03% (1.5 times the shot-noise limit). The quality of the subtraction in a RIKES application is limited because small polarization fluctuations in one beam relative to the other are magnified since the beams are highly extinguished. Both beams, though generated from the same laser, experience different birefringence and reflectivities for s- and p-polarization along their paths causing uncorrelated fluctuations. Careful matching of the paths produces a subtraction of 0.05%. Because of high losses for this configuration, the measurement was made with non-optimal extinction to reduce the effects of shot and electronic noise. To obtain spectra with optimal extinction and subtraction requires more probe power.

RESULTS

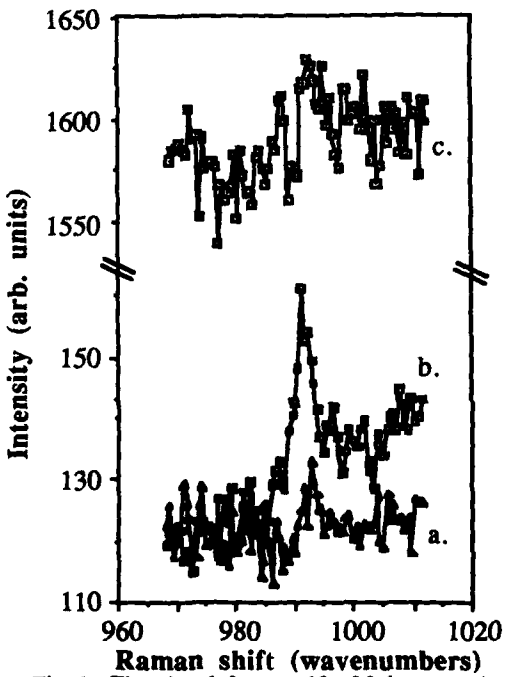

Fig. 1 The signal from a 10 mM benzene in carbon tetrachloride solution detected with a. circularly polarized pump laser light and subtraction of a reference laser's intensity from the signal beam. b. elliptically polarized pump laser light and subtraction of a reference laser's intensity from the signal beam. c. elliptically polarized pump laser light and no subtraction.

The effects of the pulse-to-pulse subtraction of a reference laser's intensity from the signal beam and the control of the pump beam's polarization are displayed in Fig. 1 showing spectra from a sample of 0.01 M benzene in carbon tetrachloride. Curves (b) and (c) show spectra recorded with and without the reference beam blocked, respectively. Curve (a) shows that a circularly polarized pump beam produced a signal that is barely seen over the fluctuations of the background. If the

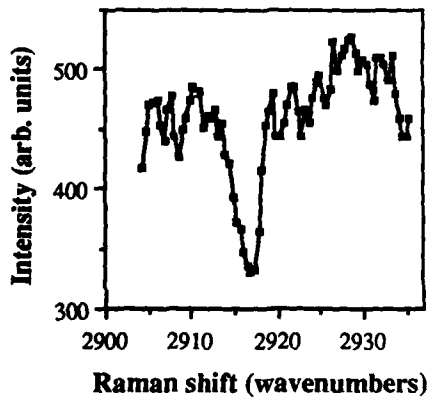

Fig.2. Methane ν_1 fundamental mode recorded at a pressure of 24 Torr

pump beam is given a slight elliptical polarization, the background shows a slight frequency dependence, but the signal increases (Fig. 1b). In the gas phase, methane spectra at pressures down to 24 Torr were recorded (Fig. 2).

FUTURE IMPROVEMENTS

The 24 Torr spectra were seen with a subtraction 60 times worse than optimal. The poor quality of the subtraction occurred when the probe was optimally extinguished and may be due to increased sensitivity to polarization fluctuations or decreased intensity on the diodes. More attention to polarization fluctuations and more probe laser power will improve the subtraction for optimal extinction. A frequency-doubled, injection-seeded Nd:YAG pump laser will increase the signal by 100 times. With these improvements signals from 4 mTorr pressures should be detectable.

1 Jacek Borysow, Roger H. Taylor and J. W. Keto, Opt. Comm. 68, 80(1988).

2 G. L. Eesley, Coherent Raman Spectroscopy, Permagon Press, New York, 1981.

3 M. D. Levenson and J. J. Song, J. Opt. Soc. Am. 66, 641(1976).

Single-Photon VUV Laser-Induced Fluorescence Spectrum of HCl

Sivaram Arepalli*, Yu-Lin Huang, Robert Callaghan, and Robert J. Gordon

Department of Chemistry, University of Illinois at Chicago, Box 4348 Chicago, Illinois 60680

Introduction

We report in this paper the first single-photon vacuum ultraviolet laser-induced fluorescence (LIF) spectrum of HCl. Earlier studies of HCl electronic spectroscopy employed conventional sources to produce high resolution absorption and emission spectra [1-6]. Recently resonance-enhanced multi-photon ionization (MPI) was used to study a number of electronically excited states between 77,000 and 87,000 cm^{-1} [7-9]. The first observation of VUV fluorescence from HCl was obtained using a broad-band (0.5 nm) synchrotron source between 105 and 123 nm [10]. Although the fluorescence cross section proved to be fairly small ($\sim 10^{-19}$ cm^2), it raised the possibility that a higher resolution LIF spectrum could be obtained.

The VUV radiation used in this study was produced by tripling the output of a commercial UV laser in a cell containing Kr or Xe gas. Third harmonic generation (THG) in atomic gases is a simple way for producing narrow-band, tunable VUV radiation which has not been widely used in molecular physics experiments [11]. Other molecules which have been studied by this method include H_2 [12], CO [12-16] and NO [15]. THG has also been extended to the XUV region, where it has been used to study H_2 [17,18], N_2, O_2 and CO_2 [19].

Experimental

The experiment was performed with a modified flash-photolysis apparatus described previously [20]. The fluorescence cell was a 15 cm monel cube machined with a 10 cm internal length. This cell was equipped with 5 cm long baffle arms at each port containing 6 mm diam apertures. Attached to one face was a cylindrical tripling cell equipped with a 2.5 cm focal length S1 UV quartz focussing lens at its entrance and a 2 mm thick LiF window separating it from the fluorescence cell. The focussing lens was located 5.5 cm away from the back window and 14.8 cm away from the center of the fluorescence cell. Both the fluorescence and tripling cells were filled statically, using capacitance manometers to measure the pressure. At right angles to the tripling cell was mounted a telescope flushed with dry N_2 and containing two 7.5 cm focal length MgF_2 lenses, followed by a solar blind photomultiplier tube (EMR 541G-08-17) sensitive between 120 and 200 nm. The tube was operated in analog mode and was biased at -3 KV. Current from this tube was amplified by a

*Present address: Lockheed ESC, P. O. Box 58561, Houston, Texas 77258-8561

factor of 10 (Tektronix TM 503), averaged with a boxcar integrator (Stanford Research SR 250), and displayed on a strip chart recorder.

The VUV radiation used to produce the fluorescence was generated in three stages. First, a YAG-pumped dye laser (Quantel 581C/TDL50) operating with LD698 dye produced 35 mj of 698 nm radiation. This beam was then doubled in a KDP crystal, producing 4 to 5 mj of UV radiation. Finally the UV beam was focussed into the tripling cell, which is expected to have a conversion efficiency of approximately 10^{-6} [18]. The optimum rare gas pressures at 115 nm were 90 Torr for Kr and 230 Torr for Xe. The bandwidth of the resulting VUV radiation was ~0.5 cm^{-1}.

Results and Discussion

The LIF spectrum of HCl was recorded between 114.8 and 116.4 nm. The fluorescence intensity increased linearly with HCl pressure up to approximately 0.2 Torr, reached a maximum at 0.5 Torr, and declined at higher pressures. The deviation from linearity is caused by absorption of the laser beam and radiative trapping of the fluorescence [21].

The spectral lines were assigned by comparison with a tabulated high resolution absorption spectrum [23]. All the observed strong lines arise from transitions from $X(^1\Sigma^+, v''=0)$ to $V(^1\Sigma^+, v''=15,16,17)$. Figure 1 shows a low resolution spectrum of much of the $v'=15$ band and part of the $v'=16$ band, while Figure 2 shows a portion of the $v'=15$ band at higher resolution, both recorded at a neat pressure of 0.1 Torr. These spectra were not normalized for variation of the VUV laser intensity with wavelength. The approximately 6 cm^{-1} splitting caused by the two isotopes of chlorine can be discerned clearly even in the low-resolution spectrum.

Diffuseness in some of the lines previously observed in the absorption spectrum [3] indicated that the V state interacts with other overlapping $^1\Sigma^+$ states, resulting in predissociation of some of the vibrational levels. This is not the case for the $v'=15,16$ and 17 levels seen here, in agreement with the emission [3], absorption [3,6] and MPI [7] studies. The previous synchrotron excitation study [10] showed no rotational structure and only partial vibrational resolution. The assignments in that study are consistent with the present results.

Aside from adjusting the HCl and rare gas pressures, no attempt was made to optimize the sensitivity of the apparatus. A significant improvement in the signal-to-noise ratio is possible by replacing the exit window of the tripling cell with a LiF collimating lens. Since none of the noise in the spectra was due to scattered laser light, a further increase in sensitivity is obtainable by photon counting. Finally, since the fluorescence is linear in laser intensity, additional improvement could be achieved by shot-to-shot normalization. For the sake of comparison, we also recorded the LIF spectra of the $X \rightarrow B$ transition of CO and the $X \rightarrow B$ transition of H_2 [22]. Both were an order of magnitude more intense than the HCl fluorescence. In the case of H_2 a sensitivity of better than 10^9 cm^{-3} per quantum level has been achieved by LIF [12,18]. The ease with

which we obtained the LIF spectrum of HCl, its linearity, and its high potential sensitivity make this technique an ideal detection method for studying elementary reaction dynamics.

Acknowledgments

We wish to thank Dr. Mitsuo Koshi for his help in setting up the VUV laser. Support by the Department of Energy under Grant no. DE-FG02-88ER13827 is gratefully acknowledged.

References

1. J. Romand, Ann. Phys. 4 (1949) 527.
2. J. K. Jacques and R. F. Barrow, Proc. Phys. Soc. London 73 (1958) 538.
3. A. E. Douglas and F. R. Greening, Can. J. Phys. 57 (1979) 1650.
4. S. G. Tilford, M. L. Ginter, and J. T. Vanderslice, J. Mol. Spectrosc. 33 (1970) 505.
5. S. G. Tilford and M. L. Ginter, J. Mol. Spectrosc. 40 (1971) 568.
6. D. S. Ginter and M. L. Ginter, J. Mol. Spectrosc. 90 (1981) 177.
7. S. Arepalli, N. Presser, D. C. Robie, and R. J. Gordon, Chem. Phys. Lett. 118 (1985) 88.
8. R. Callaghan, S. Arepalli, and R. J. Gordon, J. Chem. Phys. 86 (1987) 5273.
9. T. A. Spiglanin, D. W. Chandler, and D. H. Parker, Chem. Phys. Lett. 137 (1987) 414.
10. J. B. Nee, M. Suto, and L. C. Lee, J. Chem. Phys. 85 (1986) 719.
11. R. Hilbig, G. Hilber, A. Lago, B. Wolff, and R. Wallenstein, Comments At. Mol. Phys. 18 (1986) 157.
12. F. J. Northrup, J. C. Polanyi, S. C. Wallace, and J. M. Williamson, Chem. Phys. Lett. 105 (1984) 34.
13. H. Zacharias, H. Rottke, and K. H. Welge, Optics Commun. 35 (1980) 185.
14. R. Hilbig and R. Wallenstein, IEEE J. Quant. Elect. QE-17 (1981) 1566.
15. J. C. Miller, R. N. Compton, and C. D. Cooper, J. Chem. Phys. 76 (1982) 3967.
16. H. Rottke and H. Zacharias, Opt. Commun. 55 (1985) 87.
17. M. Rothschild, H. Egger, R. T. Hawkins, J. Bokor, H. Pummer, and C. K. Rhodes, Phys. Rev. A23 (1981) 206.
18. E. E. Marinero, C. T. Rettner, R. N. Zare, and A. H. Kung, Chem. Phys. Lett. 95 (1983) 486.
19. T. P. Softley, W. E. Ernst, L. M. Tashiro, and R. N. Zare, Chem. Phys. 116 (1987) 299.
20. J. C. Miller and R. J. Gordon, J. Chem. Phys. 78 (1983) 3713.
21. Y. P. Vlahoyannis, M. Koshi, and R. J. Gordon, Chem. Phys. Lett. 118 (1985) 179.
22. Y. Huang, S. Arepalli, R. Callaghan, and R. J. Gordon (unpublished results).
23. M. L. Ginter, private communication.

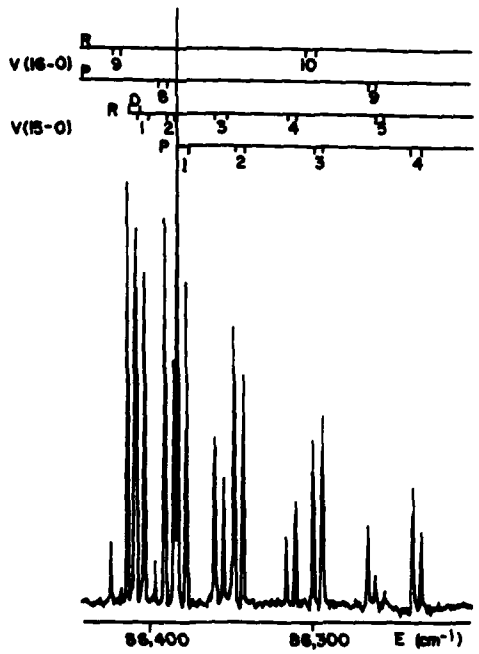

Figure 1. Part of the low resolution excitation spectrum of HCl showing P and R bands of the $X(^1\Sigma^+,v''=0) \rightarrow V(^1\Sigma^+,v'=15$ and 16) transitions. The doublets arise from the isotopic splitting of Cl.

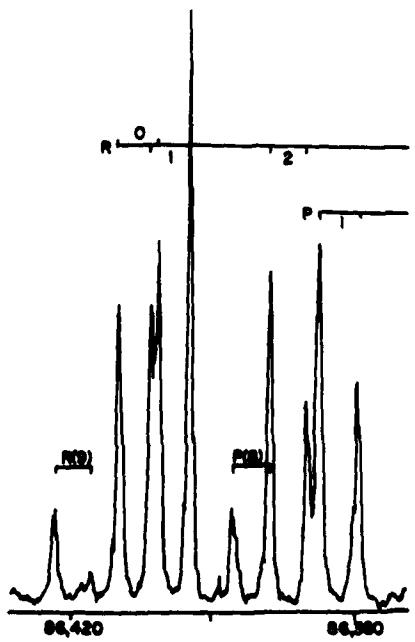

Figure 2. Part of the high resolution excitation spectrum of HCl. The spectrum was not corrected for shot-to-shot fluctuation of the laser intensity.

Resonant Two-Photon Ionization Electronic Spectroscopy of the Silver Trimer

P. Y. Cheng and M. A. Duncan

Department of Chemistry
School of Chemical Sciences
University of Georgia
Athens, GA 30602

Abstract

Silver metal clusters are produced by excimer laser vaporization (308 nm) in a pulsed supersonic nozzle cluster source. The triatomic species is selectively ionized in a resonant two-photon absorption process via an excited electronic state with an origin at 26971±10 cm^{-1} (3.35 eV). Vibronic structure extending over 1500 cm^{-1} involves cleanly resolved bands at low energy merging to a quasi-continuum at higher energy. Vibronic analysis are considered for a triangular structure with or without Jahn-Teller interaction in the excited state. No simple analytic expression successfully fits the level structure. However, the spectrum is qualitatively consistent with a $^2E''$ excited state with intermediate Jahn-Teller interaction.

Introduction

Although metal clusters have been a very active research field for a decade, gas phase polyatomic spectroscopy has been limited to triatomic sodium[1], copper[2,3], aluminum[4] and nickel[5]. In this report we describe the first observation of a vibrationally resolved electronic spectrum for triatomic silver in the gas phase.

The silver trimer has been the subject of UV-VIS, ESR, and resonance Raman experiments in the rare gas matrixes[6], as well as several recent theoretical calculations[7,8]. The ground state is generally regarded as a Jahn-Teller distorted $^2E''$ state with nominal D_{3h} symmetry, which become a $^2B_2$ minimum energy species in C_{2v} symmetry. Excited states have been calculated recently by Walch[8], and have been observed with matrix UV absorption.

Experimental

Silver clusters are produced by pulsed-nozzle laser vaporization at 308 nm in a molecular beam apparatus described previously[9]. Nd:YAG pumped dye laser (Quanta-Ray PDL-2) radiation is mixed with the 1064 nm fundamental, producing tunable UV light in the 380-360 nm region.

This laser is used for one-color resonant two-photon ionization spectroscopy, selectively detecting Ag_3 in a TOF mass spectrometer. Additional two-color ionization experiments combine a XeF excimer laser (350 nm) with a visible dye laser in the 400-500 nm region.

Results and Discussion

Figure 1 shows the wavelength dependence of the Ag_3^+ signal between 371 and 365 nm. There are 14 cleanly resolved vibronic bands. No additional cold bands are observed within the region 200 cm^{-1} to the red of this system. At higher photon energy the spectrum becomes quite congested. The same strong Ag_3^+ signal is observed for R2PI with a XeF excimer laser (350 nm), indicating that the absorption system extends as far as 1500 cm^{-1} above the indicated origin. At reduced power, the XeF laser can be combined with a tunable dye laser in the 420-490 nm region, producing a two-color Ag_3 signal. The upper limit of the Ag_3 IP is thus measured as 6.07 eV. Since Ag_3 is not ionized by the KrF excimer laser (249 nm, 4.98 eV), the IP of Ag_3 is placed between 4.98 eV and 6.07 eV.

A triangular geometry (D_{3h}) is considered for the excited state of this spectrum. As shown in Figure 1, the spectrum has been assigned to the symmetric stretch, the doubly degenerate bending mode, and combination bands.

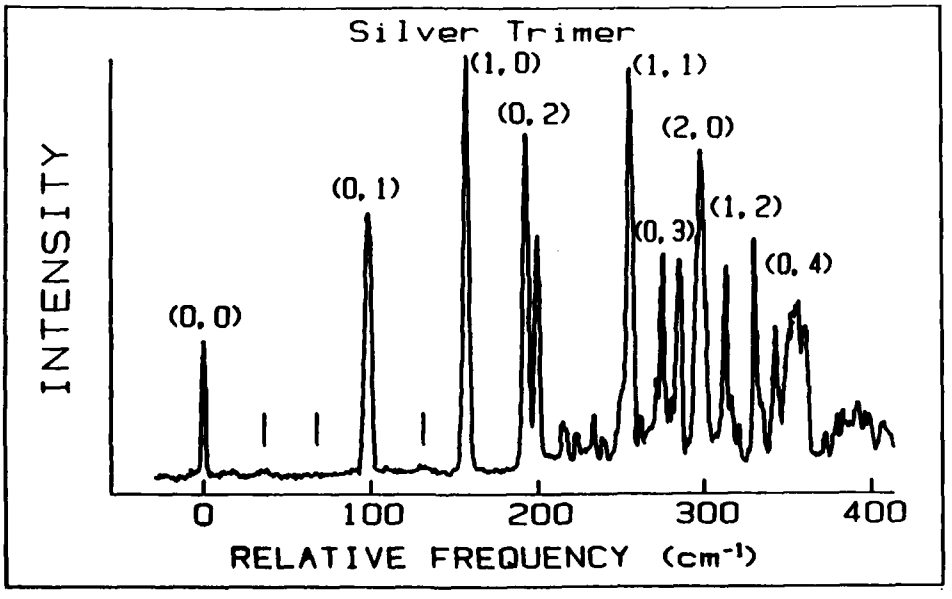

Figure 1. The 370 nm absorption band of silver trimer.

The splittings associated with the bending mode are due to Jahn-Teller vibronic coupling if the excited electronic state is also doubly degenerate ($^2E'$ or $^2E''$). Both the non-degenerate and degenerate excited electronic states were considered in this work. For the latter cases, two extreme Jahn-Teller interaction cases, namely very weak and very strong, were considered because vibronic energy levels in these extremes are described by simple analytic expressions. None of these cases were able to explain energy levels of the observed spectrum successfully. However, since (1) the $^2E''$ excited state with very weak and strong Jahn-Teller interaction qualitatively explains the vibronic levels, and (2) the most intense transition around 3 eV in Walch's calculation is a $^2E''$ state at 3.26 eV, the $^2E''$ excited state is believed to be responsible for the spectrum. This analysis suggests that this system is an example of the intermediate case of Jahn-Teller interaction, in which pseudorotation is hindered by a significant barrier to rearrangement. Spectral splittings begin near 200 cm^{-1} of total vibronic energy, suggesting that the barrier to pseudorotation has approximately this value. Vibrational analysis at low energy determines the stretching and bending frequencies to be 178.6 cm^{-1} and 103.9 cm^{-1} respectively, in general agreement with the predictions of Walch.

References

(1) G. Delacretaz, E. R. Grant, R. L. Whetten, L. Woste, and Zwanziger, Phys. Rev. Lett. 56, 2598 (1986)
(2) M. D. Morse, J. B. Hopkins, P. R. R. Langridge-Smith, and R. E. Smalley, J. Chem. Phys. 79, 5316 (1983)
(3) M. D. Morse, Chem. Phys. Lett. 133, 8 (1987)
(4) Z. Fu, G. W. Lemire, Y. M. Hamrick, S. Taylor, J. C. Shui, and M. D. Morse, J. Chem. Phys. 88, 3524 (1988)
(5) J. R. Woodward, S. H. Cobb, and J. L. Gole, J. Phys. Chem. 92, 1404 (1988)
(6) a) W. Schulze, H. U. Becker, and H. Abe, Chem. Phys. 35, 177 (1978); b) G. A. Ozin, H. Huber, and S. A. Mitchell, Inorg. Chem. 18, 2932 (1979); c) J. A. Howard, R Sutcliffe, and B. Mile, Surf. Sci. 156, 214 (1985)
(7) S. P. Walch, C. W. Bauschlicher, and S. R. Langhoff, J. Chem. Phys. 85, 5900 (1986)
(8) S. P. Walch, J. Chem. Phys. 87, 6776 (1987)
(9) K. LaiHing, R. G. Wheeler, W. L. Wilson, and M. A. Duncan, J. Chem. Phys. 87, 3401 (1987)

RESONANT ENHANCED MULTIPHOTON DISSOCIATION SPECTROSCOPY OF MOLECULAR IONS: TECHNIQUE AND APPLICATION TO CH_3I^+/CD_3I^+

U. Boesl, R. Weinkauf, K. Walter
Inst. f. Phys. u. Theor. Chemie, Technische Universität München
Lichtenbergstr.4, 8046 Garching, FRG

ABSTRACT

We present in this paper our techniques for performing photodissociation spectroscopy of molecular radical cations. These methods involve multiphoton ionization as an ion source and mass spectroscopic techniques for distinguishing between molecular and fragment ions, as well as between fragment ions of different origins. Photodissociation spectroscopy includes predissociation as well as resonant enhanced multiphoton dissociation. The latter allows access to non-fluorescing and non-dissociating ionic states. A special method allows determination of metastable decay times for very large mass differences of molecular and fragment ions. This information can be used to assign predissociation spectra. We applied our methods to CH_3I^+ and CD_3I^+ where we could, for the first time, scan down to the electronic origin of the A X transition and observe assignable rotational fine structure.

I. Multiphoton Dissociation Spectroscopy of Molecular Ions

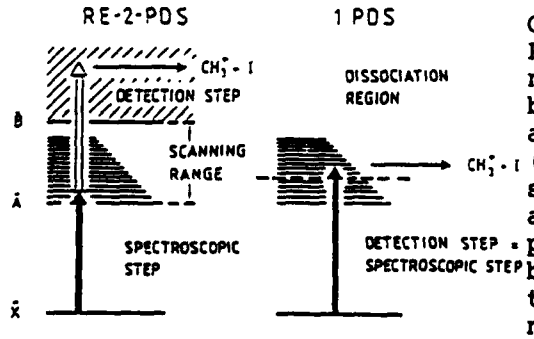

Fig.1. Schemes for PDS of CH_3I^+

One-Photon Dissociation (1-PDS) allows spectroscopy of non-fluorescing ionic states, but is limited to states above a dissociation threshold (dashed line in fig.1, right side). The separation of photon absorption for spectroscopy and photon absorption for detection by dissociation allows access to non-fluorescing, as well as non-predissociating states (see fig.1, left side). We call this resonant enhanced multiphoton dissociation spectroscopy (RE-MPDS)[1]. With RE-MPDS a large class of molecular ionic states can be investigated. Especially in low lying states of radical cations fluorescence is often suppressed by fast internal conversion and predissociation is not yet active. As an example: the origin and low lying vibrational levels of the A-state of CH_3I^+ could not be observed with conventional ion spectroscopic methods. RE-MPDS overcomes this problem. The combination with multiphoton ionization as an ion source on the other hand improves the capability of photodissociation spectroscopy considerably. The main advantages are high ion densities in a small volume and the production of state selected molecular ions[2].

II. Experimental Apparatus

Fig.2 shows our experimental setup[1]. A supersonic beam of argon gas with some percent of sample molecules is directed into the ion source consisting of two plane electrodes. At the repelling electrode a voltage of +1kV is applied. With laser1 resonance enhanced multiphoton ionization is achieved. The molecular ions are formed at a potential of 820 eV. Laser 2 is responsible for the spectroscopic and dissociation steps of these ions. All ions are extracted into a time-of-flight analyzer consisting of a field free drift region and an ion reflector with a decelerating and a reflecting electric field. The signal from the ion detector, falling within a preset time window, is registered as a function of the wavelength of laser 2. Two problems have to be solved with photodissociation spectroscopy.

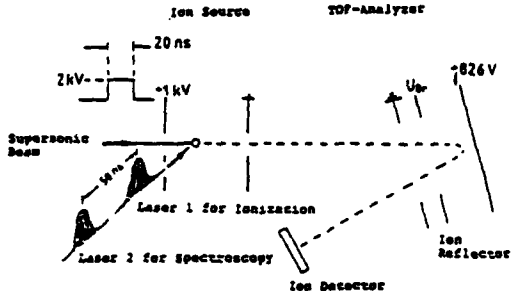

Fig.2. Experimental setup

1. Discrimination of molecular and fragment ions:
For PDS one has to discriminate between molecular ions and fragment ions. We use therefore a special, high resolution time-of-flight spectrometer[3] (Reflectron) (see fig.2). By reflecting the ions in an electric field with an exactly tuned slope, the different energies of ions with the same mass can be compensated without any loss in total ion current; this leads to a narrowing of the ion peaks by a factor of 10 and more compared to conventional linear time-of-flight analyzers. This allows narrow time gates for the ion detection and therefore very good signal-to-noise ratios.

2. Discrimination between fragment ions of different origins:
Due to undesired photodissociation during the ion production by multiphoton ionization, very often fragment ions are formed, which have the same mass as the secondary, desired fragment ions formed during ion spectroscopy. For discrimination between identical fragment ions from different photon processes we use a special HV-technique combined with the reflectron as an energy analyzer. As can be seen from fig.3 in the case of CH_3I^+, a large amount of CH_3^+ ions is formed during MPI. The same fragment ion is also formed during ion spectroscopy of the X A transition of CH_3I^+. In fig.3 the effect of applying our technique is demonstrated. In fig.3,a-d the time-of-flight scale is enlarged so that only the methyl fragment ions are shown. fig.3a: Only laser 1 (responsible for MPI) is active. fig.3b: laser 1 and laser 2 (delay 50 ns) are active . The secondary fragment ions appear as an unresolved shoulder of the primary fragment ions. fig.3c: HV-pulse (2 kV, delay to laser 1 20 ns) is applied to the repulsive electrode of the ion source and induces an energy transfer, which is different for fragment ions formed before and after the HV-pulse: $U(CH_3^+, \text{laser 1}) = 18eV$, $U(CH_3^+, \text{laser 2}) = 1eV$. This leads to a noticeable separation of both types of CH_3^+ fragment ions. fig.3d: The

potential of the reflector end plate is set to U_{ref} U+18 eV, so that all primary fragment ions with large kinetic energy hit the end plate and are eliminated while secondary fragment ions with low kinetic energy are reflected.

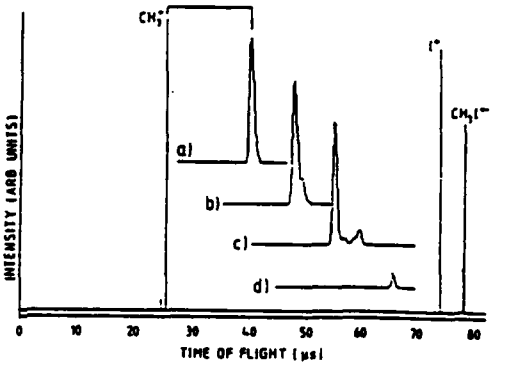

Fig.3. TOF-spectra of CH_3I^+/ CH_3^+, application of HV-pulsing and reflectron energy anlyzer. For inserts a-d see text.

III. Metastable decay rates used for molecular ion spectroscopy

Metastable decay rates in photodissociation spectroscopy can serve for discrimination between one- and multiphoton dissociation. Furthermore, at least for one-photon dissociation spectroscopy they can help to separate cold and hot bands due to different decay times of the final states. TOF-analyzers are very useful for the determination of decay rates, due to specific TOF-profiles caused by metastable decay. In a linear TOF, metastable decay in the acceleration region leads to a broad ion profile. In a corrected Reflectron, metastable decay does not cause a severe change of the ion peak profile at all[3]. In a partially corrected Reflectron (detuned reflecting field), metastable decay in the acceleration and in the drift region causes separable, relatively distinct ion peak profiles[3]. Decay rates can be determined from peak widths and intensities[4].

There is, however, a problem with large relative mass differences between molecular and fragment ions, as in the case of the molecular ion CH_3I^+ (142 amu) and the fragment ion CH_3^+ (15 amu). In linear TOF-analyzers, the profiles of such fragment ions are spread over a large TOF-range leading to very low ion peak intensities and interferences with masses between the fragment and molecular ion masses. In a non-linear Reflectron, large mass loss causes very early reflection in the ion reflecting field due to large kinetic energy loss; this is associated with such a large parallel shift of the ion trajectories, that the fragment ions miss the ion detector. Our solution[1] of this problem for a Reflectron is explained below: (1): The Reflectron works in a partial correcting mode: ions with the same mass but different energy have different times-of-flight. (2): A time window t for the ion detection at a fixed time-of-flight corresponds to an energy window U at a fixed energy U for all ions with the same mass. (3): By shifting a potential, which is superimposed onto the whole ion source, this fixed energy window U picks out metastable ions which decay at increasing positions x (increasing decay times). (4): Thus shifting this potential is like moving a time window along the decay curve of a metastable ion. However, the energy and therefore the turning point of the fragment ions in the reflector stay fixed. (5): The Reflector end plate is set to a potential at the

high energy edge of the window U. Thus all masses, which are shifted through the corresponding time window t and would interfere with the metastable mass peaks, hit the endplate and disappear from the mass spectrum.

IV. One-photon dissociation spectroscopy of CH_3I^+/CD_3I^+

Two groups have already published 1-PDS spectra of CH_3I^+ and CD_3I^+[5]. With the excellent background suppression of our technique we could increase the relative sensitivity considerably and therefore work with much smaller laser intensities. Thus all kinds of optical broadening effects could be avoided. This is demonstrated by the large increase of resolution in fig.4 (1-PDS of CH_3I^+) although we used a very similar laser system as in ref.[5a]. In fig.4 a part of the A X transition of CH_3I^+ can be seen. Due to the predissociation threshold, the spectrum suddenly breaks off at wavelengths longer than 4550 . Fig.4 shows also one single band on a very enlarged wavelength scale. Very clearly, rotational fine structure can be distinguished; one has to be aware that rotational resolved optical spectra of polyatomic molecular ions untill now are a rarity[6]. Due to the cooling of the neutral parent molecules in the supersonic beam only the lowest K level is excited which simplifies the rotational structure considerably. We tried a first assignement (see fig.4) with rotational constants given by McLoughlin et al.[5b]. These authors deduced their values from the rotational envelope and from unassigned rotational substructure. However they could not decide, if this transition belongs to the Hund's case c c or b c, which leads to different rotational constants. Our well resolved spectrum can only be simulated by the c c Hund's coupling case. For a better analysis and resolution of eventual K substructure the resolution of our dye laser has to be improved.

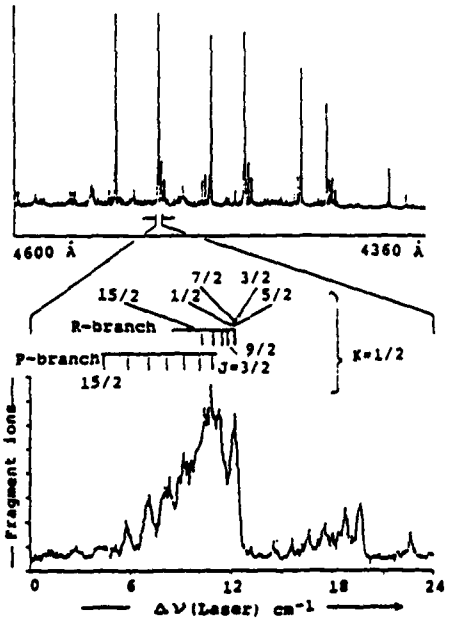

Fig.4. CH_3I^+: 1-PDS spectrum, rotational fine structure.

In fig.5a the one-photon dissociation spectrum of CD_3I^+ is shown. Also this spectrum breaks off at the predissociation threshold at 4520 . There are, however, several small peaks in the red of this threshold. The question arises, are these peaks induced by starting multiphoton dissociation or are they due to hot bands. To answer this question, we measured the metastable decay times of several bands with the method explained in chapter III. The results are displayed in fig.5a. The decay times of the bands above the threshold are between 290 and 70 ns; all of these bands could be assigned and are due to cold bands. The decay

times of small bands below this threshold are 30 and 50 ns. On the one side, this is much shorter then the values for the cold bands, on the other side this is noticeable longer than the decay times of levels reached by multiphoton absorption. Such decay times lie below the minimal values of 20 ns we can determine with our method; this is indicated in fig.5b, which shows a (1+1)PDS spectrum of CH_3I^+ at the same wavelength region as the 1-PDS spectrum in fig.5a. From these facts it can be clearly deduced that the small bands to the red of the predissociation threshold in the 1-PDS spectrum are due to hot bands.

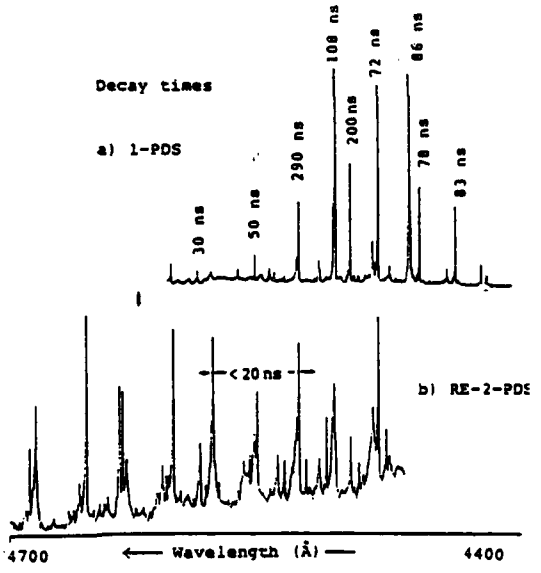

Fig.5. Decay times of final states reached during 1-PDS and RE-2-PDS of CD_3I^+

V. Multiphoton dissociation spectroscopy of CH_3I^+/CD_3I^+

In fig.5b the major advantage of multiphoton dissociation spectroscopy can be made out. Instead of breaking off at the predissociation threshold the spectrum continues without noticable interrupt to longer wavelengths. With this new ion spectroscopy the A X transition of the methyl iodide radical cation down to the true electronic origin could be investigated for the first time[1]. This radical cation is an illustrative example for many molecular radical cations with non-fluorescing or non-predissociating states.

In fig.6 parts of our RE-MPS spectra of CD_3I^+ are displayed, which consist of two spectra due to the 1/2- and 3/2-spin orbit components of the ionic ground state. These spectra can be observed separately because multiphoton ionization allows the selective preparation of methyl iodide cations in one of these spin orbit components of the ionic X state. The low intensity of hot bands in the red of the electronic origins also prove the high vibrational selectivity of ion preparation by multiphoton ionization. Furthermore, the narrow rotational envelopes of the vibronic bands demonstrate the rotational selectivity of this ion source (see also fig.4). The sudden break off in the red is now a real break off of the spectrum due to the real electronic origins. With 1-PDS the A X(3/2) spectrum starts 2700 cm^{-1} to the red of the electronic origin, which corresponds to the last vibronic band of the upper spectrum in fig.6. 90% of all bands in our RE-MPDS spectra of CH_3I^+ and CD_3I^+ could be assigned and are due to long progressions of the C-I-streching mode with different

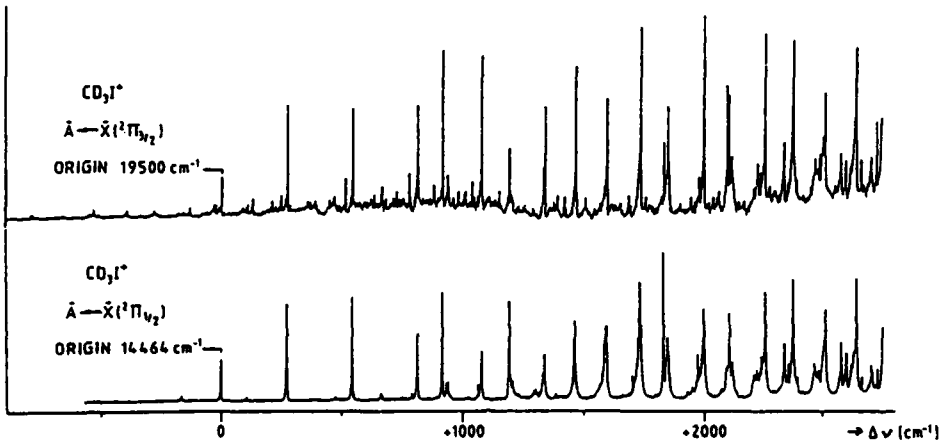

Fig.6. Re-2-PDS spectra of CD_3I^+ with the true origins of the A-X-transition. The two separated spectra are due to the two spin orbit components of the X state.

quanta of the umbrella mode as progression origins. Several new or improved molecular constants could be deduced from our RE-MPDS spectra of CH_3I^+ and CD_3I^+. For further information see refs.[1]. Recently, well resolved RE-MPDS spectra of other molecular radical cations have been published[7] confirming the importance of this ion spectroscopic method.

ACKNOWLEDGEMENT

This project has been supported by the Deutsche Forschungsgemeinschaft. The authors thank also Prof.E.W.Schlag for encouraging and stimulating discussions.

REFERENCES

1. K.Walter, R.Weinkauf, U.Boesl, E.W.Schlag, J. Chem. Phys. 89, 1914 (1988); R.Weinkauf, K.Walter, U.Boesl, E.W.Schlag, Chem. Phys. Lett. 141, 267 (1987)
2. K.S.Viswanathan, E.Sekreta, E.R.Davidson, J.P.Reilly, J. Phys. Chem. 90, 5078 (1986); A.Hiraya, Y.Achiba, N.Mikami, K.Kimura, J. Chem. Phys. 82, 1818 (1985) and ref. cited herein
3. U.Boesl, H.J.Neusser, R.Weinkauf, E.W.Schlag, J. Phys. Chem. 86, 4857 (1982) and ref. cited herein
4. H.J.Neusser, H.Kühlewind, U.Boesl, E.W.Schlag, Ber. Bunsenges. Phys. Chem. 89, 276 (1985)
5. a) A.M.Woodward, S.D.Colson, W.A.Chupka, J. Phys. Chem. 90, 274 (1966); b) R.G.McLoughlin, J.D.Morrison, D.L.Smith, A.L.Wahrhaftig, J. Chem. Phys. 82, 1237 (1985)
6. J.P.Maier, J.Electron. Spectrosc. Rel. Phenom. 40, 203 (1986)
7. X.Ripoche, I.Dimicoli, J.LeCalve, F.Piuzzu, R.Botter, to be published in Chem. Phys. (1988); P.O.Danis, T.Wyttenbach, J.P. Maier, J. Chem. Phys. 88, 3451 (1988)

CHARACTERIZATION OF THE GAS PHASE BROMOCYANOGEN CATION WITH LASER-EXCITED FLUORESCENCE SPECTROSCOPY

Maureen A. Hanratty,* Matthias Rösslein, Francis G. Celii, Thomas Wyttenbach and J. P. Maier
Institut für Physikalische Chemie, Universität Basel, Basel, Switzerland

ABSTRACT

Observation of the $\tilde{B}\,^2\Pi_{3/2} \leftarrow \tilde{X}\,^2\Pi_{3/2}$ transition of bromocyanogen cation using laser-excited fluorescence (LEF) spectroscopy is reported. On the basis of these measurements, the vibrational frequencies of the $\tilde{B}\,^2\Pi_{3/2}$ state were confirmed and the electronic origin of the $\tilde{B}\,^2\Pi_{3/2} \leftarrow \tilde{X}\,^2\Pi_{3/2}$ transition reassigned. Stimulated emission pumping (SEP) spectroscopy was used to verify the isotopic assignments as well as determine the $\tilde{X}\,^2\Pi_{3/2}$ (ν_3) frequency. Tentative assignments are made for Renner-Teller components of transitions involving ν_2 excitation in both the $\tilde{B}\,^2\Pi_{3/2}$ and $\tilde{X}\,^2\Pi_{3/2}$ states. Analysis of the rotationally-resolved spectra yielded values for the ground state rotational constants from which the R_s structure of the $\tilde{X}\,^2\Pi_{3/2}$ state was derived. Consideration of the spectroscopic parameters determined for different vibronic levels of the $\tilde{B}\,^2\Pi_{3/2}$ state indicate that some of the levels are perturbed.

INTRODUCTION

Although the bromocyanogen cation, $BrCN^+$, is isoelectronic with such well-studied polyatomic cations as CO_2^+ [1], N_2O^+ [2], OCS^+ [3] and CS_2^+ [4], the electronic spectroscopy has not been as extensively investigated. From the initial gas-phase emission[5] and matrix isolation absorption[6] studies of the $BrCN^+$ $\tilde{B}\,^2\Pi_{3/2} \leftarrow \tilde{X}\,^2\Pi_{3/2}$ transition, it was suggested that the complexity of the spectrum was due to Fermi and Renner-Teller interactions as is the case for the other 15 valence electron species mentioned above. Additional evidence for interelectronic coupling in $\tilde{B}\,^2\Pi_{3/2}$ $BrCN^+$ has been provided by time-resolved emission studies[7]. The rotationally-resolved LEF spectra of $BrCN^+$ which we now report provides further characterization of this interesting polyatomic radical cation[8].

EXPERIMENTAL

$BrCN^+$ was produced by Penning ionization of neutral bromocyanogen using He or Ne metastables in a cooled discharge lamp[9]. A Nd:YAG-pumped dye laser provided tunable visible light. Total fluorescence was collected perpendicular to the laser propagation direction with an f/1 lens and photomultiplier in combination with appropriate filters. Simultaneous monitoring of I_2 or $^{130}Te_2$ fluorescence spectra provided absolute frequency calibration. SEP experiments were performed on a similar instrument which utilized a second spatially-overlapped and temporarally-delayed ($\Delta t \sim 5$ nsec) laser as has been described previously[10].

RESULTS

A portion of $\tilde{B}\,^2\Pi_{3/2} \leftarrow \tilde{X}\,^2\Pi_{3/2}$ LEF spectrum of $BrCN^+$ ($\Delta\nu = 0.25$ cm^{-1}) is displayed in figure 1. Long progressions in ν_3 (C-Br stretch) as well as combination

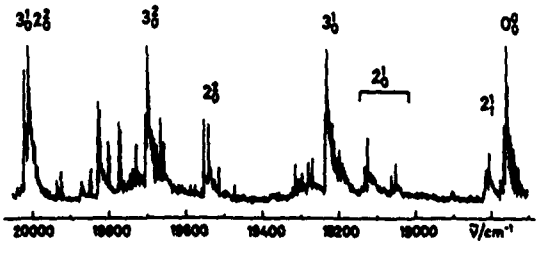

Figure 1: $\tilde{B}\,^2\Pi_{3/2} \leftarrow \tilde{X}\,^2\Pi_{3/2}$ laser excitation spectrum of $BrCN^+$ with vibrational assignments indicated above the bands.

bands involving ν_2 (Br-CN bend) are observed, indicative of a large geometry change between the two ionic states[11]. The main vibrational bands in figure 1 are all similar in appearance, having two closely spaced bandheads, one for each of the equally abundant bromine isotopes, which are degraded to longer wavelength. The frequencies of the main bands are displayed in table I. The spectrum conforms to the expectations for a $^2\Pi - ^2\Pi$ Hund's case (a) transition, with all bands assigned to transitions within the $\Omega = 3/2$ manifold, since the higher energy $\widetilde{X}\,^2\Pi_{1/2}$ (v=0) level is not populated at the temperature of this experiment ($A'' = -1477$ cm^{-1}).

Table I: Band origin and isotope shifts in the $\widetilde{B}\,^2\Pi_{3/2} \leftarrow \widetilde{X}\,^2\Pi_{3/2}$ transition of $BrCN^+$.§

Transition	$^{79}BrCN^+$	Frequency interval	$^{81}BrCN^+$	Frequency interval	Isotope shift
0_0^0	18759.79(2)		18756.46(4)		3.33
		473.09		473.35	
3_0^1	19232.88(3)		19229.81(2)		3.07
		471.13		468.62	
3_0^2	19704.01(3)		19698.43(2)		5.58
2_0^2	19552.51(20)†		19540.31(20)†		12.20
		468.83		469.92	
$3_0^1 2_0^2$	20021.34(3)		20010.23(2)		11.11

§ All values in cm^{-1} with one standard deviation shown in parentheses.
† Frequency of bandhead.

The lowest energy bands observed in the LEF spectrum have maxima located at 18,761.05 cm^{-1} and 18,757.75 cm^{-1}, and are attributed to the origin bands of the $BrCN^+$ $\widetilde{B}\,^2\Pi_{3/2} \leftarrow \widetilde{X}\,^2\Pi_{3/2}$ transition. Bands in this region were not observed in the previously reported emission spectrum of $BrCN^+$[5], and this reassignment of the origin results in closer agreement with the matrix value[6].

Irregularities in both the frequency intervals between successive 3_0^m bands and the isotope splitting within bands (table I), as well as difficulties in the initial rotational analysis, prompted a double resonance SEP experiment to be performed. The PUMP laser, tuned to the wavelength of a particular 3_0^i bandhead, produced a constant level of fluorescence. The DUMP laser, when resonant with the $\widetilde{B}\,^2\Pi_{3/2} \rightarrow \widetilde{X}\,^2\Pi_{3/2}$ 3_1^i transition frequency, caused a decrease in the detected fluorescence. The ν_3'' frequency was determined consistently to be 649.39±.05 cm^{-1} and 647.89±.05 cm^{-1} for $^{79}BrCN^+$ and $^{81}BrCN^+$, respectively. Due to the isotopic shift in the ν_3'' frequency, unambiguous identification of the bandheads was possible, with the shorter wavelength bandhead assigned to $^{79}BrCN^+$ for all bands investigated. Both the frequency intervals and isotopic splitting inconsistencies appear to be a result of perturbations in the upper states, presumably due Fermi resonances which are also manifest in the spectrum of the neutral BrCN molecule[12].

Rotationally resolved spectra ($\Delta\nu = 0.04$ cm^{-1}) for the $\widetilde{B}\,^2\Pi_{3/2} \leftarrow \widetilde{X}\,^2\Pi_{3/2}$ 0_0^0, 3_0^1, 3_0^2, and $3_0^1 2_0^2$ bands yielded line positions which were fit directly by describing the eigenvalues of each level by:

$$F_v(J) = \nu_0 + B_{eff}\{(J+1/2)^2 - 1\} - D_{eff}\{(J+1/2)^2 - 2\}^2, \qquad (1)$$

where B_{eff} and D_{eff} are the effective rotational and centrifugal distortion constants, respectively. Simultaneous fits to all but the $^{79}BrCN^+$ 3_0^1 and $^{81}BrCN^+$ 0_0^0 bands were used to determine the respective spectroscopic parameters displayed in table II. Inclusion of the $^{79}BrCN^+$ 3_0^1 or $^{81}BrCN^+$ 0_0^0 bands resulted in a significant increase in the standard deviation; therefore these bands were fit separately with a restricted number of variables. Inspection of table II reveals several anomalies in the determined rotational parameters. Most obvious is that $^{81}B_{eff}$ for $\widetilde{B}\,^2\Pi_{3/2}$ ($\nu = 0$) is larger than

the corresponding value for $^{79}B_{eff}$. In addition, there is not a smooth variation in the values of B'_{eff} for the 3_0^m series (m = 0,1,2) for either isotope. These results suggest that the $^{79}BrCN^+$ 3^1 and $^{81}BrCN^+$ 0^0 levels are perturbed. The nature of the states responsible for the perturbations have not yet been identified.

Table II: Spectroscopic constants determined for $^{79}BrCN^+$ and $^{81}BrCN^+$ §

Vibronic State	$^{79}BrCN^+$ ν_0	B_{eff}	$D_{eff} \times 10^{-7}$	$^{81}BrCN^+$ ν_0	B_{eff}	$D_{eff} \times 10^{-7}$
$\tilde{B}$ ($3^1 2^2$)	20,021.328(36)	.12782(6)	1.69(44)	20,010.216(24)	.12781(3)	1.71(25)
$\tilde{B}$ (3^2)	19,704.014(43)	.12610(6)	3.02(45)	19,698.428(33)	.12502(3)	1.05(20)
$\tilde{B}$ (3^1)	19,232.871(38)	.12615(6)	0.30†	19,229.827(17)	.12504(2)	0.30†
$\tilde{B}$ (0^0)	18,759.791(65)	.12747(5)	5.13(34)	18,756.201(8)	.12928(3)††	13.36(22)††
$\tilde{X}$ (0_0)		.14160(5)	1.10(37)		.14077(3)	1.29(14)

§ All values in cm^{-1} with one standard deviation shown in parentheses.
† Value held constant.
†† Ground state parameters held constant.

Rotational analysis of selected $\tilde{B}\,^2\Pi_{3/2} \leftarrow \tilde{X}\,^2\Pi_{3/2}$ bands of the ^{13}C and ^{15}N substituted $BrCN^+$ ions yielded a consistent set of spectroscopic parameters for the ground state from which an R_s structure for $\tilde{X}\,^2\Pi_{3/2}$ $BrCN^+$ was derived. The C–Br bond length of 186.3 ± 6.0 pm and C–N bond distance of 110.4 ± 5.9 pm have been determined [13].

ACKNOWLEDGEMENTS

This work is funded by the "Schweizerischer Nationalfonds zur Föderung der wissenschaftlichen Forschung." Ciba-Geigy SA, Sandoz SA, and F. Hoffmann-la Roche & Cie SA, Basel are also thanked for financial support.

REFERENCES

* Present address: Code 6110, Naval Research Lab, Washington, D.C., 20375-5000.
1. F. Bueso-Sanllehi, *Phys. Rev.* **60**, 556 (1941); D. Gauyacq, M. Horani, S. Leach and J. Rostas, *Can. J. Phys.* **53**, 2040 (1975); M. A. Johnson, J. Rostas and R. N. Zare, *Chem. Phys. Lett.* **92**, 225 (1982).
2. J. H. Callomon and F. Creutzberg, *Phil. Trans. R. Soc.*, **277**, 157 (1974); J. F. M. Aarts and J. H. Callomon, *Chem. Phys. Lett.*, **91**, 419 (1982).
3. M. Ochsner, M. Tsuji and J. P. Maier, *Chem. Phys. Lett.*, **115**, 373 (1985).
4. J. H. Callomon, *Proc. R. Soc. A*, **244**, 220 (1958).
5. J. Fulara, D. Klapstein, R. Kuhn and J. P. Maier, *J. Phys. Chem.*, **89**, 4213 (1985); M. Allan and J. P. Maier, *Chem. Phys. Lett.* **41**, 231 (1976).
6. S. Leutwyler, J. P. Maier and U. Spittel, *J. Chem. Phys.*, **83**, 506 (1985).
7. O. Braitbart, E. Castellucci, G. Dujardin and S. Leach, *J. Phys. Chem.*, **89**, 3252 (1985); E. Castellucci, G. Dujardin and S. Leach, *J. Chem. Soc. Faraday Trans.*, **82**, 1271 (1986).
8. For a full account see : M. A. Hanratty, M. Rösslein, F. G. Celii, T. Wyttenbach and J. P. Maier, *Molec. Phys.*, **64**, 865 (1988).
9. D. Klapstein, J. P. Maier and L. Misev, in "Molecular Ions Spectroscopy, Structure and Chemistry," edited by T. A. Miller and V. E. Bondybey (North Holland, Amsterdam, 1983), p. 175.
10. F. G. Celii, J. P. Maier and M. Ochsner, *J. Chem. Phys.*, **85**, 6230 (1986); F. G. Celii and J. P. Maier, these proceedings.
11. E. Heilbronner, V. Hornung, and K. A. Muszkat, *Helv. Chim. Acta*, **53**, 347 (1970).
12. A. G. Maki and C. T. Gott, *J. Chem. Phys.*, **36**, 2282 (1962).
13. M. A. Hanratty, M. Rösslein, and J. P. Maier, to be published.

SPECTRUM (310 TO 360 nm) AND IONIZATION POTENTIAL OF THE SILYL RADICAL

Russell D. Johnson III, Bilin P. Tsai†, Jeffrey W. Hudgens
Chemical Kinetics Division
National Institute of Standards and Technology
(formerly National Bureau of Standards)
Gaithersburg, Maryland 20899

ABSTRACT

The spectra of the silyl radical (SiH_3) and its perdeuterated analogue (SiD_3) have been observed by resonance enhanced multiphoton ionization spectroscopy. The spectra arise from two-photon excitation to the 5p, 6p and 7p Rydberg states. In the SiH_3 5p state a vibrational progression of the symmetric deformation mode ν_2 with spacings of ~825 cm^{-1} are observed. The vibrational spacings are 600-620 cm^{-1} for SiD_3. The observation of several Rydberg states allows a determination of the ionization potentials. They are 8.128 eV for SiD_3 and 8.135 eV for SiH_3.

INTRODUCTION

This paper continues our work on the silyl radical[1,2], extending the wavelength region investigated further to the blue, allowing the observation of more Rydberg states and from these a determination of the ionization potential. The optical spectra of silyl has only recently been observed[1], though attempts were made at least as early as the 1960's using flash photolysis[3]. The interest in the spectrum of the silyl radical comes from a desire to continue the homologous series which begins with the methyl radical and also to provide a laser-based diagnostic technique for monitoring silyl radicals.

The ionization potential of SiH_3 has been determined by a number of methods, including photoionization spectroscopy[4,5], and reactive ion beam scattering[6]. The two photoionization measurements produce conflicting ionization potentials of 8.14 ± 0.01 eV and 8.01 ± 0.02 eV respectively. The ion beam scattering produces a value of 8.11 ± 0.07 eV. By extrapolating a Rydberg series we should be able to determine the ionization potential to an order of magnitude better precision than previously determined.

† On sabbatical from the University of Minnesota, Duluth.

EXPERIMENTAL METHODS

The apparatus has been previously described[7]. Briefly, it consists of a flow reactor in which Cl or F atoms react with silane (SiH_4 or SiD_4) to produce SiH_3 (SiD_3) radicals. A portion of the flow reactor effluent leaks through a skimmer and into the ion optics of a time-of-flight mass spectrometer. The SiH_3 radicals are ionized by the focused light from an excimer-laser-pumped tunable dye laser. The ions were extracted into the time-of-flight mass spectrometer and the mass resolved m/z 31 or 34 (corresponding to SiH_3 or SiD_3) ion currents were recorded. The vacuum chamber which enclosed the mass spectrometer was operated at a pressure of $\sim 10^{-5}$ torr. Based upon our calculations, which conservatively assume 100% conversion of SiH_4 into SiH_3, we can detect concentrations as low as 10^9 radicals/cm^3 in the ionization region of the mass spectrometer with a single laser shot.

RESULTS AND DISCUSSION

Vibronic progressions are observed from 310 to 430 nm (which corresponds to a two-photon energy range of 64000 cm^{-1} to 47000 cm^{-1}). In SiH_3 we observe bands from the 4p and 5p Rydberg states. In SiD_3 we observe bands from the 4p, 5p, 6p, and 7p Rydberg states. SiD_3 gives stronger signal for the higher Rydberg states than SiH_3. The stronger signal from the deuterated species has also been observed in the spectra of the methyl radical[8]. The origins and vibrational spacings are listed in Table I. The origins of the SiD_3 5p, 6p, and 7p Rydberg states can be fit using the Rydberg formula:

$$h\nu = IP - \frac{R}{(n-\delta)^2}$$

Where $h\nu$ is the observed origin, IP is the ionization potential, R is the Rydberg constant (109 737 cm^{-1}), n is the principal quantum number, and δ is the quantum defect. Since the first member of a molecular Rydberg series is often perturbed from where it is expected based on the Rydberg formula the 4p state was not used for the determination of the IP. The energies of the 5p, 6p, and 7p origins can be fit using a quantum defect of 1.446 ± 0.002 and an ionization potential of 65560 ± 10 cm^{-1} (8.128 ± 0.001 eV). This ionization potential provides the 4p state with a quantum defect of 1.472. A slight increase in the quantum defect is expected for the lowest member of a Rydberg series. An increase of 0.02 to 0.05 has been observed for other systems, such as methyl[8] and flouromethyl[9] radicals.

TABLE I. Band origins and vibrational spacings for SiH_3 and SiD_3. The origins are ± 10 cm^{-1}.

State	SiH_4 Origin	SiH_4 ω_2	SiD_4 Origin	SiD_4 ω_2
$\tilde{X}\ ^2A_1$	0	725	0	541
$4p\ ^2A_2''$	48 438	800	48 388	588
$5p\ ^2A_2''$	56 925	822	56 874	607
$6p\ ^2A_2''$			60 267	613
$7p\ ^2A_2''$			62 002	615

This ionization potential is for the vibrational ground state of the SiD_3 ion and therefore includes zero point energy. To derive the ionization potential for SiH_3 the difference in zero point energies must be used. Assuming the zero point energies of the upper Rydberg states mimic the zero point energy of the ion the ionization potential for SiD_3 can be scaled by the shift of the 5p origin energies from SiD_3 to SiH_3 of 51 cm^{-1} (see Table I). A value of 8.135 eV is obtained for SiH_3.

Our measured IP can be compared with the photoelectron measurements. The photoelectron measurements are difficult to interpret because of the relatively small cross section for excitation to the vibrational ground state of the ion, and the interference from hot bands. Both of these problems make it difficult to determine which member of a progression is the origin and even whether the origin has been observed. In contrast we can distinguish hot bands by their smaller energy spacings (ω'=820 cm^{-1}, ω''=725 cm^{-1}) because our measurements are more precise (± 0.001 eV vs ± 0.01 eV or ± 10 cm^{-1} vs ± 100 cm^{-1}. We also observe the spectra of the perdeuterated silyl radical, and the vibrational progressions of the same state of the two different species must converge to the same origin. We have confirmed the 5p origin by observing it in both SiH_3 and SiD_3. Thus the recommended values for the ionization potentials are SiH_3 : 8.135 eV and SiD_3 : 8.125 eV.

ACKNOWLEDGMENT

Dr. Bilin P. Tsai thanks the University of Minnesota for support through the Bush Sabbatical Program.

REFERENCES

1) R. D. Johnson III, J. W. Hudgens
Chem. Phys. Lett. **141**, 163, (1987).
2) R. D. Johnson III, B. P. Tsai, J. W. Hudgens
Advances in Laser Science-III.
3) G. Herzberg, R. D. Verma
Can. J. Phys. **42**, 395, (1964).
4) J. M. Dyke, N. Jonathan, A. Morris, A. Ridha, and M. J. Winter
Chem. Phys. **81**, 481, (1983).
5) J. Berkowitz, J. P. Greene, H. Cho, B. Ruscic
J. Chem. Phys. **86**, 1235, (1987).
6) B. H. Boo and P. B. Armentrout
J. Am. Chem. Soc. **109**, 3549, (1987).
7) R. D. Johnson III, B. P. Tsai, J. W. Hudgens
J. Chem. Phys. **89**, 4558, (1988).
8) J. W. Hudgens, T. G. DiGiuseppe, M. C. Lin
J. Chem. Phys. **79**, 571, (1983).
9) J. W. Hudgens, C. S. Dulcey, G. R. Long, D. J. Bogan,
J. Chem. Phys. **87**, 4546, (1987).

AROMATIC MOLECULAR CLUSTERS AND THEIR PREDISSOCIATION DYNAMICS STUDIED BY PICOSECOND TIME-RESOLVED FLUORESCENCE SPECTROSCOPY

A.J. Kaziska, S.A. Wittmeyer, M.I. Shchuka, A.L. Motyka and M.R. Topp

Department of Chemistry, University of Pennsylvania,
Philadelphia, PA 19104-6323

ABSTRACT

One-photon resonant, two-photon ionization experiments are capable of determining the masses of simple molecular complexes, provided that the system has low internal energy. Yet, where larger amounts of internal energy are involved, so that cluster fragmentation can take place, the route by which a system arrives at ionized photofragments is often not clear. In view of the lack of experimental information, the current work has used time-resolved fluorescence spectroscopy to determine the vibrational predissociation dynamics of *neutral* complexes of the aromatic species perylene. The results show clearly that simple argon complexes, for internal energies <2x the binding energy, generally predissociate on a nanosecond time scale. On the contrary, methane complexes involving similar amounts of internal energy are found to undergo predissociation in the picosecond domain, as a result of efficient internal coupling of vibrational energy.

INTRODUCTION

The binding energies of 1:1 van der Waals complexes of Ar and CH_4 with perylene in the S_1 electronic state have been estimated using atom-atom pair potential techniques to be 610 cm^{-1} and ≈900 cm^{-1}, respectively. These estimates have been confirmed by fluorescence spectroscopy following the excitation of complexes into different vibronic levels. Yet the main object of interest in such studies is not so much the binding energy, but the *rate* of predissociation, since this provides a very straightforward case for unimolecular reaction dynamical analysis. One complication of such an approach using molecular S_1 states is that, although the experimental technique is far simpler than a ground state study, competition exists in the excited state between different relaxation channels. In particular, the role of nonradiative coupling to the triplet manifold must be considered.

EXPERIMENTAL

The experimental technique involved irradiation of a jet-cooled sample with the output from a mode-locked, frequency-doubled dye laser, cavity-dumped at 3.8 MHz. A proximity-focused microchannel-plate photomultiplier tube was used as a detector, behind a single 0.25 meter monochromator. This gave <50 cm^{-1} spectral resolution – sufficient to resolve resonances due to the complexes from those of free perylene. The overall time resolution of the apparatus using time-correlated

single-photon counting electronics was 160 ps, limited by photon transit-time dispersion in the monochromator.

RESULTS

Fluorescence spectra for 1:1 complexes of perylene are shown in Fig. 1. First, the onset of predissociation is revealed at 705 cm^{-1} and 900 cm^{-1}, for the Ar and CH_4 complexes, respectively. Yet, more importantly, we observe that the Ar complexes, even slightly above the predissociation energy, still give rise to a substantial amount of "resonance" emission identifiable with the optically prepared "zero-order" vibronic state 353^2. On the other hand, the CH_4 data at 705 cm^{-1}, now below the predissociation threshold, show little evidence of a resonant component, indicating extensive vibrational level mixing. At 900 cm^{-1}, this "hot" emission from the complex is completely replaced by a simple spectrum characteristic of "cold", free perylene generated by ultrafast predissociation.

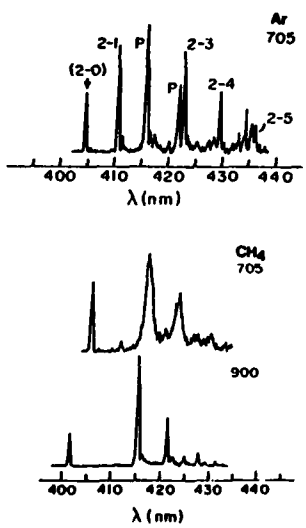

Fig. 1: Emission profiles following the excitation of perylene 1:1 complexes with Ar at 705 cm^{-1} vibrational energy (353^2; top), and with CH_4 at 705 cm^{-1} (middle) and 900 cm^{-1} (353^1550^1; lower). In the top spectrum, the numbers indicate a resonant progression in 353cm^{-1}; P indicates free perylene liberated by predissociation. The Ar data show a substantially mixed spectrum due to weak internal coupling, while the CH_4 data reveal strong coupling and rapid predissociation.

The time profiles for the growth and decay of free perylene following excitation at 705 cm^{-1} and 900 cm^{-1} of the 1:1 complex with argon are compared in Fig. 2 (top) and 2 (middle). As can be seen, the increased internal energy causes a decrease in the rise time of the fragment signal, from 2.02 to 1.09 ns, according to a single-exponential fit. Yet analysis of the fluorescence spectra (time-integrated) recorded for these two excitation conditions shows that the actual *predissociation* lifetime (i.e. k_{VP}^{-1}) decreases about an order of magnitude over this ≈200 cm^{-1} range. The difference is that singlet-triplet coupling accounts for most of the rate constant

measured following 705 cm^{-1} excitation, and that the value k_{VP}^{-1} is >10 ns.

Data presented in Fig. 2 (lower) show the CH_4/perylene 1:1 complex to fragment on a picosecond time scale for an internal energy of 900 cm^{-1}. The difference in behavior may be inferred from Fig. 1, which shows that the CH_4 complex exhibits substantial vibrational coupling below the predissociation threshold (i.e. 705 cm^{-1}), while the argon complex predissociates with little evidence of other internal coupling of the vibrational energy.

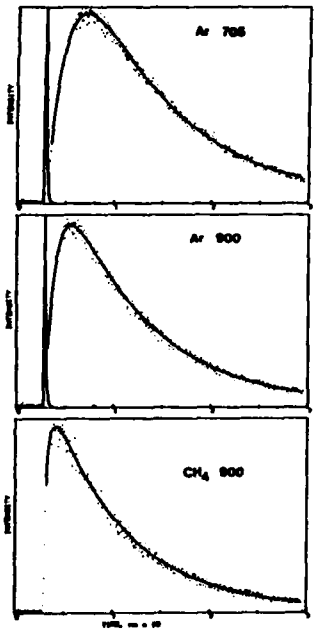

Fig. 2: Sequence of time profiles for fluorescence of free perylene liberated by excitation of 1:1 argon: 705 cm^{-1} (top), 900 cm^{-1} (middle), and by excitation of 1:1 methane complexes at 900 cm^{-1} (lower). The molecular complexes exhibit substantially faster predissociation due to more effective internal coupling.

Related experiments have shown the complex involving an argon dimer adsorbed onto perylene to undergo substantially more rapid predissociation at 705 cm^{-1} than the 1:1 complex, the photofragments exhibiting a rise time of 630 ps. In this case, more than 80% of the complexes are found to cross to the triplet manifold before predissociation can take place on the singlet surface. This behavior, and the increased predissociation rate, can be attributed to more effective internal coupling due to the presence of low-frequency modes generated by formation of the adsorbed dimer species. By contrast, we note that the fluorescence quantum efficiency associated with predissociation of the CH_4 complex is about 100%. In this case, vibrational coupling within the singlet state is sufficiently extensive, and the "relaxation" dynamics sufficiently fast that the triplet state is largely irrelevant to the predissociation dynamics of methane complexes.

High-order harmonic generation by hydrogenic ions

C. W. Clark, L. Pan,† and K. T. Taylor £

National Institute of Standards and Technology, Gaithersburg MD 20899
† also *Institute for Physical Science and Technology, University of Maryland, College Park MD 20742*
£ *Royal Holloway and Bedford New College, Egham, Surrey TW20 0EX, England*

Harmonic generation in gases is among the most widely studied processes in nonlinear optics,[1] but until recently most work in the field has been concerned with processes of the lowest orders of nonlinearity, i.e. 3rd and 5th harmonic generation, at intensities below ~ 10^{12} W cm^{-2}. In such cases there has been little reason to doubt that the nonlinear response of the atom to the driving radiation field is given correctly by lowest-order perturbation theory. Where it has been possible to carry out the appropriate atomic calculations with reasonable confidence (e.g. for alkali atoms[2]), lowest-order perturbation theory has been found to give satisfactory quantitative agreement with experiment.

In the past two years there have been several independent observations of generation of harmonics of much higher order in noble gases irradiated by intense picosecond pulses. McPherson et al.[3] have used a KrF driver (248 nm) at an intensity of $I_0 \sim 10^{16}$ W cm^{-2} to generate harmonic radiation of orders up to $n_{max} = 13$ in He and $n_{max} = 17$ in Ne. The Nd:YAG fundamental (1064 nm) at $I_0 \sim 10^{13}$ W cm^{-2} has been used by Ferray et al.[4] to produce harmonics of $n_{max} = 33$ in Ar, and of slightly lower values in other noble gases.

These studies are evidently in an early stage, since they have provided little quantitative information on the dependence of the harmonic yield upon driver frequency and intensity, and no absolute measurements of yields have been reported. However, one result appears to stand out clearly in both sets of data: *the harmonic yield does not exhibit a monotonic decrease with respect to order.* This is contrary to what one would expect from perturbation theory in the low-intensity limit, in which the radiated power of the nth harmonic should decrease as I_0^n. The observations instead exhibit a "plateau" region, typically for orders $n > 7$, where the yield fluctuates as the order increases. This phenomenon is generally not attributable to atomic multiphoton resonances.

Any statement about the conflict between the experimental results and the predictions of perturbation theory must be qualified by the recognition that, to date, no calculated values of atomic susceptibilities at such high orders of nonlinearity have been published in the open literature. We present here some initial results of such calculations, which have given nonlinear susceptibilities χ_n of hydrogenic ions, for $n \leq 99$ at selected frequencies (at least two other groups[5] are currently engaged in similar calculations). The key finding of our work is as follows. The χ_n are found to increase with n *more rapidly than a geometrical progression*, and in fact grow roughly as n! It follows that, for a given order n, there is a *critical driving intensity* $I_c(n)$ at which the radiated harmonic power increases indefinitely with order; or, correspondingly, that for a given I_0 there exists a *critical order* $n_c(I_0)$ beyond which the harmonic yield increases. For cases that seem comparable to those of the experiments, e.g. atomic hydrogen excited by Nd:YAG radiation, our calculated values of n_c are very close to the harmonic orders n_p that mark the onset

of the experimental plateau region (though it must be noted that the relationship between I_0 and n_p has not yet been established). The value of I_c establishes some sort of boundary on the range of applicability of lowest-order perturbation theory, since it indicates where higher-order processes become dominant; the values of I_c that are encountered in these examples are around $10^{13} - 10^{14}$ Wcm^{-2}.

Our computational method is fairly straightforward. We proceed from the standard expression (in atomic units) for the n^{th}-order frequency-dependent susceptibility $\chi_n(\omega)$ of an atom in an initial state g with energy ω_g:

$$\chi_n(\omega) = \sum_{k=1}^{n+1} \sum_{i_1, i_2, \ldots, i_n} \frac{d_{gi_1} d_{i_1 i_2} \cdots d_{i_{n-1} i_n} d_{i_n g}}{(\omega_{i_1 g} - s_{k1}\omega)(\omega_{i_2 g} - s_{k2}\omega) \cdots (\omega_{i_n g} - s_{kn}\omega)} , \qquad (1)$$

where the index k and integers s_{kj} characterize the possible sequences of virtual absorption of n photons of frequency ω; the inner sums run over all (discrete and continuum) atomic states i_m; and d_{im} is the dipole matrix element between states i and m and ω_{im} the difference of their energies. For example, the four sequences of absorption ($\uparrow$) of three photons @ ω and emission ($\Downarrow$) of one photon @ 3ω that contribute to $\chi_3(\omega)$ can be represented as follows, along with the associated matrix s_{kj} :

k = 1:	$\uparrow\uparrow\uparrow\Downarrow$	$s_{1j} =$	1	2	3
k = 2:	$\uparrow\uparrow\Downarrow\uparrow$	$s_{2j} =$	1	2	–1
k = 3:	$\uparrow\Downarrow\uparrow\uparrow$	$s_{3j} =$	1	–2	–1
k = 4:	$\Downarrow\uparrow\uparrow\uparrow$	$s_{4j} =$	–3	–2	–1

One can readily generalize this picture to higher order by regarding each $\omega_g + s_{kj}\,\omega$ as the energy of a virtual intermediate state.

Equation (1) is evaluated by expressing each sum over atomic states in terms of the solution ϕ_j in a hierarchy of inhomogeneous differential equations:

$$(H - \omega_g - s_{kj}\,\omega)\,\phi_j = d\,\phi_{j-1} , \qquad (2)$$

where H is the Hamiltonian of a hydrogenic ion, and $\phi_0 \equiv g \equiv$ the 1s state in cases presented here. The functions ϕ_j are expanded in products of spherical harmonics and Sturmian radial functions

$$S_{nl}^{(\zeta)}(r) = \sqrt{\frac{(n-l-1)!}{2(n+l)!}} (\zeta r)^{l+1} e^{-\zeta r/2} L_{n-l-1}^{(2l+1)}(\zeta r), \qquad (3)$$

which converts (2) to inhomogeneous linear equations.[6] The Sturmian functions possess several desirable features: they resemble hydrogenic radial functions, and thus can represent both long- and short-range behavior of the solutions efficiently; they constitute a complete denumerable basis, so that the contribution of the atomic continuum to the virtual states is fully included; and their matrix elements are sparse and simple, which greatly facilitates the solution of eq. (2) to high order. Computation of $\chi_n(\omega)$ for all $n < 100$ at one fixed value of ω takes about two hours of CYBER 205 CPU time, without extensive optimization of code. Our

use of Sturmian functions of real scale parameter ζ restricts our treatment to cases where no virtual state lies in the continuum, i.e. for which $n\omega + \omega_g < 0$.

We now discuss some main features of the results. Application of hydrogenic scaling of dipole moments and energies to eq. (1) shows that the susceptibilities $\chi_n(Z, \omega)$ of an ion of nuclear charge Z are related to those of hydrogen at a scaled frequency by $\chi_n(Z, \omega) = Z^{-(3n+1)}\chi_n(1, \omega Z^{-2})$. The variation of $\chi_n(\omega)$ in the discrete spectrum is dominated by the influence of $1s \rightarrow nl$ multiphoton resonances. Their effect is indicated most clearly by viewing χ_n as a function of $\nu = 1/\sqrt{1 - 2n\omega / Z^2}$, which is the *effective principal quantum number* of the highest virtual state attained in absorption: $-Z^2/2 + n\omega = -Z^2/2\nu^2 = \varepsilon$. This representation effects hydrogenic scaling of the frequency, and also exhibits the analytic structure of the susceptibility near the ionization threshold $\varepsilon \rightarrow 0$. Figure 1 displays a plot of this type for the third-order susceptibility of hydrogen. It can be shown[6,7] that as $\varepsilon \rightarrow 0$,

$$\chi_n(\omega) = a_n(\varepsilon) + b_n(\varepsilon)\cot(\pi\nu), \qquad (4)$$

where a_n and b_n are analytic functions of ε near $\varepsilon = 0$. The solid curve of Fig. 1 is a fit of the computed values of χ_3 to eq. (4), with a and b represented by quadratic functions. The parameters of this fit should enable one to determine χ_3 with good accuracy throughout the remainder of the discrete spectrum ($\nu \rightarrow \infty$). To the best of our knowledge, previous calculations[8] of $\chi_3(\omega)$ have not been carried beyond $\nu = 2$, nor has any systematic study of frequency dependence been done for higher orders of nonlinearity. Figure 2 provides an illustration of similar analytic structure in the 11th-order susceptibility. There, however, the energy dependence of the functions a and b is complicated by 9- and 10-photon resonances, which give poles at the energies indicated.

The variation of $\chi_n(\omega)$ with order n is entangled with the strong frequency dependence, but systematic behavior can be observed in regions far from resonances. We have undertaken calculations of $\chi_n(\omega)$ at low frequencies, e.g. CO_2 laser radiation, where more than 50 photons are required to hit the first resonance. Typical results are shown in Fig. 3, which depicts the example of hydrogen-like carbon, C^{5+}, excited by KrF radiation, and the corresponding scaled case of hydrogen excited at a wavelength of 36×248 nm = 8.928 μ. The first resonance in this case requires absorption of 74 photons. The use of ln(n!) as the abscissa reveals (clearly for H) the key result: $\chi_n(\omega) \sim n!$, where "~" includes some factor γ^n that reflects the choice of a system of units. This dismissive treatment of such a factor is motivated by the result, to follow below, that its presence does not affect the essential properties of the critical intensity $I_c(n)$. The susceptibilities of C^{5+} exhibit the influence of a factor $(1/216)^n$ deriving from hydrogenic scaling; thus $\chi_n(\omega)$ decreases rapidly at first, but the factorial growth

Fig. 1 (overleaf) Third-order susceptibility of the ground state of atomic hydrogen vs. effective principal quantum number ν of the highest virtual state. Crosses: computed values; solid line: fit of computed data to eq. (4), giving $a = -1324 + 26789\,\varepsilon - 234442\,\varepsilon^2$, $b = 3259 + 10751\,\varepsilon + 132908\,\varepsilon^2$. The susceptibility diverges at three-photon resonances, i.e. when ν is an integer. The upper limit $\nu = 11$ is arbitrary; the observed periodic structure persists as $\nu \rightarrow \infty$.

Fig. 2 (overleaf) Square of the 11th-order susceptibility of H 1s in the same representation as Fig. 1. The analogous periodic structure of 11-photon resonances is apparent, though it is complicated by intervening 9- and 10-photon resonances involving the states indicated.

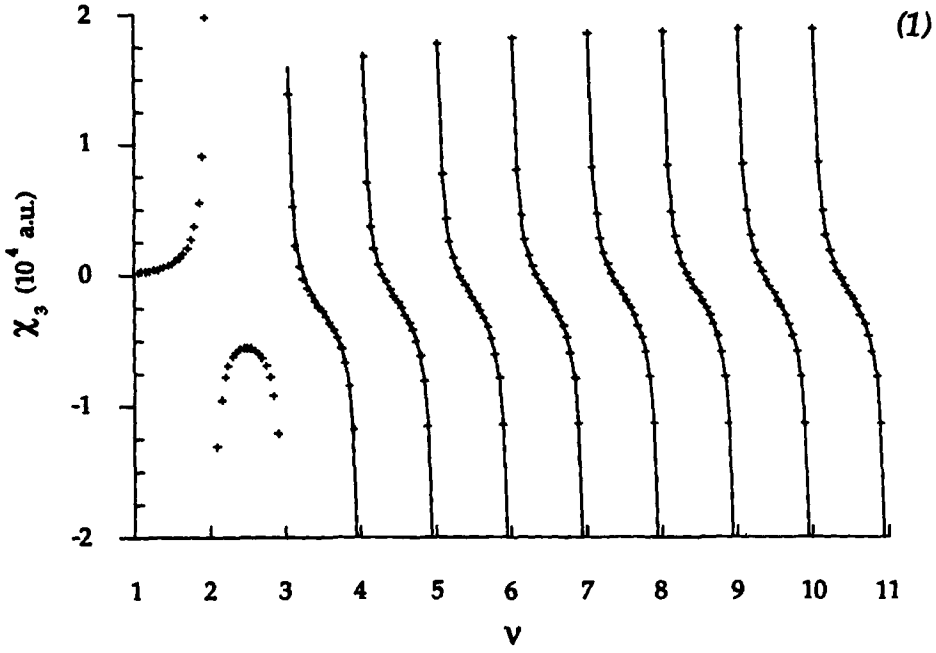
(1)
2
1
0
-1
-2
χ_3 (10^4 a.u.)
1 2 3 4 5 6 7 8 9 10 11
ν

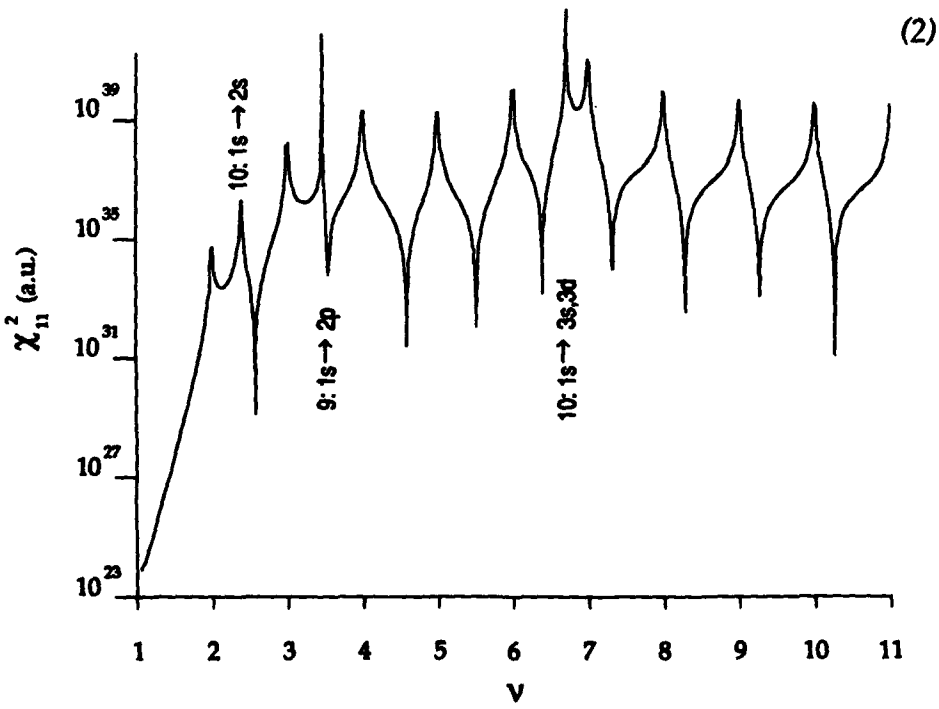
(2)
10^{39}
10^{35}
10^{31}
10^{27}
10^{23}
χ_{11}^2 (a.u.)
10: 1s → 2s
9: 1s → 2p
10: 1s → 3s,3d
1 2 3 4 5 6 7 8 9 10 11
ν

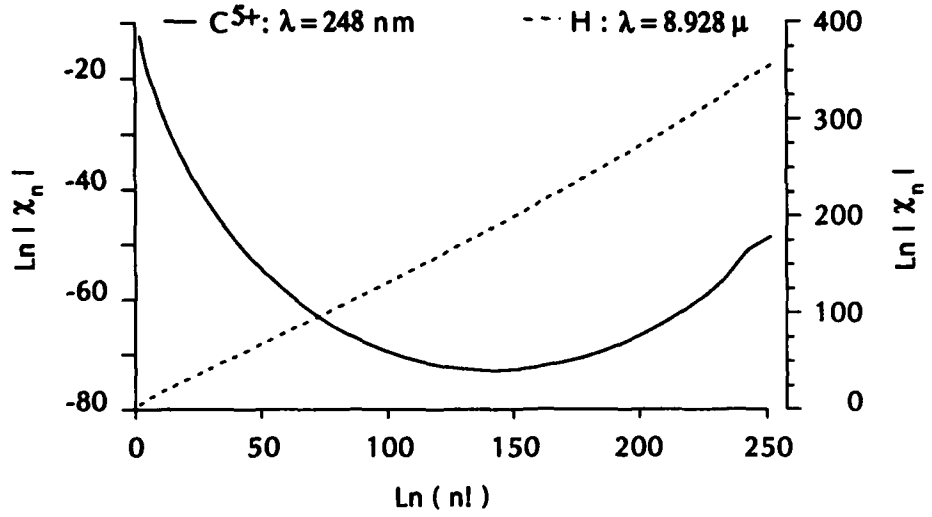

Fig. 3 Nonlinear susceptibilities for C^{5+} at the KrF wavelength, and the scaled result for H, as a function of ln (n!) where n is the harmonic order. This range corresponds to $3 \leq n \leq 73$. The first resonance occurs at n = 74, and 98 photons are required to ionize the atom.

Fig. 4 Critical intensity (eq. 5) for the case of H above, as a function of order.

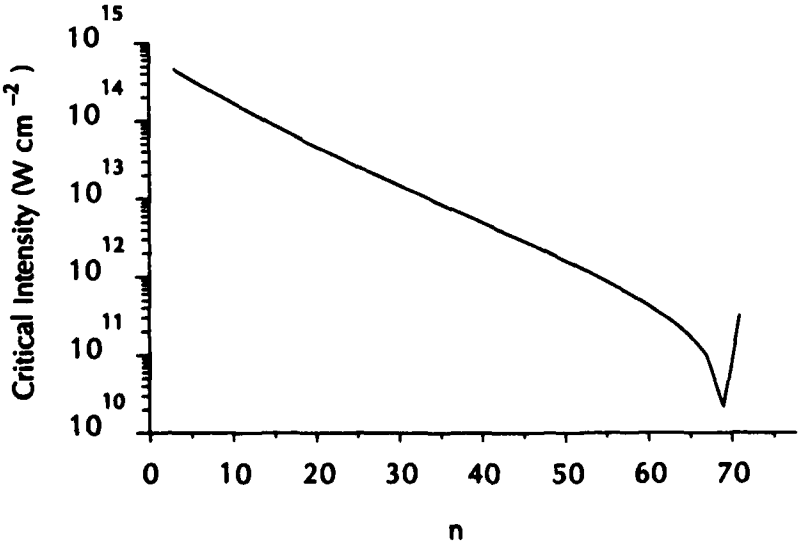

eventually dominates. Factorial divergence of this type also occurs in the Rayleigh-Schrödinger series for the energy of the hydrogen atom in a static electric field,[9] the expressions for which are similar to eq. (1) with $\omega = 0$. It is therefore not surprising that it appears in the low-frequency susceptibilities. It can also be obtained in a simple model evaluation of eq. (1) in which all energy denominators are replaced by an average value ω_a, and the sums over states are done by closure.

Now consider the critical driving intensity $I_c(n)$, defined as the intensity at which the radiated power in the n+2nd harmonic equals that of the n^{th}. If we suppose that effects of phase matching do not depend upon harmonic order, then[1]

$$I_c(n) = \frac{c}{2\pi}\frac{n}{n+2}\left|\frac{\chi_n}{\chi_{n+2}}\right| . \qquad (5)$$

The factorial growth of χ_n thus causes $I_c(n)$ to decrease indefinitely with increasing order. Figure 4 shows this behavior for the case of H in Fig. 3; the corresponding intensities for C^{5+} can be obtained by multiplying these values by $Z^6 = 46{,}656$. Lowest-order perturbation theory thus states that H irradiated by $I_c(3) = 5 \times 10^{14}\,\mathrm{Wcm^{-2}}$ of $\lambda \sim 10\ \mu$ radiation will produce harmonics of intensities that increase monotonically with order. The corresponding value for Nd:YAG radiation is about $2 \times 10^{14}\,\mathrm{Wcm^{-2}}$, and the critical intensities at 5th and 7th orders (the experimental plateau region for $I_0 \sim 10^{13}\,\mathrm{Wcm^{-2}}$) are respectively 4×10^{13} and $10^{12}\,\mathrm{Wcm^{-2}}$.

Lowest-order perturbation theory thus does not predict a monotonic decrease of harmonic yield with increasing order at presently attainable driving intensities. It is clear that the dominance of higher harmonics implies that *higher-order* processes in the generation of a given harmonic must also be taken into account. It is also probable that the factorial growth observed here ceases when the highest virtual state enters the continuum. These possibilities remain to be tested by comparison with nonperturbative results.

Support of our work by the U. S. Air Force Office of Scientific Research is gratefully acknowledged.

1. J. Reintjes, *Nonlinear Optical Parametric Processes in Liquids and Gases* (Academic Press, New York 1984)
2. R. E. Miles and S. E. Harris, IEEE J. Quant. Electronics QE-9, 470 (1973) and refs. therein.
3. A. McPherson, G. Gibson, H. Jara, U. Johann, T. S. Luk, I. A. McIntyre, K. Boyer, and C. K. Rhodes, J. Opt. Soc. Am. B 4, 595 (1987)
4. M. Ferray, A. L'Huillier, X. F. Li, L. A. Lompré, G. Mainfray, and C. Manus, J. Phys. B: At. Mol. Opt. Phys. 21, L31-L35 (1988)
5. A. F. Starace and B. Gao, private communication; R. M. Potvliege and R. Shakeshaft (to be published).
6. L. Pan, K. T. Taylor, and C. W. Clark, Phys. Rev. Lett. 61, 2673 (1988); and to be published.
7. a similar discussion of two-photon ionization has been given by M. G. J. Fink and P. Zoller (*Phys. Rev. A in the press*, 1989)
8. J. Mizuno, J. Phys. B: At. Mol. Phys. 5, 1149-1154 (1972); D. P. Shelton, Phys. Rev. A 36, 3032-3041 (1987), and refs. therein.
9. S. Graffi and V. Grecchi, Commun. Math. Phys. 62, 83 (1978)

DYNAMICS OF COUPLED SINGLE PARTICLE ELECTRON AND COLLECTIVE NUCLEAR MOTION IN A LASER FIELD

F. X. Hartmann*
Institute for Defense Analyses, Alexandria, Virginia, 22311
D. W. Noid
Oak Ridge National Laboratory, Oak Ridge, Tennessee, 37831
Y. Y. Sharon†
Princeton University, Princeton, New Jersey, 06540

ABSTRACT

A simple model of coupled electronic and collective nuclear motion is used to study energy transfer processes in the presence of a laser field. The complete classical Hamiltonian of the model includes nuclear, electronic and laser field terms. A semi-classical method (Ref. 1) to extract spectral information from the generated trajectories is used to calculate transition intensities and frequencies for the coupled quantum mechanical transitions. The nuclear term describes a deformed heavy nucleus with potential well parameters based on the recent work by Sharon and Naumann (Ref. 2); it sufficiently treats collective nuclear rotational motion lower in frequency than in the single particle nucleon model (Ref. 3). We report on the dynamics of this model in the presence of a laser field; a problem of interest in laser-driven nuclear excitation.

INTRODUCTION

Interactions between electronic transitions of an atom and nucleonic transitions of its nucleus are of interest in the excitation of nuclei from ground states to low-lying excited states or the excitation of short-lived states from long-lived isomeric states.

Part of the initial motivation for the recent work in this area by a number of groups evolves from interests in investigating the feasibility of making a laser based on nuclear transitions (Ref. 4). Even in the simplest picture, though, the required population inversions can hypothetically only be achieved in the one hour, or greater, lifetime (radiochemical) range whereas resonant absorption cross sections are generally significant only in the nanosecond to microsecond lifetime (Mossbauer) range (Ref. 5). Switching from a long-lived to short-lived state is one suggested idea but the current numbers show that the energy sources required to achieve this are very demanding and consequently are thus quite inconsistent with the critical requirements needed to observe even the Mossbauer effect (conditions for laser gain are listed in Ref. 6).

At the extrema of these two requirements we can consider two experimental possibilities of physical interest: first, in the radiochemical regime, experiments to investigate the transition from a long-lived state to a shorter-lived nuclear excited state signaled by the rapid emission of (non-stimulated) gamma-rays not attributable to the slower decay of the initial isomer or, second, in the Mossbauer range, experiments which study the excitation of small numbers of nuclei which undergo

enhanced decays (Ref. 7). In the latter, we currently suspect that the number of such participating nuclei will probably be quite small (Ref. 8). Acknowledging that many techniques exist for the excitation of nuclei, we restrict ourselves here to the general topic of excitation via electronic motions noting, as well, that photonuclear absorption can also lead to isomeric depopulation (Ref. 9).

Theoretical investigations of energy transfer to the nucleus by electronic motions in this context have been recently reported by a few researchers. In 1985, Baldwin, Biedenharn, Rinker, and Solem (Los Alamos, eg. Ref. 10), addressed the energy transfer problem by focusing on the laser-electron interaction with a perturbative approach (Ref. 11) to estimate nuclear excitation probabilities. Alternately, Noid, Hartmann and Koszykowski (Oak Ridge, Ref. 12) proposed a study of the coupled dynamics of the system in a semiclassical approach. Berger, Gogny, and Weiss (Livermore, Ref. 13) have examined the physics of laser-driven free classical electron motion with a perturbative approach to the nuclear matrix element.

In this brief report we describe a simple laser-electron-nucleon model where the nucleus has collective rotational dynamics. As noted previously, although the dynamics of energy transfer in coupled systems is of fundamental interest in making new laser materials (eg. Ref. 14), when applied to single-particle nucleon models the frequencies are simply much too high to be of practical importance. The collective nuclear term which we subsequently introduce here more closely characterizes many of the actual rotational nuclei and provides a significant improvement in studying energy transfer to the nucleus by laser driven electron motions at lower frequencies. This approach is one which solves Hamilton's dynamical equations of motion for the electron and nucleon from initial quantum conditions, and treats the laser field classically as an explicit function of time.

MODEL

A simple model of coupled electronic and nucleonic independent particle motion is used as a first step to study energy transfer processes in the presence of a laser field. The time dependent Hamiltonian, H(p,r,t) for the coupled system is:

$$H(p,r,t) = H_n(p_n,r_n) + H_e(p_e,r_e) + H_c(r_e,r_n) + H_{laser}(r_e,r_n,t) \quad (1)$$

where H_n is the nuclear term, H_e is the electronic term, H_c is the electron-nuclear coupling term, and H_{laser} is the time dependent laser term. The nuclear Hamiltonian describes the motion of a reduced mass μ in a potential well; it treats the case of a deformed rotating nucleus with a variable moment of inertia:

$$H_n(p_n,r_n) = \mu c^2\left[\left(\frac{p_n^2 + \mu^2c^2}{\mu^2c^2}\right)^{1/2} - 1\right] + \frac{\alpha}{2r_n^2} + \frac{\beta r_n^N}{N} \quad (2)$$

The parameters α, β and N are fitted to the rotational (L) energy level spacings:

$$E(L) = \left(\frac{1}{2} + \frac{1}{N}\right)\beta^{2/(N+2)}\left[\alpha + \left(L+\frac{1}{2}\right)^2\frac{h^2}{\mu}\right]^{N/(N+2)} \quad (3)$$

The remaining terms of the Hamiltonian are as described previously in Ref. 3. Briefly, the electron kinetic energy takes a form similar to that for the nuclear mass μ above and it moves in a Coulomb well associated with the stationary charge (Z-k) of the core nucleons. The coupling term is given by the Coulomb interaction between the moving charge k associated with the collective reduced mass μ and the electron. Finally, the laser term is given by the product of the total system dipole moment and the time dependent electric field.

The model thus described is comparable to that of Ref. (13) with the obvious distinction that we are proceeding in a semi-classical approach with its own advantages and limitations. The laser field essentially drives the motion of a single electron which transfers energy to the nucleus. Some differences are that the motion of the electron does not necessarily have to follow the laser field precisely as if it were free, thus the competition between the Coulomb well and the electric field strength can be explored--this is the feature we will highlight here.

RESULTS

In this model we have used the excited state spectrum of U-238 to fit our parameters because an investigation of a number of rotational heavy nuclei reveals some simplistic features for the ground state rotational band of this nucleus. We find $V(r_n) = (330\ \text{MeV-Fm}^2)/r_n^2 + (0.028\ \text{MeV/Fm}^2)r_n^2$ and use μ=26.2 in units of the proton rest mass. These parameters provide a simple model crudely characterizing a doubly-magic core with twenty neutrons and ten protons outside the closed shell; certainly meeting the requirements for collectivity, Ref. 15.

The units are summarized as follows. The frequency ω is in units of inverse time units, where one time unit is the time for light to travel one Fermi. The frequency is converted to energy units of MeV by multiplying by 197. The electric field (E) has units of $\text{MeV}^{1/2}\,\text{Fm}^{3/2}$. In these convenient units $e^2 = 1.44$ MeV·Fm and $e^2/2\pi hc$ is 1/137. Thus in atomic units $e/(a_0)^2 = 4.29 \times 10^{-10}\ \text{MeV}^{1/2}\,\text{Fm}^{3/2}$. We prefer to introduce the quantity E1 = eE, then power (watts/cm^2) is equal to $2.64 \times 10^{35}\,E1^2$ where E1 has units MeV/Fm. (A typical E1 is 10^{-10} MeV/Fm).

Classical trajectories in momentum and coordinate space are generated from the complete Hamiltonian using Hamilton's equations. The initial conditions for the trajectories are chosen from states of the separable Hamiltonian, that is, with the coupling term neglected and using a WKB approximation to find the outer turning points of the nuclear well. The outer turning points for the electron are given analytically by solution of the single particle relativistic Coulomb problem. We ignore screening thus the electron trajectories characterize energy transfer rates which can be compared to Ref. 13.

The semi-classical approach follows Ref. 12 and is described in greater detail in Ref. 1. The trajectories are used to calculate autocorrelation functions of the total system dipole moment. The absorption band shape (power spectrum) is given by the Fourier transform of the appropriate autocorrelation function. With the laser field off, the power spectrum is used to understand the basic dynamical frequencies. These calculations are carried out on a Cray computer at Oak Ridge. We integrate Hamilton's equations for an ensemble of 64 trajectories each with a different initial phase for the laser; evenly distributed over two pi radians. This phase ensemble conveniently exploits the vector capability of the computer.

We report initial results from a study of three regimes in the model: the low energy gamma-ray regime where we study the frequency and intensity behavior of the energy transfer at a coupled resonance; the x-ray regime where we illustrate the spatial dependence of the energy transfer as dependent on the orbital electron positions in the presence of the central Coulomb well; and finally, the high intensity optical photon regime where we illustrate, crudely, excitation probabilities of a typical low energy rotational transition. In this brief report we will limit ourselves to an illustration of results in the x-ray regime .

The laser is first scanned through a range of frequencies at a fixed high intensity for various electron shells. For each fixed frequency, the ensemble averaged nucleon energy, electron energy and total energy are computed as a function of time. This procedure allows us to map out interesting regimes where energy transfer is enhanced. In Fig. 1. we show the ensemble averaged energy transfer for the electronic energy change and the nuclear energy change with a laser in the x-ray regime at an intensity E1=1x10(-10) MeV/Fm. Various starting points for the electron trajectory (corresponding to the outer turning points associated with principle quantum number orbits in the relativistic single-electron Coulomb well for Z=92) are depicted. The energy transfer is expected to increase reaching a maximum at the K shell in a simple model where one treats the electron motions as free and following the laser field. Here, though, we find the competing Coulomb field counters the strong electric field and the shells with maximum transfer move out from the nuclear center. Using the energy transfer values and assuming the excitation is to the next higher nuclear quantum level one can estimate the time dependent excitation rate. At lower laser frequencies, thus far, we find photoionization of outer shell electrons occurs; with the inner shells behaving as in the x-ray regime. From these initial runs (which take much longer to compute) we deduce reasonable estimates for excitation probabilities.

CONCLUSION

We explore the application of a semi-classical dynamical approach to laser-electron-nuclear energy transfer where the collective features of a rotational nucleus are included. An illustration of the behavior of the model in the gamma-ray (at a K-resonance), in the x-ray (elaborated above) and initial results in the UV energy regimes were presented. This model, having some advantages in its simplicity, is useful in understanding the nature of energy transfer in non-radiatively coupled systems and should be readily adaptable to further refinements in modelling more complicated electron motions.

We gratefully acknowledge the support of the Dept. of Energy (Basic Energy Sciences), the National Science Foundation (YYS) and a Stockton Sabbatical and Distinguished Faculty Research Grant (YYS). We additionally thank K. K. Garcia for computer programming assistance.

* Work performed at Oak Ridge National Laboratory.

† Prof. Sharon is a Visiting Scientist in the Physics Dept. at Princeton; permanent address: Stockton State College, Pomona, NJ.

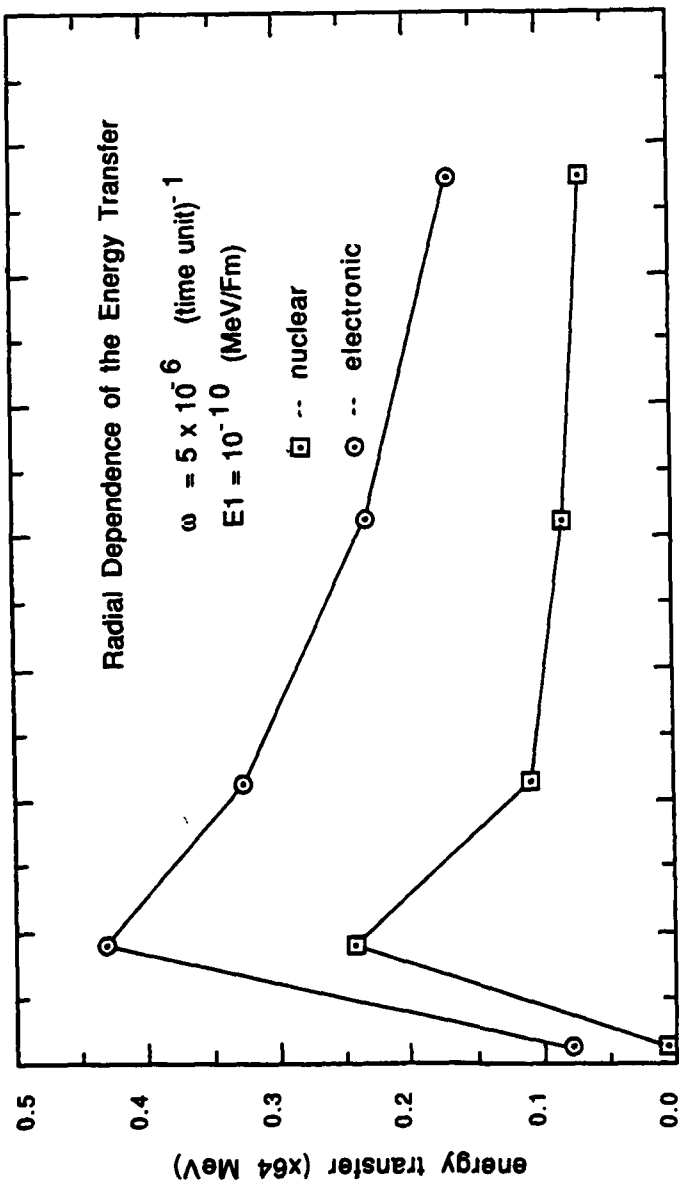

Figure 1. Averaged electron and nuclear energy transfer as a function of the initial single-particle orbital electron outer turning point radial distance in the presence of an x-ray laser field. One key feature is the drop in energy transfer at the K-shell due to the competing effects of the laser field strength and the Coulomb potential.

REFERENCES

1. D. W. Noid, M. L. Koszykowski and R. A. Marcus, J. Chem. Phys. 67 , 404 (1977).

2. Y. Y. Sharon and R. A. Naumann, Proc. of the Conf. on High Spin Nuclear Structure and Novel Nuclear Shapes, Argonne National Lab, Argonne, 1988 (in press).

3. F. X. Hartmann, K. K. Garcia, J. K. Munro, Jr. and D. W. Noid in Advances in Laser Science III, A. C. Tam, J. L. Gole and W. C. Stwalley eds., AIP Conference Proceedings 172, AIP, New York, NY (1988).

4. G. C. Baldwin, J. C. Solem and V. Goldanskii, Rev. Mod. Phys. 53, 687 (1981).

5. G. C. Baldwin, Physics Today, 33, February 1975.

6. G. C. Baldwin and M. S. Feld, J. Appl. Phys. 59 3665 (1986).

7. J. P. Hannon and G. T. Trammel, Phys. Rev. 169, 315 (1968), G. Faigel, D. P. Siddons, J. B. Hastings, P. E. Haustein, J. R. Grover, J. P. Remeika and A. S. Cooper, Phys. Rev. Lett. 58, 2699 (1987); U. van Burck, R. L. Mossbauer, E. Gerdau, R. Ruffer, R. Hollatz, G. V. Smirov and J. P. Hannon, Phys. Rev. Lett 59, 355 (1987).

8.F. X. Hartmann, S. R. Rotman and K. K. Garcia, Phys. Rev. Lett. 60, 2226 (1988)

9. C. B. Collins, C. D. Eberhard, J. W. Glesener and J. A. Anderson, Phys. Rev. C, May, 1988.

10. L. C. Biedenharn, K. Boyer and J. Solem, in Advances in Laser Science I, W. C. Stwalley and M. Lapp eds., AIP Conference Proc. No. 146, p. 50, AIP, New York, NY (1986).

11. G. A. Rinker, J. C. Solem and L. C. Biedenharn in Advances in Laser Science II , M. Lapp, W. C. Stwalley and G. A. Kenney-Wallace eds., AIP Conference Proceedings 160, p. 87, AIP, New York, NY (1987).

12. D. W. Noid, F. X. Hartmann and M. L. Koszykowski, in Advances in Laser Science II , M. Lapp, W. C. Stwalley and G. A. Kenney-Wallace eds., AIP Conference Proceedings 160, p. 69, AIP, New York, NY (1987).

13. J. F. Berger, D. Gogny and M. S. Weiss, J. Quant. Spect. and Rad. Transfer 40, Dec. 1988 (in press).

14. S. R. Rotman and F. X. Hartmann, Chem. Phys. Letts. 1988 (in press).

15. Y. Y. Sharon, Phys. Rev. C37, 1768 (1988).

SELF-FOCUSING OF VERY INTENSE CW LASER BEAMS IN SATURABLE ABSORBERS

J. Teichmann*, Y. Claude* and M. Burgess*, F.P. Mattar#,
J.P. Babuel-Peyrissac+; J.P. Marinier+ and C. Bardin+
Departement de Physique, Universite de Montreal*, Montreal, Canada
Department of Physics#, New York University, New York, NY 10003 and
Photonics Engineering#, Department of Electrical Engineering,
City College of New York, New York, NY 10031
Departement de Physico-Chimie, Centre d'Etudes,
Nucléaires de Saclay+, Gif/Yvette, France

ABSTRACT

Synthesis of analytical and numerical analyses is reported to describe the physical insights in the self-focusing of CW beams that are more intense than the saturation intensity in optically thick media. The saturable absorber clips the beam wings. It reduces the Gaussian profile into a parabolic one as exhibited by perturbation. Analytic description of free-space propagation of a parabolic beam has been obtained. Comparison between the simple physical picture and the rigorous computational approach is excellent.

I. EQUATIONS OF MOTION

The propagation of an intense CW Gaussian laser-beam in a two-level saturable absorber was rigorously and independently solved by LeBerre et al.[1-2] and Boshier et al.[3]. The first group analysis lead to the prediction of conical rings that were subsequently observed in sodium[4]. The second calculation[3] predicted a surprising on-resonance CW self-focusing. Its physical interpretation was pursued by two groups, the first one at Orsay[5] and the second one at Montreal[6-7].

In the CW regime the Maxwell-Bloch equations reduce to the nonlinear scalar field equation which reads as follows:

$$\frac{\partial \mathcal{E}}{\partial \eta} + ic_1 \nabla_T^2 \mathcal{E} = gP(\mathcal{E}) \quad (1) \quad , \quad P = r_2^2 W_0^0 \mathcal{E}(1 - ir_2^2\delta)/1 + r_2^2\delta^2 + r_1 r_2 |\mathcal{E}|^2 \quad (2)$$

with $\mathcal{E} = \frac{\mu}{\hbar} r_p E$ (3) the Rabi-frequency, r_1, r_2 the relaxation times, and W_0 the population difference $W_0 = \sigma_{22} - \sigma_{11}$ (4)

where $c_1 = \lambda \ell_0 / 4\pi r_p^2 = 1/4F$ (5), with F the Fresnel number

$g = 4\pi^2 \mu^2 r_p \ell_0 N / \lambda \hbar$ (6), the nonlinear gain

N = number of atoms/cm^3, δ the detuning, μ the dipole moment, λ the wavelength, and $\hbar$ the Plank constant

$\eta = \eta/\ell_0$ (7a), $\rho = r/r_p$ (7b), with ℓ_0, r_p the characteristic longitudinal & transverse lengths r_p the characteristic time

On resonance $\delta = 0$, $P(\mathcal{E})$ = reduces to $r_2 W_0 \mathcal{E}/1 + r_1 r_2 |\mathcal{E}|^2$ (8)

Initial condition in the $\eta = 0$ plane

$$\mathcal{E}(\eta 0, \rho) = \mathcal{E}_0 \exp(-\rho^2/a^2) \exp[-ik\rho^2/f_\ell] \quad (9) \text{ with } f_\ell \text{ a focal length, } a^2 = \log^2/2 \quad (10)$$

#Supported by ARO, AFSOR, ONR & NSF at NYU; CNRS at Orsay & CEA in Saclay

Two transverse phenomena are examined in our model. The first regime is described as the shell annular model. Its validity is predominant for large Fresnel numbers. Each shell experiences a radially dependent absorption/gain thus sees a distinct polarization. Every shell evolves independently as a uniform-plane-wave UPW propagation.

The second mechanism is the diffraction coupling that is predominant for small Fresnel numbers. Through the Laplacian, the different shells across the beam communicate with each other. A mutual influence on each other results through transverse energy flow across the beam leading to strong departure from the plane wave solution.

II. NONLINEAR ABSORPTION DOMINANT

Following LeBerre et al.[1,2] we consider diffraction as a perturbative process. Thus the field amplitude can be expanded in powers of the reciprocal of the Fresnel number $c_1 = 1/4F$ (11):

$$e(\eta,\rho) = \sum_{j=0}^{\infty} e_{2j}(\eta,\ell)c_1^{2j} + i \sum_{j=0}^{\infty} e_{2j+1}(\eta,\rho)c_1^{2j+1} \qquad (12)$$

the perturbative field is purely imaginary. The diffraction coupling leads to self-phase evolution.

Then we have for e_0 and e_1:

$$\frac{\partial e_0}{\partial \eta} = g r_2 W_0 \frac{e_0}{1+r_1 r_2 |e_0|^2} \quad (13), \qquad \frac{\partial e_1}{\partial \eta} - \nabla_T^2 e_0 = g r_2 W_0 \frac{e_1}{1+r_1 r_2 |e_1|^2} \quad (14)$$

The zeroth order i.e., the UPW solution e_0 was given by Icsevgi and Lamb[8]. The input beam consists of family of one-dimensional fields whose amplitude is radially dependent. Thus, the rate of growth of e_1 and its sign depends on the profile variation of e_0 whether it is Gaussian or superGaussian. From the properties of e_0, the growth of e_1 and of the associated self-phase modulation $\phi = \tan^{-1}[c_1 e_1/e_0]$ (15), and of the transverse energy-flow $J_T = |e_0|^2 \, \partial\phi/\partial\rho$ (16) are calculated. Figure 1 below illustrates a numerical computation for the functions e_0 and e_1, which elucidates the stripping phenomenon. This shows us that as far as we can consider the diffraction as perturbative, stripping will occur, i.e. the beam edges are more absorbed than the center, where the intensity is stronger. The Gaussian-beam whose wings have been clipped has reshaped approximately into a 'parabolic' beam. Thus, a z-dependent, soft aperture[5], is formed.

III. POST STRIPPING FREE SPACE PROPAGATION

We can expect that the stripping leads to an aperture formation, and then diffraction effects can no longer be considered as perturbative. In fact, they become predominant. The effect of the medium can now be neglected as discussed by LeBerre et al.[5] in their harsh aperture model. To emphasize this, we consider the free-space propagation of a 'parabolic' beam instead of a clipped Gaussian beam[9-10]; i.e., the equations are:

$$\frac{\partial e}{\partial \eta} + i c_1 \nabla_T^2 e = 0 \quad (17), \qquad c_1 = \frac{1}{4F} = \frac{\lambda \ell_0}{4\pi r_\rho^2} \quad (18)$$

$$e(\eta_0,\rho) = e_{0a}(1-\rho^2/a^2) \text{ if } \rho \le 1/a \quad (19a), \quad e(\eta_0,\rho) = 0 \text{ otherwise} \quad (19b)$$

This problem can be handled analytically[9], using Hankel transform, and we get:

$$e(\eta,\rho) = 2e_{0a}\int_0^\infty J_0(k\rho)J_2(k/a)\exp(ic_1k^2\eta)\frac{dk}{k} \tag{20}$$

and for $\rho = 0$

$$e(\eta,0) = 2e_{0a}\int_0^\infty J_2(k/a)\exp(ic_1k^2\eta)\frac{dk}{k} \tag{21}$$

Finally we can integrate and this leads:

$$e(\eta,0) = e_{0a}[1+4ic_1-4ic_1\exp(-i/4c_1)] \tag{22}$$

and:

$$|e(\eta,0)|^2 = e_{0a}^2\left[1+(2/f_d^2)(1-\cos f_d) - \frac{2}{f_d}\sin f_d\right] \tag{23}$$

where $f_d = \frac{\pi r_{max}^2}{\lambda\eta}$ (24), Fresnel number associated to the diaphragm aperature with $r_{max} = r_a/a$

Figure 2 presents the variation of the on-axis numerically computed energies versus η. In Fig. 3 we present the analytically attainable solution. We note that the analytical and numerical result qualitatively agrees. However, the analytical function which is continuous for $\eta = 0$, presents an infinity number of oscillations at the vicinity of $\eta = 0$. This results from the fact that the derivative of $e(\eta_0,\rho)$ is not continuous at the boundary for $\rho = 1/a$.

IV. ABSORPTION CONSIDERED AS PERTURBATIVE EFFECT

We observe in Fig. 4 below that the maximum of the on-axis intensity is similar when we neglect absorption, however this maximum is larger than when absorption is accounted for. Thus, after stripping has taken place, we treat absorption by perturbation[11] and express the solution as:

$$e(\eta,\rho) = \zeta_0(\eta,\rho) + g\zeta_1(\eta,\rho) + O(g^2) \tag{25}$$

where $\zeta_0(\eta,\rho)$ is the 'parabolic' solution corresponding to pure diffraction, previously described:

$$\zeta_0(\eta,\rho) = 2e_{0a}\int_0^\infty J_0(k\rho)J_2(k/a)\exp(ic_1k_\eta^2)\frac{dk}{k} \tag{26}$$

The system of equations for ζ_0 and ζ_1 is:

$$\frac{\partial\zeta_0}{\partial\eta} + ic_1\nabla_T^2\zeta_0 = 0 \quad (27a), \qquad \frac{\partial\zeta_1}{\partial\eta} + ic_1\nabla_T^2\zeta_1 = gP(\zeta_0) \quad (27b)$$

$$\text{with } P(\zeta_0) = r_2W_0\frac{\zeta_0}{1+r_1r_2|\zeta_0|^2} \tag{27c}$$

The integral representation of ζ_0 can be expanded in a series involving hypergeometric functions f that reduce to polynomials of m^{th} degree. We have

$$\zeta_0(\eta,\rho) = e_{0a}\sum_{m=0}^{\infty}\frac{(-1)^m}{(m+2)!}\left(\frac{i}{4a^2c_1\eta}\right)^{m+1}F(-m,-(m+2);1;a^2\rho^2) \tag{28}$$

V. SUMMARY OF THE PHYSICAL PICTURE

The on-resonance CW self-focusing is explained as a sequence of two processes: at first, absorption effects are predominant, this will cause a z-dependent "wings-stripping". During this evolution of a soft-aperturization diffraction can be treated as perturbative from the pure absorption solution of the Gaussian-beam. After stripping has taken place, diffraction becomes predominant, because of aperturization effects. This will cause an inward radial flux flow and an on-axis focusing. During this stage, absorption can be treated as perturbative, evolving from the free-space propagation of a parabolic beam. The validity of this physical model was ascertained by numerical computations and by two experimental observations in Na[12].

VI - PARAMETRIC DEPENDENCE

Using a self-consistent numerical algorithm implemented as LR1CCP® we have analyzed the range of physical domain. In particular we present three parametric studies: the first one with respect to the input beam Power $|E_0|^2$, the second with the Fresnel number varying while the third one with a different input spatial chirp.

In Fig. 5, a comparison of the longitudinal reshaping along η for different concentric cylindrical shells is shown. In graph a, we compare LR1CCP3,4,5. In graph b, we contrast the energy obtained from simulation LR1CCP9,10 & 11. In graph c, the distinct signature of calculations LR1CCP17,18,19 & 20 is presented.

In Fig. 6 we show the on-axis energy for a family of constant input power across the beam and variable on-axis value (Fig. 3) and variable on-axis power without necessitating that the total power be constant from one experiment to the other.

In Fig. 7, we display the on-axis energy versus η for different input beam widths. By modifying the diffraction coupling one affects the energy flux redistribution towards the beam center.

In Fig. 8 we report the influence of the input wavefront on the emergence of the CW self-focusing. Depending on the focal length of the lens at the input plane and its sign convergent or divergent phase compensation can be introduced. This in turn causes either an acceleration or a delay in the evolution of the self-focusing.

The role of incident detuning [13] is expected to play a significant role. The dispersion-induced phase associated with the detuning can compensate for or lead to a constructive interference with the diffraction-induced phase.

VII - CONCLUSION

We have reported the physical mechanisms that lead to on-resonant CW self-focusing in saturable absorbers.

REFERENCES

1. M. LeBerre et al., Phys. Rev. A25, 1604 (1982).
2. M. LeBerre et al., SPIE 369. 269 (1982).
3. M.G. Boshier and W.J. Sandle, Opt. Commun. 42, 371 (1982).
4. J. Teichmann and F.P. Mattar, Annual Meet. Canadian Assoc. Physicists & Astronomical Soc., Victoria, BC, Canada (June,1983).
5. M. LeBerre et al., in Coherence and Quantum Optics V, ed. L. Mandel and E. Wolf (Plenum, 1984) pp. 347-354.
6. M. LeBerre et al., in Coherence & Quantum Optics V, ed. L. Mandel & E. Wolf (Plenum,1984) pp.331-337; & Phys. Rev. A29,2669 (1984).
7. M. LeBerre et al., J. Opt. Soc. Am. B1, 591 (1984)
8. J. Teichmann et al., Opt. Commun. 54, 33 (1985).
9. A. Icevgi and W.E. Lamb, Jr., Phys. Rev. 185, 517 (1969).
10. J.P. Babuel-Peyrissac et al, SPIE 540, 569 (1985).

11. J. Teichmann et al., in Advances in Laser Science ILS-1, ed. W.C. Stwalley & M. Lapp, (AIP, 1986) pp. 320-323.
12. K. Tai et al., Opt. Lett. 9, 243 (1984).
13. M. LeBerre et al., J. Opt. Soc. Am. B2, 956 (1985).

FIGURE CAPTIONS

Fig. 1 A perturbational description of the imaginary component of a resonant uniform-phase Gaussian input field is evolving due to transverse coupling.

Fig. 2 A numerically computed on-axis energy is plotted versus η with diffraction rigorously accounted for.

Fig. 3 An analytically computed on-axis energy is plotted versus η.

Fig. 4 We compare the on-axis energy plotted versus η for the rigorous numerical calculation with the approximate analytical description of the field. The analytical calculation emulate the physics by describing the problem first as a perturbational treatment of diffraction with the saturable nonlinearity considered followed by a free-space propagation of a parabolic beam. The parabolic beam results from the wings clipping of the Gaussian beam due to the saturable nonlinearity. A refinement of the analysis is realized by treating absorption as perturbation unto the free-space propagation of the parabolic beam.

Fig. 5 The longitudinal and transverse reshaping of the intense laser beam in a saturable absorber is shown for a family of simulations to describe the domain of physical dependence.

Fig. 6 The role of e_0, the incoming on-axis field strengths is presented. First a comparison of the on-axis energies with e_0 varying. The second plot displays the individual characteristic by presenting (a) the on-axis energies versus η while (b) displays the energies profile versus ρ for different η.

Fig. 7 The Fresnel dependance of the on-axis energy is displayed as a function of r_p^{-1}(TBRHO).

Fig. 8 The effect of either a positive or negative lens before the cell (FOCLEN) was computed. Two diagnostic functions are shown namely the on-axis energy and the effective Marburger's radius (RAYMAR) are presented versus η. Both negative, positive or a composite of the two curvatures has been calculated.

LRPERT SIMULATION NO. 21

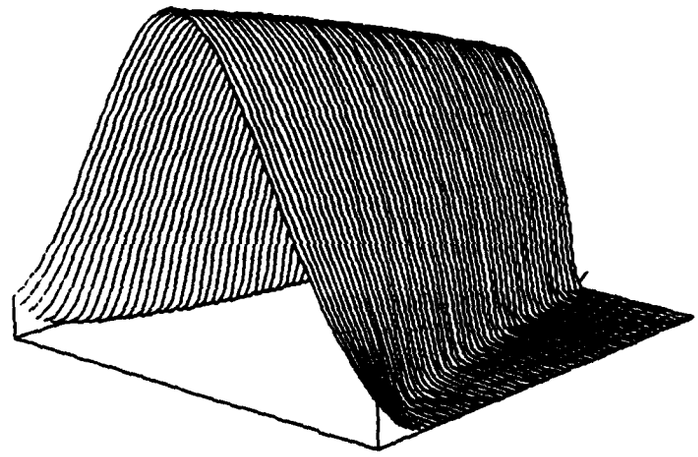

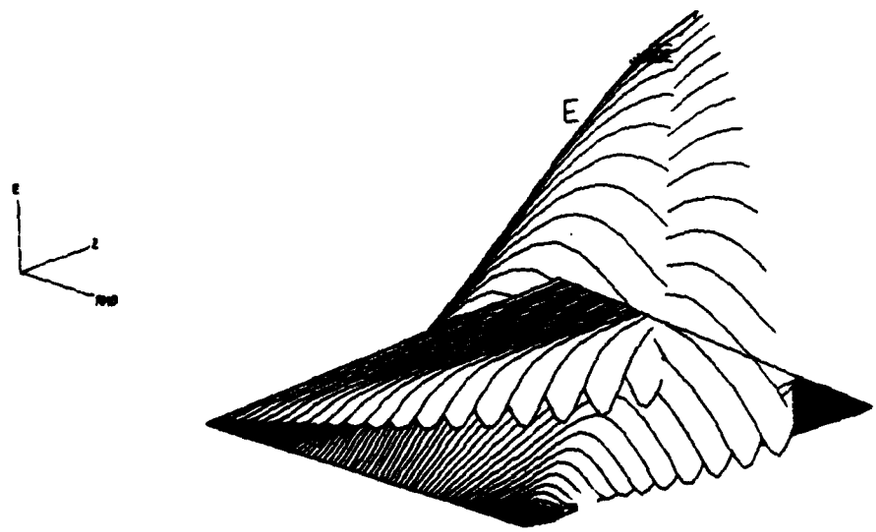

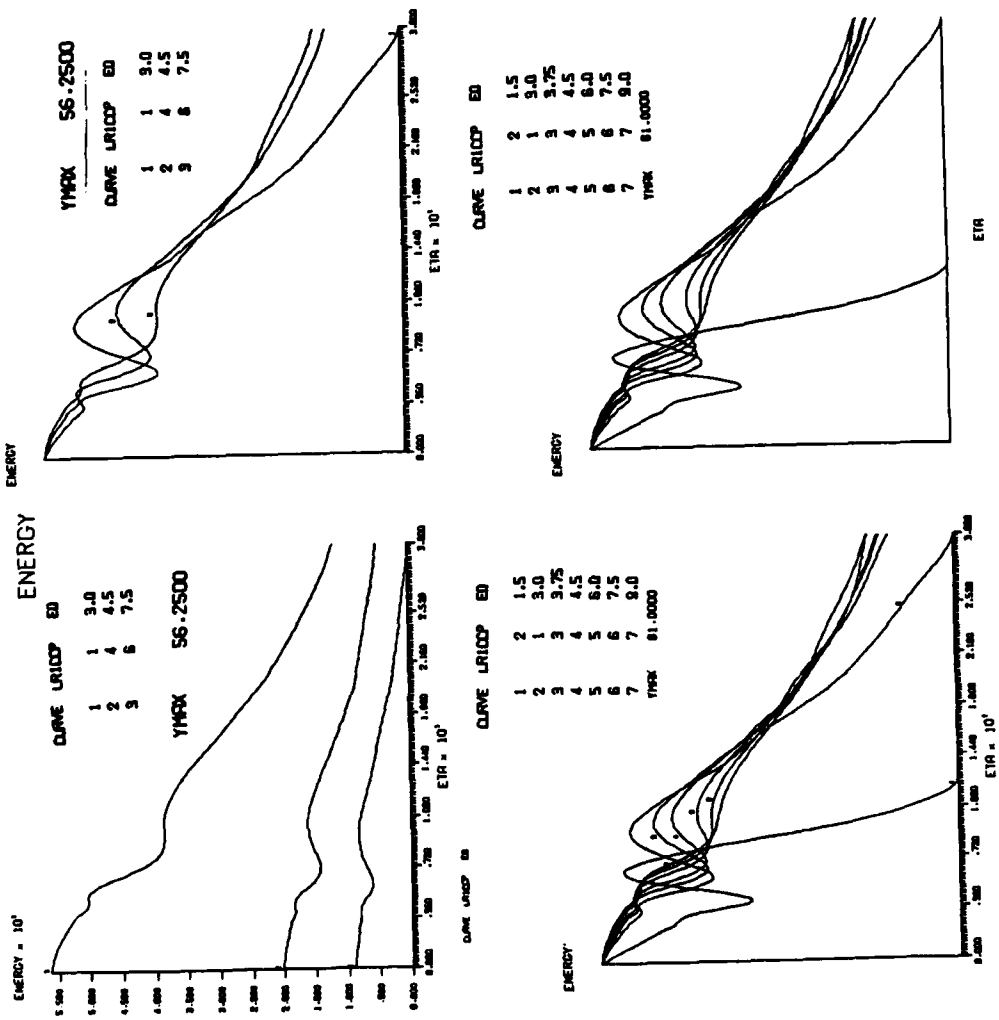
ENERGY
YMAX 56.2500
CURVE LRLOOP ED
1 1 3.0
2 4 4.5
3 6 7.5
ETA x 10¹
ENERGY x 10¹
YMAX 56.2500
CURVE LRLOOP ED
1 1 3.0
2 4 4.5
3 6 7.5
ETA x 10¹
ENERGY
CURVE LRLOOP ED
1 2 1.5
2 1 3.0
3 3 3.75
4 4 4.5
5 5 6.0
6 6 7.5
7 7 9.0
YMAX 81.0000
ETA x 10¹
ENERGY
CURVE LRLOOP ED
1 2 1.5
2 1 3.0
3 3 3.75
4 4 4.5
5 5 6.0
6 6 7.5
7 7 9.0
YMAX 81.0000
ETA

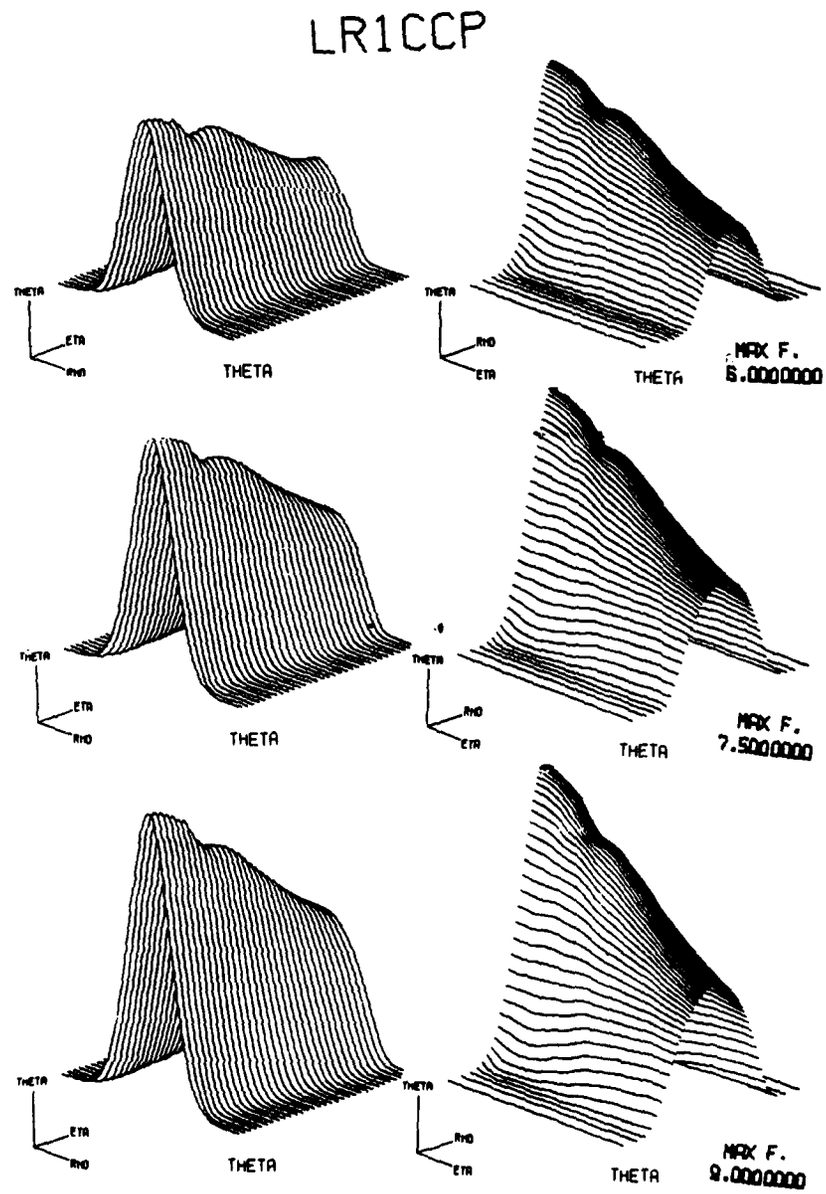

ROLE OF VARYING THE INPUT BEAM POWER/AREA ON THE CW SELF-FOCUSING IN SATURABLE ABSORBERS WHILE KEEPING THE DIFFRACTION LENGTH/FRESNEL NUMBER CONSTANT

NOTE THAT NO SCALING IN TRANSVERSE RESHAPING APPLIES.

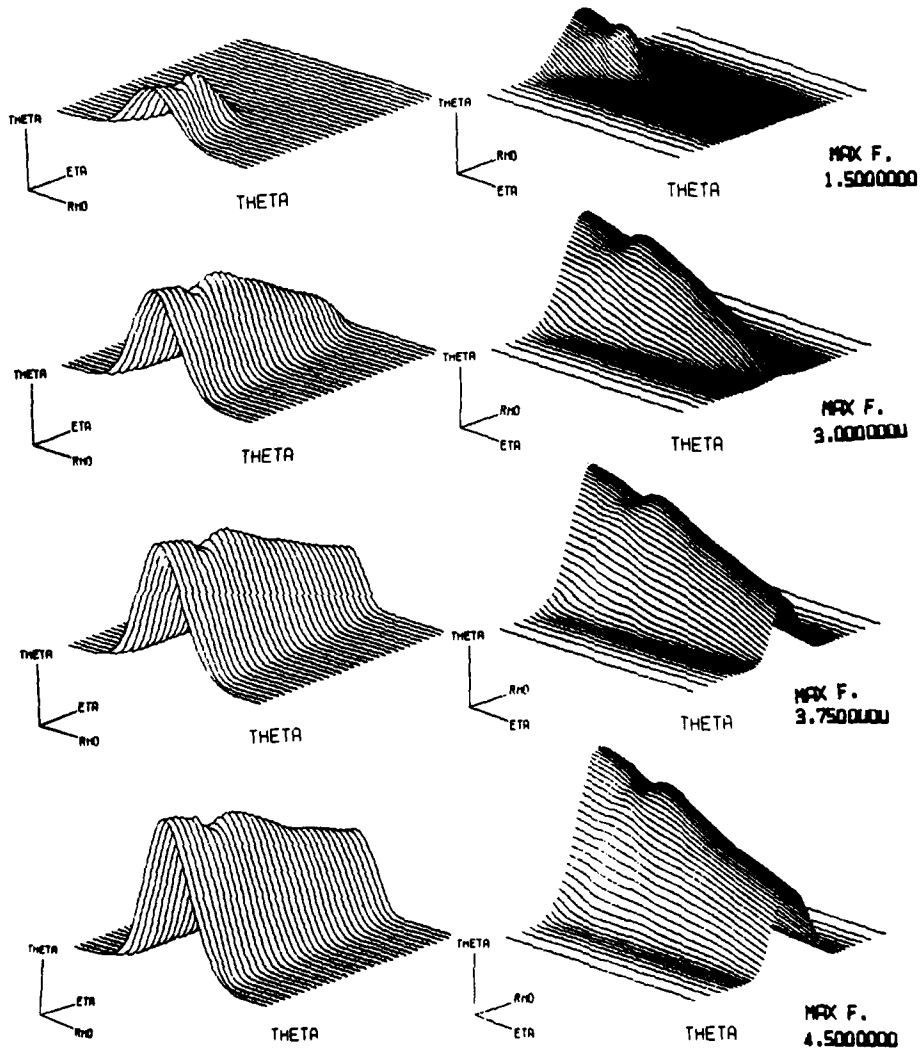

ROLE OF VARYING THE INPUT BEAM POWER/AREA ON THE CW SELF-FOCUSING IN SATURABLE ABSORBERS WHILE KEEPING THE DIFFRACTION LENGTH/FRESNEL NUMBER CONSTANT

NOTE THAT NO SCALING IN TRANSVERSE RESHAPING APPLIES.

LRICCP SIMULATION NO. 17

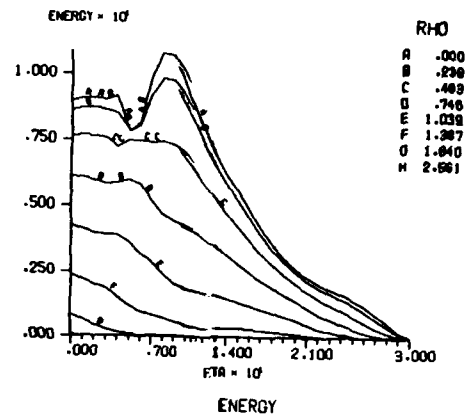

LRICCP SIMULATION NO. 18

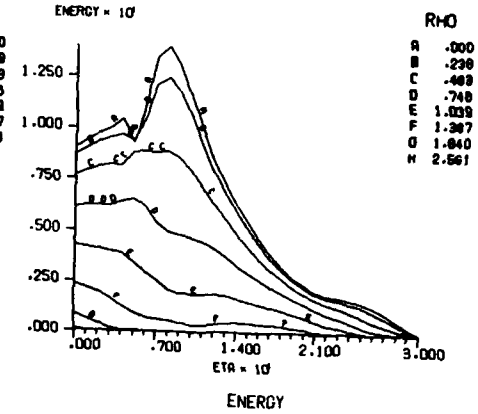

LRICCP SIMULATION NO. 19

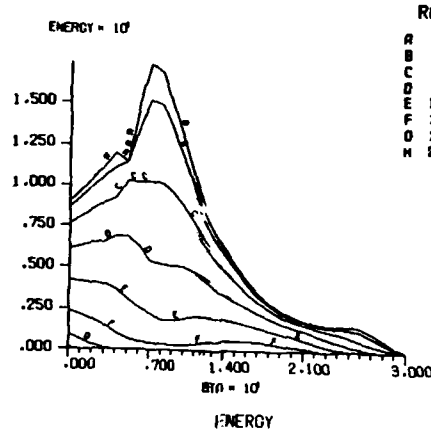

LRICCP SIMULATION NO. 20

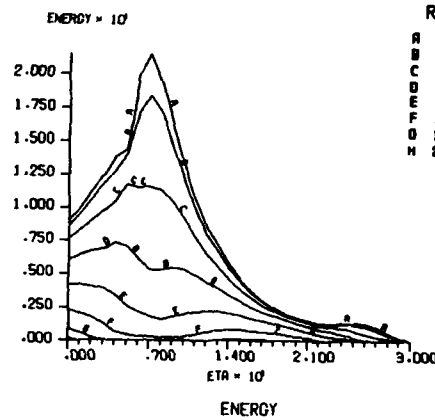

LRICCP SIMULATION NO. 3

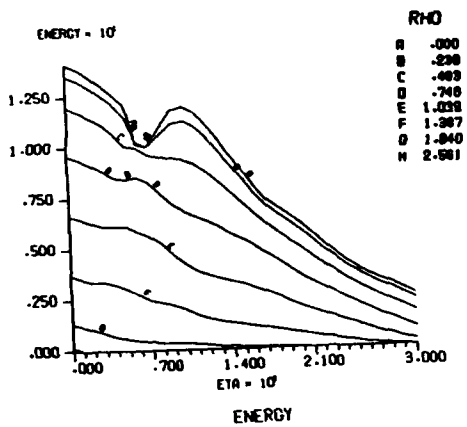

LRICCP SIMULATION NO. 4

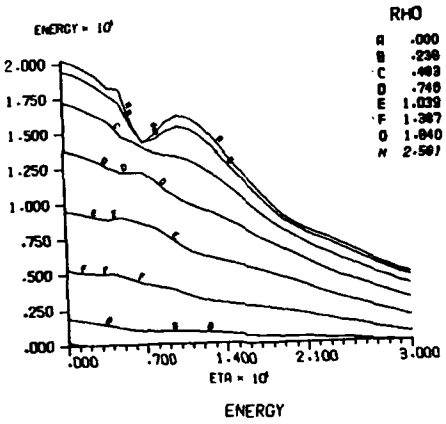

LRICCP SIMULATION NO. 5

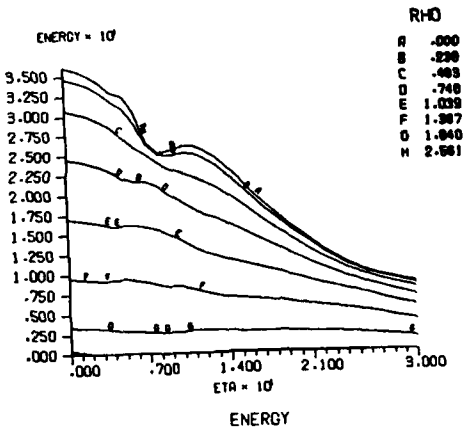

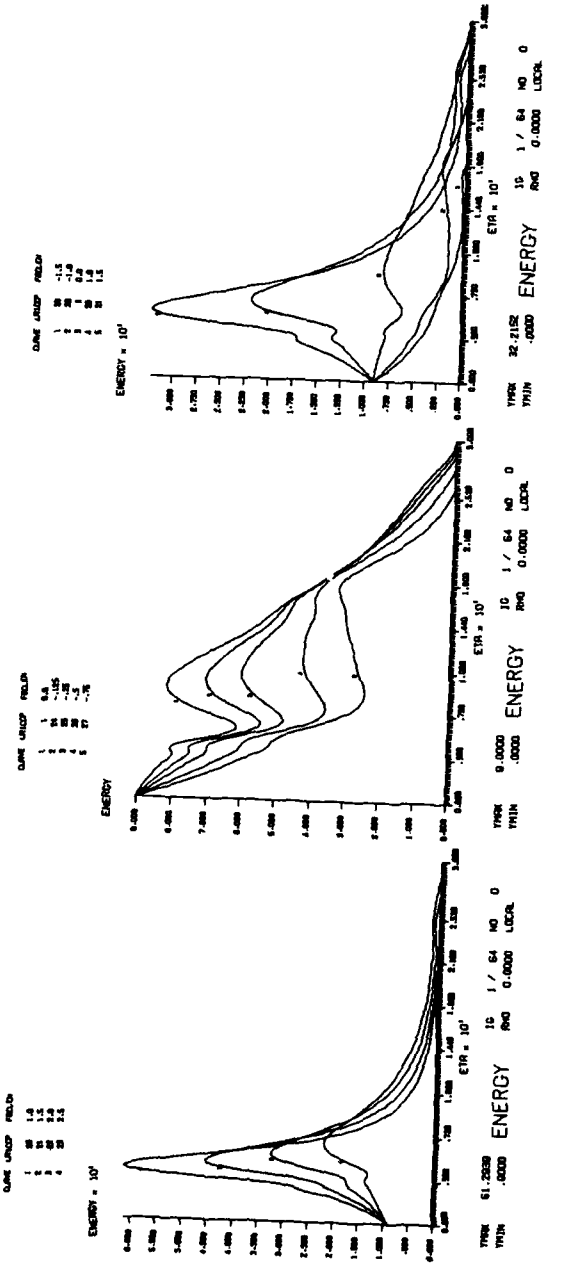
ENERGY
ENERGY
ENERGY

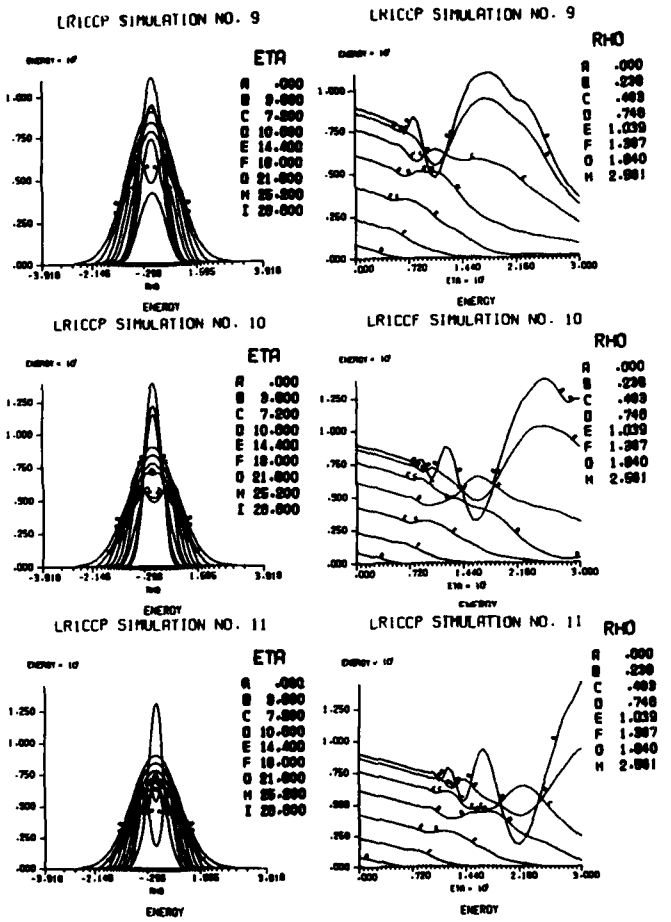
LRICCP SIMULATION NO. 9
ETA
A .000
B 3.600
C 7.200
D 10.800
E 14.400
F 18.000
G 21.600
H 25.200
I 28.800
ENERGY
LRICCP SIMULATION NO. 9
RHO
A .000
B .238
C .483
D .748
E 1.039
F 1.367
G 1.840
H 2.981
ENERGY
LRICCP SIMULATION NO. 10
ETA
A .000
B 3.600
C 7.200
D 10.800
E 14.400
F 18.000
G 21.600
H 25.200
I 28.800
ENERGY
LRICCF SIMULATION NO. 10
RHO
A .000
B .238
C .483
D .748
E 1.039
F 1.367
G 1.840
H 2.981
LRICCP SIMULATION NO. 11
ETA
A .000
B 3.600
C 7.200
D 10.800
E 14.400
F 18.000
G 21.600
H 25.200
I 28.800
ENERGY
LRICCP STMULATION NO. 11
RHO
A .000
B .238
C .483
D .748
E 1.039
F 1.367
G 1.840
H 2.981
ENERGY

CURVE	LRLOOP	FBCLEN
1	20	1.0
2	21	1.5
3	22	2.0
4	23	2.5

Fig 8

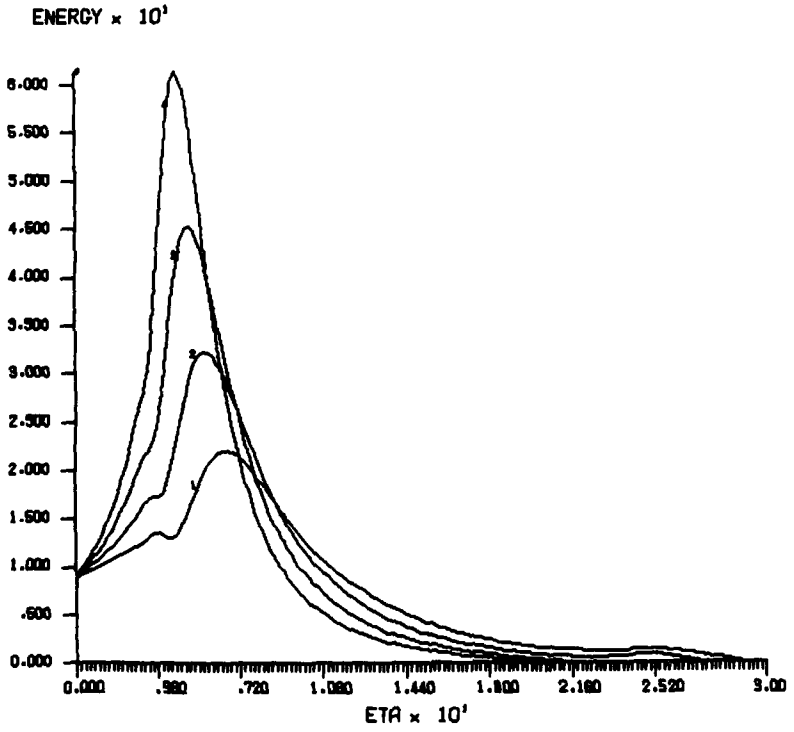

THE MOMENT THEORY FOR CROSS-COUPLING OF TWO INTENSE FIELDS THROUGH A KERR MEDIUM

J. Teichmann*, and F.P. Mattar**
Department de Physique*, Université de Montreal, Montreal, Canada and Physics Department**, New York University, New York and Electrical Engineering Department, City College of New York**, New York

ABSTRACT

We present a generalization of the Theory of Moments that characterize the nonlinear propagation from one beam to two beams. This was realized in order to verify the validity of a computational algorithm developed for pump-probe and Raman-Stokes dynamics. By reproducing the physics described analytically one develops confidence into the code. The average description of the transverse energy current distribution is calculated by determining its zero first and second moments at the input plane. The sum of the two beam widths satisfies a quadratic extension whose coefficients are these two moments.

I. INTRODUCTION

Following Vlasov et al.[1], Suydam[2], Lam and co-workers[3], Newstein and Ramakrishnan[4] and Mattar and Teichmann's[5] analysis for one beam we have determined using the moments of the transverse flux for two beams, at the input plane the form of the function itself. The knowledge of the moments provides an analytical formulism that verifies the validity of the numerical computation.

The calculation of the moments is based on the existence of two invariants, namely, the mass and the energy associated with the cubic nonlinear Schroedinger NLS equation. In nonlinear optics [6-10], the propagation of a CW beam in a medium whose refractive index n_2 is assumed proportional to the field intensity. The time variable in the NLS equation denotes the distance of propagation and r_T (x,y) the transverse beam coordinates. A catastrophic self-focusing singularity evolves. It corresponds to an extreme magnification of the field.

When Raman Amplification[11-14] is studied two NLS equations are required. The nonlinearity consists of two parts; the first one is a self-term while the second term refers to a cross-coupling. The latter is twice as large as the first one. The construction of the moment solution is extracted from the total or bi-chromatic Mass and total Energy expressions.

II. MOMENT THEORY

The propagation of two beams (or pulses) in nonlinear medium with cubic nonlinearity is described by the system of coupled equations:

$$-\frac{i}{2k}\nabla_T^2 E_{a,b} + \frac{\partial}{\partial z} E_{a,b} = \gamma_{a,b}(|E_{a,b}|^2 + 2|E_{b,a}|)E_{a,b}^2 \qquad (1)$$

where E_a, E_b are the complex electric field envelopes in the SVEA approximation for the beam a and the beam b respectively, ∇_T^2 is the transverse Laplacian, γ_a, γ_b are the corresponding gain.

The energy equation will read as follows:

$$\frac{\partial}{\partial z}|E_{a,b}|^2 + \frac{i}{2k}(E_{a,b}\nabla_T^2 E^*_{a,b} - E^*_{a,b}\nabla_T^2 E_{a,b}) = (\gamma_{a,b}+\gamma_{a,b})(|E^2_{a,b}|+2|E_{b,a}|^2)|E_{a,b}|^2 \qquad (2)$$

**Supported by ARO, AFOSR, ONR and NSF at NYU and NSERG at U. Montreal

The gain coefficients are assumed to be purely imaginary, $\gamma_j = i\bar{\gamma}_j$. We now define the transverse energy currents (j = a,b) as:

$$\underline{J}_{Tj} = -\frac{i}{2k}\,(E_j\,\nabla_T\,E_j^* - E_j^*\,\nabla_T\,E_j)\quad,\quad J_{\|j} = |E_j|^2\,. \tag{3}$$

Then Eq. (2) can be written as

$$\frac{\partial}{\partial z}\,(J_{\|a} + J_{\|b}) = -\,\nabla_T \cdot (\underline{J}_{Ta} + \underline{J}_{Tb}) \tag{4}$$

or, denoting

$$w = J_{\|a} + J_{\|b} \qquad \text{and} \qquad \underline{J}_T = \underline{J}_{Ta} + \underline{J}_{Tb} \tag{5}$$

$$\frac{\partial}{\partial z}\,w = -\,\nabla_T \cdot \underline{J}_T \tag{6}$$

The rate of change of the Energy depends on the net flux through an arbitrary surface.

Let us seek for a tensor $\underline{\underline{T}}$ which would verify the second moment equation, namely:

$$\frac{\partial}{\partial z}\,\underline{J}_T = \nabla_T \cdot \underline{\underline{T}} \tag{7}$$

where $\underline{\underline{T}} = (1/2k^2)\,[(\nabla_T E^*)(\nabla_T E)+(\nabla_T E)(\nabla_T E^*) - 1/2\,\nabla_T(\nabla_T|E|^2)]$

$$\frac{\partial}{\partial z}(\underline{J}_{aT}+\underline{J}_{bT}) = -\frac{i}{4k^2}\,[\nabla_T(\nabla_T^2(|E_a|^2+|E_b|^2)] - \frac{i}{2k^2}\,\nabla_T[(\nabla_i E_a)(\nabla_j E_a^*)+(\nabla_i E_a^*)(\nabla_j E_a)]$$

$$- \frac{i}{2k^2}\,\nabla_T[(\nabla_i E_b)(\nabla_j E_b^*) + (\nabla_i E_b^*)(\nabla_j E_b)] + \frac{\bar{\gamma}_a}{k^2}\,\nabla_T|E_a|^4 + \frac{\bar{\gamma}_b}{k^2}\,\nabla_T|E_b|^4$$

$$+ \frac{2}{k}\,(\bar{\gamma}_a|E_a|^2\nabla_T|E_b|^2 + \bar{\gamma}_b|E_b|^2\nabla_T|E_a|^2) \tag{8}$$

We observe, that the Eq. (7) can be satisfied if and only if $\bar{\gamma}_a = \bar{\gamma}_b$, for the tensor T_{ij} one has then ($\bar{\gamma} = \bar{\gamma}_a = \bar{\gamma}_b$):

$$T_{ij} = -\frac{i}{2k^2}\,((\nabla_i E_a)(\nabla_j E_a^*) + (\nabla_i E_a^*)(\nabla_j E_a) + (\nabla_i E_b)(\nabla_j E_b^*) + (\nabla_i E_b^*)(\nabla_j E_b))$$

$$+ \frac{i}{4k^2}(\nabla_T^2[|E_a|^2+|E_b|^2])\,\delta_{ij} + \frac{\bar{\gamma}}{2k}\,(|E_a|^4+|E_b|^4)\,\delta_{ij} + \frac{2\bar{\gamma}}{k}|E_a|^2|E_b|^2\delta_{ij} \tag{9}$$

The third moment equation should read

$$\frac{\partial}{\partial z}\,T_r\,\underline{\underline{T}} = -\,\nabla_T \cdot \underline{Q} \quad (10a) \qquad \frac{\partial}{\partial z}\sum_{\ell=1}^{3} T_{\ell\ell} = -\,\operatorname{div} Q \tag{10b}$$

To find the vector $\underline{Q}$ we first calculate the trace of the tensor T_{ij}.

$$T_r\,T_{ij} = \frac{i}{2k^2}\,((\nabla_T^2 E_a)E_a^* + (\nabla_T^2 E_a^*)E_a) + \frac{\bar{\gamma}}{k}\,|E_a|^4$$

$$+ \frac{i}{2k^2}\,((\nabla_T^2 E_b)E_b^* + (\nabla_T^2 E_b^*)E_b) + \frac{\bar{\gamma}}{k}\,|E_b|^4 + \frac{4\bar{\gamma}}{k}\,|E_a|^2|E_b|^2 \tag{11}$$

The first term:

$$\frac{\partial}{\partial z}\{\frac{i}{2k^2}[(\nabla_T^2 E_a)E_a^* + (\nabla_T^2 E_a^*)E_a] + \frac{\tilde{\gamma}}{k}|E_a|^4\}$$
$$- \frac{i}{4k^2}\{E_a^*\nabla_T^2(\nabla_T^2 E_a) - E_a\nabla_T^2(\nabla_T^2 E_a^*)\}$$
$$+ \frac{i\tilde{\gamma}}{2k^2}\{-[|E_a|^2 + 2(|E_b|^2]E_a^*(\nabla_T^2 E_a) + [|E_a|^2 + 2|E_b|^2]E_a(\nabla_T^2 E_a^*)$$
$$+ E_a^*\nabla_T^2[(|E_a|^2 + 2|E_b|^2)E_a] - E_a\nabla_T^2[(|E_a|^2 + 2|E_b|^2)E_a^*]\} \quad (12)$$

Using the identity:

$$E^*\nabla\cdot[(\nabla^2 E)] = \nabla\cdot[E^*\nabla(\nabla^2 E) + (\nabla E)(\nabla^2 E^*) - E\nabla(\nabla^2 E^*) - (\nabla E^*)(\nabla^2 E)] \quad (13)$$

and:

$$\nabla_T^2(|E_a|^2 E_a) = 2(\nabla_T E_a)\cdot(\nabla_T|E_a|^2) + E_a(\nabla_T^2|E_a|^2 + |E_a|^2(\nabla_T^2 E_a) \quad (14)$$

We have for the first term:

$$\frac{i}{4k^3}\nabla_T\cdot\{E_a^*\nabla_T(\nabla_T^2 E_a) + (\nabla_T E_a)(\nabla_T^2 E_a^*) - E_a\nabla_T(\nabla_T^2 E_a^*) - (\nabla_T E_a^*)(\nabla_T^2 E_a)\}$$
$$+ \frac{\tilde{\gamma}}{ik^2}\cdot\{|E_a|^2[E_a(\nabla_T E_a^*) - E_a^*(\nabla_T E_a)]\} + \frac{i\tilde{\gamma}}{k^2}\{[E_a^*(\nabla_T E_a) - E_a(\nabla_T E_a^*)]\cdot\nabla_T|E_b|^2\} \quad (15)$$

The second term is obtained by changing $a \to b$, $b \to a$.
The third term can be written as

$$\frac{2\tilde{\gamma}}{ik^2}\{|E_b|^2\nabla_T\cdot[E_a(\nabla_T E_a^*) - E_a^*(\nabla_T E_a)] + |E_a|^2\nabla_T\cdot[E_b(\nabla_T E_b^*) - E_b^*(\nabla_T E_b)]\} \quad (16)$$

We observe that all four terms with crossed terms for E_a and E_b can be combined to give

$$\frac{2\tilde{\gamma}}{ik^2}\{\nabla_T\cdot[|E_b|^2[E_a(\nabla_T E_a^*) - E_a^*(\nabla_T E_a)]] + \nabla_T\cdot[|E_a|^2[E_b(\nabla_T E_b^*) - E_b^*(\nabla_T E_b)]]\} \quad (17)$$

Finally

$$\frac{\partial}{\partial z}T_r T_{ij} = \frac{i}{4k^3}\nabla_T\cdot\{E_a^*\nabla_T(\nabla_T^2 E_a) + (\nabla_T E_a)(\nabla_T^2 E_a^*) - E_a\nabla_T(\nabla_T^2 E_a^*) - (\nabla_T E_a^*)(\nabla_T^2 E_a)\}$$
$$+ \frac{\tilde{\gamma}}{ik^2}\nabla_T\cdot\{|E_a|^2[E_a(\nabla_T E_a^*) - E_a^*(\nabla_T E_a)]\}$$
$$+ \frac{2\tilde{\gamma}}{ik^2}\nabla_T\cdot\{|E_b|^2[E_a(\nabla_T E_a^*) - E_a^*(\nabla_T E_a)]\}$$
$$+ \frac{i}{4k^3}\nabla_T\cdot\{E_b^*\nabla_T(\nabla_T^2 E_b) + (\nabla_T E_b)(\nabla_T^2 E_b^*) - E_b\nabla_T(\nabla_T^2 E_b^*) - (\nabla_T E_b^*)(\nabla_T^2 E_b)\}$$
$$+ \frac{\tilde{\gamma}}{ik^2}\nabla_T\cdot\{|E_b|^2[E_b(\nabla_T E_b^*) - E_b^*(\nabla_T E_b)]\}$$
$$+ \frac{2\tilde{\gamma}}{ik^2}\nabla_T\cdot\{|E_a|^2[E_b(\nabla_T E_b^*) - E_b^*(\nabla_T E_b)]\} \quad (18)$$

The vector $\underline{Q}$ is then defined as

$$\underline{Q} = \frac{i}{4k^3}\{E_a\nabla_T(\nabla_T^2 E_a^*) + (\nabla_T E_a^*)(\nabla_T^2 E_a) - E_a^*\nabla_T(\nabla_T^2 E_a) - (\nabla_T E_a)(\nabla_T^2 E_a^*)$$

$$+ E_b\nabla_T(\nabla_T^2 E_b^*) + (\nabla_T E_b^*)(\nabla_T^2 E_b) - E_b^*\nabla_T(\nabla_T^2 E_b) - (\nabla_T E_b)(\nabla_T^2 E_b^*)\}$$

$$+ i\frac{\gamma}{k^2}\{|E_a|^2[E_a(\nabla_T E_a^*) - E_a^*(\nabla_T E_a)] + |E_b|^2[E_b(\nabla_T E_b^*) - E_b^*(\nabla_T E_b)]\}$$

$$+ i\frac{2\gamma}{k^2}\{|E_b|^2[E_a(\nabla_T E_a^*) - E_a^*(\nabla_T E_a)] + |E_a|^2[E_b(\nabla_T E_b^*) - E_b^*(\nabla_T E_b)]\} \quad (19)$$

We can now define the moments, following Vlasov et al.[1]:

$$\bar{w} = \int_{\bar{v}} w\, d\bar{v} \quad (20), \qquad \underset{\sim}{R} = \frac{1}{\bar{w}}\int_{\bar{v}} \underset{\sim}{r}\, w d\bar{v} \quad (21), \qquad \bar{a}^2 = \frac{1}{\bar{w}_0}\int_{\bar{v}} r^2\, w d\bar{v} \quad (22)$$

The integrals are defined in the volume occupied by the fields, $\underset{\sim}{r}$ is the position vector. For the moments:

$$\frac{\partial}{\partial z}\bar{w} = 0 \quad (23), \qquad \frac{\partial^2}{\partial z^2}\underset{\sim}{R} = 0 \quad (24), \qquad \frac{\partial^3}{\partial z^3}(\bar{a}^2) = 0 \quad (25)$$

Assuming that $\underset{\sim}{n} \cdot \underset{\sim}{J}_T = 0$ (26), $\underset{\sim}{n} \cdot \underset{\sim}{Q} = 0$ (27) and $\underset{\sim}{n} \cdot \underset{\sim}{T} = 0$ (28) at the boundary of the volume V, $\underset{\sim}{n}$ being the normal vector to the boundary. Then

$$\hat{W} = \hat{W}_0 \quad (29), \qquad \underset{\sim}{R} = \underset{\sim}{R}_0 + \underset{\sim}{v}z \quad (30), \qquad (\bar{a}^2) = (\bar{a}_0)^2 + 2Bz + Cz^2 \quad (31)$$

Note that $\bar{w}_0$, $\underset{\sim}{R}_0$, $(\bar{a}_0)^2$, B and C are constants.

For the remaining quantities one has:

$$\underset{\sim}{v} = \frac{1}{\bar{w}_0}\int \underset{\sim}{J}_T d\bar{v}\Big|_{z=0} \quad (32), \qquad B = \frac{1}{\bar{w}_0}\int_v (\underset{\sim}{r}\cdot\underset{\sim}{J}_T) d\bar{v}\Big|_{z=0} \quad (33), \qquad C = -\frac{1}{\bar{w}_0}\int_v (T_r \underset{\sim}{T}) d\bar{v}\Big|_{z=0} \quad (34)$$

III. CONCLUSION

A simplified analytical solution was constructed in the CW regime to verify the validity of a finite difference scheme [15] developed to study co-propagation effects in optically thick media.

REFERENCES

1. S.N. Vlasov, V.A. Petrishchev & V.I. Talanov, Izvest. Vysshi. Ucheb. Zav. VUZ Radio fiz, 14, 1353 (1971).
2. B.R. Suydam, IEEE J. Quantum Electron. QE-10, 837 (1974) and QE-11, 225 (1975).
3. J.E. Lam, B. Lipman & F.D. Tappert, Phys. Fluids 20, 1179 (1977).
4. M.C. Newstein & D. Ramakrishnan, Tech. Rept. Polytechnic Institute of New York, POLY-MRI-1394-78 (1978).
5. F.P. Mattar & J. Teichmann, Comp. Phys. Commun. 22, 1 (1981).
6. G. Askary'yan, Sov. Phys. JETP 42, 1568 (1962), and Sov. Usp. Fiz. Nauk 111, 249 (1973).
7. P.L. Kelley, Phys. Rev. Lett. 15, 1005 (1965).
8. H.A. Haus, Appl. Phys. Lett. 8, 128 (1966); and Waves and Fields in Opto Electronics (Prentice Hall, 1984).
9. J.H. Marburger, Progress Quantum Electronics, Vol. V, ed. J.M. Sanders & S. Stenholm (Pergamon Press, 1975) pp. 35-110.
11. N.Bloembergen, Nonlinear Optics, 2nd Ed.(Benjamin/Cummings,1977).
12. Y.R. Shen, The Principles of Nonlinear Optics (Wiley, 1984).
13. G.I. Kachen, Jr. & W.H. Lowdermilk, J. Quantum Electron. QE-10, 746 (1974).
14. F.P. Mattar, Advances in Laser Sciences - II, ed. W.C. Stwalley & M. Lapp, (AIP, 1987) pp. 422-429.
15. F.P. Mattar, Appl. Phys. 17, 53 (1978).

LASER COOLING OF Mg AND Ca ATOMIC BEAMS

N. Beverini, E. Maccioni, D. Pereira, F. Strumia, G. Vissani,
Dipartimento di Fisica dell'Università di Pisa (CISM)
and INFN, Sezione di Pisa, P.Torricelli 2, 56126 Pisa , Italy

The extension of the laser cooling technique from Na and Cs to Ca and Mg is of great interest for time and frequency metrology [1]. The laser deceleration (cooling) can be achieved by irradiating a thermal Ca or Mg atomic beam with a counterpropagating laser beam in resonance with the $^1S_0$–$^1P_1$ transition at 422 nm and 285 nm, for Ca and Mg respectively. In particular, atoms with an initial velocity v_0 are stopped, in a laser field of constant intensity I, after a distance

$$L(S) = \frac{v_0^2 M \lambda \tau}{h}\left(1 + \frac{1}{2S}\right) \qquad (1)$$

where τ is the radiative lifetime of the upper $^1P_1$ level, λ the resonance wavelength, M the atom mass, and S=I/Is the saturation parameter. Only a small fraction of the atoms in the thermal velocity distribution can absorb the laser radiation when a monochromatic single-frequency laser beam is used. It consists of those atoms for which the laser frequency offset is compensated within the natural linewidth by the Doppler effect. As soon the deceleration process starts, the velocity is reduced, the atoms are Doppler shifted out of resonance, and absorption become negligible. The Zeeman tuning of the atomic absorption was used to overcome this difficulty by frequency shifting the atomic line with a magnetic field B(z) of appropriate intensity along the atomic beam axis [2]. This way a continuous beam of cooled atoms can be produced. For a linear Zeeman effect, as in Mg and Ca, and a constant laser intensity, the magnetic field intensity required to keep the atoms in resonance along the beam is

$$B(z) = B(0)\sqrt{1 - \frac{z}{L(S)}} \qquad (2)$$

In fact the above equation is just giving the minimum value of the field B(z) for any initial value B(0). Other field profiles are allowed but, since the acceleration has a finite value, there is also an upper limit on the field gradient, that must satisfy the boundary condition

$$\frac{dB}{dz} \le \frac{\dot{v}}{\mu \lambda v} \qquad (3)$$

where μ= 1.4 MHz/gauss for Mg and Ca. If the above constraint is not satisfied, the Zeeman frequency tuning is too fast for the cooling rate and the atoms are shifted out of resonance.

The experimental apparatus is shown in fig.1. A thermal beam of Mg or Ca atoms was produced from an effusive source at a temperature of about 760°K or 900°K respectively, and interacted with a counterpropagating laser beam, resonant with the $^1S_0$ - $^1P_1$ transition . A single frequency, CW laser beam was produced from a Coherent 699/21 ring dye laser with single mode TEM_{00} operation, and r.m.s. line width of ≈1 MHz . The modified velocity distribution was analyzed with a second laser beam scanning the frequency around the resonance line. It was also produced by a frequency stabilized dye laser, whose intensity was chopped at about 1 kHz in order

to discriminate, with a lock-in amplifier, against the stronger fluorescence signal from the cooling laser beam.

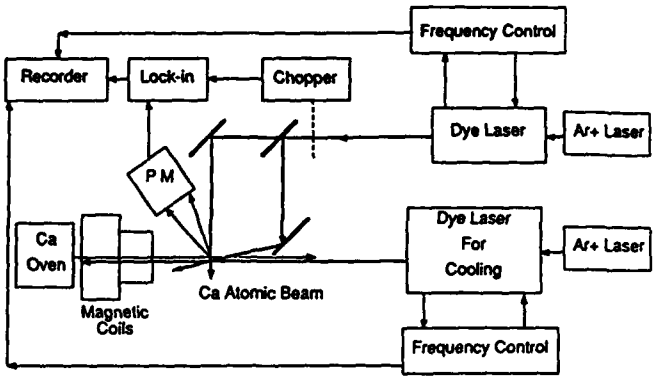

Fig. 1. Experimental apparatus

In the case of Mg the laser radiation at 285.2 nm was obtained by intracavity frequency doubling the radiation at 570.4 nm obtained from the Rhodamine 6G dye. Evidence of the deceleration of a Mg atomic beam was recently demonstrated [3] as shown in fig.2, where two identical scans of the analyzing laser are superimposed: the first in presence of the cooling laser beam of about 1mW, the second one without it.

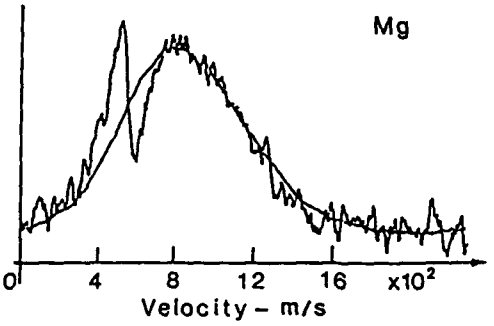

Fig.2

In the case of a Calcium the 422.6 nm laser beam was obtained by using Stilben 3 dye pumped with an UV Ar laser, and the available power was larger than 20 mW. However there is a further problem caused by the presence of a $^1D_2$ level at an energy lower than that of the $^1P_1$ level. It is then possible that the cooling cycle should be interrupted by the spontaneous emission from the $^1P_1$ towards the $^1D_2$ level, the corresponding atoms being lost because the lifetime of the $^1D_2$ level is much longer than the cooling process. A careful analysis of the available theoretical data shoved that the branching ratio between the two spontaneous transition could be large enough to not affect significantly the laser cooling[1]. In fact the experimental result shown in fig. 3 demonstrate an effective laser deceleration in presence of the Zeeman tuning.
The atoms of the original maxwellian distribution with a velocity lower than 750 m/s, are pushed by the laser radiation in a narrow velocity peak around 290 m/s. The axial

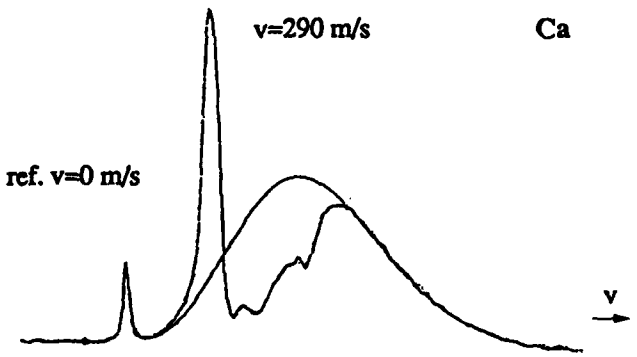

Fig. 3. Ca laser cooling observed in presence of magnetic field

magnetic field, whose intensity profile adequately fitted the theoretical requirements, was generated in the deceleration region by an ensemble of three solenoids and properly designed iron poles [1]. The magnetic field intensity B(z) decreased from its maximum to zero in about 25 cm, which was the maximum cooling length with the field on.
Ca atomic beams with a velocity as low as 10 m/s were observed corresponding to a thermal source of less than 1 K. by using different frequency settings of the cooling laser beam, in agreement with the predictions.as shown in fig.4.

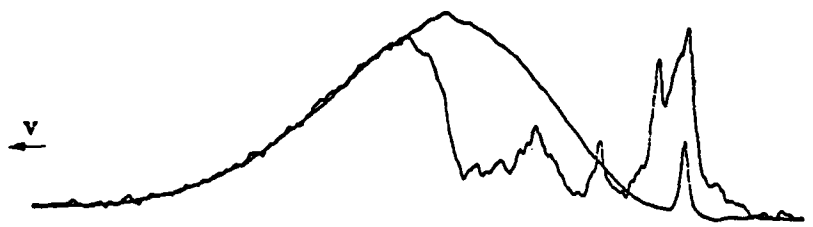

fig. 4. As in fig.3, but with a final velocity v=0±8 m/s

It is also worth to note that the velocity distributions shown in the figures where observed at a distance of about 20 cm from the decelerating magnet demonstrating that the diamagnetic properties of Mg and Ca ground state, differently from alkali atoms, make also easy the extraction from the deceleration region of low velocity atomic monochromatic beams.

1- F. Strumia ."Application of laser cooling to the atomic frequency standards".in " Laser science and technology " Eds. A.N.Chester and S.Martellucci ,(Plenum Press, November 1988).
2- W.D.Phillips, J.V.Prodan, H.J.Metcalf, A.Migdall,I.So,J.Dalibard : Phys. Rev. Lett., 54,992 (1985)
3- N. Beverini, S.De Pascalis, E. Maccioni, D. Pereira, F. Strumia,G. Vissani, Y.Z. Wang, C. Novero : in press
N. Beverini, E. Maccioni, D. Pereira, F. Strumia,G. Vissani : Proc.VI Symp. on Frequency Standards and Metrology, Springer Verlag 1988 , in press

Bound-Continuum Transitions in Diatomic Molecules*,†

William C. Stwalley
Center for Laser Science and Engineering
Department of Chemistry and
Department of Physics and Astronomy
University of Iowa, Iowa City, Iowa 52242

ABSTRACT

Bound-continuum radiative transitions in diatomic molecules are described with emphasis on comparison of theoretical calculations (with no adjustable parameters) with well-calibrated experimental results. The theoretical calculations are usually expressed in terms of Einstein A coefficients for spontaneous emission and B coefficients for stimulated emission and absorption and are based on reliable potential energy curves (e.g. RKR) and ab initio electric dipole transition moments. Examples will include Na_2 studies where laser-induced fluorescence, optical-optical double resonance, optically pumped laser and related laser spectroscopic studies have been carried out. Similar results exist for other alkali metal diatomics. Of particular interest are single electronic-vibrational-rotational emissions where rich oscillatory structure is observed and predicted.

I. Introduction

The absorption and emission of light by diatomic systems (bound molecules or colliding atoms) is now relatively well understood, with increasingly accurate prediction of such quantities from reliable empirically-based potential energy curves and reliable (typically ab initio) electric dipole transition moments. These predictions are absolute and involve no adjustable parameters. Especially for simple molecules such as the alkali metal diatomics ("visible hydrogen"), the comparison between theory and precise experiments is very good. Here, the principles of bound-bound transitions will be summarized in Section II. and extended in Section III. to the less-commonly discussed bound-free (continuum) transitions. For an excellent and more complete discussion, the review of Tellinghuisen[1] is highly recommended.

---

* Supported in part by the Air Force Office of Scientific Research and the National Science Foundation.

† Portions of the work reported here were carried out in collaboration with K. K. Verma, M. E. Koch, J. T. Bahns, A. R. Rajaei-Rizi, W. T. Zemke, G. Pichler, K. M. Sando, D. D. Konowalow, L. Li, R. W. Field, W. Müller, W. T. Luh, V. Zafiropulos, S. P. Heneghan, K. P. Chakravorty, A. M. Lyyra and P. D. Kleiber.

II. Bound-Bound Spectra

The absorption and emission process which might be considered for a simple molecule such as Na_2 are summarized in Table I (for simplicity, stimulated emissions are not explicitly listed; they correspond to adding a photon to both sides of each spontaneous emission equation). The emphasis here is on processes B. 1. and 2. in this section and the following section, respectively. However, very similar considerations apply to all 8 processes listed and all such radiative processes can be treated by similar techniques using reliable potential energy curves and electric dipole transition moments. Moreover, Na_2 will be used as the prime example in the following. References to these other processes and to other molecules may be found in Tellinghuisen's review[1].

Table I. Single photon absorption and spontaneous emission processes in Na_2 involving ground state atom or molecules.

A. Absorption		
1.	$Na_2 + h\nu \rightarrow Na_2^*$	bound-bound (ordinary)
2.	$Na_2 + h\nu \rightarrow Na^* + Na$	bound-free (photodissociation)
3.	$Na + Na + h\nu \rightarrow Na_2^*$	free-bound (photorecombination)
4.	$Na + Na + h\nu \rightarrow Na^* + Na$	free-free (line broadening)
B. Spontaneous Emission		
1.	$Na_2^* \rightarrow Na_2 + h\nu$	bound-bound (ordinary)
2.	$Na_2^* \rightarrow Na + Na + h\nu$	bound-free ("excimer")
3.	$Na + Na^* \rightarrow Na_2 + h\nu$	free-bound (photorecombination)
4.	$Na + Na^* \rightarrow Na + Na + h\nu$	free-free (line broadening)

The history of Na_2 molecular spectroscopy goes back to 1874[2] when the red-orange $A^1\Sigma_u^+ - X^1\Sigma_g^+$ and blue-green $B^1\Pi_u - X^1\Sigma_g^+$ absorption bands of Na_2 were observed (but not, of course, yet identified; for a bibliography of Na_2 spectroscopy, see reference 3). For

reference, selected relevant potential energy curves of Na_2 are summarized in Figure 1; see references 3 and 4 for the sources of these curves).

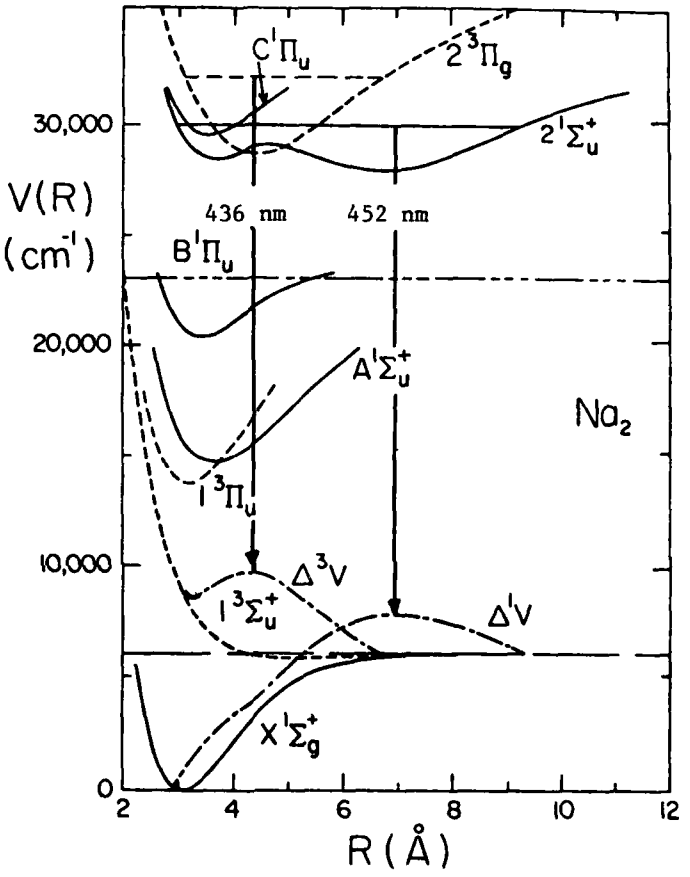

Figure 1. Selected low-lying empirically-based potential energy curves of Na_2. Also shown are the positions and Mulliken difference potentials for the "violet band" upper levels $2^1\Sigma_u^+$ ($v' = 41$, $J' = 60$) (Δ^1V) and $2^3\Pi_g$ ($v' = 44$, $J' = 12$) (Δ^3V), with "satellite" emissions (vertical arrows) peaking at 452 and 436 nm, respectively.

The procedures involved in analyzing bound-bound emission spectra, determining (or extending) potential energy curves (and estimating dissociation energies), calculating bound-bound radiative transition probabilities and radiative lifetimes, etc. (summarized in Table II) are nicely illustrated by the example (Figure 2) of the $A^1\Sigma_u^+$ ($v' = 34$, $J' = 50$) $\leftarrow$ $X^1\Sigma_g^+$ ($v'' = 3$, $J'' = 51$) transition of the Na_2 molecule excited by the 568.2 nm yellow line of the krypton ion laser[3].

In Figure 2, the spectral lines can readily be measured as to wavelength and the pairs of lines readily identified as P, R pairs for different v" values in the $X^1\Sigma_g^+$ state of Na_2. How can the various indicated quantum numbers v', v", and $J' = J'' \pm 1$ be identified? In this case[3], this is readily accomplished based on earlier work on the same A-X bands, e.g. Kusch and Hessel[5]. This tentative

Table II. Procedures involved in analysis of a bound-bound spontaneous emission spectrum (laser-induced fluorescence).

A.	Bound-bound spontaneous emission spectrum
	↓ measurement and v, J assignments
B.	Vibrational-rotational energy level spacings in lower electronic state
	↓ Rydberg-Klein-Rees (RKR) calculation
C.	Lower state potential energy curves
	↓ Schrödinger equation for radial nuclear motion
D.	Vibrational-rotational energies (check with B.) and wavefunctions
	↓ electric dipole transition moment matrix element
E.	Einstein A (and B) coefficients
	↓ summation over all lower levels
F.	Radiative lifetimes

assignment is very strongly confirmed by the intensity and other calculations discussed below. In general, however, it is relatively straightforward to obtain such quantum number assignments[6,7].

Given the assignments, the Rydberg-Klein-Rees (RKR) procedure (see e.g. references 8, 9, 10) can be used to calculate (semiclassically) the effective $X^1\Sigma_g^+$ potential energy ($U_J(R)$, here for J" = 50) between the inner and outer classical turning points of the v" = 56, J" = 50 level (R_{v-} = 2.2250 Å and R_{v+} = 8.6782 Å). The ordinary (J" = 0) potential energy curve (V(R)) can then be calculated by subtracting the centrifugal term ($\hbar^2 J(J+1)/2\mu R^2$) from the effective potential ($U_J(R)$). At internuclear distances outside the empirically-based 2.2250-8.6782 Å region, one must extrapolate the potential (or interpolate to the dissociation region if the dissociation energy and long-range forces are known (see e.g. reference 11)). Often ab initio calculations provide a useful basis for extrapolation, as in this $X^1\Sigma_g^+$ case[3]. The resulting "hybrid" potential is then defined at all internuclear distances, but the energy levels for v" ≤ 56 depend primarily on the interior (RKR) region and only slightly on the exterior regions of extrapolation. This is also confirmed by the comparisons of theory and experiment given below. It might be noted that in lighter molecules, e.g. LiH, the semiclassical RKR approximation involves errors ≳ 1 cm^{-1}, so an inverse

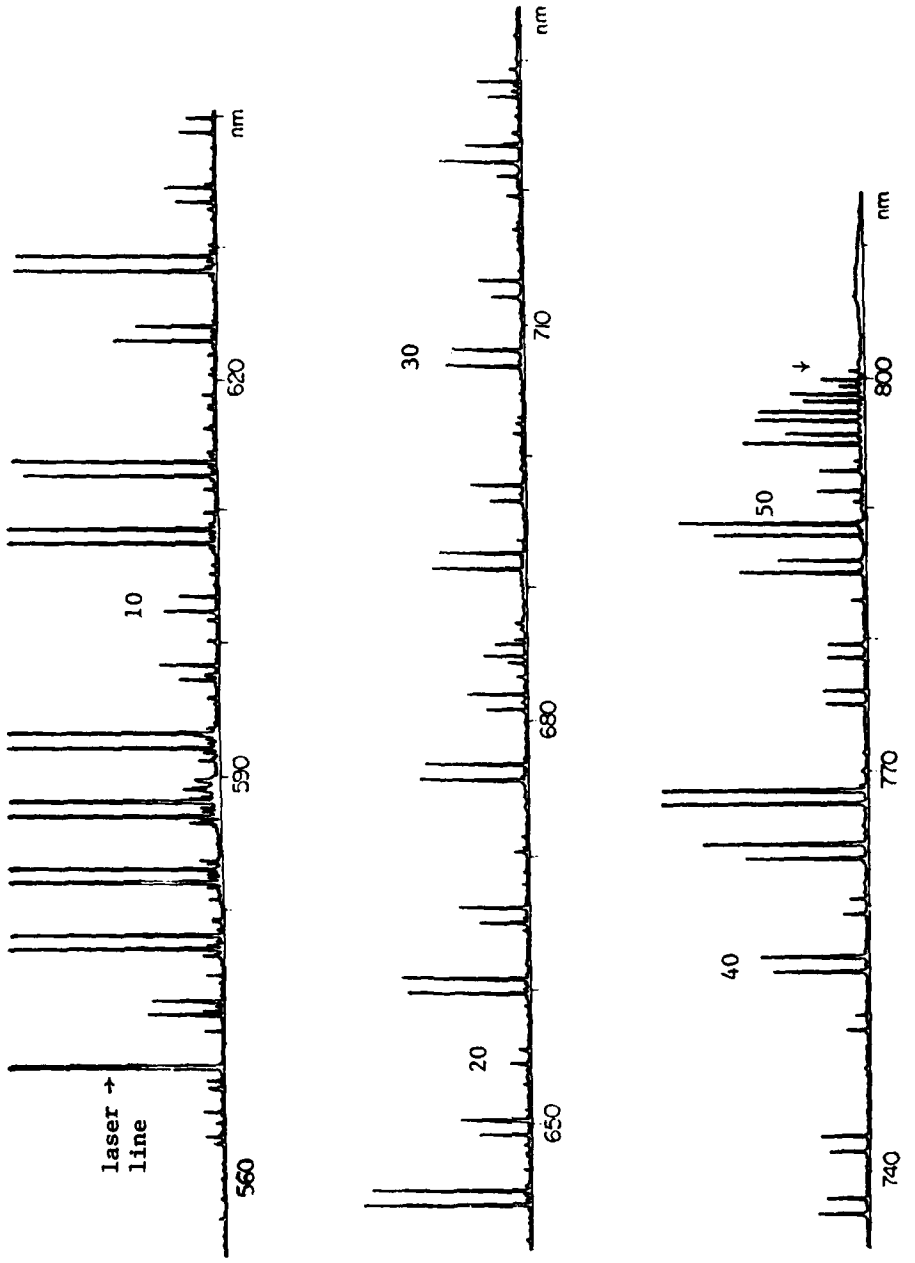

Figure 2. The laser-induced fluorescence spectrum of Na_2 excited by the 568.2 nm yellow line of the krypton ion laser and corresponding primarily to the transitions $A^1\Sigma_u^+$ (v' = 34, J' = 50) → $X^1\Sigma_g^+$ (v" or k", J" = 49, 51). The arrow indicates the position of the continuum onset[3]. Note there is a weak continuum on the long wavelength side of 801 nm.

perturbation theory has been worked out to iteratively remove such small discrepancies between the semiclassical RKR potential and the accurate quantum mechanical adiabatic potential[12-14]. Such details are unimportant for Na_2, however.

The potential (V(R)) or equivalently the effective potential ($U_J(R) = V(R) + \hbar^2 J(J+1)/2\mu R^2$) can then be used in the radial Schrödinger equation for nuclear motion corresponding to particles of reduced mass μ

$$\left[-\frac{\hbar^2}{2\mu}\frac{\partial^2}{\partial R^2} + V(R) + \frac{\hbar^2 J(J+1)}{2\mu R^2} \right] \psi_{v,J}(R) = E_{v,J}\, \psi_{v,J}(R) \qquad (1)$$

to obtain virtual exact numerical results (see reference 1 for references) for the energy $E_{v,J}$ and radial (vibrational) wavefunction $\psi_{v,J}(R)$. The angular solutions in this central force problem are, of course, just the spherical harmonics $Y_{JM}(\theta,\varphi)$. Some sample lines measured in the A-X bands of Na_2[15] are compared with calculated energies in Table III; clearly differences are significantly less than 1 cm^{-1} and thus adequately self-consistent for the present discussion.

Table III. Examples of R lines in the A-X bands of Na_2.

v'-v"	line	cm^{-1} expt.	cm^{-1} thry.	$\Delta(cm^{-1})$
14-10	R(44)	14644.60	14644.63	-0.03
16-5	R(16)	15657.01	15657.02	-0.01
22-10	R(85)	15241.66	15241.61	+0.05
25-10	R(86)	15523.54	15523.32	+0.22

Given the radial wavefunctions $\psi_{v",J"}(R)$ for the lower $X^1\Sigma_g^+$ state, the corresponding radial wavefunction $\psi_{v',J'}(R)$ for the upper $A^1\Sigma_u^+$ state (based on a V(R) obtained from other empirical data) and an ab initio electrical dipole transition moment function D(R) for the A-X transition, one can calculate the Einstein A coefficient for each v', J' → v", J" transition:

$$A_{v',J'\to v",J"} = C\left|\int_0^\infty dR\ \psi_{v',J'}(R)\ D(R)\ \psi_{v",J"}(R)\right|^2 \nu^3 \qquad (2)$$

where

$$\nu = \frac{E^*(v',\ J') - E(v",\ J")}{h} \qquad (3)$$

and $C = 7.2356 \times 10^{-6}\ S_J$ (S_J being a Hönl-London factor[6]) and where

A is in S^{-1}, ν is in cm^{-1} and D(R) is in eÅ units[16]. Such calculations agree very well with our carefully calibrated experimental results (Figure 3). It might be noted, for example, that the outer turning points of v' = 34 and v" = 43 are almost identical; since the wavefunctions have enhanced amplitude near their outer turning points, the v' = 34 → v" = 43 lines are especially intense.

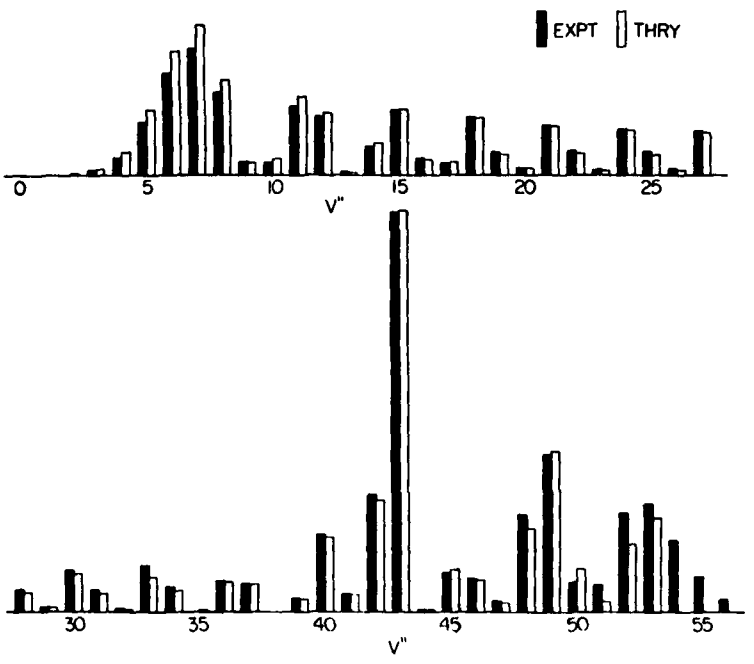

Figure 3. A comparison of experimental and theoretical intensities for lines corresponding to the Na_2^* lines $A^1\Sigma_u^+$ (v' = 34, J' = 50) → $X^1\Sigma_g^+$ (v", J" = 49 and 51) bound-bound emission in Figure 2 (levels corresponding to v" = 54-56 are quasi-bound).

If the various $A_{v',J'\rightarrow v'',J''}$ values are summed over all lower levels v", J", one obtains a total spontaneous emission rate $A_{v',J'}$ which is the reciprocal of the radiative lifetime. Again, agreement with experiment[17] is quite good (Table IV).

Table IV. Illustrative Na_2^* $A^1\Sigma_u^+$ (v', J') lifetimes.

	$\tau_{v',J'}$ (ns)	
v', J'	expt.	thry.
14, 45	~12.5	12.59
16, 17	~12.5	12.53
22, 86	12.6 ± 0.2	12.79
25, 87	12.8 ± 0.2	12.79
22, 49	12.6 ± 0.2	12.63

Such calculations can also be used for other purposes, e.g. to predict the occurrence of Na_2 A-X optically-pumped laser transitions. For example, all transitions as strong as the $A^1\Sigma_u^+$ (v' = 34, J' = 50) → $X^1\Sigma_g^+$ (v" = 40, J" = 49, 51) lines are expected to lase if those corresponding to v" = 40 do; one finds that v" = 40, 42, 43, 48, 49, 52, 53 and 54 lines do in fact all lase[18].

In summary then, the accurate empirical potential energy curves and ab initio dipole transition moment for the A-X transition of Na_2 allow one to reliably predict the energy levels, radiative transition probabilities, radiative lifetimes, laser transitions, etc. for these bound-bound spectra.

III. Bound-Free Transitions

We now note that our analysis in Figure 2 was not quite complete; in particular, there is weak continuous emission past the last line ($P_{56}(51)$) near 800 nm. This continuous bound-free emission clearly arises from the same upper level as the bound-bound line emission and exhibits three clear maxima (labeled n = 1, 2 and 3), decreasing in intensity with increasing wavelength (Table V). How can such spectra be included in the above bound-bound analysis? Note that we already have our potential V(R) and transition moment D(R) functions. All we need to do therefore is to calculate appropriate matrix elements to calculate Einstein A coefficients to a continuum state with wavenumber k" (where the asymptotic kinetic energy is $\hbar^2\, k"^2/2\mu$)

$$A_{v',J'\to k",J"} = C\left|\int dR\ \psi_{v',J'}(R)\ D(R)\ \psi_{k",J"}(R)\right|^2 \nu^3 \qquad (4)$$

Again excellent agreement between theory and experiment is achieved with regard to the position and relative intensity of the continuum maxima. Because the bound-free emission is so weak here, the radiative lifetimes are negligibly affected (<0.1 ns).

Table V. Na_2 $A^1\Sigma_u^+$ (v' = 34, J' = 50) bound-free maxima.

n	cm^{-1}		I_n/I_1	
	expt.	thry.	expt.	thry.
1	12385 ± 1	12385.0 ± 1	1	1
2	12211 ± 2	12210.0 ± 1	0.25 ± 0.02	0.259
3	12029 ± 5	12025.8 ± 1	0.05 ± 0.02	0.0433

The bound-free spectrum we have discussed is, however, not typical of diffuse spectra in general. How can we understand such spectra in general, especially where only an indistinct broad continuum is observed (perhaps roughly a Gaussian or an asymmetric distortion of a Gaussian)? In such cases, the secret is observation of

single vibrational-rotational level emission, rather than emission from a broad distribution of levels. Such single level emissions are highly structured, high information content emissions which arise from the structure of the emitting level wavefunction (e.g. $\psi_{v''} = 34$ has 34 zeroes!) and from interference between emission at "different internuclear distances" with the same semiclassical transition frequency.

The quantum mechanical calculation of this structured emission is straightforward[1] using equation 4. However, it is useful to discuss this emission semiclassically in terms of the "Mulliken Difference Potential" (MDP)

$$\begin{aligned} MDP(R) &= KE_{v',J'}(R) + V''(R) \\ &= E_{v',J'} - V'(R) + V''(R) \end{aligned} \tag{5}$$

where $KE_{v',J'}(R)$ is the classical nuclear kinetic energy at distance R. In a sense, the MDP simply corresponds to application of the Franck-Condon principle[6] that the nuclear kinetic energy is conserved during an electronic transition. It has an origin in the line broadening theories of Jablonski[19] and in the diatomic analyses of Mulliken[20] and has been popularized especially by Tellinghuisen[1]. The corresponding frequency of emission at internuclear distance R is then

$$\nu(R) = E_{v',J'} - MDP(R) = V'(R) - V''(R). \tag{6}$$

The simplest possibilities for MDP(R) are monotonic (M), single extremum (S) and double extrema (D). Two cases are shown in Figure 1 for states involving bound-free emission. The $2^1\Sigma_u^+ - X^1\Sigma_g^+$ ($^1\Delta V$) line and the $2^3\Pi_g - 1^3\Sigma_u^+$ ($^3\Delta V$) line represent an S case and a D case (partially M), respectively, which have recently been analyzed[4] for the oldest diffuse bands in sodium, the so-called "violet bands". These bands, first observed by Bartels in 1932[21] as two indistinct violet-degraded features peaking at 436 and 452 nm in the violet, have long been a mystery. Over 25 papers reported these bands without a convincing assignment[4]. However, the MDP concept allows us to easily make an assignment given single vibrational-rotational level excitation.

First let us consider the monotonic (M) case for the MDP. In this case, the classical emission frequency varies monotonically with internuclear distance and one sees only the "reflection" of the structure of the upper state wavefunction off the lower state MDP (not the true potential V"(R) as is sometimes incorrectly assumed). The emission then simply shows regular oscillatory structure. Excimer emissions from a bound upper state to an unbound lower state are often like this with MDP(R) decreasing rapidly with increasing R. At high frequencies, this is true of the MDP(R) for the $2^3\Pi_g - 1^3\Sigma_u^+$ transition in Figure 1.

Next let us consider the S case of a single extremum. Here, in addition to the structure of the upper state wavefunction, there will be two internuclear distances for most classical emission frequencies up to a limit (the extremum or "satellite" frequency) and none past that frequency. This will impose an additional modulation on the rapid "wavefunction" oscillations which always occur. Also there will be a fairly sharp cutoff (exponentially decaying intensity) beyond the satellite position, which itself will be relatively intense (as dMDP/dR goes to zero). The $2^1\Sigma_u^+$ - $X^1\Sigma_g^+$ curve in Figure 1 is an S case.

The D case will be even more complex, the three internuclear distances corresponding to a given frequency and with two cutoff satellite positions. The $2^3\Pi_g$ - $1^3\Sigma_u^+$ curves in Figure 1 is such a D case (partially M for high frequencies).

The above analysis allows one to easily assign the experimental spectra shown in Figure 4 and 5 to case S and to case M/D, respectively. This is confirmed by the full quantum mechanical simulation also shown in these figures. Note that even many of the minor features in these spectra are accurately reproduced in these calculations and also that these calculations include no adjustable

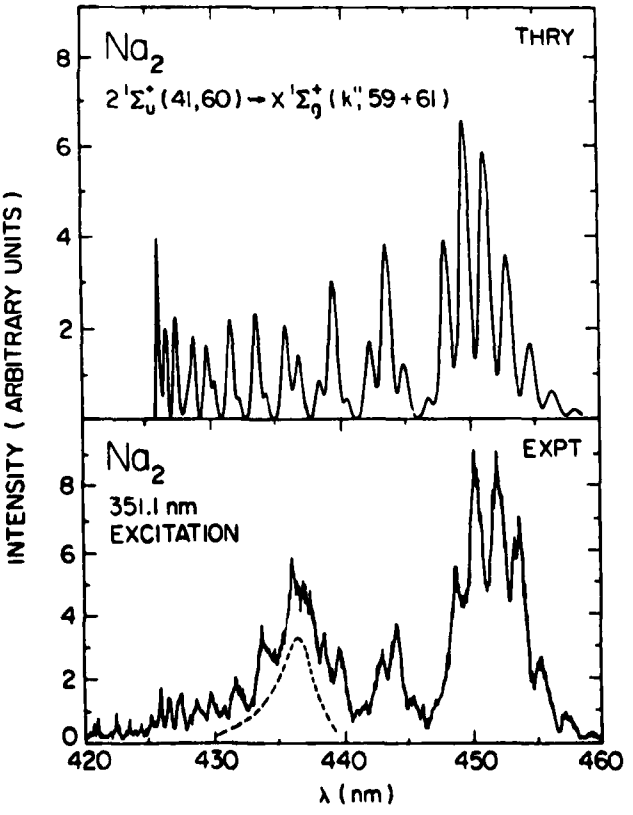

Figure 4. The laser-induced fluorescence spectrum of Na_2 excited by the 351.1 nm line of the argon ion laser and corresponding primarily to the transitions $2^1\Sigma_u^+$ (v' = 41, J' = 60) → $X^1\Sigma_g^+$ (v" or k", J" = 59, 61). The dashed line in the experimental spectrum is collision-induced triplet emission (see Figure 5) and should be subtracted out in comparing with theory. The spectrum corresponds to a single extremum case (S) for the Mulliken difference potential.

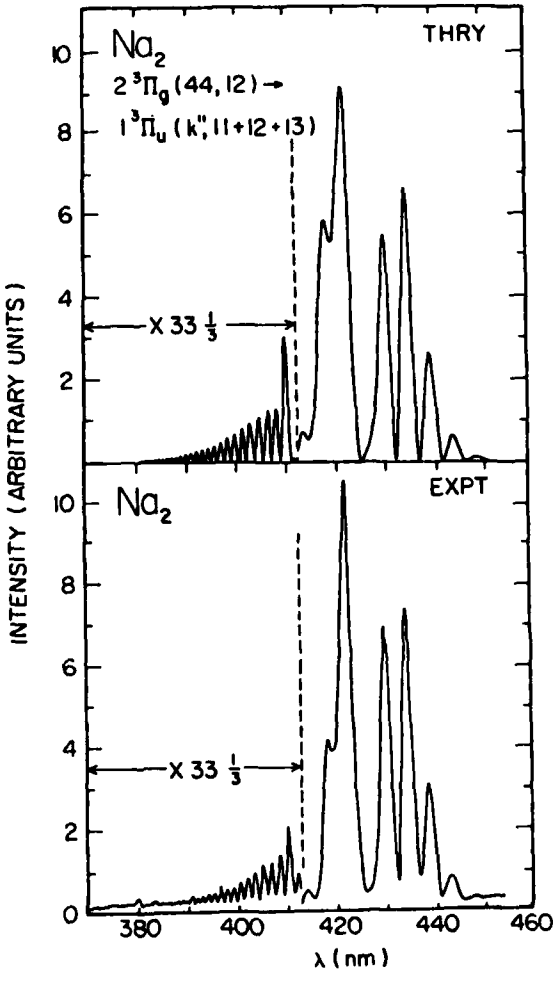

Figure 5. The laser-induced fluorescence spectrum of Na_2 excited by optical-optical double resonance and corresponding to the transitions $2^3\Pi_g$ (v' = 44, J' = 12) → $1^3\Sigma_u^+$ (v" or k", J" = 11, 12 or 13). The region λ < 412 nm corresponds to a monotonic (M) Mulliken difference potential, while λ > 412 nm represents a region of double extrema.

parameters.

In summary, theoretical and spectroscopic tools are now available for precise determination of radiative transition probabilities in diatomic molecules; these tools have been accurately tested in the alkali metal diatomics (e.g. several bands of Na_2) with outstanding consistency.

1. J. Tellinghuisen, in K. P. Lawley, editor, Photodissociation and Photoionization (Wiley, New York, 1985), p. 299.

2. H. E. Roscoe and A. Schuster, Proc. Roy. Soc. ondon 22, 362 (1874).

3. K. K. Verma, J. T. Bahns, A. R. Rajaei-Rizi, W. C. Stwalley and W. T. Zemke, J. Chem. Phys. 78, 3599 (1983).

4. G. Pichler, J. T. Bahns, K. M. Sando, W. C. Stwalley, D. D. Konowalow, L. Li, R. W. Field and W. Müller, Chem. Phys. Lett. 129, 425 (1986).

5. P. Kusch and M. M. Hessel, J. Chem. Phys. 68, 2591 (1978).

6. G. Herzberg, Spectra of Diatomic Molecules (Van Nostrand Reinhold, New York, 1950).

7. W. Demtröder, Laser Spectroscopy (Springer Verlag, New York, 1982)

8. R. N. Zare, J. Chem. Phys. 40, 1934 (1964).

9. W. C. Stwalley, J. Chem. Phys. 56, 2485 (1972).

10. Y. K. Hsieh, S. C. Yang, A. C. Tam and W. C. Stwalley, J. Chem. Phys. 68, 1448 (1978).

11. W. C. Stwalley, Contemp. Phys. 19, 65 (1978).

12. W. M. Kosman and J. Hinze, J. Mol. Spectrosc. 56, 93 (1975).

13. C. R. Vidal and H. Scheingraber, J. Mol. Spectrosc. 65, 46 (1977).

14. Y. Chan, D. R. Harding, W. C. Stwalley and C. R. Vidal, J. Chem. Phys. 85, 2436 (1986).

15. W. T. Zemke, K. K. Verma, T. Vu and W. C. Stwalley, J. Mol. Spectrosc. 85, 150 (1981).

16. W. T. Zemke and W. C. Stwalley, J. Chem. Phys. 68, 4619 (1978).

17. T. W. Ducas, M. G. Littman, M. L. Zimmerman and D. Kleppner, J. Chem. Phys. 65, 842 (1976).

18. J. T. Bahns, K. K. Verma, A. R. Rajaei-Rizi and W. C. Stwalley, Appl. Phys. Lett. 42, 336 (1983).

19. W. Jablonski, Phys. Rev. 68, 78 (1945).

20. R. S. Mulliken, J. Chem. Phys. 55, 309 (1971).

21 H. Bartels, Z. Physik 73, 203 (1932).

PRECISE LASER WAVELENGTH MEASUREMENTS: WHAT CAN WE LEARN FROM CLASSICAL SPECTROSCOPY?

Craig J. Sansonetti
National Institute of Standards and Technology*
Gaithersburg, Maryland 20899

ABSTRACT

The wavelengths of cw dye lasers are typically measured using Michelson wavemeters, but the absolute accuracy of such instruments is limited by their sensitivity to alignment of the laser beams. This systematic problem can be largely eliminated by diffusely scattering the beams and using classical spectroscopic methods to measure the wavelength. We have developed a laser wavemeter, based on a static Fabry-Perot interferometer, with an accuracy of a few parts in 10^9 and an update rate of about 2 Hz. The system is insensitive to the alignment and collimation of the incoming laser beams. The potential for a more precise wavemeter based on techniques of Fourier transform spectroscopy is also considered.

INTRODUCTION

Commercial single-frequency cw dye lasers have a linewidth of less than 1 MHz or a part in 10^9 of the optical frequency. Such lasers have been available for a decade, but there remains a need for a convenient method for measuring their wavelengths with accuracy comparable to the linewidth. Commercial wavemeters are limited to a part in 10^6, and the more precise wavemeters built in many laboratories do not consistently produce results better than a part in 10^8. Higher accuracy can be achieved by high-precision interferometric techniques[1] or direct frequency measurements,[2] but these techniques are not adapted to routine laboratory use.

MICHELSON WAVEMETERS

Over the last decade a variety of wavemeter designs have been reported (i.e. Refs. 3 - 9), but only variations of the Michelson wavemeter have seen wide use for precise measurements of cw lasers. A Michelson wavemeter of reasonable size can achieve a resolution of a part in 10^7 by using simple fringe counting. This can be improved to better than a part in 10^9 by multiplying the fringe frequency in a phase-locked loop.[4]

Although high precision Michelson wavemeters have been built in a number of laboratories, they have not achieved absolute accuracy comparable to their resolution. Some of their sources of uncertainty are quantifiable and can be controlled by appropriate design and laboratory practice. Among these are the uncertainties in the diffraction correction, the correction for the dispersion of

* Formerly National Bureau of Standards.

air, and the wavelength of the reference laser.

In contrast to these uncertainties which can be controlled to a part in 10^9, other less predictable sources of error can be identified. Laser amplitude instabilities characteristic of dye lasers can cause errors in the fringe counting and multiplication circuitry leading to a large scatter and systematic bias in the wavemeter results. This problem is readily detectable but may not be easy to eliminate. Not so easily detected are systematic errors due to misalignment of the laser beams. Two types of alignment error can be distinguished. First, the beams may not be aligned parallel to the motion of the travelling mirror. In some geometries this causes lateral shifts between the interfering beams at the fringe detector, and in any case it causes the beams to move about in the travelling retroreflector. These effects can cause phase errors in the observed fringes. Second, the unknown laser may not be aligned parallel to the reference beam. If the angle of inclination between the beams is θ, the relative error in the measured wavelength is $\theta^2/2$. To obtain a relative error smaller than a part in 10^9 the angle θ must be less than 4.5×10^{-5} rad. It is very difficult to maintain alignment at this level, and there is no readily observable condition that signals misalignment.

A good discussion of uncertainties in Michelson wavemeters has been given by Castell et al.[10] in a report on tests of the high-resolution instrument at Kaiserslautern. With very careful alignment they were able to obtain a relative uncertainty of 5×10^{-9} in measurements of an argon ion laser. When a cw dye laser was substituted for the argon ion laser the relative uncertainty increased to 1×10^{-8}. And in routine use the authors estimated that a relative uncertainty of 3×10^{-8} could be expected.

In summary, the routine accuracy of Michelson wavemeters is limited mainly by the difficulty of maintaining proper alignment of the laser beams through the instrument. Misalignment is not readily detectable and may easily cause systematic errors far greater than the statistical spread of a series of independent measurements.

CLASSICAL METHODS

Classical methods for wavelength measurement are techniques developed to determine the wavelength of spectral features in an incoherent emission source. Such a source can be regarded as a spatially extended collection of independent point emitters each of which radiates isotropically. As a consequence, the illumination of a spectroscopic instrument can be determined by the aperture of the instrument rather than by the characteristics of the source.

The most precise classical wavelength measurements are made by using Fabry-Perot interferometry or Fourier transform spectroscopy. In careful experiments accuracy better than a part in 10^8 can be obtained. Typically the accuracy is limited not by the technique or instrumentation but rather by the spectral line width and limited coherence length of the source. Since lasers can readily overcome these source limitations, it is worthwhile to consider the application of classical methods to laser wavelength measurements.

FABRY-PEROT WAVEMETER

A complete discussion of precise wavelength measurements by Fabry-Perot interferometry has been given by Meissner.[11] Briefly, the interferometer is illuminated by an extended source and the transmitted light is imaged by an achromatic lens to form a pattern of concentric interference rings. For an evacuated interferometer

$$(P + \epsilon)\lambda = 2t \qquad (1)$$

where P is the integer and ϵ the fractional order of interference at the center of the fringe pattern, λ is the wavelength, and t is the spacer length. ϵ can be determined from the observed radii of the interference rings. Using Eq. 1 one can calculate the spacer length t from a standard line, and the wavelength of an unknown line can be determined by using the equation a second time. To use Eq. 1 it is necessary to know t accurately enough to determine the integer order for the standard line and the unknown wavelength accurately enough to determine the integer order for the unknown line. In practice the optical path difference in the interferometer is slightly wavelength dependent due to phase shifts on reflection from the aluminium coatings. To obtain the highest accuracy this phase shift must be determined and taken into account.

A schematic diagram of the Fabry-Perot wavemeter developed at the National Institute of Standards and Technology is shown in Fig. 1. It differs in design principles and accuracy from earlier Fabry-Perot based instruments.[6,10] The interferometer has a 218 mm Invar spacer. Its 10 cm fused quartz plates are flat to better than $\lambda/50$ and are coated with aluminum to 85% reflectivity.

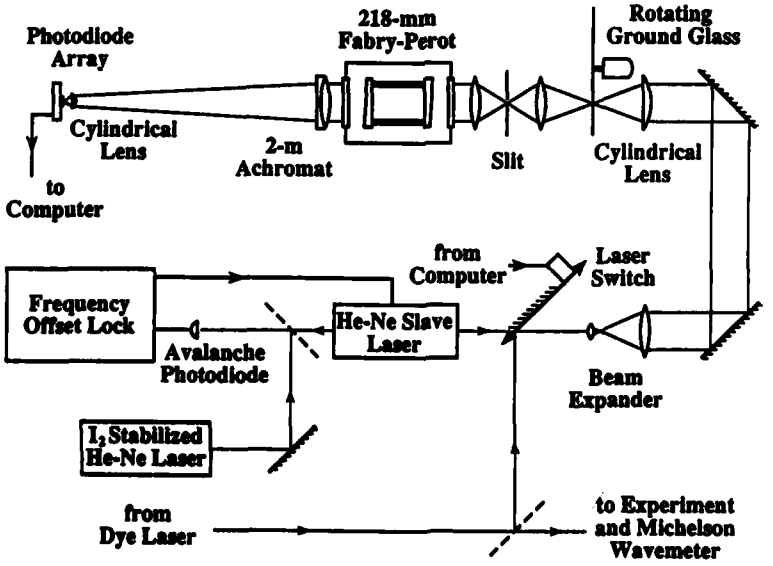

Figure 1. Schematic diagram of the Fabry-Perot wavemeter.

It is housed in a vacuum chamber at a pressure below 10 mTorr to eliminate the need for index-of-refraction corrections. The quartz plates are pressed against the spacer by springs whose tension can be adjusted from outside the vacuum housing to obtain parallelism of the plates.

The Fabry-Perot is illuminated by laser light scattered from a rotating ground glass plate. This emulates a classical source in that it is extended in space and each point on the ground glass scatters light into a solid angle large enough to fill the aperture of the instrument. The laser beam is expanded and imaged by a cylindrical lens as a line on the ground glass. The interferometer is mounted in collimated light, and the interference rings are projected by a 2-m achromat on a photodiode array of 1024 elements on 25 μm centers. A short focal length cylindrical lens just before the array increases its effective width from 25 to 200 μm. This optical system makes efficient use of the laser light and assures that all parts of the interferometer send light to all parts of the fringe pattern. In this way misalignment or imperfection in the plates broadens the fringes but does not distort the pattern.

In operation the interferometer is illuminated alternately by the dye laser and by a He-Ne reference laser which is used to determine the etalon length. This provides a continuous calibration of the system in terms of an internationally recognized standard and eliminates need for thermal stabilization of the apparatus. The reference laser is a single-mode He-Ne that is frequency-offset locked to an I_2 stabilized He-Ne. Use of a slave laser is required to provide sufficient power for the interferometer and to eliminate the frequency modulatation used to lock the I_2 stabilized laser.

Control and data reduction is provided by a minicomputer which selects the laser illuminating the interferometer and reads the fringe patterns from the photodiode array. Each pattern is analyzed to find the fractional order of interference at the center of the pattern, and the fractional order numbers are used to calculate t and the dye laser wavelength. The initial wavelength required to determine the integer order number is obtained from a low precision Michelson wavemeter. Once an initial value has been provided the Fabry-Perot wavemeter operates continously at a rate of about 2 Hz without additional input unless the stabilized dye laser is unlocked or is scanned more rapidly than 200 MHz/sec.

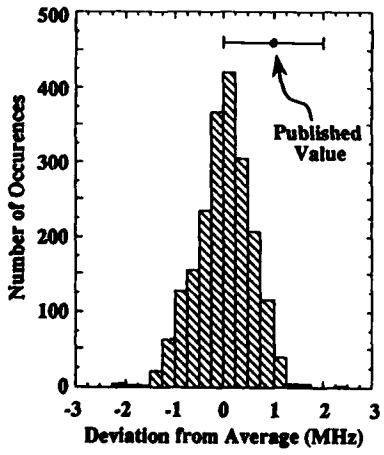

Figure 2. Distribution of wavemeter test results.

The performance of the Fabry-Perot wavemeter is shown in Fig. 2. A dye laser was locked to the $^{127}I_2$ R(66)13-2o transition and its wavelength was measured at intervals of one minute. More than 2000 measurements were accumulated over

nine days with full realignment of the instrument each day. The results fell in a narrow distribution with 93% of the individual values within 1 MHz of the mean. The average of all measurements is 1 MHz lower than the best literature value for the line[12] and agrees within the stated uncertainties. Additional measurements of many I_2 lines for which precise values have been reported indicate that an absolute accuracy better than 2 MHz is routinely obtained. Tests have shown that errors due to any plausible misadjustment of the apparatus or illumination are smaller than 1 MHz. The primary limitation of the system is its need for an initial wavelength with an accuracy of a few parts in 10^7 from another source.

FOURIER TRANSFORM WAVEMETER

The limitations of the Fabry-Perot wavemeter can be overcome by a wavemeter based on the techniques of Fourier transform spectroscopy. Such a wavemeter with an accuracy of a part in 10^7 has been described by Juntilla et al.[9] Here we will discuss the use of a high resolution Fourier spectrometer[13] as a wavemeter and estimate the accuracy it could obtain. The procedure described would take about 5 minutes per measurement, but an instrument designed for wavemeter use could operate much more rapidly.

Assume that the aperture of the Fourier spectrometer is illuminated simultaneously by diffusely scattered light from a dye laser and a reference laser whose wave number is accurately known. For a 0.1 mm aperture, errors due to finite aperture size would be negligible. A small aperture need not decrease the instrumental throughput since the intrinsic source brightness can be increased by focussing the lasers at the scatterer. One would first record and transform a short densely-sampled single-sided interferogram to obtain an initial dye laser wave number in an unaliased spectrum. A 5 mm optical path difference and 1550 Å sampling interval would yield a 32,000 cm^{-1} free spectral range with 1 cm^{-1} resolution from a 2^{15} point transform. This would be followed by a long sparsely-sampled double-sided scan to obtain high resolution in a highly aliased spectrum. A 5 m optical path difference with 155 μm step size would give 0.001 cm^{-1} resolution and 32 cm^{-1} free spectral range from a 2^{16} point transform. The results from the initial scan would be used in choosing the actual step size to ensure that the aliased spectra of the dye and reference laser would be well resolved. The high resolution spectrum would be interpolated in the vicinity of the lines and analyzed to determine dye and reference wave numbers based on the nominal interferogram step size. Finally a multiplicative correction to the wave number scale would be determined from the reference laser result and applied to obtain the wave number of the dye laser.

The accuracy obtainable can be estimated from the expression

$$\delta\sigma = \frac{\text{FWHM}}{n(S/N)}. \qquad (2)$$

Here FWHM=0.001 cm^{-1} is the width of the line, n=1 is the number of primary transform points on the profile, and (S/N) is the signal to

noise ratio. With an instrument of this type (S/N)>10^5 is typical for a strong emission line in an unaliased spectrum of 10^6 points. For our case (S/N) is reduced by a factor of 4 because we are using only 64,000 interferogram points and by an additional factor of 32 because we are operating in an aliased spectrum of order 1000. Applying these factors we expect (S/N)>800 producing a random uncertainty in each of the laser wave numbers of 1.25×10^{-6} cm^{-1}. Using the reference laser wave number for absolute calibration eliminates systematic bias but increases the statistical uncertainty by 2 giving a final uncertainty of 1.75×10^{-6} cm^{-1} or a relative uncertainty of 9 parts in 10^{11} for visible light. This suggests that the ultimate accuracy of such a wavemeter might at this point be limited by the uncertainty of the reference laser.

CONCLUSIONS

Classical methods for wavelength measurements are readily adapted to laser sources and provide a level of accuracy that is not generally obtained by conventional wavemeters. The Fabry-Perot wavemeter developed at NIST gives rapid convenie - wavelength measurements for cw dye lasers with an acccuracy of a few parts in 10^9. The system is easy to adjust and insensitive to laser alignment, collimation, and amplitude instabilities. A Fourier transform wavemeter similar to existing Fourier spectrometers has potential to provide wavelength measurements with an accuracy limited only by the uncertainty of the I_2 stabilized He-Ne laser.

REFERENCES

1. F. Biraben, J.C. Garreau, L. Julien, Europhys. Lett. 2, 925 (1986).
2. D. A. Jennings, C. R. Pollock, F. R. Petersen, R. E. Drullinger, K. M. Evenson, J. S. Wells, J. L. Hall, H. P. Layer, Opt. Lett. 8, 136 (1983).
3. P. Juncar and J. Pinard, Rev. Sci. Instrum. 53, 939 (1982).
4. J. L. Hall and S. A. Lee, Appl. Phys. Lett. 29, 367 (1976).
5. J. J. Snyder, Laser Spectroscopy III, J. L. Hall and J. L. Carlsten, Eds. (Springer-Verlag, New York, 1977), p. 419.
6. R. L. Byer, J. Paul, M. D. Duncan, Laser Spectroscopy III, J. L. Hall and J. L. Carlsten, Eds. (Springer-Verlag, New York, 1977) p. 414.
7. R. Salimbeni and R. V. Pole, Opt. Lett. 5, 39 (1980).
8. F. Docchio, F. P. Schafer, J. Jethwa, J. Jasny, J. Phys. E: Sci. Instrum. 18, 849 (1985).
9. M-L. Juntilla, B. Ståhlberg, E. Kyrö, T. Veijola, J. Kauppinen, Rev. Sci. Instrum. 58, 1180 (1987).
10. R. Castell, W. Demtröder, A. Fischer, R. Kullmer, H. Weickenmeier, K. Wickert, Appl. Phys. B 38, 1 (1985).
11. K. W. Meissner, J. Opt. Soc. Am. 31, 405 (1941).
12. L. Hlousek and W. M. Fairbank, Jr., Opt. Lett. 8, 322 (1983).
13. B. A. Palmer, Technical Bulletin LALP-85-16 (Los Alamos National Laboratory, Los Alar , N.M., 1985).

MEASUREMENT OF THE RYDBERG CONSTANT BY DOPPLER-FREE SPECTROSCOPY OF ATOMIC HYDROGEN

M.Allegrini(*), F.Biraben, B.Cagnac, J.C.Garreau and L.Julien
Laboratoire de Spectroscopie Hertzienne de l'E.N.S.,
4 Place Jussieu, Tour 12 E01, 75252 Paris Cedex 05, France

INTRODUCTION

Recent measurements of the Rydberg constant R_∞ [1-5], steming from the study of different transitions in atomic hydrogen and deuterium, agree very well with each other (see table 1). The accuracy of all these measurements (a few parts in 10^{10}) is approaching the precision (1.6×10^{-10}) of the I_2-stabilized He-Ne laser which serves as primary frequency/wavelength standard in the visible region. Here we present a new measurement of R_∞ [6], (reported in the last line of table 1), whose precision with respect to the frequency/wavelength standard is 4.4×10^{-11}. Thus our measurement of the Rydberg constant is not limited by the uncertainties inherent in the experiment, but rather by the precision with which absolute frequencies are measured in the optical domain. In other words our result shows that the present realization of the metre is no longer satisfactory in the optical domain and that better optical frequency standards are required.

The present measurement of R_∞ has been obtained after several improvements of the set-up used for the Doppler-free two-photon laser spectroscopy experiment of ref.[1].

MEASUREMENT METHOD AND APPARATUS

We measure the Rydberg constant by comparing the H- and D-transitions from the metastable 2S-state to the Rydberg states 8D, 10D and 12D, with a home-made I_2-stabilized He-Ne laser, whose calibration has been made with respect to the standard He-Ne lasers of the Bureau International des Poids et Mesures. The basic structure of the experiment can be divided in three blocks: i) metastable beam apparatus, ii) dye laser apparatus iii) frequency measurement apparatus.

i) There are three vacuum chambers; in the first one a ground state effusive atomic beam, obtained from molecular hydrogen (or deuterium) through r.f.discharge, is excited to the metastable 2S state by electron bombardment. In the second chamber where electric and magnetic stray fields are minimized, (<2mV/cm, <50mG), the 2S-atoms are excited to the nD Rydberg states by two counter-propagating laser beams. The geometry is such that the atomic metastable beam is collinear with the laser beams along the axis of a Fabry-Perot cavity, mounted to enhance the two-photon absorption. In a third chamber an applied electric field quenches the 2S-level and the

(*) Permanent address: Istituto di Fisica Atomica e Molecolare del C.N.R., Via del Giardino 7, 56100 Pisa, Italy

Table 1. Recent values obtained for the Rydberg constant by laser spectroscopy of atomic hydrogen and deuterium

Transition	R_∞ ($-109737 cm^{-1}$)	Relative(*) precision (rms error)	Group	Ref.
H,D: 2S- 8D, 2S-10D	.31569(6)	5×10^{-10}	PARIS, 1986	1
H,D: 2S- 3P	.31569(7)	6×10^{-10}	YALE, 1986	2
H,D: 2S- 4P	.31573(3)	3×10^{-10}	YALE, 1987	3
H : 1S- 2S	.31571(7)	6×10^{-10}	STANFORD, 1987	4
H,D: 1S- 2S	.31573(3)	3×10^{-10}	OXFORD, 1987	5
H,D: 2S- 8D 2S-10D 2S-12D	.315714(19)	1.7×10^{-10}	PARIS, 1988	6

(*) The absolute frequency calibration of ref. [1-3] and [6] is done against a I_2-stabilized He-Ne laser, whose accuracy is 1.6×10^{-10}. Works of ref.[4,5] use as intermediate standard molecular tellurium vapor ($^{130}Te_2$) whith an accuracy of 4×10^{-10} [4] and 2.7×10^{-10} [5].

metastable atoms are detected through the resulting Lyman-α fluorescence. The two-photon transitions are observed as a decrease of the metastable beam intensity. Typical values are $\approx 10^6$ atoms/s of flux (or a metastable density of few atoms per c.c.), $\approx 10^4$ W/cm^2 laser power density in the excitation chamber, up to 15% quenching of the metastables and a signal-to-noise ratio up to 30 in the detection chamber.

ii) The laser used to excite the 2S-nD transitions is a home made, cw, single-mode, ring, LD 700 dye laser, pumped by a Kr^+ laser. The frequency stabilization is made by active locking to an external auxiliary Fabry-Perot cavity while the scanning is done through an acousto-optic device. The modulation frequency of the acousto-optic crystal is provided by a computer-controlled frequency synthesizer and the result is a very precise control of the dye laser frequency. The overall characteristics of the dye laser are $\approx$ 1 W power in the 730-780 nm region of our interest, $\approx$ 50 kHz linewidth and $\approx$ 250 MHz tunability without mode-hopping, centered at any desired frequency.

iii) The absolute frequency position of the two-photon transitions is done by comparing the wavelengths of the i.r. dye laser and of the red He-Ne reference laser. This comparison is done inside a nonconfocal Fabry-Perot cavity of high finesse and kept under high

vacuum. The construction of this cavity requires the use of optical adhesion technique and metallic mirrors of good quality. An auxiliary He-Ne laser as well as the dye laser are mode-matched and locked to this optical cavity while the beat frequency between the two He-Ne lasers is measured. Two lengths of the Fabry-Perot cavity are used (10 cm and 50 cm) so that the phase shift due to the metallic mirror reflection is eliminated by the method of the virtual mirrors.

RESULTS AND CONCLUSIONS

We have measured the frequency of the three transitions $2S_{1/2}$-$8D_{5/2}$, $2S_{1/2}$-$10D_{5/2}$ and $2S_{1/2}$-$12D_{5/2}$ in both atomic hydrogen and deuterium and we have corrected them for h.f.s. splitting, second-order Doppler effect and light shift. Using Erickson s values for the 2P-nD interval [7], the experimental value of H-2S Lamb-shift [8] and the theoretical value of the D-2S Lamb-shift [9], we have deduced six independent values of the Rydberg constant which give as final result:

$$R_\infty = 109737.315714(19)\ cm^{-1}$$

From the analysis of the error sources we find that the determination of the frequency of the standard laser gives the limit to the precision of our measurement of R_∞. In fact our precision with respect to the standard laser is less than 5×10^{-11} while the reliability of the standard laser is 1.6 parts in 10^{10} [10]. Work is in progress in order to reach a more refined analysis of our data, including the effects of the velocity distributions inside the atomic beam.

This work is partially supported by the Bureau National de Métrologie under grant BNM-87 2 46 0017 and by the European Economic Community under grant EEC-ST2*0423.

REFERENCES

1. F.Biraben, J.C.Garreau and L.Julien, Europhys.Lett. 2, 925 (1986)
2. P.Zhao, W.Lichten, H.P.Layer and J.C.Bergquist, Phys. Rev. A34, 5138 (1986)
3. P.Zhao, W.Lichten, H.P.Layer and J.C.Bergquist, Phys. Rev. Lett. 58, 1293 (1987)
4. R.G.Beausoleil et al., Phys. Rev.A35, 4878 (1987)
5. M.G.Boshier et al., Nature 330, 463 (1987)
6. M.Allegrini, F.Biraben, B.Cagnac, J.C.Garreau and L.Julien, in "The Hydrogen Atom", G.F.Bassani, T.W.Hänsch and M.Inguscio Eds., (Springer Verlag, in press)
7. G.W.Erickson, J. Phys. Chem. Ref. Data 6, 831 (1977)
8. V.G.Pal'chikov, Yu.L.Sokolov and V.P.Yakovlev, JEPT Lett. 38, 418 (1983)
9. G.W.Erickson and H.Grotch, Phys. Rev. Lett. 60, 2611 (1988)
10. D.A.Jennings et al., Opt. Lett. 8, 136 (1983)

STATE MIXING IN RYDBERG ATOM - NOBLE GAS COLLISIONS

K.-D. Heber, P. J. West and E. Matthias
Freie Universität Berlin, Fachbereich Physik, D-1000 Berlin 33, FRG

ABSTRACT

Pressure shift and broadening rates, caused by thermal collisions with xenon atoms, have been measured for 5snd $^1D_2$ and 5snd $^3D_2$ Rydberg states of SrI in the range $8 \leq n \leq 25$ by means of Doppler-free two-photon excitation and thermionic detection. The results show drastically different resonant collisional admixtures for $^1D_2$ and $^3D_2$ states between $13 \leq n \leq 19$. Above n=20 non-resonant systematic deviations of shifts and broadenings between singlet and triplet 5snd states are observed.

TEXT

Compared to atoms in low lying excited states, Rydberg atoms exhibit a number of unusual properties[1], amongst them an extreme sensitivity to "environmental" perturbations, such as surrounding gases. Therefore broadening and shifting of Rydberg states by

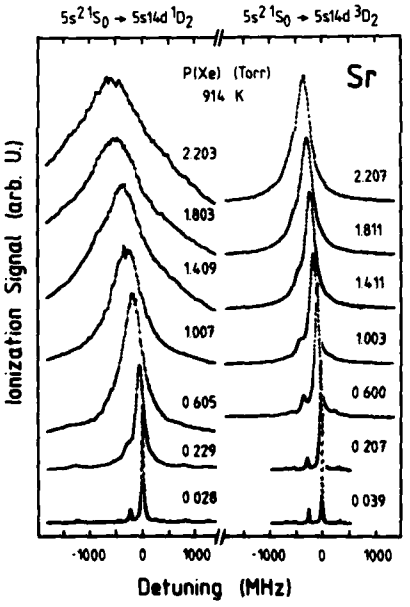

Figure 1. Line shift of the 5s 14d $^1D_2$ and $^3D_2$ Rydberg states of SrI due to different Xe densities.

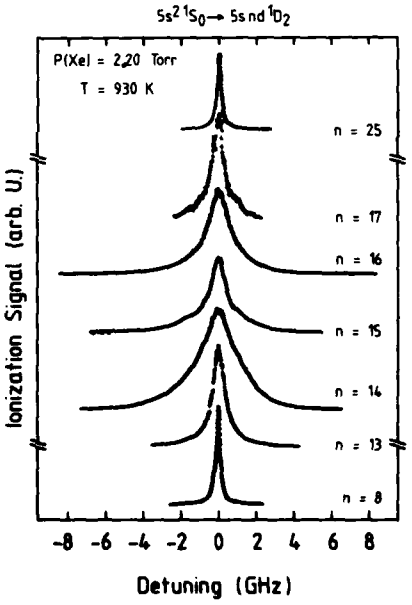

Figure 2. Line broadening (shift suppressed) of several members of the 5snd $^1D_2$ Rydberg series of SrI in Xe at 2.2 Torr.

collisions with neutral particles has received considerable attention because from the results one expects a more fundamental under-

standing of the scattering process. Many experimental studies of various aspects of Rydberg atom scattering have been reported in the past several years[1-5]. The theoretical description of atom-atom-collisions is difficult in general[6]. Almost all theoretical treatments of collisions of highly excited Rydberg atoms with neutral particles[2,7-9] are based on two terms: the scattering of the quasi-

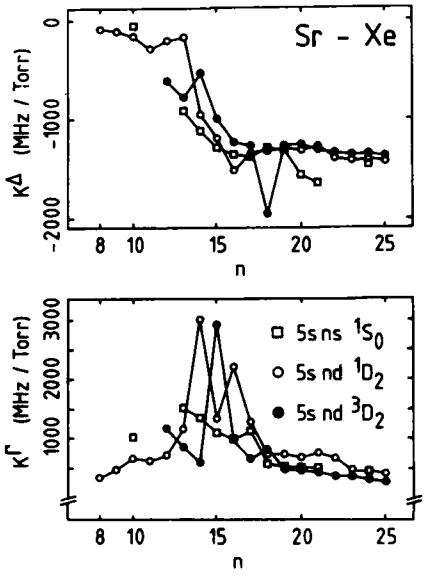

Figure 3. Pressure shift (K^{Δ}) and broadening rates (K^{Γ}) of 5snd $^1D_2$ and $^3D_2$ Rydberg states due to Xe.

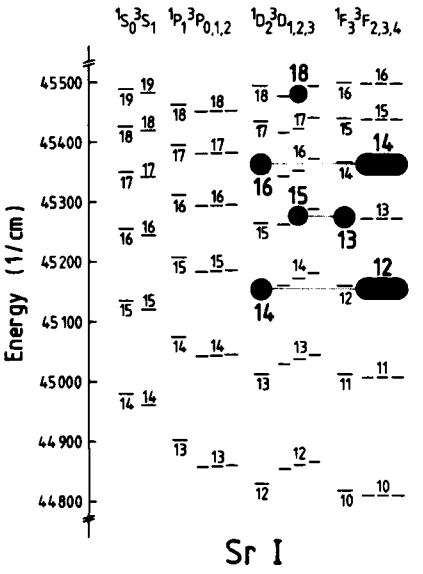

Figure 4. Quasidegeneracies causing the resonances in broadening and shifting rates shown in Fig. 3.

free Rydberg electron on the perturbing neutral particle, and the polarization of the perturbing particles by the ionic core. Both interactions are finite in range and can be treated separately in the limit of high principal quantum numbers. In this way the experimental asymptotic shifts and broadendings of high Rydberg levels have been successfully explained[3,4].

In the range of intermediate principal quantum numbers, a variety of phenomena are observed[5,10-12] which cannot be described by theory in a unified way, although some progress has been made recently[13,14]. Here pressure shifts and broadenings are strongly n - and ℓ - dependent, and inelastic collisions changing the quantum state of the Rydberg electron become important. Further complications are expected when Rydberg states of two-electron atoms are considered. The presence of singlet and triplet configurations as well as doubly excited and autoionizing states leads to irregularities in the spectra of such elements, which may be retraced in the pressure shift and broadening of Rydberg states of group II elements.

To that purpose, we have performed measurements of the pressure

shift and broadening due to noble gases of 5sns $^1S_0$, 5snd $^1D_2$ and 5s nd $^3D_2$ Rydberg states of ^{88}Sr I in the range of high ($35 \leq n \leq 150$)[4] and intermediate ($8 \leq n \leq 25$)[15] quantum numbers by means of Doppler-free two-photon excitation, thermionic detection and comparison with a molecular I_2 frequency standard[16]. We have shown that the pressure shifts and broadenings of highly excited Rydberg states behave similarly for group I and group II elements, and that low energy electron scattering lengths for all noble gases can be evaluated with good accuracy, and dipole polarizabilities with reasonable accuracy.

In the range of intermediate quantum numbers, large resonant inelastic contributions caused by collisionally induced state mixing can be observed[11,6]. The pressure shift and broadening show striking differences between the singlet and triplet states as shown e.g. in Fig.1 and (for the rates) in Fig.3. Broadening resonances of singlet states at n=14 and n=16 (see Fig.2) can be correlated to nearby 5d12f $^{1,3}F_3$ and 5d14f $^{1,3}F_3$ levels[11], while in the triplet series only the 5s15d $^3D_2$ is strongly broadened due to near-degeneracy with 5d13f $^{1,3}F_3$ (Fig.4). Recent theoretical approaches including a multichannel quantum defect treatment seems a promising way to describe these resonances in terms of collisonal induced state mixing.[14,17]. For n - values above 20, triplet states are significantly less shifted and broadened compared to singlet states. Despite local deviations due to inelastic processes, this picture suggests a subtle but global influence of the total spin on the pressure shift and broadening of a Rydberg state, up to now not discussed by theory.

REFERENCES

1. *Rydberg States of Atoms and Molecules*, edited by R. F. Stebbings and F. B. Dunning (Cambridge University Press, Cambridge, 1983)
2. N. Allard and J. Kielkopf, Rev. Mod. Phys. 54, 1103 (1982)
3. D.C. Thompson, E. Kammermayer, B.P.Stoicheff and E.Weinberger, Phys. Rev. A 36, 2134 (1987)
4. K.-D.Heber, P.J.West and E.Matthias, Phys. Rev. A 37, 1438 (1988)
5. K.S. Bhatia,D.M Bruce and W.W. Duley, Optics Comm. 53, 302 (1985)
6. *Atomic Collisions and Spectra*, by U. Fano and A. R. P. Rau (Academic Press, London, 1986)
7. E. Fermi, Nuovo Cimento 11, 157 (1934)
8. A. Alekseev and I. I. Sobel'man, Sov. Phys. - JETP 22, 882 (1965)
9. A. Omont, J. Phys. (Paris) 38, 1343 (1977)
10. D. C. Thompson, E. Weinberger, G. - X. Xu and B. P. Stoicheff, Phys. Rev. A 35, 690 (1987)
11. K.H.Weber and K.Niemax, Z. Phys. A 307,13(1982); A 309, 19 (1982)
12. F.Gounand, J.Szudy, M.Hugon, B.Sayer and P.R.Fournier, Phys. Rev. A 26, 831 (1982)
13. B. Kaulakys, J. Phys. B 17, 4485 (1984) and B.P.Kaulakys, Sov. Phys. JETP 64 (2), 229 (1986)
14. K. Ueda, J. Quant. Spectrosc. Radiat. Transfer 33, 77 (1985)
15. K.-D. Heber,P.J. West and E. Matthias, J.Phys.D: 21,63-66 (1988)
16. H. Gerhardt *et al*. Appl. Phys. 22, 361 (1980)
17. N. Y. Du and C. H. Greene, Phys. Rev. A 36, 971 (1987)

LINE SHAPE VARIATIONS OF SPIN-FORBIDDEN TWO-PHOTON TRANSITIONS *

H.R.Xia, J.W.Xu and I.S.Cheng
Department of Physics, East China Normal University
Shanghai 200062, People's Republic of China

The detailed features of Doppler-free line shapes of molecular spin allowed equal-frequency two-photon transitions have been carefully studied /1-3/. The regularities of the line shape variations in the aspects of total intensity of a two-photon absorption line, the ratio of the Doppler-free peak to its Doppler-broadened background , and the symmetry of their composed profile in the dependences on the offset value of an effectual intermediate enhancing level, on laser power and on the versions of experimental setup have been demonstrated /2,3/.

Recently we have found many new line shapes during the studies of molecular spin-forbidden two-photon transitions, which can neither be explained by the previous obtained expressions for a two-photon transition in a three-level system nor be explained by the general formula of the two-photon excitation probability with the simple summing up of enhancing factors over multiple intermediate levels /4-7/. However they show good agreement with the formulas derived from semiclassical theory for a four-level system, which is introduced for simulating a two-photon transition, for example, from an initial level a in a singlet state to a final level c in a triplet state, enhanced by a pair of near-resonant singlet-triplet mixing levels b_1 and b_2 as illustrated in Fig.1.

The experimental setup was similar to that of previous studies /2,8/. CR-599-21 single frequency scanning laser was operated at red region with DCM dye solution. A stainless steel cross oven was heated upto around optimum temperature for the interesting observations (about 450° C) without buffer gas. While two laser beams were counterpropagating along axial arms of the oven, the two-photon excitation signals were detected at the side windows of the oven by two photomultipliers behind narrow band interference filters for separately monitoring the characteristic fluorescence bands from the upper triplet state and the intermediate states.

Some of the observed line shapes are shown in Fig.2, where for clarity the Doppler-free peaks at $(\omega_{ac}/2)_i$ of the indiviually recorded traces have been moved to be aligned in a vertical line. The symbols Δ_1 and Δ_2 respect to the offsets of the intermediate levels b_1 and b_2 in Fig.1. We were surprised to find that there are opposite directions of the Doppler-free to Doppler-broadened peak-ratio reducing down to below 1 depending on the offsets, rather than one as in three-level case where the peak-ratio is towards an asymptotic value of $(\Delta\nu_D/\Delta\nu_h)$ for $\Delta>\Delta\nu_D$ /2/. The two reducing directions are pointed out by two short vertical arrows at the right side of the traces in Fig.2. In fact, here the upward arrow reasonably presents a similar variation regularity with that of spin-allowed case of three-level system as only one out of two enhancing levels is dominant. The downward

arrow, however, provides the new results observed in the special cases of two-photon transitions in four-level schemes where a pair of mixed intermediate levels with comparable magnitudes of the offsets but in opposite signs. For example, the trace f in Fig.2 remarkably shows the Doppler-free line shape of a two-photon absorption transition without a Doppler-free peak !

The upward direction of DF/DB decreasing therefore can be explained on account of the gradually increasing of the negative contribution of sixth order corrections to the lowest order solution of the density matrix element as Δ decreasing to finally result in such a line shape composed of a seriously reduced Doppler-free peak sitting on the top of its quite symmetric Doppler-broadened background in the case of $\Delta << \Delta\nu_D$ /3/. The downward direction of DF/DB decreasing is explained by the semiclassical calculations taking into account the new enhancing channels introduced by the quantum superposition of the mixed intermediate states. These new channels can be briefly expressed as

$$\rho_{aa}^{(0)} \rightarrow \rho_{ai}^{(1)} \rightarrow \rho_{ac}^{(2)} \rightarrow \rho_{jc}^{(3)} \rightarrow \rho_{cc}^{(4)} \qquad (1)$$

$$\rho_{aa}^{(0)} \rightarrow \rho_{ai}^{(1)} \rightarrow \rho_{ij}^{(2)} \rightarrow \rho_{jc}^{(3)} \rightarrow \rho_{cc}^{(4)} \qquad (2)$$

where $i,j=b_1$ or b_2 with $i=j$ in the contrast with that of $i=j$ for independent multiple enhancing levels. The new excitation channels create the kind of enhancing factors as

$$\rho_{cc}^{(4)} \propto \left(\frac{1}{\left|\Delta_{ab_1}\right|^2} + \frac{1}{\left|\Delta_{ab_2}\right|^2} - \frac{(\Delta_1 - \Delta_2)^2 + (\gamma_{ab_1} - \gamma_{ab_2})^2}{\left|\Delta_{ab_1}\right|^2 \left|\Delta_{ab_2}\right|^2} \right) \qquad (3)$$

Where $\Delta_{abi} = (\omega - \omega_{abi} + k\,v) + i\,\gamma_{abi}$. The formula obviously shows that the opposite signs of the offsets Δ_1 and Δ_2 can provide negative terms which result in by the destructive interference of the two-photon excitation probability, reducing the signal most seriously at its Doppler-free peak from the side-distributed Doppler-broadened signals at the distances corresponding to the relative offsets of the enhancing levels. The detailed theoretical analyses and computer fittings of the observed traces will be published elsewhere /9/.

The application potential of this study is clear. On one hand, it directly provides the hyperfine structure of the final level in the molecular forbidden electronic states (e.g. multiple Doppler-free peaks in Fig.2.b) without the influence of the splittings of the intermediate levels; On the other hand it reveals the relative positions of the relevent levels, where the interval between the pair of intermediate mixing levels and its variation by the experimental conditions is difficult to measure.

*Project supported by the National Natural Science Foundation of China

References:

1. J.P.Woerdman and M.F.H.Schuurmans, Opt. Commun. 21, 243 (1977);
2. H.R.Xia, G.Y.Yan and A.L.Schawlow, Opt. Commun. 39 , 153 (1981);
3. G.Y.Yan and H.R.Xia, Scientia Sinica (Series A), 28, 504 (1985);
4. L.S.Vesilenko, V.P.Chebotayev and A.V.Shishayev, Zh. Eksp. Teor. Fiz. Pis'ma 12, 161 (1970);
5. F.Biraben, B.Cagnac and G.Grynberg, Phys. Rev. Lett. 32, 643 (1974);
6. M.D.Levenson and N.Bloembergen, Phys. Rev. Lett. 32, 645 (1974);
7. T.W.Hansch, K.Harvey, G.Meisel and A.L.Schawlow, Opt. Commun. 11, 50 (1974);
8. H.R.Xia, L.S.Ma, J.W.Xu, M.Yuan and I.S.Cheng, paper submited to Opt. Commun.
9. J.W.Xu, H.R.Xia and I.S.Cheng, to be published

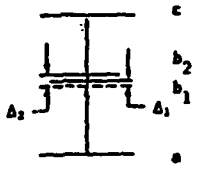

Fig.1 Two-photon transition in a four-level system

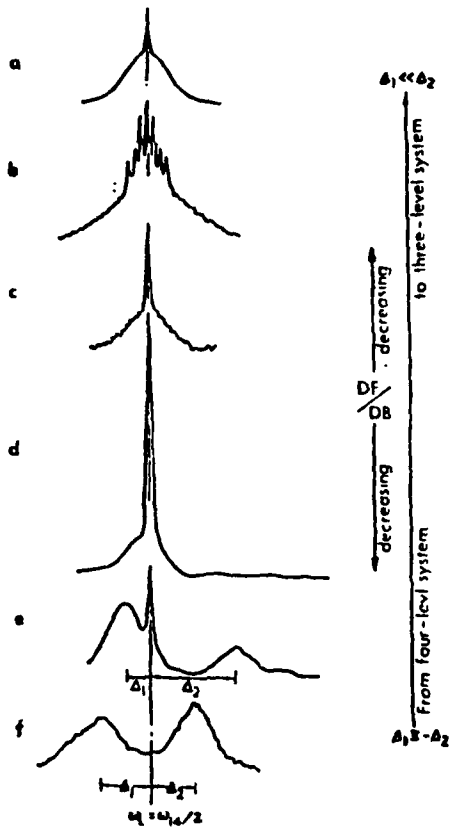

Fig.2 Two-photon line shape variations from (a) to (f) caused by the gradually increasing of destructive interference effects out of two near-resonant enhancing levels

HIGH RESOLUTION RESONANCE - ENHANCED DISSOCIATION SPECTROSCOPY OF CHLOROBENZENE CATION PREPARED BY MPI

X. Ripoche, F. Morlet-Savary, I. Dimicoli,
F. Piuzzi, J. Le Calvé, R. Botter

CEA - CEN Saclay, IRDI/DESICP, Département d'étude des Lasers et de la Physico-Chimie, 91191 Gif sur Yvette CEDEX, FRANCE

ABSTRACT

The well-resolved absorption spectrum of a large non-radiative aromatic ion like chlorobenzene has been obtained by the method of resonance-enhanced multiphoton dissociation (REMPDI). The cations are prepared in the ground electronic state with well-defined rovibrational energy excess by resonance-enhanced two-photon ionization (R2PI). The light of a second laser excites the ions through a (1+1) process into predissociative states which dynamics has been first studied. The wavelength dependence of the fragment ion yield reflects the spectroscopy of the intermediate ionic state reached by the first photon. In this work, we present the completely vibrationally resolved spectrum of the $\tilde{B} \leftarrow \tilde{X}$ transition of φCl^+. For the first time the rotational contour of the vibronic bands of R2PI-prepared ions has been calculated. The comparison with the experimental band shapes has brought additional arguments for the assignement of the spectral features.

INTRODUCTION

Ion spectroscopy can bring interesting information about ionic molecular species if high resolution is achieved. There exists a large variety of spectroscopic techniques which have more or less strong limitations[1,2]. In principle only laser induced fluorescence (LIF) experiments[2,3] circumvent both resolution and congestion problems but this method works only on radiative states. Multiphoton photodissociation spectroscopy[4-6], in which fragment ions are the detected species, has provided an important supplement of this technique because of : i) the possibility of observing other than fluorescing ionic states ; and ii) the ability of mass selective preparation and mass selective detection. Moreover, when compared to conventional one-photon dissociation spectroscopy the restriction to only predissociative states implying a narrow energy range of applicability has been removed.

In this paper we present the first well-resolved spectrum of a large non-radiative ion like chlorobenzene obtained by this method. The cations are formed by resonance-enhanced two-photon ionization (R2PI) using a first laser. The light of a second laser excites the ions through a (1+1)-process into predissociative states. Therefore gas phase ion absorption spectra can be measured by monitoring its dissociation. An important advantage of the R2PI method for ion production, compared to conventional ones such as electron impact or

plasma discharge, is that using "soft" ionization conditions mainly the parent ion can be formed and allmost all perturbing processes due to fragmentation can be prevented. The use of shift in time and space between the first and second laser pulses as well as of time-of-flight mass analyser enables a complete discrimination of unwanted photo- processes[6] . Another advantage is that ions in selected (even single) vibronic states can be prepared. Indeed the room-temperature vibrational population of the neutral molecule is not transfered by the multiphoton-ionization process. Concerning the rotational energy, the ion is formed with only a restricted part of the original Boltzmann distribution depending on the laser spectral width and the rotational contour of the resonant transition in the molecule. It can be noted here that given the rotational state density for such a asymmetric top molecule even with the highest possible resolution (0.01 cm^{-1}) and by employing a supersonic beam for cooling the neutrals there is no hope of resolving individual rotational transitions. What is observed (in the ionic vibronic band) is an intensity contour with a characteristic shape.

We here wish to present new results obtained by the method of resonance-enhanced dissociation spectroscopy concerning the $\tilde{B} \leftarrow \tilde{X}$ forbidden transition of chlorobenzene cation and in particular about the rotational band contour analysis of vibronic transitions in non-thermal ionic systems.

EXCITATION AND IONIZATION PATHWAYS OF CHLOROBENZENE

The energy level diagram for the chlorobenzene molecule and its ion is shown in fig. 1. Chlorobenzene, a molecule of C_{2v} symmetry, has 30 vibrational modes and its spectroscopy in the ground and first excited states has been widely investigated[7,8]. In our experiment the cation is prepared by resonant (1+1)-multiphoton ionization with the laser wavelength λ_1 fixed on the origine transition of the first excited neutral S_1 state. In this case only few totally symmetric A_1 vibrational modes of the ionic ground state can be populated, the maximal energy excess being about 980 cm^{-1}. By setting the laser wavelength on different vibronic bands of the $S_1 \leftarrow S_0$ transition the rovibrational energy of the φCl^+ cation can be varied. The φCl^+ cation has four bound electronic states within approximately 4 eV, the $\tilde{B}$ state being related to excitation of the in-plane ($4b_2$) lone pair of chlorine. The photoelectron spectrum [9] indicates the position of these states. The experimental threshold for the first fragmentation pathway of the cation ($\varphi^+ + Cl$, 3.81 eV above the ionization energy of φCl) involving simple breaking of the C-Cl bond is indicated by a dashed line. The rate constant of the one-photon (UV) dissociation process as a function of the internal energy of the ion has been measured by analysis of the asymmetric form of the fragment ion peak[10]. When two or more photons (visible) of the second laser λ_2 are absorbed by the ion, excitation also occur above this threshold. In this case, one can expect that the fragment ion yield versus wave-

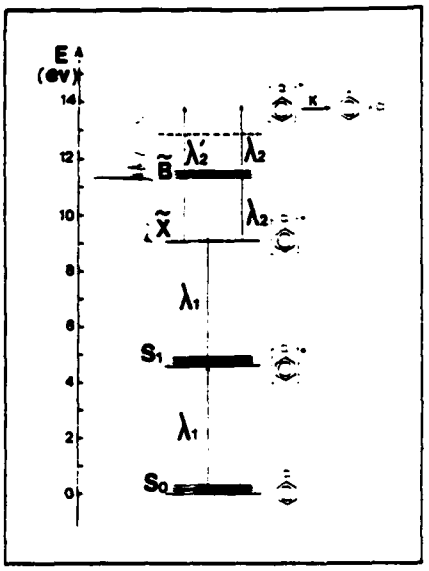

Figure 1 Schematic energy diagram of chlorobenzene.

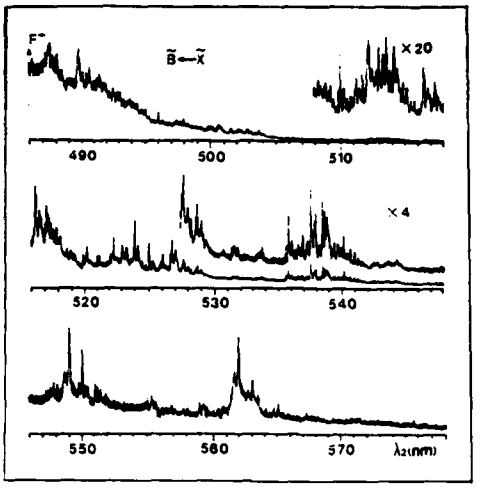

Figure 2 REMPDI- spectrum of the φCl^+ $\tilde{B} \leftarrow \tilde{X}$ transition.

length will reveal the spectrum of states reached by the first photon. The arguments allowing us to believe that the obtained spectra concern only a λ_2-photon absorption process of φCl^+ ions formed by the first laser has been discussed in detail previously[6]. The structured spectrum observed by varying λ_2 between 480 and 580 nm has been assigned to the $\tilde{B}(^2B_2) \leftarrow \tilde{X}(^2B_1)$ transition. This transition is forbidden in the C_{2v} symmetry group, which is the symmetry reasonably admitted for both $\tilde{X}$ and $\tilde{B}$ states. The spectra observed occur through vibronic interactions between the $\tilde{B}$ and near lying $\tilde{C}$ states. The coupling can be induced by vibrational modes of A_2 symmetry.

RESULTS AND DISCUSSION

The resonance-enhanced multiphoton dissociation spectrum of the $\tilde{B} \leftarrow \tilde{X}$ transition of φCl^+ is shown in fig. 2. A simple consideration of this spectrum reveals several intense progression and sequence bands. The tentative vibrational analysis, based on the knowledge of the vibrational frequencies of the ground and excited states of the neutral chlorobenzene, has allowed the following conclusions[6] :

- The $\tilde{B} \leftarrow \tilde{X}$ electronic transition is forbidden. The deduced location of the origin transition is at about 554.5 nm.

- Two of the three possible vibrational modes of A_2 symmetry (16a and 10a) have been supposed to participate in the combination modes with some vibrations of A_1 symmetry (6a, 1 and 7a). The frequencies of these modes in the ground and excited ionic states have been determined.
- The observation of sequencies up to v" = 2 level of the 6a mode (420 cm^{-1}) is consistent with the maximal internal energy of φCl^+ in our experiment.

However the complexity of the REMPDI-spectrum is also due to rotational structure. As mentioned above, the ions have been prepared with a restricted rotational energy distribution. This rotational excitation varies when the first wavelength is scanned to different positions of the rotational envelop of the 0_0^0 $S_1 \leftarrow S_0$ transition. The observed changes in the structure of the ionic vibronic transition bands between 526 and 530 nm (sequence bands $6a\,{}^2_0 16a^1_0$, $6a^3_1\,16a^1_0$, $6a^4_2 16a^1_0$ and the overtone $16a^5_0$) for small variations of λ_1 have been assigned to different rotational excitations of the ground state ions.

In fact the shape of a rotational contour is strongly dependent on the rotational selection rules which are different for the different type of contours (A, B, C or hybrid as function of the direction

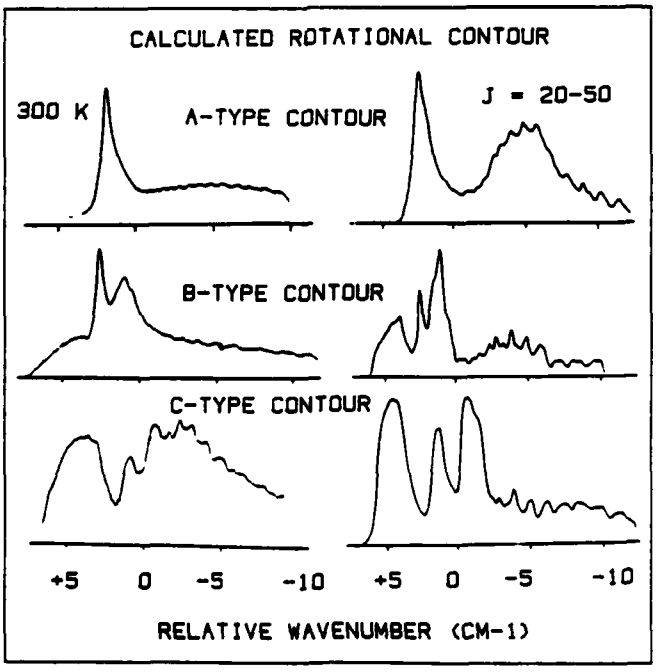

Figure 3 Calculated rotational band contours for two different rotational excitations of the chlorobenzene cation.

of the dipole moment relative to a rotational axis of the system) and on the changes of rotational constants (ΔA, ΔB, ΔC) from the ground- to the excited-state[11]. The shape of the contour depends moreover on the population of J, K_a and K_c rotational levels excited in the ion which population is not thermal for R2PI-prepared ions. Important changes in the shape can be expected as compared to conventional contours observed for room temperature ionic or neutral systems. This effect is illustrated on the fig. 3 for three types of contour and two different rotational excitations. The calculations has been performed using the program ASYROT with the spectroscopic perameters of the neutral molecule considered as near prolate symmetric rotor[11].

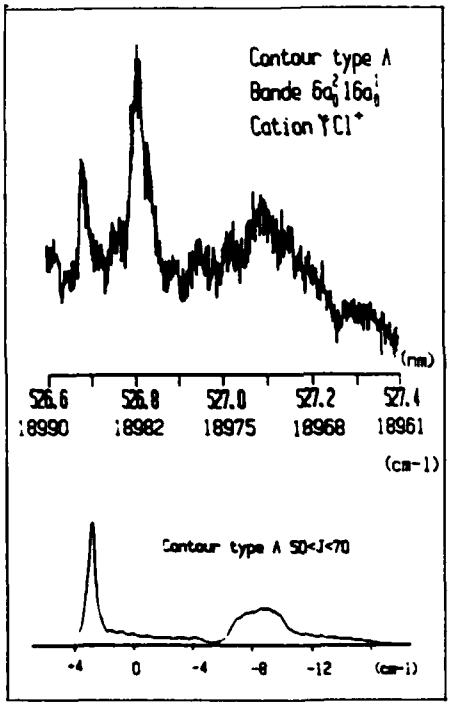

Figure 4 Experimental and calculated contour of the $6a_0^2 16a_0^1$ vibronic band in φCl^+.

In order to analyse the rotational structure of the present spectrum (the vibronic band at 526.9 nm for example) it was necessary to determine the ion rotational excitation and the type of contour. The ions have been formed with λ_1 fixed on the maximum of the $0_0^0 S_1 \leftarrow S_0$ transition and the excited rotational quantum numbers J in the ion have been estimated to lye between 50 and 70. Following our vibrational assignement an A-type contour is expected for the considered band. This hypothesis has been corroborated by the rotational contour calculations which will be discussed in details elsewhere[12]. The calculated A-type rotational contour for this J- range is shown on the fig. 4b. It consists of two peaks (one narrow and one broad)

separated by 10 cm^{-1}. On the same fig. 4a the measured contour of the sequence band $6a_0^2$ $16a_0^1$ mentioned previousely is shown. A possible explanation for the additional narrow peak is the existence of isotopic effect for this 6a vibrational mode. The necessary condition that no Cl isotopic effects exists on the $0_0^0 S_1 \leftarrow S_0$ transition has been checked. Both Cl isotopic ionic species are formed by the first laser. In fact two A-type contours are superposed, the blue shifted being due to the $\varphi\ ^{37}Cl^+$. The intensity ratio is in agreement with the natural abondance. An additional argument supporting the Cl isotope hypothesis is given by the presence of an isotopic peak in the $7a_0^1 10a_0^1$ vibronic band (7a, Cl-sensitive, 510.1 nm) and its absence in the $1_0^1 16a_0^1$ vibronic band (1, C-C twist, 524 nm).

CONCLUSION

The vibrationally well-resolved spectrum of the $\tilde{B} \leftarrow \tilde{X}$ forbidden electronic transition of the φCl^+ cation is reported. For the first time the rotational contour of ionic vibronic bands for R2PI-prepared ions has been calculated. Our work illustrates the high potentialities of this new spectroscopic method, in particular for the study of non-radiative states of large organic cations. The rotational band contour analysis has brought additional data wich agree with our initial tentative assignment[6]. The isotopic shifts of three totally symmetric vibronic transitions have been measured.

REFERENCES

1 . R.C. Dunbar, Gas phase ion chemistry, 2-3 (Academic Press, New York, 1979).
2 . V.E. Bondybey and T.A. Miller, Molecular ions : spectroscopy, strusture and chemistry (North-Holland, Amsterdam, 1983) p. 125.
3 . J.P. Maier, J. Electron. Spectry. 40, 203 (1986).
4 . R. Weinkauf, K. Walter, U. Boesl and E. W.Schlag, Chem. Phys. Lett. 141, 267 (1987).
5 . J.A. Syage and J.E. Wessel, J. Chem. Phys. 87, 3313 (1987).
6 . X. Ripoche, I. Dimicoli, J. Le Calvé, F. Piuzzi and R. Botter, Chem. Phys. 124, 305 (1988).
7 . H.D. Bist, V.N. Sarin, A. Ojha and Y.S. Jain, Appl. Spectry. 24, 292 (1970).
8 . Y.S. Jain and H.D. Bist, J. Mol. Spectry. 47, 126 (1973).
9 . A.W. Potts, M.L. Lyus, E.P.F. Lee and G.H. Fattahallah, J. Chem. Soc. Faraday II 76, 556 (1980).
10 . X. Ripoche, I. Dimicoli, F. Piuzzi and R. Botter, in preparation.
11 . T. Cvitas and J.M. Hollas, Mol. Phys. 18, 101 (1970).
12 . F. Morlet-Savary et al., in preparation.

The Absolute Vibrational Numbering and Molecular Constants of the Na_2 $2^3\Pi_g$ and $1^3\Delta_g$ States

X. Xie* and R. W. Field
Department of Chemistry, Massachusetts
Institute of Technology, Cambridge, MA 02139

L. Li*, A. M. Lyyra, J. T. Bahns† and W. C. Stwalley
Center for Laser Science and Engineering,
University of Iowa, Iowa City, IA 52242-1294

ABSTRACT

Twenty additional $2^3\Pi_g$ vibrational levels and 5 additional $1^3\Delta_g$ vibrational levels of Na_2 below the previously reported levels have been observed by Perturbation Facilitated Optical-Optical Double Resonance (PFOODR) spectroscopy. Absolute vibrational numberings and molecular constants of these two states are determined.

Thirty-six vibrational levels of the $2^3\Pi_g$ state and ten vibrational levels of the $1^3\Delta_g$ state of Na_2 have been previously observed by using Perturbation Facilitated Optical-Optical Double Resonance (PFOODR) spectroscopy with only relative vibrational numbering[1,2]. Because these levels are very high vibrational levels of the $2^3\Pi_g$ and $1^3\Delta_g$ states and also because the $2^3\Pi_g$ levels are strongly perturbed by the $3^3\Pi_g$ state, absolute vibrational numberings and molecular constants had been very uncertain. We report here additional low vibrational levels observed by PFOODR, absolute vibrational numberings, and molecular constants of these two Rydberg triplet states.

The experimental set up is the same as reported in Refs. [1,2]. This time DCM and LD700 dyes were used for both pump and probe lasers.

Twenty additional low vibrational levels ($v = v^* - 67$ through $v^* - 63$ and $v^* - 58$ through $v^* - 43$, according to the previous relative v-numbering) of the $2^3\Pi_g$ state have been observed. No levels

* Permanent address: Dalian Institute of Chemical Physics, Dalian, People's Republic of China.
† Present address: Pacific Sierra Research Corporation, 12340 Santa Monica Blvd., Los Angeles, CA 90025.

were seen at the predicted $v = v^* - 68$ and $v^* - 69$ positions. An absolute vibrational numbering of $v^* = 67$ has been determined from the $2^3\Pi_g \rightarrow a^3\Sigma_u^+$ fluorescence. The resolved fluorescence spectrum from the $v = v^* - 67$ level has only one maximum (Fig. 1a), indicating that the upper level is a $v = 0$ level. The fluorescence spectrum from $v = v^* - 66$ level has two maxima (Fig. 1b), implying the upper level is $v = 1$, etc. The $v^* = 67$ from node counting has been confirmed by a comparison of the observed $2^3\Pi_g \rightarrow a^3\Sigma_u^+$ resolved fluorescence spectra with calculated spectra.

The newly observed low vibrational levels of the $1^3\Delta_g$ state are $v = v_x - 32$ through $v_x - 28$ according to the previous relative v-numbering. In order to determine the absolute v-numbering, resolved fluorescence from these low-v levels to the $b^3\Pi_u$ $v' = 0 - 10$ levels was observed. With $v_x = 33$, 34, 35, and 36, molecular constants for each assumed v_x could be fitted, hence RKR potential curves and $1^3\Delta_g - b^3\Pi_u$ Franck-Condon factors could be calculated. However, comparing the calculated Franck-Condon factors with the relative intensities of the observed $1^3\Delta_g \rightarrow b^3\Pi_u$ resolved fluorescence spectra, only $v_x = 35$ gives satisfactory agreement.

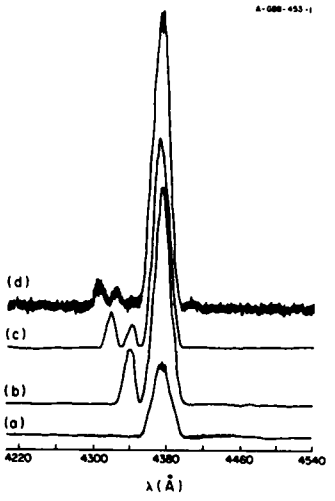

Figure 1. Resolved fluorescence spectra. The number of nodes that appear in these spectra provide the primary evidence for the vibrational assignments of the $2^3\Pi_g$ levels.

a) $2^3\Pi_{0g}$ $v = 0$, $J = 41e \rightarrow a^3\Sigma_u^+$
b) $2^3\Pi_{0g}$ $v = 1$, $J = 39e \rightarrow a^3\Sigma_u^+$
c) $2^3\Pi_{2g}$ $v = 2$, $J = 41e \rightarrow a^3\Sigma_u^+$
d) $2^3\Pi_{0g}$ $v = 3$, $J = 15e \rightarrow a^3\Sigma_u^+$

Table 1 gives the molecular constants of the $2^3\Pi_{0g}$ and $1^3\Delta_g$ states. From a preliminary fit to $\Omega = 0, 1, 2$ levels of $2^3\Pi_g$ $v = 2$, values for B_2 $(2^3\Pi_g) = 0.07412$ (10) cm^{-1} and $A_2 = 4.04$ (10) cm^{-1} were obtained. The B_e and R_e values appropriate for a $^3\Pi_g$ state and for comparison to ab initio values are therefore B_e $(2^3\Pi_g) = 0.07501$ (30) cm^{-1} and $R_e = 4.442$ (9) Å.

Table 1. Molecular constants of the $2^3\Pi_{0g}$ and the $1^3\Delta_g$ [a] states. All in cm^{-1} except R_e. 1σ uncertainties are in parenthesis.

	$2^3\Pi_{0g}$	$1^3\Delta_g$
T_e	28789.49 (6)	28 030.3 (4)
ω_e	94.35 (1)	131.01 (2)
$\omega_e x_e$	0.3760 (7)	0.4806 (14)
$\omega_e y_e$	0.00191 (2)	$1.457\ (40) \times 10^{-3}$
$\omega_e z_e$	$-0.134\ (2) \times 10^{-4}$	$-2.425\ (34) \times 10^{-5}$
B_e	0.07316 (23)	0.1227 (4)
α_e	$2.20\ (7) \times 10^{-4}$	$7.302\ (66) \times 10^{-4}$
D_e	–	$4.0\ (9) \times 10^{-7}$
R_e(Å)	4.477 (6)	3.457 (6)

[a] The rotational energy was fit to: $F_v(N) = B_vN(N+1) - D_vN^2(N+1)^2$

References

[1] Li Li and R. W. Field, J. Mol. Spectrosc. 117, 245-282 (1986).

[2] Li Li, Qingshi Zhu and R. W. Field, J. Mol. Spectrosc., in press.

OODR Fluorescence and Polarization Spectroscopy of K_2: Rydberg States and the $A^1\Sigma_u^+$ State

A. M. Lyyra[1,2], H. Wang[2], L. Li[3], W. T. Luh[4],
V. Zafiropulos[1] and W. C. Stwalley[1,2]
Center for Laser Science and Engineering
University of Iowa, Iowa City, IA 52242-1294

ABSTRACT

We have observed K_2 Rydberg electronic states of $^1\Delta_g$ and $^1\Sigma_g^+$ symmetry using CW optical-optical double resonance techniques in the energy range 28920 - 30050 cm^{-1} above the ground state minimum. Resolved fluorescence from the $^1\Sigma_g^+$ states to the $A^1\Sigma_u^+$ state allows us to observe the lowest ($v < 12$) vibrational levels of the $A^1\Sigma_u^+$ state. Using the polarization optical-optical double resonance technique we are able to observe $A^1\Sigma_u^+$ vibrational levels in the range $v = 21$ to 62. We are able to determine also the absolute vibrational numbering of one $^1\Delta_g$ Rydberg state. Major molecular constants are given for the $^1\Delta_g$ Rydberg state.

INTRODUCTION

The molecular Rydberg states are less well studied than those of atoms. Molecular hydrogen, H_2, is an exception due to its large rotational constant which made possible observation and detailed interpretation of its high lying Rydberg states before high resolution laser spectroscopic techniques were developed [1]. Schawlow et al. [2] demonstrated the potential of these techniques in their work on Na_2 Rydberg states. Since this early work, excellent experimental results have been reported for Li_2 and Na_2 [3-8]. Highly excited Rydberg states of K_2 near the ionization limit have been observed with unresolved rotational structure via two and three-photon ionization [9,10]. However, very little is known about the lower members of the Rydberg series. Doppler-free two-photon excitation into

[1] Also Department of Chemistry
[2] Also Department of Physics and Astronomy
[3] Dalian Insitute of Chemical Physics, Chinese Academy of Sciences, Dalian, People's Republic of China
[4] Present address: Department of Physics, Lehigh University, Bethlehem, PA 18015

Rydberg states in the energy region of 31000 - 32000 cm^{-1} has been reported by Engelke et al. [11]. Here we report our observation of Rydberg states of $^{39}K_2$ using CW sub-Doppler OODR fluorescence excitation spectroscopy in the 28920 - 30050 cm^{-1} region above the ground state minimum. Using laser-induced fluorescence from these Rydberg states to the $A^1\Sigma_u^+$ state we are able to observe the lowest levels of this state. Previously $A^1\Sigma_u^+$ molecular constants were given by Ross et al. [12]. These were based on observed levels v=12-18 and deperturbation of the data ($b^3\Pi_u \sim A^1\Sigma_u^+$). In this work we also use polarization OODR spectroscopy to extend the $A^1\Sigma_u^+$ potential beyond the known v=12-18 region [12].

EXPERIMENTAL

Potassium vapor is generated in a five arm stainless steel cross heatpipe which allows for detection of the fluorescence perpendicular to the laser beam. The heatpipe is operated at 1 - 2 Torr pressure. Figure 1 shows the excitation schemes for studying (a) the Rydberg states and the v<12 region of the $A^1\Sigma_u^+$ state and (b) the v>18 region of the $A^1\Sigma_u^+$ state. OODR fluorescence excitation, OODR resolved fluorescence and OODR polarization spectroscopy are used, respectively. Single mode tunable dye laser (CR 699-29) pumped by krypton ion laser is used with LD 700 and LD 800 dyes for the probe laser, and CR 599-21 or CR 699-29 dye laser pumped by argon ion laser is used with DCM dye for the pump laser. Laser-induced fluorescence of iodine is used for absolute wavelength calibration. For the LD 800 dye region, neon lines are used for calibration from optogalvanic spectroscopy using a hollow cathode lamp. This dye was used for observation of $A^1\Sigma_u^+$ levels from v=21 to 41. LD 700 was used for observation of levels v=42 to 62.

In the OODR fluorescence excitation experiments the pump and probe beams (modulated at f_1 and f_2, respectively) are combined using a dichroic mirror that passes $\lambda < 6900$ Å and reflects $\lambda > 7000$ Å. The chosen $B^1\Pi_u$ intermediate levels are $B^1\Pi_u$ v'=0, J'= 14e, v'=2, J'=14e,f and v'=4, J'=55e,f. These levels are excited from ground state levels $X^1\Sigma_g^+$ v"=0, 1 and 4, respectively, which have large Franck-Condon factors with v'=0, 2 and 4 levels of the $B^1\Pi_u$ state. When the pump laser is tuned to a specific B←X transition, the probe laser is scanned and the OODR fluorescence to low vibrational levels of the $A^1\Sigma_u^+$ state is detected with a filter-PMT-lock-in system at frequency f_1-f_2. The OODR signals via the chosen

intermediate level are identified from those via unexpected intermediate levels by using pump laser excitation from $X^1\Sigma_g^+$ v", J" = J'-1 and J"=J'+1 levels and scanning the probe for both cases. Only those signals appearing in both spectra with identical frequencies and intensities are from the selected intermediate level. The OODR fluorescence was also dispersed using a 0.8 m double monochromator (Spex 1404).

In the OODR polarization spectroscopy experiments a circularly polarized pump beam (modulated at frequency 1.1 kHz) is crossed at a small angle with the polarized counterpropagating probe beam in the center of the heatpipe. The probe propagates through crossed polarizers. The pump beam causes partial orientation of the K_2 molecules and if the probe beam now interacts with the same molecules as the pump beam, its polarization is altered from linear to slightly elliptic and thus some light can pass through the second polarizer to the detector. The pump beam modulates the population of the initial level and for assignment purposes the OODR polarization signals corresponding to the chosen pump transition are identified from other signals by a similar procedure as described above for the OODR fluorescence excitation technique (J'=J"+1 and J'=J"-1 pumping). Ground state levels v"=5, J"=19, v"=8, J"=13, 19, 45 and v"=10, J"=13, 19 are chosen for $A^1\Sigma_u^+$ levels v=42-62 as pump transitions with $B^1\Pi_u$ levels which have good Franck-Condon factors with these levels. For the $A^1\Sigma_u^+$ levels v=21-41, several pump transitions are used.

RESULTS AND DISCUSSION

From $B^1\Pi_u$ intermediate levels, states of $^1\Sigma_g^+$, $^1\Sigma_g^-$, $^1\Pi_g$ and $^1\Delta_g$ symmetry can be reached. However, our fluorescence detection from Rydberg states to the $A^1\Sigma_u^+$ state favor $^1\Sigma_g^+$ and $^1\Pi_g$ states. More than 100 levels in the energy region of 28920 - 30050 cm^{-1} are observed. Among them, 42 are assigned to a $^1\Delta_g$ state. The $^1\Delta_g$ state is a "dark" state when fluorescence to the $A^1\Sigma_u^+$ state is observed. When the probe excites $^1\Delta_g$ levels, we observe fluorescence from collisionally populated ($^1\Delta_g \rightarrow {}^1\Sigma_g^+$) $^1\Sigma_g^+$ levels to the $A^1\Sigma_u^+$ state. The electronic assignment of the Rydberg states is based on the excitation spectral pattern as well as the resolved fluorescence spectrum to the $A^1\Sigma_u^+$ state. $^1\Sigma_g^+$,v $\leftarrow B^1\Pi_u$ v',J'e excitation consists of a P-R pair of lines and $^1\Sigma_g^+$,v $\leftarrow B^1\Pi_u$ v',J'f excitation consists of a Q line. $^1\Pi_g/^1\Delta_g$ v $\leftarrow B^1\Pi_u$ v',J'e/f transitions contain P, Q and R

lines, although the $^1\Delta_g$ state cannot directly radiate to $A^1\Sigma_u^+$. Using the $A^1\Sigma_u^+$ state as the final state allows us to study collisional energy transfer involving Rydberg states. Details of these collisions will be reported later. Table I lists the molecular constants of the $^1\Delta_g$ state. The vibrational numbering, on which these constants are based, was determined by a comparison of the calculated Franck-Condon factors of the $^1\Delta_g \leftarrow B^1\Pi_u$ system with observed spectral intensity patterns. Only the Franck-Condon factors calculated from the v-numbering represented by the molecular constants of Table I give good agreement with observations. The results will be presented in more detail in a forthcoming paper [13].

Table I. Molecular constants of the $^1\Delta_g$ Rydberg state. The reported error is 1σ.

Dunham coefficients [cm^{-1}]	
Y_{00}	29349.582(8)
Y_{10}	70.8690(93)
Y_{20}	-0.3178(38)
Y_{30}	-0.0125(4)
Y_{01}	0.04338(4)
Y_{11}	$-0.244(2)\times10^{-3}$
Y_{02}	$-0.676(80)\times10^{-7}$
R_e	4.46 Å

Vibrational numbering and molecular constants for the $A^1\Sigma_u^+$ state are available from Ross et al. [12] based on observations covering v=12-18 levels. This experiment allows us to confirm the vibrational numbering of Ross et al [12] since no vibrational levels below the predicted v=0 level are observed and all vibrational levels v=0 to 11 are observed. Using the polarization OODR scheme we observe levels v=21 to 62. The analysis of data is in progress and the molecular constants and the $A^1\Sigma_u^+$ RKR curve based on constants by Ross et al. [12] for the v=12-18 range and our data for the regions v=0 to 12 and v=21 to 62, will be published shortly [14]. A quick comparison of the molecular constants of the $^1\Delta_g$ Rydberg state [12] and the $A^1\Sigma_u^+$ state indicates that the $A^1\Sigma_u^+$ state is surprisingly similar to the Rydberg state.

a)

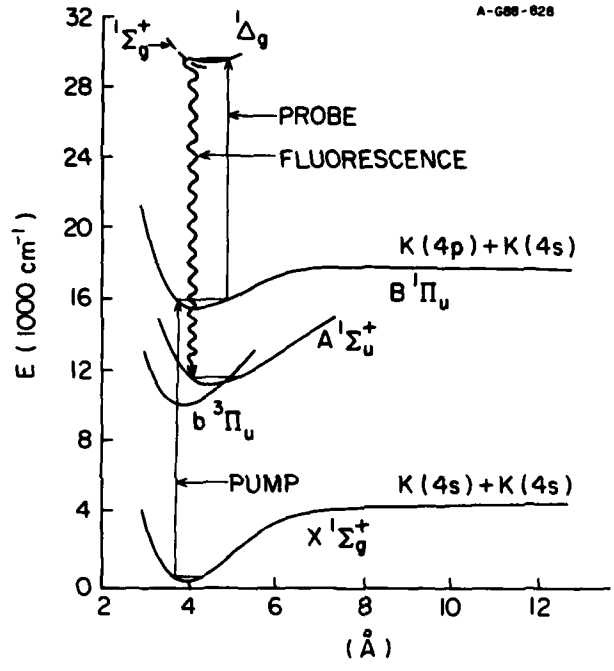

b)

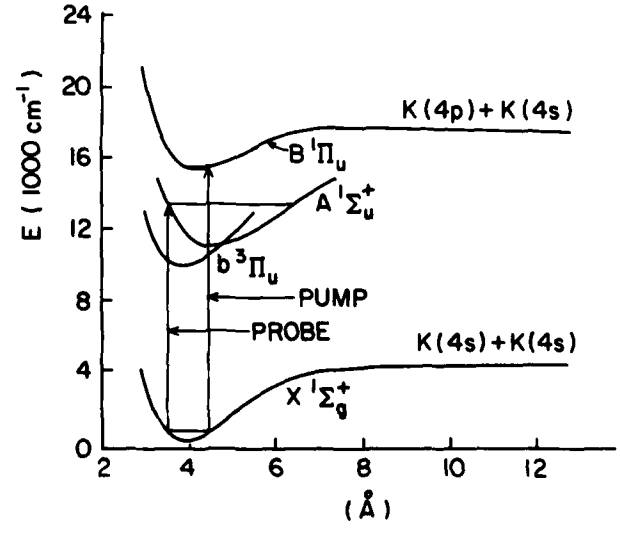

Figure 1. A Schematic for:

a) OODR fluorescence spectroscopy
b) OODR polarization spectroscopy

ACKNOWLEDGMENTS

We gratefully acknowledge the support of this work by NSF (CHE-87-17954). We also thank Professors R. W. Field and D. D. Konowalow for helpful discussions.

REFERENCES

1. G. Herzberg and Ch. Jungen, J. Mol. Spectrosc. 41, 425 (1972).
2. N. W. Carlson, A. J. Taylor and A. L. Schawlow, Phys. Rev. Lett. 45, 18 (1980); N. W. Carlson, A. J. Taylor, K. M. Jones and A. L. Schawlow, Phys. Rev. A 24, 822 (1980).
3. R. A. Bernheim, L. P. Gold and T. Tipton, J. Chem. Phys. 78, 3635 (1983).
4. S. Martin, J. Chevaleyre, M. Ch. Bordas, S. Valignat, M. Broyer, B. Chabaud and A. Hoareau, J. Chem. Phys. 79, 4132 (1983).
5. R. Bombach, B. Hemmerling and W. Demtröder, Chem. Physics 121, 439 (1988).
6. B. Hemmerling, R. Bombach and W. Demtröder, J. Chem. Phys. 87, 5186 (1987).
7. L. Li and R. W. Field, J. Mol. Spectrosc. 117, 245 (1986).
8. X. Xie and R. W. Field, J. Mol. Spectrosc. 117, 228 (1986).
9. A. F. J. van Raan, J. E. M. Haverkort, B. L. Mehta and J. Korving, J. Phys. B, 15, L669 (1982).
10. M. Broyer, J. Chevaleyere, G. Delacretaz, S. Martin and L. Wöste, Chem. Phys. Lett. 99, 206 (1983).
11. F. Engelke and V. Schühle, Chem. Phys. Lett. 123, 289 (1986).
12. A. J. Ross, P. Crozet, C. Effantin, J. d'Incan and R. F. Barrow, J. Phys. B. 20, 6225 (1987).
13. H. Wang, L. Li, A. M. Lyyra and W. C. Stwalley, to be submitted.
14. A. M. Lyyra, W. T. Luh, L. Li, H. Wang and W. C. Stwalley, to be submitted.

Na_2 $1^3\Sigma_u^+ \rightarrow 1^3\Sigma_u^+$ LASING WITH PEAK AROUND 892.0nm*

Wang Qi, Lu Zhiwei, Liu Wei, Wu Tao, Xing Da and Ma Zuguang
Institute of Opto-Electronics, Harbin
Institute of Technology, Harbin, China

ABSTRACT

The first laser oscillation of Na_2 $1^3\Sigma_u^+ \rightarrow 1^3\Sigma_u^+$ transition has been obtained by using UV dye laser in the range of 337.0nm to 342.0 nm. The cavity effect, small beam divergence (7 mrad), the pump energy threshold ($\sim 80\mu J$) and the narrowing linewidth have been observed in this experiment.

INTRODUCTION

In 1980, D.D.Konowalow[1] first suggested that the $1^3\Sigma_u^+ \rightarrow 1^3\Sigma_u^+$ transition in Na_2 may be used as a source of tunable, high-power lasers. In 1981, Ma Zuguang[2,3] first observed the emission spectra of the lowest triplet transition under the condition of the UV pumping laser and the lower buffer gas pressures. Ref. [4-8] also observed this emission spectra in different conditions, respectively.

In this paper, the $1^3\Sigma_u^+ \rightarrow 1^3\Sigma_u^+$ laser oscillation pumped by UV laser, to our knowledge, is first reported.

EXPERIMENTAL SETUP AND OPERATING CONDITIONS

The experimental setup is shown in Fig.1 in which the reflectivities of M_1 and M_2 are R_1=98% and R_2=85%, respectively. Fig.2 shows the fluorescent spectra of Na_2 pumped by 339.57nm without cavity (M_1 and M_2). The continuous spectra centred at 892 nm demonstrate the lowest triplet transition.

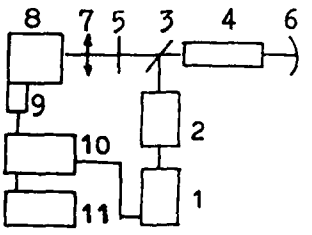

Fig.1 Experimental setup
1. XeCl excimer laser (EMG201MSC)
2. PTP dye laser (FL2002E)
3. dichroic mirror M_3
4. heatpipe
5. cavity mirror M_2
6. cavity mirror M_1
7. lens
8. monochrometer (SPEX1780)
9. PMT (RCA8852)
10. Boxcar (M162, M165)
11. recorder (K200)

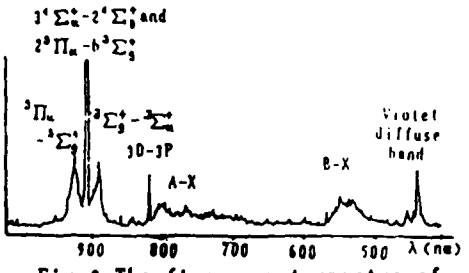

Fig.2 The fluorescent spectra of Na_2 pumped by 339.57nm

★ Supported by the Science Fund of the Chinese Academy of Science.

The operating conditions to obtain the laser oscillation are, the optimum temperature of about 710℃; the optimum buffer gas (Ar) pressure of 5-6torr and the pumping wavelength range of 337.0--342.0 nm in which these are several resonant pumping regions.

CHARACTERISTICS OF LASER OSCILLATION

(1) cavity effect

The cavity composed of M_1 and M_2 (in Fig.1) is adjusted in order, so we obtain the laser output. As the mirror M_1 is detuned, the output intensity decreases rapidly (Fig.3, curve 1 and 2 shows the output intensities when the cavity is detuned and is in order, respectively) and then completely disappears. The output intensity is sensitive to the mirror M_1.

When the mirror M_2 is detuned no more than 3～4mrad, the output intensity decreases to about 1/4. Let I_0 be the laser output intensity as the cavity is in order and I_1 be the output intensity as M_2 is detuned. Only consider that the oblique mirror M_2 will cause the light out of the cavity and make the output intensity decrease, the calculated result is $I_0/I_1=1.4$. While our experimental result is $I_0/I_1=4$. This indicates that the light is amplificated when it travels to and fro in the cavity, so we say that the laser oscillation is really generated in our case.

(2) beam divergence

Fig.4 shows the space distribution of the beam intensity. The divergence angle is 6.9 mrad.

(3) threshold effect

The threshold energy is 70～80μJ in our experiment.

(4) the narrowing of the spectral width

In Fig.5, curve 1 shows the fluorescent spectral width while curve 2 shows the laser oscillation spectral width, which illustrates the spectral width decreases to about 1/2. This is just one of the important mark of the stimulated emission.

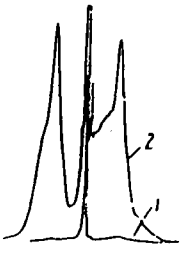

Fig.3 cavity effect

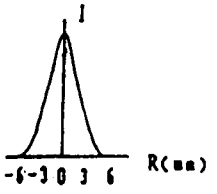

Fig.4 The beam divergence

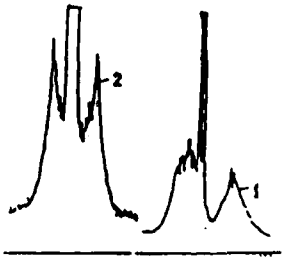

Fig.5 The spectral width

PUMPING MECHANISM

Fig.6 shows the potential energy curves of Na_2[9]. When pumping wavelength is in the range of 337.0-342.0 nm, the probable way of generating Na_2 $1^1\Sigma_u^+ \rightarrow 1^1\Sigma_g^+$ transition is roughly and tentatively interpreted as follow.

Molecules at $X^1\Sigma_g^+$ state can be pumped to the $3^1\Sigma_g^+$ and $2^1\Pi_u$ state, and then transport to the $2^1\Pi_u$ state by perturbation among the $3^1\Sigma_g^+$, $2^1\Pi_u$ and $2^1\Pi_u$ states. The $1^1\Sigma_g^+$ state is populated by $2^1\Pi_u \rightarrow 1^1\Sigma_g^+$ transition, so the laser oscillation centered at 892 nm is obtained while the population inversion exists between $1^1\Sigma_g^+$ and $1^1\Sigma_u^+$ states.

The discussion about the pumping mechanism in detail will be published in another paper.

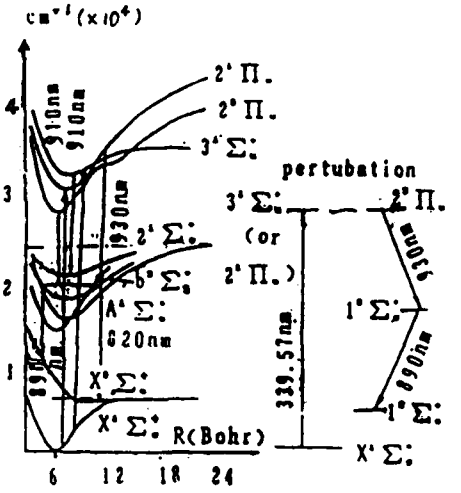

Fig.6 The potential energy curves of Na_2

CONCLUSION

Pumping by the UV laser of 337.0～342.0 nm, molecules in the ground state are populated to the $2^1\Pi_u$ state by the energy perturbation. By cascade transition, the $1^1\Sigma_g^+$ is populated and the laser oscillation in $1^1\Sigma_u^+ \rightarrow 1^1\Sigma_g^+$ is obtained.

REFERENCES

1. D.D.Konowalow, M.E.Rosenkrantz and M.L.Olson, J.Chem.Phys., 72, 2612 (1980)
2. Z.G.Ma, Acta Optica Sinica, 6, 233 (1982)
3. S.Shahdin, B.Wellegehausen and Z.G.Ma, Appl.Phys., B39, 195 (1982)
4. J.Huennekens, S.Schaefer, M.Ligare and W.Happer, J.Chem.Phys., 80, 4794 (1984)
5. S.G.Dinev, I.G.Koprinkov and I.L.Stefanov, Opt.Commun., 52, 199 (1984)
6. Ma Zuguang, Wang Qi, Xing Da and Liu Wei, 8th International Laser Conference (1985)
7. Wang Qi, Xing Da, Liu Wei and Ma Zuguang, Acta Optica, 6, 233 (1985)
8. M.Palle, S.Milosevic, D.Veza and G.Pichler, Opt.Commun., 57, 394 (1986)
9. G.Jeung, J.Phys.B.At.Mol.Phys. 16, 4289 (1983)

STUDY OF THE NEW 600.0nm DIFFUSE BAND

Yuezhen Sun, Xinghua Li, Qi Wang and Yongkang Cheng
Institute of Opto-Electronics, Harbin Institute of Technology, Harbin, China

ABSTRACT

Using a pulsed dye laser to pump the potassium vapor, we have observed the 600.0nm diffuse band. Analysis of the theoretical calculation and experimental result has shown that it is originated from the $3^1\Sigma_u^+ \rightarrow x^1\Sigma_u^+$ transition.

INTRODUCTION

In 1981 Z. G. Ma discovered a new diffuse band using XeF(351nm) and KrF (248nm) lasers to pump the potassium vapor[1,2]. The peak of the diffuse band is about 601.2nm. The origin of this new diffuse band was not explained in the paper.

Using a UV tunable pulsed dye laser to pump the potassium vapor, we have found the new diffuse band with intensity peak at 600.0nm. Based on the experimental results and theoretical calculation, it is concluded that the 600.0nm diffuse band originates from the $3^1\Sigma_u^+ \rightarrow x^1\Sigma_u^+$ transition.

EXPERIMENTAL SET-UP

An excimer laser (XeCl) is used to pump the dye laser. A cyclohexan solution of TMQ is used as a dye. The tuning range and the linewidth of the dye laser is 338-360nm and 0.016nm, respectively. The dye laser energy is about 1.5mj per pulse when the laser wavelength is 344.0nm. The dye laser beam is reflected into the stainless steel heat pipe containing potassium vapor. Passing through the dichroic plate, the fluorescence is focused onto the monochromator by a focal lens. After spectral analysis by the monochromator, the fluorescence is received by the photomultiplier tube. Then the signal is sent to the boxcar averager and recorded by the recorder.

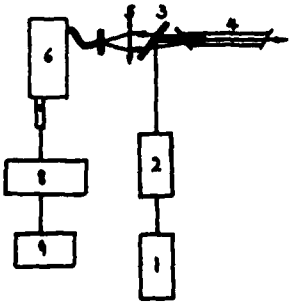

1. Excimer laser; 2. Dye laser;
3. Dichroic plate; 4. Heat pipe;
5. Focal lens; 6. Monochromator
7. Detector; 8. Boxcar averager;
9. Chart recorder.

Fig.1 Experimental set-up

EXPERIMENTAL RESULT AND DISCUSSION

The 600.0nm diffuse band is observed in the whole tuning range of the dye laser. Fig.2 is the 550.0→800.0nm spectrum pumped by the λ_L=350.0nm dye laser.

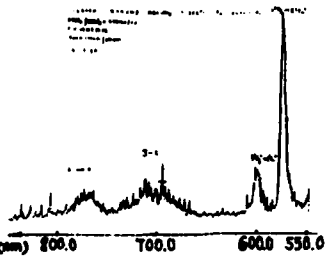

Fig.2 550→800nm spectrum when the laser wavelength is 350.0nm

There are many possible transitions exsisted when the pumping wavelength is 350.0nm. Based on the molecular constants of the K_a high-lying states and considering the Boltzmann distribution of the population of the $X^1\Sigma_g^+$ state, we have calculated the possible transitions as follows,

$$X^1\Sigma_g^+ \rightarrow C^1\Pi_u,\ D^1?_u,\ E^1?_u,\ F^1?_u,\ G^1?_u$$

the fluorescence from the high-lying ungerade singlet state transitting to the lower state is not observed in our experiment because the dichroic plate has a very high reflectivity in UV range.

The molecules in the high-lying excited singlet states frequently collide with the ground state atoms, resulting in the population of the upper states of the diffuse band. Through self-relaxation process, the population in the upper state of the diffuse band is near Boltzmann distributed. It is found that the population thermalization in the upper levels of the diffuse band is very fast(less than 10ns)[8,9]. In our experiment, the aperture duration is 50ns which is very large in comparison with the thermalization time of the upper levels. Therefore, the shape of the diffuse band we have observed in our experiment must originate from the upper levels which are in the thermal equilibrium condition. This demonstrates that the origin of the 600.0nm diffuse band is not the same as that of the 575.0nm diffuse band.

Fig.3 is the variation of the intensity of the diffuse band versus a) the pumping energy, b) temperature, c) buffer gas pressure.

From Fig.3 a)we see that the intensity of the diffuse band is linear with the pumping energy. This shows the prosess as follows, The molecules in the $x^1\Sigma_g^+$ state are excited to the high-lying singlet states by the laser photons. Then they collide with atoms, resulting in the population in the upper levels of the diffuse bands and the diffuse band produced. The intensity of the diffuse bands is proportional to the number of the molecules in the high-lying singlet states, in the unsaturated situation the number of the molecules

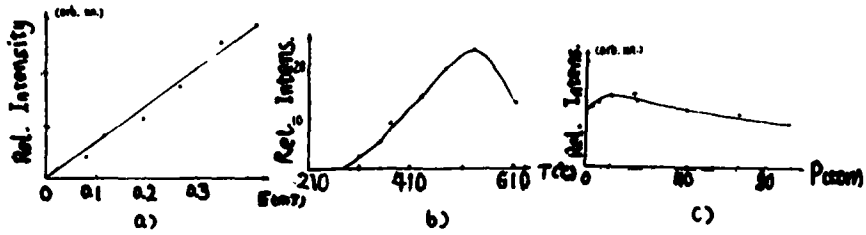

Fig.3 The variation of the intensity of the 600.0nm diffuse band with a)pumping energy b)temperature c)buffer gas pressure

in the high-lying singlet states is proportional to the laser energy. Therefore the intensity of the diffuse bands is linear with the pumping energy.

Fig.3 b), c) show that the optimum temperature of the 600.0nm diffuse band is T=530℃, the optimum buffer gas pressure is P_{opt}=10 torr.

THEORETICAL CALCULATION

For a two-level system in which the upper state is a bound level and the lower is a repulsive or weak-bounded level, the absolute intensity $I(\omega)$ for a quantum transition $\hbar\omega$ can be expressed as[8],

$$I_{v'J'\to v''J''}(\omega) \propto N_{v'J'}\,\omega^4 \times \sum_{J''} \frac{S_{J'J''}}{2J'+1} |\langle E'', J''|d_e(R)|V', J'\rangle|^2$$

Because there is no publicated results available, we have scaled the K_2 triplet curves from Na_2 using the method proposed by D.D. Konowalow[8]. According to the triplet energy curves, the K_2 $3^3\Sigma_u^+$ state is the most probable candidate for producing the 600.0nm diffuse band. It is impossible that the 600.0nm diffuse band originates from the $4^3\Sigma_u^+$ (or $3^3\Pi_u$)$\to x^3\Sigma_g^+$ transition.

Based on the potential energy curve of $3^3\Sigma_u^+$ state and the $x^3\Sigma_g^+$ curve calculated by A Valance et al[4], assuming that the dipole moment is a constant, we have calculated the peak wavelength of the $3^3\Sigma_u^+\to x^3\Sigma_g^+$ transition is 610nm in the condition of Boltzmann distribution. Considering the error of the potential energy curves and the dipole moment is a function of the internuclear distance, we concluded that the new diffuse band we observed in the experiment originates from the $3^3\Sigma_u^+\to x^3\Sigma_g^+$ transition.

REFERENCE

1. Z.G.Ma, J.Quant.Electron.(Chinese), Vol.1, (1984)
2. P. Kowalczyk et al, Chem. Phys. Lett., Vol.102, 377(1986)
3. G. Herzberg, Molecular Structure and Molecular Spectra, Vol. II.
4. A Valance and Q Nguyen Tuan, J. Phys. B, At. Mol. Phys., Vol.15, 17(1982)
5. D. D. Konowalow and M. E. Rosenkrantz, ACS symposium seris, Vol.179, (ACS, Washington, 1982), p.3

V. STATE-SPECIFIC PHOTOPHYSICS AND PHOTOCHEMISTRY

SEMIQUANTITATIVE LASER-INDUCED FLUORESCENCE FLAME MEASUREMENTS

David R. Crosley
Molecular Physics Laboratory
SRI International
Menlo Park, California 94025

ABSTRACT

The technique of laser-induced fluorescence (LIF) is a sensitive, selective and nonintrusive means of measuring intermediates important in combustion chemistry. In this article we briefly examine how LIF can be used in a semiquantitative manner to gain insight into aspects of flame chemistry mechanisms. Included are experiments on NH and NS, and extension to simultaneous multiple-species detection.

INTRODUCTION

Chemical processes govern a number of key problems in combustion, among them formation of the pollutants NO_x, SO_x and soot, ignition and inhibition phenomena, and the emission of radiation in the ultraviolet and visible wavelength regions. An understanding of the pertinent kinetics and mechanisms is best achieved through detection of those species which are the reactive intermediates in these multistep processes. To detect intermediates at low concentration levels, laser-induced fluorescence (LIF) is often the method of choice. Small (diatomic, triatomic) molecules can be detected with relative ease at the part-per-million level in an atmospheric pressure flame, with a high degree of species selectivity and a nonintrusive character. Typical molecules important in combustion chemical networks and monitored in flames using LIF are OH, CH, NH, NCO, CN, etc.

The common mode of LIF flame measurements furnishes concentration profiles as a function of distance above a burner. These profiles are compared with those calculated using large-scale computer models of the detailed chemical reaction networks, sometimes adjusting the rate constants to achieve agreement. Such quantitative comparisons require accurate absolute concentration determinations, which must be approached with considerable care.[1] An important concern is the fluorescence quantum yield, governed under most flame conditions by collisional quenching of the electronically excited state. An accurate value for the quenching rate can be limited by both unknown rate constants and a lack of knowledge of the composition of the flame gases at the point of measurement.

LIF can also be used in a semiquantitative manner.[2] Determining the presence of some particular species in the flame, at some estimated concentration, can provide important insight into the flame chemistry; relative concentrations of two or more species can permit choices among alternative reaction mechanisms. In this short article we describe such experiments on the NH and NS radicals, and the simultaneous detection of as many as four reactive radicals in a flame.

NH AND NS

We first consider measurements in an atmospheric pressure flame of CH_4 burning in N_2O. The N-N bond strength in N_2O is much stronger than the N-O bond strength, and a simple approach might consider a flame involving reactions of O atoms plus inert N_2. The emission spectra of such flames have long been known to contain bands belonging to NH, NH_2, CN, and NO, all of which can be formed only with breakage of the N-N bond. However, this emission likely results from direct chemiluminescent formation of the excited state and does not necessarily signal significant ground state concentrations. In a simple experiment,[3] we measured LIF of both OH and NH in this flame at atmospheric pressure to determine the ground state concentration. At the time, early 1980, nothing was known about OH quenching at high temperature and NH quenching had not been measured at all. An estimate of equal quantum yields indicated that the NH concentration was about 4% of that of OH; a separate absorption measurement showed that hydroxyl radicals were present at their usual high levels, near 10^{16} cm^{-3}. This amount of NH is quite sufficient for it to be of chemical significance, and the result indicated that this radical should no longer be excluded from the mechanism of this flame's chemistry. Although accurate profile measurements are now available, that early, simple semiquantitative determination showed the importance of this flame species in the mechanism of flames burning in nitrous oxide, and chemical models for such flames now include pathways for its formation and destruction.

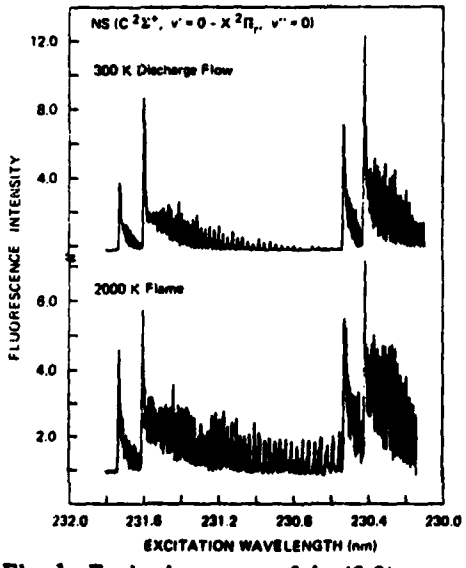

Fig. 1. Excitation scans of the (0,0) band of the $C^2\Sigma^+$-$X^2\Pi$ transition of the NS molecule. Top: NS in a room temperature discharge flow system, produced by a microwave discharge in N_2 and SCl_2. Bottom: NS in an atmospheric pressure flame of CH_4 burning in N_2O and seeded with SF_6.

A more recent example is the NS molecule,[4] observed previously only in spectroscopic experiments but never in flames. Coal can contain fuel-bound nitrogen and fuel-bound sulfur, and we wondered whether the interaction between the chemistry of NO_x and SO_x production cycles might form NS. The NS studies began with a series of spectroscopic measurements[5] performed in a microwave discharge in N_2 mixed with SCl_2 in a low pressure, room temperature flow cell. The top panel of Fig. 1 is an excitation scan of the (0,0) band of the $C^2\Sigma^+$-$X^2\Pi$ transition near 230 nm, showing four band heads and individual rotational lines. A CH_4/N_2O mixture seeded with SF_6 was then burned on a small burner at atmospheric pressure, and the laser beam directed into the flame front. The resulting excitation scan is shown in the lower panel. The identification as NS is unambiguous, illustrating the selectivity of LIF for these purposes. The larger number of lines in the flame spectrum arises from the higher temperature and larger population in higher rotational levels.

For more careful measurements, a coal flame was simulated by burning methane in oxygen seeded with small amounts of NH_3 and H_2S as the fuel nitrogen and sulfur. NS was observed in all such flames, and even in a flame of natural gas burning in N_2O, where the sulfur source was the methyl mercaptan added at 2 ppm by the gas company to produce an odor.

To estimate the NS concentration from the LIF signal intensity, several parameters are needed. The Einstein emission coefficient was taken from an ab initio calculation; it plus measured Franck-Condon factors and calculated rotational line strengths furnished the absorption coefficient. The C-state lifetime is governed by predissociation, and its value was taken from Hanle effect measurements. The major uncertainty is in the collisional quenching rate, which has never been studied for this state. Estimates of cross sections were made by analogies to NO, PO, and the $B^2\Pi$ state of NS. This resulted in peak NS concentrations which were typically 0.1% of the amount of the added sulfur, and sometimes as much as 5%. Together with experimental errors, the overall uncertainty in these absolute concentrations is about a factor of three. This level of accuracy is quite ample to make important deductions about the chemistry of these flames. A large fraction of the fuel sulfur is being processed through this one radical. The disappearance of the signal as the laser beam was moved away from the flame front allowed us to conclude that the NS was produced by a reaction between a radical present at perhaps 10 ppm and a stable species at a concentration of 0.1 mole percent or greater, and removed by a reactant present at similar levels of some tenths of a mole percent.

From this we conclude that NS may be an important reaction intermediate in the reducing region of rich hydrocarbon flames containing fuel-bound nitrogen and sulfur. Little further can be said at this point, because nothing is known about the reaction rates of NS. It may play a major role in the chemistry of the interaction between NO_x and SO_x formation. This observation of the radical does not prove that it plays such a role, but clearly indicates that further reaction rate and flame studies are needed.

MULTIPLE SPECIES LASER-INDUCED FLUORESCENCE

The detection of one intermediate species in a flame can provide valuable insight into the flame chemistry, as the examples of NH and NS show. Even more useful would be the detection of more than one kind of molecule at a time. One example is found in the chemistry of NO_x production in flames of hydrocarbons seeded with NH_3, again to represent fuel nitrogen. Whether CN or NH appears first under a variety of conditions would be very informative concerning the mechanism involved. In the small number of studies in which more than one radical have been probed, the approach has been the use of different excitation wavelengths, often different lasers, each optimized for one of the desired molecules. Because of differences in beam sizes and divergences, considerable care must be taken to ensure that the same volume in the flame is probed in each case. An imprecise spatial match among concentrations (or concentration and temperature) can render meaningless a comparison with calculated flame models. The problem is exacerbated in turbulent flames, where each laser would need to be fired simultaneously, and where there can exist severe optical inhomogeneities making it difficult to sample the same volume.

A different approach[6] sought particular laser wavelengths at which more than one species could be excited, with the objective of using one laser to detect two or more

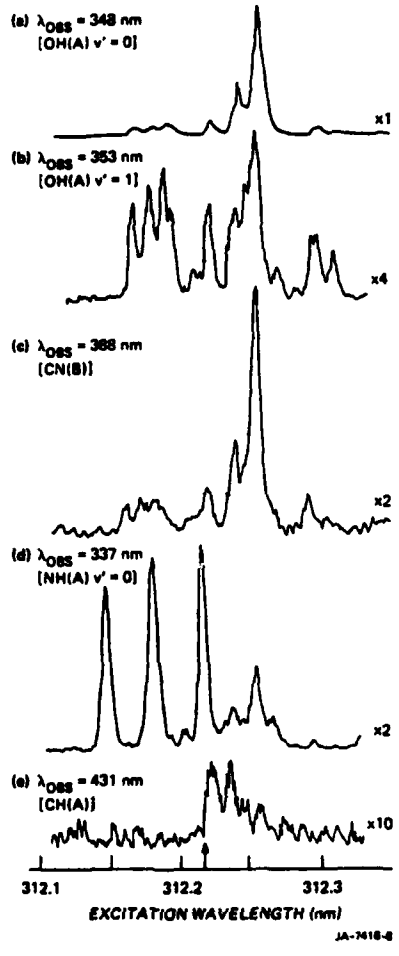

Fig. 2. Excitation spectra taken over the same wavelength region, with detection at various fluorescence wavelengths as marked. The arrow at the bottom shows where all excitations overlap. The flame is CH_4/N_2O at atmospheric pressure. (a) excitation of (0,0) band of the A-X transition of OH; (b) excitation in the (1,1) band of OH; (c) excitation of CN in the $\Delta v=3$ bands of the B-X system and via energy transfer from excited OH; (d) excitation of the (2,1) band of the A-X system of NH; (e) excitation of the (0,0) band of the C-X system of CH.

molecules in the same probed volume within the flame. This was developed in experiments performed in a CH_4/N_2O flame burning at atmospheric pressure on a small glassblowing torch. This flame contains many different reactive radicals and thus forms a good test system. In the ultraviolet, near 300 nm, there exist bands belonging to electronic transitions of the molecules OH, NH, CH, CN and NCO. In many cases, there are individual absorption lines of these molecules which overlap within the Doppler width, ~0.2 cm^{-1} at flame temperatures. This is close to the typical 0.3 cm^{-1} bandwidth of many tunable lasers. These overlaps permit the simultaneous detection of these species, using spectrally dispersed or filtered fluorescence to discriminate among the excited molecules.

A series of excitation scans near 312 nm, shown in Fig. 2, illustrates this concept. Five excitation scans are shown, each over the same wavelength region but detected at a different fluorescence wavelength through a monochromator. In the first four panels, emission from the directly excited electronic state of the radical is observed. The CH molecule is excited to the v'=0 level of its $C^2\Sigma^+$ state but detected via emission from the $A^2\Delta$ state, which is populated by C→A energy transfer in the flame. Attempts to detect the C-X emission directly were unsuccessful because of the much higher background due to lines of the OH molecule (present at much higher concentration than CH) in this same spectral region.

At the wavelength 312.22 nm, denoted by the arrow in the bottom panel of Fig. 2, all four of these diatomics absorb the laser radiation. With the laser tuned to this wavelength, a fluorescence scan shows the emission from each molecule in a different wavelength region as seen in Fig. 3. Note that there are two peaks in the CN B-X radiation. That at

shorter wavelength is from the directly excited CN, fluorescing in the (3,3) and (4,4) bands, while that at longer wavelength is the (0,0) and (1,1) bands, formed by energy transfer into $B^2\Sigma^+$ CN from laser-excited $A^2\Sigma^+$ OH.

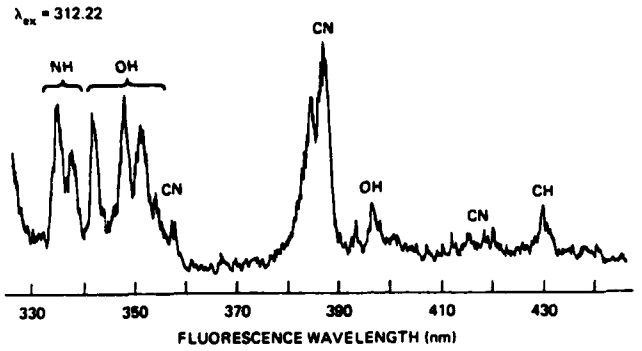

Fig. 3. Fluorescence spectrum, exciting at 312.22 nm as shown by the arrow in Fig. 2. LIF from directly excited OH and NH is seen. The CH $A^2\Delta$ state is populated by energy transfer from the excited C-state. The two peaks in the CN spectra correspond to direct excitation and energy transfer from laser-excited OH in the flame.

These spectroscopic coincidences will permit instantaneous correlation measurements among several species, using pointwise or imaged detection, avoiding complications of alignment of two or more separate laser beams and pulse-to-pulse variation in spatial and temporal profiles. This can be useful in a stable, laminar flame, but is likely essential in a turbulent system. A single optical system would be used to collect the fluorescence, which would be directed through appropriate filters and/or dichroic separate detector for each radical. The higher throughput of such a system, compared to the monochromator used for the scan in Fig. 3, would yield much higher signal levels.

CONCLUSION

LIF is a sensitive, selective and nonintrusive way to measure the concentrations of reactive intermediates in combustion chemistry. When possible, the goal is quantitative comparison with detailed predictions from computer models of that chemistry. However, semiquantitative measurements can provide much insight into the reaction mechanism. Correlations among more than one reactive species could prove especially valuable for that purpose.

ACKNOWLEDGEMENTS

I thank Richard Copeland, Jay Jeffries, and Gregory Smith for their participation in these experiments and in many discussions. The research described here has been supported by the U. S. Army Research Office, the Department of Energy, the National Science Foundation and the Gas Research Institute.

REFERENCES

1. K. Kohse-Höinghaus, J. B. Jeffries, R. A. Copeland, G. P. Smith and D. R. Crosley, Twenty-Second Symposium (International) on Combustion, in press, 1989.

2. D. R. Crosley, Comb. Flame, in press, 1989.

3. D. R. Crosley, Opt. Engr. **20**, 511 (1981).

4. J. B. Jeffries and D. R. Crosley, Comb. Flame **64**, 55 (1986).

5. J. B. Jeffries, D. R. Crosley and G. P. Smith, J. Phys. Chem., in press, 1989.

6. J. B. Jeffries, R. A. Copeland, G. P. Smith and D. R. Crosley, Twenty-First Symposium (International) on Combustion, The Combustion Institute, Pittsburgh, 1988, p. 1709.

STATE-SELECTIVE PHOTODISSOCIATION DYNAMICS OF NOCl: SCALAR AND VECTOR PROPERTIES

A. Ogai, C.X.W. Qian, L. Iwata and H. Reisler
Department of Chemistry, University of Southern California,
Los Angeles, CA 90089-0482

ABSTRACT

The photodissociation of jet-cooled NOCl following excitation in the three lowest absorption bands is reported. The transitions are assigned using photofragment spectroscopy with polarized lasers. Dissociation on T_1 exhibits state specific effects and the low NO rotational excitation results from a small torque on the NO fragment. Dissociation on S_1 and S_3 shows large final-state interactions. State specific spin-orbit and Λ-doublet effects are also observed.

INTRODUCTION

Understanding the relation between product distributions and initially prepared parent states is crucial to understanding photodissociation dynamics. Correct assignments of the excited states are likewise important, since they allow description of the photodissociation dynamics in terms of detailed motions on specific potential energy surfaces (PES). Today, there exist a variety of polarized laser spectroscopic techniques[1-6] that, in conjunction with tunable laser photolysis and photofragment yield (PHOFRY) spectroscopy can facilitate the assignments of dissociative states.

The important vectors that play a role in the elucidation of the electronic structure of dissociative states are μ, the recoil velocity v of the photofragment, its rotational angular momentum J, and the direction of the singly occupied π lobes of radicals in Π electronic states. For triatomic molecules, the situation is further simplified by the sensible assumptions that the dissociation is planar, the recoil is nearly axial and the diatomic fragment rotates in the plane of the parent molecule.[1] The pair-wise correlations that can be obtained by using polarized lasers for photolysis and detection of the photofragments are:[1,5] (i) the direction of μ relative to v (recoil anisotropy parameter β);[1,3,5] (ii) the direction of μ relative to J, and therefore the plane of the parent molecule (rotational alignment parameter, $A_0^{(2)}$);[1,4,5] and (iii) the direction of the singly occupied π lobe relative to J (Λ-doublet populations), which in the absence of extensive electronic reorganization during dissociation can be related to the initially excited orbital in the parent molecule.[6]

NOCl is an excellent prototypical molecule for application of the vector correlation methods, since it possesses several low lying dissociative excited states that give rise to electronic transitions in the uv and visible. The absorption spectrum has been obtained by Goodeve and Katz and shows several broad features (Fig.1).[7] The B band was assigned by Busch and Wilson[8] as an A'← A' transition with μ nearly parallel to the N-Cl bond. About 70% of the excess

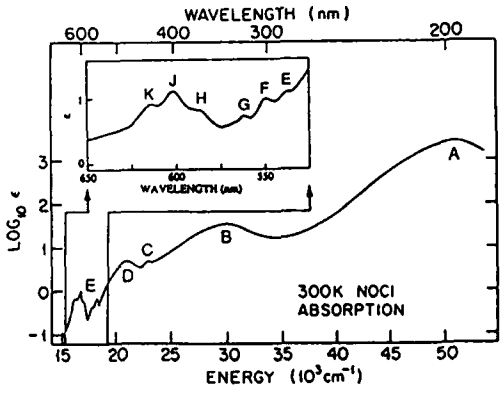

Figure 1. The absorption spectrum of NOCl

energy was found in translation, whereas dissociation in the **A** continuum (e.g. 248 and 193 nm) gave rise to highly vibrationally excited NO.[9] Recently, Bruno *et al.* reported a study of the photodissociation of 300 K NOCl in the region of the **D** and **C** bands and obtained the symmetry of the transitions from the measured Doppler profiles of NO rotational lines.[10] Independently, we found that the excitations in the **D** and **B** regions involve perpendicular and parallel transitions, respectively, and yield inverted NO rotational distributions.[11] Preliminary results on **E** band excitation showed that the rather cold rotational distributions depend strongly on the excitation wavelength.[12]

Very recently, we reported new *ab initio* calculations on the low-lying states of NOCl, which also included triplet states.[13] Based on the new calculations and the experimental results, we reassigned the electronic spectrum:[13] (i) $T_1(1^3A'') \leftarrow S_0(1^1A')$ - **E** band. The transition borrows intensity by mixing with remote singlet states, predominantly the $4^1A'$ state: (ii) $S_1(1^1A'') \leftarrow S_0(1^1A')$ - **D** and **C** bands; (iii) $S_3(2^1A') \leftarrow S_0(1^1A')$ - **B** band; (iv) $S_5(4^1A') \leftarrow S_0(1^1A')$ - **A** band;

The *ab initio* CI calculations indicate that all excitations involve promotions of electrons from Cl orbitals to NO π^* orbitals. The T_1 and S_1 surfaces have shallow minima, while the other surfaces are purely repulsive.[13] Below, we describe our experimental findings regarding dissociation in the **E**, **D**+**C** and **B** bands, and interpret them based on the new spectral assignments.

EXPERIMENTAL

The experimental arrangement is very similar to the one used in our previous studies.[11-13] Premixed NOCl samples (10/500 Torr in He) are prepared and expanded via a pulsed valve into the fluorescence chamber. The NO fragments are probed by one-photon LIF via the $A^2\Sigma \leftarrow X^2\Pi$ transition at ~226 nm. Two configurations of the lasers and detector were used. In most of the sub-Doppler resolution spectroscopy experiments, the two laser beams and the pulsed nozzle were mutually orthogonal. The PMT was located at 45° in the same plane as the lasers. An intracavity etalon (FSR = 1 cm^{-1}) was used to narrow the laser linewidth, and the frequency was pressure tuned with N_2. In the spatial anisotropy and Λ-doublet experiments, the two laser beams were collinear and counterpropagating, but perpendicular both to the PMT and the pulsed valve. The probe laser was maintained at a vertical polarization, and the polarization of the photolysis laser was rotated.

RESULTS AND DISCUSSION

1. The E band ($T_1(1^3A")$ state) - The lowest NOCl absorption consists of two groups of peaks (three per group) separated by 1580 cm^{-1} (NO stretch, ν_1').[7] The interval between successive vibrational bands within each group is 380 cm^{-1}, corresponding to ν_3', the ClNO bend.[7] No rotational structure is observed,[7] and the origin (16,240 cm^{-1}) lies well above D_0 (13,000 cm^{-1}).[8] Thus, it is possible to prepare excited states of NOCl with ν_1'=0,1 and ν_3'=0,1,2

With excitation in the E band, both the recoil anisotropy ($\beta = 1.9 \pm 0.1$, Fig. 2) and the rotational alignment are typical of a parallel transition with μ nearly parallel to ν (A'←A' transition). The oscillator strength, however, is quite small, ~ 1 x 10^{-5}, and Goodeve and Katz suggested that it may involve a forbidden transition[7]. We ascribe this transition to spin-orbit (L.S) coupling between the $1^3A"$ state, and higher lying strongly absorbing singlet states of A' symmetry.[13] The experimental oscillator strength compares favorably with the estimated value based on intensity borrowing from the $4^1A'$ state, and thus spin-orbit coupling can account for the intensity and symmetry of the transition. We emphasize that although mixing with singlet states is responsible for the oscillator strength and thus determines the values of β and $A_0^{(2)}$, only 2% of the $4^1A'$ wave function is required to yield the experimentally observed oscillator strength. Thus, the T_1 state, which derives from a promotion of an electron from the highest occupied molecular orbital (MO 16, a' symmetry), to MO 17, which is of a" symmetry, has predominantly $1^3A"$ character, and the Λ-doublet populations indeed reflect the a" symmetry of the excited state orbital.

By varying the photolysis wavelength while monitoring NO 80 ns after dissociation, a PHOFRY spectrum is obtained. With jet-cooling, the peaks are better resolved than in the 233 K absorption spectrum,[7] but their relative intensities depend on the specific NO($X^2\Pi$, v",J") state probed. Also, when monitoring NO(v"=0), only the first group of three peaks is observed, whereas v"=1 yields only the second group. Vibrational state specificity has been observed before for several NO-containing molecules.[14] However, we find that the NO v"=0 and 1 rotational distributions depend strongly on the number of bending quanta in the parent excited state. In Fig. 3, we display NO(v"=0) rotational distributions associated with excitation in the first group of peaks. Each rotational distribution corresponds to a peak in the absorption spectrum. The most striking feature is the multimodal character of the distributions associated with excitation of bending quanta in the parent. When ν_3'=1 is excited, a second peak appears in the distribution, whereas excitation of ν_3'= 2 leads to two additional rotational peaks. Similar distributions were obtained when monitoring NO(v"=1) following excitation in the second group of peaks, corresponding to ν_1'=1 and ν_3'=0,1 We also observe a large propensity for the production of the higher spin-orbit state, NO($^2\Pi_{3/2}$), relative to NO($^2\Pi_{1/2}$). The plotted distributions are not corrected for alignment effects, and their analysis shows that $\mu \perp J$ and the Π(A") Λ-doublet component is preferentially populated. We also find that the FWHM of the absorption peaks (determined from the PHOFRY spectra) are 300-400 cm^{-1},

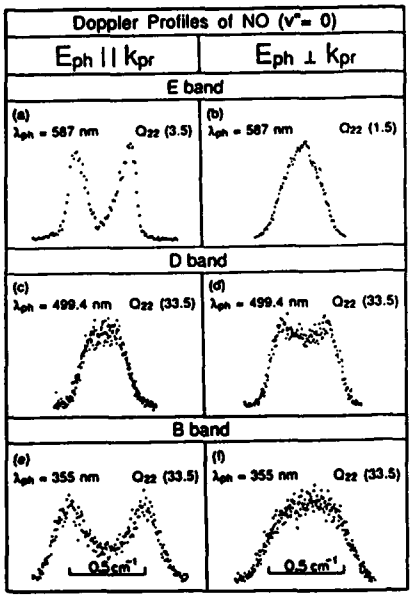

Figure 2. NO(v=0) Doppler profiles

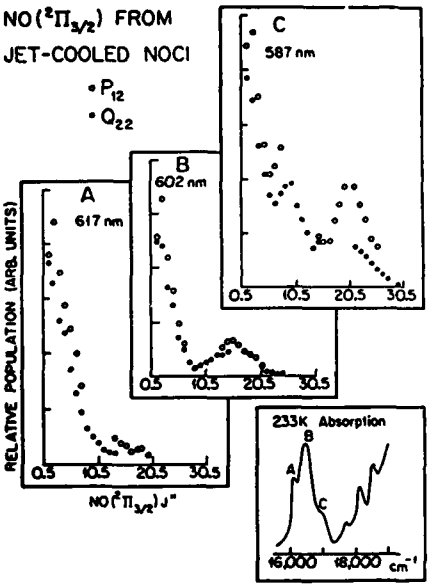

Figure 3. NO rotational populations following E band excitation.

corresponding to lifetimes ~ 20 fs (*i.e.* the order of one vibrational period).

The results indicate strong dependences of the product state distributions on the initial excitations in the upper electronic state. The evolution of the bending and stretching motions appear to be uncoupled with the latter adiabatically evolving into product vibrational excitation. The multimodal rotational distributions exhibit two prominent features: (i) a large 'cold' component indicating that very little torque is exerted in the dissociation (small angular anisotropy in the potential), and (ii) 'hotter' components that are strongly dependent on the number of excited bending quanta, but are independent of the number of excited NO stretching quanta. The state-specific peaks in the rotational distributions may reflect the nodal structure of the bending wave function, and the evolution of the excited bending motion on the (PES) along the N-Cl reaction coordinate. Recent *ab initio* calculations indicate that the excited state is bent and the PES is rather flat along the reaction coordinate, but has a shallow minimum.[13] Since the lifetime of the excited state is sufficiently long to sustain a diffuse vibrational structure, the rotational distributions may be a reflection of the fully developed bending wave function and its evolution along the reaction coordinate. Another likely scenario that may explain the multimodal rotational distributions involves surface crossings in the exit channel. A crossing by a second triplet surface which is linear has been identified in the *ab initio* calculations at separations > 2.4 Å,[13] and the influence of the surface crossings will be examined in detail in the future.

2. The D and C bands ($S_1(1^1A")$ state) - We assign the D absorption band to excitation of the $S_1(1^1A")$ state. The Doppler profiles indicate that μ is perpendicular to v with $\beta \sim -1$ (Fig. 2), and from the alignment data we conclude that the transition is of A" symmetry. The experimental Λ-doublet data for

$NO(^2\Pi_{1/2})$, which yield $\Pi(A'') > \Pi(A')$ (Fig. 4), are consistent with this assignment, since excitation is predominantly to MO 17 whose symmetry is a", as is the overall symmetry of the transition.

We believe that excitation to $S_1(1^1A'')$ is responsible for both the D and the C bands, as the two peaks are separated by ~1670 cm^{-1},[7] a value which is close to the NO stretch frequency (*i.e.* the C band arises from excitation of S_1 with one quantum of NO stretch). This assignment is based on the following observations: (i) In the PHOFRY spectrum, a peak similar to the C band appears only when monitoring NO(v"=1), but not when monitoring NO(v"=0); (ii) The NO(v"=1) recoil anisotropy parameter corresponds to a predominantly perpendicular transition; (iii) At comparable wavelengths, NO(v"=0) show a large parallel component deriving from dissociation on the $S_3(2^1A')$ surface.

The NO rotational distributions,which peak at high J", are inverted and similar to those obtained in a number of other NO containing compounds.[14] The same impulsive model that was used to interpret the translational energy distributions in NO in the 347 nm dissociation of NOCl[8] and of alkyl nitrites[14] describes qualitatively the rotational distributions obtained following dissociation on S_1. In this model, fragment rotation arises from the torque exerted on the fragments along the bond that breaks, and it is assumed that each fragment is fairly rigid. The available energy is transferred to motion along the breaking bond and is distributed mainly between fragment rotation and translation, and less into vibration.

The most striking result concerning the NO Λ-doublet populations (Fig.4) is that while the $^2\Pi_{1/2}$ state shows a clear preference for the Π(A") Λ-doublet component, no such preference is observed for the $^2\Pi_{3/2}$ state of NO.[11] The *ab initio* calculations show that the $S_1(1^1A'')$ state is crossed by the $T_2(1^3A')$ state whose vertical excitation energy is 2.90 eV, and whose equilibrium geometry is close to linear.[13] No vibration exists which can couple states of A' and A" symmetry, but they can be coupled by spin within the C_s point group, and this coupling occurs in an M_s specific fashion. If such coupling is efficient, it could account for the state-specific Λ-doublet behavior.

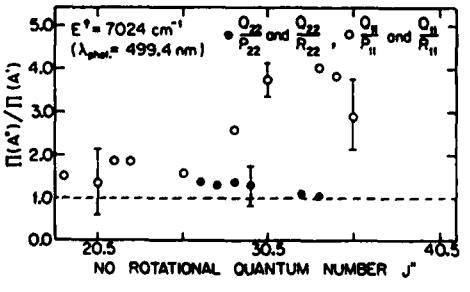

Figure 4. NO Λ-doublet populations following D band excitation.

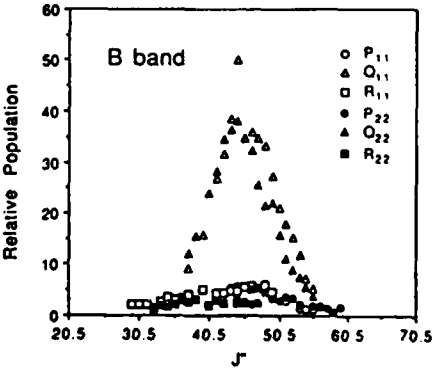

Figure 5. NO(v=0) rotational populations following B band excitation.

3. The B band ($S_3(2^1A')$ state) - The nature of the B band is consistent with the computed features of the $S_3(2^1A')$ state. The experimental recoil anisotropy parameter is typical of a parallel transition with μ nearly parallel to v (Fig. 2), confirming the A' overall nature of the upper state, and the rotational alignment is consistent with this interpretation. Finally, the Λ-doublet data show $\Pi(A'') > \Pi(A')$ (Fig. 5), an observation consistent with the fact that this state results from excitation to MO 17 whose symmetry is a". This orbital is predominantly of NO π^*(a") character, suggesting that very little charge redistribution takes place during the dissociation, despite the final state interactions that result in large rotational excitation in the NO fragment. The v"=0 rotational distributions following dissociation in the B band are very similar to those obtained in excitation in the D band, but peak at higher J" (43.5 with 355 nm excitation). The NO spin-orbit populations, however, show a slight preference for NO($^2\Pi_{1/2}$).

ACKNOWLEDGMENTS

The authors thank G.A. Segal and Y.Y. Bai for helpful discussions. Support from NSF and ARO under the auspices of the Center for the Study of Fast Transient Processes is gratefully acknowledged.

REFERENCES

1. P.L. Houston, J. Phys. Chem. 91, 5388 (1987) and references cited therein.
2. J.P. Simons, J. Phys. Chem. 91, 5378 (1987).
3. a) R.N. Zare and D.R. Herschbach, Proc. IEEE 51, 173 (1963).
4. C.H. Greene and R.N. Zare, Ann. Rev. Phys. Chem. 33, 119 (1982).
5. R.N. Dixon, J. Chem. Phys. 85, 1866 (1986).
6. a) P. Andresen and E.W. Rothe, J. Chem. Phys. 82, 3634 (1985); b) M.H. Alexander and P.J. Dagdigian, J. Chem. Phys. 80, 4863 (1984); c) M.H. Alexander et al., J. Chem. Phys. 89, 1749 (1988).
7. C.F. Goodeve and S. Katz, Proc. Roy. Soc. (London) A172 432 (1939).
8. G.E. Busch and K.R. Wilson, J. Chem. Phys. 56, 3655 (1972).
9. M.D. Moser, E. Weitz and G.C. Schatz, J. Chem. Phys. 78, 757 (1983).
10. a) A.E. Bruno, U. Bruhlmann, and J.R. Huber, Chem. Phys. 122, 155 (1988); b) A. Ticktin, A.E. Bruno, U. Bruhlmann, and J.R. Huber, Chem. Phys. 125, 403 (1988).
11. A. Ogai, C.X.W. Qian, L. Iwata, and H. Reisler, Chem. Phys. Lett. 146, 367 (1988).
12. C.X.W. Qian, A. Ogai, L. Iwata, and H. Reisler, J. Chem. Phys. 89, 6547 (1988)
13. Y.Y. Bai, A. Ogai, C.X.W. Qian, L. Iwata, G.A. Segal, and H. Reisler, J. Chem. Phys. (submitted).
14. H. Reisler, M. Noble, and C. Wittig, in Molecular Photodissociation Dynamics, Roy. Soc. Chem. p. 137 (1987), and references cited therein.

LASER INDUCED SHIFTS IN CHEMICAL EQUILIBRIA

R.A. Bernheim and Chun He
Department of Chemistry, The Pennsylvania State University,
152 Davey Laboratory, University Park, PA 16802

G. Alzetta
Institute of Physics, University of Pisa, Piazza Torricelli 2,
56100 Pisa, Italy

ABSTRACT

The effect of an optically pumped atomic spin orientation on the atom-dimer equilibrium in lithium vapor has been observed. The shift arises from a redistribution of spin-determined bonding and antibonding collision trajectories. The orientation of the $2^2S_{1/2}$ ground state Li atoms is produced by optical pumping with a single mode cw dye laser. The effects of ortho-para nuclear spin distribution in the Li_2 molecules is also discussed.

In 1965 it was predicted by one of us (R.A.B.) that an atomic spin orientation, produced by optical pumping, would cause a shift in the atom-dimer chemical equilibrium.[1] The shift would be in a direction to decrease the dimer density and is caused by the fact that the oriented atoms can collide only along triplet antibonding trajectories. In the absence of atomic orientation, collisions along singlet bonding trajectories are also possible which can lead to bond formation, with a third body collision removing energy to stabilize the bond. Most experimental observations of the shift have used coincidences between various laser line frequencies and molecular transitions to monitor the dimer density in the presence of atomic optical pumping. In the first experimental observation of the effect the 632.8 nm He-Ne laser line was used to monitor K_2 in a sodium-potassium vapor mixture.[2] More recently, [3,4] the 488.0 nm line of an Ar^+ laser and the 647.1 nm line of a Kr^+ laser have been used to monitor Na_2 and K_2 in the same mixture. It was also shown that atomic orientation changes the relative abundances of the ortho and para nuclear spin modifications of Na_2 dimers as well as the Na_2 density in sodium vapor[5]. In cesium vapor the change in Cs_2 atomic orientation has been observed using 1 cm^{-1} bandwidth laser radiation at 13170 cm^{-1} to monitor the Cs_2 concentration by laser induced fluorescence of the $B^1\Pi_u \leftarrow X^1\Sigma_g^+$ transition.[6] In this experiment the radiation is sufficiently broad-band to sample an average of the ortho and para nuclear spin varieties of Cs_2. Observations of the shift in chemical equilibrium could be made over a temperature range of 383K to 421K with a change in molecular density of up to 50% possible at the lower temperatures.

The experimental situation in lithium vapor is much more interesting because the spectral transitions from individual rotational levels are easily resolved, and it is possible to study in detail the change in rotational population distribution resulting from the optically pumped shift in chemical equilibrium.

For the studies on lithium vapor a single mode dye laser is used to excite the D_1 resonance transition of ^7Li at 670 nm using the ground state alkali atom optical pumping configuration of Dehmelt.[7] Using only 3 mW of D_1 optical pumping radiation, an atomic orientation of S = 0.5 can be achieved with typical experimental conditions of T = 319C, 300 torr He buffer gas, the sample contained in a 1.9" I.D. stainless steel crossed heat pipe cell, and an applied longitudinal magnetic field of 35.8G. Experimental studies of the shift vs atomic orientation S are possible which can be used to test the predictions of Kastler concerning this point.[8]

An experimental observation of the shift is shown in Fig. 1 for the conditions of T = 354C, 300 torr He buffer gas, 0.76 mW optical pumping power, approximately S = 0.1 atomic orientation, and 35.8G. The molecular excitation spectrum is scanned (A) in the absence of, and (B) in the presence of the optical pumping radiation. 80 mW of 1 cm^{-1} tunable dye laser power was used to record the segment of the molecular spectrum shown.

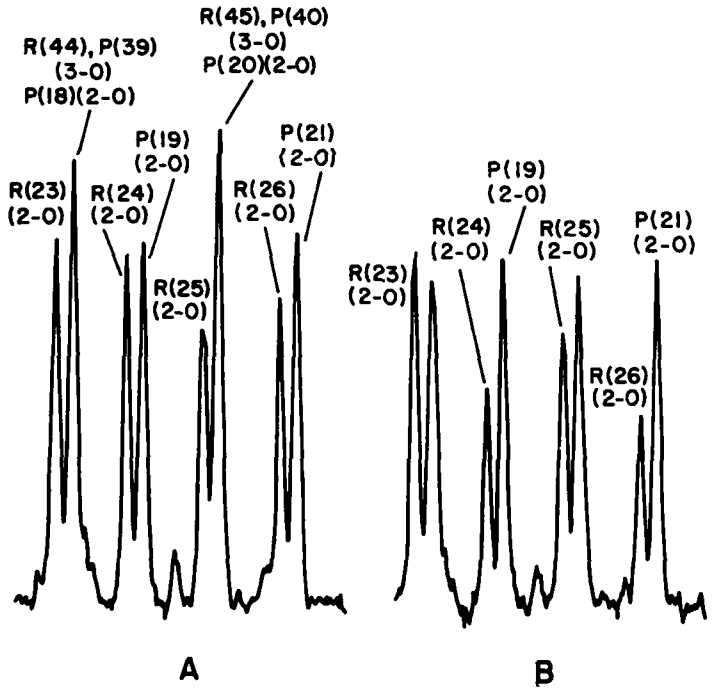

Fig. 1. A portion of the LIF spectrum of $^7Li_2$ (A) in the absence of Li atomic spin orientation, and (B) in the presence of Li atomic spin orientation showing the marked decrease of molecules having a para nuclear spin configuration.

Several salient features are immediately evident. First, the transitions that originate from levels with even values of J in the ground $X^1\Sigma_g^+$ state decrease in intensity when a Li atomic orientation is produced. The even values of J are due to the para molecular varieties having total nuclear spin T = 2 or 0. Second, the transitions that originate from the ground state levels with odd values of J retain nearly the same intensity when the optical pumping radiation is switched on. The odd values of J are due to the ortho molecules having total nuclear spin T = 3 or 1. Lastly, the transitions that are overlapped and are due to mixtures of ortho and para molecules decrease in intensity in the presence of an atomic orientation. If the intensities of the ortho and para transitions are summed, the combined intensity is found to drop by about 20% for the above conditions.

These results can be explained as arising from a combination of two effects. First, the total molecular density drops by 20% consistent with the prediction of a shift in the point of chemical equilibrium for the reaction $2Li = Li_2$. Second, the ortho/para ratio increases, consistent with the observation of Weber and Stock who point out that the atomic spin orientation can induce a molecular nuclear spin orientation. The T = 3 or ortho modification of the molecular species will be favored at the expense of the para species if (a) oriented atoms can chemically exchange with atoms in the dimer, and (b) an atomic election spin - molecular nuclear spin exchange interaction can take place.

Support by the National Science Foundation is gratefully acknowledged.

1. R. Bernheim, Optical Pumping. An Introduction (Benjamin, New York, 1965), p. 64.
2. G. Alzetta, A. Gozzini, and L. Moi, C.R. Acad. Sci. (Paris) 274B, 39, (1972).
3. M. Allegrini, G.Alzetta, P.Bicchi, and S.Gozzini, 12th EGAS Conference, 1980. Summaries of Contributions, p. 95.
4. M. Allegrini, P. Bicchi, and S. Gozzini, J. Chem. Phys. 82 457, (1985).
5. H.G. Weber and M. Stock, Phys. Lett. A50, 343 (1974).
6. J. J. Ho, Chongye Wang, and R.A. Bernheim, J. Chem. Phys. 89, 2635, (1988).
7. H. Dehmelt, Phys. Rev. 105, 1487, (1957).
8. A. Kastler, Act. Phys. Pol. 34, 693, (1968).

POLARIZATION STUDIES AS A PROBE OF PHOTODISSOCIATION DYNAMICS

V. Zafiropulos, P. D. Kleiber, K. M. Sando
X. Zeng, A. M. Lyyra and W. C. Stwalley
Center for Laser Science and Engineering, The University of Iowa, Iowa City, IA 52242-1294

ABSTRACT

A linearly polarized tunable CW dye laser was used to photodissociate K_2 from the ground $X^1\Sigma_g^+$ state through the continuum of the $B^1\Pi_u$ state. By monitoring the resultant atomic D_2 fluorescence, we were able to measure the pure bound-free absorption profile. At the same time, the polarization of the atomic fluorescence was measured as a function of laser excitation frequency. We believe this to be the first observation of a large variation in the polarization, ranging from *plus* 15±2% to *minus* 6.3±0.4% as a function of laser wavelength. The results can be explained in terms of molecular rotation during dissociation. These results are consistent with a completely adiabatic model for the dissociation. However, there are significant discrepancies between these model results and the experimental observations when hyperfine depolarization effects are included in the calculation. The origin of these discrepancies is not understood.

In 1968, Van Brunt and Zare[1] showed that one could obtain valuable information concerning the dynamics of the dissociation process ($AB + h\nu \longrightarrow A + B^*$) by studying the polarization of the light emitted by the excited atom B*, as this polarization is sensitive to the angular momenta of the photofragments. Since then, a considerable amount of work (both theoretical and experimental) has been carried out[2-10].

In this report a linearly polarized tunable CW dye laser (CR-599-21 broad band) was used to excite a K_2 molecular beam from the ground $X^1\Sigma_g^+$ state into the continuum of the $B^1\Pi_u$ state, producing excited atomic $K(^2P_{3/2})$ which radiates on the resonance D_2 line at 766.5nm. The process can be described by the following three steps:

$$K_2(X^1\Sigma_g^+) + h\nu(\text{laser}) \longrightarrow K_2^*(B^1\Pi_u) \quad \text{(excitation)}$$
$$K_2^*(B^1\Pi_u) \longrightarrow K(^2S_{1/2}) + K^*(^2P_{3/2}) \quad \text{(dissociation)}$$
$$K^*(^2P_{3/2}) \longrightarrow K(^2S_{1/2}) + h\nu'(766.5\text{nm}) \quad \text{(fluorescence)}$$

where the notation K_2^* indicates a continuum state above the dissociation threshold. A detailed description of the molecular beam apparatus and the experimental conditions are given elsewhere[9,10].

The bound-free absorption profile of K_2 and the polarization of atomic fluorescence as a function of excitation wavelength are shown in figure 1 (a and b respectively). The excitation function is found by normalizing the D_2 atomic fluorescence to the incident laser power, the error bars representing the standard deviation of many measurements. The absorption profile is quite similar to that measured by Janson and Papernov[11] in a gas cell experiment, though

shifted slightly to lower frequencies due to the somewhat higher temperature in our experiment. We have not observed expected quasibound resonances in the atomic excitation profile[12]. This may be due to the heavy thermal averaging in this experiment.

The observed polarization is sensitive to the excitation wavelength and, therefore, to the dissociation dynamics including both the molecular rotation and nonadiabatic electronic mixing during the "half collision". We have developed a semiclassical theoretical model to include these effects and semiquantitatively explain the observed polarization profile. While the molecular rotation and nonadiabatic electronic mixing associated with the radial motion are not rigorously separable, they can be approximately separated within the context of the orbital following model we employ[13,14].

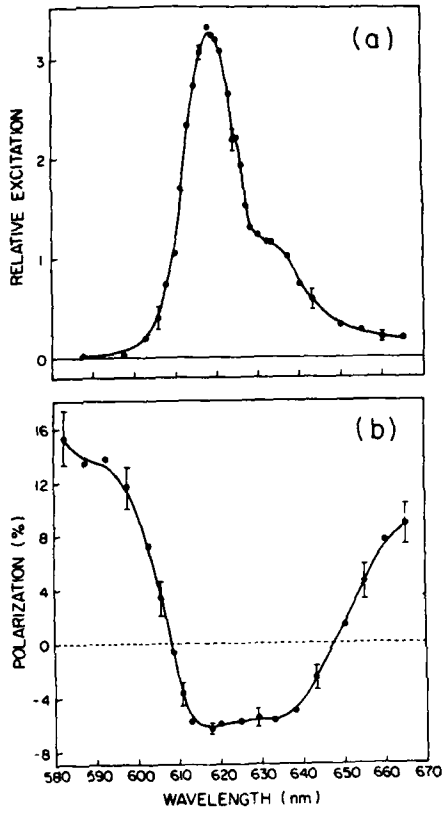

Fig. 1 (a) Relative absorption (bound-free excitation) and
(b) polarization profiles in the photodissociation of K_2

In this model we assume that following excitation (and as the molecule dissociates) the molecular orbital rotates through an angle α. This angle depends on the initial molecular state (v'',J'') and on the laser wavelength (through the continuum energy E), and must be evaluated for each individual transition. Because of the B state barrier, the asymptotic kinetic energy will in general be considerable. As a result, α typically will be restricted to relatively small values ($<2\pi$); for $\alpha \ll 1$, we approach the usual axial recoil limit[1].

For given rotation angle α and final state amplitudes resulting from the dissociation, we can evaluate the asymptotic radiation matrix element[9,10]. Then, by squaring, averaging over initial molecular orientations and summing over final states, the observed initial molecular polarization of the atomic fluorescence can be evaluated. The final state amplitudes are found by carrying out a classical trajectory calculation, numerically integrating the Schrödinger equation following coherent excitation of the $^1\Pi_u$ molecular state.

This calculation follows closely the work of Gordeev et al.[15] and includes the resonance and spin-orbit terms in the interaction. At these low energies the population of the $^2P_{1/2}$ states is near zero.

The polarization of the atomic fluorescence due to a single photodissociation event as a function of α for three different models (final state populations) is shown in figure 2. By comparing the experimental with the theoretical results (figures 1b and 2) we conclude that the observed negative polarization values can be explained by assuming the dissociation is essentially adiabatic with respect to the m_j state populations. The crude semiclassical calculation seriously overestimates the effect of nonadiabatic m_j state mixing at least for kinetic energies near $300cm^{-1}$. This is perhaps surprising since the calculation neglects potentially important rotational effects which might naively be expected to enhance the nonadiabatic mixing.

Furthermore, when hyperfine depolarization is included using the theory of Fano and Macek[7], the observed negative polarization values are roughly twice as big as theory predicts. This may suggest that atoms produced by photodissociation don't behave as free atoms even at very long internuclear distances (especially perhaps under a resonant interaction), and a new theory similar to that of Fano and Macek should be developed for depolarization due to the hyperfine interaction in a long-range molecule. An alternative explanation for the discrepancy between theory and experiment could be that the Fano-Macek hyperfine depolarization theory can be applied to photodissociation products, but our simple semiclassical model for the dissociation dynamics neglects something important, e.g. hyperfine coherences or Coriolis effects. If this is the case, then the adiabatic model may not be correct.

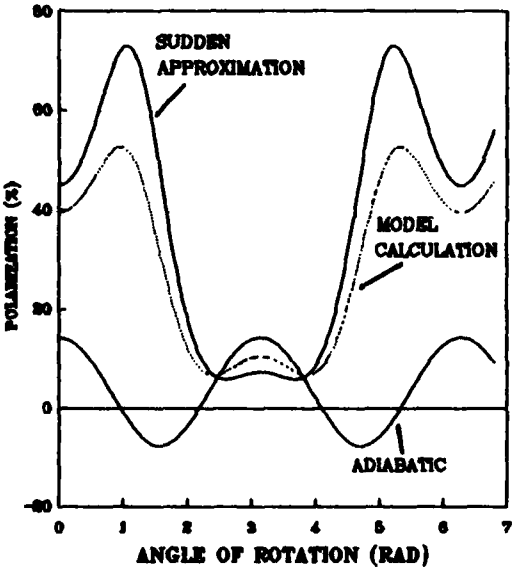

Fig. 2 Polarization of the fluorescence emitted by a single excited atom as a function of the angle of rotation α. At high kinetic energies (>>1eV), where the sudden approximation is valid, α is near zero and the upper curve cannot be observed experimentally.

The polarization results depend on laser excitation wavelength, and on the initial molecular v'',J'' state; this dependence occurs both in the final state distribution and in the final rotation angle α. The observed polarization profile will require a weighted average over initial v'',J'' levels of the ground state, for each laser wavelength[10]. Even without detailed calculation, however, the shape of the experimental polarization profile can be explained in terms of a rough correspondence between excitation wavelength and the degree of molecular rotation, α.

Consideration of the Franck-Condon factors of the $B^1\Pi_u$-$X^1\Sigma_g^+$ bound-free transitions for K_2 indicates that at short (~590nm) and at long (~660nm) wavelengths λ, excitation from high lying vibrational levels is favored, while at middle range λ's (~620nm) excitation occurs predominately from the lowest lying levels. Furthermore, the value of J with the largest contribution to photodissociation increases as λ increases. Thus short wavelengths result in photodissociating states of relatively high kinetic energy and low rotational energy leading to rotation angles α of the order of 0.1 rad, i.e. approaching the axial recoil limit where the adiabatic model predicts the maximum polarization (figure 2). As the wavelength of the laser increases the excitation occurs from lower lying levels, and the kinetic energy of the free states decreases; at the same time the average rotational energy increases and α approaches $\pi/2$ at ~620nm. The polarization therefore approaches the maximum negative value. At longer wavelengths the high lying vibrational levels become important again, and the average rotational energy increases. This leads to a wide distribution of rotation angles α centered around π and ranging roughly from $\pi/2$ to $3\pi/2$. The average value of the polarization in this range is positive but considerably reduced from that near 590nm.

It is clear that this work reveals significant information about the dynamics of the photodissociation process, such as nonadiabatic transition probabilities, molecular rotation, the degree of orbital following and the effects of hyperfine interactions.

ACKNOWLEDGMENTS

We gratefully acknowledge Sherwin Singer and Paul Julienne for helpful discussions. This work was supported by grants from the National Science Foundation.

REFERENCES

1. R. J. Van Brunt and R. N. Zare, J. Chem. Phys. 48, 4304 (1968).
2. U. Fano and J. H. Macek, Rev. Mod. Phys. 45, 553 (1973).
3. C. H. Greene and R. N. Zare, Ann. Rev. Phys. Chem. 33, 119 (1982).
4. J. Vigué, J. A. Beswick and M. Broyer, J. Phys. (Paris), Colloq. 44, 1225 (1983).
5. P. S. Julienne and F. H. Mies, Phys. Rev. A 30, 831 (1984).

6. S. J. Singer, K. F. Freed and Y. B. Band, in Advances in Chemical Physics, Vol. 61, ed. I. Prigogine and S. A. Rice, (John Wiley & Sons 1985), p. 1.
7. E. W. Rothe, U. Krause and R. Düren, Chem. Phys. Lett. 72, 100 (1980).
8. J. Vigué, P. Grangier, G. Roger and A. Aspect, J. Phys. (Paris), Lett. 42, L-531 (1981).
9. V. Zafiropulos, P. D. Kleiber, K. M. Sando, X. Zeng, A. M. Lyyra and W. C. Stwalley, Phys. Rev. Lett. 61, 1485 (1988).
10. V. Zafiropulos, Ph.D. Thesis, University of Iowa (1988).
11. M. L. Janson and S. M. Papernov, J. Phys. B: At. Mol. Phys. 15, 4175 (1982).
12. W. S. Struve, S. J. Singer and K. F. Freed, Chem. Phys. Lett. 110, 588 (1984).
13. E. L. Lewis, M. Harris, W. J. Alford, J. Cooper and K. Burnett, J. Phys. B 16, 553 (1983).
14. I. V. Hertel, H. Schmidt, A. Bähring and E. Meyer, Rep. Prog. Phys. 48, 375 (1985).
15. E. A. Gordeev, E. E. Nikitin and A. I. Shushin, Mol. Phys. 33, 1611 (1977).

SELF-INDUCED POLARIZATION EFFECTS IN GASES

S.A.Bakhramov, A.T.Berdikulov, A.M.Kokharov,
P.K.Khabibullaev, V.V.Tikhonenko.
Thermophysics Department AS Uzb.SSR, Gazzet "PRAVDA" str., 28, Chilanzar, Tashkent 700135, USSR.

ABSTRACT

The one-photon effect of the resonance self-induced optical activity (SIOA) in a atomic rubidium vapour has been experimentally investigated for the first time. Data on optical polarization rotation are presented and interpreted in terms of the resonance behavior of the third order susceptibility and finite elliptical polarization of real lasers. The limitations introduced by SIOA on the sensetivity of polarization spectroscopy is also discussed.

INTRODUCTION

In the present comminication we report the first observation of self-induced optical activity (SIOA) in a resonant centrosymmetric medium. It is demonstrated that the one-photon resonance interaction of an intense laser field with the rubidium $5S-5P_{3/2}$ transition results in considerable polarization rotation even for extremly small polarization ellipticity of initial the laser beam.

RESULTS AND DISCUSSION

A dye laser with a two-stage amplifier, pumped by a ruby laser was used. The laser output beam with 150-kW peak power, 25-ns pulse duration, and 0.5-cm^{-1} bandwidth was passed through a linear polarizer before it was directed into the 20-cm - long glass cell, which contained the rubidium vapour at concentrations not exceeding 10^{13} cm^{-3}. The vapour pressure was controlled by a two-chamber oven according to standard techniques. We did not use a buffer gas in the cell. Experiments were performed with a collimated beam. The cell and oven windows were checked for optical activity during heating. After passing through the vapour cell, the laser beam was spatially filtered to control self-focusing/defocusing effects. The frequency of the dye.laser was selected by interference filters. The analysis of the output beam polarization was accomplished by an analizer prizm and a photodiode in the polarization control channel. Other parts of the beam were deflected by beam splitters in to a second photodiode(laser energy control channel), and in to a monochromator (spectral reference

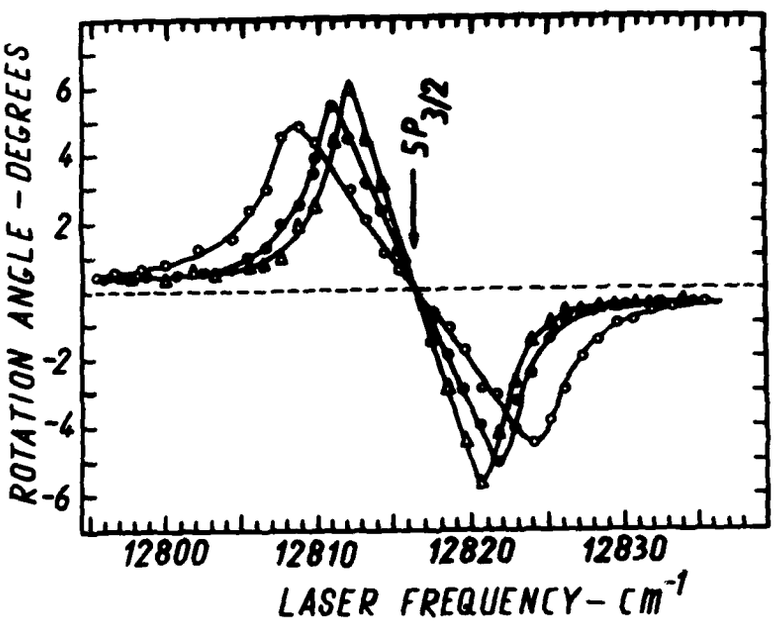

Figure 1. Frequency dependencies of polarization ellipse rotation in the vicinity of Rb $5S-5P_{3/2}$ resonance.

channel). The experimental data were then processed and stored in a computer /1/. Figure 1 shows the frequency dependence of the rotation of the polarization ellipse in the vicinity of the Rb D_2 line. The corresponding laser intensities were: 1,2 MW/cm^2 (open circles), 0.7 MW/cm^2 (full circles), and 0.35 MW/cm^2 (triangles); the polarization ellipticity was $5 \cdot 10^{-4}$, the concentration of the metal vapour was 10^{13} cm^{-3}. We assign an uncertainty of 10% to the values of the rotation angles obtained. Note that the transsmitted pulse energy was constantly monitored during the experiments. No variation of the energy in the vicinity 5S-5P resonance was observed. These proved that self-focusing, defocusing effects unimportend for the laser intensities and pressures emploed. As can be seen from Fig.1, each dependence shows a dispersion-like symmetrical contour centered about the 5S-5P resonance. In contrast to previoce polarization spectroscopy experiments /2/ we observed that the rotation angle decreses to zero as the resonance frequency is approchead. Figure 1 also shows that the maximum value of the self-rotation angle increases with decreasing laser flux. It also should be noted that we have observed an essential deformation of the polarization ellipse at exact resonance. The one-photon

self-induced rotation of the polarization ellipse /3/ may in this case be explained as a result of the AC Stark shift and the splitting of the degenerate Zeeman sublevels of the atomic ground and resonance states. Thus, the intensity-dependent difference in the refraction of the right - and left - handed circular polarized components of the transmitted beam is due to field induced changes in the refractive indeces of Zeelmeier matrix. The difference between the refractive indeces is resonantly enhanced near the rubidium D_2 line changing sign at the resonance frequency as expected. We point out that our results for SIOA differ from previously described polarization rotation effect /2-4/ which were based on the two-photon dispersion properties of S-to-S transitions of alkaly atoms. Moreover, we have directly verified in our experiments the effect of laser polarization ellipticity on SIOA. This was accomplished by placing an electrically-driven Pockel's cell before the entrance window of the oven. The parameters of the input beam-polarization-ellipse were controlled by a high voltage applied to the Pockel's cell and checked with the apparatus mentioned above in the absence of the rubidium vapour. Typical dependencies of the rotation of polarization-ellipse versus initial ellipticity are shown in Fig.2. The upper curve corresponds to a 5-cm^{-1} - low-frequency detuning from the 5S-5P resonance, while the lower curve corresponds to a 10-cm^{-1} - detuning. The total laser-power density applied was kept constant near 300 kW/cm^2 and the atomic concentration of the rubidium was again 10^{13} cm^{-3}.

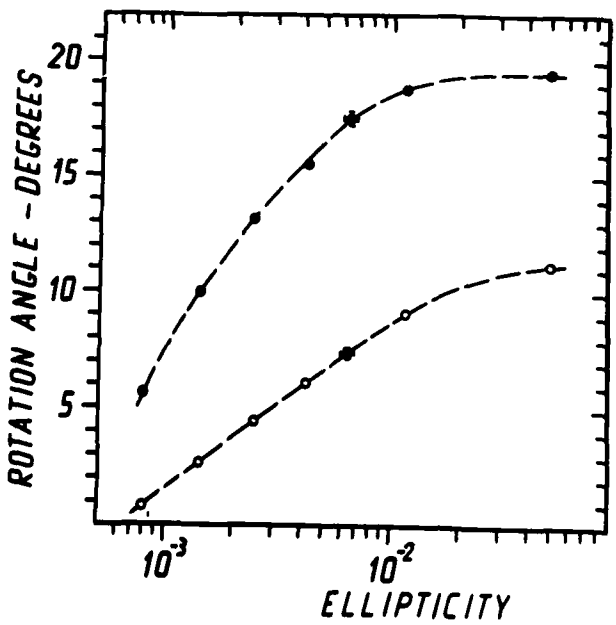

Figure 2. Polarization rotation dependencies on the passing beam ellipticity.
(Detuning from D_2 line: full circles - 5 cm^{-1}; open circles - 10 cm^{-1}.

The observed dependencies are nonlinear and the nonlinearity increases with decreasing detuning from the D_2 line. Unfortunately, the existing apparatus does not allow us to achieve higher ellipticities, but saturation obviously occures when the polarization becomes circular. The intensity dependencies of the self-induced polarization-rotation were also investigated. Figure 3 presents the experimental data obtained in the red wing of rubidium D_2-line for low frequency deturning: 5.5 cm^{-1} (triangles), 8 cm^{-1} (full circles), and 11 cm^{-1} (open circles). The initial ellipticity and Rb atomic concentration were the same as in Fig.1

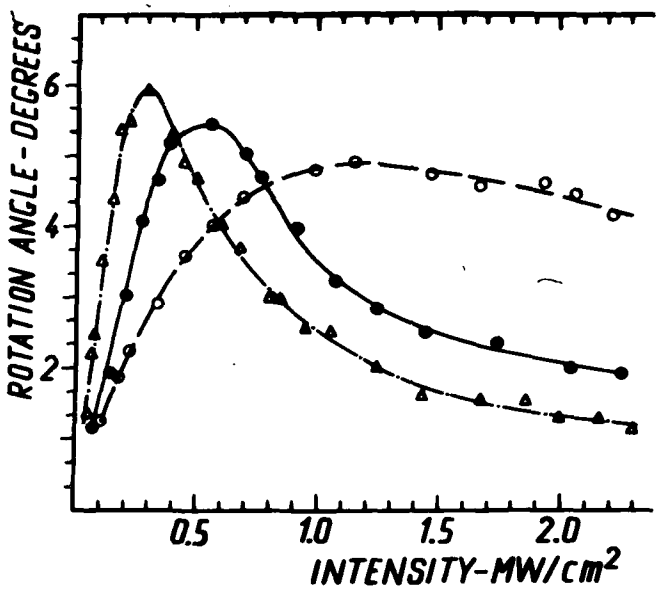

Figure 3. The self-induced polarization rotation dependencies on the laser intensity for different low-frequency detuning from the $5S-5P_{3/2}$ resonance.

A general review of our data suggests several remarks:
1. The experimental data confirm that the mechanism of SIOA is based on a non zero ellipticity of real linear polarized laser beam.
2. In contrast to the self-induced, elliptical rotation in isotropic nonresonant media proposed earlier /3/, the SIOA in atomic vapours has a resonant character due to the inherent resonant behavior of the third-order atomic susceptibility.
3. The dependence of the self-induced rotation in the "anomalous dispersion" region, seen in Fig.1 is connected with the decreas in nonlinearity due to a saturation of the 5S-5P transition by the intense laser field. In fact, our estimate indicates a good correllation between the Rabi splitting at a given intensity, and separation between the extrema of the polarization angle:

Table 1. Separation of extrema and Rabi splitting

(calculation) vs intensity.

Intensity (MW/cm^2)	Rabi splitting (cm^{-1})	Exstrema separation (cm^{-1})
0,35	8.8	8.7
0.70	11.4	11.8
1.20	15.2	15.0

CONCLUSION

We wish to point out that the resonant SIOA reported here may degrade the vectoral phase-conjugation prosess exploited in many resonant four-wave parametric generators. It also leads to sensetivity limitation for resonance polarization spectroscopy. The intensity behavior of the dispersion curves of Fig.1 and the data of Fig.3 allow us to suggest that the highest SIOA effect may be obtained with extremly narrowband cw dye lasers. These is due to the small power broadening of the relevant transitions and the maximum achievable resonant enhancement.

Another concequency of SIOA is a systematic error introduce in experimental verifications of parity nonconservation effects /5-7/.

REFERENCES

1. S.A.Bakhramov, K.N.Drabovich, A.M.Kokharov et al, Opt.Commun. 60, 32 (1986).
2. P.L.Liao, G.C.Bjorklund, Phys.Rev. A 15, 2009 (1975).
3. P.D.Maker, R.W.Terhune, C.M.Savage, Phys. Rev. Lett. 12, 507 (1964).
4. V.M.Arutunyan, I.I.Papazyan, G.G.Adonts et al, JETF 68, 44 (1975).
5. J.V.Bogdanov, I.I.Sobelman, V.N.Sorokin et al, JETF Pisma 31, 234 (1980).
6. L.L.Lewis, J.H.Hollister, D.C.Soreide et al, Phys. Rev. Lett. 39, 795 (1977).
7. P.E.G.Baird, M.W.S.M.Brimicombe, R.G.Hunt et al, Phys. Rev. Lett. 39, 798 (1977).

VIBRATIONAL PREDISSOCIATION DYNAMICS OF OVERTONE-EXCITED HN_3

B.R. Foy, M.P. Casassa, J.C. Stephenson, and D.S. King
Molecular Spectroscopy Division
National Institute of Standards and Technology
Gaithersburg, Maryland 20899

ABSTRACT

Vibrational overtone photodissociation is used to examine rotationally resolved spectra of HN_3 near E_{vib} = 15100 cm^{-1} and 17700 cm^{-1}. The spectra exhibit extensive coupling of the NH stretching overtones to background vibrational states. Lifetimes for vibrational predissociation, $HN_3(\tilde{X}) \rightarrow NH(X) + N_2(X)$, are 210 nsec and 0.95 nsec for the levels v_{NH} = 5 and 6, respectively.

INTRODUCTION

Vibrational overtone excitation of molecules offers a powerful means of studying ground-electronic state unimolecular fragmentation. Reactants may be prepared in a highly state-specific manner, and time- and state-resolved analysis of the products can reveal important details of the dissociation dynamics. Experiments by Crim and co-workers on HOOH illustrate these advantages well.[1] We have recently described similar experiments[2] on hydrazoic acid, HN_3, in which the v_{NH} = 5 and 6 levels, populated by direct overtone pumping from the ground vibrational state, yield NH and N_2 fragments by the spin-forbidden process $HN_3(\tilde{X}^1A') \rightarrow NH(X^3\Sigma^-) + N_2(X^1\Sigma_g^+)$. Here we report a picosecond measurement of the $6\nu_{NH}$ dissociation lifetime and molecular-beam overtone photodissociation spectra of $5\nu_{NH}$ and $6\nu_{NH}$. These spectra enable us to examine the degree of vibrational level mixing at high vibrational energy in the ground state ($\tilde{X}$).

PHOTODISSOCIATION SPECTRA

Molecular-beam cooling of HN_3 eliminates the rotational congestion that plagues the 300 K spectra of the overtone bands.[3] Figure 1 shows the photodissociation spectrum of the $5\nu_{NH}$ band. This was obtained by scanning the frequency of the overtone-pump laser near 15,121 cm^{-1} and monitoring fluorescence (LIF) excited by a probe laser tuned to a NH fragment transition ($A^3\Pi$-$X^3\Sigma^-$, $R_1(1)$ line near 336 nm). HN_3 is cooled to a rotational temperature of ~8 K in a free-jet expansion (5% HN_3 in Ar, 1 atm backing pressure). Linewidths in the spectrum are determined by the 0.03 cm^{-1} bandwidth of the pump laser. As expected, we observe the simple P,R-branch structure for a parallel band of a near-prolate top. Unexpectedly, though, the (J,K=0) transitions appear as multiplets of up to three features rather than as single peaks. These features are separated by 0.02-0.18 cm^{-1}, and the patterns of the multiplets vary erratically with J. Identical patterns show up in the P and R branches for transitions with a common upper state J'. The

combination-differences of these lines are consistent with the known rotational constants of the ground vibrational state.[4] Possible causes of the extra lines such as K>0 transitions, hot-band transitions, and absorptions of van der Waals clusters can all be excluded by known spectroscopic data[3] and the fact that similar spectra are obtained in different expansion gases. These sets of transitions can only arise by mixing of the ($n\nu_{NH}$,J,K=0) rovibrational levels of HN_3 with other rovibrational states of the molecule.

The photodissociation spectrum of the $6\nu_{NH}$ overtone (17,671 cm^{-1}) is similarly perturbed by neighboring vibrational states.[5] More components (from three to five) appear in this spectrum than in $5\nu_{NH}$, reflecting the increase in the density of background states with vibrational energy. Separations of features are larger, up to 0.39 cm^{-1}, indicating an increase in the coupling matrix elements between the vibrational states. In both the $5\nu_{NH}$ and $6\nu_{NH}$ spectra, the J'=0 levels are perturbed to the same extent as higher J, suggesting that the mixing is principally anharmonic (or Fermi) in nature. We have estimated the size of the coupling matrix elements by performing a deperturbation of the patterns of mixing in Fig. 1,[5] and we find that these matrix elements are in the range 0.010-0.065 cm^{-1} for $5\nu_{NH}$, and up to 0.1 cm^{-1} for $6\nu_{NH}$. In both the $5\nu_{NH}$ and $6\nu_{NH}$ levels, the density of features that appear in the spectrum is comparable to the calculated density of vibrational states (ρ_{vib} = 7 and 13 states/cm^{-1} for v_{NH} = 5 and 6, respectively). This remarkable comparison suggests that the NH stretching overtones can couple to any neighboring states that fall within the coupling strength of ~0.1 cm^{-1}, regardless of the type of motion involved.

VIBRATIONAL PREDISSOCIATION LIFETIMES

We previously measured the vibrational predissociation lifetime (τ_{vp}) of the $5\nu_{NH}$ level at 300 K, at which a broad distribution of rotational levels was excited.[2] Lifetimes were measured by varying

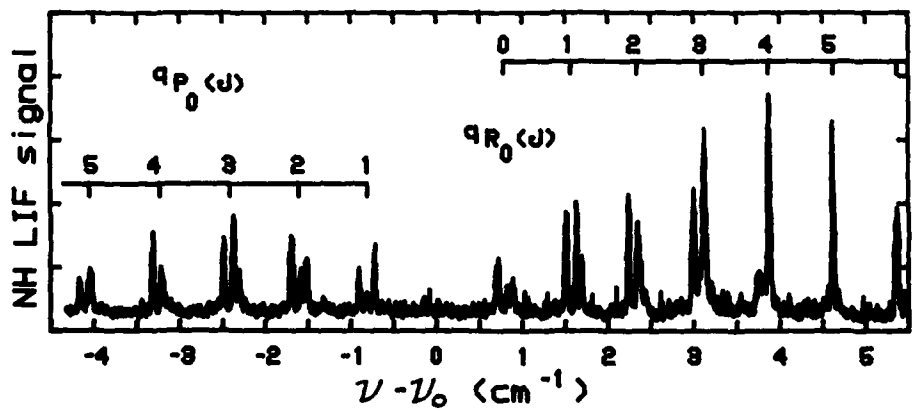

Figure 1. Photodissociation spectrum of HN_3 ($5\nu_{NH}$). Fragment LIF signal plotted vs. pump laser frequency; ν_0 = 15121.23 cm^{-1}.

the pump-probe time delay and monitoring the increase of fragment LIF. In molecular beam experiments, one can measure the lifetimes of individual (J,K) levels of $5\nu_{NH}$, and of the Fermi resonance components of those rotational levels. For the spectral features shown in Fig. 1, we find dissociation lifetimes on the order of 210 nsec. Surprisingly, a few particular Fermi resonance components have lifetimes that differ by as much as a factor of 2; this will be discussed in a separate publication.[5] Aside from this deviation, however, τ_{vp} is not strongly dependent on rotational level at these low J values (J = 0-7, K=0).

The $6\nu_{NH}$ overtone state dissociates much more rapidly, and picosecond pump and probe pulses are required to measure its lifetime. Our apparatus consists of independently tunable picosecond lasers that generate pulses of duration $\leq$ 15 psec; it has been described elsewhere.[6] We measure a lifetime of 950 $\pm$ 150 psec for $6\nu_{NH}$, with no rotational state dependence at low J. This represents about a 200-fold increase in the vibrational predissociation rate for a 17% increase in vibrational energy. Statistical theory predicts a less dramatic increase in the rate with energy and ρ_{vib}: RRKM calculations give only a factor of 4 increase at these energies.[5] More detailed theories may be required to account for the observed rates $k_{uni}(E_{vib})$.

In summary, we have found that rotationally resolved overtone photodissociation spectra for HN_3 near 15121 cm^{-1} and 17671 cm^{-1} exhibit extensive mixing of the NH stretching states with background states. The matrix elements associated with this mixing are in the range 0.01-0.1 cm^{-1}, increasing slightly with the number of stretching quanta v_{NH}. Vibrational predissociation rates for HN_3 in its ground electronic state increase rapidly with v_{NH}, more so than predicted by statistical theory.

This work was supported in part by the Air Force Office of Scientific Research.

REFERENCES

1. F.F. Crim in Molecular Photodissociation Dynamics, M.N.R. Ashfold and J.E. Baggott eds., (Royal Society of Chemistry, London, 1987); X. Luo, P.T. Rieger, D.S. Perry, and T.R. Rizzo, J. Chem. Phys. 89, 4448 (1988).
2. B.R. Foy, M.P. Casassa, J.C. Stephenson, and D.S. King, J. Chem. Phys. 89, 608 (1988).
3. David T. Halligan, Ph.D. Thesis, Rice University (1988).
4. J. Bendtsen and F.M. Nicholaisen, J. Mol. Spectrosc. 119, 456 (1986).
5. B.R. Foy, M.P. Casassa, J.C. Stephenson, and D.S. King, submitted to J. Chem. Phys.
6. M.P. Casassa, J.C. Stephenson, and D.S. King, J. Chem. Phys. 89, 1966 (1988).

VIBRATIONAL AND ROTATIONAL ENERGY TRANSFER IN $X^2\Pi_i$ OH

David R. Crosley, Karen J. Rensberger and Jay B. Jeffries
Molecular Physics Laboratory
SRI International
Menlo Park, California 94025

ABSTRACT

Vibrational and rotational energy transfer in the $X^2\Pi_i$ state of the OH radical has been studied in a low pressure flow system, using a novel two-laser pump-and-probe technique. The OH is prepared in v=2 by overtone pumping in the infrared and monitored by laser-induced fluorescence in the (1,2) or (0,1) band of the A-X electronic system in the ultraviolet. Varying the time delay between the lasers produces decay rates for individual level populations due to collisional transfer with added collider gases. Rotational relaxation with He is determined under single-collision conditions. Vibrational relaxation from v=2 proceeds like that of hydrogen halides but, except for polar ammonia and water, is much slower than for the $A^2\Sigma^+$ state of OH.

INTRODUCTION

The OH molecule is of both practical and fundamental interest. It is a key intermediate in the chemistry of the atmosphere and in combustion, and is small enough that *ab initio* calculations of potential surfaces with simple colliders is feasible. OH has a large dipole moment, vibrational frequency and rotational constant like HCl and HF but, as a free radical, has a very different chemical reactivity than those molecules. In its $A^2\Sigma^+$ excited state, which also has a large dipole moment, OH undergoes vibrational energy transfer (VET), as well as collisional quenching, in a manner governed by attractive forces and collision complex formation. The hydrogen halides undergo self-relaxation at a rate which decreases with increasing temperature, behavior typical of systems where attractive forces dominate. The study of ground electronic state OH is therefore of particular interest in an overall understanding of the mechanisms for vibrational and rotational energy transfer (RET).

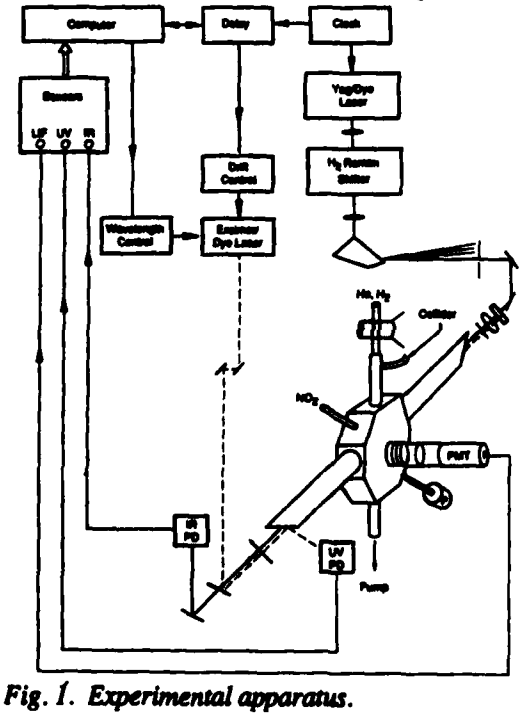

Fig. 1. Experimental apparatus.

EXPERIMENTAL METHOD

The apparatus for this study[1] is shown in Fig. 1. Hydrogen atoms are produced in a microwave discharge in helium with trace amounts of H_2 added; these react with NO_2 just above

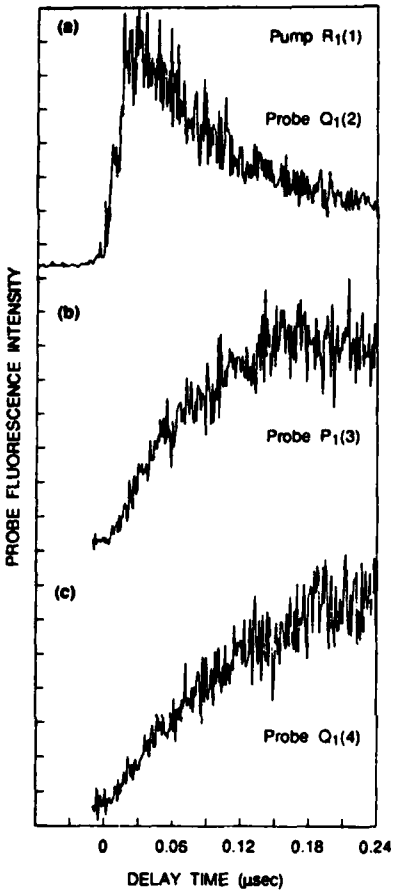

Fig. 2. Time dependence of signals from rotational levels N=2, 3, and 4 following pumping of N=2 in water vapor at 0.2 Torr.

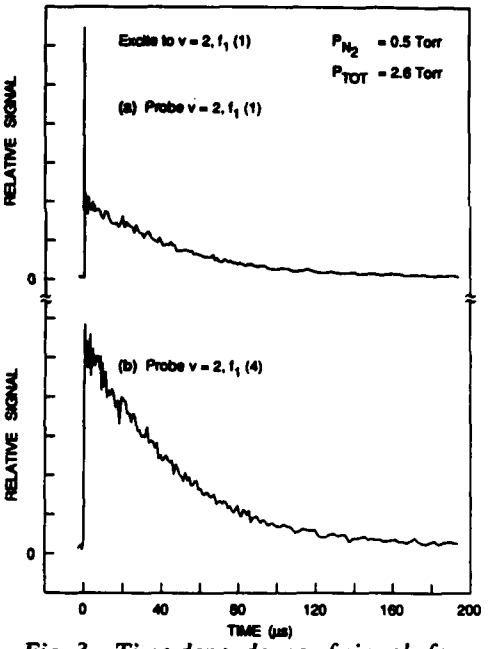

Fig. 3. Time dependence of signals from N=1 and 4 following pumping of N=1 in 0.5 Torr N_2 and 2.1 Torr He.

the laser interaction region to form OH radicals. The rare gas carrier pressure is about 2 Torr for the VET studies, and as low as 650 mTorr for the RET measurements. Collider gas is added upstream of the interaction region to facilitate good mixing. The second Stokes component of the Raman-shifted output of a tunable dye laser (~7000 cm^{-1}, 0.9 mJ, 0.15 cm^{-1} bandwidth) excites the OH to both λ-doublet components of a specific rotational level in v=2 via the first overtone transition. Ultraviolet light from a second laser probes one of the rotational levels in v=2 or 1 via the (1,2) or (0,1) bands of the A-X system. The infrared beam is focused to 0.5 mm diameter at cell center and the ultraviolet beam is five times larger. Both laser beam energies are monitored by photodiodes. The fluorescence is collected and focused onto a filtered photomultiplier tube, whose output is amplified and captured by a boxcar integrator.

A computer varies the time delay between the lasers and collects the fluorescence and photodiode signals. For lower pressure and short delays, traces such as those shown in Fig. 2 are obtained. The top panel monitors the intially excited rotational level, $f_1(2)$, which rises steeply and then decays as the molecules rotationally transfer due to collisions, in this case H_2O at 0.2 Torr. At the same time, the populations of the other rotational levels in v=2, initially zero, begin to increase as seen

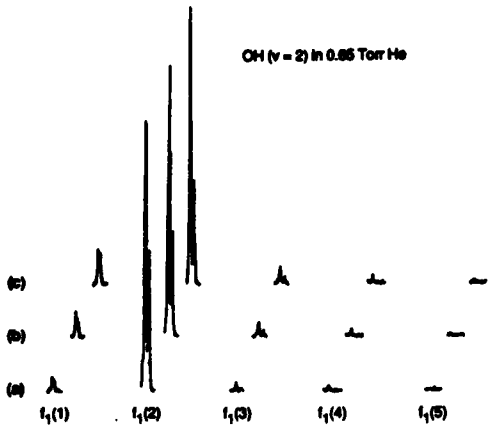

Fig. 4 LIF signals for $1 \leq N \leq 5$ after exciting $f_1(2)$ in v=2 for delays of (a) 0, (b) 60, and (c) 100 ns between the pump and probe laser pulses in 0.65 Torr of He.

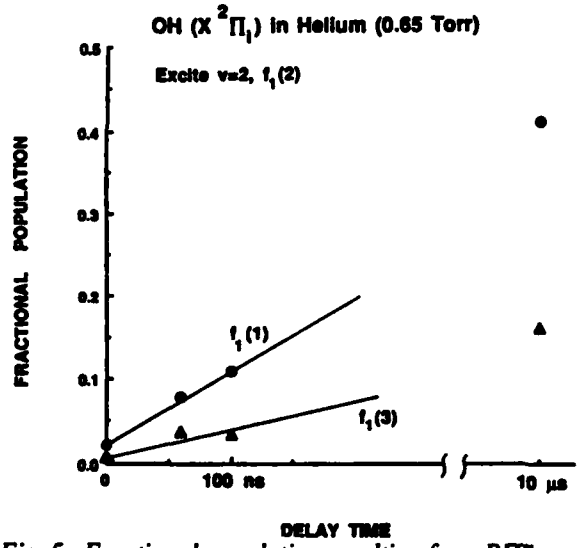

Fig. 5. Fractional population resulting from RET versus collision time for $f_1(1)$ and $f_1(3)$ from the data in Fig. 4.

in traces (b) and (c) in which the $f_1(3)$ and $f_1(4)$ levels are probed. At longer times, the rotational level populations reach thermalization and begin to decay out of the v=2 level at the much slower VET rate. This is shown in Fig. 3, where RET is caused by collisions with the added N_2 and the He bath gas. In this case, the decay rate of the v=2 population can be seen to be the same for both the intially pumped level and the level populated by rapid RET.

ROTATIONAL ENERGY TRANSFER

To date, quantitative RET measurements have been made for only one level and He as a collider. The OH is initially excited to the $f_1(2)$ level in v=2, and the probe laser tuned to excite $1 \leq N \leq 5$. The LIF signal for each of these levels is shown in Fig. 4 for delays of 0, 60, and 100 ns. It is important to work toward the single collision limit to obtain state-to-state cross sections. With a 100 ns delay between the pump and probe laser pulses, only 15% of the population in $f_1(2)$ is transferred to other levels at a He pressure of 0.65 Torr. Figure 5 shows the fractional population in the levels $f_1(1)$ and $f_1(3)$ versus delay time from the data in Fig. 4; the points at 10 µs delay are the 300 K thermal populations. The slopes of the lines yield cross sections of $\sigma(2\rightarrow1) = 3$ Å^2 and $\sigma(2\rightarrow3) = 1$ Å^2. Qualitative observations of other levels and for other colliders show transfer as high as $f_1(5)$, with possible contributions from both multiquantum and multi-collision transfer. In an earlier version[2] of this experiment with H_2O as a collider, a definite propensity was found for conservation of λ-doublet components during RET. In the present measurements both components are initially

populated, but future experiments will include rates specific to λ-doublet and spin-orbit components of the $^2\Pi$ state.

VIBRATIONAL ENERGY TRANSFER

At higher carrier gas pressures, rotational equilibration is achieved before VET takes place (see Fig. 3). The signals are fit to single exponentials and the resulting decay constants show a linear dependence on collider gas pressure. The intercepts are due to diffusive and transit time considerations and change slightly with carrier pressure, flow rates, and beam diameters. The slopes yield the desired VET rate constants,[1] presented in Table 1. Chemical reaction could contribute to the removal rates for the colliders NH_3, CH_4, and N_2O, but the rate constants for those reactions (with OH, v=0) are two to three orders of magnitude smaller. The effects of vibrational excitation of the OH on those reaction rates is not known, but it is expected to be small as the OH bond is not broken in the reaction. Therefore, we conclude that the observed removal is primarily by vibrational relaxation out of v=2.

Table 1. Vibrational Relaxation Constants ($cm^3\ s^{-1}$)

Collider	$X^2\Pi_i$, v=2	$A^2\Sigma^+$, v=1 (Refs. 3-6)
NH_3	1.2×10^{-10}	1.2×10^{-10}
CH_4	2.3×10^{-12}	4.4×10^{-10}
CO_2	6.7×10^{-13}	3.1×10^{-10}
N_2O	4.6×10^{-13}	3.4×10^{-10}
O_2	2.6×10^{-13}	3.8×10^{-10}
N_2	$<1 \times 10^{-14}$	2.8×10^{-10}
H_2	$<1 \times 10^{-14}$	1.9×10^{-10}

The vibrational relaxation of OH follows many of the same trends as the relaxation of HF and HCl. The hydrogen halides often relax by vibration-to-vibration transfer into some mode of the collision partner; the efficiency of the process is greater as the energy defect, i.e., the excess energy going into translation and rotation, is smaller. In OH, four of the colliders studied follow this pattern, as seen in Fig. 6 where the rate constant is plotted logarithmically vs. the energy defect. The role of long-range attractive forces is evident in the case of the polar molecule NH_3, whose rate constant is enhanced by a factor of thirty over predictions from the energy defect; it also relaxes HF and HCl rapidly. Preliminary experiments indicate that H_2O, another polar molecule, also relaxes OH rapidly.

The four colliders He, Ar, H_2 and N_2 are not shown in Fig. 6, as we could determine only upper limits for their rate constants; all inefficiently relax v=2 of OH. The rare gases have, of course, no vibrational degree of freedom, but have rate constants at least threefold smaller than predicted by the energy defect. Transfer to H_2 is endoergic for single quantum transfer and should also proceed only by transfer to translation and rotation. Relaxation by nitrogen, however, is unexpectedly slow. The energy defect of 1070 cm^{-1} is similar to that for CO_2 but the rate constant is at least sixty times smaller. The fact that N_2 has an infrared inactive mode is not the reason, for O_2 falls on the line predicted by energy defect (see Fig. 6). Relaxation of HF and HCl by both N_2 and O_2 is slow.

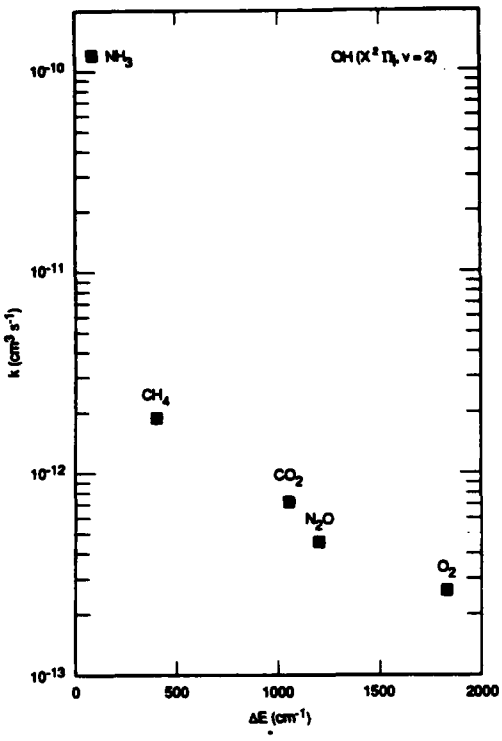

Fig. 6 Measured rate constant vs. rotationless vibration-to-vibration energy defect for five colliders.

COMPARISON WITH VET IN OH $A^2\Sigma^+$

The results contrast starkly with those for vibrational relaxation of the v=1 level of the $A^2\Sigma^+$ electronically excited state of the OH radical. Rate constants for that process[3-6] are also included in Table 1. For all colliders save NH_3, the excited state rate constants are 100 to 10,000 times larger than for the ground state. The large cross sections for both VET and quenching of the A-state has been explained by a collision mechanism involving the formation of a transitory complex,[3] the dynamics of whose formation are governed by attractive interactions between the excited OH and the collision partner. A simple picture involving multipole interactions[6-8] accounts for most features of these collisions.

Both the ground and excited states of OH have large dipole moments, and the attractive interactions might be expected to be similar for the two states. The polar collider NH_3 has long-range dipole-dipole forces and nearly identical VET cross sections, so similar mechanisms governed by attractive forces may be operating in both states. However, this is not the case for any of the other colliders studied here, and it is necessary to consider the entire potential, not just the attractive part. Potentials for the interaction of OH with the colliders studied here are not available. However, recent laser-induced fluorescence experiments[9] on OH-Ar van der Waals complexes have furnished potential curves for that molecule. Two features are evident: a much smaller well depth in the ground electronic state, 70 cm^{-1}, compared to 700 cm^{-1} in the excited state; and a repulsive wall occurring at a larger OH-Ar separation in the ground state. We do not know if the potentials for the colliders studied here are similar, but nonetheless speculate on possible effects. The differences could give rise to two effects leading to smaller ground state cross sections. Complex formation in the ground state will be less favorable due to the smaller well depth. Also, the onset of repulsion at larger separation could prevent vibration-to-vibration transfer caused directly by the attractive force part of the curve, a process known to be efficient.

ACKNOWLEDGMENT

This work was supported by the National Aeronautics and Space Administration and by the Air Force Office of Scientific Research.

REFERENCES

1. K. J. Rensberger, J. B. Jeffries and D. R. Crosley, J. Chem. Phys., in press, 1989.

2. R. A. Copeland and D. R. Crosley, J. Chem. Phys. **81**, 6400 (1984).

3. R. K. Lengel and D. R. Crosley, Chem. Phys. Lett. **32**, 261 (1975); J. Chem. Phys. **68**, 5309 (1978).

4. K. R. German, J. Chem. Phys. **64**, 4065 (1976).

5. J. Burris, J. J. Butler, T. J. McGee and W. S. Heaps, Chem. Phys. **124**, 251 (1988).

6. R. A. Copeland, M. L. Wise and D. R. Crosley, J. Phys. Chem. **92**, 5710 (1988).

7. P. W. Fairchild, G. P. Smith and D. R. Crosley, J. Chem. Phys. **79**, 1795 (1983).

8. R. A. Copeland, M. J. Dyer and D. R. Crosley, J. Chem. Phys. **82**, 4022 (1985).

9. M. T. Berry, M. R. Brustein and M. I. Lester, Chem. Phys. Lett., in press, 1988.

ENERGY TRANSFER COLLISIONS IN LASER EXCITED MIXTURES OF ALKALI VAPORS

M.Allegrini, S.Gozzini, G.Squadrito, C.Gabbanini and L.Moi
Istituto di Fisica Atomica e Molecolare del C.N.R.
Via del Giardino, 7 - 56100 Pisa, Italy

ABSTRACT

Energy transfer collisions between two laser excited alkali atoms of different species have been investigated in cell experiments using an intermodulation technique. Cross sections have been measured for the potassium/rubidium mixture and evidence of three-body collisions in presence of a buffer gas has been obtained in the sodium/potassium mixture.

INTRODUCTION

The collisions involving two atoms both in an excited state play an important role in different fields of atomic and molecular physics. The colliding atoms may evolve to several exit channels giving quite different products : ions plus electrons through associative ionization, very excited atoms through electronic energy transfer and excited molecules through atom/molecule energy transfer or molecule formation. At first these collisions have risen much interest as a mean to produce plasmas at very low laser power[1]. Later on they have been considered as a possible mechanism for population inversion in atomic and molecular levels with consequent opportunity for new laser sources[2,3]. More recently the associative ionization has been considered as a limiting process in the atom density achievable with cooling techniques[4]. The population transfer from the initial laser excited atoms to higher levels has been extensively studied in alkali vapors. We have pointed out the interest of extending these studies to mixtures of different alkalis[5] and designated a set of experiments to measure the relative cross sections of heteronuclear energy transfer collisions.

The processes we consider are

$$\begin{aligned} A^*(nP) + B^*(mP) &\longrightarrow A^{**}(n'L) + B(mS) \\ &\longrightarrow A(nS) + B^{**}(m'L) \end{aligned} \qquad (1)$$

where [A(nS), B(mS)], [A*(nP), B*(mP)] and [A**(n'L), B**(m'L)] indicate two alkali atoms of different species in the ground state, in the first excited state and in highly-lying states respectively. The energy transfer is effective only to A**(n'L) and B**(m'L) levels such that the energy defect $|\Delta E|$ from initial to final energy of the reaction is comparable with kT. In order to measure the cross sections of reactions (1), atoms A and B are optically excited to the first P-level and fluorescence intensities are measured from the A**(n'L) and B**(m'L) states. Two dye lasers (cw in our experiments) are required for the selective excitation of the two alkali species. Because A*(nP) and B*(mP) atoms are simultaneously produced, the fluorescence spectrum contains emission also from levels populated through homonuclear collisions

$$\begin{aligned} A^*(nP) + A^*(nP) &\longrightarrow A^{**}(n''L) + A(nS) \\ B^*(mP) + B^*(mP) &\longrightarrow B^{**}(m''L) + B(mS) \end{aligned} \qquad (2)$$

This contribution may predominate over the fluorescence lines coming from highly excited atoms populated by heteronuclear collisions and must be eliminated. To this purpose we have adopted an intermodulation technique, whose details have been described in reference [6], which involves modulation of the two laser beams at two different frequencies ω_1 and ω_2 and phase sensitive detection of the fluorescence at the sum frequency $\omega_1 + \omega_2$. The alkali vapors are produced in a sealed pyrex cell containing an amalgam of the two different metals under study. The amount of the two metals in the amalgam are chosen in such a way that at a given temperature the two species have comparable densities. The determination of the cross sections requires also knowledge of the excited atoms A* and B* densities; these have been indipendently deduced from the effective radiative lifetimes measured in a resonance fluorescence experiment under pulsed excitation. For processes (2) absolute cross sections have been measured in several cases; cross sections for heteronuclear processes (1) are, however, more difficult to measure because many independent parameters are needed. For that reason we have found convenient to determine the cross sections of processes (1) relatively to suitable cross sections of processes (2).

RESULTS

Table I shows the results obtained for the sodium/potassium and potassium/rubidium mixture while table II lists the absolute cross sections for sodium/sodium and rubidium/rubidium collisions used as reference.

Table I. List of levels populated by the collisions of column 1. The cross sections reported in column 5 have been measured relatively to the absolute cross sections (a) and (b) reported in table II.

Collision process	Atom	Level	T(^{0}C)	$\sigma x10^{15} cm^2$	Reference process	Ref.
Na(3P)/K(4P)	Na	3D	240	2.8 ± 1.4	(a)	[6]
	K	5D	240	3.8 ± 1.9	(a)	[6]
		7S	240	1.8 ± 0.9	(a)	[6]
K(4P)/Rb(5P)	Rb	5D	220	58 ± 29	(b)	[7]
		7S	220	6.4 ± 3.2	(b)	[7]
Rb(5P)/Rb(5P)	Rb	7S	180	2.8 ±1.4	(b)	[7]

The values for Na/K collisions reported in reference [6] have been doubled to take into account the correction introduced by Bezuglov et al.[8], valid for experiments performed in cells rather than in beams. The preliminary results for the potassium/rubidium mixture are reported here for the first time. For the moment they are restricted to collisions involving Rb atoms excited to the $5P_{3/2}$; however, work is in progress to

investigate collisions involving also the lower $5P_{1/2}$ level. The measurement of the cross section in this case may be of particular interest because one of the collisionally populated levels is in the midst of the four fine structure levels K*(4P) + Rb*(5P). The last cross section in table I is for energy transfer in pure rubidium. In previous studies[9] of the process

$$Rb^*(5P) + Rb^*(5P) \longrightarrow Rb^{**}(n^nL) + Rb(5S) \qquad (3)$$

population transfer was observed only to the 5D state. Since we use the absolute cross section σ_{5D}(Rb/Rb) of process (3) as reference (see table II) in the measurement of the cross sections for the heteronuclear potassium/rubidium collisions, we have checked if our apparatus give a σ_{5D}(Rb/Rb) value in agreement with that of reference [9], (which is the case). During this experiment we have observed fluorescence also from the 7S level and therefore measured σ_{7S}(Rb/Rb) relatively to σ_{5D}(Rb/Rb). The resulting value matches other cross sections[3] for population transfer collisions in alkali vapors involving similar energy defects (in this case about 2kT).

Table II. List of collision processes and measured absolute cross sections used as reference for measuring the cross sections of table I

	Collision process	Atom	Level	Absolute $\sigma \times 10^{15} cm^2$	Ref.
(a)	Na(3P)/Na(3P)	Na	5S	$3.6 \pm 1.3^{(*)}$	[10](**)
(b)	Rb(5P)/Rb(5P)	Rb	5D	$64 \pm 26^{(*)}$	[9]

(*) The original values have been doubled according to ref. [8].

(**) We have made an average of the two values from ref. [10].

THREE-BODY COLLISIONS

Heteronuclear collisions in a sodium/potassium mixture have been investigated also in presence of a foreign buffer gas[11]. The experiment has been performed using as cell the bulb of a Na spectral lamp which, in addition to sodium, contains a few torr of neon and potassium as impurity. Fluorescence spectra have been recorded upon three different excitation : i) with a single laser tuned to one of the Na D-lines, ii) with a second single laser tuned to one of the K D-lines and iii) with both lasers. While the intensity of fluorescence lines originated by sodium levels does not change significantly in the three spectra, that due to potassium levels exibits a nonlinear increase. Assuming that heteronuclear collisions are responsible for this behaviour, we have adopted the intermodulation technique to distinguish their contribution from that of homonuclear collisions. This intermodulation spectrum exibits new lines with respect to the analogous intermodulation spectrum observed without buffer gas. Moreover some of the fluorescence lines have opposite phase, which indicate a depopulation process of the level emitting the fluorescence. It is well known that the buffer gas increases the energy transfer rate between close levels, however the binary collisions involving alkali and buffer gas atoms can not modify the frequency modulation of the fluorescence. Therefore, in order to explain the modifications observed in the intermodulation spectrum, we have to consider a process able to affect both the population distribution and the modulation frequency of the fluorescence. A process that satisfies these two requirements is the three body collision

$$Na(3P) + K(4S) + M \longrightarrow Na(3S) + K(4P) + M \qquad (4)$$

where M indicates a buffer gas atom. The ratio between the number of three-body and two-body collisions can be expressed[12] as $R = k_3 N / k_2$, where k_3 is the three-body collision rate constant, N is the buffer gas density and k_2 is the two-body rate constant, which has been measured in reference [13]. Comparison of the intermodulation spectrum in presence and absence of buffer gas, suggests a lower value of $R \approx 10\text{-}100$, from which we deduce a lower limit for k_3 of $10^{-27} cm^6 s^{-1}$.

CONCLUSIONS

The intermodulation technique has been proved to be very useful to study the energy pooling collisions in mixtures of alkali atoms. The measured cross sections confirm the fact that the efficiency of these collisions decreases rapidly with increasing energy defects. With the same technique we have also demonstrated the effects of the buffer gas on these collisional processes.

REFERENCES

1. see for example T.B. Lucatorto and T.J. McIlrath, Appl. Opt. 19, 3948 (1980)
2. W. Muller and I.V. Hertel, Appl. Phys. 24, 33 (1981)
3. M. Allegrini, C. Gabbanini and L. Moi, J. Physique Colloq. 46, C1-61 (1985)
4. P.L. Gould, P.D. Lett, P.S. Julienne, W.D. Phillips, H.R. Thorsheim and J. Weiner, Phys. Rev. Lett. 60, 788 (1988)
5. A. Cremoncini, S.A. Abdullah, M. Allegrini, S. Gozzini and L. Moi, Proc. Intern. Conf. LASERS' 85, C.P. Wang Ed., (STS Press -McLean, 1986) pag. 98
6. S. Gozzini, S.A. Abdullah, M. Allegrini, A. Cremoncini and L. Moi, Opt. Commun. 63, 97 (1987)
7. C. Gabbanini, S. Gozzini, G. Squadrito, M. Allegrini and L. Moi, to be published
8. N.N. Bezuglov, A.N. Klucharev and V.A. Sheverev, J. Phys. B20, 2497 (1987)
9. L. Barbier and M. Cheret, J. Phys. B16, 3213 (1983)
10. J. Huennekens and A. Gallagher, Phys. Rev. A27, 771 (1983); M. Allegrini, P. Bicchi and L. Moi, Phys. Rev. A28, 1338 (1983)
11. S.A. Abdullah, M. Allegrini, S. Gozzini and L. Moi, Nuovo Cimento D9, 1467 (1987)
12. J.B. Hasted, *Physics of Atomic Collisions*, (Butterworths, London (1972)
13. M. Allegrini, G. Alzetta, L. Moi and D. Giulietti, Nuovo Cimento B28, 69 (1975)

PHOTOCHEMICAL PRODUCTION OF XeCl(B) INITIATED BY TWO-PHOTON EXCITATION OF Xe AND Xe_2*

Michael R. Berman
McDonnell Douglas Research Laboratories, St. Louis, MO, 63166

ABSTRACT

The excited state of xenon chloride, XeCl(B), has been produced in gas-phase mixtures of Xe and Cl_2 by reactions initiated by the two-photon excitation of atomic xenon and xenon dimers in the wavelength region 246.5 to 258 nm. Studies of the time dependence of the emission from XeCl(B) reveal that the two-photon excitation of xenon atoms at low laser intensities produces excited Xe atoms which react with Cl_2 to produce XeCl(B). Production of XeCl(B) initiated by two-photon excitation of xenon dimers, Xe_2, proceeds by a mechanism involving ionic species. At the laser intensities required for the excitation of two-photon transitions in Xe_2, two-photon absorption is followed by absorption of a third photon ionizing either the excited Xe_2 or an excited Xe atom produced by predissociation of excited Xe_2.

INTRODUCTION

Photochemical production of the rare-gas halide excimer XeCl(B) has been observed at a number of excitation wavelengths.[1-5] In this work, the mechanisms and kinetics of production of XeCl(B) initiated by the two-photon excitation of atomic xenon and xenon dimers are studied.

EXPERIMENTAL

The output of an excimer-pumped tunable dye laser (Lambda Physik FL2002E) having a nominal bandwidth of 0.2 cm^{-1} was doubled in a BBO crystal and passed through a reaction cell containing static mixtures of Xe and Cl_2. Fluorescence was detected at right angles to the laser beam by photomultipliers fitted with filters that passed either XeCl emission peaked at 308 nm or Xe_2Cl emission between 450 and 500 nm. The photomultiplier signals were sent to a gated boxcar integrator (SRS 265) for fluorescence excitation spectra or were recorded by a transient digitizer (Tektronix 7912AD) for time-resolved profiles.

RESULTS AND DISCUSSION

At Xe pressures less than 1 kPa and Cl_2 pressures of 0.04 kPa, emission from XeCl(B) at 308 nm was observed when the laser was resonant with the spectrally narrow, dipole-dipole allowed two-photon

*This work was conducted under the McDonnell Douglas Independent Research and Development program.

transitions in Xe. The intense atomic transition broadened asymetrically as the Xe pressure increased and additional features which corresponded to the absorptions of Xe_2 molecules grew into the fluorescence excitation spectrum. For Xe pressures of 113 kPa at 300 K, it is estimated that the xenon dimer concentration is 0.7 kPa. Spectral features arising from excitation of atomic Xe and molecular Xe_2 were both found to be quadratically dependent on laser power; thus, observed spectra were normalized by the square of the laser power. At high Xe pressures, similar excitation spectra were obtained by monitoring the XeCl(B) or the Xe_2Cl^* emission.

Figure 1 shows an excitation spectrum from a sample of 113-kPa Xe and 0.3-kPa Cl_2 obtained by scanning the dye laser between 246.5 and 258 nm and detecting the 308-nm emission. Vibrational progressions of Xe_2 were observed converging toward levels of excited Xe atoms. The observed line positions of the vibrational transitions converging toward the $5d[7/2]_3$ level of Xe at 247.0 nm are in good agreement with the work of Dehmer, Pratt, and Dehmer[6] who produced cold Xe_2 by a supersonic nozzle expansion and used MPI detection, and the work of Gornik et al.[7] who detected VUV and IR emission following excitation of Xe_2. In the present work, detection is shifted to the near UV or visible by reactions with Cl_2 initiated by the two-photon excitation of Xe_2. These reactions produce the diatomic or triatomic rare-gas halide excimers which emit with high quantum yields. The molecular transitions converging to Xe $5d[7/2]_3$ are not obscured by the atomic transition because transitions from the ground state of atomic xenon to the $5d[7/2]_3$ level are not allowed by dipole-dipole selection rules.

Features of the mechanisms of XeCl(B) production are illustrated in Figure 2 by the temporal profiles of emission produced by excitation of atomic Xe and molecular Xe_2 in samples of approximately 14-kPa Xe and 0.04-kPa Cl_2. When the $6p[1/2]_0$ level of Xe is excited at low laser fluence (2 mJ/cm^2), the XeCl(B) emission rises rapidly and decays exponentially. The time dependence of the emission is consistent with prompt production of excited Xe atoms which react with Cl_2 to produce XeCl(B).[8] Production of XeCl(B) following excitation of Xe_2 occurs only under the high laser fluences produced

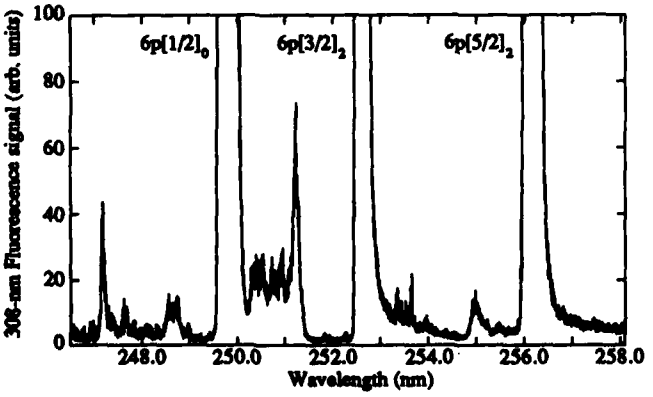

Figure 1.
Fluorescence excitation spectrum produced by irradiation (800 mJ/cm^2) of 113-kPa Xe and 0.3-kPa Cl_2.

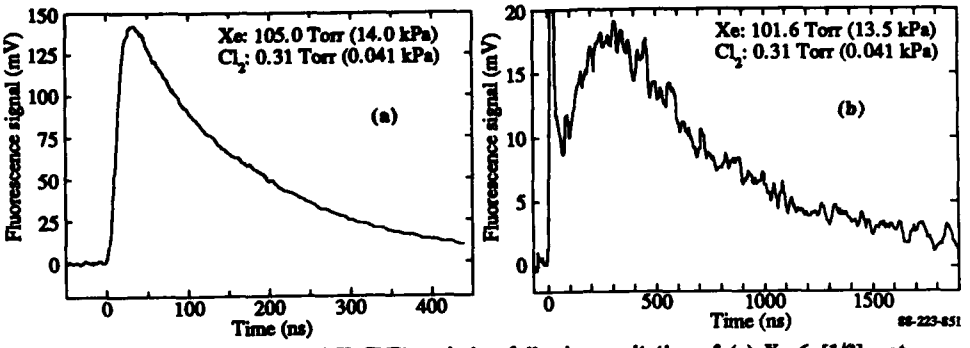

Figure 2. Temporal profiles of XeCl(B) emission following excitation of (a) Xe $6p[1/2]_0$ at 249.63 nm, 0.08 mJ/pulse, unfocused and (b) Xe_2 at 247.16 nm, 0.20 mJ/pulse, focused. Both traces are for 100 shots but note different time scales for (a) and (b).

by focusing the laser beam (>200 mJ/cm^2). The temporal profile of the XeCl(B) produced in this manner possesses much slower rise and fall times characteristic of a mechanism in which the species reacting to produce XeCl(B) are not produced directly. The time profile of the fluorescence is consistent with a mechanism involving ionic species initiated by the (2+1) photoionization of Xe_2. Photoelectron spectra[6] have shown that some states of Xe_2^* predissociate and the resulting excited Xe atoms are ionized. Non-predissociative levels of Xe_2^* are ionized to various states of Xe_2^+, many of which are dissociative. We obs ve evidence that excitation of Xe_2 through a non-predissociative level of Xe_2^* leads to a slightly earlier rise in the XeCl(B) emission than when a predissociative level is excited. This earlier production of XeCl(B) occurs because Xe_2^+, a key intermediate in the ionic mechanism, produced directly by photoionization, eliminates the need for the three-body reaction to produce Xe_2^+ which is required when Xe^+ is produced initially.

REFERENCES

1. V. S. Dubov, Ya. E. Lapsker, A. N. Samoilova, and L. V. Gurvich, Chem. Phys. Lett. 83, 518 (1981); H. P. Grieneisen, H. Xue-Jing, and K. L. Kompa, Chem. Phys. Lett. 82, 421 (1981).
2. B. E. Wilcomb and R. Burnham, J. Chem. Phys. 74, 6784 (1981).
3. J. K. Ku, G. Inoue, and D. W. Setser, J. Phys. Chem. 87, 2989 (1983).
4. G. Inoue, J. K. Ku, and D. W. Setser, J. Chem. Phys. 80, 6006 (1984); A. W. McCown and J. G. Eden, J. Chem. Phys. 81, 2933 (1984).
5. T. Ishiwata, A. Tokunaga, and I. Tanaka, Chem. Phys. Lett. 112, 356 (1984).
6. P. M. Dehmer, S. T. Pratt, and J. L. Dehmer, J. Chem. Phys. 85, 13 (1986); J. Phys. Chem. 91, 2593 (1987).
7. W. Gornik, S. Kindt, E. Matthias, and D. Schmidt, J. Chem. Phys. 75, 68 (1981).
8. J. E. Velasco, J. H. Kolts, and D. W. Setser, J. Chem. Phys. 69, 4357 (1978).

Alignment Effects in Ca-He (5^1P_1 - 5^3P_J) Energy Transfer Half-Collisions

K. C. Lin
Department of Chemistry, National Taiwan University
and Institute of Atomic and Molecular Sciences,
Academica Sinica, Taipei 10764, Taiwan

S. Ananthamurthy, P. D. Kleiber,
J. X. Wang and W. C. Stwalley
Department of Physics and Astronomy and the
Center for Laser Science and Engineering,
The University of Iowa, Iowa City, IA 52242

Stephen R. Leone
Joint Institute for Laboratory Astrophysics and
Departments of Chemistry and Biochemistry, National Bureau
of Standards and University of Colorado, Boulder, CO 80309

ABSTRACT

We have studied Ca-He spin changing collisions using far wing laser scattering "half-collision" techniques. We have observed a strong red wing-blue wing asymmetry which we interpret in terms of an orbital alignment preference in the energy transfer cross section. This orbital alignment effect approaches 100%.

We report studies of the spin changing energy transfer process $Ca^*(5^1P_1^0) + He \rightarrow Ca^*(5^3P_J^0) + He + \Delta E$, using far wing laser scattering techniques. This report closely parallels previously published work [1] but extends those measurements to larger frequency shifts and hence smaller internuclear separations of the collision complex. In polarized crossed beam experiments on this CaHe system Leone and co-workers [2,3] have determined a stronger preference for the energy transfer to occur when the $Ca^*(5^1P)$ orbital is aligned perpendicular to the internuclear axis, than if aligned parallel. In the orbital locking and following model [4], it is assumed that the $Ca^*(^1P)$ orbital locks onto the Ca-He axis at long range and follows the axis adiabatically through the collision. In such a scheme, a parallel alignment at long range correlates at short range with a molecular Σ state, while a perpendicular alignment at long range correlates with a Π molecular state at short range. Within the context of this model, the observed alignment effect [2,3] can be expressed in terms of a polarization,

$$P = \frac{\sigma_\Pi - \sigma_\Sigma}{\sigma_\Pi + \sigma_\Sigma} \approx 24\%$$

Here $\sigma_\Pi(\sigma_\Sigma)$ is the energy transfer cross section for collisions occurring on the $^1\Pi(^1\Sigma^+)$ molecular states. This result has been explained in terms of a curve crossing model [3]. The attractive $^1\Pi$ state curve (correlating with the $Ca^*(5^1P$ asymptote)) is likely to cross the repulsive $^3\Sigma$ state (correlating with the lower-lying

$Ca^*(5^3P)$ manifold); such a curve crossing may facilitate this energy transfer process.

Pouilly and Alexander [5], however, have questioned the validity of the orbital locking and following model. They point out that long range non-adiabatic mixing between the $^1\Sigma$ and $^1\Pi$ states correlating with the 5^1P asymptote, will tend to "scramble" the correlation between the asymptotic orbital alignment and the short-range molecular state. The observed polarization includes such an orbital scrambling.

Our approach is to study the "half-collision" dynamics by exciting the Ca-He collision complex directly and monitoring the subsequent branching into the 5^3P and 5^1P exit channels. Based on crude but reasonable arguments concerning the expected shapes of the potential curves [1], we expect that far red wing absorption corresponds predominantly to excitation of the attractive $^1\Pi$ molecular state, whereas blue wing absorption corresponds predominately to excitation of the repulsive $^1\Sigma^+$ molecular state. The polarization effect should then be apparent in a red wing/blue wing asymmetry for the $(5^3P)/(5^1P)$ branching ratio. Since the excitations occur at relatively short range, the results may be less affected by long range nonadiabatic mixing leading to an enhanced polarization.

The experimental setup is described in detail in reference [1]. The major modifications here were: a) the use of Courmarin 540 A laser dye; and b) replacement of the monochromator with 10nm band pass filters to improve atomic fluorescence collection efficiency.

We have measured the population branching ratio

$$R = \frac{N(^3P)}{N(^1P) + N(^3P)}$$

as a function of helium pressure and as a function of detuning. Here $N(^3P)$ [$N(^1P)$] is the population of the 5P triplet [singlet] level. These populations are determined through measurements of the fluorescence intensities $I(^3P)$ and $I(^1P)$ on the $Ca^*(5^3P_J - 3^3D_J)$ and the $Ca^*(5^1P_1 - 3^1D_2)$ transitions, respectively. The fluorescence measurements are scaled to the population ratios as

$$\frac{I(^3P)}{I(^1P)} = \theta \frac{N(^3P)}{N(^1P)}$$

where θ is a scaling factor that depends on the radiative branching, detection system efficiencies, etc. This factor can be estimated by measuring the intensity ratio at high pressures (>100 Torr) where collisional mixing leads to approximately Boltzmann equilibrium in the populations, $N(^3P)/N(^1P) \approx [g(^3P)/g(^1P)]e^{-\Delta E/kT} \approx 4$. The measurement of θ is made tricky by an unfortunate accidental fluorescence coincidence of the $Ca^*(5^3S_1 \rightarrow 4^3P_J)$ multiplet, which falls within our detection bandpass and which must be subtracted out in the calibration.

The population branching ratios R, are strong functions of

pressure and at high pressure collisional mixing leads to a value of R ~ 0.8. At low pressures R can be extrapolated to the zero pressure limit, to obtain the "single collision" branching ratio, R_0. This extrapolation is carried out by fitting to the solution of a simple two-state rate equation model which allows for collisional mixing between the (5^1P) and (5^3P) levels. Fig. 1 shows R_0 as a function of detuning and clearly exhibits the red wing-blue wing asymmetry. The qualitative shape of the branching ratio profiles agree with previously published results at lower frequency detunings [1] but the absolute scale of the branching ratios differs somewhat. This is due to the use of an incorrect scaling factor in the previous measurements; the influence of the additional $5^3S \rightarrow 4^3P$ fluorescence channel was not taken into account. It should be noted that there is still a systematic uncertainty in the absolute magnitudes of the branching ratios due to the use of the two state rate equation model in the extrapolation procedure.

We may define the line profile asymmetry,

$$A(\Delta) = \frac{R_0 \text{ (red)} - R_0 \text{ (blue)}}{R_0 \text{ (red)} + R_0 \text{ (blue)}} .$$

Correlating the red (blue) wing signals with the $^1\Pi(^1\Sigma^+)$ molecular state absorptions, this quantity can be equated to the polarization

$$P = \frac{\sigma_\Pi(\Delta) - \sigma_\Sigma(\Delta)}{\sigma_\Pi(\Delta) + \sigma_\Sigma(\Delta)}.$$

The dramatic increase in the polarization (approaching 100%) shown in Fig. 2 suggests that absorption in the far wings indeed occurs in a region where nonadiabatic $^1\Pi - {}^1\Sigma$ mixing can be neglected. These results indicate a complete correlation between the Π state excitation and the energy transfer process, in agreement with the curve crossing model. These results may also be used to define very accurately the region over which "orbital scrambling" occurs. Thus, these techniques allow a very sensitive probe of nonadiabatic effects in multichannel collision processes.

Acknowledgments

We gratefull acknowledge helpful discussions with Dr. Alan Gallagher. This work was supported by the National Science Foundation through Grant No. CHE86-15118.

References

1. K. C. Lin, P. D. Kleiber, J. X. Wang, W. C. Stwalley and S. R. Leone, J. Chem. Phys. 89, 4771 (1988).
2. M. O. Hale, I. V. Hertel and S. R. Leone, Phys. Rev. Lett. 53, 2296 (1984).
3. Bussert, W. D. Neuschäfer and S. R. Leone, J. Chem. Phys. 87, 3833 (1987).
4. I. V. Hertel, H. Schmidt, A. Bähring and E. Meyer, Rep. Prog. Phys. 48, 375 (1985).
5. B. Pouilly and M. H. Alexander, J. Chem. Phys. 86, 4790 (1987).

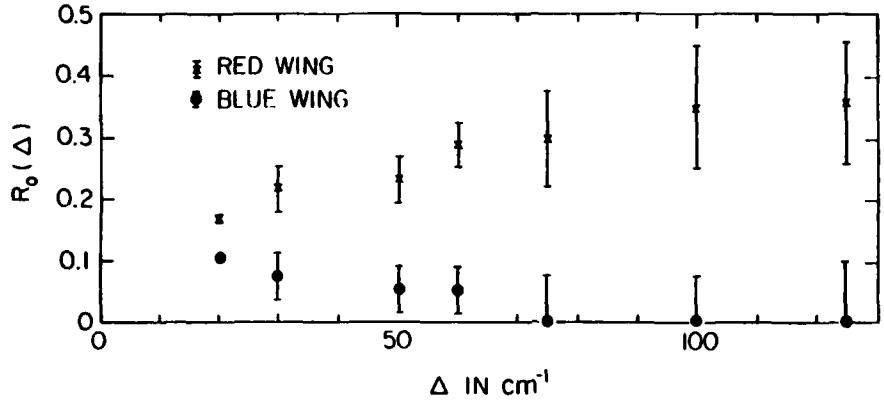

Figure 1. Extrapolated zero pressure triplet branching ratio as a function of detuning.

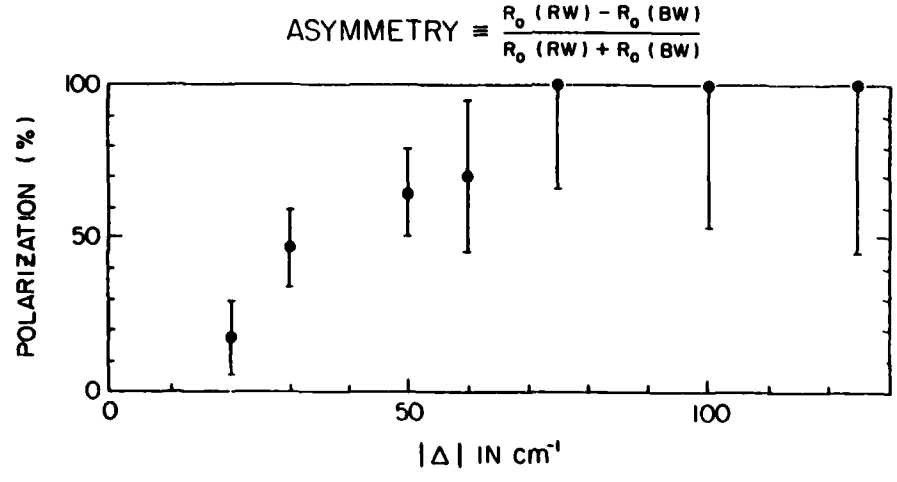

Figure 2. The red/blue profile asymmetry or polarization as a function of detuning.

SPECTROSCOPIC MAPPING OF THE OH-Ar STRETCHING POTENTIAL[a)]

Mary T. Berry, Mitchell R. Brustein, and Marsha I. Lester
Department of Chemistry
University of Pennsylvania, Philadelphia, Pennsylvania 19104-6323

ABSTRACT

Intermolecular potentials between Ar($^1S_0$) and hydroxyl radicals in the A $^2\Sigma^+$ and X $^2\Pi_{3/2}$ states are constructed along the OH-Ar van der Waals (vdW) stretching coordinate. The interaction potentials are derived from analysis of the OH-Ar fluorescence excitation spectrum observed about the OH A(v'=0) - X(v"=0) transition. The OH-Ar potential is found to be dramatically changed upon electronic excitation of the OH moiety.

INTRODUCTION

Spectroscopic experiments on weakly bound van der Waals (vdW) complexes provide an important means to probe the intermolecular potential between the molecules. Although the potential well region has been spectroscopically mapped for many closed shell molecular systems, little is known about the intermolecular potential in open shell systems. Complexes of the hydroxyl radical with argon represent a model case for determining the interaction potential in an open shell system since OH-Ar is both experimentally observable[1-3] and theoretically tractable.

OH-Ar vdW complexes are formed in a pulsed supersonic expansion of ultraviolet photolyzed nitric acid in argon carrier gas. The complexes are probed via laser-induced fluorescence in the vicinity of the OH A $^2\Sigma^+$ (v'=0) - X $^2\Pi_{3/2}$ (v"=0) transition. We have identified new spectroscopic features, positioned at 31944.1, 32078.2, 32193.8, 32291.3, 32371.3, and 32432.9 cm^{-1}, which have been assigned to a vibrational progression in the OH-Ar stretching mode of the excited electronic state. As an example, the feature centered at 32371.3 cm^{-1} is shown in Fig. 1. Through analysis of the rotation-vibration structure of the features in the progression, we are able to evaluate the OH-Ar stretching potential for hydroxyl radicals in the A $^2\Sigma^+$ and X $^2\Pi_{3/2}$ states.

VIBRATIONAL ANALYSIS

We have performed a Birge-Sponer analysis of the vdW vibrational progression in OH-Ar to estimate the binding energy of Ar to OH in the A(v'=0) state, as well as the fundamental vibrational frequency ω_e' and anharmonicity $\omega_e'x_e'$ of the OH-Ar vdW stretch.[1] A Birge-Sponer plot of the spacing between successive vibrational bands versus vdW vibrational quantum number was linear, indicating that a simple anharmonic oscillator well characterizes the vibrational

a)This research was supported by the Division of Chemical Sciences, Office of Basic Energy Sciences of the Department of Energy.

motion in the spectroscopically accessed portion of the well. Some of the derived potential parameters depend on the vibrational quantum number assignments. We adopt the numbering scheme reported for an analogous vibrational progression in the fluorescence excitation spectrum of OH imbedded in an argon matrix.[4] This yields a fundamental vibrational frequency $\omega_e'=170$ cm^{-1} and an anharmonicity $\omega_e'x_e'=9$ cm^{-1}. The binding energy is estimated from a linear Birge-Sponer extrapolation to be $D_0(v'=0)=718$ cm^{-1}.

The binding energy of Ar to OH in the X(v"=0) state is evaluated from the spectroscopic shift of the assigned vdW vibrational origin relative to the $P_1(1)$ transition of free OH and the binding energy of OH-Ar in the excited state, yielding $D_0(v"=0)=69$ cm^{-1}.

ROTATIONAL ANALYSIS

Four vibronic bands in the OH-Ar vdW stretching progression have been analyzed by assuming a linear structure for OH-Ar.[2] The linear model readily accounts for the experimentally observed rotational structure. A least-squares fit of calculated P_1, Q_1, R_1, and $^sR_{21}$ rotational line positions to experimental positions yield vibrationally averaged rotational constants B_v' in the excited state as well as a rotational constant for the vibrationless level of OH-Ar in the ground state ($B_0"= 0.110$ cm^{-1}).

A stick spectrum constructed from the calculated line positions and intensities is superimposed on the spectral feature shown in Fig. 1. The mere fact that the OH-Ar spectral features can be fit by a linear model does not confirm that the structure is indeed linear. Since the mass of H is so small relative to O and Ar, a nonlinear structure would exhibit a similar rotational profile. The rotational constants derived from the spectral analysis yield vibrationally averaged vdW bond lengths, defined as the distance between the Ar atom and the OH center-of-mass. The average vdW bond length is 3.6 Å at the zero point level of the ground state. In the excited electronic state, the vibrationally averaged rotational constants have been extrapolated to give $B_e'=0.169$ cm^{-1} and $r_e'=2.9$ Å, the vdW bond length at the equilibrium position of the potential well.

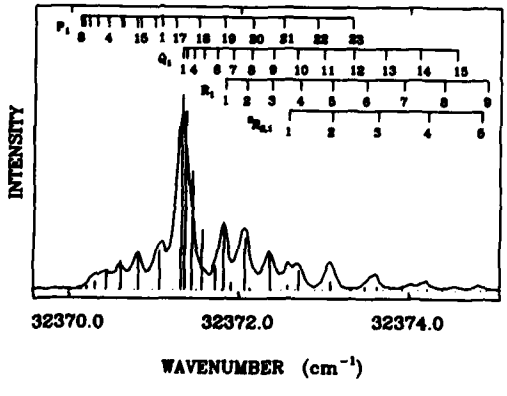

Fig. 1. Fluorescence excitation spectrum of one member of the OH-Ar vibrational progression.

OH-Ar INTERACTION POTENTIAL

The vdW vibrational constants, together with the r_e determined in the rotational analysis, can be used to define a Morse potential correlating to OH A(v′=0) + Ar ($^1S_0$). A Morse potential, which approximates the actual excited state OH-Ar potential, is plotted in Fig. 2 as a function of the OH–Ar separation distance. The vibrational levels predicted for the OH-Ar vdW stretching mode are displayed; only the vdW vibrational levels 1-6 have been experimentally observed.

Much less information is available about the ground state OH-Ar potential which correlates with OH X(v″=0) + Ar ($^1S_0$). In order to construct a Morse potential for the ground state of OH-Ar, we use the ground state binding energy and the average vdW bond length at the zero point level determined here and estimate the vibrational frequency of the OH-Ar stretch.[2] The resultant potential curve is also shown in Fig. 2.

As illustrated in Fig. 2, the OH (center-of-mass) to Ar distance is substantially reduced (Δr_e=0.6 Å) and Ar becomes much more tightly bound to CH upon electronic excitation of OH. We expect that these changes will have a marked effect on the full- and half-collision dynamics taking place on these surfaces.

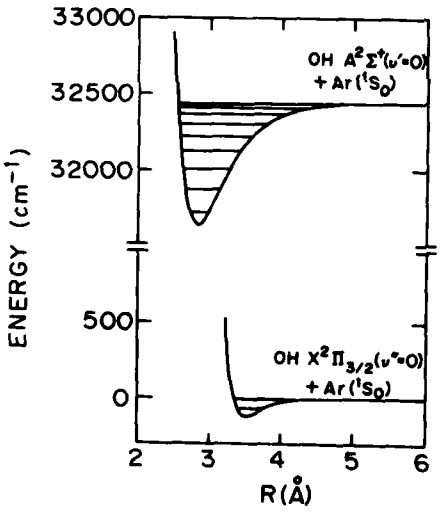

Fig. 2. Morse potential curves for OH-Ar.

REFERENCES

1. M. T. Berry, M. R. Brustein, J. R. Adamo, and M. I. Lester, J. Phys. Chem. 92, 5551 (1988).
2. M. T. Berry, M. R. Brustein, and M. I. Lester, Chem. Phys. Lett. 153, 17 (1988).
3. W. M. Fawzy and M. C. Heaven, J. Chem. Phys. 89, 7030 (1988).
4. J. Goodman and L. R. Brus, J. Chem. Phys. 67, 4858 (1977).

PHOTODISSOCIATION STUDIES OF BORANE CARBONYL

H. H. Nelson
Chemistry Division, Naval Research Lab, Washington, DC 20375

ABSTRACT

Several experiments have been performed to determine the energy disposal into the primary products of the 193 nm photolysis of borane carbonyl (BH_3CO). It has been shown that the BH_3 product, while formed with substantial internal energy, is below the energy threshold to dissociate to $BH + H_2$. This dissociation has been shown both experimentally and theoretically to involve a small (1-3 kcal/mole) barrier. The nascent CO product has been shown to contain ~5.9 kcal/mole of vibrational energy and ~0.6 kcal/mole of rotational energy. Product translation is presumed to account for the remaining energy available, although the CO doppler profile is not entirely consistent with this explanation. The internal energies measured are larger than might be expected from a purely impulsive dissociation of BH_3CO although they are much lower than a statistical theory would predict.

INTRODUCTION

Although many laboratories have been able to completely determine the energy distribution into the products of the photolysis of small molecules, it is rare to have the chance to be able to probe the photodissociation of a larger molecule in this detail. This is especially true for weakly bound molecules in which the amount of energy to be disposed into the products is large. BH_3CO is a very attractive molecule for studies of this nature since both of the primary photoproducts, BH_3 and CO, as well as the other possible boron hydride products can be spectroscopically probed. An energy level diagram for the BH_3CO photodissociation system is shown in figure 1. As can be seen from this figure, there are several energetically allowed channels in this photodissociation. Dissociation to form BH_3 and CO requires only 20.7 kcal/mole[1]; this leaves 127 kcal/mole available for disposal into the product degrees of freedom (E_{av} in the figure). It is likely that the products of this channel will contain substantial amounts of internal as well as translational energy. BH_3CO is known[2] to have a structure consisting of a pyramidal BH_3 unit and a CO bond length almost exactly that for free CO. Simple impulsive notions about this dissociation would predict large amounts of internal energy for the BH_3 fragment, primarily in the umbrella bending mode, and considerable product translation. In fact, if a substantial amount of the available energy is partitioned into BH_3 internal degrees of freedom, one might expect the BH_3 formed to decompose unimolecularly into BH and H_2. In our laboratory, we have used the photodissociation of BH_3CO to

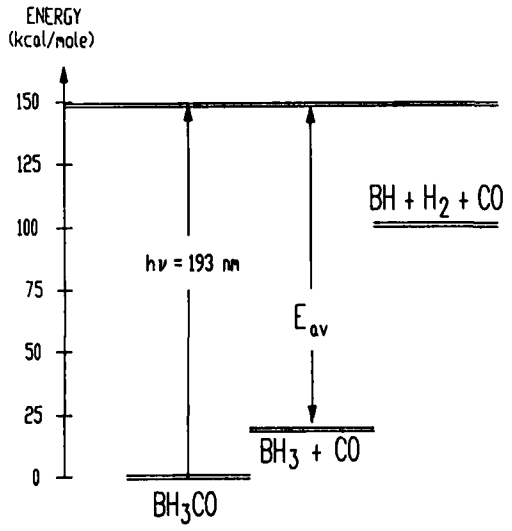

Figure 1 Relative energy levels of the products of the 193 nm photolysis of BH_3CO.

produce BH_3[3] and BH[4] for kinetics studies. Fluence measurement[5] in our laboratories as well as the earlier observation of BH from the flash photolysis of BH_3CO[6] indicate that the BH we observe is formed in a single photon process. In order to help determine if there are two channels in this photodissociation or if the BH results from the decomposition of highly energized BH_3, we have undertaken a series of measurements of the energy disposal into the various degrees of freedom of the primary products of the photodissociation of BH_3CO.

In this paper, I report our preliminary results on the energy distribution into the BH_3 and CO photoproducts. In addition, I will present some pertinent theoretical and experimental results on the recombination reaction of BH with H_2 that address the issue of the subsequent dissociation of energized BH_3 into BH and H_2 and provide an upper limit to the internal energy of the BH_3 product.

EXPERIMENTAL

Each of the measurements reported here was carried out in the "pump-probe" configuration. In all cases, the photolysis laser was an excimer laser operating on ArF at 193 nm. The BH_3 photoproduct is detected in its ground vibrational state using tunable, infrared diode laser absorption near 1140 cm^{-1} as has been described previously[3]. A schematic diagram of the apparatus used for these experiments is shown in figure 2. Unfortunately, the seven lines originating in $v'' = 0$ reported by Kawaguchi *et al.*[7] are the only spectral features assigned to BH_3. This same apparatus was used to measure the doppler profile of the nascent CO near 2111 cm^{-1}. The diode laser, with its high resolution capabilities, is very effective at resolving the absorption lines of BH_3 from those of the parent and measuring the CO absorption linewidth. It is much more difficult to determine absolute absorption strengths however. For this reason, the vibrational energy distribution in the CO product is measured with a cw, grating-tuned CO laser system that has been described in detail recently[8]. These measurements are made on a timescale and at a pressure such that rotations are thermalized while vibrations are not. In order to measure the rotational energy distribution in CO we use single photon VUV laser induced fluorescence (lif) on the CO ($A^1\Pi - X^1\Sigma^+$) fourth positive system near 140 nm[9]. The excitation frequency is generated by a nonresonant four wave mixing process in Hg vapor via the process $\omega_{VUV} = \omega_{UV} + 2\omega_{VIS}$ as has been described by Wallenstein[10].

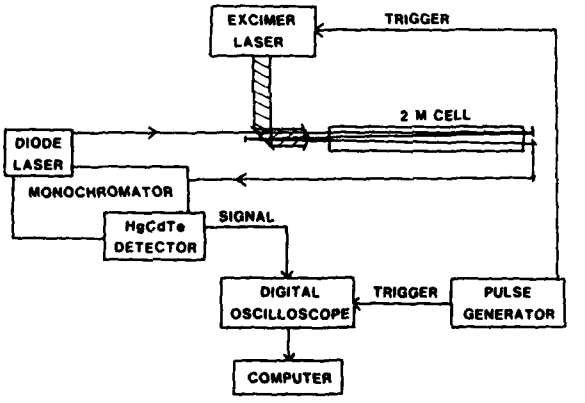

Figure 2 Schematic diagram of the diode laser apparatus used for several of the measurements reported in this paper.

In all experiments except the VUV lif, the BH_3CO is slowly flowed through the gas cell used at a pressure of 1 - 30 mTorr. In some cases, He or N_2 is used as a buffer gas, in others the BH_3CO is used neat. In the VUV experiment, a 1-5% BH_3CO in CO mixture is admitted to the photolysis cell through a pulsed supersonic nozzle. BH_3CO is synthesized following the method of Burg and Schlesinger[11] and is stored at liquid N_2 temperature prior to use.

RESULTS

We have examined each of the primary products of the photodissociation in order to determine the energy disposal into each degree of freedom. I will report the results in three sections; CO internal energy, BH_3 internal energy and translational energy.

CO INTERNAL ENERGY

Pasternack, Weiner and Baronavski[9] have measured the nascent rotational distribution of the CO product in $v'' = 0$ and 1. A semilog plot of the populations in each rotational level versus the rotational energy for $v'' = 0$ is shown in figure 3. The lowest 8 levels are obscured by absorption due to free CO in the expansion from the decomposition of BH_3CO in the nozzle. These data can be characterized by a temperature of 362 ± 22K. A similar experiment on the $v'' = 1$ level results in a rotational temperature of 175 ± 8K.

Pasternack, Weiner, Prather, Rosenfeld and Nelson[12] have used transient absorption of a cw CO laser to measure the vibrational distribution in CO. The results of these measurements are shown plotted versus vibrational energy in figure 4. The average vibrational energy of CO formed in the dissociation is 5.9 kcal/mole and average rotational energy is 0.6 kcal/mole.

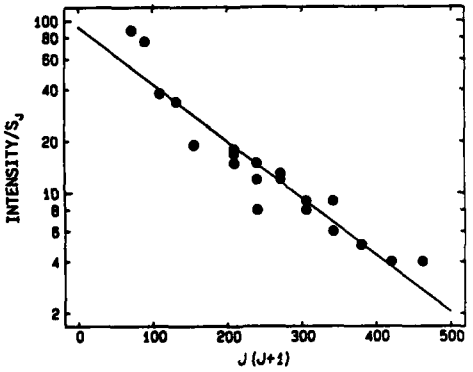

Figure 3. Plot of the CO(v''= 0) rotational population versus rotational energy. The solid line is a fit to the data and corresponds to a rotational temperature of 362 ± 22K.

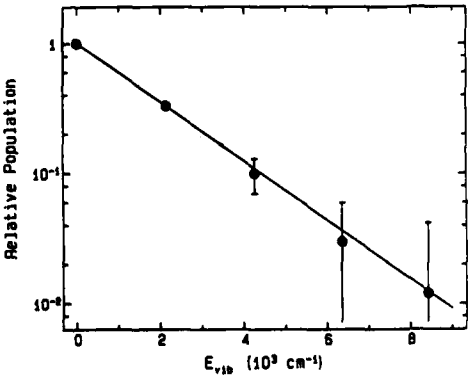

Figure 4 Plot of the relative vibrational population of the CO fragment versus vibrational energy. The siolid line is a fit to the data and corresponds to a vibrational temperature of 1111K.

BH_3 INTERNAL ENERGY

Pasternack, *et al.*[12] have shown that BH_3 is the primary ($\Phi = 0.7 \pm 0.3$) boron containing product of this photolysis. They reference the BH_3 formed in the photolysis of BH_3CO to that formed in the photolysis of B_2H_6 which is known to have a quantum yield of 2. The uncertainty in the measurement arises from the fact that the BH_3 formed in the photolysis of BH_3CO appears in the ground vibrational state, the only level presently able to be probed, only after a delay of many microseconds. This delay varies with the identity of the buffer gas used (the delay with N_2 is shorter than that with He) and varies inversely with the buffer gas pressure. The time scales and pressures involved make it unlikely that thermalization of rotational excitation is responsible for the delay but, rather, thermalization of nascent vibrational excitation. The only other feasible explanation for the observed delay would be relaxation of

electronically excited BH_3 although this appears unlikely. The lowest excited singlet state of BH_3 has been calculated[13] to lie 6.08 eV above the ground state and the lowest triplet 5.48 eV up, above the energy range accessible to this experiment.

Since we observe BH_3 with such a large quantum yield, it must be formed with less energy than that required to dissociate to BH and H_2. In order to place an accurate upper limit on the internal energy of BH_3, Caldwell, Rice, Page, Adams and Nelson[14], investigated this dissociation in two ways. Experimentally, the reverse reaction of BH with H_2 to form BH_3 was found to have an activation energy of ~2.5 kcal/mole. To confirm this, they performed a high quality MCSCF-CI calculation on the BH_3 surface yielding the structure and vibrational frequencies of the transition state for the $BH_3 \rightarrow BH + H_2$ reaction as well as an activation energy that agrees well with the measured value. An RRKM calculation using the calculated values shows that BH_3 excited as little as 0.1 kcal/mole above the barrier has a lifetime of < 1 ns, which would preclude our observation of BH_3 as the major photoproduct. Thus, we are able to place an upper limit of 82 kcal/mole on the nascent internal energy of BH_3.

PRODUCT TRANSLATION

Pasternack *et al.*[12] have used diode laser absorption to measure the Doppler profile of the absorption of the CO product. These measurements were taken under conditions such that the average CO had undergone 0.4 collisions with the bath gas. Thus, some translational thermalization is expected to have occurred. An example of the measured profiles, in this case for the CO v" = 0,P8 line, is shown in figure 5. Note that the FWHM of the observed profile is ~0.015 cm^{-1} while a room temperature absorption line has a Doppler width of ~0.005 cm^{-1}. Since CO is formed in several vibrational levels, the absorption is proportional to the difference in population of the upper and lower states. It is likely that molecules in the upper vibrational level contain less translational energy than those in the lower level. This will lead to an absorption that is double peaked, as has been described.[15] We have assumed that the CO product is ejected from the precursor isotropically, with a gaussian distribution of velocities determined by the distribution of internal energy in the BH_3 product. After accounting for the fact that the population of v" = 1 is approximately 30% of that in the ground state, we are able to fit the observed line profile with a CO translational energy of ~5 ± 2 kcal/mole for v = 0 and 3 ± 2 kcal/mole for v = 1. This places a lower limit on total product translation of ~15 kcal/mole.

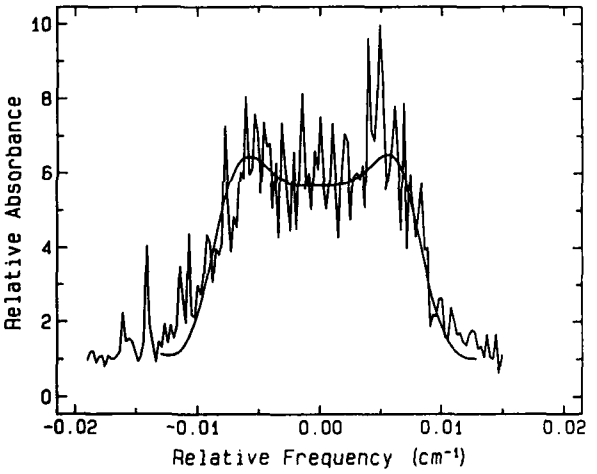

Figure 5 Doppler profile of the CO v" = 0, P8 line measured after a delay of 2 μs at 6 mTorr total pressure.

SUMMARY

The photodissociation of BH_3CO into the products BH_3 and CO at 193 leaves 127 kcal/mole to be distributed into the various degrees of freedom of the products. We have shown that BH_3 is not formed with enough energy to dissociate to BH and H_2. As we have also shown by both experiement and calculation that the dissociation of BH_3 proceeds over a barrier of 1-3 kcal/mole and that the lifetime of BH_3 excited as little as 0.1 kcal/mole above the barrier is < 1 ns, we are able to place an upper limit of ~82 kcal/mole (ΔH + 2 kcal) on the internal energy in BH_3. This leaves ~45 kcal/mole for CO internal energy and product translation. The CO rotational energy is ~0.6 kcal/mole and the CO vibrational energy is ~5.9 kcal/mole. Thus, the 15 kcal/mole we quote as the lower limit on the translational energy released in the dissociation must be far from the correct value. Resolution of this issue will require more accurate measurements of the translational energy release, presumably by a time-of-flight technique.

The internal energy of the CO product, while a small fraction of the available energy, is much larger than would be predicted by a simple "Golden Rule" calculation. Energy is clearly coupled into the CO oscillator on the timescale of the dissociation. A simple inpulsive calculation would predict ~60% of the available energy, or 72 kcal/mole, would appear as product translation. This is far less than the 23 kcal/mole we observe although a portion of the difference may be due to relaxation before our measurement. A better theoretical desciption of the dissociation will clearly be required for a detailed understanding of the process.

ACKNOWLEDGEMENTS

The work reported here is due to several groups at two laboratories. The scientists involved are Louise Pasternack, Brad Weiner, Andy Baronavski, Jack Caldwell and Jane Rice of the NRL Chemistry Division; Mike Page of the NRL Laboratory for Computational Physics; and Kim Prather and Robert Rosenfeld of the Department of Chemistry, UC Davis.

REFERENCES

1. S.H. Bauer, in: *Advances in boron and the boranes*, eds. J.F. Liebman, A. Greenberg and R.E. Williams (VCH Publishers, New York, 1988)
2. A.C. Venkatachar, R.C. Taylor and R.L. Kuczkowski, J. Mol. Struc., *38*, 17 (1977)
3. L. Pasternack, R.J. Balla and H.H. Nelson, J. Phys. Chem., *92*, 1200 (1988).
4. J.K. Rice, N. J. Caldwell and H.H. Nelson, J. Phys. Chem., in press.
5. J.K. Rice, C.H. Douglass and H.H. Nelson, manuscript in preparation.
6. S. H. Bauer, G. Herzberg and J.W.C. Johns, J. Molec. Spectrosc., *13*, 256 (1964).
7. K. Kawaguchi, J.E. Butler, C. Yamada, S.H. Bauer, T. Minowa, H. Kanamori and E. Hirota, J. Chem. Phys., *87*, 2438 (1987)
8. B.I. Sonobe, T.R. Fletcher and R.N. Rosenfeld, Chem. Phys. Lett., *105*, 322 (1984)
9. L. Pasternaack, B.R. Weiner and A.P. Baronavski, Chem. Phys. Lett., in press.
10. R. Hillbig, G. Hilber and R. Wallenstein, Appl. Phys. B, *41*, 225 (1986)
11. A.B. Burg and H.I. Schlesinger, J. Am. Chem. Soc., *59*, 780 (1937)
12. B.R. Weiner, H.H. Nelson, K. Prather, R.N. Rosenfeld and L. Pasternack, manuscript in preparation
13. W.C. Swope, H.F. Schaefer III and D.R. Yarkony, J. Chem. Phys., *73*, 407 (1980)
14. N.J. Caldwell, J.K. Rice, M. Page, G. Adams and H.H. Nelson, manuscript in preparation.
15. H. Kanamori and E. Hirota, J. Chem. Phys., *86*, 3903 (1987)

PHOTODISSOCIATION DYNAMICS OF FERROCENE AT 193 NM

Urmi Ray and Matthew Vernon
Columbia University, New York, New York 10027

Hui-qi Ho
Dept. Nuclear Science, Fudan University, Shanghai, PRC

Zhuangjian Zhang
Dept. of Physics, Fudan University, Shanghai, PRC

ABSTRACT

A molecular beam of ferrocene has been photodissociated with 193 nm excimer laser radiation. Two channels were observed. The major channel involves the incoherent absorption of two photons by ferrocene, followed by sequential elimination of the two Cp ligands. A minor, single photon channel produces FeCp in an excited (ligand field?) state. The energy disposal in both cases can be predicted by statistical, microcanonical models. The two photon channel occurs despite the fact that a single photon has sufficient energy to remove both Cp ligands, because the electronic energy interconverts to the ground electronic state. The RRKM dissociation rate after a single photon absorption is slow compared to the incoherent photon absorption rate, so a second photon is absorbed.

INTRODUCTION

Metallocenes are a large class of organometallic molecules with intense ultraviolet absorptions. As part of an experimental program to investigate the gas-phase decomposition mechanism of organometallic molecules to develop quantitative models which describe how laser radiation can be used to control the product branching ratios and energy distributions, we have measured the product translational energy distributions for the 193 nm excimer laser photolysis of ferrocene.

The experiment was performed using a crossed molecular beams apparatus configured for photodissociation[1]. The ferrocene molecular beam was made by flowing Ar gas at 400 torr through a heated stainless steel vessel containing the ferrocene solid. The nozzle temperature was 160°C. Mass spectroscopy of the molecular beam shows no evidence of cluster formation. The molecular beam velocity distribution was measured using a rotating disk as described elsewhere[1]. Photofragment velocity distributions were recorded at Fe^+, $FeCp^+$, and Cp^+ masses at a laser fluence of ~10 mj/cm^2.

DATA ANALYSIS

The velocity distributions at the three photofragments were analyzed using the method-of-moments[2] procedure to obtain the center-of-mass (cm) photofragment distributions. The cm distributions indicate that the data at all three ions can be described by a Gaussians, indicating that the energy disposal, as far as the nuclear motions is concerned, is statistically governed. Two models of the photodissociation were considered, differing in the sequence of photon absorption and Cp eliminations.

Model A: $FeCp_2 + hv \rightarrow FeCp + Cp$

$FeCp + hv \rightarrow Fe + Cp$

Model B: $FeCp_2 + 2\,hv \rightarrow FeCp^* + Cp$

$FeCp^* \rightarrow Fe + Cp$

where $FeCp^*$ is an unstable intermediate.

Model A can fit the observed data when free adjustment of the Gaussian parameters for the two Cp eliminations is allowed. However, the model cannot explain two features of the data. First, the FeCp velocity distribution observed is too narrow to result from the statistical dissociation from the ground state of ferrocene. Since the bond energies[3] and vibrational frequencies[4] are available from other investigations, the deviation of the observed distributions from the calculated dissociation via the ground electronic state cannot reasonably arise from the approximations of the statistical calculation. Instead, the FeCp fragments are assigned as the products of ferrocene dissociating to an excited electronic state of FeCp located ~40 kcal/mole above the ground state. Calculations of the $FeCp_2$ dissociation rate using a simple RRKM model show that if the electronic energy interconverts to the ground electronic state, the dissociation rate is too slow to produce FeCp fragments on the time scale of the photodissociation experiment. The second major deficiency is that the ratio of Cp's produced by the one and two photon steps of model A are inconsistent. The fit to the data results in 25 times as many Cp's produced from the second step as in the first step, clearly impossible for the sequential mechanism.

Model B however can predict the observed velocity distributions at Fe^+ and Cp^+ assuming dissociation along the ground electronic states for each Cp elimination with the correct ratio of Cp ligands. In this case, the dissociation rate of ferrocene after absorbing two photons is sufficiently fast to produce the fragments we observe.

CONCLUSION

The dissociation of ferrocene at 193 nm can happen in two different ways. The minor channel is a one photon process where a single Cp ligand is eliminated and FeCp is produced in an excited electronic state. The major channel is Model B. The energy disposal for the nuclear motions for both channels is statistical. Microcanonical calculations of the product energy distributions using the known bond energies and frequencies agree exactly with the experimental measurements. Model B is also consistent with the RRKM dissociation rates required for detection by our experiment .

REFERENCES

1. U.Ray, S.L. Brandow,G. Bandukwalla, B.K. Venkataraman, Z. Zhang, M. Vernon, accepted, *J. Chem. Phys.*
2. G. Bandukwalla and M. Vernon, *J. Chem. Phys.*, **88**, 7387 (1988).
3. Karen E. Lewis and Gregory P. Smith, *J. Am. Chem. Soc.*, **106**, 4650, (1984).
4. Heinz P. Fritz, *Adv. Organometallic Chemistry*, F.G.A. Stone and R. West eds., **1**, 239 (1964).

ACKNOWLEDGEMENTS

This work was supported by grants CHE-85-19082 and CHE-85-52744 from the National Science Foundation.

LASER-INDUCED FLUORESCENCE IN THE $B^2\Sigma^+$-$X^2\Pi_i$ SYSTEM OF OH

Andrew D. Sappey, David R. Crosley and Richard A. Copeland
Molecular Physics Laboratory, SRI International
Menlo Park, California 94025

ABSTRACT

Laser-induced fluorescence in the previously unobserved B-X system is used to detect the high vibrational levels of ground state OH generated by the reaction of H and O_3. Light (220-240 nm) from a frequency-doubled tunable dye laser excites the (0,8), (0,9) and (1,8) vibrational bands of the B-X system. The B state then fluoresces predominantly to the $A^2\Sigma^+$ state between 400 and 600 nm. Weaker fluorescence to the X state is also observed. From the temporal evolution of the fluorescence, lifetimes are extracted for different vibrational, rotational, and fine-structure levels of the B state. Large variations are observed between these levels indicating an unexpected predissociation.

INTRODUCTION AND EXPERIMENTAL APPROACH

High vibrational levels of the OH radical ($X^2\Pi_i$, $v'' \leq 9$) are produced in the earth's upper atmosphere by the reaction of H and O_3. These highly excited molecules then fluoresce via vibrational transitions within the ground state giving rise to visible and near-infrared light. This emission is used as a diagnostic for upper atmosphere temperature, concentrations, and dynamics. Models of this emission require as input absolute vibrational band transition strengths and rotational and vibrational energy transfer rate constants and mechanisms. A sensitive and state selective method of probing high vibrational levels in OH is required to characterize these collisional energy transfer processes. In this work, we describe the development of such a method, B-X laser-induced fluorescence (LIF).

The OH radicals are produced in $v'' \leq 9$ in a microwave-discharge flow cell by the reaction of H with O_3 and excited to the $B\ ^2\Sigma^+$ state by light between 220 to 240 nm (~1 mJ) from a frequency-doubled excimer-pumped dye laser. The total cell pressure can be varied from 0.2 to 2 Torr with helium as the major component. The LIF is monitored by a filtered photomultiplier and also dispersed by a monochromator. The signals are amplified and detected with either a boxcar integrator or a 100 megasample s^{-1} transient digitizer. A complete description of the experimental approach can be found in Ref. 1.

DISPERSED FLUORESCENCE RESULTS

We have measured the intensity of the dispersed fluorescence from both $v' = 0$ and 1 of the B state following excitation of the overlapped $Q_1(1)$ and $^QP_{21}$ rotational feature.[1] We observe fluorescence to levels $3 \leq v \leq 9$ of $A^2\Sigma^+$ between 350 and 600 nm. The three strongest vibrational bands from $v' = 0$ are (0,7), (0,8) and (0,6) at 510, 550, and 470 nm, while those from $v' = 1$ are (1,6), (1,9) and (1,5) at 460, 555, and 420 nm. These bands lie at significantly longer wavelengths than the excitation laser so scattered laser light is not a problem in the LIF detection. The fluorescence cuts off abruptly to the red of the (0,9) and (1,9) B-A bands, because $v = 10$ of the A state is not bound. The expected minimum in the fluorescence pattern from $v' = 1$

occurs in the vicinity of the (1,8) band. The relative vibrational band transition probabilities for the B-A bands agree very well with recent theoretical calculations by Langhoff et al.[2]

In the ultraviolet we detect small signals that result from fluorescence in the (0,9) and (0,10) bands of the B-X electronic system.[1] These bands are similar in intensity to the weakest bands of the B-A system and we find that I[B-A(0,3)]/ I[B-X(0,10)] = 1.6 ± 0.5; about 0.3% of the B-A fluorescence occurs in the (0,3) band. The theoretical result[2] for the above ratio is 0.5 which differs from the experimental result by about a factor of three.

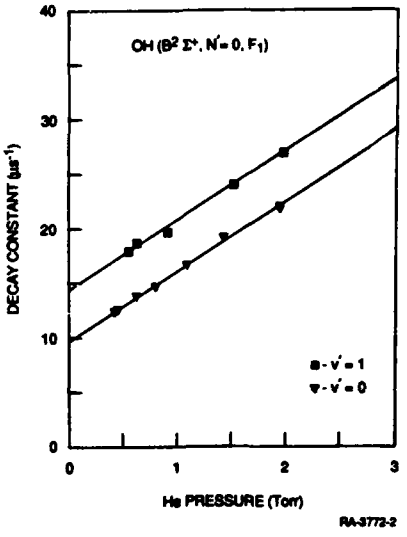

Figure 1

FLUORESCENCE LIFETIMES OF THE B STATE

Fluorescence lifetimes for the B state are obtained from the zero pressure intercept of a plot of the fluorescence decay constant versus the He pressure as shown in Figure 1. We fit the time-dependent fluorescence signals from 90 to 10% of the peak value to a single exponential to obtain the decay constants. In Fig. 1, the boxes are data taken exciting v' = 0, N' = 0, J'=0.5 while the triangles are taken exciting the same rotational state in v' = 1. The lines are the best linear least squares fit to the data. Note the larger zero pressure intercept for v' = 1 indicating a longer fluorescence lifetime,τ for v'=0. The characteristic slope of each line is due to collisional removal of the excited rotational level and will be discussed in detail in a future publication. We have made zero pressure lifetime measurements for the F_1 and F_2 spin components of rotational levels, N = 0, 1,and 2 in v' = 0, and 1 of the B state. The results are presented in Figure 2 where we have chosen to plot the lifetimes versus the total angular momentum J. The data for the F_1 components are obtained by exciting to only the F_1 level, while the points for F_2 are extracted from data in which a mixture of F_1 and F_2 fine-structure levels are populated. We estimate an experimental uncertainty of in the fluorescence lifetimes of ±15% for the F_1 levels and ±50% for the F_2 levels.

The significant variation of τ with N, v, F_1 and F_2 seen in Fig. 2 signals a predissociation in the B state. (Note that the lifetime of the F_1 component of rotational level N-1 is nearly equal to that of the F_2 component of level N.) This conclusion is supported by a calculated radiative lifetime[2] of ~300 ns for v = 0 and ~510 ns for v = 1, which is much longer than we observe in the experiments. Our lifetimes are over an order of magnitude shorter than obtained by previous indirect measurements[3] and, coupled with the theoretical results,[2] indicate that the B fluorescence lifetimes of Ref. 3 are in error. Although we can not definitively assign the predissociation based on our limited data, several points can be made with certainty. First, the magnitude of our values (20-100 ns) indicates that the predissociation is weak. A weak predissociation may be due to second order effects (especially spin-orbit) in the electronic matrix element, or small vibrational overlap factors resulting from non-crossing curves.[4] Second, the lifetimes for the F_1 levels in both v' = 0, and 1 decrease as J increases

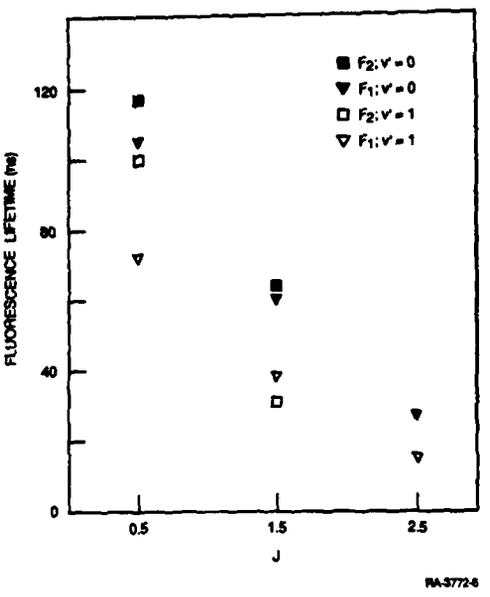

Figure 2

(Fig. 2). This type of behavior is characteristic of rotational and gyroscopic predissociations.[4] Rotational predissociation can be eliminated because we are observing levels well below the dissociation limit of the B state. The predissociation observed here is therefore distinct from the rotational predissociation of higher rotational levels of the B state discussed by Felenbok.[5]

On a more speculative level, further information is gained from consideration of possible perturbing states that could induce a gyroscopic predissociation ($\Delta\Lambda\pm1$, $\Delta S=0$). The lower lying asymptote, $O(^1D) + H(^2S)$, gives rise to three doublet states, $^2\Sigma^+$, $^2\Pi$, and $^2\Delta$. The first of these constitutes the well-known $A^2\Sigma^+$ state. Of the remaining states, only the $^2\Pi$ state is capable of predissociating the $B^2\Sigma^+$ state through first order effects. Calculations show a crossing (barely) between the $B^2\Sigma^+$ and repulsive $^2\Pi$ states on the inner limb; this is the only curve which appears to cross the B state.[6] However, the $^2\Sigma^+$-$^2\Pi$ gyroscopic interaction should be strong. The weakness of the observed interaction suggests that the curves may not actually cross, or that another predissociation mechanism is occurring. Further experiments investigating predissociation in OD and in higher rotational levels should unambiguously characterize this predissociation.

ACKNOWLEDGMENT

This work was sponsored by the Air Force Geophysics Laboratory under contract No. F19628-87-K-0043, AFOSR task 231064.

REFERENCES

1. A. D. Sappey, D. R. Crosley and R. A. Copeland, J. Chem. Phys., in press (1989).
2. S. R. Langhoff, E. F. van Dishoeck, R. Wetmore and A. Dalgarno, J. Chem. Phys. 77, 1379 (1982).
3. T. Bergeman, P. Erman and M. Larsson, Chem. Phys. 54, 55 (1980).
4. H. Lefebvre-Brion and R. W. Field, Perturbations in the Spectra of Diatomic Molecules, (Academic Press, New York, 1986), pp. 331-381.
5. P. Felenbok, Ann. Astrophys. 26, 393 (1963).
6. I. Easson and M. H. L. Pryce, Can. J. Phys., 51, 518 (1973).

PHOTOCHEMISTRY OF FORMYL FLUORIDE

Brad R. Weiner[1] and Robert N. Rosenfeld*
Department of Chemistry,
University of California, Davis, California 95616

ABSTRACT

The photochemistry of formyl fluoride, HFCO, at 193- and 248-nm has been studied by using the technique of time-resolved CO laser absorption spectroscopy. Measurements of CO product formation rates suggest that the initial photochemical event is bond fission, yielding H+FCO or F+HCO. The triatomic product undergoes secondary decomposition to an atom and CO. The rate of this secondary dissociation depends on the internal energy of the triatomic. The photochemistry of HFCO qualitatively differs from its thermal chemistry. The latter results in molecular elimination to form HF and CO in a single elementary step.

INTRODUCTION

We report here recent experimental results on the photodissociation of formyl fluoride, HFCO, using time-resolved CO laser absorption spectroscopy to probe the carbon monoxide product following pulsed laser photolyses at 248- and 193-nm.[2] Berry and co-workers[3] have used chemical laser gain and infrared absorption spectroscopic methods to detect the HF photoproduct following the broad-band ultraviolet (UV) excitation of HFCO, (1), and report that the vibrational energy distribution of the HF thus

$$HFCO + h\nu \rightarrow HF + CO \qquad (1)$$

formed is inverted. However, HF vibrational energy accounted for less than 7% of the total available energy, and rotational, translational, or CO vibrational energy distributions were not measured. The decomposition of chemically activated, ground electronic state HFCO has been studied.[4] These results raise the possibility that, in HFCO, different reaction channels are accessed from the ground and excited electronic states. Data on the kinetics and dynamics of CO formation [*cf.* (1)], especially as a function of excitation wavelength, may be useful in addressing this question.

EXPERIMENTAL RESULTS

The instrumentation used in our time-resolved CO laser absorption experiments has been previously described in detail.[5] Transient CO laser absorption, *i.e.*, CO formation, is observed following the photolysis of HFCO at 248 and 193 nm. In all cases, absorption amplitudes were found to be linearly dependent on the UV laser fluence.

Photochemistry of HFCO at 248 nm. The photolysis of HFCO at 248-nm results in the production of CO which can be detected by transient absorption spectroscopy using the $P_{v+1,v}(11)$ CO laser lines, where v=0-2. A representative transient absorption curve is shown in Figure 1a. The risetime of the absorption signal is orders of magnitude longer than the detection system risetime (*ca.* 10^{-7} s). This result holds for all v=0-2. The rising portion of these absorption curves can be fit with single-exponential functions, as determined by non-linear regression analysis. The risetime and amplitude of the transient absorption curve recorded by using the $P_{1,0}(11)$ CO laser line is independent of the pressure of added He, Ar, SF_6, C_2H_6 or C_4H_{10} over the pressure range 0-25 Torr.

Photochemistry of HFCO at 193 nm. The photolysis of HFCO at 193-nm results in the formation of CO, which can be detected by using $P_{v+1,v}(11)$ CO laser lines, where v=0-4. Two distinct types of transients are observed, depending on the values of v. The rising portion of the $P_{5,4}(11)$ and $P_{4,3}(11)$ transients can be fit with single-exponential functions and have slow risetimes, comparable to those observed in the 248-nm experiments. Transient absorptions recorded by using the $P_{v+1,v}(11)$ CO laser lines, where v=0-2, could not be fit by single-exponential functions, but could be well-fit by using biexponential functions. See Figure 1b. In these cases, the rising portion of each transient consisted of (at least) two components: One with a detector-limited risetime, independent of pressure (region I, Figure 1b), and another with a rise time comparable to that observed in the 248-nm photolysis (region II, Figure 1b). Nascent CO product vibrational energy distributions can be obtained only for the channel corresponding to region I in Figure 1b. In this case, peak absorption amplitudes are obtained by non-linear regression analyses of the transients. Relative vibrational populations are obtained from the amplitudes as previously described. The results are $N_0:N_1:N_2$ = 1.00:(0.13±0.05):(0.04±0.02), corresponding to an effective vibrational temperature of *ca.* 1300K.

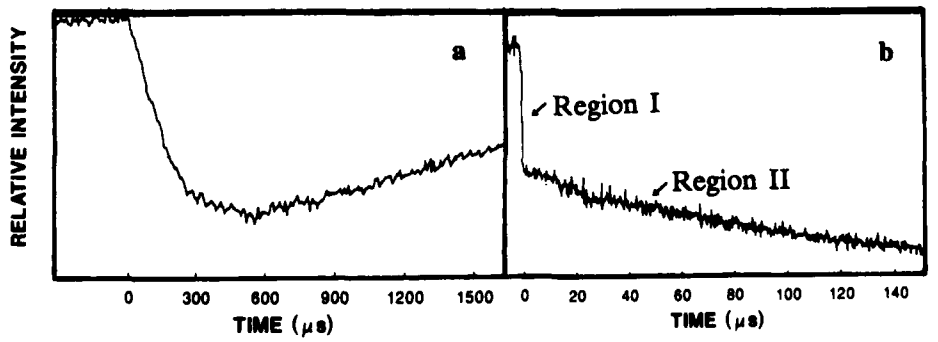

Figure 1. *Time resolved* absorption of the $P_{1,0}(11)$ CO laser line following the 248-nm (a) and 193-nm (b) photolyses of HFCO. Regions I and II in (b) correspond to detector-limited and slow production of CO, respectively.

DISCUSSION

The HFCO($\tilde{A}^1A''$) prepared by 248- or 193-nm excitation can only decompose to ground electronic state HF + CO following internal conversion, since the molecular elimination process, (1), is symmetry forbidden from the first excited singlet.[3b] RRKM calculations indicate that HFCO($\tilde{X}^1A'$) with either 115 or 148 kcal/mole of internal energy, corresponding to 248- or 193-nm photoactivation respectively would decay to HF + CO with a rate constant $>10^7$ s^{-1}. The CO absorption signals observed following 248-nm excitation of HFCO have risetimes of *ca.* 10^4 s^{-1}. The non-radiative decay rate of the HFCO($\tilde{A}^1A''$) prepared by 248-nm excitation has been reported to be *ca.* 10^8 s^{-1}.[3c] This indicates that internal conversion is not responsible for CO production in our experiments, and allows us to conclude that UV photolysis of HFCO does not result in the direct formation of molecular products, HF + CO.

These considerations point to a simple bond fission, (2), as the primary

$$HFCO(\tilde{A}^1A'') \rightarrow F(H) + HCO(FCO) \qquad (2)$$

chemical event following the UV excitation of HFCO. 248-nm excitation does not, by itself, impart sufficient energy for a subsequent dissociation of the triatomic (primary) product to yield an atom + CO. Therefore, the additional energy required to form CO must come from the high energy component of the energy distribution for the HCO or FCO photoproduct. Note that under our experimental conditions (pressures $\geq$ 1 Torr), the triatomic product is likely thermalized via collisions rapidly, relative to the timescale for its dissociation. The energy supplied by a 193-nm photon is sufficient to yield H+F+CO(v=0-2), but insufficient to yield CO(v>2). Thus, any CO(v>2) formed must originate from the high-energy component of the distribution of triatomic species produced by photodissociation. CO(v=0-2) can be formed promptly (region I), or slowly following thermalization (region II).

REFERENCES

1. Current Address: Department of Chemistry, University of Puerto Rico, Rio Piedras, PR 00931.

2. B.R. Weiner and R.N. Rosenfeld, J. Phys. Chem. 92, 4640 (1988).

3. a. D.E. Klimek and M.J. Berry, Chem. Phys. Lett. 30, 141 (1973); b. D.E. Klimek Ph.D. Diss., Univ. of Wisconsin, Madison, WI (1975); c. S.T. Amimoto Ph.D. Diss., Univ. of Wisconsin, Madison, WI (1979).

4. D.J. Donaldson and J.J. Sloan, J. Chem. Phys. 82, 1873 (1985).

5. B.I. Sonobe, T.R. Fletcher and R.N. Rosenfeld, J. Am. Chem. Soc. 106, 4352 (1984).

ENERGETICS AND SPIN SELECTIVITY IN THE INFRARED MULTIPHOTON DISSOCIATION $HN_3(\tilde{X}^1A') \rightarrow N_2(X^1\Sigma_g^+) + NH(X^3\Sigma^-, a^1\Delta)$

Millard H. Alexander, Department of Chemistry, University of Maryland
College Park, Maryland 20742

Paul J. Dagdigian, Department of Chemistry, The Johns Hopkins University
Baltimore, Maryland 21218

ABSTRACT

The dissociation of $HN_3(\tilde{X}^1A')$ into ground state $N_2(X^1\Sigma_g^+)$ and the NH radical in its ground ($X^3\Sigma^-$) or first excited ($a^1\Delta$) electronic state, studied experimentally by Stephenson, King, Cassassa and Foy at NBS using infrared multiphoton and overtone pumping, involves a crossing between the lowest energy singlet and triplet HN_3 potential energy surfaces. *Ab initio* CASSCF and MCSCF calculations have been used to locate the transition states for both channels. The symmetry of the ground state HN_3 wavefunctions as well as of the relevant spin-orbit Hamiltonian with respect to reflection of the spatial and spin components of all the electrons in the plane of the molecule implies that NH products can be formed only in states in which the wavefunction (electronic + rotational) is also symmetric with respect to this operation. This implies that for NH in the $X^3\Sigma^-$ electronic state only the F_1 and F_3 multiplets will be populated in the dissociation process, as seen experimentally.

I. INTRODUCTION

The distribution of the products of photodissociation reactions among accessible fine-structure levels can provide insight into the dynamics. As an example, the non-statistical population of the Λ-doublet levels[1] of $OH(X^2\Pi)$, observed in a number of photodissociation processes,[2,3] can be interpreted by analysis of the evolution of the molecular orbitals in the precursor species which correlate with the unfilled π molecular orbital in the OH fragment.

Unequal populations have also been observed in photodissociation products in $^{2S+1}\Sigma$ electronic states, namely $CN(X^2\Sigma^+)$[4,5] and $NH(X^3\Sigma^-)$.[6,7] The spin multiplets of a molecule in a $^{2S+1}\Sigma$ electronic state correspond to the allowed vector coupling of the spin (S) and nuclear rotational (N) angular momentum.[1] The origin of spin selectivity appears to be qualitatively different than that of Λ doublet specificity since the selectivity corresponds in the former case to a preferential orientation of the electronic *spin* relative to some internal axis, rather than a preferential *spatial* orientation of the electronic wavefunction.[2]

In this article we shall discuss the recent experiments of Stephenson, King, and co-workers[6,7] who have found preferential population of the product spin multiplet levels in the IRMPD dissociation of deuterated hydrazoic acid (DN_3),

$$DN_3(\tilde{X}\,^1A') \xrightarrow{nh\nu} ND(X\,^3\Sigma^-) + N_2(X\,^1\Sigma_g^+) \quad . \qquad (1)$$

and in the analogous dissocation of HN_3 by IR overtone pumping. Process (1) is spin-forbidden; the spin-allowed pathway would lead to the lowest electronically excited product channel of singlet multiplicity, $NH(a^1\Delta)$, lying ~ 12,700 cm^{-1} higher,[8] which is also observed in both the IRMPD and IR overtone experiments.[6,7] The spin selectivity is manifest in the virtually complete absence of NH ($X^3\Sigma^-$) products in the F_2 multiplet level.

Process (1) occurs by a spin-orbit induced crossing between the singlet surface correlating asymptotically to $N_2(X^1\Sigma_g^+) + NH(a^1\Delta)$ and the lowest triplet surface, which correlates asymptotically with the ground state product channel [$NH(X^3\Sigma^-)$]. As illustrated schematically in Fig. 1, the lower, triplet product channel correlates in the molecular region with an electronically excited triplet state of HN_3.

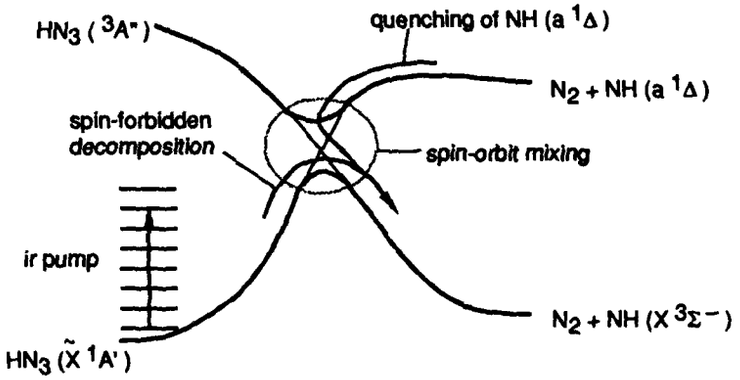

Fig. 1. Schematic reaction coordinate diagram for the energetics of the dissociation of HN_3 by infrared pumping on the ground electronic surface. Also indicated is the expected mechanism for the quenching of $NH(a^1\Delta)$ by N_2.

II. *AB INITIO* STUDIES OF THE TOPOLOGY OF THE EXIT CHANNEL IN THE DECOMPOSITION OF HN3

In its ground ($\tilde{X}\,^1A'$) electronic state the HN_3 molecule is planar with a nearly linear N_3 moiety and the H–N bond strongly bent with respect to the N_3 backbone (see Fig. 2).[9] The wavefunction can be written in a single-configuration approximation as $1a'^2...9a'^2\ 1a''^2\ 2a''^2$. Of these, the 9a' orbital corresponds to the NH σ bonding orbital, the 1a" orbital to

the N_2 π bonding orbital, and the 2a" orbital, to a weak π bond involving the three N atoms. This orbital correlates asymptotically with the N 2p non-bonding orbital in NH.

Complete active space self-consistent field (CASSCF)[10] and multireference configuration-interaction (MCSCF-CI)[11,12] techniques have been used to characterize quantitatively the orbitals and energetics of the HN_3 molecule, in particular in the region of large N_2–NH separation which influence the dynamics of the dissociation to both the singlet ($a^1\Delta$) and triplet ($X^3\Sigma^-$) channels. A large basis set consisting of 94 contracted Gaussian type functions of s,p, and d symmetry on N and s and p on H was used. The CASSCF calculations involved allocating either all the 16 valence electrons or the 10 valence electrons (exclusive of the N 2s electrons) within an active space of the 4a'–12a' and 1a"–3a" orbitals. The largest configurations from these CASSCF calculations were then used as reference for the MCSCF-CI calculations.

The lowest crossing between the $^1A'$ and $^3A"$ surfaces, which corresponds to the barrier for appearance of NH($X^3\Sigma^-$) products, occurs for a trans HN_3 geometry with $\angle_{HNN}$≈ 85° and a nearly linear N_3 backbone ($\angle_{NNN}$≈165°). The terminal N—N bond distance and a N—H bond distance were very close to the equilibrium internuclear separations in the ground electronic states of these two molecules, and the interior N—N distance was approximately 3.55 bohr. At this point the singlet-triplet crossing lies *ca.*15,250 cm^{-1} above the calculated energy of $HN_3(X^1A')$ at the experimental equilibrium geometry. Due to a better description of electron correlation in the HN_3 molecule, this barrier is somewhat higher than our previous theoretical estimate[13] (~12,500 cm^{-1}) and also higher than the experimental activation energy[14] (12,700 cm^{-1}) for the decomposition of HN_3. The discrepancy with experiment may be reduced somewhat by addition of zero-point corrections, which will probably be larger for the equilibrium geometry of HN_3.

Since the bond distances of the N_2 and NH fragments at the position of lowest singlet-triplet crossing are identical to those in the isolated N_2 and NH molecules (both $X^3\Sigma^-$ and $a^1\Delta$), the dissociation process will be vibrationally adiabatic. A contour plot of the crossing seam between the singlet and triplet potential energy surfaces in the region of this minimum is shown in Fig. 2. Since the seam lies nearly perpendicular to the direction of steepest descent, on both the singlet and triplet sides, we anticipate that product recoil will occur with very little rotational torque on the NH fragment. This is consistent with the experimental findings.[6,7] At equilibrium the $HN_3(X^1A')$ is planar.[9] Calculations were not carried out at non-planar geometries. Nevertheless, at the point of lowest singlet-triplet crossing the terminal N–N bond and the N–H bonds are nearly perpendicular, so that the energy will be nearly independent of the dihedral angle between the terminal N–N and the N–H bonds. Consequently, there will be no torques exerted on the fragments causing a loss of planarity.

It appears from the experimental work of Stephenson, Casassa, and King[6] that there

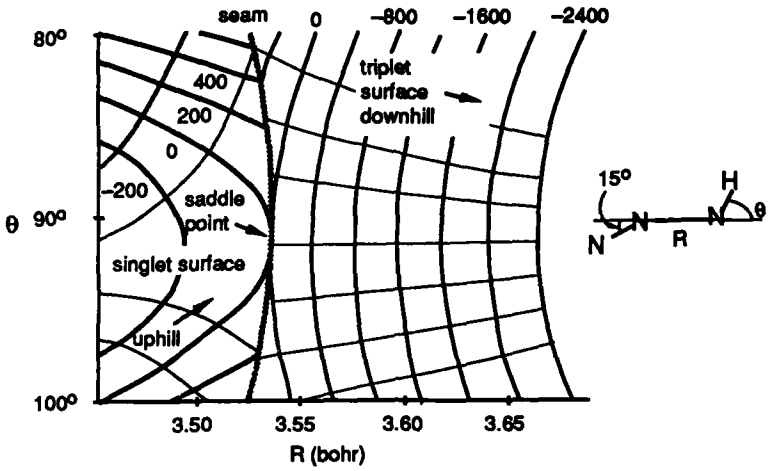

Fig. 2. Contour plot illustrating the region of crossing between the lowest singlet ($^1A'$) and lowest triplet ($^3A''$) surfaces of HN_3 as a function of the NN–NH distance and the NNH angle. The zero of energy refers to the minimum singlet–triplet crossing. The singlet surface is energetically lower to the left of the seam; the triplet surface, to the right.

may exist a barrier in the lowest singlet channel leading to $NH(a^1\Delta)$. The dynamics of the spin-allowed dissociation of hydrazoic acid is related intimately to that of the quenching of $NH(a^1\Delta)$ by N_2,[15] which can proceed by approach on the singlet surface followed by crossing to the triplet surface (Fig. 1). The low rate constant for this process at room termperature[15] is a further indication of the existence of a barrier in the singlet product channel. We have carried out an extensive series of CASSCF calculations to explore this feature. From these calculations we have located the minimum barrier in the singlet channel at a geometry very similar to the minimum singlet–triplet crossing (trans HN_3 geometry with $\angle HNN \approx 90°$ and $\angle NNN \approx 165°$), but at an interior N–N distance of ~4.5 bohr, beyond the singlet-triplet crossing. This singlet barrier lies ~2000 cm^{-1} above this singlet-triplet crossing and also ~1000 cm^{-1} above the N_2 + $NH(a^1\Delta)$ asymptote. This barrier arises from electronic constriction: At long range the 10a' and 2a" orbitals are equivalently occupied by the 2p NH electrons. In the presence of the N_2 molecule the 10a' orbital becomes energetically unfavorable, due to Fermi repulsion with the $2p\sigma$ N_2 orbitals.

III. ORIGIN OF THE SPIN SELECTIVITY IN THE DISSOCIATION OF HN_3 TO GIVE NH ($X^3\Sigma^-$)

At the point of lowest singlet-triplet crossing, the molecule will be nearly planar. As the N_2 and NH fragments separate, there will be little or no dihedral torques. Thus if no out-of-plane wagging vibrations in the HN_3 molecule are initially excited, then the rotational motion of the nascent NH and N_2 molecules will be confined to the initial HN_3 plane. In the ground

state (X^1A') the electronic wavefunction of HN_3 is symmetric with respect to reflection of the spin and space coordinates of the electrons in the molecular plane. Similarly, the $l_z s_z$ term in the spin-orbit Hamiltonian,[16] which is responsible for the coupling between the lowest singlet and lowest triplet surfaces, is symmetric with respect to reflection of the spin and space coordinates of the electrons in any plane containing the NH bond axis — here the HN_3 molecular plane. Thus coupling will be possible only to final states which are also symmetric.

Since the wavefunction of the ground state of $N_2(X^1\Sigma_g^+)$ is symmetric with respect to reflection of the electronic coordinates in a plane containing the molecular axis, this symmetry restriction implies that the wavefunction of the nascent NH molecules in the $X^3\Sigma^-$ state must also be symmetric with respect to inversion. There are 3 spin states for molecules in $^3\Sigma$ electronic states; these are Ω=1 *e* and *f* and Ω=0 in case (a).[16,17] The reflection symmetry in a plane containing the molecular axis is the expectation value of the operators $\sigma_v(xz)$ and $\sigma_v(yz)$ corresponding to reflection of the spatial *and* spin coordinates of all the electrons. Inclusion of the spin coordinates is especially relevant in the case (a) limit, where the spins are coupled to the molecular axis. Omitting the algebraic details here, we state the final result:[13] In the case (a) limit for a $^3\Sigma^-$ electronic state, the *e* levels for both Ω=0 and Ω=1 are *symmetric* with respect to reflection in the plane of rotation, while the Ω=1, *f* level is *antisymmetric.*

The Ω=0 and Ω=1 *e* levels are mixed by the electronic-rotation term (B J·S) in the molecular Hamiltonian.[16] It is conventional spectroscopic practice to label the molecular eigenstates of a given J as F_1, F_2, and F_3 in order of increasing energy.[1] In the case (b) limit, where the spin-spin interaction is negligible compared to the rotational spacings, the wave functions are labelled by the quantum number N, where N = J – S, and equals J–1, J, and J+1 for the F_1, F_2, and F_3 levels. The corresponding wave functions can be expressed as linear combinations of the case (a) functions.[17] The F_1 and F_3 levels can be shown to be *symmetric* with respect to reflection of the electronic spatial *and* spin coordinates through this plane, while the F_2 levels are *antisymmetric.*[13] The reflection symmetry does not change between the case (a) and (b) limits.

In a coplanar dissociation the plane of rotation of the NH fragment will be the same as the plane of rotation of the initial HN_3 molecule. Since the wavefunctions in the F_1 and F_3 spin-multiplet levels are symmetric with respect to reflection of the electronic coordinates in this plane of rotation, only these two levels, and not the F_2 level, whose wavefunction is antisymmetric, should be produced. This is what has been found experimentally by Stephenson, Casassa, Foy, and King.[6,7] This spin selectivity is particularly evident in the overtone pumping experiments of Foy *et al.*,[7] as compared with the IRMPD experiments,[6] since out-of-plane motion is substantially less in the former case.

ACKNOWLEDGMENT

The research described here was partially supported by the U. S. Air Force Office of Scientific Research under contract F49620-88-C-0056. Most of the *ab initio* calculations were carried out at the San Diego Supercomputer Center, under an allocation of time to MHA in connection with NSF grant CHE-8705828. These calculations could not have been carried out without the help of Professor Hans-Joachim Werner (Universität Bielefeld, FRG). MHA is grateful to David King, John Stevenson, and Bernard Foy for several discussions about their experimental work.

REFERENCES

1. G. Herzberg, *Molecular Spectra and Molecular Structure. I. Spectra of Diatomic Molecules* (D. Van Nostrand, Princeton, 1950).
2. M. H. Alexander and P. J. Dagdigian, J. Chem. Phys. **80**, 4325 (1984); B. Pouilly, P. J. Dagdigian, and M. H. Alexander, *ibid.* **87**, 7118 (1987).
3. For a review, see J. P. Simons, J. Phys. Chem. **91**, 5378 (1987).
4. F. Shokoohi, S. Hay, and C. Wittig, Chem. Phys. Lett. **110**, 1 (1984); I. Nadler, D. Mahgerefteh, H. Reisler, and C. Wittig, J. Chem. Phys. **82**, 3885 (1985).
5. H. Joswig, M. A. O'Halloran, R. N. Zare, and M. S. Child, Faraday Disc. Chem. Soc. **82**, 83 (1986).
6. J. C. Stephenson, M. P. Casassa, and D. S. King, J. Chem. Phys. **89**, 1378 (1988).
7. B. R. Foy, M. P. Casassa, J. C. Stephenson, and D. S. King, J. Chem. Phys. **89**, 608 (1988).
8. C. R. Brazier, R. S. Ram, and P. F. Bernath, J. Molec. Spectrosc. **120**, 381 (1986).
9. B. P. Winnewiser, J. Molec. Spectrosc. **82**, 220 (1980).
10. P. J. Knowles and H.-J. Werner, Chem. Phys. Lett. **115**, 259 (1985).
11. H.-J. Werner and E. A. Reinsch, in *Advanced Theories and Computational Approaches to the Electronic Structure of Molecules*, edited by C.E. Dykstra (D. Reidel, 1984), p. 79
12. H.-J. Werner and P. J. Knowles, J. Chem. Phys., submitted.
13. M. H. Alexander, H.-J. Werner, and P. J. Dagdigian, J. Chem. Phys. **89**, 1388 (1988).
14. O. Kajimoto, T. Yamamoto, and T. Fueno, J. Phys. Chem. **83**, 429 (1979).
15. F. Freitag, F. Rohrer, and F. Stuhl, J. Phys. Chem., submitted.
16. H. Lefebvre-Brion and R. W. Field, *Perturbations in the Spectra of Diatomic Molecules* (Academic, New York, 1986).
17. M. H. Alexander and P. J. Dagdigian, J. Chem. Phys. **79**, 302 (1983).

STUDY OF HYDROGEN ABSTRACTION REACTIONS BY NEGATIVE ION PHOTOELECTRON SPECTROSCOPY

S. E. Bradforth, A. Weaver, R. B. Metz, and D. M. Neumark.
Department of Chemistry, University of California,
Berkeley, CA 94720

ABSTRACT

Photoelectron spectra of the negative ions IHI^-, $BrHI^-$ and $(CH_3OH)F^-$ have been recorded at 266 nm and 213 nm. The vibrational structure observed in each spectrum is assigned to the corresponding unstable neutral complex for the bimolecular reaction X + HY -> XH + Y. In the case of the centrosymmetric IHI^- ion, the neutral complex formed lies near the collinear reaction transition state. For the asymmetric reactions, the geometry of the precursor anion determines whether the reactant or product valley of the reactive surface is probed. The peak positions and widths describe the potential energy surface for the neutral reaction, and in the case of I + HI have been interpreted in terms of a vibrationally adiabatic model.

INTRODUCTION

We are interested in the dynamics of elementary bimolecular reactions such as hydrogen abstraction reactions

$$X + HY \longrightarrow XH + Y$$

where X and Y are halogen atoms or alkoxy radicals. These reactions are direct and in the case of $X \neq Y$ often proceed with a small barrier. We have developed a spectroscopic technique to investigate the transition state region of such reactions; the goal of this work is to invert the spectroscopic data to obtain accurate reaction potential energy surfaces. Our approach is to prepare a stable negative ion XHY^- whose equilibrium geometry is similar to the neutral transition state complex. The photoelectron spectrum of such an ion exhibits vibrational structure which is a direct and detailed probe of the neutral potential energy surface near the transition state. We have used this method to explore the I + HI, Br + HI and F + CH_3OH reactions by photodetaching IHI^-, $BrHI^-$ and $(CH_3OH)F^-$.

The I + HI reaction has been the subject of many theoretical investigations in recent years. It is the prototypical heavy + light-heavy reaction, and scattering calculations on model potential energy surfaces have predicted interesting dynamical effects such as 'vibrational bonding' and sharp reactive resonance structure.[1] The potential energy surface is poorly characterized for this reaction, however, since no experimental scattering or kinetic data exist. Our experiment provides (a) the first experimental results on the I + HI reaction and (b) a direct test of the existence of the dynamical effects predicted in the theoretical work.

The asymmetric hydrogen abstraction reactions have been the focus of numerous experimental investigations using infra-red chemiluminescence and crossed molecular beam techniques.[2] The results of these studies, in conjunction with classical trajectory calculations, have been used to construct model potential energy surfaces for several of these reactions. The sensitivity of our method to the details of the potential energy surface near the transition state means we can readily test the proposed surfaces and improve on them. Our experiment also probes electronically excited potential energy surfaces for these reactions. Although experiments examining non-adiabatic effects in these reactions have yielded useful results,[3] the nature of the excited state surfaces responsible for these effects is poorly understood.

EXPERIMENTAL

A negative ion time-of-flight photoelectron spectrometer[4] is used in this work. Negative ions are generated by crossing a pulsed molecular beam with a 1 kV electron beam. The gas mixture expanded through the molecular beam valve for generation of IHI^- and $BrHI^-$ is 5% HI in Argon and 0.25% HI / 5% HBr in Argon respectively. For the $(ROH)F^-$ experiments, NF_3 was passed over the liquid alcohol before entering the pulsed valve. The negative ions formed in the free jet expansion are expected to be internally cold. The ions are extracted perpendicularly from the beam by a pulsed electric field and injected into a time of flight mass spectrometer.[5] The mass-selected ions are photodetached with a pulsed Nd:YAG laser operating at fourth or fifth harmonic (266 nm, 4.66 eV and 213 nm, 5.825 eV respectively). A small fraction of the ejected electrons is detected at the end of a 100 cm field-free flight tube; electron energies are analyzed by time of flight. The laser is polarized at 54.7° with respect to the electron collection direction. The spectrometer resolution is 8 meV at 0.65 eV and scales as $E^{3/2}$ at higher electron energy. Peaks at highest electron kinetic energy correspond to molecular states of lowest internal energy.

RESULTS AND DISCUSSION

I + HI:

The photoelectron spectra of IHI^- and IDI^- are shown in Fig. 1. They show a series of well resolved peaks with differing widths. The peaks at highest electron energy in each spectrum coincide, but the spacing of the following peaks is reduced significantly in the IDI^- spectra. The peaks are therefore assigned to a vibrational progression, which primarily involves hydrogen atom motion, in the neutral complex, and the highest electron energy peak is the 0-0 transition. Assuming that the ion is linear and centrosymmetric,[6,7] and that the minimum energy path for the I + HI reaction is collinear,[1] we would not expect to see any excitation of the bending mode (v_2). Hence the observed progression is ascribed to the antisymmetric stretching motion (v_3) of the hydrogen atom between the two iodine atoms.

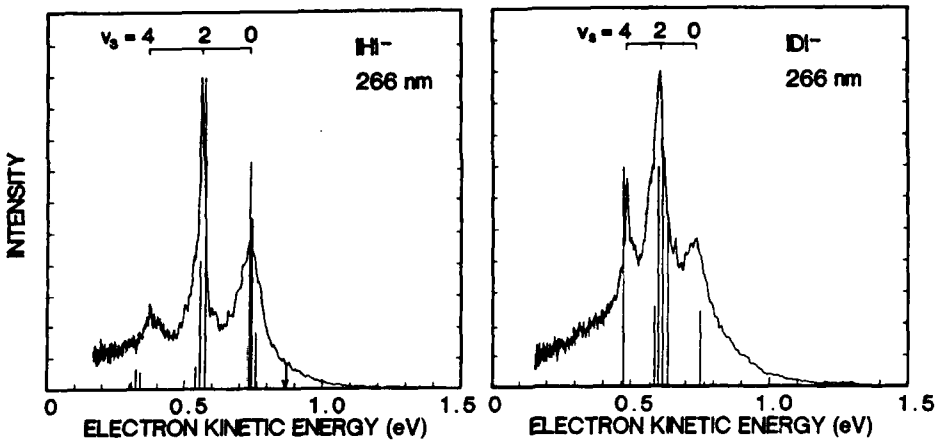

Fig. 1 Photoelectron spectra of IHI^- and IDI^- at 266 nm. The arrow indicates the energy for the reaction asymptote corresponding to I ($^2P_{3/2}$) + HI (v=0), calculated from thermochemical data. Simulated stick spectra are superimposed on the experimental spectra allowing the v_3= 0 sticks to line up with experimental v_3= 0 peak.

Considering that the v_3= 0 ion nuclear wavefunction is totally symmetric, only transitions to symmetric v_3 levels of the neutral will have non-zero intensity. The measured spacing between the 0-0 and the 2-0 peaks is 1360 ± 100 cm^{-1} and 1020 ± 120 cm^{-1} in the IHI^- and IDI^- spectra respectively. The fact that these spacings are much smaller than the stretching frequency of the free HI (DI) molecule indicates that the H atom is interacting strongly with both iodine atoms. This corresponds to the intuitive idea that in the transition state there is expected to be a bond order of one half between the H and each of the I atoms.

We have presented an interpretation[8] of the IHI^- and IDI^- spectra in terms of vibrational motion on a model collinear potential energy surface of the London-Eyring-Polanyi-Sato (LEPS) form. All the features in each spectrum correspond to dissociative states of the IHI [IDI] complex that lie above I + HI [DI] (v=0). The existence of a progression in the antisymmetric stretch can be explained by the poor coupling of that mode to the dissociation coordinate in a heavy-light-heavy reaction. The peak widths can be explained by considering symmetric stretch motion on the neutral surface. Although this mode is strongly coupled to dissociation, a number of symmetric stretch (v_1) states exist for each even v_3 level, within the framework of an adiabatic approximation.[1] These bound and quasi-bound states are responsible for 'vibrational bonding' and reactive resonances respectively.

We can simulate our experimental spectrum by calculating the two-dimensional Franck-Condon factors between the ground state of the ion and the symmetric and antisymmetric stretch states supported by the LEPS surface. The results of the simulation are superimposed on the experimental spectra. The three groups of lines in each

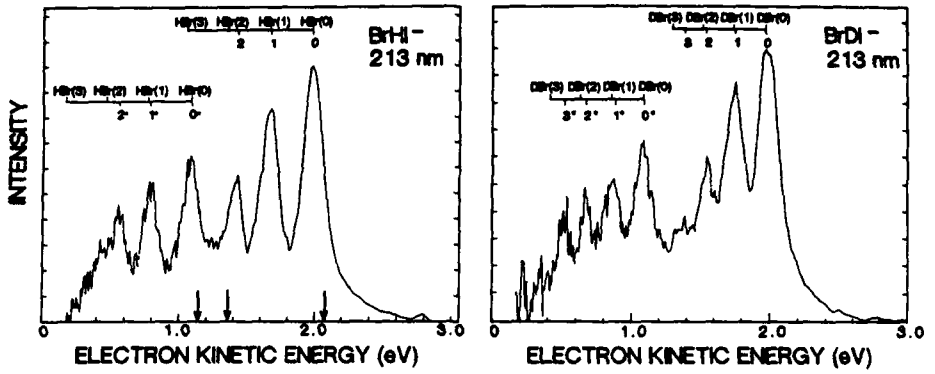

Fig. 2 Photoelectron spectra of $BrHI^-$ and $BrDI^-$ at 213 nm. Peak spacings for progression originating at 1.98 eV for $BrHI^-$ [free HBr] in cm^{-1}: 0-1 2510 [2559], 1-2 1960 [2468]. Spacings for $BrDI^-$ [free DBr]: 0-1 1810 [1839], 1-2 1670 [1794], 2-3 1270 [1748]. The vibrational spacings in the free diatomics HBr (DBr) are shown assuming observed band origin. Arrows indicate the energies for asymptotes corresponding to the reaction channels (left to right): $I(^2P_{1/2})$ + HBr(v=0), $Br(^2P_{3/2})$ + HI(v=0) and $I(^2P_{3/2})$ + HBr(v=0).

simulation correspond to different antisymmetric stretch levels of the IHI (IDI) complex, while the closely spaced lines within each set correspond to symmetric stretch levels. The individual symmetric stretch levels are not resolved in the experimental spectra, and the shape of each experimental peak is interpreted as the envelope of the underlying closely spaced symmetric stretch states which have good overlap with the ion. The agreement of the experimental spectrum with the simulated peak shapes is encouraging given the approximate nature of the model potential surface employed.

Although collinear calculations on the I + HI reaction show sharp resonance structure due to quasi-bound IHI states, there has been considerable discussion in the literature about the nature of these states in three dimensions. The narrowness of the v_3= 4 peak in the IDI^- experimental spectrum (12 meV) provides strong evidence for the existence of these states as well as a lower limit of 0.1 ps for their lifetime. Higher resolution experiments on the I + HI system in progress in our laboratory should provide further insight into the properties of these long-lived states.

Br + HI:

The photoelectron spectra of $BrHI^-$ and $BrDI^-$ were recorded at 213 nm and are shown in Fig. 2. There are two vibrational progressions in each spectrum with band origins at 1.98 and 1.08 eV. The spacing of the peaks in each progression is slightly less than that of free HBr (DBr). The 0.90 eV interval between the band

origins is very close to the spin-orbit splitting in the free iodine atom (0.943 eV). All peaks are broad (approx. 160 meV). The electron energies required to form ground state I + HBr (v=0) products and Br + HI (v=0) reactants are indicated in the figure with arrows. The most intense peak in the 1.98 eV progression comes from a transition to the neutral complex that lies just above the energy required to form I + HBr(v=0). There is little or no intensity at the Br + HI(v=0) asymptotic energy.

The peak spacings and intensity distributions in the vibrational progressions that start at 1.98 eV indicate that we are accessing the product valley of the Br + HI reaction where the nascent HBr bond is nearly complete. This is reasonable because HI is a stronger gas phase acid than HBr, and the ion should thus resemble I^-(HBr). Photodetachment therefore results in an asymmetric neutral complex with the same geometry. The peak spacings and intensities can in fact be simulated assuming the hydrogen atom moves in an asymmetric double well potential which represents the weak interaction between an I atom and the nearly formed HBr bond.

The progressions starting at 1.08 eV appear to be from an electronically excited state of the neutral complex that is best described as spin-orbit excited I* weakly interacting with HBr. This excited state lies on an adiabatic potential surface joining Br^* + HI and I^* + HBr, which is expected to have a very large collinear barrier.[3] As such it is surprising that the excited state progression shows peaks no wider than the ground state and that the separation of the band origins is, if anything, smaller than that of free iodine, while the vibrational spacings in the excited state still indicate a vibrational interaction with the iodine similar to that on the ground state surface.

F + CH_3OH:

All asymmetric bihalide photoelectron spectra show structure largely sensitive to the product valley of the neutral reaction, because the hydrogen favors the same halogen atom in the neutral as in the anion. In contrast, HF is a stronger gas phase acid than methanol despite the fact that the O-H bond in methanol is weaker than an H-F bond; this effect is due to the low electron affinity of the methoxy radical compared to atomic fluorine. The hydrogen bonded anion derived from this pair is therefore of the form[9] $(CH_3OH).F^-$ and photodetachment will access the reactant valley for the F + CH_3OH system.

Hydrogen abstraction by fluorine from methanol is highly exothermic and extremely fast. While abstraction occurs from both the hydroxyl and the methyl groups,[10] our experiment examines only the hydroxyl abstraction channel. The saddle point to this reaction is probably at a collinear geometry where the barrier is small and 'early'. The strong binding energy of the fluoride-methanol anion,[11a] and the reasonably small difference in the gas phase acidity of HF and CH_3OH,[11b] suggests that the anion has a geometry suitable for looking at the transition state of the neutral reaction: a tight complex with the hydrogen fairly substantially

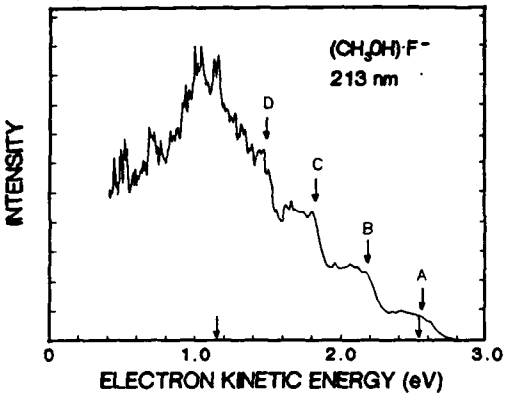

Fig. 3 The photoelectron spectrum of $(CH_3OH)F^-$ at 213 nm. Threshold spacings in cm^{-1} [spacings in HF]: A-B 3200 [3959], B-C 2850 [3779], C-D 2750 [3600]. Baseline arrows indicate the energies for asymptotes corresponding to channels (left to right) : $F + CH_3OH$ and $CH_3O + HF(v=0)$.

displaced by the fluoride ion from the equilibrium O-H distance in methanol . Ab initio calculations[12] confirm this prediction and suggest the ion is linear about the hydrogen bond.

The 213 nm photoelectron spectrum of the $(CH_3OH)F^-$ ion is shown in Fig. 3. A sequence of broad steps is observed over a range of 1.5 eV. On the basis of a corresponding $(CH_3OD)F^-$ spectrum (not shown) we assign the sequence of peaks as a hydrogen stretching vibrational progression in the neutral just as in the bihalide spectra. The spacings between step thresholds, at higher electron energy where it is possible to distinguish them, are considerably smaller than the vibrational spacing in HF as well as the OH stretch in CH_3OH. This shows the H atom is interacting strongly with both the F atom and the methoxy radical and indicates that the experiment indeed probes the transition state region for this reaction.

The $F + CH_3OH$ reactant and $HF + CH_3O$ product asymptotic energies are indicated with arrows in the figure. In contrast to the $BrHI^-$ spectrum, the intensity increases with higher vibrational excitation of the neutral complex until the reactant channel is energetically allowed. This again is in accord with the expected geometry of the anion and our consequent supposition that the best overlap will be with the reactant valley. The spectrum becomes more complex at these high internal energies as states correlating to both reactants and products are superimposed.

Finally, it is perhaps surprising that photodetaching $(CH_3OH)F^-$ to form a system as large as the $F + CH_3OH$ collision complex results in <u>any</u> vibrational structure in the photoelectron spectrum. It appears that most of the vibrational modes of the complex are not excited upon photodetachment of the ion, although enough excitation is occurring to broaden the features in the spectrum relative to the triatomic systems. The results for this system are encouraging with regard to future plans to apply our method to even more complex systems, particularly hydrogen abstraction reactions of the OH radical.

REFERENCES

1: Manz, J.; Meyer, R.; Pollak, E.; Romelt, J.; Schor, H.H.R. Chem. Phys. 83, 333 (1984); Kaye, J.A.; Kuppermann, A. Chem. Phys. Lett. 77, 573 (1981); Clary, D.C.; Connor, J.N.L. J. Phys. Chem. 88, 2758 (1984).

2: B.S. Agrawalla and D.W. Setser in 'Gas-Phase Chemiluminescence and Chemi-ionization' ed. Fontijn, Elsevier (1985); Maylotte, D.H.; Polanyi, J.C., Woodall K.B. J. Chem. Phys. 57, 1547 (1972); Grover, J.R.; Iden, C.R.; Lilenfeld, H.V. J. Chem. Phys. 64, 4657 (1976); McDonald, J.D.; Ph.D. Thesis Harvard University (1971).

3: Bergmann, K.; Leone, S.R.; Moore, C.B. J. Chem. Phys. 63, 4161 (1975); Hepburn, J.W.; Liu, K.; MacDonald R.G., Northrup F.J.; Polanyi, J.C. J. Chem. Phys. 75, 3353 (1981).

4: Metz, R.B.; Kitsopoulos, T.N.; Weaver, A.; Bradforth, S.E.; Neumark, D.M., to be published; Posey, L.A.; DeLuca, M.J.; Johnson, M.A. Chem. Phys. Lett. 131, 170 (1986)

5: Wiley, W.C.; McLaren, I.H. Rev. Sci. Instr. 26, 1150 (1955).

6: Ellison, C.M.; Ault, B.S. J. Phys. Chem. 83, 832 (1979).

7: Kawaguchi, K.; Hirota, E. J. Chem. Phys. 87, 6838 (1987); Kawaguchi, K. J. Chem. Phys. 88, 4186 (1988).

8: Weaver, A.; Metz, R.B.; Bradforth, S.E.; Neumark D.M. J. Phys. Chem. 92, 5558 (1988).

9: Moylan, C.R.; Dodd, J.A.; Han, C.; Brauman, J.I. J. Chem. Phys. 86, 5350 (1987)

10: Wickramaaratchi, M.A.; Setser, D.W.; Hildebrandt, H.; Korbitzer, B.; Heydtmann, H. Chem. Phys. 94, 109 (1985); MacDonald, R.G.; Sloan, J.J.; Wassell, P.T. Chem. Phys. 41, 201 (1979).

11: a) Larson, J.W.; McMahon, T.B. J. Am. Chem. Soc. 105, 2944 (1983) b) Moylan, C.R.; Brauman, J.I. J. Phys. Chem. 88, 3175 (1984).

12: Optimized geometry at MP2/6-31++g(p,d) has r(O-H)=1.056 Å, r(F-H)=1.378 Å and <FHO=176°.

DOUBLE RESONANCE STUDIES OF ROTATIONAL ENERGY TRANSFER IN THE N_2 $B^3\Pi_g$ STATE

P. J. Dagdigian and A. Ali*
Department of Chemistry, The Johns Hopkins University
Baltimore, Maryland 21218

ABSTRACT

Rotationally inelastic collisions of N_2 $B^3\Pi_g$ with argon have been investigated by optical-optical double resonance. Specific B state rotational levels are prepared by pulsed pump laser excitation of metastable $N_2(A)$ molecules, which have been prepared in a flow system, on isolated rotational lines in the B–A (3,0) band near 688 nm. A probe laser interrogates the B state rotational populations after a short delay by fluorescence excitation in the C–B (0,3) band near 406 nm. Results on collisional transfer from incident levels in all 3 spin-orbit manifolds of the B state will be reported. For molecules initially in the F_1 (Ω=0) manifold, a preference for conservation of fine-structure label with even ΔJ changes was observed. By contrast, inelastic collisions involving the F_2 (Ω=1) and F_3 (Ω=2) manifolds do not exhibit a significant propensity to conserve fine-structure label. These experimental results are compared to the propensity rules expected for homonuclear $^3\Pi$ rotationally inelastic collisions, both in the case (a) and (b) limits.

I. INTRODUCTION

There has been a long-standing interest in understanding the detailed mechanisms that govern energy flow in systems containing electronically excited nitrogen molecules.[1] The optical-optical double resonance (OODR) technique is applied in this paper to the study, with initial and final rotational state resolution, of collisional transitions in the N_2 $B^3\Pi_g$ state. The present study, for which a fuller description is given elsewhere,[2] extends a recent investigation of the same process by Katayama.[3]

II. EXPERIMENTAL

An extensive description of the experimental apparatus and OODR technique employed for the determination of state resolved inelastic cross sections has been given previously in connection with our studies of the CN radical.[4] Here, nitrogen molecules are prepared in the metastable $A^3\Sigma_u^+$ state through the $Ar(^3P_{0,2})+N_2$ excitation transfer process in a flow of 3.3 Torr of argon by the addition of a small amount of nitrogen to a flow containing metastable argon atoms, which were produced in a low-current dc hollow-cathode discharge.[1] Thus, the collision partner in these experiments is predominantly argon. Fluorescence induced by the pump and probe lasers was observed by a photomultiplier (EMI 9816 or 9813) perpendicular to the gas flow direction and the laser beams, which were combined

*Present address: Ames Laboratory, Iowa State University, Ames, IA 50011

on a dichroic mirror. The pump and probe sources were dye lasers pumped by a Nd:YAG and XeCl laser, respectively; typical dye laser pulse energies were 25 and 2 mJ at a 10 Hz repetition rate. The delay between the ca. 10 nsec long pump and probe laser pulses was controlled electronically and was typically less than 50 nsec. Individual rotational levels in the $B^3\Pi_g$ v=3 manifold were populated by pulsed pump laser irradiation on isolated lines in the first positive B – A (3,0) band[5] near 688 nm. Both the initially excited and collisionally populated rotational levels were monitored by laser fluorescence detection of C – B (0,0) band emission through a uv filter (340 center wavelength, 10 nm bandpass) upon probe laser excitation in the second positive $C^3\Pi_u$ – $B^3\Pi_g$ (0,3) band near 406 nm.[5]

III. RESULTS

Figure 1 shows the energies of the low-lying rotational levels in the $B^3\Pi_g$ v=3 manifold of N_2. The average collision energy in this experiment is *ca.* 200 cm^{-1}, or kT for a room-temperature Maxwell-Boltzmann distribution. Thus there is sufficient translational energy for excitation into F_2 and F_3 from the F_1 manifold.

Double resonance spectra of the C–B (0,3) band were obtained for small pump-probe delays for a range of initially excited rotational levels in all 3 spin-orbit

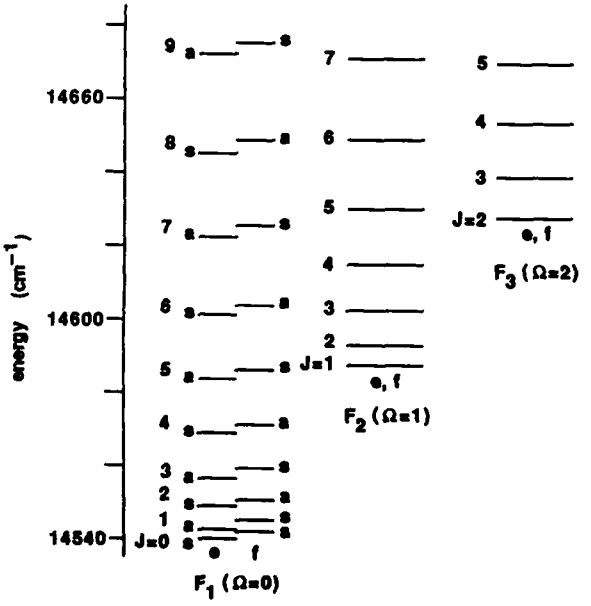

Figure 1. Rotational energies (referred to the lowest level of $A^3\Sigma_u^+$) of N_2 $B^3\Pi_g$ v=3.

manifolds of $B^3\Pi_g$ v=3. Typical pump-probe delays were 10 to 20 nsec; multiple collision effects became evident for delays greater than 50 nsec. Figure 2 displays a spectrum when the J=6 F_1 es level is initially excited. It can be seen that there is a propensity for even ΔJ changes within the F_1 manifold. This even ΔJ propensity rule

was anticipated by the general analysis of inelastic collisions of $^3\Pi$ case (a) molecules given by Pouilly and Alexander.[6] Also evident in our spectrum is the presence of weaker features which correspond to transitions into the F_2 and F_3 manifolds, as well as to odd ΔJ fine-structure-conserving transitions.

The observed relative intensities of resolved rotational lines in OODR spectra such as that displayed in Fig. 2 were used to determine the relative populations in the final rotational states. The derived populations are displayed in Fig. 3 for incident levels of varying J in the F_1 manifold. The propensity toward even ΔJ fine-structure-conserving collisional transitions is clearly evident. This is expected from the fact that the coupling matrix element V vanishes[6] for odd ΔJ transitions

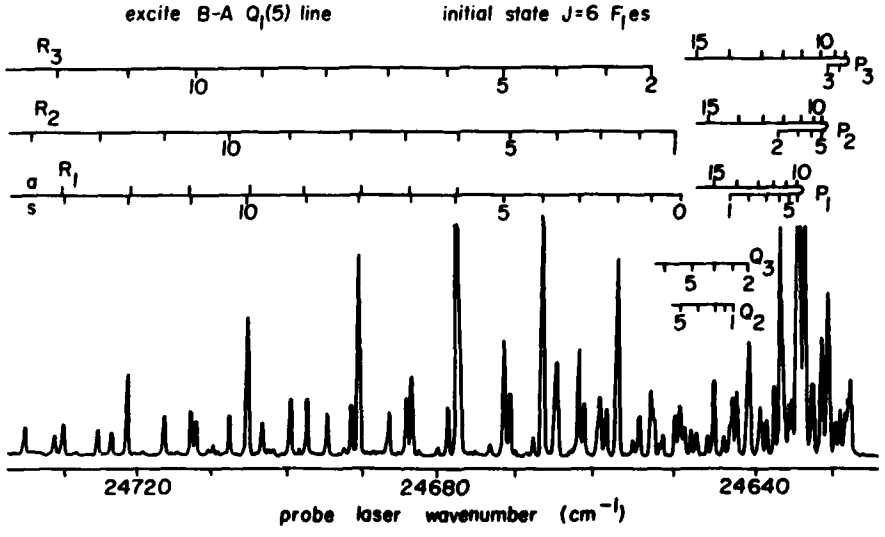

Figure 2. OODR spectrum of the $C^3\Pi_u - B^3\Pi_g$ (0,3) band with the J=6 F_1 es state initially excited. The pump-probe delay was 10 ns.

in collisions of a $^3\Pi_0$ homonuclear molecule in case (a) coupling. Figure 3(a) shows that the cross sections for odd ΔJ transitions from the incident J=0 level are less than 10% of those for even ΔJ. It can be seen from Figs. 3(b) through 3(d) that the amplitude of this even-odd oscillation decreases monotonically as the angular momentum J of the initial level increases. For J=12, the populations of final levels for odd ΔJ transitions has grown to 60-70% of those for even ΔJ. In addition, the importance of fine-structure-changing transitions increases with increasing initial J. By contrast, we find that fine-structure-changing transitions occur with almost the same probability (not shown here) as fine-structure-conserving ones for F_2 and F_3 initial levels for all initial J levels studied.[2]

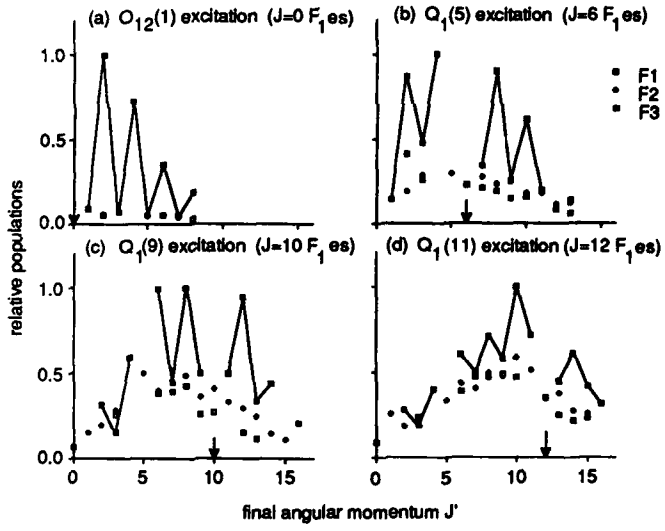

Figure 3. Final state populations for different initial levels in the F_1 manifold. For ease of viewing, populations in the incident manifold are connected with solid lines.

IV. DISCUSSION

Pouilly and Alexander[6] have considered the quantum collision dynamics for rotationally inelastic collisions involving molecules in $^3\Pi$ electronic states and have derived matrix elements of the interaction potential in a case (a) basis. To understand the present results, we extend their treatment to intermediate case coupling. The intermediate case wave functions, which are eigenfunctions of the rotational + spin-orbit Hamiltonian,[7,8] can be expressed as follows:

$$|JMF_i\varepsilon\rangle = \sum_{\Omega=0}^{2} C^{\Omega}_{JF_i\varepsilon} |JM\Omega\varepsilon\rangle. \qquad (1)$$

For simplicity, we have suppressed the labels S and v in Eq. (1). Here ε is a symmetry index,[9] and $|JM\Omega\varepsilon\rangle$ is a symmetrized case (a) wave function.

The approach of Ar to $N_2(B)$ removes the twofold degeneracy of the Π state and yields two potentials, $V_{A'}$ and $V_{A''}$. $N_2(B)$–Ar potential energy surfaces of interaction, as well as calculated inelastic cross sections, are not available for comparison with these experimental results. In the absence of calculated cross sections, it is useful to look at the magnitude of the matrix elements of the interaction potential between initial and final states. In this comparison, we are assuming that cross sections are directly proportional to coupling matrix elements. In a $|JF_i\varepsilon LJM\rangle$ basis,[10] these elements are given by

$$\langle {}^3\Pi J'F_i'\varepsilon'L'JM|\,V\,|{}^3\Pi JF_i\varepsilon LJM\rangle = (-1)^{J+J'+J}[(2L+1)(2L'+1)(2J+1)$$

$$\times (2J'+1)]^{1/2} \sum_l \begin{pmatrix} L' & l & L \\ 0 & 0 & 0 \end{pmatrix} \begin{Bmatrix} J' & L' & J \\ L & J & l \end{Bmatrix} \frac{1}{2}[1 + \varepsilon\varepsilon'(-1)^{J+J'+l}]$$

$$\times [A^l_{JF_i'\varepsilon',JF_i\varepsilon} V_{l0}(R) + B^l_{JF_i'\varepsilon',JF_i\varepsilon} V_{l2}(R)], \qquad (2)$$

where

$$A^l_{JF_i'\varepsilon',JF_i\varepsilon} = \sum_{\Omega=0}^{2} (-1)^{\Omega} C^{\Omega}_{JF_i'\varepsilon'} C^{\Omega}_{JF_i\varepsilon} \begin{pmatrix} J' & l & J \\ -\Omega & 0 & \Omega \end{pmatrix}, \qquad (3a)$$

$$B^l_{JF_i'\varepsilon',JF_i\varepsilon} = \varepsilon \sum_{\Omega=0}^{2} (-1)^{\Omega} C^{2-\Omega}_{JF_i'\varepsilon'} C^{\Omega}_{JF_i\varepsilon} \begin{pmatrix} J' & l & J \\ \Omega-2 & 2 & -\Omega \end{pmatrix}. \qquad (3b)$$

The radial terms $V_{l0}(R)$ and $V_{l2}(R)$ are coefficients in the expansion of the sum V_{sum} and difference V_{diff}, respectively, of $V_{A'}$ and $V_{A''}$ in terms of the Legendre and associated Legendre polynomials $P_l(\cos\beta)$ and $P^2_l(\cos\beta)$.[10] For a homonuclear molecule, such as N_2, only even l terms are allowed in Eq. (2).

In the case (a) limit, the coupling is zero for odd ΔJ transitions in the Ω=0 manifold of homonuclear molecules.[6] This explains the observed strong propensity for even ΔJ transitions for the J=0 F_1 es initial level [see Fig. 3(a)]. Calculation[2] of the coefficients A and B in Eq. (3) for even and odd ΔJ transitions within the F_1 manifold indicate that it is V_{sum} and V_{diff}, respectively, that principally enable these transitions. Since the importance of odd ΔJ transitions is seen in Fig. 3 to grow rapidly with initial J in the F_1 manifold as the molecular coupling goes away from case (a), we conclude that V_{diff} is significant in comparison with V_{sum} for N_2(B)–Ar.

Pouilly and Alexander[6] have shown that, in the case (a) limit, fine-structure-changing transitions are enabled by the difference potential V_{diff}. This also holds true to a large extent for intermediate case coupling, while in the high-J limit such transitions become forbidden.[2] We see from Fig. 3 that the cross sections for such processes are comparable in magnitude to odd ΔJ transitions within the F_1 manifold. Moreover, collisional change of fine-structure level is facile for F_2 and F_3 initial levels.[2] This also indicates the importance of V_{diff} for this collision system.

Our experimental results show that for N_2(B)–Ar collisions the difference potential V_{diff} is not insignificant compared to the sum potential V_{sum}. The predominant electron configuration for N_2(B) is[5] ...$1\pi_u^4 3\sigma_g 1\pi_g$. We infer from the present study that there is a significant variation in the interaction between N_2 in the B state and an argon atom when the $1\pi_g$ electron is in the triatomic molecular scattering plane as compared to when it is perpendicular to it. Thus, the orientation of the $1\pi_g$ electron, which corresponds to an antibonding $2p\pi$ orbital, has a significant effect on the N_2(B)–Ar interaction.

It is interesting to compare these inferences on the N_2(B)–Ar system with what is known about NO($X^2\Pi$)–Ar. The NO(X) electron configuration differs from that for N_2(B) only in the addition of another electron to fill the $3\sigma_g$ orbital. Both experimental crossed beam studies[11] and quantum scattering calculations[12] show that fine-structure-changing collisional transitions are approximately an order

of magnitude less probable than those in which the fine-structure label is conserved. In the nearly pure case (a) coupling appropriate for NO(X), the probability of fine-structure-changing transitions is related to the magnitude of the difference potential $V_{diff.}$ This implies that for NO(X)–Ar the interaction potential depends weakly on the orientation of the unfilled π orbital with respect to the triatomic plane. This suggests that for NO(X)–Ar the filled orbitals shield the incoming perturber atom from interacting strongly with the unfilled $1\pi_g$ orbital. Also, this orbital would also be expected to be somewhat more compact in NO(X) than in N_2(B) because of a slightly higher ionization potential (9.3 vs 8.2 eV[13]). It would be interesting to compare our qualitative conclusions about the N_2(B)–Ar interaction potential, and the comparison with NO(X)–Ar, with actual *ab initio* computations of these potential energy surfaces.

ACKNOWLEDGMENTS

The authors appreciate the help of Millard Alexander for insights into the quantum theory of inelastic scattering of open-shell molecules. This work has been supported by NSF grant CHE-8705912.

REFERENCES

1. J. H. Kolts and D. W. Setser, in *Reactive Intermediates in the Gas Phase*, edited by D. W. Setser (Academic, New York, 1979), p. 151.
2. A. Ali and P. J. Dagdigian, J. Chem. Phys. **87**, 6915 (1987).
3. D. H. Katayama, J. Chem. Phys. **84**, 1477 (1986).
4. N. Furio, A. Ali, and P. J. Dagdigian, J. Chem. Phys. **85**, 3860 (1986); Guo Jihua, A. Ali, and P. J. Dagdigian, *ibid.* **85**, 7098 (1986); A. Ali, Guo Jihua, and P. J. Dagdigian, *ibid.* **87**, 2045 (1987).
5. A. Lofthus and P. H. Krupenie, J. Phys. Chem. Ref. Data **6**, 113 (1977).
6. B. Pouilly and M. H. Alexander, J. Chem. Phys. **79**, 1545 (1983).
7. J. T. Hougen, Natl. Bur. Stand. (U.S.) Monogr. **115** (1970).
8. H. Lefebvre-Brion and R. W. Field, *Perturbations in the Spectra of Diatomic Molecules* (Academic, New York, 1986).
9. B. Pouilly, P. J. Dagdigian, and M. H. Alexander, J. Chem. Phys. **87**, 7118 (1987).
10. M. H. Alexander, Chem. Phys. **92**, 337 (1985).
11. H. Joswig, P. Andresen, and R. Schinke, J. Chem. Phys. **85**, 1904 (1986).
12. G. C. Corey and M. H. Alexander, J. Chem. Phys. **85**, 5652 (1986).
13. K. P. Huber and G. Herzberg, *Molecular Spectra and Molecular Structure. IV. Constants of Diatomic Molecules* (Van Nostrand Reinhold, New York, 1979).

COLLISIONAL QUENCHING AND ENERGY TRANSFER IN NS $B^2\Pi$

Ingrid J. Wysong, Jay B. Jeffries, and David R. Crosley
Molecular Physics Laboratory
SRI International, Menlo Park, California 94025

ABSTRACT

Measurements of the collisional removal and vibrational energy transfer rate constants for a series of vibrational levels of the NS $B^2\Pi$ electronic state show surprising specificity on both collider and vibrational level. Total removal rate constants are obtained from the time resolved decay of fluorescence following pulsed laser excitation of v'=4-7 in the presence of collider in a room temperature discharge flow. For CO_2, N_2O, SF_6, and N_2 as collision partners, the rate constants double from v'=0 to 1, are a minimum at v'=4, increase at 5, decrease at 6, and increase at 7. In contrast, the rate constants for O_2 and H_2 increase nearly monotonically with v'. Fluorescence dispersed through a monochromator provides a measure of the vibrational relaxation within the B state. A significant amount of $\Delta v=2$ transfer is observed for the three polyatomic colliders.

INTRODUCTION

The NS $B^2\Pi$ state is a good candidate for a detailed study of collisional energy transfer, as it has a series of eleven vibrational levels below the dissociation limit which can be excited from the ground state with uv laser light. A previous study of NS[1] revealed that $k_D(6)<k_D(0),k_D(1)$ for some colliders, where $k_D(v)$ is the total removal rate constant from a given vibrational level of the B state. We present measurements here, and in more detail elsewhere,[2] of the total collisional removal rates and vibrational energy transfer rates for a series of vibrational levels. The collisional removal rates of the NS B state show a surprising specificity on both vibrational level and collider, indicating that the underlying physical mechanism is not simply understood.

NS radicals, dilute in a bath gas, are produced in a room-temperature flow cell and excited to the $B^2\Pi$ electronic state with a pulsed, doubled dye laser. Laser-induced fluorescence (LIF) is collected at right angles through a monochromator with a sufficiently broad band pass to observe an entire vibrational band. The temporal behavior of the LIF from a specific band may be analyzed with a transient digitizer, or the monochromator may be scanned to observe a time-integrated fluorescence spectrum.

QUENCHING

Although the laser pumps only one (or possibly a few overlapped) rotational level, a room-temperature rotational distribution is achieved almost immediately through background gas collisions. The entire vibrational manifold can then be seen to decay in a single exponential, which can be described by a decay constant. In a plot of decay

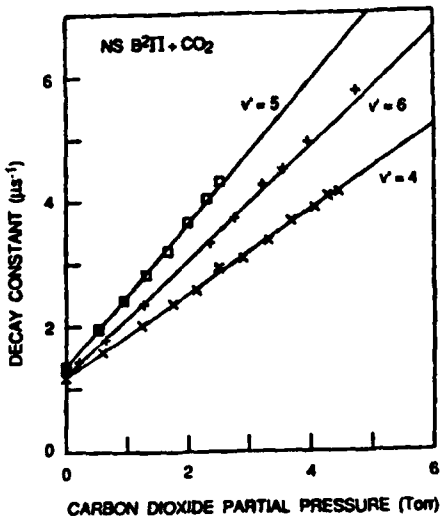

Fig. 1 Carbon dioxide partial pressure dependence of the fluorescence decay constant for three vibrational levels.

constant for a given vibrational level vs. partial pressure of added collider, as shown in Figure 1 for CO_2, the slope is $k_D(v)$, the total removal rate constant. $k_D=k_V+k_Q$, i.e., the total removal is the sum of the vibrational energy transfer (VET) and the electronic energy transfer (quenching, Q). Note that CO_2 quenches v'=5 more rapidly than either v'=4 or v'=6. The intercept of the line is the sum of the radiative decay and the collisional removal by the background and bath gases. These results have been obtained for v'=4-7, and in Table 1 are combined with results from the previous study[1] of v'=0 and 1 (v'=2 and 3 are severely perturbed by quartet states). We might expect that $k_D(v'=1)>k_D(0)$, since the added channel of VET opens up for v>0, and that k_D would continue to rise or level off at a constant value for higher v'. This is the behavior observed for the colliders O_2 and H_2, where k_D increases with increasing v'. The other colliders studied, however, have a minimum in k_D at v'=4 and then an oscillatory behavior. Since none of these vibrational levels are significantly perturbed, we find this result to be surprising.

Table 1. Total Removal Rate Constants for NS($B^2\Pi$) ($10^{-11}cm^3\ s^{-1}$)

	v'=0	v'=1	v'=4	v'=5	v'=6	v'=7
O_2	1.2	2.6	1.6	3.2	3.9	5.4
H_2		1.3	0.9	1.8	1.6	2.0
N_2	1.0	2.5	0.1	0.9	0.3	0.6
CO_2		12.7	2.1	3.6	2.8	3.1
N_2O	6.4	11.1	1.3	2.6	1.9	2.0
SF_6	1.0	3.8	0.9	1.8	1.5	2.2
He	0.04	0.1	0.03	0.3	0.2	0.3
Ar			0.07	0.5	0.2	0.4

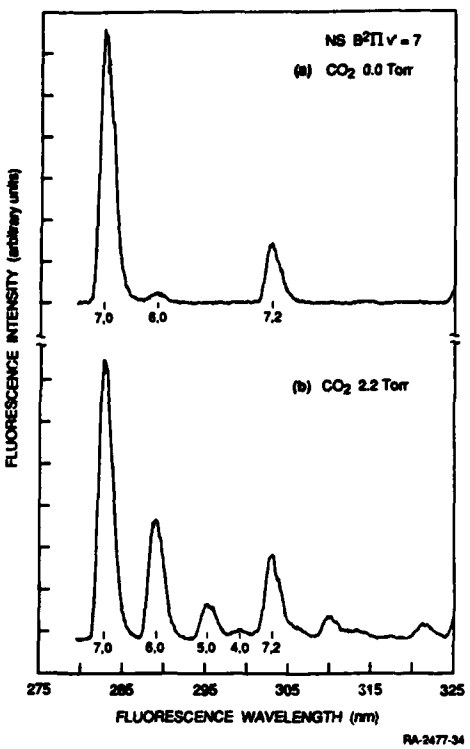

Fig. 2 Wavelength dependence of the LIF following excitation of NS $B^2\Pi$ v'=7, with and without added CO_2 collider.

VIBRATIONAL ENERGY TRANSFER

We have measured the fraction of k_D which is VET. A specific level v' is excited and the wavelength-resolved fluorescence is recorded with and without added collider, using a long boxcar gate to integrate the whole signal and observe a steady-state population distribution; an example is displayed in Figure 2. Knowing k_D for each v' and the relative band emission strengths,[3] we may calculate the VET rate constants k_V. H_2 and the three polyatomics (SF_6, CO_2, and N_2O) have substantial k_V values (k_V=20-80% of k_D), which increase as v' increases from 4 to 7. If we subtract k_V from k_D to obtain k_Q, however, we still observe a minimum in k_Q at v'=4 for most of the colliders studied.

The data clearly show that $\Delta v=2$ transfer from v'=5 occurs for the three polyatomic colliders. In analyzing the v'=5 fluorescence spectra, we first measure the 5→4 VET rate and then calculate the amount of fluorescence from v'=3 that is due to subsequent $\Delta v=1$ collisional cascading, using the 4→3 rate from the v'=4 fluorescence scans. The excess population in v'=3 is due to direct transfer from v'=5; a preliminary value for k(5→3)/k(5→4) is 0.5 for CO_2 and SF_6.

ACKNOWLEDGEMENT

This study was supported by the Air Force Office of Scientific Research.

REFERENCES

1. J. B. Jeffries and D. R. Crosley, J. Chem. Phys. 86, 6839 (1987).

2. I. J. Wysong, J. B. Jeffries, and D. R. Crosley, in preparation.

3. J. B. Jeffries, G. P. Smith, and D. R. Crosley, J. Phys. Chem., in press, 1989.

STATISTICAL SPECTROSCOPY: INSIGHT OR NONSENSE?#

Jean-Paul Pique*, Yongqin Chen†, David M. Jonas,
James K. Lundberg, Charles E. Hamilton**, George W. Adamson,
Robert J. Silbey, and Robert W. Field
Department of Chemistry and George R. Harrison Spectroscopy
Laboratory, Massachusetts Institute of Technology, Cambridge,
MA 02139

ABSTRACT

Stimulated Emission Pumping (SEP) spectra of acetylene, in an energy region intrinsically unassignable in terms of the usual vibrational quantum numbers, are uniquely suited to decoding by statistical methods such as: averaged square-modulus of the Fourier transform[1], autocorrelation, and cross-correlation. The key to the utility of statistical measures is that SEP spectra are nearly pure sequences, i.e. each spectrum contains features belonging to only one value of all rigorous quantum numbers. The short-time dynamical information quantum mechanically encoded in the vibrational spectrum is revealed directly by statistical reduction rather than indirectly via the traditional reduction to molecular constants.

INTRODUCTION

Rotation-Vibration spectra of vibrationally highly excited polyatomic molecules can be very complex and congested. Much of the congestion is removable by double resonance and/or supersonic jet rotational cooling. Let us assume that a spectrum has been maximally simplified so that it consists entirely of transitions into a single, known J-value and rovibronic symmetry (Γ_{rve}) species. The energy levels derivable from such an irreducibly complex spectra form a "pure sequence". It is possible that no labels, in addition to the rigorous quantum numbers E, J, and Γ_{rve}, can be associated with any of the pure sequence levels.

#Supported by DoE grant FE-FG02-87ER13671 and NATO International Travel Grant 693/84.

*Present address: Laboratoire de Spectrométrie Physique, Université Scientifique, Technologique et Médicale de Grenoble, B.P. 87, 38402 Saint Martin d'Hères, France.

†Present address: Department of Chemistry, University of Southern California, Los Angeles, CA 90084-0482.

**Present address: Spectra Technology, 2755 Northup Way, Bellevue, WA 98004.

Nonrigorous quantum numbers, such as "C-C stretch", "torsion", "in-plane bend", or even the chemical bonding name of the molecule, which are eigenvalues of an operator that does not commute with the exact molecular Hamiltonian, may become intrinsically unknowable.

If each level in a spectrum of an N-atom molecule cannot be asigned 3N-6 vibrational mode quantum numbers, no information about the molecule's potential energy surface can be derived from the spectrum by traditional spectrum-inversion techniques. The traditional spectrum - assignment process is based on a very special form of pattern recognition. It is possible that new kinds of pattern recognition schemes can be devised which will be capable of extracting structural and dynamical information from spectra which are intrinsically unassignable eigenstate-by-eigenstate. In this paper we discuss several statistically-based schemes for extracting short-time dynamical information from pure sequence spectra of the acetylene molecule in its $\tilde{X}^1\Sigma_g^+$ electronic ground state.

It is no accident that we focus on short-time dynamics rather than molecular constants derived by fitting molecular eigenstates to an effective Hamiltonian model. Molecules are inherently classical systems of balls and springs. Energy quantization can be thought of as an awkward encoding of the classical dynamics, limited at long time only by the energy resolution at which the spectrum is recorded or, at infinite resolution, by the time corresponding to the symmetry-sorted vibrational density of states ($t \lesssim \rho/c$ where ρ is in cm units). Eigenstates encode the longest time information about the dynamics. They are therefore sensitive to global details of the potential surface. On the other hand, low resolution pure-sequence spectra are sensitive only to short time dynamics. The short time dynamics subsequent to a localized initial excitation samples a local region of the potential energy surface. Low resolution pure-sequence spectra violate Klemperer's first law, namely that all low resolution spectra are either misassigned or worthless.

THE SEP TECHNIQUE

Stimulated Emission Pumping (SEP) is a variant of Optical Optical Double Resonance utilizing two pulsed dye lasers (PUMP and DUMP). The PUMP excites a single rovibronic transition in the $\tilde{A} \leftarrow \tilde{X}(v=0)$ electronic system, thereby populating a single rotational level of an assignable low vibrational level (therefore highly localized) of an electronically excited state. Undispersed, collisionally unrelaxed (ensured by working at $\sim$ 0.1 Torr) side fluorescence from the PUMP-populated level is monitored as the frequency of the DUMP laser is scanned. When the DUMP laser frequency matches a downward $\tilde{A} \rightarrow \tilde{X}(v'' = 0)$ transition

from the PUMP populated level, an ~ 10% dip in the intensity of side-fluorescence results. An SEP spectrum is a fluorescence - depletion excitation spectrum recorded as the DUMP frequency is scanned. Since all transitions in a given SEP spectrum originate from the same $\tilde{A}$-state rotation-vibration level, the term values of all high-v $\tilde{X}$ state rotation-vibration terminal levels are determined absolutely. Selection rules typically limit the levels sampled in one SEP spectrum to 3 or fewer J-values and one rovibronic symmetry (Γ_{rve}) for each J. Thus SEP spectra are nearly pure-sequence spectra, and many be sorted into pure sequences merely by comparing spectra recorded from two $\tilde{A}$-state J-values or via two DUMP polarizations from the same J-level.

A COMPARISION OF SEP TO OTHER TYPES OF SPECTRA

An SEP spectrum is essentially identical to the spectrum of dispersed fluorescence originating from a single $\tilde{A}$-state rotation-vibration level. Aside from an important technical advantage of SEP over dispersed fluorescence, there is no physical difference between spectra recorded via stimulated vs. spontaneous emission. There is, however, an essential difference between SEP and high-overtone spectra. Overtone spectra, because they involve transitions between v=0 and v>>0 vibrational levels belonging to the same electronic state, derive their intensity entirely from overtones of a highly localized, high frequency, "local R-H" stretching basis state. This class of bright basis state is very special, being nearly perfectly localized into a single R-H bond excitation and into a single molecular eigenstate. The vast majority of the other nearby basis states are strongly coupled to many other basis states, consequently most of the nearby eigenstates are less localized than the states accessed in an overtone spectrum. The dynamics sampled by overtone excitation will be atypical. SEP transitions, because they are between a v~0 level of an electronically excited state ($\tilde{A}$) and a v>>0 level of the electronic ground state ($\tilde{X}$), derive their intensity from Franck-Condon factors. Typically, the equilibrium structures and force constants for the $\tilde{A}$ and $\tilde{X}$ states will be very different, and this difference usually involves distortions along several normal modes. Thus the bright basis states in SEP spectra are combinations rather than overtones and involve normal modes affecting the entire molecular framework rather than a localized R-H bond excitation.

The eigenstates that appear in an SEP spectrum are more like the "typical" eigenstate (delocalized, mixed) than those in a high overtone spectrum (localized, unmixed). This important difference is illustrated by the evolution of the appearance of the SEP spectrum as the vibrational excitation energy is increased. In HCCH, at $E \lesssim 10{,}000\ cm^{-1}$, the number of states per

cm^{-1} that appear in the SEP spectrum (typically, in any ~ 1000 cm^{-1} spectral region, the weakest observable transitions are 10^{-2} as strong as the strongest), the spectral density of states (ρ_{SP}), is equal to the number of states predicted to be observable on the basis of Franck-Condon factors, the Franck-Condon density of states (ρ_{FC}). ρ_{FC} is typically 10 to 100 times smaller than ρ_{TOT}, where ρ_{TOT} is the total density of symmetry accessible states. By E≈16,000 cm^{-1}, $\rho_{SP} \approx \rho_{TOT}$. This implies that the vast majority of eigenstates appear in an SEP spectrum, whereas the typical density of states appearing in an overtone spectrum (within a factor of 100 intensity range), ρ_{ovtn}, is much smaller than that in an SEP spectrum. This difference between ρ_{SP} and ρ_{ovtn} becomes increasingly profound as the vibrational excitation increases.

SEP spectra are more "democratic" than overtone spectra, but SEP spectra do contain information about the phase space localization of the wave packet initially transferred into the $\tilde{X}$-state from the $\tilde{A}$ $v=0$ state. Because SEP and overtone spectra differ so profoundly in the nature of the initial localization and its subsequent dynamics, quite different techniques are required for extracting this information from the spectra. The democratic nature of SEP spectra suggests a statistical approach where one seeks information about the structure of phase space in a given energy region. For example, how many "bottlenecks" of unspecified nature divide energetically and symmetry accessible phase space? How long does it take for a piece of the initial wave packet to explore the volume of phase space confined behind a bottleneck? What is the rate of population flow through a bottleneck? The "names" of the bottlenecks and the actual processes described by the rates remain to be determined by other experiments (especially SEP spectra of isotopically substituted species) or theoretical calculations. On the other hand, the bond-localized nature of the overtone excitation invites spectroscopic assignment (in a local mode zero-order model) and mechanistic modelling (e.g. energy flows from R-H stretch to "wag" to "bath"). A statistical approach seems vague, mysterious, and far less satisfying than a mechanistic one. However, by telling us how many unspecified quantum numbers are approximately good and for how long, multi-dimensional trajectory calculations can be guided into the right time and energy regimes and specific mechanistic hypotheses can be tested. When spectra are intrinsically unassignable, we have no choice, it's statistics or nothing!

DYNAMICS FROM EIGENSTATES?

Eigenstates are stationary states! Individually, they exhibit no dynamics whatsoever. The only way to get motion in the probability distribution, $\Psi^*\Psi$, is to construct Ψ out of several eigenstates,

$$\Psi(\underline{x},t) = \sum_i a_i(t)\psi_i(\underline{x})e^{-E_i t/\hbar} \quad . \tag{1}$$

It is a standard exercise in introductory quantum mechanics courses to associate a dynamical process (e.g. tunnelling through a barrier in a symmetric-double-minimum potential) with a systematic pattern of eigenstates (the energy splitting between the two components of a tunnelling doublet).

Molecular rotation-vibration spectra contain complicated patterns of eigenstates that encode dynamics. Dynamical information can be inferred from spectra which are free of any detectable homogeneous broadening of transitions. The intensities and frequencies of spectra are expected and observed to be reproducible line-by-line, even in energy regions where the classical dynamics is chaotic. The final states in an SEP spectrum, as in any eigenstate-resolved spectrum, are <u>stationary</u> states of the molecular Hamiltonian.

So how is a spectrum related to a time-dependent $\Psi^*\Psi$? The initial state in the SEP process, $|\tilde{A},\underline{v}_i\rangle$, is transferred onto onto the $\tilde{X}$ state surface by the transition dipole operator, $\underline{\mu}$. This produces a t=0 wave packet on the $\tilde{X}$ surface which is not an eigenstate of the $\tilde{X}$-state Hamiltonian, but which can be expanded in the $\tilde{X}$-state eigenbasis,

$$|0\rangle = \underline{\mu}|\tilde{A},\underline{v}_i\rangle = \sum_j c_j|\tilde{X},\underline{v}_j\rangle \quad , \tag{2}$$

where

$$c_j \equiv \langle\tilde{X},\underline{v}_j|\underline{\mu}|\tilde{A},\underline{v}_i\rangle \tag{3}$$

by completeness. The autocorrelation of $|0\rangle$ with the time-evolving version of itself, $|t\rangle$,

$$|t\rangle \equiv \sum_j c_j|\tilde{X},\underline{v}_j\rangle e^{-iE_j t/\hbar} \quad , \tag{4}$$

$$\langle t|0\rangle = \sum_j |c_j|^2 e^{iE_j t/\hbar} \quad . \tag{5}$$

Thus the SEP spectrum, $I(\omega)$, is merely the Fourier transform of the autocorrelation of $|0\rangle$

$$FT[\langle t|0\rangle] = \sum_j |c_j|^2 \delta(E_j/\hbar - \omega) = I(\omega). \tag{6}$$

The factor $|c_j|^2$ contains the usual $|\langle\tilde{A}|\underline{\mu}|\tilde{X}\rangle|^2$ electronic transition moment and $|\langle\underline{v}_i|\underline{v}_j\rangle|^2$ Franck-Condon factors. Thus it

is evident that the spectrum, taken as a collection of transition frequencies and intensities, contains a specific kind of dynamical information about a time-evolving initial state.

The dynamical information about $\langle t|0\rangle$ present in an SEP spectrum is precisely the same as would be produced in a time resolved PUMP-DUMP-PROBE experiment using a δ-function (in time) DUMP pulse. No phase information is lost! The energy resolution (~ 0.03 cm^{-1}) and capability of $>10^3$ cm^{-1} spectral coverage give SEP access to a dynamical time regime ranging from 1 fs to 1 ns! When a spectrum can be fully resolved, or when the envelope of a partially resolved spectrum contains hundreds of features, frequency-domain experiments such as SEP will yield higher quality dynamical information than any time-domain experiment.

The SEP initial state is localized in any one of several selectable, assigned and fully characterized normal mode vibrational eigenstates of the $\tilde{A}$-state, none of which are even approximately eigenstates of the $\tilde{X}$-state. Thus a variety of SEP spectra can be recorded, each displaying the dynamics of a wave packet initially localized in a different region of phase space in the $\tilde{X}$-state.

SEP provides information about the time autocorrelation of the initial wavepacket as a function of several variables at the disposal of the experimentalist: (i) total vibrational energy on the $\tilde{X}$-state potential surface, $\bar{E}$, where the energy resolution is set by the width, ΔE, of the spectral region centered about $\bar{E}$ which contains a sufficient number of features (>>100) to yield meaningful statistical measures; (ii) type of initial localization on the $\tilde{X}$-state via selection of intermediate $\tilde{A}$-state $\underline{v}_i$; (iii) rigorous symmetry such as Γ_{rve} or J, where J can be selected to minimize or maximize specific types of Coriolis and centrifugal distortion effects; (iv) isotopic species, where a particular symmetry can be strongly ($H^{12}C^{12}CD$) or weakly ($H^{12}C^{13}CH$) broken, the frequency of a crucial vibrational motion may be drastically altered (HCCH vs. DCCD), or the nature of the intermediate state altered from normal mode (HCCH bending vibrations) to local mode (HCCD $\tilde{A}$ has a highly local DCC bend).

STATISTICAL MEASURES

Three statistical measures have proven useful: (i) The averaged square modulus of the Fourier transform of the spectrum

$$\overline{C(t)} \equiv \langle |\mathrm{FT}\ I(\omega)|^2 \rangle, \tag{7}$$

where the averaging may be done either by cutting the spectrum over the $\omega_{min}<\omega<\omega_{max}$ interval into N segments of length $(\omega_{max}-\omega_{min})/N$ and summing the $|\mathrm{FT}\ I(\omega)|^2$ from each spectral segment or by convolving c(t) with a suitable window function,

$\Omega(t-t')$,

$$\overline{c(t)} = \int c(t')\Omega(t-t')dt'; \tag{8}$$

(ii) the spectral autocorrelation

$$A(\Delta) = \int_{\omega_{min}}^{\omega_{max}} I(\omega)I(\omega-\Delta)d\omega \tag{9}$$

which can be shown to be identical to

$$A(\Delta) = FT[|FT\ I(\omega)|^2]; \tag{10}$$

(iii) and the spectral cross-correlation, $I_{1x2}(E_{vib}/\hbar)$, is the locally averaged overlap between two SEP spectra, $I_1(\omega)$ and $I_2(\omega-\Delta)$, recorded out of two different same-J, same-Γ_{rve} $\tilde{A}$-state vibrational levels, E_1 and E_2,

$$E_1 - E_2 \equiv \hbar\Delta,$$

where I_2 is shifted by Δ so that features in the two spectra are displayed on the same absolute energy scale. The quantity actually computed is

$$I_{1x2}(\omega) = \int I'_1(\omega')I'_2(\omega'-\Delta)\Omega(\omega-\omega')N(\omega')d\omega'$$

where

$$I'_i(\omega) \equiv dI_i/d\omega$$

and $N(\omega')$ is a suitable intensity normalization factor.

The $\underline{\langle|FTI(\omega)|^2\rangle}$ is the most mysterious of the three statistical measures. It is designed to contrast the locally averaged (over the interval $\omega_{min},\omega_{max}$) properties of the energy level spacing distribution in $I(\omega)$ (in particular the difference between the pair distribution function, $P(\omega_1, \omega_2)$, and the uncorrelated average $\rho(\omega_1)\rho(\omega_2)$) to two generic limiting cases, the Poisson limit, which corresponds to an "assignable" spectrum with many non-rigorous but well defined quantum numbers, and the GOE (or random real symmetric matrix) limit, which corresponds to an intrinsically unassignable spectrum possessing no approximate quantum numbers. Because of their universality, the two limiting cases contain no molecule-specific information. However, they are useful as templates in a pattern-recognition scheme whereby molecule-specific features are revealed as systematic departures from the limiting patterns.

There are several qualitatively distinct dynamical features in $\langle|FT\ I(\omega)|^2\rangle$: an exponentional fall from a maximum at t=0

(which corresponds to the rate at which the wave packet explores the initially dynamically accessible region of phase space), a "correlation hole" with complete recovery by $t<\rho/c$ (which implies uniform or "chaotic" exploration of the initially accessed region of phase space), the possibility that the recovery from the correlation hole is complete by $t\sim(\rho/c)/N$ (where, if N is an integer > 1, it implies that the initial wavepacket samples ~N regions of phase space between which there is negligible flow of probability on the time scale limited by the resolution of the spectrum), and recurrences (which correspond to stable large amplitude motions). Spectra recorded at low and high resolution often have very similar appearing $\langle|FT\ I(\omega)|^2\rangle$, but on vastly different time scales. A hierarchy of unnamed rate processes, periods of energetically stable orbit types, and bottleneck structures can be revealed by $\langle|FT\ I(\omega)|^2\rangle$. Supplementary information (from systematic variation of intermediate state, isotopic substitution, trajectory calculations, and inspired guessing) is needed to infer the mechanistic nature of the statistically revealed dynamical features.

The spectral autocorrelation is a brute force search technique which will reveal an often repeated interval, $\Delta\Omega$, concealed in a spectrum where the average separation between transitions, $\Delta\omega$, is much smaller than $\Delta\Omega$. For example, in our SEP spectra of linear acetylene, the interval between J=1, ℓ=0 and J=2, ℓ=2 should appear in every vibrational level of the $\tilde{X}^1\Sigma_g^+$ state sampled by the spectrum. Every J=1, ℓ=0 level will have a J=2, ℓ=2 partner and vice versa. However, one expects a large dispersion in the ℓ=0, ℓ=2 spacing, so this interval should wash out in the spectral autocorrelation. In contrast, the vinylidene isomer of H_2C_2 is an asymmetric top. If the SEP spectrum samples the vinylidene region of phase space, it should repeatedly sample the interval between J=1,K=0 and J=2,K=2 of vinylidene, for which less dispersion is expected than for the corrresponding interval in linear acetylene. In SEP spectra of HCCD, an ~ 37 cm^{-1} interval appears repeatedly in the spectral autocorrelation for energy regions centered at 14,200 cm^{-1} to 17,400 cm^{-1} above the $\tilde{X}$-state vibrational origin. An A rotational constant of $[E_{J=K=2} - E_{J=1,K=0} - 4B]/4 \sim (37-4)/4=8$ cm^{-1} is plausible for monodeuterated vinylidene.

The spectral autocorrelation, $A(\Delta)$, contains information similar to that in $\langle|FT\ I(\omega)|^2\rangle$, although in a quite different format. The averaging of $|FT\ I(\omega)|^2$ throws away information present in $A(\Delta)$ at large Δ. Convolution of $I(\omega)$ or $A(\Delta)$ with a window function to improve the S/N of $A(\Delta)$ throws away long-t information present in $\langle|FT\ I(\omega)|^2\rangle$. It remains to be seen whether there are special advantages to the presentation of information in $A(\Delta)$ vs. $\langle|FT\ I(\omega)|^2\rangle$.

The spectral cross-correlation contains information of a profoundly different nature from that contained in $\langle|FT\ I(\omega)|^2\rangle$ and $A(\Delta)$. The spectral cross-correlation compares spectra ($I_1(\omega)$ and $I_2(\omega)$) originating from two selectable, localized, and maximally different initial preparations ($|\tilde{A},v_1\rangle$ and $|\tilde{A},v_2\rangle$). If the selected difference corresponds to two different values of an approximate constant of motion, and this constant of motion is conserved on the time scale set by ρ/c or the spectral resolution (whichever is shorter), then the two spectra will be profoundly different and $I_{1x2}(\omega)\approx 0$.

For example, v_1 could be 3 quanta of the HCCH $\tilde{A}$-state trans-bend and v_2 could be one quantum of C-C stretch plus two quanta of the antisymmetric in-plane bend, then $\tilde{X}$-state vibrational levels having only zero or only non-zero quanta in the cis-bend (ν_5) would be Franck-Condon accessible from v_1 or v_2, respectively. At low energy in the $\tilde{X}$-state, where ν_5 is a good quantum number, $I_{1x2}(\omega)\approx 0$. At high energy, where ν_5 is not a good quantum number, memory of the difference between v_1 and v_2 is lost rapidly and $I_{1x2}(\omega)\approx 1$.

Of course, the interesting region is at intermediate energy where $I_{1x2}(\omega)$ is evolving from 0 to 1. This evolution could be monotonic, but it is more likely to display "resonances", local regions of ω where I_{1x2} passes through a local maximum ≈ 1. The ω-regions of these I_{1x2} resonances would mark the location of "promoter" levels (basis states which are especially effective in destroying the selected approximate quantum number) and the widths of these I_{1x2} resonances would provide a measure of the rate at which memory of the selected quantum number is lost.

The spectral cross-correlation is the least "statistical" of the statistical measures applied to SEP spectra. A question is being asked about the loss of memory of a specific, experimentally selected quantum number. Although the nature of the promoter level remains to be inferred from supplementary experimental or theoretical information, the nature of the initially selected localization is known a priori. This will facilitate a much more purposeful and systematic exploration of phase space structures than the mechanistically blind $\langle|FT\ I(\omega)|^2$ and $A(\Delta)$ measures. A particularly promising area for the $I_{1x2}(\omega)$ measure is isomerization onsets and the vibration-rotation structure of unstable isomers. Often, rotation-dependent symmetry properties based on the complete nuclear permutation-inversion group will permit isomer-related effects to be distinguished from rigid molecule Fermi resonances.

INSIGHT OR NONSENSE?

SEP spectroscopy is capable of producing enormous quantitites

of high quality, pure-sequence spectra. The availability of pure-sequence spectra raises the possibility of applying many new kinds of pattern recognition techniques to gain information from otherwise uninterpretable spectra. Statistical measures are very blunt tools; when applied to non-pure-sequence spectra they would probably only be capable of detecting that several pure sequences were superimposed. There is much remaining to be learned about how experimental limitations (resolution, dynamic range, spectral coverage) degrade statistical measures. Surely pattern recognition schemes, based on the short-time-dynamics of initially localized system preparations, must be capable of generating information complementary to that obtainable by the powerful but limited, traditional spectroscopic, eigenstate-assignment methods.

GAS PHASE TRANSITION METAL SPECIES: ELECTRONIC STRUCTURE AND REACTIVITY

G. Eiden, S. Hanton, J. Harrington, D. Ritter, L. Sanders and J.C. Weisshaar
Department of Chemistry, University of Wisconsin–Madison, Madison, Wisconsin 53706

ABSTRACT

We survey recent results on the chemical reactivity and electronic structure of gas phase transition metal species. For the reaction of specific spin-orbit levels $V^+(a^3F_J)$ with C_2H_6, we find no dependence of the single collision, total reaction cross section on the quantum number J. For the neutral transition metal atoms $Ti(a^3F)$, we present 300K bimolecular rate constants for abstraction of oxygen atoms from NO, O_2, and N_2O. We have used multiphoton ionization-photoelectron spectroscopy to refine the accuracy of the first ionization energy of VO, confirm the assignment of the VO^+ ground state as $X^3\Sigma^-$, and measure the ground state vibrational frequency. The energy ordering of the known electronic states of the metal monoxide cations TiO^+ and VO^+ can be understood in terms of a simple molecular orbital model.

J-SPECIFIC CROSS SECTIONS FOR $V^+(a^3F_J) + C_2H_6 \rightarrow VC_2H_4^+ + H_2$

We have used resonant two-photon ionization in conjunction with time-of-flight photoelectron spectroscopy to create slow V^+ beams in well-characterized electronic state distributions.[1] In previous work using pulsed time-of-flight mass spectrometry,[2] we demonstrated that the second excited electronic term of $V^+, 3d^34s(a^3F)$ at 1.1 eV, reacts with C_2H_6 at 0.2 eV collision energy at least 200 times more efficiently than either the ground $3d^4(a^5D)$ term or the first excited $3d^34s(a^5F)$ term at 0.4 eV. This provides strong evidence of the importance of electron spin conservation in metal cation activation of C-H bonds of alkanes.

More recently, we have obtained angle integrated, J-resolved photoelectron spectra at different ionization wavelengths and measured relative, state-averaged reaction cross sections for a variety of different spin-orbit level distributions within $V^+(a^3F)$. This allows us to check for the possibility of J-dependent cross sections, which might confuse the interpretation of the a^3F reactivity as primarily an effect of electron spin.

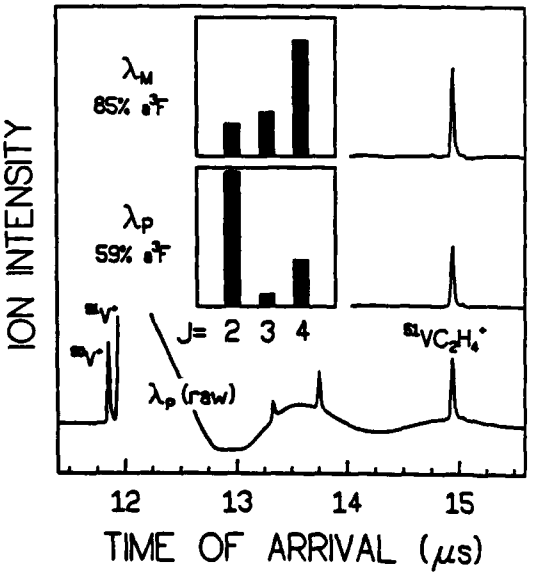

Fig. 1. Time-of-flight mass spectra for $V^+ + C_2H_6$ reaction using two different ionization wavelengths. Lower trace: raw signal at λ_P; upper traces: signal-background at λ_P and λ_M. Histogram shows J-distributions within $V^+(a^3F)$ term at λ_P and λ_M.

The experimental results are illustrated in Fig. 1; relative cross sections are displayed in Table I. Within the uncertainty associated with the raw data and with extraction of state-specific cross sections by a least squares fitting procedure, we find no J-dependence of the reaction cross section. This suggests that non-adiabatic transitions between potential energy surfaces correlating with J = 2, 3, and 4 are rapid on the time scale of reagent approach. The absence of severe spin-orbit effects validates the common assumption that transition metal cation reaction cross sections depend only on the metal electron configuration, L, and S.

Table I. State specific relative reaction cross sections for $V^+ + C_2H_6 \rightarrow VC_2H_4^+ + H_2$ at E = 0.21 ± .04eV.

V^+State		V^+ Internal Energy (eV)	$\sigma_i/\langle\sigma_J\rangle$
Term	J		
$3d^4, a^5D$	0-4	0.017	≤ 0.0049
$3d^34s, a^5F$	1-5	0.353	≤ 0.0043
$3d^34s, a^3F$	2-4	1.098	1.02 ±0.02
$3d^34s, a^3F$	2	1.071	1.09 ±0.19
	3	1.096	0.89 ±0.71
	4	1.128	1.02 ±0.33

OXYGEN ATOM ABSTRACTION REACTIONS OF Ti(a^3F) WITH NO, O_2, and N_2O

By coupling a laser vaporization source of gas phase metal atoms[3] to a fast flow reactor, we have developed a quite general technique for measurement of 300K reaction rate constants of *neutral* metal atoms in 0.4-1.0 torr of He buffer gas. Near-UV laser induced fluorescence (LIF) provides electronic state-specific detection of most neutral transition metal atom reactants and of some neutral products as well.

Table II. Effective bimolecular rate constants for reactions of Ti(a^3F) and TiO($X^3\Delta$) with oxidants at 300 K in 0.75 torr He.

Reaction	$-\Delta H^0_{298}$ (kcal − mol^{-1})	k (10^{-12}cm^3 − s^{-1})	$\langle\sigma\rangle^a$ (Å^2)	Collision Number[b]
Ti(a^3F) + NO	10 ± 4	7.8 ± 0.6	1.34	32
Ti(a^3F) + O_2	41 ± 3	1.5 ± 0.4	0.26	170
Ti(a^3F) + N_2O	121 ± 3	0.40 ± 0.14	0.07	640
TiO($X^3\Delta$) + NO	−6 ± 6	2.2 ± 0.4	0.45	120

[a] Average cross section $\langle\sigma\rangle = k/\langle v\rangle$, where $\langle v\rangle$ is the mean relative velocity at 300 K.

[b] Estimated hard spheres collision cross sections are 43-49 Å^2.

For the oxygen atom transfer reactions $Ti(a^3F) + OX \rightarrow TiO + X$ with $OX = NO, O_2$, and N_2O, the 300K rate constants are collected in Table II. All three reactions are exothermic yet inefficient at 300K, indicating the presence of activation barriers. We can also detect the TiO products by LIF and obtain the $TiO(X^3\Delta) + NO$ reaction rate constant, which is also slow (Table II).

A state correlation argument based on separated Ti + O + X fragments can explain the inefficiency of all three $Ti(3d^24s^2, a^3F)$ reactions. All low-lying TiO states of appropriate spin have only *single* occupancy of the molecular orbital that correlates with the Ti(4s) orbital. The need to switch electron configurations along low energy adiabatic paths from ground state reactants to energetically accessible TiO + OX product states is the probable origin of the energy barrier. This same argument should apply to many atom abstraction reactions of metal atom ground states having the chemically inert ns^2 configuration.

ELECTRONIC STRUCTURE OF VO

Laser vaporization of a vanadium target rod in the throat of a pulsed nozzle expansion of 5% O_2 in 2 atm of Ar creates an intense beam of rotationally cold VO molecules from the $V + O_2$ reaction, as described previously for TiO.[4] The skimmed beam is ionized by absorption of four red dye laser photons (nominal 1 + 3 multiphoton ionization). The neutral resonant states are the B and C states of VO. We obtain photoelectron spectra of cold VO by time-of-flight electron analysis.

We observe as many as ten vibrational states of the VO^+ ground electronic state. The threshold yields the first ionization energy $I_1(VO) = 58,313 \pm 20\ cm^{-1} = 7.230 \pm 0.003$ eV, in good agreement with the previous measurement of 7.25 ± 0.02 eV.[5] Absence of spin-orbit structure in the spectra is consistent with Dyke's assignment of the ground state as $X^3\Sigma^-$, which was based on *ab initio* electronic structure calculations.[5] We refine the ground state fundamental vibrational frequency to $\Delta G_{1/2} = 1038 \pm 15 cm^{-1}$.

It is increasingly clear that nominally isoelectronic neutral and cationic transition metal monoxide pairs, such as TiO and VO^+ or ScO and TiO^+, are electronically *dissimilar*, i.e., the energy ordering of corresponding states is quite different in neutral and cation. For example, the ScO state ordering is $X^2\Sigma^+, A^2\Delta$ at 1.87 eV, $A'^2\Pi$ at 2.05 eV, and $B^2\Sigma^+$ at 2.56 eV. In contrast, the ordering of the known TiO^+ states is $X^2\Delta, A^2\Sigma^+$ at 1.27 eV, and $B^2\Sigma^+$ at 1.39 eV.

Merer[6] has explained the structure of the early transition metal neutral oxides in terms of single electron configurations built from a simple orbital energy diagram. He finds that the Coulomb and exchange interactions that split configurations into molecular terms transfer quite well from molecule to molecule. We find that a similar picture can explain the observed TiO^+ and VO^+ states if the molecular orbital σ_s is placed *above* the orbitals δ, π^*, and σ^* (Fig. 2); σ_s is primarily M(4s) in character, while δ, π^*, and σ^* all involve M(3d) atomic orbitals. In contrast, in the neutral metal oxides σ_s lies just below δ.[6] This rearrangement of orbital energies is qualitatively sensible in that the 3d atomic orbitals lie below 4s in M^+ but above 4s in neutral Sc and Ti. The differences in MO^+ and MO electronic structure for isoelectronic pairs primarily reflect differences in relative orbital energies of the atomic asymptotes.

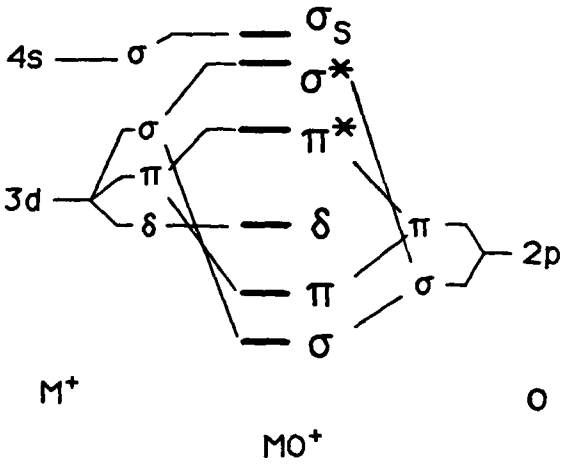

Fig. 2. Schematic molecular orbital energy diagram for early first transition series metal monoxide cations, MO^+. In contrast to the neutrals, $M^+(3d)$ lies below $M^+(4s)$, leading to σ_s *above* δ, π^*, and σ^*.

The diagram of Fig. 2 readily explains the $^2\Delta$ ground state of TiO^+ ($\sigma^2\pi^4\delta$ configuration) as well as the existence of two low-lying excited $^2\Sigma^+$ states (σ and σ_s configurations); it also predicts that a $^2\Pi$ state (from π^*) will lie between $X^2\Delta$ and the $^2\Sigma^+$ states. The same picture explains the $^3\Sigma^-$ ground state of VO^+ as arising from the $\sigma^2\pi^4\delta^2$ configuragion.

ACKNOWLEDGMENTS

We thank the donors of the Petroleum Research Fund, administered by the American Chemical Society and the National Science Foundation (Grant No. CHE-8703076) for support of this research.

REFERENCES

1. L.Sanders, A.D. Sappey, and J.C. Weisshaar, *J. Chem. Phys.* **85**, 6952 (1986).
2. L. Sanders, S. Hanton, and J.C. Weisshaar, *J. Phys. Chem.* **91**, 5145 (1987); and *J. Phys. Chem.*, in press.
3. R. Tonkyn, M. Ronan, and J.C. Weisshaar, *J. Phys. Chem.***92**, 92 (1988).
4. A.D. Sappey, J. Harrington, G. Eiden, and J.C. Weisshaar in *Advances in Laser Sciences-III*, A.C. Tam, Editor (AIP, New York, 1988), p. 399.
5. J.M. Dyke, B.W. Gravenor, M.P. Hastings, and A. Morris, *J. Phys. Chem.***89**, 4613 (1985).
6. A.J. Merer, G. Huang, A.S.-C. Cheung, and A.W. Taylor, *J. Mol. Spectros.***125**, 465 (1987).

Stability and Oxidation of Metal-Based CO and CO_2 Complexes

M. J. McQuaid and J. L. Gole

High Temperature laboratory
Center for Atomic and Molecular Science
School of Physics
Georgia Institute of Technology
Atlanta, Georgia 30332

Introduction

The investigation of the electronic structure and bonding of coordinatively unsaturated transition metal carbonyls, $M(CO)_x$, has been an area of intense research in recent years.[1] Much of the interest in this area has been motivated, in part, by the proposed role which these species play as intermediates in homogeneous catalytic and photochemical reactions, and as models for heterogeneous bulk metal catalysts.[1] This paper summarizes results obtained using a novel gas phase approach for the formation of and characterization of $M(CO)_x$ species as well as a study of their oxidation to form chemiluminescing reaction products. The formation and oxidation of $Al \cdot CO_2$ is also examined.

Experimental Method

The experiments were carried out using a single chamber entrainment burner system similar to that described elsewhere.[2] The chamber was evacuated by a two stage rotary vacuum pump. Metal is vaporized from an appropriately designed crucible fitted into a resistively heated tungsten basket heater, entrained in a rare gas, CO, or CO_2, and transported to the reaction zone where a reactive encounter with O_3, N_2O, or NO_2 occur. Typical total operating pressures ranged from one to ten Torr, with the entrainment gas contributing the bulk of this measured pressure. The oxidant pressures were typically 10 to 100 mTorr.

Results and Discussion

Metal Carbonyl Binding Energies.

The first row transition metals and aluminum when entrained in a rare gas (Ar) and oxidized with O_3, N_2O, or NO_2 to form diatomic metal oxides via the reaction

$$M + OX + Ar \rightarrow MO^{*} + X + Ar \qquad (1)$$

These reactions are highly exothermic and the nascent metal oxides (MO) may be formed in various excited electronic states from which they subsequently chemiluminesce. The optical signature corresponding to the products of the reaction (1) can be used to determine the stability and electronic structure of the product MO electronic states. The short wavelength (high energy) onset of this optical signature also provides a lower bound to the heat of reaction. The highest accessible energy levels of MO^{*}, and therefore the highest energy vibronic transitions observed in a study of the oxidation process must lie at energies lower than those accessible to the total reaction exothermicity.

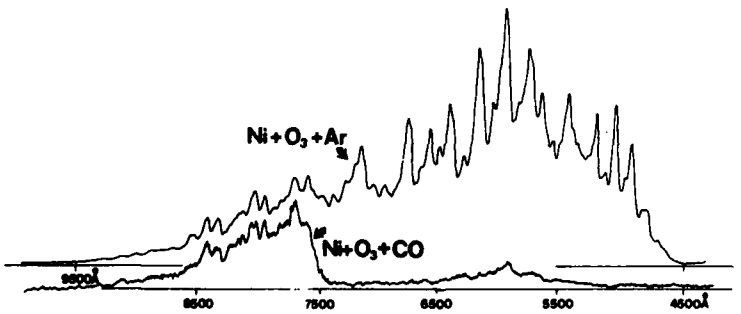

Figure 1: Chemiluminescent spectra for the multiple collision oxidation of nickel atoms with ozone to form the excited states of nickel oxide. a) Spectrum obtained when nickel atoms entrained in argon ($Ni + O_3 + Ar \rightarrow NiO^{*} + O_2 + Ar$) are oxidized to yield a spectrum onsetting at 4480 Å; $P_{Total}(Ar) \simeq 4.3$ Torr. b) Spectrum obtained when a high flux of nickel atoms entrained in CO ($Ni + O_3 + CO \rightarrow NiCO + O_3 \rightarrow NiO^{*} + O_2 + CO$) are oxidized to yield a spectrum onsetting at $\simeq$ 7500 Å; $P_{Total}(CO) \simeq 3.8$ Torr. Spectral resolution for both scans is 12 Å.

Figure 1 compares the emission spectra for electronically excited NiO formed (1) via reaction (1) and (2) when CO replaces argon as the entrainment gas to form $Ni(CO)_x$ complexes which are subsequently

oxidized. It is observed that the NiO emission onsets at a considerably longer wavelength (7500Å v. 4480Å) when CO is used as the entrainment gas. This indicates that NiO is formed via a reaction which is considerably less exothermic than the reaction (1). This occurs because the chemiluminescent process now corresponds to the sequence,

$$M + xCO \rightarrow M(CO)_x \qquad (2a)$$

$$M(CO)_x + OA \rightarrow MO^* + A + xCO \qquad (2b)$$

where the exothermicity of the process forming NiO^* is diminished by the magnitude of the total M-CO binding energy.

We can employ the difference in the spectral wavelength onset for the two NiO emission scans, to deduce a value for the Ni-CO binding energy. Using the appropriate energy conserving cycle, we find $E_{binding} = E_{4480Å}$ (22300)-$E_{7500Å}$ (13300) = 9000 cm^{-1} (1.12eV). This lower bound value is in excellent agreement with the calculations of Bauschlicher et al.[3] for $^1\Sigma^+$ NiCO (D_e = 1.10 eV). Similarly, the M-CO binding energies for $Ti(CO)_{x\geq 2}$, $V(CO)_{x=1or2}$ and $A\ell(CO)_2$ have been determined to be ~ 1.75, 1.5 ± 0.4, and ~ 0.7 eV, respectively,[1,3] through comparison of the chemiluminescent emissions associated with reactions (1) and (2). We are presently working towards unambiguously determining the stoichiometry of the titanium and vanadium complexes.

Weakly Bound Electronically Excited Metal Oxide - CO or CO_2 Complexes Formed in Metal Based Oxidations.

In Figure 2, we present the surprising results obtained upon chemiluminescent oxidation of aluminum atoms entrained and solvated in CO_2 at pressures ranging from 0.4 to 0.6 Torr,[4] the pressure range associated with maximum chemiluminescent intensity. A virtually unresolved spectral signature with enhanced features clearly associated with the $A\ell O\ B^2\Sigma^+ - X^2\Sigma^+$ sequence groupings is observed. This signature is compared to both the $A\ell + Ar + O_3$ and $A\ell + CO + O_3$ systems which yield well resolved vibrational structure at gas pressures between 0.4 and 0.6 Torr. These results indicate that, in

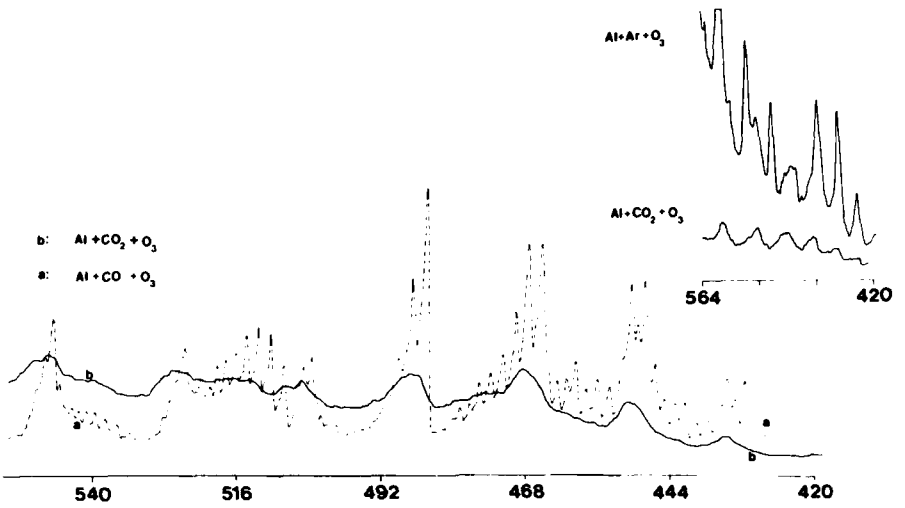

Figure 2: Comparison of chemiluminescent spectra for multiple collision processes in which aluminum entrained in argon, CO, or CO_2 is oxidized with O_3 (a) chemiluminescent spectrum corresponding to the oxidation of CO entrained aluminum atoms to produce $A\ell O^*$ $B^2\Sigma^+ - X^2\Sigma^+$ emission. (b) chemiluminescent spectrum resulting from the multiple collision oxidation of an $A\ell CO_2$ complex and attributed to the process $A\ell CO_2+O_3+CO_2 \rightarrow A\ell\overset{O^*}{\underset{CO_2}{<}} + O_2+CO_2$. Note that the unresolved vibrational structure in this spectrum correlates closely with the $A\ell O$ B-X sequence groupings. (c) Inset: Comparison of spectra for the multiple collision interactions $A\ell+O_3+Ar \rightarrow A\ell O^*+O_2+Ar$ and $A\ell CO_2+O_3+CO_2 \rightarrow A\ell\overset{O^*}{\underset{CO_2}{<}} +O_2+CO_2$ as in (b) above. Spectral resolution is 10Å and intensities are uncorrected for instrumental response.

lieu of a reaction mechanism similar to reaction (2b) where the ligand (CO) is lost within a few vibrational periods, CO_2 solvates $A\ell O$. In this case, the reaction sequence is thought to correspond to,

$$A\ell + x\ CO_2 \rightarrow A\ell CO_2 + (x-1)CO_2 \qquad (3a)$$

$$A\ell CO_2 + O_3 \rightarrow A\ell\overset{O^*}{\underset{(CO_2)}{<}} + O_2 \qquad (3b)$$

The characteristic $A\ell O$-based vibrational level structure is lost in excited state complex formation.[4] Similar results have been observed involving $MOCO^*$ complex formation where M = Sc, Cr, Co, and Fe.[2]

Conclusion

The results obtained in a number of CO and CO_2 systems indicate

that the techniques outlined here provide a means to (1) evaluate $M(CO)_x$ (x=1,2) binding energies, (2) study long lived MOCO or $MOCO_2$ solvation complexes, and (3) characterize the spectroscopy of M-CO and $M-CO_2$ complexes. The metal atom based solvation complexes present an opportunity to study interactions extending in various degrees from weak van der Waal binding to strong chemical bonds.

References

1. For discussions of these compounds see G. A. Somorjai, Chemistry in Two Dimensions: Surfaces, Cornell Univ. Press, Ithaca (1981) and references contained therein. M. Poliakoff and E. Weitz, Acc. of Chem. Res. 20, 408-411 (1987) and references cited therein. See also, D. H. Stedman, D. A. Tammaro, D. K. Branch, and R. Pearson, Jr., Anal. Chem. 51, 2340 (1979). D. A. Hikade, D. H. Stedman, J. G. Walega, Anal. Chem. 56, 1629 (1984). and references in these articles which discuss pertinent chemiluminescence detection of the nickel carbonyls. For photodissociation studies see J. A. Welch, V. Vaida, and G. L. Geoffrey, J. Phys. Chem. 87, 3635 (1983), J. A. Welch, K. S. Peters, and V. Vaida, J. Phys. Chem. 86, 1941 (1982), L. J. Rothberg, D. P. Gerrity, and V. Vaida, J. Chem. Phys. 74, 2218 (1981), D. G. Leopold and V. Vaida, J. Am. Chem. Soc. 105, 6809 (1983), D. G. Leopold and V. Vaida, J. Am. Chem. Soc. 106, 3720 (1984).

2. M. J. McQuaid, K. Morris, and J. L. Gole, J. Am. Chem. Soc. 110, 5280-5285 (1988).

3. C. W. Bauschlicher Jr., P. S. Bagus, C. Nelin, and B. O. Roos, J. Chem. Phys. 85, 354- (1986).

4. M. McQuaid, J. R. Woodward, and J. L. Gole, J. Phys. Chem. 92, 252-255 (1988).

Mode-Selective Intramolecular Vibrational Redistribution (IVR) to the van der Waals' Modes in *trans*-Stilbene van der Waals' Complexes

by Timothy S. Zwier
Department of Chemistry, Purdue University, West Lafayette, IN 47907

We report a detailed study[1,2] of vibrational predissociation and intramolecular - intermolecular state mixing in the first excited singlet state of *trans*-stilbene van der Waals complexes with helium and hydrogen. We present evidence that the helium atom in stilbene-He and the H_2 molecule in stilbene-H_2 possess very low frequency van der Waals bending levels involving delocalization of the complexed species over both phenyl rings. In stilbene-He, the mode-selective, strong coupling of the out-of-plane phenyl ring modes (such as v_{36}, the out-of-plane phenyl bend and v_{37}, the out-of-plane phenyl torsion) with the pseudo-translation van der Waals bending modes leads to a dramatic broadening of the transitions to several times the breadth of in-plane stilbene-He vibrations (see Fig. 1a). Dispersed fluorescence spectra from the peaks of the $36^1_0 37^1_0$ and 37^2_0 stilbene-He transitions show that vibrational predissociation occurs on a time-scale fast compared to fluorescence (2.7 nsec).[3] Stilbene products are formed primarily in the 0^0 level in both cases. We use this fact to our advantage in wavelength-resolved excitation scans which were taken of the broadened transitions in which only fluorescence from a 6 cm^{-1} region centered on the 0^0_0 band of the parent stilbene molecule was collected. In so doing we have enhanced emission from the dissociating stilbene-He complex by comparison to all other emissions. Such a scan is shown in Figure 1b. Note that the stilbene-He transitions are fully as broad in this spectrum as in the total fluorescence spectrum above it.

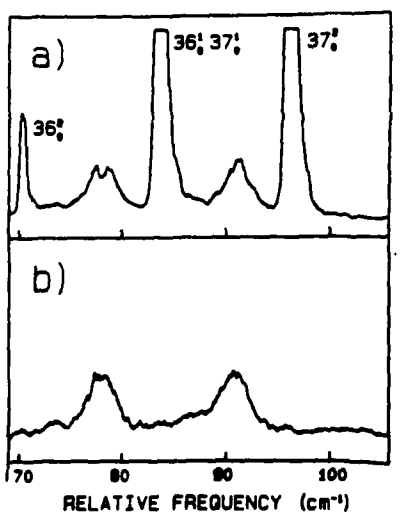

Fig. 1: a) Fluorescence excitation spectrum in the region of the broadened $36^1_0 37^1_0$-He and 37^2_0-He transitions when collecting the total fluorescence. b) Corresponding wavelength-resolved excitation scan.

Dispersed fluorescence spectra were taken at other positions in the broadened $36^1_0 37^1_0$ and 37^2_0 contours. The 37^2_0-He contour shows a $37^1/0^0$ stilbene product ratio which changes from less than 5% to over 50% as one goes from red to blue in the contour. The broadening is thus inhomogeneous in character.

In stilbene-H_2, the mode selective coupling of out-of-plane phenyl ring motions with the in-plane van der Waals' levels exhibits itself as a splitting of the out-of-plane transitions in to a set of 5-6 closely spaced transitions separated by about 1 cm^{-1} (Fig. 2).

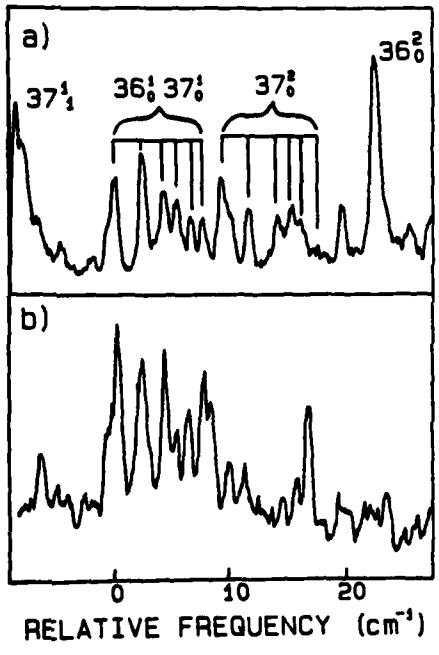

Fig. 2: Fluorescence excitation spectrum a) in the region of the $36^1_0 37^1_0$-H_2 and 37^2_0-H_2 transitions, and b) in the region of $25^1_0 36^1_0 37^1$-H_2 and $25^1_0 37^2$-H_2 transitions.

Since excitation occurs to energies only 80 cm^{-1} above the origin, these closely spaced transitions can only be the result of a very low frequency bending mode vibration for the complex involving motion of the H_2 molecule between the two phenyl rings. In fact, if we model the vibration as a translation of the H_2 molecule in a 10 A one-dimensional square well, then the spacing between the lowest pseudo-translational energy levels will be about 1 cm^{-1}, just as we observe. These transitions, which are just resolvable in stilbene-H_2, are the likely cause of the unresolved broadening we observe in stilbene-He as well, where the spacing between levels would be about 0.5 cm^{-1}.

We have taken dispersed fluorescence spectra of several stilbene-H_2 transitions which do not have enough energy to predissociate. These spectra show two kinds of

fluorescence: (i) structured resonance fluorescence from the level carrying the oscillator strength in absorption and (ii) broadened emission centered on the major 0^0 levels of the complex which can be ascribed to state mixing with the van der Waals modes. The ratio of structured to broadened emission reflects the degree of state mixing. As expected, even when predissociation cannot occur, the out-of-plane modes exhibit a significantly greater degree of state mixing than in-plane vibrations, even when the latter levels are several times higher in energy.

The vibrational predissociation product state distributions from out-of-plane levels also reflects this extensive state mixing. In particular, the 37^4_0-He dispersed fluorescence spectrum shows emission primarily from two levels of the stilbene product: the *lowest* energy gap 37^3 level and the *highest* energy gap 0^0 level. While the former would be expected based on vibrational predissociation theory, the latter must result from levels possessing considerable van der Waals' state character. In fact, a better interpretation of the observed product state distributions would be to view them as giving rough estimates of the percentage van der Waals' character in the laser-accessed states rather than measuring the vibrational predissociation rate constants.

The strong coupling observed between out-of-plane phenyl ring vibrations and the pseudo-translational van der Waals mode occurs primarily for kinematic reasons. The position of the complexed atom or molecule is almost certainly[4] above the plane of the phenyl rings. Thus, phenyl bending or torsional motion will involve motion directly against the van der Waals-bound species. In fact, we often refer to the out-of-plane phenyl ring modes as "paddleball" modes since the phenyl ring interaction with the complexed atom is much like that of a racquet against a ball. In addition, the small energy mismatch between the very low frequency, large amplitude phenyl ring vibrations and the van der Waals vibrations should enhance the coupling between the motions.

It will be interesting to carry out similar measurements on other large-molecule van der Waals complexes in order to determine the generality of the large, mode-selective state mixing we oberve here.

Acknowledgements: This work has been supported by the National Science Foundation Research in Undergraduate Institutions Program (CHE8710016) and was performed at Calvin College.

1. D.O. DeHaan, A.L. Holton, and T.S. Zwier, J. Chem. Phys. (in press).

2. C.A. Taatjes, W.B. Bosma, and T.S. Zwier, Chem. Phys. Lett. 128, 127 (1986).

3. D.H. Semmes, J.S. Baskin, and A.H. Zewail, J. Amer. Chem. Soc. 109, 4104 (1987).

4. J.S. Baskin, P.M. Felker, and A.H. Zewail, J. Chem. Phys. 84, 4708 (1986).

DYNAMICS OF NCS FORMATION FROM PHOTOLYSIS OF RNCS

F.J. Northrup and Trevor J. Sears
Department of Chemistry, Brookhaven National Laboratory
Upton, New York 11973

ABSTRACT

Laser induced fluorescence (LIF) was used to probe the internal energy modes of NCS resulting from the 248 nm photolysis of compounds RNCS (R=Me,Et). Accurate spectroscopic constants were determined for the excited vibrational levels for the first time. The NCS fragment was found to be highly excited in all three vibrational modes. Rotational motion was not as highly excited. The dissociation was found to preferentially populate the upper spin-orbit component of the ground $^2\Pi$ state.

INTRODUCTION

The linear radical, NCS, is chemically important because of its similarity to NCO, an important species in combustion reactions. It is readily formed by ultraviolet photolysis of RNCS compounds. The spectroscopy of this radical is of interest because of the Renner-Teller interaction in the υ_2 bending mode and the large spin-orbit splitting in the ground electronic state. The spectroscopy was studied previously [1,2], but greater detail is available from this study.

EXPERIMENTAL

Compounds RNCS were photolyzed with a KrF excimer laser at 248 nm and the NCS fragment was probed by LIF using a pulsed dye laser tuned from 355-460 nm. For detailed spectroscopic studies, the photolysis was carried out in the throat of a pulsed supersonic jet and the NCS was probed downstream, after cooling. Internal energy distributions were studied in 0.1 torr of pure RNCS flowing in a gas cell. Variable delay between the pulse and probe lasers allowed the nascent distribution or relaxed vibrational distributions to be probed.

SPECTROSCOPY

Laser induced fluorescence spectra were recorded for

both the B-X ($^2\Sigma^+$-$^2\Pi$) and A-X ($^2\Pi$-$^2\Pi$) transitions of NCS. Both systems showed extensive band structure that was badly overlapped under cell conditions. The pulsed jet experiments allowed observation and assignment of individual vibronic levels. The stronger A-X transition was found to be highly off-diagonal in the two stretching modes and was used for the subsequent dynamics studies. Hot bands were identified in this transition up to the (v_1,v_2,v_3)= (2,0,0) and (0,0,5) levels. Bending mode levels lie at lower energies and are not readily assigned above v_2=2. New spectroscopic constants were determined and will be presented elsewhere. The vibrational energies for the three modes were found to be 1942 cm^{-1} for υ_1, 378 cm^{-1} for υ_2 and 700 cm^{-1} for υ_3. The spin-orbit splitting for the vibrationless ground $^2\Pi$ state is 323.6 cm^{-1} and this varies with vibrational level.

PHOTODISSOCIATION DYNAMICS

LIF spectra of nascent NCS (eg. Fig.1) showed very broad, densely structured features indicative of extensive internal excitation of the fragment. The nascent internal energy distributions were determined by following the appearence of the spectrum as delay time between photolysis and probe lasers was varied (Fig.2). This showed clearly that the nascent spectrum is composed of excited stretching and bending level transitions from excited rotational levels. Excitation of NCS was seen up to $2\upsilon_1$ (4200 cm^{-1}) and up to $5\upsilon_3$ (3700 cm^{-1}). Bending level excitation was extensive, but not readily determined because of the band density and rapid relaxation of these levels. Relative populations for the various excited levels are not yet available because the relevant Franck-Condon factors are still being determined.

An R-N bond energy of 78 kcal $mole^{-1}$ implies 12500 cm^{-1} of energy left after R-NCS dissociation at 248 nm. NCS vibrational levels are found with greater than 30% of this energy. At least two and probably all three of the modes show comparable excitation. This suggests a long-lived RNCS excited state that predissociates. Unresolved structure in the RNCS absorption spectrum[3] tends to support this. Rotational excitation is considerably lower than this in agreement with the R-NCS geometry being similar in the ground and first excited states.

The spectra show evidence for spin-orbit selectivity. As seen in Fig.1, about 80% of the population for the $0v_20$ levels is in the upper spin-orbit manifold. This inversion

continues up to at least $4v_3$.

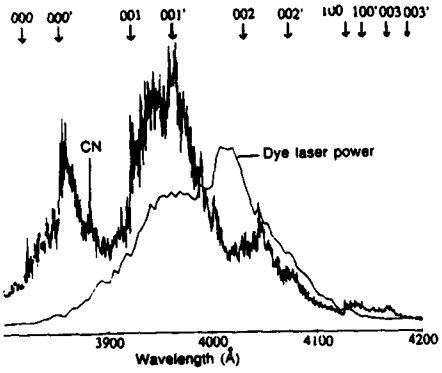

Fig.1 Broad scan through part of the nascent NCS A-X hot band region. Arrows mark bandhead positions of transitions from $X(v_1, v_2, v_3)$ to A 000. Unprimed levels are for the $^2\Pi_{3/2}$ species and primed are $^2\Pi_{1/2}$.

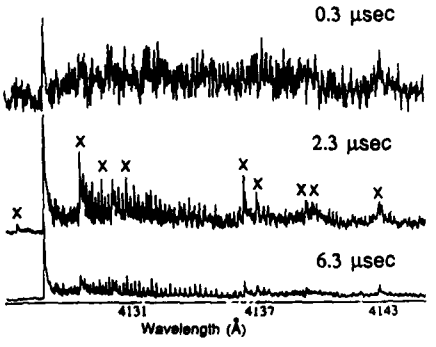

Fig.2 000←100 band head region as a function of delay time between photolysis and probe lasers. Transitions from bending levels excited in combination with 100 are marked by x.

An attempt to study the wavelength dependence of the photolysis was unsuccessful. Only two-photon absorption was observed for 308 nm and 355 nm, and 193 nm absorption produced NCS directly in the A electronic state.

Dissociation of MeNCS showed the same nascent spectrum as EtNCS. EtSCN looked similar but showed a larger dissociation channel leading to CN.

Work is continuing to quantify these results.

ACKNOWLEDGEMENT

This research was carried out at Brookhaven National Laboratory under contract DE-AC02-76CH00016 with the U.S. Department of Energy and supported by its Division of Chemical Sciences, Office of Basic Energy Science.

REFERENCES

1. R.N. Dixon and D.A. Ramsay, Can. J. Phys. 46, 2619 (1968).
2. H. Ohtoshi, K. Tsukiyama, A. Yanagibori, K. Shibuya, K. Obi, and K. Tanaka, Chem. Phys. Lett. 111, 136 (1984).
3. J.R. McDonald, V.M. Scherr and S.P. McGlynn, J. Chem. Phys. 51, 1723 (1969).

The Resolution and Characterization of Distinct *ortho*- and *para*-D_2 Complexes with *trans*-Stilbene in a Supersonic Jet

by D.O. DeHaan[a] and Timothy S. Zwier
Department of Chemistry, Purdue University, West Lafayette, Indiana 47907

A supersonic free jet expansion has been used to prepare *trans*-stilbene-H_2 and D_2 complexes.[1] The cooling in the jet collapses most of the *ortho* and *para* H_2 and D_2 rotational population to the lowest rotational levels of a given nuclear spin symmetry: j=0 and j=1. As seen in Fig. 1, the laser-induced fluorescence excitation spectrum of stilbene-D_2 shows a well-resolved doublet at the origin due to stilbene-D_2(j=0) and stilbene-D_2(j=1) complexes.

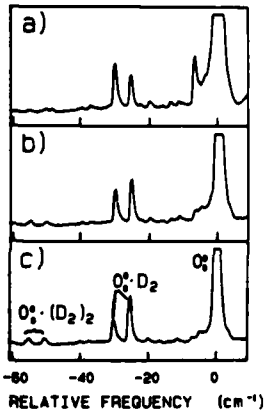

Fig. 1: Total fluorescence excitation spectrum near the stilbene origin taken with vayring D_2 concentrations in the expansion.
a) 1% D_2 in helium.
b) 2% D_2 in helium.
c) 5% D_2 in helium.

We assign these transitions in this fashion for the following reasons: First, at high D_2 flows in the expansion (Fig. 1c), the relative intensities of the members of the doublet approach the 2:1 intensity ratio given by the (j=0)/(j=1) nuclear spin statistics. Second, the dispersed fluorescence spectra of these transitions are identical to one another (Fig. 2). Given this assignment, the 4.9 cm^{-1} splitting of the transitions indicates that the D_2 molecule is undergoing hindered internal rotation in the complex and that the barrier to internal rotation changes upon electronic excitation.

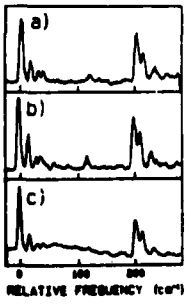

Fig. 2: Dispersed fluorescence spectra of a) the red member of the stilbene-D_2 doublet at the origin, b) the blue member, and c) the single peak in the stilbene-H_2 origin.

By contrast, in stilbene-H_2 (Fig. 3a), we observe only a single transition at the origin which we assign to stilbene-H_2(j=1). We are able to place an upper bound on the stilbene-H_2(j=0) transition intensity of 5% of the stilbene-H_2(j=1) intensity. This is at least a factor of 6 less than the expected intensity ratio based on nuclear spin statistics (33%).

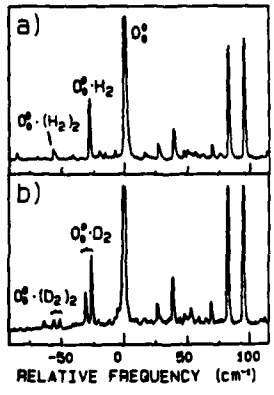

Fig. 3: Total fluorescence excitation spectrum of a) stilbene-H_2, and b) stilbene-D_2.

The fact that stilbene-H_2(j=0) complexes are missing in the stilbene/H_2 expansion while stilbene-D_2(j=0) complexes are readily observed in stilbene/D_2 expansions is intriguing and perhaps quite general. For instance, we see similar behavior[1] in p-methyl-*trans*-stilbene-H_2/D_2. Even more startling, exactly analogous behavior has been observed in the infrared spectrum of HF-H_2 and HF-D_2 by Nesbitt and co-workers[2,3]; that is, readily observable transitons due to both HF-D_2(j=0) and D_2(j=1) in the infrared spectrum of HF-D_2, with only HF-H_2(j=1) observed in H_2-containing expansions.

We have carried out several experiments designed to determine the reason for the absence of stilbene-H_2(j=0) complexes in the expansion. Dispersed fluorescence spectra are used to bracket the binding energies of the stilbene-H_2/D_2 complexes in both ground and excited states. In the ground states of stilbene-H_2(j=1) and stilbene-D_2(j=0,1) complexes, 169 $cm^{-1} \leq D_0' \leq 249\ cm^{-1}$, so that the stilbene-$H_2$(j=0) transitions cannot be mising by virtue of the complex being unbound. We propose that kinetic selection may contribute to the enhancement of stilbene-H_2(j=1) complexes. The recent careful analysis of Lovejoy, *et. al.*[2,3] on HF-

H_2/D_2 has shown that the H_2(j=1) or D_2(j=1) molecules are more strongly bound to HF than are their j=0 counterparts. The added stability of the j=1 complexes arises from dynamic stabilization of the complex caused by the preferential orientation of the j=1 molecule with respect to the HF molecule. We expect similar behavior in the stilbene-H_2 /D_2 complexes. If this is the case, then exchange reactions in which the more strongly bound H_2(j=1) preferentially displaces H_2(j=0) from stilbene could contribute to the enrichment of stilbene-H_2(j=1) complexes in the jet.

The presence of H_2(j=2) molecules in the expansion could further suppress stilbene-H_2(j=0) formation. The stilbene-H_2(j=2) complex is not bound because it possesses enough energy to predissociate:

$$\text{stilbene-}H_2(j=2) \longrightarrow \text{stilbene} + H_2(j=0). \qquad (1)$$

As a result, if H_2(j=2) molecules interact with stilbene more strongly than H_2(j=0) molecules (once again by dynamic stabilization of a preferred orientation of the H_2(j=2) molecules), then the two-body exchange reactions:

$$\text{stilbene-}H_2(j=0) + H_2(j=2) \longrightarrow \text{stilbene-}H_2(j=2) + H_2(j=0) \qquad (2)$$

will favor stilbene-H_2(j=2) products, which will subsequently predissociate via reaction (1). Such a process is not available for stilbene-D_2 since stilbene-D_2(j=2) is bound.

It will be interesting to pursue similar investigations in other X-H_2/D_2 complexes in order to further characterize this unusual behavior.

Acknowledgements: This work has been supported by the National Science Foundation Research in Undergraduate Institutions Program (CHE8710016)and was performed at Calvin College.

[a]Present address: Dept. of Chemistry, Calvin College, Grand Rapids, MI 49506.

1. D.O. DeHaan and T.S. Zwier, J. Chem. Phys. (in press).

2. C.M. Lovejoy, D.D. Nelson, Jr., and D.J. Nesbitt, *J. Chem. Phys.* 87, 5621 (1987).

3. C.M. Lovejoy, D.D. Nelson, Jr., and D.J. Nesbitt, *J. Chem. Phys.* (in press).

APPLICATION OF EXCITATION TRANSFER TO STUDIES OF COLLISIONAL DEACTIVATION OF VIBRATIONALLY EXCITED ISOTOPICALLY LABELLED NITROUS OXIDE BY SULFUR HEXAFLUORIDE

M. C. Longuemare R. Morrison, and R. D. Bates, Jr.
Georgetown University, Dept. of Chemistry, Washington, D.C. 20057

ABSTRACT

Discovery of a direct pumping scheme for CO_2 laser excitation of $^{14}N^{14}NO$ and $^{14}N^{15}NO$ has facilitated studies of collisional deexcitation of these molecules by efficient collision partners like SF_6. Comparison of other isotopically substituted nitrous oxide molecules has been hindered by the lack of a direct pumping scheme with a readily available pulsed or Q-switched laser. An indirect pumping scheme by which laser-excited CO_2 acts as a vibrational sensitizer of N_2O facilitates studies of quenching by SF_6 in these species. Application of this method gives observed rate constants for $^{14}N^{14}NO$-SF_6 of 1030 $ms^{-1}torr_{SF_6}^{-1}$ and for $^{14}N^{15}NO$-SF_6 of 1180 $ms^{-1}torr_{SF_6}^{-1}$ for samples containing 0.5 to 1.0% SF_6 and 10% CO_2. The rate constant for $^{14}N^{14}NO$ is comparable to that measured by direct excitation, and that for $^{15}N^{15}NO$ is much faster than the value of 200 $ms^{-1}torr_{SF_6}^{-1}$ obtained for $^{14}N^{15}NO$. These results indicate that there is an efficient deactivation pathway for $^{15}N^{15}NO$ by SF_6 either directly to the ground state or through an intermediate level.

INTRODUCTION

Direct examination of the behavior of laser-excited $^{14}N^{14}NO$ and of $^{14}N^{15}NO$ with a range of collision partners has been facilitated by the discovery of a CO_2 laser line that can pump each of these species to the 001 level, from which fluorescence at 4.5 μm provides a probe of the rate of vibrational energy redistribution through collisions.[1]

These direct pump experiments have provided data on the deactivation of both $^{14}N^{14}NO$ and $^{14}N^{15}NO$ by SF_6, giving pseudo-first order rate constants of 1000 $ms^{-1}torr_{SF_6}^{-1}$ for $^{14}N^{14}NO$ and 200 $ms^{-1}torr_{SF_6}^{-1}$ for $^{14}N^{15}NO$.[2]

For comparison, data for the other isotopically substituted N_2O molecules is very important. But there is no source by which the others can be pumped directly. Thus excitation through a transfer mechanism has been employed.

RESULTS

Three component mixtures containing predominantly the N_2O species to be studied with 10% CO_2 and a small amount of SF_6 were used. A Q-switched CO_2 laser excited the CO_2 to the 001 level, which then rapidly shared its energy with the corresponding N_2O levels.[3] Deactivation by collisions, predominantly by the very

efficient collisions of SF_6 with N_2O, was monitored by observing the combined N_2O-CO_2 fluorescence.

The results for experiments with CO_2-$^{14}N^{14}NO$ give a value of 1030 $ms^{-1}torr_{SF_6}^{-1}$ for the deactivation of the N_2O by SF_6, as shown in Table I. All samples contained 10% CO_2, the indicated amount of SF_6, the balance being $^{14}N^{14}NO$.

Table I. Rate constants for deactivation of $^{14}N^{14}NO$ by SF_6 in mixtures of CO_2-$^{14}N^{14}NO$-SF_6 excited by a CO_2 laser.

PERCENTAGE SF_6	RATE (ms^{-1} $torr_{SF_6}^{-1}$)
0.3 %	940 ± 100
0.5 %	1060 ± 40
1.0 %	1090 ± 90

The results for experiments with CO_2-$^{15}N^{15}NO$ give a value of 1180 $ms^{-1}torr_{SF_6}^{-1}$ for the deactivation of the N_2O by SF_6, as shown in Table II. All samples contained 10% CO_2, the indicated amount of SF_6, the balance being $^{15}N^{15}NO$.

Table II. Rate constants for deactivation of $^{15}N^{15}NO$ by SF_6 in mixtures of CO_2-$^{15}N^{15}NO$-SF_6 excited by a CO_2 laser.

PERCENTAGE SF_6	RATE (ms^{-1} $torr_{SF_6}^{-1}$)
0.5 %	1270 ± 110
0.8 %	1190 ± 90
1.0 %	1070 ± 40

DISCUSSION

Indirect excitation of N_2O by transfer provides an effective means by which to study deexcitation through collisions with an efficient quencher like SF_6. The results for $^{14}N^{14}NO$ by different methods agree. The rate constants for deactivation by SF_6 of $^{14}N^{14}NO$ are similar to those for $^{15}N^{15}NO$, but the SF_6-$^{14}N^{15}NO$ process is considerably less efficient, as shown in Table III.

The deactivation of vibrationally excited CO_2 (00^01) by SF_6 probably takes CO_2 from (00^01) to (02^00) at 961 cm^{-1}, which can be referred to as a 10 μm mechanism.[5] For N_2O a 4 μm mechanism

Table III. Results for deexcitation of N_2O by SF_6 by different methods.

N_2O SPECIES	METHOD	$k_{N_2O-SF_6}$ (ms^{-1} $torr_{SF_6}^{-1}$)	REF
$^{14}N^{14}NO$	direct with N_2O laser	1200	4
$^{14}N^{14}NO$	direct with CO_2 laser	1000	1
$^{14}N^{14}NO$	indirect by transfer	1030	this paper
$^{14}N^{15}NO$	direct with CO_2 laser	200	1
$^{15}N^{15}NO$	indirect by transfer	1180	this paper

involving deactivation of N_2O (00^01) to the ground state has been hypothesized.[4] The relevant energy levels are shown in Table IV. The deactivation of N_2O by SF_6 is extremely fast with a cross section a fraction of gas kinetic; it proceeds by near resonant intermolecular processes. The larger energy gap in $^{14}N^{15}NO$ results in a decrease in efficiency. The energy gaps increase further for $^{15}N^{15}NO$, but the efficiency is again high. A simple explanation for these results has not yet been found.

Table IV. Vibrational frequencies in cm^{-1} for N_2O species and their match-up with SF_6 frequencies.

MOLECULE	ν_1	ν_2	ν_3	$\nu_3-\nu_1$	$\nu_3-2\nu_2$	$\Delta E_{SF_6-N_2O}$ 4 μm	$\Delta E_{SF_6-N_2O}$ 10 μm
CO_2	1285	667	2349	1063	961	-118	-13 (-116)
$^{14}N^{14}NO$	1285	588	2224	938	1046	7	9 (-98)
$^{14}N^{15}NO$	1281	575	2178	896	1026	53	51 (-78)
$^{15}N^{15}NO$	1266	572	2156	890	1018	75	57 (-71)

REFERENCES

1. K.L. McNesby, M.C. Longuemare, and R.D. Bates, Jr., in Advances in Laser Science-III, AIP Conference Processdings No. 172, (American Institute of Physics, New York, 1988), p. 650.
2. K. McNesby, Ph.D. thesis, Georgetown University, 1987.
3. L. Doyennette, M. Margottin-Maclou, H. Gueguen, A. Carion, and L. Henry, J. Chem. Phys. 60 (1974) 697.
4. A. Fakhr and R.D. Bates, Jr., Chem. Phys. Letters 71 (1980) 381; A. Fahr and R.D. Bates, Jr., Chem. Phys. 105 (1986) 449.
5. J.C. Stephenson and C.B. Moore, J. Chem. Phys. 52, 2333 (1970).

VI. DIAGNOSTIC AND ANALYTICAL APPLICATIONS OF LASERS

VI.A. Advances in Raman Spectroscopy

VI.B. Lasers and Chromotography

VI.C. Advances in Photothermal Spectroscopy

VI.D. Lasers in Trace Analysis

VI.E. Lasers in Combustion Analysis

VI.F. Advances in Plasma Diagnostics

Surface Enhanced Raman Spectroscopy of Neurotransmitters

Michael L. McGlashen, Kevin L. Davis and Michael D. Morris*
The University of Michigan Chemistry Department
Ann Arbor, Michigan 48105

Abstract

The surface-enhanced Raman spectra (SERS) of neurotransmitters in biological matrices and synthetic solutions are described. The effects of protein adsorption on catecholamine SERS intensity are discussed. Techniques for obtaining dopamine SERS spectra in cerebrospinal fluid and rat brain dialysate are demonstrated. Preliminary SERS of histamine and tele-methylhistamine are presented.

Introduction

There are about two hundred molecules which are known or suspected to function as neurotransmitters.[1-3] These include several aromatic amines, such as the catecholamines, histamine and serotonin, several amino acids, and a large number of oligo- and polypeptides. In addition, neurobiologists and pharmacologists have studied numerous closely related molecules, either as pharmaceuticals, or as probes of the important features of neurotransmitter and receptor function and structure.

Because the synaptic cleft in mammalian neurons is no more than 20 nm across, neither optical or physical probes of neurotransmitter concentrations in this region are practical. Instead, researchers have usually relied on probes placed in the extracellular fluid.

Three general methods of real-time neurotransmitter measurement are flow perfusion, dialysis perfusion and voltammetry.[4] Flow perfusion techniques are based on the diffusion of materials into a stream of synthetic cerebrospinal fluid flowing into and out of the test area. The stream is pumped from a reservoir into a small tube (cannula) inserted into the test area of the brain or brain slice and removed by pumping from a concentric cannula placed outside the input tube. The time constants are reasonably fast (10 sec), but materials are badly diluted by the flow process. Any convenient assay technique can be used on the perfusate. Immunoassay, liquid chromatography with electrochemical or fluorescence detection and gas chromatography/mass spectrometry are among the common finishes.

Dialysis perfusion techniques are based on transport of the neurotransmitter across a membrane which terminates a perfusion probe. The neurotransmitters are isolated and measured externally. Membranes with a molecular weight cutoff of 5,000 a.m.u. and lower have been used.[5,6] Dialysis perfusion is attractive because the protein burden of the sample is greatly reduced. In addition, dialysis decreases the extent of tissue damage at the probe site because the tissue is not directly exposed to fluid flow. The assay techniques are the same as those used in push-pull perfusion.

Measurements of catecholamines, serotonin and their metabolites can be made by anodic voltammetry at a carbon electrode.[4,7] Voltammetry provides close to real-time response. Carbon electrodes range in size from 40–50 μm diameter graphite epoxy disks[7] to 1 μm diameter carbon fibers[8]. Response times are a few seconds.[9]

Voltammetry is not problem free. It can be used only with catecholamines and serotonin, and some of their metabolites, precursors or synthetic analogs. Further, the range of oxidation potentials within a class of molecules is small. In general, a neurotransmitter and its metabolites or precursors can not be completely resolved voltammetrically[7].

In addition, ascorbic acid is more easily oxidized than catecholamines or serotonin. On untreated carbon electrodes, an ascorbate signal badly overlaps catecholamine signals. The problem can be overcome in several ways. Two effective methods are the use of chemically treated carbon paste electrodes[10] and use of Nafion coated graphite electrodes.[11]

Histamine presents a special analytical challenge. It is not electroactive and it absorbs deep in the UV, $\lambda_{max} = 207$ nm, making LC detection difficult without derivatization. Radioenzymatic assay remains the commonly used finish to histamine perfusion studies. Histamine assays are notoriously difficult. Problems arise in part from the assay itself and in part from the variability in histamine content with the method used to sacrifice the test animal.[12]

Theory

Surface enhancement of Raman spectra occurs as the result of several processes which take place on structured metal surfaces[13]. These can be divided into two classes: electromagnetic effects[14,15] and chemical (or charge transfer) effects.[16] Since chemical enhancement is normally accompanied by electromagnetic enhancement, the total enhancement is the product of both processes. In this case, good spectra can be observed from molecules adsorbed from $10^{-6}M$ solutions. Detection limits are for adsorption from solutions 10^{-7} to $10^{-8}M$.

Biogenic amine neurotransmitters such as dopamine, histamine and serotonin are nearly ideal SERS substrates. As aromatic amines, they form strong complexes with silver, copper or gold. Charge transfer enhancement contributes to good SERS sensitivity. Each neurotransmitter can be viewed as an aromatic ring system with different substituents defining the neurotransmitter and its metabolites. Distinguishing among such compounds is a classic strength of vibrational spectroscopy.

Hsieh *et al.*[17] have recently reported the SERS spectra of the naturally-occuring catecholamines and some metabolites and analogs on silver electrodes. They demonstrated that the major bands in the spectra were aromatic ring modes due to the catechol moiety. Table I summarizes band positions and assignments in that system.

Table I.
SERS shifts (cm^{-1}) of catecholamines and related compounds.

bands	DA[a]	NOR[a]	MTA[a]	catechol
ν_{15}	1152	1150		1149
ν_{C-O}	1269	1272	1273	1258
ν_3	1331	1329	1363	1331
ν_{19a}	1424	1422	1441	
ν_{19b}	1479	1479		1469
ν_{8a}	1572		1578	
ν_{8b}	1584		1601	

[a]Abbreviations: DA, dopamine; NOR, norepinephrine; MTA 3-methoxytyramine.

The intense band near 1480cm^{-1} has been assigned[17] to the benzene ν_{19b} mode. This band is generally the most convenient for quantitative measurements. Its absence distinguishes the methoxylated compounds from the catechol compounds. The band near 1270 cm^{-1} is the phenolic C–O stretch. It may also be used for quantification.

Although the band positions in dopamine and norepinephrine are quite similar, the relative intensities are not. For example, ν_3 is strong in dopamine spectra, but quite weak in norepinephrine spectra. Thus, band intensity ratios can be used to distinguish dopamine from norepinephrine.

Catecholamines with highly substituted ethylamine side chains give weak spectra. Bulky substituents apparently force an unfavorable adsorbate orientation. Spectra of anionic (acetate) metabolites have not been observed. For strong catecholamine adsorption, the electrode potential must be near the potential of zero charge. Under these conditions, anions are desorbed from the electrode surface.

Hsieh *et al.*[17] worked only in synthetic electrolyte solutions. In the brain, however, the extracellular fluid (ECF) contains electrolytes as well as small amounts of serum albumin, immunoglobins and other proteins. Cerebrospinal fluid is essentially the equivalent of the brain ECF. Other neurochemical samples, such as extracts of tissue homogenates, contain high protein burdens as well as lipids and other surface-active molecules. Because these surfactants could interfere with SERS measurements, it is important to investigate neurotransmitter SERS in these media.

Catecholamines in Neurochemical Media

We present catecholamine SERS obtained in several neurochemical media using silver electrodes. The experimental apparatus and procedures were generally similar to those described by Hsieh *et al.*[17] The silver electrode was maintained at −0.9 V vs. S.C.E. For all experiments, a Spex Triplemate spectrograph equipped with a Tracor Northern or a PARC 1420 intensified diode array detector was employed. Integration times of 100 sec were used. Spectra were obtained using 30 mW of Ar^+ 514.5 nm excitation. Sample volumes were 0.2–0.5 ml.

We have investigated the effects of protein adsorption on catecholamine SERS intensity. For this work, we have used albumin, which is the major protein in cerebrospinal fluid. Figure 1 shows the effect of albumin addition on dopamine SERS intensity. At 0.5% albumin concentration, SERS intensity is reduced to roughly half its value in protein-free solutions, and there is a clear decrease in the quality of the spectrum. When the protein burden reaches 1%, the spectrum is barely visible.

Figure 2 shows the SERS spectrum of cerebrospinal fluid (CSF, Sigma Diagnostics) spiked with approximately $2 \times 10^{-5} M$ dopamine. This concentration is near the upper end of the useful range for neurochemistry. The four major bands of the dopamine SERS spectrum are present but the signal magnitude and signal/noise ratio are slightly less than in the simple electrolyte solutions used by Hsieh *et.al.*[17]

In general, CSF has a protein concentration of between 15 and 40 mg per 100ml.[18] The assay value for the sample used here is 31 mg/100ml (0.31%). About 65% of the protein is serum albumin. CSF is viscous and the protein surfactants can cause extensive foaming. Consequently, CSF requires more careful handling than synthetic electrolyte solutions which contain only small molecules or ions. Standard addition may be used for quantification. However, the addition must be followed by thorough stirring to avoid artifacts. The Sigma CSF samples also contain 0.05% sodium azide as a preservative. The effects of azide, if any, are not yet known.

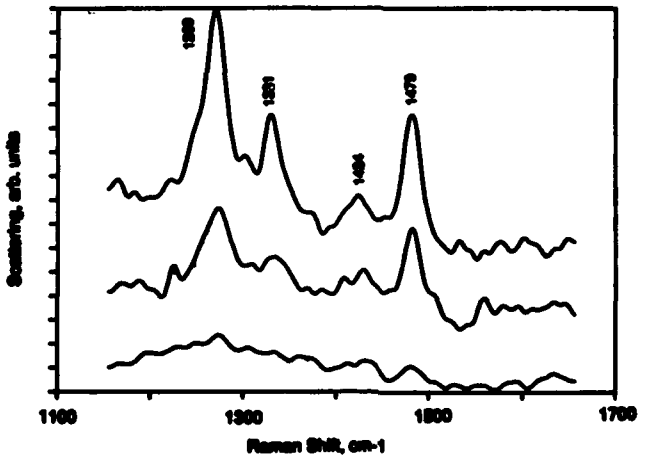

Figure 1. Effects of Albumin Concentration on Catecholamine SERS Intensity at pH 7.
Top: 0%, Middle: 0.5%, Bottom: 1.0%

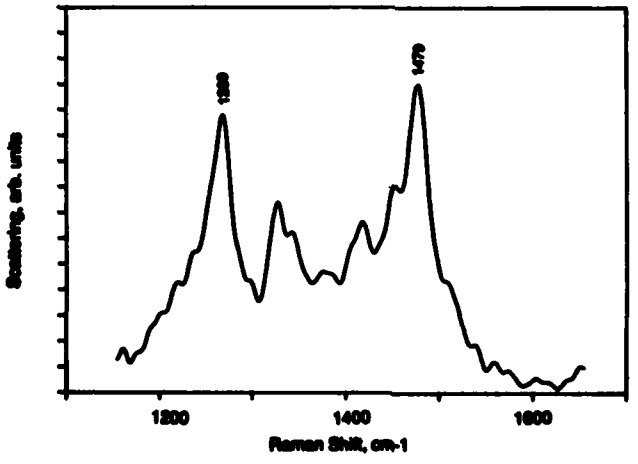

Figure 2. SERS Spectrum of Cerebrospinal Fluid, Spiked with $2 \times 10^{-5} M$ Dopamine.

Figure 3 shows the spectrum of a dialysate sample obtained from a rat brain striatum by Professors Jill Becker and Terry Robinson (University of Michigan, Department of Psychology). The sample is spiked with $5 \times 10^{-6} M$ dopamine. With its low residual protein content, the dialysate sample is nearly the equivalent of a synthetic electrolyte matrix. The signal magnitude and signal/noise ratio approach those obtained with simple aqueous solutions.

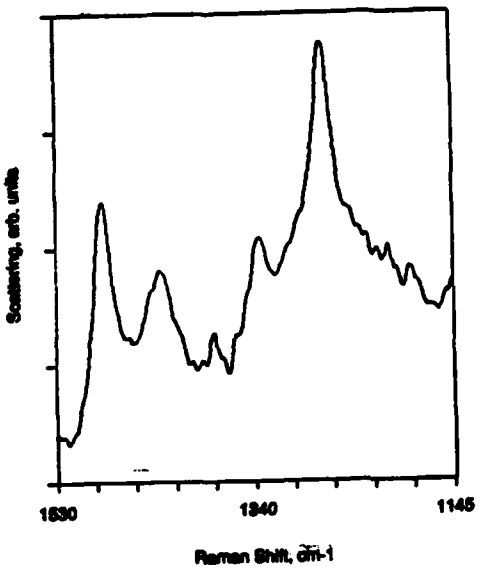

Figure 3. SERS of Rat Brain Striatum Dialysate, Spiked with $5 \times 10^{-6} M$ *Dopamine*.

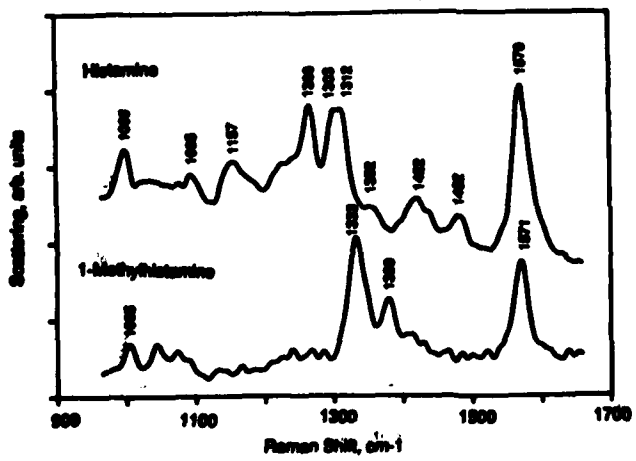

Figure 4. SERS Spectra of Histamine and *tele*-Methlyhistamine at pH 7.

Histamine

We have also made preliminary SERS measurements of histamine and its primary metabolite tele-methyl histamine on a silver electrode. As shown in Figure 4, the spectra of histamine and its metabolite are readily distinguished. In particular, the intense histamine bands at 1266, 1302 and 1312 cm^{-1} are missing in the methylated compound, which has the single strong 1332 cm^{-1} band in this region. The signal magnitudes and signal/noise ratios obtained in these spectra are similar to those of the catecholamines.

Conclusions

We are actively developing SERS as a multi-purpose probe of neurotransmitter concentrations. We have verified the feasibility of catecholamine SERS analysis of real biological matrices and have demonstrated useful SERS from histamine and its methylated metabolite. We are developing new techniques to minimize protein interference. Very preliminary results with Nafion-coated electrodes suggest that excellent catecholamine SERS can be obtained from coated electrodes. This technique may prove the key to practical SERS measurements in a variety of neurochemical matrices.

References

1. Noback, C.R.; Demarest, R.J. *The Human Nervous System. Basic Principles of Neurobiology,* McGraw-Hill, New York, **1975.**
2. Guroff, G. *Molecular Neurobiology,* Marcel Dekker, New York, **1980.**
3. Bradford, H.F. *Chemical Neurobiology,* Freeman, New York, **1986.**
4. Marsden, C.A., Ed. *Measurement of Neurotransmitter Release* In Vivo, Wiley, New York, **1984.**
5. Blaha, J.J., in *Vibrational Spectra and Structure, Vol. 10,* Durig, J.R., Ed., Dekker, New York, **1981,** pp. 227–268.
6. Van Duyne, R.P.; Haller, K.L.; Altborn, R.I. *Chem. Phys. Lett.* **1986,** 190–196
7. Adams, R.N.; Marsden, C.A. in *New Techniques in Psychopharmacology,* Iversen, L.E.; Iversen, S.D.; Snyder, S.H., Eds., Plenum, New York, **1982,** pp. 1–74.
8. Meulemans, A.; Poulain, B.; Baux, G.; Tauc, L.; Henzel, D. *Anal. Chem.* **1986,** *58,* 2088–2091.
9. Rice, M.E.; Gerhardt, G.A.; Hierl, P.M.; Nagy, G.; Adams, R.N. *Neurosci.* **1985,** *15,* 891–902.
10. Gelbert, M.B.; Curran, D.J. *Anal. Chem.* **1986,** *58,* 1028–1032.
11. Gerhardt, G.A.; Oke, A.F.; Nagy, G.; Moghaddam, B.; Adams, R.N. *Brain Res.* **1984,** *290,* 390–395.
12. Hegstrand, L.R.; Hine R.J. *Neurochem. Res.* **1985,** *10,* 307–314.
13. Chang, R.K.; Furtak, T.E., Eds. *Surface Enhanced Raman Spectroscopy,* Plenum, New York, **1982.**
14. Kerker, M.E. *Acc. Chem. Res.* **1984,** *17,* 271–277.
15. Moskovits, M. *Rev. Mod. Phys.* **1985,** *57,* 783–826.
16. Furtak, T.E.; Roy, D. *Surf. Sci.* **1985,** *158,* 126–146.
17. Hsieh, Y.-Z.; Paisley, R.F.; Morris, M.D. *Anal. Chem.* **1988,** *60,* 1198.
18. Ganong, W.F. *Review of Medical Physiology, 12th Ed.* Lange, California **1985.** 85–94.

OBSERVATION OF THE SRS SPECTRUM OF SECONDARY VIBRATIONAL FOUNDAMENTAL FREQUENCY ν_4 IN CH_4

Wang Yuezhu, Wang Qi, Lin Dianyang, Cheng Yongkang and Ma Zuguang
Institute of Opto-Electronics, Harbin
Institute of Technology, Harbin, China

ABSTRACT

With a Q-switching Ruby laser, the stimulated Raman vibrational line ν_4 of CH_4, which was much difficult to observe, was first observed and the scattering feature between CH_4 and H_2 was compared.

INTRODUCTION

SRS is one of the simpliest and feasible ways which may obtain coherent light source of multiple-frequence. Attention is further paid to SRS which is considered to be possible for improving the beam quality of high-intensity. In this experiment, the SRS of secondary vibrational foundamental frequency ν_4 in CH_4 with the purity of 99.9 percent pumped with a Q-switching Ruby laser with pulse duration of 30 ns and energy range of 80~1500mJ was first observed and the thresholds and scattering features between CH_4 and H_2 are compared and analysed.

EXPERIMENTAL RESULT AND ANALYSIS

CH_4, a *five-atomic molecule has four* vibrational foundamental frequencies $\nu_1 \sim \nu_4$ which are Raman active, but the ν_2 and ν_4 are also infrared active. ν_1=2916cm^{-1} and ν_3=3020cm^{-1} have been observed in Raman spectrum and ν_2=1306 cm^{-1} observed also in infrared spectrum[1]. ν_4 of these frequencies is more difficult to observe. ν_4 calculated from the observation of vibration combination bands was 1526 cm^{-1}. The spontaneous Raman spectrum of ν_4 was observed by M. A. Thomas et al. in 1960[2].

In this experiment, we first observed the stimulated vibrational Raman spectrum of ν_4 in CH_4, and took a distinct spectral photograph of ν_4.

The first overtone $2\nu_4$=3071cm^{-1} of ν_4 is close to ν_1=2916cm^{-1} which gives the strongest Raman line, thus, Raman line of $2\nu_4$ is much more stronger than that of ν_4 due to Fermi resonance. Therefore, when the pumping energy is lower, only Raman spectrum of $2\nu_4$ occurs, but that of ν_4 does not occur. When the pumping energy is high enough, output of ν_4 is considerable and SRS of ν_4 may be observed in the experiment.

1. Observation of the SRS thresholds of ν_1 and ν_4, comparison between thresholds of ν_1, ν_4 and H_2

Changing the parameters of the experimental setup, SRS of ν_1 occurs for pumping energy of 1000 mJ and pressure of 40 atm while the power density at focal point is about 2.5GW/cm^2. The spectral lines are shown in Fig. 1.

In Fig. 1, the central white line is a burned trace of the pump-

ing beam at 694.3nm. The right line is 1st Stokes of ν_1 at 870.7nm with energy of 90mJ. The left yellow-green line is a anti-Stokes of ν_1 at 577.5 nm.

Fig.1 SRS spectral lines for pumping energy of 1000mJ.

When the pumping energy goes up to 1200mJ, the left yellow-green line shown in Fig.2 consists of three lines with energy of 10mJ. The main one is a anti-Stokes of ν_1 at 577.5 nm. The other two are anti-Stokes lines of ν_2 at 574.0nm and $2\nu_2$ at 572.3 nm, respectively.

Fig.2 SRS spectral lines for pumping energy of 1200mJ.

The relation between the scattered energy and the medium pressure is shown in Fig.3. The relation between the scattered energy and the medium gain volume is shown in Fig.4.

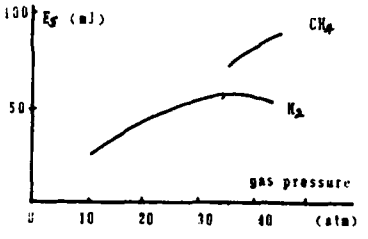

Fig.3 The relation between the scattering energy and madium pressure for CH_4 and H_2.

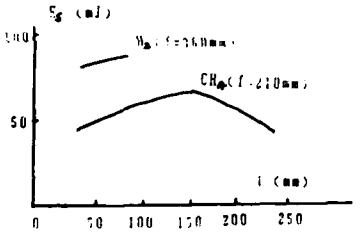

Fig.4 The relation between the scattering energy and medium gain volume for CH_4 and H_2.

For energy of 1400mJ, pressure of 40atm and f=210mm, SRS of ν_2 appears while the power density at the focal point is about 3GW/cm^2. The stimulated Raman spectrum is shown in Fig.5.

Fig.5 SRS spectral lines for pumping energy of 1400mJ, the orange line is anti-Stokes of ν_2.

In Fig.5, the orange line is the anti- Stokes of ν_2 at 627.9 nm with output energy of 0.5mJ (1st Stokes of ν_2 being infrared, sensi-

tivity of which is very low to the film used in the experiment).

Comparing Fig.1、Fig.2 and Fig.5 with wavelength curve of drum read of the monochromator, Fig.6 is obtained.

The threshold of SRS in H_2 is less about one order of magnitude than that of SRS in CH_4. When pumping energy is 80mJ, SRS in H_2 appears. In experiment, the gain of ν_1 is about 7/5 of that of ν_2 in CH_4.

2. The scattering light spots of CH_4 is taken white spectrum is measured. From the spots, the divergence angle of the inside wedge of light ring of AS(ν_1) in CH_4 is 13mrad and that of the outside wedge of light ring is 30 mrad.

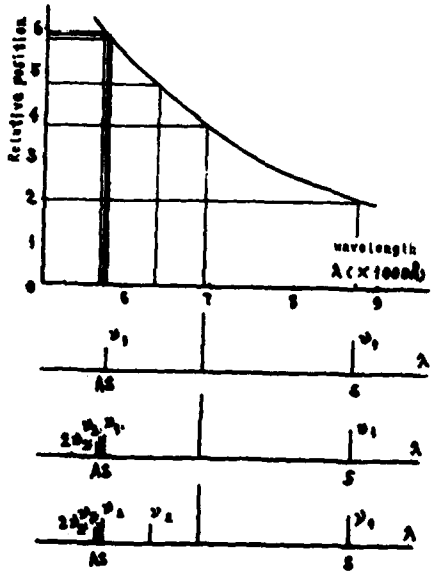

Fig.6 SRS spectum obtained by comparison Fig.1, Fig.2 and Fig.5 with the wavelength curve of drum read of the monochromator.

CONCLUSION

In this experiment, for the first time we observed the SRSof the secondary vibrational foundamental frequence ν_2 in CH_4.

The features of SRS are summarized as follows,

1. The Raman line of ν_2 has obvious threshold. When pumping energy is less than 1400mJ, the line does not appear, and it was reproduced very well.

2. It has obvious diretionality. The divergence angle of SRS beam for ν_1 and ν_2 are less than that of the pumping.

3. It has obvious monochromatic. The line-width of AS(ν_2) is not larger than that of the pumping which is 0.05cm^{-1}.

4. The intensity of stimulated Raman line of ν_2 is much less than that of ν_1 and $2\nu_2$. It is consistent with theory.

All these features provide sufficient evidence that the orange line would be SRS line of ν_2 in CH_4.

REFERENCES

1. G. Herzberg, Molecular Spectra and Molecular Structure II (D. Van Nostrand, 1951).
2. M.A. Thomas et al. Canad. J. Phys., 38, 1291 (1960)

NOVEL APPROACHES IN DETECTOR INSTRUMENTATION FOR PROCESS LIQUID CHROMATOGRAPHY

Robert E. Synovec
Center for Process Analytical Chemistry
Department of Chemistry, BG-10
University of Washington, Seattle, WA 98195

ABSTRACT

A position-sensitive detector (PSD) has been incorporated into a simple and rugged dual-beam absorbance detector that simultaneously measures refractive index (RI). By operating the PSD at both electronic and optical null conditions, excellent absorbance detectibilities of 3×10^{-5} AU ($3 \times$ rms noise) are routinely obtained. Off-axis focusing at a capillary flow cell with the incident sample beam allows RI information to be detected at the PSD. The absorbance and RI signals are readily deconvoluted. The dual-beam PSD based absorbance detector is useful for liquid chromatography (LC), and also process monitoring. The concentration gradient of solutes passing through a well designed flow cell may be sensitively monitored by probing the refractive index gradient (RIG). The analytical signal in RIG detection is a beam deflection that is measured with a single beam PSD arrangement. Concentration gradients are readily encoded with translational diffusion information of the solutes, thus a method to characterize polymers via a RIG detection based system is described. Low ppm concentrations of polymers may be characterized.

INTRODUCTION

Process control is a critical task in the industrial work place.[1] Scientists are generally asked to solve process control problems with a tool box of techniques and instrumentation that were originally designed for bench-top, or off-line, analyses. Unfortunately, the best solution to many process control problems is to perform analyses either at-line, on-line, in-line, or non-invasively, but not off-line. Information in process analysis must be obtained in a timescale that allows corrective measures to be taken, if necessary, while it is still possible to make proper adjustments to the process. Thus, instrumentation suitable for process analysis applications must be less sensitive to environmental conditions while providing comparable or superior information as is available from off-line analysis. Paramount in routine chemical analysis is the use of liquid chromatography (LC)[2] and related techniques. Successful separation and detection of process samples on-line is a challenge. Use of position-sensitive detectors (PSD) in process LC detector technology has been explored, with developments in absorbance[3] and RI[4] detection. First, a dual-beam PSD based absorbance detector for process LC is described.[3] Second, a refractive index gradient (RIG) detector using a PSD is described,[5] and applied to size-exclusion chromatography (SEC) of polymers,[6] and used in diffusion controlled measurements of polymer solutions.[7]

DUAL-BEAM PSD-BASED MEASUREMENTS

The dual-beam optical arrangement utilizing PSD is shown in Fig. 1. The dual-beam arrangement, coupled with the PSD, affords advantages in absorbance detection over conventional dual-detector approaches and amplitude modulation techniques.[3] The dual-beam PSD-based absorbance detector does not require moving parts or matched photodiodes, while being quite rugged and inexpensive. A laser may be used, or any other suitable light source. From a signal processing standpoint, the absorbance information is automatically obtained at a very sensitive detection limit (DL).

The PSD is shown in the dual-beam configuration in Fig. 2 with respect to the sample and reference beams, I_{Sample} and I_{Ref}, respectively. Photocurrents from I_{Sample} and I_{Ref} are measured at electrodes a and b, with the photocurrents denoted as I_a and I_b. A uniform resistive laser across the length, L, of the PSD controls the magnitude of the contributions of beam intensities I_{Sample} and I_{Ref} to photocurrents I_a and I_b. The PSD is electronically configured to yield ratio and sum outputs

$$ratio = \frac{I_a - I_b}{I_a + I_b} \tag{1}$$

$$sum = I_a + I_b \tag{2}$$

For optimum performance I_{Sample} should equal I_{Ref} in intensity (optical null) prior to any absorbance, and futhermore, the two beams should then be equidistant from the PSD center (electronic null).[3] The ratio output is related to Beer's law absorbance, A, by

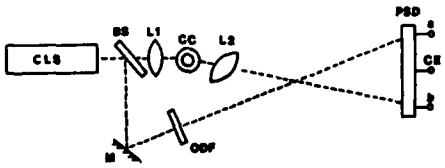

Fig. 1. CLS – collimated light source, BS – beam splitter, L1, L2, – lenses, CC – capillary flow cell, M – mirror, ODF – optical density filter, PSD – position sensitive detector (See Fig. 2).

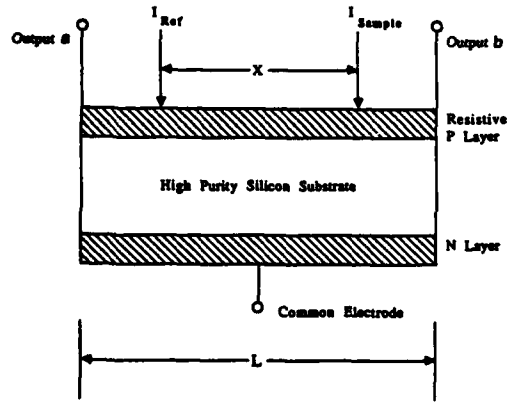

Fig. 2. Dual-beam position sensitive detection: I_{Ref} and I_{Sample} (incident beams) separated by distance X for PSD of total length L, with outputs a and b relative to common electrode CE.

$$ratio = \frac{X}{L}\left(\frac{1-10^{-A}}{1+10^{-A}}\right) \tag{3}$$

which for small A reduces to

$$ratio = \frac{X}{L}\left(\frac{2.303}{2}\right)A \tag{4}$$

Furthermore, one may also obtain absorbance information from the sum output as a relative change from baseline conditions, since for small A

$$sum = I_0(2 - 2.303A) \tag{5}$$

where the baseline output at no background absorbance is simply $2I_0$, which corresponds to the sum of the photocurrents resulting from I_{Sample} and I_{Ref} prior to absorbance. In practice the absorbance measurement obtained from the dual-beam ratio output has a better DL than the sum output since the sum output offers no light source noise reduction. Applications of the dual beam PSD-based absorbance and RI detector for process LC are abundant. In Fig. 3 is shown the reversed-phase microbore separation of two isomers of FD & C Blue Dye 2 followed by absorbance detection. In Fig. 4 is shown the reversed-phase microbore LC separation of acetonitrile and acetone from water, followed by RI detection. RI detection is facilitated by off-center focusing to a capillary flow cell, where beam deflection due to RI charges can be as high as 3 rad RI^{-1} .[4] It is possible to obtain both absorbance and RI information simultaneously by off-center focusing of the sample beam to a capillary flow cell, or to "tune-out" the RI information by center focusing.[3,4]

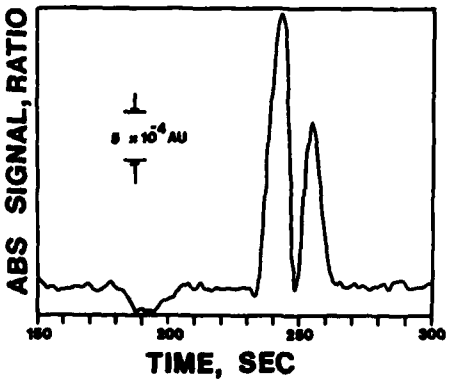

Fig. 3. Reversed-phase microbore HPLC separation and dual-beam absorbance detection (ratio signal) of two isomers of FD&C Blue Dye 2 (6.4 ng injected).

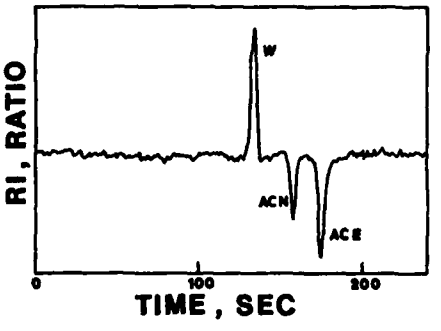

Fig. 4. Reversed-phase microbore HPLC separation and RI detection (ratio signal) of water (W), acetonitrile (ACN), and acetone (ACE).

REFRACTIVE INDEX GRADIENT MEASUREMENTS

The laser diode based RIG detector, shown in Fig. 5, may be coupled with either LC or as a diffusion controlled flow system. The RIG effect is measured as an angular beam deflection θ,[5,7-9] that is dependent upon the existence of a concentration gradient dC/dx

$$\theta = \frac{y}{n_o}\frac{dn}{dC}\frac{dC}{dx} \tag{6}$$

where y is the probed path length orthogonal to dC/dx, n_0 is the solvent RI, and dn/dC is a sensitivity factor for a given solute in a given solvent. Although equation 6 was derived for straight tube flow,[9] orthogonal to the incident light beam, data from our apparatus (Fig. 5) qualitatively follow the same relationship between θ and dC/dx. Thus, since the PSD directly measures θ, one directly measures the solute concentration gradient dC/dx. It is critical to preserve dC/dx on a microscopic level, i.e., turbulent flow must be avoided in the flow cell during RIG detection. Presently, our RIG detector has a DL of about 1 μrad. The diode laser output was at 780 nm, generally a non-absorbing wavelength for most solutes and solvents.

A simple diffusion controlled flow method employing RIG detection was designed and tested as a potential on-line and at-line process monitor for polymer characterization.[7] Consider a solute concentration distribution that has boundary conditions of zero concentration at both beginning and ending points, and reaches a maximum concentration in between, in a reference frame dependent upon time and distance. A typical example is a Gaussian function or another suitable function dependent upon the hydrodynamic conditions and history of the solute concentration distribution. For a continuous function so defined, there exists a maximum and minimum in dC/dx. For a Gaussian function the maximum and minimum occur such that[9]

$$\theta \propto \frac{dC}{dx} \propto \frac{1}{\sigma^2} \tag{7}$$

where σ^2 is the variance of the concentration distribution. For a well designed diffusion controlled apparatus the RIG signal, θ, is experimentally observed to correlate with the solute translational diffusion coefficient D, following from equations 6 and 7,[7]

$$\theta \propto \frac{1}{D} \tag{8}$$

since from the Einstein relation σ^2 is equal to 2Dt, where t is the diffusion time. For linear polystyrenes in a good solvent, D is related to the weight average molecular weight, M_w, by[7]

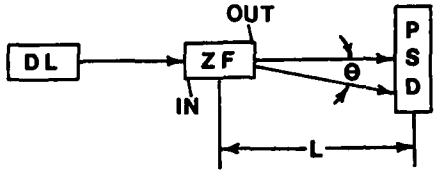

Fig. 5. RIG detector: DL-diode laser with focusing (780 nm, 5mW), ZF – z-configuration flow cell (5 μL volume), IN – inlet, OUT – outlet, PSD – position sensitive detector, θ – RIG signal (eq 6), L – length of 25 cm.

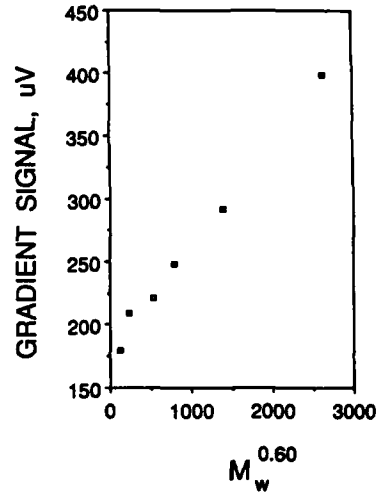

Fig. 6. RIG signal for linear polystyrenes of varying M_w, in CH_2Cl_2, using diffusion controlled apparatus.

$$D \propto M_w^{-0.6} \tag{9}$$

Thus, one would expect the detected angular data θ to readily correlate to M_w. The exponential relation between D and M_w (equation 9) is polymer shape and solvent dependent, for linear polymers the detected RIG signal is given by

$$\theta \propto M_w^{0.6} \tag{10}$$

Experimentally, equation 10 is supported by the data shown in Fig. 6 for linear polystyrenes in CH_2Cl_2 at a constant injected concentration of $5x10^{-4}$ g mL^{-1}. The ability to distinguish subtle changes in polymer M_w has been demonstrated and described in detail in an earlier description.[7]

An example of using RIG detection following the SEC of linear polystyrenes is shown in Fig. 7. For comparison the same polystyrene mixture was detected with a commercial UV-vis absorbance detector as shown in Fig. 8. Note that the commercial absorbance detector has a typical DL of about $5x10^{-5}$ AU and is operated at a favorable wavelength for the polystyrenes (270 nm). The RIG detector outperforms the commercial absorbance detector in terms of DL by at least an order of magnitude for each polymer. The DL for the 500,000 g mol^{-1} polystyrene in Fig. 7 was better than 500 pg injected polymer, and about 2 ng for the 9,000 g mol^{-1} polystyrene. The sensitivity of the RIG detection mechanism is being explored in more detail, since the performance of the device is quite remarkable relative to other universal detection approaches for LC.

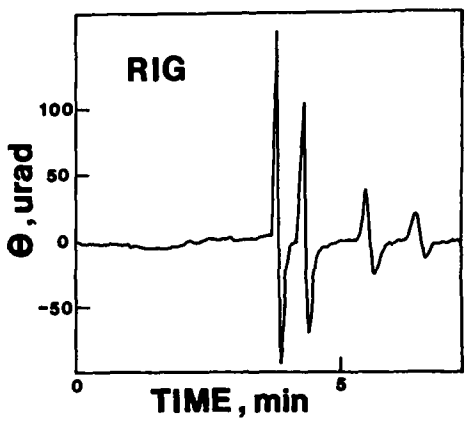

Fig. 7. SEC and RIG detection of linear polystyrenes with 150 ng each injected: 500,000 g mol^{-1}, 170,000 g mol^{-1}, 34,500 g mol^{-1}, and 9,000 g mol^{-1} (elution order in CH_2Cl_2 eluent).

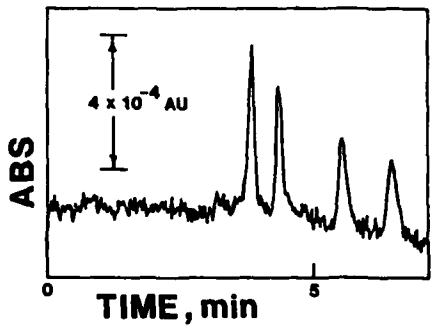

Fig. 8. SEC and UV-vis absorbance detection at 270 nm of same polymer sample as in Fig. 7.

ACKNOWLEDGMENT

R.E.S. thanks Curtiss N. Renn and Darrell O. Hancock for their participation in this work, and the Center for Process Analytical Chemistry for partial support.

REFERENCES

1. T. Hirshfeld, J.B. Callis and B.R. Kowalski, *Science*, 226, 312 (1984).
2. L.R. Snyder and J.J. Kirkland, *Introduction to Modern Liquid Chromatography* (Wiley, N.Y., 1979).
3. C.N. Renn and R.E. Synovec, *Anal. Chem*, 60, 1188 (1988).
4. R.E. Synovec, *Anal. Chem*, 59, 2877 (1987).
5. D.O. Hancock and R.E. Synovec, *Anal. Chem.*, 60, 1915 (1988).
6. C.N. Renn and R.E. Synovec, *Anal. Chem*, 60, 200 (1988).
7. D.O. Hancock and R.E. Synovec, *Anal. Chem.*, 60, 2812 (1988).
8. M. Born and E. Wolf, *Principles of Optics*, (Pergamon, N.Y., 1980), pp. 121–124.
9. J. Pawliszyn, *Anal. Chem.*, 58, 243 (1986).

ArF LASER-GENERATED MICROPLASMAS FOR CHEMICAL ANALYSIS

J.B. Morris,* A.W. Miziolek, R.C. Sausa, B.E. Forch
U.S. Army Ballistic Research Laboratory, APG, MD, 21005-5066

ABSTRACT

ArF laser-generated microplasmas are used to detect the presence of hydrocarbons in the effluent of a gas chromatograph (GC). The microplasma is detected by optogalvanic, photoacoustic, and photometric techniques. The current detection limits for acetylene samples using these three techniques are 500 ng, 500 ng, and 10 ng, respectively, with rf pick-up being the noise-limiting factor.

INTRODUCTION

Recent studies show that UV lasers can be used to produce microplasmas efficiently in gaseous flows.[1,2] One application for the use of such laser-produced microplasmas is the detection of species in the effluent gas of a GC. Desirable characteristics for such a GC detector include: high sensitivity, no flame requirements, multidimensional detection possibilities, and wide selectivity. The hypothesis behind this work is that laser-produced microplasmas occur only when a hydrocarbon analyte is present in the He carrier gas flow and not in the presence of the flow alone.

Microplasma formation is a sequential process involving the following steps. The first step involves the production of "seed" electrons within the laser focal volume. Additional electron population can then be produced by collisional processes, initiated by the intense electric fields in the laser focal volume, involving the "seed" electrons and molecular species. Finally, some of the remaining laser radiation is absorbed via inverse bremsstrahlung. Typically, between 10 and 100 μJ of laser radiation is absorbed to produce the microplasma. Characteristics of the microplasma which make it a suitable source for a GC detector include: (a) the presence of mostly singly ionized atomic and molecular species and electrons, (b) a shockwave, and (c) the emission of electromagnetic radiation. These three properties of the microplasma form the basis for optogalvanic, photoacoustic, and photometric detection schemes.

EXPERIMENTAL SETUP

A schematic of the experimental apparatus is presented in Figure 1. Briefly, the output from an ArF excimer laser (unstable resonator, 10 mJ/pulse, 10 pps, 15 ns pulse width) is focused into the effluent of a 530 μm i.d. capillary column using a 50 mm UV grade synthetic quartz lens. The laser beam is focused ca. 500 μm above

* NAS/NRC Postdoctoral Associate

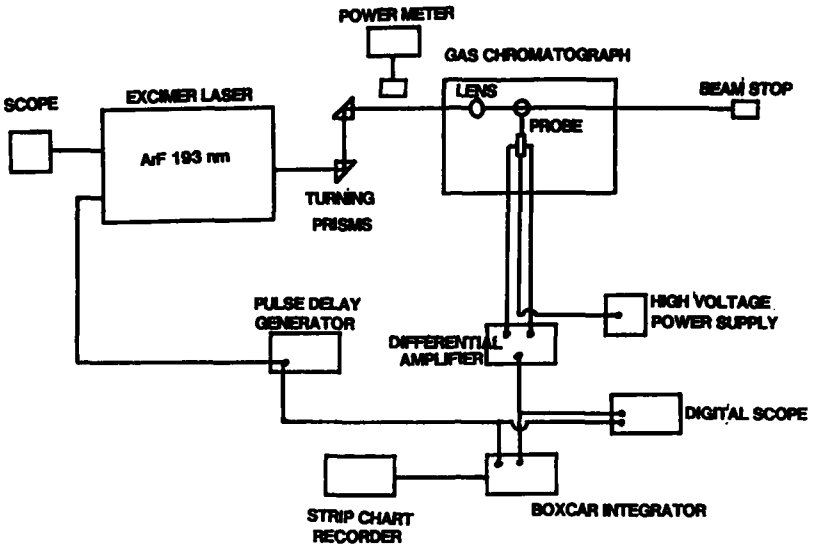

Figure 1. Experimental Setup.

the end of the column, with a waist of about 50 μm. High purity He is used as the carrier gas through the column with a flow rate of approximately 10 ml/min. A 3/8" diameter sheath surrounding the column is used to flow additional He to reduce mixing of room air with the effluent gas. Acetylene samples are injected into the column using a calibrated 10 μl gas-tight syringe.

An optogalvanic probe (point electrode) is used for collecting the electrons produced in the microplasma. The probe was designed and built by Prof. T.A. Cool of Cornell University.[3] Its 1 mm diameter anode is biased to +300 volts and placed ca. 500 μm above the microplasma. For photoacoustic detection, a commercial microphone replaces the optogalvanic probe. In the case of photometric detection, emission from the microplasma is imaged onto the slits of a 1/4 m monochromator equipped with a PMT. All of the signals are processed using a boxcar integrator whose output is directed to a strip chart recorder.

RESULTS AND DISCUSSION

Detection limits for the three microplasma detection techniques were determined by injection of varying amounts of acetylene. The optogalvanic probe (electron detection) and microphone (photoacoustic detection) give similar sensitivities of ca. 500 ng. The linearity of the detector signal for the two detection schemes was checked from 500 ng to 10 μg. Figure 2 shows the detector response for the optogalvanic probe. Both the optogalvanic and photoacoustic detectors are presently limited by rf pickup from the laser system. An additional limitation with the optogalvanic

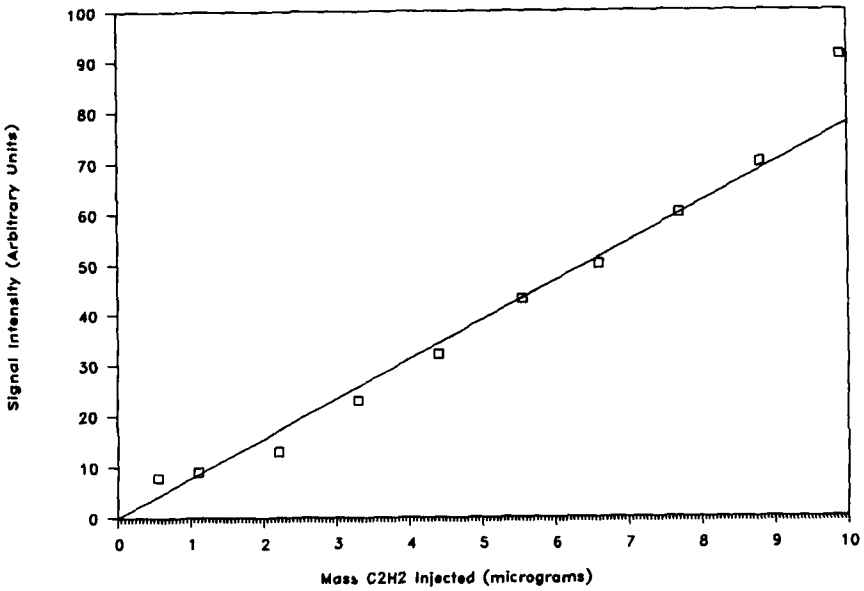

Figure 2. Optogalvanic Probe Response vs. Mass Acetylene Injected.

probe is the likelihood that space-charge effects are interfering with its electron collection efficiency.

Photometric detection of carbon atom emission at 247.9 nm is much more sensitive than the other two detection schemes tried. The use of carbon atom emission exemplifies the "multidimensional" facet of the photometric technique: atom (or molecule) selectivity. Other species whose emission was detected from acetylene include H (486 nm) and CH (431 nm). The current detection limit obtained using carbon atom emission from acetylene is 10 ng. The photometric detector response is linear over the range checked (10 - 100 ng). The major factor which presently determines the detection limit is rf pickup from the laser system by the detection electronics. Current efforts are involved in reducing this interference by shielding the laser better; once this is accomplished, the sensitivity of the photometric detection technique should show a dramatic increase.

ACKNOWLEDGEMENTS

The authors would like to thank Prof. T.A. Cool for the optogalvanic probe he supplied to us. This research was supported by US Army in-house funds.

REFERENCES

1. B.E. Forch, A.W. Miziolek, Opt. Lett., 11, 129 (1986).
2. B.E. Forch, A.W. Miziolek, Comb. Sci. and Tech., 52, 151 (1987).
3. P.J.H. Tjossem, T.A. Cool, Chem. Phys. Lett., 100, 479 (1983).

Hadamard Transform Techniques in Photothermal Spectroscopy

Patrick J. Treado and Michael D. Morris*
Department of Chemistry, The University of Michigan
Ann Arbor, Michigan 48109-1055

ABSTRACT

Hadamard transform imaging is shown to be generally applicable to any linear spectroscopy and to be useful where locally high power densities are undesirable. Application to transverse photothermal deflection and Raman spectroscopies is reviewed. The modulation transfer functions (MTF) of both source-encoded and signal-encoded Hadamard imagers are described. Preliminary results from a signal-encoded imager are presented.

INTRODUCTION

Hadamard transform imaging is a multiplexing technique that provides spatially resolved images from unfocused laser beams[1-6]. Because it operates with distributed light intensity, Hadamard imaging is advantageous for use with lasers whose peak or average power would otherwise damage samples. The method is a convenient alternative to the rastering and tight focusing employed in conventional laser microscopy, such as the Raman microprobe[7,8].

The need for laser power distribution is clear if pulsed lasers are employed. Even if CW lasers are employed, power density reduction remains important. A 50 mW beam tightly focused through a microscope objective can easily produce local temperature rises of 50°–100° in absorbing solids. While thermal decomposition or ablation is unlikely, melting or phase changes can easily occur.

There are two forms of Hadamard transform imaging. In source-encoded imaging, the signal is obtained by exciting the sample with a mask-encoded laser beam. In signal-encoded imaging, the sample is illuminated with an unfocused laser beam and the spectroscopic signal image is encoded by a series of Hadamard masks before presentation to a spectrometer.

Source-encoded Hadamard imaging is required where it is difficult or impossible to observe and manipulate an image of the analytical signal. Indirect absorption techniques, including transverse photothermal deflection spectroscopy (PDS) and photoacoustic spectroscopy (PAS) are important examples. In principle, source-encoded imaging is applicable to most spectroscopies. The only requirements are that the signals from the spatial elements of the sample be independent and that the detector generate the sum or weighted sum of the signals from illuminated spatial elements.

If the analytical signal can be imaged, as in Raman scattering, signal encoding is preferred. Signal encoding allows use of masking devices, such as photographic masks or spatial light modulators, which can not withstand high source intensities. Aperture diffraction is less severe, because the analytical signal from a coherent source is usually incoherent or only partially coherent.

We describe here the theory which describes both schemes, and the strengths and limitations of various experimental configurations in photothermal and Raman imaging. Photothermal imaging provides high sensitivity and is applicable to thin layer chromatography,[1-4] and to densitometry of protein blots. Raman imaging provides complete vibrational spectra at moderate sensitivity, with the potential for diffraction-limited spatial resolution.[5,8] The power distribution advantage of Hadamard techniques

may allow extension of Raman microscopy to pulsed laser excitation, which should prove extremely useful in ultraviolet resonance Raman studies of biological materials.

THEORY

Hadamard transform theory and application to spectroscopy and imaging have been reviewed.[9-11] The exciting laser beam or the signal from the illuminated sample is encoded with a series of n independent masks. Each mask is composed of a pseudo-random array of binary elements. The spatial distribution from the n resolution elements can be recovered from the set of n independent linear equations for the n mask configurations. In matrix notation, equation 1 describes the system.

$$\mathrm{Y} = \mathrm{S} \cdot \mathrm{X} \tag{1}$$

In equation 1, Y is a matrix consisting of the measured signals, y_i for the n mask configurations. X is a matrix representing the individual signals x_i for the n positions on the sample. The matrix S describes the configurations of the n masks and is called an S-matrix. S-matrices are derived from Hadamard matrices.[11] The decoded data can be recovered by equation 2.

$$\mathrm{X} = \mathrm{S}^{-1} \cdot \mathrm{Y} \tag{2}$$

Recovery of the data is facilitated if the number of elements encoded is $2^n - 1$. In these cases, the fast Hadamard transform (FHT) can be used, reducing the number of steps from $n^2 - n$ to $n\log_2 n$. Algorithms for constructing mask sequences and for generating fast Hadamard transforms have been published.[11]

Resolution of an imaging system is described by its modulation transfer function (MTF), which is a plot of image contrast versus spatial frequency.[12,13] We have presented approximate treatments of the modulation transfer function of a source-encoded Hadamard imaging system.[3,4] Here, we extend these arguments to the signal-encoded Hadamard imaging system. We describe contributions to the transfer function in a two-dimensional mask sequence of unit square aperture, d, using image magnification, M, to improve spatial resolution.

Equation 3 describes the effect of convolution with the finite width, d of the aperture.

$$MTF_a = \Lambda\left(\frac{f_x d}{M}\right) \tag{3}$$

In equation 3, Λ is the triangle function. The significance of this equation is that the magnified image is resolved to higher spatial frequencies than the inverse of the physical size of the mask unit aperture.

In addition, the MTF will have contributions from aperture diffraction, MTF_d, and lens aberrations, MTF_l, if present. Diffraction should be less severe for signal-encoding than for source-encoding. Lens aberrations are insignificant at the spatial frequencies reached in our experiments. MTF_l is assumed to be unity for all of the classical monochromatic aberrations. For the Hadamard imager, the modulation transfer function, MTF, is approximated as the product of all contributing terms.

HADAMARD MASKS

The encoding mask is the central element in Hadamard transform methods. Spatial light modulators are an elegant mask technology for spectroscopy in the visible and near-infrared.[14-16] However, currently available spatial light modulators are too delicate for

most source-encoded imaging. Existing spatial light modulator technology does not allow access to the ultraviolet. For these applications, mechanically translated masks remain indispensable. We have employed mechanically translated masks, fabricated as slits milled in brass[1,5] or as photographic positives on high contrast film.[3–5]

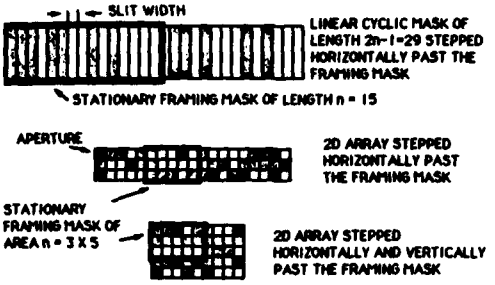

Figure 1. One- and Two-Dimensional Hadamard Mask Systems. Top: 15 element mask arranged for line-encoding; Middle: folded 3×5 array, with one axis translation; Bottom: 3×5 array folded to use x-axis and y-axis translation.

Several mask arrangements and mask translation schemes are possible. These are shown in Figure 1. The Hadamard masks can be one-dimensional, as in the upper drawing. The Hadamard sequences can be folded to give two dimensional mask sequences requiring only one-dimensional translations. The principle is shown in the center drawing of Figure 1. Here, a 15 element sequence has been folded into three rows of five elements each. The data remains an array of 15 sequential measurements and the data transformation is mathematically the same as in the one-dimensional case.

Alternatively, a folded mask sequence can be shifted in both the x and y directions, as shown in the bottom drawing of Figure 1. This motion requires two translation mechanisms, but can be implemented with a more compact mask. Two-dimensional translation is necessary with 2K element masks to avoid extraordinarily long masks.

There are constraints on the aspect ratios available, if the FHT is required for data transformation. The available aspect ratios depend on the factors of $2^n - 1$. For example, a 255-element mask can be folded into a 15×17 array a 5×51 array or an 3×85 array. In practice the roughly square array will usually be preferred. Curiously, neither a 511 element sequence nor a 2047 element sequence can be folded into approximately square arrays. However, a 1023 element sequence can be folded into a 31×33 array and a 4095 element sequence can be folded into a 45×91 array or a 63×65 array.

Advances in stepping motor and translation stage design have reduced or eliminated many of the disadvantages of mechanical motion. Commercial 10μm step devices provide positioning to within ± 5 μm and can be translated several million inches with no detectable mechanical wear and no missed steps. The largest source of error is thermal expansion of the translation stage lead screw, caused by heat transfer from the motor.

Because the Hadamard masks are used in multiplexing systems, random positioning errors are reduced by $\sqrt{N}$, where N is the number of elements in a Hadamard mask. This factor alone reduces the average error to 0.5 μm or less.[4] The unit aperture of the mask is usually 50–400 μm. The positioning error is 1% or less of this value.

THE MTF OF A SIGNAL-ENCODED HADAMARD IMAGER

The MTF is measured by evaluating the system response to a standard USAF 1951 resolution target supplied as photographic positive on glass. The target contains sets of patterns in spatial frequency increments of $\sqrt[6]{2}$, from 1 line pair per millimeter (lp/mm) to 228 lp/mm.

Our laboratory has introduced the use of transverse photothermal deflection for measurement of transfer functions of source-encoded Hadamard transform imaging systems.[3,4] Colloidal silver photographic positives give strong photothermal signals over a wide range of excitation wavelengths. Our data support the simple resolution model for Hadamard imaging summarized here. Ideally, sampling, that is convolution with the finite area of the aperture, and aperture diffraction, govern the system response.

We have also measured the MTF of a signal-encoded Hadamard microprobe. For these measurements, photothermal techniques are inappropriate. Conventional resolution targets are chromium, silver or aluminum films on quartz or glass and do not not give appreciable Raman or fluorescence signals. The MTF can be measured by encoding the image of a negative target uniformly illuminated from below with a defocused incoherent source, as shown in Figure 2.

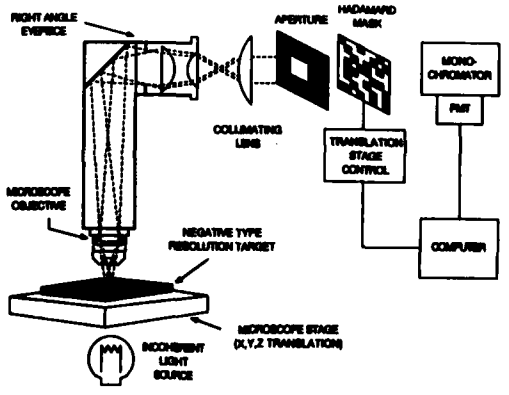

Figure 2. Apparatus for measurement of modulation transfer function of signal-encoded Hadamard imager.

A tungsten bulb beneath a ground glass diffuser serves as the light source. The light coming through the target will behave approximately as Raman scattering originating from the bar patterns. The spectrometer is operated as a monochromator (1-10 cm^{-1} band pass), with a photomultiplier tube.

The system employs a 10× objective, a 10× eyepiece and an 80 mm f.l. collimating lens for an overall magnification of 40×. In this system, the magnification is less then the product of the objective and eyepiece magnifications because of the collimating lens.

Figure 3 is a two-dimensional image of a 3-bar pattern from the resolution target. The bar centers are positioned 13.9 μm apart, which corresponds to a spatial frequency of 71.84 lp/mm. With the 190 μm element mask used in these experiments convolution with the mask unit aperture limits resolution (zero contrast) to 4.8 μm. The Rayleigh diffraction limit is approximately 1 μm. With judicious choice of objective, eyepiece, and mask aperture size there appears to be no theoretical impediment to true diffraction-limited resolution.

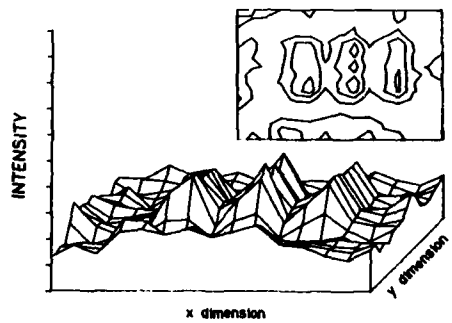

Figure 3. Two-dimensional image of resolution bar target. 40× magnification, 4.8 μm resolution. Target: 71.84 lp/mm. Bar separation: 13.9 μm.

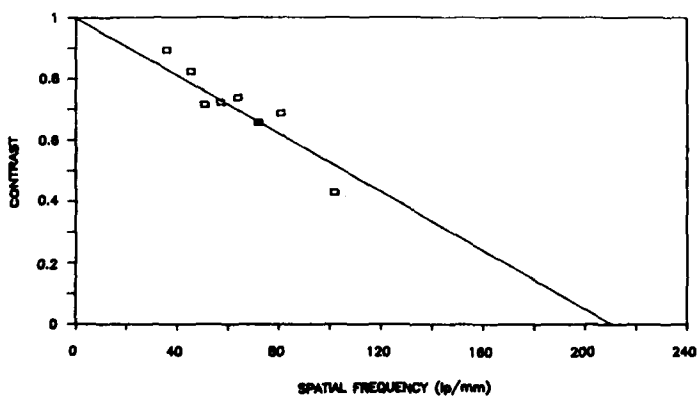

Figure 4. Modulation transfer function of a signal-encoded Hadamard transform microprobe. 40× magnification. Solid line: aperture convolution contribution to MTF.

Figure 4 shows the modulation transfer function for the signal-encoded Hadamard transform microprobe. The solid line represents the theoretical contribution from convolution with the unit aperture. Contrast is measured for cross sections of the two-dimensional image. Good agreement is observed between the measured values and the theoretical prediction. Contributions from aperture diffraction, lens aberrations, and focusing errors are small in this case. To construct a Hadamard imaging system in which diffraction by the microscope objective or aberrations in the microscope optics are resolution limiting, it should only be necessary to decrease the size of the unit aperture or increase the overall magnification of the system.

A SIGNAL-ENCODED HADAMARD RAMAN MICROPROBE

Details of a Hadamard transform Raman microprobe have been described.[8] Figure 5 shows a Raman image of a bensoic acid crystal obtained with this instrument. The apparent crystal dimensions obtained from the Raman image agree well with the directly (reticle) measured dimensions. The intensity scale does not faithfully represent the crystal shape, because illumination and collection efficiency depend on the angles the crystal facets make with the optical system.

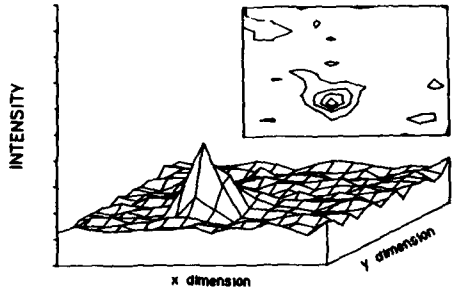

Figure 5. Hadamard transform Raman image of benzoic acid crystal. *Excitation:* 150 mW, 514.5 nm. Observation at 542 nm (992 cm^{-1}); 10 cm^{-1} spectral resolution; 4.8 μm spatial resolution. 40× magnification.

CONCLUSION

Hadamard transform multiplexing represents a generally useful approach to spatial imaging using intense light sources. The technique is applicable to any linear spectroscopy. Photothermal spectroscopy and other indirect absorption techniques will continue to employ source-encoding. However, Raman scattering and fluorescence imaging will use signal-encoding, to minimize diffraction problems and to enable use of delicate spatial light modulators.

REFERENCES

1. F.K. Fotiou, M.D. Morris, Appl. Spectrosc. **40**, 704 (1986).
2. F.K. Fotiou, M.D. Morris, Anal. Chem. **59**, 185 (1987).
3. F.K. Fotiou, M.D. Morris, Anal. Chem. **59**, 1446 (1987).
4. P.J. Treado, M.D Morris, Appl. Spectrosc. **42**, (in press) (1988).
5. Treado, P.J.; M.D. Morris, Appl. Spectrosc. **42**, 897 (1988).
6. Treado, P.J., M.D. Morris, Appl. Spectrosc. **43**, (in press) (1989).
7. J.J. Blaha, in J.R. Durig, ed. *Vibrational Spectra and Structure, Vol. 10* Elsevier: Amsterdam, 1981, p. 227.
8. G.J. Rosasco in R.J.H. Clark, R.E. Hester, Eds. *Advances in Infrared and Raman Spectroscopy, Vol 10,* Wiley: Chicester, 1981, p. 223.
9. R.M. Hammaker, J.A. Graham, D.C. Tilotta, W.G. Fateley in J. Durig, ed. *Vibrational Spectra and Structure, Vol. 15,* Dekker: New York, 1986, p. 401.
10. W. Stinson, Chem. Engin. News, February 29, 22 (1988).
11. M. Harwit, N.J.A. Sloane, *Hadamard Transform Optics;* Academic Press: New York, 1979.
12. J.W. Goodman, *Introduction to Fourier Optics;* McGraw-Hill: New York, 1968.
13. H.C. Andrews, *Computer Techniques in Image Processing;* Academic Press: New York, 1970.
14. D.C. Tilotta, R.M. Hammaker, W.G. Fateley, Appl. Spectros. **41**, 727 (1987).
15. D.C. Tilotta, R.M. Hammaker, W.G. Fateley, Appl. Opt. **26**, 4825 (1987).
16. D.C. Tilotta, R.D. Freeman, W.G. Fateley, Appl. Spectros. **41**, 1280 (1987).

INTENSITY OF THE SPECTRAL LINES IN THE OPTOGALVANIC EFFECT

B. R. Reddy, Putcha Venkateswarlu and M. C. George
Department of Physics, Alabama A&M University,
Normal, Alabama 35762

ABSTRACT

An experimental demonstration is given to explain the discrepancies between the intensities of the spectral lines in optogalvanic effect and those in emission. An explanation is also given for the signal polarity changes occuring when the discharge voltage is varied. A technique has been suggested to record a maximum number of spectral lines in OGE.

Optogalvanic effect (OGE) is the response of the discharge voltage to an optical pulse stimulation. A pulsed laser beam axially irradiates the discharge in a hollow cathode lamp filled with neon or argon as buffer gas and the voltage across the discharge tube varies whenever the laser frequency is in resonance with the gap between the energy levels of the species. The amplitude of the signal in OGE depends on the lower level population, transition probability for photon absorption and collisional ionization probability of the higher level. We have recorded about 300 lines in neon and about 200 lines in argon in the wavelength interval 4100-6700Å and majority of them are recorded for the first time in the OG spectrum. The line density spectrum in OGE is more like the emission spectrum than the absorption spectrum, because in a discharge species, electrons exist in higher levels also. In a small wavelength region it is expected that the relative intensities of the spectral lines in OGE would be proportional to those in emission. But some strong lines of the emission spectra are sometimes either too weak or absent in OGE. Also peaks of some of the lines in the OG spectrum show up on either side of the stripchart recordings when the discharge voltage is varied, leading to discrepancies in the assignment of OG signal polarities. An experimental study of these important contradictions is presented and an explanation is given as to why such discrepancies arise.

For several of the OG signals in neon the temporal evolution[1] is successfully described by the equation

$$\Delta v = -\text{const.}\ [a_2 \exp(-t/T_2) - a_1 \exp(-t/T_1)] \qquad (1)$$

where Δv is the amplitude of the signal, a_1 and a_2 relate to the rates of ionization from levels 1 and 2 and T_1 and T_2 are the relaxation times for the discharge populations to reach the steady state values. For $a_2 > a_1$ and $T_1 = T_2$, equation (1) predicts a -ve signal while for $a_2 > a_1$ and $T_1 \gg T_2$ equation (1) predicts a sharp -ve signal followed by a broad +ve signal. The temporal evolution of a typical signal at 6046Å is shown in Fig. 1a, which has a sharp -ve peak around 3 μsec followed by a broad +ve portion peaking around 25 μsec

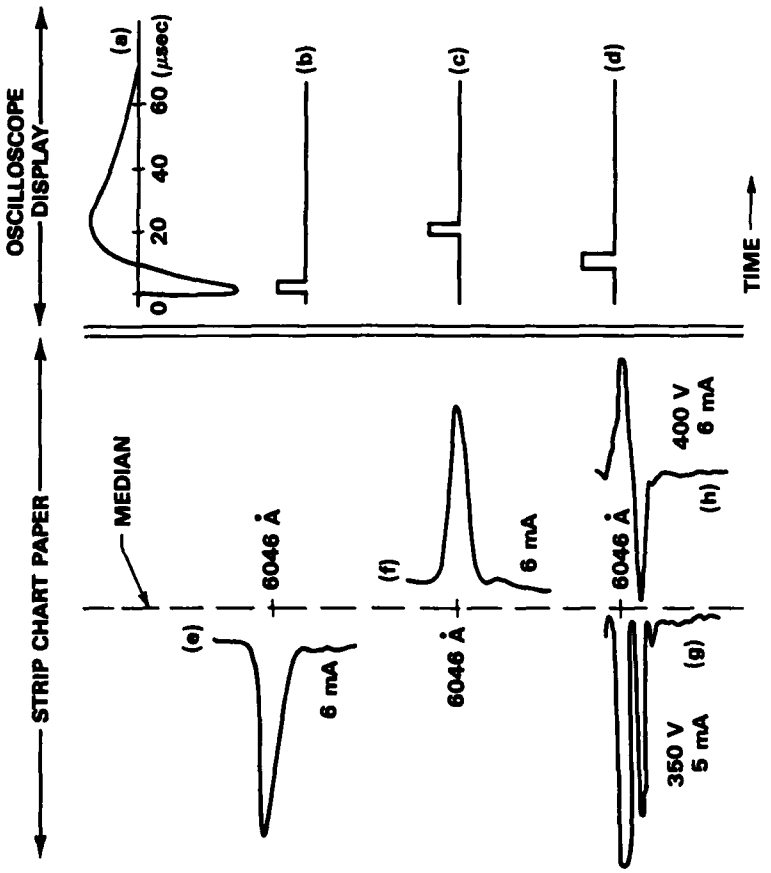

Figure 1(a). Temporal evolution of the signal in OGE at 6046 Å in Ne discharge. (b), (c), (d) are the boxcar aperture settings and (e), (f) and g(h) are the respective OG spectra in the region at 6046 A.

and finally reaching steady state discharge condition at about 60 μsecs. Equation (1) was used to fit the data of figure 1 and the best fit values are $a_2/a_1 = 2.2$, $T_1 = 50.8$ μsec and $T_2 = 8.8$ μsec.

The shape and polarity of the waveform remained the same for a range of discharge currents (0-10mA). When pulsed laser sources are used for irradiation a boxcar/gated integrator is used to process the signals. To record the OG spectrum in a certain wavelength region, the gate duration and delay time are set to optimum values to sample a small portion of the waveform and then the laser frequency is tuned in the desired spectral region. Assume that the gate was timed to sample the signal entirely from the -ve part as in Fig. 1b, then the spectral peak appeared to the left half on a stripchart recording (Fig. 1e) when the laser was tuned in the region. When the gate was timed to sample from the +ve portion as in Fig. 1c, then the same peak appeared to the right half on the chart paper (Fig. 1f). When the gate was set to either of these two positions, the peaks did not change sides though the discharge current was varied from 0-10mA. However, an entirely different situation was encountered when the gate was set to an intermediate position as in Fig. 1d, where the gate sampled some part of the -ve signal and some part of the +ve signal. For a discharge voltage of 350V or less the peak appeared to the left half (Fig. 1g) and for 400V and above the peak appeared to the right half (Fig. 1h). For an intermediate voltage no peak was observed. The explanation is given below. At 350 volts the gate sampled a larger portion of the -ve component than the +ve component and hence, the peak appeared to the left half. When the voltage was increased to 400V the +ve part had grown faster than the -ve part causing the gate to sample a larger portion of the +ve component. Hence, the peak appeared to the right half; and at an intermediate voltage, the +ve and -ve parts sampled by the gate are exactly equal resulting in no signal output. The timings at which the signal reaches the peak amplitudes are characterized by the values a_1, a_2, T_1 and T_2 of the levels and hence, these values differ for different levels. So, the sampling parameters, gate duration and delay time which are optimum for one wavelength are not optimum values for all the wavelengths. Hence, the OG signal strengths do not always agree with the signal strengths/transition probabilities found from the emission spectra. So, it is also not possible in OGE to record all the spectral lines of emission (in any wavelength interval) with one set of sample parameters. By varying the sampling parameters we are able to record for the first time several of the weakest lines reported in emission but not observed in the OG spectrum in the past[2] (for example the 6328.2Å line).

REFERENCES

1. G. Erez, S. Lavi and E. Miron, IEEE J Quant. Elec., QE-15, 1328 (1979).
2. K. C. Smyth and P. K. Schenck, Chem. Phys. Letts. 55, 466 (1978).

THE OLD TECHNIQUE APPLIED TO DIAGNOSTICS OF THE ATMOSPHERIC SIMULATION CHAMBER

Richard Anderson
University of Missouri, Department of Physics
Rolla, MO 65401

ABSTRACT

The present remote sensing diagnostic techniques of the atmospheric simulation chamber is Mie scattering from the droplets and the optoacoustic laser beam deflection technique is an additional method.

INTRODUCTION

The chamber and experimental apparatus are shown in Figure 1. A pulsed laser is directed into the chamber

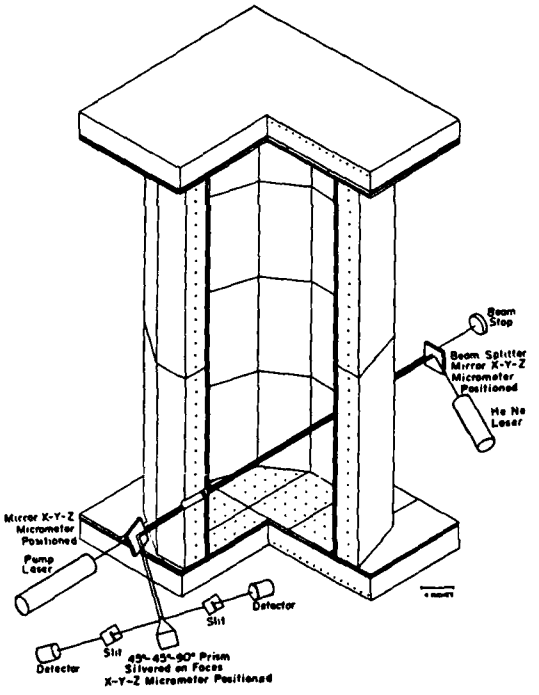

Figure 1. Experimental Arrangement

which can excite species of clusters or it is absorbed by a particulate scavenged by the droplets. This pulse heats the gas along the path and the heat pulse has the same profile as the laser beam. The heat pulse moves

radially outward at the speed of sound changing the index of refraction which deflects probe laser beams. The probes are HeNe lasers which are slightly displaced from each other and the pump beam. A single probe beam determines molecular species and two beams determine the speed and temperature of the gas. The index of refraction change is

$$n(r) = n_o - n_o\eta \exp(-r^2/a^2) \quad (1)$$

and for small η, $n(r) = n'' + n'r^2/a^2$, (2)

where $n' = n_o\eta$ and $n'' = n_o - n_o\eta$.

THEORY

At atmospheric pressure the radiation absorbed is lost by quenching so the absorbed energy is deposited heat. For opaque material scavenged by the droplets this is also true. Then the heat absorbed is approximately

$$H = N_o B_{12} I_o h\nu\tau = I_o\alpha l\tau , \quad (3)$$

where N_o is the molecular density, B_{12} is the absorption coefficient, τ is the pump pulse width, I_o is the incident laser power, l is the path length, and α is the linear absorption coefficient of the medium.

When two probe lasers are used, their separation is accurately known and the time between deflects is measured and the pulse speed v is evaluated. It is related to the temperature by the relation

$$T = v^2 M \left\{ R \left[1 + R/C_v(T) \right] \right\}^{-1} \quad (4)$$

so T is evaluated. T_i is the initial gas temperature and $\Delta T = T - T_i$. Then linear absorption coefficient is

$$\alpha = N_o Ac_v \Delta T/I_o\tau \quad (5)$$

and if the molecular density is not known, the linear absorption coefficient per molecule is

$$\alpha' = \alpha/N = c_v \Delta T/I_o l\tau \quad . \quad (6)$$

where N is the total number of molecules.

The amount of beam deflection can be calculated from the energy conservation equation

$$\rho c_p\left[\partial T(r,t)/\partial t+v\ \partial T(r,t)/\partial r\right] = k\ \partial^2 T(r,t)/\partial r^2+I(r,t). \quad (7)$$

Neglecting conduction in steady state (7) becomes

$$\rho c_p v \partial T(r,t)/\partial r = I(r,t). \tag{8}$$

The angular deflection in the direction of propagation is gradient

$$d\phi/dz = \left\{\partial n/\partial T \; \partial T/\partial r\right\}/n \tag{9}$$

$$\text{so} \qquad \Delta\phi = \left\{\partial n/\partial T \left[2 \; \alpha' \; N \; E_o \; 1/\pi \; a^2 \tau \rho c_p \; v\right]\right\}/n, \tag{10}$$

From the Gladstone-Dale equation the index of refraction is

$$n = n \; + \delta_o \; T_i/T, \tag{11}$$

where $\delta_o = \rho\langle R_G\rangle$ and $R_G = \sum_{i=0}^{n} R_{Gi} \; X_i$. Then $\partial n/\partial T \simeq \delta_o T_i/T^2$ and assume $1/n \simeq 1$ so

$$\Delta\phi = -2 \; \delta_o T_i \; \alpha' \; N \; E_o 1/\pi \; a^2 T^2 \; \rho\tau c_p v \tag{12}$$

CONCLUSIONS

Filtered, dried outside air is used in the chamber and this technique along with FFT spectroscopy may allow impurities to be determined. Also cluster absorption in the IR can be studied and opaque particulate scavenging can be measured.

REFERENCE

1. K. Tennal, G. J. Salamo, and R. Gupta, Minority concentration in flames by the photoacoustic technique, Appl. Opt. 21, 2133 (1982).

2. J. A. Sell, Quanitative photothermal deflection spectroscopy in a flowing stream of gas, Appl. Opt. 23, 1586 (1984).

3. W. C. Gardner, Jr., Y. Hidaka, and T. Tanzawa, Refractivity of combustion gases, Flame 40, 213 (1981).

4. L. A. Melton, Soot diagnostics based on laser heating, Appl. Opt. 23, 2201 (1984).

QUANTUM-LIMITED FM SPECTROSCOPY WITH A LEAD-SALT DIODE LASER

CARLISLE, C.B. and COOPER D. E.
SRI International
333 Ravenswood Avenue, Menlo Park, CA 94025

ABSTRACT

We report the attainment of quantum-limited sensitivity in FM spectroscopy with a lead-salt diode laser. This sensitivity has been demonstrated at 4.8 μm in the detection of CO_2 and CO. The improved sensitivity and reproducibility of our FM apparatus can be attributed to several new features. Recently obtained MBE-grown lasers have exhibited much better mode and filamentation characteristics and as a consequence much more reproducible measurements. Our technique of optical fringe filtering using frequency discrimination[1] has effectively alleviated the chronic fringe problems associated with diode laser absorption spectroscopy. Improved optical processing of our beam has allowed us to collect more of the laser output onto the detector with reduced feedback and multipassing effects. Finally, operation of the laser in the saturated regime of optical power vs. injection current essentially eliminates residual amplitude modulation (RAM) problems.

INTRODUCTION

Since its inception,[2] FM spectroscopy has been touted as the only method of linear absorption spectroscopy that is in principle quantum-noise limited. An ideal FM apparatus is limited only by the quantum (often termed shot) noise which is inherent to the statistics of the photodetection process. In practice such sensitivity has proven difficult to attain for every implementation of the technique. A variety of different "technical" noise sources conspire to degrade sensitivity unless extremely careful attention is paid to a number of experimental details. In fact, it is the circumvention of these technical noise sources which constitutes the effective application of FM spectroscopy.

FM spectroscopy as originally conceived employs modulation of the laser carrier with a single rf component, with demodulation at the same frequency. A later version of FM, which uses two distinct but closely spaced rf components and demodulation at their difference frequency is termed Two-Tone FM spectroscopy (TTFMS).[3] This variation has found somewhat greater application than the original version due to its reduced detector bandwidth requirements and RAM susceptibility.[4] These considerations are particularly important for IR diode laser FMS, as detectors have limited bandwidths and RAM is always present.

Quantum-limited sensitivity has been achieved for visible[5,6] laser-based FMS. However, rather sophisticated dual-beam techniques were required using extremely well-stabilized lasers. Since semiconductor diode lasers produce highly divergent, invisible beams, sophisticated optical processing techniques are difficult if not impossible to apply to them. Further, these lasers are much less stable and much more sensitive to feedback than other lasers due to the low reflectivity of their output couplers. The major experimental obstacles encountered in performing diode laser FMS are: (1) optical fringes from transmissive optics; (2) lack of optical power; (3) feedback-induced noise and excess laser noise; (4) thermal drift of signal and background; (5) laser RAM. Effective methods of dealing with all of these problems must be devised in order to achieve quantum-limited detection sensitivity.

Perhaps the most persistently troublesome phenomenon encountered by diode laser spectroscopists is the etalon effect. The relatively wide sideband spacing in FM laser light makes it acutely susceptible to this effect of optical fringes. Our method of rapid, repetitive scanning of the laser combined with post mixer IF low pass filtering to frequency discriminate against fringes virtually eliminates the problem. Figure 1 illustrates the effect of the technique.

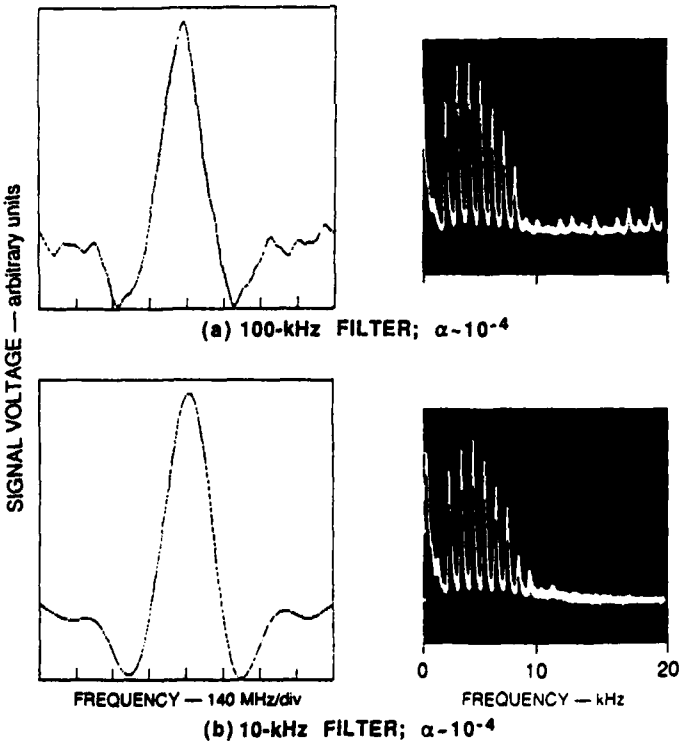

Figure 1. TTFMS SCANS USING LOW-PASS FILTER

Lead-salt diode lasers have been very low output devices since their invention, with typical output powers of hundreds of μW. Their beam emerges as a 60-80 degree light cone, making collimation and optical processing in general difficult. Ordinary spherical optical lenses and parabolic mirrors cannot collimate such a beam without excessive aberrations. We have found that only special aberration-free doublets or aspherics are capable of properly collimating and focusing a lead-salt laser beam. Using conventional lenses or off-axis paraboloids imparts such strong aberrations to the beam that only about 10-20% of the total output power can be imaged on to our photodetector (which has an active area = 250 μm squared).

Excess, classically correlated laser noise can be a problem with diode lasers, especially at frequencies below a few MHz. Of course, the entire motivation behind FMS is to move the detection frequency beyond this region and thus avoid such noise. However, in the presence of optical feedback or near a cavity mode-hop this noise can extend to tens or even hundreds of MHz. Judicious selection of the laser's operating temperature and current and careful optical alignment can reduce it to an acceptable level.

Tunable diode lasers are known to be extremely sensitive to heat bath fluctuations[7] as well as self-heating, non-linear cavity effects. This phenomenon is not of great concern for laboratory applications where manual readjustment of the laser settings can be performed. However, for practical, fieldable instruments such drifts are intolerable and an automated feedback system must be employed. Preliminary experiments using sample-cell line-locking indicate that a stable device can be constructed quite easily.

Laser RAM is always a difficulty in FMS. We have found that operation in the saturation region of power vs. injection current suppresses RAM effects greatly, especially for TTFMS applications, where RAM effects are second order functions of the AM index. TTFMS is also preferable because of the increased dynamic range allowed for the preamplification necessary to have the detector shot noise above any downstream Johnson noise.

Some data taken on CO and CO_2 lines is shown in Figure 2. These scans exhibit, to the authors' best knowledge, the first discernible lineshapes of absorptions of $\alpha < 10^{-6}$ from a linear absorption technique. Moreover, these data provide convincing evidence of the speed and sensitivity of diode laser FMS. These scans were acquired in approximately 2-4 seconds. The sloping baselines are due to long free spectral range etalons from the transmissive optics.

Our limiting noise voltage is taken to be the complete, peak-to-peak noise value measured on our digitizer. This amounts to equating our noise voltage with the width of its Poisson distribution well into the wings of the distribution. Conventional FMS calculations

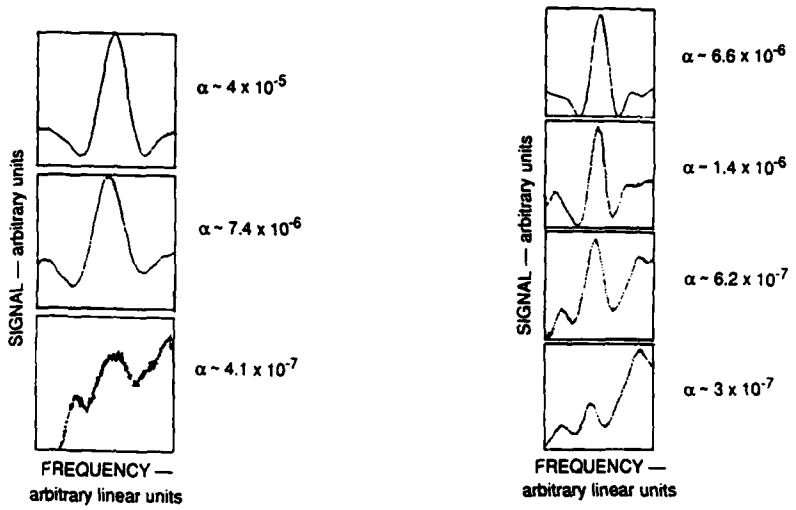

(a) Over Weak CO Lines (b) Over Weak CO_2 Lines

Figure 2. TTFMS SCANS

take their limit to be the rms value, or half-width at half-max, of the noise envelope. Consequently, our value measured directly from the digitizer data is consistently a factor of 2 to 4 above the limit calculated for an rms noise voltage. By statistically analyzing our noise and obtaining an rms value, we conclude that our measurements are indeed quantum-noise limited.

CONCLUSIONS

We have demonstrated quantum-noise limited sensitivity with a lead-salt diode laser monitoring CO and CO_2 lines around 4.8 μm. Our techniques are applicable to all IR diodes of sufficient spectral quality and ultrasensitive detection for absorptions as small as 10^{-7} should be possible throughout the IR regions accessible to the laser sources.

REFERENCES

1. D. E. Cooper and C. B. Carlisle, Opt. Lett., 13, 719 (1988).
2. G. C. Bjorklund, Opt. Lett., 5, 15 (1980).
3. G. R. Janik, C. B. Carlisle, and T. F. Gallagher, JOSA B 3, 1070 (1986).
4. D. E. Cooper and R. E. Warren, JOSA B 4, 470 (1986).
5. M. Gehrtz, G. C. Bjorklund, and E. A. Whittaker, JOSA B 2, 1510 (1985).
6. N. C. Wong and J. L. Hall, JOSA B 2, 1527 (1985).
7. H. Yasaka and H. Kawaguchi, Appl. Phys. Lett., 53, 1360 (1988).

REAL-TIME HIGH RESOLUTION MONITOR FOR AMBIENT METHANE BASED ON A ZEEMAN-SPLIT HeNe LASER

P.L. Kebabian and J.B. McManus
Aerodyne Research, Inc., Billerica, Massachusetts 01821

ABSTRACT

We report the construction of an atmospheric methane measurement instrument based upon a Zeeman-split IR HeNe laser. The laser has a transverse magnetic field over ~2/3 of its gain length, and can oscillate at an (unsplit) frequency (2947.9 cm^{-1}) centered on a methane absorption line, or at ±0.055 cm^{-1} from the center, with low CH_4 absorption. The laser is tuned to dwell sequentially at each frequency, giving two differential absorption measurements in each 46 ms tuning cycle. There are two atmospheric measurement channels, with fast (0.75 sec) and slow (5 sec) flow response times. Fluctuations in ambient CH_4 of ~20 ppb (RMS, 1 sec TC) are detected, with fringe effects the dominant noise source. The instrument has operated in a field experiment (NASA GTE/ABLE-3A) in Alaska.

1. INTRODUCTION

The precision measurement of atmospheric methane recently has become a topic of widespread interest. Methane, with a tropospheric concentration near 1.7 ppm, plays important roles in both atmospheric chemistry[1-2] and global heat transfer.[3,4] The tropospheric CH_4 concentration is currently increasing at the rate of ~1% per year.[5] An extensive program of world wide surface and airborne measurements has begun to gather the systematic data necessary for an understanding of methane sources and sinks, photochemistry, and the changing methane content of the atmosphere. We have constructed and demonstrated an optical instrument that we expect will advance the state-of-the-art in measurement of atmospheric methane.

This instrument was constructed to take part in the NASA Atmospheric Boundary Layer Experiment,[6] which is a broadly based set of experiments on the land and in aircraft to study the sources and distribution of trace gases in the tropospheric boundary layer. The instrument was sent to a field site during the summer of 1988, to collect data on the evolution of CH_4 from arctic tundra. The instrument has two measurement channels, a slow response (~5 sec) channel for measuring the vertical concentration profile (from 0.5 to 12 meters) and a fast response (0.75 sec) channel for eddy correlation measurements at a fixed height (12m).

2. INSTRUMENT DESIGN

Our methane instrument is based on the well known[7] coincidence of the 3.39 μm (2947.9 cm^{-1}) output line of a HeNe laser with the P7 absorption line in the ν_3 band of CH_4. It uses a HeNe laser with a transverse magnetic field (~1 kG) over ~2/3 of the gain length, which can oscillate at the center (unsplit) frequency that is

coincident with the methane absorption line, and at two Zeeman split lines (±0.055 cm^{-1}) that lie to either side of the absorption line. While magnetic tuning of an infrared HeNe laser with a transverse field has been reported previously,[8] our laser is novel in that the splitting is quite broad, and the laser is controlled by a novel system of feedback loops. By sequentially tuning the laser to each of the three lines, one absorbed by CH_4 and two unabsorbed, we can make two differential absorption measurements with a single laser. The atmospheric gas samples are drawn into multipass absorption cells of the type described by Herriott,[9] with two atmospheric sampling cells and a third reference cell that is nominally identical to the two sample cells, and contains standard air at the same pressure. A control loop uses the reference cell signal to equalize the power on the three laser lines, precompensated for CH_4 absorption. Ideally then, differences in detected power between the split and unsplit lines result from a difference in CH_4 concentration between the sampled atmospheric air and the standard.

A piezo-transducer on the rear laser mirror tunes the cavity between the unsplit and two split lines in cycles lasting ~46 ms, where the output dwells sequentially on each line for about a quarter of the cycle. The output is ~10 μW on each line, with the output going to zero between the lines. The laser tuning waveform contains a small sinusoidal component to dither the tuning mirror while dwelling on the unsplit line, which enables us to lock the cavity length. On short timescales, the cavity length control loop adds an offset to the piezo drive voltage. On longer timescales, a heated germanium Brewster window within the cavity introduces compensating length changes. The signal processing and laser control functions are performed digitally by a dedicated microprocessor.

The absorption cells are designed to have the minimum practical volume, giving the minimum gas exchange time with a limited flow of sampled atmospheric gas. The cells are operated at reduced pressure (~100 Torr) which gives the optimum differential absorption signal for the 0.055 cm^{-1} splitting ($\Delta I/I = 5.5 \times 10^{-4}$/ppm-m). The beam makes 72 passes of the 16.2 cm long cell, for 11.7m path length in a cell of only 42 cm^3. We experience a relatively high level of interference fringes, of ~5×10^{-3} of the total transmitted power, which is comparable to the CH_4 absorption level. The high fringe level is a consequence of the close spacing of beam spots on the mirrors and the small cell size. We use piezo transducers to oscillate the rear mirror of each cell to average out the fringes. The instrument was built on a small honeycombed table measuring 44 x 74 cm, and was enclosed with a Lexan cover (33 cm high).

3. RESULTS AND CONCLUSIONS

We have tested the prototype methane instrument in both a laboratory setting and at a field site, as part of the NASA GTE ABLE-3A experiment. The operation in the field was substantially the same as in the laboratory. The signal to noise ratio for both data channels is similar, at ~75 (RMS, 1 sec TC), relative to the response to ambient CH_4. Thus, we detect changes in atmospheric

CH_4 of ~20 ppb with SNR = 1 at 1 sec TC. The noise is well above that expected from either laser shot noise or detector noise, with the excess due to the large cell fringes. The maximum long-term drift is ~0.16 ppm/hr, or ~10%/hr of atmospheric CH_4 concentration. The drift is largely due to fringes in the germanium detector windows.

Our HeNe laser system may be used in other methane sensing applications. For example, the wide magnetic splitting used in our laser would be appropriate to broad (0.15 cm^{-1} FWHM) absorption lines at atmospheric pressure. The laser may be used in an open path eddy correlation flux measurement system, of the type we have already demonstrated[10] with a tunable diode laser (TDL) source, and we anticipate that the HeNe laser will allow a much lighter and more rugged instrument. The cells also may be operated at lower pressure in conjunction with a laser with lower splitting, which would be appropriate for high altitude aircraft measurements. We are currently developing a more sensitive version of the instrument, with a goal of detecting methane fluctuations of 5 ppb (1 sec).

In general, rare-gas discharge lasers may be applied to monitoring other atmospheric trace gases, when there are close coincidences between emission lines and molecular absorption lines. This technique is less flexible than using TDL's, but for dedicated monitors of particular gases, the rare gas laser has some advantages, such as high reliability, plenty of power in a single mode and good beam quality. In addition, one can avoid some of the bulky elements of TDL systems. We will continue to explore the application of rare gas lasers to sensing other atmospheric trace gases.

We wish to acknowledge the assistance of M.S. Zahniser, A. Freedman, S.A. Anderson and S. Kallelis, all at Aerodyne Research, and of S.C. Wofsy, P.S. Bakwin and S.M. Fan of Harvard University. This work was supported by the NSF Atmospheric Chemistry Division and the NASA Tropospheric Chemistry Program.

REFERENCES

1. J.A. Logan, M.J. Prather, S.C. Wofsy, M.B. McElroy, J. Geophys. Res. 86, 7210 (1981).
2. R.J. Cicerone, Science 237, 35 (1987).
3. W.C. Wang, G. Molner, J. Geophys. Res. 90, 12971 (1985).
4. V. Ramanthan, R.J. Cicerone, H.G. Singh, J.T. Keith, J. Geophys. Res. 90, 5547 (1985).
5. D.R. Blake, F.S. Rowland, Science 239, 1129 (1988).
6. R.J. McNeal, J.P. Mugler, R.C. Harriss, J.M. Hoell, Eos Trans. AGU 64, 561 (1983).
7. A.S. Pine, J. Opt. Soc. Am. 66, 97 (1976).
8. R.L. Fork, C. Patel, Proc. IEEE 52, 208 (1964).
9. D.R. Herriott, H. Kogelnik, R. Kompfner, Appl. Opt. 3, 523 (1964).
10. M.S. Zahniser, P.L. Kebabian, S.A. Anderson, A. Freedman, C.E. Kolb, in "Advances in Laser Science - II," M. Lapp, W.C. Stwalley, G.A. Kenny-Wallace, eds. [AIP, New York, 1987], 690.

IMAGING OF SUPERSONIC FLOW USING PLANAR LASER-INDUCED FLUORESCENCE

P. H. Paul, J. Seitzman, M. P. Lee, B. McMillin and R. K. Hanson
High Temperature Gasdynamics Laboratory, Mechanical Engineering Dept.
Stanford University, Stanford, CA, 94305

The use of "molecular velocimetry", the measurement of flowfield velocity by means of Doppler-shifted absorption with fluorescence detection, as a diagnostic tool was first proposed by Measures[1]. Hiller and Hanson[2] have described an extension of this technique, for supersonic flows, which yields simultaneous two-dimensional measurements of two velocity components and pressure based on planar laser-induced fluorescence (PLIF). The use of molecular velocimetry is of particular advantage in supersonic flows where the use of particle-based techniques may be precluded by practical considerations or strongly biased by the slip of the particles in regions of high shear. Additionally, the use of PLIF can provide access to a wide range of 2-d species concentration and temperature concepts[3].

Previous molecular velocimetry techniques have relied on the detection of fluorescence from an absorption line of a seed species excited with a narrowband laser[2]. In brief, a change in the fluorescence signal reflects a velocity-induced Doppler effect, i.e., the shift of an absorption line across a spectrally narrow, fixed-frequency laser line. The demand for a narrowband excitation source has limited prior work to the use of continuous-wave lasers. The use of low intensity CW lasers in turn has required seeding with efficient fluorescing species and has required relatively long exposure times, such that the velocity measurements are not instantaneous (flow-stopping).

The approach employed here is similar to that described by Hiller and Hanson[2] with one critical difference: broadband excitation is used[4]. Based on a simple two level, weak excitation model, the number of fluorescence photons per pixel, S, arriving at the detector is proportional to the convolution of the laser and absorption lineshapes. For the broadband technique described here, the convolution lineshape is that of the laser, $g_l(\nu_a-\nu_l,\Delta\nu_l)$, which is constant at all points in the flow. Here ν_a and ν_l are the absorption and laser frequencies respectively and $\Delta\nu_l$ is the laser linewidth.

The fluorescence signal at the unshifted line position (zero velocity component) is proportional to the convolution lineshape $g(\nu_a-\nu_l)$, while the signal resulting from a Doppler shift of $\pm\Delta\nu_D$ is given by S^+ and $S^- \propto g(\nu_a\pm\Delta\nu_D-\nu_l)$. The superscripts refer to the signals that are recorded with the laser sheets in the forward, "+", and counterpropogating, "-", directions (see figure 1). The Doppler shift is given by the scalar product between the velocity and laser wave vector, $\Delta\nu_D = -(u/\lambda)\cos\theta$, where u is the velocity magnitude and θ is the angle between the laser and velocity unit vectors. The velocity algorithm is obtained by expanding S^+ and S^- in Taylor series

about ν_a. Taking the difference between S^+ and S^- leaves only the odd terms in the series while taking the sum leaves only the even terms. Thus, to first order in $\Delta\nu_D$,

$$\Delta\nu_D\,(g'/g) = [2\,S^+/(S^+ - S^-)] - 1 \qquad (1)$$

where g' is the slope of the laser profile evaluated at ν_a. Velocity imaging is performed by acquiring the S^+ image and a sum image, $S^{\pm} = S^+ + S^-$.

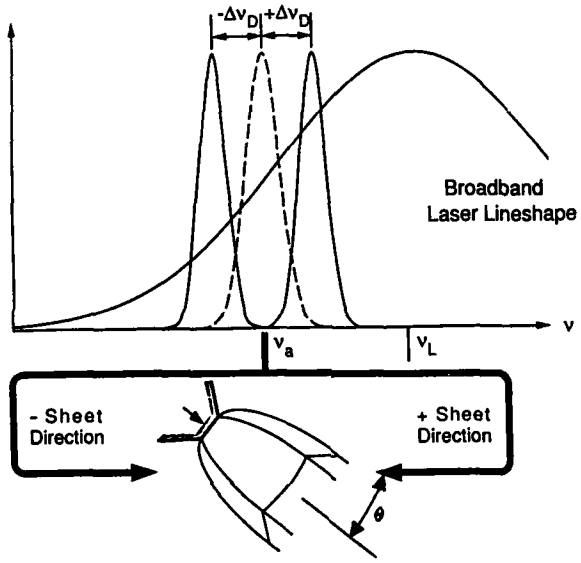

Figure 1. Schematic diagram showing the imaging geometry and the velocity induced Doppler shift effect.

The flow facility used to investigate the broadband concept consists of a chamber fitted with UV-silica windows in which a converging conical quartz nozzle was mounted. Nitrogen seeded with 0.5% NO was supplied to the nozzle at a reservoir pressure of $P_0 = 760$ Torr and at room temperature. After passing through the 1.65 mm ID nozzle the flow was expanded into the main chamber with a background pressure of 5 Torr, maintained by continuous pumping. The maximum flow velocity is ~1 km/s, corresponding to a maximum Doppler shift with respect to the laser direction (oriented θ=60° to the flow direction) of 4.4 GHz. NO florescence was obtained by pumping the $Q_1(6)$ line in the A-X (0-0) system at 226.234 nm with an excimer pumped dye laser doubled in beta barium borate. The doubled linewidth was measured to be 10.5 GHz FWHM. The laser beam was expanded into a thin, ~100 μm thick, sheet which intersected the flow through the jet centerline. The broadband fluorescence was imaged through a UG-5 Schott glass filter and an f/1.2 lens onto an intensified CCD array detector (240x512 pixels).

Figure 2 shows a corresponding false-color display of the velocity component (θ=60°). Strong radial flow may be seen as sudden changes of signal in passing from the jet core (axial flow) through the incident shock (strong outflow) through the

cocoon (axial flow) and finally to the shear layer (radial inflow). Though the maximum velocity occurs near the Mach disk on the jet centerline, the maximum velocity component at 60° occurs above centerline and closer to the nozzle as evidenced by the region of very high signal at this location. For this image we estimate a random error (noise in signal) of 2% and systematic errors of <3% due to variations in absorption lineshape with pressure and temperature, <5% from nonlinear lineshape, and <10% from the measured laser linewidth. The S^+ and $S^\pm$ data have excellent signal-to-noise throughout the image, even though the gas density varies over nearly three orders of magnitude. The signal variation with gas density is partially balanced by the temperature dependence of the $Q_1(6)$ line.

Figure 2. Velocity image showing the velocity component at θ=60° to the flow axis. The vertical striations are a laser sheet artifact. White corresponds to 780 m/s and black corresponds to -110 m/s.

A promising extension of the technique described here is to employ a second laser (possibly a second dye laser driven with the same pump laser) tuned to pump a different transition in the same species. The second laser, delayed in time with respect to the first laser, would be employed to obtain a second component of velocity, using two additional cameras to record the $S^\pm$ and S^+ images as described above. The sum images from each laser, $S^\pm(\lambda_1)$ and $S^\pm(\lambda_2)$, which correspond to images of the non-Doppler shifted flow, could then be used to obtain simultaneous images of temperature and of the partial pressure of the absorbing species[3].

This work was supported by the U.S. AFOSR under contract 87-0057.

1. R. M. Measures, J. Appl. Phys., 39, 5232-5245, (1968).
2. B. Hiller and R. K. Hanson, Appl. Opt., 27, 33-48, (1988).
3. R. K. Hanson, *21st Symposium (International) on Combustion*, (The Combustion Inst., 1986), p1677.
4. P. H. Paul, M. P. Lee and R. K. Hanson, (submitted to Opt. Lett., Sept., 21, 1988).

IN-SITU DETECTION OF GAS PHASE SPECIES IN THE FILAMENT-ASSISTED DIAMOND GROWTH ENVIRONMENT

F.G. Celii,* P.E. Pehrsson, H.-t. Wang, H.H. Nelson and J.E. Butler
Chemistry Division, Naval Research Laboratory, Washington, D.C. 20375-5000

ABSTRACT

The use of in-situ optical diagnostics for probing the gaseous chemistry in the chemical vapor deposition (CVD) of diamond is described. Both radical (H, CH_3) and stable (CH_4, C_2H_2, C_2H_4) species have been detected. We report here the resonance-enhanced multiphoton ionization (REMPI) detection of CH_3 and atomic hydrogen under diamond CVD conditions. The H atom concentration, found to be quite sensitive to initial CH_4/H_2 fraction (F_0), decreased with increasing F_0 and was severely depleted with F_0= 3.0% and filament temperatures below 2200 C. Our present model of the filament-assisted gas phase environment is one in which thermodynamically-favored species (e.g., C_2H_2, CH_3) are formed at high temperature near the filament, followed by depletion of the more reactive species during transport to the diamond growth surface. An interference effect due to third harmonic generation in atomic hydrogen was also observed in the REMPI experiments.

INTRODUCTION

The outstanding material properties of diamond, such as extreme hardness and high thermal conductivity,[1] are well known. The same properties make diamond exceedingly difficult to modify (*e.g.*, by machining or doping). Since modification can more easily be accomplished during vapor phase deposition, diamond CVD is of great practical importance. Crucial to the development of improved deposition techniques is an understanding of the mechanisms leading to preferential formation of diamond, a metastable form of carbon under typical CVD temperature and pressure conditions. While it is known[2] that supersaturation of atomic hydrogen is important for diamond deposition, the postulated carbon-transport species are generally hydrocarbon pyrolysis products, most notably CH_3,[2,3] and reactive carbon species, such as C.[4] Only recently have in-situ gas phase measurements[5,6] enabled testing of these hypotheses.

EXPERIMENTAL

The chamber used for the deposition of diamond films and IR absorption measurements has been described previously.[5] Briefly, a tungsten filament was suspended 1.5 cm above a substrate (e.g., Si wafers or Ni foil) and mounted in the center of a stainless steel 6-way cross. For the REMPI experiments, the substrate holder was biased to provide efficient collection of photoelectrons at a Pt probe wire inserted 2-4 mm above the subtrate and 1-2 mm from the focal volume of the laser.[7] Typical growth conditions utilized a slow flow (100 sccm) of <1.0% CH_4 in H_2 at 25 Torr total pressure. With the filament temperature (T_{fil}) at ~2000 C, the substrate temperature is maintained in the range necessary for diamond growth (~900 C). A focussed dye laser beam (1-15 mJ/pulse, $\Delta\nu \sim 0.2\ cm^{-1}$), made 1 or 2 passes through the chamber for the laser-excited fluorescence (LEF) and REMPI experiments.

RESULTS AND DISCUSSION

The films deposited in this chamber were analyzed using Raman spectroscopy, Auger electron spectroscopy, X-ray photoelectron spectroscopy, scanning electron microscopy and x-ray diffraction, and were shown to be polycrystalline diamond.[5] All spectroscopic investigations were conducted under similar diamond growth conditions, although deposits were not always analyzed.

With F_0= 0.5% and T_{fil}= 2000 C, the following gas phase species concentrations present during diamond CVD were determined from infrared absorption measurements: CH_4, $8 \pm 3x10^{14} cm^{-3}$ (~50 mTorr @ 300 C); CH_3, $2 \pm 1.5x10^{12}$; C_2H_4, $6 \pm 2x10^{12}$; and C_2H_2, $2 \pm 1x10^{14}$. No absorption lines due to C_2H_6 or stable C_3H_y species were

found. These observations can be rationalized by consideration of the initial gas mixture at elevated temperatures (1300<T<2500 C), where C_2H_2 is the thermodynamically-favored carbon-containing molecule. LEF detection of transient species including C_2, CH and C_3 was attempted, but only a weak signal tentatively assigned to C_3 was seen. The absence of C_2 and CH in detectable concentration indicates that while these species may be produced at the hot filament, they are consumed by reactions occuring at lower temperature during transport to the surface. Harris, *et al.*[6] also observed significant conversion of CH_4 to C_2H_2 and used kinetic modeling to predict radical species concentrations, which are in agreement with our results. As a results of these studies, it is found that the probable carbon-transport species in this system are CH_3, C_2H_2, CH_4 and C_2H_4, with preference given to CH_3 and C_2H_2 based on reactivity.[6]

The 2+1 REMPI band at 333.5 nm[8] was employed for in-situ detection of CH_3. The spatial resolution of the REMPI detection provides relative concentration measurements in a volume directly above the growth surface. Both the CH_3 REMPI signal and the C_2H_2 concentration (from IR absorption) increased as a function of F_0 (Fig. 1), with the C_2H_2 growing at perhaps a faster rate.

The concentration of atomic hydrogen was monitored[7] using the 3+1 REMPI line at 364.7 nm.[9] With a single pass (travelling wave–TW) geometry, the REMPI feature (Fig. 2(a)) shifted to shorter wavelength as T_{fil} increased, reaching 364.54 nm for T_{fil}= 2350 C. The scan shown in (Fig. 2b) was obtained using standing-wave (SW) excitation (a spherical mirror re-focussed the UV beam back along the optical axis). An additional REMPI feature observed at 364.68 nm increased in intensity, but did not shift wavelength with increased T_{fil}. These observations are consistent with theoretical predictions[10] and experimental verifications[11] of an interference effect between odd harmonics of the laser field. In our case, the third harmonic light at 121.57 nm, (generated in atomic hydrogen) drives the 2p population 180° out of phase from the harmonic (365.7 nm), which results in elimination of the REMPI signal in the TW geometry. The third harmonic field is suppressed in the SW case, so the resonant REMPI signal is observed. The non-resonant REMPI feature, also produced through 4-wave mixing, is present in both excitation geometries. The shift in wavelength of

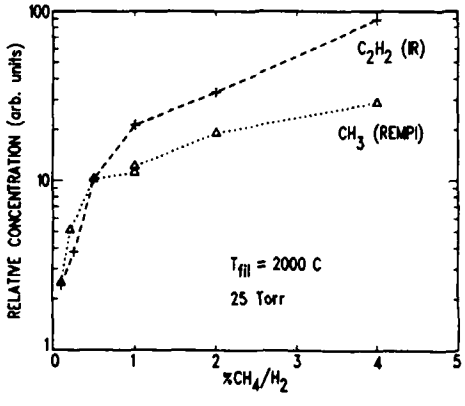

Figure 1: Relative concentrations of C_2H_2 (crosses, from infrared absorption), and CH_3 (triangles, REMPI measurements) *vs.* F_0. The IR measurements are not spatially resolved.

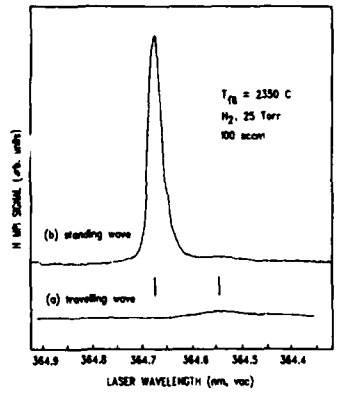

Figure 2: Observed H atom REMPI signals: (a) non-resonant REMPI signal with TW excitation; (b) With SW excitation, the dominant REMPI signal occurs resonantly with the 2p ← 1s transition.

this feature with T_{fil} is qualitatively consistent with the atomic hydrogen concentration change deduced from the intensity of the 365.68 nm peak.

The T_{fil} dependence of the H atom REMPI signal at 365.68 nm for pure H_2 (Fig. 3(a)) is in agreement with the known thermodynamics for H_2 dissociation. The signal attenuation at F_0= 0.5% and 1.0% reflects a loss in H atom concentration, probably due to gas-phase reactions. The F_0=3% curve (Fig. 3(d)) suggests a poisoning of the filament surface resulting in severely reduced H atom concentration for T_{fil} less than 2200 C. The diminished H atom flux for F_0>1% correlates with observations[12] of increased deposition of graphitic and amorphous carbon under these conditions, whereas the measured concentration of CH_3 and C_2H_2 both increase with F_0 (Fig. 1). We suggest that the primary role of atomic hydrogen in diamond growth is surface-related (e.g., dangling surface bond termination, and/or preferential etching of non-diamond carbon forms), rather than generation of gas-phase intermediates.

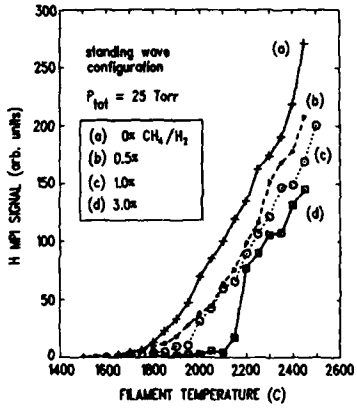

Figure 3: Relative H atom concentrations *vs.* filament temperature. The reactant CH_4/H_2 fractions (F_0) are given. The lines are merely to connect data points of a given F_0. All data are for a filament-probe separation of 8 mm.

ACKNOWLEDGEMENTS

We thank Dr. Earl Skelton for the X-ray diffraction measurements and Drs. John Reintjes, Steve Harris, H. Doug Ladouceur and Ms. Tina Shih for helpful and insightful discussions. This work was supported in part by the Office of Naval Research.

REFERENCES

* National Research Council Postdoctoral Fellow.
1. J.E. Field, *"The Properties of Diamond,"* Academic Press, New York, 1979.
2. For excellent reviews, see: R.C. DeVries, *Ann. Rev. Mater. Sci.*, **17**, 161 (1987); J.C. Angus and C.C. Hayman, *Science*, **241**, 913 (1988); A.R. Badzian and R.C. DeVries, *Mat. Res. Bull.*, **23**, 385 (1988).
3. Y. Hirose and Y. Terasawa, *Jap. J. Appl. Phys.*, **25**, L519 (1986).
4. S. Matsumoto, Y. Sato, M. Tsutsumi and N. Setaka, *J. Mater. Sci.*, **17**, 3106 (1982).
5. F.G. Celii, P.E. Pehrsson, H.-t. Wang, and J.E. Butler, Appl. Phys. Lett., 52, 2043 (1988).
6. S. J. Harris, A. M. Weiner and T. A. Perry, *Appl. Phys. Lett.*, **53**, 1605 (1988).
7. F.G. Celii and J.E. Butler, *Appl. Phys. Lett.*, submitted for publication.
8. J.W. Hudgens, T.G. DiGuiseppe and M.C. Lin, *J. Chem. Phys.*, **79**, 571 (1983).
9. P.J.H. Tjossem and T.A. Cool, *Chem. Phys. Lett.*, **100**, 479 (1983).
10. D.J. Jackson and J.J. Wynne, *Phys. Rev. Lett.*, **49**, 543 (1982); M.G. Payne, W.R. Garrett and W.R. Ferrell, *Phys. Rev. A*, **34**, 1143 (1986).
11. J.H. Glownia and R.K. Sander, *Phys. Rev. Lett.*, **49**, 21 (1982).
12. B. Singh, Y. Arie, A.W. Levine, and O.R. Mesker, *Appl. Phys. Lett.*, **52**, 451 (1988).

SIMULTANEOUS DETERMINATION OF TEMPERATURE AND SPECIES CONCENTRATIONS OF HIGH TEMPERATURE GASES USING TUNABLE LASER ABSORPTION SPECTROSCOPY

X. Ouyang, P. L. Varghese, and D. S. Cline
The University of Texas at Austin, Austin, TX 78712

ABSTRACT

A systematic and practical method was developed to retrieve temperature and species concentrations from absorption spectra with multiple overlapping lines. The technique was used to make measurements in a heated gas mixture.

INTRODUCTION

Continuously tunable laser absorption spectroscopy has several advantages over other optical methods, but the application of the technique to high temperature gas measurements was greatly restricted by difficulties in data reduction.[1-3] The techniques developed previously are not very practical. For temperature measurement, one had to find two closely spaced absorption lines from the same absorption species under strict conditions.[1,2] Concentration measurements required that a single fully resolved line be recorded.[3] These requirements are often difficult or impossible to meet in real combustion measurements, since the spectra of the major and minor combustion species often overlap, especially at high temperatures.

In this work, an experimental data reduction technique was developed to relax the restrictions described above. The new technique can deal with absorption spectra with multiple overlapping lines from several absorbing species, thus making absorption measurements much more practical. The retrieval of temperature and concentrations requires two steps: first the experimental record is fitted to a mathematical model, then the temperature and concentrations are calculated from the model parameters extracted from the curve fit. In this paper, the technique is discussed, and an example is given to demonstrate its application.

THE CURVE FIT MODEL AND PROGRAM

The experimentally recorded transmissivity as a function of frequency, $\tau(\nu)$, is equal to the ratio of the transmitted and incident laser intensity, I and I_0 respectively. It is related to the absorption coefficient α (= partial pressure × integrated absorption = pS), the Voigt line shape function, V, (with line position and line broadening parameters ν_0 and y respectively), and a base line shift parameter, Δ. The mathematical model used is:

$$\tau(\nu) = \frac{I(\nu)}{I_0(\nu)} = \exp\left(- A \sum_{ij} \alpha_{ij} V\left(\frac{\nu - \nu_{0ij}}{B}, y_{ij}\right) \right) + \Delta. \qquad (1)$$

Here *i* and *j* are indices for absorption line and species respectively. The constants A and B are related to each other by $A = L/(B\sqrt{\pi})$ where L is the absorption path length of the laser beam. Adjusting B, so that the collisional broadening parameters y_{ij} in the Voigt functions are around unity, makes the curve fitting procedure more efficient. The parameter y_{ij} is related to the normalized collision width γ_{ij} by $y_{ij} = 2\gamma_{ij}p/B$, where p is the total pressure of the gas.

There are several advantages of this model. Unlike previous models, all the parameters in the new model are linearly independent and can be determined directly from a curve fit procedure. We use the Voigt line shape here since the parameters in the Voigt function are relatively insensitive to experimental noise. When collision narrowing is significant the Voigt function cannot be used to determine true line shape parameters.[4] However, Eq. 1 is still a very

good model for the determination of temperature and concentration because only the absorption coefficients α_{ij} are used in the calculation and the values of α_{ij} from the curve fit are not sensitive to the line shape model used.[5] Fitting the transmissivity directly avoids non-linear manipulation of the experimental data, and permits the addition of the shift parameter Δ to the curve fit procedure. The introduction of the shift parameter makes the data acquisition and analysis much easier since the shift of the experimental record from the base line can be corrected automatically by the curve fit procedure.

A FORTRAN code, TFIT, has been developed using Eq. 1 as a fitting function. The algorithms used in TFIT are the same as in the previously developed code GALFIT.[5] TFIT can deal efficiently with absorption records with multiple overlapping lines.

DETERMINATION OF TEMPERATURE AND PARTIAL PRESSURES

The absorption coefficients extracted from the curve fit procedure are used to determine the temperature and partial pressures. The temperature is first calculated from the ratio of the sums of the absorption coefficients of two groups of lines (I and II) from the same absorbing species,

$$\frac{\sum_m \alpha^{I}_{mj}}{\sum_n \alpha^{II}_{nj}} = \frac{\sum_m S^{I}_{mj}(T)}{\sum_n S^{II}_{nj}(T)} \approx F_j(T) \tag{2}$$

If the temperature can be calculated from several species, averaging the results reduces error by cancelling possible systematic errors in the F functions arising from neglect of weak lines or inaccurate integrated absorptions. After the temperature is calculated, the partial pressure of the j-th species is calculated by

$$p_j = \frac{\sum_i \alpha_{ij}}{\sum_i S_{ij}(T)} . \tag{3}$$

In constructing Eqs. 2-3, two primary arguments were used. Firstly, when developing TFIT it was found that the curve fitted value of $\sum\alpha_{ij}$ of a group of lines is not affected by strong overlapping of individual lines, provided the group as a whole is reasonably well resolved. Thus line overlap does not restrict the applicability of this procedure. Secondly, statistics show that the uncertainty in $\sum S_{ij}(T)$ is less than the uncertainty in the individual S_{ij}. Thus there is an advantage to using multiple (possibly overlapping) lines to infer temperature and concentrations.

EXAMPLE

Fig. 1 is a set of absorption data near 2874 cm^{-1} obtained with a tunable diode laser in a formaldehyde-methane (H_2CO-CH_4) mixture in a heated absorption cell. The fitted curve is also shown in the figure. There are 13 absorption lines in the frequency range scanned: 5 H_2CO lines marked by F, and 8 CH_4 lines indicated by M. Only the 10 strongest lines are included in the curve fitting procedure. The other 3 weak lines cannot be resolved. Line F2 is very weak, and Lines M3 and F5 are overlapped by much stronger lines. The curve fit results are shown in Table 1.

The temperature and partial pressure calculations are shown in Table 2. The table also gives the thermocouple measurement and the mixture composition computed from measured partial pressures. The temperature of the mixture is calculated both from the H_2CO and CH_4 lines. Some of the H_2CO lines recorded have been assigned to the ν_5 band;[6] the assignments are

shown in the Table. Lines F1 and F3 are used for the calculation. The temperature dependence of the integrated absorption of these lines is calculated from the expression,

$$S(T) = S(T_0)\frac{Q(T)}{Q(T_0)}\frac{T}{T_0}\exp\left(\frac{hcE''}{k}\left(\frac{1}{T_0}-\frac{1}{T}\right)\right)\frac{1-\exp(-hc\nu/kT)}{1-\exp(-hc\nu/kT_0)} \qquad (4)$$

where $S(T_0)$ is the integrated absorption at a reference temperature T_0, Q is the internal partition function, which was calculated from the RRHO model, E" is the energy of the lower level of the absorption transition, ν is the transition frequency, h is Planck's constant, c is the velocity of light, and k is Boltzmann's constant. For CH_4, lines M4 and M6 are used for the temperature calculation. The temperature dependence of the strengths of these lines were determined directly from separate experiments. Equation 4 was not used for the calculation since these transitions have not been assigned.

The temperatures calculated from the CH_4 and H_2CO lines are not equal. When considering the systematic errors due to the unresolved weak lines M3 and F5 and the behavior of the corresponding F functions (Eq. 2) used to calculated the temperatures, one finds that the temperature estimated from formaldehyde is over-predicted while the temperature from CH_4 lines is under-predicted. Averaging helps to cancel the systematic errors and the average agrees well with the thermocouple measurement. The exact correspondence of the two results is fortuitous.

The partial pressure calculations are shown in Table 2. The partial pressures of methane and formaldehyde from the absorption measurements are both within the uncertainty of the mixture composition. Note that very good results are obtained even with weak unresolved lines. In practical combustion measurements such departures from ideal conditions are to be expected.

CONCLUSIONS

A systematic and practical method was developed for experimental data analysis of tunable laser absorption measurements for homogeneous conditions. The new technique relaxes many of the restrictions which had been imposed on the selection of laser operation frequency. The requirements for the new technique are: (1) the temperature dependence of the integrated absorptions for some of the reasonably well resolved lines or groups of lines be known; (2) the slope of the F function in Eq. 2 be large enough to achieve the necessary sensitivity for the temperature measurements. The feasibility of simultaneous temperature and multiple species concentration determination for high temperature gases was demonstrated by an experiment in a heated absorption cell. This work will be extended to the non-homogeneous case and the feasibility of temperature and concentration profile measurements by tunable laser absorption will be investigated.

This work was supported by the Center for Energy Studies, The University of Texas at Austin. Additional support was provided by the National Science Foundation under grant ECS-8604411.

REFERENCES

1. S. A. Gearhart and M. E. Thomas, Appl. Opt. **27**, 3630 (1988).
2. R. K. Hanson and P. K. Falcone, Appl. Opt. **17**, 2477 (1978).
3. R. K. Hanson, P. A. Kuntz, and C. H. Kruger, Appl. Opt. **16**, 2045 (1977).
4. P. L. Varghese and R. K. Hanson, Appl. Opt. **23**, 2376, (1984).
5. X. Ouyang and P. L. Varghese, "A Reliable and Efficient Program for Fitting Galatry and Voigt Profiles to Spectral data on Multiple Lines", Applied Optics, in press.
6. L. R. Brown, R. H. Hunt, and A. S. Pine, J. Mol. Spectrosc. **75**, 406 (1979).

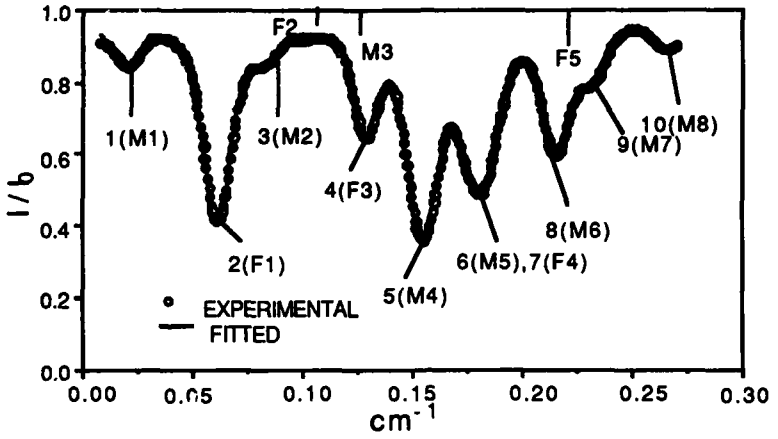

Figure 1. Absorption record from a H_2CO-CH_4 mixture at 2874 cm^{-1} and the fitted curve

Table 1. Curve fitting results of experimental data of Fig.1 by TFIT

INDEX	SPECIES	ID	TRANSITION	ω_0(cm^{-1})	α (cm^{-2})
1	CH_4	M1		0.0198	0.61×10^{-4}
2	H_2CO	F1	$13_{2,12} \leftarrow 13_{1,13}$	0.0615	2.72×10^{-4}
3	CH_4	M2		0.0835	0.41×10^{-4}
4	H_2CO	F3	$27_{2,25} \leftarrow 27_{1,26}$	0.1288	1.05×10^{-4}
5	CH_4	M4		0.1552	3.42×10^{-4}
6	CH_4	M5		0.1772	1.27×10^{-4}
7	H_2CO	F4	$3_{2,2} \leftarrow 2_{1,1}$	0.1845	1.16×10^{-4}
8	CH_4	M6		0.2156	1.49×10^{-4}
9	CH_4	M7		0.2316	0.61×10^{-4}
10	CH_4	M8		0.2661	0.36×10^{-4}

Table 2. Temperature and concentration determination from curve-fitted absorption coefficients

Temperature				
H_2CO	$F = \alpha_2/\alpha_4 = 2.6$	$\Rightarrow T_{H_2CO} = 480$ K	$\Rightarrow$	$T_{ave} = 473$ K
CH_4	$F = \alpha_5/\alpha_8 = 2.3$	$\Rightarrow T_{CH_4} = 467$ K		
Thermocouple				T = 473 (±2) K

Partial pressures		Absorption	Actual
P_{H_2CO}	$= (\alpha_2+\alpha_4)/(S_{F1}+S_{F3})$	= 0.81 Torr	0.79 (± 0.05) Torr
P_{CH_4}	$= (\alpha_5+\alpha_8+\alpha_9)/(S_{M4}+S_{M6}+S_{M7})$	= 37.9 Torr	37.95 (± 0.1) Torr

SIMULTANEOUS CONCENTRATION MEASUREMENT OF CO_2 AND H_2 WITH MULTIPLEX CARS IN COMBUSTION ENVIRONMENTS

J. P. Singh and F. Y. Yueh
Diagnostic Instrumentation and Analysis Laboratory
Mississippi State University
Mississippi State, Mississippi 39762

ABSTRACT

Multiplex CARS was used to measure CO_2 and H_2 concentrations simultaneously in a combustion environment. CARS spectra of pure CO_2 and various mixtures of CO_2, N_2 and CO_2, N_2, H_2 were recorded using a quartz cell kept in a furnace at various temperatures. The computer code was tested with the CO_2 spectra taken at different temperatures. The CO_2 and H_2 concentrations extracted from CARS data were compared with preanalysis data provided by the vendor. The sensitivity of H_2 concentration measurements using the pure rotational S(5) line was compared with those using the S(4) and S(9) lines.

INTRODUCTION

Coherent anti-Stokes Raman Spectroscopy (CARS) is an advanced laser based technique for nonintrusive measurement of temperature and species concentration in hostile, high luminous and harsh combustion environments. It can provide measurements with high spatial and temporal resolution. It also can be collected with high efficiency due to its laser like signal. This technique has been successfully used to probe many combustion environments.[1]

Since carbon dioxide is a principal combustion product, it is possible to extract the temperature and CO_2 concentration from the CO_2 CARS spectra. CO_2 CARS temperature measurement[2] and preliminary work on CO_2 concentration measurement[3] have been reported. The main aim of the present study was to test the computer code of CO_2 CARS spectra using the data taken in a furnace with known temperatures and concentrations. This study can supply valuable information for future CO_2 concentration measurements.

It has been found that the hydrogen pure rotational S(5) line, which can be used to monitor the H_2 concentration, is in the spectral region of CO_2 CARS.[3] Recently Yueh and Beiting[4] have used the pure rotational S(9) line of hydrogen to estimate H_2 concentration. Since the H_2 S(9) line is not well populated until about 1000 K, it is difficult to extract the H_2 concentration from this line. The hydrogen pure rotational S(4) line has been used qualitatively to estimate H_2 concentration in a Scramjet engine recently.[4] A series of calculations have been performed to compare the detection sensitivity of the H_2 S(5) line with that of the H_2 S(4) and S(9) lines.

EXPERIMENTAL

The experimental configuration used in the present experiment was modified from one used previously.[3] In brief, the output of a Nd-YAG

laser was frequency doubled to yield the 532 nm (green) laser beam. The residual Nd-YAG beam from the frequency doubler was again frequency doubled and was used to pump the oscillator of the dye laser. One third of the main green beam was used to pump the amplifier of the dye laser. The residual main green beam was divided into two equal intensity and parallel beams. The green and dye laser beams were kept parallel to each other which is needed for BOXCARS phase matching geometry. Ten percent of the green and dye laser beams were reflected from a special beam splitter, which was constructed with two 532 nm and one 600 nm reflecting mirrors of 1 inch diameter, and then focused into a reference cell to generate a nonresonant CARS reference signal. The residual beams were focused into the test media to generate the CARS signal. The CARS signal and the laser beams were recollimated through a lens. Then the CARS signal was separated from the laser beams using beam blocks and dichroic mirrors. Signals from the test media and the reference cell were aligned so that both could be seen simultaneously (at different heights) on the detector.

The preanalyzed gas sample was placed in a quartz cell which was placed in a furnace. The temperature inside the furnace was varied up to 1500 K and was monitored with a thermocouple.

RESULTS AND DISCUSSION

CO_2 CARS spectra have been recorded in a CH_4/O_2 flame with the dye laser center wavelength at 5730 A. These spectra have two CO_2 band progressions at 1388 cm^{-1} and 1285 cm^{-1}, respectively. Since the intensity of the 1388 cm^{-1} progression is higher than that of the 1285 cm^{-1} progression, the 1388 cm^{-1} progression was selected for the CO_2 concentration measurement. It has been found the pure rotational H_2 S(5) line at 1447 cm^{-1} is superimposed on the 13301 $\rightarrow$ 23301, 04401 $\rightarrow$ 14401 CO_2 bands of the 1388 cm^{-1} progression. This line was used for the H_2 concentration measurement. There is another H_2 line at 1246 cm^{-1} in the 1285 cm^{-1} CO_2 progression which has been assigned to the pure rotation S(4) line. The intensity of the S(4) line is weaker than that of the S(5) line due to nuclear statistics.

Some CO_2 CARS spectra were also recorded with the dye laser center wavelength at 5770 A. These spectra contained CO_2, H_2, and O_2 CARS signal which can be used to measure these three species concentrations simultaneously. To extract quantitative information from these spectra, the combined CO_2, H_2 and O_2 CARS spectra need to be carefully modeled. At present only combined CO_2 and H_2 data has been modeled. The CO_2 CARS spectra have been modeled using the new rotational constants for CO_2.[6] The Raman linewidth expression was obtained from Papineau and Pealat.[7] The computer code of CO_2 CARS has been tested by comparing the furnace data with the computer simulation spectra. In order to model the CO_2 CARS spectrum accurately, the dye laser profile has to be known accurately. Since the dye laser profile tends to shift during measurement, a nonresonant CARS signal recorded along with the CO_2 CARS furnace data was used to extract the dye laser profile. By using this method to obtain the dye laser profile the temperatures inferred from the CO_2 CARS furnace data were in good agreement with the thermocouple

temperatures. The fitting results of the CO_2 CARS data are shown in Figure 1.

CARS spectra of a premixed gas sample of CO_2, H_2 and N_2 were also recorded in a furnace of 900 K. These spectra were used to determine the hydrogen S(5) line position to be 1447.67 cm^{-1}. This line position was used for the combined CO_2 and H_2 model. A typical fit of the combined CO_2 and H_2 CARS spectrum is shown in Figure 2. The observed spectrum was taken 7 mm above a CH_4/O_2 flame. Both the CO_2 and H_2 concentrations were extracted from this spectrum.

The sensitivity of H_2 concentration measurement with the H_2 S(5) line was compared with that of the S(4) and S(9) lines. It depends on the intensity and position of the line with respect to the CARS signal of other molecules in the nearby spectral region. It was found that the S(5) line has less interference at flame temperature from other molecules than do the S(4) and S(9) lines. A series of intensity calculations for the S(4), S(5) and S(9) lines have been performed at various temperatures. The intensity ratios of S(5) to S(9) and of S(5) to S(4) were also calculated. These ratios are plotted in Figure 3. It shows the intensity of the S(5) line at a flame temperature of 2000 K is 17.5 times as high as that of the S(9) line and 7.23 times as high as that of the S(4) line. Obviously the H_2 concentration measurement is better performed by using the H_2 S(5) line than the S(4) or S(9) line.

CONCLUSIONS

CO_2 CARS spectra have been modeled more precisely than in previous work. The model has been successfully tested with the furnace data. The hydrogen pure rotational S(5) line has been included into the CO_2 CARS model to be used for H_2 concentration measurement. A study of the sensitivity of H_2 concentration measurement from S(5), S(9) and S(4) lines was performed. The results show the S(5) line has the best detection sensitivity among those lines.

REFERENCES

1. R. J. Hall and A. C. Eckbreth, Laser Applications, Vol. 5, J. F. Ready and R. K. Erf, Eds. (Academic, San Diego, 1984).
2. R. J. Hall and H. Stufflebeam, Appl. Opt. 23, 4319 (1984).
3. J. P. Singh and F. Y. Yueh, Proc. Int. Conf. Laser '87, 925 (1987).
4. F. Y. Yueh and E. J. Beiting, Appl. Opt. 27, 3233 (1988).
5. A. C. Eckbreth, T. J. Anderson and G. M. Dobbs, Appl. Phys. B45, 215 (1988).
6. L. S. Rothman, Appl. Opt. 25, 1795 (1986).
7. N. Papineau and M. Pealat, Appl. Opt. 24, 3002 (1985).

ACKNOWLEDGMENT

This work was supported by DOE Contract DE-AC02-80ET-15601.

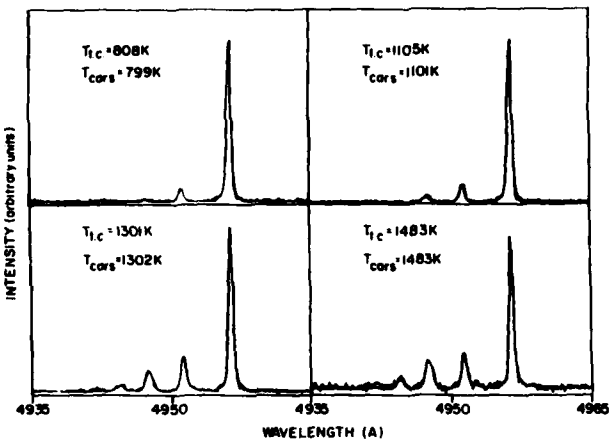

Fig. 1. Fitting of the computer simulated spectra with observed spectra at various temperatures in a furnace.

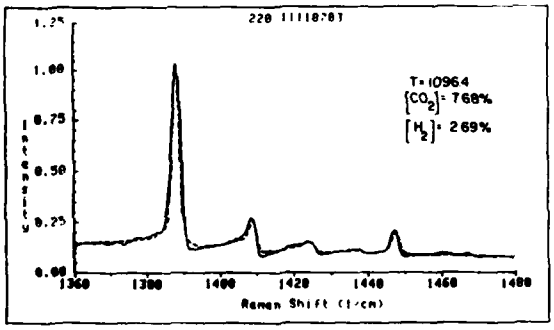

Fig. 2. A fit of the combined CO_2 and H_2 CARS spectrum taken in a CH_4/O_2 flame.

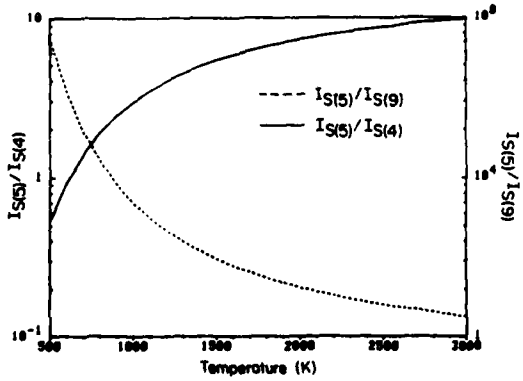

Fig. 3. Plot of $I_{S(5)}/I_{S(9)}$ and $I_{S(5)}/I_{S(4)}$ with temperature.

LASER-INDUCED FLUORESCENCE AND DISSOCIATION OF ACETYLENE IN FLAMES

George A. Raiche, David R. Crosley and Richard A. Copeland
Molecular Physics Laboratory, SRI International
Menlo Park, California 94025

ABSTRACT

Laser-induced fluorescence and photoinduced dissociation of acetylene is observed in both room temperature cells and low-pressure flames. Acetylene is excited via the $\tilde{A}$-$\tilde{X}$ electronic transition between 210 and 230 nm. The fluorescence exhibits long vibronic progressions due to the different equilibrium geometries; acetylene is trans-planar in the $\tilde{A}$ state and linear in the $\tilde{X}$ state. Intense fluorescence from electronically excited carbon radicals (C_2^*) is also observed upon resonant excitation of C_2H_2 at room and flame temperatures. In addition, a non-resonant laser-induced production of C_2^* is observed in the flame. The effects of C_2H_2 pressure (i.e., electronic quenching) and laser fluence on fluorescence are examined.

INTRODUCTION

Acetylene is an important chemical intermediate in hydrocarbon combustion and is likely a key species in soot formation. Although its fundamental spectroscopy and photophysics have been well studied,[1] its optical detection in the high temperature environment of flames has proven difficult.[2] Acetylene absorbs at many discrete wavelengths in the 210-240 nm region and fluoresces throughout the ultraviolet in the $\tilde{A}$-$\tilde{X}$ electronic system. In multiphoton experiments at 193 nm C_2H_2 photodissociates into electronically excited C_2^* and CH* radicals that emit throughout the visible.[3] We report here on the detection of C_2H_2 in both low-pressure flames and a room temperature flow cell via laser-induced fluorescence (LIF) and photodissociation methods. In these experiments the output of a frequency-doubled excimer-pumped dye laser (210 to 240 nm) excites C_2H_2, and the resulting fluorescence is dispersed by a monochromator and monitored with a photomultiplier tube. The amplified signals are then captured by a transient digitizer or a boxcar integrator.

ACETYLENE FLUORESCENCE AND PHOTODISSOCIATION

We have observed strong fluorescence signals from both acetylene and C_2^* following resonant excitation of rotationally resolved vibronic bands in the C_2H_2 $\tilde{A}$-$\tilde{X}$ electronic system. The ultraviolet and visible emissions resulting from excitation of the $v_3 = 4$ level of the A-state at 215.9 nm are depicted in Figure 1, which has not been corrected for the wavelength response of the detection setup. The dominant features in the spectrum are emissions from the C_2 Swan ($d^3\Pi_g$-$a^3\Pi_u$) and Deslandres-d'Azambuja ($C^1\Pi_g$-$A^1\Pi_u$) systems, although C_2H_2 $\tilde{A}$-$\tilde{X}$ LIF is also observed. The C_2^* emission signals rise promptly with the laser pulse, indicating a unimolecular mechanism for formation of both excited states. Higher resolution emission scans reveal vibrational structure and show population up to v = 3 in the C state and v = 6 in the d state.

The apparent ratios of the C_2^* to $C_2H_2^*$ signal intensities are the result of three experimentally controlled parameters: C_2H_2 pressure, laser fluence, and excited vibrational level in the $\tilde{A}$ state. From the temporal evolution of fluorescence for the different emissions, individual decay constants are determined by fitting the decay to a

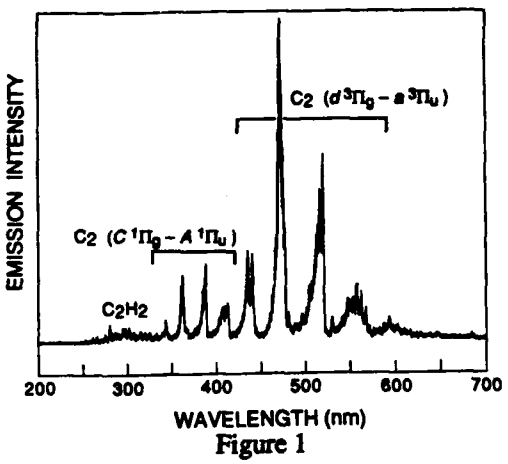

Figure 1

single exponential, while phenomenological total removal rate constants are taken from the slope of the line relating these decay constants to C_2H_2 pressure. The intercepts correspond to the radiative lifetime. We find that the emission from C_2H_2 is rapidly quenched ($\sim 5 \times 10^{-10}$ cm^3 s^{-1} for $\nu_3 = 3$) while quenching of the C and d states of C_2^* is approximately two and four times slower, respectively. At the ~1 Torr pressure of Fig. 1, the C_2^* d-state signal is enhanced relative to the other emissions and probably will be stronger in higher pressure flame conditions.

Another contribution to this ratio is the non-linear nature of the C_2^* production mechanism. While a detailed mechanism has not been isolated, the energetic requirements of the dissociation of C_2H_2 to C_2^* (C, d) dictate that at least one additional photon must be absorbed by the $\tilde{A}$ state in order to photodissociate to electronically and vibrationally excited C_2. In this wavelength region, we observe C_2^* production only with resonant excitation of the $\tilde{A}$ state. In fact, dissociation through a 1+1 mechanism would require the concerted elimination of H_2, an unlikely event. A more likely scenario involves absorption of one photon to the $\tilde{A}$ state and two more photons by the $\tilde{A}$ state (or a rapid predissociation product, possibly C_2H) to allow sequential elimination of hydrogen. Our power dependence studies indicate that the C_2^* signal scales approximately as the laser power squared, while the C_2H_2 signal is slightly less than linear between ~0.2 and 2.0 GW cm^{-2}. Because of these different laser power functions, the C_2^* signals are strongly enhanced at high power and tight focusing (Fig. 1, ~5 GW cm^{-2}).

The ratio also strongly depends on the C_2H_2 excitation wavelength. For a fixed laser power C_2^* signal intensity increases with increasing ν_3' in the $\tilde{A}$ state. At ~1.4 GW cm^{-2}, the C_2^* signal varies from approximately five times the C_2H_2 LIF signal to negligible, as excitation in ν_3 varies from 3 to 1 quanta. An apparent threshold for C_2^* production, observed between $\nu_3' = 1$ and $\nu_3' = 2$ (231.0 and 225.6 nm, respectively), is consistent with an excitation mechanism that involves a rapid predissociation from C_2H_2 $\tilde{A}$ to a C_2^* precursor, possibly C_2H. In summary, high pressures, high laser fluence, and shorter excitation wavelengths all favor the production of C_2^* emission over C_2H_2 LIF.

ACETYLENE FLAME STUDIES

All of the above-mentioned factors determine that C_2^* emission may be a very suitable diagnostic for C_2H_2 flame concentrations. Our studies have shown that the excitation spectrum of acetylene, useful as a "fingerprint" in room temperature experiments, can also be used to identify acetylene in the flame environment with rotational resolution. Using C_2^* laser-induced emission as the acetylene diagnostic, and tuning to a known C_2H_2 transition, we measure a one-dimensional spatial distribution

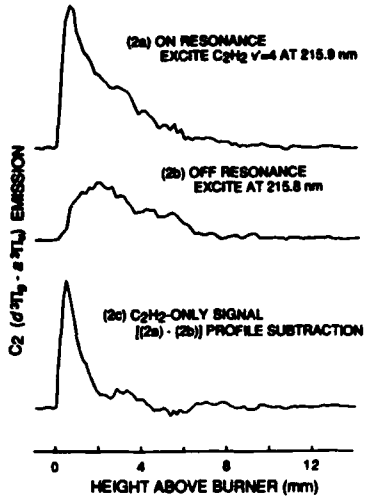

Figure 2

of C_2^* signal in a stoichiometric, 3 Torr C_2H_2/O_2 flame. Figure 2a is such a profile of C_2^* emission intensity as a function of the height of the laser beam above the burner surface. These profiles are useful as maps of acetylene concentrations in flames only to the extent that the C_2^* emission signal can be directly related to C_2H_2 concentration. Room temperature C_2^* production is strictly a resonant process through C_2H_2; however, the laser-correlated production of C_2^* in flames is observed even when the excitation laser is tuned off a C_2H_2 resonance, as shown in Fig. 2b. This nonresonant C_2^* excitation constitutes an interference to its use as a diagnostic for acetylene. In Fig. 2a note the sharp rise and slower decay of the signal over ~5 mm. In Fig. 2b note the slow signal rise, which we also attribute to C_2^* emission. Since the non-resonant background signal is not a strong function of laser wavelength, it also contributes to the Fig. 2a signal which therefore represents the sum of the resonantly and nonresonantly produced C_2^* emissions. A subtraction, representing the emission directly attributable to C_2H_2 excitation, is shown in Fig. 2c. Note the sharp rise and decay of the emission signal, indicating the rapid consumption of acetylene in the flame front. Clearly, some of the C_2^* laser-induced emission observed in the flame cannot be directly attributed to C_2H_2 excitation. The emission spectrum of the nonresonant excitation is identical with that of the resonantly-produced emission, suggesting a common excitation pathway following thermal or laser-induced dissociation of C_2H_2. In most flames this interference has not hampered our detection of C_2H_2, and upon further investigation should prove interesting in its own right.

ACKNOWLEDGEMENT

This work is supported by the Aero Propulsion Laboratory of the Air Force Wright Aeronautical Laboratories and the Physical Sciences Department of the Gas Research Institute.

REFERENCES

1. J.K.G. Watson, M. Herman, J. C. Van Craen, and R. Colin, J. Mol. Spectrosc. 95, 101 (1982); J. C. Stephenson, J. A. Blazy, and D. S. King, Chem. Phys. 85, 31 (1984); J. C. Van Craen, M. Herman, R. Colin, and J.K.G. Watson, J. Mol. Spectrosc. 111, 185 (1985); M. Fujii, A. Haijima, and M. Ito, Chem. Phys. Lett. 150, 380 (1988).

2. R. L. Farrow, R. P. Lucht, W. L. Flower, and R. E. Palmer, Proceedings of the Twentieth International Symposium on Combustion, p. 1307, The Combustion Institute, 1984.

3. J. R. McDonald, A. P. Baronarski, and V. M. Donnelly, Chem. Phys. 33, 161 (1978); H. Okabe, R. J. Cody, and J. E. Allen, Jr., Chem. Phys. 92, 67 (1985).

LASER-INDUCED FLUORESCENCE MEASUREMENT OF PLASMA ION DISTRIBUTION FUNCTIONS: ERRORS DUE TO SPATIALLY INHOMOGENEOUS LASER INTENSITIES

M.J. GOECKNER, J. GOREE, AND T.E. SHERIDAN
Department of Physics and Astronomy
The University of Iowa, Iowa City, Iowa 52242-1479
November 12, 1988

Abstract

When using laser-induced fluorescence to measure plasma ion velocity distribution functions, high power inhomogeneous laser intensities produce important undesirable changes in the Doppler broadened fluorescence line width. A basic model of laser-induced fluorescence is discussed. As typical examples, fluorescence from the ArII $3d'^2G_{9/2} \leftrightarrow 4p'^2F^0_{7/2} \rightarrow 4s'^2D_{5/2}$ transition with three spatial laser intensity modes are examined. The ion velocity distribution function can be measured correctly only if the maximum intensity for all regions of the laser beam is below the saturation broadening threshold. A procedure to determine if this is achieved is described.

Introduction

A correct measurement of low plasma ion energies is an important and difficult task.[1] A reliable diagnostic enables the accurate study of ion heating, ion acoustic waves, and related phenomena. These processes can be important in gas discharge, fusion, and other plasmas.[2] One possible diagnostic uses laser-induced fluorescence from the ions.

Laser-induced fluorescence,[3] LIF, may be used for a variety of measurements; here we consider measuring only ion velocity distributions. Ion velocity distribution functions are determined by measuring the Doppler broadened spectral line shape. Measurements of velocity distributions will be in error if other other processes broaden the spectral line.

Power broadening of the spectral line, an instrumental broadening encountered with the use of high intensity pulsed lasers, is the result of saturation of the probed transition for ions in a velocity range v to v + dv. Saturation occurs when the stimulated photon emission rate is balanced by the photon absorption rate and is much larger than the spontaneous photon emission rate. Increasing the laser intensity will increase the saturated velocity range but will not change this balance for velocities already saturated.

Power broadening can be reduced by decreasing the laser intensity. However, decreasing the laser intensity will lower the detected fluorescence signal. An optimum laser intensity will balance between a strong signal and minimal broadening. We have discussed three methods of optimizing the intensity for a spatially homogeneous laser beam in an earlier paper.[4] Inhomogeneous laser beams complicate these optimization methods.

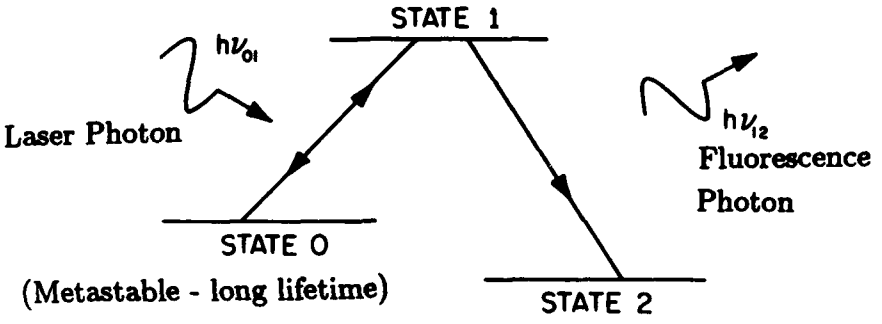

Fig. 1 - *Ion states in the LIF process. Laser photons, ν_{01}, are used to probe the 0 - 1 state transition. The collected fluorescence photons, ν_{12}, reveal the number of ions in state 1.*

When saturation broadening occurs in some areas of the laser beam and not others, the Doppler broadened fluorescence line is distorted. By examining how inhomogeneities in the laser intensity distort the fluorescence signal, this undesirable distortion can be avoided.

We examined three spatial intensity cases: a homogeneous laser beam, the sum of two homogeneous components, and a Gaussian spatial distribution. We show that the distortions take the form of false tails in the ion velocity distribution functions, which we call pseudo-temperatures.

Theory

The LIF process is dominated by transitions between three states of an ion. These states, labeled 0, 1, and 2, along with the laser photon, ν_{01}, and the fluorescence photon, ν_{12}, are shown in Fig. 1. The laser photons are used to probe the Doppler broadened 0 - 1 transition. The relative signal from the detected fluorescence photons is plotted as a function of the laser's tuned frequency. Doppler shift, $2\pi\Delta\nu = \mathbf{k}\cdot\mathbf{v}$, gives the velocity distribution function.

We consider only three spatial intensity modes, homogeneous, two component, and Gaussian. However, the fluorescence line shapes from two modes will be the same if there is a one to one and on to spatial mapping of the laser intensities.

The number of fluorescence photons detected in a solid angle, $d\Omega$, is[4]

$$\begin{aligned} N_{obs} &= \frac{d\Omega}{4\pi} A_{12} \int d^3x \int d^3v\, f_0(\mathbf{x},\mathbf{v},t=0) B_{10} \Phi (\Gamma\chi)^{-1} \Big[4\Gamma^{-1} \\ &\quad - \left(2\Gamma^{-1}(1+(1-\chi)^{-1/2}) - \tau_1 \chi (1-\chi)^{-1/2} \right) \\ &\quad \exp\left(-\frac{T}{2}\Gamma(1-(1-\chi)^{-1/2}) \right) \end{aligned}$$

PARAMETER	VALUE	UNITS	REFERENCE
$\delta\nu_l$	1.0	GHz	
λ_0	611.492	nm	5
A_{10}	0.212	$10^8 s^{-1}$	6
A_{12}	0.759	$10^8 s^{-1}$	6
B_{10}	121.9	$10^{11} m^2 (Js)^{-1}$	
B_{01}	97.55	$10^{11} m^2 (Js)^{-1}$	
τ_1	8.51	ns	
τ_0	≥ 1.0	ms	
T	17.0	ns	
m_i	39.962	amu	

Table 1 - *The parameters used in Figs. 2 - 4. They correspond to probing the ArII transition,* $3d'^2G_{9/2} \leftrightarrow 4p'^2F^0_{7/2} \rightarrow 4s'^2D_{5/2}$, *with a typical broad bandwidth high intensity pulsed laser. The laser intensity,* $I(\nu)$, *is assumed to be a Gaussian with a FWHM,* $\delta\nu_l$, *of 1.0 GHz.*

$$+\left(2\Gamma^{-1}(1-(1-\chi)^{-1/2})-\tau_1\chi(1-\chi)^{-1/2}\right)$$
$$\exp\left(-\frac{T}{2}\Gamma(1+(1-\chi)^{-1/2})\right)\Big] \ , \qquad (1)$$

where

$$\Gamma(\mathbf{x},\mathbf{v},t)=\left(\frac{1}{\tau_0}+\frac{1}{\tau_1}+(B_{01}+B_{10})\Phi\right),$$

$$\chi(\mathbf{x},\mathbf{v},t)=\frac{4}{\Gamma^2}\left[\frac{1}{\tau_0\tau_1}+\Phi\left(B_{01}(\tau_1^{-1}-A_{10})+\frac{B_{10}}{\tau_0}\right)\right],$$

and

$$\Phi(\mathbf{x},\mathbf{v},t)=\frac{1}{4\pi}\int_0^{+\infty} d\nu\ L(\nu,\nu_{01},\mathbf{v})I(\mathbf{x},\nu,t).$$

Here $\Phi(\mathbf{x},\mathbf{v},t)$ is an effective isotropic laser intensity, $L(\nu,\nu_{10},\mathbf{v})\,d\nu d\mathbf{v}$ is the absorption probability, $I(\mathbf{x},\nu,t)$ is the laser intensity, $f_0(\mathbf{x},\mathbf{v},t)$ is the distribution function for state 0, B_{01} is the Einstein coefficient of absorption for isotropic intensity light, B_{10} is the Einstein coefficient of stimulated emission from state 1 to state 0 for isotropic intensity light, A_{1i} is the Einstein coefficient of spontaneous emission from state 1 to state i, τ_i is the lifetime of state i, and ν_{10} is the transition frequency from state 1 to state 0.

The theoretical prediction of the fluorescence line shape is found by plotting N_{obs} as a function of the laser frequency. This theoretical line shape may be plotted as a function of energy by using the Doppler shift of the ion transition, $2\pi\Delta\nu = \mathbf{k}\cdot\mathbf{v}$, and the energy equation, $E = mv^2/2$.

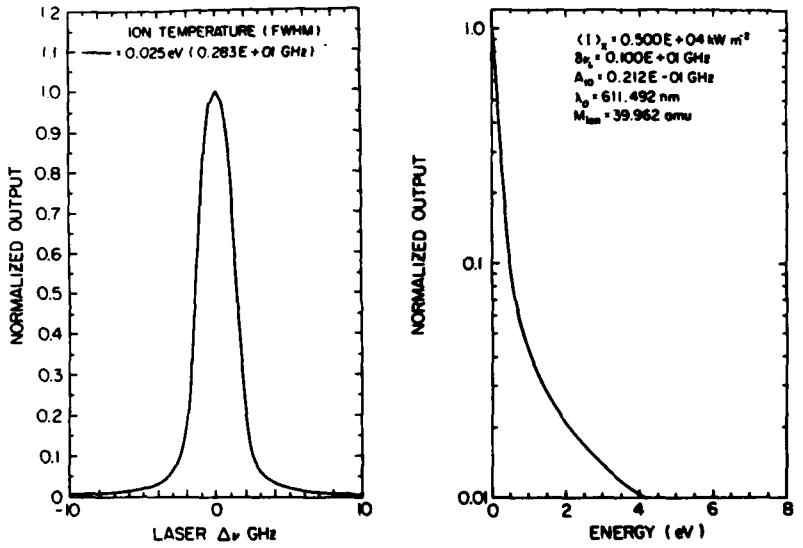

Fig. 2 - *The LIF signal for a homogeneous spatial intensity mode. These graphs show the same normalized fluorescence signal. The signal is a function of frequency in the left graph and energy in the right graph. They are related by the Doppler shift,* $2\pi\Delta\nu = \mathbf{v} \cdot \mathbf{k}$, *and the energy equation,* $\mathrm{E} = \mathrm{mv}^2/2$.

An undistorted Maxwellian ion velocity distribution, $f(v) \propto \exp(-v^2)$, will give a straight line when the log of the fluorescence signal is plotted as a function of energy. The ion temperature, in units of energy, may be found from the slope of this line using the formula, $T_i = -(\text{slope})^{-1}$. A distortion of a Maxwellian distribution will manifest as a second line added to the correct distribution. The slope of the false secondary line gives a pseudo-temperature.

Not all ion velocity distributions are Maxwellian. This precludes ignoring a measured tail of a velocity distribution. The tail may be real and an important part of the distribution.

We used the ArII transition $3d'^2G_{9/2} \leftrightarrow 4p'^2F^0_{7/2} \rightarrow 4s'^2D_{5/2}$ to examine distortion of the velocity distribution. This transition has been used by Anderegg et al. [2] to observe ion heating. They employed a laser with a bandwidth, $\delta\nu_l$, of 1 GHz and a pulse duration, T, of 17 ns. The parameters used in our computations are provided in Table 1.

Pseudo-temperatures may result from two mechanisms. The first mechanism is weak saturation broadening in all regions of the laser beam. This shown for homogeneous laser beams in Fig. 2. Saturation broadening, an undesirable effect, can be controlled by reducing the laser intensity.[4]

The second mechanism, an enhancement of the first mechanism, is caused

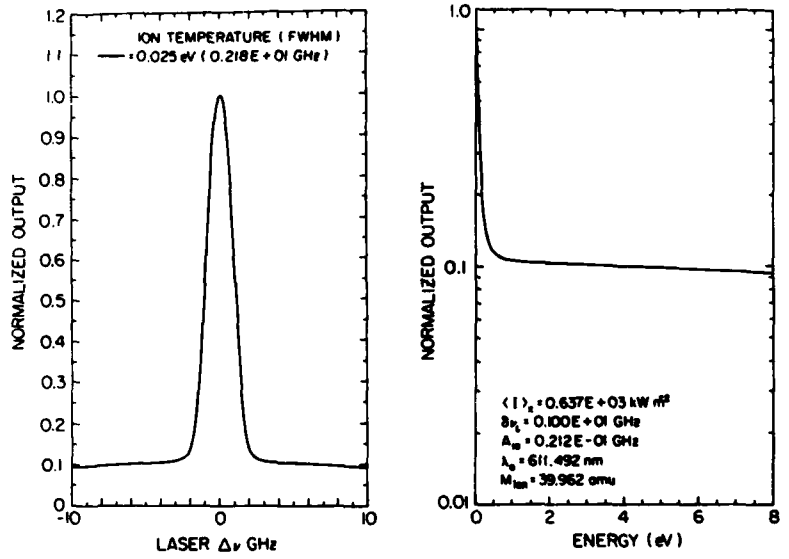

Fig. 3 - *The LIF signal for a two component spatial intensity distribution.*

by a small bright portion of an inhomogeneous laser beam saturating the ion transition while the rest of the laser mode is less intense and does not saturate the transition. We call this inhomogeneous saturation broadening. Figure 3 shows inhomogeneous saturation broadening for a beam composed of two homogeneous components, a high intensity area and a low intensity area. The ratio of the high intensity area to the low intensity area is 1:10.

Figure 4 is the LIF signal for a Gaussian spatial laser intensity distribution. The pseudo-temperature seen in this figure is produced by a combination of the two mechanisms. Because spatial changes in intensity are not steplike, this distribution most realistically models actual experimental conditions.

Pseudo-temperatures are caused by saturation of the ion transition in any part of the laser beam. Elimination of distortion in the measured ion velocity distribution requires that no portion of the laser beam saturates the ion transition. This requirement allows the experimenter a simple procedure to determine if any distortion of the measured distribution occurred.

The procedure involves repeating the measurement at a lower laser intensity. The ion velocity distribution is measured. The laser intensity is lowered, by at least a factor of ten. The velocity distribution function is measured again. If the measured velocity distribution does not change, that distribution is correct. If the measured distribution does change, the laser intensity must be reduced again. This procedure is repeated until the correct distribution is measured.

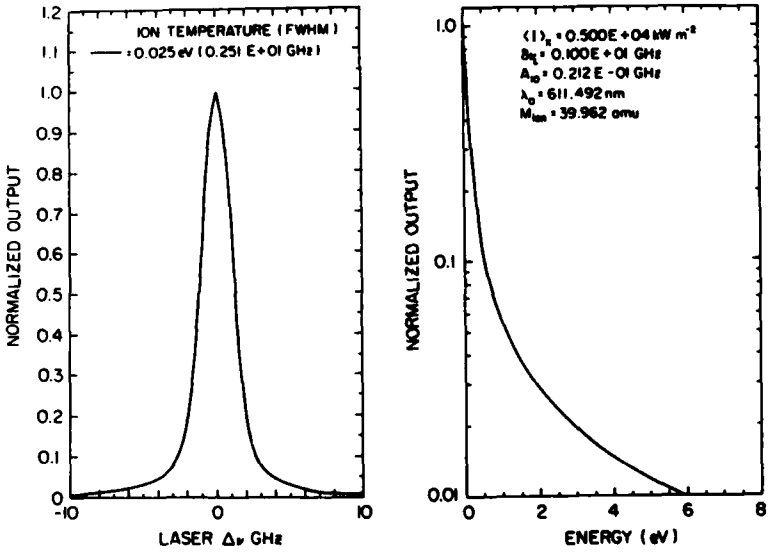

Fig. 4 - *The LIF signal for a Gaussian spatial intensity distribution.*

Conclusions

Distortions of the ion velocity distribution function determined using LIF will occur if a portion of the laser beam saturates the ion transition. These distortions may be eliminated by attenuating the laser intensity.

To avoid these distortions, an experimenter can make repeated measurements of a velocity distribution, lowering the laser intensity between each measurement. If lowering the laser intensity does not change the measured velocity distribution, this type of distortion has not occurred.

Acknowledgment

This work is supported by The Iowa Department of Economic Development.

References

[1] N. D'Angelo and M. J. Alport, Plasma Phys. 24, 1291 (1982).

[2] F. Anderegg, R. A. Stern, B. A. Hammel, M. Q. Tran, P. J. Paris, and P. Kohler, Phys. Rev. Lett. 57 329, (1986) and references therein.

[3] R. A. Stern and J. A. Johnson, Phys. Rev. Lett. 24, 1548 (1975).

[4] M. J. Goeckner and J. Goree J. Vac. Sci. Technol. A 7, (in press) (May/June 1989).

[5] Göran Nolén, Physica Scripta 8, 249 (1973).

[6] Gustavo García and José Campos, J. Quant. Spectrosc. Radiat. Transfer 34, 85 (1985).

MEASUREMENT OF H AND H_2 POPULATIONS IN A LOW-TEMPERATURE PLASMA BY VACUUM ULTRAVIOLET LASER ABSORPTION SPECTROSCOPY

A.T. Young, G.C. Stutzin, A.S. Schlachter, J.W. Stearns,
K.N. Leung, and W.B. Kunkel
Lawrence Berkeley Laboratory
Berkeley, California 94720

G.T. Worth and R.R. Stevens
Los Alamos National Laboratory
Los Alamos, New Mexico 87545

ABSTRACT

A new technique, vacuum ultraviolet laser absorption spectroscopy, has been developed to quantitatively determine the absolute density of H and H_2 within a plasma. The technique is particularly well suited to measurement in a plasma, where high charged particle and photon backgrounds complicate other methods of detection. The high selectivity and sensitivity of the technique allows for the measurement of the rotational-vibrational state distribution of H_2 as well as the translational temperature of the atoms and molecules. The technique has been used to study both pulsed and continuous plasma discharges. H_2 state distributions show a high degree of internal excitation, with levels up to v=5 and J=8 being observed. Hydrogen atom measurements indicate that, even for modest discharge currents, the fraction of H_2 molecules dissociated can be greater than 0.15.

INTRODUCTION

The measurement of atomic and molecular hydrogen density and temperature is of crucial importance to the understanding of the chemistry occurring in hydrogen plasmas. In particular, for plasmas with a low electron temperature, the formation of H^- is thought to be sensitive to the density and temperature of the H atoms present as well as the vibrational state distribution of the H_2 molecules. Unfortunately, many of the current laser-based detection schemes of H and H_2 are difficult to apply to plasma measurements within the discharge volume because of the large background of photons and charged particles produced by the plasma. To overcome these difficulties, a new technique, vacuum ultraviolet laser absorption spectroscopy, has been developed. The method allows for the direct absolute measurement of the density of atomic and molecular hydrogen in the plasma. The high sensitivity and selectivity of the technique makes possible internal state distribution measurements on the molecules and translational energy distribution measurements on both atoms and molecules.

EXPERIMENTAL ARRANGEMENT

The VUV laser spectrometer has been previously described in detail.[1] Briefly, four-wave sum-frequency mixing is used to produce narrow-bandwidth pulses of coherent VUV. Two excimer-pumped dye lasers provide photons at frequencies ω_1 and ω_2. Mercury vapor is used as the mixing medium, with VUV output occurring at $2\omega_1 + \omega_2$. To enhance the efficiency, $2\omega_1$ is chosen to be resonant with a mercury transition, with continuous tunability of the VUV provided by tuning ω_2. By varying the resonant state, VUV has been produced from 97 to 128 nm, encompassing portions

of the atomic Lyman series and the molecular Lyman (B-X) and Werner (C-X) bands. Bandwidth of the VUV is 0.27 cm-1, and an estimated 10^9 photons are produced. The plasma chamber is cylindrical, 31 cm long and 20 cm in diameter. The VUV is directed through the chamber parallel to the cylinder axis. The transmitted VUV is detected using microchannel plates.

The data are recorded as absorbance spectra, defined as -ln (I_p/I_o), where Ip is the VUV signal measured with the plasma discharge on, and I_o the VUV signal measured with the discharge off. Using published values of the absorption line strength, the average density of the H or H_2 can be determined absolutely. Analysis of the width and shape of the absorption profile provides information on the translational temperature of the species of interest.

ATOMIC HYDROGEN MEASUREMENTS

Figure 1 shows a representative absorption spectrum of atomic hydrogen. This spectrum was obtained with a continuous discharge using the Lyman-γ transition and corresponds to a hydrogen atom density of 9.4×10^{12} atoms cm^{-3}. The lineshape is best fit by the sum of two Gaussians, leading to a velocity distribution characterized by two temperatures. Although the bulk of the atoms have a temperature of 700 K, ~40% of the atoms could be assigned a temperature in excess of 7300 K.

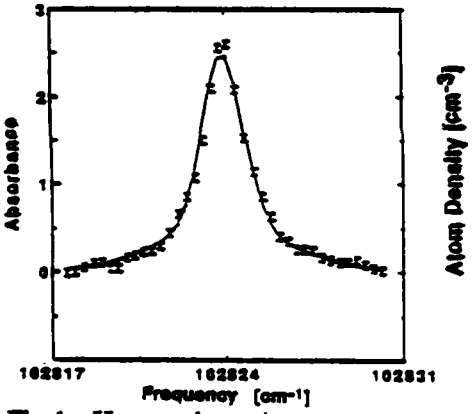

Fig 1. H-atom absorption spectrum using the Lyman-γ transition. Discharge parameters are 25 A and 150 V with H_2 pressure of 7 mT. The line is a bi-Gaussian fit to the data.

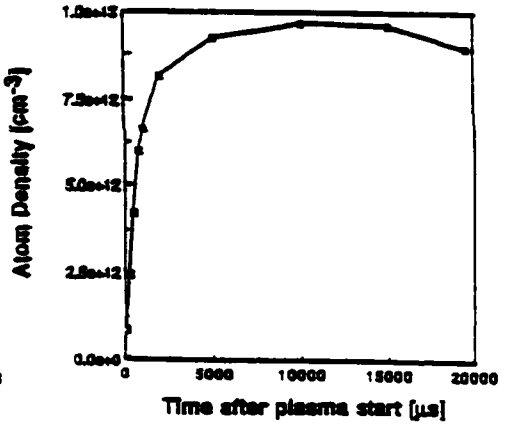

Fig. 2 H-atom temporal evolution in a pulsed discharge. Discharge parameters are 5 A, 300 V, pulse width of 20 msec, with H_2 pressure of 1 mT.

Using a pulsed discharge allows the temporal evolution of the H atoms to be measured. Figure 2 shows the H-atom density as a function of delay time from the beginning of the discharge pulse. The discharge current was 5A at 300V. The pulse length was 20 milliseconds, hence, all the data shown were obtained within the discharge pulse. Initial H_2 pressure was 1.0 mTorr. The risetime of the atom density, ~3 msec, is much longer than the discharge current risetime, ~200 μsec, and is indicative of the kinetics of the formation and destruction of the atoms. The steady-state value for the atom density, 9.5×10^{12} atoms cm^{-3}, corresponds to 15% of the H_2 initially present being dissociated. Experiments performed at higher discharge currents show a decrease in the rise time of the atom density and an increase in the

steady-state atom density, with a density of 1.8 x 10^{13} measured for 50 A. These studies are continuing and will help elucidate the mechanisms taking place within the plasma.

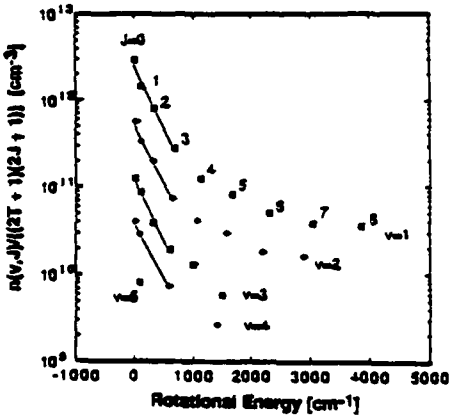

Fig. 3. H_2 rovibrational state distribution in a continuous discharge. Plotted are the absolute state populations divided by the degeneracies. Discharge parameters are 25 A and 150 V with H_2 pressure of 8 mT.

MOLECULAR HYDROGEN ROTATIONAL-VIBRATIONAL STATE DISTRIBUTIONS

H_2 state distributions were obtained with a continuous discharge plasma.[2] These populations, divided by the rotational and nuclear spin degeneracies, are plotted in Figure 3. Vibrational levels up to 5 and rotational levels up to 8 have been observed, showing that the H_2 are highly excited. Although the rotational distributions are similar for all the vibrational levels measured, they are not Boltzmann. A quasi-temperature has been derived using the lower J values. This temperature, 500 K, is the same for all vibrational levels and is represented on Figure 3 by the straight lines. The vibrational state distribution, in contrast to the rotational distributions, is thermal. Analysis of the data for v=1 to v=5 yields a vibrational temperature of 4200 K. Work is presently underway to detect higher-lying vibrational states in both continuous and pulsed plasmas.

SUMMARY

VUV laser absorption spectroscopy has been used to quantitatively determine the hydrogen atom density and the rotational-vibrational state distribution of hydrogen molecules within a plasma. In addition, the translational temperature of both species has been measured. A large fraction of the atoms possess a translational temperature in excess of 7300 K, while the H_2 shows a high degree of internal excitation.

This work has been supported by the U.S. Department of Energy under contract DE-AC03-76SF00098, the Air Force Office of Scientific Research under contract AFOSR-155A-88-003, and Los Alamos National Laboratory

REFERENCES

1. G.C. Stutzin, A.T. Young, A.S. Schlachter, J.W. Stearns, K.N. Leung, W.B. Kunkel, G.T. Worth, and R.R. Stevens, Rev. Sci. Instrum. 59 (1988) 1364; Rev. Sci. Instrum 59 (1988) 1479.
2. G.C. Stutzin, A.T. Young, A.S. Schlachter, K.N. Leung, and W.B. Kunkel. (To be published.)

PHOTODETACHMENT OF He^-: ANGULAR DISTRIBUTIONS OF PHOTOELECTRONS

J. S. Thompson and D. J. Pegg*
Department of Physics, University of Tennessee
Knoxville, Tennessee 37996, U.S.A.

R. N. Compton§ and G. D. Alton
Oak Ridge National Laboratory
Oak Ridge, Tennessee 37831-6377, U.S.A.

ABSTRACT

Energy- and angle-resolved photoelectron detachment spectroscopy has been used to study the spectral dependence of the angular distributions of electrons photodetached from a beam of He^- ions.

INTRODUCTION

In this paper, we report on a recent study of the spectral dependence of the angular distributions of electrons ejected from metastable He^- ions in the photodetachment process: $h\nu + He^-(1s2s2p\ ^4P) \rightarrow He\ (1s2p\ ^3P) + e\ (kp)$. The threshold for this detachment channel is 1.22 eV. Our measurements were made in the photon energy range 1.77 – 2.46 eV. With the exception of H^-, He^- represents the simplest system for probing the effects of correlation on electron emission following photodetachment. Spin-dependent interactions are small for a light ion such as He^-. Configuration interaction calculations show that the lowest He^- state, $(1s2s2p)^4P$, is 96% pure.[1] Correlation effects in the initial state are therefore small.

EXPERIMENTAL TECHNIQUE

The apparatus used in the energy- and angle-resolved spectroscopic measurements on the detached electrons has been described in detail by Pegg et al.[2] It consists of a fast beam of He^- ions that is crossed perpendicularly by a beam of photons from a pulsed dye laser. The tenuous He^- ion beam is produced by sequential double charge transfer when a momentum-analyzed beam of He^+ ions is passed through a Li vapor cell. Photoelectrons, ejected from the interaction region in the direction of motion of the ion beam, are energy analyzed by means of an electron spectrometer. The angular distributions of the photoelectrons were measured by determining the yield of electrons as a function of the angle θ, between the fixed collection direction and the variable direction defined by the electric field vector of the linearly polarized laser beam. For linearly polarized radiation and a randomly polarized target, the shape of the emission pattern should take the form,

---

* Also with the Physics Division, Oak Ridge National Laboratory.
§ Also with the Chemistry Department, University of Tennessee.

$f(\theta) = 1 + \beta P_2(\cos\theta)$ in the electric dipole approximation. The quantity, β, is the asymmetry parameter and $P_2(\cos\theta)$ is the second-order Legendre polynomial. The apparatus was tested by measuring the spectral dependence of the angular distribution of electrons produced by photodetaching a beam of $D^-(H^-)$ ions under the same experimental conditions. Since all the photon energies used were below the threshold for leaving the residual D atom in an excited state, the emission process should be well described by an independent electron model which neglects correlation. The observed $\cos^2\theta$ ($\beta = 2$) distribution at all photon energies is in agreement with the predictions of Cooper and Zare.[3] A kinematic correction to the angular distributions is made in all cases. In general, this transformation from the laboratory frame to the ion frame involves amplitude and phase constants that depend on the velocity of the ion beam. In forward-directed electron spectroscopy, the phase factor is zero.

RESULTS AND DISCUSSION

The spectral dependence of the asymmetry parameter, β, is shown in Figure 1. At the highest photon energy used, the measured value of $\beta = 2$ is consistent with the predictions of the independent electron model. As the photon energy is reduced, however, the value of β is seen to decrease sharply over a small range of energies and then level off at $\beta \approx 1.6$. Correlation, in some form, appears to be the cause of a depolarization of the ejected electrons as the threshold is approached. In photoionization studies, this kind of behavior is commonly explained in terms of an anisotropic final state interaction between the outgoing electron and the residual ion. The electron could be re-oriented, for example, by an exchange of angular momentum via electrostatic multipole forces. In the present photodetachment study, the residual

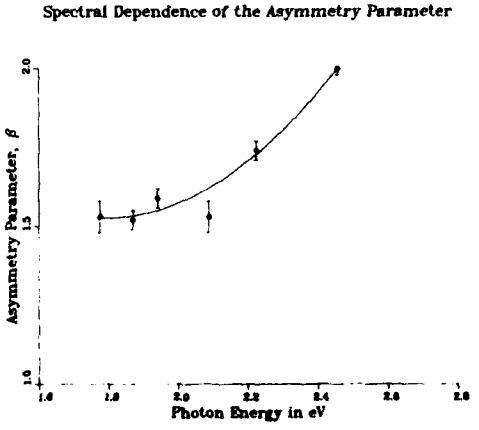

Fig. 1. The spectral dependence of β for the process: $h\nu + He^-(1s2s2p\ ^4P) \rightarrow He(1s2p\ ^3P) + e$. The solid line is a weighted least squares polynomial fit to the data.

excited He atom is nonspherical and the electron-atom interaction should be dominated by the quadrupole force which, in principle, can exert a "torque" on the outgoing electron. The permanent and induced dipole moments are expected to be small for this non-hydrogenic system.

An alternative explanation of the observed spectral dependence of β involves the consideration of the influence of the $(1s2p^2)^4P$ shape resonance on the emission process. This resonance has been found by Peterson et al.[4] to lie ≈11 meV above the $(1s2p)^3P$ threshold. Our measurements correspond to a range of energies that lie ~0.5 – 1.0 eV above this resonance. The resonance is, however, very strong and it appears from a calculation by Watanabe[5] that it can make a non-negligible contribution to the photodetachment cross section in the energy range of our measurements. In our experiment, this resonance will be anisotropically excited. The photoexcitation process is necessarily state selective as a result of the use of linearly polarized incident radiation and the restriction imposed on the possible final states by the Pauli exclusion principle. The electrons subsequently ejected in the autodetachment of this resonance will carry away the anisotropy. The emission pattern, in this case, will be characterized by a value of β that is considerably smaller than those observed in our measurements. One intriguing possibility is that the shape of the spectral dependence of β observed in the photodetachment of He^- arises from an interference between direct and resonant photodetachment pathways to the common $(1s2skp)^4P$ final state. The measured value of β at any particular photon energy would, in this model, be the result of an appropriate weighting of the β's from the two different pathways. These weighting factors, which will be determined by the relative cross sections for the two interfering processes, are expected to change as a function of the photon energy.

Two of us (JST and DJP) acknowledge research support from the U.S. Department of Energy, Office of Basic Energy Sciences, Division of Chemical Sciences through the University of Tennessee. Two of us (RNC and GDA) acknowledge suport from the U.S. Office of Naval Research. Oak Ridge National Laboratory is operated by Martin Marietta Energy Systems, Inc. under Contract No. DE-AC05-840R21400.

REFERENCES

1. A. V. Bunge and C. F. Bunge, Phys. Rev. 19, 452 (1979).
2. D. J. Pegg, J. S. Thompson, R. N. Compton, and G. D. Alton, Phys. Rev. Lett. 59, 2267 (1987).
3. J. Cooper and R. N. Zare, in Lectures in Theoretical Physics: Atomic Collision Processes, ed. by S. Geltman, K. T. Mahanthappa, and W. E. Brittin (Gordon and Breach, New York, 1969), Vol. XI-C, pp. 317-337.
4. J. R. Peterson, Y. K. Bae, and D. L. Huestis, Phys. Rev. Lett. 55, 692 (1985).
5. S. Watanabe, Phys. Rev. 25, 2074 (1982).

AUTHOR INDEX

A

Ackerhalt, J. R., 112
Adams, R. G., 112
Adamson, G. W., 673
Alexander, M. H., 651
Alfano, R. R., 33
Ali, A., 664
Allegrini, M., 554, 621
Allman, S. L., 276
Alton, G. D., 770
Alzetta, G., 599
Ananthamurthy, S., 630
Anderson, R., 734
Arepalli, S., 481
Arlinghaus, H. F., 436
Armstrong, R. L., 351

B

Babuel-Peyrissac, J. P., 303, 515
Bahns, J. T., 569
Bajic, S. J., 466
Bakhramov, S. A., 607
Bandyopadhyay, P. K., 106
Bardin, C., 515
Bates, Jr., R. D., 701
Bedair, S. M., 442
Berdikulov, A. T., 607
Berman, M. R., 627
Bernheim, R. A., 599
Berry, M. T., 634
Beverini, N., 533
Bierlein, J. D., 54
Biraben, F., 554
Biswas, A., 351
Bockhop, B., 415
Boesl, U., 488
Borysow, J., 478
Botter, R., 563
Boulon, G., 109
Bourkoff, E., 324
Bradforth, S. E., 657
Braichotte, D., 439
Brenna, J. T., 403
Brustein, M. R., 634
Buoncristiani, A. M., 125
Burgess, M., 131, 137, 164, 219, 241, 249, 515
Butler, J. E., 747
Byer, R. L., 1

C

Cagnac, B., 554
Calaway, W. F., 436
Callaghan, R., 481
Carlisle, C. B., 737
Casassa, M. P., 612
Celii, F. G., 472, 494, 747
Chang, C. C., 420
Chang, Y.-C., 318
Chase, L. L., 436
Chen, C. H., 354, 460
Chen, Y. Q., 673
Cheng, I. S., 560
Cheng, P. Y., 485
Cheng, Y. K., 91, 285, 581, 713
Chuang, T., 77
Clark, C. W., 503
Claude, Y., 131, 137, 164, 219, 241, 249, 515
Cline, D. S., 750
Cobb, S. H., 63, 68
Comly, J. C., 119
Compton, R. N., 466, 770
Cooper, D. E., 737
Copeland, R. A., 645, 758
Cox, J. N., 400
Creasy, W. R., 403
Crosley, D. R., 587, 615, 645, 670, 758
Cuykendall, R. R., 369, 415
Czuchlewski, S. J., 119

D

Dagata, J. A., 379, 445
Dagdigian, P. J., 651, 664
Davis, K. L., 707
DeBeer, D., 271
DeHaan, D. O., 698
Dehmer, J. L., 451
Dehmer, P. M., 451
Deijch, R., 339
DeLettrez, J., 303
Deshmukh, S., 430
Dimicoli, I., 563
Du, R., 198

Duczynski, E. W., 45
Duncan, M. A., 485
Duncan, M. D., 265
Dunn, D. S., 375
Dutta, B., 420

E

Ehrt, D., 45
Eiden, G., 683
Elg, A. P., 394
Eres, D., 382

F

Farrow, R. L., 262
Feigerle, C. S., 457
Field, R. W., 569, 673
Forch, B. E., 722
Foy, B. R., 612
Friedrich, L., 400
Furtak, T. E., 412

G

Gabbanini, C., 621
Garapon, C., 109
Garreau, J. C., 554
Garrett, W. R., 268, 273, 276, 279, 282
Garrido, C., 439
Gaur, A., 327
Gayen, S. K., 33
Geohegan, D. B., 382
George, M. C., 731
Goeckner, M. J., 761
Gole, J. L., 63, 68, 687
Gordon, R. J., 481
Goree, J. A., 761
Gouveia-Neto, A. S., 336
Gozzini, S., 621
Greene, D. P., 119
Gruen, D. M., 436

H

Hamilton, C. E., 673
Han, K. S., 82, 85
Hanratty, M. A., 494
Hanson, D. E., 112, 119
Hanson, R. K., 744
Hanton, S., 683
Harrington, J., 683
Harris, J. M., 360
Hartmann, F. X., 509
Hartmann, S. R., 271
He, C., 599
Heath, L. L., 400
Heber, K.-D., 557
Hedge, M. S., 420
Heller, D. F., 39
Helvajian, H., 433
Heumann, E., 45
Ho, H.-Q., 642
Horwitz, J. S., 445
Hsu, D. S. Y., 397
Huang, J. M., 216
Huang, Y.-L., 481
Huber, G., 45
Hudgens, J. W., 475, 497
Huo, W. M., 463

I

Inam, A., 420
Iwata, L., 593

J

Jacobs, D. C., 426
James, R. B., 318
Jeffries, J. B., 615, 670
Johnson III, R. D., 475, 497
Joly, A. G., 333
Jonas, D. M., 673
Judish, J. P., 276, 279, 282
Julien, L., 554

K

Karam, N. H., 442
Kaziska, A. J., 500
Kebabian, P. L., 741
Keto, J. W., 478
Khabibullaev, P. K., 607
Kim, K. H., 50
King, D. S., 612
Kleiber, P. D., 602, 630
Kofman, A. G., 128
Kohler, B., 330
Kokharov, A. M., 607
Kolasinski, K. W., 426
Kolenkow, R., 400
Krohn, B. J., 119
Kubodera, S., 74

Kumar, P., 216
Kunkel, W. B., 767

L

L'Huiller, A., 466
Lahiri, J., 469
Lambropoulos, P., 466
Latifi, H., 351
Lau, A. M. F., 262, 463
Le Calve, J., 563
Ledig, M., 45
Lee, J. H., 50, 82, 85
Lee, M. P., 744
Lee, S. M., 82
Leon, B., 439
Leone, S. R., 630
Lester, M. I., 634
Leung, K. N., 767
Levenson, M. D., 207
Levine, A. M., 128
Lezama, A., 291
Li, L., 363, 569, 572
Li, X. H., 285, 581
Lin, D. Y., 713
Lin, K. C., 630
Lin, M. C., 379, 397, 445
Liu, H., 442
Liu, W., 578
Liu, X. Y., 324
Liu, Y. H., 363
Longuemare, M. C., 701
Lowndes, D. H., 382
Lu, Z. W., 91, 578
Luh, W. T., 572
Lundberg, J. K., 673
Lyyra, A. M., 569, 572, 602

M

Ma, Z.G., 91, 578, 713
Maccioni, E., 533
Mahon, R., 265
Maier, J. P., 472, 494
Manassah, J., 297
Manson, S. T., 469
Mansueto, E. S., 357
Marinier, J. P., 515
Marion, J. E., 103
Mashburn, D. N., 382
Mattar, F. P., 131, 137, 164, 198, 219, 241, 249, 297, 303, 515, 529
Matthias, E., 394, 557
McCann, M. P., 279, 354, 460
McCown, A. W., 119
McGlashen, M. L., 707
McManus, J. B., 741
McMillin, B., 744
McQuaid, M. J., 687
Megli, D., 415
Meixler, L., 57
Merkle, L. D., 106
Metcalf, H., 77, 94
Metz, R. B., 657
Michie, R. B., 112
Miller, J. C., 294, 457
Miragliotta, J., 412
Miziolek, A. W., 722
Moi, L., 621
Monteil, A., 109
Moore, M. A., 268, 273
Morgan, J. R., 348
Morlet-Savary, F., 563
Morris, J. B., 722
Morris, M. D., 707, 725
Morrison, R., 701
Mossberg, T. W., 291
Motyka, A. L., 500
Myers, J. F., 39

N

Nam, C. H., 57
Nam, K., 85
Natarajan, L. V., 348
Nelson, H. H., 637, 747
Nelson, K. A., 330, 333
Neumark, D. M., 657
Noack, F., 339
Noid, D. W., 509
Normandin, R., 366
Northrup, F. J., 695
Novakoski, L. V., 397

O

O'Halloran, M. A., 451
Ogai, A., 593
Oh, C. H., 88
Ouderkirk, A. J., 375
Ouyang, X., 750

P

Pan, L., 503
Paul, P. H., 744
Payne, M. G., 268, 273, 276, 279, 282, 460
Pegg, D. J., 770
Pehrsson, P. E., 747
Pellin, M. J., 436
Pennycook, S. J., 382
Pereira, D., 533
Perez-Amor, M., 439
Pertica, A. J., 103
Petricevic, V., 33
Petzoldt, S., 394
Pinnick, R. G., 351
Pique, J.-P., 673
Piuzzi, F., 563
Poirier, P., 39
Postovalos, W. E., 339
Powell, R. C., 1
Pratt, S. T., 451
Prior, Y., 128

Q

Qian, C. X. W., 593

R

Raiche, G. A., 758
Rawers, J., 391
Ray, U., 642
Raymond, T. D., 112
Reck, G. P., 430
Reddy, B. R., 731
Reif, J., 394
Reintjes, J., 265
Reiser, C., 112
Reiser, H., 593
Reitz, W., 391
Rensberger, K. J., 615
Rice, J. K., 112
Ripoche, X., 563
Ritter, D., 683
Roberts, L. F., 125
Roesslein, M., 494
Rosenfeld, R. N., 648
Rother, E. W., 430
Rudolph, W., 339

S

Sanders, L., 683
Sando, K. M., 602
Sansonetti, C. J., 548
Sappey, A. D., 645
Sauerbrey, R., 74
Sausa, R. C., 722
Schearer, L. D., 42, 97
Scheps, R., 39
Schlachter, A. S., 767
Sears, T. J., 695
Seeber, W., 45
Seitzman, J., 744
Shang, S.-Q., 94
Sharma, A. K., 327
Sharon, Y. Y., 509
Shaw, R. W., 288
Shchuka, M. I., 500
Shelby, R. M., 207, 210
Sheridan, T. E., 761
Shinn, D. W., 445
Silbey, R. J., 673
Singh, J. P., 754
Singh, R. D., 327
Smith, D. D., 345
Smith, D. H., 288
Soln, J., 80
Sombra, A. S. B., 336
Squadrito, G., 621
Stearns, J. W., 767
Stephenson, J. C., 612
Stevens, R. R., 767
Stokowski, S. E., 103
Strobl, K. H., 369, 415
Strumia, F., 533
Stutzin, G. C., 767
Stwalley, W. C., 536, 569, 572, 602, 630
Suckewer, S., 57
Suh, U. C., 88
Sun, B. L., 400
Sun, Y. Z., 285, 581
Swetits, J. J., 125
Synovec, R. E., 716

T

Tang, T. W., 357
Tang, X., 466
Tankersley, L. L., 265
Taylor, J. R., 336

Taylor, K. T., 503
Taylor, R. H., 478
Teichmann, J., 137, 164, 219, 241, 249, 515, 529
Thompson, J. S., 770
Tighe, W., 57
Tikhonenko, V. V., 607
Tin, P., 42
Tischler, J. Z., 382
Tom, H. W. K., 406
Tomkins, F. S., 451
Topp, M. R., 500
Treado, P. J., 725
Tsai, B. P., 475, 497
Tsang, T., 345

U

Usadi, E., 271

V

van den Bergh, H., 439
v. d. Heide, H. J., 45
Van der Meer, P., 366
Vanherzeele, H., 54
Varghese, P. L., 750
Venable, D. D., 82
Venkatesan, T., 420, 731
Venkateswarlu, P., 731
Vernon, M., 642
Villa, E., 379
Vissani, G., 533

W

Walling, J. C., 1
Walter, K., 488
Wan, K., 366
Wang, H., 572
Wang, H.-T., 747
Wang, J. X., 630
Wang, Q., 91, 285, 578, 581, 713
Wang, W. C., 363
Wang, Y. Z., 713
Weaver, A., 657
Weiner, B. R., 648
Weinkauf, R., 488
Weisshaar, J. C., 683
Welle, R., 433
West, P. J., 557
Wight, C. A., 357
Wigley, P. G. J., 336
Wisoff, P. J., 74
Wittmeyer, S. A., 500
Woodward, J. R., 63, 68
Worth, G. T., 767
Wu, T., 91, 578
Wu, X. D., 420
Wunderlich, R. K., 273, 282
Wysong, I. J., 670
Wyttenbach, T., 494

X

Xia, H. R., 560
Xie, X., 569
Xing, D., 578
Xu, J. W., 560

Y

Yoshida, I., 442
Young, A. T., 767
Young, C. E., 436
Young, J. P., 288
Yu, G. D., 363
Yueh, F. Y., 754

Z

Zafiropulos, V., 572, 602
Zaibel, R., 128
Zare, R. N., 426
Zeng, X., 602
Zhang, Z. J., 642
Zhang, Z. M., 363
Zhu, X. R., 360
Zhu, Y., 291
Zumsteg, F. C., 54
Zwier, T. S., 692, 698

AIP Conference Proceedings

		L.C. Number	ISBN
No. 1	Feedback and Dynamic Control of Plasmas – 1970	70-141596	0-88318-100-2
No. 2	Particles and Fields – 1971 (Rochester)	71-184662	0-88318-101-0
No. 3	Thermal Expansion – 1971 (Corning)	72-76970	0-88318-102-9
No. 4	Superconductivity in *d*- and *f*-Band Metals (Rochester, 1971)	74-18879	0-88318-103-7
No. 5	Magnetism and Magnetic Materials – 1971 (2 parts) (Chicago)	59-2468	0-88318-104-5
No. 6	Particle Physics (Irvine, 1971)	72-81239	0-88318-105-3
No. 7	Exploring the History of Nuclear Physics – 1972	72-81883	0-88318-106-1
No. 8	Experimental Meson Spectroscopy –1972	72-88226	0-88318-107-X
No. 9	Cyclotrons – 1972 (Vancouver)	72-92798	0-88318-108-8
No. 10	Magnetism and Magnetic Materials – 1972	72-623469	0-88318-109-6
No. 11	Transport Phenomena – 1973 (Brown University Conference)	73-80682	0-88318-110-X
No. 12	Experiments on High Energy Particle Collisions – 1973 (Vanderbilt Conference)	73-81705	0-88318-111-8
No. 13	π-π Scattering – 1973 (Tallahassee Conference)	73-81704	0-88318-112-6
No. 14	Particles and Fields – 1973 (APS/DPF Berkeley)	73-91923	0-88318-113-4
No. 15	High Energy Collisions – 1973 (Stony Brook)	73-92324	0-88318-114-2
No. 16	Causality and Physical Theories (Wayne State University, 1973)	73-93420	0-88318-115-0
No. 17	Thermal Expansion – 1973 (Lake of the Ozarks)	73-94415	0-88318-116-9
No. 18	Magnetism and Magnetic Materials – 1973 (2 parts) (Boston)	59-2468	0-88318-117-7
No. 19	Physics and the Energy Problem – 1974 (APS Chicago)	73-94416	0-88318-118-5
No. 20	Tetrahedrally Bonded Amorphous Semiconductors (Yorktown Heights, 1974)	74-80145	0-88318-119-3
No. 21	Experimental Meson Spectroscopy – 1974 (Boston)	74-82628	0-88318-120-7
No. 22	Neutrinos – 1974 (Philadelphia)	74-82413	0-88318-121-5
No. 23	Particles and Fields – 1974 (APS/DPF Williamsburg)	74-27575	0-88318-122-3
No. 24	Magnetism and Magnetic Materials – 1974 (20th Annual Conference, San Francisco)	75-2647	0-88318-123-1
No. 25	Efficient Use of Energy (The APS Studies on the Technical Aspects of the More Efficient Use of Energy)	75-18227	0-88318-124-X

No. 26	High-Energy Physics and Nuclear Structure – 1975 (Santa Fe and Los Alamos)	75-26411	0-88318-125-8
No. 27	Topics in Statistical Mechanics and Biophysics: A Memorial to Julius L. Jackson (Wayne State University, 1975)	75-36309	0-88318-126-6
No. 28	Physics and Our World: A Symposium in Honor of Victor F. Weisskopf (M.I.T., 1974)	76-7207	0-88318-127-4
No. 29	Magnetism and Magnetic Materials – 1975 (21st Annual Conference, Philadelphia)	76-10931	0-88318-128-2
No. 30	Particle Searches and Discoveries – 1976 (Vanderbilt Conference)	76-19949	0-88318-129-0
No. 31	Structure and Excitations of Amorphous Solids (Williamsburg, VA, 1976)	76-22279	0-88318-130-4
No. 32	Materials Technology – 1976 (APS New York Meeting)	76-27967	0-88318-131-2
No. 33	Meson-Nuclear Physics – 1976 (Carnegie-Mellon Conference)	76-26811	0-88318-132-0
No. 34	Magnetism and Magnetic Materials – 1976 (Joint MMM-Intermag Conference, Pittsburgh)	76-47106	0-88318-133-9
No. 35	High Energy Physics with Polarized Beams and Targets (Argonne, 1976)	76-50181	0-88318-134-7
No. 36	Momentum Wave Functions – 1976 (Indiana University)	77-82145	0-88318-135-5
No. 37	Weak Interaction Physics – 1977 (Indiana University)	77-83344	0-88318-136-3
No. 38	Workshop on New Directions in Mossbauer Spectroscopy (Argonne, 1977)	77-90635	0-88318-137-1
No. 39	Physics Careers, Employment and Education (Penn State, 1977)	77-94053	0-88318-138-X
No. 40	Electrical Transport and Optical Properties of Inhomogeneous Media (Ohio State University, 1977)	78-54319	0-88318-139-8
No. 41	Nucleon-Nucleon Interactions – 1977 (Vancouver)	78-54249	0-88318-140-1
No. 42	Higher Energy Polarized Proton Beams (Ann Arbor, 1977)	78-55682	0-88318-141-X
No. 43	Particles and Fields – 1977 (APS/DPF, Argonne)	78-55683	0-88318-142-8
No. 44	Future Trends in Superconductive Electronics (Charlottesville, 1978)	77-9240	0-88318-143-6
No. 45	New Results in High Energy Physics – 1978 (Vanderbilt Conference)	78-67196	0-88318-144-4
No. 46	Topics in Nonlinear Dynamics (La Jolla Institute)	78-57870	0-88318-145-2
No. 47	Clustering Aspects of Nuclear Structure and Nuclear Reactions (Winnepeg, 1978)	78-64942	0-88318-146-0
No. 48	Current Trends in the Theory of Fields (Tallahassee, 1978)	78-72948	0-88318-147-9

No. 49	Cosmic Rays and Particle Physics – 1978 (Bartol Conference)	79-50489	0-88318-148-7
No. 50	Laser-Solid Interactions and Laser Processing – 1978 (Boston)	79-51564	0-88318-149-5
No. 51	High Energy Physics with Polarized Beams and Polarized Targets (Argonne, 1978)	79-64565	0-88318-150-9
No. 52	Long-Distance Neutrino Detection – 1978 (C.L. Cowan Memorial Symposium)	79-52078	0-88318-151-7
No. 53	Modulated Structures – 1979 (Kailua Kona, Hawaii)	79-53846	0-88318-152-5
No. 54	Meson-Nuclear Physics – 1979 (Houston)	79-53978	0-88318-153-3
No. 55	Quantum Chromodynamics (La Jolla, 1978)	79-54969	0-88318-154-1
No. 56	Particle Acceleration Mechanisms in Astrophysics (La Jolla, 1979)	79-55844	0-88318-155-X
No. 57	Nonlinear Dynamics and the Beam-Beam Interaction (Brookhaven, 1979)	79-57341	0-88318-156-8
No. 58	Inhomogeneous Superconductors – 1979 (Berkeley Springs, W.V.)	79-57620	0-88318-157-6
No. 59	Particles and Fields – 1979 (APS/DPF Montreal)	80-66631	0-88318-158-4
No. 60	History of the ZGS (Argonne, 1979)	80-67694	0-88318-159-2
No. 61	Aspects of the Kinetics and Dynamics of Surface Reactions (La Jolla Institute, 1979)	80-68004	0-88318-160-6
No. 62	High Energy e^+e^- Interactions (Vanderbilt, 1980)	80-53377	0-88318-161-4
No. 63	Supernovae Spectra (La Jolla, 1980)	80-70019	0-88318-162-2
No. 64	Laboratory EXAFS Facilities – 1980 (Univ. of Washington)	80-70579	0-88318-163-0
No. 65	Optics in Four Dimensions – 1980 (ICO, Ensenada)	80-70771	0-88318-164-9
No. 66	Physics in the Automotive Industry – 1980 (APS/AAPT Topical Conference)	80-70987	0-88318-165-7
No. 67	Experimental Meson Spectroscopy – 1980 (Sixth International Conference, Brookhaven)	80-71123	0-88318-166-5
No. 68	High Energy Physics – 1980 (XX International Conference, Madison)	81-65032	0-88318-167-3
No. 69	Polarization Phenomena in Nuclear Physics – 1980 (Fifth International Symposium, Santa Fe)	81-65107	0-88318-168-1
No. 70	Chemistry and Physics of Coal Utilization – 1980 (APS, Morgantown)	81-65106	0-88318-169-X
No. 71	Group Theory and its Applications in Physics – 1980 (Latin American School of Physics, Mexico City)	81-66132	0-88318-170-3
No. 72	Weak Interactions as a Probe of Unification (Virginia Polytechnic Institute – 1980)	81-67184	0-88318-171-1
No. 73	Tetrahedrally Bonded Amorphous Semiconductors (Carefree, Arizona, 1981)	81-67419	0-88318-172-X

No. 74	Perturbative Quantum Chromodynamics (Tallahassee, 1981)	81-70372	0-88318-173-8
No. 75	Low Energy X-Ray Diagnostics – 1981 (Monterey)	81-69841	0-88318-174-6
No. 76	Nonlinear Properties of Internal Waves (La Jolla Institute, 1981)	81-71062	0-88318-175-4
No. 77	Gamma Ray Transients and Related Astrophysical Phenomena (La Jolla Institute, 1981)	81-71543	0-88318-176-2
No. 78	Shock Waves in Condensed Matter – 1981 (Menlo Park)	82-70014	0-88318-177-0
No. 79	Pion Production and Absorption in Nuclei – 1981 (Indiana University Cyclotron Facility)	82-70678	0-88318-178-9
No. 80	Polarized Proton Ion Sources (Ann Arbor, 1981)	82-71025	0-88318-179-7
No. 81	Particles and Fields –1981: Testing the Standard Model (APS/DPF, Santa Cruz)	82-71156	0-88318-180-0
No. 82	Interpretation of Climate and Photochemical Models, Ozone and Temperature Measurements (La Jolla Institute, 1981)	82-71345	0-88318-181-9
No. 83	The Galactic Center (Cal. Inst. of Tech., 1982)	82-71635	0-88318-182-7
No. 84	Physics in the Steel Industry (APS/AISI, Lehigh University, 1981)	82-72033	0-88318-183-5
No. 85	Proton-Antiproton Collider Physics –1981 (Madison, Wisconsin)	82-72141	0-88318-184-3
No. 86	Momentum Wave Functions – 1982 (Adelaide, Australia)	82-72375	0-88318-185-1
No. 87	Physics of High Energy Particle Accelerators (Fermilab Summer School, 1981)	82-72421	0-88318-186-X
No. 88	Mathematical Methods in Hydrodynamics and Integrability in Dynamical Systems (La Jolla Institute, 1981)	82-72462	0-88318-187-8
No. 89	Neutron Scattering – 1981 (Argonne National Laboratory)	82-73094	0-88318-188-6
No. 90	Laser Techniques for Extreme Ultraviolt Spectroscopy (Boulder, 1982)	82-73205	0-88318-189-4
No. 91	Laser Acceleration of Particles (Los Alamos, 1982)	82-73361	0-88318-190-8
No. 92	The State of Particle Accelerators and High Energy Physics (Fermilab, 1981)	82-73861	0-88318-191-6
No. 93	Novel Results in Particle Physics (Vanderbilt, 1982)	82-73954	0-88318-192-4
No. 94	X-Ray and Atomic Inner-Shell Physics – 1982 (International Conference, U. of Oregon)	82-74075	0-88318-193-2
No. 95	High Energy Spin Physics – 1982 (Brookhaven National Laboratory)	83-70154	0-88318-194-0
No. 96	Science Underground (Los Alamos, 1982)	83-70377	0-88318-195-9

No. 97	The Interaction Between Medium Energy Nucleons in Nuclei – 1982 (Indiana University)	83-70649	0-88318-196-7
No. 98	Particles and Fields – 1982 (APS/DPF University of Maryland)	83-70807	0-88318-197-5
No. 99	Neutrino Mass and Gauge Structure of Weak Interactions (Telemark, 1982)	83-71072	0-88318-198-3
No. 100	Excimer Lasers – 1983 (OSA, Lake Tahoe, Nevada)	83-71437	0-88318-199-1
No. 101	Positron-Electron Pairs in Astrophysics (Goddard Space Flight Center, 1983)	83-71926	0-88318-200-9
No. 102	Intense Medium Energy Sources of Strangeness (UC-Sant Cruz, 1983)	83-72261	0-88318-201-7
No. 103	Quantum Fluids and Solids – 1983 (Sanibel Island, Florida)	83-72440	0-88318-202-5
No. 104	Physics, Technology and the Nuclear Arms Race (APS Baltimore –1983)	83-72533	0-88318-203-3
No. 105	Physics of High Energy Particle Accelerators (SLAC Summer School, 1982)	83-72986	0-88318-304-8
No. 106	Predictability of Fluid Motions (La Jolla Institute, 1983)	83-73641	0-88318-305-6
No. 107	Physics and Chemistry of Porous Media (Schlumberger-Doll Research, 1983)	83-73640	0-88318-306-4
No. 108	The Time Projection Chamber (TRIUMF, Vancouver, 1983)	83-83445	0-88318-307-2
No. 109	Random Walks and Their Applications in the Physical and Biological Sciences (NBS/La Jolla Institute, 1982)	84-70208	0-88318-308-0
No. 110	Hadron Substructure in Nuclear Physics (Indiana University, 1983)	84-70165	0-88318-309-9
No. 111	Production and Neutralization of Negative Ions and Beams (3rd Int'l Symposium, Brookhaven, 1983)	84-70379	0-88318-310-2
No. 112	Particles and Fields – 1983 (APS/DPF, Blacksburg, VA)	84-70378	0-88318-311-0
No. 113	Experimental Meson Spectroscopy – 1983 (Seventh International Conference, Brookhaven)	84-70910	0-88318-312-9
No. 114	Low Energy Tests of Conservation Laws in Particle Physics (Blacksburg, VA, 1983)	84-71157	0-88318-313-7
No. 115	High Energy Transients in Astrophysics (Santa Cruz, CA, 1983)	84-71205	0-88318-314-5
No. 116	Problems in Unification and Supergravity (La Jolla Institute, 1983)	84-71246	0-88318-315-3
No. 117	Polarized Proton Ion Sources (TRIUMF, Vancouver, 1983)	84-71235	0-88318-316-1

No. 118	Free Electron Generation of Extreme Ultraviolet Coherent Radiation (Brookhaven/OSA, 1983)	84-71539	0-88318-317-X
No. 119	Laser Techniques in the Extreme Ultraviolet (OSA, Boulder, Colorado, 1984)	84-72128	0-88318-318-8
No. 120	Optical Effects in Amorphous Semiconductors (Snowbird, Utah, 1984)	84-72419	0-88318-319-6
No. 121	High Energy e^+e^- Interactions (Vanderbilt, 1984)	84-72632	0-88318-320-X
No. 122	The Physics of VLSI (Xerox, Palo Alto, 1984)	84-72729	0-88318-321-8
No. 123	Intersections Between Particle and Nuclear Physics (Steamboat Springs, 1984)	84-72790	0-88318-322-6
No. 124	Neutron-Nucleus Collisions – A Probe of Nuclear Structure (Burr Oak State Park - 1984)	84-73216	0-88318-323-4
No. 125	Capture Gamma-Ray Spectroscopy and Related Topics – 1984 (Internat. Symposium, Knoxville)	84-73303	0-88318-324-2
No. 126	Solar Neutrinos and Neutrino Astronomy (Homestake, 1984)	84-63143	0-88318-325-0
No. 127	Physics of High Energy Particle Accelerators (BNL/SUNY Summer School, 1983)	85-70057	0-88318-326-9
No. 128	Nuclear Physics with Stored, Cooled Beams (McCormick's Creek State Park, Indiana, 1984)	85-71167	0-88318-327-7
No. 129	Radiofrequency Plasma Heating (Sixth Topical Conference, Callaway Gardens, GA, 1985)	85-48027	0-88318-328-5
No. 130	Laser Acceleration of Particles (Malibu, California, 1985)	85-48028	0-88318-329-3
No. 131	Workshop on Polarized ^{3}He Beams and Targets (Princeton, New Jersey, 1984)	85-48026	0-88318-330-7
No. 132	Hadron Spectroscopy–1985 (International Conference, Univ. of Maryland)	85-72537	0-88318-331-5
No. 133	Hadronic Probes and Nuclear Interactions (Arizona State University, 1985)	85-72638	0-88318-332-3
No. 134	The State of High Energy Physics (BNL/SUNY Summer School, 1983)	85-73170	0-88318-333-
No. 135	Energy Sources: Conservation and Renewables (APS, Washington, DC, 1985)	85-73019	0-88318-334-X
No. 136	Atomic Theory Workshop on Relativistic and QED Effects in Heavy Atoms	85-73790	0-88318-335-8
No. 137	Polymer-Flow Interaction (La Jolla Institute, 1985)	85-73915	0-88318-336-6
No. 138	Frontiers in Electronic Materials and Processing (Houston, TX, 1985)	86-70108	0-88318-337-4
No. 139	High-Current, High-Brightness, and High-Duty Factor Ion Injectors (La Jolla Institute, 1985)	86-70245	0-88318-338-2

No. 140	Boron-Rich Solids (Albuquerque, NM, 1985)	86-70246	0-88318-339-0
No. 141	Gamma-Ray Bursts (Stanford, CA, 1984)	86-70761	0-88318-340-4
No. 142	Nuclear Structure at High Spin, Excitation, and Momentum Transfer (Indiana University, 1985)	86-70837	0-88318-341-2
No. 143	Mexican School of Particles and Fields (Oaxtepec, México, 1984)	86-81187	0-88318-342-0
No. 144	Magnetospheric Phenomena in Astrophysics (Los Alamos, 1984)	86-71149	0-88318-343-9
No. 145	Polarized Beams at SSC & Polarized Antiprotons (Ann Arbor, MI & Bodega Bay, CA, 1985)	86-71343	0-88318-344-7
No. 146	Advances in Laser Science–I (Dallas, TX, 1985)	86-71536	0-88318-345-5
No. 147	Short Wavelength Coherent Radiation: Generation and Applications (Monterey, CA, 1986)	86-71674	0-88318-346-3
No. 148	Space Colonization: Technology and The Liberal Arts (Geneva, NY, 1985)	86-71675	0-88318-347-1
No. 149	Physics and Chemistry of Protective Coatings (Universal City, CA, 1985)	86-72019	0-88318-348-X
No. 150	Intersections Between Particle and Nuclear Physics (Lake Louise, Canada, 1986)	86-72018	0-88318-349-8
No. 151	Neural Networks for Computing (Snowbird, UT, 1986)	86-72481	0-88318-351-X
No. 152	Heavy Ion Inertial Fusion (Washington, DC, 1986)	86-73185	0-88318-352-8
No. 153	Physics of Particle Accelerators (SLAC Summer School, 1985) (Fermilab Summer School, 1984)	87-70103	0-88318-353-6
No. 154	Physics and Chemistry of Porous Media—II (Ridge Field, CT, 1986)	83-73640	0-88318-354-4
No. 155	The Galactic Center: Proceedings of the Symposium Honoring C. H. Townes (Berkeley, CA, 1986)	86-73186	0-88318-355-2
No. 156	Advanced Accelerator Concepts (Madison, WI, 1986)	87-70635	0-88318-358-0
No. 157	Stability of Amorphous Silicon Alloy Materials and Devices (Palo Alto, CA, 1987)	87-70990	0-88318-359-9
No. 158	Production and Neutralization of Negative Ions and Beams (Brookhaven, NY, 1986)	87-71695	0-88318-358-7

No. 159	Applications of Radio-Frequency Power to Plasma: Seventh Topical Conference (Kissimmee, FL, 1987)	87-71812	0-88318-359-5
No. 160	Advances in Laser Science–II (Seattle, WA, 1986)	87-71962	0-88318-360-9
No. 161	Electron Scattering in Nuclear and Particle Science: In Commemoration of the 35th Anniversary of the Lyman-Hanson-Scott Experiment (Urbana, IL, 1986)	87-72403	0-88318-361-7
No. 162	Few-Body Systems and Multiparticle Dynamics (Crystal City, VA, 1987)	87-72594	0-88318-362-5
No. 163	Pion–Nucleus Physics: Future Directions and New Facilities at LAMPF (Los Alamos, NM, 1987)	87-72961	0-88318-363-3
No. 164	Nuclei Far from Stability: Fifth International Conference (Rosseau Lake, ON, 1987)	87-73214	0-88318-364-1
No. 165	Thin Film Processing and Characterization of High-Temperature Superconductors	87-73420	0-88318-365-X
No. 166	Photovoltaic Safety (Denver, CO, 1988)	88-42854	0-88318-366-8
No. 167	Deposition and Growth: Limits for Microelectronics (Anaheim, CA, 1987)	88-71432	0-88318-367-6
No. 168	Atomic Processes in Plasmas (Santa Fe, NM, 1987)	88-71273	0-88318-368-4
No. 169	Modern Physics in America: A Michelson-Morley Centennial Symposium (Cleveland, OH, 1987)	88-71348	0-88318-369-2
No. 170	Nuclear Spectroscopy of Astrophysical Sources (Washington, D.C., 1987)	88-71625	0-88318-370-6
No. 171	Vacuum Design of Advanced and Compact Synchrotron Light Sources (Upton, NY, 1988)	88-71824	0-88318-371-4
No. 172	Advances in Laser Science–III: Proceedings of the International Laser Science Conference (Atlantic City, NJ, 1987)	88-71879	0-88318-372-2
No. 173	Cooperative Networks in Physics Education (Oaxtepec, Mexico 1987)	88-72091	0-88318-373-0
No. 174	Radio Wave Scattering in the Interstellar Medium (San Diego, CA 1988)	88-72092	0-88318-374-9
No. 175	Non-neutral Plasma Physics (Washington, DC 1988)	88-72275	0-88318-375-7

No. 176	Intersections Between Particle and Nuclear Physics (Third International Conference) (Rockport, ME 1988)	88-62535	0-88318-376-5
No. 177	Linear Accelerator and Beam Optics Codes (La Jolla, CA 1988)	88-46074	0-88318-377-3
No. 178	Nuclear Arms Technologies in the 1990s (Washington, DC 1988)	88-83262	0-88318-378-1
No. 179	The Michelson Era in American Science: 1870–1930 (Cleveland, OH 1987)	88-83369	0-88318-379-X
No. 180	Frontiers in Science: International Symposium (Urbana, IL 1987)	88-83526	0-88318-380-3
No. 181	Muon-Catalyzed Fusion (Sanibel Island, FL 1988)	88-83636	0-88318-381-1
No. 182	High T_c Superconducting Thin Films, Devices, and Application (Atlanta, GA 1988)	88-03947	0-88318-382-X
No. 183	Cosmic Abundances of Matter (Minneapolis, MN 1988)	89-80147	0-88318-383-8
No. 184	Physics of Particle Accelerators (Ithaca, NY 1988)	87-07208	0-88318-384-6
No. 185	Glueballs, Hybrids, and Exotic Hadrons (Upton, NY 1988)	89-83513	0-88318-385-4
No. 186	High-Energy Radiation Background in Space (Sanibel Island, FL 1987)	89-083833	0-88318-386-2
No. 187	High-Energy Spin Physics (Minneapolis, MN 1988)	89-083948	0-88318-387-0
No. 188	International Symposium on Electron Beam Ion Sources and their Applications (Upton, NY 1988)	89-084343	0-88318-388-9
No. 189	Relativistic, Quantum Electrodynamic, and Weak Interaction Effects in Atoms (Santa Barbara, CA 1988)	89-084431	0-88318-389-7
No. 190	Radio-frequency Power in Plasmas (Irvine, CA 1989)	89-045805	0-88318-397-8